Synthese zweifach-koordinierter, quasilinearer Übergangsmetall(II/I)-Komplexe

Kumulative Dissertation

Zur Erlangung des akademischen Grades eines

Doktors der Naturwissenschaften

(Dr. rer. nat.)

dem

Fachbereich Chemie der Philipps-Universität Marburg

vorgelegt von

Ruth Anja Weller (M. Sc.)

aus Forchheim

Marburg (Lahn) 2021

Hochschulkennziffer 1180

Synthese zweifach-koordinierter, quasilinearer Übergangsmetall(II/I)-Komplexe

Kumulative Dissertation

Zur Erlangung des akademischen Grades eines

Doktors der Naturwissenschaften

(Dr. rer. nat.)

dem

Fachbereich Chemie der Philipps-Universität Marburg

vorgelegt von

Ruth Anja Weller (M. Sc.)

aus Forchheim

Marburg (Lahn) 2021

Erstgutachter: Dr. C. Gunnar Werncke

Zweitgutachter: Prof. Dr. Carsten von Hänisch

Hochschulkennziffer 1180

Die vorliegende Arbeit wurde in der Zeit von Dezember 2017 bis November 2021 am Fachbereich Chemie der Philipps-Universität Marburg unter der Leitung von Herrn Dr. C. Gunnar Werncke angefertigt.

Erstgutachter: Dr. C. Gunnar Werncke
Zweitgutachter: Prof. Dr. Carsten von Hänisch

Annahme der Dissertation: 17.11.2021
Tag der Disputation: 09.12.2021

Erklärung

Ich erkläre, dass eine Promotion noch an keiner anderen Hochschule als der Philipps-Universität Marburg, Fachbereich Chemie, versucht wurde. Weiterhin versichere ich, dass ich meine vorgelegte Dissertation mit dem Titel

„Synthese zweifach-koordinierter, quasilinearer Übergangsmetall(II/I)-Komplexe“

selbst und ohne fremde Hilfe verfasst, nicht andere als die in ihr angegebenen Quellen oder Hilfsmittel benutzt, alle vollständig oder sinngemäß übernommenen Zitate als solche gekennzeichnet sowie die Dissertation in der vorliegenden oder einer ähnlichen Form noch bei keiner anderen in- oder ausländischen Hochschule anlässlich eines Promotionsgesuchs oder zu anderen Prüfungszwecken eingereicht habe.

Marburg, den 17.11.2021

_____

Ruth Anja Weller

- *Meiner Familie gewidmet* **-**

"Ich habe keine Ahnung, wo Ideen herkommen, und ich hoffe, ich finde es nie heraus.
Es würde mir die Aufregung verderben, wenn sich herausstellen sollte,
dass ich einfach eine lustige kleine Stelle in meinem Gehirn habe, die mich dazu bringt,
über unsichtbare Bahnsteige nachzudenken."

- J. K. Rowling –

Inhaltsverzeichnis

Liste verwendeter Abkürzungen und Symbole

Ada	Adamantyl
AILFT	ab-initio Ligandfeldtheorie-Analyse (Englisch: ab-initio ligand field theory analysis)
Äquiv. / equiv.	Äquivalent (Englisch: equivalent)
B	Flussdichte
BDE	Bindungsdissoziationsenergie
BnK	Benzylkalium
cAAC	zyklisches Alkylaminocarben (Englisch: cyclic (alkyl)(amino)carbene)
calcd.	Berechnet; Englisch: calculated
CHD	1,4-Zyklohexadien
CO	Carbonyl
crypt-222	[2.2.2]-Kryptand = 4,7,13,16,21,24-Hexaoxa-1,10-diazabizyklo[8.8.8]hexacosan
d	Dublett (Kernspinresonanzspektroskopie)
δ	Chemische Verschiebung
DBU	1,8-Diazabizyklo[5.4.0]undec-7-en
DFT	density functional theory
Dppbz	1,2-Bis(diphenylphosphino)benzol
Dppe	1,2-Bis(diphenylphosphino)ethan
Dipp	2,6-Di-*iso*-propylphenyl
E	Energie
ε	Extinktionskoeffizient
ESR	Elektronenspinresonanz
h	Stunde
H	externes Magnetfeld
HOMO	höchstes besetztes Molekülorbital (Englisch: highest occupied molecular orbital)
Hz	Hertz
i	*ipso*
IDipp	1,3-Di-*iso*-propylimidazol-2-yliden

IMes	1,3-Dimesitylimidazol-2-yliden
IR	Infrarot
^{i}Pr	*iso*-Propyl
J	Kopplungskonstante (Kernspinresonanzspektroskopie)
J	Gesamtdrehimpulsquantenzahl
KZ	Koordinationszahl
L	Ligand
L	Bahndrehimpuls
λ	Wellenlänge
LUMO	niedrigstes unbesetztes Molekülorbital
	(Englisch: lowest unoccupied molecular orbital)
M	Metallatom/ -zentrum
M	(molare) Magnetisierung
m	mittel (IR Spektroskopie)
m	*meta*
m	Multiplett (Kernspinresonanzspektroskopie)
m	Maskierungsreagenz (18-Krone-6 oder crypt-222)
M^{A}	Alkalimetall
Mes/Mesityl	2,4,6-Trimethylphenyl
μ	Magnetisches Moment
μ_{eff}	Effektives magnetisches Moment
$\mu_{S.O.}$	Spin-Only-Wert des magnetischen Moments
nacnac	β-Diketiminato
[(NHC)PR]	NHC-stabilisiertes Phosphiniden
NMR	Kernspinresonanz (Englisch: nuclear magnetic resonance)
o	*ortho*
OxZ	Oxidationsstufe/ -zahl
p	*para*
Ph	Phenyl
ppm	Englisch: parts per million
PPMS	Englisch: physical properties measurement system
R	Substituent/Rest
S	Spinquantenzahl
s	Singulett (Kernspinresonanzspektroskopie)

s	stark (IR Spektroskopie)
sIDipp	1,3-Di-*iso*-propylimidazolin-2-yliden
sIMes	1,3-Dimesitylimidazolin-2-yliden
SIM	Einzelionenmagnet (Englisch: single-ion magnet)
SMM	Einzelmolekülmagnet (Englisch: single-molecule magnet)
SQUID	supraleitende Quanteninterferenzeinheit (Englisch: superconducting interference device)
t	Triplett (Kernspinresonanzspektroskopie)
^{t}Bu	*tert*-Butyl
THF	Tetrahydrofuran
ÜM	Übergangsmetall
ÜM-SMM	Übergangsmetall-Einzelmolekülmagnet (Englisch: transition metal single-molecule magnet)
TMS	Tetramethylsilan
Tolan	Diphenylacetylen
Tripp	2,4,6-Tri-*iso*-propylphenyl
U_{eff}	magnetische Relaxationsbarriere
UV/Vis	Englisch: ultraviolet/visible
$\tilde{\nu}$	Wellenzahl
w	schwach (IR-Spektroskopie; Englisch: weak)
18c6	18-Krone-6 = 1,4,7,10,13,16-Hexaoxazyklooctadecan
χ	molare magnetische Suszeptibilität

Abbildungsverzeichnis

Schemenverzeichnis

1 Einführung

Die vorliegende Arbeit beschäftigt sich mit der Synthese und Reaktivität der jungen und relativ unerforschten Substanzklasse (quasi-)linearer 3d-Metall(I)-Komplexe. Durch die elektronisch und koordinativ ungesättigten Metallzentren sind die Verbindungen sehr reaktiv und erfordern eine gewissenhafte Handhabung. Erste Studien zeigten bereits interessante Reaktivitäten gegenüber kleinen Molekülen und Substraten. Einblicke in ihr magnetisches Verhalten deuten ebenfalls auf ein vielversprechendes Potenzial hin. Bislang sind allerdings nur vereinzelte Spezies in der Literatur beschrieben.

Diese Arbeit soll zur Verbesserung des allgemeinen Verständnisses über die strukturellen sowie magnetischen Eigenschaften und Reaktivitäten Silylamid-basierter Metall(I)-Komplexe sowie deren Metall(II)-Vorläufer beitragen. Zusätzlich soll das Spektrum linearer 3d-Metall(II/I)-Komplexe auf Heteroatome, wie Phosphor, erweitert werden.

Im folgenden Kapitel wird das Wissen über bekannte 3d-Metall(II)- und 3d-Metall(I)-Komplexe zusammengefasst, um die in dieser Arbeit erhaltenen Ergebnisse mit der Literatur in Einklang zu bringen.

2 Theoretischer Hintergrund

2.1 Die Anfänge der Koordinationschemie

Die Anfänge der Koordinationschemie zu beschreiben ist schwierig, da kein definierter Beginn existiert. Bereits im Altertum wurde die Herstellung von Substanzen beschrieben, deren Inhaltsstoffe Koordinationsverbindungen darstellen. Dazu gehören Farblacke oder aus Tierblut extrahierte Häm-Derivate.[1]

Wissenschaftlich belegt wurden die ersten Substanzen in der Neuzeit, wobei die Charakterisierungen erst Jahrhunderte später erfolgten. Darunter fällt beispielsweise der Tetraamminkupfer(II)-Komplex $[Cu(NH)_3)_4]^{2+}$, der 1597 von LIBAVIUS entdeckt wurde (**Abbildung 1**). Dieser beschrieb die Blaufärbung einer Lösung aus $Ca(OH)_2$ und $[NH_4]Cl$ bei Zugabe von Bronze (Kupfer-Zinn-Legierung), konnte diese aber nicht erklären.[1,2] Auch das ‚Cadet's fuming liquid' − eine Mischung aus Kakodyl ($As_2(CH_3)_4$) und Kakodyloxid ($[(CH_3)_2As]_2O$) − wurde im Jahr 1757 von DE GASSICOURT synthetisiert, jedoch erst 1843 von BUNSEN strukturell aufgeklärt.[3,4]

Generell konnten im 19. Jahrhundert eine Reihe weiterer Komplexe synthetisiert und charakterisiert werden. Neue Verbindungen erhielten meist den Namen ihres Entdeckers, da noch keine Nomenklatur existierte. Darunter fällt unter anderem das ‚Zeise's Salz', $K[PtCl_3(CH_2H_4)]$, die erste reine organometallische Verbindung. Sie ist bis heute eines der einfachsten Beispiele für die Komplexierung zwischen Übergangsmetallen und Olefinen (**Abbildung 1**).[5]

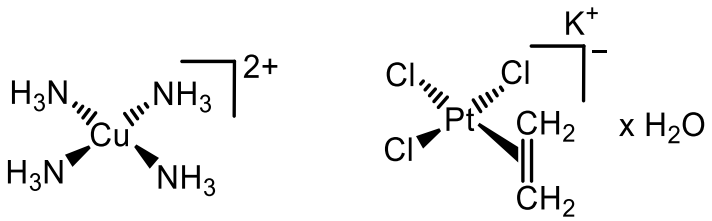

Abbildung 1. Beispielhafte Verbindungen der anfänglichen Koordinationschemie: $[Cu(NH_3)_4]^{2+}$ (links) und $K[PtCl_3(C_2H_4)] \times H_2O$ (rechts).[5]

Durch die systematische Darstellung einiger Amminchlorocobalt(III)-Verbindungen versuchte JØRGENSEN im späten 19. Jahrhundert, eine Theorie für die Bindungsverhältnisse in Komplexen zu entwickeln und etablierte den Begriff der ‚Kettentheorie'. Der Einfluss der organischen Strukturchemie ist dabei offenkundig, da er oligomere Ammoniak-Ketten postulierte, in denen die Stickstoffatome formal fünfbindig sind (**Abbildung 2**). Trotz der für heutige Verständnisse seltsamen

Vorstellungen und Annahmen nutzte WERNER diesen Ansatz als Vorlage für seine Koordinationstheorie, welche er 1893 verfasste und die als Grundstein für das heutige Verständnis der Komplexchemie gilt.[1,6]

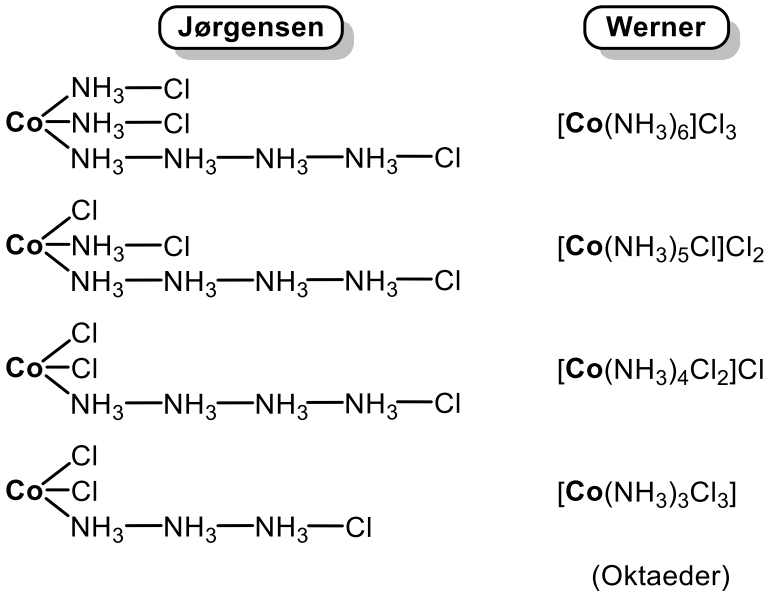

Abbildung 2. Vergleich der Konstitutionsformeln von Amminchlorocobalt(III)-Verbindungen nach JØRGENSEN (links) und WERNER (rechts).[1,6]

WERNER postulierte, dass sich Liganden um ein Metallzentrum mit charakteristischen Koordinations- und Ligandenzahlen anordnen, wodurch Koordinationsgeometrien wie oktaedrisch, tetraedrisch oder quadratisch planar am Metallzentrum entstehen (**Abbildung 3**).

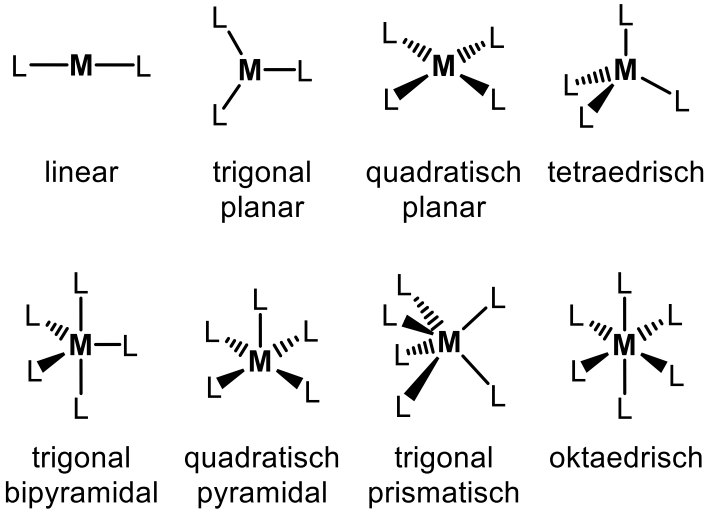

Abbildung 3. Mögliche Koordinationsgeometrien mit Koordinationsnummern von zwei bis sechs (M = Metall, L = Ligand).[7]

Diese Überlegungen basieren überwiegend auf der Verwendung einfacher Moleküle bzw. Ionen, die als Liganden fungieren. Sie dienen als Quelle negativer Ladungsdichte, welche über das Bindungsatom auf ein Metallkation gerichtet ist bzw.

auf dieses übertragen wird.[8–12] Beispiele sind CO, CN^-, PR_3, H^-, CH_3^-, NO_2^-, Ethylendiamin, NH_3, Pyridin, NCS^-, H_2O, O^{2-}, $C_2O_4^{2-}$, OH^-, F^-, N_3^-, SCN^-, S^{2-}, Br^-, I^- usw., welche oft in spektrochemischen Spannungsreihen aufgelistet werden.[12–14] Die Fähigkeit, d-Orbitale eines Metallatoms durch Koordination energetisch aufzuspalten, nimmt dabei von CO zu I^- sukzessive ab. Es können sich bis zu sechs dieser kleinen Moleküle um ein 3d-Übergangsmetallion anordnen, wodurch eine oktaedrische Koordinationssphäre generiert wird.[7]

Auf Basis dieses Konzepts wurden neue Theorien entwickelt, die das Wissen über Metallkomplexe weiter ausbauten. LEWIS erarbeitete 1916 beispielsweise das Elektronenpaarkonzept oder SIDGWICK 1923 die 18-Elektronen-Regel. Auch die Valenzbindungs-, Molekülorbital- oder Kristall-/Ligandfeldtheorien sind essentiell für das heutige Verständnis von Komplexen. Da diese Konzepte jedoch als Grundlage für heutige Forschungen herangezogen werden und sie Bestandteil vieler Sach- und Lehrbücher sind, wird an dieser Stelle auf eine detaillierte Beschreibung verzichtet.

2.2 Lineare 3d-Metall(II)-Komplexe

2.2.1 Historische Entwicklung

Im Laufe der späten 1950er- und 1960er-Jahre wurde der sterische Anspruch von Liganden sukzessive erhöht, um deren Auswirkungen auf die Struktur und Bindungsverhältnisse in Übergangsmetallkomplexen zu untersuchen.[15] Die Verwendung von Substituenten wie $-O^tBu$ und $-NMe_2$ führte dabei zur Entwicklung von Übergangsmetallalkoxiden und −amiden, die Koordinationszahlen von vier bzw. fünf aufwiesen.[16–19] Durch die Einführung des sperrigen Silylamid-Liganden $-N(SiMe_3)_2$ gelang BÜRGER und WANNAGAT in den 1960er-Jahren die Darstellung der 3d-Metallkomplexe $[M(N(SiMe_3)_2)_3]$ (M = Cr, Fe) und $[M(N(SiMe_3)_2)_2]$ (M = Mn, Co, Ni).[20,21] Durch eine Salzeliminierungsreaktion wird das entsprechende Metallhalogenid ($[MX_2]$ bzw. $[MX_3]$, X = Cl^-, I^-) mit zwei bzw. drei Äquivalenten $M^AN(SiMe_3)_2$ (M^A = Na, Li) umgesetzt (**Schema 1**).[20,21]

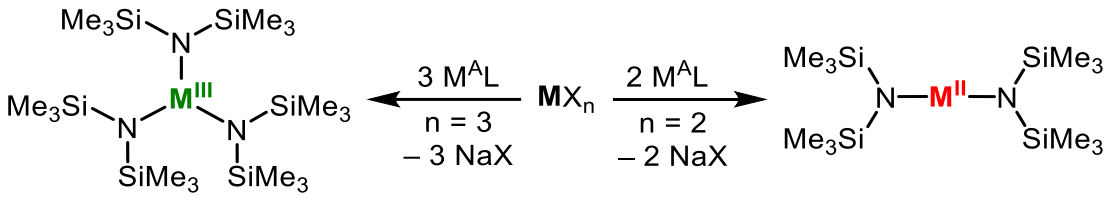

Schema 1. Synthese der postulierten Komplexe [M(N(SiMe$_3$)$_2$)$_3$] (M = Cr, Fe) und [M(N(SiMe$_3$)$_2$)$_2$] (M = Mn, Co, Ni) nach BÜRGER und WANNAGAT.[20,21]

Die Substrate lagen in der Gasphase als monomere, zwei- und dreifach-koordinierte Verbindungen vor, zeigten einen relativ niedrigen Siedepunkt und eine hohe Löslichkeit in kohlenwasserstoffhaltigen Lösungsmitteln. Aufgrund dieser Eigenschaften und ihrer hohen Reaktivität war eine vollständige Charakterisierung der Verbindungen zur damaligen Zeit schwierig. Die Existenz eines trigonal-planar-koordinierten Eisenzentrums in [Fe(N(SiMe$_3$)$_2$)$_3$] konnte erst im Jahr 1969 bestätigt werden.[22] Noch anspruchsvoller ist der Umgang mit den voraussichtlich zweifach-koordinierten Derivaten. 1971 wurde monomeres [Co(N(SiMe$_3$)$_2$)$_2$] durch Kryoskopie (in Lösung) und Massenspektrometrie (in der Gasphase) nachgewiesen, doch weitere Charakterisierungen waren vorerst nicht möglich. Die Forschungen konzentrierten sich daher in den folgenden Jahren überwiegend auf dreifach-koordinierte Verbindungen inklusive deren Eigenschaften und Reaktivitäten.[23–28] In diesem Zuge wurden Komplexe mit sterisch anspruchsvolleren Ligandsystemen entwickelt. Die so erhaltenen Amido-, Aryloxido-, Triorganosiloxido- oder Arylthiolato-Derivate erweitern das Spektrum von trigonalen Komplexen der Gruppen 5,6, 8 und 9 maßgeblich.[24–27] Als besonders interessant galten die schweren Homologe Niob, Tantal, Molybdän und Wolfram (Gruppe 5 und 6), da ihnen unter anderem die Fähigkeit zur Aktivierung kleiner Moleküle, wie CO oder N_2, nachgewiesen werden konnte.[27,28]

1978 konnte die postulierte zweifach-koordinierte Verbindung [Mn(N(SiMe$_3$)$_2$)$_2$] röntgenkristallographisch untersucht werden. Statt Monomeren liegen im Festkörper Dimere vor, in welchen zwei −N(SiMe$_3$)$_2$-Einheiten verbrückend zwischen zwei Metallatomen zur Stabilisierung der Verbindungen beitragen. Die Mn-Zentren sind damit trigonal planar umgeben (**Schema 2**).[29]

Für die beiden ebenfalls offenschaligen 3d-Übergangsmetall(II)-Silylamide des Eisens und Kobalts wurden in den darauffolgenden Jahren analoge Ergebnisse erhalten.[30,31] Mittels ^{1}H-NMR-spektroskopischen Untersuchungen an [Co(N(SiMe$_3$)$_2$)$_2$] wurde

entdeckt, dass sich selbst in Lösung ein Monomer-Dimer-Gleichgewicht einstellt, welches sowohl durch die Temperatur als auch das Lösungsmittel beeinflusst wird.[32]

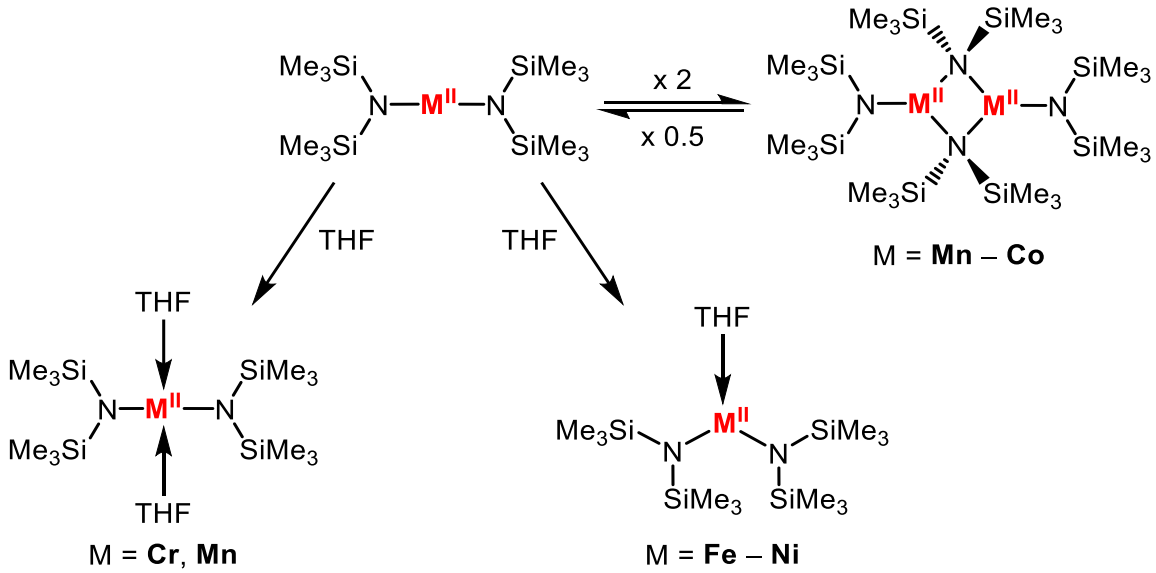

Schema 2. Stabilisierung von $[M(N(SiMe_3)_2)_2]$ durch Dimerisierung im Festkörper (rechts) oder Adduktbildung durch LEWIS-Basen in Lösung (unten), gezeigt am Beispiel THF.[29,31–36]

Durch die Addition von LEWIS-Basen, welche reversibel an die Metallzentren binden, wird die dimere Struktur aufgebrochen und so monomere Verbindungen im Festkörper erhalten. Die N−M−N-Achse ist dabei entweder linear wie beispielsweise im quadratisch planaren $[Cr(THF)_2(N(SiMe_3)_2)_2]$[33] oder gewinkelt, wie am Beispiel des trigonal planaren $[Co(THF)(N(SiMe_3)_2)_2]$[32,34] gezeigt wurde.

All diese Nachweise belegten, dass der sterische Anspruch des $-N(SiMe_3)_2$-Liganden nicht ausreichte, um die Linearität im Festkörper zu gewährleisten. Eine Erhöhung der Sterik durch Verwendung des Systems $-C(SiMe_3)_3$ führte im Jahr 1985 schließlich zur Isolierung des ersten zweifach-koordinierten Komplexes, $[Mn(C(SiMe_3)_3)_2]$ (**Abbildung 1**). Die Linearität am Metallzentrum wurde röntgenkristallographisch durch einen C−Mn−C Winkel von 180°, generiert durch ein kristallographisches Inversionszentrum im zentralen Manganatom, bestätigt.[37]

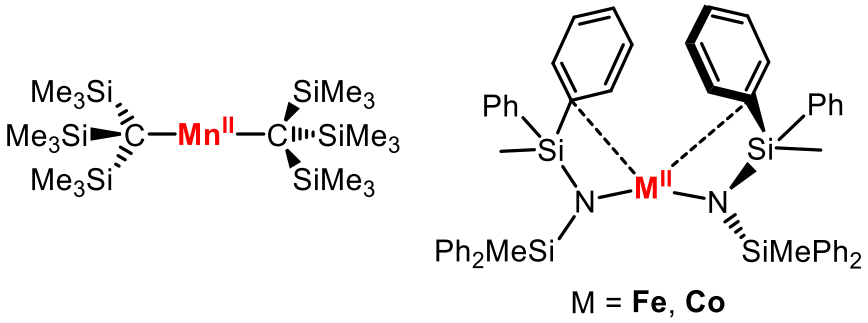

Abbildung 4. Struktur des ersten linearen 3d-Metallkomplexes $[Mn(C(SiMe_3)_3)_2]$ (links) und von $[M(N(SiMePh_2)_2)_2]$ (M = Fe, Co, rechts).[37,38]

Nach Veröffentlichung dieser Struktur wurden weitere homoleptische und lineare Verbindungen entwickelt. Beispiele sind $[Mn(CH_2{}^tBu)_2]$[39] oder $[M(N(SiMePh_2)_2)_2]$ (M = Fe, Co),[38] in welchen der sterische Anspruch des Ligandsystems genau zwischen dem von $[M(N(SiMe_3)_2)_2]$ und $[Mn(C(SiMe_3)_3)_2]$ liegt. Im Fall der beiden Silylamid-Spezies $[M(N(SiMePh_2)_2)_2]$ (M = Fe, Co) führte die geringere sterische Abschirmung und die Einführung eines Aryl-Substituenten jedoch zu einer (schwachen) Abwinklung der N−M−N-Achse (Fe: 169.0°, Co: 147.0°). Ursache ist die zusätzliche Ausbildung von d-π-Wechselwirkungen zwischen dem partiell positiven Zentralatom und dem elektronenreichen Arylsystem.

2.2.2 Bindungsverhältnisse und Geometrieeinflüsse zweifach-koordinierter Übergangsmetall(II)-Komplexe

Zum besseren Verständnis der Bindungsverhältnisse in linearen Komplexen wird zu Beginn nur die Symmetrie am Zentralatom, d. h. des Metallzentrums und den beiden daran bindenden Atomen, betrachtet. Aufgrund der hoch ungesättigten Koordination und der resultierenden linearen Geometrie am Metallzentrum besitzen zweifach-koordinierte Komplexe ein schwaches Ligandenfeld.[40] Im Grundzustand liegen die Komplexe mit Elektronenkonfigurationen von d^1 bis d^9 somit als *High-Spin*-Komplexe vor.[15,41] Bei den nachfolgenden Überlegungen werden vorerst lediglich σ-M/L-Wechselwirkungen berücksichtigt.[42]

Durch eine $D_{\infty h}$-Symmetrie orientieren sich die bindenden Ligandatome um das Metallzentrum entlang einer Achse, welche nach Konvention der Z-Achse entspricht. Die beiden Orbitale d_{xy} und $d_{x^2-y^2}$ liegen am energetisch günstigsten, wohingegen das d_{z^2}-Orbital energetisch am höchsten liegt. Wie die Orbitale unterschiedlicher Elektronenkonfigurationen im Grundzustand besetzt werden, ist vereinfacht in **Abbildung 5** für Konfigurationen von d^4 bis d^7 dargestellt.

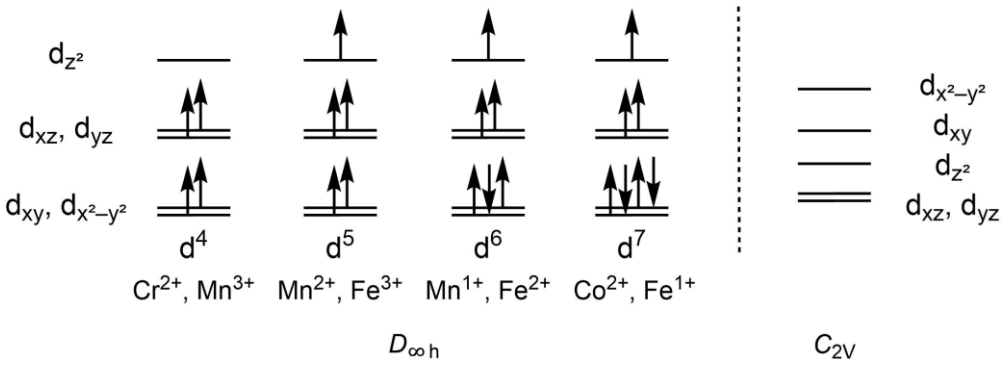

Abbildung 5. d-Orbitalaufspaltung und Grundzustände der Elektronenkonfigurationen d^1 bis d^9 in einem vereinfachten, linearen Kristallfeld nach $D_{\infty h}$-Symmetrie.[15]

In der Praxis zeigt sich, dass die meisten zweifach-koordinierten Komplexe eine leicht gewinkelte L−M−L Anordnung besitzen. Durch die damit einhergehende Verringerung der Symmetrie zu C_{2V} findet eine energetische Umverteilung statt.[15] Werden mehr Atome im Komplex betrachtet, so wird die Symmetrie weiter verringert. Der Silylamid-Komplex $[Fe(N(SiMe_3)_2)_2]$ weist beispielsweise eine D_{2d}-Symmetrie in seiner $Fe(NSi_2)_2$-Einheit auf.[43]

Neben Wechselwirkungen zwischen dem Metallzentrum und elektronenreichen Substituenten[44] kann auch der RENNER-TELLER Effekt eine gewinkelte Umgebung am Zentralatom verursachen.[41] So sind z. B. lineare Eisen(II)-Spezies im *High-Spin*-Zustand von Natur aus intrinsisch instabil. Die im linearen Fall energetisch separierten, nicht-bindenden $d_{x^2-y^2}$ und d_{xy} Orbitale werden durch eine abgewinkelte Geometrie mit den π- (d_{xz}, d_{yz}) und σ- (d_{z^2}) Orbitalen der Liganden vermischt. Folglich können sie an (anti-)bindenden Wechselwirkungen mitwirken und die Gesamtenergie der Komplexe senken.[41] Das Umgehen all dieser Effekte ist jedoch durch den Einsatz sterisch anspruchsvoller Liganden möglich, wodurch eine lineare Achse erzwungen wird.[41] Des Weiteren wird eine perfekt lineare Koordination am Metallzentrum häufig durch ein Inversionszentrum im zentralen Metallatom vorgetäuscht, wenn die Charakterisierung mithilfe der Einkristallstrukturanalyse erfolgt.[37]

Durch das Vorliegen eines sowohl sterisch als auch elektronisch ungesättigten Metallzentrums in einem schwachen Ligandenfeld weisen zweifach-koordinierte 3d-Metallkomplexe interessante magnetische Eigenschaften auf. Dies kann bis hin zum Verhalten eines Einzelmolekülmagneten führen. Im folgenden Kapiteln wird eine Übersicht über theoretische Grundlagen und bestehende Übergangsmetall-basierte Einzelmolekülmagnete gegeben.

2.2.3 Magnetismus in Übergangsmetallkomplexen

Um das magnetische Verhalten eines Systems zu evaluieren, werden Verbindungen einem äußeren Magnetfeld der Stärke *H* ausgesetzt. Die Differenz der Feldstärken außerhalb (*H*) und innerhalb (Flussdichte *B*) der Probe kann durch die Magnetisierung *M* berechnet werden. Hierfür wird zunächst von einem Mol Probensubstanz ausgegangen, wodurch die molare Magnetisierung *M* durch **Gleichung 1** ausgedrückt werden kann. Die Vakuumpermeabilität μ_0 dient dabei als Proportionalitätsfaktor.[1]

$$M = \frac{1}{\mu_0} B - H \qquad (1)$$

Ist *M* positiv (*B* > *H*), liegen paramagnetische Proben vor. Für *B* < *H* ist *M* negativ und entsprechende Verbindungen sind diamagnetisch. Die Abhängigkeit der molaren Magnetisierung vom externen Magnetfeld wird als molare magnetische Suszeptibilität χ bezeichnet. Bei geringen Feldstärken ist χ unabhängig vom Magnetfeld und kann als Proportionalitätsfaktor zwischen *M* und *H* angesehen werden (**Gleichung 2**).

$$M = \chi H \tag{2}$$

Die magnetische Suszeptibilität χ setzt sich aus einem diamagnetischen (χ_{dia}) und einem paramagnetischen (χ_{para}) Anteil zusammen (**Gleichung 3**).

$$\chi = \chi_{dia} + \chi_{para} \tag{3}$$

Der Diamagnetismus ist eine grundlegende Eigenschaft jeglicher Materie, wodurch auch paramagnetische Substanzen den diamagnetischen Beitrag χ_{dia} besitzen. Dieser Faktor ist unabhängig von der äußeren Feldstärke und der Temperatur und kann durch die sogenannten Pascal-Konstanten für jedes Atom berechnet werden. Der Beitrag ist stets negativ und liegt in der Größenordnung von -10^{-4} bis -10^{-6} cm^3 G Mol^{-1}. χ_{para} dagegen ist mit positiven Werten von 10^{-2} bis 10^{-5} cm^3 G Mol^{-1} wesentlich größer und bestimmt die magnetische Suszeptibilität in paramagnetischen Proben. Um die magnetische Suszeptibilität zu bestimmen, muss der diamagnetische Anteil jedoch berücksichtigt und experimentell erhaltene Werte müssen um den Beitrag von χ_{dia} korrigiert werden. In den folgenden Betrachtungen wird davon ausgegangen, dass diese Korrektur bereits stattgefunden hat.[1,45]

Molekularer Magnetismus

Aufgrund seiner Spin- und Bahndrehimpulse erzeugt ein Elektron ein magnetisches Moment μ, während es um einen positiv geladenen Atomkern herum radial beschleunigt wird (**Abbildung 6**). Der Wert von μ eines einzelnen Elektrons im Grundzustand wird durch das BOHRSCHE MAGNETON μ_B ausgedrückt und dient als Einheit für Systeme mit mehreren Elektronen.[45]

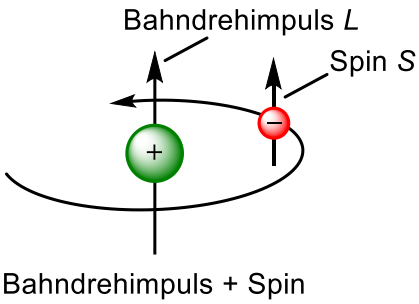

Abbildung 6. Vereinfachte Darstellung der Spin- und Bahndrehimpulse *S* und *L* eines Elektrons in einem Atom.

Dieses Moment setzt sich aus dem Eigendrehimpuls μ_S und dem Beitrag des Bahndrehimpulses μ_L zusammen (**Gleichung 4**).[1]

$$\mu = \mu_L + \mu_S \tag{4}$$

Befinden sich nur gepaarte Elektronen in einem Atom bzw. Molekül, gleichen sich die einzelnen magnetischen Momente der Elektronen aus und diamagnetische Substanzen liegen vor.[46,47] Sind jedoch ungepaarte Elektronen präsent, entstehen interne Magnetfelder und die Verbindungen sind paramagnetisch.[46–48]

Ohne die Präsenz eines äußeren Magnetfeldes *H* sind die Ausrichtungen der einzelnen magnetischen Momente energetisch entartet. Beim Anlegen von *H* wird diese Entartung aufgehoben, wodurch die Ausrichtungen des Gesamtdrehimpulsvektors *J* (*J* = *L* + *S*) unterschiedliche Energien besitzen. Dieser Effekt wird auch als ZEEMAN-Effekt bezeichnet. Die magnetischen Dipole ordnen sich nun BOLTZMANN-verteilt parallel bzw. antiparallel zum angelegten Feld an. Durch eine Senkung der Temperatur *T* steigt die Wahrscheinlichkeit, dass sich die Dipole parallel zum Magnetfeld ausrichten und die Magnetisierung der Probe, ausgedrückt durch χ, nimmt zu. Die Temperaturabhängigkeit der magnetischen Suszeptibilität lässt sich durch das CURIESCHE GESETZ (**Gleichung 5**) beschreiben, wobei die CURIE-Konstante *C* stoffspezifisch ist.[1]

$$\chi = \frac{C}{T} \tag{5}$$

Theoretisch kann diese Beziehung aus der VAN-VLECK-Gleichung hergeleitet werden, welche die Temperaturabhängigkeit der magnetischen Suszeptibilität als Bolzmann-Verteilung über die Zeeman-aufgespalteten Gesamtspin-/Gesamtdrehimpuls-Zustände der Moleküle angibt. Aus ihr lässt sich unmittelbar folgern, dass das Produkt χT temperaturunabhängig ist. Zudem ist in **Abbildung 7** zu sehen, dass die

Auftragung der reziproken Suszeptibilität gegen die Temperatur eine Ursprungsgerade darstellt. Diese idealisierte Vorstellung weicht allerdings von der Praxis ab, da das CURIE-Gesetz nur in einem bestimmten Temperatur- und Feldstärkenbereich aussagekräftig ist. Liegen beispielsweise zu niedrige Temperaturen bei gleichzeitig hohen Feldstärken vor, wird ein Sättigungswert erreicht, da alle Dipole parallel zum Magnetfeld ausgerichtet sind. Das CURIE-Gesetz ist außerdem nur auf Systeme mit isolierten Zentren in thermisch isolierten Grundzuständen anwendbar.

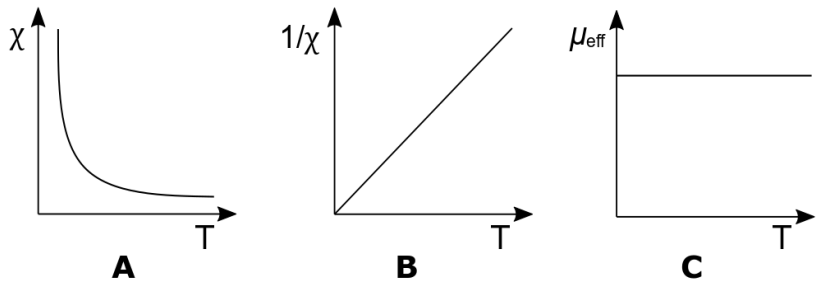

Abbildung 7. Idealisierte Darstellungen der Auftragungen **A** χ vs. *T*, **B** 1/χ vs. *T* und **C** μ_{eff} vs. T.[1]

Der Zusammenhang zwischen der magnetischen Suszeptibilität χ und dem effektiven magnetischen Moment μ_{eff}, welches das magnetische Moment einer Komplexverbindung angibt, lässt sich durch **Gleichung 6** mit den Konstanten N (AVOGADRO-Konstante), μ_B (BOHR Magneton) und k (BOLTZMANN-Konstante) beschreiben.[1,45]

$$\mu_{eff} = \sqrt{\frac{3k}{N\mu_B^2}}\sqrt{\chi T} = 2.828\sqrt{\chi T} \tag{6}$$

Der Spin-Only-Wert

In einem Übergangsmetallkomplex besitzen Metall−Ligand-Bindungen keinen direkten Einfluss auf den Spinzustand des Zentralions. Unabhängig vom Ligandenfeld ergibt sich für einen *High-Spin*-Mn(II)-Komplex mit einer d^5-Konfiguration beispielsweise ein maximaler Gesamtspin von 5/2. Bei d^1 bzw. d^9 Besetzungen (z. B. Sc^{2+}, Cu^{2+}) ist *S* mit einem Wert von 1/2 für paramagnetische Systeme minimal.[48]

Dem gegenüber ist der Bahndrehimpuls und somit auch μ_L stark vom vorliegenden Ligandenfeld abhängig. In einem freien Ion besitzen die P-, D-, F-Terme einen Bahndrehimpuls und somit ein magnetisches Moment. Befindet sich dieses Ion in einem Ligandenfeld, kann die Entartung der Terme aufgehoben werden und der Bahnbeitrag zum gesamten magnetischen Moment wird ‚gelöscht' („orbital quenching"). Im extremen Fall, dem Spin-Only-Fall, ausgedrückt durch $\mu_{S.O.}$, wird

dieser Bahnmoment durch die Ligandfeldaufspaltung vollständig unterdrückt. Das effektive magnetische Moment, μ_{eff}, ist somit nur noch vom Spin und nicht mehr vom Bahndrehimpuls abhängig. Der Komplex verhält sich wie ein freies Ion.[1]
Unter Berücksichtigung dieser Annahmen vereinfacht sich die VAN-VLECK-Gleichung zu **Gleichung 7** mit dem Landé-Faktor des freien Elektrons g und dem Gesamtspin *S*.

$$\chi = \frac{Ng^2\mu_B^2}{3kT} S(S+1) \tag{7}$$

Wird die magnetische Suszeptibilität nun durch das effektive magnetische Moment ersetzt, ergibt sich für den Spin-Only-Fall die Beziehung

$$\mu_{eff} = \mu_{S.O.} = \sqrt{g^2 S(S+1)} = \sqrt{4S(S+1)} \quad (\text{mit } g \approx 2). \tag{8}$$

Die die zu erwartenden μ_{eff} von Übergangsmetallkomplexen im *High-Spin*-Zustand mit einer d^n-Konfiguration können mit dieser vereinfachten Formel einfach abgeschätzt werden, da S = n/2.[1,45] Es ergibt sich

$$\mu_{eff} = \mu_{S.O.} = \sqrt{n(n+2)}. \tag{9}$$

In linearen 3d-Metallkomplexen liegt durch eine minimierte Wechselwirkung zwischen den Liganden und den d-Orbitalen nur ein schwaches Ligandenfeld vor. Der Bahndrehimpuls *L* wird nicht mehr vollständig unterdrückt und trägt zum magnetischen Moment μ_{eff} bei.[47] Dieser Effekt kann so stark sein, dass das magnetische Moment zweifach-koordinierter Komplexe an Werte freier Metallionen heranreicht.[48,49]

Einzelmolekülmagnete

Einige wenige Verbindungen sind in der Lage, ihre Magnetisierung in Abwesenheit eines äußeren Magnetfels für eine gewisse Zeitspanne bei niedrigen Temperaturen aufrechtzuerhalten (**Abbildung 8**).[50] Solche Substrate werden als Einzelmolekülmagnete (SMMs, engl. für single-molecule magnets) bezeichnet. Aus magnetischer Sicht sind sie bistabil, wodurch sie eine Energiebarriere des Spinumkehrs (U_{eff}) von $+M_S$ bis $-M_S$ besitzen.[51] Sie zeigen eine langsame magnetische Relaxation, d. h. eine magnetische Hysterese, unterhalb einer bestimmten Blocktemperatur (T_B).[52]

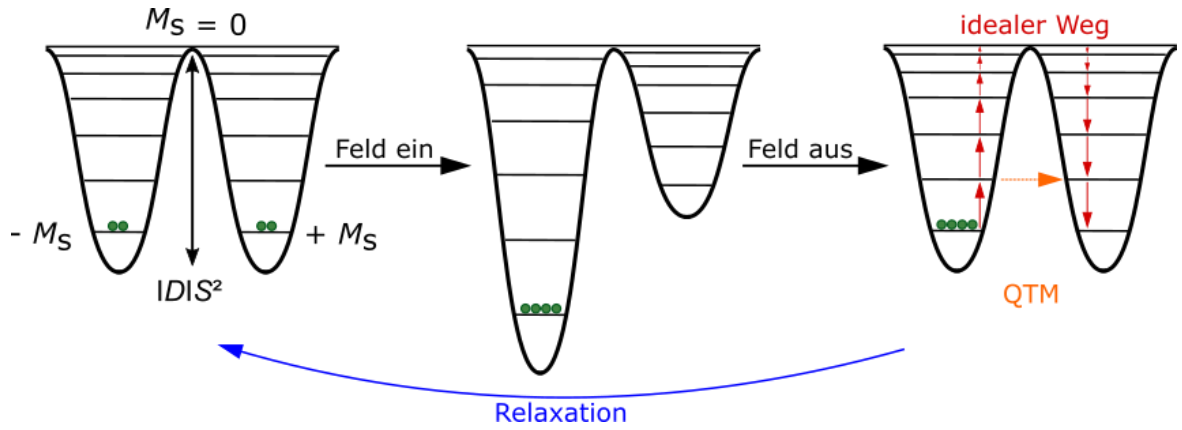

Abbildung 8. Veranschaulichung möglicher Prozesse in Einzelmolekülmagneten (QTM = Quantentunneln der Magnetisierung).[52]

Durch eine Vielzahl ungepaarter Elektronen liegt in Einzelmolekülmagneten ein hoher Wert für den Spins *S* vor. In Kombination mit einer großen magnetischen Anisotropie im Molekül, d. h. einer großen Richtungsabhängigkeit der Magnetisierung, entsteht eine Hysterese.[53] Die Anisotropie wird bestimmt durch den Parameter *D*, welcher die axiale Nullfeldaufspaltung (ZFS, engl. für zero-field splitting; Beschreibung der Energieaufspaltung ohne Anlegen eines äußeren Magnetfeldes) angibt.[54] Dieses Phänomen ist allein auf einen molekularen Ursprung zurückzuführen, was sie von ‚klassischen' Magneten unterscheidet. Weitere physikalische Eigenschaften wie Berry-Phasen Interferenz,[55] das Quantentunneln der Magnetisierung (QTM, vgl. **Abbildung 8**)[56] oder auch Quantenkohärenz[57] wurden bei SMMs beobachtet. Durch ihre magnetische Bistabilität weisen sie zudem ein hohes Potenzial für die Anwendung als Quantencomputer[58] oder Informationsspeicher mit hoher Dichte auf.[59]

Nicht verwunderlich ist daher das Interesse, das sie in vielen Forschungsbereichen, wie der Chemie, Physik oder auch den Material- bzw. Nanowissenschaften, wecken.[50,54–60]

Im Laufe der letzten Jahrzehnte wurde eine Reihe an Einzelmolekülmagneten entwickelt, die sich sowohl strukturell als auch magnetisch in ihrer potenziellen Leistung unterscheiden. Die Energiebarriere des Spinumkehrs, U_{eff}, und die magnetische Blocktemperatur, T_B, stellen zusammen die zwei wichtigsten Kenngrößen zur Einordnung dieser Leistung dar. Je größer die Werte sind, desto besser sind die Eigenschaften des Einzelmolekülmagneten.[50]

Der erste Einzelmolekülmagnet, der 1980 beschrieben wurde, war ein multinuklearer [Mn_{12}]-Komplex, der ein U_{eff} von 51 cm^{-1} und eine T_B von 3 K mit einer außerordentlichen magnetischen Hystereseschleife besitzt (**Abbildung 9**).[61]

Wie bereits erwähnt, ist die Barriere U in Übergangsmetall-Einzelmolekülmagneten (ÜM-SMMs) vom Spin S des Grundzustandes und der axialen Nullfeldaufspaltung D abhängig.[54] Dabei gilt $U = S^2 |D|$ für gerade bzw. $U = (S^2 - 1/4) |D|$ für ungerade Spins.[54]

Erste Bestrebungen lagen darin, S und damit auch U_{eff} durch die Entwicklung weiterer Metall-Cluster zu erhöhen. Dies war allerdings nur mäßig erfolgreich, da eine inverse Korrelation zwischen D und S^2 beobachtet wurde.[53,62]

Neuere Synthesestrategien fokussieren sich auf die Erhöhung der magnetischen Anisotropie innerhalb eines Moleküls. Einer der wichtigsten Ansätze dabei ist die Entwicklung und Synthese von mononuklearen SMMs mit Übergangsmetall-, Lanthanoid- oder Actinoidionen, welche auch als Einzelionmagnete (SIM, engl. für single-ion magnet) bezeichnet werden.[50,52] Lanthanoid-SIMs weisen wesentlich höhere U_{eff} als ÜM-SMMs auf, weshalb diese in den vergangenen Jahren primär erforscht wurden. In dem einzigartigen Beispiel des Dysprosium(III)-Komplexes $[(Cp^{iPr5})Dy(Cp^*)]^+$ konnte sogar ein U_{eff} von 1541 cm^{-1} bei einer Blocktemperatur von 80 K erzielt werden (**Abbildung 9**).[63,64]

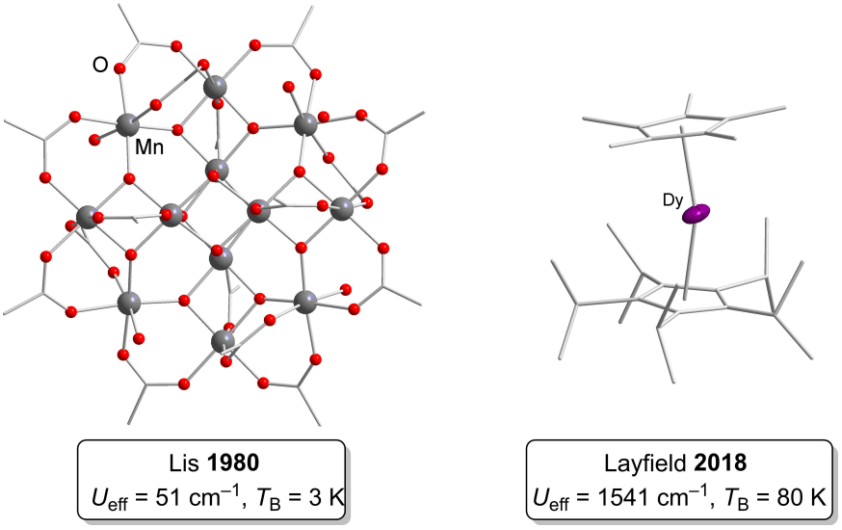

Abbildung 9. Molekülstruktur des ersten multinuklearen SMMs $[Mn_{12}O_{12}(O_2CMe)_{16}(H_2O)_4]$ (links) und das Anion des Lanthanoid-SIMs $B(C_6F_5)_4[(Cp^{iPr5})Dy(Cp^*)]$ (rechts). H-Atome werden aus Gründen der Übersichtlichkeit nicht gezeigt.[53,61,64,65]

Entwicklung von 3d-Metall(II)-SIMs

Die Verwendung von 3d-Übergangsmetallen für SIMs scheint im Vergleich zu Lanthanoiden auf den ersten Blick nicht sehr vielversprechend, da sie z. B. kleinere magnetische Momente und geringere Spin-Bahn-Kopplungskonstanten besitzen. Des Weiteren besteht die Möglichkeit, dass ein Teil des Bahndrehimpulses durch das Ligandenfeld abgeschwächt wird.[52] Allerdings sind sie wesentlich günstiger, haben

ein größeres natürliches Vorkommen und sind vor allem in der Lage, stark gekoppelte Spinsysteme auszubilden.[50] 2003 konnten dem ersten oktaedrischen Kobalt(II)-Komplex $[Co(SCN)_2(4\text{-dzbpy})_4]$ (dzbpy = diazobenzylpyridin) Charakteristika eines Einzelmolekülmagneten mit einem U_{eff} von 89 cm^{-1} und einer Hystereseschleife bei 3.5 K nachgewiesen werden.[66] Jedoch wurde diese Struktur *in situ* durch Bestrahlung mit Licht erzeugt und war nicht isolierbar, weshalb die genauere Beschaffenheit des Komplexes nicht beschrieben werden konnte. Ebenso ist die Quelle der Spins aufgrund der Koordination eines Carbens nicht alleine dem Metall zuzuordnen. Dieser Komplex zählt aus diesem Grund zwar als erste mononukleare 3d-Metall-haltige Verbindung, jedoch nicht als ‚reiner' SIM.

Im Laufe der Jahre konnten einige Kobalt-basierte SIMs in Koordinationsumgebungen von zwei bis sechs entwickelt werden.[50,52] Der erste ‚reine' ÜM-SIM ist der vierfach-koordinierte Fe(II)-Komplex $[(tpa^{Mes})Fe]^-$ aus dem Jahr 2010 (**Abbildung 10**).[67] Seither wurde eine Vielzahl weiterer SIMs in den Elektronenkonfigurationen d^4 bis d^9 für 3d-Übergangsmetalle (Cr − Ni) in unterschiedlichen Koordinationsmodi (zwei bis acht) veröffentlicht, wobei die Mehrheit auf den Metallen Kobalt und Eisen basiert.[48,52]

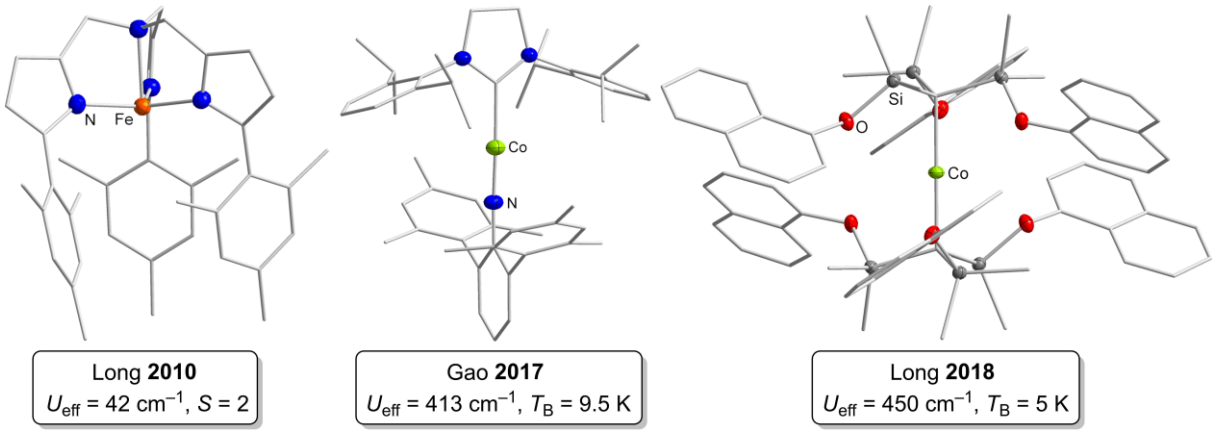

Abbildung 10. Molekülstrukturen der 3d-Metall-SIMs $[(tpa^{Mes})Fe]^-$ (links), [(sIDipp)CoNDmp] (Mitte) und $[Co(C(SiMe_2ONaph)_3)_2]$ (rechts). rechts). H-Atome werden aus Gründen der Übersichtlichkeit nicht gezeigt.[67–70]

Ein wesentlicher Aspekt bei der Entwicklung von SIMs ist das Aufrechterhalten des Bahndrehimpulses *L* innerhalb des Moleküls. Wie in Kapitel 2.2.3 beschrieben, kann dies speziell durch die Verwendung linearer, zweifach-koordinierter Verbindungen erzielt werden. Mit angelegten Magnetfeldern zwischen 61.9 K und 260 K zeigten so berechnete Beispiele der Fe(II)-Komplexe $[Fe(C(SiMe_3)_3)_2]$, $[Fe(N(Dipp)SiMe_3)_2]$ (Dipp = 2,6-Di-*iso*-propylphenyl), $[Fe(OAr')_2]$ und $[Fe(N(H)Ar)_2]$ typisches Verhalten von SIMs auf (**Abbildung 11**).[41] Wird die N−Fe−N-Achse jedoch abgewinkelt, wie in $[Fe(N(H)Ar^{\#})_2]$,[71] so liegt kein SIM-Verhalten vor (**Abbildung 11**, rechts).

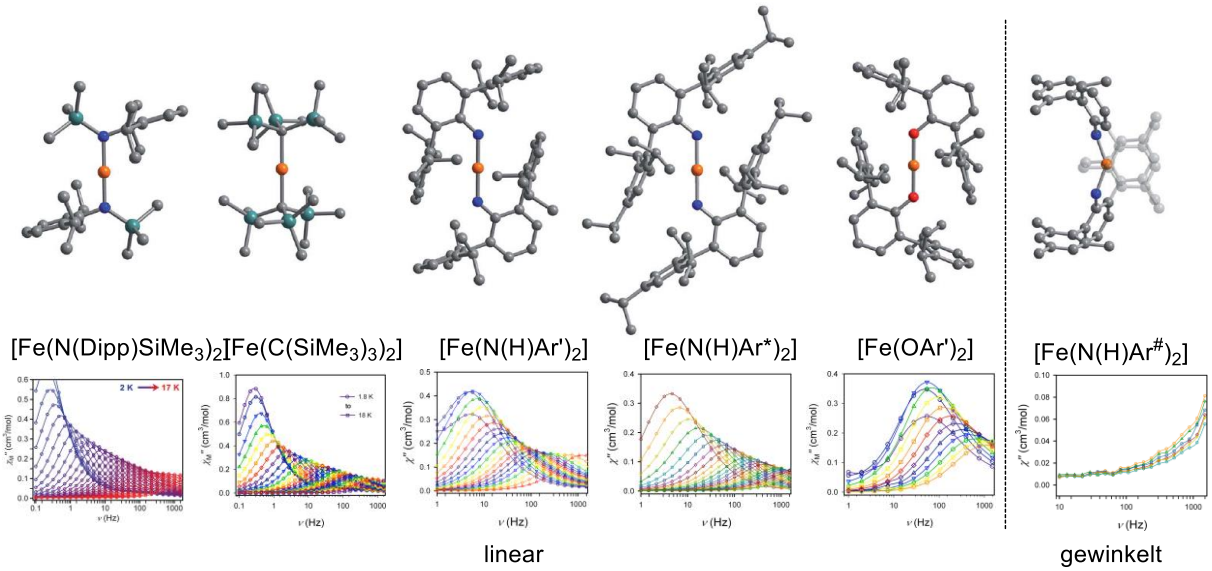

Abbildung 11. Vergleich des magnetischen Verhaltens linearer Fe(II)-Komplexe gegenüber dem eines gewinkelten (rechts).[52,72]

Bessere Werte als die eben diskutierten Fe(II)-Komplexe besitzt der heteroleptische Co(II)-Imido Komplex [(sIDipp)CoNDmp] (Dmp = 2,6-dimesitylphenyl), mit einer langsamen magnetischen Relaxation unterhalb von 50 K und einem U_{eff} von 413 cm^{-1} (**Abbildung 10**).[69] Diese unglaublichen Werte wurden nur ein Jahr später durch den linearen Dialkyl-Co(II)-Komplex, $[Co(C(SiMe_2ONaph)_3)_2]$, mit einem U_{eff} von 450 cm^{-1} übertroffen, welcher die bisher größte Energiebarriere zum Spinumkehr in ÜM-SIMs besitzt.[68] Der Bahndrehimpuls im Komplex ist maximal, verursacht durch eine Gesamtdrehimpulsquantenzahl *J* von 9/2. Dies führt zu einer langsamen magnetischen Relaxation bei Temperaturen von bis zu 70 K und einer magnetischen Hysterese bei niedrigen Temperaturen (**Abbildung 12**).[68]

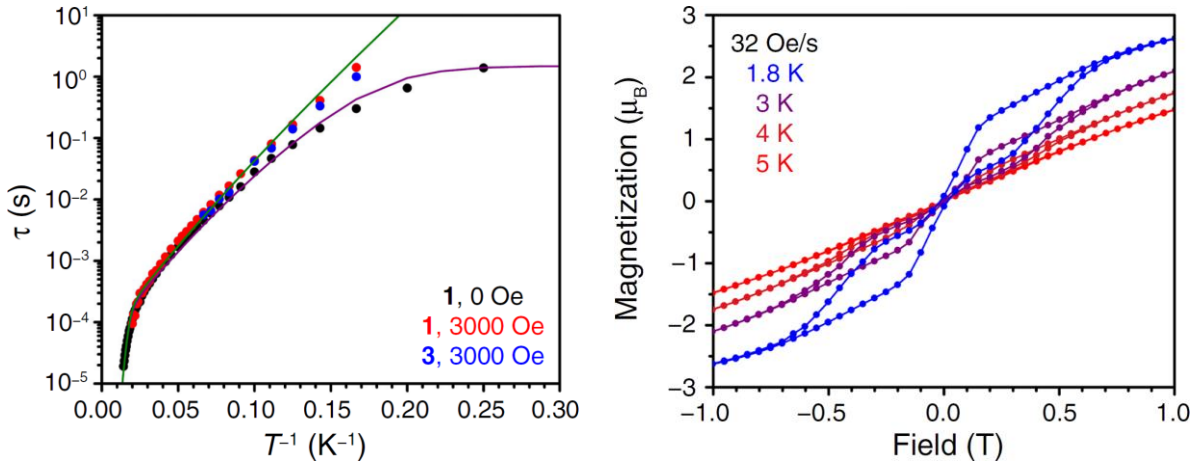

Abbildung 12. Magnetische Relaxationsdynamiken von $[Co(C(SiMe_2ONaph)_3)_2]$. Links: Arrhenius-Plot (schwarz: ohne angelegtes DC-Feld; rot: mit angelegtem DC-Feld (3000 Oe); blau: irrelevant in diesem Kontext). Rechts: Magnetische Hystereseschleife im Temperaturbereich von 1.8 K – 5 K bei einer Durchlaufgeschwindigkeit von 32 Oe/s.[68]

2.2.4 Darstellung linearer 3d-Metall(II)-Komplexe

Die Darstellung linearer 3d-Metall(II)-Komplexe von Chrom bis Kobalt erfolgt hauptsächlich durch Salzeliminierungs- oder Ligandaustauschreaktionen (**Schema 3**).[73–75]

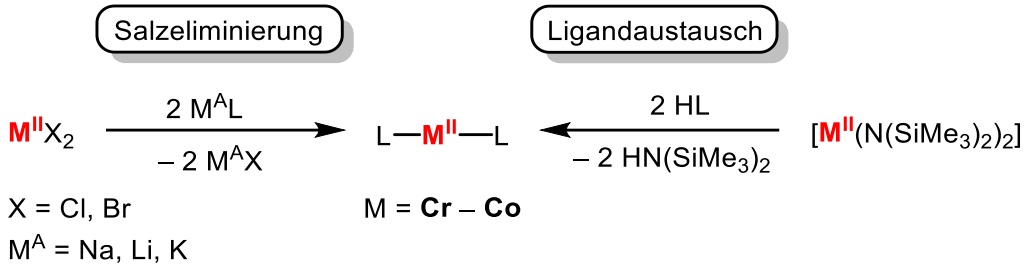

Schema 3. Möglichkeiten zur Synthese von Metall(II)-Komplexen.

Bei einer Salzeliminierungsreaktion wird ein Metall(II)-Halogenid MX_2 (X = Cl, Br) mit zwei Äquivalenten des entsprechenden Alkalisalzes M^AL (M^A = Na, K, Li; L = Ligand) umgesetzt. Gerade für Amido-Liganden ist diese Synthesestrategie sehr erfolgreich. BÜRGER und WANNAGAT nutzten diese Variante bereits zur Synthese von $[M(N(SiMe_3)_2)_2]$ (M = Mn − Co) (vgl. Kapitel 2.2.1).[20,21] Neben den damals eingesetzten Na-Salzen werden in neueren Publikationen vermehrt Li- oder K-Salze verwendet.[76,77]

Bei einer Ligandaustauschreaktion werden die Silylamid-Komplexe $[M(N(SiMe_3)_2)_2]$ (M = Mn − Co) als Präkursoren eingesetzt und mit zwei Äquivalenten des protonierten Ligands (HL), wie ein Phenol oder primäres/sekundäres Phosphan, umgesetzt.[73–75] Das entstehende Nebenprodukt, $HN(SiMe_3)_2$, kann auf einfache Weise durch Trocknung im Vakuum oder Destillation abgetrennt werden.

Salzeliminierungs- oder Ligandaustauschreaktionen werden auch in dieser Arbeit angewendet. Seltene Beispiele zeigen Darstellungen über Eliminierungs- oder Insertionsreaktionen[78] sowie der Abspaltung eines Halogenids von einem Metall(III)-Halogenido-Komplex. Diese Methoden sind jedoch für diese Arbeit irrelevant und werden an dieser Stelle nicht weiter diskutiert.

2.2.5 Stabilisierung von 3d-Metall(II)-Komplexen

Stabile, (quasi)lineare und offenschalige Übergangsmetall(II)-Komplexe (d^1 − d^9) sind bis heute wenig untersucht. Die Gründe hierfür sind vielseitig, lassen sich aber meist auf die fehlende koordinative und/oder elektronische Absättigung des Metallzentrums zurückführen, wodurch die Synthese erschwert wird.[20,21,76,77,79]

Die Komplexe neigen neben Disproportionierunsgreaktionen zur Dimerisierung[20,21] oder, bei sehr kleinen Liganden (wie z. B. Halogeniden), sogar zur Ausbildung von Aggregaten, wodurch die Koordinationszahl am Metallzentrum auf bis zu sechs erhöht wird.[80] Der einfachste und sicherste Weg, um ein solches Verhalten zu umgehen, ist die Verwendung sterisch anspruchsvoller Systeme, wie die für diese Arbeit relevanten Amido-Liganden.[81] Diese müssen zuvor oft im Labor hergestellt werden.[76,82] Ausnahmen sind z. B. die Silylamide $HN(SiMe_xPh_y)_2$, (x = 1 − 3; y = 3 − x), die kommerziell erworben und in einer einfachen Reaktion in das benötigte Lithium-Salz überführt werden können.[83] Relativ leicht herzustellen ist das Salz $LiN(Dipp)SiMe_3$, welches in dieser Arbeit zur Synthese der Metall(II)-Präkursoren $[M(N(Dipp)SiMe_3)_2]$ (M = Mn − Co) verwendet wird (**Schema 4**).[82]

In einem ersten Schritt wird das Amin $HN(Dipp)SiMe_3$ durch Reaktion von 2,6-Di-*iso*-propylanilin, *n*-Butyllithium und Trimethylsilylchlorid dargestellt. Anschließend wird das isolierte Amin mit einem weiteren Äquivalent *n*-Butyllithium zu $LiN(Dipp)SiMe_3$ lithiiert.[82]

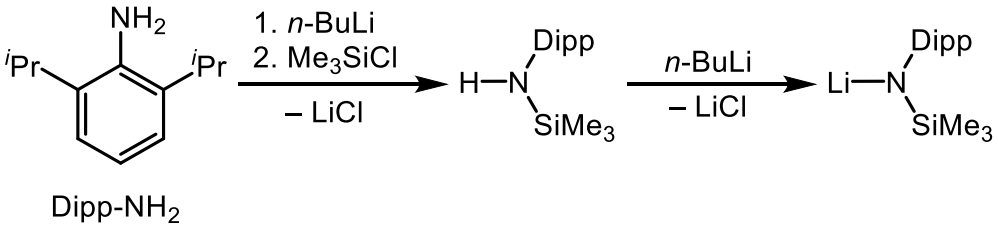

Schema 4. Darstellung des Silylamid-Salzes $LiN(Dipp)SiMe_3$.[82]

Das Vorliegen einer linearen N−M−N-Achse in den homoleptischen Komplexen $[M(N(Dipp)SiMe_3)_2]$ (M = Mn − Ni) konnte röntgenkristallographisch gezeigt werden (**Abbildung 13**).[72,76,79]

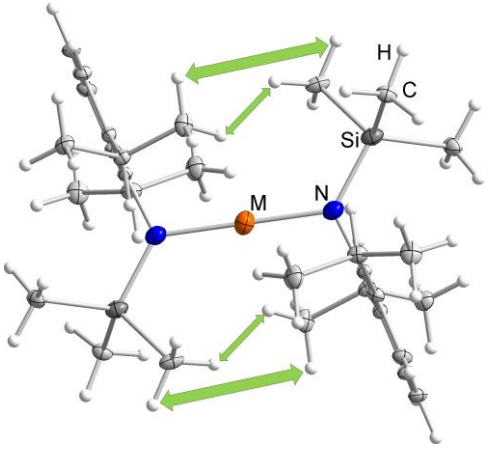

Abbildung 13. Stabilisierung von $[M(N(Dipp)SiMe_3)_2]$ (M =Mn – Co) durch Dispersionswechselwirkungen (grün) nach POWER.[76,79]

Die Komplexe werden nicht nur durch den sterischen Anspruch der Liganden selbst, sondern zusätzlich durch intramolekulare Dispersionswechselwirkungen (22 − 29 kcal/mol) stabilisiert.[76]

Im Fall von Chrom reicht die Größe der Liganden und die Ausbildung von Dispersionskräften allerdings nicht aus, um [Cr(N(Dipp)SiMe$_3$)$_2$] erfolgreich zu stabilisieren.[76] Stattdessen erfolgt eine H-Abstraktion einer CH$_3$-Gruppe durch ein Cr^{2+}-Atom, sodass der vierkernige Cluster [Cr(N(Dipp)(SiMe$_2$CH$_2$)$_2$Cr]$_2$(THF) entsteht (**Abbildung 14**). Erst durch Verwendung des sterisch anspruchsvolleren Liganden −N(Dipp)Si^{i}Pr$_3$ konnte eine lineare Cr(II)-Verbindung, [Cr(N(Dipp)Si^{i}Pr$_3$)$_2$], dargestellt werden.[77]

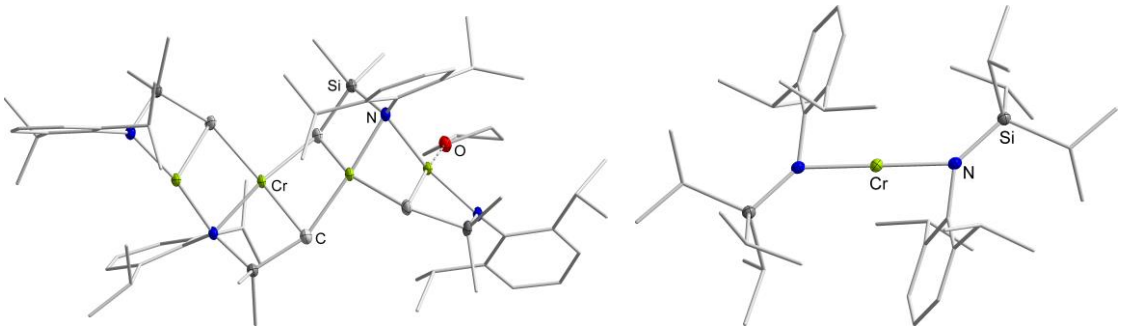

Abbildung 14. Molekülstrukturen des vierkernigen Chrom-Clusters [Cr(N(Dipp)(SiMe$_2$CH$_2$)$_2$Cr]$_2$(THF) (links) und der linearen Verbindung [Cr(N(Dipp)Si^{i}Pr$_3$)$_2$] (rechts). H-Atome sind aus Gründen der Übersichtlichkeit nicht gezeigt.[76,77]

Die Verwendung sterisch anspruchsvoller Liganden ist keine Garantie für eine lineare Koordination am Metallzentrum. Durch die Präsenz elektronenreicher, oft arylischer, Substituenten im Ligandrückgrat werden Komplexe durch die Ausbildung sekundärer d-π-Wechselwirkungen zwischen Metall und Substituent zusätzlich stabilisiert. Dies führt zu einer Abwinklung der L−M−L-Achse. Bei geringen Abweichungen von 180° wird von quasilinearen Substanzen gesprochen.[84–86]

POWER fand 2012 heraus, dass lediglich 13 der damals knapp 80 bekannten Verbindungen im Festkörper Abwinklungen von weniger als 10° ($\sphericalangle$ L−M−L > 170°) aufwiesen und als (quasi)linear gelten.[87] Gerade Chrom-Verbindungen sind häufig stark gewinkelt, da sie zum einen den größten Atomradius der verglichenen Metalle besitzen und zum anderen eine quadratisch planare Koordination aufgrund ihrer vier d-Elektronen bevorzugen.[77]

Die Verbindung mit dem kleinsten N−Cr−N Winkel von 110.8° ist der Borylamid-Komplex [Cr(NPh(BMes$_2$))$_2$] (Mes = Mesityl = 2,4,6-trimethylphenyl), in dem das zentrale Cr-Atom zusätzliche Wechselwirkungen zu zwei nahe gelegenen Mesityl-Einheiten ausbildet (**Abbildung 15**).[88]

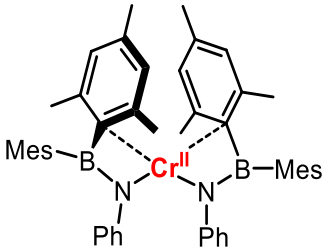

Abbildung 15. Stark abgewinkelte N−Cr−N-Achse (110.8°) in $[Cr(NPh(BMes_2))_2]$.[88]

Zur koordinativen Sättigung neigen die Metallzentren neben der Stabilisierung durch sekundäre Wechselwirkungen und trotz des Einsatzes großer Ligandsysteme dazu, LEWIS-Basen wie THF, Pyridin, Phosphane oder mono- bzw. polyatomare Anionen zu koordinieren. Diese Affinität gilt auch weiteren kleinen Molekülen wie O_2, N_2O oder H_2O, wodurch die Komplexe extrem luft- und feuchtigkeitsempfindlich sind.[28,89–91] Um Zersetzungsreaktionen zu vermeiden, müssen sowohl die Synthese und Aufbewahrung als auch die Durchführung verschiedenster Messmethoden unter Schutzgas erfolgen.

Trotz des schwierigen Umgangs rücken zweifach-koordinierte Komplexe immer mehr in den Fokus verschiedenster Forschungsprojekte. Gerade die noch nicht vollständig verstandenen Wechselwirkungen zwischen Metall und Substituent oder die hohe Reaktivität der koordinativ ungesättigten Metallzentren weisen ein noch wenig erforschtes Potenzial auf

2.2.6 Phosphanid-stabilisierte 3d-Metall(II)-Komplexe

Wie in den vorherigen Kapiteln angedeutet, basiert der Großteil an Metall(II)-Komplexen auf der Verwendung von Amidoliganden des Typs −NRR‘. Des Weiteren existieren vereinzelte Beispiele für Aryl-, Alkyl-, Alkoxo- oder Thiolato-Derivate.[15,40,43,74,78,92–95] Konträr dazu sind kaum Verbindungen auf Basis schwererer p-Block-Elemente, wie Phosphor, bekannt. Das hohe Reduktionspotenzial von Phosphaniden erschwert deren Isolierung im Vergleich zu Amiden. Statt der Ausbildung linearer Komplexe wird die Reduktion des Metallzentrums in Zusammenhang mit einer P−P-Bindungsknüpfung beobachtet. Der einzige homoleptische und lineare Vertreter ist der Bis(phosphanido)-Komplex $[Zn(P(SiPh_3)_2)_2]$, der allerdings nicht im Festkörper nachgewiesen werden konnte und eine d^{10}-Konfiguration besitzt (**Abbildung 16**).[96] Homoleptische, aber dimerisierte Komplexe konnten für Zink und Mangan mit dem Liganden $-P(SiMe_3)_2)_2$ erhalten werden.[73,97] Deren Stabilität wurde durch die volle bzw. halbvolle Besetzung der d-Orbitale in den Konfigurationen d^{10} (Zn) und d^5 (Mn) erklärt.

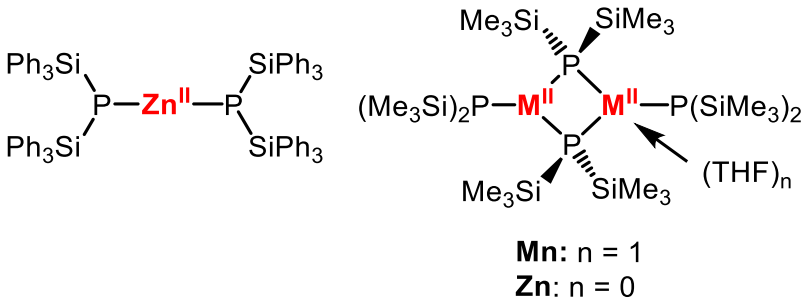

Abbildung 16. Bekannte homoleptische Bis(phosphanido)-Komplexe.[73,96,97]

Des Weiteren konnten durch Ligandaustauschreaktionen heteroleptische und dimerisierte Komplexe isoliert werden (**Schema 5**). Der Austausch des zweiten Silylamid-Liganden scheiterte, wurde aber mit dem großen sterischen Anspruch der Substituenten und nicht durch mögliche Zersetzungsreaktionen begründet.[75]

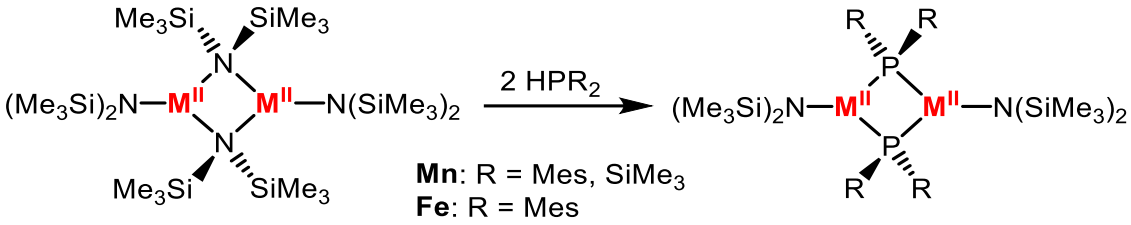

Schema 5. Synthese bekannter heteroleptischer 3d-Metall-Phosphanid-Komplexe.[75]

Die Entwicklung des vierkernigen Fe-Phosphanid-Clusters, mit Eisen in der formalen Oxidationsstufe +1.5, ist ein weiteres Beispiel für das Potenzial neuartiger homoleptischer 3d-Metall-Phosphanid-Komplexe.[98] Das Interesse an ihnen betrifft nicht nur die Schwierigkeit der Isolierung, auch Eigenschaften elektronischer und magnetischer Natur können einen interessanten Einblick in zukünftige Anwendungen geben.

Um die Natur von Metall−Phosphor-Bindungen in niederkoordinierten 3d-Metallkomplexen besser zu verstehen, beschäftigt sich diese Arbeit mit der Reaktivität von Metall(II)-Komplexen gegenüber Phosphinidenen bzw. Phosphinideniden. Aus diesem Grund wird im folgenden Kapitel ein Einblick in deren Chemie gegeben.

2.3 Phosphinidene

Die Elektronegativitäten von Phosphor (EN(P) = 2.15) und Kohlenstoff (EN(C) = 2.55) unterscheiden sich nur leicht, weshalb Phosphor als Gruppe 15 Äquivalent des Kohlenstoffs angesehen wird. So wird die Gruppe der Phosphinidene (oder Phosphanylidene, [PR]) auch gerne als Carben (R_2C:) -Analoga bezeichnet.[99,100]

Phosphinidene besitzen die formale Oxidationsstufe ±1 und gehören mit ihren sechs Valenzelektronen zu Elektronenmangelverbindungen.[100,101] In diesen hochreaktiven Spezies liegen die Elektronen analog zu Carbenen entweder im Singulett- oder im Triplett-Zustand vor. Laut quantenchemischen Berechnungen wird der Triplett-Zustand aufgrund eines energetisch abgesenkten Grundzustandes und zwei entarteten p-Orbitalen bevorzugt. Experimentell konnte dies durch ESR-Messungen anhand von Mesitylphosphiniden ([PMes]) bestätigt werden.[101,102] Aufgrund des vorliegenden Triplett-Zustands oligomerisieren Phosphinidene nahezu barrierefrei zu Zyklophosphanen (n [PR] → $[PR]_n$) (vgl. **Schema 6**, Kapitel 2.3.2).[103]
Durch das Anbringen starker π-Donorsubstituenten R wird die Entartung der beiden p-Orbitale am Phosphoratom aufgehoben. Dies führt zur Verkleinerung des Triplett-Singulett-Abstands und einer erleichterten Stabilisierung des Singulett-Zustands.
Dennoch sind freie Phosphinidene im Singulett-Grundzustand nicht stabil und neigen zum Ausgleich des Elektronenmangels am Phosphinidenid-P-Atom dazu, Phosphor−Phosphor-Mehrfachbindungen auszubilden.[104,105] Aufgrund der bevorzugten Oligomerisierungsreaktionen wurden Methoden entwickelt, Phosphinidenide zu stabilisieren. Dazu gehört die Komplexierung in einem Phosphiniden-Metallkomplex oder die Stabilisierung durch ein *N*-heterozyklisches Carben (NHC, engl. *N*-heterocyclic carbenes).

2.3.1 Komplexierung von Phosphinidenen

Phosphinidene besitzen vier Valenzelektronen, die an einen Stabilisierungspartner, wie z. B. ein Übergangsmetall, binden können und fungieren so als 2- oder 4-Elektronendonoren. Es können sowohl verbrückende ($[(R)P(ML_n)_2]$) als auch terminale ($[(R)PML_n]$) Phosphinidenkomplexe entstehen. Wenn alle vier Elektronen beteiligt sind, werden lineare ([(R)P═M]), μ-planare, μ_3-tetraedrische oder μ_4-bipyramidale Komplexe gebildet.[106] Chemisch interessanter sind jedoch Verbindungen, in denen nur zwei Elektronen zur Stabilisierung beitragen und freie Koordinationsstellen vorliegen. Befinden sich das Phosphiniden im Singulett-Zustand (**Abbildung 17**, links), werden elektrophile, FISCHER-ähnliche Komplexe ausgebildet. Alternativ kann das [PR]-Fragment im Triplett-Zustand vorliegen und nukleophile, SCHROCK-ähnliche Phosphinidenkomplexe entstehen (**Abbildung 17**, rechts).[107]

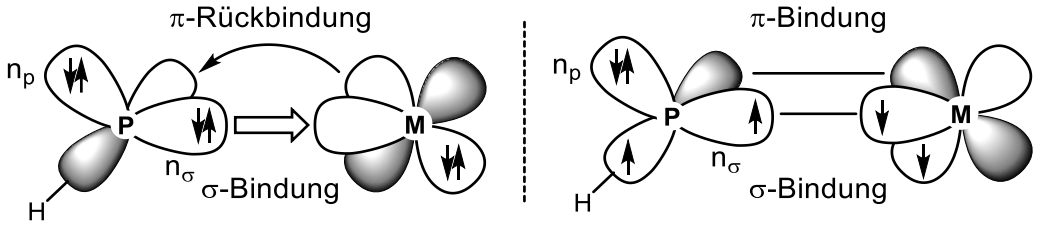

Abbildung 17. Bindungsverhältnisse in elektrophilen (links) und nukleophilen (rechts) terminalen Phosphinidenkomplexen.[106]

In welchem der beiden Zustände (Singulett oder Triplett) sich das Phosphoratom befindet, hängt bedeutend vom Metallzentrum und dessen Liganden ab, jedoch ist der Triplett-Zustand stark bevorzugt.[108] Sind weitere Liganden am Metall starke σ-Donoren, erhöht sich die Nukleophilie am Phosphoratom durch Erhöhung der Elektronendichte. Koordinieren π-Akzeptorliganden (wie CO) an das Metallatom, vergrößert sich die Elektrophilie im Phosphiniden durch Verringerung der Elektronendichte am Phosphoratom.[101,108]

Neben Hauptgruppen- und Actinoidkomplexen handelt es sich bei den in der Literatur bekannten Verbindungen hauptsächlich um Übergangsmetallkomplexe. Eine kleine Auswahl wird in **Abbildung 18** gegeben.[101,109–113]

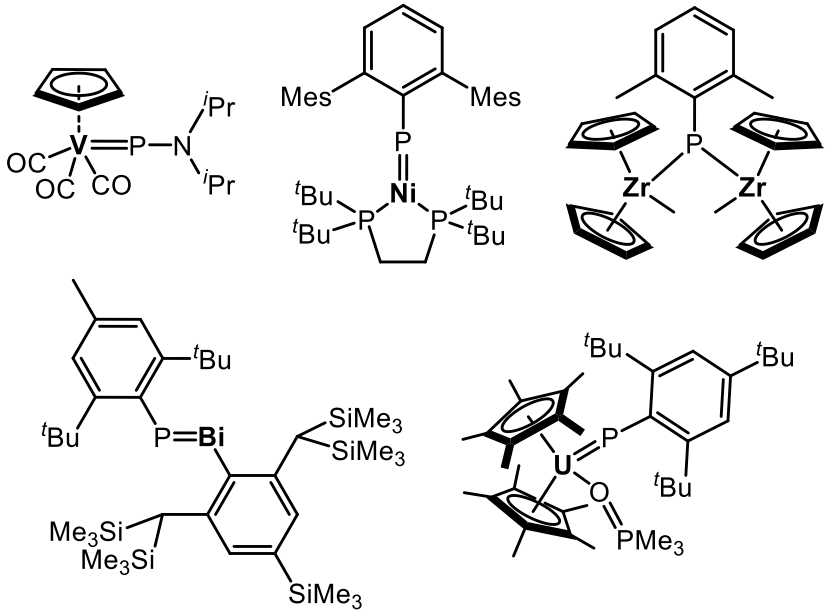

Abbildung 18. Auswahl bekannter Metall-Phosphiniden-Komplexe.[109–113]

2.3.2 NHC-stabilisierte Phosphinidene: [(NHC)PR]

Phosphinidene können statt der Komplexierung an Übergangsmetalle auch durch die Ausbildung eines Addukts mit Elektronenpaardonoren, wie Phosphinen oder NHCs, stabilisiert werden.[114–116]

Das Interesse, p-Block Elemente an NHCs zu binden, besteht, seitdem ARDUENGO im Jahr 1991 das erste *N*-heterozyklische Carben auf Basis eines Imidazolin-2-ylidens gebildet hat.[117] Es wurde festgestellt, dass Reaktionen mit zyklischen Oligomeren von Alkyl- bzw. Arylphosphinidenen, wie $(PPh)_5$, möglich sind (**Schema 6**).[116,118]

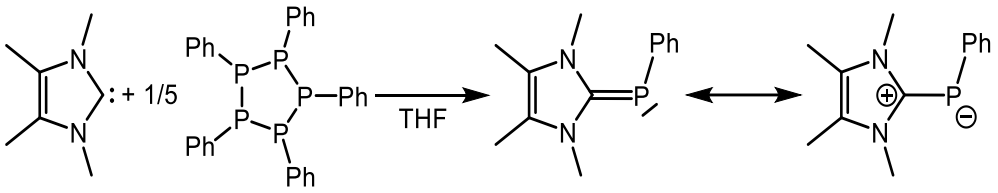

Schema 6. Darstellung des ersten NHC-substituierten Phosphinidens.[118]

Während die Stabilisierung substituierter Phosphinidene nach der Entdeckung durch ARDUENGO in den darauffolgenden Jahren vermehrt beschrieben wurde,[100,114,119] konnte der einfachste Repräsentant, [(NHC)PH], aufgrund seiner hohen Reaktivität lange Zeit nur theoretisch behandelt werden.[120]

‚parent' Phosphinidene: [(NHC)PH]

ROBINSON und seine Mitarbeiter legten 2010 den Grundstein für die Entwicklung Carben-stabilisierter Phosphinidene des Typs [(NHC)PH], den sogenannten ‚parent' Phosphinidenen. Durch Reaktion des freien NHCs IDipp (1,3-Di-*iso*-propylimidazol-2-yliden) mit PCl_3 und sukzessiver Reduktion erhielten sie das erste lithiierte Phosphiniden (**Schema 7**). Die im anfänglichen Schritt erhaltene, hypervalente Verbindung [(IDipp)PCl_3] wurde mit KC_8 zum Carben-stabilisierten Diphosphor $[(IDipp)P]_2$ (OxZ(P) = 0) reduziert, welches wiederum mit elementarem Lithium in THF zu [(^{Li}IDipp)PH] (OxZ(P) = +I) weiter reagierte.[121]

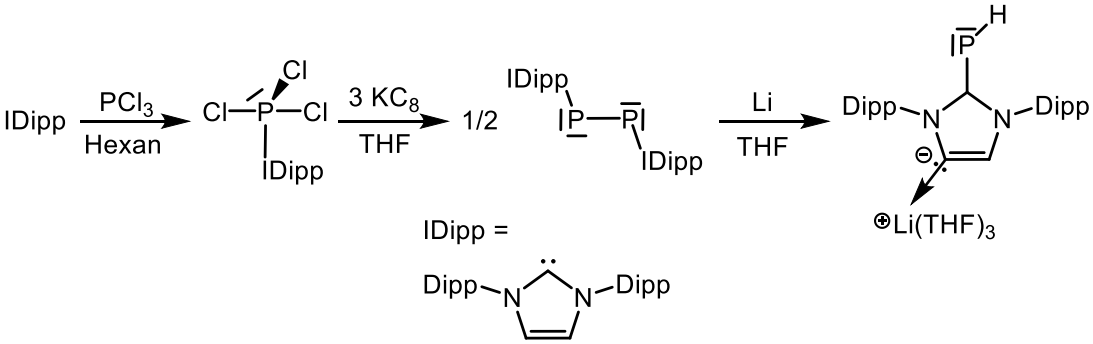

Schema 7. Synthese des ersten NHC-stabilisierten ‚parent' Phosphinidens [(NHC)PH] durch ROBINSON und seine Mitarbeiter.[121]

Der vorliegende Mechanismus ist ungeklärt, da sowohl die zentrale P−P-Bindung von $[(IDipp)P]_2$ gespalten wurde als auch eine Lithium-basierte C−H Aktivierung im NHC-Rückgrat stattfindet.[121] Mittlerweile konnten mehrere ‚parent' Phosphinidenide

dargestellt werden. Die erfolgreichen Isolierungen basieren allerdings auf nicht universell anwendbaren Synthesestrategien, die auf die jeweiligen Substrate angepasst werden müssen.[122]

Das ‚parent' Phosphiniden [(IDipp)PH] kann hingegen auf mehrere Weisen dargestellt werden, wie z. B. durch die Desilylierung des Carben-Addukts [(IDipp)PSiMe$_3$] mit Methanol oder[123] durch Reaktion von [Na(OCP)] bzw. $P_7(SiMe_3)_3$ mit dem entsprechenden Imidazolium Salz NHC•HCl in THF.[124] Die Synthese des gesättigten Analogons [(sIDipp)PH] wurde erstmals durch Reaktion des Imidazolium Salzes mit [(Na_3P_7)(DME)$_x$] zugänglich.[125] VON HÄNISCH und seine Mitarbeiter modifizierten die ursprüngliche Vorschrift und konnten so die ungesättigten Verbindungen [(sIMes)PH][126] und [(sIDipp)PH][127] auf einem atom-effizienteren Weg erzielen (**Schema 8**). Für [(sIDipp)PH] suspendieren sie das Imidazolium Salz sIDipp*HCl mit [Na(OCP)] in Benzonitril und rühren das Gemisch bei erhöhter Temperatur für mehrere Tage. Das Lösungsmittel wird im Anschluss evaporiert und der Rückstand in einer Soxhlett-Apparatur für mehrere Tage mit *n*-Pentan erhitzt. Abschließend wird das Lösungsmittel im Vakuum entfernt und [(sIDipp)PH] als beige- bzw. orangefarbener kristalliner Feststoff in moderaten Ausbeuten erhalten.

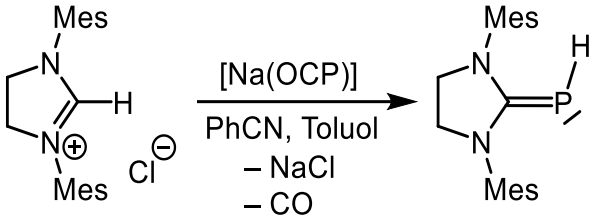

Schema 8. Darstellung von [(sIMes)PH] nach VON HÄNISCH.[126]

Bindungssituation in [(NHC)PR] bzw. [(NHC)PH]

Die Bindungssituation in [(NHC)PR] ist bis heute stark umstritten, da die vorliegenden Phosphor(I)-Spezies delokalisierte Elektronen besitzen. Dies bedeutet, dass die C−P-Bindung sowohl Doppelbindungscharakter aufweisen (**I**) als auch rein koordinativer Natur (**III**) sein kann (**Abbildung 19**).[120,123]

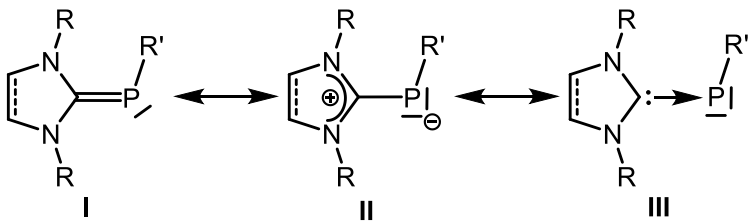

Abbildung 19. Mögliche Resonanzstrukturen in NHC-stabilisierten Phosphinidenen.[123]

Quantenchemische Berechnungen weisen auf eine Ylid-Struktur hin, weshalb von einer bevorzugten Bindungssituation zwischen den Grenzstrukturen **I** und **II** ausgegangen wird.[120] Am besten trifft demnach die Beschreibung als invers polarisiertes Phosphaalken zu, da Phosphinidene durch eine schwache π-Rückbindung vom Phosphoratom zum Carben-C-Atom ein negativ polarisiertes Phosphoratom aufweisen (**II**). Untersuchungen mittels ^{31}P-NMR-Spektroskopie indizieren darüber hinaus eine hohe Elektronendichte am Phosphoratom. In Phosphaalkanen hingegen ist das Phosphoratom positiv polarisiert. Experimentelle Beobachtungen bestätigen diese Beschreibung als invers polarisierte Phosphaalken, da bei der Umsetzung von [(NHC)PR]s mit Übergangsmetallen häufig eine Koordination über nur ein Elektronenpaar beobachtet wird, wie am Beispiel [(IMes)PH(W(CO)$_5$)] in **Abbildung 20** gezeigt.[128] In selteneren Fällen konnte die Verfügbarkeit eines zweiten Elektronenpaares durch eine rein dative Bindung des NHCs zum Phosphoratom (**III**, **Abbildung 19**) und das daraus resultierende Verhalten als LEWIS-Base dennoch nachgewiesen werden. Bei der Reaktion von [(IMes)PR] (R = H, Ph) mit BH_3 koordinieren beispielsweise zwei Äquivalente des Borans am Phosphorzentrum.[128,129]

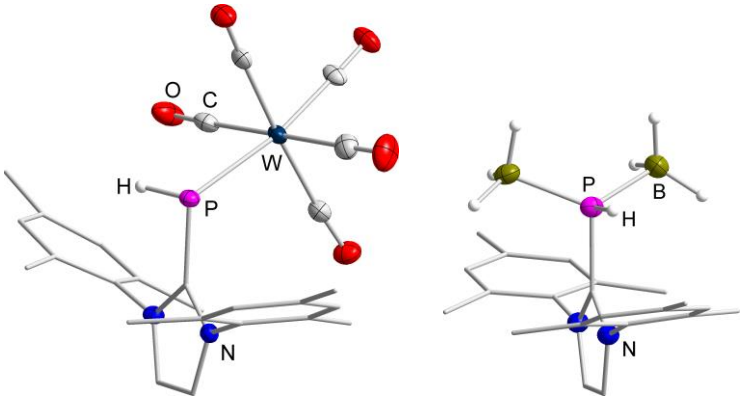

Abbildung 20. Bindung eines Phosphinidens zu Stabilisierungspartnern über ein (links, [IMesPH(W(CO)$_5$)]) oder zwei (rechts, [IMesPH(BH$_3$)$_2$]) freie Elektronenpaare. Protonen am Liganden werden aus Gründen der Übersichtlichkeit nicht gezeigt.[128]

Die Elektronendichte am Phosphoratom in [(NHC)PR]s ist auch vom verwendeten Carben und dessen π-Akzeptor-Eigenschaften abhängig. Als Indikation für mögliche Rückbindungen wurden chemische Verschiebungen im ^{31}P-NMR verglichen, die eine Hochfeldverschiebung der Phosphorsignale für ungesättigte NHCs im Vergleich zu ihren gesättigten Analoga ergaben.[130] Dies ist gut am Beispiel der beiden Verbindungen IDipp (1,3-Di-*iso*-propylimidazol-2-yliden) und sIDipp (1,3-Di-*iso*-propylimidazolin-2-yliden) zu erkennen (**Abbildung 21**). Mit Verschiebungen von δ = −18.9 ppm (sIDipp) und δ = −10.2 ppm (IDipp) ergibt sich eine Differenz von

Δδ = 8.7 ppm. Folglich befindet sich eine geringere Elektronendichte am Phosphorzentrum in Phosophinidenen mit gesättigten NHCs, was auf bessere π-Akzeptoreigenschaften schließen lässt. Diese Tendenz steht im Einklang mit weiteren Studien über NHCs.[130]

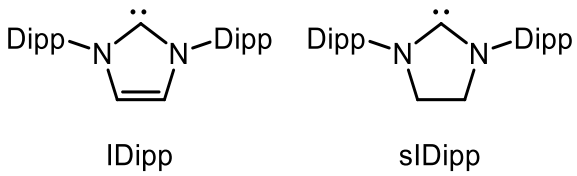

Abbildung 21. Gesättigtes NHC IDipp (links) und ungesättigtes NHC sIDipp (rechts).[131]

2.3.3 Übergangsmetall-stabilisierte Phosphinidenidkomplexe: [(NHC)PML$_n$]

Im Vergleich zu Phosphinidenen ist noch weniger über ihre anionischen Analoga, den Phosphinideniden ([NHC)P]$^-$), bekannt. Es sind nur wenige Komplexe des Typs [(NHC)PML$_n$], die mindestens einen anionischen Phosphinidenid-Liganden tragen, publiziert.[123,132,133]

Die Arbeitsgruppe von TAMM erzeugte diese erstmals durch die Umsetzung des bereits erwähnten [(IDipp)PSiMe$_3$] mit verschiedenen Übergangsmetallchloriden, wodurch sowohl terminale als auch verbrückende Phosphinidenid-Verbindungen unter Abspaltung von Trimethylsilylchlorid entstanden (**Abbildung 22**).[123,134]

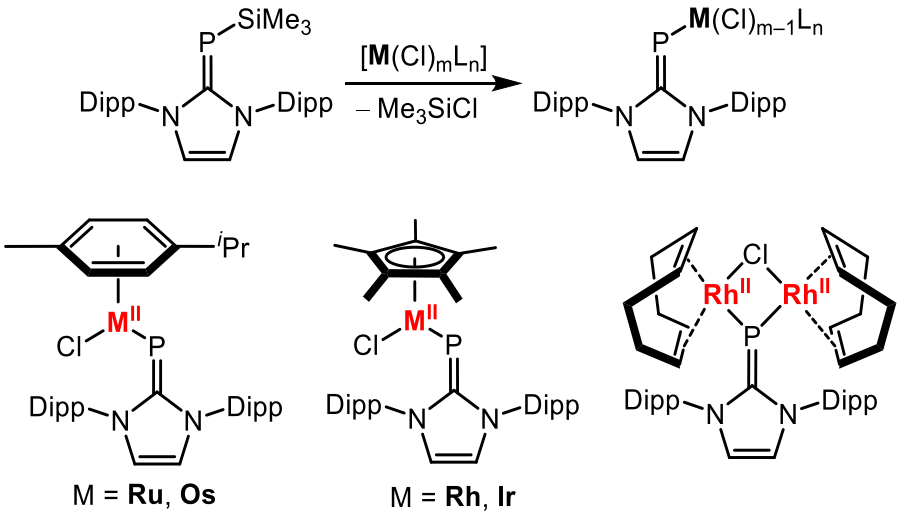

Abbildung 22. Synthese ÜM-substituierter Phosphinidenide ausgehend vom Carben-Phosphiniden-Addukt [(IDipp)PSiMe$_3$] (oben) mit Beispielen (unten).[123]

Durch die kurzen M−P-Bindungen und die tieffeldverschobenen Signale im ^{31}P-NMR-Spektrum konnte die Analogie zu terminalen Phosphiniden-Komplexen gezogen werden. Der [(IDipp)P]-Ligand wird als monoanionischer NHC-Phosphiniden-Ligand angesehen, der als 2σ,2π-Elektronendonor fungiert. In Anbetracht der hohen Metall-

Phosphor-Kovalenz könnte der Ligand andererseits auch als kationische NHC-Phosphiniden-Spezies binden. Die Stärke der π-Rückbindung zwischen Metall und Ligand ist dabei stark von den π-Akzeptor-Eigenschaften des NHCs abhängig, wie durch die mesomeren Grenzstrukturen ersichtlich wird (**Abbildung 23**).[134]

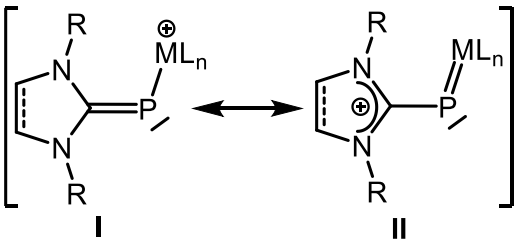

Abbildung 23. Mögliche Bindungsverhältnisse in Phosphinidenid-Komplexen des Typs [(NHC)PML$_n$] auf Grundlage mesomerer Grenzstrukturen.[134]

Durch Umsetzung eines Äquivalents $HgCl_2$ mit zwei Äquivalenten der Phosphinidene [(IDipp)PH] bzw. [(sIDipp)PH] in Anwesenheit der starken Base DBU (DBU = 1,8-Diazabizyklo[5.4.0]undec-7-en) gelang die Darstellung der beiden homoleptischen Quecksilber(II)-Komplexe [Hg(P(NHC))$_2$] (NHC = IDipp, sIDipp).[135] Messungen *via* Einkristallstrukturanalyse ergaben, dass sich das zentrale Quecksilber(II)-Atom auf einem symmetriegeneriertem Inversionszentrum befindet, wodurch der ∢ P−Hg−P Winkel 180° beträgt (**Abbildung 24**). Im Vergleich zu den freien Phosphinidenen bleiben die C1−P-Bindungslängen in [Hg(P(NHC))$_2$] mit Werten von 1.752(1) Å (NHC = IDipp) bzw. 1.743(2) Å (NHC = sIDipp) identisch. Zusätzlich werden die Komplexe durch die Aryl-Einheiten im Ligandrückgrat stabilisiert, da sich diese orthogonal zum Zentralatom mit einem Hg−C$_{ipso}$ Abstand von 3.067(5) Å orientieren.

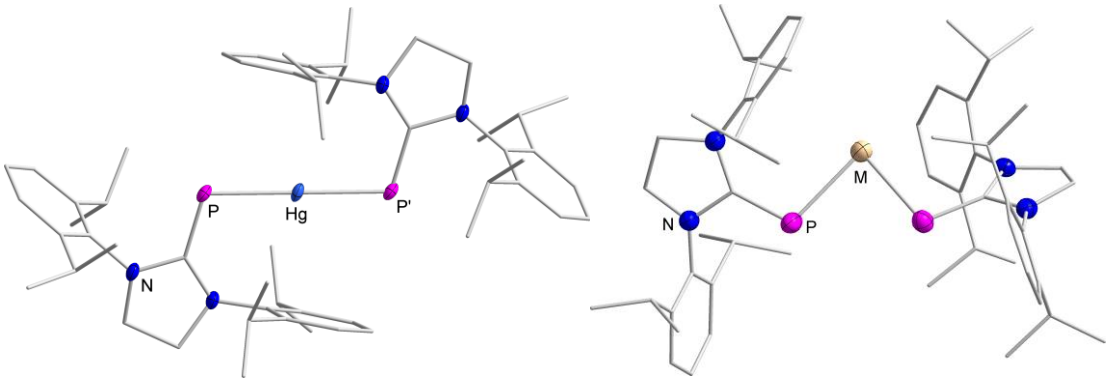

Abbildung 24. Molekülstrukturen der homoleptischen Komplexe [M(PsIDipp)$_2$] (links: M = Hg; rechts: M= Sn, Ge, Pb). H-Atome sind aus Gründen der Übersichtlichkeit nicht angezeigt. Ausgewählte Bindungslängen und -winkel: C1−P 1.754(6) Å (Hg), 177.0(2)−177.3(2) Å (Ge), 176.5(4)−176.8(5) Å (Sn), 174.3(10)−175.4(10) Å (Pb); M−P 2.407(1) Å (Hg), 229.6(1)−230.2(1) Å (Ge), 249.2(2)−249.9(2) Å (Sn), 258.0(3)−258.2(3) Å (Pb); P1−M−P2 180° (Hg), 87.4(1)° (Ge), 85.8(3)° (Sn), 84.6(1)° (Pb).[127,135]

In der Oxidationsstufe +2 und der daraus resultierenden d^{10}-Elektronenkonfiguration sind die Eigenschaften und die Reaktivität von Quecksilber eher mit denen eines

Hauptgruppenelements des p-Blocks vergleichbar. So gelang es, analoge Komplexe mit den Tetrelen Zinn, Germanium und Blei zu synthetisieren.[127] Aufgrund freier Elektronenpaare liegt in diesen Fällen jedoch eine gewinkelte Koordination am Zentralatom vor (**Abbildung 24**).[127]

Das P-gebundene Proton in [(NHC)PH]‘s ist verhältnismäßig unreaktiv gegenüber Basen.[126] Dennoch gelang der Arbeitsgruppe VON HÄNISCH die Deprotonierung mit der starken Base Benzylkalium (BnK), wodurch die beiden Kalium-Salze [(sIMes)PK] und [(sIDipp)PK] (**Abbildung 25**) isoliert werden konnten. Die beiden orangefarbenen Substanzen sind stark hydrolyseempfindlich und zersetzen sich in Gegenwart von heteroatomhaltigen Lösungsmitteln wie Diethylether. Zudem sind sie in aliphatischen bzw. aromatischen Lösungsmitteln unlöslich, wodurch sie nur aus der Suspension heraus reagieren.[126,127] Die Synthese der oben beschriebenen Komplexe $[M(P(sIDipp))_2]$ (M = S, Ge, Pb) bestätigt dies.

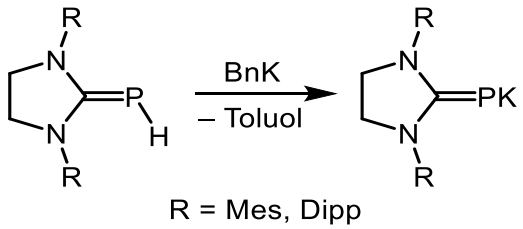

Abbildung 25. Synthese der beiden Kalium-Salze [(NHC)PK] (NHC = sIMes, sIDipp).[126,127]

2.4 Lineare 3d-Metall(I)-Komplexe

Neben der Entwicklung neuartiger, linearer 3d-Metall(II)-Komplexe beschäftigt sich diese Arbeit intensiv mit der Synthese und Reaktivität (quasi-)linearer 3d-Metall(I)-Komplexe von Chrom bis Kobalt. Vertreter dieser jungen und unerforschten Verbindungsklasse liegen in der Oxidationsstufe +1 vor, die für offenschalige Metalle sehr ungewöhnlich ist. Sie zeigen interessante Reaktivitäten hinsichtlich verschiedener Substratklassen auf (vgl. Kapitel 2.4.3) und sind gleichzeitig hochempfindlich gegenüber Zersetzungsreaktionen. Aus diesem Grund werden zu ihrer Stabilisierung, analog zu den Metall(II)-Komplexen, sterisch anspruchsvolle oder/und elektronisch stabilisierende Ligandsysteme verwendet.

Während zweifach-koordinierte Metall(II)-Ionen in Neutralkomplexen mithilfe zweier monoanionischer Liganden komplexiert werden, können Metall(I)-Ionen sowohl über anionische Liganden als auch Neutralliganden, wie NHCs oder cAACs (zyklische Alkylaminocarbene, engl. cyclic (alkyl)(amino)carbenes), komplexiert werden. Auf diese Weise entstehen geladene oder neutrale Verbindungen, die entweder zwei

gleiche (homoleptisch) oder zwei unterschiedliche (heteroleptisch) Liganden koordinieren.

2.4.1 Heteroleptische 3d-Metall(I)-Komplexe

Heteroleptische Metall(I)-Komplexe sind neutrale Verbindungen, in denen das zentrale Atom sowohl einen anionischen als auch einen neutralen, LEWIS-basischen Liganden koordiniert. Die meisten Verbindungen basieren auf Nickel, da die Oxidationsstufe +1 für Nickel im Vergleich zu den leichteren 3d-Metallen Chrom bis Kobalt relativ stabil ist.[136,137] So konnten Phosphanid-stabilisierte Komplexe des Typs [Ni(PR$_3$)L] (R = ^{t}Bu, ^{i}Pr; L = −N(Dipp)SiMe$_3$, −O(2,6-^{t}Bu-4-Me-C$_6$H$_2$) dargestellt werden (**Abbildung 26**).[138] In den meisten Fällen stabilisiert jedoch ein NHC das Metall(I)-Fragment, da NHCs starke σ-Donor- und vor allem π-Akzeptoreigenschaften besitzen und sowohl elektronisch als auch sterisch unkompliziert an die benötigten Bedürfnisse angepasst werden können.[136,137]

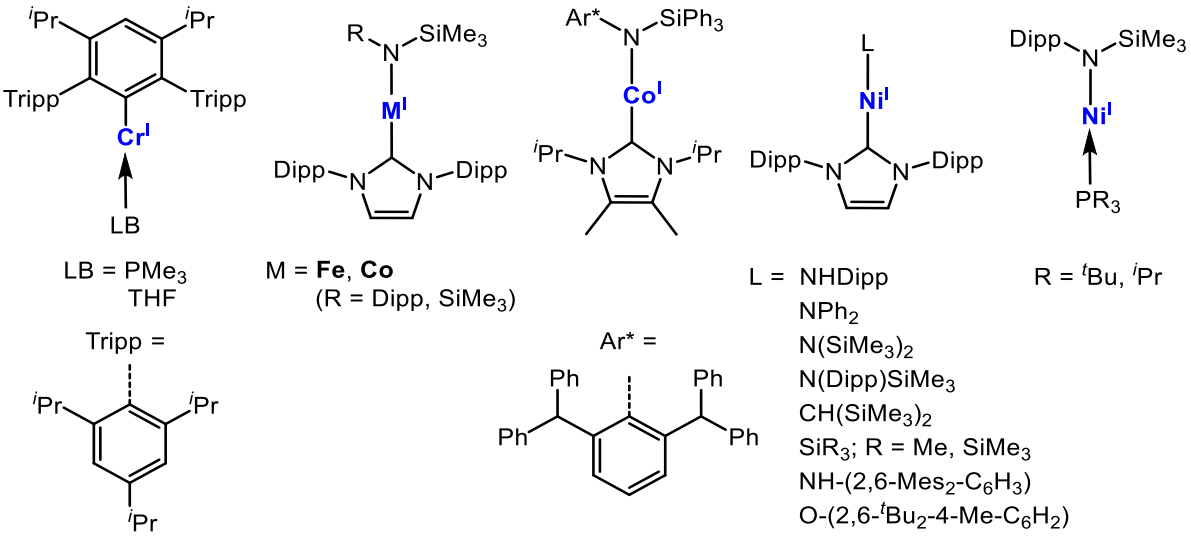

Abbildung 26. Bekannte heteroleptische 3d-Metall(I)-Komplexe von Chrom bis Nickel.[69,136–144]

Neben Nickel-Komplexen konnten auch Vertreter mit Chrom-, Eisen- und Kobalt-Zentren synthetisiert und charakterisiert werden. In **Abbildung 26** sind alle in der Literatur bekannten heteroleptischen 3d-Metall(I)-Komplexe, die sowohl einen anionischen als auch einen neutralen Liganden tragen, aufgeführt.[69,136–143]

Zusätzlich besteht die Möglichkeit, Metall(I)-Fragmente heteroleptisch durch intra- bzw. intermolekulare Aren-Wechselwirkungen zu stabilisieren (**Abbildung 27**).[140,145–149] In diesen Fällen ist das Metallfragment formal mehr als zweifach-koordiniert, weshalb an dieser Stelle nicht näher darauf eingegangen wird.

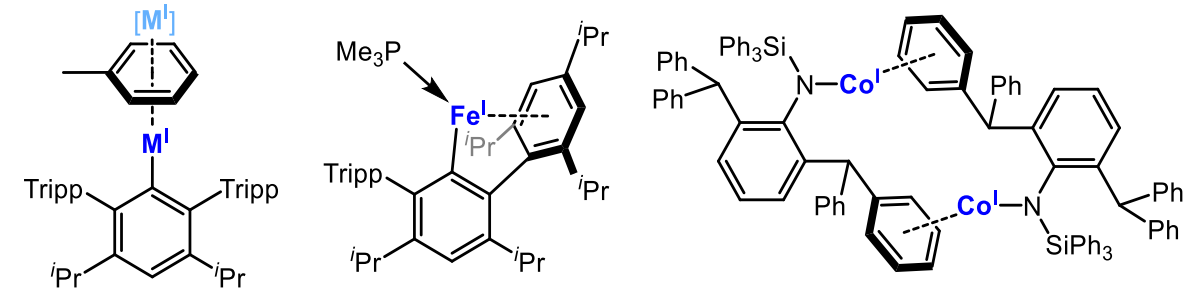

Mononuklear: **Cr**, **Fe**, **Co**
Dinuklear: **Mn**

Abbildung 27. Auswahl bekannter Aren-stabilisierter 3d-Metall(I)-Fragmente.[140,145–147]

Die Darstellung linearer heteroleptischer Spezies erfolgt auf Grundlage unterschiedlicher Synthesestrategien. So wurden die Komplexe [Cr(LB)Ar‘] (LB = THF, PMe_3; Ar‘ = 2,6-(Trip)$_2$-3,5 (^{i}Pr)$_2$-C_6H mit Tripp = 2,4,6-Tri-*iso*-propylphenyl), die beiden ersten literaturbeschriebenen linearen 3d-Metall(I)-Verbindungen, durch Reduktion des Chromchlorid Präkursors [Cr(Ar’)Cl] mit KC_8 in THF (und im Fall von [Cr(Ar‘)PMe_3] in Anwesenheit von PMe_3) unter Abspaltung von KCl erhalten.[150] Auf eine ähnliche Weise konnten die Verbindungen [Ni(IDipp)L] (L = −N(SiMe$_3$)$_2$, −NH(Dipp)) synthetisiert werden. Dabei wurde das dimere [(IDipp)Ni(μ-Cl)]$_2$ mit den entsprechenden Alkalisalzen NaN(SiMe$_3$)$_2$ und LiNH(Dipp) in einer Salzeliminierungsreaktion umgesetzt (**Schema 9**).[136]

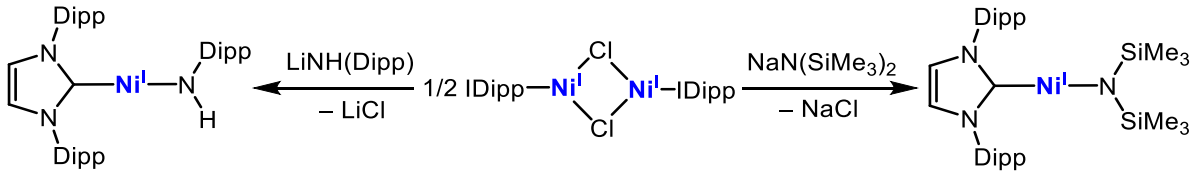

Schema 9. Synthese der heteroleptischen Ni(I)-Spezies [Ni(IPr)R] (R = −N(H)Dipp, −N(SiMe$_3$)$_2$).[136]

Heteroleptische Metall(I)-Spezies können auch ausgehend von homoleptischen Metall(II)-Präkursoren synthetisiert werden (**Schema 10**). In einer Eintopf-Synthese kann der Nickel(II)-Komplex [Ni(N(Dipp)SiMe$_3$)] mit KC_8 zu [KNi(N(Dipp)SiMe$_3$)] reduziert werden, bevor die schwache Säure NEt_3*HCl (Triethylamin Hydrochlorid) zugegeben wird. Nach Freisetzung des Amins HN(Dipp)SiMe$_3$ und KCl wird die entstehende intermediäre Ni(I)-Spezies mit einem Äquivalent IDipp bzw. PMe_3 abgefangen.[138] Im Laufe der Jahre konnte die Reihenfolge der einzelnen Syntheseschritte variiert werden. Im analogen System basierend auf Eisen (und später auch Kobalt) wurde beispielsweise erst die Säure zugegeben, bevor die Substitution eines Liganden durch das NHC erfolgte. Die entstandene Fe(II)-Chlorido-Spezies

wurde anschließend unter Abspaltung des Chlorido-Liganden mit interkaliertem Kalium (KC_8) reduziert.[143,151]

In beiden Eintopf-Synthesen konnten die Intermediate weder isoliert noch charakterisiert werden. Die Möglichkeit, trigonale Chlorido-Spezies des allgemeinen Typs [(NHC)MCl(L)] zu reduzieren, konnte erst drei Jahre später am Beispiel von [(IDipp)MCl(N(SiMe$_3$)$_2$)] (M = Fe, Co) bewiesen werden.[139]

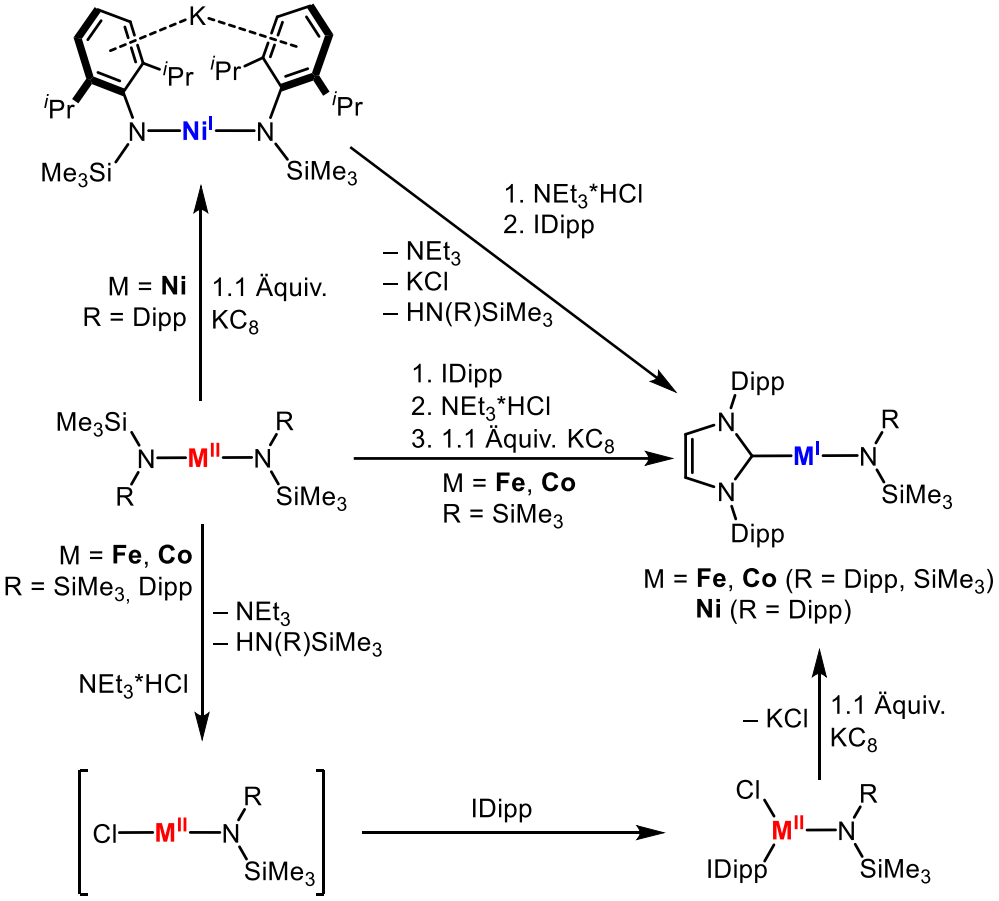

Schema 10. Darstellung heteroleptischer Metall(I)-Verbindungen ausgehend von Metall(II)-Vorläufern.[138,143,151]

Die beiden Komplexe [(IDipp)MCl(N(SiMe$_3$)$_2$)] (M = Fe, Co) besitzen hohe magnetische Momente von 5.91 μ_B (Fe) und 6.25 μ_B (Co) bei Raumtemperatur.[139] Dies ist sehr ungewöhnlich, da der Wert im Fall von Kobalt höher ist als der für ein freies Co(I)-Ion erwartete Wert von μ_{eff} = 5.59 μ_B. Diese anfänglich unerklärbaren μ_{eff} wurden durch das formale Vorliegen von M(II)-Zentren, die über Austauschwechselwirkungen nach HEISENBERG und DIRAC VAN VLECK mit einem Elektron (S = 1/2) wechselwirken und dieses über den gesamten Liganden bzw. Komplex delokalisieren, bewiesen. Die vorliegenden Elektronenkonfigurationen sind somit „3d^n + e$^-$“ (n = 6 (Fe), 7 (Co)) mit theoretischen magnetischen Momenten von 6.93 μ_B (Fe) und 6.86 μ_B (Co).[139]

2.4.2 Homoleptische 3d-Metall(I)-Komplexe

Monovalente, homoleptische 3d-Übergangsmetallkomplexe von Chrom bis Nickel sind erst seit einem knappen Jahrzehnt bekannt.[152] Im Gegensatz zu den heteroleptischen Derivaten tragen sie zwei identische Liganden. Sind diese neutral, entstehen kationische Spezies. Anionische Liganden erzeugen dagegen einfach negativ geladene Komplexionen.

Kationische 3d-Metall(I)-Komplexe

Kationische Metall(I)-Komplexe werden durch zwei neutrale Liganden stabilisiert. Verwendung finden *N*-heterozyklische Carbene oder auch zyklische Alkylaminocarbene.[153–168]

Die Möglichkeit, Metallatome linear durch zwei NHCs zu stabilisieren, entdeckte ARDUENGO im Jahr 1994.[165] Durch Reaktion des NHCs IMes (1,3-Dimesitylimidazol-2-yliden) mit olefinischen Ni(0) und Pt(0) Komplexen erhielt er die beiden Verbindungen [M(IMes)$_2$] (M = Ni, Pt) (**Abbildung 28**).[165,166] Er postulierte eine Übertragung der Elektronendichte vom Carben auf das Metallfragment durch dπ-pπ-Wechselwirkungen.

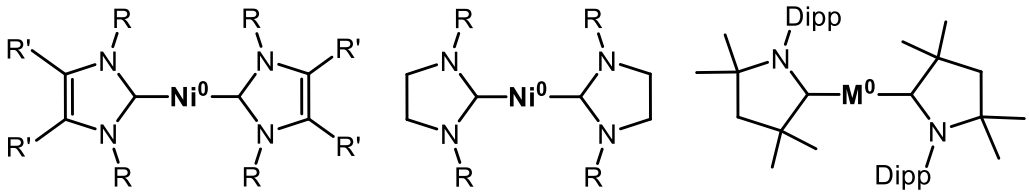

Abbildung 28. Bekannte lineare Metall(0)-Komplexe der 3d-Metalle von Cr **–** Ni.[155–160,165–168]

2012 untersuchten DENG und seine Mitarbeiter mögliche intramolekulare C(sp^3)−H Aktivierungen an niedervalenten Co(I)-Spezies. Während die Umsetzung der trigonalen Co(I)-Verbindung [Co(Cl)(PPh$_3$)$_3$] mit Natrium-Amalgam gewünschtes Ergebnis lieferte, führte die Addition von Na[BPh$_4$] zu [Co(Cl)(PPh$_3$)$_3$] zur ersten ionischen und linearen Verbindung, BPh$_4$[Co(IMes)$_2$], unter Abspaltung von NaCl (**Schema 11**).[169] BPh$_4$[Co(IMes)$_2$] weist bei Raumtemperatur ein magnetisches Moment von 4.1 μ_B auf, welches stark vom Spin-Only-Wert von 2.83 μ_B (S = 1) abweicht. Dies lässt auf einen signifikanten Beitrag des Bahndrehimpulses zum *High-Spin*-Co(I)-Zentrum mit einer d^8-Elektronenkonfiguration schließen. Weitere

kationische Komplexe auf Basis von Eisen und Kobalt mit NHC-Derivaten konnten in den darauffolgenden Jahren erzielt werden.[154,170]

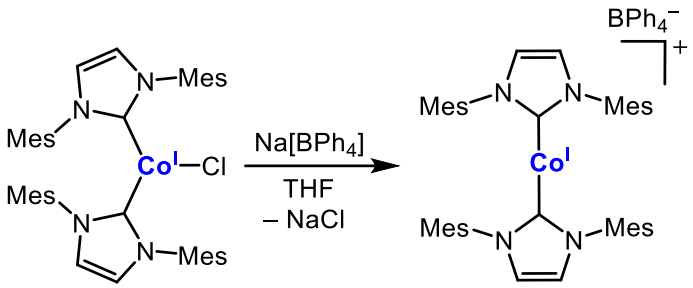

Schema 11. Darstellung des ersten homoleptischen M(I)-Komplexes BPh$_4$[Co(IMes)$_2$].[169]

Der Arbeitsgruppe um ROESKY gelang es, homoleptische cAAC-stabilisierte 3d-Metall(I)-Komplexe von Chrom bis Eisen zu isolieren,[158,164,171] wobei das Eisen-Derivat zeitgleich auch von PETERS, DENG und deren Mitarbeitern publiziert wurde.[172,173] Durch ihre magnetischen Eigenschaften, wie eine langsame magnetische Relaxation, war diese Verbindung von besonderem Interesse.[164,172]

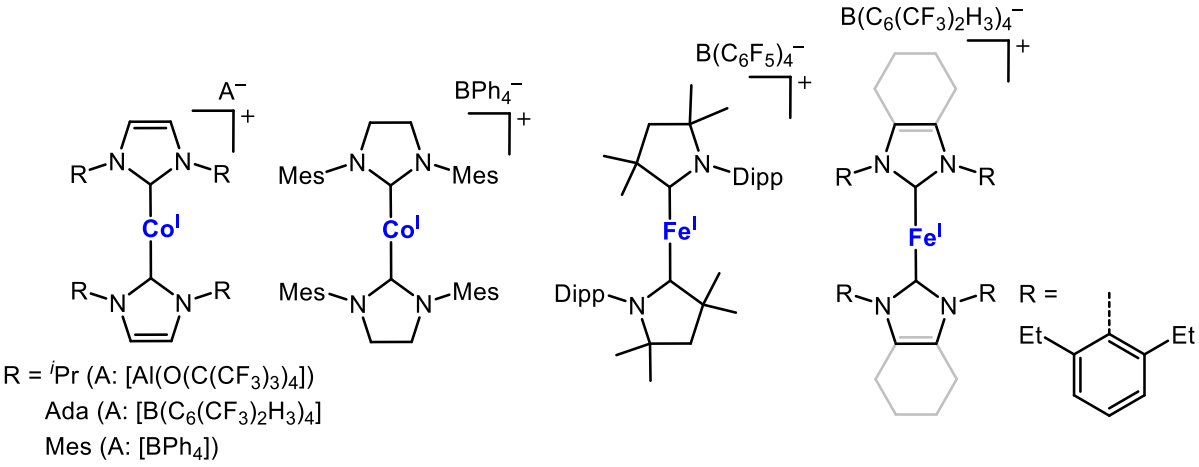

Abbildung 29. Bekannte kationische 3d-Metall(I)-Komplexe.[153,154,161–164]

Anionische 3d-Metall(I)-Komplexe

(Quasi-)lineare, anionische 3d-Metall(I)-Komplexe stellen die für diese Arbeit wichtigste Gruppe zweifach-koordinierter monovalenter Verbindungen dar. In ihnen koordinieren zwei monoanionische, sterisch anspruchsvolle Liganden L der Form −C(SiMe$_3$)$_3$, −N(Ar)SiR$_3$ oder –N(SiR$_3$)$_2$ an das zentrale Metallatom. Bisherige Vertreter wurden bisher ausschließlich durch Reduktion ihres linearen Metall(II)-Vorläufers [ML$_2$] mit KC$_8$ synthetisiert.[77,141,174] Das Kalium-Kation wird meist durch eines der Maskierungsreagenzien (m) 18-Krone-6 (18c6, 1,4,7,10,13,16-Hexaoxazyklooctadecan) oder crypt-222 (4,7,13,16,21,24-Hexaoxa-1,10-diazabizyklo[8.8.8]hexacosan) komplexiert und so von der anionischen

Komplexeinheit separiert (**Abbildung 30**). Die zentralen Metall(I)-Atome erfahren geometriebedingt nur eine schwache Ligandfeldaufspaltung und befinden sich somit im *High-Spin*-Zustand.[70,77,79,141,174–179]

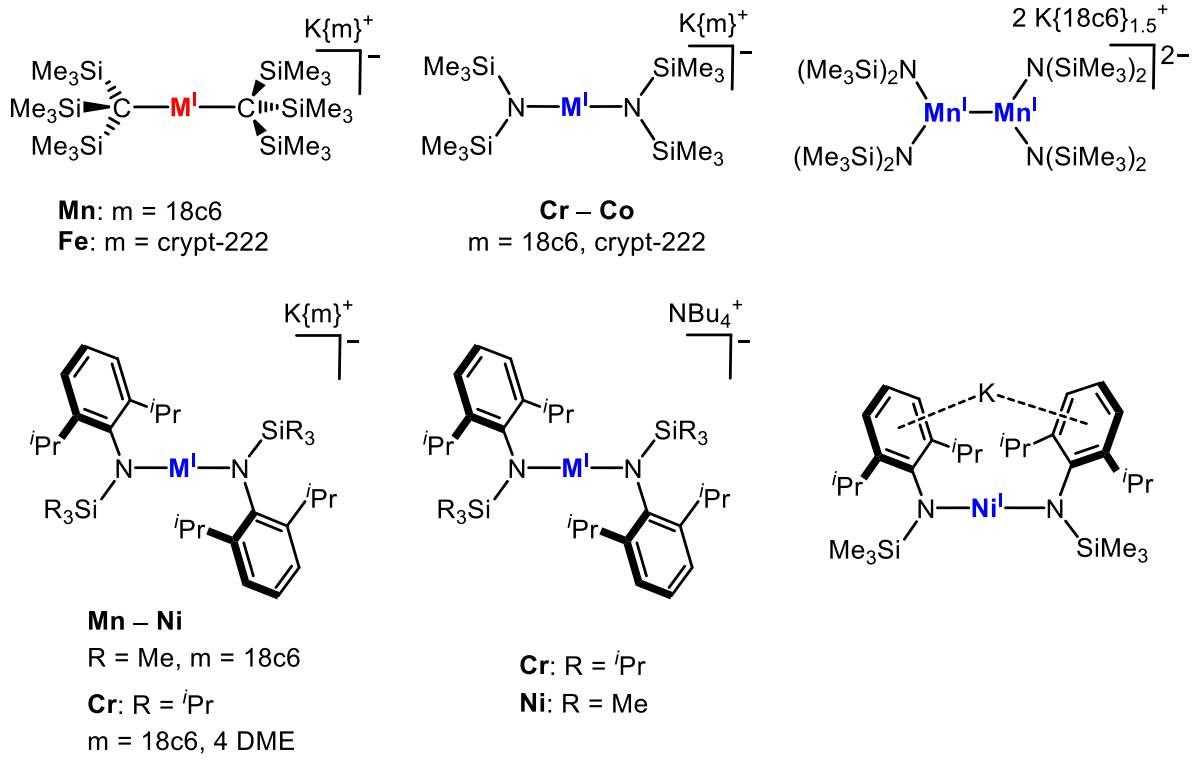

Abbildung 30. Übersicht bekannter anionischer Metall(I)-Verbindungen.[70,77,79,141,174–179]

Die Methanid-Komplexe des Typs $[M(C(SiMe_3)_3)_2]^-$ (M =Mn, Fe) weisen eine perfekt lineare C−M−C-Achse von 180° auf.[70,174] Gerade das Eisen-Derivat erlangte besonderes Interesse, da es phänomenale magnetische Eigenschaften besitzt und sich wie ein Einzelmolekülmagnet verhält.[70] Die experimentell bestimmte Relaxationsbarriere von U_{eff} = 226 cm^{-1} bei einer Blocktemperatur T_B = 4.5 K ist die zweithöchste Barriere, die für einen mononuklearen 3d-Metallkomplex erreicht werden konnte. Sie wurde seither nur von der Co(II)-Spezies $[Co(C(SiMe_2ONaph)_3)_2]$ übertroffen (vgl. Kapitel 2.2.3).[68,70] Ein Aspekt, der zu diesen erstaunlichen Werten beiträgt, ist die hohe Symmetrie im Komplex, welche durch den dreizähnigen Liganden $-C(SiMe_3)_3$ möglich ist.[70]

WERNCKE reduzierte einige Zeit später die dimeren Metall(II)-Verbindungen $[M(N(SiMe_3)_2)_2]_2$ (M = Cr − Co) ebenfalls mit KC_8 in Anwesenheit von 18c6 bzw. crypt-222 (**Schema 12**).[79,176] Im Gegensatz zu ihren divalenten Analoga liegen die anionischen Silylamid-Metall(I)-Komplexe $[M(N(SiMe_3)_2)_2]^-$ (M = Cr, Fe, Co) trotz des verhältnismäßigen kleinen sterischen Anspruchs der Liganden auch im Festkörper als Monomer mit einer linearen Koordination von 180° am Zentralatom vor.[79,176] Die

zusätzliche Darstellung des Eisen-Komplexes aus den trigonalen Metall(II)-Vorläufern [Fe(L)(N(SiMe$_3$)$_2$)$_2$] (L = THF, PCy$_3$) beweist ebenfalls, dass eine lineare Geometrie des Edukts nicht zwingend erforderlich ist.[176]

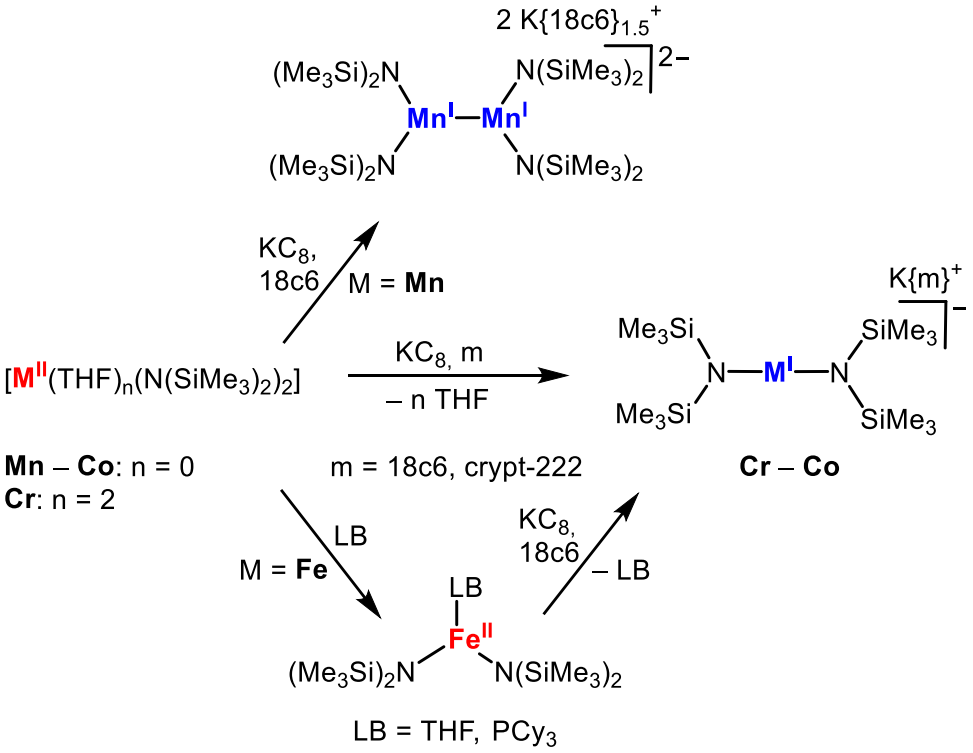

Schema 12. Synthese der linearen 3d-Metall(I)-Komplexe K{m}[M(N(SiMe$_3$)$_2$)$_2$] (M = Cr – Co; m = 18c6, crypt-222).[79,176]

Quantenchemische Berechnungen der Eisen-Derivate K{m}[Fe(N(SiMe$_3$)$_2$)$_2$] (m = 18c6, crypt-222) bestätigen, dass das dz²-Orbital konträr zu den Metall(II)-Analoga durch Wechselwirkung mit dem 4s-Orbital energetisch stark abgesenkt ist (**Abbildung 31**).[176] Die magnetischen Momente von 5.12 μ_B (18c6) und 5.14 μ_B (crypt-222) bei Raumtemperatur liegen höher als der erwartete Spin-Only-Wert eines S = 3/2-Spinsystems von 3.87 μ_B und nahe dem Wert eines freien Ions mit d^7-Konfiguration (d^7: 5.19 μ_B). Dies lässt auf einen hohen Beitrag des Bahndrehimpulses schließen. Gemessene Energiebarrieren von 43 cm^{-1} (18c6) und 64 cm^{-1} (crypt-222) sind jedoch circa viermal kleiner als im Methanid-Komplex K{crypt-222}[Fe(C(SiMe$_3$)$_3$)$_2$]. Berechnungen zur Folge liegen die d-Orbitale in [Fe(C(SiMe$_3$)$_3$)$_2$]$^-$ energetisch höher, wodurch das größere U_{eff} erklärt wird. Des Weiteren verursachen die freien Elektronenpaare der Amidliganden im anionischen [Fe(N(SiMe$_3$)$_2$)$_2$]$^-$-Fragment eine Aufspaltung der d$_{yz}$- und d$_{xz}$-Orbitale, wodurch die Symmetrie auf C$_{2V}$ reduziert wird. Folglich ist der Beitrag des Bahndrehimpulses und die magnetische Anisotropie vermindert, wodurch die magnetische Relaxation beschleunigt wird (vgl. Kapitel 2.2.3).[176]

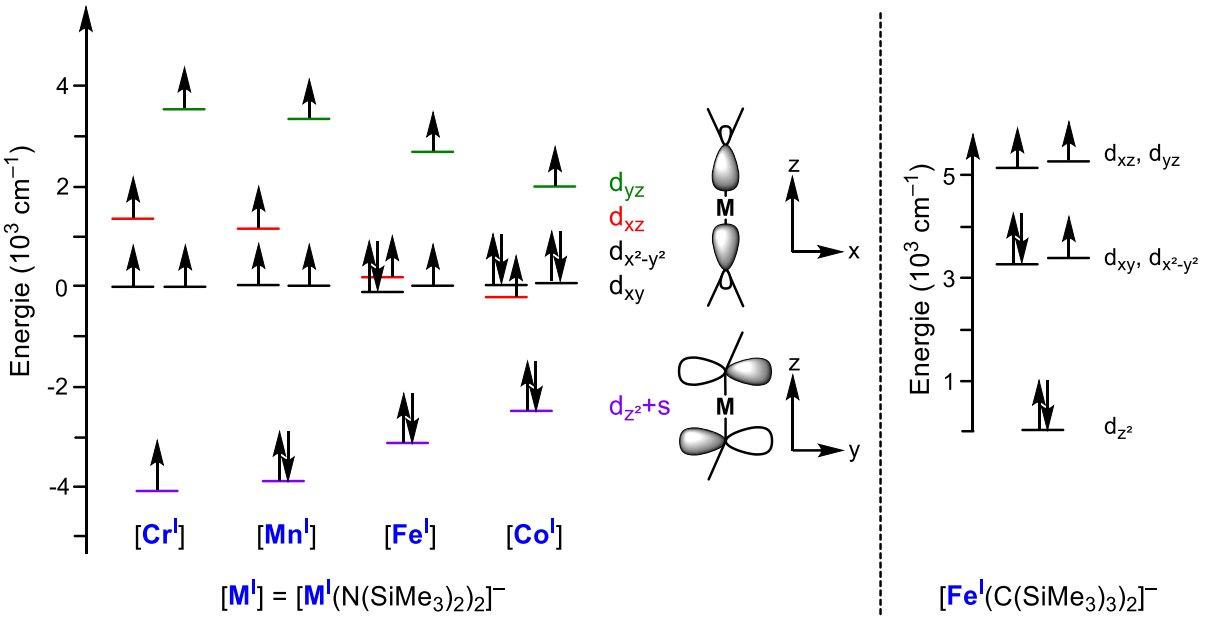

Abbildung 31. Berechnete Grenzorbitaldiagramme für K{18c6}[M(N(SiMe$_3$)$_2$)$_2$] (M = Cr – Co) (links; Berechnungen für Mn anhand des Fe-Derivats) und K{crypt-222}[Fe(C(SiMe$_3$)$_3$)$_2$] (rechts).[70,79,176]

Die Reduktion der analogen Mn-Spezies [Mn(N(SiMe$_3$)$_2$)$_2$] führt zum sehr reaktiven und nur kurzlebigen Dimer (K{18c6})$_2$[Mn(N(SiMe$_3$)$_2$)$_2$]$_2$. Konträr zum dimeren Mn(II)-Präkursor liegen im Festkörper keine verbrückten Silylamid-Liganden, sondern eine nicht-Ligand-stabilisierte Mn−Mn-Bindung der Länge 2.721 Å vor. Trotz Kühlung disproportioniert die dunkelviolette Verbindung schnell zu K{18c6}N(SiMe$_3$)$_2$, K{18c6}[Mn(N(SiMe$_3$)$_2$)$_3$] und elementarem Mangan.[79] Die langfristige Stabilisierung eines Mangan(I)-Ions war nur durch die Verwendung des sterisch anspruchsvolleren Ligandsystems −N(Dipp)SiMe$_3$ möglich. In K{18c6}[Mn(N(Dipp)SiMe$_3$)$_2$] zeigt das Zentralatom eine leicht gewinkelte Geometrie auf (N−Mn−N 167.12(14)°).[79]

Neben dem Mangan-Derivat existiert die Serie [M(N(Dipp)SiMe$_3$)$_2$]$^-$ auch für die Metalle Eisen bis Nickel, wobei im Fall von Eisen zwei zusätzliche Diethylether-Moleküle an das Kalium-Kation koordinieren.[177] Aufgrund der verhältnismäßigen schwachen Donoreigenschaften von Et$_2$O kann dieser während eines Farbumschlags des Komplexes von grün zu orange durch Trocknung im Vakuum zersetzungsfrei entfernt werden. Gerade für die Eisen-haltige Verbindung war das Interesse an den magnetischen Eigenschaften sehr groß. Eine leichte Winkelung der N−Fe−N-Achse von circa acht Grad verhindert jedoch einzelmolekülmagnetisches Verhalten. Demgegenüber besitzen die Strukturen von Kobalt und Nickel eine lineare Koordination am Zentralatom. Zusammengefasst stimmen die experimentell erlangten Werte magnetischer Messungen für Eisen und Nickel nur schlecht mit simulierten Berechnungen überein. Die Behauptungen einer großen axialen Anisotropie und eines

erhöhten Beitrags des Bahndrehimpulses *L* zu μ_{eff} für Fe(I) und Co(I) als auch die Behauptung eines verringerten Beitrags von *L* im Fall von Ni(I) sind daher mit Vorsicht zu behandeln.[48,177]

Da der Magnetismus in Metall(I)-Komplexen noch nahezu unerforscht ist, ist ein besseres Verständnis der Eigenschaften dieser Systeme und im Speziellen von Eisen(I)-Derivaten sehr wichtig. Die d^7-Elektronenkonfiguration eines Eisen(I)-Atoms ist zu der eines Co(II)-Atoms identisch. Des Weiteren werden Eisen(I)-Spezies in vielen (bio)chemischen Prozessen als reaktive Intermediate postuliert.[180]

Wie bereits angedeutet, wird das Kalium-Gegenion in anionischen (quasi-)linearen 3d-Metall(I)-Komplexen hauptsächlich durch einen Kryptanden stabilisiert. Anstelle dieser Maskierungsreagenzien konnte das K^+-Ion im Fall von Chrom durch vier Äquivalente DME (= 1,2-Dimethoxyethan) komplexiert werden (**Schema 13**).[77] Ein Austausch des anorganischen Ions durch ein NBu_4^+-Kation war durch die anschließende Umsetzung mit [NBu_4]Br möglich. NBu_4[Cr(N(Dipp)Si^{i}Pr)$_2$] ist ein seltenes Beispiel eines anionischen 3d-Metall(I)-Komplexes mit einem organischen Gegenion. Die Triebkraft für den Kationenaustausch liegt in der Bildung des in Diethylether nahezu unlöslichen Salzes KBr.[77]

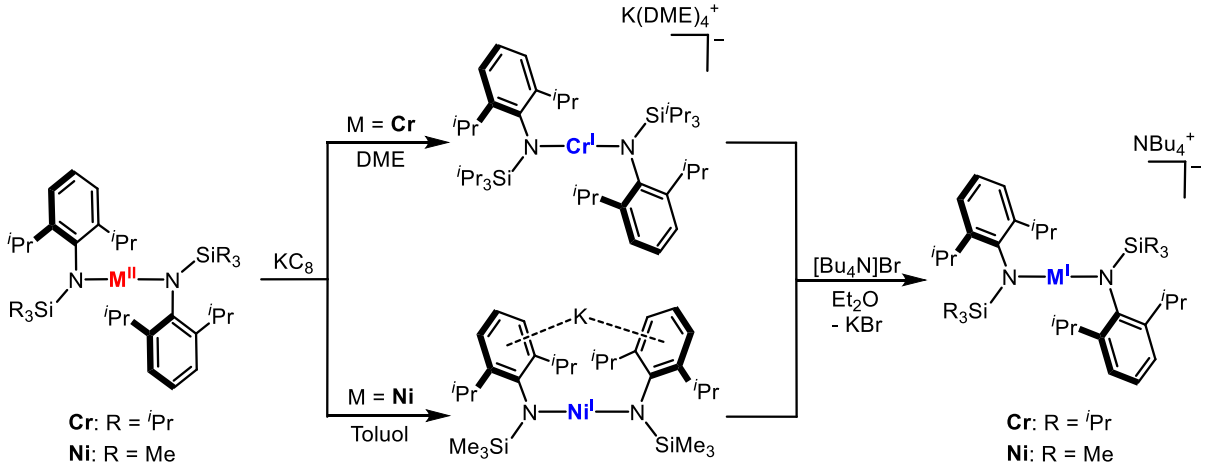

Schema 13. Darstellung der Kryptand-freien Komplexe K(DME)$_n$[M(N(Dipp)SiR$_3$)$_2$] (M = Cr, (R = ^{i}Pr, n = 4); Ni (R = Me, n = 0)) und NBu_4[M(N(Dipp)SiR$_3$)$_2$] (M = Cr (R = ^{i}Pr); Ni (R = Me).[77,141]

Der Komplex [KNi(N(Dipp)SiMe$_3$)$_2$] ist das bisher einzige literaturbekannte Beispiel, in dem das Kalium-Kation intramolekular ohne weitere Hilfsreagenzien fixiert wird (**Schema 13**).[141] In der monomeren und formal neutralen Verbindung befindet sich das Kation zwischen zwei Arylsystemen gegenüberliegender Silylamid-Liganden. Verglichen mit der ladungsseparierten Spezies K{18c6}[Ni(N(Dipp)SiMe$_3$)$_2$] (1.8493(9) Å) bleiben die Ni−N-Bindungslängen (beide 1.8436(15) Å) nahezu unverändert. Die Ni−K Distanz beträgt 3.4428(7) Å. Die Geometrie am Nickelzentrum

ist weiterhin linear. Während in der ladungsseparierten Ni(I)-Spezies ein Torsionswinkel von 180° vorliegt, verursacht die Reduktion von Ni(II) zu Ni(I) eine Rotation entlang der N−Ni−N-Achse mit einer drastischen Minimierung des Torsionswinkels zu 0.131° bei Abwesenheit eines Maskierungsreagenz. An diesem Beispiel ist zu erkennen, dass nur minimale Rotationsbarrieren in $[M(N(Dipp)SiMe_3)_2]^{0,-}$ vorliegen müssen. Die Relevanz der sekundären Dispersionswechselwirkungen, welche die sterisch und elektronisch ungesättigten Metall-Zentren maßgeblich stabilisieren sollen, ist bisher ungeklärt (vgl. Kapitel 2.2.5).[76] Die Umsetzung von $[KNi(N(Dipp)SiMe_3)_2]$ mit $[NBu_4]Br$ verursachte analog zu $K(DME)_4[Cr(N(Dipp)Si^iPr_3)_2]$ einen Austausch des Kations.[141]

2.5 Reaktivität linearer 3d-Metall(I)-Komplexe

In einer Vielzahl biologischer, synthetischer und industrieller Reaktionen spielt die Aktivierung von kleinen Molekülen oder funktionellen Gruppen eine wichtige Rolle.[181–184] Die Präsenz von Übergangsmetallverbindungen und deren katalytische Fähigkeiten sind dabei essenziell, wobei ablaufende Mechanismen bis heute häufig nicht vollständig verstanden sind. Der Grund ist die Generierung kurzlebiger und hochreaktiver Schlüsselintermediate während einer Reaktion. In ihnen liegen die Metallzentren in für sie außergewöhnlichen, oft niedrigen, Oxidationsstufen oder/und seltenen Koordinationsmodi vor. Die Erforschung der Reaktivität von niederkoordinierten Metallverbindungen, im Speziellen von mononuklearen linearen 3d-Metall(I)-Komplexen, kann daher sehr aufschlussreich sein.

Kationische Metall(I)-Fragmente der Form $[M(cAAC)_2]^+$ können beispielsweise mit KC_8 oder Natrium-Amalgam zu ihren nullvalenten Analoga $[M(cAAC)_2]$ reduziert werden.[172] Im Fall von Mangan führt die Reduktion jedoch zu einer Mn(I)-Verbindung, mit einem ungepaarten und delokalisierten Elektron (Spin 1/2) auf den cAAC-Liganden. Aufgrund dieser Eigenschaft ist mit dem Mangan-Derivat sogar die Spaltung von Wasserstoff möglich.[158] Der Erfolg dieser Synthesen ist allerdings zum Großteil den Elektronenakzeptor-Eigenschaften der Carbenliganden zuzuschreiben.

In Diethylether führt die Reduktion eines kationischen Eisen(II)-Dihalogenid-Derivats mit KC_8 und anschließender Zugabe von $Na[BAr^F_4]$ zur linearen Eisen(I)-Verbindung $BAr^F_4[(Fe(sIMes)_2]$. In THF dagegen koordiniert ein THF-Molekül äquatorial an das Eisenzentrum und der T-förmige Komplex $BAr^F_4[(Fe(THF)(sIMes)_2]$ wird generiert. Die Koordination ist jedoch reversibel.[154]

Reaktivitätsstudien neutraler und anionischer 3d-Metall(I)-Komplexe wurden bislang hauptsächlich in den Arbeitsgruppen von TILLEY und WERNCKE durchgeführt (**Schema 14**).[77,138,143,178–180,185–190]

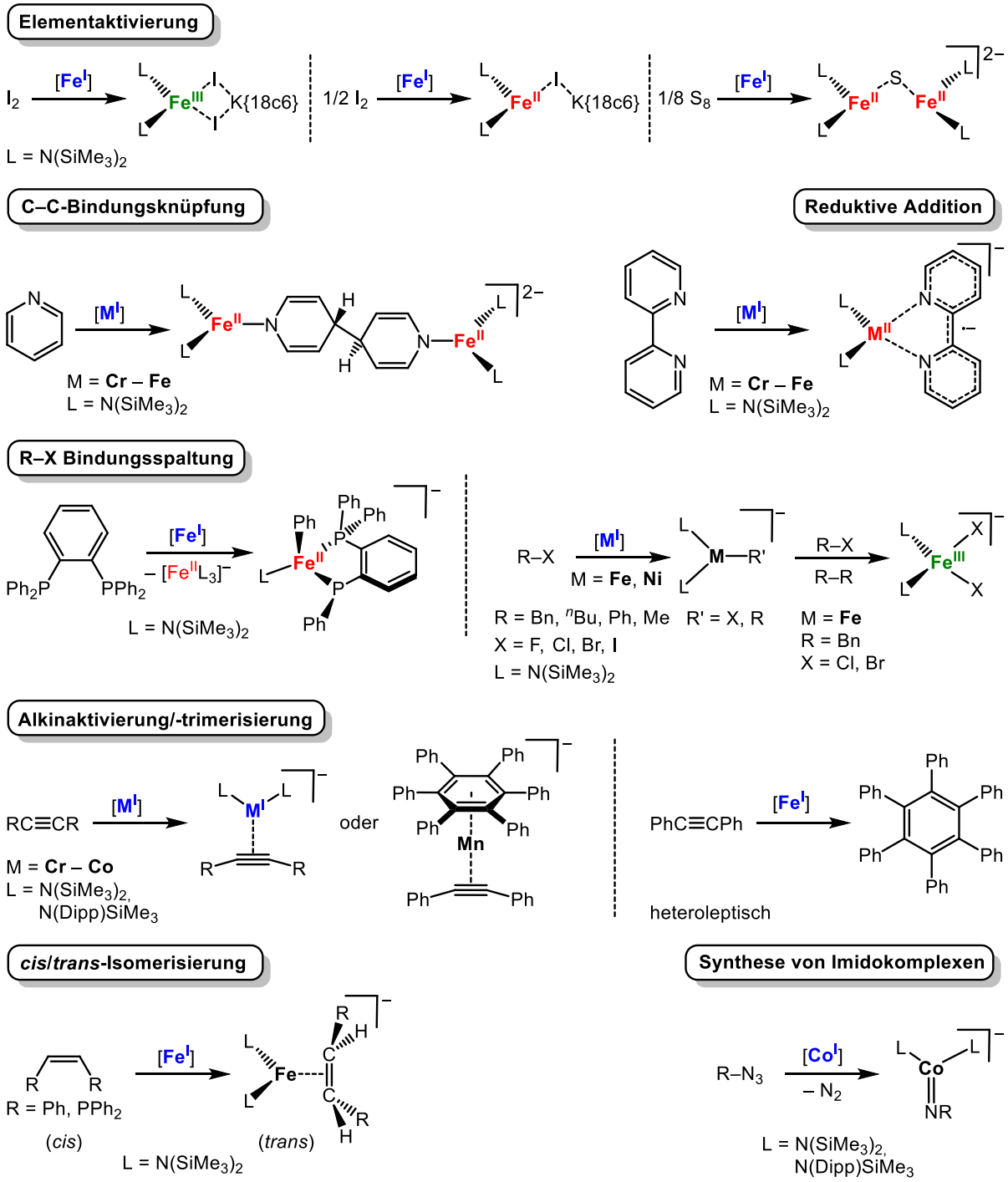

Schema 14. Übersicht über bekannte Reaktivitäten linearer Metall(I)-Komplexe. Kationen werden aus Gründen der Übersichtlichkeit nicht gezeigt.[77,138,143,178–180,185–190]

Homoleptische (quasi-)lineare Metall(I)-Komplexe können Elemente, wie Chalkogene oder Halogene, aktivieren.[77,180,186] Die Möglichkeit zur Elektronenübertragung auf ein Substrat zeigten die Metall(I)-Verbindungen auch bei der reduktiven Addition von 2,2'-Bipyridin[185] oder der reduktiven Kopplung von (Fluoro-)Pyridin in *para*-Position.

Beim Einsatz von Perfluoropyiridin konnte sogar eine C−F-Bindungsspaltung nachgewiesen werden, wodurch seltene Metall(II)-Fluoride entstehen.[188]
Durch Umsetzung von [KNi(N(Dipp)SiMe$_3$)$_2$] mit Methyliodid ist es möglich, eine Methyl-Gruppe reduktiv an das Nickel-Zentrum zu addieren.[141] Dieses Ergebnis konnte ebenfalls mit der ladungsseparierten Verbindung K{18c6}[Fe(N(SiMe$_3$)$_2$)$_2$] erzielt und auf aromatische (Phenyllithium, PhLi) bzw. benzylische (Benzylkalium, BnK) Substrate erweitert werden.[186] Im Produktgemisch waren jeweils ein seltenes dreifach-koordiniertes Eisen(II)-Halogenid und ein Organoeisen(II)-Komplexen zu finden. Mit Ausnahme von BnX (X = Cl, Br) fand trotz Zugabe weiterer Äquivalente Organohalogenid keine weitere Reaktion mit den trigonalen Eisen(II)-Komplexen statt. Die C−X-Bindungsspaltung erfolgt über einen radikalischen Ein-Elektronen-Prozess, wie die Umsetzung mit der Radikaluhr Zyklopropylmethylbromid aufklärte.[186] Die Reaktivität gegenüber C−X-Bindungen von weiteren 3d-Metallen, wie Mangan und Kobalt, wurde bisher nicht untersucht.
Neben diesen Ergebnissen zeigen (quasi-)lineare Metall(I)-Komplexe auch interessante Reaktivitäten gegenüber Olefinen auf. Diese werden im nächsten Kapitel ausführlicher behandelt, da sich die vorliegende Arbeit unter anderem mit intermolekularen Alkinumsetzungen bzw. intramolekularen Alkensubstituenten beschäftigt. Es wird sowohl auf die theoretischen Hintergründe von Metall-Olefin-Wechselwirkungen als auch bekannte Reaktionen zwischen 3d-Metall(I)-Komplexen und C−C-Mehrfachbindungen eingegangen. Im Anschluss werden auf analoge Weise Organoazide vorgestellt, bevor deren Reaktion mit anionischen 3d-Metall(I)-Komplexen und die dabei entstehenden Imidokomplexe beschrieben werden.

2.5.1 Reaktivität von 3d-Metall(I)-Komplexen gegenüber Olefinen

Das DEWAR-CHATT-DUNCANSON-Modell

In der metallorganischen Chemie sind Wechselwirkungen zwischen niedervalenten 3d-Metallen und C−C-Mehrfachbindungen von fundamentaler Bedeutung. Sie sind Grundlage vieler katalytischer Prozesse wie der Bindungsmetathese, der Alkintrimerisierung oder allgemeiner in Zyklisierungs- bzw. Oligomerisierungs-mechanismen.[191–194] Aus diesem Grund werden bereits einige Übergangsmetall-katalysierte Mechanismen, wie die PAUSON-KHAND-Zykloadditionsreaktion[192,194,195] oder die SIMMONS-SMITH-Zyklopropanierung,[192,196] in der Literatur beschrieben.

Um Reaktionswege besser steuern und vorhersagen zu können, ist die Kenntnis der Metall-Olefin-Wechselwirkung von fundamentaler Bedeutung. Bereits 1951 schrieb DEWAR ein Review über die ‚Theorie von π-Komplexen', welche später durch CHATT und DUNCANSON in das heute bekannte DEWAR-CHATT-DUNCANSON-Modell erweitert wurde.[197,198] In diesem Modell wird die Bindungssituation zwischen einem Übergangsmetall und einer Mehrfachbindung, z. B. in Alkenen, Alkinen, oder kleinen Molekülen (CO etc.), beschrieben. Laut dem Modell überträgt das π-azide Olefin Elektronendichte aus seinem HOMO (höchstes besetztes Molekülorbital; engl. highest occupied molecular orbital) in ein leeres d-Orbital mit passender Symmetrie des Metallzentrums, wodurch sich eine σ-Bindung bildet (**Abbildung 32**, links). Gleichzeitig ist das Metallatom in der Lage, Elektronendichte über ein gefülltes d-Orbital in das leere π*-Orbital (LUMO; niedrigstes unbesetztes Molekülorbital; engl. lowest unoccupied molecular orbital) des Olefins zurück zu donieren (π-Rückbindung). Beide Effekte reduzieren die Bindungsordnung der C−C Mehrfachbindung unter Aufweitung der Bindungslänge. Im Fall eines Alkins können weitere π-Bindungen zwischen Metall und Olefin diesen Effekt verstärken.

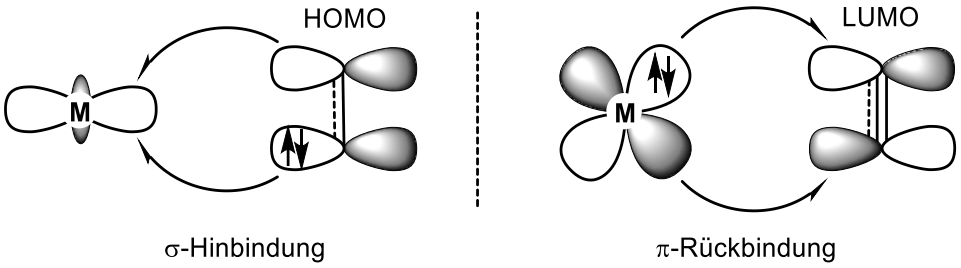

Abbildung 32. σ-Hin (links) und π-Rückbindung (rechts) einer Interaktion zwischen einem 3d-Metall und einem Olefin nach dem DEWAR-CHATT-DUNCANSON-Modell. Weitere π-Bindungen im Falle eines Alkins sind nicht gezeigt.[199]

Die Stärke der Wechselwirkungen ist von mehreren Faktoren abhängig. Sind starke π-Akzeptor-Coliganden, wie CO, präsent, konkurrieren diese mit der C−C Mehrfachbindung um die Elektronendichte des Metallzentrums und die π-Rückbindung zum Olefin wird geschwächt. Mit starken σ-Donor-Liganden am Zentralatom wird die π-Rückbindung zum Olefin hingegen verstärkt. Einen weiteren Einfluss hat das Olefin selbst. Bindet es stark elektronegative Substituenten, wie in Tetrafluorethen, besitzt es starke π-Akzeptor-, aber schwache σ-Donoreigenschaften. Dies macht sich durch eine verkürzte Metall−Olefin-Bindung und eine verlängerte C−C-Mehrfachbindung bemerkbar.

Durch die Koordination eines Olefins an ein Metallfragment wird die Planarität eines Alkens bzw. die Linearität eines Alkins der organischen Verbindung aufgehoben. Nach

der BENT'schen Regel nimmt die Abwinklung mit steigender Elektronegativität der Substituenten am Olefin zu, da elektronegativere Liganden zur Ausbildung von Hybridorbitalen mit erhöhtem p-Orbital-Anteil neigen.[200] Zudem führt eine starke π-Rückbindung zur energetischen Absenkung des π*-Orbitals, wodurch eine d-p-Orbitalüberlappung begünstigt wird.

Ist die Abweichung der Planarität bzw. Linearität sehr groß, werden die vorliegenden Komplexe besser als Metallazyklopropane (Alken) bzw. -propene (Alkin) statt als π-Komplexe beschrieben (**Abbildung 33**). Die realen Bindungsverhältnisse liegen allerdings oft zwischen beiden Modellvorstellungen und müssen für jede Verbindung neu evaluiert werden.[199]

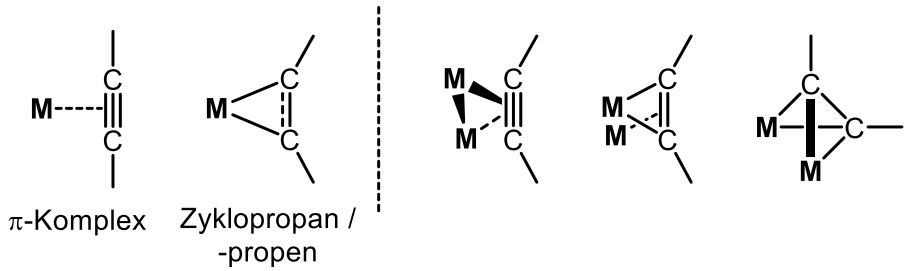

Abbildung 33. Mögliche Bindungsmodi in Metall-Alkin-Komplexen.[4,197,199,201]

Gleiche Überlegungen gelten für die Art des Metallzentrums. Während elektronenreiche Metallatome zur π-Komplex-Bildung neigen,[201,202] werden Olefin-Komplexe mit elektronenarmen Übergangsmetallen, wie Titan, besser als Metallazyklopropane/-propene mit zwei kovalenten Metall-Kohlenstoff-Bindungen beschrieben.[203,204]

Für Alkine lässt sich neben diesen beiden *side-on*-Koordinationen noch eine Bandbreite weiterer Koordinationsmodi beobachten. Diese sind jedoch nicht immer eindeutig und hängen stark von den unterschiedlichen Bindungspartnern und -typen ab.[4] In **Abbildung 33** ist eine Auswahl dieser Motive aufgelistet.

Niedervalente 3d-Metall-Alkin-Komplexe

In den meisten bekannten Übergangsmetall-Alkin-Komplexen der mittleren 3d-Reihe (M = Cr − Co) koordinieren Liganden wie Zyklopentadienyl (Cp), Carbonyl (CO) oder Phosphane (PR_3) an das zentrale Metallatom und verursachen ein starkes Ligandenfeld.[205–212] Durch Kombination mit einer hohen Koordinationszahl (KZ) am zentralen Atom bilden sich stabile *Low-Spin*-Komplexe aus. Demgegenüber konnten nur wenige niederkoordinierte 3d-Metall-Alkin-Komplexe (M = Cr − Co, KZ ≤ 4) im *High-Spin*-Zustand erhalten werden.

Erstmals war dies zwei Arbeitsgruppen im Jahr 2005 durch Umsetzung von β-Diketiminato- (nacnac-) Fe-Präkursoren mit einem Alkin möglich.[213–215] Während die Gruppe von HOLLAND einen dinuklearen [((nacnac)Fe)$_2$N$_2$]-Komplex mit einem Überschuss Alkin umsetzte,[213,214] addierte CHIRIK ein Äquivalent Alkin zu einer *in situ* Reduktion einer Eisen-Dichlorido-Verbindung mit Natrium-Amalgam und erhielt die *side-on*-Komplexe [(nacnac)Fe(RCCR)] (R = Ph, SiMe$_3$) (**Abbildung 34**, Mitte unten).[215] Die vorliegenden C≡C-Bindungslängen von circa 1.29 Å und magnetischen Momente von 2.9 μ_B (R = SiMe$_3$) und 3.2 μ_B (R = Ph) deuten auf eine rein koordinative Metall-Alkin-Wechselwirkungen hin. Nach dem CHATT-DEWAR-DUNCANSON-Modell werden sie daher am besten als π-Komplexe mit den Eisen-Zentren in der Oxidationsstufe +1 beschrieben.

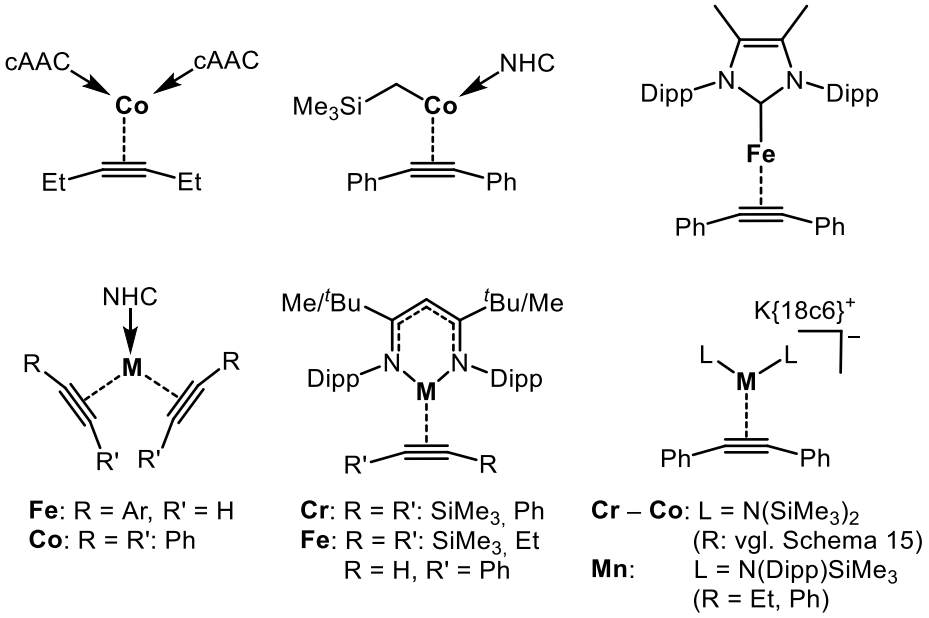

Abbildung 34. Bekannte 3d-Metall-Alkin-Komplexe im *High-Spin*-Zustand.[156,213–220]

Konträr dazu weisen die beiden analogen Chrom-Derivate [(nacnac)Cr(RCCR)] (R = Ph, SiMe$_3$) C−C Olefin-Bindungslängen von ca. 1.3 Å und magnetische Momente von 3.9 μ_B (R = SiMe$_3$) bzw. 3.6 μ_B (R = Ph) auf. Dies lässt auf eine Zweifachreduktion des Alkins und Chrom(III)-Zentren schließen, wodurch eher Metallazyklopropene vorliegen.[216–218]

Hinweise über Bindungssituationen und elektronische Eigenschaften in neu entwickelten Komplexen durch einen Vergleich bestehender Komplexe zu erlangen, ist kaum möglich. Die sterischen und elektronischen Einflüsse der verwendeten Ligandsysteme weichen dafür zu stark voneinander ab.

2020 gelang es MÜLLER, die Reihe der (quasi-)linearen Silylamid-3d-Metall(I)-Komplexe K{18c6}[M(N(SiMe$_3$)$_2$)$_2$] (M = Cr − Co) erfolgreich mit internen Alkinen

umzusetzen. Es wurden die trigonalen *side-on*-Komplexe K{18c6}[M(N(SiMe$_3$)$_2$)$_2$(η^2-RCCR)] (R = Ph (M = Mn, Fe, Co), R = SiMe$_3$ (M = Cr), R = Et, ^{n}Pr (M = Fe)) erhalten und röntgenkristallographisch analysiert (**Schema 15**).[84]

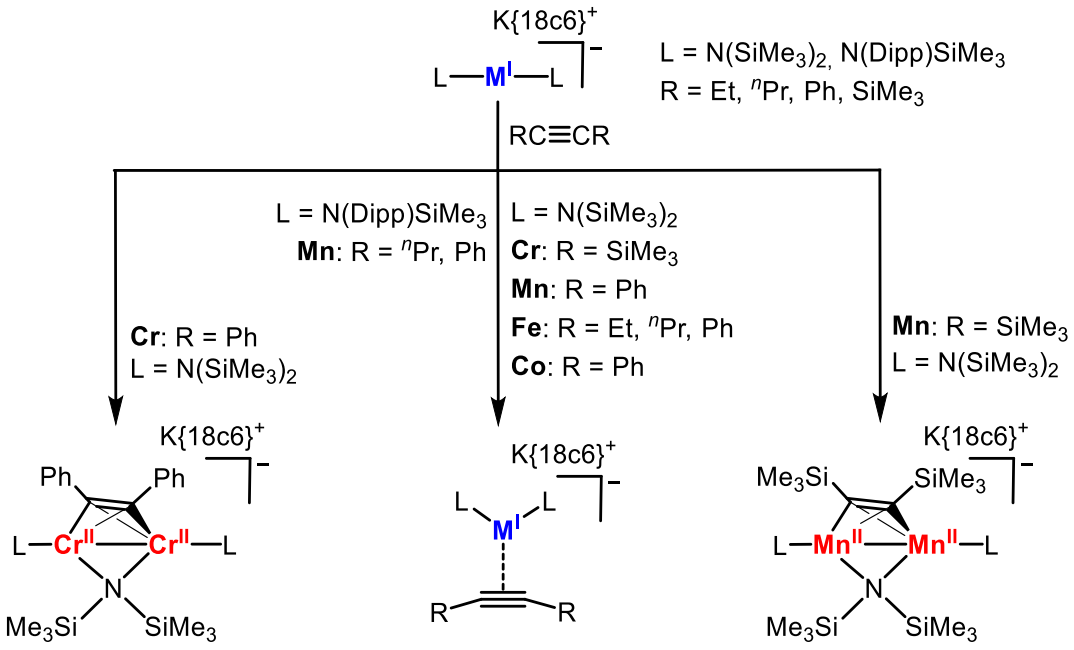

Schema 15. Darstellung niedervalenter 3d-Metall-Alkin-Komplexe der Metalle Chrom bis Kobalt mit dem flexiblen Ligandsystem –N(SiMe$_3$)$_2$.[84]

Die interessantesten Komplexe dieser Reihe sind die beiden Mangan-haltigen Vertreter K{18c6}[Mn(L)$_2$(RCCR)] (L = −N(SiMe$_3$)$_2$ (R = Ph), −N(Dipp)SiMe$_3$ (R = ^{n}Pr, Ph), **Schema 15**, Mitte). Sie sind die ersten niederkoordinierten Mangan-Alkin-Komplexe in einer *High-Spin*-Konfiguration. Während mit dem sterisch anspruchsvolleren Ligandsystem über längere Zeit hinweg stabile *side-on*-Mangan-Komplexe erhalten wurden, führte das kleinere −N(SiMe$_3$)$_2$-System zu einer Reihe weiterer C≡C-Dreifachbindungsaktivierungen (**Schema 16**). Es wurde ein Reaktionsverlauf postuliert, in welchem die Manganzentren das Alkin zum Dianion unter sukzessiver Abspaltung der −N(SiMe$_3$)$_2$-Liganden reduzieren. Nach weiteren Umlagerungen, die nicht aufgeklärt werden konnten, entsteht der Silylamid-freie Komplex K{18c6}[Mn(HPB)(η^2-PhCCPh)] (HPB = Hexaphenylbenzol). In ihm wird das zentrale Manganzentrum durch ein *side-on*-koordiniertes, leicht gewinkeltes Tolan-Molekül sowie einem η^6-koordinierten HPB-Substituenten gebunden, welcher sich aus einer Zyklotrimerisierungsreaktion des Diphenylacetylens bildet. Die Oxidationsstufe war nicht bestimmbar, jedoch ergaben quantenchemische Berechnungen des Eisen-Analogons K{18c6}[Fe(HPB)(η^2-PhCCPh)] der Gruppe von WOLF das Vorliegen einer seltenen Eisen(−I)-Spezies, weshalb das Mn-Derivat ebenfalls in der Oxidationsstufe −1 vorliegen könnte.[84,221]

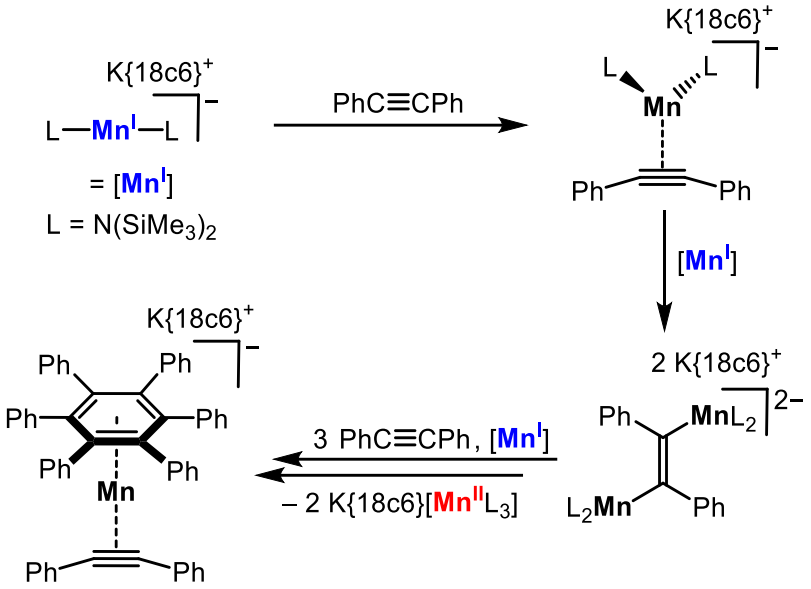

Schema 16. Postulierter Reaktionsverlauf bei Umsetzung von K{18c6}[Mn(N(SiMe$_3$)$_2$)$_2$] mit Diphenylacetylen.[84]

Die Fähigkeit der Alkintrimerisierung wurde linearen Metall(I)-Komplexen erstmals durch den heteroleptischen Komplex [(IDipp)Fe(N(Dipp)SiMe$_3$)] nachgewiesen.[143] Unter milden Bedingungen und mit Beladungen von 2 − 5 mol% war es möglich, sowohl interne als auch terminale Alkine in Ausbeuten von bis zu > 99% zu trimerisieren. In einer ersten Studie wurde die Funktion des heteroleptischen Komplexes als Präkatalysator postuliert, welcher sich in ein katalytisch aktives, ebenfalls paramagnetisches Intermediat umwandelt. Nach beendeter Katalyse konnte die Ausgangsverbindung zurückgewonnen werden. In diesem Zyklus wurde die Präsenz von sowohl M(I)- als auch M(III)-Spezies angenommen, obwohl solche Redoxprozesse eher für Übergangsmetalle der zweiten und dritten Periode bekannt sind.[143]

Um einen detaillierteren Einblick in den Mechanismus zu erlangen, wurden die Forschungen auf das sterisch anspruchsvollere Substrat Tolan erweitert.[222] Die 1:1-Umsetzung von [(IDipp)Fe(N(Dipp)SiMe$_3$)] mit dem internen Alkin führte zur bimetallischen Verbindung [Fe(N(Dipp)SiMe$_3$)(PhCCPh)]$_2$ (**I**, **Schema 17**). Röntgenkristallographische Analysen ergaben eine im Vergleich zum freien Tolan (C≡C 1.204(2) Å) verlängerte C≡C-Dreifachbindung (1.316(6) Å) mit einer gewinkelten Geometrie (C−C−Ph 142.7°). Durch das Erhitzen auf 60 °C in Toluol (**A**) koppeln die beiden verbrückenden Alkinfragmente, wodurch ein Dimetallazyklopentadien-Komplex erhalten wird (**II**, **Schema 17**). Bestätigt mittels ^{57}Fe-Mößbauer-Spektroskopie, werden die beiden Fe-Atome dabei formal durch je ein Elektron zu Fe(II) oxidiert. Basierend

auf diesen isolierten Verbindungen und mechanistischen DFT-Berechnungen konnte ein Reaktionsmechanismus der Alkintrimerisierung postuliert werden (**Schema 17**).[222]

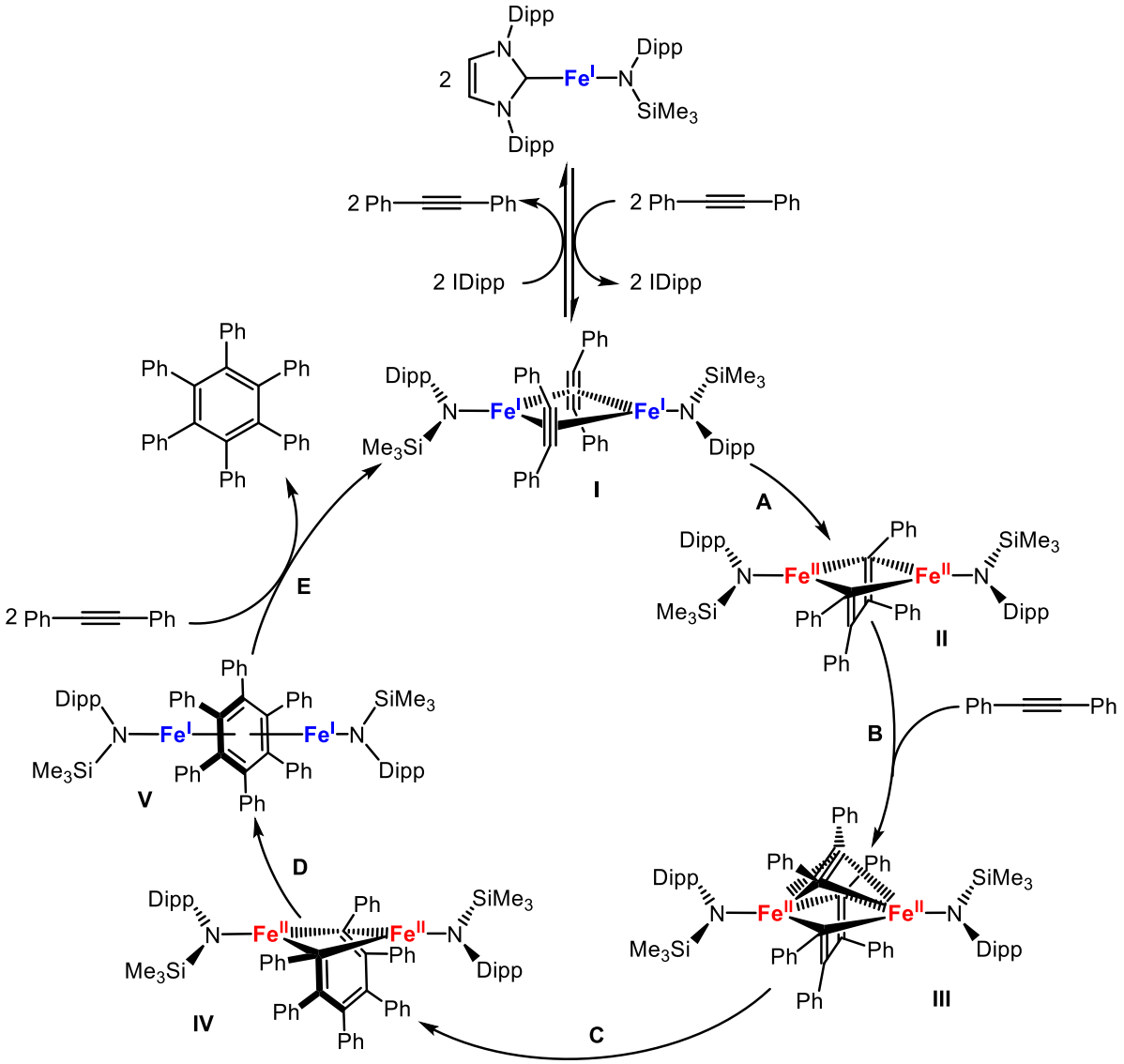

Schema 17. Postulierter Mechanismus der Zyklotrimerisierung von Tolan mittels [(IDipp)Fe(N(Dipp)SiMe$_3$)].[222]

Nach der anfänglichen Bildung von **I** führt eine oxidative Kopplung der beiden verbrückenden Alkine (**A**) unter Reduktion der Fe-Zentren zu Komplex **II**. Nach Addition eines weiteren Äquivalents Alkin (**B**) insertiert dieses in einer μ-η^2-Koordination zwischen die beiden Metallzentren (**III**). Die Umlagerung von Elektronen führt zu einer Alkintrimerisierung (**IV**, **C**). Durch Übertragung von Elektronen von den Eisen-Kernen auf das organische Fragment (**D**) findet ein Ringschluss statt. Der inverse Sandwichkomplex **V** kann nun unter Freisetzung des geformten Arens (**E**) erneut zwei Äquivalente Alkin aufnehmen, wodurch der Zyklus von Neuem durchlaufen wird. Die Bildung von **V** konnte nur indirekt über Berechnungen nachgewiesen werden.

Die Präsenz ist dennoch nicht abwegig, da die Struktur der eines isolierten nacnac-Komplexes ähnelt.[223,224]

Dieser postulierte Mechanismus gibt einen ersten Einblick in den möglichen Ablauf einer Alkintrimerisierungsreaktion. Die Untersuchungen und das Verständnis der ablaufenden Prozesse stehen jedoch noch am Anfang, da dieser Mechanismus nur anhand eines Komplexes postuliert wurde. Eine Ausweitung auf andere Metall-Zentren, wie z. B. Mangan, kann daher sehr aufschlussreich sein.

Niedervalente 3d-Metall-Alken-Komplexe

Weniger als über die Reaktivität von niedrig-koordinierten 3d-Metallkomplexen mit Alkinen ist über entsprechende Umsetzungen mit Alkenen bekannt. Der Arbeitsgruppe von DENG gelang es jedoch, die nullvalenten Derivate [(NHC)M(H_2CCHPh)] (M = Mn – Co, NHC = IDipp, IMes) darzustellen (**Abbildung 35**).[225,226] THEOPOLD und HOLLAND isolierten nacnac-basierte Verbindungen, in denen ein Alken entweder μ-η^2:η^2-verbrückend zwischen zwei Metallzentren wirkt oder *side-on* an ein Zentrum koordiniert.[214,227–229] Diese Ergebnisse sind mit denen der Alkin-Komplexe vergleichbar.

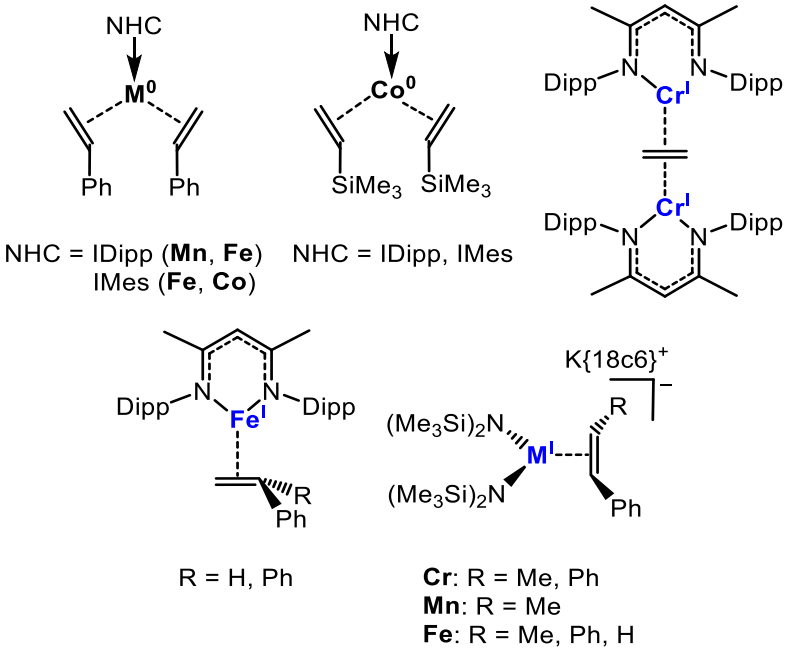

Abbildung 35. Auswahl bekannter niederkoordinierter Metall-Alken-Komplexe.[69,190,214,225–230]

Analog zu diesen Spezies konnte die *side-on*-koordinierte Verbindung K{18c6}[Fe(N(SiMe$_3$)$_2$(CH$_2$=CHPh)] bei Reaktion des anionischen Eisen(I)-Komplexes K{18c6}[Fe(N(SiMe$_3$)$_2$)$_2$] mit Styrol (H_2C=CHPh) erhalten werden.[190] Bei Verwendung eines internen Alkens, *cis*-Stilben (PhHC=CHPh), beobachtete MÜLLER

neben einer *side-on*-Koordination eine *Z*/*E*-Isomerisierung zu *trans*-Stilben (**Schema 18**).[190] Eine Metall-katalysierte Isomerisierung ist für allylische Doppelbindungen nicht ungewöhnlich, erfolgt normalerweise jedoch unter Beteiligung einer Metall-Hydrid-Spezies.[231–233] Da in Stilben keine allylische Doppelbindung präsent ist, wurden die Beobachtungen durch Vorarbeiten und Berechnungen von GANO erklärt.[234] Die Übertragung eines Elektrons vom Metall auf das Olefin verursacht die Bildung eines radikalischen Monoanions, dessen *Z*/*E*-Isomerisierung im Vergleich zu einem neutralen Olefin energetisch stark begünstigt ist. Diese Überlegungen stehen im Einklang mit einem 3d-Metall-freien Alken-Radikalanion, welches im Zuge der gleichen Studie strukturell charakterisiert werden konnte.[190]

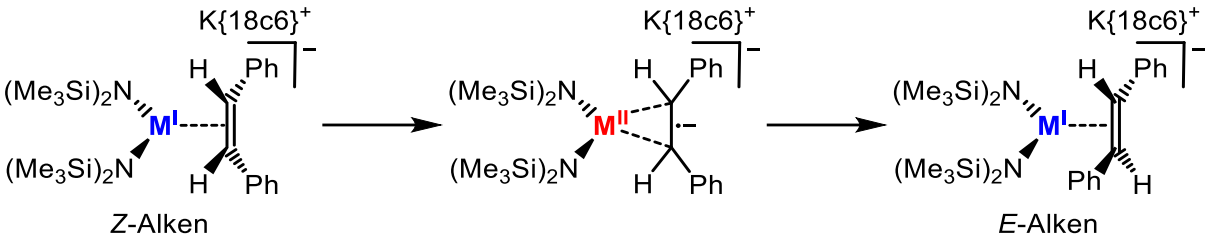

Schema 18. Postulierter Reaktionsverlauf der *Z*/*E*-Alken Isomerisierung von Stilben.[190]

Eine analoge Eisen-katalysierte *Z*/*E*-Isomerisierung, die sogar katalytisch erfolgt, wurde für 1,2-Bis(diphenylphosphino)ethen (dppe) beobachtet, welches ebenfalls keine allylischen Doppelbindungen aufweist.[84] Dieses Ergebnis ist erstaunlich, da die Alken-Koordination einer Wechselwirkung zwischen einer Phosphan-Einheit und dem Eisenzentrum bevorzugt ist.

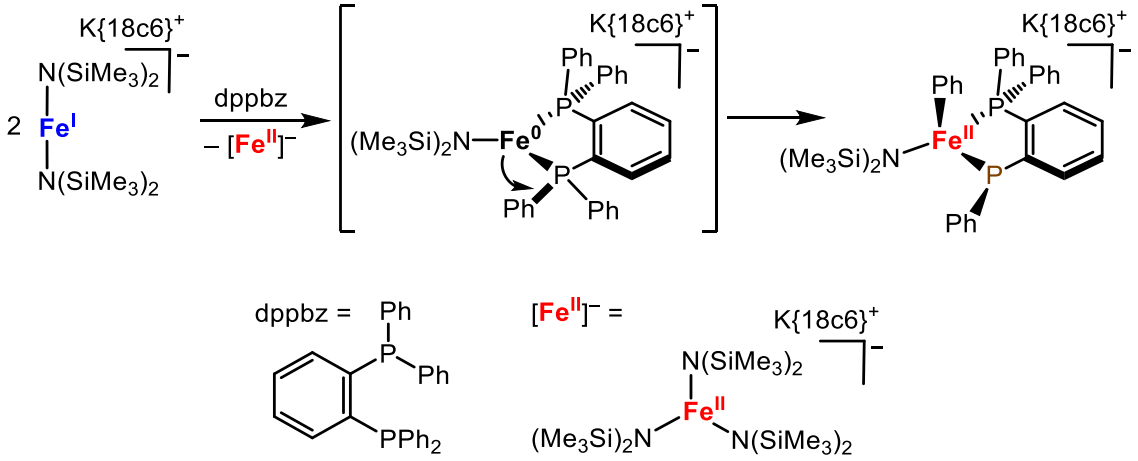

Schema 19. Postulierter Mechanismus der P-Aryl Bindungsspaltung bei Reaktion von K{18c6}[Fe(N(SiMe$_3$)$_2$)$_2$] mit dppbz.[84]

Bei Präsenz einer delokalisierten Doppelbindung in einem Diphosphin, wie in dppbz (1,2-bis(diphenylphosphino)benzol), findet keine Isomerisierung statt. Stattdessen erfolgt eine seltene P−C-Bindungsspaltung, bei der die freiwerdende Aryl-Einheit auf

das Metallzentrum übertragen und ein tetraedrischer Phenyleisen(II)-Komplex gebildet wird (**Schema 19**).[84]

In allen literaturbekannten Reaktionen wurden nur intermolekulare Umsetzungen zwischen niedervalenten 3d-Metallkomplexen und Alkenen beschrieben. Über intramolekulare Alken−Metall-Wechselwirkungen sind bisher keine Informationen bekannt.

2.5.2 Reaktivität von 3d-Metall(I)-Komplexen gegenüber Organoaziden

Seit GRIESS im Jahr 1862 zum ersten Mal die Synthese von Phenylazid beschrieb, erweckten Derivate organischer Azide vielseitiges Interesse.[235,236] Gerade in den 1950er- und 1960er-Jahren wurden einige neue Vertreter wie Acyl-, Aryl- oder Alkylazide entwickelt und als funktionelle Gruppen in Medikamenten eingesetzt oder zur Synthese von Heterozyklen herangezogen.[237]

Organoazide sind sehr energiereiche und flexible Verbindungen, die sich explosionsartig zersetzen können.[237] Der Ursprung ihrer hohen Reaktivität liegt in der Labilität der N_α−N_β-Bindung (**Schema 20**). Eine thermische oder photochemische Aktivierung führt zur Freisetzung von Distickstoff (N_2) und einem hochreaktiven Nitrenfragment ([RN]).[238]

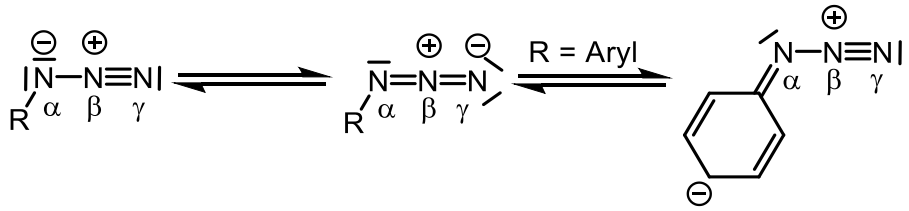

Schema 20. Mesomere Grenzstrukturen eines Organoazids.[238]

Aufgrund der möglichen Nitren-Bildung eignen sich Organoazide für die Umsetzung mit Übergangsmetallkomplexen. Während Organoazide über N_α und N_γ Mehrfachkoordinationen an einem Metallzentrum ausbilden und als verbrückende Liganden dienen können, ist es ihnen ebenfalls möglich, als Imido-Derivate über Mehrfachbindungen an ein Metallzentrum zu koordinieren.[238,239]

Das allgemeine Interesse an M−L Mehrfachbindungen steigt, da Komplexe mit diesem Bindungsmotiv lange Zeit als zu instabil zur Isolierung galten. M−L Mehrfachbindungen sind Bestandteil hochreaktiver Zwischenstufen, in denen eine Heteroatomfunktion auf

ein vermeintlich unreaktives Substrat übertragen wird, z. B. beim Einbau einer [NR]-Funktionalität in eine unreaktive C−H-Bindung.[239–242]

Das Bindungsmotiv zwischen einem Metall und einem [NR]-Fragment kann sehr unterschiedlich sein. Bindet das Stickstoffatom über eine einzelne, kovalente Bindung an das Metallatom, liegt ein Nitren-Komplex vor.[239–241] Das Stickstoffatom ist darin monosubstituiert und besitzt ein Elektronensextett (**Abbildung 36**). Befinden sich formal insgesamt sieben Valenzelektronen am Heteroatom, entsteht ein anionischer Imidyl-Ligand des Typs [NR^{-}] mit Radikalcharakter. Bei einem Elekronenoktett am N-Atom wird von einem dianionischen Imid bzw. von Imido-Liganden gesprochen.

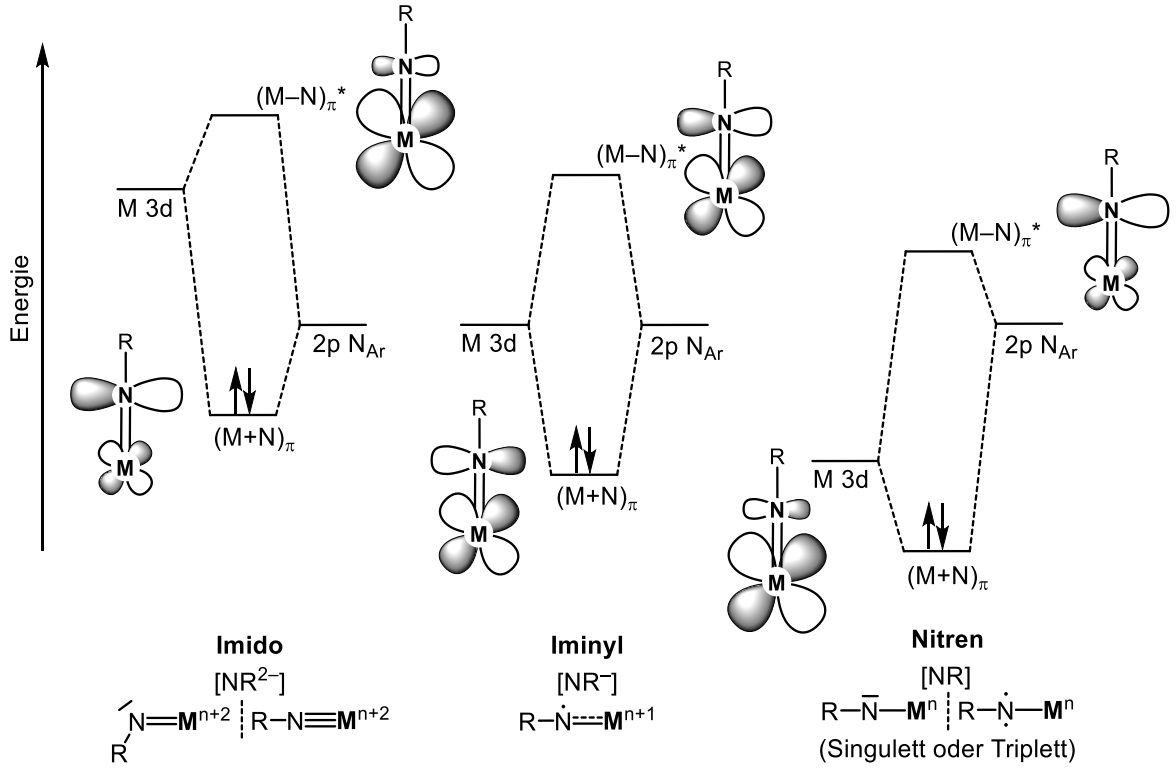

Abbildung 36. Energetische Auftragung der Grenzmolekülorbitale in Komplexen der Form [M(NR)L_n] abhängig vom Oxidationszustand des Metalls.[239,241]

Welches der drei Bindungsmotive vorliegt, hängt nicht nur vom Rest R des organischen Fragments, sondern auch stark vom verwendeten Metallzentrum und dessen Orbitalenergien ab. Frühe 3d-Übergangsmetalle besitzen beispielsweise wenige Valenzelektronen und sind elektrophil. Die Bindung eines nukleophilen und dianionischen Imido-Ligandens unter Bildung einer stark polarisierten M−L-Bindung ist bevorzugt.[241] Die Polarisierung in entsprechenden Derivaten kann bis hin zu einer Dreifachbindung führen, da je nach Symmetrie des Komplexes bis zu drei Elektronenpaare (p_z (σ-Bindung), p_x/p_y (π-Bindung)) des Imids mit den d-Orbitalen des Metallzentrums wechselwirken können. Wird die Reihe der 3d-Elemente hin zu mittelständigen Übergangsmetallen verfolgt, nimmt die Elektronendichte am

Metallatom sukzessive zu und die Bindungssituation ändert sich. Die Metall-Ligand Mehrfachbindungen erlangen kovalenteren Charakter und die Bildung von Imidyl-Komplexen ist begünstigt.[241]

Die Isolierung von elektronenreichen 3d-Metallkomplexen mit einer M−N-Mehrfachbindung ist selten, obwohl das Bindungsmotiv Bestandteil verschiedener Transfer-katalytischer Prozesse ist.[241] Durch eine hohe Elektronendichte am Metall bei gleichzeitig geringer räumlicher als auch energetischer Überlappung der Metall- und Ligand-Orbitale ist eine Inversion der Orbitalenergien möglich (**Abbildung 36**, rechts). Durch das invertierte Ligandenfeld sind die Grenzmolekülorbitale überwiegend Ligand-zentriert und das Metall liegt in einem reduzierten Zustand vor.

Die genaue elektronische Struktur ist nicht pauschal vorhersagbar. Ein gutes Indiz für den vorliegenden Bindungsmodus ist die vorliegende M−N-Bindungslänge, da der kovalente Anteil im Laufe der 3d-Periode ansteigt und die M−N-Distanz aufgeweitet wird (**Abbildung 37**). Die Bindungslänge hängen jedoch auch vom Oxidationszustand und Radius des Metallzentrums ab, weshalb ein Vergleich von Metallkomplexen untereinander schwierig ist.[187,239–241]

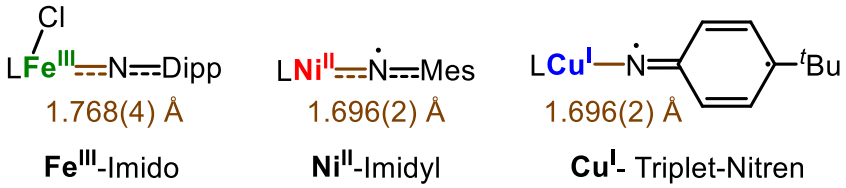

Abbildung 37. Vergleich der Bindungslängen in Imido- (links), Imidyl- (Mitte) und Nitren- (rechts) Komplexen am Beispiel literaturbekannter Verbindungen.[240,241,243]

Während bereits einige Eisen-haltige Imido-Komplexe veröffentlicht wurden, sind nur wenige Derivate später 3d-Metalle (Kobalt bis Kupfer) bekannt. In den meisten Kobalt-Imido-Komplexen liegt das Metallzentrum in einem *Low-Spin*-Zustand vor, wodurch die Spezies allgemein stabiler und weniger reaktiv sind.[70,77,141,174,175,177] Offenschalige *High-Spin*-Komplexe gibt es dagegen nur sehr wenige (**Abbildung 38**).[178,179,187,239,244,245]

Durch teilweise gefüllte d-Orbitale wird die Donierung von Elektronen vom [NR]-Fragment zum Metallzentrum verringert und das Ligandenfeld abgeschwächt. Das Metallzentren liegt im *High-Spin*-Zustand vor und die Reaktivität des Systems wird gesteigert. Zur Stabilisierung dieser offenschaligen Imido-Komplexe werden daher spezielle Hilfsliganden eingesetzt. Durch Verwendung eines sterisch anspruchsvollen, dreizähnigen Chelatliganden konnten so 2005 die beiden ersten

literaturbeschriebenen Kobalt-Derivate dargestellt werden (**Abbildung 38**, oben links).[244]

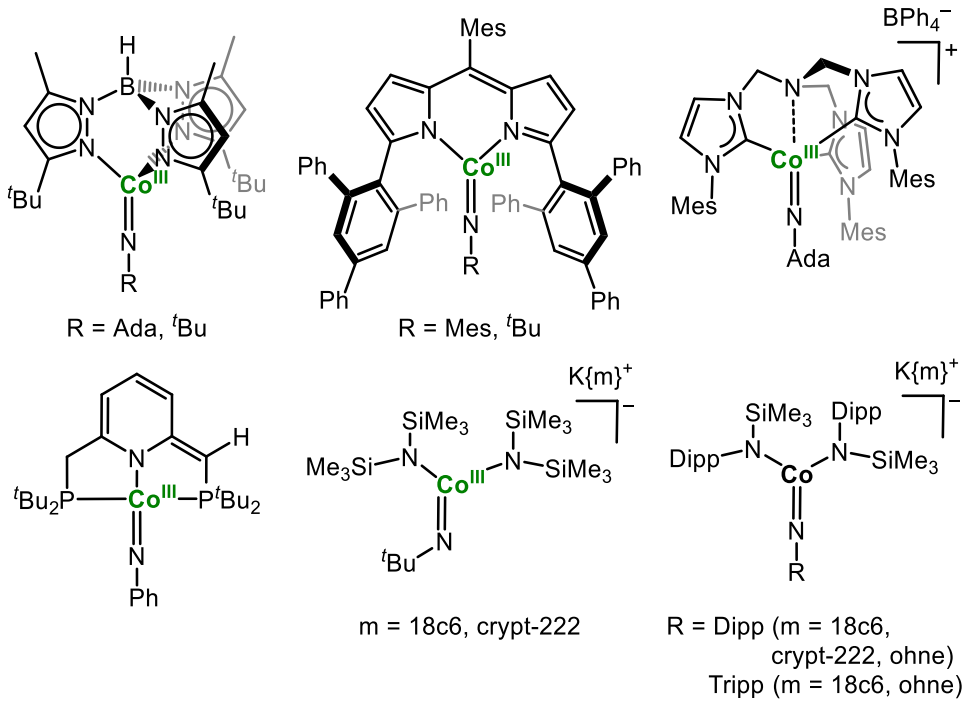

Abbildung 38. Bekannte Kobalt-Imido-Komplexe in höheren Spinzuständen.[178,179,187,239,244–247]

2020 konnte RECKZIEGEL den sterischen Anspruch der Hilfsliganden drastisch minimieren. Durch die Reaktion von *tert*-Butylazid mit dem quasilinearen Co(I)-Komplex K{18c6}[Co(N(SiMe$_3$)$_2$)$_2$] stellte er die anionischen Kobalt(III)-Imido-Komplexe K{m}[Co(N^{t}Bu)(N(SiMe$_3$)$_2$)$_2$] (m = 18c6, crypt-222) dar.[178,179] Dies ist bemerkenswert, da das Metallzentrum im Vergleich zu anderen bekannten Kobalt-Imido-Komplexen keine chelatisierenden oder stark abschirmenden Liganden trägt. Mit 1.7067(12) Å besitzt das anionische [Co(N^{t}Bu)(N(SiMe$_3$)$_2$)$_2$]$^-$-Fragment eine relativ lange Co−N-Bindung (zuvor bekannte Co−N$_{Imid}$ Längen: 1.61 Å − 1.70 Å)),[248] die durch einen *Intermediate-Spin*-Triplett-Grundzustand (S = 1) erklärt wird.[178,179] Außerdem ist die Co−N−C-Bindungsachse mit 160.78(12)° gewinkelt. Im Vergleich zu vielen anderen Kobalt-Imido-Komplexen ist [Co(N^{t}Bu)(N(SiMe$_3$)$_2$)$_2$]$^-$ unreaktiv gegenüber Nitren-Transferreaktionen (z. B. auf Phosphine oder Alkene), kann aber intermolekulare C−H-Bindungen mit Bindungsdissoziationsenergien (BDE) von bis 92 kcal mol^{-1} aktivieren, wodurch ein Kobalt(II)-Amido-Komplex erhalten wird (**Schema 21**). Dies war bis dato mit keinem anderen Imido-Komplex möglich. Interessanterweise ist die Amidoverbindung ebenfalls in der Lage, eine C−H-Bindung zu aktivieren, wodurch schließlich freies *tert*-Butylamin und die regenerierte Ausgangsverbindung K{18c6}[Co(N(SiMe$_3$)$_2$)$_2$] zurückgewonnen wird.[178,179]

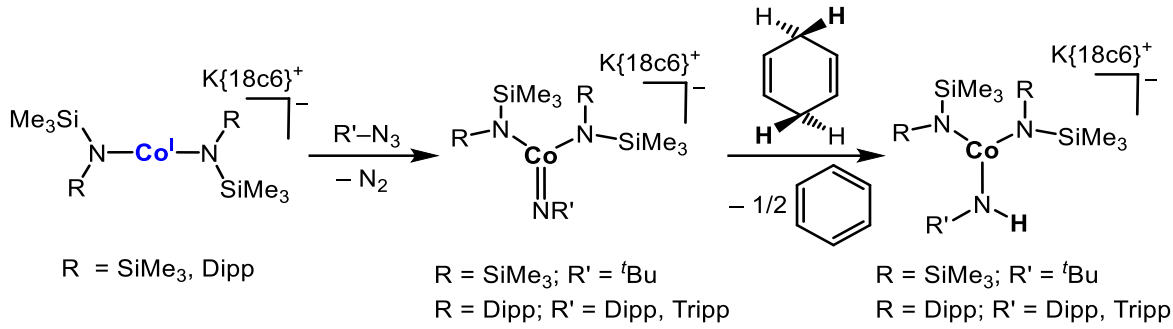

R = $SiMe_3$, Dipp

R = $SiMe_3$; R' = ^{t}Bu
R = Dipp; R' = Dipp, Tripp

R = $SiMe_3$; R' = ^{t}Bu
R = Dipp; R' = Dipp, Tripp

Schema 21. Intermolekulare H-Abstraktion mit den Imido-Komplexen K{18c6}[Co(NR‘)(N(R)$SiMe_3$)$_2$] (R = $SiMe_3$, Dipp; R‘ = ^{t}Bu, Dipp, Tripp) am Beispiel von CHD.[178,179,187]

In einer Folgestudie wurden die Untersuchungen auf das sterisch anspruchsvollere Ligandsystem −N(Dipp)$SiMe_3$ ausgeweitet.[187] Durch Reaktion von [Co(N(Dipp)$SiMe_3$)$_2$]$^-$ mit den beiden arylischen Aziden Dipp−N_3 und Tripp−N_3 wurden die ionischen Verbindungen [Co(NR)(N(Dipp)$SiMe_3$)$_2$]$^-$ (R = Dipp, Tripp) synthetisiert (**Abbildung 38**). Mit ca. 1.75 Å besitzen sie die mit Abstand längsten bekannten Co−N_{Imid}-Bindungslängen.[242,248–251] Röntgenkristallographische und quanten-theoretische Ergebnisse ergaben eine niedrige Co−N- (0.6) und eine erhöhte C−N-Bindungsordnung (1.3) sowie ein *High-Spin*-Kobaltzentrum. EPR-Messungen zeigten zudem einen Imidyl-Charakter des organischen Substituenten, weshalb die beiden Spezies als Kobalt-Imidyl-Komplexe eingestuft wurden.

Durch diese außergewöhnlichen Ergebnisse ist es von großem Interesse, weitere Kobalt-Imido-Komplexe zu entwerfen und deren Reaktivitäten zu untersuchen.

3 Motivation und Aufgabenstellung

Wie in Kapitel 2 erläutert, besitzen (quasi-)lineare 3d-Metall(I)-Komplexe ein hohes Potenzial bezüglich ihrer Eigenschaften und Reaktivitäten. Bisherige Publikationen beschränken sich jedoch hauptsächlich auf die beiden Silylamid-basierten Systeme $[M(N(Dipp)SiR_3)_2]^-$ (M = Cr (R = ^{i}Pr), Mn − Ni (R = Me)) und $[M(N(SiMe_3)_2)_2]^-$ (M = Cr − Co), deren Untersuchungen hinsichtlich der Variation des Metallzentrums (Chrom bis Nickel) sowie deren Umsetzung mit verschiedenen Substraten. Strukturelle bzw. elektronische Veränderungen der Komplexe selbst wurden kaum begutachtet, weshalb dies im Fokus dieser Arbeit stehen soll.

Zur Untersuchung struktureller Aspekte sollten in einem ersten Schritt 3d-Metall(II)-Komplexe mit elektronenreichen Substituenten im Ligandsystem dargestellt werden (**Schema 22**). Der Einfluss der eingeführten Fragmente auf die Struktur und die Reduzierbarkeit der divalenten Spezies sollten im Anschluss untersucht werden. Des Weiteren sollten potenziell entstehende Metall(I)-Derivate hinsichtlich ihrer Reaktivität gegenüber Organoaziden analysiert werden.

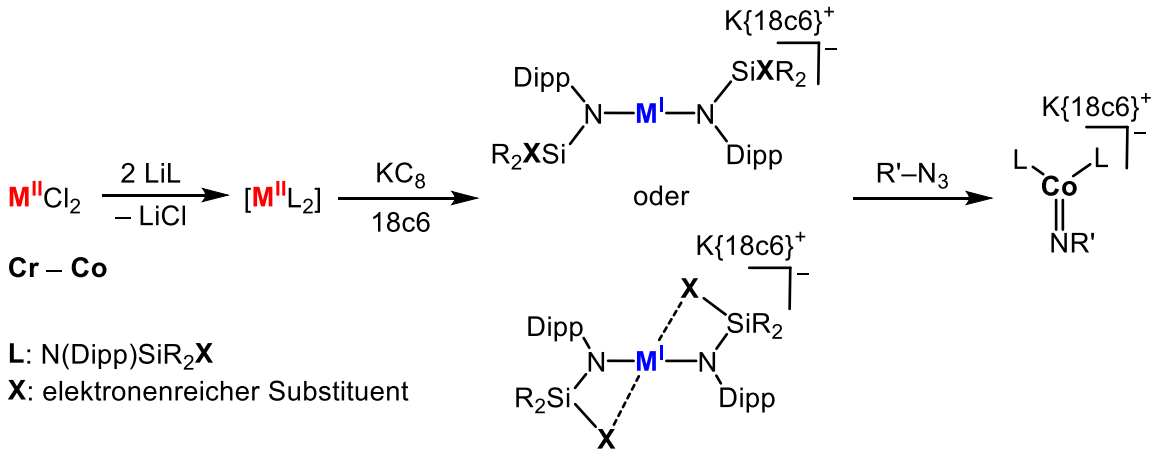

Schema 22. Synthese neuartiger 3d-Metall(I)-Komplexe mit elektronenreichen Ligandsubstituenten und deren Reaktivität gegenüber Organoaziden.

Da in der Literatur bisher ausschließlich interkaliertes Kalium (KC_8) als Reduktionsmittel eingesetzt wurde, besitzen anionische 3d-Metall(I)-Komplexe ein Kalium-Gegenion. Die Reduzierbarkeit von Metall(II)-Präkursoren mit weiteren Alkalimetallen sollte aus diesem Grund getestet werden. Analog zu $NBu_4[M(N(Dipp)SiR_3)_2]$ (M = Cr (R = ^{i}Pr), Ni (R = Me))[77,141] sollte ebenfalls überprüft werden, ob der Austausch des Kaliumions durch ein organisches Kation, wie z. B. NBu_4^+, auch mit anderen 3d-Metallen (Mn − Co) möglich ist (**Schema 23**).

Das Kalium-Gegenion in Metall(I)-Komplexen wird zur Stabilisierung und zur Vermeidung ungewollter Zersetzungsreaktionen durch einen Kryptanden (18c6 oder crypt-222) interkaliert und vom Anion separiert. Demgegenüber wurde anhand von [KNi(N(Dipp)SiMe$_3$)$_2$] gezeigt, dass das Kation auch intramolekular durch Ausbildung einer formal neutralen Verbindung stabilisiert werden kann.[141] Welche Auswirkungen diese Art der Stabilisierung und die dadurch resultierende Fixierung der Liganden auf die Reaktivität und die elektronischen Eigenschaften der Komplexe besitzen, sollte durch die Synthese und Analyse der monomeren Verbindungen [KM(N(Dipp)SiR$_3$)$_2$] (M = Cr (R = ^{i}Pr), Mn − Co (R = Me)) ermittelt werden (**Schema 23**). Zum Testen der Reaktivität sollte sich die Umsetzung mit Alkinen eignen, da in der Literatur bereits variierende Ergebnisse wie *side-on*-Koordinationen oder Trimerisierungsreaktionen beschrieben wurden. Bei erfolgreichen Umsetzungen sollten die Silylamid-basierten 3d-Metall(II/I)-Komplexe auch bezüglich katalytischer Fähigkeiten kontrolliert werden.
Zur Untersuchung der elektronischen Beschaffenheit der monovalenten Komplexe [KM(N(Dipp)SiMe$_3$)$_2$] (M =Cr − Co) sollte die Analyse auf die Fe-Spezies fokussiert werden. Dies erlaubt einen Einblick in die elektronische Struktur mittels ^{57}Fe-Mößbauer-Spektroskopie und zum anderen beschreiben ausgewählte Literaturbeispiele einzelmolekülmagnetisches Verhalten für Eisen(I)-Verbindungen (vgl. Kapitel 2.4.2). Experimentell erhaltene Ergebnisse sollten durch quantenchemische Berechnungen bestätigt werden.

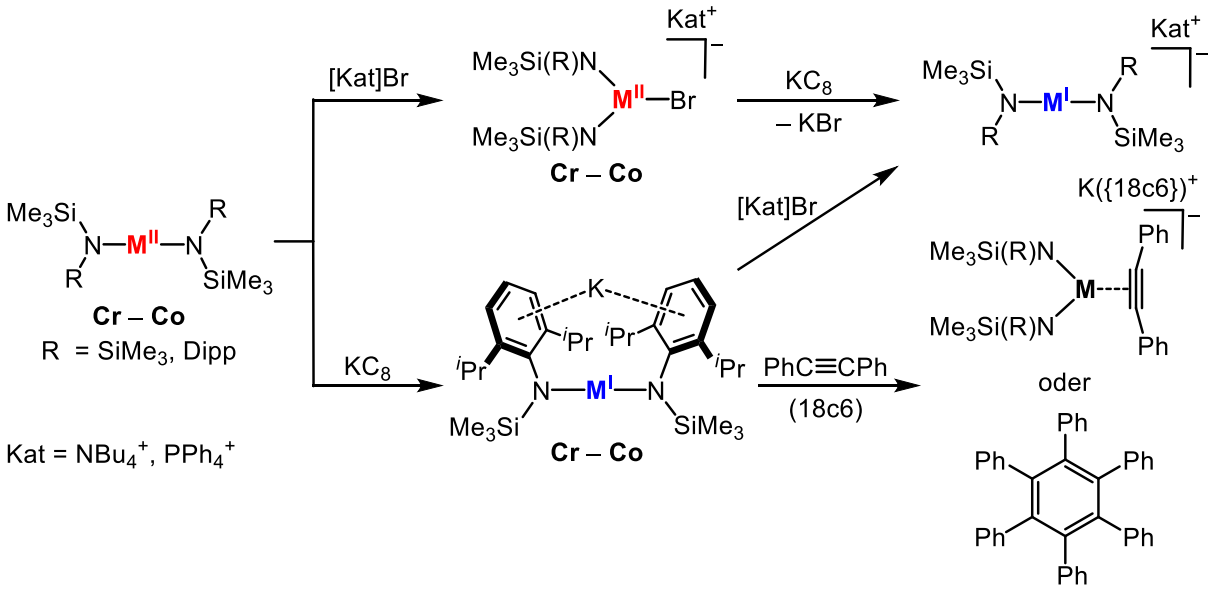

Schema 23. Synthetische Vorgehensweise zur Aufklärung des Kationeneinflusses auf Struktur, Eigenschaft und Reaktivität von linearen 3d-Metall(I)-Komplexen.

Bis auf Silylamid- bzw. Methanid-basierte Derivate sind keine quasilinearen 3d-Metall(I)-Komplexe bekannt. Im zweiten Teil dieser Arbeit sollten daher Verbindungen

auf Basis weiterer Heteroatome dargestellt werden. Es sollte versucht werden, lineare Metall(II)-Komplexe über eine Ligandaustauschreaktion durch Umsetzung von $[M(N(SiMe_3)_2)_2]$ (M = Mn − Co) mit Phosphor-haltigen Verbindungen zu synthetisieren (**Schema 24**). Anschließend sollten diese mit KC_8 zu Metall(I)-Derivaten reduziert werden. Hierfür eignen sich Phosphiniden- bzw. Phosphinidenid-Derivate [(sIDipp)PR] (R = H, K). Anhand der Übergangsmetallkomplexe $[(IDipp)PML_n]$ wurde gezeigt, dass Phosphinidensubstituenten als σ-Donor- und π-Akzeptor-Liganden fungieren und die entstehenden M−P-Bindungen Doppelbindungscharakter besitzen können (**Abbildung 23**).[123,134] Des Weiteren wurde die Ausbildung sekundärer Wechselwirkungen in $[Hg(P(NHC))_2]$ (NHC = sIDipp, sIMes) beschrieben, welche den Phosphinidenid-Komplex zusätzlich stabilisieren. Diese Eigenschaften könnten essenziell für die erfolgreiche Synthese neuartiger 3d-Metall(I)-Komplexe der allgemeinen Form $[M(PR)_2]^-$ sein.[135]

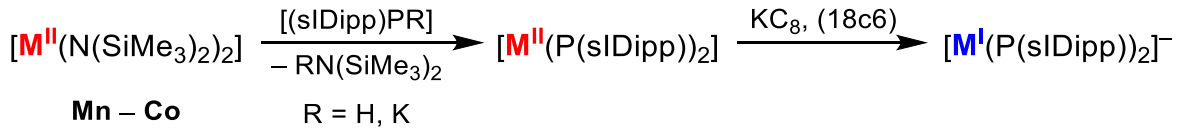

Schema 24. Möglicher Syntheseweg zur Darstellung von $[M(P(sIDipp))_2]^{0,-}$ (M = Mn − Co).

4 Übersicht über die im kumulativen Teil enthaltenen Publikationen

Im Zuge dieser Arbeit sind sieben Projekte entstanden, welche im Folgenden aufgelistet sind. Neben drei veröffentlichten Publikationen befinden sich drei Artikel unter Begutachtung und ein weiterer in den letzten Vorbereitungen. Die Nummerierung bzw. Abkürzungen aller Verbindungen werden in den einzelnen Zusammenfassungen analog zu den Originalpublikationen verwendet. Die elektronischen Zusatzinformationen („Supporting Information“, ESI) befinden sich in Kapitel 11.

1 *“Homoleptic quasilinear metal(I/II) silylamides of Cr − Co with phenyl and allyl functions − impact of the oxidation state on secondary ligand interactions”*
R. Weller, L. Ruppach, A. Shlyaykher, F. Tambornino, C. G. Werncke, *Dalton Trans.* **2021**, *50*, 10947−10963. DOI: 10.1039/d1dt01543e

2 „*Quasilinear 3d-metal(I) complexes [KM(N(Dipp)SiR$_3$)$_2$] (M = Cr − Co) − structural diversity, solution state behaviour and reactivity”*
R. Weller, I. Müller, C. Duhayon, S. Sabo-Etienne, S. Bontemps, C. G. Werncke, *Dalton Trans.* **2021**, *50*, 4890−4903. DOI: 10.1039/d1dt00121c

3 *“On the Synthesis and Reduction of Trigonal Halido Bis(silylamido) Metalates of Chromium to Cobalt”*
R. Weller, L. Völlinger, C. G. Werncke*, Eur. J. Inorg. Chem.* **2021**, 4383−4392; DOI: 10.1002/ejic.202100716

4 *“Catalytic 1,3-H Atom Shift of a Terminal Benzylic Alkyne by Iron and Alkali Metal Silylamides − Switching between Allene and Internal Alkyne”*
R. Weller, I. Müller, C. G. Werncke, *eingereichtes Manuskript.*

5 *“Magnetic Blocking in a Conformationally Restricted Quasilinear Iron(I) Silylamide”*
R. Weller, M. Atanasov, S. Demeshko, I. Mohelsky, M. Orlita, F. Meyer, F. Neese, C. G. Werncke, *Manuskript in Vorbereitung.*

6 "*NHC-Stabilized Parent Phosphinidene Adducts of Metal(II) Hexamethyldisilazanides of Manganese − Cobalt and Their Lability in Solution*" R. Weller, A. Gonzalez, H. Gottschling, C. von Hänisch, C. G. Werncke, *eingereichtes Manuskript.*

7 "*Synthesis of the Open-Shell 3d-Transition Metal(II) Bis(phosphinidenide) [Mn(P(sIDipp))$_2$]*"
R. Weller, M. Balmer, C. von Hänisch, C. G. Werncke, *eingereichtes Manuskript.*

5 Kumulativer Teil

5.1 „Homoleptic quasilinear metal(I/II) silylamides of Cr − Co with phenyl and allyl functions − impact of the oxidation state on secondary ligand interactions“

Ruth Weller, Lutz Ruppach, Alena Shlyaykher, Frank Tambornino,
C. Gunnar Werncke

Dalton Transactions **2021**, *50*, 10947−10963.
DOI: 10.1039/d1dt01543e
https://pubs.rsc.org/en/content/articlelanding/2021/dt/d1dt01543e

Abstract

Herein we describe the synthesis and characterization of a variety of new quasilinear metal(I/II) silylamides of the type $[M(N(Dipp)SiR_3)_2]^{0,-}$ (M = Cr − Co) with different silyl substituents (SiR_3 = $SiPh_{3-n}Me_n$ (n = 1 − 3), $SiMe_2$(allyl)). By comparison of the solid state structures we show that in case of phenyl substituents secondary metal ligand interactions are suppressed upon reduction of the metal. Introduction of an allyl substituted silylamide gives divalent complexes with additional metal-π-alkene interactions with only weak activation of the C═C bond but substantial bending of the principal N–M–N axis. $1e^-$-reduction leads for cobalt to a more strongly bound alkene substituent, whereas for chromium reduction and intermolecular dimerisation of the allyl unit is observed. It thus indicates that the general view of low-coordinate 3d-metal ions as electron deficient seems not apply to anionic metal(I) complexes. Additionally, obtained cobalt(I) complexes are reacted with an aryl azide giving trigonal imido metal complexes. These can be regarded as rare examples of high-spin imido cobalt compounds from their structural and solution magnetic features.

Zusammenfassung

In dieser Publikation wird die Synthese und Charakterisierung einer Vielzahl neuer quasilinearer 3d-Metall(II/I)-Silylamide des Typs $[M(N(Dipp)SiR_3)_2]^{0,-}$ (M = Cr − Co) mit verschiedenen Silylsubstituenten (SiR_3 = $SiPh_{3-n}Me_n$ (n = 1 − 3; (L^1 − L^3)), $SiMe_2$(allyl) (**L^4**)) im Ligandrückgrat beschrieben. Anhand dieser Verbindungen wird die Präsenz

sekundärer Metall−Aren Wechselwirkungen und deren strukturelle Auswirkung untersucht. Analog zu literaturbekannten Verbindungen, wie $[Cr(N(SiMe_2Ph)_2)_2]$,[86] werden beim Einbau von Phenylsubstituenten ($L^1 - L^3$) in Metall(II)-Komplexe sekundäre Wechselwirkungen ausgebildet, die eine erhebliche Abwinklung der N−M−N-Achsen verursachen. Interessanterweise verschwinden diese Metall−Aren Interaktionen in Eisen- und Kobalt-Derivaten bei Reduktion zu den entsprechenden Metall(I)-Komplexen. Dies geschieht unabhängig von der Anzahl vorhandener Phenylringe im Ligandrückgrat und dem einhergehenden sterischen Druck. Auf einer rein strukturellen Ebene scheinen anionische 3d-Metall(I)-Ionen deshalb, konträr zu ihren divalenten Analoga, eine vernachlässigbare LEWIS-Azidität zu besitzen. Im Fall von Mangan findet durch die Reduktion mit KC_8 eine C−H Aktivierung einer Methylgruppe im Silylfragment statt (**Schema 25**).

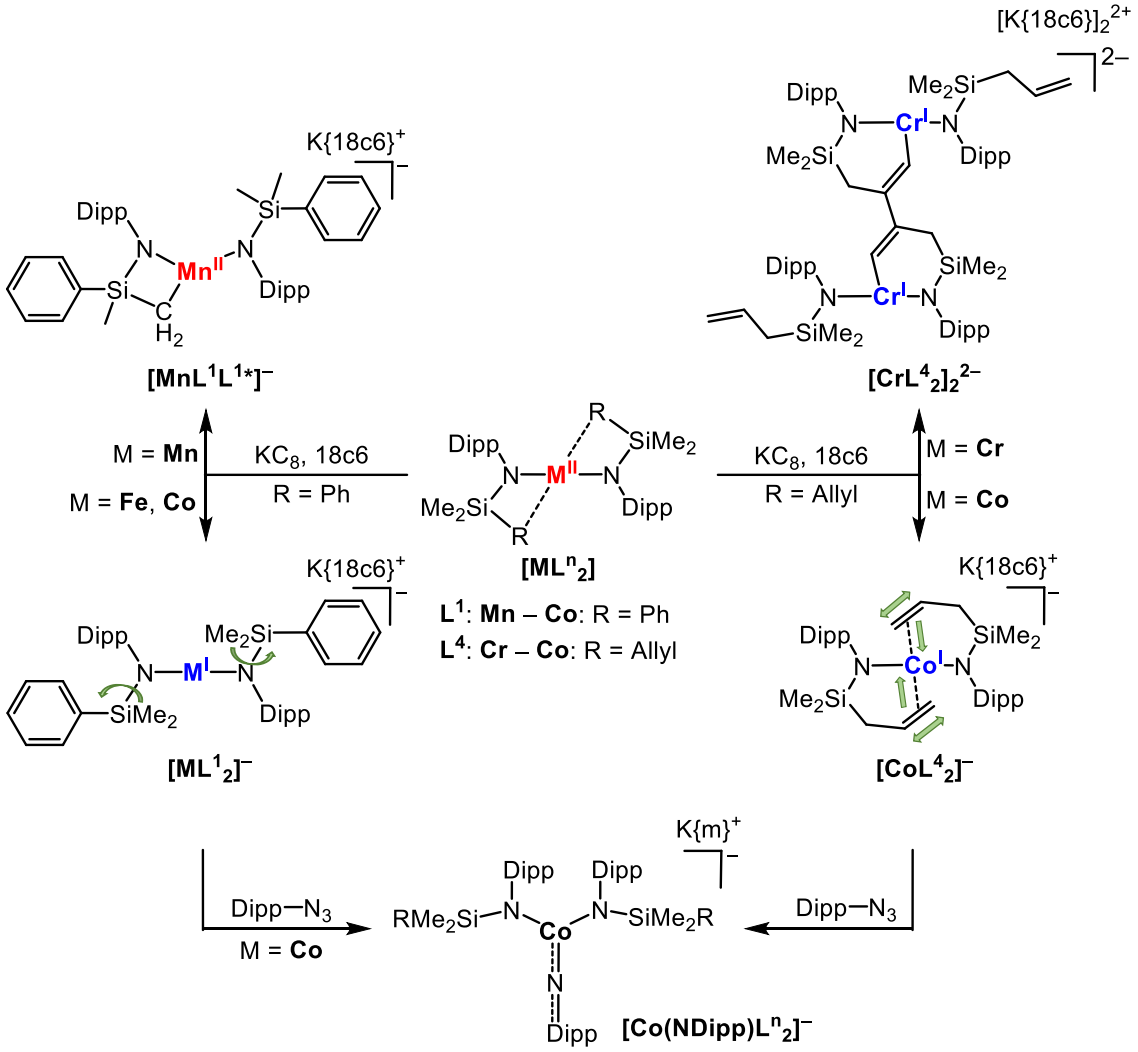

Schema 25. Auswirkung unterschiedlicher Oxidationsstufen auf die Ausbildung intramolekularer Metall-π-Wechselwirkungen am Beispiel von Metall(II/I)-Komplexen des Typs $[ML^n_2]^{0,-}$ (L^1: M = Mn − Co), L^4: M = Cr − Co)).

Durch die Einführung einer Allyl-Funktion in die Silyl-Einheit entstehen zweiwertige Komplexe des Typs [ML^4_2] (M = Cr − Co), die eine stark abgewinkelte N−M−N-Hauptachse aufweisen. Dies geschieht durch die zusätzliche Ausbildung von Metall-π-Alken-Wechselwirkungen. Aufgrund langer Metall−Alken Distanzen (ca. 2.44 Å (Co) − 2.66 Å (Mn)) und C═C-Bindungslängen von 1.33 Å (Mn) − 1.35 Å (Cr) können diese Wechselwirkungen als schwach angesehen werden. Das Mangan-Derivat stellt den ersten zweiwertigen Mangan-Komplex mit einer intramolekularen Aren-Koordination dar.

Konträr zu den Phenyl-basierten Interaktionen verstärken sich die Metall-Aren-Wechselwirkungen durch Reduktion der divalenten Verbindungen mit KC_8 in Anwesenheit von 18-Krone-6. Während im Fall von Kobalt, **[CoL^4_2]$^-$**, eine erhöhte π-Rückbindung beobachtet wird, führt die Reduktion von **[CrL^4_2]** gar zu einer intermolekularen C−C-Kopplung bzw. Dimerisierung der Propenyl-Einheiten und der binukleare Chrom(II)-Alkyl-Komplex **[$CrL^4_2]_2^{2-}$** wird gebildet. Diese Beobachtungen lassen darauf schließen, dass niedrig-koordinierte 3d-Metall(I)-Ionen eher als elektronenreich bezeichnet werden sollten.

Um den Einfluss der eingeführten Phenyl- und Allyl- Einheiten auf die Reaktivität von 3d-Metall(I)-Silylamiden zu testen, werden die erhaltenen Kobalt(I)-Komplexe mit Dipp-Azid zu trigonalen Metall-Imido-Komplexen umgesetzt. Diese können aufgrund ihrer strukturellen und magnetischen Eigenschaften in Lösung als weitere Beispiele für seltene *High-Spin*-Kobalt-Imido-Verbindungen angesehen werden. Erstaunlicherweise findet in **[Co(NDipp)L^4_2]$^-$** keine Reaktion zwischen dem intramolekular gebundenen Alken und der Imidyl-Einheit statt.

Beiträge der Autoren

Die Planung und Durchführung des Projektes sowie die Synthese und Charakterisierung aller Verbindungen lag in meiner Hand. Bis auf K{18c6}**[MnL^1L^{1*}]**, K{18c6}**[FeL^3_2]**, K{18c6}**[Co(NDipp)L^1_2]** und K{18c6}**[Co(NDipp)L^4_2]** wurden alle erhaltenen Verbindungen zuvor entweder von Lutz Ruppach im Rahmen seiner Bachelorarbeit oder von Alena Shlyaykher im Rahmen eines Vertiefungspraktikums unter meiner Leitung dargestellt und teilweise analysiert. Alle von ihnen erhaltenen Ergebnisse wurden jedoch von mir reproduziert, ergänzt und für diese Publikation aufbereitet. Zusätzlich war ich für die Aufnahme aller an den Diffraktometern IPDS2 bzw. IPDS2T der Firma STOE gemessenen Daten zuständig. Messungen am Quest

D8 Diffraktometer der Firma BRUKER wurden von Dr. C. Gunnar Werncke und der zentralen Serviceabteilung für Kristallstrukturanalyse am Fachbereich Chemie der Philipps-Universität Marburg unter der Leitung von Dr. Klaus Harms und Dr. Sergei Ivlev ausgeführt. Alle Datensätze, die mittels Einkristallstrukturanalyse erhalten wurden, wurden von mir gelöst und verfeinert. Bei der Verfeinerung von **[MnL$^{1}_{2}$]**, K{18c6}**[MnL^{1}L^{1}*]** (K{18c6})$_2$**[CrL$^{4}_{2}$]$_2$,** und NBu$_4$**[Co(Br)L$^{1}_{2}$]** erhielt ich Hilfestellung von Dr. Frank Tambornino. Mit der Unterstützung der hausinternen NMR-Abteilung des Fachbereichs Chemie der Philipps-Universität Marburg unter der Leitung von Dr. Xiulan Xie nahm ich alle Evans-Messungen auf und wertete diese selbständig aus. Elementaranalytische Untersuchungen wurden von Lutz Ruppach, Alena Shlyaykher und mir vorbereitet und durch mich ausgewertet. Die Messungen selbst führte die hausinterne Abteilung für Massenspektrometrie und Elementanalytik des Fachbereichs Chemie der Philipps-Universität Marburg unter der Leitung von Dr. Uwe Linne durch. ^{1}H-NMR-, IR- und UV/Vis-Messungen wurden von Lutz Ruppach, Alena Shlyaykher und mir ausgeführt. Die Auswertungen wurden von mir übernommen. Das Manuskript wurde von mir in Zusammenarbeit mit Dr. C. Gunnar Werncke verfasst.

Dalton Transactions

ROYAL SOCIETY OF CHEMISTRY

PAPER

View Article Online
View Journal | View Issue

Cite this: *Dalton Trans.*, 2021, **50**, 10947

Homoleptic quasilinear metal(I/II) silylamides of Cr–Co with phenyl and allyl functions – impact of the oxidation state on secondary ligand interactions†

Ruth Weller, Lutz Ruppach, Alena Shlyaykher, Frank Tambornino and C. Gunnar Werncke *

Received 12th May 2021,
Accepted 7th July 2021

DOI: 10.1039/d1dt01543e

rsc.li/dalton

Herein we describe the synthesis and characterization of a variety of new quasilinear metal(I/II) silylamides of the type $[M(N(Dipp)SiR_3)_2]^{0,-}$ (M = Cr–Co) with different silyl substituents (SiR_3 = $SiPh_{3-n}Me_n$ (*n* = 1–3), $SiMe_2(allyl)$). By comparison of the solid state structures we show that in the case of phenyl substituents secondary metal–ligand interactions are suppressed upon reduction of the metal. Introduction of an allyl substituted silylamide gives divalent complexes with additional metal–π-alkene interactions with only weak activation of the C=C bond but substantial bending of the principal N–M–N axis. $1e^-$-reduction makes cobalt a more strongly bound alkene substituent, whereas for chromium, reduction and intermolecular dimerisation of the allyl unit are observed. It thus indicates that the general view of low-coordinate 3d-metal ions as electron deficient seems not to apply to anionic metal(I) complexes. Additionally, the obtained cobalt(I) complexes are reacted with an aryl azide giving trigonal imido metal complexes. These can be regarded as rare examples of high-spin imido cobalt compounds from their structural and solution magnetic features.

Introduction

Open-shell, linear complexes $[ML_2]$ are a rare class in coordination chemistry, which show promise in the fields of (catalytic) bond and element activation as well as molecular magnetism.[1–3,4–10] These complexes are mostly found in the +II oxidation state bearing bulky anionic ligands such as amides,[11,12] (thio)phenolates,[6,13–15] or terphenyls.[8,9,13,16] The steric encumbrance of the ligands shields the sterically and coordinatively unsaturated metal, and by that prevent dimerisation.[17] A common trait in linear compounds are secondary interactions between the unsaturated metal ion and ligand substituents. This is especially prevalent for adjacent phenyl groups and leads to bending of the ligand–metal–ligand axis.[1,2,4,6,13,15,18–21] While these interactions shield and stabilize the metal centre, they are unwanted in the case of molecule magnetism due to quenching of orbital angular momentum.[4,9,12,20,22–24]

In the case of open-shell monovalent compounds, which are less numerous, the situation is less clear. For neutral linear metal(I) compounds, interactions of aryl substituents with the electron richer metal(I) are observable, as for example for mixed ligated NHC/amide or amidate nickel(I) compounds.[18,19,25–27] Similarly, cationic complexes such as $[M(NHC)_2]^+$ give also evidence of an unsaturated metal ion *via* adduct formation, such as by THF or additional NHCs.[28] In contrast, for *anionic* linear metal(I) complexes $[ML_2]^-$, which are obtained by the reduction of the aforementioned $[ML_2]$ compounds, substantial metal–ligand interactions were so far not observed.[5,7,10,29–31] Moreover, a singular report on the chromium complex $[Cr(N(Dipp)Si^iPr_3)_2]^{0,-}$ (Dipp = 2,6-di-isopropylphenyl) hints at distinct differences with respect to the oxidation state, whereas only in the divalent case secondary ligand interactions are observed *via* pronounced bending of the Dipp moiety towards the metal ion (Fig. 1).[29]

Recent reports by us and others concerning the behaviour of two-coordinate metal(I) ions bearing two anionic silylamide ligands also indicated a diverging behaviour of the metal(I) ion and an indifference of a two-coordinate metal(I) ion in $[ML_2]^-$ towards σ-donor ligands,[6,30,32] that contrasts the situation of their divalent counterparts.[33,34] Interactions of $[ML_2]^-$ with substrates were only observed if π-backbonding with or even formal $1e^-$ reduction of the substrate was possible.[35]

Fachbereich Chemie, Philipps-Universität Marburg, Hans-Meerwein-Straße 4, D-35032 Marburg, Germany. E-mail: gunnar.werncke@chemie.uni-marburg.de

† Electronic supplementary information (ESI) available. CCDC 2073678–2073682, 2074223–2074237, 2074256 and 2074317. For ESI and crystallographic data in CIF or other electronic format see DOI: 10.1039/d1dt01543e

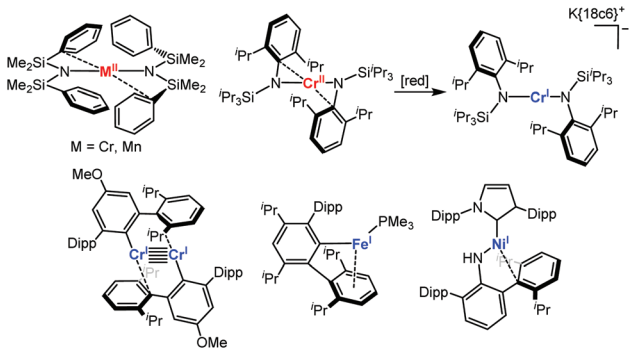

Fig. 1 Examples of low-coordinate metal(I/II) complexes with secondary metal–ligand interactions (Dipp = 2,6-di-iso-propylphenyl).[18,19,25,27,29]

Furthermore, in the case of formally neutral metal amides with intramolecular counter ion complexation ([KM(N(Dipp)$SiR_3)_2$]), donor ligands exclusively coordinate to the counter ion, but not to the transition metal.[36] This evoked the question of the apparent lack of Lewis acidity of the 3d-metal(I) ion in these anionic compounds is an intrinsic feature or rather due to the absence of conformationally accessible arenes or other functionalities. In our general quest to broaden the usability of linear metal(I) silylamides, we aimed at the deliberate introduction of functionalities in quasilinear metal(I) complexes. This stems in part from their use as platforms for unusual metal-multiple bonds, which was recently shown for imido cobalt complexes.[37,38]

In this report we present the synthesis of quasilinear metal(II) bis(silylamide) complexes [ML_2] (M = Cr–Co) bearing a –N(Dipp)$SiMe_2$Ph ligand (=**L**^{1}), with a coordinatively accessible phenyl function. In the solid state, these complexes show arene–metal interactions expectantly, which also exist in non-coordinating solvents. For chromium this is extended to –N(Dipp)$SiMePh_2$ (**L**^{2}), and for iron to –N(Dipp)$SiPh_3$ (**L**^{3}). Reduction of these complexes leads to anionic metal(I) complexes of type K{18c6}[ML_2] (**L**^{1}: Fe, Co; **L**^{2}: Fe), in which such secondary metal–arene interactions are absent, and for manganese, intramolecular C–H activation is observed. This is extended to allyl substituents (–N(Dipp)$SiMe_2$(allyl), **L**^{4}), in which the metal–alkene interaction is substantially stronger in the reduced state. In the case of chromium, one-electron reduction of the allyl function under concomitant Cr–C and intermolecular C–C bond formation is observed. For cobalt, the obtained monovalent compounds are used to obtain some additional rare imido cobalt complexes, which is remarkable in the presence of an allyl unit.

Results and discussion

The synthesis of homoleptic, linear metal(I) complexes bearing anionic ligands is, thus far, restricted to silylamide ligands such as –N(Dipp)$SiMe_3$,[6,7] –N(Dipp)Si^iPr_3 [29] and –$N(SiMe_3)_2$ [7] or the silylmethanide –$C(SiMe_3)_3$.[5,10] In these compounds secondary interactions are absent likely due to steric reasons and lack of suitable functionalities. This holds also true for their direct divalent counterparts, with the exception of [Cr(N(Dipp)$Si^iPr_3)_2$] (Fig. 1). As such, we sought to modify the –N(Dipp)SiR_3 ligand sets accordingly by installing accessible phenyl functions ($SiMe_{3-n}Ph_n$, n = 1–3) at the Si atom. All aryl(silyl) amines were obtained by reacting stoichiometric amounts of 2,6-di-iso-propyl aniline with *n*-butyl lithium at −20 °C followed by chlorosilane addition (Scheme 1).[39,40] Work-up gave the amines as colourless oils (HN(Dipp)$SiMe_{3-n}Ph_n$: **HL**^{1} (n = 1), **HL**^{2} (n = 2)) or as white solids (HN(Dipp)$SiPh_3$: **HL**^{3}) in very good yields and purity. The most salient ^{1}H NMR spectroscopic feature of these amines is the signal of the NH protons which are found among 4.05 ppm (**HL**^{3}), 2.90 (**HL**^{2}) and 2.46 ppm (**HL**^{1}) as broad singlets. The corresponding lithium salts were obtained by subsequent deprotonation of the amine with *n*-butyl lithium in Et_2O (**LiL**^{3}) or *n*-pentane (all other) as white solids in yields of 77% to 96%.

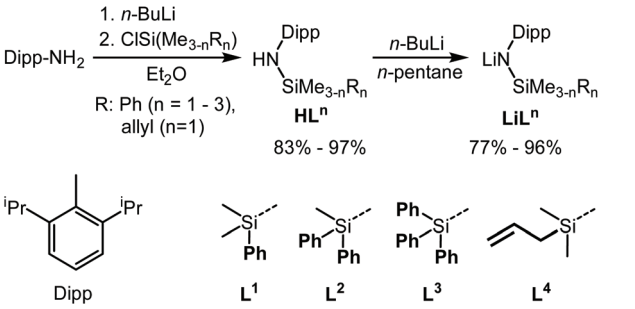

Scheme 1 Synthetic pathway to the used lithio silylamides.

Crystalline **LiL**^{1},[41] shows a dimeric structure in the solid state, with a nearly symmetric Li_2N_2 core (Li–N: 1.987(3) Å and Li–N′: 2.025(3) Å; Fig. 2, left). The phenyl group of each ligand is oriented towards an adjacent lithium cation (Li–C1: 2.708(3) Å). Furthermore, a Me_{Dipp} group of each ligand is oriented towards a lithium cation with C–Li 2.864(3) Å which is in the range of weak electrostatic interactions (for comparison: agostic Li–H_3C interactions are between 2.0 and 2.2 Å).[42] **LiL**^{2} and **LiL**^{3} are monomeric in the solid state, with the coordination sphere of lithium

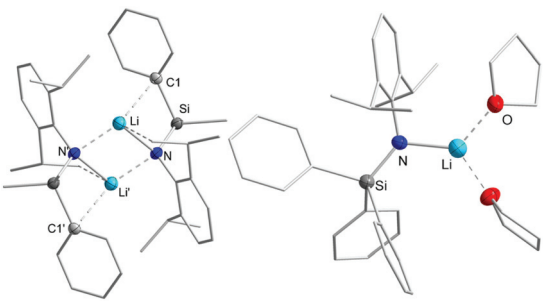

Fig. 2 Crystal structures of the dimeric (LiN(Dipp)$SiMe_2$Ph)$_2$ (**LiL**^{1}, left) from a saturated *n*-pentane solution and the monomeric $LiL^3 \times (THF)_2$·(**LiL**^{3}, pentane layered saturated THF solution, right). All hydrogen atoms are omitted for clarity.

saturated by THF. Accordingly Li–aryl interactions are absent (Li–C1: 3.772(3) Å (**LiL^2**); 3.663(3) Å (**LiL^3**)).

Metal complexes bearing a phenyl substituent

The quasilinear metal(II) complexes **[ML$^n{}_2$]** were obtained by reacting one equivalent of the metal chloride (M = Cr–Co) with two equivalents of the respective lithium salt (**LiL^1–LiL^3**) in diethyl ether. This was comprehensively conducted using **LiL^1** (M = Cr–Fe), whereas for **LiL^2** and **LiL^3** only conceptual reactions were performed with chromium (**[CrL$^2{}_2$]**) or iron (**[FeL$^3{}_2$]**) (Scheme 2).

After stirring overnight a colour change of the respective reaction mixtures was observed (Cr: dark green; Mn: beige; Fe: orange/brown; Co: dark red). All volatiles were then removed under reduced pressure, and the solid was redissolved in *n*-pentane to allow separation from the formed lithium chloride. A crystalline material was obtained from saturated *n*-pentane solutions of the compounds at −40 °C in moderate yields. For **L^1** neutral complexes **[ML$^1{}_2$]** (M = Mn–Co) were obtained as crystalline solids in yields of 54% (**[MnL$^1{}_2$]**), 79% (**[FeL$^1{}_2$]**) and 78% (**[CoL$^1{}_2$]**); for chromium only intractable oily substances were observed. This is not particularly surprising, given the reported instability of the related, elusive [Cr(N(Dipp)SiMe$_3$)$_2$], for which self-deprotonation and cluster formation were observed.[43] Only an increase of the steric profile of the silyl substituents (Si^{i}Pr$_3$ or SiMe^{t}Bu$_2$) gave linear chromium(II) silyl amides.[21,29] In **[ML$^1{}_2$]** (M = Mn–Co) the M–N bond lengths shorten along the series from *ca.* 1.94 Å (**[MnL$^1{}_2$]**) to 1.86 Å (**[CoL$^1{}_2$]**) (Table 1), which is due to the decrease of ion radii along the series and in agreement with other literature known complexes of the type [M(N(Dipp)SiR$_3$)$_2$] (M = Mn–Co).[7,43–45] The introduced phenyl ring is clearly oriented towards the metal center with M–C1$_{ipso}$ distances of only 2.800(7) Å for **[MnL$^1{}_2$]**, 2.696(2) Å for **[FeL$^1{}_2$]** and 2.856(2) Å for **[CoL$^1{}_2$]**. Consequently, the ◁ N1–M–N2 angles deviate from linearity (compared to [M(N(Dipp)SiMe$_3$)$_2$]: 180°) with values of 152.29(17)° (Mn), 150.69(6)° (Fe) and 164.31(7) (Co) and narrower ◁ M–N–Si bond angles with values of 110.9(2)° (Mn), 108.86(8)° (Fe) and 114.35(8) (Co) ([M(N(Dipp)SiMe$_3$)$_2$]: ≈125°).[44]

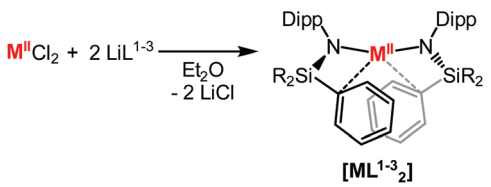

L^1: M = **Mn** (54%), **Fe** (79%), **Co** (78%) **L^2**: M = Cr (10%) **L^3**: M = **Fe** (53%)

Scheme 2 Synthesis of quasilinear metal(II) silylamide complexes [ML$^n{}_2$] (L^1 = N(Dipp)SiMe$_2$Ph (M = Mn–Co); L^2 = N(Dipp)SiMePh$_2$ (M = Cr); L^3 = N(Dipp)SiPh$_3$ (M = Fe).

For chromium, a comparable complex was obtained employing the more encumbering diphenyl silyl derivative **LiL^2** yielding **[CrL$^2{}_2$]**, which was pure by combustion analysis. X-ray analysis on suitable crystals revealed, besides **[CrL$^2{}_2$]** (see Fig. 3), the presence of co-crystallized (LiL^2)$_2$ (17%, see Fig. S84†). In **[CrL$^2{}_2$]**, one of the phenyl rings of one ligand is clearly orientated towards the chromium ion with a Cr–C$_{ipso}$ distance of only 2.372(3) Å. Consequently, the ◁ N1–Cr–N2 bond angle deviates with 140.02° strongly from linearity and the geometry in **[CrL$^2{}_2$]** is better described as Y-shaped, accounting for the substantial chromium–carbon interaction. The even more sterically demanding triphenylsilyl (**L^3**) ligand set was also probed using iron as a representative. **[FeL$^3{}_2$]** was obtained by reaction of 2 equivalents of **LiL^3** with FeCl$_2$. In the solid state the closest secondary arene–metal interaction of **[FeL$^3{}_2$]** is 2.980(2) Å and thus significantly longer than that of **[FeL$^1{}_2$]** (2.696(2) Å) (Table 1). The metal–arene interaction M–C2 to the second ligand weakens to a higher extent with a distance of 3.173(2) Å, highlighting the larger steric demand of the **L^3** ligand. Unsurprisingly, the N1–Fe–N2 axis is closer to linearity (162.26(10)°) in comparison to **[FeL$^1{}_2$]**, whereas the Fe–N slightly shortens to 1.884(2) Å.

The inherent paramagnetism of the samples leads to highly broadened signals in ^{1}H NMR and prevents any signal assignment for **[MnL$^1{}_2$]**, as well as **[CrL$^2{}_2$]** and **[FeL$^3{}_2$]**.[7,36] In contrast, the proton spectrum of **[CoL$^1{}_2$]** is rather well behaved and – together with the one of [Co(N(Dipp)SiMe$_3$)$_2$][34] – allowed for a signal assignment. In C$_6$D$_6$ the broad signal at 93.4 ppm corresponds to the methyl groups at the silyl moieties of **[CoL$^1{}_2$]** (see Fig. S9†). Two contrary shifted signals at 41.6 ppm and −173.2 ppm indicate different electronic environments for the iso-propyl-methyl groups and therefore a hindered rotation

Table 1 Selected bond lengths and angles of compounds **[ML$^{1-3}{}_2$]$^{0/-}$** (L^1: M = Mn–Co; L^2: M = Cr; L^3: M = Fe) and **[MnL^{1}L^1*]$^-$** (* smallest N–Si–C$_{Ph}$ angle)

	Compound	M–N1/M–N2/Å	M–C1/M–C2/Å	N1–M–N2/°	M–N–Si*	N–Si–C$_{Ph}$*	Torsion angle
Cr	**[CrL$^2{}_2$]**	1.9515(13)/1.9274(11)	3.318(8)/2.372(3)	140.02(5)	101.75(7)	97.41(11)	39.67(12)
Mn	**[MnL$^1{}_2$]**	1.955(4)/1.941(3)	2.900(4)/2.800(7)	152.29(17)	110.9(2)	100.5(2)	40.0(4)
	[MnL^{1}L^1*]$^-$	2.042(11)/2.160(12)	2.11(2)/3.70(2)	134.4(4)	89.6(5)/134.2(6)	101.4(8)	177.71(10)
Fe	**[FeL$^1{}_2$]**	1.9100(15)/1.9098(15)	2.696(2)/2.8780(18)	150.69(6)	108.86(8)	100.56(8)	40.03(16)
	[FeL$^1{}_2$]$^-$	1.905(4)/1.903(4)	3.938(3)/3.859(7)	172.10(17)	116.2(2)	114.4(1)	14.9(5)
	[FeL$^3{}_2$]	1.889(2)/1.884(2)	2.980(2)/3.173(2)	162.26(10)	112.89(12)	104.01(12)	36.1(2)
	[FeL$^3{}_2$]$^-$	1.911(3)/1.905(3)	3.605(4)/3.417(3)	172.50(13)	116.64(16)	110.29(15)	45.2(2)
Co	**[CoL$^1{}_2$]**	1.8610(15)/1.8562(15)	2.856(2)/3.2158(17)	164.31(7)	114.35(8)	100.73(7)	37.42(16)
	[CoL$^1{}_2$]$^-$	1.883(3)/1.881(3)	3.642(5)/3.707(4)	172.55(13)	113.35(16)	111.34(19)	29.6(4)

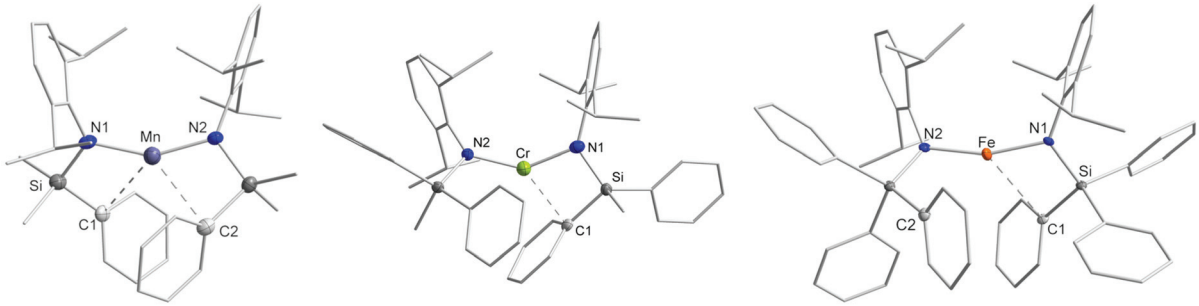

Fig. 3 General structures of $[ML^{1-3}_2]$ (left: $[ML^1_2]$ (M = Mn–Co, depicted for manganese); middle: $[CrL^2_2]$ (solid solution with dimeric $(LiL^2)_2$ (17%, not depicted, see also Fig. S84†); right: $[FeL^3_2]$). All hydrogen atoms are omitted for clarity.

of the ligand sets in solution. The arylic protons of the Dipp moiety cause singlets at 45.6 ppm (*m*-C**H**$_{Dipp}$) and −45.7 ppm (*p*-C**H**$_{Dipp}$). The remaining signals at −55.8 ppm and −128.0 ppm can be attributed to the phenyl rings of the silyl fragments. Changing from C_6D_6 to the coordinating THF-d_8, a broadened signal of the methyl groups at the silyl moieties is now located at 14.2 ppm, whereas the two signals at 24.9 ppm and −30.0 ppm correspond to the methyl groups of the isopropyl groups (see Fig. S10†). While the paramagnetic influence to the protons in *meta*- (41.8 ppm) and *para*- (−31.0 ppm) positions seem to be largely unaffected by the solvent, the three highfield shifted signals at −4.55 ppm, −16.4 ppm and −42.2 ppm indicate a less paramagnetically shifted environment for the phenyl rings. Furthermore, the signal for methine protons, absent in C_6D_6, is observed at 99.4 ppm. From these observations we tentatively conclude that in coordinating solvents such as THF-d_8 the metal–phenyl interactions are likely replaced by solvent coordination.[34] For $[FeL^1_2]$, similar observations were made, with respect to the solvent dependency (Fig. S7/8†).

Treatment of the metal(II) complexes $[ML^1_2]$ (M = Mn–Co) with 1.1 equivalents of potassium graphite in diethyl ether in the presence of one equivalent of 18-crown-6 leads to an immediate colour change of the reaction mixture (Mn: beige → dark violet; Fe: orange → red; Co: dark red → light green). A crystalline material was obtained by diffusion of *n*-pentane into a diethyl ether solution of each compound at −40 °C yielding violet K{18c6}$[MnL^1L^{1*}]$, light green K{18c6}$[FeL^1_2]$, and light green K{18c6}$[Co(L^1)_2]$ in yields up to 77% (Scheme 3). Similarly, greenish K{18c6}$[FeL^3_2]$ was obtained, whereas only decomposition was observed for $[CrL^2_2]$. X-ray diffraction analysis of $[FeL^1_2]^-$ and $[CoL^1_2]^-$ revealed the presence of quasilinear complexes ($[FeL^1_2]^-$: 172.10(17)°; $[CoL^1_2]^-$: 172.55(13)°) with widening of the ∢ M–N–Si bond angles to values of 116.2(2) ($[FeL^1_2]^-$) and 113.35(16)° ($[CoL^1_2]^-$) (Fig. 4, middle; Table 1). By losing the metal–arene interaction, the ligands rotate into an eclipsed conformation with torsion angles of 14.9(5)° for $[FeL^1_2]^-$ and 29.6(4)° for $[CoL^1_2]^-$. The M–N bond lengths are mostly unaffected by the reduction of the metal. $[MnL^1L^{1*}]^-$ showed intramolecular C–H activation under Mn–C bond formation. A similar behaviour was

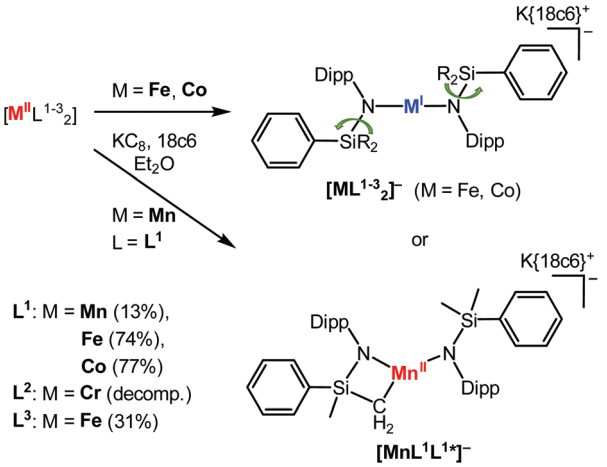

Scheme 3 Reduction of $[ML^{1-3}_2]$ with potassium graphite in the presence of 18-crown-6 lead to the reduced metal(I) complexes $[MnL^1L^{1*}]^-$, $[ML^1_2]^-$ (M = Fe, Co) and $[FeL^3_2]^-$.

described for the reaction of $CrCl_3$ with LiN(Dipp)SiMe$_3$ under C–H bond activation of a CH_3 unit of the Dipp moiety.[46] In the solid state structure of $[MnL^1L^{1*}]^-$, whose data set suffers from weakly diffracting crystals, the manganese atom is disordered over two positions (ratio 2 : 1), which is correlated with the bonding to the CH_2-group of either of the two amide ligands (Fig. 4, left). This leads to a strongly bent N1–Mn–N2 bond axis (134.4(4)°) and a distorted trigonal ligand geometry of the resulting manganese(II) ion.

Similar to the compounds comprising the SiMe$_2$Ph function (L^1), metal–arene interactions are also absent in $[FeL^3_2]^-$ with its multiple phenyl functions (Fig. 4, right). The N–M–N bond angle is closer to linear (172.50(13)° in $[FeL^3_2]^-$), with the phenyl rings facing away from the iron center, resulting in a torsion angle of 45.2(2)°. All other bond lengths and angles in the ligand sets remain the same within standard deviations. This indicates that, even when crowding the metal's sphere with phenyl functions, the metal(I) center in anionic silylamides lacks arene–metal interactions which indicates the absence of significant Lewis-acidity of the 3d-metal(I) ion in linear compounds bearing two anionic ligands.

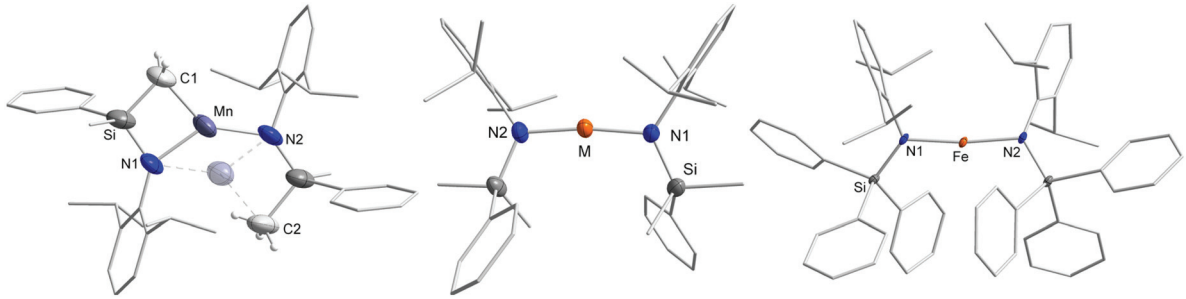

Fig. 4 Sections of the molecular structures of K{18c6}[MnL^1L^{1*}] and K{18c6}[ML^n_2] in the solid state (left: $[MnL^1L^{1*}]^-$; middle: $[ML^1_2]^-$ (M = Fe, Co); right: $[FeL^3_2]^-$). The K{18c6} counter ions and hydrogen atoms are generally omitted for clarity. For $[MnL^1L^{1*}]^-$ the disorder of the manganese atom is indicated.

^{1}H NMR spectroscopy also proved expectantly difficult for the monovalent complexes and was only informative for $[CoL^1_2]^-$. By using $[Co(N(Dipp)SiMe_3)_2]^-$ as a reference,[31,36] the aliphatic signals of the Dipp moiety of $[CoL^1_2]^-$ are found at 17.0/−84.9 ppm ($CH(CH_3)_2$) and at 23.3 ppm ($CH(CH_3)_2$), respectively. Aryl protons in *meta*- and *para*-positions correspond to signals at 14.6 ppm and 2.85 ppm. At 21.4 ppm a broad singlet likely represents the two methyl groups at the silyl moiety, whereas signals at −2.59 ppm, −7.39 ppm and −38.1 ppm belong to protons of the phenyl substituent of the $SiMe_2Ph$ group.

Complexes bearing an allyl substituent

Recently we reported on the distinct interaction of linear anionic metal(I) complexes with alkyne and phosphine substituted alkene substrates.[32,47] In these cases either the formation of π-complexes or subsequent substrate transformation was observed. As such we wanted to elaborate intramolecular alkene coordination which would also allow for assessing the impact of the oxidation state on the metal–olefin interaction in this coordination geometry. For that we chose –N(Dipp)$SiMe_2$(allyl) (**L^4**) as a representative. LiN(Dipp)$SiMe_2$(allyl) (**LiL^4**) was obtained in good yields in two steps upon reaction of $ClSiMe_2$(allyl) with LiNHDipp and subsequent deprotonation of the obtained HN(Dipp)$SiMe_2$(allyl) (**HL^4**) with *n*-butyl lithium (see Scheme 1). The most salient ^{1}H NMR spectroscopic feature of **HL^4** is the signal for the NH proton at 2.26 ppm measured in C_6D_6, which is low-field shifted compared to **$HL^{1–3}$** (see above). The allyl moiety of **HL^4** shows a multiplet from 4.99 to 5.05 ppm for the two terminal alkene protons and a multiplet from 5.81 to 5.95 ppm ($CH{=}CH_2$), which shifts upon lithiation of the amide to 5.00–5.11 ppm and 6.08–6.25 ppm, respectively. Solid state analysis of **LiL^4** could unfortunately not be performed due to the rapid melting of the crystals. Next, two equivalents of **LiL^4** were reacted with the respective metal(II) chloride giving $[ML^4_2]$ (M = Cr–Co) in yields of 47%–79% (Scheme 4). In the solid state the amide ligands are arranged in a bent, quasilinear fashion with ◁ N1–M–N2 angles ranging from 143.61(4)° (Fe) to 150.24(5)° (Cr) (Fig. 5). Both the alkene ligands are situated on the opposing side of the metal with an alkene–M–alkene' angle between 144.3° ($[MnL^4_2]$) and 148.5° ($[FeL^4_2]$), the alkene–M–alkene' axis is perpendicular towards the N1–M–N2 axis leading to geometries best described as intermediates between the seesaw and tetrahedron ($\tau_4' \approx 0.43–0.47$). The M–N bond lengths shorten from Cr (2.0129(13) Å) to Co (1.9262(7) Å) (see Table 2), but are overall longer than those in $[ML^1_2]$, probably due to the higher coordination number. M–alkene distances amount to 2.3243(4) Å (Cr), 2.6475(4) Å (Mn), 2.4351(3) Å (Fe) and 2.4437(3) Å (Co), with C=C bond lengths of 1.330(3) Å (Mn) or around 1.34 Å (Cr: 1.346(2) Å, Fe: 1.3418(17) Å, and Co: 1.3421(13) Å), respectively. Structural examples of metal(II)–alkene interactions are absent for manganese and generally scarce for other 3d metals. In these,

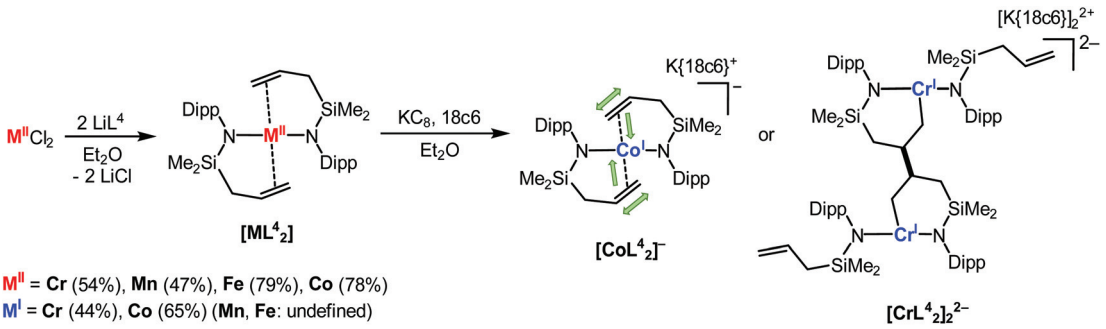

Scheme 4 Synthesis of $[ML^4_2]$ (M = Cr–Co) and stepwise reduction to $[CoL_4^2]^-$ and $[CrL^4_2]_2^{2-}$.

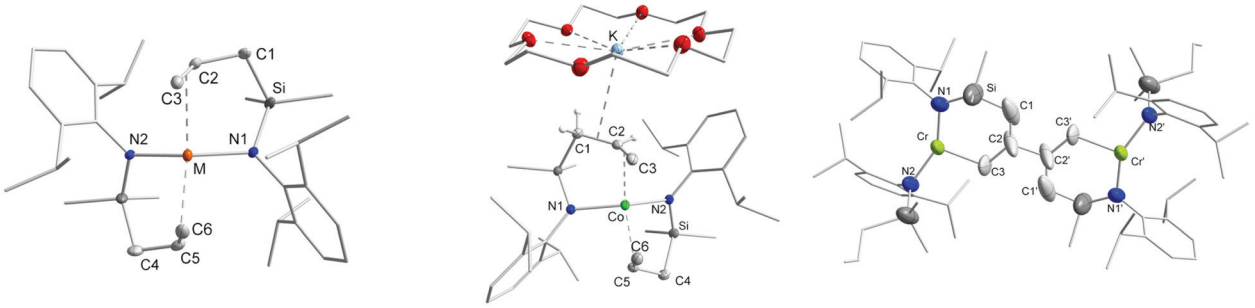

Fig. 5 Molecular structures of $[ML^4_2]$ (M = Cr–Co; left), $[CoL^4_2]-$ (middle) and the anionic section of $[CrL^4_2]_2^{2-}$ (right). Non-coordinating K{18c6} moieties and unnecessary hydrogen atoms are omitted for clarity.

Table 2 Selected structural values of the neutral $[ML^4_2]$ (M = Cr–Co) and the reduced species $[CoL^4_2]^-$

	Compound	M–N1/M–N2/Å	C2═C3/C5═C6	M···C═C	N1–M–N2/°	CC–M–CC/°
Cr	$[CrL^4_2]$	2.0155(12)/2.0129(13)	1.346(2)/1.348 (2)	2.3243(4)/2.3457(3)	150.24(5)	147.33(1)
Mn	$[MnL^4_2]$	2.0040(15)/2.0030(15)	1.330(3)/1.337(3)	2.6618(3)/2.6475(4)	149.26(6)	144.30(1)
Fe	$[FeL^4_2]$	1.9546(9)/1.9544(9)	1.3418(17)/1.343(2)	2.4824(3)/2.4351(3)	143.61(4)	148.59(1)
Co	$[CoL^4_2]$	1.9262(7)/1.9280(7)	1.3421(13)/1.3444(16)	2.4653(3)/2.4437(3)	144.37(3)	144.49(1)
	$[CoL^4_2]^-$	2.0142(14)/2.0248(14)	1.379(3)/1.369(3)	2.0337(3)/2.0646(4)	138.08(6)	138.53(1)

longer C═C bond distances are found for chromium (1.43 Å),[48] iron (1.36–1.41 Å)[49–53] and cobalt (1.37–1.38 Å)[54,55] complexes with closer distances between the metal and the alkene (Cr: 2.13 Å;[48] Fe: 1.93–2.23 Å;[49–53] Co: 1.94–1.95 Å (ref. 54 and 55)). The observed C═C lengths in $[ML^4_2]$ are close to non-coordinating allylsilyl units[56] and cationic magnesium(II)–π-alkene compounds, in which backbonding is absent (C═C: 1.32–1.35 Å).[57] From this we conclude that the metal–alkene interactions in $[ML^4_2]$ are weak and mostly electrostatic. Similar to $[ML^{1-3}_2]$, the evaluation of $[ML^4_2]$ *via* ^{1}H NMR spectroscopy was only partially possible due to the compound's paramagnetism. Best results were again received for cobalt ($[CoL^4_2]$), with similarities to the signal distribution of $[CoL^1_2]$ (compare Fig. S33 and 34†)

In C_6D_6 the methyl groups of the silyl fragment experience smaller paramagnetic shifting effects with a signal at 26.5 ppm. Additionally, the allylic chain in $[CoL^4_2]$ evokes broad signals at 57.1 ppm, −48.0 ppm and −164 ppm. Interestingly, no remarkable changes in the shifts are observable by measuring $[CoL^4_2]$ in THF-d_8, indicating persistent coordination of the alkene unit to the cobalt ion, or by preventing THF coordination.

Reduction of $[ML^4_2]$ (M = Cr–Co) with 1.1 equivalents of potassium graphite in diethyl ether in the presence of one equivalent of 18-crown-6 was subsequently conducted. For manganese and iron only the formation of lightly coloured, unidentifiable solids, which led to decomposition, were obtained. For cobalt, the envisioned silylamide complex $[CoL^4_2]^-$ could be obtained in 65% yield, whose structure was verified by X-ray diffraction analysis. In comparison to the divalent $[CoL^4_2]$, the interaction between the metal ion and the allyl unit is stronger, with a shorter Co–alkene distance of 2.0337(3) Å in $[CoL^4_2]^-$ (−0.4 Å *vs.* $[CoL^4_2]$) as well as elongation of the C═C bond to 1.379(3) Å (+0.035 Å *vs.* $[CoL^4_2]$). The C═C bond activation is slightly lower than that found for other low-valent, low-coordinate cobalt–alkene complexes (1.39–1.44 Å),[54,58] which speaks to only moderate π-backbonding in $[CoL^4_2]^-$. In comparison to the parent $[Co(N(Dipp)SiMe_3)_2]^-$, the ^{1}H NMR signals of the alkene unit in $[CoL^4_2]^-$ are found at 47.4 ppm, 23.4 ppm and 9.71 ppm, which indicates coordinative interactions also in solution. For chromium, a green compound was isolated, whose combustion data were in agreement with $[CrL^4_2]^-$. However, X-ray diffraction analysis revealed the presence of a dimeric compound in which two $[CrL^4_2]$ units are connected *via* a C–C bond in the β-position of an allyl substituent. Although the structure suffered from intrinsic crystallographic flaws, due to weakly diffracting crystals, tentative examination of the bond lengths shows the presence of a C–C single bond of the former C═C bond unit as well as a clear presence of a Cr–C bond. The second allyl ligand of each complex part is pointing away from the respective metal ion, which contrasts the observations for $[CoL^4_2]^-$. This gives a T-shaped coordination geometry around each chromium ion. We rationalize the formation of $[CrL^4_2]_2^{2-}$ as follows: first, reduction of $[CrL^4_2]$ leads to the envisioned monovalent chromium complex "$[CrL^4_2]^-$" with internal π-alkene coordination. This can alternatively be described as a chromium(II) ion bound to an alkene radical anion, similar to the observations made by us and others for related metal alkyne complexes.[47,59] These radical anions would undergo subsequent intermolecular C–C coupling which gives the dimeric complex $[CrL^4_2]_2^{2-}$. The behaviour of the bound alkene unit overall resembles the electrochemical reductive dimerisation of activated alkenes.[60] $[CrL^4_2]_2^{2-}$ exhibits a magnetic moment of 6.17μ_B which speaks to weakly antiferromagnetically coupled high-spin chromium(II) ions.

Magnetic properties of $[ML^n{}_2]^{-,0}$ complexes in solution

Having understood the different behaviours of the functional groups (Ph *vs.* allyl) in solution, we were interested in how the secondary ligand coordination impacts the magnetic properties of **[ML$^{1-4}{}_2$]** in solution which we probed with the Evans method (Table 3). The μ_{eff} of 5.65μ_B for **[MnL$^1{}_2$]** is close to the spin-only value of 5.92μ_B and similar to [Mn(N(Dipp)SiMe$_3$)$_2$] (6.09μ_B).[7]

[FeL$^1{}_2$] and **[CoL$^1{}_2$]** exhibit expectantly higher than spin-only values due to orbital contributions. For **[CrL$^2{}_2$]** the effective magnetic moment of μ_{eff} = 3.24μ_B is substantially lower than the spin-only value of 4.89μ_B (quintet state (d^4)) and in stark contrast to comparable complexes like [Cr^{II}(N(Dipp)Si^{i}Pr$_3$)$_2$] (μ_{eff} = 4.9μ_B).[29] Unquenched negative orbital contributions are to be expected for a d^4 system, however, the extent in the case of **[CrL$^2{}_2$]** indicates further unresolved differences in the electronic structure. The magnetic moment of **[FeL$^3{}_2$]** of 4.88μ_B equals the spin-only value ($\mu_{S.O.}$ = 4.89) without any further orbital contributions. Similarly, a high-spin character was found for all **[ML$^4{}_2$]** complexes. For **[CrL$^4{}_2$]**, μ_{eff} amounted to 4.45μ_B, which is slightly less than the spin-only value of 4.89μ_B (S = 2). For **[MnL$^4{}_2$]**, the μ_{eff} value (5.27μ_B) is also lower than the expected $\mu_{S.O.}$ value (5.92μ_B, S = 5/2). In contrast, for iron (5.14μ_B; $\mu_{S.O.}$ = 4.89μ_B) and especially cobalt (4.84μ_B; $\mu_{S.O.}$ = 3.87μ_B), values higher than the spin-only values are again obtained. This is in general agreement with other linear metal(II) complexes. Diminished contributions from orbital angular momentum are generally observed which is expected due to deviations from linearity and additional coordinative interactions.[4,9,12,20,22–24] With an effective magnetic moment of 5.37μ_B ($\mu_{S.O.}$ = 5.92μ_B), **[MnL^{1}L^1*]$^-$** is a high-spin metal(II) complex with five unpaired electrons. **[FeL$^{1/3}{}_2$]$^-$** and **[CoL$^1{}_2$]$^-$** retain their higher than spin-only values with μ_{eff} = 4.52μ_B/4.60μ_B ($\mu_{S.O.}$ = 3.87μ_B) and μ_{eff} = 3.94μ_B ($\mu_{S.O.}$ = 2.83μ_B), respectively. Those values resemble the ones for [M(N(Dipp)SiMe$_3$)$_2$]$^-$ (M = Fe (μ_{eff} = 4.34μ_B); Co (μ_{eff} = 3.93μ_B))[36] is to be expected given the proposed absence of any metal–aryl interactions. The magnetic susceptibility of **[CoL$^4{}_2$]$^-$** (μ_{eff} = 4.04μ_B) is comparable to that of **[CoL$^1{}_2$]$^-$** indicating that here the additional allyl coordination does not negatively impact the orbital contributions to the magnetic moment. However, pronounced contributions from a description of **[CoL$^4{}_2$]$^-$** as a cobalt(II) bound alkene radical anion, mimicking π-alkyne adducts of linear metal(I) silylamides,[47] are also possible.

Table 3 Magnetic susceptibilities in solution using the Evans method (C_6D_6 for neutral, THF-d_8 for anionic complexes)[61,62]

	Compound	μ_{eff} [μ_B] ($\mu_{S.O.}$ [μ_B])
Cr	**[CrL$^2{}_2$]**	3.24 (4.89)
	[CrL$^4{}_2$]	4.45 (4.89)
	[CrL$^4{}_2$]$_2^{2-}$	6.17 (6.93)
Mn	**[MnL$^1{}_2$]**	5.65 (5.92)
	[MnL^{1}L^1*]$^-$	5.37 (5.92)
	[MnL$^4{}_2$]	5.27 (5.92)
Fe	**[FeL$^1{}_2$]**	5.23 (4.89)
	[FeL$^1{}_2$]$^-$	4.52 (3.87)
	[FeL$^3{}_2$]	4.88 (4.89)
	[FeL$^3{}_2$]$^-$	4.60 (3.87)
	[FeL$^4{}_2$]	5.14 (4.89)
Co	**[CoL$^1{}_2$]**	4.89 (3.87)
	[CoL$^1{}_2$]$^-$	3.94 (2.83)
	[CoL$^4{}_2$]	4.84 (3.87)
	[CoL$^4{}_2$]$^-$	4.04 (2.83)
	[Co(NDipp)L$^1{}_2$]$^-$	4.87 (4.89)
	[Co(NDipp)L$^4{}_2$]$^-$	5.05 (4.89)

Imido cobalt complexes

As recently shown, linear cobalt(I) silylamides are valuable platforms for the generation of unique imido cobalt complexes in higher spin states.[37,38] Those studies also showed that these imido cobalt units do not interact with alkenes (*e.g.* under C=C bond aziridation) or other electron rich substrates (phosphines). In contrast, it is highly competent in H atom abstraction from external C–H bonds.[38] To elaborate further on the suitability of linear cobalt(I) complexes to support an [NR] unit in higher spin states, we conducted respective studies using **[CoL$^1{}_2$]$^-$** and **[CoL$^4{}_2$]$^-$** as examples. The latter was of special interest due to possible intramolecular aziridation. **[CoL$^1{}_2$]$^-$** and **[CoL$^4{}_2$]$^-$** were reacted with one equivalent of Dipp–N$_3$, respectively, which was recently used to yield unique cobalt imidyl radical complexes using the parent silylamide complex K{m}[Co(N(Dipp)SiMe$_3$)$_2$]$^-$ (m = none, 18c6, crypt).[38] The corresponding reactions in a 1 : 1 (v/v) mixture of THF/Et$_2$O gave dark green **[Co(NDipp)L$^1{}_2$]$^-$** and dark red **[Co(NDipp)L$^4{}_2$]$^-$** in yields of 67% and 65%, respectively (Scheme 5).

In both compounds (Fig. 6), the cobalt ions exhibit a trigonal planar coordination motif with two amide and one NDipp ligands. For **[Co(NDipp)L$^1{}_2$]$^-$**, the Co–N$_{imido}$ bond length amounts to 1.7707(17) Å with a symmetry generated linear Co–N–Dipp axis (180°). For **[Co(NDipp)L$^4{}_2$]$^-$** the situation is similar (Co–N$_{imido}$ 1.7555(16) Å, Co–N–Dipp 176.95(16)°). The observed cobalt imide bond lengths are remarkable, as they are usually found between 1.61 and 1.70 Å.[63] They slightly surpasses even those of the recently reported K{18c6}[Co(NDipp)(N(Dipp)SiMe$_3$)$_2$] (Co–N 1.751(2)), a unique high-spin system with substantial imidyl radical character on the imide nitrogen.[37] For **[Co(NDipp)L$^1{}_2$]$^-$** and **[Co(NDipp)L$^4{}_2$]$^-$** magnetic moments of 4.87μ_B and 5.05μ_B are observed, indicating a quintet state. As such the obtained imido complexes are tenta-

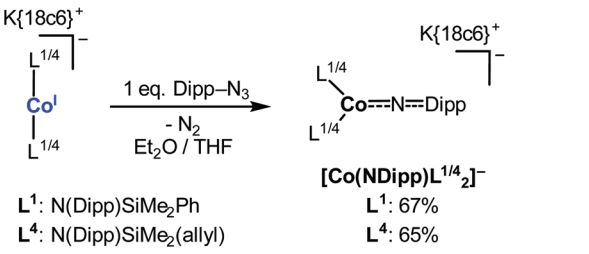

Scheme 5 Reactivity of **[CoL$^{1/4}{}_2$]$^-$** towards Dipp-N$_3$ resulting in the imido complexes **[Co(NDipp)L$^{1/4}{}_2$]$^-$**.

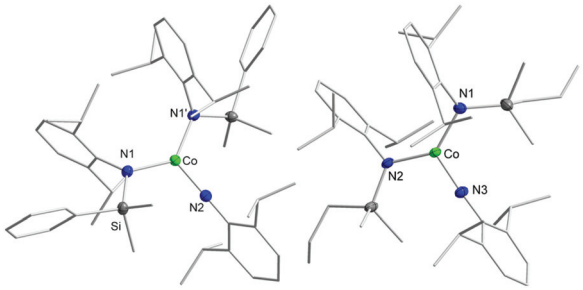

Fig. 6 Sections of the crystal structures $[Co(NDipp)L^1_2]^-$ (left) and $[Co(NDipp)L^4_2]^-$ (right). Cations and H atoms are omitted for clarity. $[Co(NDipp)L^1_2]^-$: Co–N2 1.7707(17) Å, Co–N1/N1′ 1.9493(12) Å, N1–Co–N1′ 128.17(7), Co–N2–C 180.0°; $[Co(NDipp)L^4_2]^-$: Co–N3 1.7555(16) Å, Co–N1 1.9378(18) Å, Co–N2 1.9230(18) Å, N1–Co–N1′ 134.35(7)°, Co–N3–C 176.95(16)°.

tively described as very rare examples of high-spin imido cobalt species.[37,64] The case of $[Co(NDipp)L^4_2]^-$ is especially remarkable as it exhibits an alkene function in the vicinity of the [MNR] unit. Generally, late 3d-metal imido complexes are potent in the aziridation of alkene substrates,[65] which is not observed here, even after prolonged storage at ambient temperature, heating to 50 °C or light irradiation (400 nm). Steric constraints or a pronounced nucleophilic character of the imidyl radical, which mitigates its aziridation reactivity, might be the reason for this.

Conclusion

We reported the synthesis of quasilinear homoleptic metal(II) complexes $[M(N(Dipp)SiMe_nPh_{3-n})_2]$ of Cr–Co. The presence of phenyl substituents gives rise to secondary metal–arene interactions, reflected by a bent N–M–N axis. Reduction of these compounds with KC_8 in the presence of 18-crown-6 gave the corresponding metal(I) complexes for iron and cobalt, where metal–arene interactions are absent. These findings show, at the structural level, that in anionic quasilinear metal complexes the metal(I) ion exhibits negligible Lewis acidity, contrasting the situation in the divalent, neutral counterparts. For manganese, C–H bond activation of a $SiMe_3$-unit is observed. The introduction of a propenyl substituent into the ligand set (using –N(Dipp)$SiMe_2$(allyl)) gave divalent complexes with intramolecular alkene coordination, a feature not reported so far for divalent manganese. The propenyl–metal interaction is rather weak which is indicated by long M–alkene and C=C bond lengths. For cobalt, reduction leads to enhanced π-backbonding and for chromium even to an intermolecular reductive C–C coupling of the propene unit upon formation of a binuclear chromium(II) alkyl complex. These results emphasize the intricacies of metal–bond interactions in the case of low-valent and low-coordinate metal ions, and reveal that in anionic linear metal(I) complexes, the metal ion should not be regarded as coordinatively and electronically deficient, but rather electron rich. The obtained cobalt complexes were further reacted with an aryl azide, resulting in rare examples of high-spin imido cobalt complexes. This is remarkable in the case of propenyl substituted ancillary ligands, as the alkene function does not react with the imido metal unit, an usually observed behaviour for imido metal units. The aptitude of silylamides in the stabilization of imido metal units in higher spin states as well as the potential to introduce (coordinatively labile) functionalities in the vicinity of a quasi-two-coordinate metal ion is currently developed in our lab.

Experimental section

Materials and methods

All manipulations were carried out in a glovebox under a dry argon atmosphere, unless indicated otherwise. Used solvents were dried by continuous distillation over sodium metal for several days, degassed *via* three freeze–pump–thaw cycles and stored over molecular sieves 4 Å. Deuterated solvents were used as received, degassed *via* three freeze-pump cycles and stored over molecular sieves 4 Å. The ^{1}H NMR spectra were recorded on a Bruker AV 500, a Bruker HD 500 or a Bruker HD 300 NMR spectrometer (Bruker Corporation, Billerica, USA). Chemical shifts are reported in ppm relative to the residual proton signals of the solvent (for ^{1}H). $w_{1/2}$ is the line width of a signal at half its maximum intensity. Integrals of the broad signals of the ligand set were obtained directly or by peak fitting (in the case of overlapping signals) using the MestreNova software package (Mestrelab, Santiago de Compostela, Spain). Solution magnetic susceptibility was determined using the Evans method from at least two independent samples.[61,62] IR measurements were conducted on a Bruker Alpha ATR-IR spectrometer (Bruker Corporation, Billerica, USA). The UV/VIS measurement was recorded on an AnalytikJena Specord S600 using the WinASPECT software. Elemental analysis was performed by the "in-house" service of the Chemistry Department of Philipps University Marburg, Germany, using a CHN(S) analyser vario MICRO cube (Elementar Analysensysteme GmbH, Langenselbold, Germany).

–N(Dipp)$SiMe_2$Ph (L^1) containing compounds

HL^1. The compound is known in the literature, but so far not isolated and used without analysis.[39,41] 5.62 mL of 2,6-di-iso-propylaniline (30 mmol, 1 equiv.) were cooled to −20 °C in Et_2O before adding 1 equivalent of *n*-BuLi (30 mmol, 1 equiv.) dropwise. The mixture was stirred at room temperature for one hour before it was cooled to −20 °C, again. A precooled solution of 5.00 mL of chloro(dimethyl)phenyl silane (30 mmol, 1 equiv.) in Et_2O was added slowly, whereas a light yellow solution and a colourless precipitate appeared. The reaction mixture was allowed to stir overnight at room temperature before the solvent was removed *in vacuo*. After condensation of the remaining residue (120 °C, 10^{-3} mbar), the desired product (HL^1) was obtained as a colourless, viscous liquid in a yield of 97%. **Yield:** 9.10 g (29 mmol, 97%). **^{1}H NMR:**

(300.2 MHz, C_6D_6, 300 K, ppm): δ = 7.54–7.57 (m, 2 H, Ar**H**), 7.19–7.26 (m, 3 H, Ar**H**), 7.04–7.11 (m, 3 H, Ar**H**), 3.40 (h, 2 H, $^3J_{H,H}$ = 6.82 Hz, C**H**$(CH_3)_2$), 2.46 (bs, 1 H, N**H**), 1.12 (d, 12 H, $^3J_{H,H}$ = 6.84 Hz, CH(C**H**$_3)_2$), 0.32 (s, 6 H, Si(C**H**$_3)_2$). **^{13}C-{^{1}H} NMR**: (75.5 MHz, C_6D_6, 300 K, ppm): δ = 144.2 (s, N**C**$_{ipso}$), 140.0 (s, *o*-**C**$_{Dipp}$), 139.5 (s, Si**C**$_{ipso}$), 133.6 (s, *o*-**C**H$_{Ph}$), 129.5 (s, *p*-**C**H$_{Ph}$), 128.1 (*m*-**C**H$_{Ph}$), 124.2 (s, *p*-**C**H$_{Dipp}$), 123.4 (s, *m*-**C**H$_{Dipp}$), 28.6 (s, **C**H$(CH_3)_2$), 23.8 (s, CH(**C**H$_3)_2$), −0.70 (s, Si(**C**H$_3)_2$).

LiL^1. The compound is known in the literature, but so far not isolated and used without analysis.[41] 6.50 g (20.8 mmol, 1 equiv.) of **HL^1** were dissolved in 20 mL of *n*-pentane. It was cooled to −20 °C and *n*-BuLi (20.8 mmol, 1 equiv.) was added dropwise, while a white precipitate appeared immediately. After stirring for a further 30 minutes, the solid was filtered off and washed with *n*-pentane before drying *in vacuo*. **LiL^1** could be obtained as a white solid in a yield of 77%. **Yield**: 5.06 g (16.0 mmol, 77%). Crystals, suitable for X-ray diffraction analysis, were obtained from a saturated *n*-pentane solution of **LiL^1** at −40 °C. **^{1}H NMR**: (300.2 MHz, C_6D_6, 300 K, ppm): δ = 7.81–7.83 (m, 2 H, *m*-C**H**$_{Dipp}$), 7.32–7.37 (m, 2 H, *m*-C**H**$_{Ph}$), 7.21–7.26 (m, 1 H, *p*-C**H**$_{Dipp}$), 6.81–6.93 (m, 3 H, *o*/*p*-C**H**$_{Ph}$), 3.07 (h, 2 H, $^3J_{H,H}$ = 6.83 Hz, C**H**$(CH_3)_2$), 1.16 (d, 6 H, $^3J_{H,H}$ = 6.67 Hz, CH(C**H**$_3)_2$), 0.52 (d, 6 H, $^3J_{H,H}$ = 7.01 Hz, CH(C**H**$_3)_2$), 0.30 (s, 6 H, Si(C**H**$_3)_2$). **^{13}C-{^{1}H} NMR**: (300.2 MHz, C_6D_6, 300 K, ppm): δ = 149.3 (s, N**C**$_{ipso}$), 143.1 (s, *o*-**C**$_{Dipp}$), 142.9 (s, Si**C**$_{ipso}$), 133.4 (s, *o*-**C**H$_{Ph}$), 129.9 (m, *m*/*p*-**C**H$_{Ph}$), 124.3 (s, *m*-**C**H$_{Dipp}$), 120.3 (s, *p*-**C**H$_{Dipp}$), 27.7 (s, **C**H$(CH_3)_2$), 25.3 (s, CH(**C**H$_3)_2$), 24.7 (s, CH(**C**H$_3)_2$), 0.98 (s, Si(**C**H$_3)_2$). **^{1}H NMR**: (300.2 MHz, THF-d_8, 300 K, ppm): δ = 7.54–7.57 (m, 2 H, *m*-C**H**$_{Ph}$), 7.05–7.16 (m, 3 H, *o*/*p*-C**H**$_{Ph}$), 6.73 (d, 2 H, $^3J_{H,H}$ = 7.45 Hz, *m*-C**H**$_{Dipp}$), 6.37 (d, 1 H, $^3J_{H,H}$ = 7.41 Hz, *p*-C**H**$_{Dipp}$), 4.05 (h, $^3J_{H,H}$ = 6.90 Hz, 2 H, C**H**$(CH_3)_2$), 0.99 (d, 12 H, $^3J_{H,H}$ = 6.93 Hz, CH(C**H**$_3)_2$), 0.17 (s, 6 H, Si(C**H**$_3)_2$). **^{13}C-{^{1}H} NMR**: (75.5 MHz, THF-d_8, 300 K, ppm): δ = 157.4 (s, N**C**$_{ipso}$), 149.2 (s, Si**C**$_{ipso}$), 143.8 (s, *o*-**C**$_{Dipp}$), 134.5 (s, *o*-**C**H$_{Ph}$), 127.4 (s, *m*-**C**H$_{Ph}$), 127.2 (s, *p*-**C**H$_{Ph}$), 122.5 (s, *m*-**C**H$_{Dipp}$), 115.4 (s, *p*-**C**H$_{Dipp}$), 27.2 (s, **C**H$(CH_3)_2$), 25.3* (s, CH(**C**H$_3)_2$), 2.96 (s, Si(**C**H$_3)_2$). *, The signal partially overlaps with the solvent signal. Elemental analysis of $C_{20}H_{28}LiNSi$ (317.48 g mol^{-1}): calcd: N 4.41, C 75.67, H 8.89; found: N 4.91, C 76.11, H 8.89%. **IR** (ATR, cm^{-1}): $\tilde{\nu}$ = 3068 (w), 3043 (w), 3007 (w), 2958 (m), 2922 (w), 2903 (w), 2866 (m), 1586 (w), 1458 (w), 1418 (s), 1387 (w), 1363 (w), 1308 (m), 1231 (s), 1188 (s), 1143 (w), 1104 (m), 1050 (w), 1040 (m), 997 (w), 921 (vs), 882 (m), 824 (m), 813 (m), 798 (m), 775 (vs), 755 (vs), 737 (s), 701 (s), 668 (m), 619 (w), 593 (w), 572 (m), 531 (m), 478 (m), 451 (w), 436 (m), 413 (m).

[ML$^1_2$] (M = Mn–Co). One equivalent of MCl_2 (M = Mn–Co) and two equivalents of **LiL^1** were suspended in 15 mL of diethyl ether. It was allowed to stir overnight at room temperature, while a change in colour was observed (Mn: beige → dark beige; Fe: yellow → orange-brown; Co: light yellow → dark red-brown). All volatiles were removed under reduced pressure before resolving the obtained residue in *n*-pentane. The lithium chloride was filtered off and it was cooled to −40 °C for crystallization. After several days the solution was decanted off. Crystalline **[ML$^1_2$]** (M = Mn–Co) was obtained in yields of 54–79%.

[MnL$^1_2$]. Using 79 mg of $MnCl_2$ (0.63 mmol, 1 equiv.), **[MnL$^1_2$]** could be obtained as a yellow-orange crystalline solid. **Yield**: 230 mg (0.34 mmol, 54%). Crystals, suitable for X-ray diffraction analysis, were obtained from a saturated *n*-pentane solution of **[MnL$^1_2$]** at −40 °C. Elemental analysis of $C_{40}H_{56}MnN_2Si_2$ (676.01 g mol^{-1}): calcd: N 4.14, C 71.07, H 8.35; found: N 4.56, C 70.67, H 8.27%. **IR** (ATR, cm^{-1}): $\tilde{\nu}$ = 3068 (w), 3050 (w), 3015 (w), 2954 (s), 2924 (m), 2865 (m), 1588 (w), 1563 (w), 1482 (w), 1457 (m), 1425 (s), 1400 (w), 1380 (m), 1360 (m), 1310 (s), 1239 (s), 1195 (s), 1159 (w), 1145 (w), 1104 (s), 1049 (w), 1039 (m), 997 (w), 972 (w), 924 (s), 879 (w), 834 (s), 795 (m), 779 (vs), 766 (vs), 733 (s), 714 (w), 704 (s), 692 (s), 672 (m), 644 (w), 621 (w), 592 (m), 536 (m), 503 (w), 466 (m), 441 (m), 426 (s). **Evans** (500.1 MHz, 300 K, C_6D_6 + 1% TMS): μ_{eff} = 5.65μ_B; $\mu_{S.O.}$ = 5.92μ_B.

[FeL$^1_2$]. Using 60 mg of $FeCl_2$ (0.47 mmol, 1 equiv.), **[FeL$^1_2$]** could be obtained as a yellow-orange crystalline solid. **Yield**: 250 mg (0.37 mmol, 79%). Crystals, suitable for X-ray diffraction analysis, were obtained from a saturated *n*-pentane solution of **[FeL$^1_2$]** at −40 °C. **^{1}H NMR** (300.2 MHz, C_6D_6, 300 K, ppm): δ = 98.0 (bs, 12 H, $w_{\frac{1}{2}}$ = 1870 Hz, Si(C**H**$_3)_2$), 40.8 (bs, 4 H, $w_{\frac{1}{2}}$ = 450 Hz, *m*-C**H**$_{Dipp}$), 29.6 (bs, 14 H, $w_{\frac{1}{2}}$ = 580 Hz, CH(C**H**$_3)_2$), −32.0 (bs, $w_{\frac{1}{2}}$ = 222 Hz, C**H**$_{Ph}$), −50.3 (bs, 2 H, $w_{\frac{1}{2}}$ = 266 Hz, *p*-C**H**$_{Dipp}$), −61.3 (bs, 4 H, $w_{\frac{1}{2}}$ = 460 Hz, C**H**$_{Ph}$), −108 (bs, 4 H, $w_{\frac{1}{2}}$ = 2000 Hz, C**H**$_{Ph}$), −136.9 (bs, 12 H, $w_{\frac{1}{2}}$ = 2470 Hz, CH(C**H**$_3)_2$). **^{1}H NMR** (300.2 MHz, THF-d_8, 300 K, ppm): δ = 61.4 (s, 4 H, $w_{\frac{1}{2}}$ = 150 Hz, *m*-C**H**$_{Dipp}$), 38.6 (bs, 4 H, $w_{\frac{1}{2}}$ = 2140 Hz, C**H**$(CH_3)_2$), 23.7 (s, 12 H, $w_{\frac{1}{2}}$ = 160 Hz, CH(C**H**$_3)_2$), 13.8 (bs, 12 H, $w_{\frac{1}{2}}$ = 565 Hz, Si(C**H**$_3)_2$), −3.53 (bs, $w_{\frac{1}{2}}$ = 48 Hz, C**H**$_{Ph}$), −8.73 (s, $w_{\frac{1}{2}}$ = 86 Hz, C**H**$_{Ph}$), −26.0 (bs, $w_{\frac{1}{2}}$ = 74 Hz, *p*-C**H**$_{Dipp}$), −26.3 (bs, $w_{\frac{1}{2}}$ = 1020 Hz, C**H**$_{Ph}$), −64.1 (bs, 12 H, $w_{\frac{1}{2}}$ = 690 Hz, CH(C**H**$_3)_2$). Elemental analysis of $C_{40}H_{56}FeN_2Si_2$ (676.92 g mol^{-1}): calcd: N 4.14, C 70.97, H 8.34; found: N 4.43, C 70.60, H 8.24%. **IR** (ATR, cm^{-1}): $\tilde{\nu}$ = 3050 (w), 3016 (w), 2954 (m), 2925 (m), 2865 (m), 1588 (w), 1563 (w), 1482 (w), 1457 (m), 1425 (s), 1401 (w), 1381 (m), 1360 (m), 1332 (w), 1310 (s), 1239 (s), 1193 (s), 1159 (w), 1146 (w), 1105 (s), 1050 (w), 1039 (m), 996 (w), 956 (w), 918 (s), 879 (w), 839 (s), 782 (vs), 767 (vs), 733 (s), 715 (m), 701 (s), 674 (m), 595 (m), 535 (m), 464 (m), 442 (m), 426 (s). **Evans** (500.1 MHz, 300 K, C_6D_6 + 1% TMS): μ_{eff} = 5.20μ_B; $\mu_{S.O.}$ = 4.89μ_B.

[CoL$^1_2$]. Using 82 mg of $CoCl_2$ (0.63 mmol, 1 equiv.), **[CoL$^1_2$]** could be obtained as a dark red crystalline solid. **Yield**: 333 mg (0.49 mmol, 78%). Crystals, suitable for X-ray diffraction analysis, were obtained from a saturated *n*-pentane solution of **[CoL$^1_2$]** at −40 °C. **^{1}H NMR** (300.2 MHz, C_6D_6, 300 K, ppm): δ = 93.4 (bs, 12 H, $w_{\frac{1}{2}}$ = 1330 Hz, Si(C**H**$_3)_2$), 45.6 (bs, 4 H, $w_{\frac{1}{2}}$ = 358 Hz, *m*-C**H**$_{Dipp}$), 41.6 (bs, 12 H, $w_{\frac{1}{2}}$ = 345 Hz, C**H**$(CH_3)_2$), −45.7 (bs, 2 H, $w_{\frac{1}{2}}$ = 271 Hz, *p*-C**H**$_{Dipp}$), −55.8 (bs, 8 H, w = 326 Hz, C**H**$_{Ph}$), −128.0 (bs, 2 H, $w_{\frac{1}{2}}$ = 1560 Hz, C**H**$_{Ph}$), −173.2 (bs, 12 H, $w_{\frac{1}{2}}$ = 1780 Hz, CH(C**H**$_3)_2$). **^{1}H NMR** (300.2 MHz, THF-d_8, 300 K, ppm): δ = 99.4 (s, 4 H, $w_{\frac{1}{2}}$ = 1080 Hz, C**H**$(CH_3)_2$), 41.8 (s, 4 H, $w_{\frac{1}{2}}$ = 67 Hz, *m*-C**H**$_{Dipp}$), 24.9 (bs, 12 H, $w_{\frac{1}{2}}$ = 76 Hz, CH(C**H**$_3)_2$), 14.2 (bs, 12 H, $w_{\frac{1}{2}}$ = 355 Hz, Si(C**H**$_3)_2$), −4.55 (s, 2 H, $w_{\frac{1}{2}}$ = 40 Hz,

p-C**H**$_{Ph}$), −16.4 (s, 4 H, $w_{\frac{1}{2}}$ = 61 Hz, C**H**$_{Ph}$), −30.0 (bs, 12 H, $w_{\frac{1}{2}}$ = 700 Hz, CH(C**H**$_3$)$_2$), −31.0 (s, 2 H, $w_{\frac{1}{2}}$ = 67 Hz, *p*-C**H**$_{Dipp}$), −42.2 (bs, 4 H, $w_{\frac{1}{2}}$ = 640 Hz, C**H**$_{Ph}$). Elemental analysis of $C_{40}H_{56}CoN_2Si_2$ (680.01 g mol^{-1}): calcd: N 4.12, C 70.65, H 8.30; found: N 4.29, C 70.25, H 8.15%. **IR** (ATR, cm^{-1}): $\tilde{\nu}$ = 3068 (w), 3047 (w), 3014 (w), 2964 (m), 2950 (m), 2932 (m), 2867 (w), 1586 (w), 146 (w), 1450 (w), 1426 (m), 1382 (w), 1360 (w), 1311 (m), 1253 (m), 1236 (m), 1186 (m), 1107 (m), 1098 (m), 1051 (w), 1038 (w), 998 (w), 961 (w), 910 (s), 879 (m), 848 (s), 824 (s), 789 (vs), 767 (s), 734 (s), 699 (s), 650 (m), 588 (m), 534 (m), 474 (m), 439 (w), 424 (m), 412 (m). **Evans** (500.1 MHz, 300 K, C_6D_6 + 1% TMS): μ_{eff} = 4.89μ_B; $\mu_{S.O.}$ = 3.87μ_B.

K{18c6}[ML$^1_2$] (M = Mn–Co). One equivalent of **[ML$^1_2$]** (M = Mn−Co) and one equivalent of 18-crown-6 were dissolved in 5 mL of diethyl ether. After adding KC_8 (1.1 equiv.) the reaction mixture was stirred for several minutes at room temperature, while a change in colour was observed (Mn: beige → dark violet; Fe: orange → red; Co: dark red → light green). The graphite was filtered off, layered with *n*-pentane and cooled to −40 °C for several days for crystallization. The solution was decanted off and the remaining crystals were dried *in vacuo*. Crystalline K{18c6}**[ML$^1_2$]** (M = Mn–Co) was obtained in yields of 24–77%.

K{18c6}[MnL^{1}L^1*]. Using 56 mg of **[MnL$^1_2$]**, K{18c6}**[MnL^{1}L^1*]** could be obtained as a dark violet crystalline solid. **Yield**: 20 mg (0.02 mmol, 24%). Crystals, suitable for X-ray diffraction analysis, were obtained from a *n*-pentane layered solution of K{18c6}**[MnL^{1}L^1*]** in Et_2O at −40 °C. Elemental analysis of $C_{52}H_{80}MnKN_2O_6Si_2$ (979.43 g mol^{-1}): calcd: N 2.86, C 63.77, H 8.23; found: N 3.26, C 64.27, H 8.14%. **IR** (ATR, cm^{-1}): $\tilde{\nu}$ = 3060 (w), 3039 (w), 3003 (w), 2951 (m), 2895 (m), 2861 (m), 1584 (w), 1454 (m), 1421 (s), 1377 (w), 1351 (m), 1312 (m), 1284 (w), 1237 (s), 1192 (m), 1104 (vs), 1039 (m), 961 (m), 926 (s), 881 (w), 823 (s), 782 (s), 770 (m), 749 (w), 736 (m), 725 (w), 700 (s), 680 (m), 641 (m), 618 (w), 584 (m), 530 (m), 503 (w), 475 (m), 434 (m). **Evans** (500.1 MHz, 300 K, THF-d_8 + 1% TMS): μ_{eff} = 5.37μ_B; $\mu_{S.O.}$ = 5.92μ_B.

K{18c6}[FeL$^1_2$]. Using 100 mg of **[FeL$^1_2$]**, K{18c6}**[FeL$^1_2$]** could be obtained as a light green crystalline solid. **Yield**: 109 mg (0.11 mmol, 74%). Crystals, suitable for X-ray diffraction analysis, were obtained from a *n*-pentane layered solution of K{18c6}**[FeL$^1_2$]** in Et_2O at −40 °C. **^{1}H NMR** (300.2 MHz, THF-d_8, 300 K, ppm): δ = 26.6 (bs, $w_{\frac{1}{2}}$ = 480 Hz), 25.9 (bs, $w_{\frac{1}{2}}$ = 610 Hz), 12.9 (bs, 6 H, $w_{\frac{1}{2}}$ = 2070 Hz, Si(C**H**$_3$)$_2$), 9.89 (bs, $w_{\frac{1}{2}}$ = 200 Hz), 2.64 (s, 24 H, $w_{\frac{1}{2}}$ = 21.8 Hz, 18c6), −7.68 (s, $w_{\frac{1}{2}}$ = 76 Hz, C**H**$_{Ph}$), −12.8 (s, $w_{\frac{1}{2}}$ = 76 Hz, C**H**$_{Ph}$), −54 (bs, $w_{\frac{1}{2}}$ = 3800 Hz), −105.0 (bs, $w_{\frac{1}{2}}$ = 1400 Hz, CH(C**H**$_3$)$_2$). Elemental analysis of $C_{52}H_{80}FeKN_2O_6Si_2$ (980.33 g mol^{-1}): calcd: N 2.86, C 63.71, H 8.23; found: N 3.34, C 63.30, H 8.15%. **IR** (ATR, cm^{-1}): $\tilde{\nu}$ = 3061 (w), 3043 (w), 2951 (m), 3899 (m), 2860 (m), 1583 (w), 1472 (m), 1454 (m), 1420 (m), 1376 (w), 1351 (m), 1312 (m), 1284 (w), 1237 (s), 1193 (m), 1100 (vs), 1053 (m), 1040 (m), 997 (w), 962 (s), 925 (s), 883 (w), 866 (w), 834 (s), 866 (w), 834 (s), 804 (s), 781 (s), 727 (m), 702 (m), 685 (m), 671 (w), 640 (m), 621 (w), 583 (w), 531 (m), 476 (m), 430 (m). **Evans** (500.1 MHz, 300 K, THF-d_8 + 1% TMS): μ_{eff} = 4.52μ_B; $\mu_{S.O.}$ = 3.87μ_B.

K{18c6}[CoL$^1_2$]. Using 70 mg of **[CoL$^1_2$]**, K{18c6}**[CoL$^1_2$]** could be obtained as a light green crystalline solid. **Yield**: 75 mg (0.08 mmol, 77%). Crystals, suitable for X-ray diffraction analysis, were obtained from a *n*-pentane layered solution of K{18c6}**[CoL$^1_2$]** in Et_2O at −40 °C. **^{1}H NMR** (300.2 MHz, THF-d_8, 300 K, ppm): δ = 23.3 (bs, 4 H, $w_{\frac{1}{2}}$ = 500 Hz, C**H**(CH$_3$)$_2$), 21.4 (bs, 12 H, $w_{\frac{1}{2}}$ = 160 Hz, Si(C**H**$_3$)$_2$), 17.0 (bs, 12 H, $w_{\frac{1}{2}}$ = 38 Hz, CH(C**H**$_3$)$_2$), 14.6 (bs, 4 H, $w_{\frac{1}{2}}$ = 28 Hz, *m*-C**H**$_{Dipp}$), 3.01 (s, 24 H, $w_{\frac{1}{2}}$ = 19.9 Hz, 18c6), 2.85 (s, 2 H, $w_{\frac{1}{2}}$ = 15.5 Hz, *p*-C**H**$_{Dipp}$), −2.59 (s, 2 H, $w_{\frac{1}{2}}$ = 14.8 Hz, C**H**$_{Ph}$), −7.39 (s, 4 H, $w_{\frac{1}{2}}$ = 19.7 Hz, C**H**$_{Ph}$), −38.1 (bs, 4 H, $w_{\frac{1}{2}}$ = 218 Hz, C**H**$_{Ph}$), −84.9 (bs, 12 H, $w_{\frac{1}{2}}$ = 100 Hz, CH(C**H**$_3$)$_2$). Elemental analysis of $C_{52}H_{80}CoKN_2O_6Si_2$ (983.42 g mol^{-1}): calcd: N 2.85, C 63.51, H 8.20; found: N 3.24, C 63.71, H 8.13%. **IR** (ATR, cm^{-1}): $\tilde{\nu}$ = 3060 (w), 3045 (w), 2953 (m), 2913 (w), 2900 (w), 2859 (m), 1582 (w), 1475 (w), 1454 (m), 1420 (m), 1380 (w), 1351 (m), 1312 (m), 1284 (w), 1239 (m), 1196 (m), 1102 (vs), 1055 (m), 1039 (m), 992 (w), 961 (m), 933 (m), 830 (m), 803 (s), 780 (s), 760 (w), 741 (w), 727 (m), 702 (m), 668 (w), 640 (m), 588 (w), 540 (m), 533 (m), 478 (m), 436 (m). **Evans** (500.1 MHz, 300 K, THF-d_8 + 1% TMS): μ_{eff} = 3.94μ_B; $\mu_{S.O.}$ = 2.83μ_B.

–N(Dipp)SiMePh$_2$ (L^2) containing compounds

HL^2. 4.48 mL of 2,6-di-iso-propylaniline (24 mmol, 1 equiv.) were cooled to −20 °C in Et_2O before adding 1 equivalent of *n*-BuLi (24 mmol, 1 equiv.) dropwise. It was stirred at room temperature for one hour before it was cooled to −20 °C, again. A precooled solution of 5.00 mL of chloro(dimethyl) phenyl silane (24 mmol, 1 equiv.) in Et_2O was added slowly, whereas a light yellow solution and a colourless precipitate appeared. The reaction mixture was allowed to stir overnight at room temperature before the solvent was removed *in vacuo*. To extract the desired product, *n*-pentane was added and the white residue (LiCl) was filtered off afterwards. The solvent was removed *in vacuo* to obtain a colourless, viscous liquid (**HL^2**) in a yield of 99%. **Yield:** 8.89 g (0.024 mmol, 99%). **^{1}H NMR:** (300.2 MHz, C_6D_6, 300 K, ppm): δ = 7.56–7.59 (m, 4 H, *m*-C**H**$_{Ph}$), 7.14–7.17* (m, 6 H, *o*/*p*-C**H**$_{Ph}$), 7.01–7.08 (m, 3 H, C**H**$_{Dipp}$), 3.37 (h, 2 H, $^3J_{H,H}$ = 6.86 Hz, C**H**(CH$_3$)$_2$), 2.90 (bs, 1 H, N**H**), 1.04 (d, 12 H, $^3J_{H,H}$ = 6.84 Hz, CH(C**H**$_3$)$_2$), 0.54 (s, 3 H, Si(C**H**$_3$)). **^{13}C-{^{1}H} NMR:** (75.5 MHz, C_6D_6, 300 K, ppm): δ = 143.7 (s, N**C**$_{ipso}$), 139.4 (s, *o*-**C**$_{Dipp}$), 138.2 (s, Si**C**$_{ipso}$), 134.7 (s, *o*-**C**H$_{Ph}$), 129.8 (s, *p*-**C**H$_{Ph}$), 128.1 (s, *m*-**C**H$_{Ph}$), 124.1 (s, *p*-**C**H$_{Dipp}$), 123.5 (s, *m*-**C**H$_{Dipp}$), 28.8 (s, **C**H(CH$_3$)$_2$), 23.7 (s, CH(**C**H$_3$)$_2$), −2.63 (s, Si(**C**H$_3$)). *, The signal partially overlaps with the solvent signal.

LiL^2. 3.00 g (8.03 mmol, 1 equiv.) of **HL^2** were dissolved in 20 mL of *n*-pentane. It was cooled to −20 °C and *n*-BuLi (8.03 mmol, 1 equiv.) was added dropwise, while a white precipitate appeared immediately. After stirring for a further 30 minutes the solid was filtered off and washed with *n*-pentane before drying *in vacuo*. **LiL^2** could be obtained as a white solid in a yield of 77%. **Yield**: 2.69 g (7.09 mmol, 88%). Crystals, suitable for X-ray diffraction analysis, were obtained from a *n*-pentane layered solution of **LiL^2** in THF at −40 °C. **^{1}H NMR:** (300.2 MHz, C_6D_6, 300 K, ppm): δ = 7.49–7.52 (dd, 4 H,

$^3J_{H,H}$ = 7.61 Hz, $^3J_{H,H}$ = 1.80 Hz, *m*-C**H**$_{Ph}$), 7.11–7.21* (m, 6 H, *o*/*p*-C**H**$_{Ph}$), 6.84–6.93 (m, 3 H, C**H**$_{Dipp}$), 3.09 (h, 2 H, $^3J_{H,H}$ = 6.84 Hz, C**H**(CH$_3$)$_2$), 0.92 (d, 6 H, $^3J_{H,H}$ = 6.06 Hz, CH(C**H**$_3$)$_2$), 0.61 (d, 6 H, $^3J_{H,H}$ = 6.46 Hz, CH(C**H**$_3$)$_2$), 0.51 (s, 3 H, Si(C**H**$_3$)). *, The signal overlaps with the solvent signal. **^{13}C-{^{1}H} NMR**: (75.5 MHz, C_6D_6, 300 K, ppm): δ = 149.1 (s, N**C**$_{ipso}$), 143.1 (s, Si**C**$_{ipso}$), 141.4 (s, *o*-**C**$_{Dipp}$), 134.8 (s, *o*-**C**H$_{Ph}$), 129.5 (s, *p*-**C**H$_{Ph}$), 129.0 (s, *m*-**C**H$_{Ph}$), 124.6 (s, *m*-**C**H$_{Dipp}$), 120.7 (s, *p*-**C**H$_{Dipp}$), 28.2 (s, **C**H(CH$_3$)$_2$), 25.2 (s, CH(**C**H$_3$)$_2$), 24.9 (s, CH(**C**H$_3$)$_2$), 1.96 (s, Si(**C**H$_3$)). **^{1}H NMR**: (300.2 MHz, THF-d_8, 300 K, ppm): δ = 7.48–7.51 (m, 4 H, *m*-C**H**$_{Ph}$), 7.10–7.13 (m, 6 H, *o*/*p*-C**H**$_{Ph}$), 6.76 (d, 2 H, $^3J_{H,H}$ = 7.46 Hz, *m*-Ph**H**), 6.43 (t, 1 H, $^3J_{H,H}$ = 7.43 Hz, *p*-Ph**H**), 4.01 (h, $^3J_{H,H}$ = 6.90 Hz, 2 H, C**H**(CH$_3$)$_2$), 0.93 (d, 12 H, $^3J_{H,H}$ = 6.90 Hz, CH(C**H**$_3$)$_2$), 0.45 (s, 3 H, Si(C**H**$_3$)). **^{13}C-{^{1}H} NMR**: (300.2 MHz, THF-d_8, 300 K, ppm): δ = 156.4 (s, N**C**$_{ipso}$), 147.1 (s, *o*-**C**$_{Dipp}$), 143.6 (s, Si**C**$_{ipso}$), 135.5 (s, *o*-**C**H$_{Ph}$), 127.6 (s, *p*-**C**H$_{Ph}$), 127.4 (s, *m*-**C**H$_{Ph}$), 122.7 (s, *m*-**C**H$_{Dipp}$), 115.8 (s, *p*-**C**H$_{Dipp}$), 27.6 (s, **C**H(CH$_3$)$_2$), 24.9* (s, CH(**C**H$_3$)$_2$), 2.45 (s, Si(**C**H$_3$)). *, The signal (partially) overlaps with the solvent signal. Elemental analysis of $C_{25}H_{30}LiNSi$ (379.55 g mol^{-1}): calcd: N 3.69, C 79.11, H 7.97; found: N 3.85, C 79.56, H 8.07%. **IR** (ATR, cm^{-1}): $\tilde{\nu}$ = 3065 (w), 3048 (w), 2962 (w), 2949 (m), 2921 (w), 2899 (w), 2862 (m), 1587 (w), 1486 (w), 1455 (m), 1421 (s), 1384 (m), 1362 (w), 1339 (w), 1302 (m), 1248 (m), 1234 (s), 1187 (m), 1157 (w), 1145 (w), 1100 (s), 1067 (w), 1037 (m), 997 (w), 942 (s), 930 (s), 879 (w), 811 (m), 788 (s), 770 (s), 736 (s), 702 (vs), 672 (m), 645 (m), 618 (w), 600 (w), 577 (m), 530 (s), 480 (s), 453 (m), 422 (s).

[CrL$^2_2$]. 49 mg of $CrCl_2$ (0.40 mmol, 1 equiv.) and 300 mg of **LiL^2** (0.56 mmol, 2 equiv.) were suspended in 15 mL of diethyl ether. It was stirred overnight at room temperature, while a change in colour to dark brown was observed. All volatiles were removed under reduced pressure before resolving the obtained residue in *n*-pentane. The lithium chloride was filtered off and it was cooled to −40 °C for crystallization. After several days, the solution was decanted off and the remaining orange crystals were dried *in vacuo*. Crystalline **[CrL$^2_2$]** was obtained in a yield of 10%. **Yield**: 22 g (0.03 mmol, 10%). Elemental analysis of $C_{50}H_{60}CrN_2Si_2$ (797.21 g mol^{-1}): calcd: N 3.51, C 75.33, H 7.59; found: N 3.62, C 75.13, H 7.90%. **IR** (ATR, cm^{-1}): $\tilde{\nu}$ = 3064 (w), 3047 (w), 2954 (m), 2925 (m), 2925 (m), 2863 (m), 1586 (w), 1483 (w), 1458 (m), 1424 (s), 1380 (w), 1359 (w), 1313 (m), 1252 (m), 1204 (m), 1184 (m), 1155 (w), 1142 (w), 1105 (s), 1041 (m), 996 (w), 951 (m), 893 (m), 873 (m), 854 (m), 824 (m), 812 (m), 787 (s), 766 (s), 734 (s), 698 (vs), 652 (m), 590 (m), 529 (m), 482 (s), 448 (m), 425 (m), 403 (w). **Evans** (500.1 MHz, 300 K, C_6D_6 + 1% TMS): μ_{eff} = 3.24μ_B; $\mu_{S.O.}$ = 4.89μ_B.

–N(Dipp)SiPh$_3$ (L^3) containing compounds

HL^3. The synthesis of these compounds was described in the literature *via* an alternative pathway with no analytical data.[66] 1.60 mL of 2,6-di-iso-propylaniline (8.50 mmol, 1 equiv.) was cooled to −20 °C in Et_2O before adding 1 equivalent of *n*-BuLi (8.50 mmol) dropwise. It was stirred at room temperature for one hour before it was cooled to −20 °C, again. A precooled solution of 2.51 mg of chlorotriphenylsilane (8.50 mmol, 1 equiv.) in Et_2O was added dropwise, whereas a light yellow solution and a colourless precipitate appeared. The reaction mixture was allowed to stir overnight at room temperature before the solution was filtered off and the residue was washed with *n*-pentane. After drying *in vacuo*, **HL^3** could be obtained as a colourless oil in a yield of 97%. **Yield:** 3.63 g (8.34 mmol, 97%). Crystals, suitable for X-ray diffraction analysis, were obtained from a solution of **HL^3** in *n*-pentane at −40 °C. **^{1}H NMR**: (300.2 MHz, THF-d_8, 300 K, ppm): δ = 7.46–7.48 (m, 6 H, *m*-C**H**$_{Ph}$), 7.24–7.36 (m, 9 H, *o*/*p*-C**H**$_{Ph}$), 6.91 (m, 3 H, C**H**$_{Dipp}$), 4.05 (bs, 1 H, N**H**), 3.43 (h, $^3J_{H,H}$ = 6.64 Hz, 2 H, C**H**(CH$_3$)$_2$), 0.83 (d, 12 H, $^3J_{H,H}$ = 6.84 Hz, CH(C**H**$_3$)$_2$). **^{13}C-{^{1}H} NMR**: (75.5 MHz, THF-d_8, 300 K, ppm): δ = 145.9 (s, N**C**$_{ipso}$), 139.8 (s, *o*-**C**$_{Dipp}$), 136.8 (s, Si**C**$_{ipso}$), 136.5 (s, *o*-**C**H$_{Ph}$), 130.2 (s, *p*-**C**H$_{Ph}$), 128.3 (s, *m*-**C**H$_{Ph}$), 124.6 (s, *p*-**C**H$_{Dipp}$), 123.5 (s, *m*-**C**H$_{Dipp}$), 29.2 (s, **C**H(CH$_3$)$_2$), 23.7 (s, CH(**C**H$_3$)$_2$).

LiL^3. 3.35 g (7.69 mmol, 1 equiv.) of **HL^3** were dissolved in 20 mL of Et_2O. It was cooled to −20 °C and *n*-BuLi (7.69 mmol, 1 equiv.) was added dropwise, while a white precipitate appeared immediately. After stirring for a further 30 minutes, the solid was filtered off and washed with *n*-pentane before drying *in vacuo*. **LiL^3** could be obtained as a white solid in a yield of 96%. **Yield**: 3.26 g (7.38 mmol, 96%). Crystals, suitable for X-ray diffraction analysis, were obtained from a *n*-pentane layered solution of **LiL^3** in THF at −40 °C. **^{1}H NMR**: (300.2 MHz, THF-d_8, 300 K, ppm): δ = 7.41–7.44 (m, 6 H, *m*-C**H**$_{Ph}$), 7.13–7.15 (m, 9 H, *o*/*p*-C**H**$_{Ph}$), 6.75 (d, 2 H, $^3J_{H,H}$ = 7.48 Hz, *m*-C**H**$_{Dipp}$), 6.44 (t, 1 H, $^3J_{H,H}$ = 7.51 Hz, *p*-C**H**$_{Dipp}$), 3.90 (h, 2 H, $^3J_{H,H}$ = 6.85 Hz, C**H**(CH$_3$)$_2$), 0.77 (d, 12 H, $^3J_{H,H}$ = 6.69 Hz, CH(C**H**$_3$)$_2$). **^{13}C-{^{1}H} NMR**: (75.5 MHz, THF-d_8, 300 K, ppm): δ = 155.4 (s, N**C**$_{ipso}$), 144.8 (s, Si**C**$_{ipso}$), 143.5 (s, *o*-**C**$_{Dipp}$), 136.5 (s, *o*-**C**H$_{Ph}$), 128.0 (s, *p*-**C**H$_{Ph}$), 127.4 (s, *m*-**C**H$_{Ph}$), 122.8 (s, *m*-**C**H$_{Dipp}$), 116.2 (s, *p*-**C**H$_{Dipp}$), 28.0 (s, **C**H(CH$_3$)$_2$), 24.5 (s, CH(**C**H$_3$)$_2$). Elemental analysis of $C_{30}H_{32}LiNSi$ (441.62 g mol^{-1}): calcd: N 3.17, C 81.59, H 7.30; found: N 3.56, C 81.78, H 7.45%. **IR** (ATR, cm^{-1}): $\tilde{\nu}$ = 3060 (w), 3043 (w), 2953 (m), 2881 (m), 2861 (m), 1584 (m), 1481 (w), 1458 (m), 1416 (s), 1375 (w), 1354 (w), 1336 (m), 1317 (m), 1275 (m), 1253 (s), 1205 (m), 1180 (w), 1152 (w), 1140 (w), 1098 (s), 1040 (s), 972 (w), 960 (m), 919 (m), 886 (m), 807 (w), 764 (m), 746 (s), 698 (vs), 675 (m), 652 (m), 617 (w), 594 (w), 572 (m), 528 (m), 497 (s), 442 (m), 424 (m).

[FeL$^3_2$]. 35 mg of $FeCl_2$ (0.28 mmol, 1 equiv.) and 350 mg of **LiL^3** (0.56 mmol, 2 equiv.) were suspended in 15 mL of diethyl ether. It was stirred overnight at room temperature, while a change in colour from beige to yellowish green was observed. All volatiles were removed under reduced pressure before resolving the obtained residue in *n*-pentane. The lithium chloride was filtered off and it was cooled to −40 °C for crystallization. After several days, the solution was decanted off and the remaining orange crystals were dried *in vacuo*. Crystalline **[FeL$^3_2$]** was obtained in a yield of 53%. **Yield**: 135 mg (0.14 mmol, 53%). Crystals, suitable for X-ray diffraction analysis, were obtained from a saturated *n*-pentane solution of **[FeL$^3_2$]** at −40 °C. **^{1}H NMR** (300.2 MHz, C_6D_6, 300 K, ppm): δ =

44.9 (bs, $w_{\frac{1}{2}}$ = 2310 Hz), 42.0 (bs, $w_{\frac{1}{2}}$ = 230 Hz), 18.7 (bs, $w_{\frac{1}{2}}$ = 930 Hz), 14.5 (bs, $w_{\frac{1}{2}}$ = 860 Hz), −3.90 (bs, $w_{\frac{1}{2}}$ = 200 Hz), −10.3 (bs, $w_{\frac{1}{2}}$ = 180 Hz). −27.0 (bs, $w_{\frac{1}{2}}$ = 360 Hz), −32.6 (bs, $w_{\frac{1}{2}}$ = 530 Hz), −41.7 (bs, $w_{\frac{1}{2}}$ = 430 Hz). Elemental analysis of $C_6H_{64}FeN_2Si_2 \times C_4H_{10}O$ (999.32 g mol^{-1}): calcd: N 2.80, C 76.92, H 7.46; found: N 2.94, C 76.84, H 7.55% **IR** (ATR, cm^{-1}): $\tilde{\nu}$ = 3066 (w), 3050 (w), 2958 (m), 2923 (w), 2863 (w), 1586 (w), 1482 (w), 1457 (w), 1426 (m), 1380 (w), 1359 (w), 1311 (m), 1254 (m), 1240 (m), 1185 (m), 1104 (s), 1040 (m), 996 (w), 908 (m), 878 (w), 829 (m), 788 (s), 737 (m), 697 (vs), 595 (m), 535 (m), 497 (vs), 444 (m), 429 (m), 408 (w). **Evans** (500.1 MHz, 300 K, C_6D_6 + 1% TMS): μ_{eff} = 4.88μ_B; $\mu_{S.O.}$ = 4.89μ_B.

K{18c6}[FeL$^3_2$]. 30 mg of **[FeL$^3_2$]** (0.03 mmol, 1 equiv.) and 8.5 mg of 18-crown-6 (0.03 mmol, 1 equiv.) were dissolved in 5 mL of THF. After adding KC_8 (0.04 mmol, 1.1 equiv.) the reaction mixture was stirred for several minutes at room temperature, while a change in color from orange to dark red was observed. The graphite was filtered off before layering with *n*-pentane. It was allowed to crystallize at −40 °C for several days before the solution was decanted off. After washing with *n*-pentane the dark red crystals were dried *in vacuo*. Crystalline K{18c6}**[FeL$^3_2$]** was obtained in a yield of 31%. **Yield**: 12 mg (0.010 mmol, 31%). Crystals, suitable for X-ray diffraction analysis, were obtained from a *n*-pentane layered solution of **[FeL$^3_2$]**$^-$ in THF at −40 °C. **^{1}H NMR** (300.2 MHz, THF-d_8, 300 K, ppm): δ = 23.7 (bs, $w_{\frac{1}{2}}$ = 740 Hz), 20.4 (bs, $w_{\frac{1}{2}}$ = 670 Hz), 2.97 (s, 24 H, $w_{\frac{1}{2}}$ = 25.5 Hz, 18c6), −101.8 (bs, $w_{\frac{1}{2}}$ = 1360 Hz). Elemental analysis of $C_{72}H_{88}FeKN_2O_6Si_2$ (1228.62 g mol^{-1}): calcd: N 2.28, C 70.39, H 7.22; found: N 2.51, C 70.72, H 7.33%. **IR** (ATR, cm^{-1}): $\tilde{\nu}$ = 3060 (w), 3040 (w), 2951 (m), 2896 (m), 2859 (m), 1584 (w), 1564 (w), 1471 (m), 1454 (m), 1422 (s), 1376 (w), 1351 (m), 1313 (m), 1284 (w), 1241 (m), 1189 (m), 1100 (vs), 998 (w), 960 (m), 929 (m), 878 (w), 821 (m), 779 (s), 738 (m), 697 (vs), 593 (m), 533 (m), 501 (s), 443 (w), 427 (m), 415 (w). **Evans** (500.1 MHz, 300 K, THF-d_8 + 1% TMS): μ_{eff} = 4.60μ_B; $\mu_{S.O.}$ = 3.87μ_B.

−N(Dipp)SiMe$_2$(allyl) (L^4) containing compounds

HL^4. 2.79 mL of 2,6-di-iso-propylaniline (14.8 mmol, 1 equiv.) were cooled to −20 °C in Et_2O before adding 1 equivalent of *n*-BuLi (14.8 mmol) dropwise. It was stirred at room temperature for one hour before it was cooled to −20 °C, again. A precooled solution of 2.51 mg of chloro(dimethyl)allyl silane (14.8 mmol, 1 equiv.) in Et_2O was added slowly, whereas a colourless precipitate appeared. The reaction mixture was allowed to stir overnight at room temperature before the solvent was removed *in vacuo*. The desired product (**HL^4**) was obtained after condensation of the remaining residue (80 °C, 10^{-3} mbar) as a colourless, viscous liquid in a yield of 86%. **Yield**: 3.49 g (12.7 mmol, 86%). **^{1}H NMR**: (300.2 MHz, C_6D_6, 300 K, ppm): δ = 7.16–7.23* (m, 3 H, *m*/*p*-C**H**$_{Dipp}$), 5.81–5.95 (m, 1 H, C**H**=CH$_2$), 4.99–5.05 (m, 2 H, CH=C**H**$_2$), 3.53 (h, 2 H, $^3J_{H,H}$ = 6.80 Hz, C**H**(CH$_3$)$_2$), 2.23 (bs, 1 H, N**H**), 1.70 (d, 2 H, $^3J_{H,H}$ = 7.78 Hz, SiC**H**$_2$), 1.27 (d, 12 H, $^3J_{H,H}$ = 6.87 Hz, CH(C**H**$_3$)$_2$), 0.16 (s, 6 H, Si(C**H**$_3$)$_2$). *, The signal overlaps with the solvent signal. **^{13}C-{^{1}H} NMR**: (75.5 MHz, C_6D_6, 300 K, ppm): δ = 144.7 (s, N**C**$_{ipso}$), 139.5 (s, *o*-**C**$_{Dipp}$), 134.9 (s, **C**H=CH$_2$), 124.4 (s, *p*-**C**H$_{Dipp}$), 123.4 (s, *m*-**C**H$_{Dipp}$), 113.7 (s, CH=**C**H$_2$), 28.5 (s, **C**H(CH$_3$)$_2$), 26.2 (s, SiC**H**$_2$), 23.9 (s, CH(**C**H$_3$)$_2$), −1.26 (s, Si(**C**H$_3$)$_2$).

LiL^4. 3.00 g (10.8 mmol, 1 equiv.) of **HL^4** were dissolved in 20 mL of *n*-pentane. It was cooled to −20 °C and *n*-BuLi (10.8 mmol, 1 equiv.) was added dropwise, while a white precipitate appeared immediately. After stirring for a further 30 minutes, the solid was filtered off and washed with *n*-pentane before drying *in vacuo*. **LiL^4** could be obtained as a white solid in a yield of 80%. **Yield**: 2.44 g (8.67 mmol, 80%). **^{1}H NMR**: (300.2 MHz, C_6D_6, 300 K, ppm): δ = 6.93 (d, 2 H, $^3J_{H,H}$ = 7.60 Hz, *m*-C**H**$_{Dipp}$), 6.83 (t, 1 H, $^3J_{H,H}$ = 6.88 Hz, *p*-C**H**$_{Dipp}$), 6.08–6.25 (m, 1 H, C**H**=CH$_2$), 5.00–5.11 (m, 2 H, CH=C**H**$_2$), 3.25 (h, 2 H, $^3J_{H,H}$ = 6.83 Hz, C**H**(CH$_3$)$_2$), 1.73 (d, 2 H, $^3J_{H,H}$ = 8.08 Hz, SiC**H**$_2$), 1.17 (d, 6 H, $^3J_{H,H}$ = 6.69 Hz, CH(C**H**$_3$)$_2$), 0.80 (d, 6 H, $^3J_{H,H}$ = 6.64 Hz, CH(C**H**$_3$)$_2$), 0.18 (s, 6 H, Si(C**H**$_3$)$_2$). **^{13}C-{^{1}H} NMR:** (75.5 MHz, C_6D_6, 300 K, ppm): δ = 150.2 (N**C**$_{ipso}$), 143.0 (*o*-**C**$_{Dipp}$), 140.9 (**C**H=CH$_2$), 124.3 (*m*-**C**H$_{Dipp}$), 120.2 (*p*-**C**H$_{Dipp}$), 112.1 (CH=**C**H$_2$), 29.9 (Si**C**H$_2$), 27.9 (**C**H(CH$_3$)$_2$), 25.2 (CH(**C**H$_3$)$_2$), 24.9 (CH(**C**H$_3$)$_2$), 1.03 (Si(**C**H$_3$)$_2$). **^{1}H NMR**: (300.2 MHz, THF-d_8, 300 K, ppm): δ = 6.72 (d, 2 H, $^3J_{H,H}$ = 7.45 Hz, *m*-C**H**$_{Dipp}$), 6.35 (t, 1 H, $^3J_{H,H}$ = 7.40 Hz, *p*-C**H**$_{Dipp}$), 5.75–5.90 (m, 1 H, C**H**=CH$_2$), 4.53–4.64 (m, 2 H, CH=C**H**$_2$), 4.03 (h, 2 H, $^3J_{H,H}$ = 6.93 Hz, C**H**(CH$_3$)$_2$), 1.54 (d, 2 H, $^3J_{H,H}$ = 8.27 Hz, SiC**H**$_2$), 1.05 (d, 12 H, $^3J_{H,H}$ = 6.93 Hz, CH(C**H**$_3$)$_2$), −0.08 (s, 6 H, Si(C**H**$_3$)$_2$). **^{13}C-{^{1}H} NMR:** (75.5 MHz, THF-d_8, 300 K, ppm): δ = 157.7 (N**C**$_{ipso}$), 143.7 (*o*-**C**$_{Dipp}$), 141.0 (**C**H=CH$_2$), 122.4 (*m*-**C**H$_{Dipp}$), 115.2 (*p*-**C**H$_{Dipp}$), 109.2 (CH=**C**H$_2$), 30.8 (Si**C**H$_2$), 27.2 (**C**H(CH$_3$)$_2$), 1.87 (Si(**C**H$_3$)$_2$). *, The signal of the CH(**C**H$_3$)$_{2-}$ group overlaps with the solvent signal. Elemental analysis of $C_{17}H_{28}LiNSi$ (281.44 g mol^{-1}): calcd: N 4.98, C 72.55, H 10.03; found: N 5.29, C 72.25, H 10.13%. **IR** (ATR, cm^{-1}): $\tilde{\nu}$ = 3078 (w), 3047 (w), 3007 (w), 2957 (m), 2867 (m), 1628 (m), 1617 (m), 1589 (w), 1457 (m), 1419 (s), 1385 (m), 1362 (m), 1305 (m), 1247 (s), 1229 (s), 1185 (s), 1142 (m), 1107 (m), 1038 (m), 1008 (w), 991 (w), 927 (vs), 897 (s), 819 (s), 783 (s), 768 (s), 744 (m), 723 (m), 690 (w), 663 (m), 631 (m), 578 (m), 559 (w), 528 (s), 453 (m), 435 (m).

[ML$^4_2$] (M = Cr–Co). One equivalent of MCl_2 (M = Cr–Co) and two equivalents of **LiL^4** were suspended in 15 mL of diethyl ether. It was allowed to stir overnight at room temperature, while a change in colour was observed (Cr: green → dark green; Mn: beige → dark beige; Fe: brown → dark yellow; Co: light yellow → dark red-brown). All volatiles were removed under reduced pressure before resolving the obtained residue in *n*-pentane. The lithium chloride was filtered off and it was cooled to −40 °C for crystallization. After several days, the solution was decanted off and the obtained crystals were dried *in vacuo*. Crystalline **[ML$^4_2$]** (M = Cr–Co) was obtained in yields of 47–78%.

[CrL^4]$_2$. Using 109 mg of $CrCl_2$ (0.89 mmol, 1 equiv.), **[CrL$^4_2$]** could be obtained as a dark green crystalline solid. **Yield**: 289 mg (0.48 mmol, 54%). Crystals, suitable for X-ray diffraction analysis, were obtained from a saturated *n*-pentane solution of **[CrL$^4_2$]** at −40 °C. **^{1}H NMR** (300.2 MHz, C_6D_6, 300 K,

ppm): δ = 14.6 (bs, $w_{\frac{1}{2}}$ = 940 Hz), 9.5 (bs, $w_{\frac{1}{2}}$ = 380 Hz), 6.0 (bs, $w_{\frac{1}{2}}$ = 460 Hz), 3.3 (bs, $w_{\frac{1}{2}}$ = 1190 Hz). Elemental analysis of $C_{34}H_{56}CrN_2Si_2$ (601.00 g mol^{-1}): calcd: N 4.66, C 67.95, H 9.39; found: N 5.03, C 67.88, H 8.91%. **IR** (ATR, cm^{-1}): $\tilde{\nu}$ = 3064 (w), 3044 (w), 3009 (w), 2955 (m), 2929 (m), 2865 (m), 1587 (w), 1570 (m), 1460 (w), 1422 (m), 1380 (w), 1359 (w), 1307 (m), 1235 (s), 1194 (m), 1162 (w), 1142 (w), 1107 (s), 1052 (w), 1039 (w), 1002 (m), 923 (s), 891 (m), 825 (s), 772 (vs), 734 (m), 702 (w), 671 (m), 641 (m), 595 (m), 573 (w), 527 (m), 426 (m). **Evans** (500.1 MHz, 300 K, C_6D_6 + 1% TMS): μ_{eff} = 4.45μ_B; $\mu_{S.O.}$ = 4.89μ_B.

[MnL$^4_2$]. Using 89 mg of $MnCl_2$ (0.71 mmol, 1 equiv.), **[MnL$^4_2$]** could be obtained as a yellow crystalline solid. **Yield**: 203 mg (0.34 mmol, 47%). Crystals, suitable for X-ray diffraction analysis, were obtained from a saturated *n*-pentane solution of **[MnL$^4_2$]** at −40 °C. **^{1}H NMR**: (300.2 MHz, C_6D_6, 300 K, ppm): δ = 30.8 (bs, $w_{\frac{1}{2}}$ = 2100 Hz), 11.9* (bs), −27.5 (bs, $w_{\frac{1}{2}}$ = 4300 Hz). *, The half width could not be determined. Elemental analysis of $C_{34}H_{56}MnN_2Si_2$ (603.94 g mol^{-1}): calcd: N 4.64, C 67.62, H 9.35; found: N 4.91, C 67.15, H 9.07%. **IR** (ATR, cm^{-1}): $\tilde{\nu}$ = 3052 (w), 2954 (m), 2902 (w), 2864 (m), 1592 (m), 1458 (m), 1424 (s), 1381 (w), 1358 (w), 1309 (m), 1254 (w), 1240 (s), 1195 (s), 1175 (w), 1154 (w), 1142 (w), 1104 (s), 1040 (m), 1025 (m), 926 (vs), 903 (m), 891 (s), 825 (s), 788 (s), 772 (s), 729 (m), 699 (m), 674 (m), 643 (m), 593 (m), 562 (m), 530 (m), 424 (m). **Evans** (500.1 MHz, 300 K, C_6D_6 + 1% TMS): μ_{eff} = 5.27μ_B; $\mu_{S.O.}$ = 5.92μ_B.

[FeL$^4_2$]. Using 90 mg of $FeCl_2$ (0.71 mmol, 1 equiv.), **[FeL$^4_2$]** could be obtained as a yellow crystalline solid. **Yield**: 293 mg (0.48 mmol, 68%). Crystals, suitable for X-ray diffraction analysis, were obtained from a saturated *n*-pentane solution of **[FeL$^4_2$]** at −40 °C. **^{1}H NMR** (300.2 MHz, C_6D_6, 300 K, ppm): δ = 157.6 (bs, $w_{\frac{1}{2}}$ = 2250 Hz, C**H**$_{allyl}$), 48.9 (s, 4 H, $w_{\frac{1}{2}}$ = 270 Hz, *m*-C**H**$_{Dipp}$), 35.1 (bs, 4 H, $w_{\frac{1}{2}}$ = 1590 Hz, C**H**(CH$_3$)$_2$), 24.0 (s, 12 H, $w_{\frac{1}{2}}$ = 335 Hz, CH(C**H**$_3$)$_2$), 22.2 (bs, 12 H, $w_{\frac{1}{2}}$ = 666 Hz, Si(C**H**$_3$)$_2$), 16.7 (bs, $w_{\frac{1}{2}}$ = 3400 Hz, C**H**$_{allyl}$), −28.2 (s, 12 H, $w_{\frac{1}{2}}$ = 710 Hz, CH(C**H**$_3$)$_2$), −37.5 (s, 2 H, $w_{\frac{1}{2}}$ = 150 Hz, *p*-C**H**$_{Dipp}$), −135.2 (bs, $w_{\frac{1}{2}}$ = 2630 Hz, C**H**$_{allyl}$). **^{1}H NMR** (300.2 MHz, THF-d_8, 300 K, ppm): δ = 147.3 (bs, $w_{\frac{1}{2}}$ = 1490 Hz, C**H**$_{allyl}$), 49.2 (s, 4 H, $w_{\frac{1}{2}}$ = 160 Hz, *m*-C**H**$_{Dipp}$), 34.0 (bs, 4 H, $w_{\frac{1}{2}}$ = 1200 Hz, C**H**(CH$_3$)$_2$), 23.2 (s, 12 H, $w_{\frac{1}{2}}$ = 240 Hz, CH(C**H**$_3$)$_2$), 20.2 (bs, 12 H, $w_{\frac{1}{2}}$ = 530 Hz, Si(C**H**$_3$)$_2$), 15.5 (bs, $w_{\frac{1}{2}}$ = 2400 Hz, C**H**$_{allyl}$), −31.3 (bs, 12 H, $w_{\frac{1}{2}}$ = 580 Hz, CH(C**H**$_3$)$_2$), −37.1 (s, 2 H, $w_{\frac{1}{2}}$ = 110 Hz, *p*-C**H**$_{Dipp}$), −121.5 (bs, $w_{\frac{1}{2}}$ = 3200 Hz, C**H**$_{allyl}$). Elemental analysis of $C_{34}H_{56}FeN_2Si_2$ (604.85 g mol^{-1}): calcd: N 4.63, C 67.52, H 9.33; found: N 4.58, C 67.20, H 9.16%. **IR** (ATR, cm^{-1}): $\tilde{\nu}$ = 3051 (w), 3012 (w), 2956 (m), 2901 (m), 2865 (m), 1577 (w), 1460 (m), 1424 (s), 1381 (w), 1359 (w), 1307 (m), 1255 (m), 1236 (s), 1191 (s), 1154 (w), 1142 (w), 1104 (s), 1053 (w), 1040 (m), 1005 (m), 952 (w), 917 (s), 885 (m), 826 (s), 787 (s), 774 (vs), 728 (m), 699 (m), 677 (m), 645 (m), 596 (m), 569 (m), 532 (m), 426 (m). **Evans** (500.1 MHz, 300 K, C_6D_6 + 1% TMS): μ_{eff} = 5.14μ_B; $\mu_{S.O.}$ = 4.89μ_B.

[CoL$^4_2$]. Using 90 mg of $CoCl_2$ (0.71 mmol, 1 equiv.), **[CoL$^4_2$]** could be obtained as a yellow crystalline solid. **Yield**: 335 mg (0.55 mmol, 78%). Crystals, suitable for X-ray diffraction analysis, were obtained from a saturated *n*-pentane solution of **[CoL$^4_2$]** at −40 °C. **^{1}H NMR** (300.2 MHz, C_6D_6, 300 K, ppm): δ = 57.1 (bs, $w_{\frac{1}{2}}$ = 650 Hz, C**H**$_{allyl}$), 56.1 (bs, 4 H, $w_{\frac{1}{2}}$ = 124 Hz, *m*-C**H**$_{Dipp}$), 39.5 (bs, 12 H, $w_{\frac{1}{2}}$ = 141 Hz, CH(C**H**$_3$)$_2$), 26.5 (bs, 12 H, $w_{\frac{1}{2}}$ = 420 Hz, Si(C**H**$_3$)$_2$), −32.1 (s, 2 H, $w_{\frac{1}{2}}$ = 56 Hz, *p*-C**H**$_{Dipp}$), −48 (bs, $w_{\frac{1}{2}}$ = 2740 Hz C**H**$_{allyl}$), −79.7 (bs, 12 H, $w_{\frac{1}{2}}$ = 390 Hz, CH(C**H**$_3$)$_2$), −164 (bs, $w_{\frac{1}{2}}$ = 1780 Hz, C**H**$_{allyl}$). **^{1}H NMR** (300.2 MHz, THF-d_8, 300 K, ppm): δ = 59.2 (bs, $w_{\frac{1}{2}}$ = 580 Hz, C**H**$_{allyl}$), 53.2 (bs, 4 H, $w_{\frac{1}{2}}$ = 130 Hz, *m*-C**H**$_{Dipp}$), 37.2 (bs, 12 H, $w_{\frac{1}{2}}$ = 160 Hz, CH(C**H**$_3$)$_2$), 25.4 (bs, 12 H, $w_{\frac{1}{2}}$ = 470 Hz, Si(C**H**$_3$)$_2$), −34.7 (s, 2 H, $w_{\frac{1}{2}}$ = 94 Hz, *p*-C**H**$_{Dipp}$), −80.3 (bs, 12 H, $w_{\frac{1}{2}}$ = 440 Hz, CH(C**H**$_3$)$_2$), −138.0 (bs, $w_{\frac{1}{2}}$ = 960 Hz, C**H**$_{allyl}$), −192.6 (bs, $w_{\frac{1}{2}}$ = 1220 Hz, C**H**$_{allyl}$). Elemental analysis of $C_{34}H_{56}CoN_2Si_2$ (607.94 g mol^{-1}): calcd: N 4.61, C 67.17, H 9.29; found: N 4.89, C 66.85, H 9.08%. **IR** (ATR, cm^{-1}): $\tilde{\nu}$ = 3060 (w), 3011 (w), 2956 (m), 2927 (w), 2903 (w), 2865 (m), 1583 (m), 1463 (w), 1424 (s), 1381 (w), 1358 (w), 1307 (m), 1252 (m), 1238 (s), 1193 (s), 1142 (w), 1101 (s), 1051 (w), 1041 (w), 1101 (w), 1051 (w), 1041 (m), 1010 (w), 920 (vs), 886 (s), 826 (vs), 790 (s), 774 (vs), 730 (m), 697 (m), 676 (m), 647 (m), 595 (m), 567 (m), 532 (m), 426 (m). **Evans** (500.1 MHz, 300 K, C_6D_6 + 1% TMS): μ_{eff} = 4.84μ_B; $\mu_{S.O.}$ = 3.87μ_B.

(K{18c6})$_2$[CrL$^4_2$]$_2$. Using 50 mg of **[CrL$^4_2$]**, (K{18c6})$_2$**[CrL$^4_2$]$_2$** could be obtained as a green crystalline solid. **Yield**: 32 mg (0.035 mmol, 44%). Crystals, suitable for X-ray diffraction analysis, were obtained from a *n*-pentane layered solution of (K{18c6})$_2$**[CrL$^4_2$]$_2$** in Et_2O at −40 °C. **^{1}H NMR** (300.2 MHz, THF-d_8, 300 K, ppm): δ = 34.1 (bs, $w_{\frac{1}{2}}$ = 1060 Hz), 14.9 (bs, $w_{\frac{1}{2}}$ = 590 Hz), 12.2 (bs, $w_{\frac{1}{2}}$ = 780 Hz), 8.1 (bs, $w_{\frac{1}{2}}$ = 770 Hz), 3.57* (s, 24 H, 18c6), −16.5 (bs, $w_{\frac{1}{2}}$ = 470 Hz). *, The signal overlaps with the solvent signal. Elemental analysis of $C_{46}H_{80}CrKN_2O_6Si_2$ (904.42 g mol^{-1}): calcd: N 3.10, C 61.09, H 8.92; found: N 3.41, C 61.12, H 8.90%. **IR** (ATR, cm^{-1}): $\tilde{\nu}$ = 3036 (w), 2950 (m), 2899 (m), 2860 (m), 1624 (w), 1583 (w), 1470 (w), 1454 (m), 1418 (m), 1376 (w), 1351 (m), 1314 (m), 1283 (w), 1244 (m), 1196 (m), 1172 (w), 1132 (m), 1103 (vs), 1054 (m), 1033 (m), 991 (w), 960 (m), 931 (m), 881 (w), 821 (s), 771 (s), 736 (m), 666 (m), 632 (m), 578 (m), 559 (w), 530 (m), 447 (m), 423 (m). **Evans** (500.1 MHz, 300 K, THF-d_8 + 1% TMS): μ_{eff} = 6.17μ_B; $\mu_{S.O.}$ = 6.93μ_B.

K{18c6}[CoL$^4_2$]. Using 100 mg of **[CoL$^4_2$]**, K{18c6}**[CoL$^4_2$]** could be obtained as a dark greenish brown crystalline solid. **Yield**: 97 mg (0.11 mmol, 65%). Crystals, suitable for X-ray diffraction analysis, were obtained from a *n*-pentane layered solution of K{18c6}**[CoL$^4_2$]** in Et_2O at −40 °C. **^{1}H NMR** (300.2 MHz, THF-d_8, 300 K, ppm): δ = 47.4 (bs, $w_{\frac{1}{2}}$ = 220 Hz, C**H**$_{allyl}$), 23.4 (bs, 2 H, $w_{\frac{1}{2}}$ = 320 Hz, C**H**$_{allyl}$), 18.0 (s, 4 H, $w_{\frac{1}{2}}$ = 18.7 Hz, *m*-C**H**$_{Dipp}$), 9.71 (bs, 2 H, $w_{\frac{1}{2}}$ = 180 Hz, C**H**$_{allyl}$), 6.73 (s, 12 H, $w_{\frac{1}{2}}$ = 88 Hz, Si(C**H**$_3$)$_2$), 4.57 (s, 12 H, $w_{\frac{1}{2}}$ = 20 Hz, CH(C**H**$_3$)$_2$), 3.52 (s, 24 H, $w_{\frac{1}{2}}$ = 7.0 Hz, 18c6), −3.34 (bs, 4 H, $w_{\frac{1}{2}}$ = 450 Hz, C**H**(CH$_3$)$_2$), −4.84 (s, 2 H, $w_{\frac{1}{2}}$ = 17 Hz, *p*-C**H**$_{Dipp}$), −31.7 (bs, 12 H, $w_{\frac{1}{2}}$ = 84 Hz, CH(C**H**$_3$)$_2$), −53.8 (bs, 4 H, $w_{\frac{1}{2}}$ = 250 Hz, C**H**$_{allyl}$). Elemental analysis of $C_{46}H_{80}CoKN_2O_6Si_2$ (911.36 g mol^{-1}): calcd: N 3.07, C 60.62, H 8.85; found: N 2.90, C 60.75, H 8.77%. **IR** (ATR, cm^{-1}): $\tilde{\nu}$ = 3031 (w), 2954 (m), 2900 (m), 2861 (m), 1581 (w), 1461 (m), 1416 (m), 1377 (w), 1353 (w), 1311 (m), 1284 (w), 1243 (s), 1200 (m), 1101 (vs), 1053 (m),

1042 (m), 1008 (w), 956 (s), 898 (m), 821 (s), 769 (s), 729 (m), 700 (w), 659 (m), 604 (w), 572 (w), 519 (m), 428 (m). **Evans** (500.1 MHz, 300 K, THF-d_8 + 1% TMS): μ_{eff} = 4.04μ_B; $\mu_{S.O.}$ = 2.83μ_B.

Imido complexes

K{18c6}[Co(NDipp)L$^1_2$]. 48 mg of K{18c6}[CoL$^1_2$] (0.05 mmol, 1 equiv.) were dissolved in an Et_2O : THF mixture (1 : 1, v/v). Dipp azide (10 mg, 0.05 mmol, 1 equiv.) was added, while a spontaneous colour change from dark green to dark brown was observable. After allowing to crystallize at −40 °C for several days, the grown crystals were isolated and dried *in vacuo*. K{18c6}[Co(NDipp)L$^1_2$] was obtained as a dark green crystalline solid in a yield of 67%. **Yield**: 38 mg (0.03 mmol, 67%). **^{1}H NMR** (300.2 MHz, THF-d_8, 300 K, ppm): δ = 117 (bs, $w_{\frac{1}{2}}$ = 1500 Hz), 66.2 (bs, $w_{\frac{1}{2}}$ = 1320 Hz), 44.2 (bs, $w_{\frac{1}{2}}$ = 660 Hz), 37.6 (bs, $w_{\frac{1}{2}}$ = 970 Hz), 31.7 (bs, $w_{\frac{1}{2}}$ = 600 Hz), 28.1 (bs, $w_{\frac{1}{2}}$ = 820 Hz), 21.3 (bs, $w_{\frac{1}{2}}$ = 160 Hz), 17.0 (s, $w_{\frac{1}{2}}$ = 36 Hz), 14.6 (s, $w_{\frac{1}{2}}$ = 27 Hz), 9.37 (bs, $w_{\frac{1}{2}}$ = 560 Hz), 7.61 (s, $w_{\frac{1}{2}}$ = 14 Hz), 7.25 (s, $w_{\frac{1}{2}}$ = 26 Hz), 6.92 (s, $w_{\frac{1}{2}}$ = 66 Hz), 3.67 (s, 24 H, $w_{\frac{1}{2}}$ = 6.4 Hz, 18c6), 3.61 (s, $w_{\frac{1}{2}}$ = 9.1 Hz, $THF_{coord.}$), 2.86 (s, $w_{\frac{1}{2}}$ = 23 Hz), 1.77 (s, $w_{\frac{1}{2}}$ = 9.9 Hz, $THF_{coord.}$), −1.93 (bs, $w_{\frac{1}{2}}$ = 1300 Hz), −2.62 (s, $w_{\frac{1}{2}}$ = 13 Hz), −7.43 (s, $w_{\frac{1}{2}}$ = 18 Hz), −14.5 (bs, $w_{\frac{1}{2}}$ = 180 Hz), −18.0 (bs, $w_{\frac{1}{2}}$ = 700 Hz), −31.8 (bs, $w_{\frac{1}{2}}$ = 140 Hz), −38.1 (bs, $w_{\frac{1}{2}}$ = 160 Hz), −84.9 (bs, $w_{\frac{1}{2}}$ = 94 Hz). Elemental analysis of $C_{64}H_{97}CoKN_3O_6Si_2$ (1158.70 g mol^{-1}): calcd: N 3.63, C 66.34, H 8.44; found: N 3.61, C 65.71, H 8.57%. **IR** (ATR, cm^{-1}): $\tilde{\nu}$ = 3065 (w), 3053 (w), 3039 (w), 2948 (m), 2897 (m), 2860 (m), 2827 (w), 2791 (w), 1584 (w), 1469 (w), 1454 (m), 1421 (s), 1391 (w), 1376 (w), 1350 (m), 1312 (m), 1282 (w), 1237 (s), 1192 (m), 1103 (vs), 1055 (m), 960 (s), 931 (m), 908 (m), 883 (w), 831 (s), 802 (s), 767 (s), 741 (m), 726 (w), 701 (s), 683 (m), 651 (m), 576 (w), 541 (m), 528 (m), 477 (m), 431 (m). **Evans** (500.1 MHz, 300 K, THF-d_8 + 1% TMS): μ_{eff} = 4.87μ_B; $\mu_{S.O.}$ = 4.89μ_B.

K{18c6}[Co(NDipp)L$^4_2$]. 45 mg of K{18c6}[CoL$^4_2$] (0.05 mmol, 1 equiv.) were dissolved in an Et_2O : THF mixture (1 : 1, v/v). Dipp azide (10 mg, 0.05 mmol, 1 equiv.) was added to the above mixture, while a spontaneous colour change from dark green to dark brown was observable. After allowing to crystallize at −40 °C for several days, the grown crystals were isolated and dried *in vacuo*. K{18c6}[Co(NDipp)L$^4_2$] was obtained as a dark red crystalline solid in a yield of 54%. **Yield**: 29 mg (0.03 mmol, 65%). **^{1}H NMR** (300.2 MHz, THF-d_8, 300 K, ppm): δ = 84.7 (bs, $w_{\frac{1}{2}}$ = 300 Hz), 30.5 (bs, $w_{\frac{1}{2}}$ = 680 Hz), 26.2 (bs, $w_{\frac{1}{2}}$ = 780 Hz), 7.1 (bs, $w_{\frac{1}{2}}$ = 130 Hz), 4.42 (s, 24 H, $w_{\frac{1}{2}}$ = 12 Hz, 18c6), 3.61 (s, 8 H, $w_{\frac{1}{2}}$ = 9.1 Hz, $THF_{coord.}$), 1.77 (s, 8 H, $w_{\frac{1}{2}}$ = 8.2 Hz, $THF_{coord.}$), −25.1 (bs, $w_{\frac{1}{2}}$ = 150 Hz), −26.1 (s, $w_{\frac{1}{2}}$ = 190 Hz), −52.4 (bs, $w_{\frac{1}{2}}$ = 18 Hz), −53.4 (bs, $w_{\frac{1}{2}}$ = 15 Hz). Elemental analysis of $C_{58}H_{97}CoKN_3O_6Si_2$ (1086.63 g mol^{-1}): calcd: N 3.87, C 64.11, H 9.00; found: N 3.80, C 63.68, H 8.84%. **IR** (ATR, cm^{-1}): $\tilde{\nu}$ = 3067 (w), 3049 (w), 3025 (w), 2951 (m), 2897 (m), 2862 (m), 1624 (m), 1584 (w), 1456 (m), 1421 (s), 1392 (w), 1377 (w), 1351 (m), 1337 (w), 1311 (m), 1283 (w), 1236 (s), 1188 (m), 1132 (w), 1104 (vs), 1054 (m), 1037 (w), 993 (w), 961 (m), 930 (w), 903 (s), 878 (m), 835 (s), 799 (s), 782 (m), 739 (m), 705 (w), 675 (m), 646 (m), 585 (w), 556 (m), 537 (m), 437 (m). **Evans** (500.1 MHz, 300 K, THF-d_8 + 1% TMS): μ_{eff} = 5.05μ_B; $\mu_{S.O.}$ = 4.89μ_B.

X-ray diffraction analysis

Data for compounds **LiL^2** (CCDC 2073681†), **LiL^3_b** (CCDC 2073682†), **[FeL$^1_2$]** (CCDC 2074225†), **[CoL$^1_2$]** (CCDC 2074223†), K{18c6}[CoL$^1_2$] (CCDC 2074226†), **[FeL$^3_2$]** (CCDC 2074224†), K{18c6}[FeL$^3_2$] (CCDC 2074234†), **[CrL$^4_2$]** (CCDC 2074229†), **[FeL$^4_2$]** (CCDC 2074232†), **[CoL$^4_2$]** (CCDC 2074236†), $(K\{18c6\})_2$ **[CrL$^4_2$]$_2$** (CCDC 2074256†) and K{18c6}[Co(NDipp)L$^4_2$] (CCDC 2074231†) were collected at 100 K on a Bruker Quest D8 diffractometer (Bruker Corporation, Billerica, USA) using Incoatec Microfocus Source Mo-Kα radiation and equipped with an Oxford Instrument Cooler Device (Oxford Instruments, Abingdon, UK) and a Photon 100 detector. Data for compound K{18c6}[MnL^1*L] (CCDC 2074317†) were collected at 100 K on an STOE Stadivari diffractometer using Cu-Kα radiation and a DECTRIS Pilatus R 300 K detector. Data for compounds **LiL^1** (CCDC 2073679†), **HL^3** (CCDC 2073678†), **LiL^3_a** (CCDC 2073680†), K{18c6}[FeL$^1_2$] (CCDC 2074235†) and **[MnL$^4_2$]** (CCDC 2074233†) were collected at 100 K on an STOE IPDS2 diffractometer (STOE & Cie GmbH, Darmstadt, Germany) and data for compounds **[MnL$^1_2$]** (CCDC 2074237†), **[CrL$^2_2$]** (CCDC 2074230†), K{18c6}[CoL$^4_2$] (CCDC 2074228†) and K{18c6}[Co(NDipp)L$^1_2$] (CCDC 2074227†) were collected at 100 K on an STOE IPDS2T diffractometer using graphite-monochromated Mo-Kα radiation (λ = 0.71073 Å) and equipped with an Oxford Instrument Cooler Device (Oxford Instruments, Abingdon, UK). The structures have been solved using OLEX SHELXT V2014/1[67] and refined by means of least-squares procedures on F^2 with the aid of the program SHELXL-2016/6[68] included in the software package WinGX version 1.63[69] or using CRYSTALS.[70] In the case of **[CoL$^1_2$]**, the structure was refined using olex2.refine. The atomic scattering factors were taken from International Tables for X-ray Crystallography.[71] All non-hydrogen atoms were refined anisotropically. All hydrogen atoms were refined by using a riding model. Disorders were found for **LiL^2** (a coordinating THF molecule), **LiL^3_a** (a coordinating THF molecule), **LiL^3_b** (coordinating THF molecules), K{18c6}[MnL^{1}L^1*] (all atoms), K{18c6}[FeL$^1_2$] (two phenyl rings and two iso-propyl groups), K{18c6}[CoL$^1_2$] (methyl group), [CrL$^2_2$] ($SiMePh_2$ fragment), **[FeL$^3_2$]** (a free *n*-pentane molecule), K{18c6}[FeL$^3_2$] (a coordinated THF molecule and a free *n*-pentane molecule), $(K\{18c6\})_2$**[CrL$^4_2$]$_2$** (crown ether, coordinated THF molecules, iso-propyl and allyl groups), K{18c6}[Co(NDipp)L$^1_2$] (a coordinated THF molecule) and K{18c6}[Co(NDipp)L$^4_2$] (coordinated THF molecules, allyl groups) and were modelled accordingly. The structures of **[MnL$^1_2$]**, K{18c6}[MnL^{1}L^1*] and K{18c6}[FeL$^1_2$] were refined as inversion twins. For $(K\{18c6\})_2$**[CrL$^4_2$]$_2$** weakly diffracting crystals and intrinsic crystallographic flaws could not be overcome despite multiple attempts. Absorption corrections were introduced by using the MULTISCAN and X-Red programs.[72] Drawings of molecules are performed using the DIAMOND program (Crystal Impact, Bonn, Germany) with 50% probability displacement ellipsoids for non-H atoms. Additional details are given in the ESI.†

Author contributions

The manuscript was written through contributions of all authors. All authors have given approval to the final version of the manuscript.

Conflicts of interest

There are no conflicts to declare.

Acknowledgements

Special thanks to Dr Sergei Ivlev for helping with some of the crystallographic problems. C. G. W. thanks the Deutsche Forschungsgemeinschaft (grant WE 5627/4-1) and the Philipps-University for financial support.

Notes and references

1 P. P. Power, *Chem. Rev.*, 2012, **112**, 3482–3507.
2 D. L. Kays, *Dalton Trans.*, 2011, **40**, 769–778.
3 (*a*) S. Roy, K. C. Mondal and H. W. Roesky, *Acc. Chem. Res.*, 2016, **49**, 357–369; (*b*) P. C. Bunting, M. Atanasov, E. Damgaard-Møller, M. Perfetti, I. Crassee, M. Orlita, J. Overgaard, J. van Slageren, F. Neese and J. R. Long, *Science*, 2018, **362**(6421), eaat7319; (*c*) R. J. Witzke and T. D. Tilley, *Chem. Commun.*, 2019, **55**, 6559–6562; (*d*) M. I. Lipschutz, T. Chantarojsiri, Y. Dong and T. D. Tilley, *J. Am. Chem. Soc.*, 2015, **137**, 6366–6372; (*e*) A. M. Bryan, C.-Y. Lin, M. Sorai, Y. Miyazaki, H. M. Hoyt, A. Hablutzel, A. LaPointe, W. M. Reiff, P. P. Power and C. E. Schulz, *Inorg. Chem.*, 2014, **53**, 12100–12107; (*f*) J. Du, L. Wang, M. Xie and L. Deng, *Angew. Chem., Int. Ed.*, 2015, **54**, 12640–12644; (*g*) C. A. Laskowski, D. J. Bungum, S. M. Baldwin, S. A. Del Ciello, V. M. Iluc and G. L. Hillhouse, *J. Am. Chem. Soc.*, 2013, **135**, 18272–18275; (*h*) G. Ung and J. C. Peters, *Angew. Chem., Int. Ed.*, 2015, **54**, 532–535; (*i*) C. G. Werncke, P. C. Bunting, C. Duhayon, J. R. Long, S. Bontemps and S. Sabo-Etienne, *Angew. Chem., Int. Ed.*, 2015, **54**, 245–248; (*j*) M. I. Lipschutz and T. D. Tilley, *Angew. Chem., Int. Ed.*, 2014, **53**, 7290–7294; (*k*) J. N. Boynton, W. A. Merrill, W. M. Reiff, J. C. Fettinger and P. P. Power, *Inorg. Chem.*, 2012, **51**, 3212–3219; (*l*) C. L. Wagner, L. Tao, E. J. Thompson, T. A. Stich, J. Guo, J. C. Fettinger, L. A. Berben, R. D. Britt, S. Nagase and P. P. Power, *Angew. Chem., Int. Ed.*, 2016, **55**, 10444–10447; (*m*) H. Lei, J.-D. Guo, J. C. Fettinger, S. Nagase and P. P. Power, *J. Am. Chem. Soc.*, 2010, **132**, 17399–17401; (*n*) C. Schneider, S. Demeshko, F. Meyer and C. G. Werncke, *Chem. – Eur. J.*, 2021, **27**, 6348–6353.
4 K. Freitag, C. R. Stennett, A. Mansikkamäki, R. A. Fischer and P. P. Power, *Inorg. Chem.*, 2021, **60**, 4108–4115.
5 J. M. Zadrozny, D. J. Xiao, M. Atanasov, G. J. Long, F. Grandjean, F. Neese and J. R. Long, *Nat. Chem.*, 2013, **5**, 577–581.
6 A. M. Bryan, G. J. Long, F. Grandjean and P. P. Power, *Inorg. Chem.*, 2014, **53**, 2692–2698.
7 C. G. Werncke, E. Suturina, P. C. Bunting, L. Vendier, J. R. Long, M. Atanasov, F. Neese, S. Sabo-Etienne and S. Bontemps, *Chem. – Eur. J.*, 2016, **22**, 1668–1674.
8 H. R. Sharpe, A. M. Geer, L. J. Taylor, B. M. Gridley, T. J. Blundell, A. J. Blake, E. S. Davies, W. Lewis, J. McMaster, D. Robinson and D. L. Kays, *Nat. Commun.*, 2018, **9**, 3757.
9 C. Ni, T. A. Stich, G. J. Long and P. P. Power, *Chem. Commun.*, 2010, **46**, 4466.
10 C.-Y. Lin, J. C. Fettinger, N. F. Chilton, A. Formanuik, F. Grandjean, G. J. Long and P. P. Power, *Chem. Commun.*, 2015, **51**, 13275–13278.
11 (*a*) A. E. Ashley, A. R. Cowley, J. C. Green, D. R. Johnston, D. J. Watkin and D. L. Kays, *Eur. J. Inorg. Chem.*, 2009, **2009**, 2547–2552; (*b*) H. Chen, R. A. Bartlett, M. M. Olmstead, P. P. Power and S. C. Shoner, *J. Am. Chem. Soc.*, 1990, **112**, 1048–1055; (*c*) H. Chen, R. A. Bartlett, H. V. R. Dias, M. M. Olmstead and P. P. Power, *J. Am. Chem. Soc.*, 1989, **111**, 4338–4345; (*d*) R. A. Bartlett and P. P. Power, *J. Am. Chem. Soc.*, 1987, **109**, 7563–7564.
12 W. M. Reiff, C. E. Schulz, M.-H. Whangbo, J. I. Seo, Y. S. Lee, G. R. Potratz, C. W. Spicer and G. S. Girolami, *J. Am. Chem. Soc.*, 2009, **131**, 404–405.
13 C. Ni and P. P. Power, *Chem. Commun.*, 2009, 5543–5545.
14 T. Nguyen, A. Panda, M. M. Olmstead, A. F. Richards, M. Stender, M. Brynda and P. P. Power, *J. Am. Chem. Soc.*, 2005, **127**, 8545–8552.
15 J. J. Ellison, K. Ruhlandt-Senge and P. P. Power, *Angew. Chem., Int. Ed. Engl.*, 1994, **33**, 1178–1180.
16 D. L. Kays and A. R. Cowley, *Chem. Commun.*, 2007, 1053–1055.
17 (*a*) R. A. Andersen, K. Faegri, J. C. Green, A. Haaland, M. F. Lappert, W. P. Leung and K. Rypdal, *Inorg. Chem.*, 1988, **27**, 1782–1786; (*b*) B. D. Murray and P. P. Power, *Inorg. Chem.*, 1984, **23**, 4584–4588; (*c*) D. C. Bradley, M. B. Hursthouse, K. M. A. Malik and R. Möseler, *Transition Met. Chem.*, 1978, **3**, 253–254; (*d*) T. Deschner, K. W. Törnroos and R. Anwander, *Inorg. Chem.*, 2011, **50**, 7217–7228; (*e*) G. A. Sigel, R. A. Bartlett, D. Decker, M. M. Olmstead and P. P. Power, *Inorg. Chem.*, 1987, **26**, 1773–1780; (*f*) M. M. Olmstead, P. P. Power and S. C. Shoner, *Inorg. Chem.*, 1991, **30**, 2547–2551; (*g*) B. D. Murray, H. Hope and P. P. Power, *J. Am. Chem. Soc.*, 1985, **107**, 169–173; (*h*) P. P. Power and S. C. Shoner, *Angew. Chem., Int. Ed. Engl.*, 1991, **30**, 330–332.
18 R. Wolf, C. Ni, T. Nguyen, M. Brynda, G. J. Long, A. D. Sutton, R. C. Fischer, J. C. Fettinger, M. Hellman, L. Pu and P. P. Power, *Inorg. Chem.*, 2007, **46**, 11277–11290.
19 C. Ni, B. D. Ellis, T. A. Stich, J. C. Fettinger, G. J. Long, R. D. Britt and P. P. Power, *Dalton Trans.*, 2009, 5401.
20 A. M. Bryan, W. A. Merrill, W. M. Reiff, J. C. Fettinger and P. P. Power, *Inorg. Chem.*, 2012, **51**, 3366–3373.

21 I. C. Cai, M. S. Ziegler, P. C. Bunting, A. Nicolay, D. S. Levine, V. Kalendra, P. W. Smith, K. V. Lakshmi and T. D. Tilley, *Organometallics*, 2019, **38**, 1648–1663.
22 M. Atanasov, J. M. Zadrozny, J. R. Long and F. Neese, *Chem. Sci.*, 2013, **4**, 139–156.
23 W. M. Reiff, A. M. LaPointe and E. H. Witten, *J. Am. Chem. Soc.*, 2004, **126**, 10206–10207.
24 W. A. Merrill, T. A. Stich, M. Brynda, G. J. Yeagle, J. C. Fettinger, R. D. Hont, W. M. Reiff, C. E. Schulz, R. D. Britt and P. P. Power, *J. Am. Chem. Soc.*, 2009, **131**, 12693–12702.
25 C. A. Laskowski, G. R. Morello, C. T. Saouma, T. R. Cundari and G. L. Hillhouse, *Chem. Sci.*, 2013, **4**, 170–174.
26 (*a*) D. D. Beattie, E. G. Bowes, M. W. Drover, J. A. Love and L. L. Schafer, *Angew. Chem., Int. Ed.*, 2016, **55**, 13290–13295; (*b*) J. Hicks and C. Jones, *Organometallics*, 2015, **34**, 2118–2121.
27 S. N. König, D. Schneider, C. Maichle-Mössmer, B. M. Day, R. A. Layfield and R. Anwander, *Eur. J. Inorg. Chem.*, 2014, **2014**, 4302–4309.
28 (*a*) Z. Ouyang, J. Du, L. Wang, J. L. Kneebone, M. L. Neidig and L. Deng, *Inorg. Chem.*, 2015, **54**, 8808–8816; (*b*) Z. Ouyang, Y. Meng, J. Cheng, J. Xiao, S. Gao and L. Deng, *Organometallics*, 2016, **35**, 1361–1367.
29 I. C. Cai, M. I. Lipschutz and T. D. Tilley, *Chem. Commun.*, 2014, **50**, 13062–13065.
30 M. I. Lipschutz, X. Yang, R. Chatterjee and T. D. Tilley, *J. Am. Chem. Soc.*, 2013, **135**, 15298–15301.
31 C.-Y. Lin, J. C. Fettinger, F. Grandjean, G. J. Long and P. P. Power, *Inorg. Chem.*, 2014, **53**, 9400–9406.
32 C. G. Werncke and I. Müller, *Chem. Commun.*, 2020, **56**, 2268–2271.
33 (*a*) C. G. Werncke, L. Vendier, S. Sabo-Etienne, J.-P. Sutter, C. Pichon and S. Bontemps, *Eur. J. Inorg. Chem.*, 2017, **2017**, 1041–1406; (*b*) A. M. Bryan, G. J. Long, F. Grandjean and P. P. Power, *Inorg. Chem.*, 2013, **52**, 12152–12160; (*c*) R. T. Baker, J. C. Gordon, C. W. Hamilton, N. J. Henson, P.-H. Lin, S. Maguire, M. Murugesu, B. L. Scott and N. C. Smythe, *J. Am. Chem. Soc.*, 2012, **134**, 5598–5609; (*d*) R. A. Layfield, J. J. W. McDouall, M. Scheer, C. Schwarzmaier and F. Tuna, *Chem. Commun.*, 2011, **47**, 10623–10625; (*e*) A. Massard, P. Braunstein, A. A. Danopoulos, S. Choua and P. Rabu, *Organometallics*, 2015, **34**, 2429–2438; (*f*) N.-J. H. Kneusels, J. E. Münzer, K. Flosdorf, D. Jiang, B. Neumüller, L. Zhao, A. Eichhöfer, G. Frenking and I. Kuzu, *Dalton Trans.*, 2020, **49**, 2537–2546.
34 C.-Y. Lin, J. C. Fettinger and P. P. Power, *Inorg. Chem.*, 2017, **56**, 9892–9902.
35 (*a*) C. G. Werncke, J. Pfeiffer, I. Müller, L. Vendier, S. Sabo-Etienne and S. Bontemps, *Dalton Trans.*, 2019, **48**, 1757–1765; (*b*) I. Müller, C. Schneider, C. Pietzonka, F. Kraus and C. G. Werncke, *Inorganics*, 2019, **7**, 117; (*c*) I. Müller and C. G. Werncke, *Chem. – Eur. J.*, 2021, **27**, 4932–4938.
36 R. Weller, I. Müller, C. Duhayon, S. Sabo-Etienne, S. Bontemps and C. G. Werncke, *Dalton Trans.*, 2021, **50**, 4890–4903.
37 A. Reckziegel, M. Kour, B. Batistella, S. Mebs, K. Beuthert, R. Berger and G. Werncke, *Angew. Chem., Int. Ed.*, 2021, **60**, 15376–15380.
38 A. Reckziegel, C. Pietzonka, F. Kraus and C. G. Werncke, *Angew. Chem., Int. Ed.*, 2020, **59**, 8527–8531.
39 J. Wang, R. Liu, W. Ruan, Y. Li, K. C. Mondal, H. W. Roesky and H. Zhu, *Organometallics*, 2014, **33**, 2696–2703.
40 M. A. Petrie, K. Ruhlandt-Senge and P. P. Power, *Inorg. Chem.*, 1993, **32**, 1135–1141.
41 X. Wang, J. Li, S. Chen, W. Liu, Q. Ye and H. Zhu, *Dalton Trans.*, 2016, **45**, 6709–6717.
42 D. Braga, F. Grepioni, K. Biradha and G. R. Desiraju, *J. Chem. Soc., Dalton Trans.*, 1996, 3925.
43 C.-Y. Lin, J.-D. Guo, J. C. Fettinger, S. Nagase, F. Grandjean, G. J. Long, N. F. Chilton and P. P. Power, *Inorg. Chem.*, 2013, **52**, 13584–13593.
44 J. M. Zadrozny, M. Atanasov, A. M. Bryan, C.-Y. Lin, B. D. Rekken, P. P. Power, F. Neese and J. R. Long, *Chem. Sci.*, 2013, **4**, 125–138.
45 C. L. Wagner, L. Tao, J. C. Fettinger, R. D. Britt and P. P. Power, *Inorg. Chem.*, 2019, **58**, 8793–8799.
46 H.-J. Liu, I. C. Cai, A. Fedorov, M. S. Ziegler, C. Copéret and T. D. Tilley, *Helv. Chim. Acta*, 2016, **99**, 859–867.
47 I. Müller, D. Munz and C. G. Werncke, *Inorg. Chem.*, 2020, **59**, 9521–9537.
48 P. Betz, P. W. Jolly, C. Krueger and U. Zakrzewski, *Organometallics*, 1991, **10**, 3520–3525.
49 C. Lichtenberg, M. Adelhardt, M. Wörle, T. Büttner, K. Meyer and H. Grützmacher, *Organometallics*, 2015, **34**, 3079–3089.
50 C. Lichtenberg, L. Viciu, M. Adelhardt, J. Sutter, K. Meyer, B. de Bruin and H. Grützmacher, *Angew. Chem., Int. Ed.*, 2015, **54**, 5766–5771.
51 L. Wang, L. Hu, H. Zhang, H. Chen and L. Deng, *J. Am. Chem. Soc.*, 2015, **137**, 14196–14207.
52 A. Cutler, D. Ehnholt, P. Lennon, K. Nicholas, D. F. Marten, M. Madhavarao, S. Raghu, A. Rosan and M. Rosenblum, *J. Am. Chem. Soc.*, 1975, **97**, 3149–3157.
53 T. Chen, S. Jiang and E. Turos, *Tetrahedron Lett.*, 1994, **35**, 8325–8328.
54 B. J. Barrett and V. M. Iluc, *Inorg. Chem.*, 2014, **53**, 7248–7259.
55 Y. Tian, T. Maulbetsch, R. Jordan, K. W. Törnroos and D. Kunz, *Organometallics*, 2020, **39**, 1221–1229.
56 J. B. Lambert, C. L. Stern, Y. Zhao, W. C. Tse, C. E. Shawl, K. T. Lentz and L. Kania, *J. Organomet. Chem.*, 1998, **568**, 21–31.
57 K. Thum, A. Friedrich, J. Pahl, H. Elsen, J. Langer and S. Harder, *Chemistry*, 2021, **27**, 2513–2522.
58 (*a*) S. Deblon, L. Liesum, J. Harmer, H. Schönberg, A. Schweiger and H. Grützmacher, *Chem. – Eur. J.*, 2002, **8**, 601–611; (*b*) C. Chan, A. E. Carpenter, M. Gembicky, C. E. Moore, A. L. Rheingold and J. S. Figueroa, *Organometallics*, 2019, **38**, 1436–1444; (*c*) S. Asghar, S. B. Tailor, D. Elorriaga and R. B. Bedford, *Angew. Chem., Int. Ed.*, 2017, **56**, 16367–16370; (*d*) S. Pelties, T. Maier,

D. Herrmann, B. de Bruin, C. Rebreyend, S. Gärtner, I. G. Shenderovich and R. Wolf, *Chem. – Eur. J.*, 2017, **23**, 6094–6102.

59 J. C. Ott, H. Wadepohl and L. H. Gade, *Inorg. Chem.*, 2021, **60**, 3927–3938.

60 (*a*) H. Lund, *J. Electrochem. Soc.*, 2002, **149**, S21; (*b*) J. H. P. Utley, T. Fanghänel, I. Grenthe, W. R. Salaneck, R. Sillanpää, G. Bernáth, J. Szúnyog and B. Långström, *Acta Chem. Scand.*, 1998, **52**, 237–249.

61 D. F. Evans, *J. Chem. Soc.*, 1959, 2003.

62 E. M. Schubert, *J. Chem. Educ.*, 1992, **69**, 62.

63 (*a*) T. A. Betley and J. C. Peters, *J. Am. Chem. Soc.*, 2003, **125**, 10782–10783; (*b*) X. Hu and K. Meyer, *J. Am. Chem. Soc.*, 2004, **126**, 16322–16323; (*c*) E. R. King, G. T. Sazama and T. A. Betley, *J. Am. Chem. Soc.*, 2012, **134**, 17858–17861; (*d*) D. M. Jenkins, T. A. Betley and J. C. Peters, *J. Am. Chem. Soc.*, 2002, **124**, 11238–11239; (*e*) X. Dai, P. Kapoor and T. H. Warren, *J. Am. Chem. Soc.*, 2004, **126**, 4798–4799; (*f*) C. Jones, C. Schulten, R. P. Rose, A. Stasch, S. Aldridge, W. D. Woodul, K. S. Murray, B. Moubaraki, M. Brynda, G. La Macchia and L. Gagliardi, *Angew. Chem., Int. Ed.*, 2009, **48**, 7406–7410; (*g*) Y. Liu, J. Du and L. Deng, *Inorg. Chem.*, 2017, **56**, 8278–8286; (*h*) S. Aghazada, D. Fehn, F. W. Heinemann, D. Munz and K. Meyer, *Angew. Chem., Int. Ed.*, 2021, **60**, 16480–16486; (*i*) P. J. Chirik, Y. Park, S. P. Semproni and H. Zhong, *Angew. Chem., Int. Ed.*, 2021, **60**, 14376–14380.

64 M. J. T. Wilding, D. A. Iovan and T. A. Betley, *J. Am. Chem. Soc.*, 2017, **139**, 12043–12049.

65 (*a*) G. Coin, R. Patra, S. Rana, J. P. Biswas, P. Dubourdeaux, M. Clémancey, S. P. de Visser, D. Maiti, P. Maldivi and J.-M. Latour, *ACS Catal.*, 2020, **10**, 10010–10020; (*b*) K. Ray, F. Heims and F. F. Pfaff, *Eur. J. Inorg. Chem.*, 2013, **2013**, 3784–3807; (*c*) P. F. Kuijpers, J. I. van der Vlugt, S. Schneider and B. de Bruin, *Chem. – Eur. J.*, 2017, **23**, 13819–13829.

66 S. Anga, Y. Sarazin, J.-F. Carpentier and T. K. Panda, *ChemCatChem*, 2016, **8**, 1373–1378.

67 O. V. Dolomanov, L. J. Bourhis, R. J. Gildea, J. Howard and H. Puschmann, *J. Appl. Crystallogr.*, 2009, **42**, 339–341.

68 G. M. Sheldrick, *Acta Crystallogr., Sect. C: Struct. Chem.*, 2015, **71**, 3–8.

69 L. J. Farrugia, *J. Appl. Crystallogr.*, 1999, **32**, 837–838.

70 P. W. Betteridge, J. R. Carruthers, R. I. Cooper, K. Prout and D. J. Watkin, *J. Appl. Crystallogr.*, 2003, **36**, 1487.

71 C. P. Brock, E. Arnold, M. I. Aroyo, A. Authier, G. Chapuis, Th. Hahn, S. R. Hall, D. M. Himmel, V. Kopský, D. B. Litvin, B. McMahon, U. Müller, E. Prince, M. G. Rossmann, U. Shmueli, T. R. Welberry and H. Wondratschek, *International tables for crystallography*, International Union of Crystallography, Springer, Chester, England, New York, 1st edn, 2006.

72 (*a*) *SADABS-2016/2*, Bruker, 2016; (*b*) X.-R. , *X-Area*, STOE, 2016.

5.2 „Quasilinear 3d-metal(I) complexes [KM(N(Dipp)SiR$_3$)$_2$] (M = Cr − Co) − structural diversity, solution state behaviour and reactivity”

Ruth Weller, Igor Müller, Carine Duhayon, Sylviane Sabo-Etienne, Sébastien Bontemps, C. Gunnar Werncke

Dalton Transactions **2021**, *50*, 4890−4903.
DOI: 10.1039/d1dt00121c
https://pubs.rsc.org/en/content/articlehtml/2021/dt/d1dt00121c

Abstract

The synthesis and characterization of neutral quasilinear 3d-metal(I) complexes of chromium to cobalt of the type [KM(N(Dipp)SiMe$_3$)$_2$] (Dipp = 2,6-di-*iso*-propylphenyl) are reported. In solid state these metal(I) complexes either occur as isolated molecules (Co) or are part of a potassium ion linked 1D-coordination polymer (Cr − Fe). In solution the potassium cation is either ligated within the ligand sphere of the metal silylamide or is separated from the complex depending on the solvent. For iron, we showcase that it is possible to use sodium or lithium metal for the reduction of the metal(II) precursor. However, in these cases the resulting iron(I) complexes can only be isolated upon cation separation using an appropriate crown-ether. Further, the neutral metal(I) complexes are used to introduce NBu_4^+ as an organic cation in case of cobalt and iron. The impact of the intramolecular cation complexation was further demonstrated upon reaction with diphenyl acetylene which lead to bond formation processes and redox disproportionation instead of η^2-alkyne complex formation.

Zusammenfassung

In dieser Publikation wird die Synthese und Charakterisierung neutraler quasilinearer 3d-Metall(I)-Komplexe des Typs [KM(N(Dipp)SiR$_3$)$_2$] (M = Cr (R = ^{i}Pr) **1**, M = Mn – Co (R = Me), **2** − **4**) beschrieben. Sie stellen neben [KNi(N(Dipp)SiMe$_3$)$_2$][141] die ersten Verbindungen dar, die das Kalium-Kation durch Wechselwirkungen mit den anionischen Komplexionen und nicht durch ein Maskierungsreagenz stabilisieren. Für **4** geschieht dies, analog zu Nickel, intramolekular in Form isolierter Monomere. Intermolekulare Wechselwirkungen generieren dagegen polymere Ketten von Chrom

(**1**) bis Eisen (**3**). Durch Verwendung koordinierender Lösungsmittel bzw. Hilfsreagenzien können allerdings auch monomere Spezies für Chrom (**1**.3THF) und Eisen (**3**.Et$_2$O, **3**.DMAP) erhalten werden. Interessanterweise koordinieren die Lösungsmittelmoleküle dabei ausschließlich an das Kalium-Kation und nicht an die elektropositiven Metallzentren.

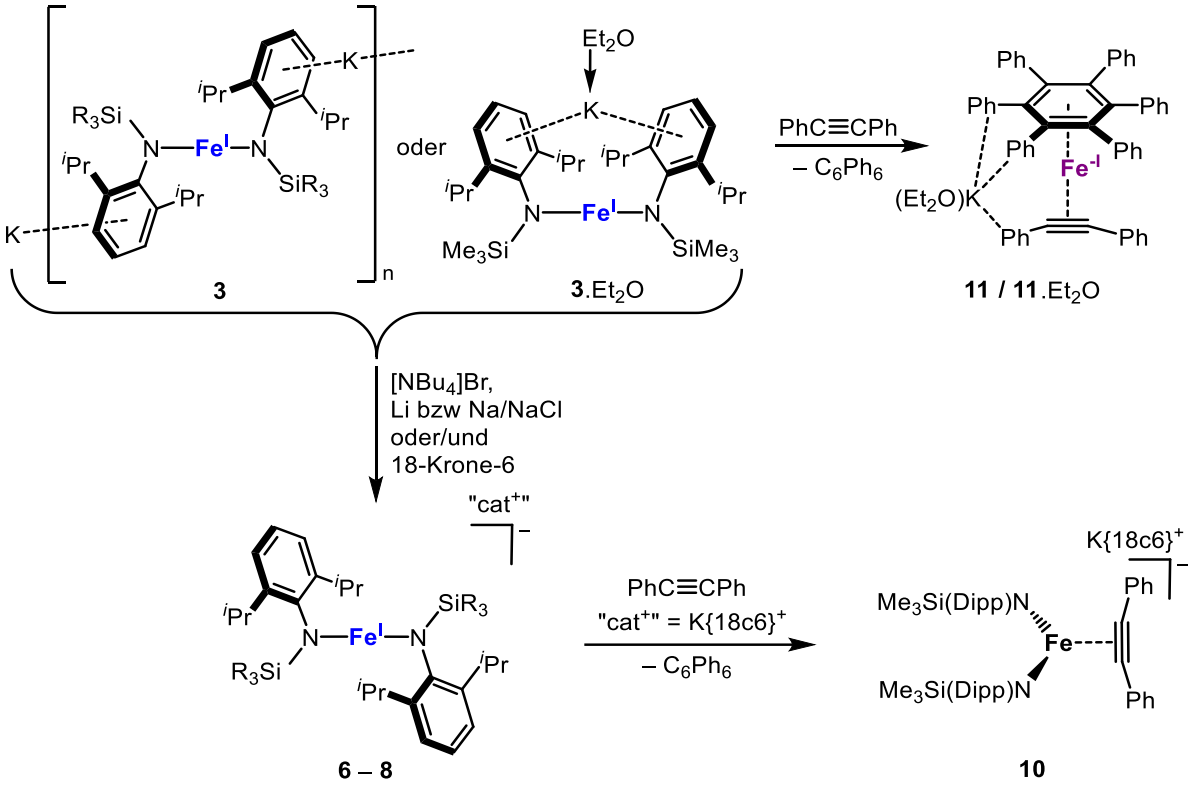

Schema 26. Struktureller Kationeneinfluss in linearen 3d-Metall(I)-Komplexen und Auswirkung einer Ladungsseparierung auf die Reaktivität am Beispiel von Eisen.

^{1}H-NMR-spektroskopische Untersuchungen zeigten eine Ionenseparierung in Lösung bei Verwendung koordinierender Lösungsmittel wie THF. Beim Lösen in nicht- oder schwach-koordinierenden Lösungsmitteln, wie Benzol oder Diethylether, wird das K^+-Ion weiterhin durch das Anion stabilisiert. Eine nachträgliche Interkalation des Kalium-Kations in Maskierungsreagenzien, wie 18-Krone-6, ist ohne signifikanten Ausbeuteverlust möglich.

Alle literaturbekannten 3d-Metall(I)-Komplexe wurden bisher ausschließlich durch Reduktion der Metall(II)-Vorläufer mit KC_8 erhalten. Aus diesem Grund wurde die Reduzierbarkeit von Metall(II)- zu Metall(I)-Spezies mit weiteren Alkalimetallen am Beispiel von Eisen getestet. Sowohl bei Verwendung von Lithium (elementar) als auch Natrium (5 % in NaCl) konnten die erfolgreichen Umsetzungen ^{1}H-NMR-spektroskopisch verfolgt werden. Die Isolierung entsprechender Komplexe erforderte jedoch die Anwesenheit von Maskierungsreagenzien (Verbindungen **6** und **7**). Des

Weiteren konnte für Eisen und Kobalt gezeigt werden, dass ein Austausch des Kalium-Kations durch ein organisches Ion, hier NBu_4^+, möglich ist (Verbindungen **8** und **9**). Unterschiedlichste räumliche Ligand-Anordnungen (*cis*, *trans* oder orthogonal) zeigen, dass nicht nur intra-, sondern auch intermolekulare Wechselwirkungen die Geometrie der Komplexionen ohne Beeinflussung der Metall−Amid-Bindungslängen bestimmen. Die in der Literatur diskutierten intramolekularen Dispersionswechselwirkungen sind somit wichtige, aber keine essenziellen Stabilisierungsfaktoren in linearen 3d-Metall(I)-Verbindungen.

In ersten weiterführenden Reaktionen wurde nachgewiesen, dass die Anwesenheit von Maskierungsreagenzien die Reaktivität der Komplexe beeinflusst. Dies wurde durch Umsetzungen von [KM(N(Dipp)SiMe$_3$)$_2$] (M = Mn, Fe) bzw. K{18c6}[Fe(N(Dipp)SiMe$_3$)$_2$] mit Diphenylacetylen getestet. Während durch die Ionenseparierung eine *side-on*-Koordination des Alkins begünstigt wird (**10**), wird das Alkin mit Neutralkomplexen sukzessive unter Abspaltung der Silylamid-Liganden trimerisiert (**11** − **12**). Die neutralen Verbindungen fungieren somit sowohl als Koordinationspartner als auch als Reduktionsmittel. Die ungewöhnlichen Intermediate können für die Aufklärung von Alkintrimerisierungen mit 3d-Metall(I)-Komplexen sehr hilfreich sein.

Beiträge der Autoren

Die Verantwortlichkeit für die Durchführung des Projektes lag in meiner Hand. Die in dieser Publikation beschriebenen Verbindungen wurden von Dr. Igor Müller (Verbindungen **10**, **12** und **13**) und mir (Verbindungen **1** − **9**, **11**) synthetisiert und analysiert. Eine Ausnahme stellt Verbindung **3**.Et$_2$O dar, die von Dr. C. Gunnar Werncke in Toulouse im Rahmen seines Projekts als Postdoktorand erhalten wurde. Die Analyse von **3**.Et$_2$O mittels Röntgendiffraktometrie wurde aus diesem Grund in Toulouse durch Dr. C. Duhayon und Dr. S. Sabo-Etienne unter Leitung von Prof. Dr. C. Bontemps durchgeführt. Für die Aufnahme aller gemessenen Daten (Ausnahme: Strukturen **10**, **12** und **13**) an den Diffraktometern IPDS2 bzw. IPDS2T der Firma STOE war ich zuständig. Messungen am Quest D8 Diffraktometer der Firma BRUKER wurden von Dr. C. Gunnar Werncke und der zentralen Serviceabteilung für Kristallstrukturanalyse am Fachbereich Chemie der Philipps-Universität Marburg unter der Leitung von Dr. Klaus Harms ausgeführt. Mit Ausnahme von **3**.Et$_2$O, **10**, **12** und **13** wurden alle Datensätze, die mittels Einkristallstrukturanalyse erhalten wurden, von mir

gelöst und verfeinert. Mit der Unterstützung der hausinternen NMR-Abteilung des Fachbereichs Chemie der Philipps-Universität Marburg unter der Leitung von Dr. Xiulan Xie nahm ich alle ^{1}H-NMR spektroskopischen Untersuchungen sowie Evans-Messungen auf und wertete diese selbständig aus. Elementaranalytische Untersuchungen wurden von mir vorbereitet und ausgewertet. Die Messungen selbst führte die hausinterne Abteilung für Massenspektrometrie und Elementanalytik des Fachbereichs Chemie der Philipps-Universität Marburg unter der Leitung von Dr. Uwe Linne durch. IR- und UV/Vis-Messungen wurden ebenfalls von mir geplant, durchgeführt und ausgewertet. Das Manuskript wurde von mir in Zusammenarbeit mit Dr. C. Gunnar Werncke verfasst.

Dalton Transactions

ROYAL SOCIETY OF CHEMISTRY

PAPER

View Article Online
View Journal | View Issue

Check for updates

Cite this: *Dalton Trans.*, 2021, **50**, 4890

Quasilinear 3d-metal(I) complexes [KM(N(Dipp)SiR$_3$)$_2$] (M = Cr–Co) – structural diversity, solution state behaviour and reactivity†

Ruth Weller,[a] Igor Müller,[a] Carine Duhayon,[b] Sylviane Sabo-Etienne,[b] Sébastien Bontemps[b] and C. Gunnar Werncke*[a]

Received 13th January 2021,
Accepted 2nd March 2021

DOI: 10.1039/d1dt00121c

rsc.li/dalton

The synthesis and characterization of neutral quasilinear 3d-metal(I) complexes of chromium to cobalt of the type [KM(N(Dipp)SiMe$_3$)$_2$] (Dipp = 2,6-di-iso-propylphenyl) are reported. In solid state these metal(I) complexes either occur as isolated molecules (Co) or are part of a potassium ion linked 1D-coordination polymer (Cr–Fe). In solution the potassium cation is either ligated within the ligand sphere of the metal silylamide or is separated from the complex depending on the solvent. For iron, we showcase that it is possible to use sodium or lithium metal for the reduction of the metal(II) precursor. However, in these cases the resulting iron(I) complexes can only be isolated upon cation separation using an appropriate crown-ether. Further, the neutral metal(I) complexes are used to introduce NBu_4^+ as an organic cation in the case of cobalt and iron. The impact of the intramolecular cation complexation was further demonstrated upon reaction with diphenyl acetylene which leads to bond formation processes and redox disproportionation instead of η^2-alkyne complex formation.

Introduction

Complexes with two-coordinate, open-shell 3d-metal(I) ions, known for chromium to nickel, are a young and rare class of compounds in coordination chemistry.[1,2–11] They combine an uncommon coordination motif with an unusual oxidation state. The isolation of such compounds relies mostly on the use of sterically encumbering and/or electronically stabilizing ligands, such as bulky amides or N-heterocyclic carbenes. Thereby intramolecular dispersion forces are generally thought to be crucial for their kinetic stabilisation of two-coordinate metal ions.[11,12] Given the labile nature of two-coordinate metal(I) complexes, the physical properties, as well as their reactivity concerning small molecules and various substrates is only partially explored. Reports concerning their respective behaviour indicate a high potential, *e.g.* remarkable single molecule magnetic properties.[2,4] These stem from the fact that these compounds can exhibit magnetic moments higher than the expected spin-only values, due to unquenched orbital momentum, as well as a strong magnetic anisotropy, attributed to their (near) linear ligand arrangement.[4,13–15] Further, linear metal(I) complexes are shown to mediate intriguing bond activation processes like cleavage of H_2, P–aryl, and C–F bonds or trimerisation of alkynes.[7,9,10,16] The number of homoleptic, linear metal(I) complexes bearing anionic ligands is very limited, and restricted to silylmethanides and silylamides. For silylamides this gave so far few examples of complex salts of the type [K{18c6}][M(N(Dipp)SiR$_3$)$_2$] (Cr – Cu; 18c6 = 18-crown-6; Dipp = 2,6-di-iso-propylphenyl) or [K{m}][M(N(SiMe$_3$)$_2$)$_2$] (Cr, Fe, Co; m = 18c6 or crypt.222).[2,3,6,8,11] Their synthesis is achieved by reacting a two-coordinate metal(II) precursor with potassium graphite in the presence of a cryptand or crown-ether. The latter is generally thought to be needed to sequestrate the cation, and by that to prevent decomposition of the homoleptic complex anion, which was demonstrated in case of [Fe(N(SiMe$_3$)$_2$)$_2$]$^-$.[2] A notable exception was reported by Tilley and co-workers in the case of the nickel(I) complex [KNi(N(Dipp)SiMe$_3$)$_2$],[5] for which the monovalent state is comparably stable. Here the potassium ion is ligated within the ligand sphere (Fig. 1), leading to an overall neutral compound.[5,6]

Given the fundamental interest of expanding the coordination chemistry of two-coordinate 3d-metal ions we wanted to elucidate the synthesis of monovalent compounds of the type [KM(L)$_2$] of the earlier 3d-transition metals. The presence of an unmasked alkali metal cation in the vicinity of a 3d-metal is prospective of distinct reactivity due to synergistic effects, as shown

[a]*Department of Chemistry, Philipps-University Marburg, Hans-Meerwein-Straße 4, D-35032 Marburg, Germany. E-mail: gunnar.werncke@chemie.uni-marburg.de*
[b]*CNRS, LCC (Laboratoire de Chimie de Coordination), 205 route de Narbonne, 31077 Toulouse and Université de Toulouse, UPS, INPT, 31077 Toulouse, France*

†Electronic supplementary information (ESI) available: ^{1}H-NMR-, UV/Vis spectra, crystallographic details. CCDC 2010651, 2010659, 2010661–2010666, 2011200, 2011213, 2011333, 2011409, 2011410 and 2047637–2047641. For ESI and crystallographic data in CIF or other electronic format see DOI: 10.1039/d1dt00121c

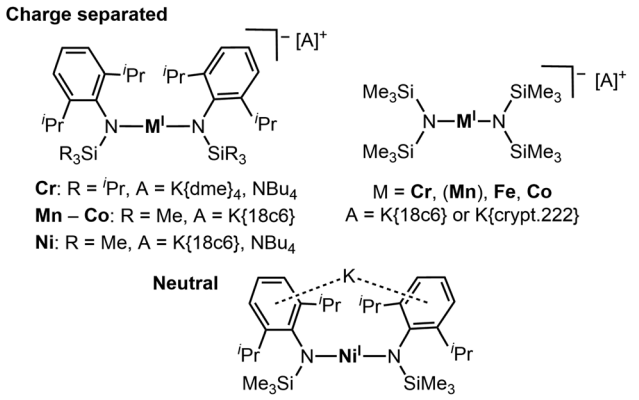

Fig. 1 Known anionic or neutral quasilinear open-shell 3d-metal(I) silylamides.

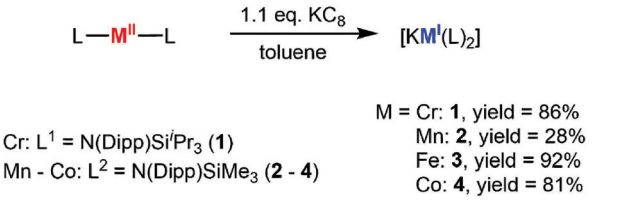

Scheme 1 Synthesis of solvent and cryptand free $[KM(L)_2]$ (M = Cr–Co) (**1–4**) (Dipp = 2,6-di-iso-propylphenyl).

for example for low-coordinate alkali metal ferrates or manganates,[17] may labilise the 3d-metal–amide bond or can be used for introduction of further functionalities or other cations.

Herein we report the isolation of quasilinear complexes of the type $[KM(L)_2]$ (L^1 = N(Dipp)Si^{i}Pr$_3$ (Cr); L^2 = N(Dipp)SiMe$_3$ (Mn – Co)), with intra- or intermolecular complexation of the potassium cation, leading to unusual coordination polymers bearing open-shell, two-coordinate metal(I) ions. For iron we showcase the first use of lithium or sodium metal as reductants, whereas respective compounds are unstable and have to be stabilized by masking of the alkali metal cation. In due course a large structural variety of the ligand arrangement within the quasilinear silyl amide complexes can be observed that depends on interligand as well as cation···anion interactions. We provide insights into the solution state dependence of the $[KM(L)_2]$ complexes, also revealing how the alkali metal ion is extracted in donor solvents. First studies on the reactivity of $[KM(L)_2]$ complexes towards diphenyl acetylene hint to the consequences of the lack of persistent cation separation.

Results and discussion

Synthesis and structure of $[KM(L)_2]$ complexes

The quasilinear metal(II) complexes $[M(L)_2]$ (L^1 = N(Dipp)Si^{i}Pr$_3$ (Cr, due to reported instability of the SiMe$_3$ derivative);[5] L^2 = N(Dipp)SiMe$_3$ (Mn – Co)) were reacted with 1.1 equivalent KC_8 in toluene at room temperature (Scheme 1) leading to an instantaneous change of colour in each case (Cr: dark red → red; Mn: colourless → dark violet; Fe: red → greenish brown; Co: red violet → green). Crystalline material was obtained from diffusion of *n*-pentane into a toluene solution of each compound at −40 °C giving green $[KCr(L^1)_2]$, **1**, violet $[KMn(L^2)_2]$, **2**, red brown $[KFe(L^2)_2]$, **3**, and green $[K(toluene)Co(L^2)_2]$, **4**. X-Ray diffraction analysis of compounds revealed for compounds **1–3** a polymeric structure (Fig. 2), where formally [M

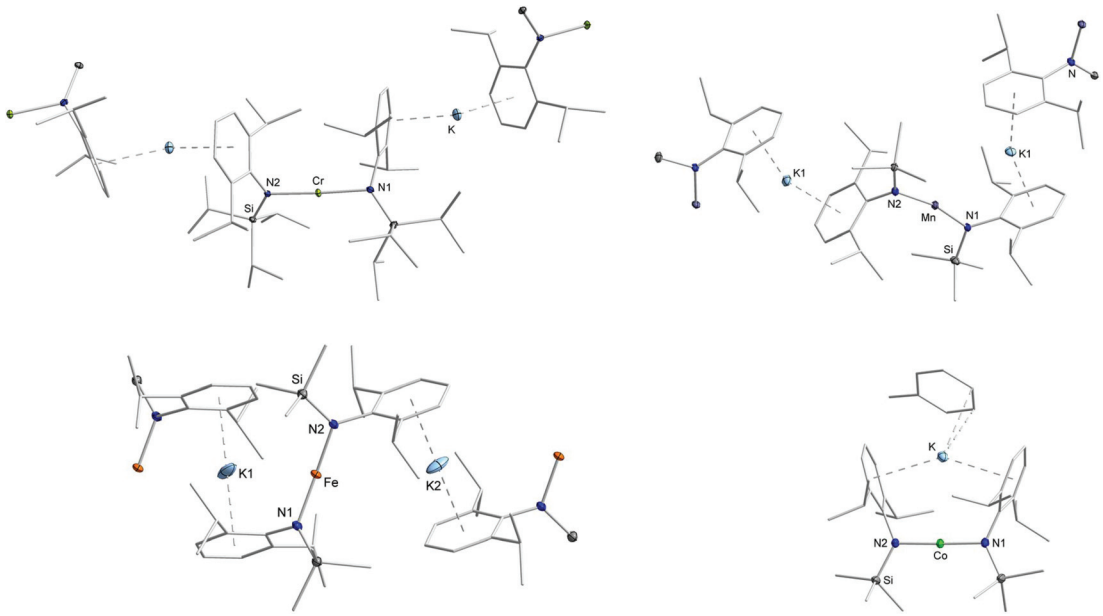

Fig. 2 Sections of the crystal structure of **1** (top left), **2** (top right), **3** (bottom left) and **4** (bottom right). H atoms are omitted for clarity. For compounds **1–3** the amide unit of neighbouring complex molecules is shown.

$(L)_2]^-$ anions are linked *via* potassium cations, which are situated between the aryl rings of two neighbouring molecules. The potassium ion are located at the outer (**1**, Cr), inner and outer (**2**, Mn) or inner (**3**, Fe) side of the respective aryl ring. In case of compound **3** (Fe), the potassium ion is situated directly between two aryl rings with no apparent Fe⋯K interaction (Fe–K 4.3564(3) Å), whereas in **2** (Mn) it is clearly oriented towards the transition metal (Mn–K 3.8423(5) Å). These structural features lead to a zig-zag 1D-polymer chain for **2** (Mn) and **3** (Fe), and a more linear chain for **1** (Cr). This is also reflected by the intermolecular M–M′ distances, which gives for **1** (Cr) a Cr–Cr′ distance of 12.4099(9) Å within and of 9.9095(8) Å between the chains (Table 1). For **2** (Mn) and **3** (Fe), the situation is inverse with shorter intra- (**2**: 9.8350(5) Å; **3**: 8.7128(5) Å) than inter-chain M–M′ distances (**2**: 11.0784(5) Å; **3**: 11.6773(6) Å). The chain-like arrangement in solid state for compounds **1–3** is a so far unknown feature of complexes with open-shell, two-coordinate transition metal ions. It contrasts the situation of the related $[KNi(L)_2]$,[5] where the potassium ion is ligated in an intramolecular fashion. Such a situation is observed for the cobalt derivative **4** (Co), where a toluene molecule is completing the coordination sphere of the potassium ion (Co–K distance of 3.5652(6) Å). The N–M–N bond angles within the polymeric compounds are almost linear in the case of chromium (177.44(10)°, **1**) and slightly bent in manganese (165.56(6)°, **2**) and iron (170.59(5)°, **3**). For the monomeric cobalt compound **4**, the N–Co–N bond angle amounts to 178.43(8)°. The M–N bond lengths shorten along the series from *ca.* 2.07 Å (**1**, Cr) to 1.96 Å (**2**, Mn) and down to 1.88 Å (**4**, Co).

A large variety was observed for the C_{aryl}–N–N′–C'_{aryl} torsion angles (Table 1). While in **1** the opposing aryl rings twist with a torsion angle of 60(2)°, the rings are standing more or less *trans* to each other in **2** (161.68(14)°) and **3** (123.65(15)°). These large differences originate likely from respective aryl–K interaction as well as inter- or intramolecular dispersion forces between an iso-propyl group and an aryl ring of a second ligand. In the cobalt complex **4**, the aryl rings of both ligands are facing each other (torsion angle of 1.22(23)°) which is enforced by the potassium ion. The intramolecular K⋯arene distances in **4** are with 3.1419(7) Å longer than in polymeric **1–3** (approx. 2.8 Å), probably due to the enforced proximity of opposing iso-propyl groups. Together with literature known $[M(L^2)_2]^-$ complexes, as well as further examples presented below, it reveals a rotational flexibility of the amide ligands around the N–M–N axis. This structural diversity contrasts the situation of the divalent precursors which exhibit a (symmetry generated) linear N–M–N axis with *trans*-oriented aryl rings only.[18] As such, the amide ligand orientation is dictated by K-arene and not by interligand dispersion interactions *via* CH_3⋯arene or CH_3⋯CH_3 units.

Solution state behaviour of $[KM(L)_2]$ complexes

^{1}H NMR spectroscopy. Given the observed structural variability of compounds **1–4** in solid state and their envisioned use for substrate activation, we sought further insights into their behaviour in solution with respect to the potassium cation speciation. Thereby it is important to note that **1–4** are highly soluble in toluene or Et_2O, contrasting the congeners with 18-crown-6 masked potassium cations (only slightly soluble in Et_2O). All complexes were first examined by ^{1}H NMR spectroscopy in non-coordinating C_6D_6 revealing their paramagnetic nature by strongly shifted (in comparison with their

Table 1 Selected structural metrics of compounds **1–9** (L^2 = –N(Dipp)$SiMe_3$)

Metal	Compound	M–N1/Å	M–N2/Å	M–M′/Å	N1–M–N2/°	Torsion angle/°	Shortest, interligand C–C distance
Cr	**1**	2.076(2)	2.070(2)	9.9095(8)[a] 12.4099(9)	177.44(10)	59.97(23)	3.719(4) ($CH_{3(Si^iPr_3)}$⋯$CHMe_{2(Si^iPr_3)}$) 3.796(3) (Ph⋯$CH_{3(Dipp)}$) 3.680(4) ($CH_{3(Dipp)}$⋯$CHMe_{2(Si^iPr_3)}$)
	5	2.0576(14)	2.0528(14)	11.1564(9)	174.12(5)	42.41(12)	3.954(2) ($CH_{3(Si^iPr_3)}$⋯$CH_{3(Si^iPr_3)}$) 3.536(1) (Ph⋯$CH_{3(Dipp)}$)
Mn	**2**	1.9653(16)	1.9681(15)	9.8350(5) 11.0784(5)[a]	165.56(6)	161.68(14)	3.979(2) (Ph⋯$CH_{3(SiMe_3)}$)
	$[K\{18c6\}][Mn(L^2)_2]$[8]	1.961(3)	1.954(3)	10.8687(11)	167.12(14)	49.1(2)	3.867(5) (Ph⋯$CH_{3(SiMe_3)}$) 4.661(7) ($CH_{3(SiMe_3)}$⋯$CH_{3(SiMe_3)}$)
Fe	**3**	1.9005(15)	1.9014(13)	8.7128(5) 11.6773(6)[a]	170.59(5)	123.65(15)	4.139(3) ($CH_{3(Dipp)}$⋯$CH_{3(SiMe_3)}$)
	3·2DMAP	1.9121(3)	1.9121(3)[b]	10.7640(19)	180[b]	16.8(3)	4.469(7) ($CH_{3(SiMe_3)}$⋯$CH_{3(SiMe_3)}$)
	6	1.911(3)	1.915(3)	10.5043(9)	175.34(13)	148.9(3)	4.825(5) (Ph⋯$CH_{3(SiMe_3)}$) 4.200(10) ($CH_{3(Dipp)}$⋯$CH_{3(SiMe_3)}$)
	7	1.894(4)	1.903(4)	11.518(2)	170.82(14)	7.0(4)	3.804(9) ($CH_{3(Dipp)}$⋯$CH_{3(Dipp)}$) 4.136(9) ($CH_{3(SiMe_3)}$⋯$CH_{3(SiMe_3)}$)
	8	1.915(2)	1.918(2)	10.8837(18)	175.27(7)	111.35(17)	3.604(2) (Bu_4N⋯Ph) 4.089(4) ($CH_{3(Dipp)}$⋯$CH_{3(SiMe_3)}$)
	$[K\{18c6\}][Fe(L^2)_2]$[3]	1.9135(14)	1.9147(14)	10.625(17)	172.65(6)	95.05(15)	3.936(2) ($CH_{3(Dipp)}$⋯$SiCH_3$)
Co	**4**	1.8787(23)	1.8782(24)	7.7857(8)	178.43(8)	1.22(23)	3.416(4) ($CH_{3(Dipp)}$⋯$CH_{3(Dipp)}$) 4.391(5) ($CH_{3(SiMe_3)}$⋯$CH_{3(SiMe_3)}$)
	9	1.878(2)	1.884(2)	11.1161(7)	176.28(10)	3.93(25)	3.500(3) (Bu_4N⋯Ph) 3.497(4) ($CH_{3(Dipp)}$⋯$CH_{3(Dipp)}$) 4.121(4) ($CH_{3(SiMe_3)}$⋯$CH_{3(SiMe_3)}$)
	$[K\{18c6\}][Co(L^2)_2]$[3]	1.8835(10)	1.8835(10)[b]	10.5574(6)	180[b]	180[b]	3.951(2) ($CH_{3(Dipp)}$⋯$CH_{3(SiMe_3)}$)

[a] M–M′ distances along the 1D chain. [b] Generated *via* a crystallographic inversion centre on the metal atom.

Table 2 ^{1}H NMR signals of the complex anions of **1–9** with R = ^{i}Pr (Cr), Me (Mn–Co) in ppm. The signal(s) belonging to the K{18c6} or NBu_4 cations are found around their diamagnetic positions

Metal	Compound	solvent	SiR_3	CH_3	$CHMe_2$	*m*-Ph	*p*-Ph
Cr	**1**	C_6D_6	6.81	No signal attribution possible			
		THF-d_8	No signal attribution possible				
	5	THF-d_8	No signal attribution possible				
Mn	**2**	C_6D_6/THF-d_8	No signal attribution possible				
Fe	**3**	C_6D_6	−1.65	−78.0/39.7	59.3	23.4	4.33
		THF-d_8	−0.09	−103.1/—	—	—	—
	3·2DMAP	C_6D_6	−3.63	−78.6/39.4	—	26.6	19.4
	6	THF-d_8	−1.03	−99.8/—	—	—	—
	7	THF-d_8	−0.49	−102.2/—	—	—	—
	8	THF-d_8	—	−102.3/—	—	—	—
Co	**4**	Toluene-d_8	3.67	−72.3/29.3	5.79	21.4	9.26
		THF-d_8	13.9	−86.5/17.7	29.7	16.5	4.27
	9	THF-d_8	14.0	−88.0/17.4	30.1	16.0	7.31

expected diamagnetic signal position) and broadened proton signals. The paramagnetic shift comes primarily from interactions of the respective proton with the metal(I) ion *via* through-bond (contact shift) and through-space (pseudo-contact shift) interactions.[19] In some cases, signal assignments were thus hampered (Table 2), *e.g.* for chromium (**1**) and manganese (**2**) only very broad signatures were detected. The proton spectra of **3** (iron, Fig. S5†) and especially **4** (cobalt, Fig. 3, left) are better behaved allowing for signal assignment *via* signal positions and integral intensities (Table 2). In **4**, which shows rather sharp signatures, the signal belonging to the $SiMe_3$ fragment in **4** is found at 3.67 ppm whereas the iso-propyl groups give rise to two signals at −72.3 and 29.3 ppm. Looking at the solid state structure the latter two signals likely represents the inward and outward positioned methyl functions of each iso-propyl group, suggesting suppression of the free rotation of the iso-propyl groups in solution. The huge paramagnetic shift difference between these two signals is remarkable and likely comes from pseudo-contact interactions, given the identical bond connection but different spacial distances to the metal ion (average d(Co–C_{in}) 4.3 Å *vs.* d(Co–C_{out}) 5.1 Å). Together with differences in line-broadening it suggests that the stronger paramagnetically influenced signal at −72.3 ppm belongs to the inward oriented methyl group and that the pseudo-contact and contact shifts have opposing signs. The *meta*-positioned protons of the aromatic systems are shifted downfield to 21.4 ppm, whereas the impact of the paramagnetic centre to the *para*-positioned ones (9.26 ppm) are weaker. The signal of the methine protons (5.79 ppm) are again strongly broadened due to the proximity of the cobalt(I) ion. Given the well-behaved ^{1}H NMR spectrum of **4** (Co), we conducted further experiments to get qualitative insights into the speciation in solution, especially with respect to the location of the potassium ion (within the complex or as separated cation). The switch to the coordinating solvent THF-d_8 impacted significantly the signal positions in comparison to the non-coordinating solvent toluene-d_8 (Fig. 3, right). The highest impact of changing the solvent was detected for the methine protons, which are now found at 29.7 ppm ($\Delta\delta$ = 26 ppm). While the signal of the trimethylsilyl protons is shifted downfield by approx. 10 ppm to 13.9 ppm, signals of the methyl groups of the Dipp-units are shifted by around 12 ppm to higher field and are found at −86.5 ppm and 17.7 ppm, respectively (toluene-d_8: −72.3, 29.3 ppm). The spectrum of **4** (Co) in THF-d_8 is thereby analogous to the one obtained for the potassium ion separated complex [K{18c6}][Co(L^2)$_2$] (THF-d_8, Fig. S19†),[7] speaking to the complete solvation of the potassium ion by THF. Thereby, the process of the extraction of the potassium ion by THF requires a large excess of THF as addition of up to 20 equivalents of THF to a toluene-d_8 solution of **4** (Co) led just to a slight shift of its ^{1}H proton signals. In contrast, upon Et_2O addition no shifting signals were observed, even using pure Et_2O. This reflects the weak ability of THF and inability of Et_2O to fully solvate the potassium cation. At low temperatures, the spectra of **4** in THF-d_8 and toluene-d_8 did not coincide (Fig. S20 and S22†), which indicated a persistent diverging potassium cation speciation between these solvents. All paramagnetic signals of **4** (Co) follow the Curie–Weiss law ($\delta(T) \sim 1/T$) in THF-d_8 (Fig. S23†) as well as in toluene-d_8 (Fig. S21†). Together with the absence of signal splitting,[2,8] this showed that, like the cation/anion interaction, the electronic situation and complex geometry remained unchanged over the examined temperature range.

With these results for **4** (Co) in mind, the solvent dependencies of the ^{1}H NMR signals were also examined for complexes **1** (Cr), **2** (Mn) and **3** (Fe). For all three compounds similar the spectra in toluene-d_8 or C_6D_6 (also in Et_2O for **3**) differed significantly from those in THF-d_8. The latter are thereby identical to the ^{1}H NMR spectra of the [K{18c6}][M(L_2)] complexes (Table 2), whereas [K{18c6}][Cr(L^1)$_2$], **5**, had to be synthesized first.[3,6,8] Overall, ^{1}H NMR spectroscopy showed for the [KML_2] compounds that in non/weakly-coordinating solvents the K^+ cation is likely connected to the complex anion, presumably residing between the aryl rings as in the solid state structure of **4**, whereas in THF it is present as a solvent-separated counter-ion.

UV/Vis spectroscopy. Given the observed ^{1}H NMR spectroscopic features of compounds **1–4**, a variable-temperature UV/Vis spectroscopic analysis was conducted. In case of the chro-

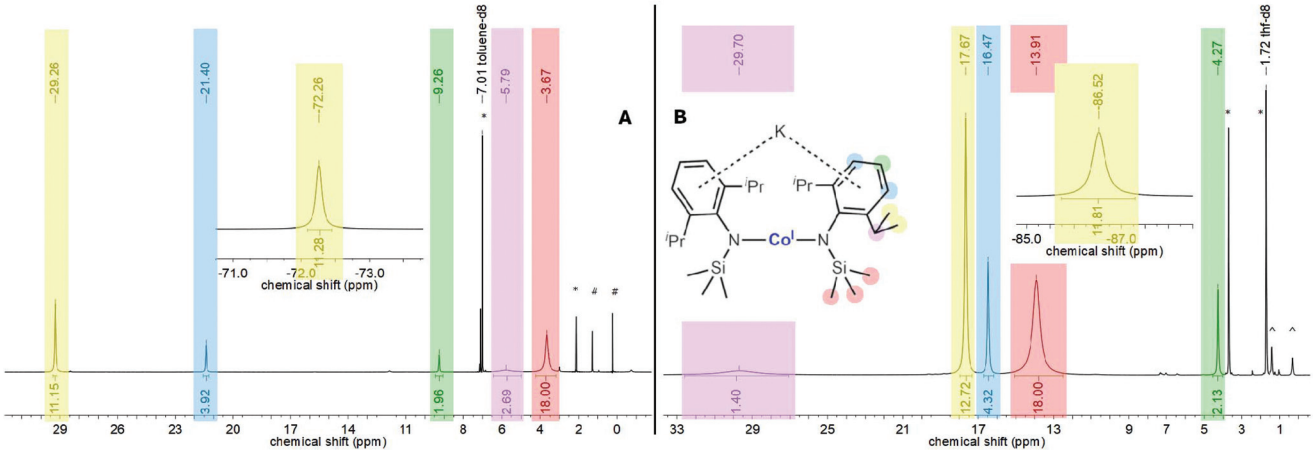

Fig. 3 ^{1}H NMR spectrum (500.1 MHz, 300 K) of **4** in toluene-d_8 (left (A), * solvent, # *n*-pentane) and THF-d_8 (right (B), ^ impurities).

mium compound **1**, a UV/Vis spectrum recorded in THF showed three absorption bands at 286 nm (ε > 7930 L mol^{-1} cm^{-1}), 343 nm (ε = 4440 L mol^{-1} cm^{-1}) and 426 nm (ε = 3320 L mol^{-1} cm^{-1}). These bands can be ascribed to ligand to metal charge transfer (LMCT) transitions (Table 3),[3,12] and mimic those of **5** (Cr). When switching to toluene or Et_2O only one absorption maximum was observed for **1** (Cr) (toluene: 431 nm, $\varepsilon \approx$ 5210 L mol^{-1} cm^{-1}; Et_2O: 435 nm, $\varepsilon \approx$ 6940 L mol^{-1} cm^{-1}), speaking for a similar electronic situation for **1** in these two solvents. Cooling the respective solutions to −110 °C had no significant effect. For **2** (Mn) examinations were restricted to diethyl ether, due to decomposition in toluene and THF under these dilute conditions. Two absorption maxima at 448 nm ($\varepsilon \approx$ 1610 L mol^{-1} cm^{-1}) and 565 nm ($\varepsilon \approx$ 2410 L mol^{-1} cm^{-1}) were observed that superpose those of [K{18c6}][MnL$^2_2$].[8] For complex **3** (Fe) maxima at 421 nm (ε = 2120 L mol^{-1} cm^{-1}), 610 nm (ε = 160 L mol^{-1} cm^{-1}) and 773 nm (ε = 120 L mol^{-1} cm^{-1}) were observed in THF (Fig. 4),

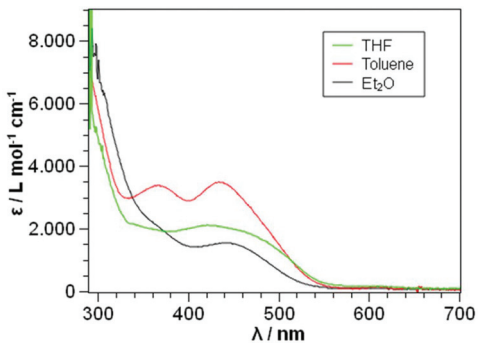

Fig. 4 UV/Vis spectrum (290–700 nm) of **3** in different solvents at 22 °C.

whose positions are akin to the ones found for [K{18c6}][Fe(L$_2$)$_2$].[3] The latter two maxima are tentatively assigned to d–d transitions.[3,12] When switching to toluene as solvent, both

Table 3 UV/Vis absorption maxima of **1–9** and [K{18c6}][M(L^2)$_2$] (M = Fe, Co, L^2 = −N(Dipp)SiMe$_3$); 280–900 nm, (RT)

Metal	Compounds	Solvent	$\lambda(\varepsilon)$/nm(L mol^{-1} cm^{-1})
Cr	**1**	Toluene	431 (5210)
		THF	286 (>7930), 343 (4440), 426 (3320)
		Et_2O	435 (6940)
	5	THF	288 (7710), 338 (3880), 421 (2160)
Mn	**2**	Et_2O	448 (1610), 565 (2410), 849 (2650)
Fe	**3**	Toluene	368 (3380), 432 (3490), 602 (140)
		THF	421 (2120), 610 (160), 773 (120)
		Et_2O	442 (1540), 601 (100)
	3·2DMAP	Toluene	360 (3230), 434 (3190), 607 (130)
	6	THF	422 (1990), 771 (170)
	7	THF	420 (5020), 613 (320), 771 (260)
	8	THF	364 (1660), 420 (1900)
	[K{18c6}][FeL$^2_2$] [3]	THF	428 (4000), 626 (100)
Co	**4**	Toluene	385 (3080)
		THF	336 (2800), 385 (2300)
		Et_2O	393 (3560)
	9	THF	340 (4770), 390 (4120)
	[K{18c6}][CoL$^2_2$][a 3]	THF	337 (2380), 391 (2030), 629 (100)

[a] UV/Vis spectrum was recorded but no absorption coefficients were given in the original report.

LMCT bands at 368 nm ($\varepsilon \approx 3380$ L mol^{-1} cm^{-1}) and 432 nm ($\varepsilon \approx 3490$ L mol^{-1} cm^{-1}) appear as two distinct absorption maxima. Cooling these solutions down to −110 °C had no considerable effect on the position of the transitions. The UV/Vis spectrum of **3** (Fe) in Et_2O resembled the one in THF with a LMCT band at 442 nm ($\varepsilon \approx 1540$ L mol^{-1} cm^{-1}) and a d–d transition at 601 nm ($\varepsilon \approx 100$ L mol^{-1} cm^{-1}). Upon cooling this solution to −110 °C the reversible disappearance of the LMCT band could be observed, whose origin is yet unclear.

The UV/Vis spectrum of 4 (Co) in toluene exhibited one LMCT band at 385 nm ($\varepsilon \approx 3080$ L mol^{-1} cm^{-1}) which splits at −110 °C into two bands at 387 nm ($\varepsilon \approx 3910$ L mol^{-1} cm^{-1}) and 410 nm ($\varepsilon \approx 3850$ L mol^{-1} cm^{-1}). Measurements in THF showed two absorption bands at 336 nm ($\varepsilon \approx 2800$ L mol^{-1} cm^{-1}) and 385 nm ($\varepsilon \approx 2300$ L mol^{-1} cm^{-1}) at room temperature, which is comparable to the UV/Vis spectrum of [K{18c6}][Co(L_2)$_2$].[3] A UV/Vis spectrum of **4** (Co) in diethyl ether showed a broad band at 393 nm with additional low-intensity d–d transitions ($\varepsilon < 100$ L mol^{-1} cm^{-1}) above 600 nm. Cooling a solution of **4** (Co) in THF or Et_2O had no considerable effect onto its UV/Vis spectroscopic properties. Overall the UV/Vis spectroscopic examinations showed markedly different spectra for complexes **1** (Cr), **3** (Fe) and **4** (Co) for either THF or toluene solutions. Thereby the spectra in THF coincided with those of cation separated complexes mimicking the ^{1}H NMR spectroscopic results. In Et_2O the UV/Vis spectroscopic situation is ambiguous. Whereas for **1** and **4** the respective spectra resembled those in toluene, implicating that the potassium ion is also not separated from the complex anion, for the iron complex **3** the spectroscopic features in Et_2O are similar to those in THF. As this is not in line with the NMR spectroscopic observations, it speaks for an additional solvent effect, such as solvent coordination.

Structural effects of donor solvents on [KM(L)$_2$] complexes

Having observed the ^{1}H NMR and UV/Vis spectroscopic changes for complexes **1–4** when going from non-coordinating to coordinating solvents, we were interested if this could be somewhat retraced on a structural level. This turned out to be highly challenging as small amounts of donor solvents such as Et_2O or THF lead to a very high solubility of the respective compounds **1–4** even in *n*-pentane, indicative of solvent coordination. Upon rigorous drying of respective solutions, the donor solvents could be removed as these complexes were again insoluble in *n*-pentane. Nonetheless, in due course we could identify for iron the highly soluble diethyl ether adduct **3**·Et_2O (Fe) using X-ray diffraction analysis (Fig. 5, left). As the crystal data suffers from some flaws, its general features are only shortly discussed. In **3**·Et_2O (Fe) the potassium cation is coordinated in an intramolecular fashion by the two aryl rings, as observed for **4** (Co) and [KNiL$^2_2$].[5] It thus shows how the polymeric form is transformed to a monomer in solution. A diethyl ether molecule completes the coordination sphere of the potassium ion. As a result of the intramolecular potassium cation fixation the N–Fe–N bond axis is nearly linear with a negligible C_{Ar}–N–N′–C'_{Ar} torsion angle. Given the difficulties in the crystallization progresses, which we attributed to the volatility of the employed Et_2O in conjunction with the high solubility of **3**·Et_2O (Fe), we used DMAP as an exemplary donor ligand. This gave the stable adduct **3**·2DMAP (Fe) (Fig. 5, middle) as green crystals in yields up to 75%. Similar to **3**·Et_2O (Fe), the potassium cation is located between the two aryl rings in an intramolecular fashion and is further coordinated by two DMAP molecules. Looking at the UV/Vis spectrum of **3**·2DMAP, two distinct LMCT bands at 360 nm ($\varepsilon \approx 3230$ L mol^{-1} cm^{-1}) and 434 nm ($\varepsilon \approx 3190$ L mol^{-1} cm^{-1}) are present. This mimics the behaviour of pure **3** in toluene, corroborating for the latter a persistent intramolecular potassium cation complexation. For chromium, the monomeric complex **1**·3THF (Cr) was obtained as revealed by X-ray diffraction analysis. In **1**·3THF (Cr) the potassium cation resides on the external side of one of the aryl rings of the silylamide ligand set with three tetrahydrofuran molecules completing its coordination sphere. Together with **3**·Et_2O (Fe) and **3**·2DMAP (Fe), **1**·3THF (Cr) thus gives insight on how the potassium cation is extracted out of the aryl pocket of the [KM(L)$_2$] complexes upon addition of donor solvents. Remarkably, no coordination of donor solvent molecules to the 3d-metal ion takes place, which is observed for their divalent counterparts.[20]

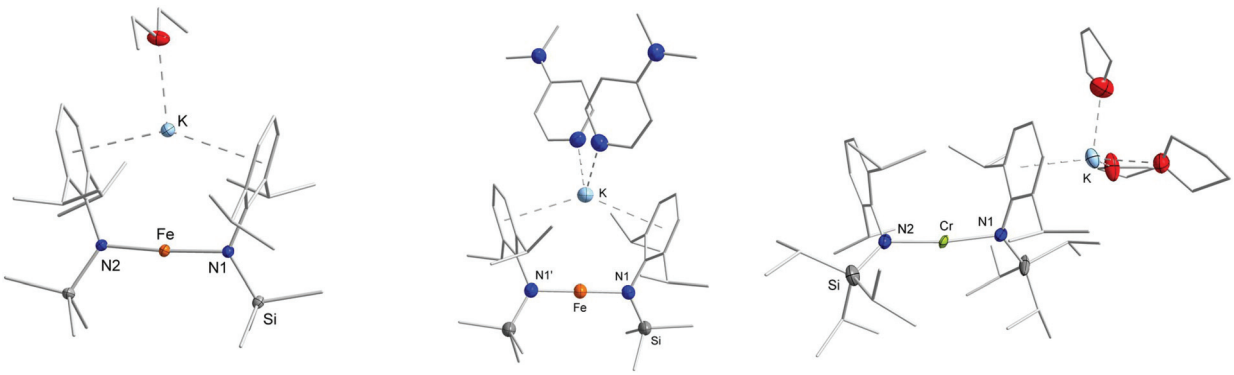

Fig. 5 Sections of the crystal structure of **3**·Et_2O (left), **3**·2DMAP (middle) and **1**·3THF (right). H atoms are omitted for clarity. In case of **1**·3THF disorders found for one THF molecule as well as for two iso-propyl groups are not depicted.

Sodium, lithium and NBu_4^+ as counter ions

The synthesis of homoleptic quasilinear metal(I) silylamides was so far exclusively approached using potassium graphite as the reductant. In view of the different solid state structures of the neutral compounds we wanted to introduce lithium and sodium as reductants for such complexes, as these smaller ions might enforce a different solid or solution state behaviour. To probe this possibility we chose the iron derivative as a representative. Treatment of $[Fe(L^2)_2]$ with lithium or sodium (5% Na dispersed in NaCl)[21] led to a slow (Li), respectively rapid (Na) colour change from orange/red to brownish green (Scheme 2). Attempts to obtain the presumed neutral reaction products $[AFe(L^2)_2]$ (A = Li, Na) led to their decomposition. This was evidenced by a colour change of the reaction solutions overnight at −40 °C or upon evaporation of the solvent and was additionally verified *via* the subsequent recrystallization of the metal(II) precursor. The initial formation of $[AFe(L^2)_2]$ could be proven *via* ^{1}H NMR spectroscopy when performing the reduction in THF-d_8. Adding either 12-crown-4 (for lithium) or 18-crown-6 (for sodium) to a solution of $[AFe(L^2)_2]$ led, after work-up, to the isolation of the respective ion-separated products $[Li\{12c4\}_2][Fe(L^2)_2]$, **6**, and $[Na\{18c6\}(Et_2O)][Fe(L^2)_2]$, **7**, as shown in Fig. 6.

Structural analysis *via* X-ray diffraction on suitable crystals showed most notably different orientations of the amide ligands within the $[Fe(L^2)_2]^-$ complex anion. In **6** (Fe), the aryl functions are pointing in the opposite direction (torsion angle 148.9(3)°), whereas in **7** (Fe), they are in an eclipsed position (torsion angle 7.0(4)°). As expected, the UV/Vis and paramagnetic ^{1}H NMR spectra in THF-d_8 for both **6** and **7** resembled those of $[K\{18c6\}][Fe(L^2)_2]$. Similar to the extraction of the alkali metal ion by crown-ethers, we also wanted to use the $[KM(L)_2]$ complexes to introduce an organic cation (Scheme 3). This was already shown in case of the related nickel complex $[KNi(L^2)_2]$ as well as in the case of chromium $[K\{dme\}_4][Cr(L^1)_2]$.[5,6]

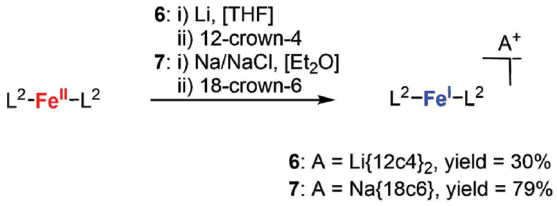

Scheme 2 Reduction of $[Fe(L^2)_2]$ (L^2 = N(Dipp)SiMe$_3$) with lithium (**6**) or sodium (**7**), respectively.

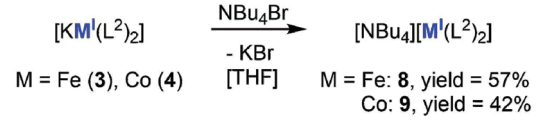

Scheme 3 Introduction of the organic cation NBu_4^+ in $[NBu_4][M(L^2)_2]$ (M = Fe (**8**), Co (**9**), L^2 = N(Dipp)SiMe$_3$).

The reaction of **2** (Mn) with NBu_4Br or PPh_4Br led to discolouring of the reaction mixture as well as to precipitation of small amounts of a black solid on the stirring bar. This indicated an insufficient stability of the cation in the presence of the highly reducing manganese(I) complex $[MnL^2_2]^-$ ($E_{red} \approx -2.5$ V *vs.* Fc/Fc^+).[8] The reaction of **3** (Fe) and **4** (Co) with NBu_4Br led, after work-up, to the isolation of the corresponding compounds $[NBu_4][Fe(L^2)_2]$, **8**, and $[NBu_4][Co(L^2)_2]$, **9** (Scheme 3). X-Ray diffraction analysis revealed that the exchange of the cation has no significant influence on the M–N bond lengths and the N–M–N angles in the anion (Table 1). However, larger differences in the torsion angles were notable. Whereas the ligand set of **9** (Co) remains in an eclipsed conformation with a torsion angle of 3.93(25)°, a rotation around the N–M–N axis took place in **8** (Fe), resulting in a staggered conformation (111.35(17)°). Both features can be attributed to interactions of the aryl rings with one of the methyl groups of the NBu_4^+ cation, whose distances are in part even shorter than intramolecular $CH_3\cdots$aryl/$CH_3\cdots CH_3$ distances (Table 1). It implicates that intramolecular dispersion forces, thought as essential for the stability of two-coordinated complexes, are here of lesser importance. The impact of attracting intramolecular dispersion interactions is further discussed to influence M–N distances.[12,22] However, the cobalt complexes **4** (KCo), **9** (NBu_4Co) and $[K\{18c6\}][Co(L^2)_2]$, for example, exhibit

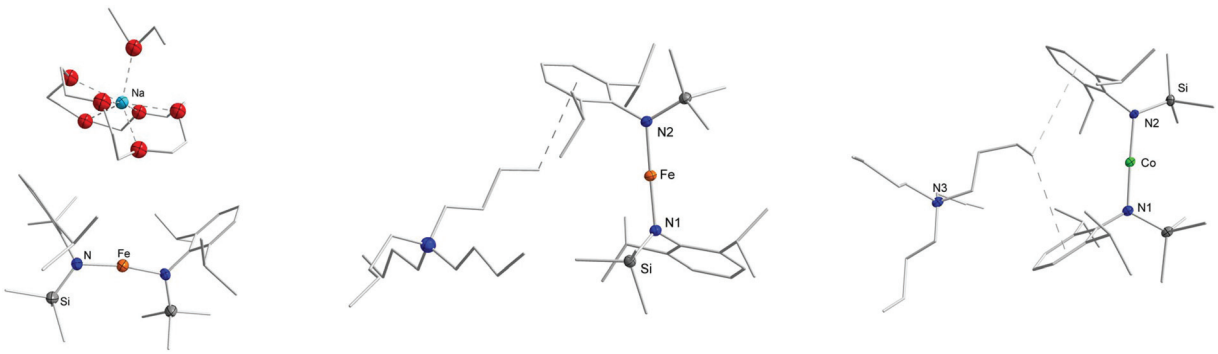

Fig. 6 Sections of the crystal structure of **7** (left), **8** (middle) and **9** (right). H atoms and a disorder of the 18-crown-6 fragment of **7** are omitted for clarity. For **8** and **9** the shortest CH_3–arene interactions are depicted (dashed line).

virtually identical Co–N distances, despite bearing drastically differing ligand orientations and interactions in solid state.

Magnetic properties in solution

Having understood the speciation of the complexes **1–4** in solution, we were briefly interested if the intramolecular potassium ion complexation of the [KML_2] complexes has a discernible impact onto the solution state magnetic properties in comparison with to their cation separated counterparts. Using Evans method (Table 4) the effective magnetic moments of **1** (Cr) and **2** (Mn) in C_6D_6 were determined to be 5.17μ_B ($\mu_{S.O.(S=5/2)}$ = 5.92μ_B) and 4.68μ_B ($\mu_{S.O.(S=2)}$ = 4.82μ_B). These are lower than the expected spin-only values (Cr^I: $\mu_{S.O.(S=5/2)}$ = 5.92μ_B, Mn^I: $\mu_{S.O.(S=2)}$ = 4.92μ_B) but are in the range of other linear chromium(I) and manganese(I) complexes (*e.g.* [K{dme}$_4$][Cr(L^1)$_2$]: 5.2μ_B, K{18c6}[Mn(L^2)$_2$]: 4.98).[6,8] Higher than spin-only values were measured for complexes **3** (Fe) (μ_{eff} = 5.31μ_B, $\mu_{S.O.(S=3/2)}$ = 3.87μ_B), **3**·2DMAP (Fe) (μ_{eff} = 4.89μ_B), and **4** (Co) (μ_{eff} = 4.50μ_B, $\mu_{S.O.(S=1)}$ = 2.83μ_B) which is expected for linear complexes with unquenched orbital contributions.[13,14,23] When switching to THF-d_8 a slight drop in the respective magnetic susceptibilities was observed for **1** (4.92μ_B), **3** (4.34μ_B) and **4** (3.93μ_B). The values in THF are comparable to those found for the respective cation separated complexes (**5–9**), stressing that the complex anion is more or less unaffected by a separated counter ion in solution. Within the limits of the Evans method this indicates a beneficial factor of intramolecular potassium ion complexation, either by blocking of the free amide rotation or fixation of a near-linear N–Fe–N axis which would overall enhance orbital contributions.

Reactivity of [$KM(L)_2$] complexes towards diphenylacetylene

Lastly, we conducted first experiments concerning the impact of the intramolecular potassium ion complexation on the reactivity of the metal(I) complexes for manganese to cobalt given the identical ligand set. For that we chose diphenyl acetylene (PhCCPh) as a probe, given our recent examination of anionic metal(I) silylamides [$M(N(SiMe_3)_2)_2$]$^-$ towards alkynes, that yielded predominantly *side-on* alkyne complexes ([$M(\eta^2$-RCCR)$(N(SiMe_3)_2)_2$]$^-$) but also some bond reduction and disproportionation processes in case of manganese.[24] In this context the –N(Dipp)$SiMe_3$ ligand set was already probed for manganese yielding relatively stable complexes of the type [$Mn(\eta^2$-RCCR)$(L^2)_2$] (R = Et, Ph).[24] As such we pursued first the isolation of the iron and cobalt derivatives. Reaction of [K{18c6}][Fe(L^2)$_2$] with PhCCPh led to the quantitative formation of the *side-on* alkyne complex [K{18c6}][Fe(L^2)$_2$(η^2-PhCCPh)], **10** (Scheme 4). The same reaction with [K{18c6}][Co(L^2)$_2$] yielded in an initial color change to red brown, but only the employed cobalt(I) precursor was isolated upon crystallisation. This is not surprising as weak and reversible binding of alkynes to cobalt silylamides was already observed in case of sterically less demanding [Co$(N(SiMe_3)_2)_2$]$^-$.[24] Treating **4** (KCo) with PhCCPh afforded also only the starting materials. In contrast, when **3** (Fe) was treated with PhCCPh in Et_2O, crystallization yielded the mixed arene/alkyne iron complex [K(D)(Fe(C_6Ph_6)(PhCCPh)], **11**·D, (D = none, Et_2O) (Fig. 7, second left, ESI†) as well as inseparable free hexaphenylbenzene (HPB). Following the reaction of **3** (Fe) in C_6D_6 by ^{1}H NMR spectroscopy showed the rapid consumption of PhCCPh and formation of minor amounts of free HPB. **11**·D corresponds to the known iron compound [K{18c6}][Fe(HPB)(η^2-PhCCPh)], obtained by reaction of the iron(–I) synthon [K{18c6}][Fe($C_{10}H_8$)$_2$] with PhCCPh,[25] as well as the

Table 4 Solution state magnetic susceptibilities of complexes **1–9** (L^2 = N(Dipp)$SiMe_3$) in THF-d_8 and C_6D_6 *via* the Evans method. Theoretical spin-only values are given for the high-spin case

Metal	Compound	Cation	μ_{eff} [μ_B] in THF-d_8	μ_{eff} [μ_B] in C_6D_6
Cr [$\mu_{S.O.}$ = 5.92μ_B]	**1**	K	4.92	5.17
	5	K{18c6}	4.21	Insoluble
Mn [$\mu_{S.O.}$ = 4.90μ_B]	**2**	K	Partial decomposition	4.68
	[K{18c6}][Mn(L^2)$_2$]	K{18c6}	4.98 [8]	Insoluble
Fe [$\mu_{S.O.}$ = 3.87μ_B]	**3**	K	4.34	4.85
	3·2DMAP	K(DMAP)$_2$	—	4.89
	6	Na{18c6}	4.74	Insoluble
	7	Li{12c4}$_2$	4.24	Insoluble
	8	NBu_4	4.30	Insoluble
Co [$\mu_{S.O.}$ = 2.83μ_B]	**4**	K	3.93	4.18
	9	NBu_4	3.58	Insoluble

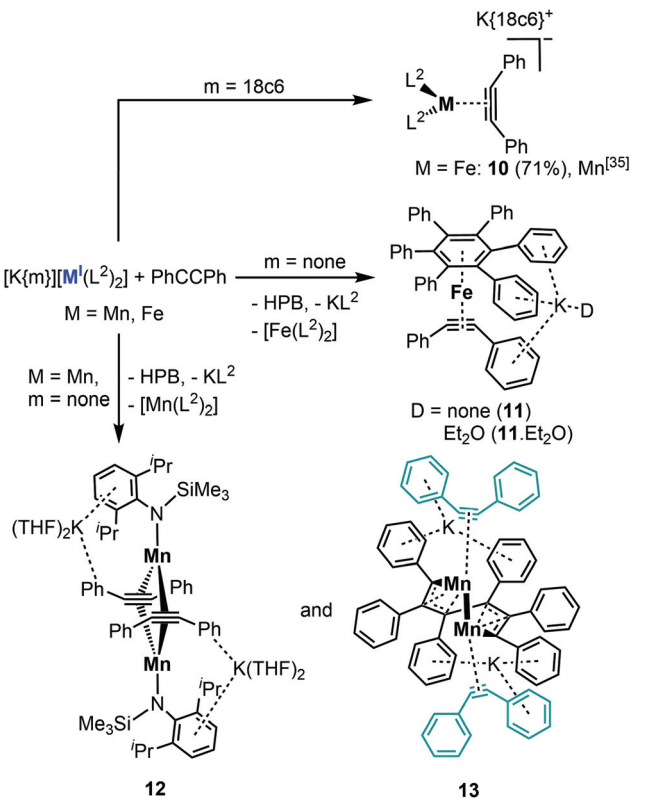

Scheme 4 Reactivity of [K{m}][$M(L^2)_2$] of manganese and iron (m = none or 18c6) towards PhCCPh (HPB = C_6Ph_6).

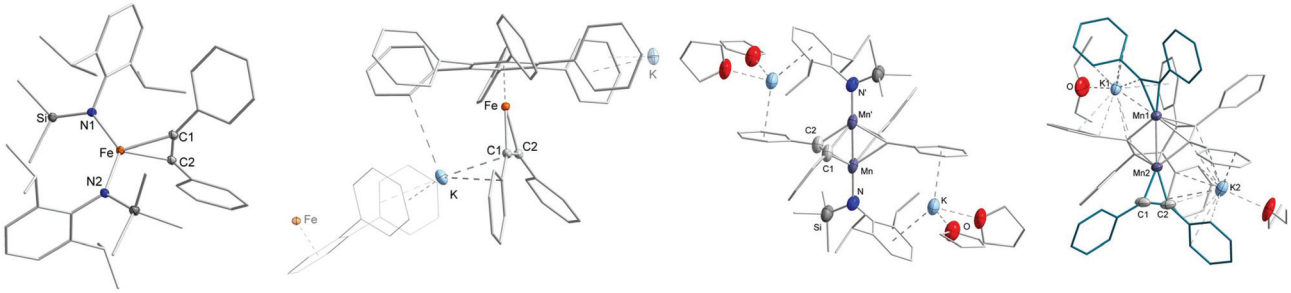

Fig. 7 Sections of the crystal structures of **10**–**13** (from left to right). H atoms and the K{18c6} unit of **10** are omitted for clarity.

manganese analogue [K{18c6}][Mn(HPB)(η^2-PhCCPh)].[24] The latter was observed during the reaction of the manganese(I) complex $[Mn(N(SiMe_3)_2)_2]^-$ with PhCCPh under redox disproportionation and ligand redistribution. For **3** (Fe) a similar mechanism is plausible, whereas **3** acts as reductant as well as source of an iron atom under formal release of KL^2 and [Fe$(L^2)_2$].

Treatment of **2** (KMn) in toluene with PhCCPh resulted also in the trimerisation product HPB. Remarkably, small amounts of crystals of the dimeric complexes **12** and **13** (Fig. 7, right, ESI†) were obtained that give insights into this manganese mediated trimerisation process. In **12** two manganese ions are bridged by two PhCCPh units, which are oriented orthogonal towards the Mn–Mn axis. The distance between the manganese atoms are with 2.434(2) Å rather short and comparable to a ketimide linked Mn^{II}/Mn^{II} dimer.[26] Similar to **11**·D, the formation of **12** is probably the result of formal redox disproportionation of the employed **2** (Mn). Compound **12** is in close resemblance to a recently reported dinuclear iron complex ([(L^2)Fe(μ-η^2-PhCCPh)$_2$Fe(L^2)], which was observed upon reacting [Fe(IDipp)(L^2)] (IDipp = 1,3-bis(2,6-di-iso-propylphenyl) imidazolin-2-ylidene) with PhCCPh.[27] It exhibits significantly less distorted alkyne ligands (C–C 1.349(7) Å, C–C–C_{phenyl} bond angle of 133.3(4)°) which speaks to a stronger π-backbonding into the π^*-orbitals of the alkyne within **12**. In the other dimeric complex **13** two manganese atoms (Mn–Mn 2.5665(11) Å) are linked *via* a C6-chain, stemming from incomplete alkyne trimerisation. Judging from the bond lengths, the carbon fragment is best described as two allyl units linked *via* a C–C single bond giving it a formal dianionic charge.[28–30] The coordination sphere of each manganese ion, that lacks any silylamide ligation, is completed by an alkyne ligand, which experiences only a moderate C–C bond elongation (1.267(7) Å and 1.287(8) Å). The presence of two potassium ions, each being located in a pocket composed of two aryl rings of the C6 fragment as well as one of an alkyne, leads to a formal oxidation state of Mn^0 for both manganese ions. The formation of the trimerised C6 fragment in **13** is remarkable as it poses a snapshot in the final step of alkyne trimerisation. Metallacycloheptatriene-like intermediates in alkyne trimerisation were so far only observed for mononuclear complexes,[28–31] whereas bimetallic derivatives were only postulated.[27] Any attempts of isolating pure **12** or **13** *via* adjustment of the reaction stoichiometry as well as reaction temperature failed so far, in part by the ubiquitous presence of the complete trimerisation product HPB. When the reaction mixture of **2** (KMn) with PhCCPh in Et_2O was layered after several minutes with 18c6 in Et_2O and stored at −35 °C, to promote crystallisation *via* cation separation, only the known η^2-alkyne complex K{18c6}[Mn$(L^2)_2(\eta^2$-PhCCPh)][24] can be isolated, showing that the formation of **12** and **13** is a slower process.

Conclusions

The syntheses and characterization of neutral quasilinear, homoleptic 3d-metal(I) silylamides of the type $[KM(L)_2]$ (L^1 = N(Dipp)Si^{i}Pr$_3$ (Cr); L^2 = N(Dipp)SiMe$_3$ (Mn – Co)) *via* the reduction of the respective quasilinear metal(II) silylamide with KC_8 in non-coordinating solvents were presented. X-Ray diffraction analysis shows that the alkali metal ion is coordinating to the aryl rings in either an intramolecular (Co) or intermolecular intermolecular fashion (Cr, Mn, Fe). For the latter this results in the presence of unprecedented 1D-coordination polymers of linear, open-shell metal(I) complexes. Detailed ^{1}H NMR spectroscopic examinations of the complexes in solution showed that, in non-coordinating solvents, the cation remains in the vicinity of the complex anion whereas, in good donor solvents like THF, these compounds exist as an ion pair. When using lithium or sodium as reductants the respective iron complexes $[AFe(L^2)_2]$ (A = Li, Na) could be generated, which were isolated by sequestrating the alkali metal. Starting off the formally neutral metal(I) silylamides, the alkali metals could also be exchanged by an organic cation in case of iron and cobalt. Upon comparison of the structural metrics of all obtained and literature reported $[M(L)_2]^-$ complexes, it is shown that the two amide ligands can virtually exhibit any orientation towards each other (*cis*, *trans* or orthogonal). This is dependent on the presence of not only intra- but also intermolecular interactions in solid states and has no considerable effect on the metal–amide bond length. It indicates that intramolecular dispersion forces are an important, but not an essential factor for the stabilization of homoleptic, two-coordinate metal(I) amides. First reactivity studies of the neutral compounds $[KM(L^2)_2]$ (M = Mn –Co) towards diphenyl acetylene showed distinct differences with respect to their cation separ-

ated counterparts K{18c6}[M(L^2)$_2$]. Whereas the latter prefer the formation of η^2-alkyne complexes, the neutral complexes serve as coordination sites as well as reductants. This leads ultimately to substrate trimerisation whereas unusual intermediates could be structurally characterized. It thus shows that the intramolecular potassium ion complexation labilises the metal amide bond and give rise to distinct reactivities The further use of neutral metal(I) silylamides as precatalysts as well as a detailed inspection of their magnetic properties is currently explored in our lab.

Experimental section

Materials and methods

All manipulations were carried out in a glovebox under a dry argon atmosphere, unless indicated otherwise. Used solvents were dried by continuous distillation over sodium metal for several days, degassed *via* three freeze–pump–thaw cycles and stored over molecular sieves 4 Å. Deuterated solvents were used as received, degassed *via* three freeze-pump cycles and stored over molecular sieves 4 Å. The ^{1}H NMR spectra were recorded on a Bruker AV 500, a Bruker HD 500 or a Bruker HD 300 NMR spectrometer (Bruker Corporation, Billerica, USA). Chemical shifts are reported in ppm relative to the residual proton signals of the solvent (for ^{1}H). $w_{1/2}$ is the line width of a signal at half its maximum intensity. Integrals of the broad signals ligand set were obtained directly or by peak fitting (in case of overlapping signals) using the MestreNova software package (Mestrelab, Santiago de Compostela, Spain). IR measurements were conducted on a Bruker Alpha ATR-IR spectrometer (Bruker Corporation, Billerica, USA). The UV/VIS measurement were recorded on an AnalytikJena Specord S600 using WinASPECT software. Elemental analysis were performed by the "in-house" service of the Chemistry Department of the Philipps University Marburg, Germany using a CHN(S) analyser vario MICRO Cube (Elementar Analysensysteme GmbH, Langenselbold, Germany). Dispersed sodium (5% Na/NaCl),[21] [Cr(N(Dipp)Si^{i}Pr$_3$)$_2$],[6] [Mn(N(Dipp)SiMe$_3$)$_2$],[8] [Fe(N(Dipp)SiMe$_3$)$_2$],[14] and [Co(N(Dipp)SiMe$_3$)$_2$],[12] were prepared according to literature procedures.

Synthesis and characterization

[KM(L)$_2$] (L^1 = N(Dipp)Si^{i}Pr$_3$ (Cr); L^2 = N(Dipp)SiMe$_3$ (Mn – Co)). One equivalent of [M(L)$_2$] (M = Cr–Co) was dissolved in either 10 mL toluene or diethyl ether. After adding KC_8 (1.1 equiv.) the reaction mixture was stirred for several minutes at room temperature, while a change in colour was observed (Cr: dark red → red; Mn: beige → dark violet; Fe: orange → red; Co: dark red → light green). The graphite was filtered off and all volatiles were removed under reduced pressure. After washing with *n*-pentane and drying *in vacuo*, [KM(L)$_2$] (**1–4**) was obtained in yields of 28–92%.

[KCr(N(Dipp)Si^{i}Pr$_3$)$_2$] (1). Using 500 mg of [Cr(N(Dipp)Si^{i}Pr$_3$)$_2$], **1** could be obtained as red solid. **Yield:** toluene: 391 mg (0.52 mmol, 74%), Et_2O: 447 mg (0.59 mmol, 86%). Crystals, suitable for X-ray diffraction analysis, were obtained from a concentrated toluene solution of **1** at −40 °C. **^{1}H NMR** (500.1 MHz, C_6D_6, 300 K, ppm): δ = 22 (bs, $w_{\frac{1}{2}}$ = 1900 Hz), 15 (bs, $w_{\frac{1}{2}}$ = 1300 Hz), 12 (bs, $w_{\frac{1}{2}}$ = 310 Hz), 7 (bs, 18 H, $w_{\frac{1}{2}}$ = 2100 Hz, Si(CH(C**H**$_3$)$_2$)$_3$), 4.0 (s, $w_{\frac{1}{2}}$ = 42 Hz), 3.6 (s, $w_{\frac{1}{2}}$ = 32 Hz), 2.4 (s, $w_{\frac{1}{2}}$ = 20 Hz), 0.29 (s, $w_{\frac{1}{2}}$ = 22 Hz), −16 (bs, $w_{\frac{1}{2}}$ = 200 Hz) ppm. (300.2 MHz, THF-d_8, 300 K, ppm): δ = 16 (bs, $w_{\frac{1}{2}}$ = 920 Hz), 12 (bs, $w_{\frac{1}{2}}$ = 810 Hz), 2.65 (s, $w_{\frac{1}{2}}$ = 17.3 Hz). Elemental analysis: $C_{42}H_{76}CrKN_2Si_2$ (756.35 g mol^{-1}): calcd: N 3.70, C 66.70, H 10.13; found: N 3.84, C 66.36, H 10.05%. **IR** (ATR, cm^{-1}): $\tilde{\nu}$ = 2941 (m), 2861 (m), 1576 (w), 1456 (m), 1407 (s), 1313 (m), 1244 (s), 1140 (w), 1101 (w), 992 (w), 925 (s), 878 (m), 804 (w), 767 (s), 719 (w), 640 (s), 554 (w), 525 (w), 487 (w), 418 (m). **EVANS** (500.1 MHz, 300 K, C_6D_6 + 1% TMS): μ_{eff} = 5.17μ_B; $\mu_{S.O.}$ = 5.92μ_B. (500.1 MHz, 300 K, C_6D_6 + 1% TMS): μ_{eff} = 4.92μ_B; $\mu_{S.O.}$ = 5.92μ_B.

[KMn(N(Dipp)SiMe$_3$)$_2$] (2). Using 100 mg of [Mn(N(Dipp)SiMe$_3$)$_2$], **2** could be obtained as dark violet solid. **Yield:** toluene: 5 mg (0.009 mmol, 5%), Et_2O: 30 mg (0.051 mmol, 28%). Crystals, suitable for X-ray diffraction analysis, were obtained from a *n*-pentane layered solution of **2** in toluene at −35 °C. **^{1}H NMR** (500.1 MHz, C_6D_6, 300 K, ppm): δ = 16 (bs, $w_{\frac{1}{2}}$ = 1400 Hz), 12 (bs, $w_{\frac{1}{2}}$ = 630 Hz), 2.11 (s, $w_{\frac{1}{2}}$ = 8.09 Hz), 2.01 (s, $w_{\frac{1}{2}}$ = 14.3 Hz), 1.4 (bs, $w_{\frac{1}{2}}$ = 450 Hz), 1.21 (s, $w_{\frac{1}{2}}$ = 8.17 Hz), 0.99 (s, $w_{\frac{1}{2}}$ = 18.0 Hz), 0.41 (s, $w_{\frac{1}{2}}$ = 15.4 Hz), 0.11 (s, $w_{\frac{1}{2}}$ = 11.0 Hz), −7.3 (bs, $w_{\frac{1}{2}}$ = 1400 Hz). (500.1 MHz, THF-d_8, 300 K, ppm): δ = 15 (bs, $w_{\frac{1}{2}}$ = 2100 Hz), 11.0 (bs, $w_{\frac{1}{2}}$ = 470 Hz), 6.10 (s, $w_{\frac{1}{2}}$ = 55.3 Hz), 3.9 (s, $w_{\frac{1}{2}}$ = 56 Hz), 2.89 (s, $w_{\frac{1}{2}}$ = 14.8 Hz), 2.29 (s, $w_{\frac{1}{2}}$ = 6.31 Hz), 0.20 (bs, $w_{\frac{1}{2}}$ = 220 Hz), −0.06 (s, $w_{\frac{1}{2}}$ = 34 Hz), −13 (bs, $w_{\frac{1}{2}}$ = 860 Hz). Elemental analysis $C_{30}H_{52}MnKN_2Si_2$ (590.96 g mol^{-1}): calcd: N 4.74, C 60.97, H 8.87; found: N 5.00, C 61.30, H 8.65%. **IR** (ATR, cm^{-1}): $\tilde{\nu}$ = 2953 (m), 2867 (w), 1577 (vw), 1459 (w), 1416 (s), 1380 (w), 1359 (w), 1313 (m), 1237 (vs), 1190 (s), 1105 (w), 1052 (w), 1039 (w), 958 (w), 916 (s), 879 (w), 824 (vs), 784 (vs), 741 (m), 666 (m), 619 (w), 571 (w), 534(m), 431 (m). **EVANS** (500 MHz, 300 K, C_6D_6 + 1% TMS): μ_{eff} = 4.68μ_B; $\mu_{S.O.}$ = 4.90μ_B.

[KFe(N(Dipp)SiMe$_3$)$_2$] (3). Using 350 mg of [Fe(N(Dipp)SiMe$_3$)$_2$], **3** could be obtained as red solid. **Yield:** toluene: 339 mg (0.57 mmol, 90%), Et_2O: 343 mg (0.58 mmol, 92%). Crystals, suitable for X-ray diffraction analysis, were obtained from a *n*-pentane layered solution of **3** in toluene at −35 °C. Crystals of **3**·Et_2O, suitable for X-ray diffraction analysis, were obtained from a *n*-pentane layered solution of **3** in minimal amounts of Et_2O at −35 °C. The Et_2O adduct is soluble in *n*-pentane whereas the one without is not. **^{1}H NMR** (500.1 MHz, C_6D_6, 300 K, ppm): δ = 60 (bs, 2 H, C**H**(CH$_3$)$_2$), 39.7 (bs, 12 H, $w_{\frac{1}{2}}$ = 620 Hz, CH(C**H**$_3$)$_2$), 23.4 (bs, 4 H, $w_{\frac{1}{2}}$ = 470 Hz, *m*-Ph**H**), 4.3 (bs, 2 H, $w_{\frac{1}{2}}$ = 290 Hz, *p*-Ph**H**), 0.15 (s, $w_{\frac{1}{2}}$ = 7.70 Hz), −1.7 (bs, 18 H, $w_{\frac{1}{2}}$ = 1800 Hz, Si(C**H**$_3$)$_3$), −78 (bs, 12 H, $w_{\frac{1}{2}}$ = 1200 Hz, CH(C**H**$_3$)$_2$). (300.2 MHz, THF-d_8, 300 K, ppm): δ = 29 (bs, $w_{\frac{1}{2}}$ = 560 Hz), 28 (bs, $w_{\frac{1}{2}}$ = 360 Hz), 12.6 (bs, $w_{\frac{1}{2}}$ = 240 Hz), 1.3 (bs, $w_{\frac{1}{2}}$ = 33 Hz), 0.26 (bs, $w_{\frac{1}{2}}$ = 20 Hz), −0.1 (bs, 18 H, $w_{\frac{1}{2}}$ = 1300 Hz, Si(C**H**$_3$)$_3$), −103 (bs, $w_{\frac{1}{2}}$ = 1500 Hz, CH(C**H**$_3$)$_2$). Elemental analysis $C_{30}H_{52}FeKN_2Si_2$ (591.87 g mol^{-1}): calcd: N

4.73, C 60.88, H 8.86; found: N 4.91, C 60.97, H 8.63%. **IR** (ATR, cm^{-1}): $\tilde{\nu}$ = 2947 (m), 2864 (w), 1582 (w), 1462 (w), 1417 (s), 1379 (w), 1357 (w), 1317 (m), 1238 (s), 1198 (m), 1141 (w), 1102 (m), 1051 (w), 1041 (w) 978 (m), 914 (s), 877 (m), 828 (vs), 787 (vs), 745 (m), 671 (m), 624 (w), 576 (w), 541 (w), 425 (m). **EVANS** (500 MHz, 300 K, C_6D_6 + 1% TMS): μ_{eff} = 4.85μ_B; $\mu_{S.O.}$ = 3.87μ_B. (500 MHz, 300 K, THF-d_8 + 1% TMS): μ_{eff} = 4.34μ_B; $\mu_{S.O.}$ = 3.87μ_B.

[K(DMAP)$_2$Fe(N(Dipp)SiMe$_3$)$_2$] (3·2DMAP). Crystals, suitable for X-ray diffraction analysis, were obtained by adding two equivalents of DMAP (20.5 mg, 0.17 mmol, 2 eq.) to 50 mg of **3** (0.08 mmol, 1 equiv.) in Et_2O, layering the solution with *n*-pentane and keeping it at −40 °C for several days. **Yield:** 49.7 mg (0.06 mmol, 75%). **^{1}H NMR** (500.1 MHz, C_6D_6, 300 K, ppm): δ = 61 (bs, $w_{\frac{1}{2}}$ = 260 Hz), 39.4 (bs, 12 H, $w_{\frac{1}{2}}$ = 600 Hz, CH(C**H**$_3$)$_2$), 26.2 (bs, 4 H, $w_{\frac{1}{2}}$ = 480 Hz, *m*-Ph**H**), 19.4 (bs, 2 H, $w_{\frac{1}{2}}$ = 170 Hz, *p*-Ph**H**), 1.8 (bs, $w_{\frac{1}{2}}$ = 290 Hz), 1.2 (bs, $w_{\frac{1}{2}}$ = 63 Hz), 0.98 (bs, $w_{\frac{1}{2}}$ = 96 Hz), 0.23 (bs, $w_{\frac{1}{2}}$ = 230 Hz), −1.75 (bs, $w_{\frac{1}{2}}$ = 550 Hz), −3.6 (bs, 18 H, $w_{\frac{1}{2}}$ = 1700 Hz, Si(C**H**$_3$)$_3$), −79 (bs, 12 H, $w_{\frac{1}{2}}$ = 1300 Hz, CH(C**H**$_3$)$_2$). Elemental analysis $C_{44}H_{72}FeKN_6Si_2$ (591.87 g mol^{-1}): calcd: N 10.05, C 63.20, H 8.68; found: N 10.38, C 62.83, H 8.50%. **IR** (ATR, cm^{-1}): $\tilde{\nu}$ = 2949 (m), 2863 (m), 1603 (s), 1534 (m), 1461 (w), 1442 (w), 1417 (s), 1387 (m), 1357 (w), 1318 (m), 1230 (s), 1200 (m), 1154 (w), 1139 (w), 1106 (m), 1056 (w), 1042 (w), 992 (s), 951 (m), 928 (s), 881 (w), 834 (vs), 801 (vs), 781 (vs), 752 (m), 669 (m), 622 (m), 527 (m), 480 (w), 430 (m). **EVANS** (500 MHz, 300 K, C_6D_6 + 1% TMS): μ_{eff} = 4.89μ_B; $\mu_{S.O.}$ = 3.87μ_B.

[KCo(N(Dipp)SiMe$_3$)$_2$] (4). Using 200 mg of [Co(N(Dipp)SiMe$_3$)$_2$], **4** could be obtained as light green solid. **Yield:** toluene: 159 mg (0.27 mmol, 74%), Et_2O: 173 mg (0.29 mmol, 81%). Crystals, suitable for X-ray diffraction analysis, were obtained from a *n*-pentane layered solution of **4** in toluene at −25 °C. **^{1}H NMR** (500.1 MHz, toluene-d_8, 300 K, ppm): δ = 29.3 (s, 12 H, $w_{\frac{1}{2}}$ = 29.4 Hz, CH(C**H**$_3$)$_2$), 21.4 (s, 4 H, $w_{\frac{1}{2}}$ = 26 Hz, *m*-Ph**H**), 9.26 (s, 2 H, $w_{\frac{1}{2}}$ = 22 Hz, *p*-Ph**H**), 5.8 (bs, 4 H, $w_{\frac{1}{2}}$ = 310 Hz, C**H**(CH$_3$)$_2$), 3.7 (s, 18 H, $w_{\frac{1}{2}}$ = 78 Hz, Si(C**H**$_3$)$_3$), −72.3 (s, 12 H, $w_{\frac{1}{2}}$ = 50 Hz, CH(C**H**$_3$)$_2$). (500.1 MHz, THF-d_8, 300 K, ppm): δ = 30 (bs, 4 H, $w_{\frac{1}{2}}$ = 800 Hz, C**H**(CH$_3$)$_2$), 17.7 (s, 12 H, $w_{\frac{1}{2}}$ = 55 Hz, CH(C**H**$_3$)$_2$), 16.5 (s, 4 H, $w_{\frac{1}{2}}$ = 43 Hz, *m*-Ph**H**), 13.9 (s, 18 H, $w_{\frac{1}{2}}$ = 210 Hz, Si(C**H**$_3$)$_3$), 4.27 (s, 2 H, $w_{\frac{1}{2}}$ = 34 Hz, *p*-Ph**H**), −86.5 (s, 12 H, $w_{\frac{1}{2}}$ = 150 Hz, CH(C**H**$_3$)$_2$). Elemental analysis $C_{30}H_{52}CoKN_2Si_2$ (594.96 g mol^{-1}): calcd: N 4.71, C 60.56, H 8.81; found: N 4.90, C 60.24, H 8.97%. **IR** (ATR, cm^{-1}): $\tilde{\nu}$ = 2953 (m), 2865 (w), 1567 (w), 1453 (m), 1415 (vs), 1367 (m), 1345 (w), 1289 (w), 1232 (s), 1134 (w), 1105 (w), 1044 (w), 978 (s), 940 (m), 829 (vs), 806 (vs), 779 (s), 755 (s), 740 (m), 726 (m), 649 (m), 609 (w), 428 (w). **EVANS** (500.1 MHz, 300 K, C_6D_6 + 1% TMS): μ_{eff} = 4.18μ_B; $\mu_{S.O.}$ = 2.83μ_B. (500.1 MHz, 300 K, THF-d_8 + 1% TMS): μ_{eff} = 3.93μ_B; $\mu_{S.O.}$ = 2.83μ_B.

[K{18c6}][Cr(N(Dipp)Si^{i}Pr$_3$)$_2$] (5). 50 mg (0.07 mmol, 1 equiv.) [Cr(N(Dipp)Si^{i}Pr$_3$)$_2$] were dissolved in 5 mL Et_2O. After adding KC_8 (0.08 mmol, 1.1 equiv.) it was stirred for several minutes at room temperature. The graphite was filtered off the red solution and the volatiles were reduced to a minimum. After layering with a solution of one equiv. 18-crown-6 in Et_2O and storing at −40 °C for several days, [K{18c6}][Cr(N(Dipp)Si^{i}Pr$_3$)$_2$] (**5**) was obtained as orange crystals in a yield of 43%. **Yield:** 31 mg (0.03 mmol, 43%). **^{1}H NMR** (500.1 MHz, THF-d_8, 300 K, ppm): δ = 23 (bs, $w_{\frac{1}{2}}$ = 2000 Hz), 16 (bs, $w_{\frac{1}{2}}$ = 1700 Hz), 3.6* (s, 24 H, 18c6), 0.4 (bs, $w_{\frac{1}{2}}$ = 2400 Hz). * Signal is overlapping with the solvent peak, why no further information can be provided. Elemental analysis $C_{54}H_{100}CrKN_2O_6Si_2$ (1020.67 g mol^{-1}): calcd: N 2.74, C 63.55, H 9.88; found: N 2.72, C 63.10, H 9.66%. **IR** (ATR, cm^{-1}): $\tilde{\nu}$ = 2953 (m), 2892 (m), 2849 (m), 1584 (w), 1469 (m), 1452 (w), 1413 (m), 1373 (w), 1350 (m), 1309 (w), 1283 (w), 1241 (s), 1196 (m), 1103 (vs), 1058 (w), 991 (m), 965 (m), 925 (m), 878 (m), 837 (m), 800 (w), 759 (s), 738 (m), 663 (m), 635 (s), 555 (m), 530 (w), 515 (w), 461 (w), 427 (m). **EVANS** (500.1 MHz, 300 K, THF-d_8 + 1% TMS): μ_{eff} = 4.21μ_B; $\mu_{S.O.}$ = 5.92μ_B.

[Li{12c4}$_2$][Fe(N(Dipp)SiMe$_3$)$_2$] (6). 100 mg (0.18 mmol, 1 equiv.) [Fe(N(Dipp)SiMe$_3$)$_2$] were dissolved in 5 mL THF. After adding a piece of lithium the reaction mixture was stirred for 2 hours at room temperature. Residual lithium was filtered off the dark red solution and the volatiles were reduced to a minimum. After layering with a solution of two equiv. 12-crown-4 in Et_2O and storing at −40 °C for several days, [Li{12c4}$_2$] [Fe(N(Dipp)SiMe$_3$)$_2$] (**6**) was obtained as green crystals in a yield of 57%. **Yield:** 94 mg (0.10 mmol, 57%). **^{1}H NMR** (300.2 MHz, THF-d_8, 300 K, ppm): δ = 29.5 (bs, $w_{\frac{1}{2}}$ = 320 Hz), 27.7 (bs, $w_{\frac{1}{2}}$ = 480 Hz), 13 (bs, $w_{\frac{1}{2}}$ = 200 Hz), 2.77 (s, 32 H, $w_{\frac{1}{2}}$ = 19.4 Hz, 12c4), 0.12 (s, 16 H, $w_{\frac{1}{2}}$ = 4.0 Hz), −1 (bs, 18 H, $w_{\frac{1}{2}}$ = 1800 Hz, Si(C**H**$_3$)$_3$), −100 (bs, $w_{\frac{1}{2}}$ = 1600 Hz, CH(C**H**$_3$)$_2$). Elemental analysis $C_{46}H_{84}FeLiN_2O_8Si_2$ (912.14 g mol^{-1}): calcd: N 3.07, C 60.57, H 9.28; found: N 3.38, C 60.19, H 9.09%. **IR** (ATR, cm^{-1}): $\tilde{\nu}$ = 3035 (vw), 2950 (m), 2913 (m), 2862 (m), 1580 (w), 1482 (w), 1443 (m), 1420 (m), 1364 (m), 1351 (w), 1313 (m), 1287 (m), 1251 (s), 1194 (m), 1134 (s), 1094 (vs), 1051 (w), 1023 (s), 921 (vs), 881 (w), 827 (vs), 778 (s), 742 (m), 666 (m), 625 (w), 554 (m), 429 (m). **EVANS** (500.1 MHz, 300 K, THF-d_8 + 1% TMS): μ_{eff} = 4.74μ_B; $\mu_{S.O.}$ = 3.87μ_B.

[Na{18c6}][Fe(N(Dipp)SiMe$_3$)$_2$] (7). 150 mg (0.27 mmol, 1 equiv.) [Fe(N(Dipp)SiMe$_3$)$_2$] were dissolved in 5 mL Et_2O. After adding Na/NaCl (5% w/w) (0.30 mmol (Na), 1.1 equiv.) the reaction mixture was stirred for several minutes at room temperature. The residuals were filtered off and the resulting dark red solution was reduced *in vacuo* to approx. 1 ml. After layering with a solution of one equiv. 18-crown-6 in Et_2O and storing at −40 °C for several days, [Na{18c6}][Fe(N(Dipp)SiMe$_3$)$_2$] (7) was obtained as red-brownish crystals in a yield of 79%. **Yield:** 180 mg (0.21 mmol, 79%). **^{1}H NMR** (300.2 MHz, THF-d_8, 300 K, ppm): δ = 29.5 (bs, $w_{\frac{1}{2}}$ = 390 Hz), 28.0 (s, $w_{\frac{1}{2}}$ = 380 Hz), 12.8 (bs, $w_{\frac{1}{2}}$ = 170 Hz), 3.45 (m, 4 H, Et_2O), 1.92 (s, 24 H, 18c6), 1.17 (m, 6 H, Et_2O), −0.5 (bs, $w_{\frac{1}{2}}$ = 540 Hz, Si(C**H**$_3$)$_3$) −102 (bs, $w_{\frac{1}{2}}$ = 540 Hz, CH(C**H**$_3$)$_2$). Elemental analysis $C_{42}H_{76}FeN_2NaO_6Si_2$ (840.08 g mol^{-1}): calcd: N 3.33, C 60.05, H 9.12; found: N 3.83, C 60.06, H 9.06%. **IR** (ATR, cm^{-1}): $\tilde{\nu}$ = 3052 (vw), 3035 (vw), 2950 (m), 2879 (m), 2862 (m), 1581 (w), 1456 (m), 1419 (s), 1375 (w), 1353 (m), 1317 (m), 1294 (w), 1233 (s), 1194 (m), 1094 (vs), 1053 (m), 1039 (w), 948 (m), 920 (s), 882 (w), 832 (vs), 781 (s), 742 (m), 666 (m), 619 (w), 576 (w), 542

(w), 530 (w), 431 (m). **EVANS** (500.1 MHz, 300 K, THF-d_8 + 1% TMS): μ_{eff} = 4.24μ_B; $\mu_{S.O.}$ = 3.87μ_B.

[NBu$_4$][Fe(N(Dipp)SiMe$_3$)$_2$] (8). 70 mg (0.12 mmol, 1 equiv.) [KFe(N(Dipp)SiMe$_3$)$_2$] and 39 mg NBu$_4$Br (0.12 mmol, 1 equiv.) were dissolved in 2 mL THF. After stirring over night at room temperature, the solvent was removed under reduced pressure. The green solid was resolved in Et$_2$O and layered with *n*-pentane, before cooling to −40 °C for crystallization. After several days, the solution was decanted off. The remaining green crystals were dried *in vacuo* and crystalline [NBu$_4$][Fe(N(Dipp)SiMe$_3$)$_2$] (**8**) was obtained in a yield of 57%. **Yield:** 54 mg (0.07 mmol, 57%). **^{1}H NMR** (300.2 MHz, THF-d_8, 300 K, ppm): δ = 28 (bs, $w_{\frac{1}{2}}$ = 550 Hz), 12.7 (s, $w_{\frac{1}{2}}$ = 180 Hz), 2.49 (s, 8 H, $w_{\frac{1}{2}}$ = 65 Hz, NBu$_4^+$), 1.0 (bs, 8 H, $w_{\frac{1}{2}}$ = 66 Hz, NBu$_4^+$), 0.57 (s, 8 H, $w_{\frac{1}{2}}$ = 81 Hz, NBu$_4^+$), 0.18 (m, 12 H, $w_{\frac{1}{2}}$ = 48 Hz, NBu$_4^+$), −36.1 (s, $w_{\frac{1}{2}}$ = 12.4 Hz), −56.1 (bs, $w_{\frac{1}{2}}$ = 12.4 Hz), −102 (bs, $w_{\frac{1}{2}}$ = 1100 Hz, CH(C**H**$_3$)$_2$). Elemental analysis $C_{46}H_{88}FeN_3Si_2$ (795.25 g mol^{-1}): calcd: N 5.28, C 69.48, H 11.15; found: N 5.43, C 69.04, H 10.76%. **IR** (ATR, cm^{-1}): $\tilde{\nu}$ = 2958 (s), 2863 (s), 1581 (w), 1482 (m), 1459 (m), 1419 (s), 1378 (w), 1356 (w), 1314 (m), 1239 (vs), 1195 (m), 1149 (w), 1102 (w), 1041 (w), 997 (w), 923 (s), 879 (m), 837 (s), 777 (s), 736 (m), 668 (s), 623 (m), 575 (w), 539 (w), 519 (w), 432 (s). **EVANS** (500.1 MHz, 300 K, THF-d_8 + 1% TMS): μ_{eff} = 4.30μ_B; $\mu_{S.O.}$ = 3.87μ_B.

[NBu$_4$][Co(N(Dipp)SiMe$_3$)$_2$] (9). 70 mg (0.12 mmol, 1 equiv.) [KCo(N(Dipp)SiMe$_3$)$_2$] and 39 mg NBu$_4$Br (0.12 mmol, 1 equiv.) were dissolved in 2 mL THF. After stirring over night at room temperature, the solvent was removed under reduced pressure. The green solid was resolved in Et$_2$O and layered with *n*-pentane, before cooling to −40 °C for crystallization. After several days, the solution was decanted off. The remaining green crystals were dried *in vacuo* and crystalline [NBu$_4$][Co(N(Dipp)SiMe$_3$)$_2$] (**9**) was obtained in a yield of 42%. **Yield:** 40 mg (0.05 mmol, 42%). **^{1}H NMR** (300.2 MHz, THF-d_8, 300 K, ppm): δ = 30 (bs, $w_{\frac{1}{2}}$ = 800 Hz, C**H**(CH$_3$)$_2$), 17.4 (s, 12 H, $w_{\frac{1}{2}}$ = 64 Hz, CH(C**H**$_3$)$_2$), 16.0 (s, $w_{\frac{1}{2}}$ = 38 Hz, *m*-Ph**H**), 14.0 (bs, 18 H, $w_{\frac{1}{2}}$ = 210 Hz, Si(C**H**$_3$)$_3$), 7.31 (s, $w_{\frac{1}{2}}$ = 9.48 Hz, *p*-Ph**H**), 3.01 (bs, 8 H, $w_{\frac{1}{2}}$ = 120 Hz, NBu$_4^+$), 0.53–1.50 (m, 28 H, NBu$_4^+$), −88.0 (bs, 12 H, $w_{\frac{1}{2}}$ = 110 Hz, CH(C**H**$_3$)$_2$). Elemental analysis $C_{46}H_{88}CoN_3Si_2$ (798.33 g mol^{-1}): calcd: N 5.26, C 69.21, H 11.11; found: N 5.65, C 68.77, H 10.63%. **IR** (ATR, cm^{-1}): $\tilde{\nu}$ = 2950 (m), 2863 (m), 1581 (w), 1477 (w), 1460 (w), 1420 (m), 1375 (w), 1318 (m), 1245 (s), 1229 (s), 1199 (m), 1142 (w), 1103 (w), 1042 (w), 1025 (w), 939 (s), 838 (vs), 778 (s), 664 (m), 616 (w), 543 (w), 436 (m). **EVANS** (500.1 MHz, 300 K, THF-d_8 + 1% TMS): μ_{eff} = 3.58μ_B; $\mu_{S.O.}$ = 2.83μ_B.

[K{18c6}][Fe(N(Dipp)SiMe$_3$)$_2$(η^2-PhCCPh)] (10). 50 mg (0.06 mmol, 1 equiv.) [K{18c6}][Fe(N(Dipp)SiMe$_3$)$_2$] and 10 mg diphenyl acetylene (0.06 mmol, 1 equiv.) were dissolved in 2 mL THF. After stirring for several minutes at room temperature, the solution was layered with *n*-pentane, before cooling to −40 °C for crystallization. After several days, the solution was decanted off. The remaining dark red crystals were dried *in vacuo* and crystalline [K{18c6}] [Fe(N(Dipp)SiMe$_3$)$_2$(η^2-PhCCPh)] (**10**) was obtained in a yield of 71%. **Yield:** 36 mg (0.04 mmol, 71%). **^{1}H NMR** (300.2 MHz, THF-d_8, 300 K, ppm): δ = 27.0 (bs, $w_{\frac{1}{2}}$ = 87 Hz), 4.67 (bs, $w_{\frac{1}{2}}$ = 530 Hz), 3.50 (s, 24 H, $w_{\frac{1}{2}}$ = 37 Hz, 18c6), 3.50 (bs, $w_{\frac{1}{2}}$ = 44 Hz), 0.8 (bs, $w_{\frac{1}{2}}$ = 99 Hz), −3.5 (bs, $w_{\frac{1}{2}}$ = 330 Hz), −8.83 (bs, $w_{\frac{1}{2}}$ = 42 Hz), −25.0 (bs, $w_{\frac{1}{2}}$ = 57 Hz). Elemental analysis $C_{42}H_{76}FeKN_2O_6Si_2$ (1034.43 g mol^{-1}): calcd: N 2.71, C 65.02, H 8.38; found: N 3.19, C 65.09, H 8.35%. **IR** (ATR, cm^{-1}): $\tilde{\nu}$ = 3054 (w), 3038 (w), 3002 (w), 2953 (m), 2911 (m), 2888 (m), 2862 (m), 1816 (w), 1587 (m), 1472 (w), 1461 (m), 1421 (s), 1376 (w), 1351 (m), 1312 (m), 1283 (w), 1235 (s), 1191 (m), 1154 (w), 1131 (w), 1104 (vs), 1054 (m), 1040 (m), 1024 (w), 997 (w), 962 (m), 928 (s), 912 (s), 879 (m), 831 (s), 777 (s), 766 (w), 760 (m), 738 (m), 695 (m), 666 (m), 640 (w), 618 (m), 591 (w), 572 (w), 554 (w), 530 (m), 507 (w), 490 (w), 438 (m). **EVANS** (500.1 MHz, 300 K, THF-d_8 + 1% TMS): μ_{eff} = 3.88μ_B; $\mu_{S.O.}$ = 3.87μ_B.

Reaction of [KMn(L^2)$_2$] (2) with diphenyl acetylene. 53 mg (0.10 mmol, 1.0 equiv.) [Mn(N(Dipp)SiMe$_3$)$_2$] and 21 mg KC$_8$ (0.15 mmol, 1.5 equiv.) were dissolved in 2 mL toluene in the presence or absence of small amounts of THF, respectively. After stirring for several minutes at room temperature, the dark violet solution was filtered in a solution of diphenyl acetylene (20 mg, 0.11 mmol, 1.1 equiv.) in the same solvent. It was layered with *n*-pentane and allowed to crystallize at room temperature. After several days, dark red crystals of both **12** and **13**, besides pale yellow crystals of hexaphenylbenzene, could be obtained, which were suitable for X-ray diffraction analysis.

Reaction of [KFe(L^2)$_2$] (3) with diphenyl acetylene. 59 mg (0.10 mmol, 1.0 equiv.) [KFe(N(Dipp)SiMe$_3$)$_2$] (**3**) and 18 mg diphenyl acetylene (0.10 mmol, 1.0 equiv.) were dissolved in 2 mL diethyl ether. It was stirred for several minutes at room temperature. The brownish solution was filtered and layered with *n*-pentane, before crystallizing at room temperature. After several days, single crystals of [K(D)Fe(η^6-HPB)(η^2-PhCCPh)] (**11**·D) (D = none, Et$_2$O) could be obtained, suitable for X-ray diffraction analysis.

[K{18c6}][Fe(N(Dipp)SiMe$_3$)$_2$].[3] 100 mg (0.18 mmol, 1 equiv.) [Fe(N(Dipp)SiMe$_3$)$_2$] were dissolved in 5 mL Et$_2$O. After adding KC$_8$ (0.20 mmol, 1.1 equiv.) the reaction mixture was stirred for several minutes at room temperature, while the colour changed to red. The graphite was filtered off and it was layered with a solution of 18-crown-6 (1.1 equiv.) in Et$_2$O. After storing at −40 °C for several days [K{18c6}][Fe(N(Dipp)SiMe$_3$)$_2$] was obtained as orange crystals in a yield of 64%. **Yield:** 99 mg (0.12 mmol, 64%). **^{1}H NMR** (500.1 MHz, THF-d_8, ppm): δ = 29.0 (bs, $w_{\frac{1}{2}}$ = 370 Hz), 27.5 (s, $w_{\frac{1}{2}}$ = 420 Hz), 12.4 (bs, $w_{\frac{1}{2}}$ = 157 Hz), 2.58 (bs, 24 H, $w_{\frac{1}{2}}$ = 40 Hz, 18c6), 1.14 (s, $w_{\frac{1}{2}}$ = 17.0 Hz), 0.11 (s, $w_{\frac{1}{2}}$ = 11.1 Hz), −0.7 (bs, $w_{\frac{1}{2}}$ = 1500 Hz, Si(C**H**$_3$)$_3$), −101 (bs, $w_{\frac{1}{2}}$ = 1400 Hz, CH(C**H**$_3$)$_2$). The spectroscopic data coincide with ^{1}H NMR measurements of [K{18c6}][Fe(N(Dipp)SiMe$_3$)$_2$] synthesized *via* literature procedure.[3]

[K{18c6}][Co(N(Dipp)SiMe$_3$)$_2$].[3] 100 mg (0.18 mmol, 1 equiv.) [Co(N(Dipp)SiMe$_3$)$_2$] were dissolved in 5 mL. After adding KC$_8$ (0.20 mmol, 1.1 equiv.) the reaction mixture was stirred for several minutes at room temperature, while the colour changed to green. The graphite was filtered off and it was layered with a solution of 18-crown-6 (1.1 equiv.) in Et$_2$O. After

storing at −40 °C for several days [K{18c6}][Co(N(Dipp)SiMe$_3$)$_2$] was obtained as light green crystals in a yield of 56%. **Yield:** 87 mg (0.10 mmol, 56%). **^{1}H NMR** (500.1 MHz, THF-d_8, 300 K, ppm): δ = 29 (bs, 4 H, $w_{\frac{1}{2}}$ = 900 Hz, C**H**(CH$_3$)$_2$), 17.3 (s, 12 H, $w_{\frac{1}{2}}$ = 48 Hz, CH(C**H**$_3$)$_2$), 16.3 (s, 4 H, $w_{\frac{1}{2}}$ = 36 Hz, *m*-Ph**H**), 13.3 (s, 18 H, $w_{\frac{1}{2}}$ = 210 Hz, Si(C**H**$_3$)$_3$), 4.04 (s, 2 H, $w_{\frac{1}{2}}$ = 23 Hz, *p*-Ph**H**), 2.85 (s, 24 H, $w_{\frac{1}{2}}$ = 26 Hz, 18c6), −86.5 (s, 12 H, $w_{\frac{1}{2}}$ = 140 Hz, CH(C**H**$_3$)$_2$). The spectroscopic data coincide with ^{1}H NMR measurements of [K{18c6}][Co(N(Dipp)SiMe$_3$)$_2$] synthesized *via* literature procedure.[3]

X-Ray diffraction analysis

Data for compounds **1** (CCDC 2010661), **1**·3THF (CCDC 2011333), **2** (CCDC 2011213), **3** (CCDC 2010659), **4** (CCDC 2010663), **5** (CCDC 2011200), **6** (CCDC 2011410), **10** (CCDC 2047637), **11** (CCDC 2047640), **11**·Et$_2$O (CCDC 2047641) and **13** (CCDC 2047638)† were collected at 100 K on a Bruker Quest D8 diffractometer (Bruker Corporation, Billerica, USA) using an Incoatec Microfocus Source Mo-Kα radiation and equipped with an Oxford Instrument Cooler Device (Oxford Instruments, Abingdon, UK) and Photon 100 detector. Data for compounds **3**·2DMAP (CCDC 2010662), **7** (CCDC 2011409) and **12** (CCDC 2047639)† were collected at 100 K on a STOE IPDS2 diffractometer (STOE & Cie GmbH, Darmstadt, Germany) and data for compound **8** (CCDC 2010664), **9** (CCDC 2010665) and [K{18c6}][Fe(N(Dipp)SiMe$_3$)$_2$]·Et$_2$O (CCDC 2010666)† were collected at 100 K on a STOE IPDS2T diffractometer using a graphite-monochromated Mo-Kα radiation (λ = 0.71073 Å) and equipped with an Oxford Instrument Cooler Device (Oxford Instruments, Abingdon, UK). Data for compound **3**·Et$_2$O (CCDC 2010651†) were collected at 100 K on a Bruker Kappa Apex2 using an Area graphite source Mo-Kα radiation equipped with an Oxford Instrument Cooler Device (Oxford Cryosystems open-flow nitrogen cryostat, Cosier & Glazer, 1986). The structures have been solved using either OLEX SHELXT V2014/1 [32] and refined by means of least-squares procedures on an F^2 (all complexes but **3**·Et$_2$O which was refined on F) with the aid of the program SHELXL-2016/6 [33] included in the software package WinGX version 1.63 [34] or using CRYSTALS.[35] The atomic scattering factors were taken from International Tables for X-ray crystallography.[36] All non-hydrogen atoms were refined anisotropically. All hydrogen atoms were refined by using a riding model. Disorders were found for **1**·3THF (a coordinating THF molecule and two iso-propyl groups), **5** (a coordinating THF molecule) and **7** (18-crown-6 unit) and were modelled accordingly. The structure of **9** was refined as an inversion twin. For **3**·Et$_2$O some data sets are probably incomplete due to strategy errors, however the structure is very good (R < 3%, 20 refl/parameter, no restrains, no disorder, low maximum/minimum residual density). Absorption corrections were introduced by using the MULTISCAN and X-Red programs.[37] Drawings of molecules are performed with the program DIAMOND (Crystal Impact, Bonn, Germany) with 50% probability displacement ellipsoids for non-H atoms. Additional details are given in the ESI.†

Author contributions

The manuscript was written through contributions of all authors. All authors have given approval to the final version of the manuscript.

Conflicts of interest

There are no conflicts to declare.

Acknowledgements

We thank the DFG (grant WE 5627/1-1 and WE 5627/4-1 for C. G. W.), the Philipps-University Marburg, the CNRS and the ANR (programme blanc "IRONHYC" ANR-12 for C. G. W., S. S.-E. and S. B.) for funding.

Notes and references

1 (*a*) P. P. Power, *Chem. Rev.*, 2012, **112**, 3482–3507; (*b*) G. Ung, J. Rittle, M. Soleilhavoup, G. Bertrand and J. C. Peters, *Angew. Chem., Int. Ed.*, 2014, **53**, 8427–8431; (*c*) S. Roy, K. C. Mondal and H. W. Roesky, *Acc. Chem. Res.*, 2016, **49**, 357–369; (*d*) Z. Mo, Z. Ouyang, L. Wang, K. L. Fillman, M. L. Neidig and L. Deng, *Org. Chem. Front.*, 2014, **1**, 1040–1044; (*e*) P. P. Samuel, K. C. Mondal, N. Amin Sk, H. W. Roesky, E. Carl, R. Neufeld, D. Stalke, S. Demeshko, F. Meyer, L. Ungur, L. F. Chibotaru, J. Christian, V. Ramachandran, J. van Tol and N. S. Dalal, *J. Am. Chem. Soc.*, 2014, **136**, 11964–11971; (*f*) P. P. Samuel, R. Neufeld, K. Chandra Mondal, H. W. Roesky, R. Herbst-Irmer, D. Stalke, S. Demeshko, F. Meyer, V. C. Rojisha, S. De, P. Parameswaran, A. C. Stückl, W. Kaim, J. H. Christian, J. K. Bindra and N. S. Dalal, *Chem. Sci.*, 2015, **6**, 3148–3153; (*g*) C.-Y. Lin, J. C. Fettinger, N. F. Chilton, A. Formanuik, F. Grandjean, G. J. Long and P. P. Power, *Chem. Commun.*, 2015, **51**, 13275–13278; (*h*) C. A. Laskowski and G. L. Hillhouse, *J. Am. Chem. Soc.*, 2008, **130**, 13846–13847; (*i*) M. I. Lipschutz and T. D. Tilley, *Angew. Chem.*, 2014, **126**, 7418–7422; (*j*) Y.-S. Meng, Z. Mo, B.-W. Wang, Y.-Q. Zhang, L. Deng and S. Gao, *Chem. Sci.*, 2015, **12**, 7156–7162.

2 C. G. Werncke, P. C. Bunting, C. Duhayon, J. R. Long, S. Bontemps and S. Sabo-Etienne, *Angew. Chem., Int. Ed.*, 2015, **54**, 245–248.

3 C.-Y. Lin, J. C. Fettinger, F. Grandjean, G. J. Long and P. P. Power, *Inorg. Chem.*, 2014, **53**, 9400–9406.

4 J. M. Zadrozny, D. J. Xiao, M. Atanasov, G. J. Long, F. Grandjean, F. Neese and J. R. Long, *Nat. Chem.*, 2013, **5**, 577–581.

5 M. I. Lipschutz, X. Yang, R. Chatterjee and T. D. Tilley, *J. Am. Chem. Soc.*, 2013, **135**, 15298–15301.

6 I. C. Cai, M. I. Lipschutz and T. D. Tilley, *Chem. Commun.*, 2014, **50**, 13062–13065.

7 P. P. Samuel, K. C. Mondal, H. W. Roesky, M. Hermann, G. Frenking, S. Demeshko, F. Meyer, A. C. Stückl, J. H. Christian, N. S. Dalal, L. Ungur, L. F. Chibotaru, K. Pröpper, A. Meents and B. Dittrich, *Angew. Chem.*, 2013, **125**, 12033–12037.
8 C. G. Werncke, E. Suturina, P. C. Bunting, L. Vendier, J. R. Long, M. Atanasov, F. Neese, S. Sabo-Etienne and S. Bontemps, *Chem. – Eur. J.*, 2016, **22**, 1668–1674.
9 C. A. Laskowski, D. J. Bungum, S. M. Baldwin, S. A. Del Ciello, V. M. Iluc and G. L. Hillhouse, *J. Am. Chem. Soc.*, 2013, **135**, 18272–18275.
10 M. I. Lipschutz, T. Chantarojsiri, Y. Dong and T. D. Tilley, *J. Am. Chem. Soc.*, 2015, **137**, 6366–6372.
11 C. L. Wagner, L. Tao, E. J. Thompson, T. A. Stich, J. Guo, J. C. Fettinger, L. A. Berben, R. D. Britt, S. Nagase and P. P. Power, *Angew. Chem., Int. Ed.*, 2016, **55**, 10444–10447.
12 C.-Y. Lin, J.-D. Guo, J. C. Fettinger, S. Nagase, F. Grandjean, G. J. Long, N. F. Chilton and P. P. Power, *Inorg. Chem.*, 2013, **52**, 13584–13593.
13 W. M. Reiff, A. M. LaPointe and E. H. Witten, *J. Am. Chem. Soc.*, 2004, **126**, 10206–10207.
14 M. Atanasov, J. M. Zadrozny, J. R. Long and F. Neese, *Chem. Sci.*, 2013, **4**, 139–156.
15 (*a*) W. M. Reiff, C. E. Schulz, M.-H. Whangbo, J. I. Seo, Y. S. Lee, G. R. Potratz, C. W. Spicer and G. S. Girolami, *J. Am. Chem. Soc.*, 2009, **131**, 404–405; (*b*) M. Atanasov, D. Aravena, E. Suturina, E. Bill, D. Maganas and F. Neese, *Coord. Chem. Rev.*, 2015, **289–290**, 177–214.
16 (*a*) C. G. Werncke, J. Pfeiffer, I. Müller, L. Vendier, S. Sabo-Etienne and S. Bontemps, *Dalton Trans.*, 2019, **48**, 1757–1765; (*b*) I. Müller, C. Schneider, C. Pietzonka, F. Kraus and C. G. Werncke, *Inorganics*, 2019, **7**, 117; (*c*) C. G. Werncke and I. Müller, *Chem. Commun.*, 2020, **56**, 2268–2271.
17 (*a*) L. C. H. Maddock, T. Nixon, A. R. Kennedy, M. R. Probert, W. Clegg and E. Hevia, *Angew. Chem., Int. Ed.*, 2018, **57**, 187–191; (*b*) E. Nagaradja, F. Chevallier, T. Roisnel, V. Jouikov and F. Mongin, *Tetrahedron*, 2012, **68**, 3063–3073; (*c*) V. L. Blair, W. Clegg, R. E. Mulvey and L. Russo, *Inorg. Chem.*, 2009, **48**, 8863–8870; (*d*) V. L. Blair, W. Clegg, B. Conway, E. Hevia, A. Kennedy, J. Klett, R. E. Mulvey and L. Russo, *Chem. – Eur. J.*, 2008, **14**, 65–72.
18 M. I. Lipschutz and T. D. Tilley, *Chem. Commun.*, 2012, **48**, 7146–7148.
19 (*a*) *NMR of paramagnetic molecules. Applications to metallobiomolecules and models*, ed. I. Bertini, C. Luchinat, G. Parigi and E. Ravera, Elsevier, Amsterdam, Netherlands, 2017; (*b*) I. Bertini, C. Luchinat, G. Parigi and R. Pierattelli, *ChemBioChem*, 2005, **6**, 1536–1549; (*c*) I. Bertini, C. Luchinat and G. Parigi, *Prog. Nucl. Magn. Reson. Spectrosc.*, 2002, **40**, 249–273; (*d*) C. L. I. Bertini, *Coord. Chem. Rev.*, 1996, **150**, 1–28; (*e*) G. N. La Mar, W. D. Horrocks and R. H. Holm, *NMR of Paramagnetic Molecules. Principles and Applications*, Elsevier Science, Burlington, 1973.
20 C.-Y. Lin, J. C. Fettinger and P. P. Power, *Inorg. Chem.*, 2017, **56**, 9892–9902.
21 J. Hicks, M. Juckel, A. Paparo, D. Dange and C. Jones, *Organometallics*, 2018, **37**, 4810–4813.
22 C. L. Wagner, L. Tao, J. C. Fettinger, R. D. Britt and P. P. Power, *Inorg. Chem.*, 2019, **58**, 8793–8799.
23 W. Alexander Merrill, T. A. Stich, M. Brynda, G. J. Yeagle, J. C. Fettinger, R. D. Hont, W. M. Reiff, C. E. Schulz, R. D. Britt and P. P. Power, *J. Am. Chem. Soc.*, 2009, **131**, 12693–12702.
24 I. Müller, D. Munz and C. G. Werncke, *Inorg. Chem.*, 2020, **59**, 9521–9537.
25 R. Wolf, N. Ghavtadze, K. Weber, E.-M. Schnöckelborg, B. de Bruin, A. W. Ehlers and K. Lammertsma, *Dalton Trans.*, 2010, **39**, 1453–1456.
26 R. A. Lewis, S. Morochnik, A. Chapovetsky, G. Wu and T. W. Hayton, *Angew. Chem., Int. Ed.*, 2012, **51**, 12772–12775.
27 R. J. Witzke, D. Hait, K. Chakarawet, M. Head-Gordon and T. D. Tilley, *ACS Catal.*, 2020, **10**, 7800–7807.
28 W.-Y. Yeh, S.-M. Peng and G.-H. Lee, *Organometallics*, 2002, **21**, 3058–3061.
29 F. Calderazzo, G. Pampaloni, P. Pallavicini, J. Straehle and K. Wurst, *Organometallics*, 1991, **10**, 896–901.
30 K. Mach and S. I. Troyanov, *J. Organomet. Chem.*, 1991, **414**, C15–C18.
31 N. E. Schore, *Chem. Rev.*, 1988, **88**, 1081–1119.
32 O. V. Dolomanov, L. J. Bourhis, R. J. Gildea, J. Howard and H. Puschmann, *J. Appl. Crystallogr.*, 2009, **42**, 339–341.
33 G. M. Sheldrick, *Acta Crystallogr., Sect. C: Struct. Chem.*, 2015, **71**, 3–8.
34 L. J. Farrugia, *J. Appl. Crystallogr.*, 1999, **32**, 837–838.
35 P. W. Betteridge, J. R. Carruthers, R. I. Cooper, K. Prout and D. J. Watkin, *J. Appl. Crystallogr.*, 2003, **36**, 1487.
36 International Union of Crystallography, *International tables for crystallography*, Springer, Chester, England, New York, 1st edn, 2006.
37 (*a*) *SADABS-2016/2*, Bruker, 2016; (*b*) *X.-R. 1. X-Area*, STOE, 2016.

5.3 „On the Synthesis and Reduction of Trigonal Halido Bis(silylamido) Metalates of Chromium to Cobalt“

Ruth Weller, Lena Völlinger, C. Gunnar Werncke

Eur. J. Inorg. Chem. **2021**, 4383−4392.
DOI: 10.1002/ejic.202100716
https://doi.org/10.1002/ejic.202100716

Abstract

A series of halido bis(silylamido) metalates of chromium to cobalt is reported. Reaction of [NBu_4]Br with linear metal silylamides [ML_2] (M = Mn − Co, L = −$N(SiMe_3)_2$, −N(Dipp)$SiMe_3$; Dipp = 2,6-^{i}Pr-C_6H_3) leads to NBu_4[M(Br)L_2] whereas for chromium either intramolecular deprotonation (L = −$N(SiMe_3)_2$) or ligand exchange (L = −N(Dipp)$SiMe_3$) is observed. Attempts for their reduction with KC_8 showed in part the formation of linear metal(I) silylamide complexes but also degradation. In contrast, analogous compounds bearing a K{18c6}$^+$ counter ion of cobalt and iron, obtained from reaction of anionic linear metal(I) complexes [$M(N(SiMe_3)_2)_2]^-$ with allyl bromide − can be cleanly reduced. The adduct formation studies are also extended to benzyl potassium yielding [KM(Bn)L_2] (M = Mn, Co) and subsequently the salt separated K{18c6}[M(Bn)L_2] using 18-crown-6 as sequestrating agent.

Zusammenfassung

In der Literatur sind erst wenige Beispiele niedervalenter Metall-Addukte mit einer M−X-Bindung (X = Halogen, Alkyl/Aryl) bekannt (vgl. Kapitel 2.4.3). Um das Potenzial dieser Substanzklasse im Fall von 3d-Metall(II)-Silylamiden besser einschätzen zu können, wird in dieser Publikation über die Umsetzung bekannter Metall(II)-Präkursoren [ML^n_2] (L^1 = −$N(SiMe_3)_2$ (M = Cr − Co), L^2 = −N(Dipp)$SiMe_3$ (M = Mn − Co), L_3 = −N(Dipp)Si^iPr_3 (M = Cr)) mit [NBu_4]Br berichtet. Während für Chrom ein Ligandaustausch (L^3) bzw. eine intramolekulare Deprotonierung (L^1) beobachtet wird, wurden für Mangan, Eisen und Kobalt trigonale Halogenido-Spezies des Typs NBu_4[M(Br)L^n_2] (M = Mn − Co, n = 1, 2) mit einer M−Br-Bindung erhalten. Sowohl die räumliche Anordnung im Einkristall als auch ^{1}H-NMR spektroskopische Untersuchungen für Kobalt deuten auf Ionenpaarung hin. Unter Abspaltung des

Bromido-Liganden können diese trigonalen Komplexe mit KC_8 zu linearen Metall(I)-Silylamiden reduziert werden. Aufgrund simultan stattfindender Zersetzungsreaktionen ist die Isolierung allerdings nur in einzelnen Fällen und in schlechten Ausbeuten möglich. Frei von Nebenprodukten war die Reduktion analoger Verbindungen mit dem klassischen Gegenion $K\{18c6\}^+$ für Eisen und Kobalt.

Statt einer trigonalen Metall(II)-Hydrid-Spezies konnte aus der Umsetzung von $NBu_4[Co(Br)L^2{}_2]$ mit $KHBEt_3$ (Kaliumtriethylborhydrid) $NBu_4[CoL^2{}_2]$ ebenfalls in guten Ausbeuten generiert werden.

Die Addition des organischen Salzes $[PPh_4]Br$ wurde ebenfalls am Beispiel von Eisen getestet. Die Isolierung von $PPh_4[Fe(Br)L^2{}_2]$ war zwar in guten Ausbeuten möglich, jedoch verhinderten Redoxprozesse die weitere Reduktion. So lässt sich die Wiedergewinnung des Edukts bzw. die Generierung des zweifach-koordinierten Metall(II)-Vorläufers $[FeL^2{}_2]$ beobachten.

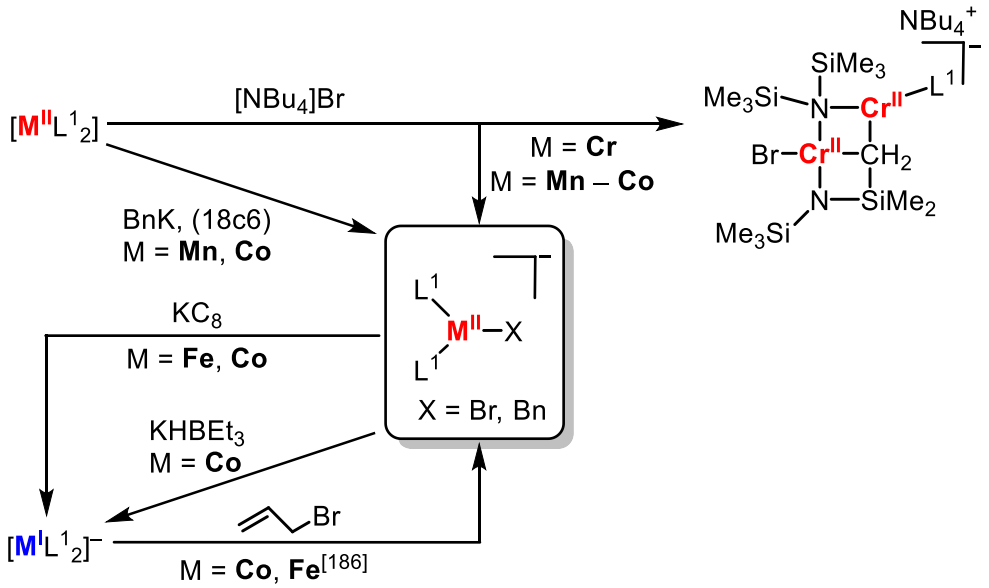

Schema 27. Zusammenhang verschiedener Additions- und Reduktionsmöglichkeiten niedervalenter Metall-Silylamide am Beispiel von $[ML^1{}_2]$ (M = Cr – Co).[186]

Analog zu $[NBu_4]Br$ konnte auch das unlösliche Benzylkalium (BnK) zu den linearen Metall(II)-Vorläufern addiert werden. Produkte sind formal neutrale und trigonale Metall(II)-Benzyl-Komplexe der Form $[KM(Bn)L^1{}_2]$ (M = Mn, Co). Durch Ausbildung polymerer Ketten wird das Kation zwischen dem aromatischen System des Benzylsubstituenten und zwei Silylamidfragmenten stabilisiert. Durch Zugabe des Maskierungsreagenz 18-Krone-6 wird das Kaliumion unter Ladungsseparierung vom Anion getrennt.

Beiträge der Autoren

Die Planung und Durchführung des Projektes sowie die Synthese und Charakterisierung aller Verbindungen lag in meiner Hand. Die Komplexe $NBu_4[M(Br)L^2_2]$ (M = Mn − Co) und $NBu_4[Cr(Br)_2L^3]$ wurden zuvor von Lena Völlinger im Rahmen ihrer Bachelorarbeit unter meiner Leitung dargestellt und teilweise analysiert. Alle von ihr erhaltenen Ergebnisse wurden jedoch von mir reproduziert, ergänzt und für diese Publikation aufbereitet. Zusätzlich war ich für die Aufnahme aller an den Diffraktometern IPDS2 bzw. IPDS2T der Firma STOE gemessenen Daten zuständig. Messungen am Quest D8 Diffraktometer der Firma BRUKER wurden von Dr. C. Gunnar Werncke und der zentralen Serviceabteilung für Kristallstrukturanalyse am Fachbereich Chemie der Philipps-Universität Marburg unter der Leitung von Dr. Klaus Harms und Dr. Sergei Ivlev ausgeführt. Alle Datensätze, die mittels Einkristallstrukturanalyse erhalten wurden, wurden von mir gelöst und verfeinert. Bei der Verfeinerung der Verbindungen $NBu_4[Fe(Br)L^1_2]$ und $NBu_4[Co(Br)L^1_2]$ erhielt ich Hilfestellung von Dr. Sergei Ivlev. Mit der Unterstützung der hausinternen NMR-Abteilung des Fachbereichs Chemie der Philipps-Universität Marburg unter der Leitung von Dr. Xiulan Xie nahm ich alle ^{1}H-NMR spektroskopischen Untersuchungen sowie Evans-Messungen auf und wertete diese selbständig aus. Elementaranalytische Untersuchungen wurden von Lena Völlinger und mir vorbereitet und durch mich ausgewertet. Die Messungen selbst führte die hausinterne Abteilung für Massenspektrometrie und Elementanalytik des Fachbereichs Chemie der Philipps-Universität Marburg unter der Leitung von Dr. Uwe Linne durch. IR-Messungen wurden von Lena Völlinger und mir durchgeführt und von mir ausgewertet. Das Manuskript wurde von mir in Zusammenarbeit mit Dr. C. Gunnar Werncke verfasst.

EurJIC
European Journal of Inorganic Chemistry

Full Papers
doi.org/10.1002/ejic.202100716

Chemistry Europe
European Chemical Societies Publishing

On the Synthesis and Reduction of Trigonal Halido Bis(silylamido) Metalates of Chromium to Cobalt

Ruth Weller,[a] Lena Völlinger,[a] and C. Gunnar Werncke*[a]

A series of halido bis(silylamido) metalates of chromium to cobalt is reported. Reaction of $[NBu_4]Br$ with linear metal silylamides ML_2 (M=Mn–Co, L=–$N(SiMe_3)_2$, –N(Dipp)$SiMe_3$; Dipp = 2,6-^{i}Pr–C_6H_3) leads to $NBu_4[M(Br)L_2]$ whereas for chromium either intramolecular deprotonation (L=–$N(SiMe_3)_2$) or ligand exchange (L=–N(Dipp)$SiMe_3$) is observed. Attempts for their reduction with KC_8 showed in part the formation of linear metal(I) silylamide complexes but also degradation. In contrast, analogous compounds bearing a $[K\{18c6\}]^+$ counter ion of cobalt and iron, obtained from reaction of anionic linear metal (I) complexes $[M\{N(SiMe_3)_2\}_2]^-$ with allyl bromide – can be cleanly reduced. The adduct formation studies are also extended to benzyl potassium yielding $[KM(Bn)L_2]$ (M=Mn, Co) and subsequently the salt separated $[K\{18c6\}][M(Bn)L_2]$ using 18-crown-6 as sequestrating agent.

Introduction

Divalent 3d-metal(II)hexamethyldisilazanides are widely used in coordination chemistry and comprise the metals of chromium to nickel (and zinc).[1,2–5] They are mostly employed as a halide-free source for molecular ligand exchange reactions (>400 references) and precursors in material as well as surface science.[6] In recent years the coordination chemistry of $[M\{N(SiMe_3)_2\}_2]$ complexes themselves is also increasingly explored. Due to the low-coordinate state of the metal, these compounds are Lewis acidic and tend to stabilize themselves by dimerisation[2,7–9] or adduct formation (e.g. phosphines, carbenes, N- or O-donor ligands).[5,7–16] This can give rise to remarkable chemical and magnetic properties owing to a low-coordinate environment and the highly basic amide ligands.[11–14,16,17] Similarly, salt-like compounds, such as $KN(SiMe_3)_2$ or KCH_2Ph, form interesting at-complexes (e.g. $[KM(CH_2Ph)\{N(SiMe_3)_2\}_2]$ or $[KFe\{N(SiMe_3)_2\}_3]$), which evoke distinct reactivities.[18,19] In addition to hexamethyldisilazanides, metal(II) complexes with bulkier silyamide ligands (e.g. –$N(SiMe_2Ph)$ or –N(Dipp)SiR_3) (Dipp = 2,6-di-*iso*-propylphenyl) also found their use with a persistent quasilinear geometry.[20–25] In recent reports it was also shown that such divalent 3d-metal silylamides can be reduced giving linear, monovalent complex anions.[22,25–29] These were employed in bond activation and substrate reduction.[19,24,27,29–34] Here, the unique role of the low-coordinate environment of the low-valent metal as well as the weak field of silylamide ligands became evident, causing unusual higher-spin imido cobalt complexes or metal bound alkyne radical anions.[31,33,34] In most of these studies the R_2N–M–NR_2 fragment is bent with angles between 120–130° to accommodate the additional substrate/ligand. Especially in case of monovalent complexes their chemistry thus resembles that of complexes bearing chelating monoanionic N-donor ligands such as β-diketiminates ("nacnac"),[35] amidinates,[36] guanidates,[37] dipyrrinates[38] or monoanionic diazabutadienes.[39] Contrasting to these ligand sets, studies on non-chelating halido metal silyl amides of the type $[M(X)L_2]^-$ (X = halide, L = e.g. –$N(SiMe_3)_2$, –N(Dipp)$SiMe_3$) and their use as potential starting points for further synthesis, like introduction of anionic ligands (e.g. hydrides or organic functionalities) or alternative entry to linear metal(I) complexes, are mostly absent. In a singular report from our group, we could recently obtain phenyl and *n*-butyl iron(II) complexes by mentioned ligand exchange using the respective organolithium reagent. In this case, the required iron bromide complex was obtained *via* oxidation of the quasilinear iron(I) silylamide $[M\{N(SiMe_3)_2\}_2]^-$ with benzyl bromide. A few other trigonal halido bis(silylamido) metalates were obtained by us in an analogous fashion using perfluoropyridine (Mn–Co)[19,32] or I_2[27] as oxidants, all starting from the respective linear metal(I) silylamide. Apart from this approach, the direct introduction of organic functional groups was also shown by us *via* reaction of $[Fe\{N(SiMe_3)_2\}_2]$ with benzyl potassium (BnK).[19]

In our quest to elaborate and understand the behaviour and broader coordination chemistry of 3d-silylamides, we herein describe on the synthesis of trigonal metal(II) complexes of the type $[NBu_4][M(Br)\{N(SiMe_3)_2\}_2]$ (M=Mn–Co) and the sterically more encumbered $[NBu_4][M(Br)\{N(Dipp)SiMe_3\}_2]$ (M=Mn–Co). For chromium, two-fold ligand displacement or self-deprotonation is observed. Reduction of the $[NBu_4][M(Br)L_2]$ complexes is possible, but limited by partial decomposition of the $[NBu_4]^+$ cation. Further, the addition reaction can be

[a] R. Weller, L. Völlinger, Dr. C. G. Werncke
Fachbereich Chemie
Philipps-Universität Marburg
Hans-Meerwein-Straße 4, 35032 Marburg, Germany
E-mail: gunnar.werncke@chemie.uni-marburg.de
https://www.uni-marburg.de/de/fb15/arbeitsgruppen/ag-werncke/

Supporting information for this article is available on the WWW under https://doi.org/10.1002/ejic.202100716

Full Papers
doi.org/10.1002/ejic.202100716

extended to benzyl potassium yielding cobalt and manganese benzyl complexes.

Results and Discussion

Starting off with hexamethyldisilazanide complexes, [ML$^1_2$] (M=Fe–Co) or CrL$^1_2$*2thf (L^1=–N(SiMe$_3$)$_2$) with one equivalent of [NBu$_4$]Br in diethyl ether and stirring for an adjusted period of time (from 10 min (Mn, Fe) up to one night (Cr)), leads to a color change to dark blue (Cr), beige (Mn, Fe) or light green (Co), respectively. After removal of unreacted [NBu$_4$]Br *via* filtration, the colored solutions were concentrated to a minimum under reduced pressure, layered with *n*-pentane and stored at −40 °C for crystallization. X-ray diffraction analysis confirmed the successful synthesis of [NBu$_4$][M(Br)L$^1_2$] (M=Mn–Co) (Scheme 1).

In solid state of all compounds (Mn–Co), the complex anion consists of a metal atom surrounded by two silylamide and one bromide ligands, with almost perfect trigonal planar geometry (Figure 1, top right). The M–N bonds exhibit lengths of 2.026(5) Å (Mn) and 1.924(2) Å (Co) as expected from the general trend of contraction of the ion radii (Table 1). The M–Br distances also shorten within the row from manganese to cobalt from 2.5357(12) Å to 2.4177(7) Å. For iron, the structure suffers from severe intrinsic flaws, why the disclosure of detailed bond length and angles is prohibited. Nonetheless, the structural metrics are similar to the only other known trigonal anionic halido metal(II) silylamides [K{18c6}][Fe(Br)L$^1_2$][19] or [Li(THF)$_3$Co(Cl)L$^1_2$],[40] with no discernible impact of the additional alkali metal coordination.

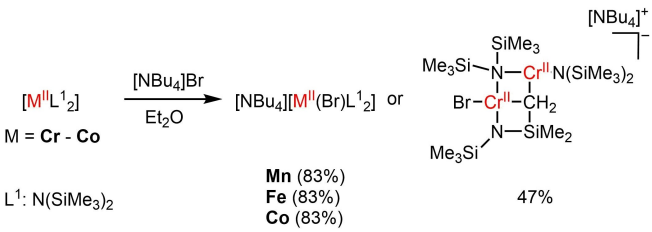

Scheme 1. Reaction of [ML$^1_2$] (M=Cr–Co) with [NBu$_4$]Br.

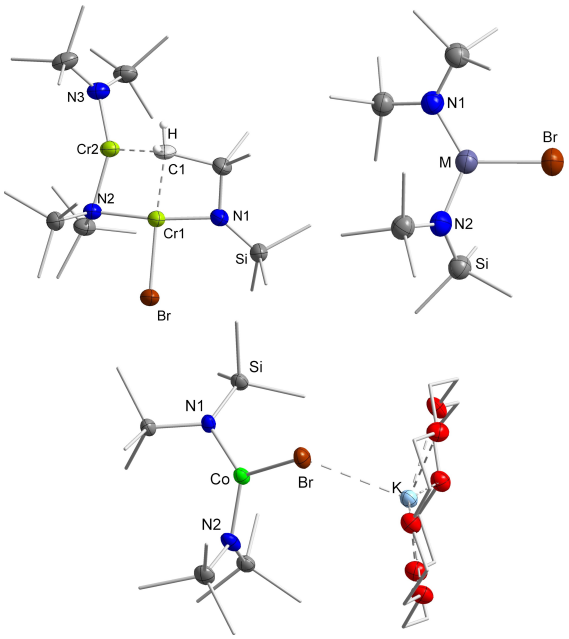

Figure 1. Sections of the crystal structures of [NBu$_4$][Cr$_2$(Br)L$^1_2$L^1*] (top left), [NBu$_4$][M(Br)L$^1_2$] (M=Mn–Co, top right) and of [K{18c6}][Co(Br)L$^1_2$] (bottom). All hydrogen atoms and [NBu$_4$]$^+$ cations are omitted for clarity.

For chromium, the binuclear complex [NBu$_4$][Cr$_2$(Br)L$^1_2$L^1*] (L^1*=η^2-N(SiMe$_3$){SiMe$_2$(CH$_2$)-κ^1N,κ^2C} is formed, bearing a hexamethyldisilazanide ligand (L^1*) with a deprotonated methyl group, which thus acts as a bidentate dianionic ligand (Figure 1, top left). The Cr1 atom is coordinated in a slightly distorted square planar fashion, which can be evidenced by the bond angles N1–Cr1–C1 and N1–Cr1–Br with values between 80.53(13)° and 95.72(8)°, respectively. With a length of 2.5355(7) Å, the Cr1–Br distance fits in the trend for M–Br lengths compared to those of [NBu$_4$][M(Br)L$^1_2$] (M=Mn–Co) as described above. The CH$_2^-$ fragment is stabilized by coordination to both chromium atoms (Cr1–C1: 2.254(4) Å, Cr2–C1: 2.149(4) Å). Furthermore, both N–Cr–N bond axes are with 166.03(12)° (N1–Cr1–N2) and 148.67(13)° (N2–Cr2–N3) slightly bent. Cr2 is coordinated by two silylamides and the bridging methyl ligand in a geometry between T- and Y-shaped (N2–Cr2–C1: 99.94(14)°, N3–Cr2–C1: 111.38(16)°). This trigonal

Table 1. Selected bond lengths and angles of compounds [NBu$_4$][M(Br)L$^1_2$] (M=Mn, Co), [NBu$_4$][Cr$_2$(Br)L$^1_2$L^1*], [K{18c6}][Co(Br)L$^1_2$], [NBu$_4$][M(Br)L$^2_2$] (M=Mn–Co), [NBu$_4$][Cr(Br)$_2$L^3] and [PPh$_4$][Fe(Br)L$^2_2$].

Compound	M–N1 [Å]	M–N2 [Å]	M–Br [Å]	N1–M–N2 [°]
[NBu$_4$][Cr$_2$(Br)L$^1_2$L^1*]	Cr1: 2.024(3) (N1) Cr2: 2.083(3) (N2)	Cr1: 2.140(3) (N2) Cr2: 1.992(3) (N3)	2.5355(7)	166.03(12) (Cr1) 148.67(13) (Cr2)
[NBu$_4$][Mn(Br)L$^1_2$]	2.029(5)	2.026(5)	2.5357(12)	128.0(2)
[NBu$_4$][Co(Br)L$^1_2$]	1.924(2)	1.9240(19)	2.4177(7)	129.15(13)
[K{18c6}][Co(Br)L$^1_2$]	1.929(7)	1.935(7)	2.4413(15)	125.7(3)
[NBu$_4$][Cr(Br)$_2$L^3]	1.978(2)	/	Br1: 2.4893(6) Br2: 2.4436(5)	/
[NBu$_4$][Mn(Br)L$^2_2$]	2.013(3)	2.018(3)	2.5253(7)	139.74(12)
[NBu$_4$][Fe(Br)L$^2_2$]	1.950(2)	1.931(2)	2.4369(4)	138.52(9)
[NBu$_4$][Co(Br)L$^2_2$]	1.917(2)	1.914(2)	2.4392(4)	132.17(9)
[PPh$_4$][Fe(Br)L$^2_2$]	1.941(3)	1.943(3)	2.4145(8)	138.72(14)

geometry is remarkable, as it indicates a three-coordinate chromium(II) as feasible. All four Cr–N distances (see Table 1) are in accordance to other silylamide chromium(II) species known in literature.[21,23] The formation of $[NBu_4][Cr_2(Br)L^1{}_2L^1*]$ can be explained by intramolecular deprotonation of one silylamide of the initially formed $[Cr(Br)L^1{}_2]^-$ by the second amide ligand under elimination of HL^1. The residual $[Cr(Br)L^1*]^-$ moiety is then stabilized *via* coordination of a second $[CrL^1{}_2]$ molecule. Such a deprotonation reaction of chromium silylamides was already observed for attempts to obtain the linear $[Cr\{N(Dipp)SiMe_3\}_2]$ as well as for trivalent homoleptic vanadium hexamethyldisilazanides.[23,41]

Looking at the ^{1}H NMR spectroscopic features of obtained compounds, strongly broadened and paramagnetically shifted signals prevent any assignments for manganese and chromium (see ESI). For iron, the signals belonging to L^1 and the $[NBu_4]^+$ cation overlap in the region from −0.38 ppm to 0.24 ppm. Although this prohibited an accurate assignment, these cation signals are signifcantly shifted from their expected diamagnetic position and thus was indicative of pronounced interactions with the paramagnetic anion. For cobalt, $[NBu_4][Co(Br)L^1{}_2]$, the signal corresponding to L^1 is found at −11 ppm (Figure 2). The four signals of the cation are located in the diamagnetic region at 0.41 ppm, attributed to the CH_3 fragments, and at 1.78 ppm, 3.78 ppm and 5.82 ppm, belonging to the CH_2 moieties. These observed isotropic shifts of the cation in $[NBu_4][Co(Br)L^1{}_2]$ also pointed to intimate interactions with the paramagnetic anion, in agreement with other paramagnetic $[NBu_4]^+$ complexes.[42] This persistent cation/anion interaction was confirmed by temperature dependent proton NMR, as the shifts of all $[NBu_4]^+$ signals followed the Curie-Weiss law ($\delta(T) \sim 1/T$) (see ESI). The shift was most pronounced for the terminal CH_3 function, which amounted to −1.0 ppm when going from 323 K to 193 K. Only little concentration dependence of all signals was observed. The analogous compound $[K\{18c6\}][Co(Br)L^1{}_2]$ exhibited two signals for the $[K\{18c6\}]^+$ cation (3.13 ppm) and the trimethylsilyl groups (−11 ppm) at room temperature (compare Figure S5). The isotropic shift of the cation is surprisingly small compared to the observations made for the $[NBu_4]^+$ cation. However, the substantial broadening of the signal upon cooling indicates a strong interaction, which mimics the solid state structure. In contrast to the observation made for the iron iodide complex $[K\{18c6\}][Fe(I)L^1{}_2]$,[27] no splitting of the crown-ether signal was observed in case of cobalt, that would indicate a persistent K–Br interaction in solution.

In order to test the reducibility of the obtained $[NBu_4][M(Br)L^1{}_2]$ complexes (Mn–Co) potassium graphite was added to the compounds in THF (Scheme 2, top). For manganese, the formed manganese(I) anion $[MnL^1{}_2]^-$, as indicated by the characteristic dark violet colored solution, degraded rapidly within seconds, preventing any attempts of measuring an *in situ* ^{1}H NMR spectrum. Nonetheless, for iron and cobalt, *in situ* measurements were performed, where the formation of the metal(I) species was evident for both metals. However, as seen for cobalt (Figure 3), the reaction is only partially successful with additional formation of the cobalt trisamide $[Co\{N(SiMe_3)_2\}_3]^-$ as well as an unknown species that implicates decomposition processes.

Similar results were obtained for iron (Figure S18). Neither solid state structures nor the isolation of the metal(I) products were achieved despite multiple attempts. This yielded only oily

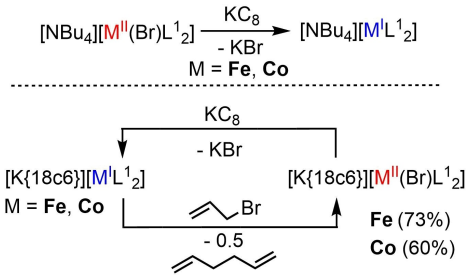

Scheme 2. Top: Reduction of $[NBu_4][M(Br)L^1{}_2]$ to $[NBu_4][ML^1{}_2]$ (M=Fe, Co) with KC_8. Bottom: Synthesis of $[K\{18c6\}][M(Br)L^1{}_2]$ (M=Fe, Co) and their reduction with potassium graphite.

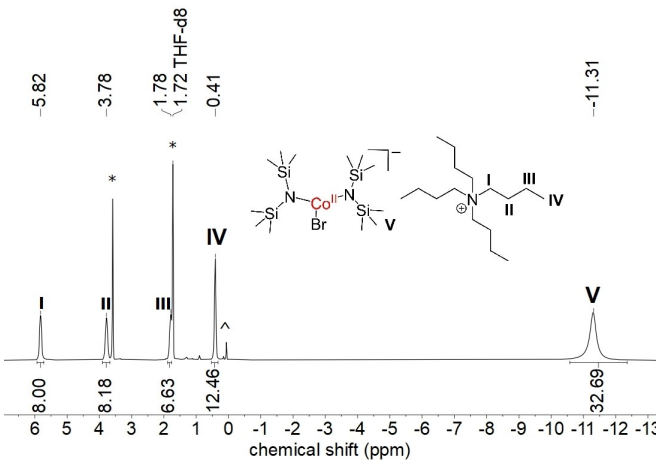

Figure 2. ^{1}H NMR spectrum (300.2 MHz, 300 K) of $[NBu_4][Co(Br)L^1{}_2]$ in THF-d_8. (* solvent, decomposition)

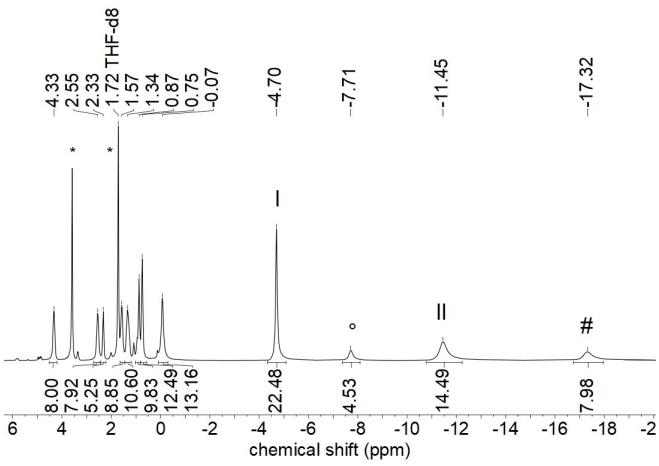

Figure 3. *In situ* ^{1}H NMR spectrum (300.2 MHz, 300 K) of reacting $[NBu_4][Co(Br)L^1{}_2]$ with KC_8 in THF-d_8. (* solvent, II: $[Co(Br)L^1{}_2]^-$, ° $[CoL^1{}_3]^-$; I: $[CoL^1{}_2]^-$; # unknown).

substances, which we attributed to the susceptibility of the organic cation and the presence of mentioned impurities.

To probe the reducibility of the halido metal complex anions $[MBr(L^1)_2]^-$ (M=Fe, Co) further, we turned to the respective K{18c6} salts $[K\{18c6\}][M(Br)L^1_2]$ (M=Fe,[19] Co), to mitigate the effect of the ammonium cation. For that, $[K\{18c6\}][Co(Br)L^1_2]$ (Figure 1, bottom) was synthesized from oxidation of $[K\{18c6\}][CoL^1_2]$ with allyl bromide with 1,5-hexadiene as byproduct (Scheme 2, bottom). In this context, we note that the analogous known iron(II) bromide can also be obtained in this fashion without any signs of overoxidation to iron(III), as observed for the use of benzyl bromide.[19] Subsequently, $[K\{18c6\}][M(Br)L^1_2]$ (M=Fe, Co) was reacted with one equivalent of potassium graphite. Monitoring the reactions by ^{1}H NMR spectroscopy showed in case of iron full conversion of the iron halide and formation of the known iron(I) complex $[K\{18c6\}][ML^1_2]$,[27] which was confirmed *via* x-ray diffraction analysis. For cobalt, only partial reduction to cobalt(I) is observed with small amounts of the unwanted cobalt(II) trisamide side product, as well.

To convey these findings to bulkier ligands, analogous reactions with the kinetically more stable $[M\{N(Dipp)SiR_3\}_2]$ (M=Cr (R=^{i}Pr), Mn–Co (R=Me)) were conducted. $[M\{N(Dipp)SiMe_3\}_2]$ (Mn–Co) was treated with one equivalent of $[NBu_4]Br$ in THF and stirred for 16 h at room temperature (Scheme 3).

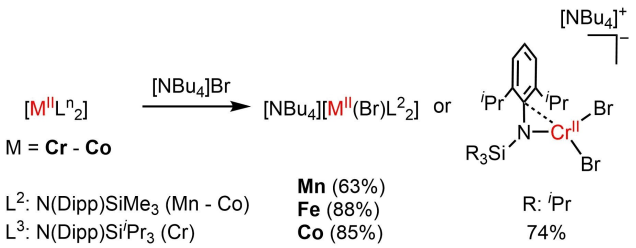

Scheme 3. Synthesis of $[NBu_4][M(Br)\{N(Dipp)SiR_3\}_2]$ (M=Cr (R=^{i}Pr), Mn–Co (R=Me)) *via* reaction of $[M\{N(Dipp)SiR_3\}_2]$ with $[NBu_4]Br$.

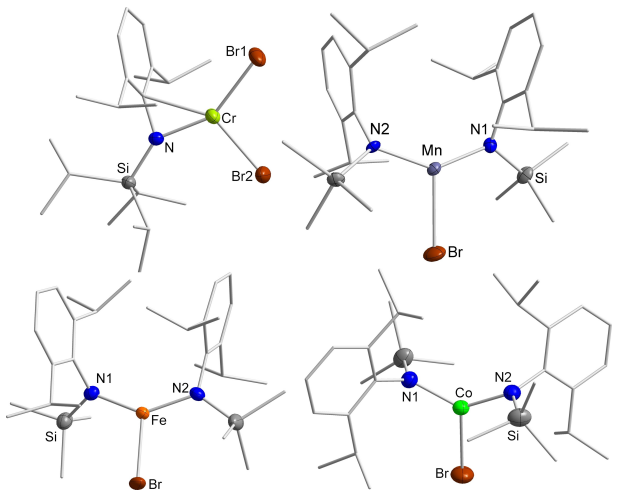

Figure 4. Sections of the solid state structure of [NBu4][Cr(Br)2 L3] (top left) and [NBu4][M(Br)L22] (M=Mn–Co). All cations and hydrogen atoms are omitted for clarity.

After filtering off residual solids, the concentrated solutions were layered with *n*-pentane and stored at −40 °C for several days to yield crystalline $[NBu_4][M(Br)L^2_2]$ (L^2=–N(Dipp)SiMe$_3$) in good yields (Mn: 63%, Fe: 88%, Co: 85%). In solid state, the complex anions from Mn to Co exhibit a trigonal planar coordination geometry (Figure 4). In comparison to the above described $[NBu_4][M(Br)L^1_2]$, the N1–M–N2 angles are larger (139.74(12)° (Mn) to 132.17(9)° (Co)) with smaller N–M–Br angles (around 110°). These deviations reflect the higher steric demand of the L^2 ligand. For chromium, the more encumbering ligand set –N(Dipp)Si^{i}Pr$_3$ (=L^3) was employed due to the known instability of the elusive $[CrL^2_2]$.[21] This yielded in the dibromide complex $[NBu_4][Cr(Br)_2L^3]$, in which one of the silylamides is replaced by a second bromide ligand. The bond lengths of both Cr–Br bonds with ca. 2.44 Å and 2.49 Å. The Cr–N bond is minimally shortened to 1.978(2) Å. The *ipso*-carbon atom of the Dipp moiety (Cr–C_{ipso}: 2.319(3) Å) is strongly oriented towards the chromium atom, which is reflected by an acute Cr–N–C_{ipso} angle of 84.57(14)°. This deformation is not surprising, knowing that chromium(II) prefers a quadratic planar coordination motif.

Having these bulkier trigonal bromido metallate complexes in hand, we also attempted their reduction. This would give an alternative approach to linear metal(I) silylamides with organic cations, which can be obtained from $[KML^2_2]$ or $[KCrL^3_2]$ by cation exchange.[21,24] For that, $[NBu_4][M(Br)L^2_2]$ (M=Mn–Co) and $[NBu_4][Cr(Br)_2L^3]$ were dissolved in diethyl ether before one equivalent of potassium graphite was added. After stirring for one hour or over night, respectively, subsequent filtration, layering with *n*-pentane and crystallization over several days at low temperature lead to the formation of green crystals for iron and cobalt, whose identity was confirmed by x-ray diffraction analysis, albeit in low yields (Scheme 4). Interestingly, the cobalt (I) complex can also be obtained by reacting $[NBu_4][Co(Br)L^2_2]$ with stoichiometric amounts of $KHBEt_3$ in good yields of 74%. In case of the manganese and chromium complexes only decomposition was observed.

To briefly examine the effect of the counter cation, a second organic ion, $[PPh_4]^+$, was tested. In this regard, $[FeL_2]$ was reacted with one equivalent of $[PPh_4]Br$ in THF. Crystallization and subsequent work-up procedures yielded in brownish $[PPh_4][Fe(Br)L^2_2]$ (Figure 5). As the organic cation is separated from the anion, all interesting bond lengths and angles are

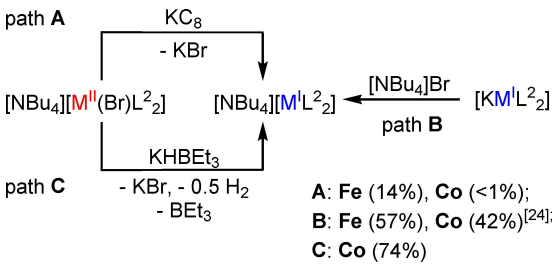

Scheme 4. Comparison of three different pathways for the synthesis of $[NBu_4][ML^2_2]$ (M=Fe, Co).[24]

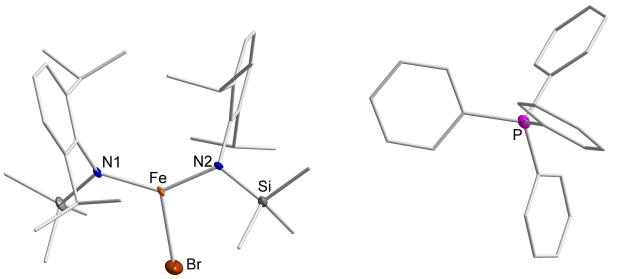

Figure 5. Molecular structure of $[PPh_4][Fe(Br)L^2{}_2]$. All hydrogen atoms and a free THF molecule are omitted for clarity.

comparable to the ones in $[NBu_4][Fe(Br)L^2{}_2]$ and can be found in Table 1. Attempts to isolate the iron(I) species $[PPh_4][FeL^2{}_2]$ upon reduction of $[PPh_4][Fe(Br)L^2{}_2]$ with potassium graphite gave only the divalent starting complex as well as $[FeL_2]$, although decoloration of KC_8 suggested reduction processes. The alternative reaction of $[KFeL_2]$ with $[PPh_4]Br$ was similarly unproductive, giving only the iron(II) complex $[PPh_4][Fe(Br)L^2{}_2]$, as well, which speaks again for degradation.

Besides the overall sluggish nature of the reduction of all these halido metal silylamide complexes, it further showed that the reactions proceeded rather slow (approx. 1 h). This contrasts the near instantaneous reduction of the linear metal(II) precursors. As such it indicates that the halide ligand in the halido complexes might have to briefly decoordinate for the reduction to take place.

Benzyl silylamide metallates

As the introduction of halides proceeded smoothly nonetheless, we fathomed also a more delicate nucleophiles. For that we chose benzyl potassium, which was already successful in case of its reaction with $[FeL^1{}_2]$.[19] As such we wished to extend to its neighbours cobalt and manganese, whereas the respective metal(II) ion is generally expected to be more (Mn) or less (Co) stable towards a reducing benzyl function. Accordingly, $[ML^1{}_2]$ (M=Mn, Co) was reacted with one equivalent of benzyl potassium in toluene with or without 18-crown-6 (Scheme 5). The colours changed to yellow (Mn) or green (Co), respectively, after stirring for a few minutes before any residue was filtered off. Complexes $[KM(Bn)L^1)_2]$ and $[K\{18c6\}][M(Bn)L^1{}_2]$ (M=Mn, Co) were obtained in moderate yields by cooling the *n*-pentane layered solutions for several days and subsequent work-up

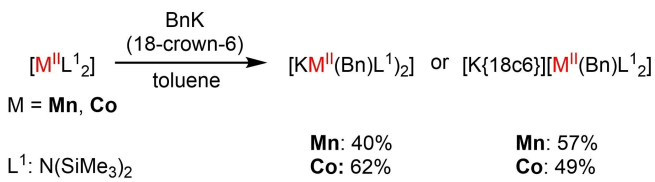

Scheme 5. Synthesis of $[KM(Bn)L^1)_2]$ and $[K\{18c6\}][M(Bn)L^1{}_2]$ (M=Mn, Co).

procedures. Looking at the molecular structures revealed by x-ray diffraction analysis, the potassium cation is either sequestrated by the masking agent $[K\{18c6\}][M(Bn)L^1{}_2]$ (Figure 6, left) or stabilized within two adjacent anions, forming polymeric chains (Figure 6, right).

In the latter, the potassium atom is located between one phenyl ring (K-aryl: 2.9216(5) Å (Mn), 2.9117(4) Å (Co)) and two silylamide ligands. Consequently, the N1–M–N2 bond angles are smaller for $[KMn(Bn)L^1{}_2]$ (113.52(6)°) and $[KCo(Bn)L^1{}_2]$ (118.45(5)°) in comparison to values of 123.92(11)° (Mn) and 125.52(6)° (Co) for K{18c6} complexes, respectively (Table 2). The values of the M–C1 bonds are all in agreement with M–C single bonds.

^{1}H NMR spectroscopic examinations are, again, only evaluable for the cobalt complexes, as the impact of the paramagnetic manganese centre is too strong. For cobalt, the silylamide ligands evoke in THF-d_8 broad signals at −22 ppm for both cobalt compounds $[KCo(Bn)L^1{}_2]$ and $[K\{18c6\}][Co(Bn)L^1{}_2]$. The benzyl fragment is represented by two singlets at 41.16 ppm/41.37 ppm (without/with 18-crown-6) and around −78.8 ppm, whereas the remaining two signals could not be observed in the region of +/−500 ppm. Small traces of the cobalt(II) side product $[CoL^1{}_3]^-$ were always present in the ^{1}H NMR spectra, indicating subsequent ligand exchanges. Beside this fact, the cobalt(I) species $[CoL^1{}_2]^-$ is also detectable, which points to a homolytic Co–C bond cleavage.[34] Using the Evans method, effective magnetic moments were determined to be 4.57 μ_B ($[KCo(Bn)L^1{}_2]$) and 4.84 μ_B ($[K\{18c6\}][Co(Bn)L^1{}_2]$). These values are higher than the expected spin-only values of $\mu_{S.O.(S=3/2)}$ = 3.87 μ_B, but are in accordance with other tridentate cobalt(II) complexes (e.g. $[Co(sIPr)\{N(SiMe_3)_2\}_2]$: μ_B = 4.8 μ_B (sIPr = 1,3-bis(2,6-di-*iso*-propylphenyl)imidazolidin-2-ylidene);[15] ^{Dipp}nacnacCo

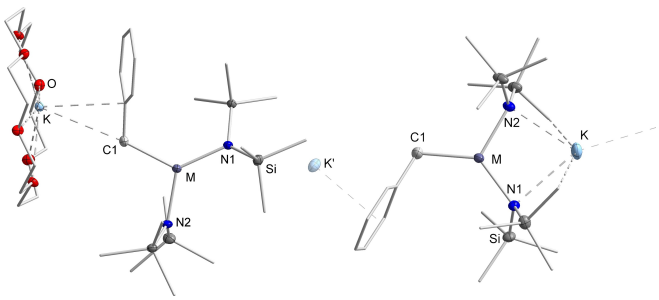

Figure 6. Molecular structure of $[K\{18c6\}][M(Bn)L^1{}_2]$ (left) and $[KM(Bn)L^1{}_2]$ (right) (M=Mn, Co). All hydrogen atoms and a coordinated THF molecule in case of $[K\{18c6\}][Co(Bn)L^1{}_2]$ are omitted for clarity.

Table 2. Selected bond lengths and angles of compounds $[KM(Bn)L^1{}_2]$ and $[K\{18c6\}][M(Bn)L^1{}_2]$ (M=Mn, Co). (* K–C_{ipso} distance)

Length [Å]/angles [°]	[KMn (Bn)$L^1{}_2$]	[K{18c6}] [Mn$L^1{}_2$]	[KCo (Bn)$L^1{}_2$]	[K{18c6}] [Co(Bn)$L^1{}_2$]
M–N1	2.0716(14)	2.047(3)	1.9710(13)	1.9601(12)
M–N2	2.0821(14)	2.059(3)	1.9798(13)	1.9548(12)
M–C1	2.1545(18)	2.192(3)	2.0541(16)	2.0747(16)
K-aryl	2.9216(5)	3.147(3)*	2.9117(4)	3.308(1)*
N1–M–N2	113.52(6)	123.92(11)	118.45(5)	125.52(6)
M–C1–Ph	112.86(12)	116.7(2)	114.26(11)	115.23(10)

(CH_3)]: $\mu_B = 4.9\ \mu_B$[43]) Lower than expected spin-only values ($\mu_{S.O.(S=5/2)} = 5.92\ \mu_B$), were found for the two benzylic manganese complexes ($[KMn(Bn)L^1)_2]$: $\mu_B = 5.58\ \mu_B$; $[K\{18c6\}][Mn(Bn)L^1{}_2]$: $\mu_B = 5.31\ \mu_B$). The benzyl complexes described herein represent rare examples of benzyl metal(II) complexes for cobalt[34,44] and manganese,[45] and the first in a three-coordinate setting.

Conclusion

In this work, the general synthesis of anionic trigonal halido metal(II) silylamides is presented. Complexes of the type $[NBu_4][M(Br)L_2]$ (M=Mn–Co, L^1=$N(SiMe_3)_2$, L^2=N(Dipp)$SiMe_3$) are obtained by addition reactions between $[ML_2]$ and $[NBu_4]Br$. ^1H NMR spectroscopic examination in case of cobalt indicated ion pairing in solution. A similar reaction in case of chromium leads to either two-fold ligand displacement or intramolecular deprotonation. Reducing the trigonal halido metal complexes with potassium graphite give linear metal(I) silylamides, although their isolation is only possible in few cases and in low yields. In an attempt to obtain a trigonal metal(II) hydride *via* reaction of $KHBEt_3$ with $[NBu_4][Co(Br)L^2{}_2]$, the clean reduction to the linear metal(I) complex $[CoL^2{}_2]^-$ is observed. In an analogous fashion, the otherwise insoluble benzyl potassium can also be introduced giving the trigonal manganese(II) and cobalt(II) benzyl complexes $[KM(Bn)L^1{}_2]$. Here, the potassium cation is stabilized by the two silylamide ligands and the aromatic system of an adjacent benzylic fragment, forming polymeric chains, and can be sequestered with 18-crown-6. Overall we give insights into the possibilities but also intricacies evolving around synthesis and use of trigonal halido and benzyl metal(II) silylamides.

Experimental Section

Materials and Methods

All manipulations were carried out in a glovebox under a dry argon atmosphere, unless indicated otherwise. Used solvents were dried by continuous distillation over sodium metal for several days and stored over molecular sieves 4 Å. Deuterated solvents were used as received, degassed *via* three freeze-pump cycles and stored over molecular sieves 4 Å. The ^1H NMR spectra were recorded on a Bruker AV 500, a Bruker HD 500 or a Bruker HD 300 NMR spectrometer (Bruker Corporation, Billerica, USA). Chemical shifts are reported in ppm relative to the residual proton signals of the solvent (for ^1H). $w_{1/2}$ is the line width of a signal at half its maximum intensity. Integrals of the broad signals ligand set were obtained directly or by peak fitting (in case of overlapping signals) using the MestreNova software package (Mestrelab, Santiago de Compostela, Spain). Magnetic moments in solution were determined by the Evans method by adding 1 vol% of tetramethylsilane (TMS) to the deuterated solvent. As reference, a capillary with the same solvent +1 vol% TMS was added to the NMR tube. Magnetic moments were calculated from the frequency differences of both TMS signals using the MestreNova software package (see above). IR measurements were conducted on a Bruker Alpha ATR-IR spectrometer (Bruker Corporation, Billerica, USA). Elemental analysis were performed by the "in-house" service of the Chemistry Department of the Philipps University Marburg, Germany using a CHN(S) analyser vario MICRO Cube (Elementar Analysensysteme GmbH, Langenselbold, Germany). $[NBu_4]Br$ and $[PPh_4]Br$ were obtained commercially and used as received. $[M\{N(SiMe_3)_2\}_2]$ (M=Mn,[4] Fe,[3] Co),[8] $[Cr(thf)_2\{N(SiMe_3)_2\}_2]$,[4] $[M\{N(Dipp)SiMe_3\}_2]$ (M=Mn,[28] Fe,[23] Co),[23] $[Cr\{N(Dipp)Si^iPr_3\}_2]$,[21] $[K\{18c6\}][M\{N(SiMe_3)_2\}_2]$ (M=Fe,[27] Co[28]) and benzyl potassium[46] were prepared according to literature procedures.

$[NBu_4][Cr_2(Br)L^1{}_2L^1{}^*]$. 100 mg (0.2 mmol, 1 equiv.) $[Cr\{N(SiMe_3)_2\}_2(thf)_2]$ and 62 mg $[NBu_4]Br$ (0.2 mmol, 1 equiv.) were dissolved in 2 mL Et_2O. The reaction mixture was stirred over night at room temperature before the blue solution was dried *in vacuo*. $[NBu_4][Cr_2(Br)L^1{}_2L^1{}^*]$ was obtained as sticky dark blue solid in yields of 47%.**Yield**: 81 mg (0.09 mmol, 47%). Crystals, suitable for x-ray diffraction analysis, were obtained from a *n*-pentane layered solution of $[NBu_4][Cr_2(Br)L^1{}_2L^1{}^*]$ in Et_2O/THF at −40 °C. **^1H NMR** (300.2 MHz, THF-d_8, 300 K, ppm): δ = 32 (bs, $w_{1/2}$ = 1210 Hz), 12 (bs, $w_{1/2}$ = 308 Hz), 7 (s, $w_{1/2}$ = 202 Hz,), 3 (bs, $w_{1/2}$ = 88 Hz), 1.0 (bs, $w_{1/2}$ = 41 Hz), 0.66 (m, $w_{1/2}$ = 80 Hz). Elemental analysis $C_{34}H_{89}BrCr_2N_4Si_6$ (906.52 g/mol): calcd: N 6.18, C 45.05, H 9.90; found: N 5.63, C 45.30, H 9.42%. **IR** (ATR, cm^{-1}): $\tilde{\nu}$ = 2943 (m), 2880 (m), 2822 (w), 1469 (m), 1385 (w), 1282 (w), 1243 (m), 1231 (m), 1175 (w), 1150 (w), 1110 (w), 1064 (s), 978 (s), 910 (m), 896 (m), 868 (s), 826 (vs), 776 (s), 758 (m), 749 (s), 718 (m), 696 (m), 662 (s), 611 (s), 499 (m), 481 (m), 434 (w), 406 (w). **EVANS** (500.1 MHz, 300 K, THF-d_8 +1% TMS): $\mu_{eff} = 4.61\ \mu_B$; $\mu_{S.O.} = 8.94\ \mu_B$.

$[NBu_4][Mn(Br)L^1{}_2]$. 100 mg (0.3 mmol, 1 equiv.) $[Mn\{N(SiMe_3)_2\}_2]$ and 86 mg $[NBu_4]Br$ (0.3 mmol, 1 equiv.) were dissolved in 2 mL Et_2O. After stirring for 10 minutes at room temperature the beige solution was filtered off. The solution was layered with *n*-pentane before cooling to −40 °C for several days. The solvent was decanted off and the obtained beige crystals were dried *in vacuo*. Crystalline $[NBu_4][Mn(Br)L^1{}_2]$ was obtained in yields of 83%. **Yield**: 157 mg (0.23 mmol, 83%). **^1H NMR** (300.2 MHz, THF-d_8, 300 K, ppm): δ = 34 (bs, 36 H, $w_{1/2}$ = 1970 Hz, $Si(CH_3)_3$), 1 (bs, $w_{1/2}$ = 286 Hz, $[NBu_4]^+$). Elemental analysis $C_{28}H_{72}BrMnN_3Si_4$ (698.09 g/mol): calcd: N 6.02, C 48.18, H 10.40; found: N 6.41, C 48.24, H 9.96%. **IR** (ATR, cm^{-1}): $\tilde{\nu}$ = 2942 (m), 2878 (m), 1484 (m), 1461 (m), 1426 (w),1383 (w), 1350 (w), 1314 (w), 1274 (w), 1247 (m), 1234 (s), 1193 (w), 1187 (w), 998 (s), 892 (m), 868 (s), 817 (vs), 774 (s), 747 (m), 698 (m), 663 (s), 609 (m), 433 (w), 404 (m). **EVANS** (500.1 MHz, 300 K, THF-d_8 +1% TMS): $\mu_{eff} = 4.86\ \mu_B$; $\mu_{S.O.} = 5.92\ \mu_B$.

$[NBu_4][Fe(Br)L^1{}_2]$. 113 mg (0.3 mmol, 1 equiv.) $[Fe\{N(SiMe_3)_2\}_2]$ and 97 mg $[NBu_4]Br$ (0.3 mmol, 1 equiv.) were dissolved in 2 mL Et_2O. After stirring for 1 hour at room temperature the beige solution was filtered off. The solution was layered with *n*-pentane before cooling to −40 °C for several days. The solvent was decanted off and the obtained colourless crystals were dried *in vacuo*. Crystalline $[NBu_4][Fe(Br)L^1{}_2]$ was obtained in yields of 77%. **Yield**: 162.3 mg (0.23 mmol, 77%). **^1H NMR** (300.2 MHz, THF-d_8, 300 K, ppm): δ = 0.2 (bs, 36 H, $w_{1/2}$ = 64.6 Hz, $Si(CH_3)_3$), 0.09 (s, $w_{1/2}$ = 9.00 Hz, $[NBu_4]^+$), −0.1 (m, $w_{1/2}$ = 28.7 Hz, $[NBu_4]^+$), −0.4 (bs, $w_{1/2}$ = 48.2 Hz, $[NBu_4]^+$). Elemental analysis $C_{28}H_{72}FeBrN_3Si_4$ (698.99 g/mol): calcd: N 6.01, C 48.11, H 10.38; found: N 6.19, C 48.40, H 10.28%. **IR** (ATR, cm^{-1}): $\tilde{\nu}$ = 2943 (m), 2878 (m), 1470 (m), 1383 (w), 1281 (w), 1235 (s), 1169 (w), 1109 (w), 1066 (w), 1035 (w), 985 (s), 924 (w), 892 (m), 862 (m), 831 (vs), 780 (s), 750 (m), 704 (m), 666 (s), 625 (m), 612 (m), 531 (w). **EVANS** (500.1 MHz, 300 K, THF-d_8 +1% TMS): $\mu_{eff} = 5.03\ \mu_B$; $\mu_{S.O.} = 4.90\ \mu_B$.

$[NBu_4][Co(Br)L^1{}_2]$. 114 mg (0.3 mmol, 1 equiv.) $[Co\{N(SiMe_3)_2\}_2]$ and 97 mg $[NBu_4]Br$ (0.3 mmol, 1 equiv.) were dissolved in 2 mL Et_2O. After stirring for 1 hour at room temperature the light green solution was filtered off. The solution was layered with *n*-pentane

before cooling to −40 °C for several days. The solvent was decanted off and the obtained colourless, light greenish crystals were dried *in vacuo*. Crystalline $[NBu_4][Co(Br)L^1_2]$ was obtained in yields of 83 %. **Yield**: 175 mg (0.25 mmol, 83 %). **^{1}H NMR** (300.2 MHz, THF-d_8, 300 K, ppm): δ = 5.82 (s, 8 H, $w_{1/2}$ = 21.9 Hz, $[NBu_4]^+$), 3.78 (s, 8 H, $w_{1/2}$ = 24.7 Hz, $[NBu_4]^+$), 1.78 (s, 8 H, $w_{1/2}$ = 22.3 Hz, $[NBu_4]^+$), 0.41 (s, 12 H, $w_{1/2}$ = 16.1 Hz, $[NBu_4]^+$), −11 (bs, 36 H, $w_{1/2}$ = 67.2 Hz, $Si(CH_3)_3$). Elemental analysis $C_{28}H_{72}BrCoN_3Si_4$ (702.08 g/mol): calcd: N 5.99, C 47.90, H 10.34; found: N 6.32, C 47.94, H 10.25 %. **IR** (ATR, cm^{-1}): $\tilde{\nu}$ = 2964 (m), 2942 (m), 2879 (m), 1469 (m), 1383 (w), 1281 (w), 1235 (s), 1169 (w), 1109 (w), 1063 (w), 1000 (s), 926 (w), 891 (m), 860 (s), 829 (vs), 777 (s), 749 (s), 702 (m), 666 (s), 623 (m), 612 (m). **EVANS** (500.1 MHz, 300 K, THF-d_8 + 1 % TMS): μ_{eff} = 4.39 μ_B; $\mu_{S.O.}$ = 3.87 μ_B.

[K{18c6}][Fe(Br)L$^1_2$].[19] 68 mg (0.1 mmol, 1 equiv.) [K{18c6}][Fe{N(SiMe$_3$)$_2$}$_2$] and 8,64 µL allyl bromide (0.1 mmol, 1 equiv.) were dissolved in 2 mL Et_2O. After stirring for several minutes at room temperature the colourless solution was filtered off. The solution was layered with *n*-pentane before cooling to −40 °C for several days. The solvent was decanted off and the obtained colourless crystals were dried *in vacuo*. Crystalline $[K\{18c6\}][Fe(Br)L^1_2]$ was obtained in yields of 73 %. **Yield**: 56 mg (0.07 mmol, 73 %). Successful synthesis was evidenced by ^{1}H NMR spectroscopy.[19]

[K{18c6}][Co(Br)L$^1_2$]. 68 mg (0.1 mmol, 1 equiv.) [K{18c6}][Co{N(SiMe$_3$)$_2$}$_2$] and 8,64 µL allyl bromide (0.1 mmol, 1 equiv.) were dissolved in 2 mL Et_2O. After stirring for several minutes at room temperature the green solution was filtered off. The solution was layered with *n*-pentane before cooling to −40 °C for several days. The solvent was decanted off and the obtained light petrol crystals were dried *in vacuo*. Crystalline $[K\{18c6\}][Co(Br)L^1_2]$ was obtained in yields of 60 %. **Yield**: 46 mg (0.06 mmol, 60 %). **^{1}H NMR** (300.2 MHz, THF-d_8, 300 K, ppm): δ = 3.13 (s, 24 H, $w_{1/2}$ = 5.10 Hz, 18c6), −11 (bs, 36 H, $w_{1/2}$ = 68.1 Hz, $Si(CH_3)_3$). Elemental analysis $C_{24}H_{60}BrCoKN_2O_6Si_4$ (763.03 g/mol): calcd: N 3.67, C 37.78, H 7.93; found: N 4.04, C 38.06, H 7.74 %. **IR** (ATR, cm^{-1}): $\tilde{\nu}$ = 2946 (m), 2892 (m), 2826 (w), 1473 (w), 1454 (w), 1433 (w), 1351 (m), 1284 (w), 1236 (s), 1105 (vs), 1057 (w), 986 (s), 962 (s), 892 (m), 862 (s), 823 (vs), 782 (s), 751 (m), 707 (m), 665 (s), 625 (m), 612 (m), 529 (w), 417 (w). **EVANS** (500.1 MHz, 300 K, THF-d_8 + 1 % TMS): μ_{eff} = 5.14 μ_B; $\mu_{S.O.}$ = 3.87 μ_B.

N(Dipp)SiR$_3$ (R=^{i}Pr (Cr), Me (Mn–Co))

[NBu$_4$][Cr(Br)$_2$L^3]. 100 mg (0.14 mmol, 1 equiv.) [Cr{N(Dipp)Si^{i}Pr$_3$}$_2$] and 45 mg [NBu$_4$]Br (0.14 mmol, 1 equiv.) were dissolved in 2 mL Et_2O. After stirring over night at room temperature the red solution was filtered off. The solution was layered with *n*-pentane before cooling to −40 °C for several days. The solvent was decanted off and the obtained green crystals were dried *in vacuo*. Crystalline $[NBu_4][Cr(Br)_2L^3]$ was obtained in yields of 74 %. **Yield**: 81 mg (0.10 mmol, 74 %). **^{1}H NMR** (300.2 MHz, THF-d_8, 300 K, ppm): δ = 7 (bs, $w_{1/2}$ = 426 Hz), 0.88–1.50 (m), −8 (bs, $w_{1/2}$ = 475 Hz). Elemental analysis $C_{37}H_{74}Br_2CrN_2Si$ (786.90 g/mol): calcd: N 3.56; C 56.48; H 9.48; found: N 3.68, C 56.41, H 9.30 %. **IR** (ATR, cm^{-1}): $\tilde{\nu}$ = 2960 (s), 2940 (s), 2863 (s), 1481 (m), 1459 (m), 1416 (m), 1381 (m), 1364 (w), 1312 (m), 1240 (s), 1199 (m), 1177 (w), 1149 (w), 1106 (m), 1066 (w), 1043 (m), 1025 (w), 993 (m), 987 (m), 958 (w), 937 (s), 877 (s), 772 (vs), 733 (m), 672 (s), 624 (m), 574 (w), 552 (w), 518 (m), 498 (m), 466 (w), 434 (s). **EVANS** (500.1 MHz, 298 K, THF-d_8 + 1 % TMS): μ_{eff} = 4.45 μ_B; $\mu_{S.O.}$ = 4.90 μ_B.

[NBu$_4$][Mn(Br)L$^2_2$]. 100 mg (0.18 mmol, 1 equiv.) [Mn{N(Dipp)SiMe$_3$}$_2$] and 58 mg [NBu$_4$]Br (0.1 mmol, 1 equiv.) were dissolved in 2 mL THF. After stirring over night at room temperature the beige solution was filtered off. The solution was layered with *n*-pentane before cooling to −40 °C for several days. The solvent was decanted off and the obtained colourless crystals were dried *in vacuo*. Crystalline $[NBu_4][Mn(Br)L^2_2]$ was obtained in yields of 63 %. **Yield**: 99 mg (0.11 mmol, 63 %). **^{1}H NMR** (300.2 MHz, THF-d_8, 300 K, ppm): δ = 28 (bs, $w_{1/2}$ = 283 Hz), 10 (bs, $w_{1/2}$ = 403 Hz), 7.28 (s, $w_{1/2}$ = 5.4 Hz), 0.09–2.33 (m, $[NBu_4]^+$), −28 (s, $w_{1/2}$ = 665 Hz). Elemental analysis $C_{46}H_{88}BrMnN_3Si_2$ (874.24 g/mol): calcd: N 4.81; C 63.20; H 10.15; found: N 5.20, C 63.10, H 9.87 %. **IR** (ATR, cm^{-1}): $\tilde{\nu}$ = 2956 (m), 2875 (m), 1580 (w), 1482 (m), 1458 (m), 1421 (s), 1379 (w), 1358 (w), 1311 (m), 1233 (s), 1186 (s), 1151 (w), 1142 (w), 1106 (m), 1049 (w), 1038 (w), 923 (s), 909 (s), 881 (m), 832 (vs), 778 (s), 745 (m), 672 (m), 620 (m), 572 (w), 537 (m), 428 (m). **EVANS** (500.1 MHz, 300 K, THF-d_8 + 1 % TMS): μ_{eff} = 5.21 μ_B; $\mu_{S.O.}$ = 5.92 μ_B.

[NBu$_4$][Fe(Br)L$^2_2$].100 mg (0.18 mmol, 1 equiv.) [Fe{N(Dipp)SiMe$_3$}$_2$] and 58 mg [NBu$_4$]Br (0.18 mmol, 1 equiv.) were dissolved in 2 mL THF. After stirring over night at room temperature the light yellow solution was filtered off. The solution was layered with *n*-pentane before cooling to −40 °C for several days. The solvent was decanted off and the obtained colourless crystals were dried *in vacuo*. Crystalline $[NBu_4][Fe(Br)L^2_2]$ was obtained in yields of 88 %. **Yield**: 139 mg (0.16 mmol, 88 %). **^{1}H NMR** (300.2 MHz, THF-d_8, 300 K, ppm): δ = 34 (bs, $w_{1/2}$ = 73.1 Hz, *m*-Ph**H**), 24 (bs, $w_{1/2}$ = 420 Hz, $CH(CH_3)_2$), 12 (bs, $w_{1/2}$ = 104.2 Hz, $Si(CH_3)_3$), −1.18 (s, 12 H, $w_{1/2}$ = 18.9 Hz, $[NBu_4]^+$), −1.74 (s, 8 H, $w_{1/2}$ = 30.0 Hz, $[NBu_4]^+$), −2.48 (m, 8 H, $w_{1/2}$ = 30.5 Hz, $[NBu_4]^+$), −2.76 (s, 8 H, $w_{1/2}$ = 32.3 Hz, $[NBu_4]^+$), −36 (bs, $w_{1/2}$ = 48.8 Hz, *p*-Ph**H**), −56 (bs, $w_{1/2}$ = 361.4 Hz, $CH(CH_3)_2$). Elemental analysis $C_{46}H_{88}FeBrN_3Si_2$ (875.15 g/mol): calcd: N 4.80; C 63.13; H 10.14; found: N 4.89, C 62.71, H 9.90 %. **IR** (ATR, cm^{-1}): $\tilde{\nu}$ = 3043 (w), 2958 (m), 2875 (m), 2860 (m), 1585 (w), 1566 (w), 1475 (w), 1458 (m), 1423 (m), 1378 (m), 1357 (w), 1312 (m), 1233 (s), 1188 (m), 1143 (w), 1106 (m), 1049 (w), 1039 (m), 902 (s), 878 (m), 845 (s), 831 (vs), 783 (s), 742 (m), 671 (m), 623 (w), 576 (w), 541 (m), 427 (m). **EVANS** (500.1 MHz, 300 K, THF-d_8 + 1 % TMS): μ_{eff} = 4.79 μ_B; $\mu_{S.O.}$ = 4.90 μ_B.

[NBu$_4$][Co(Br)L$^2_2$]. 56 mg (0.1 mmol, 1 equiv.) [Co{N(Dipp)SiMe$_3$}$_2$] and 32 mg [NBu$_4$]Br (0.1 mmol, 1 equiv.) were dissolved in 2 mL THF. After stirring over night at room temperature the light green solution was filtered off. The solution was layered with *n*-pentane before cooling to −40 °C for several days. The solvent was decanted off and the obtained light petrol crystals were dried *in vacuo*. Crystalline $[NBu_4][Co(Br)L^2_2]$ was obtained in yields of 85 %. **Yield**: 75 mg (0.09 mmol, 85 %). **^{1}H NMR** (300.2 MHz, THF-d_8, 300 K, ppm): δ = 110 (bs, 4 H, $w_{1/2}$ = 9.1 Hz, C**H**$(CH_3)_2$), 42.18 (s, 4 H, $w_{1/2}$ = 44.3 Hz, *m*-Ph**H**), 27.29 (s, 12 H, $w_{1/2}$ = 42.6 Hz, $CH(CH_3)_2$), 6 (bs, 18 H, $w_{1/2}$ = 263 Hz, $Si(CH_3)_3$), 0.30 (s, 8 H, $w_{1/2}$ = 23.3 Hz, $[NBu_4]^+$), −0.21 (s, 8 H, $w_{1/2}$ = 25.4 Hz, $[NBu_4]^+$), −0.47 (s, 8 H, $w_{1/2}$ = 25.3 Hz, $[NBu_4]^+$), −0.68 (m, 12 H, $w_{1/2}$ = 15.8 Hz, $[NBu_4]^+$), −37.99 (s, 2 H, $w_{1/2}$ = 23.9 Hz, *p*-Ph**H**), −53 (bs, 12 H, $w_{1/2}$ = 496 Hz, $CH(CH_3)_2$). Elemental analysis $C_{46}H_{88}BrCoN_3Si_2$ (878.24 g/mol): calcd: N 4.78, C 62.91, H 10.10; found: N 4.67, C 62.70, H 9.63 %. **IR** (ATR, cm^{-1}): $\tilde{\nu}$ = 2960 (m), 2873 (m), 1583 (w), 1479 (m), 1455 (m), 1424 (s), 1377 (m), 1355 (w), 1340 (w), 1312 (m), 1236 (s), 1194 (m), 1151 (w), 1105 (m), 1055 (w), 1039 (w), 1024 (w), 951 (w), 923 (s), 880 (m), 838 (s), 825 (s), 779 (vs), 740 (m), 669 (m), 623 (w), 581 (w), 536 (m), 428 (m). **EVANS** (500.1 MHz, 300 K, THF-d_8 + 1 % TMS): μ_{eff} = 4.66 μ_B; $\mu_{S.O.}$ = 3.87 μ_B.

[NBu$_4$][ML$^2_2$] (M=**Fe**, **Co**).[24] Synthetic path **A**: $[NBu_4][M(Br)L^2_2]$ (M=Fe, Co) (0.07 mmol, 1 equiv.) and $[NBu_4]Br$ (0.07 mmol, 1 equiv.) were dissolved in 2 mL Et_2O. After stirring for one hour at room temperature the green solution was filtered off. The solution was layered with *n*-pentane before cooling to −40 °C for several days. The solvent was decanted off and the obtained green crystals were dried *in vacuo*. Crystalline $[NBu_4][ML^2_2]$ (M=Fe, Co) were obtained in yields of 14 % (Fe) or less than 1 % (Co), respectively. **Yield**: Fe: 7.8 mg (0.009 mmol, 14 %); Co: 0.9 mg ($7 \cdot 10^{-4}$ mmol, < 1 %).

Synthetic path **B**: 30 mg $[NBu_4][Co(Br)L^2_2]$ (0.03 mmol) was dissolved in THF and cooled to 0 °C before $KHBEt_3$ (0.03 mol, 1 equiv.) was

added. The dark green reaction mixture was filtered and layered with *n*-pentane. After cooling to −40 °C for several days, the obtained green crystals were isolated *via* decantation, washed with *n*-pentane and dried *in vacuo*. Crystalline $[NBu_4][CoL^2_2]$ was obtained in yields of 74%. **Yield**: 20 mg (0.03 mmol, 74%)

$[PPh_4][Fe(Br)L^2_2]$. 200 mg (0.36 mmol, 1 equiv.) $[Fe\{N(Dipp)SiMe_3\}_2]$ and 152 mg $[PPh_4]Br$ (0.36 mmol, 1 equiv.) were dissolved in 2 mL THF. After stirring over night at room temperature the red solution was filtered off. The solution was layered with *n*-pentane before cooling to −40 °C for several days. The solvent was decanted off and the obtained light brownish crystals were dried *in vacuo*. Crystalline $[PPh_4][Fe(Br)L^2_2]$ was obtained in yields of 84%. **Yield**: 293 mg (0.30 mmol, 84%). **^{1}H NMR** (300.2 MHz, THF-d_8, 300 K, ppm): δ = 44 (bs, $w_{1/2}$ = 1200 Hz, C**H**$(CH_3)_2$), 34 (bs, 4 H, $w_{1/2}$ = 77.4 Hz, *m*-Ph**H**), 21 (bs, 18 H, $w_{1/2}$ = 517 Hz, Si(C**H**$_3)_3$), 12 (bs, $w_{1/2}$ = 114 Hz, CH(C**H**$_3)_2$), 6.46–6.78 (s, 20 H, PPh_4^+), −35.57 (s, $w_{1/2}$ = 47.6 Hz, *p*-Ph**H**), −52 (bs, $w_{1/2}$ = 419 Hz, CH(C**H**$_3)_2$). Elemental analysis $C_{54}H_{72}FeBrN_2PSi_2$ (972.08 g/mol): calcd: N 2.88; C 66.72; H 7.47; found: N 3.31, C 66.41, H 7.52%. **IR** (ATR, cm^{-1}): $\tilde{\nu}$ = 3058 (w), 3040 (w), 3005 (w), 2949 (m), 2896 (w), 2861 (m), 1586 (w), 1484 (w), 1457 (w), 1437 (m), 1423 (m), 1377 (w), 1357 (w), 1312 (m), 1234 (s), 1188 (m), 1107 (s), 1067 (m), 1050 (w), 1039 (w), 997 (w), 902 (s), 880 (m), 830 (s), 780 (s), 748 (m), 722 (s), 687 (s), 669 (m), 622 (w), 574 (w), 525 (vs), 433 (m). **EVANS** (500.1 MHz, 300 K, THF-d_8 + 1% TMS): μ_{eff} = 4.77 μ_B; $\mu_{S.O.}$ = 4.90 μ_B.

$[KMn(Bn)L^1_2]$. 50 mg (0.13 mmol, 1 equiv.) $[Mn\{N(SiMe_3)_2\}_2]$ and 17 mg benzyl potassium (0.13 mmol, 1 equiv.) were dissolved in 2 mL toluene at −40 °C. The solution was stirred for 5 minutes and the colour changed to yellow/green. After filtration, the yellow solution was dried *in vacuo*. Yellow $[KMn(Bn)L^1_2]$ was obtained in yields of 40%. **Yield**: 26 mg (0.05 mmol, 40%). Crystals, suitable for x-ray diffraction analysis, were obtained from a saturated solution of $[KMn(Bn)L^1_2]$ at −40 °C. **^{1}H NMR** (300.2 MHz, THF-d_8, 300 K, ppm): δ = 26 (bs, $w_{1/2}$ = 4900 Hz, Si(C**H**$_3)_3$), 3.36 (s, 2 H, $w_{1/2}$ = 18.2 Hz, *m*-C**H**/C**H**$_2$), 1.11 (s, 3 H, $w_{1/2}$ = 15.2 Hz, *o*/*p*-C**H**), −0.22 (s, 2 H, $w_{1/2}$ = 12.2 Hz, *m*-C**H**/C**H**$_2$). Elemental analysis $C_{19}H_{43}KMnN_2Si_4$ (505.94 g/mol): calcd: N 5.54; C 45.11; H 8.57; found: N 5.64, C 45.60, H 8.75%. **IR** (ATR, cm^{-1}): $\tilde{\nu}$ = 2943 (m), 2892 (m), 1587 (m), 1494 (w), 1478 (m), 1435 (w), 1360 (w), 1242 (s), 1175 (w), 1115 (m). 1069 (m), 956 (s), 863 (s), 812 (vs), 767 (m), 748 (s), 701 (m), 658 (s), 601 (s), 541 (w), 527 (w), 470 (m), 413 (m). **EVANS** (500.1 MHz, 300 K, THF-d_8 + 1% TMS): μ_{eff} = 5.58 μ_B; $\mu_{S.O.}$ = 5.92 μ_B.

$[K\{18c6\}][Mn(Bn)L^1_2]$. 49 mg (0.13 mmol, 1 equiv.) $[Mn\{N(SiMe_3)_2\}_2]$ and 34 mg 18-crown-6 (0.13 mmol, 1 equiv.) were dissolved in 2 mL toluene. Benzyl potassium (0.13 mmol, 1 equiv.) was added and it was stirred for 5 minutes at room temperature. After filtration, the yellow solution was concentrated to a minimum before layering with *n*-pentane. Cooling at −40 °C for several days yielded yellow crystals, which were washed with *n*-pentane before drying *in vacuo*. Yellow and crystalline $[K\{18c6\}][Mn(Bn)L^1_2]$ was obtained in yields of 57%. **Yield**: 57 mg (0.07 mmol, 57%). **^{1}H NMR** (300.2 MHz, THF-d_8, 300 K, ppm): δ = 32 (bs, $w_{1/2}$ = 3840 Hz), 20 (bs, $w_{1/2}$ = 560 Hz), 7.13 (s, $w_{1/2}$ = 34 Hz), 3.58* (s, 18c6). * Signal is overlapping with a solvent peak. Elemental analysis $C_{31}H_{67}KMnN_2O_6Si_4$ (770.26 g/mol): calcd: N 3.64; C 48.34; H 8.77; found: N 3.64, C 48.36, H 8.72%. **IR** (ATR, cm^{-1}): $\tilde{\nu}$ = 3057 (w), 2936 (m), 2892 (m), 2926 (w), 1585 (m), 1473 (m), 1453 (w), 1434 (w), 1351 (m), 1283 (m), 1234 (s), 1212 (m), 1175 (w), 1107 (s), 1057 (w), 1024 (w), 999 (s), 962 (s), 914 m(w), 867 (s), 822 (vs), 771 (s), 748 (s), 699 (m), 660 (s), 607 (m), 583 (m), 534 (m), 521 (w). **EVANS** (500.1 MHz, 300 K, THF-d_8 + 1% TMS): μ_{eff} = 5.31 μ_B; $\mu_{S.O.}$ = 5.92 μ_B.

$[KCo(Bn)L^1_2]$. 49 mg (0.13 mmol, 1 equiv.) $[Co\{N(SiMe_3)_2\}_2]$ and 17 mg benzyl potassium (0.13 mmol, 1 equiv.) were dissolved in 2 mL toluene at −40 °C. The reaction mixture was stirred for 5 minutes, while the colour changed to yellow/green. After filtration, the yellow solution was dried *in vacuo*. Yellow $[KCo(Bn)L^1_2]$ was obtained in yields of 62%. **Yield**: 52 mg (0.10 mmol, 62%). Crystals, suitable for x-ray diffraction analysis, were obtained from a saturated solution of $[KCo(Bn)L^1_2]$ at −40 °C. **Yield**: 52 mg (0.10 mmol, 62%). **^{1}H NMR** (300.2 MHz, THF-d_8, 300 K, ppm): δ = 41.16 (s, 5 H, $w_{1/2}$ = 17 Hz, $CH_2(C_6H_5)$), −22 (bs, 38 H, $w_{1/2}$ = 67 Hz, Si(C**H**$_3)_3$), −78.84 (s, 2 H, $w_{1/2}$ = 19 Hz, $CH_2(C_6H_5)$). Elemental analysis $C_{19}H_{43}CoKN_2Si_4$ (509.94 g/mol): calcd: N 5.49; C 44.75; H 8.50; found: N 6.16, C 45.01, H 8.60%. **IR** (ATR, cm^{-1}): $\tilde{\nu}$ = 3062 (w), 2944 (m), 2890 (m), 1586 (m), 1480 (m), 1445 (w), 1420 (w), 1399 (w), 1281 (w), 1256 (m), 1243 (s), 1215 (m), 1175 (w), 1074 (w), 1026 (w), 969 (s), 879 (m), 859 (s), 827 (vs), 768 (m), 753 (s), 703 (m), 688 (w), 662 (m), 610 (m), 534 (w), 422 (m). **EVANS** (500.1 MHz, 300 K, THF-d_8 + 1% TMS): μ_{eff} = 4.57 μ_B; $\mu_{S.O.}$ = 3.87 μ_B.

$[K\{18c6\}][Co(Bn)L^1_2]$. 49 mg (0.13 mmol, 1 equiv.) $[Co\{N(SiMe_3)_2\}_2]$ and 34 mg 18-crown-6 (0.13 mmol, 1 equiv.) were dissolved in 2 mL toluene at −40 °C. Benzyl potassium (0.13 mmol, 1 equiv.) was added and it was stirred for 5 minutes. After filtration, the green solution was concentrated to a minimum before layering with *n*-pentane. Cooling at −40 °C for several days yielded dark green crystals, which were washed with *n*-pentane before drying *in vacuo*. Green and crystalline $[K\{18c6\}][Co(Bn)L^1_2]$ was obtained in yields of 49%. **Yield**: 49 mg (0.06 mmol, 49%). **^{1}H NMR** (300.2 MHz, THF-d_8, 300 K, ppm): δ = 41.37 (s, $w_{1/2}$ = 19.6 Hz, $CH_2(C_6H_5)$), 4.23 (s, 24 H, $w_{1/2}$ = 5.9 Hz, 18c6), −22 (bs, 18 H, $w_{1/2}$ = 57.1 Hz, Si(C**H**$_3)_3$), −78.80 (s, $w_{1/2}$ = 21.8 Hz, $CH_2(C_6H_5)$). Elemental analysis $C_{31}H_{67}CoKN_2O_6Si_4$ (774.27 g/mol): calcd: N 3.62; C 48.09; H 8.72; found: N 4.06, C 47.59, H 9.14%. **IR** (ATR, cm^{-1}): $\tilde{\nu}$ = 2941 (m), 2889 (m), 2827 (w), 1590 (w), 1472 (m), 1454 (m), 1433 (w), 1352 (m), 1284 (m), 1233 (s), 1104 (vs), 1058 (w), 988 (s), 962 (s), 864 (s), 820 (vs), 777 (s), 746 (s), 709 (w), 699 (m), 660 (s), 609 (m), 544 (w), 529 (m), 462 (w), 422 (w). **EVANS** (500.1 MHz, 300 K, THF-d_8 + 1% TMS): μ_{eff} = 4.84 μ_B; $\mu_{S.O.}$ = 3.87 μ_B.

$[K\{18c6\}][CoL^1_3]$. 49 mg (0.13 mmol, 1 equiv.) $[Co\{N(SiMe_3)_2\}_2]$ and 34 mg 18-crown-6 (0.13 mmol, 1 equiv.) were dissolved in 2 mL Et_2O at −40 °C. $KN(SiMe_3)$ (0.13 mmol, 1.0 equiv.) was added and it was stirred for 5 minutes. After filtration, the green solution was concentrated to a minimum before layering with *n*-pentane. Cooling at −40 °C for several days yielded dark green crystals, which were washed with *n*-pentane before drying *in vacuo*. Green and crystalline $[K\{18c6\}][CoL^1_3]$ was obtained in yields of 74%. **Yield**: 81 mg (0.10 mmol, 74%). **^{1}H NMR** (300.2 MHz, THF-d_8, 300 K, ppm): δ = 2.90 (s, 24 H, $w_{1/2}$ = 9.7 Hz, 18c6), −8 (bs, 54 H, $w_{1/2}$ = 55 Hz, Si(C**H**$_3)_3$). Elemental analysis $C_{30}H_{78}CoKN_3O_6Si_6$ (843.51 g/mol): calcd: N 4.98; C 42.72; H 9.32; found: N 4.71, C 42.86, H 9.22%. **IR** (ATR, cm^{-1}): $\tilde{\nu}$ = 2945 (m), 2894 (m), 2827 (w), 1473 (w), 1454 (w), 1433 (w), 1352 (m), 1284 (m), 1233 (s), 1105 (s), 1055 (w), 984 (s), 961 (s), 866 (s), 822 (vs), 779 (s), 750 (m), 710 (m), 661 (s), 610 (m), 530 (m), 447 (w). **EVANS** (500.1 MHz, 300 K, THF-d_8 + 1% TMS): μ_{eff} = 5.38 μ_B; $\mu_{S.O.}$ = 3.87 μ_B.

X-ray diffraction analysis

Data for compounds **$[NBu_4][Fe(Br)L^1_2]$** (CCDC 2102354), **$[NBu_4][Co(Br)L^1_2]$** (CCDC 2101926), **$[NBu_4][Mn(Br)L^2_2]$** (CCDC 2101933), **$[NBu_4][Fe(Br)L^2_2]$** (CCDC 2101934), **$[NBu_4][Co(Br)L^2_2]$** (CCDC 2101930), **$[K\{18c6\}][CoL^1_3]$** (CCDC 2101921), **$[PPh_4][Fe(Br)L^2_2]$** (CCDC 2102355), **KL^3** (CCDC 2101924), **$[KCo(Bn)L^1_2]$** (CCDC 2101922), **$[K\{18c6\}][Co(Bn)L^1_2]$** (CCDC 2101928), **$[KMn(Bn)L^1_2]$** (CCDC 2101923) and **$[K\{18c6\}][Mn(Bn)L^1_2]$** (CCDC 2101929) were collected at 100 K on a Bruker Quest D8 diffractometer (Bruker Corporation, Billerica, USA) using an Incoatec Microfocus Source Mo–Kα radiation and equipped with an Oxford Instrument Cooler Device (Oxford Instruments, Abingdon, UK) and Photon 100 detector. Data for compounds **$[NBu_4][Cr_2(Br)L^1_2L^1$***] (CCDC 2101927), **$[NBu_4][Mn(Br)L^1_2]$**

(CCDC 2101932) and **[NBu$_4$][Cr(Br)$_2$L^3]** (CCDC 2101931) were collected at 100 K on a STOE IPDS2 diffractometer (STOE & Cie GmbH, Darmstadt, Germany) and data for compound **[K{18c6}][Co(Br)L$^1_2$]** (CCDC 2101925) were collected on a STOE IPDS2T diffractometer using a graphite-monochromated Mo–Kα radiation (λ = 0.71073 Å) and equipped with an Oxford Instrument Cooler Device (Oxford Instruments, Abingdon, UK). The structures have been solved using either OLEX SHELXT V2014/1[47] and refined by means of least-squares procedures on an F^2 with the aid of the program SHELXL-2016/6[48] included in the software package WinGX version 1.63[49] or using CRYSTALS.[50] The atomic scattering factors were taken from International Tables for x-ray Crystallography.[51] All non-hydrogen atoms were refined anisotropically. All hydrogen atoms were refined by using a riding model. Disorders were found for **[NBu$_4$][Cr$_2$(Br)L$^1_2$L^1*]** (in two butyl groups and the free solvent molecule), **[NBu$_4$][Fe(Br)L$^1_2$]** (in the NBu_4^+ cation), **[NBu$_4$][Co(Br)L$^1_2$]** (in the NBu_4^+ cation and one $SiMe_3$ moiety), **[K{18c6}][CoL$^1_3$]** (in one coordinated THF molecule), **[NBu$_4$][Fe(Br)L$^2_2$]** (in two butyl groups and one $SiMe_3$ fragment), **[NBu$_4$][Mn(Br)L$^2_2$]** (in one bromide ligand and one $SiMe_3$ fragment in one of three independent molecules), **[PPh$_4$][Fe(Br)L$^2_2$]** (in one bromide ligand in one of three independent molecules), **[K{18c6}][Co(Bn)L$^1_2$]** (in the benzyl fragment in one of two independent anions) and **[K{18c6}][Co(Bn)L$^1_2$]** (in the coordinated THF molecule) and were modelled accordingly. The structures of **[NBu$_4$][Fe(Br)L$^1_2$]**, **[K{18c6}][Co(Br)L$^1_2$]** and **[NBu$_4$][Co(Br)L$^2_2$]** were refined as twins. For **[NBu$_4$][Fe(Br)L$^1_2$]** weakly diffracting crystals and intrinsic crystallographic flaws could not be overcome despite multiple attempts. Absorption corrections were introduced by using the MULTISCAN and X-Red programs.[52] Drawings of molecules are performed with the program DIAMOND (Crystal Impact, Bonn, Germany) with 50 % probability displacement ellipsoids for non-H atoms. Additional details are given in the Supporting Information.

Deposition Numbers 2102354 (for **[NBu$_4$][Fe(Br)L$^1_2$]**), 2101926 (for **[NBu$_4$][Co(Br)L$^1_2$]**), 2101933 (for **[NBu$_4$][Mn(Br)L$^2_2$]**), 2101934 (for **[NBu$_4$][Fe(Br)L$^2_2$]**), 2101930 (for **[NBu$_4$][Co(Br)L$^2_2$]**), 2101921 (for **[K{18c6}][CoL$^1_3$]**), 2102355 (for **[PPh$_4$][Fe(Br)L$^2_2$]**), 2101924 (for **KL^3**), 2101922 (for **[KCo(Bn)L$^1_2$]**), 2101928 (for **[K{18c6}][Co(Bn)L$^1_2$]**), 2101923 (for **[KMn(Bn)L$^1_2$]**), 2101929 (for **[K{18c6}][Mn(Bn)L$^1_2$]**), 2101927 (for **[NBu$_4$][Cr$_2$(Br)L$^1_2$L^1*]**), 2101932 (for **[NBu$_4$][Mn(Br)L$^1_2$]**), 2101931 (for **[NBu$_4$][Cr(Br)$_2$L^3]**), and 2101925 (for **[K{18c6}][Co(Br)L$^1_2$]**) contain the supplementary crystallographic data for this paper. These data are provided free of charge by the joint Cambridge Crystallographic Data Centre and Fachinformationszentrum Karlsruhe Access Structures service www.ccdc.cam.ac.uk/structures.

Acknowledgements

Special thanks to Dr. Sergei Ivlev and Dr. Frank Tambornino for helping with some of the crystallographic problems. C.G.W. thanks the Deutsche Forschungsgemeinschaft (grant WE 5627/4-1) and the Philipps-University for financial support. Open Access funding enabled and organized by Projekt DEAL.

Conflict of Interest

The authors declare no conflict of interest.

Keywords: Amide ligands · 3d-Block metals · Low-coordinate · Reduction · Synthesis

[1] a) M. F. Lappert, *Metal amide chemistry*, Wiley, Chichester, U. K., **2009**; b) P. P. Power, *Chem. Rev.* **2012**, *112*, 3482; c) P. P. Power, K. Ruhlandt-Senge, S. C. Shoner, *Inorg. Chem.* **1991**, *30*, 5013.
[2] B. D. Murray, P. P. Power, *Inorg. Chem.* **1984**, *23*, 4584.
[3] H. Bürger, U. Wannagat, *Monatsh. Chem.* **1963**, *94*, 1007.
[4] H. Bürger, U. Wannagat, *Monatsh. Chem.* **1964**, *95*, 1099.
[5] M. Faust, A. M. Bryan, A. Mansikkamäki, P. Vasko, M. M. Olmstead, H. M. Tuononen, F. Grandjean, G. J. Long, P. P. Power, *Angew. Chem. Int. Ed.* **2015**, *54*, 12914.
[6] a) F. Dumestre, *Science* **2004**, *303*, 821; b) C. Desvaux, C. Amiens, P. Fejes, P. Renaud, M. Respaud, P. Lecante, E. Snoeck, B. Chaudret, *Nat. Mater.* **2005**, *4*, 750; c) M. P. Conley, M. F. Delley, G. Siddiqi, G. Lapadula, S. Norsic, V. Monteil, O. V. Safonova, C. Copéret, *Angew. Chem. Int. Ed.* **2014**, *53*, 1872; d) O. Margeat, C. Amiens, B. Chaudret, P. Lecante, R. E. Benfield, *Chem. Mater.* **2005**, *17*, 107; e) T. Deschner, K. W. Törnroos, R. Anwander, *Inorg. Chem.* **2011**, *50*, 7217; f) D. V. Baxter, M. H. Chisholm, G. J. Gama, A. L. Hector, I. P. Parkin, *Chem. Vap. Deposition* **1995**, *1*, 49; g) S. Suh, D. M. Hoffman, L. M. Atagi, D. C. Smith, *Chem. Vap. Deposition* **2001**, *7*, 81.
[7] M. M. Olmstead, P. P. Power, S. C. Shoner, *Inorg. Chem.* **1991**, *30*, 2547.
[8] A. M. Bryan, G. J. Long, F. Grandjean, P. P. Power, *Inorg. Chem.* **2013**, *52*, 12152.
[9] D. L. J. Broere, I. Čorić, A. Brosnahan, P. L. Holland, *Inorg. Chem.* **2017**, *56*, 3140.
[10] a) D. C. Bradley, M. B. Hursthouse, C. W. Newing, A. J. Welch, *Chem. Commun.* **1972**, 567; b) W. Zhou, A. N. Desnoyer, J. A. Bailey, B. O. Patrick, K. M. Smith, *Inorg. Chem.* **2013**, *52*, 2271; c) C. G. Werncke, L. Vendier, S. Sabo-Etienne, J.-P. Sutter, C. Pichon, S. Bontemps, *Eur. J. Inorg. Chem.* **2017**, *2017*, 1041; d) M. M. Hänninen, K. Pal, B. M. Day, T. Pugh, R. A. Layfield, *Dalton Trans.* **2016**, *45*, 11301; e) R. A. Layfield, J. J. W. McDouall, M. Scheer, C. Schwarzmaier, F. Tuna, *Chem. Commun.* **2011**, *47*, 10623; f) T. Bodenstein, A. Eichhöfer, *Dalton Trans.* **2019**, *48*, 15699; g) Y. Liu, L. Deng, *J. Am. Chem. Soc.* **2017**, *139*, 1798; h) A. Panda, M. Stender, M. M. Olmstead, P. Klavins, P. P. Power, *Polyhedron* **2003**, *22*, 67; i) N.-J. H. Kneusels, J. E. Münzer, K. Flosdorf, D. Jiang, B. Neumüller, L. Zhao, A. Eichhöfer, G. Frenking, I. Kuzu, *Dalton Trans.* **2020**, *49*, 2537.
[11] Y.-F. Deng, T. Han, Z. Wang, Z. Ouyang, B. Yin, Z. Zheng, J. Krzystek, Y.-Z. Zheng, *Chem. Commun.* **2015**, *51*, 17688.
[12] R. T. Baker, J. C. Gordon, C. W. Hamilton, N. J. Henson, P.-H. Lin, S. Maguire, M. Murugesu, B. L. Scott, N. C. Smythe, *J. Am. Chem. Soc.* **2012**, *134*, 5598.
[13] A. A. Danopoulos, P. Braunstein, M. Wesolek, K. Y. Monakhov, P. Rabu, V. Robert, *Organometallics* **2012**, *31*, 4102.
[14] A. Eichhöfer, Y. Lan, V. Mereacre, T. Bodenstein, F. Weigend, *Inorg. Chem.* **2014**, *53*, 1962.
[15] A. Massard, P. Braunstein, A. A. Danopoulos, S. Choua, P. Rabu, *Organometallics* **2015**, *34*, 2429.
[16] B. M. Day, K. Pal, T. Pugh, J. Tuck, R. A. Layfield, *Inorg. Chem.* **2014**, *53*, 10578.
[17] a) B. M. Day, T. Pugh, D. Hendriks, C. F. Guerra, D. J. Evans, F. M. Bickelhaupt, R. A. Layfield, *J. Am. Chem. Soc.* **2013**, *135*, 13338; b) K. Pal, O. B. Hemming, B. M. Day, T. Pugh, D. J. Evans, R. A. Layfield, *Angew. Chem. Int. Ed.* **2016**, *55*, 1690; c) A. A. Danopoulos, A. Massard, G. Frison, P. Braunstein, *Angew. Chem. Int. Ed.* **2018**, *57*, 14550; d) P.-H. Lin, N. C. Smythe, S. I. Gorelsky, S. Maguire, N. J. Henson, I. Korobkov, B. L. Scott, J. C. Gordon, R. T. Baker, M. Murugesu, *J. Am. Chem. Soc.* **2011**, *133*, 15806.
[18] a) A. M. Borys, E. Hevia, *Organometallics* **2021**, *40*, 442; b) L. C. H. Maddock, T. Nixon, A. R. Kennedy, M. R. Probert, W. Clegg, E. Hevia, *Angew. Chem. Int. Ed.* **2018**, *57*, 187; c) S. N. König, D. Schneider, C. Maichle-Mössmer, B. M. Day, R. A. Layfield, R. Anwander, *Eur. J. Inorg. Chem.* **2014**, *2014*, 4302; d) L. C. H. Maddock, T. Cadenbach, A. R. Kennedy, I. Borilovic, G. Aromí, E. Hevia, *Inorg. Chem.* **2015**, *54*, 9201.
[19] C. G. Werncke, J. Pfeiffer, I. Müller, L. Vendier, S. Sabo-Etienne, S. Bontemps, *Dalton Trans.* **2019**, *48*, 1757.
[20] a) S. N. Konig, C. Schadle, C. Maichle-Mossmer, R. Anwander, *Inorg. Chem.* **2014**, *53*, 4585; b) H. Chen, R. A. Bartlett, H. V. R. Dias, M. M. Olmstead, P. P. Power, *J. Am. Chem. Soc.* **1989**, *111*, 4338; c) R. A. Bartlett, P. P. Power, *J. Am. Chem. Soc.* **1987**, *109*, 7563; d) J. M. Zadrozny, M. Atanasov, A. M. Bryan, C.-Y. Lin, B. D. Rekken, P. P. Power,

F. Neese, J. R. Long, *Chem. Sci.* **2013**, *4*, 125; e) C.-Y. Lin, J. C. Fettinger, P. P. Power, *Inorg. Chem.* **2017**, *56*, 9892; f) C. L. Wagner, L. Tao, J. C. Fettinger, R. D. Britt, P. P. Power, *Inorg. Chem.* **2019**, *58*, 8793; g) M. I. Lipschutz, T. D. Tilley, *Chem. Commun.* **2012**, *48*, 7146; h) L. Maddock, R. Morton, A. Kennedy, E. Hevia, *Chem. Eur. J.* **2021**, DOI: 10.1002/chem.202102328.

[21] I. C. Cai, M. I. Lipschutz, T. D. Tilley, *Chem. Commun.* **2014**, *50*, 13062.

[22] I. C. Cai, M. S. Ziegler, P. C. Bunting, A. Nicolay, D. S. Levine, V. Kalendra, P. W. Smith, K. V. Lakshmi, T. D. Tilley, *Organometallics* **2019**, *38*, 1648.

[23] C.-Y. Lin, J.-D. Guo, J. C. Fettinger, S. Nagase, F. Grandjean, G. J. Long, N. F. Chilton, P. P. Power, *Inorg. Chem.* **2013**, *52*, 13584.

[24] R. Weller, I. Müller, C. Duhayon, S. Sabo-Etienne, S. Bontemps, C. G. Werncke, *Dalton Trans.* **2021**, *50*, 4890.

[25] R. Weller, L. Ruppach, A. Shlyaykher, F. Tambornino, C. G. Werncke, *Dalton Trans.* **2021**, *50*, 10947.

[26] C.-Y. Lin, J. C. Fettinger, F. Grandjean, G. J. Long, P. P. Power, *Inorg. Chem.* **2014**, *53*, 9400.

[27] C. G. Werncke, P. C. Bunting, C. Duhayon, J. R. Long, S. Bontemps, S. Sabo-Etienne, *Angew. Chem. Int. Ed.* **2015**, *54*, 245.

[28] C. G. Werncke, E. Suturina, P. C. Bunting, L. Vendier, J. R. Long, M. Atanasov, F. Neese, S. Sabo-Etienne, S. Bontemps, *Chem. Eur. J.* **2016**, *22*, 1668.

[29] M. I. Lipschutz, X. Yang, R. Chatterjee, T. D. Tilley, *J. Am. Chem. Soc.* **2013**, *135*, 15298.

[30] a) M. I. Lipschutz, T. D. Tilley, *Angew. Chem. Int. Ed.* **2014**, *53*, 7290; b) I. Müller, C. Schneider, C. Pietzonka, F. Kraus, C. G. Werncke, *Inorganics* **2019**, *7*, 117; c) C. G. Werncke, I. Müller, *Chem. Commun.* **2020**, *56*, 2268; d) C. Schneider, S. Demeshko, F. Meyer, C. G. Werncke, *Chem. Eur. J.* **2021**, *27*, 6348.

[31] I. Müller, D. Munz, C. G. Werncke, *Inorg. Chem.* **2020**, *59*, 9521.

[32] I. Müller, C. G. Werncke, *Chem. Eur. J.* **2021**, *27*, 4932.

[33] A. Reckziegel, M. Kour, B. Battistella, S. Mebs, K. Beuthert, R. Berger, C. G. Werncke, *Angew. Chem. Int. Ed.* **2021**, *60*, 15376.

[34] A. Reckziegel, C. Pietzonka, F. Kraus, C. G. Werncke, *Angew. Chem. Int. Ed.* **2020**, *59*, 8527.

[35] a) C. Chen, S. M. Bellows, P. L. Holland, *Dalton Trans.* **2015**, *44*, 16654; b) R. Bonnett, D. C. Bradley, K. J. Fisher, *Chem. Commun.* **1968**, *0*, 886; c) L. Bourget-Merle, M. F. Lappert, J. R. Severn, *Chem. Rev.* **2002**, *102*, 3031; d) Y.-C. Tsai, *Coord. Chem. Rev.* **2012**, *256*, 722.

[36] M. Asay, C. Jones, M. Driess, *Chem. Rev.* **2011**, *111*, 354.

[37] C. Jones, *Coord. Chem. Rev.* **2010**, *254*, 1273.

[38] R. Shikha Singh, R. Prasad Paitandi, R. Kumar Gupta, D. Shankar Pandey, *Coord. Chem. Rev.* **2020**, *414*, 213269.

[39] a) I. L. Fedushkin, A. A. Skatova, V. A. Chudakova, G. K. Fukin, *Angew. Chem. Int. Ed.* **2003**, *42*, 3294; b) G. van Koten, K. Vrieze in *Advances in Organometallic Chemistry*, Elsevier, **1982**, pp. 151–239; c) F. J. de Zwart, B. Reus, A. A. H. Laporte, V. Sinha, B. de Bruin, *Inorg. Chem.* **2021**, *60*, 3274; d) S. Berger, F. Baumann, T. Scheiring, W. Kaim, *Z. Anorg. Allg. Chem.* **2001**, *627*, 620.

[40] M. M. Olmstead, P. P. Power, B. M. Murray, *CSD Communication* **2018**, CCDC 1871691.

[41] P. Berno, R. Minhas, S. Hao, S. Gambarotta, *Organometallics* **1994**, *13*, 1052.

[42] a) G. N. La Mar, *J. Chem. Phys.* **1964**, *41*, 2992; b) M. Damjanović, T. Morita, Y. Horii, K. Katoh, M. Yamashita, M. Enders, *ChemPhysChem* **2016**, *17*, 3423; c) D. W. Larsen, *Inorg. Chem.* **1966**, *5*, 1109; d) D. W. Larsen, A. C. Wahl, *Inorg. Chem.* **1965**, *4*, 1281; e) I. Bertini, C. Luchina, E. Borghi, *Inorg. Chem.* **1981**, *20*, 303.

[43] J. Vela, J. M. Smith, R. J. Lachicotte, P. L. Holland, *Chem. Commun.* **2002**, 2886.

[44] a) T. R. Dugan, J. M. Goldberg, W. W. Brennessel, P. L. Holland, *Organometallics* **2012**, *31*, 1349; b) A. Enachi, D. Baabe, M.-K. Zaretzke, P. Schweyen, M. Freytag, J. Raeder, M. D. Walter, *Chem. Commun.* **2018**, *54*, 13798; c) K. Ding, W. W. Brennessel, P. L. Holland, *J. Am. Chem. Soc.* **2009**, *131*, 10804; d) Q. Liang, N. J. Liu, D. Song, *Dalton Trans.* **2018**, *47*, 9889; e) R. R. Reinig, E. L. Fought, A. Ellern, T. L. Windus, A. D. Sadow, *Dalton Trans.* **2018**, *47*, 12147; f) M. D. Fryzuk, D. B. Leznoff, R. C. Thompson, S. J. Rettig, *J. Am. Chem. Soc.* **1998**, *120*, 10126; g) J. A. DuPont, M. B. Coxey, P. J. Schebler, C. D. Incarvito, W. G. Dougherty, G. P. A. Yap, A. L. Rheingold, C. G. Riordan, *Organometallics* **2007**, *26*, 971; h) N. Shirasawa, T. T. Nguyet, S. Hikichi, Y. Moro-oka, M. Akita, *Organometallics* **2001**, *20*, 3582.

[45] a) J. Cámpora, P. Palma, C. M. Pérez, A. Rodríguez-Delgado, E. Álvarez, E. Gutiérrez-Puebla, *Organometallics* **2010**, *29*, 2960; b) M. Abubekerov, T. L. Gianetti, A. Kunishita, J. Arnold, *Dalton Trans.* **2013**, *42*, 10525; c) C. G. Howard, G. Wilkinson, M. Thornton-Pett, M. B. Hursthouse, *J. Chem. Soc. Dalton Trans.* **1983**, 2025; d) C. C. Lu, J. C. Peters, *Inorg. Chem.* **2006**, *45*, 8597; e) M. H. Al-Afyouni, V. M. Krishnan, H. D. Arman, Z. J. Tonzetich, *Organometallics* **2015**, *34*, 5088.

[46] P. J. Bailey, R. A. Coxall, C. M. Dick, S. Fabre, L. C. Henderson, C. Herber, S. T. Liddle, D. Loroño-González, A. Parkin, S. Parsons, *Chem. Eur. J.* **2003**, *9*, 4820.

[47] O. V. Dolomanov, L. J. Bourhis, R. J. Gildea, J. Howard, H. Puschmann, *J. Appl. Crystallogr.* **2009**, *42*, 339.

[48] G. M. Sheldrick, *Acta Crystallogr. Sect. C* **2015**, *71*, 3.

[49] L. J. Farrugia, *J. Appl. Crystallogr.* **1999**, *32*, 837.

[50] P. W. Betteridge, J. R. Carruthers, R. I. Cooper, K. Prout, D. J. Watkin, *J. Appl. Crystallogr.* **2003**, *36*, 1487.

[51] *International tables for crystallography*, International Union of Crystallography; Springer, Chester, England, New York, **2006**.

[52] a) SADABS-2016/2, *Bruker*, **2016**; b) X.-R. 1. X-Area, *STOE*, **2016**.

Manuscript received: August 17, 2021
Revised manuscript received: September 2, 2021
Accepted manuscript online: September 3, 2021

5.4 „Catalytic 1,3-H Atom Shift of a Terminal Benzylic Alkyne by Iron and Alkali Metal Silylamides − Switching between Allene and Internal Alkyne”

Ruth Weller, Igor Müller, C. Gunnar Werncke

- eingereichtes Manuskript -

Abstract

Herein, the examination of the transformation of alkynes by low-coordinate iron silylamides is presented. An anionic linear iron(I) silylamide ($[Fe(N(Dipp)SiR_3)_2]^-$; Dipp = 2,6-di-*iso*-propylphenyl, R = Me) acts as precatalyst for the cyclotrimerisation of diphenyl acetylene, but is unable to transform internal alkynes with aliphatic substituents or terminal alkynes accordingly. For a benzylic, terminal alkyne, however, the 1,3-H-shift to the internal alkyne is observed and proceeds *via* phenyl allene. Using 10 mol% of the iron complex, the terminal alkene is selectively transformed to phenyl allene within minutes and further fully transformed to the internal alkyne within 24 h. The transformation is retraced on a stoichiometric level and leads to the isolation of a π-alkyne complex with a shifted triple bond. Further, the anionic, trigonal iron(II) silylamide $[Fe(NR_2)_3]^-$ also mediates the catalytic conversion of the terminal alkyne but is restricted to allene formation. Overall, a deprotonation/reprotonation mechanism is assumed for these transformations. This could be ultimately proven using potassium hexamethyldisilazanide KNR_2, which is an even more active catalyst for the complete triple bond shift.

Zusammenfassung

In dieser Publikation werden die Eigenschaften niedervalenter Eisen-Derivate bezüglich katalytischer Alkinumlagerungen erforscht. Hierfür wurden je 10 mol% der Silylamide $[Fe(N\{SiMe_3\}_2)_2]^-$ (**A**), $[Fe(N(Dipp)SiMe_3)_2]^-$ (**B**), $[Fe(N(SiMe_3)_2)_3]^-$ (**C**) und $[Fe(N(SiMe_3)_2)_2]$ (**D**) mit verschiedenen internen und terminalen Alkinen mit Phenyl- und/oder Alkylsubstituenten umgesetzt und die Reaktionen *via* ^{1}H-NMR verfolgt. Es konnte gezeigt werden, dass das Eisen(I)-Derivat **B** die Zyklotrimerisierung interner Alkine katalysiert (**Abbildung 39**, oben). Diese Fähigkeit ist jedoch beschränkt auf Diphenylacetylen, welches innerhalb einer Woche zu 95% in das Benzol-Derivat HPB

umgewandelt wird. Bei Einsatz der beiden Eisen(II)-Spezies **C** und **D** als auch der Eisen(I)-haltigen Verbindung **A** fanden keine Transformationen statt. Dieses Ergebnis ist erstaunlich, da **A** sterisch anspruchsloser ist als **B** und stöchiometrische Umsetzungen von Diphenylacetylen mit sowohl **A** als auch **B** zur Ausbildung von *side-on*-Komplexen führen (vgl. Kapitel 5.2).[252]

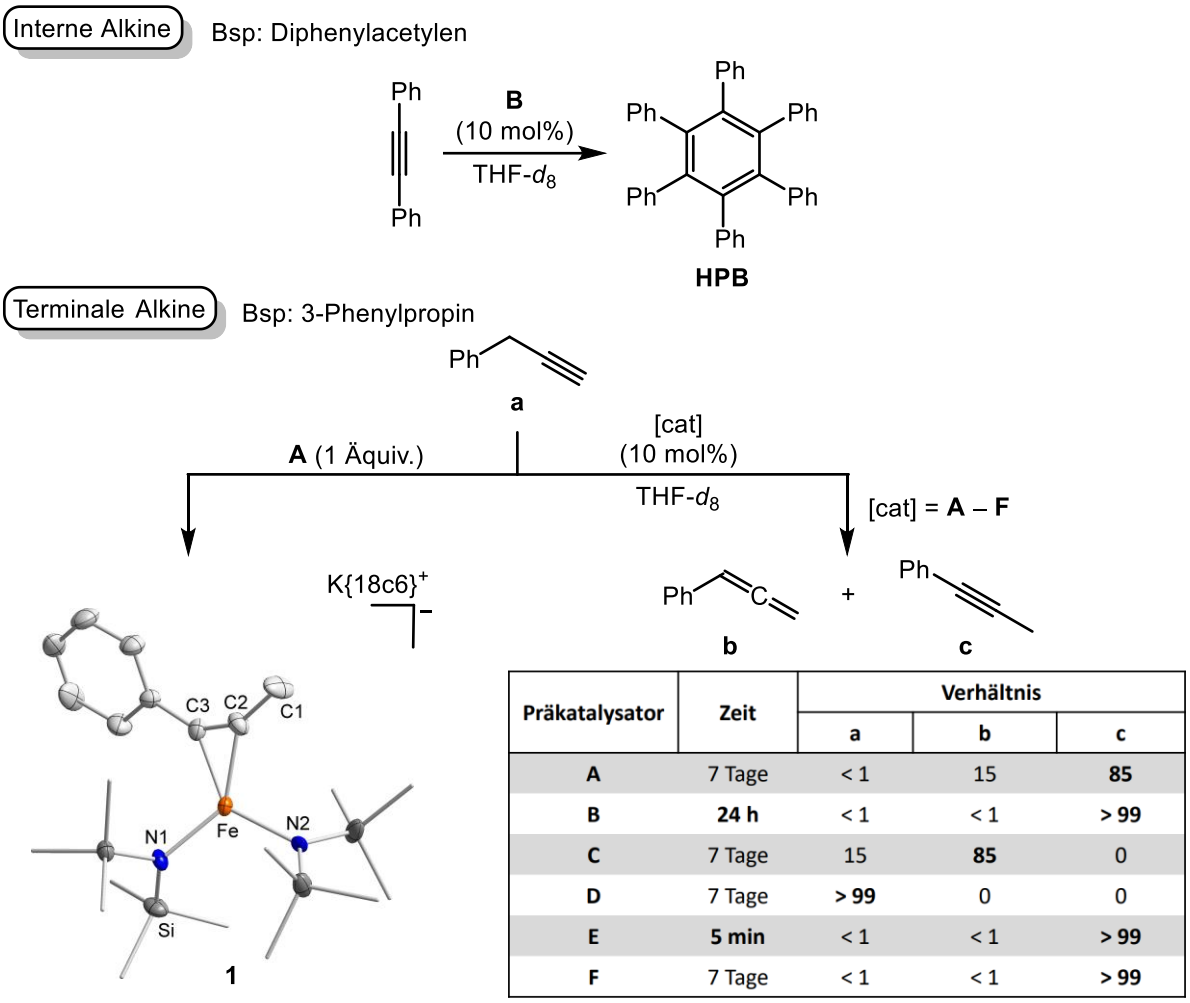

Präkatalysator	Zeit	Verhältnis		
		a	b	c
A	7 Tage	< 1	15	**85**
B	**24 h**	< 1	< 1	**> 99**
C	7 Tage	15	**85**	0
D	7 Tage	**> 99**	0	0
E	**5 min**	< 1	< 1	**> 99**
F	7 Tage	< 1	< 1	**> 99**

Abbildung 39. Übersicht über Isomerisierungsreaktionen von internen und terminalen Alkinen katalysiert durch die Eisensilylamide **A** − **D** ($[Fe(N(SiMe_3)_2)_2]^-$ (**A**), $[Fe(N(Dipp)SiMe_3)_2]^-$ (**B**), $[Fe(N(SiMe_3)_2)_3]^-$ (**C**) und $[Fe(N(SiMe_3)_2)_2]$ (**D**) bzw. die Alkalisalze **E** und **F** ($KN(SiMe_3)_2$ (**E**), $Li(N(SiMe_3)_2$ (**F**)) anhand der Beispiele Diphenylacetylen (intern) und 3-Phenylpropin (terminal).

Für terminale Alkine konnten keine Trimerisierungsreaktionen beobachtet werden. Stattdessen findet im Fall des benzylischen Alkins 3-Phenylpropin eine katalytische Umlagerung der Dreifachbindung statt (**Abbildung 39**, unten). Nach wenigen Minuten wird zunächst das intermediäre Phenylallen **b** gebildet, welches anschließend innerhalb von 24 h (**B**) bzw. sieben Tagen (**A**) zum internen Alkin 1-Phenylpropin **c** weiterreagiert. Auch in diesem Fall ist **B** reaktiver als **A**. Die Evaluation der stöchiometrischen Umsetzung zwischen 3-Phenylpropin und **B** ergab, konträr zu den katalytischen Ergebnissen, eine Umlagerung zum Allen, welche mittels ^{1}H-NMR

Spektroskopie verfolgt wurde. Die Isolierung eines olefinischen Eisenkomplexes war nicht möglich. Dies gelang jedoch durch die Umsetzung des terminalen Alkins mit **A**, wodurch der stabile Eisenkomplex **1** mit einem *side-on*-koordinierenden und umgelagerten Alkin isoliert und charakterisiert werden konnte. Diese Beobachtungen lassen auf eine höhere Bindungsaffinität des Substrates hinsichtlich **A** schließen, welche die katalytischen Eigenschaften von **A** im Vergleich zu **B** verlangsamt, aber die Bildung eines stabilen und isolierbaren Komplexes ermöglicht.

Während für das trigonale Eisen(II)-Trisamid, **C**, ähnliche Isomerisierungsprozesse zum Allen beobachtet wurden, konnte keine Reaktivität gegenüber der neutralen Verbindung **D** festgestellt werden.

Die vollständige Umlagerung der Dreifachbindung von 3-Phenylpropin zu 1-Phenylpropin mit **A** und **B** ist bemerkenswert, da die Isomerisierung terminaler Alkine durch Übergangsmetallkomplexe überwiegend Allene, Vinylidene oder seltener 1,3-Diene erzeugt.[253,254] Da in den hier beschriebenen Systemen **A** − **D** keine Metallhydride entstehen können, welche normalerweise für die Isomerisierung von terminalen Alkinen durch Übergangsmetallkomplexe verantwortlich gemacht werden, wird in den hier beschriebenen Reaktionen von De- bzw. Reprotonierungs-mechanismen ausgegangen. Diese Behauptung konnte durch Reaktionen mit den metallfreien und kommerziell erhältlichen Alkalisalzen $M^AN(SiMe_3)_2$ (M^A = K (**E**), Li (**F**)) bestätigt werden. Während beide Salze 3-Phenylpropin zum internen Alkin umlagern können, ist **E** sogar wesentlich effizienter als die oben beschriebenen Eisenkomplexe **A** und **B**.

Beiträge der Autoren

Die Planung und Durchführung des Projekts lag anfänglich in der Hand von Dr. Igor Müller. Er konnte Verbindungen **1** und **2** darstellen und mithilfe der hausinternen Serviceabteilungen ^{1}H-NMR-spekroskopisch, mittels der Evans-Methode, elementaranalytisch und röntgenkristallographisch charakterisieren. Ebenfalls wurden die IR- und UV/Vis-Messungen durch ihn durchgeführt. Die beiden Datensätze, die mittels Einkristallstrukturanalyse erhalten wurden, wurden von Dr. Igor Müller gelöst und verfeinert. Das durch ihn und Dr. C. Gunnar Werncke erstellte Rohmanuskript ist Bestandteil der Dissertationsschrift von Dr. Igor Müller.[190] Nach Abschluss seiner Promotion übernahm ich das Projekt und brachte es zum Abschluss. Dazu gehörte sowohl die Wiederholung und Ausweitung aller katalytischen Messreihen mittels

^{1}H-NMR Spektroskopie als auch die Überarbeitung des Manuskripts. Das Manuskript wurde in Zusammenarbeit aller drei Autoren verfasst.

RESEARCH ARTICLE

Catalytic 1,3-H Atom Shift of a Terminal Benzylic Alkyne by Iron and Alkali Metal Silylamides − Switching between Allene and Internal Alkyne

Ruth Weller,[a] Igor Müller[a] and C. Gunnar Werncke[a],*

[a] Ruth Weller, Dr. Igor Müller, Dr. C. Gunnar Werncke
Department of Chemistry
Philipps-University Marburg
Hans-Meerwein-Straße 4, D-35032, Marburg, Germany
E-mail: gunnar.werncke@chemie-uni-marburg.de

Supporting information for this article is given *via* a link at the end of the document.

Abstract: Herein the examination of the transformation of alkynes by low-coordinate iron silylamides is presented. An anionic linear iron(I) silylamides ([Fe(N{Dipp}SiR$_3$)$_2$]$^-$; Dipp = 2,6-diisopropylphenyl, R = Me) acts as precatalyst for the cyclotrimerisation of diphenylacetylene, but is unable to transform internal alkynes with aliphatic substituents or terminal alkynes accordingly. For a benzylic, terminal alkyne however the 1,3-H-shift to the internal alkyne is observed and proceeds via phenylallene. Using 10% of the iron complex the terminal alkene is selectively transformed to phenylallene within minutes, and further fully transfored to the internal alkyne within 24 h. The transformation is retraced on a stoichiometric level and leads to the isolation of a π-alkyne complex with a shifted triple bond. Further, the anionic, trigonal iron(II) silylamide [Fe(NR$_2$)$_3$]$^-$ also mediates the catalytic conversion of the terminal alkyne but is restricted to allene formation. Overall, a deprotonation/reprotonation mechanism is assumed for these transformations. This could be ultimately proven using potassium hexamethyldisilazanide KNR$_2$, which is an even more active catalyst for the complete triple bond shift.

Introduction

3d-transition metal complexes play a vital role in catalytic bond transformations. In contrast to compounds with second or third row metal complexes, earth abundant and benign first-row metals are often found in an open-shell configuration in higher spin states.[1] This explains their tendency to undergo an one-electron process, which makes their use challenging, but it can give rise to novel catalytic conversions.[2] In recent years, given the coordinatively and electronically unsaturated state of the metal ion, linear complexes of the middle and late 3d-transition metals have gained interest as precatalysts in this context.[3] In a seminal example, TILLEY presented the trimerisation of internal alkynes using the two-coordinate iron(I) complex ([Fe(IPr)(N{Dipp}SiMe$_3$)], which catalyses the trimerisation of alkynes to benzene derivatives *via* an unprecedented binuclear mechanism.[4] Others reported on trimerisation of terminal alkynes using the simple [Fe(N{SiMe$_3$}$_2$)$_2$], where the −N(SiMe$_3$)$_2$ functions acted as internal bases. The catalytic conversion was thereby attributed to *in situ* formed iron(0) particles.[5] Further, an iron(II) bis(terphenyl) complex was employed for the trimerisation[6] or hydrophosphination[7] of isocyanates, which result was attributed to the LEWIS acidity of the two-coordinate iron(II) ion.

Recently, we observed a *cis* → *trans* bond isomerisation of a 1,2-bisphosphine substituted ethylene by the iron(I) complex [K{18c6}][Fe^I(N{SiMe$_3$}$_2$)$_2$], **A**, even on a catalytic scale.[8] Thereby, the bond isomerisation was proposed to proceed *via* an intermittent 1e$^-$-reduction of the C=C double bond by the highly reducing metal(I) ion. The possibility of an one-electron reduction was recently shown *via* a multiple bond reduction study on the electronic structure of related metal(I) complexes bearing internal alkynes, which are described best as alkyne radical anions bound to a metal(II) ion.[9] In this case, we further observed the lability of these linear metal(I) silylamides with respect to diphenyl acetylene, which initiated oxidation state and ligand redistribution reactions as well as alkyne trimerisation, resulting in anionic arene metallates of the type [M(η_6-arene)(η_2-alkyne)]$^-$ (M = Mn, Fe).[10,9]

Results and Discussion

We now wanted to survey possible catalytic bond transformations of internal and terminal alkynes by **A** and the sterically slightly more encumbered [K{18c6}][Fe(N{Dipp}SiMe$_3$)$_2$], **B**. Using 10 mol% of the precatalysts **A** or **B** in THF-d_8, internal alkynes were tested first using 3-hexyne, diphenyl acetylene and 1-phenyl propyne as prototypical representatives for aryl/alkyl substituted alkynes. However, no conversion was observed for any substrate using **A**. Only in case of **B** and diphenyl acetylene a conversion was observed (**Scheme 1**). This gave the cyclotrimerisation product hexaphenyl benzene (HPB) that precipitated directly from the reaction mixture (isolated yield 95% after seven days). The reactivity difference between both complexes is remarkable as a) both compounds initially form π-complexes in stoichiometric conversions[10,9] and b) **A** should be more reactive due to lesser steric shielding. Trimerisation of diphenyl acetylene was already observed in case of [KFe(N{Dipp}SiMe$_3$)$_2$], the neutral analogue of **B** with intramolecular cation complexation, under redox processes and ligand distribution to the species [KFe(arene)(η^2-PhCCPh)].[10] This might also be in play for **B** in the presence of an excess of substrate, which was indirectly supported by the disappearance of the ^{1}H NMR signature of diphenyl acetylene (Figure S23−26). To elaborate on the impact of the charge, coordination number and oxidation state on ongoing processes, we also tested the iron(II) complexes [K{18c6}][Fe(N{SiMe$_3$}$_2$)$_3$],

C, and [Fe(N{SiMe$_3$}$_2$)$_2$], **D**, which, however, gave no substrate conversion at all.

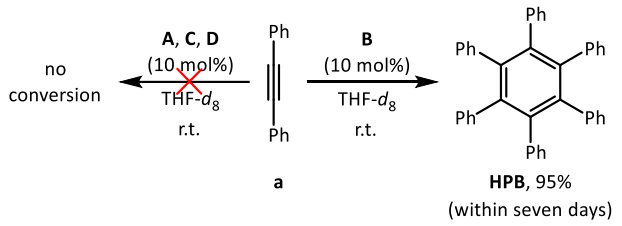

Scheme 1. Catalytical conversion of the internal alkyne diphenyl acetylene to HPB using 10 mol% catalyst **A** − **D** (HPB: hexaphenyl benzene, **A**: [Fe(N{SiMe$_3$}$_2$)$_2$]$^-$, **B**: [Fe(N{Dipp}SiMe$_3$)$_2$]$^-$, **C**: [Fe(N{SiMe$_3$}$_2$)$_3$]$^-$, **D**: [Fe(N{SiMe$_3$}$_2$)$_2$]).

Next, we turned to terminal alkynes with an alkylic (1-hexyne), arylic (phenyl acetylene) or benzylic (3-phenyl propyne) substituent. While 1-hexyne or phenyl acetylene were unaffected using 10 mol% of catalyst **A** or **B**, substrate conversion was observed in case of the benzylic alkyne by ^{1}H NMR spectroscopy. Instead of the envisioned trimerisation, the rapid transformation to phenyl allene was observed (< 5 min). This allene is converted further to the internal alkyne 1-phenyl propyne over the course of 24 h (**B**) or seven days (**A**). The trisamide, **C**, yielded a slow conversion to the allene, whereas the neutral iron(II) complex **D** was ineffective.

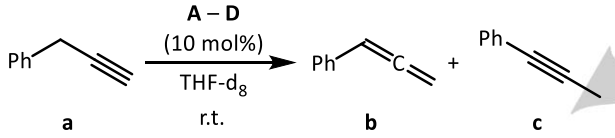

Scheme 2. Iron mediated bond isomerisation of the terminal alkyne 3-phenyl propyne with **A** − **D**. (**A**: [Fe(N{SiMe$_3$}$_2$)$_2$]$^-$, **B**: [Fe(N{Dipp}SiMe$_3$)$_2$]$^-$, **C**: [Fe(N{SiMe$_3$}$_2$)$_3$]$^-$, **D**: [Fe(N{SiMe$_3$}$_2$)$_2$])

Table 1. Iron complex mediated catalytic bond isomerisation of the terminal alkyne 3-phenyl propyne by **A** – **D**.

Precatalyst	[cat] /mol%	Time	Ratio [%]		
			a	**b**	**c**
A	10	5 min	<1	**>99**	0
		24 h	<1	**76**	24
		7 d	<1	15	**85**
B	10	5 min	<1	**>99**	0
		24 h	<1	<1	**>99**
C	10	5 min	**98**	2	0
		24 h	**94**	6	0
		7 d	15	**85**	0
D	10	7 d	**>99**	0	0

To gain some mechanistic insights, **A**, **B** and **C** were treated with stoichiometric amounts of 3-phenyl acetylene, as well. For **A**, reaction with 3-phenyl propyne in diethyl ether at −30 °C (**Scheme 3**) yielded directly in a dark red solution. This was immediately filtered, layered with *n*-pentane and stored at −35 °C. Within a few days, dark red crystals of complex **1** were obtained in moderate yields. X-ray diffraction analysis revealed an iron complex with a symmetrically bound η_2-Ph−C≡C−**CH$_3$** ligand (**Figure 1**, left), confirming a triple bond shift of the employed substrate mediated by **A**. Complex **1** can also be obtained directly in similar yields by reacting 1-phenyl propyne with **A**.

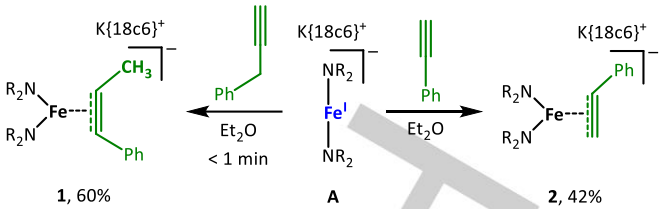

Scheme 3. Reaction of **A** with 3-phenyl propyne (left) and phenyl acetylene (right) (R = SiMe$_3$).

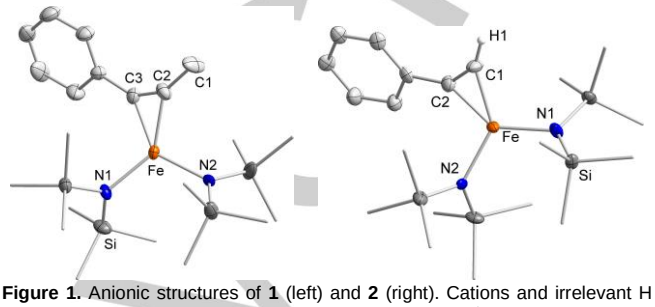

Figure 1. Anionic structures of **1** (left) and **2** (right). Cations and irrelevant H atoms are omitted for clarity. Important bond lengths (Å) and angles (°): **1**) Fe−C2 1.976(8), Fe−C3 1.959(7), Fe−N1 1.976(6), Fe−N2 1.990(6), C1−C2 1.484(11), C2−C3 1.261(10), C1−C2−C3 141.2(8), C2−C3−C$_{Ph}$ 143.2(8); **2**) Fe−C2 1.962(5), Fe−C3 1.918(5), Fe−N1 1.988(4), Fe−N2 2.085(8), C2−C3 1.262(3), C2−C3−C$_{Ph}$ 151.7(5).

While the C1−C2 distance in **1** represents a single bond with a bond length of 1.484(11) Å, a C2≡C3 triple bond is found, connected to the iron atom. Its length of 1.261(10) Å is in agreement with previous examples of related alkyne complexes.[9] The η_2-side on coordination motif is supported by bond length of 1.976(8) Å and 1.959(7) Å for Fe−C2 and Fe−C3, respectively. The C1−C2−C3 bond angle is bent to 141.2(8)°. The proton spectrum of **1** showed a singlet at −2.81 ppm. Only two signals are found for the alkyne ligand, positioned at −5.6 and −77.5 ppm. The effective magnetic moment (3.87 μ_B), determined by the Evans method, coincides with the spin-only value of 3.87 μ_B for a high spin iron(I) species. The easy formation of a complex bearing a substrate with a shifted triple bond implicates that **A** can facilitate a rapid triple bond shift, however, the substrate binds too strong to the metal center, thus reducing the overall catalytic capabilities.

For the treatment of **B** with 3-phenyl propyne an instantaneous color change from green to bluish was observed, however, only complex **B** was recrystallized from the reaction mixture. *In situ* ^{1}H NMR spectroscopic examinations of this reaction also showed the presence of **B** and complete conversion of the terminal alkyne. Very broad signals around 5.6 ppm as well as 7 ppm coincide with those of phenyl allene. This implicates weak interactions between **B** and phenyl allene, best described as a coordination equilibrium that is nearly full on the side of the separate compounds, yet sufficient for spin-polarisation of the allene. For **C** substrate conversion (85%) and selective formation of the allene were observed over the period of seven days.

To elaborate the bonding situation between a terminal alkyne and silylamide complexes, phenyl acetylene was used to prevent bond migration. For **A** this gave the η_2-complex **2** (**Figure 1**, right). The bond metrics of the bound phenyl acetylene unit itself (d$_{C\equiv C}$: 1.262(3) Å, <$_{Ph-C\equiv C}$: 151.7(5)°) is in line with those of **1** and comparable 3d-metal compounds.[11,12,13] However, the alkyne binds asymmetrically with M−C$_{Ph}$ (1.918(5) Å) being significantly

shorter than M−C_H (1.962(5) Å). This stands in contrast to the usual observation of either equidistant M−C_{alkyne}[12,13] or shorter M−C_H bonds.[14] Comparable to **1**, the singlet attributed to the silylamide ligands is found at −2.7 ppm in the ^{1}H NMR spectrum. The coordinated alkyne causes very broad signals at −5.8, 7.2 and 10.1 ppm. The measured effective magnetic moment of 3.93 μ_B is in line with the value for complex **1**. Deprotonation processes were not observed here. Similarly, treatment of phenyl acetylene with **B** and **C**, respectively, gave no conversions in any observable reactions.

The complete triple bond shift of 3-phenyl propyne to 1-phenyl propyne with **A** and **B** is remarkable as isomerisation of terminal alkynes by transition metal complexes is known to give predominantly allenes,[15] vinylidenes,[16a,17,16b] and, to a lesser extent, 1,3-dienes.[18] Thereby, the intermittent formation of a metal hydride is found to be crucial, which we deemed unlikely in our systems.[17,19] Other reactivities concern the alkyne dimerisation to 1,3-enynes.[20] Reports on the complete metal complex mediated triple bond shift from terminal to internal alkynes are restricted to magnesium and involve a bimetallic deprotonation of the alkyne.[21] Due to the basic nature of the silylamide ligands, this seems plausible here. Further, in all catalytic conversions increasing diamagnetic signals belonging to transition metal free or protonated silylamides also pointed to such deprotonation reactions. As the neutral complex **D** proved, however, catalytically incompetent, we contemplated on the beneficial role of the potassium cation in conjunction with a silylamide, present in all active complexes. And indeed, using 10 mol% of KN(SiMe$_3$)$_2$ (**E**), full conversion of the terminal to the internal alkyne is observed within a few minutes, which even surpassed by far that of the aforementioned iron amides. Reducing the catalyst loading to 1 mol%, the substrate is still converted to 71% allene and 29% internal alkyne over the same period of time, which was not feasible at all in case of 1 mol% of the iron complexes. These results contrast reports on the reverse reaction using stoichiometric amounts of lithium or potassium bases that predominantly transform internal alkynes to terminal derivatives ("Zipper" reaction).[22] In these cases, the preference for the thermodynamically less favored terminal alkyne is thereby attributed to the formation of insoluble alkali metal acetylenides.[23] The nature of the alkali metal ion is also of importance as LiN(SiMe$_3$)$_2$ (**F**) proved to be less efficient. With 10 mol%, mostly the allene is observed after 5 minutes, while complete conversion to the internal alkene needed one week. In all these cases, highly violet or bluish colored solutions were observed. The origin of the colors is still unclear as stoichiometric reactions gave only the alkali metal hexamethyldisilazanides, as revealed by proton NMR. Preliminary examinations of other terminal alkynes with complexes mentioned herein showed that aliphatic alkynes were almost unaffected. This held mostly true for terminal alkynes with heteroatoms in the *ß*-position. In case of $Me_2N-CH_2C\equiv CH$ almost full conversion was observed using **B**, although the nature of the resulting products remained inconclusive.

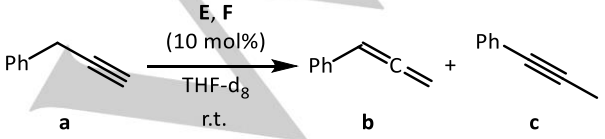

Scheme 4. Alkali metal mediated bond isomerisation of the terminal alkyne 3-phenyl propyne (**E**: KN(SiMe$_3$)$_2$, **F**: LiN(SiMe$_3$)$_2$)

Table 2. Alkali metal hexamethyldisilazanide mediated catalytic bond isomerisation of the terminal alkyne 3-phenyl propyne (**E**: KN(SiMe$_3$)$_2$, **F**: LiN(SiMe$_3$)$_2$; [cat] = **E**, **F**).

Amide	[cat] /mol%	Time	Ratio [%]		
			a	**b**	**c**
E	10	5 min	<1	<1	**>99**
	1	5 min	<1	**71**	29
		24 h	<1	16	**84**
		7 d	<1	6	**94**
F	10	5 min	21	**77**	2
		24 h	<1	56	**44**
		7 d	<1	<1	**>99**

Conclusion

Overall, we investigated the low-coordinate iron(I/II) silylamides, $[Fe^I(N\{SiMe_3\}_2)_2]^-$ (**A**), $[Fe^I(N\{Dipp\}SiMe_3)_2]^-$ (**B**) and $[Fe^{II}(N\{SiMe_3\}_2)_3]^-$ (**C**) as potential precatalysts for the transformation of alkynes using prototypical phenyl and/or alkylated substrates. For internal alkynes it was shown that only iron(I) complex **B** can effectuate the catalytic trimerisation to a benzene derivative, which is, however, restricted to diphenyl acetylene. The examinations of terminal alkynes revealed the absence of any transformation reactions, such as trimerisation, with the exception of a benzylic alkyne, namely 3-phenyl propyne. Here, a catalytic shift of the triple bond mediated by 10 mol% **A** or **B**, respectively, as precatalyst is observed. This leads first to phenyl allene and ultimately to the formation of the internal alkyne 1-phenyl propyne. The bulkier catalyst **B** is more reactive than **A**. For **A**, a stoichiometric reaction allowed the isolation of a rather stable iron complex with a *side-on* bound, rearranged alkyne, whereas no stabile substrate coordination but allene formation is observed for **B**. These findings implicate stronger substrate binding for **A**, mitigating efficient substrate turn-over. The related trigonal iron(II) trisamide $[Fe(N\{SiMe_3\}_2)_3]^-$ also effectuates double bond isomerisation but selectively remains at the allene stage. The reactions are presumed to proceed *via* a deprotonation/reprotonation mechanism. This could be proven using the transition metal free and commercially available potassium hexamethyldisilazanide. This amide also catalyzes the isomerisation of terminal to internal alkynes and is more efficient than the abovementioned iron complexes. The use of the potassium salt is of further importance as LiN(SiMe$_3$)$_2$ proved to be less efficient. This implicates an interplay between coordination and deprotonation processes for the iron complexes influencing the product selectivity. Preliminary examinations of the triple bond shift for related substrates, for example exchanging the −Ph fragment by $-NMe_2$ or −OMe, revealed no according isomerisation reactions, yet further research on concerning substrate scope is on-going.

Experimental Section

Materials and Methods

All manipulations were carried out in a glovebox under a dry argon atmosphere, unless indicated otherwise. Used solvents were dried by continuous distillation over sodium metal for several days, degassed *via* three freeze-pump-thaw cycles and stored over molecular sieves 4 Å. Deuterated solvents were used as received, degassed *via* three freeze-

pump cycles and stored over molecular sieves 4 Å. The ^{1}H NMR spectra were recorded on a Bruker AV 500, a Bruker HD 500 or a Bruker HD 300 NMR spectrometer (Bruker Corporation, Billerica, USA). Chemical shifts are reported in ppm relative to the residual proton signals of the solvent (for ^{1}H). $w_{½}$ is the line width of a signal at half its maximum intensity. Integrals of the broad signals ligand set were obtained directly or by peak fitting (in case of overlapping signals) using the MestreNova software package (Mestrelab, Santiago de Compostela, Spain). IR measurements were conducted on a Bruker Alpha ATR-IR spectrometer (Bruker Corporation, Billerica, USA). The UV/VIS measurements were recorded on an AnalytikJena Specord S600 using WinASPECT software. Elemental analysis were performed by the "in-house" service of the Chemistry Department of the Philipps University Marburg, Germany using a CHN(S) analyser vario MICRO Cube (Elementar Analysensysteme GmbH, Langenselbold, Germany). Solid alkynes and $KN(SiMe_3)_2$ were obtained commercially and used as received. All liquid alkynes were also obtained commercially, but released from stabilizers by distillation prior use. [K{18c6}][Fe(N{SiMe$_3$}$_2$)$_2$],[24][K{18c6}][Fe(N{Dipp}SiMe$_3$)$_2$],[25] [K{18c6}][Fe(N{SiMe$_3$}$_2$)$_3$],[8] [Fe(N{SiMe$_3$}$_2$)$_2$][26] and LiN(SiMe$_3$)$_2$[27] were prepared according to literature procedures.

[K{18c6}][Fe(N{SiMe$_3$}$_2$)$_2$(η^2-PhCCMe)] (**1**). **Synthetic path I**: 68 mg (0.10 mmol, 1 equiv.) [K{18c6}][Fe(N{SiMe$_3$}$_2$)$_2$] (**A**) were dissolved in diethyl ether before 3-phenyl propyne (0.10 mmol, 1 equiv.) was added. The color changed immediately from yellow-green to dark pink. After layering with *n*-pentane, the solution was allowed to crystallize at −35 °C for several days. Grown crystals were isolated *via* filtration, washed with *n*-pentane and dried *in vacuo*. Crystalline, dark pink [K{18c6}][Fe(N{SiMe$_3$}$_2$)$_2$(η^2-PhCCMe)] (**1**) was obtained in yields of 42%. **Yield:** 35 mg (0.04 mmol, 42%). **^{1}H NMR** (300.2 MHz, THF-d_8, 300 K, ppm): δ = 3.58 (bs, 24 H, 18c6), −2.78 (bs, 36 H, $w_{½}$ = 306 Hz, Si(C**H**$_3$)$_3$), −5.58 (s, $w_{½}$ = 97 Hz, alkyne), −77.0 (bs, $w_{½}$ = 390 Hz, alkyne). Elemental analysis $C_{33}H_{68}FeKN_2O_6Si_4$ (796.20 g/mol): calcd: N 3.52, C 49.78, H 8.61; found: N 3.43, C 49.55, H 7.98%. **IR** (ATR, cm^{-1}): $\tilde{\nu}$ = 2943 (w), 2888 (w), 2825 (w), 2047 (w), 1585 (w), 1471 (w), 1452 (w), 1431 (w), 1350 (m), 1283 (w), 1232 (s), 1170 (w), 1103 (vs), 983 (s), 960 (s), 890 (w), 865 (m), 825 (vs), 778 (m), 747 (m), 696 (m), 660 (m), 609 (m), 506 (w), 430 (w). **EVANS** (500.1 MHz, 300 K, THF-d_8 + 1% TMS): μ_{eff} = 3.87 μ_B; $\mu_{S.O.}$ = 3.87 μ_B. **Synthetic path II**: Using 1-phenyl-1-propine as substrate and following path **A**, **1** was obtained in yields of 53%. **Yield:** 42 mg (0.05 mmol, 53%).

[K{18c6}][Fe(N{SiMe$_3$}$_2$)$_2$(η^2-PhCCH)] (**2**). 68 mg (0.10 mmol, 1 equiv.) [K{18c6}][Fe(N{SiMe$_3$}$_2$)$_2$] (**A**) were dissolved in diethyl ether before phenyl acetylene (0.10 mmol, 1 equiv.) was added. The color changed immediately from yellow-green to dark red. After layering with *n*-pentane the solution was allowed to crystallize at −35 °C for several days. Grown crystals were isolated *via* filtration, washed with *n*-pentane and dried *in vacuo*. Crystalline, dark red [K{18c6}][Fe(N{SiMe$_3$}$_2$)$_2$(η^2-PhCCH)] (**2**) was obtained in yields of 55%. **Yield:** 47 mg (0.06 mmol, 60%). **^{1}H NMR** (300.2 MHz, THF-d_8, 300 K, ppm): δ = 10.1 (bs, $w_{½}$ = 360 Hz, alkyne), 7.2 (bs, $w_{½}$ = 270 Hz, alkyne), 3.57* (bs, 24 H, 18c6), −2.71 (bs, 36 H, $w_{½}$ = 280 Hz, Si(C**H**$_3$)$_3$), −5.80 (bs, $w_{½}$ = 64 Hz, alkyne). * Signal is overlapping with a solvent peak. Elemental analysis $C_{32}H_{66}FeKN_2O_6Si_4$ (782.17 g/mol): calcd: N 3.58, C 49.14, H 8.51; found: N 3.42, C 48.78, H 8.11%. **IR** (ATR, cm^{-1}): $\tilde{\nu}$ = 2943 (w), 2888 (w), 2826 (w), 1585 (w), 1471 (w), 1452 (w), 1432 (w), 1351 (m), 1284 (w), 1233 (s), 1171 (w), 1104 (vs), 983 (s), 961 (s), 890 (w), 865 (m), 826 (vs), 778 (m), 747 (m), 696 (m), 660 (m), 609 (m), 507 (w), 431 (w). **EVANS** (500.1 MHz, 300 K, THF-d_8 + 1% TMS): μ_{eff} = 3.93 μ_B; $\mu_{S.O.}$ = 3.87 μ_B.

Catalysis. All catalytic examinations were carried out in YOUNG NMR tubes. The corresponding substrates were dissolved in THF-d_8 and treated with 10 (**A** − **F**) or 1 mol% (**E**) catalyst, respectively. While 0.04 mmol alkyne were reacted with 10 mol% catalyst, 0.02 mmol substrate were used for 1 mol% (**E**). Conversion and yield was determined in relation to the emplpyed substrate using reported NMR spectroscopic values. For the trimerisation of diphenylacetylene yield was determined via product isolation.

X-Ray diffraction analysis

Data for compounds **1** (CCDC 2113360) and **2** (CCDC 2113361) were collected at 100 K on a Bruker Quest D8 diffractometer (Bruker Corporation, Billerica, USA) using an Incoatec Microfocus Source Mo-Kα radiation and equipped with an Oxford Instrument Cooler Device (Oxford Instruments, Abingdon, UK) and Photon 100 detector. The structures have been solved using OLEX SHELXT V2014/1[28] and refined by means of least-squares procedures on an F^2 with the aid of the program SHELXL-2016/6[29] included in the software package WinGX version 1.63[30] . The atomic scattering factors were taken from International Tables for X-ray Crystallography.[31] All non-hydrogen atoms were refined anisotropically. All hydrogen atoms were refined by using a riding model. Disorders were found for **2** in the anionic part and were modelled accordingly. Absorption corrections were introduced by using the MULTISCAN and X-Red programs.[32] Drawings of molecules are performed with the program DIAMOND (Crystal Impact, Bonn, Germany) with 50% probability displacement ellipsoids for non-H atoms. Additional details are given in the Supporting Information.

Conflicts of interest

"There are no conflicts to declare".

Keywords: Alkynes • earth abundant metals • silylamides • catalysis • isomerisation • allene

Notes and references

Spectra and further crystallographic data are given in the Electronic Supporting Information (ESI).

[1] a) B. D. Sherry, A. Fürstner, *Acc. Chem. Res.* **2008**, *41*, 1500; b) J. E. Zweig, D. E. Kim, T. R. Newhouse, *Chem. Rev.* **2017**, *117*, 11680; c) X. Du, Z. Huang, *ACS Catal.* **2017**, *7*, 1227; d) P. J. Chirik, *Angew. Chem. Int. Ed.* **2017**, *56*, 5170; e) R. L. Webster, *Dalton Trans.* **2017**, *46*, 4483; f) B. Su, Z.-C. Cao, Z.-J. Shi, *Acc. Chem. Res.* **2015**, *48*, 886; g) E. Buñuel, D. J. Cárdenas, *Chem. Eur. J.* **2018**, *24*, 11239; h) J. D. Sears, P. G. N. Neate, M. L. Neidig, *J. Am. Chem. Soc.* **2018**, *140*, 11872; i) K. Riener, S. Haslinger, A. Raba, M. P. Högerl, M. Cokoja, W. A. Herrmann, F. E. Kühn, *Chem. Rev.* **2014**, *114*, 5215; j) D. Wei, C. Darcel, *Chem. Rev.* **2019**, *119*, 2550; k) D. Bézier, J.-B. Sortais, C. Darcel, *Adv. Synth. Catal.* **2013**, *355*, 19; l) L. C. Misal Castro, H. Li, J.-B. Sortais, C. Darcel, *Green Chem.* **2015**, *17*, 2283.

[2] P. J. Chirik, K. Wieghardt, *Science* **2010**, *327*, 794.

[3] a) L. J. Taylor, D. L. Kays, *Dalton Trans.* **2019**, *48*, 12365; b) S. Roy, K. C. Mondal, H. W. Roesky, *Acc. Chem. Res.* **2016**, *49*, 357; c) P. P. Power, *Chem. Rev.* **2012**, *112*, 3482; d) A. A. Danopoulos, T. Simler, P. Braunstein, *Chem. Rev.* **2019**, *119*, 3730; e) G. Ung, J. C. Peters, *Angew. Chem. Int. Ed.* **2015**, *54*, 532; f) Y. Dong, M. I. Lipschutz, R. J. Witzke, J. A. Panetier, T. D. Tilley, *ACS Catal.* **2021**, *11*, 11160; g) S. Miyazaki, Y. Koga, T. Matsumoto, K. Matsubara, *Chem. Commun.* **2010**, *46*, 1932; h) S. Arata, Y. Sunada, *Dalton Trans.* **2019**, *48*, 2891.

[4] a) M. I. Lipschutz, T. Chantarojsiri, Y. Dong, T. D. Tilley, *J. Am. Chem. Soc.* **2015**, *137*, 6366; b) R. J. Witzke, D. Hait, K. Chakarawet, M. Head-Gordon, T. D. Tilley, *ACS Catal.* **2020**, *10*, 7800.

[5] D. Brenna, M. Villa, T. N. Gieshoff, F. Fischer, M. Hapke, A. Jacobi von Wangelin, *Angew. Chem. Int. Ed.* **2017**, *56*, 8451.

[6] H. R. Sharpe, A. M. Geer, H. E. L. Williams, T. J. Blundell, W. Lewis, A. J. Blake, D. L. Kays, *Chem. Commun.* **2017**, *53*, 937.

[7] H. R. Sharpe, A. M. Geer, W. Lewis, A. J. Blake, D. L. Kays, *Angew. Chem. Int. Ed.* **2017**, *56*, 4845.

[8] C. G. Werncke, I. Müller, *Chem. Commun.* **2020**, *56*, 2268.

[9] I. Müller, D. Munz, C. G. Werncke, *Inorg. Chem.* **2020**, *59*, 9521.

[10] R. Weller, I. Müller, C. Duhayon, S. Sabo-Etienne, S. Bontemps, C. G. Werncke, *Dalton Trans.* **2021**, *50*, 4890.

[11] a) S. A. Stoian, Y. Yu, J. M. Smith, P. L. Holland, E. L. Bominaar, E. Münck, *Inorg. Chem.* **2005**, *44*, 4915; b) A. Linden, L. Llovera, J. Herrera, R. Dorta, G. Agrifoglio, R. Dorta, *Organometallics* **2012**, *31*, 6162; c) Y. Yu, J. M. Smith, C. J. Flaschenriem, P. L. Holland, *Inorg. Chem.* **2006**, *45*, 5742.

[12] C. Chan, A. E. Carpenter, M. Gembicky, C. E. Moore, A. L. Rheingold, J. S. Figueroa, *Organometallics* **2019**, *38*, 1436.

[13] W. Bonrath, K. R. Pörschke, G. Wilke, K. Angermund, C. Krüger, *Angew. Chem. Int. Ed.* **1988**, *27*, 833.
[14] a) C. Martín, M. Sierra, E. Alvarez, T. R. Belderrain, P. J. Pérez, *Dalton Trans.* **2012**, *41*, 5319; b) A. A. Titov, V. A. Larionov, A. F. Smol'yakov, M. I. Godovikova, E. M. Titova, V. I. Maleev, E. S. Shubina, *Chem. Commun.* **2019**, *55*, 290.
[15] N. Krause, A. S. Hashmi (Hrsg.) *Modern allene chemistry*, Wiley-VCH, Weinheim, **2004**.
[16] a) M. Puerta, P. Valerga, *Coord. Chem. Rev.* **1999**, *193-195*, 977; b) Y. Wakatsuki, N. Koga, H. Yamazaki, K. Morokuma, *J. Am. Chem. Soc.* **1994**, *116*, 8105.
[17] C. Bruneau, P. H. Dixneuf, *Acc. Chem. Res.* **1999**, *32*, 311.
[18] R. Shintani, W.-L. Duan, S. Park, T. Hayashi, *Chem. Commun.* **2006**, 3646.
[19] a) M. Otsuka, N. Tsuchida, Y. Ikeda, Y. Kimura, Y. Mutoh, Y. Ishii, K. Takano, *J. Am. Chem. Soc.* **2012**, *134*, 17746; b) Y. Wakatsuki, *J. Organomet. Chem.* **2004**, *689*, 4092; c) E. Larionov, H. Li, C. Mazet, *Chem. Commun.* **2014**, *50*, 9816.
[20] Q. Liang, K. M. Osten, D. Song, *Angew. Chem. Int. Ed.* **2017**, *56*, 6317.
[21] R. Rochat, K. Yamamoto, M. J. Lopez, H. Nagae, H. Tsurugi, K. Mashima, *Chem. Eur. J.* **2015**, *21*, 8112.
[22] a) C. A. Brown, A. Yamashita, *J. Am. Chem. Soc.* **1975**, *97*, 891; b) S. Ma, Q. He, *Angew. Chem. Int. Ed.* **2004**, *43*, 988; c) A. Maercker, J. Fischenich, *Tetrahedron* **1995**, *51*, 10209; d) T. L. Jacobs, R. Akawie, R. G. Cooper, *J. Am. Chem. Soc.* **1951**, *73*, 1273.
[23] K. Avocetien, Y. Li, G. A. O'Doherty in *Modern alkyne chemistry*. *Catalytic and atom-economic transformations* (Hrsg.: B. M. Trost, C.-J. Li), Wiley-VCH Verlag GmbH & Co. KGaA, Weinheim, Germany, **2015**, S. 365–394.
[24] C. G. Werncke, P. C. Bunting, C. Duhayon, J. R. Long, S. Bontemps, S. Sabo-Etienne, *Angew. Chem. Int. Ed.* **2015**, *54*, 245.
[25] C.-Y. Lin, J. C. Fettinger, F. Grandjean, G. J. Long, P. P. Power, *Inorg. Chem.* **2014**, *53*, 9400.
[26] H. Bürger, U. Wannagat, *Monatsh. Chem.* **1963**, *94*, 1007.
[27] M. W. Rathke, *Org. Synth.* **1973**, *53*, 66.
[28] O. V. Dolomanov, L. J. Bourhis, R. J. Gildea, J. Howard, H. Puschmann, *J. Appl. Crystallogr.* **2009**, *42*, 339.
[29] G. M. Sheldrick, *Acta. Crystallogr. C* **2015**, *71*, 3.
[30] L. J. Farrugia, *J. Appl. Crystallogr.* **1999**, *32*, 837.
[31] *International tables for crystallography*, International Union of Crystallography; Springer, Chester, England, New York, **2006**.
[32] a) SADABS-2016/2, *Bruker*, **2016**; b) X.-R. 1. X-Area, *STOE*, **2016**.

Entry for the Table of Contents

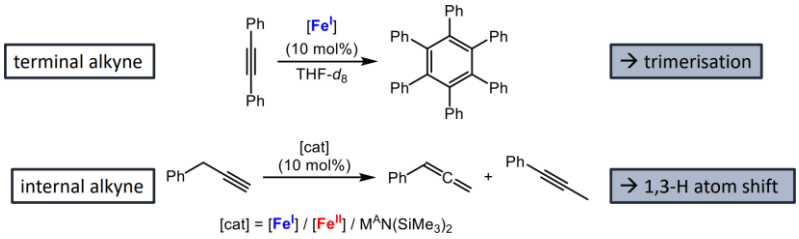

We examined the catalytic isomerisation of alkynes by low-valent and low-coordinate iron silylamides. This gives cyclotrimerisation of diphenyl acetylene as well as the 1,3-H shift for 3-phenyl propyne. The latter proceeds *via* intermediate formation of phenyl allene and likely *via* a deprotonation/reprotonation mechanism. It can also be catalyzed by simple alkali metal hexamethyldisilazanides.

Institute and/or researcher Twitter usernames: @wernckegunnar

5.5 „Magnetic Blocking in a Conformationally Restricted Quasilinear Iron(I) Silylamide”

Ruth Weller, Mihail Atanasov, Serhiy Demeshko, Ivan Mohelsky, Milan Orlita, Franc Meyer, Frank Neese , C. Gunnar Werncke

- Manuskript in Vorbereitung -

Abstract

The rational design for 3d-metal based single molecules requires a fundamental understanding of the intrinsic electronic properties and how they translate to experimentally observable features. Here, the isolation of the monomeric quasilinear iron(I) silylamide [KFe(N(Dipp)SiMe$_3$)$_2$], **1**, with intramolecular counter cation complexation is reported. Determination of its magnetic properties revealed magnetic blocking and a close-waist magnetic hysteresis below 4.5 K as well as a barrier for slow relaxation of magnetisation of U_{eff} = 184 cm^{-1}. This value corresponds well with a magnetic transition at 180 cm^{-1} as determined by field-dependent IR-spectroscopy, as well as dc-magnetic measurements (2D = 208 cm^{-1}). These observations can be perfectly described by ab-initio ligand field theory analysis (AILFT). It thereby shows that remarkable single molecule magnetic properties can be observed for two-coordinated iron(I) complexes in the presence of low-symmetric ligands like the used silylamide ligands in **1**.

Zusammenfassung

Das Interesse an 3d-Metall(I)-Komplexen mit einzelmolekülmagnetischem Verhalten ist groß. Bisherige strukturelle Konzepte konzentrieren sich auf die Konstruktion einer linearen Achse am zentralen Metallatom und eine hohe Symmetrie innerhalb des Komplexes. Auf diese Weise soll das Aufrechterhalten des Bahndrehimpulses und eine möglichst große Barriere des Spinumkehrs (U_{eff}) gewährleistet werden. In dieser Publikation wird die monomere und quasilineare Verbindung [KFe(N(Dipp)SiMe$_3$)$_2$], **1**, vorgestellt, in welcher das Kalium-Kation intramolekular interkaliert wird. Dies führt zur Fixierung der Silylamid-Liganden und einer verminderten Molekülsymmetrie. Dennoch zeigen magnetische Messungen eine ‚close-waist‘-Hysterese unterhalb der Blocktemperatur T_B von 4.5 K. Der Wert von U_{eff} (184 cm^{-1}) stimmt gut mit einem

magnetischen Übergang zwischen Grund- und erstem angeregten Zustand bei 180 cm^{-1} überein. Dieser wurde mittels feldabhängiger IR-Spektroskopie bestimmt und durch quantenchemische Berechnungen (mittels einer ab-initio Ligandfeldtheorie-Analyse, AILFT) bestätigt. Aufgrund der niedrigen Symmetrie der Liganden sowie der leichten Abwinklung der N−Fe−N-Achse sind die magnetischen Eigenschaften von **1** erstaunlich, da **1** als Einzelmolekülmagnet bezeichnet werden kann. Dieser Umstand widerspricht der vorgefassten Meinung, dass eine hohe Ligandsymmetrie (mindestens C_{3V}) essenziell für lineare SIMs ist und π/π*-Wechselwirkungen verhindert werden sollten. Die Synthese von **1** erweitert die synthetischen Möglichkeiten zur Konstruktion einkerniger SIMs.

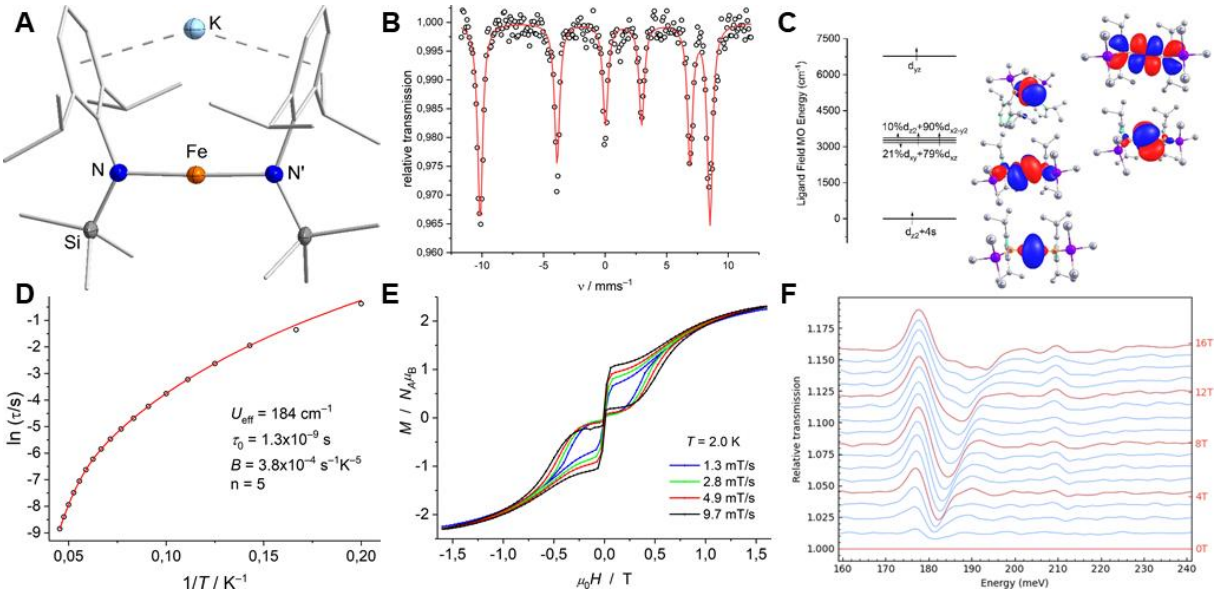

Abbildung 40. A: Molekülstruktur von **1**. H-Atome sind aus Gründen der Übersichtlichkeit nicht gezeigt; **B**: Mößbauer-Spektrum von **1** bei 7 K; **C**: d-Orbitalaufspaltung von **1** nach quantenchemischen Berechnungen (AILFT); **D**: Arrhenius-Plot von **1**; **E**: Magnetische Hystereseschleife von **1** bei unterschiedlichen Feldstärken bei 2 K; **F**: Fern-IR-Spektrum von **1** im magnetischen Feld (0 − 16 T)

Beiträge der Autoren

Die Synthese und Charakterisierung von Verbindung **1** lag in meiner Hand. Zudem war ich für die Aufnahme und Auswertung des ATR-IR-Spektrums sowie der Einkristallstrukturanalysenmessung am IPDS 2 der Firma STOE verantwortlich. Der dabei erhaltene Datensatz wurde von mir gelöst und verfeinert. Die Probenvorbereitung und Übermittlung zu den Kooperationspartnern wurden von mir organisiert. Dr. Serhiy Demeshko aus dem Arbeitskreis von Prof. Dr. Franc Meyer übernahm die Datenerfassung und Auswertung der ^{57}Fe Mößbauer spektroskopischen sowie magnetischen Messungen. Für die Durchführung der quantenchemischen Berechnungen waren Prof. Dr. Mihail Atanasov und Prof. Dr. Frank Neese zuständig.

Das Spektrum der Magneto-IR-Spektroskopie wurde von Ivan Mohelsky in der Arbeitsgruppe von Dr. Milan Orlita aufgenommen und ausgewertet. Die elementaranalytische Untersuchung von **1** wurde von mir vorbereitet und durch die hausinterne Abteilung für Massenspektrometrie und Elementanalytik des Fachbereichs Chemie der Philipps-Universität Marburg unter der Leitung von Dr. Uwe Linne durchgeführt. Das Manuskript wurde von Dr. C. Gunnar Werncke mit Unterstützung aller am Manuskript beteiligten Personen verfasst.

COMMUNICATION

Magnetic Blocking in a Conformationally Restricted Quasilinear Iron(I) Silylamide

Ruth Weller,[a] Mihail Atanasov,[b] Serhiy Demeshko,[c] Ivan Mohelsky,[d] Milan Orlita,[d] Franc Meyer,[c] Frank Neese,[b] C. Gunnar Werncke[a]

[a] M. Sc. R. Weller, Dr. C. G. Werncke Title(s)
Department of Chemistry
Philipps-University Marburg
Hans-Meerwein-Straße 4, 35043 Marburg, Germany
E-mail: gunnar.werncke@chemie.uni-marburg.de
[b] Dr. S. Demeshko, Prof. Dr. F. Meyer
Institut für Anorganische Chemie
Universität Göttingen
Tammannstr. 4, D-37077 Göttingen, Germany
[c] Prof. D. M. Atanasov, Prof. Dr. F. Neese
Max-Planck-Institut für Kohlenforschung
Kaiser-Wilhelm-Platz 1, 45470 Mülheim an der Ruhr, Germany
[b] I. Mohelsky, Dr. M. Orlita
LAB National des Champs Magnétiques Intenses
LNCMI - CNRS
25 Martyrs Avenue, BP 166, 38042 Grenoble Cedex 9, France

Supporting information for this article is given via a link at the end of the document.

Abstract: The rational design for 3d-metal based single molecules requires a fundamental understanding of the intrinsic electronic properties and how they translate to experimentally observable features. Here, the isolation of the monomeric quasilinear iron(I) silylamide [KFe(N(Dipp)SiMe$_3$)$_2$], **1**, with intramolecular counter cation complexation is reported. Determination of its magnetic properties revealed magnetic blocking and a close-waist magnetic hysteresis below 4.5 K as well as a barrier for slow relaxation of magnetisation of U_{eff} = 184 cm^{-1}. This value corresponds well with a magnetic transition at 180 cm^{-1} as determined by field-dependent IR-spectroscopy, as well as dc-magnetic measurements (2D = 208 cm^{-1}). These observations can be perfectly described by ab-initio ligand field theory analysis (AILFT). It thereby shows that remarkable single molecule magnetic properties can be observed for two-coordinated iron(I) complexes in the presence of low-symmetric ligands like the used silylamide ligands in **1**.

Single-molecule magnets (SMMs) have attained considerable interest as they pose potential for future applications in high-density information storage,[1] quantum computing,[2] and magnetic refrigeration.[3] SMMs are open-shell complexes that display slow relaxation of magnetisation that originates from the intrinsic properties of the molecular system.[4] When the complexes contain only one metal ion, they are also denoted single-ion magnets (SIMs). The key feature is the presence of large magnetic anisotropy that arises from partially filled, energetically degenerated orbitals. This can be prominently observed for trivalent lanthanide complexes, since valence 4f orbitals of Ln^{3+} are only little affected by the ligands, which allows for the coupling of non-zero orbital angular momentum with the total spin S. It gives rise to a total angular moment J, and with this a potentially large magnetic anisotropy. This has been exploited for a number of recent examples of lanthanide complexes that display large effective barriers to reversal of magnetisation (U_{eff}) and high magnetic blocking temperatures T_B. [Dy(Cp^{ttt})$_2$]$^+$ (Cp^{ttt} = 1,2,4-tri(*tert*-butyl)cyclopentadienyl) and [(Cp^{iPr5})Dy(Cp*)]$^+$ (Cp* = pentamethylcyclopentadienyl, Cp^{iPr5} = penta-*iso*-propylcyclopentadienyl) reaching T_B of 60 K and 80 K, respectively.[5]

In contrast, 3d-transition metal based SIMs face several disadvantages with regards to their lanthanide counterparts. They possess smaller magnetic moments and spin-orbit coupling constants. More importantly, strong interaction of the d-orbitals with the ligand field leads to quenching of first-order orbital contributions to the magnetic moment. Recently, it has been shown that these disadvantages can in principal be overcome for 3d-metals in a linear ligand arrangement.[6–9,10] Here, the two-coordinated metal ion can exhibit virtually unquenched orbital angular momentum due to the unusually weak ligand field and the energetic indifference to Jahn-Teller distortions.[11] As such it mimics the situation found for lanthanides. The seminal example in this regard is [Fe(C(SiMe$_3$)$_3$)$_2$]$^-$ with an effective relaxation barrier of 226 cm^{-1} at zero field with the first-time observation of magnetic blocking for a mononuclear 3d-transition metal system.[6,12]

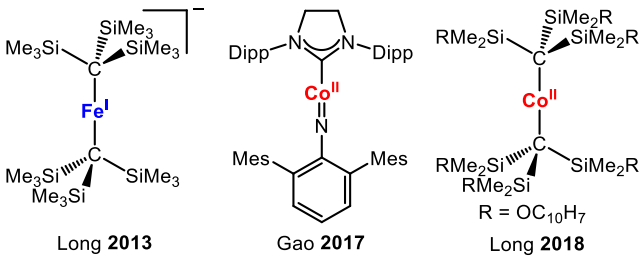

Long **2013** Gao **2017** Long **2018**

Scheme 1. Known linear 3d-metal complexes with observable magnetic blocking at low temperatures.[6–8]

More recently, two remarkable reports concerned linear cobalt(II) complexes (S = 3/2), namely [(NHC)Co(NAr*)] (U_{eff} = 413 cm^{-1})[8] and more importantly [Co(CMe$_2$OR)$_2$] with a non-Aufbau principle

L = 3 ground state with U_{eff} = 450 cm^{-1}.[7] The latter value is connected to the transition from M_J = ±9/2 to ±7/2, with a calculated separation of 476 cm^{-1}. The value is close to the calculated theoretical maximum for 3d-metals, which was detected for singly coordinated cobalt ad-atoms on a MgO surface.[13] The presence of a S = 3/2 ion in a (quasi)linear environment is thereby no sufficient criterion for the observation of magnetic blocking behaviour as it is absent for a few other quasilinear iron(I) complexes.[9,14] Hence, it implies that also other factors are in play, too, such as vibronic coupling or slight lifting of orbital degeneracy due to deviations from linearity. Some of us reported for example on K{crypt.222}[Fe(N(SiMe$_3$)$_2$)$_2$], which also showed slow relaxation of magnetisation in the absence of an applied dc-field with U_{eff} = 64 cm^{-1}.[9] This is significantly lower than for the seminal C_{3v}-symmetric [Fe(C(SiMe$_3$)$_3$)$_2$]$^-$, although ab-initio ligand-field theory (AILFT) indicated similar reversal barriers as expressed by the energy spacing between the ground and first excited M_J states.[15] This was attributed to the lower steric demand as well as the lower symmetry (C_{2V}) of the −N(SiMe$_3$)$_2$ ligands.

Herein, we report on the isolation and crystallisation of monomeric [KFe(N(Dipp)SiMe$_3$)$_2$], (Dipp = 2,6-di-*iso*-propylphenyl) with quasilinear N−Fe−N axis caused by an intramolecular potassium ion complexation. Comprehensive analysis of the magnetic properties revealed magnetic blocking below 4.5 K and an effective relaxation barrier of U_{eff} = 184 cm^{-1}. The latter corresponds to the energy spacing between the ground and first excited state obtained from magnetometry, and it was directly probed by magneto-IR-spectroscopy, the results being in full agreement with ab-initio ligand field analysis.

Initially, [KFe(N(Dipp)SiMe$_3$)$_2$], synthesized from KC_8 and [Fe(N(Dipp)SiMe$_3$)$_2$], was obtained as a polymeric compound with the potassium ions linking neighbouring iron(I) amides *via* the aryl rings.[16] However, when the reaction mixture was carried out in toluene, filtered after a few minutes and stored at −40°C without layering with *n*-pentane, this gave consistently monomeric [KFe(N(Dipp)SiMe$_3$)$_2$] (**1**) as dark red crystals, suitable for x-ray diffraction analysis (yield 88%, **Scheme 2**).

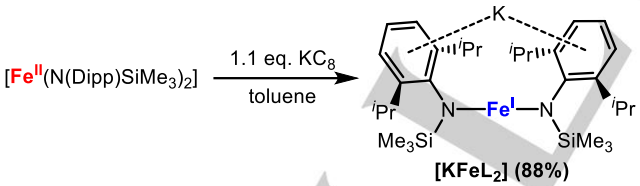

Scheme 2. Synthesis of [KFe(N(Dipp)SiMe$_3$)$_2$] (**1**).

In solid state it shows a neutral, monomeric structure with the potassium ion encapsulated by aryl rings within the ligand sphere (**Figure 1**), akin to related nickel and cobalt examples.[16,17] Accordingly, the Dipp-moieties are directly opposing each other (torsion angle of 0.3(3)°). The N−Fe−N angle is nearly linear (177.79(18)°). Disregarding small deviations, the compound can be thus attributed as C_v-symmetric.

Compound **1** was characterized by ^{57}Fe Mössbauer spectroscopy. At 80 K, no signal was observed. This phenomenon is not unexpected as it was already observed for the related iron(I) silylamide [Fe(N(SiMe$_3$)$_2$)$_2$]$^-$ and can be attributed to magnetic relaxation processes. At 7 K, the spectrum shows a sharp sextuplet with an isomer shift of δ = 0.34 mm/s, ΔE_Q = −2.31 mm/s and an internal field of H_{int} = 58.0 T, which is characteristic for linear iron complexes.[6,9,11,18]

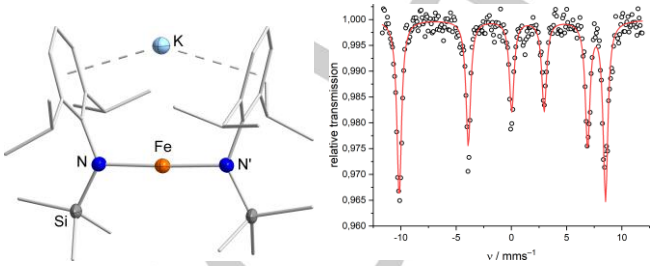

Figure 1. Left: Crystal structure of **1**. All hydrogen atoms are omitted for clarity. Selected bond lengths and angles: Fe−N 1.914(3) Å, K−Fe 3.5308(16) Å, K−Aryl 2.9290(5) Å, N−Fe−N' 177.79(18)°, torsion angle: 0.3(3)°. Right: Mössbauer spectrum of **1** at 7 K. Parameters: δ = 0.34 mm/s, ΔE_Q = −2.31 mm/s, H_{int} = 58.0 T.

Next, we turned to magnetic measurements of solid samples between 2 and 210 K (**Figure 2**). Higher temperatures were not measured to prevent melting of the perfluorinated oil used for fixating the crystals of **1**. At 200 K, the $\chi_M T$ value amounts to 3.63 cm^{3}Kmol^{-1}. Upon lowering the temperature a slight increase to 3.65 cm^{3}Kmol^{-1} at 150 K is observed, which speaks to a degenerate ground state. The curve then steadily decreases to 3.13 cm^{3}Kmol^{-1} at 10 K, which is typical for transition metal complexes with contributions from first order angular momentum. A further sharp drop to 2.73 cm^{3}Kmol^{-1} at 2 K is observed. Together with variable temperature − variable field (VTVH) magnetisation measurements the curves could be satisfactory modelled as a two-level system for an axial iron(I) with S = 3/2 (E/D = 0) using the spin Hamiltonian with Zeeman and zero field splitting $\hat{H} = \mu_B \vec{B} \boldsymbol{g} \vec{S} + D[\hat{S}_z^2 - \frac{1}{3}S(S+1) + {}^{E}/_{D}(\hat{S}_x^2 - \hat{S}_y^2)]$: This gave $g_x = g_y$ = 2.27 (±1.22), g_z = 3.31 (±0.01) and D = −104 cm^{-1} (±116), although with a large confidence interval (especially for D). Frequency dependent ac magnetic susceptibility measurements at various temperatures were performed to determine the relaxation barrier U_{eff}, for which an external magnetic field of 1000 Oe was used. Arrhenius plot of the temperature dependence clearly deviated from the linear Arrhenius law, so additional relaxation processes were considered (direct, Raman, Orbach processes and quantum tunnelling of the magnetization (QTM)). For **1**, the entire temperature range could be well fitted assuming Raman and Orbach relaxation pathways, using $\tau^{-1} = BT^n + \tau_0^{-1} \exp(-U_{eff}/k_B T)$. This gave U_{eff} = 184 cm^{-1} with B = 3.8·10^{-4} s^{-1}K^{-5}, n = 5, and τ_0 = 1.3·10^{-9} s. **1** also showed magnetic hysteresis below 4.5 K. The hysteresis is waist-restricted, which is attributed to rapid relaxation due to quantum tunnelling in the absence of any external field. These observations are comparable to those made for [Fe(C(SiMe$_3$)$_3$)$_2$]$^-$ and [Co(CMe$_2$OR)$_2$],[6,7] whereas [Co(NAr*)(IDipp)] displayed an open hysteresis.[8] The appearance of a hysteresis loop indicated magnetic blocking at low temperatures, and indeed zero-field cooled measurements revealed such a behaviour below 4.5 K.

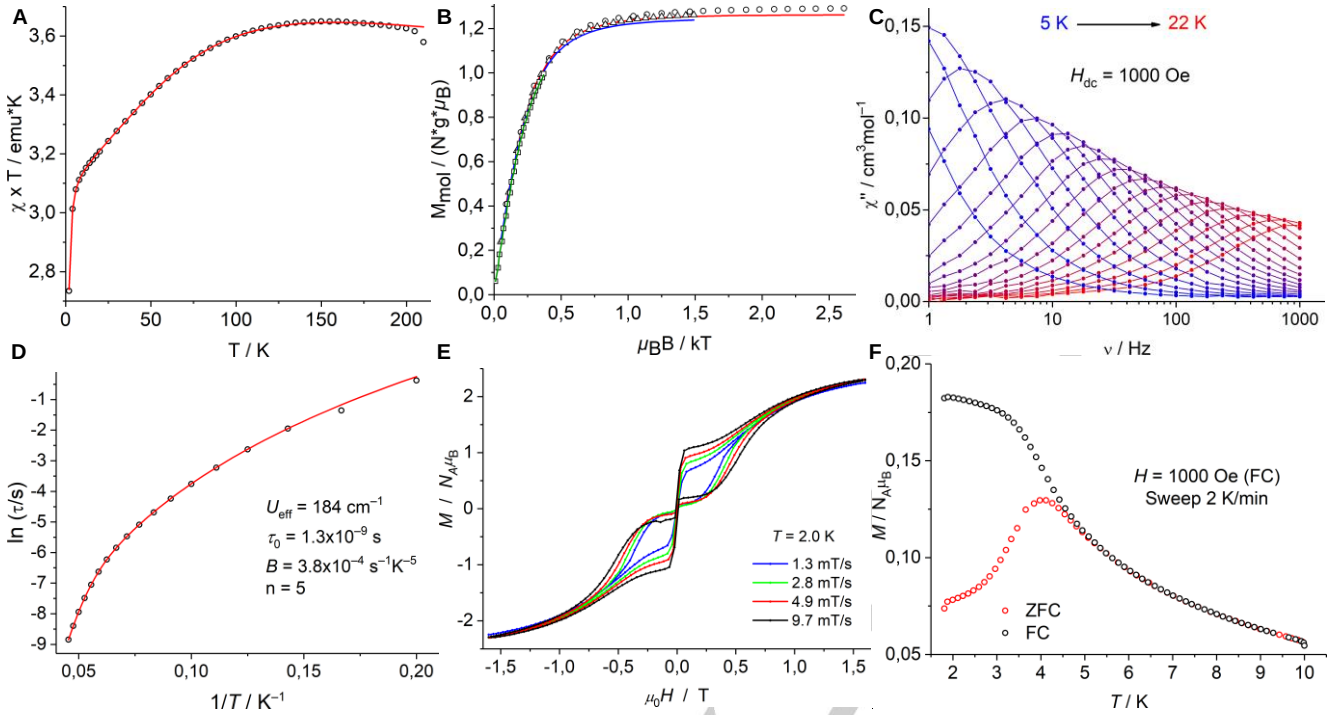

Figure 2. A) Temperature dependence of $\chi_M T$ at 5000 Oe between 2 and 210 K; **B**) VTVH magnetisation measurements at 1, 4 and 7 T; **C**) Frequency dependence of χ'' at various temperatures (ΔT = 1 K) with an applied dc field of H_{dc} = 1000 Oe; **D**) Arrhenius-Plot of the temperature dependence of τ at H_{dc} = 1000 Oe; **E**) Magnetic hysteresis loop for various field sweep rates at 2.0 K; **F**: Zero-field-cooled/field-cooled (ZFC/FC) magnetisation measurements.

To better understand the electronic situations, we turned to ab-initio ligand field analysis[19] (NEVPT2/CASCF level), which has proven as a powerful tool for delineation of single-molecule magnetic features. Looking at the orbital splitting, it gives an orbital ordering of d_{z^2}+4s, nearly degenerate d_{xy}, d_{xz} and $d_{x^2-y^2}$ and highest lying d_{yz}, which is similar to the one of the C_{2v}-symmetric $[Fe(N(SiMe_3)_2)_2]^-$.[9] The ^{4}E ground state splits into four doublets, which are best characterised by the magnetic quantum number M_J (J = total angular moment). The four doublets would then correspond to M_J = ±7/2, ±5/2, ±3/2 and ±1/2, with an energy spacing between the lowest doublets (M_J = ±7/2, ±5/2) of 212 cm^{-1}. The M_J = ±7/2 ground state is highly anisotropic (g_x = g_y = 0.018, g_z = 9.876). The energy spacing is in excellent agreement from the value obtained from the temperature dependent susceptibility data (2D = 208 cm^{-1}). The less axial anisotropic first excited magnetic state M_J = ±5/2 (g_x = g_y = 2.271, g_z = 5.321) indicates that the magnetic relaxation in **1** likely occurs *via* through-barrier tunnelling of the excited state.

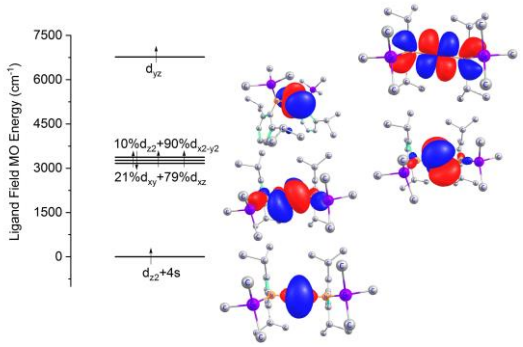

Figure 3. d-Orbital splitting from ab-initio ligand field analysis.

To confirm the experimentally and computationally determined energy spacing between the ground and first excited M_J state, we turned to field-dependent IR spectroscopy of the far-red region. This is of special importance as the common determination of D *via* the magnetisation data is subject to the fitting procedure, as can be seen by a large confidence interval (*vide supra*) and further provides only an indirect measure for the excitation from the ground to the excited state. Vibrational spectra were recorded in applied field B ranging from 0 to 16 T in the range from 100 – 400 cm^{-1} at 4 K. A field dependent absorption band was detected at 178 cm^{-1} (1 T). This is in the range of the computed (212 cm^{-1}) and experimentally determined (208 cm^{-1}) energy spacing between the ground and the first excited magnetic state. Increasing the field to 16 T leads to a blue shift of 14 cm^{-1} that perfectly matches the expected value of 15 cm^{-1}, which arises from different field dependencies of the energies of the involved states.

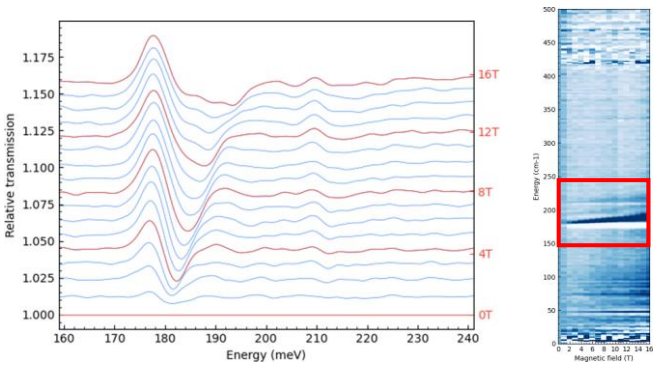

Figure 4. Far-IR region of complex **1** under an applied field (0 − 16 T). The different spectra are given in relation to the zero field spectrum.

Overall, we present the single-molecule magnetic behaviour of the quasilinear complex [KFe(N(Dipp)SiMe$_3$)$_2$] with intramolecular fixation of the amide ligand *via* secondary potassium complexation. This compound shows a close-waist hysteresis and magnetic blocking below 4.5 K as well as a barrier for slow relaxation of magnetisation of 184 cm^{-1}. Using ab-initio ligand field analysis as well as magneto-IR-spectroscopy, this behaviour could be rationalized. The remarkable magnetic features of the iron(I) silylamide are present despite its rather anisotropic, low-symmetric ligands and slight deviations from linearity. It goes against the preconceived notion that a high symmetry of the ligand architecture (C_{3V}) should be present for linear SMMs, and that π/π^*-interactions with the ligands should be avoided. This expands the synthetic possibilities beyond metal methanides for mononuclear transition metal complexes showing magnetic blocking and may inspire the development of other quasilinear ligand architectures.

Conflicts of interest

"There are no conflicts to declare."

Acknowledgements

F.M. acknowledges support of this work from the Deutsche Forschungsgesellschaft (DFG, Research Training Group BENCh, RTG 2455). C. G. W. thanks the DFG (grant WE 5627/4-1) and the Philipps-University for financial support.

Keywords: single molecule magnet • linear iron(I) • silylamides • ab-initio ligand field theory • Mössbauer spectroscopy

[1] M. Mannini, F. Pineider, P. Sainctavit, C. Danieli, E. Otero, C. Sciancalepore, A. M. Talarico, M.-A. Arrio, A. Cornia, D. Gatteschi et al., *Nature materials* **2009**, *8*, 194.

[2] a) P. C. E. Stamp, A. Gaita-Ariño, *J. Mater. Chem.* **2009**, *19*, 1718; b) A. Ardavan, O. Rival, J. J. L. Morton, S. J. Blundell, A. M. Tyryshkin, G. A. Timco, R. E. P. Winpenny, *Phys. Rev. Lett.* **2007**, *98*, 57201; c) M. N. Leuenberger, D. Loss, *Nature* **2001**, *410*, 789; d) E. Moreno-Pineda, W. Wernsdorfer, *Nat Rev Phys* **2021**.

[3] a) F. Torres, J. M. Hernández, X. Bohigas, J. Tejada, *Appl. Phys. Lett.* **2000**, *77*, 3248; b) Y.-Z. Zheng, G.-J. Zhou, Z. Zheng, R. E. P. Winpenny, *Chem. Soc. Rev.* **2014**, *43*, 1462.

[4] J. M. Frost, K. L. M. Harriman, M. Murugesu, *Chem. Sci.* **2016**, *7*, 2470.

[5] a) F.-S. Guo, B. M. Day, Y.-C. Chen, M.-L. Tong, A. Mansikkamäki, R. A. Layfield, *Angew. Chem. Int. Ed.* **2017**, *56*, 11445; b) C. A. P. Goodwin, F. Ortu, D. Reta, N. F. Chilton, D. P. Mills, *Nature* **2017**, *548*, 439; c) F.-S. Guo, B. M. Day, Y.-C. Chen, M.-L. Tong, A. Mansikkamäki, R. A. Layfield, *Science* **2018**, *362*, 1400.

[6] J. M. Zadrozny, D. J. Xiao, M. Atanasov, G. J. Long, F. Grandjean, F. Neese, J. R. Long, *Nature Chem.* **2013**, *5*, 577.

[7] P. C. Bunting, M. Atanasov, E. Damgaard-Møller, M. Perfetti, I. Crassee, M. Orlita, J. Overgaard, J. van Slageren, F. Neese, J. R. Long, *Science* **2018**, *362*.

[8] X.-N. Yao, J.-Z. Du, Y.-Q. Zhang, X.-B. Leng, M.-W. Yang, S.-D. Jiang, Z.-X. Wang, Z.-W. Ouyang, L. Deng, B.-W. Wang et al., *J. Am. Chem. Soc.* **2017**, *139*, 373.

[9] C. G. Werncke, P. C. Bunting, C. Duhayon, J. R. Long, S. Bontemps, S. Sabo-Etienne, *Angew. Chem. Int. Ed.* **2015**, *54*, 245.

[10] a) W. Alexander Merrill, T. A. Stich, M. Brynda, G. J. Yeagle, J. C. Fettinger, R. D. Hont, W. M. Reiff, C. E. Schulz, R. D. Britt, P. P. Power, *J. Am. Chem. Soc.* **2009**, *131*, 12693; b) A. M. Bryan, C.-Y. Lin, M. Sorai, Y. Miyazaki, H. M. Hoyt, A. Hablutzel, A. LaPointe, W. M. Reiff, P. P. Power, C. E. Schulz, *Inorg. Chem.* **2014**, *53*, 12100.

[11] W. M. Reiff, A. M. LaPointe, E. H. Witten, *J. Am. Chem. Soc.* **2004**, *126*, 10206.

[12] J. M. Zadrozny, D. J. Xiao, J. R. Long, M. Atanasov, F. Neese, F. Grandjean, G. J. Long, *Inorg. Chem.* **2013**, *52*, 13123.

[13] I. G. Rau, S. Baumann, S. Rusponi, F. Donati, S. Stepanow, L. Gragnaniello, J. Dreiser, C. Piamonteze, F. Nolting, S. Gangopadhyay et al., *Science* **2014**, *344*, 988.

[14] a) P. P. Samuel, K. C. Mondal, N. Amin Sk, H. W. Roesky, E. Carl, R. Neufeld, D. Stalke, S. Demeshko, F. Meyer, L. Ungur et al., *J. Am. Chem. Soc.* **2014**, *136*, 11964; b) U. Chakraborty, S. Demeshko, F. Meyer, C. Rebreyend, B. de Bruin, M. Atanasov, F. Neese, B. Mühldorf, R. Wolf, *Angew. Chem. Int. Ed.* **2017**, *56*, 7995.

[15] C. G. Werncke, E. Suturina, P. C. Bunting, L. Vendier, J. R. Long, M. Atanasov, F. Neese, S. Sabo-Etienne, S. Bontemps, *Chem. Eur. J.* **2016**, *22*, 1668.

[16] R. Weller, I. Müller, C. Duhayon, S. Sabo-Etienne, S. Bontemps, C. G. Werncke, *Dalton Trans.* **2021**, *50*, 4890.

[17] M. I. Lipschutz, X. Yang, R. Chatterjee, T. D. Tilley, *J. Am. Chem. Soc.* **2013**, *135*, 15298.

[18] W. M. Reiff, C. E. Schulz, M.-H. Whangbo, J. I. Seo, Y. S. Lee, G. R. Potratz, C. W. Spicer, G. S. Girolami, *J. Am. Chem. Soc.* **2009**, *131*, 404.

[19] M. Atanasov, D. Ganyushin, K. Sivalingam, F. Neese in *Structure and Bonding*, *Vol. 143* (Eds.: D. M. P. Mingos, P. Day, J. P. Dahl), Springer Berlin Heidelberg, Berlin, Heidelberg, **2012**, pp. 149–220.

5.6 „NHC-Stabilized Parent Phosphinidene Adducts of Metal(II) Hexamethyldisilazanides of Manganese − Cobalt and Their Lability in Solution”

Ruth Weller, Andres Gonzalez, Hannah Gottschling, Carsten von Hänisch, C. Gunnar Werncke

- eingereichtes Manuskript -

Abstract

The behavior between the *N*-heterocyclic carbene (NHC) stabilized parent phosphinidene [(sIDipp)PH] (Dipp = 2,6-di-*iso*-propylphenyl) and 3d-metal(II)-hexamethyldisilazanides is described. In solid state, the three-coordinated phosphinidene adducts [M(PH(sIDipp))(N(SiMe$_3$)$_2$)$_2$] (M = Mn − Co) are obtained. In solution, all compounds exhibit strong paramagnetism that allowed further NMR spectroscopic examinations only for cobalt. At room temperature, the system is highly fluxional, which can be overcome by cooling down to 193 K. This is further corroborated by ^{31}P NMR spectroscopy observations as small amounts of free phosphinidene can be observed at low temperatures. This implicates that in part ligand coordination competes with [M(N(SiMe$_3$)$_2$)$_2$] dimerisation and an overall weak binding of the phosphinidene. This was confirmed by adding one equivalent of PCy$_3$ to [M(PH{sIDipp})(N{SiMe$_3$}$_2$)$_2$], which leads to statistical ligand exchange (50%).

Zusammenfassung

In der Literatur sind kaum offenschalige 3d-Metall(II)-Phosphan-Komplexe bekannt. Da die Donorstärke von Phosphinidenen mit der des NHCs IDipp vergleichbar ist,[255] beschäftigt sich das vorliegende Manuskript mit der Umsetzung der 3d-Metall(II)-Hexamethyldisilazane [M(N(SiMe$_3$)$_2$)$_2$] (M = Mn − Co) mit dem ‚parent‘ Phosphiniden [(sIDipp)PH]. Aufgrund der hohen Basizität des Phosphiniden-H-Atoms findet die erwartete Ligandaustauschreaktion unter Abspaltung von HN(SiMe$_3$)$_2$ jedoch nicht statt. Stattdessen werden die dreifach-koordinierten Phosphiniden-Addukte [M(PH(sIDipp))(N(SiMe$_3$)$_2$)$_2$] (**[M]**, M = Mn − Co) gebildet. Im Festkörper besitzen die Addukte eine verzerrt T-förmige Geometrie am Metallzentrum mit einer langen M−P-Distanz von 2.45 Å (**[Co]**) − 2.60 Å (**[Mn]**). In Zusammenhang mit einer, verglichen mit

freiem [(sIDipp)PH] (1.7426(19) Å), nur leicht verlängerten P−C1-Bindung von 1.7492(19) Å ([**Fe**]) − 1.784(3) Å ([**Co**]) , lässt dies auf lediglich schwache σ- und π-Elektronendonierung vom Phosphoratom auf das Metall(II)-Fragment schließen.

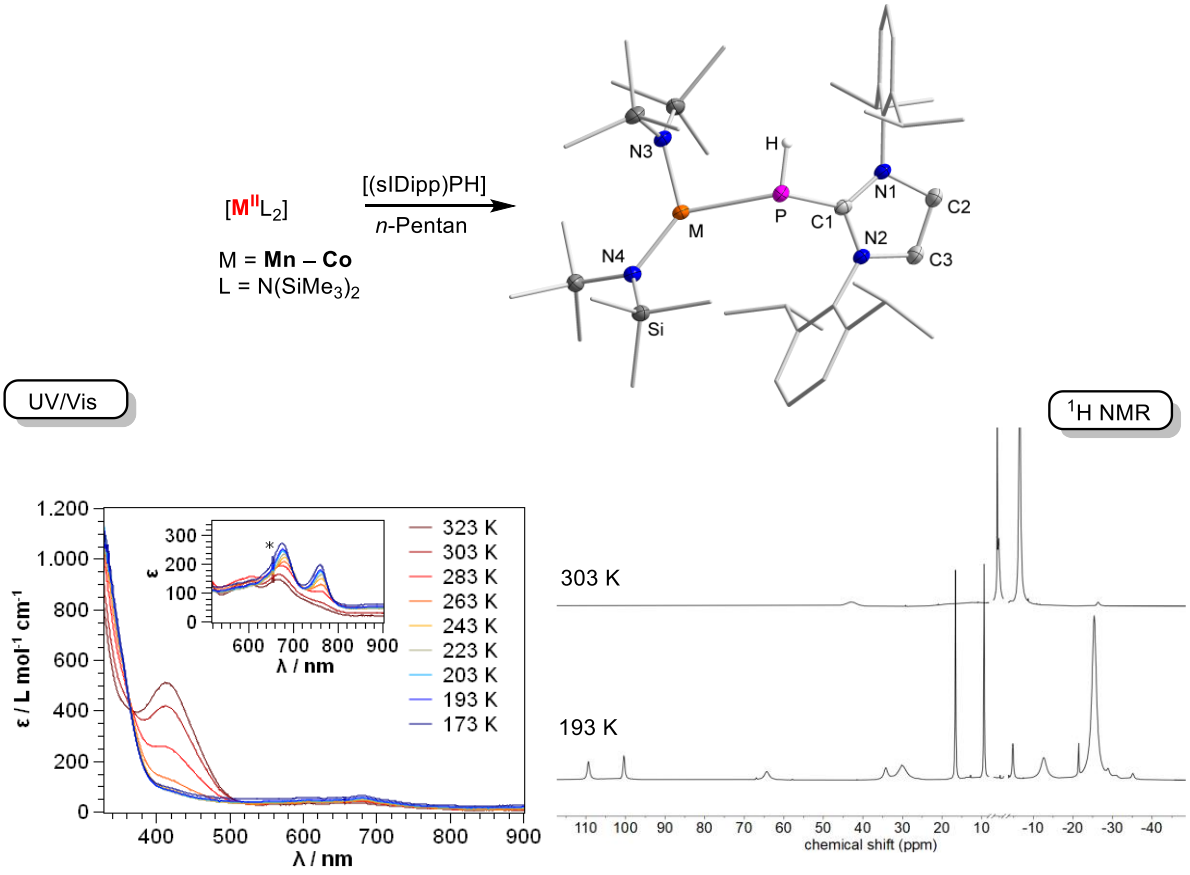

Abbildung 41. Veranschaulichung der labilen Adduktbildung bei Umsetzung des ‚parent' Phosphinidens [(sIDipp)PH] mit den zweifach-koordinierten [M(N(SiMe$_3$)$_2$)$_2$].

Die nur geringe Koordination des Phosphinidens an das elektronisch und koordinativ ungesättigte Metall(II)-Zentrum kann durch NMR-spektroskopische Messreihen im nicht-koordinierenden Lösungsmittel Toluol-d_8 bestätigt werden. Aufgrund der Nähe zu den stark paramagnetischen Metallzentren sind bei Raumtemperatur keine Signale im ^{31}P-NMR Spektrum detektierbar. Selbst durch Zugabe weiterer Äquivalente Phosphiniden entsteht kein Signal. Im ^{1}H-NMR Spektrum unterbinden die paramagnetischen Zentren ebenfalls mögliche Signalzuordnungen. Erstaunlicherweise ist dies auch in **[Co]** der Fall, obwohl die Signale in ^{1}H-NMR Spektren ähnlicher Kobalt(II)-Verbindungen üblicherweise relativ scharf und gut zuordenbar sind.[32,178,179,256] Erst durch die schrittweise Kühlung auf bis zu 193 K wird eine partielle Signalzuordnung ermöglicht. Diese Beobachtungen lassen auf fortwährende De- bzw. Rekoordinierungprozesse schließen, welche erst bei tiefen Temperaturen unterdrückt werden. Die Labilität der Metall-Phosphiniden-Addukte

kann auch durch weitere NMR-spektroskopische Messreihen, wie die Zugabe der LEWIS-Basen PCy_3 oder Et_2O, gezeigt werden. Temperaturabhängige UV/Vis-Messreihen liefern analoge Ergebnisse. In **[Co]** ist gerade bei hohen Temperaturen (263 − 323 K) stets ein kleiner Anteil des freien und monomeren $[Co(N(SiMe_3)_2)_2]$ präsent. Gleichzeitig ist in **[Co]** eine schwache Absorptionsbande (λ = 760 nm), die d-d-Übergängen zugeschrieben wird, nur bei tiefen Temperaturen sichtbar.
Der Versuch, die anfänglich erwünschte Ligandaustauschreaktion durch Erhitzen des Systems hervorzurufen, scheiterte. Statt eine intramolekulare Deprotonierung zu erzielen, wird lediglich Addukt-freies $[M(N(SiMe_3)_2)_2]$ destillativ aus dem Reaktionsgemisch entfernt.

Beiträge der Autoren

Die Planung und Durchführung des Projektes sowie die Synthese und Charakterisierung aller neuen Verbindungen (**[Mn]** − **[Co]**) lag in meiner Hand. Die Komplexe **[Co]** und **[Fe]** wurden jedoch zuvor von Andres Gonzalez unter meiner Leitung im Rahmen eines Vertiefungspraktikums dargestellt. Alle von ihm erhaltenen Ergebnisse wurden von mir reproduziert, ergänzt und für diese Publikation aufbereitet. Der Präkursor [(sIDipp)PH] wurde von Hannah Gottschling bzw. Markus Balmer im Arbeitskreis von Prof. Dr. Carsten von Hänisch dargestellt und für dieses Projekt zur Verfügung gestellt. Ich war für die Aufnahmen der Daten von **[Mn]** und **[Fe]**, gemessen am Diffraktometer IPDS2 der Firma STOE, zuständig. Die Daten für **[Co]** wurden von Dr. C. Gunnar Werncke am Quest D8 Diffraktometer der Firma BRUKER aufgenommen. Alle Datensätze, die mittels Einkristallstrukturanalyse erhalten wurden, wurden von mir gelöst und verfeinert. Mit der Unterstützung der hausinternen NMR-Abteilung des Fachbereichs Chemie der Philipps-Universität Marburg unter der Leitung von Dr. Xiulan Xie nahm ich alle ^{1}H- und ^{31}P-NMR spektroskopischen Untersuchungen sowie Evans-Messungen auf und wertete diese selbständig aus. IR-Messungen wurden von Andres Gonzalez und mir aufgenommen und von mir ausgewertet. Das Manuskript wurde von mir in Zusammenarbeit mit Dr. C. Gunnar Werncke und mit der Unterstützung von Prof. Dr. Carsten von Hänisch verfasst.

ARTICLE

NHC-Stabilized Parent Phosphinidene Adducts of Metal(II) Hexamethyldisilazanides of Manganese – Cobalt and Their Lability in Solution

Ruth Weller,[a] Andres Gonzalez,[a] Hannah Gottschling,[a] Carsten von Hänisch,[a] C. Gunnar Werncke*[a]

[a] R. Weller, A. Gonzalez, H. Gottschling, Prof. Dr. C. von Hänisch, Dr. C. G. Werncke
Department of Chemistry
Philipps-Universität Marburg
Hans-Meerwein-Straße 4, D- 35032 Marburg, Germany
E-Mail: gunnar.werncke@chemie.uni-marburg.de

Supporting information for this article is given *via* a link at the end of the document

Abstract: The behavior of the *N*-heterocyclic carbene (NHC) stabilized 'parent' phosphinidene [(sIDipp)PH] (Dipp = 2,6-di-*iso*propylphenyl) towards 3d-metal(II) hexamethyldisilazanides is described. In solid state, the three-coordinated phosphinidene adducts [M{PH(sIDipp)}{N(SiMe$_3$)$_2$}$_2$] (M = Mn − Co) are obtained. In solution, all compounds exhibit strong paramagnetism that limited further NMR spectroscopic examinations to cobalt. At room temperature, the system is highly fluxional, which can be overcome by cooling down to 193 K. This is further corroborated by ^{31}P NMR spectroscopy observations as small amounts of free phosphinidene can be observed at low temperatures. This implicates that in part ligand coordination competes with [M{N(SiMe$_3$)$_2$}$_2$] dimerisation and an overall weak binding of the phosphinidene ligand. As such it can be partially displaced by a phosphine (PCy$_3$) or even diethyl ether with persisting chemical exchange in solution.

Introduction

N-Heterocyclic carbene phosphinidene adducts [(NHC)PR] (R = aryl, SiMe$_3$, H) have enjoyed attention over the last decades since their discovery in 1997 by ARDUENGO *et al*.[1] Their electronic structure is described best within the continuum between a phosphaalkene and a NHC-stabilized phosphinidene.[2] This leads to an electron rich phosphorous atom with strong donor capabilities of the [PR] fragment. This moiety has been exploited for the formation of a limited number of main group (R = Ph[3] or H[4]) and transition metal adducts (R = SiMe$_3$,[5] aryl[5–9] or H[6,10–14]). Concerning transition metal complexes, all examples are stable 18 valence electron complexes, in which the use of the NHC-stabilized 'parent' phosphinidenes [(NHC)PH] is predominant.[6,10–13] For example, carbonyl complexes of group 6 ([M(CO)$_5$L; M = Cr, Mo, W)[6,12,14] as well as of iron ([M(CO)$_4$L])[10] and singular examples for M = Ru, Os ([M(Cl)$_2$(η^6-arene)(L)]) and M = Ir, Rh ([M(Cp*)(Cl)$_2$(L)])[11] were reported (**Figure 1**). Further, the possible coordination of the phosphinidene to two metals was also shown.[10,14] For transition metals, TAMM and co-workers evaluated that the overall donor strengths of [(NHC)PR] and [(NHC)PH] are comparable to that of the NHC IDipp (1,3-bis{2,6-di-*iso*-propylphenyl}imidazolin-2-ylidene).[6]

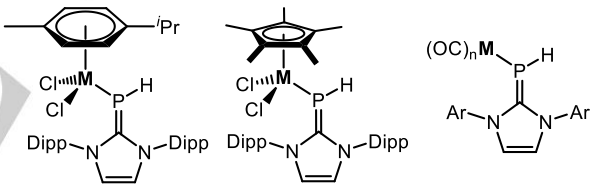

M = **Ru**, **Os** M = **Rh**, **Ir** M = **Cr**, **Mo**, **W** (n = 5) **Fe** (n = 4)

Figure 1. Rare examples of known transition metal phosphinidene complexes.[6,10–12,14]

As such we were interested to examine the respective behavior of the NHC-stabilized 'parent' phosphinidene [(sIDipp)PH] (sIDipp = 1,3-bis(2,6-di-*iso*-propylphenyl)-imidazolidine-2-ylidene) towards divalent 3d-metal(II) hexamethyldisilazanides.[15,16] These substrates are electronically and coordinatively unsaturated and thus highly susceptible to LEWIS bases such as phosphines,[17–21] NHC's[22,23] or N/O-donors (e.g. THF or (bi)pyridines).[19,20,24] The basicity of the amide ligands might also facilitate deprotonation, which would result in a rare instance of a transition metal complex bearing an anionic NHC-stabilized phosphinidenide [(NHC)P]$^-$.[11,13,25]

Herein we report on the reactivity of the phosphinidene [(sIDipp)PH] with low coordinate, LEWIS acidic metal(II) hexamethyldisilazanides of manganese to cobalt. This yields the first open-shell, three-coordinated 3d-metal(II) phosphinidene adduct complexes of the type [M{PH(sIDipp)}{N(SiMe$_3$)$_2$}$_2$] (M = Mn − Co) as evidenced by solid state analysis. Examinations in solution, however,

implicate only weak phosphinidene metal interactions with no signs of intramolecular deprotonation.

Results and Discussion

Stirring one equivalent of both [M{N(SiMe$_3$)$_2$}$_2$] (M = Mn − Co) and [(sIDipp)PH] in *n*-pentane before cooling to −40 °C resulted in the formation of highly sensitive and crystalline [M{PH(sIDipp)}{N(SiMe$_3$)$_2$}$_2$], **[M]** (M = Mn (beige, **[Mn]**); Fe (orange-brown, **[Fe]**); Co (green, **[Co]**); **Scheme 1**). Elemental analysis measurements gave good results for manganese, whereas a deviation in the carbon value of ~ 1% was repeatedly observed for iron and cobalt. Although this might hint to impurities, parallel measurements of stochiometric mixtures of the phosphinidene and [M{N(SiMe$_3$)$_2$}$_2$], only dissolved in *n*-pentane and dried *in vacuo* without further manipulations, gave similar results. X-ray diffraction analysis on suitable crystals showed the envisioned adduct formation for all compounds (**Figure 2**). Thereby, **[Mn]** and **[Fe]** crystallise isomorphous with two and **[Co]** with one molecule(s) within the unit cell in the space groups *P*2$_1$/c or *P*2$_1$/n, respectively.

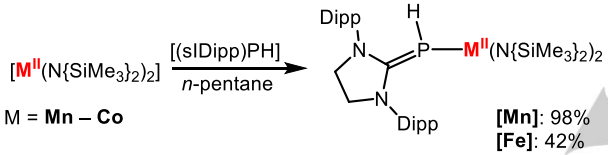

Scheme 1. Synthetic pathway to yield complexes **[Mn]** − **[Co]**.

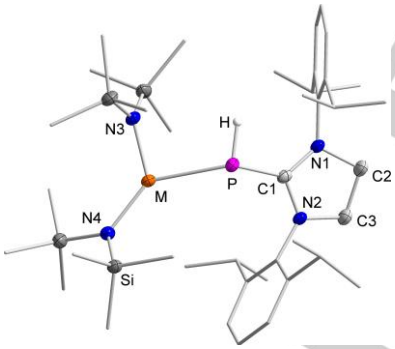

Figure 2. General crystal structure of **[M]** (M = Mn − Co). Irrelevant hydrogen atoms are omitted for clarity.

In solid state, the complexes exhibit M−P distances with values of 2.6033(10) Å (Mn), 2.5185(6) (Fe) Å and 2.4572(8) Å (Co) (**Table 1**). The shortening can be attributed to the contraction of the ion radii along the series from Mn to Co. The M−P bonds are comparably long with regard to the few other known [(NHC)PR]-3d-metal adducts such as [(NHC)P(H)Fe(CO)$_4$] (1.828(3) Å)[10] or [(NHC)P(Ph)CuCl] (1.8097(19) Å).[7] The values are more in the range of phosphine complexes [M(PR$_3$){N(SiMe$_3$)$_2$}$_2$] (M = Mn − Co, R = Cy, Cyp, Me or Ph) and most similar to those of the rather bulky PCy$_3$ ligand.[17,18,20,21,26] The P−C1 bond lengths are found between 1.7492(19) Å (**[Fe]**) and 1.784(3) Å (**[Co]**). These distances are shorter than in other [(NHC)PH] complexes (1.80 Å to 1.83 Å)[6,10–12] and only slightly longer than in free [(sIDipp)PH] (1.7426(19) Å).[13] This indicates only little σ- and π-electron donation from the phosphorous atom to the metal(II) hexamethyldisilazanide fragments why they are thus best described as phosphaalkene adducts. Most remarkably, the two N3−M−P and N4−M−P angles differ strongly from each other with angles of 94.04(8)° (**[Mn]**), 93.29(5)° (**[Fe]**) and 94.25(7)° (**[Co]**) for the first versus 134.81(9)° (**[Mn]**), 134.91(5)° (**[Fe]**) and 132.54(7)° (**[Co]**) for the latter. Together with N3−M−N4 values of 128.27(12)° (**[Mn]**), 128.25(7)° (**[Fe]**) and 132.48(9)° (**[Co]**), the complex geometry is best described as Y-shaped. This is in stark contrast to all other known adducts of the type [M(L){N(SiMe$_3$)$_2$}$_2$], which adopt a symmetric donor binding. Further, the M−P−C1 angle is with approx. 135° rather large as it is usually found around 110° for metal adducts with ligands of the type [(NHC)PH] or [(NHC)PPh].[5–8,10–12] We attribute this to the steric repulsion between the Dipp moieties of the NHC backbone and the silylamide ligand. This would also explain the long M−P distances and thus points to a rather weak metal phosphinidene interaction.

Table 1. Selected bond lengths and angles of **[M]** (M = Mn − Co).

	[Mn]	**[Fe]**	**[Co]**
M−P / Å	2.6033(10)	2.5185(6)	2.4572(8)
P−C1 / Å	1.767(3)	1.7492(19)	1.784(3)
M−N3 / Å	2.005(3)	1.8478(16)	1.926(2)
M−N4 / Å	1.998(3)	1.91878(16)	1.917(2)
C2−C3 / Å	1.504(5)	1.480(3)	1.518(4)
N3−M−N4 / °	128.27(12)	128.25(7)	132.48(9)
N3−M−P / °	94.04(8)	93.29(5)	94.25(7)
N4−M−P / °	134.81(9)	134.91(5)	132.54(7)
M–P−C1 / °	133.88(11)	133.11(7)	138.96(9)

To get a further insight into the M−P adduct, NMR spectroscopic examinations in toluene-d_8 were attempted. All compounds are highly paramagnetic, as evidenced *via* the Evans method at ambient temperatures. Obtained values were slightly lower (Mn, Fe) or higher (Co) than the spin-only values of the respective high-spin ions, whereas the deviations can be attributed to fluxional behavior in solution (*vide infra*). No signals are observable for all compounds in the ^{31}P NMR spectra at ambient conditions, which is expected for coordinative interactions of the phosphorous atom to a paramagnetic metal centre. Unsurprisingly, paramagnetic line broadening and shifting of the signals in the proton NMR spectra also prevented any signal assignments for **[Mn]** and **[Fe]** at room temperature (see ESI). This also extended to **[Co]**, where only the hexamethylsilyl moiety can be assigned at −6.55 ppm (**Figure 3**, top), although other paramagnetic cobalt(II) silylamide complexes give rather sharp signals.[17,20,27] As this hinted to a fluxional behavior, variable-temperature NMR studies were conducted on **[Co]** in toluene-d_8.

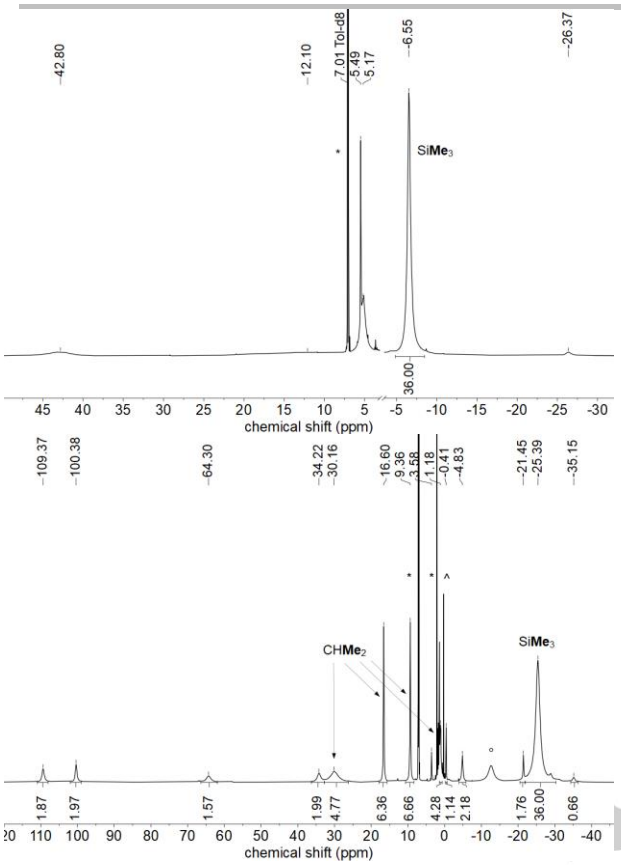

Figure 3. ^{1}H NMR spectra (500.1 MHz) of **[Co]** in toluene-d_8 at 300 K (top) and 193 K (bottom). (* solvent, ^ impurities, ° [Co(OEt$_2$){N(SiMe$_3$)$_2$}$_2$])

Indeed, upon stepwise cooling to 193 K, the evolution and decoalescence of several signals were observed, which became rather well resolved at low temperatures, thus allowing for partial signal attribution. The signal of the Si(CH$_3$)$_3$-protons is shifted to −25.4 ppm upon cooling. Due to their signal intensity, two distinct signals at 9.36 and 16.6 ppm and two broadened signals at 1.2 and 30.2 ppm are tentatively attributed to the *iso*-propyl-methyl groups of the eight Dipp units of the ligands. This speaks to a blocked rotation of the phosphinidene ligand around the Co−P axis at low temperatures. Comparing with the crystal structure, the two broadened signals likely belong to the *iso*-propyl groups pointing towards the cobalt centre, thus experiencing a stronger dipole-dipole interaction. A similar phenomenon was observed for the Dipp groups of the linear complex ion [Co{N(Dipp)SiMe$_3$}$_2$]$^-$.[28] All other paramagnetically shifted signals in the range from −35.2 to 109.4 ppm cannot be assigned further but correspond to the NHC moiety.

Lowering the temperature also give rise to a signal at −117.5 ppm in the ^{31}P NMR spectrum of **[Co]** that appears below 273 K (**Figure 4**) corresponding to free [(sIDipp)PH] (lit: −116.7 ppm).[13] This implicates constant decoordination/ recoordination processes of **[Co]** in solution, which are freezed out below 273 K with concomitant formation of unligated [Co{N(SiMe$_3$)$_2$}$_2$], presumably in the dimeric form [Co{N(SiMe$_3$)$_2$}{μ-N(SiMe$_3$)$_2$}]$_2$ (short: [Co{N(SiMe$_3$)$_2$}$_2$]$_2$). This can also be indirectly observed *via* the temperature dependence of the sigmatropic shift of the SiMe$_3$-groups for which linearity according to the Curie-Weiss law is only observed below 270 K (see ESI). Interestingly, addition of further phosphinidene (up to additional 1.5 equiv.) did not evoke any signal in the ^{31}P NMR spectrum at room temperature at all whereas the SiMe$_3$ proton signal shifted from –6.55 ppm to –12 ppm. This can be explained by rapid exchange of coordinating and free phosphinidene that allows for spin-polarization of the phosphorous atom of all employed [(sIDipp)PH] adducts.

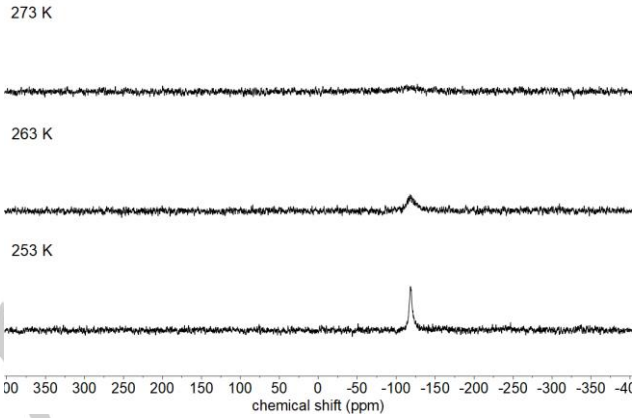

Figure 4. Temperature dependent ^{31}P NMR spectrum (202.5 MHz) of **[Co]** from 253 K to 273 K.

To corroborate these solution equilibria, temperature dependent UV/Vis measurements were performed for [Co{N(SiMe$_3$)$_2$}$_2$] and **[Co]** in *n*-pentane, as well (**Figure 5**). For [Co{N(SiMe$_3$)$_2$}$_2$], we observe a pronounced absorption band at around 415 nm (ε = 1939 L mol^{-1} cm^{-1}, 323 K) that can be ascribed to ligand-to-metal charge transfer (LMCT) transitions of the linear, monomeric form. A room temperature UV/Vis spectrum of [Co{N(SiMe$_3$)$_2$}$_2$] in *n*-hexane was already reported, however, it lacks the absorption band around 415 nm with a stronger one around 300 nm, which might be attributed to differences in the used concentration.[20] The band at 415 nm disappears almost completely upon cooling at the expense of a blue-shifted band at 349 nm (ε = 3261 L mol^{-1} cm^{-1} at 173 K), which can thus be attributed to the dimer [Co{N(SiMe$_3$)$_2$}$_2$]$_2$ with its three-coordinate cobalt(II) ions. The observation of an isosbestic point at around 370 nm supports the notion of a monomer/dimer equilibrium of [Co{N(SiMe$_3$)$_2$}$_2$] as observed by proton NMR spectroscopy.[20] The low-intensity bands between 600 and 700 nm, attributed to d-d transitions,[20] did change only little upon cooling.

For **[Co]**, the dominant band at around 300 nm is persistent throughout the whole temperature range with a marginally changing extinction coefficient (approx. 2000 L mol^{-1} cm^{-1}, see Figure S29). Only at elevated temperatures a minor band at around 415 nm, attributed to the monomeric, adduct free [Co{N(SiMe$_3$)$_2$}$_2$], can be detected. As such, the band at 300 nm is indicative for the presence of a three-coordinate cobalt(II) silylamide as found in [**Co**] as well as dimeric [Co{N(SiMe$_3$)$_2$}$_2$]$_2$. A weak band at 760 nm (ε = 196 L mol^{-1} cm^{-1} at 173 K) becomes visible at lower temperatures for **[Co]**. This is also absent for

$[Co\{N(SiMe_3)_2\}_2]_2$ at low temperatures but visible for the related phosphine adduct $[Co(PMe_3)\{N(SiMe_3)_2\}_2]_2$,[20] thus confirming phosphinidene coordination in **[Co]**.

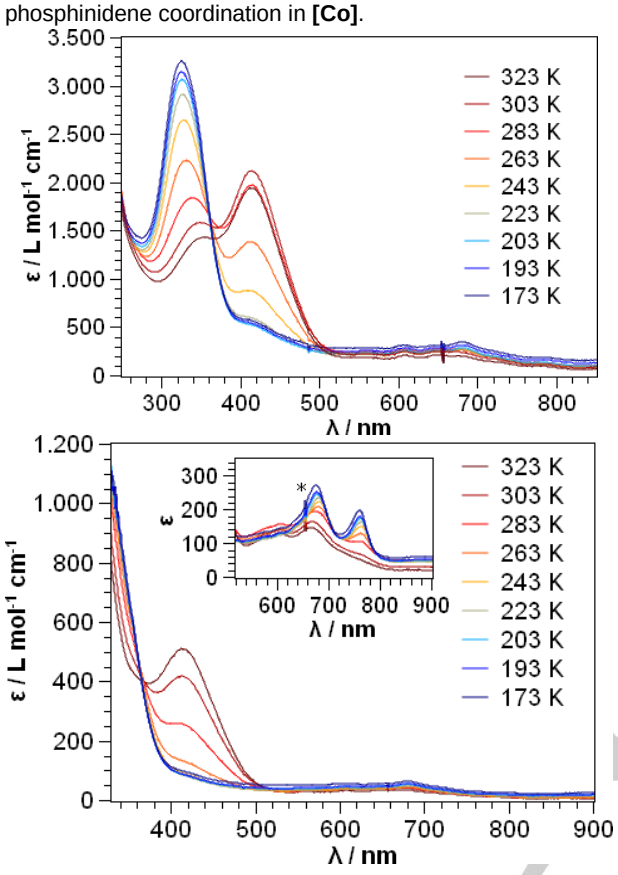

Figure 5. UV/Vis spectra of $[Co\{N(SiMe_3)_2\}_2]$ (top) and **[Co]** (bottom) at different temperatures in *n*-pentane. (* signal caused by lamp exchange)

To further evaluate the donor strength of [(sIDipp)PH], one equivalent of PCy_3 or diethyl ether, respectively, were added to **[Co]**. For PCy_3, it yielded in a 1:1 integral ratio of free phosphinidene and free PCy_3. In the case of Et_2O, the signal of the silylamide protons is shifted to −15.3 ppm in the ^1H NMR spectrum. This pointed towards the presence of $[Co(OEt_2)\{N(SiMe_3)_2\}_2]$, which was confirmed by addition of Et_2O to donor-free $[Co\{N(SiMe_3)_2\}_2]$. Hereby, one equivalent of Et_2O is sufficient for $[Co(OEt_2)\{N(SiMe_3)_2\}_2]$ formation as addition of further Et_2O did not change the position of the $SiMe_3$ protons (16 ppm) and shifted the signals, attributed to the ligated Et_2O, closer to its diamagnetic position. Previously, similar observations were also made for stronger donors such as DMAP or THF.[20] No liberated [(sIDipp)PH] was observed in case of [**Co**], which speaks nonetheless for its constant chemical exchange with diethyl ether concerning ligation to the metal in solution. Analogous observations with respect to detection of free phosphinidene *via* ^{31}P NMR spectroscopy at low temperatures were subsequently also made for **[Mn]** and **[Fe]**, which point to an overall weak phosphinidene coordination in these complexes. Driven by these observations, we also examined the temperature behavior of known $[Co(PCy)_3\{N(SiMe_3)_2\}_2]$[18] (Figure S24). Here, the appearance of free phosphine was also observed at low temperatures in the ^{31}P NMR spectrum. Overall, this implicates an indifference of the cobalt silylamide towards the nature of the P-donor and overall weak $C-P_{Donor}$ bonds. These observations contribute to the general donor ligand lability of metal(II) hexamethyldisilazanides which was reported in case of THF with regards to $[M\{N(SiMe_3)_2\}_2]$ (M = Co, Fe)[29] as well as NHC coordination to $[Fe\{N(SiMe_3)_2\}_2]$, [23].

At last, we attempted the intramolecular deprotonation of obtained adducts by heating the isolated solids *in vacuo*. However, only destillative removal of the adduct free hexamethyldisilazanides $[M\{N(SiMe_3)_2\}_2]$ was observed.

Conclusion

Concluding, we presented the adduct formation between NHC-stabilized 'parent' phosphinidenes and monomeric metal(II) silylamide complexes giving complexes of the type $[M\{PH(sIDipp)\}\{N(SiMe_3)_2\}_2]$ (M = Mn − Co). They exhibit a distorted T-shaped geometry at the metal centre and a rather long M−P bond. Solution state examinations *via* NMR spectroscopy revealed a rather weak and fluxional binding of the phosphinidene to the otherwise electronically and coordinatively deficient metal(II) hexamethyldisilazanides, which was supported by exchange reactions with PCy_3 or diethyl ether. Further, heating of obtained complexes *in vacuo* did not yield intramolecular deprotonation but destillative removal of the adduct free $[M\{N(SiMe_3)_2\}_2]$ compounds.

Experimental Section

Materials and Methods

All manipulations were carried out in a glovebox under a dry argon atmosphere unless indicated otherwise. Used solvents were dried by continuous distillation over sodium metal for several days, degassed *via* three freeze-pump-thaw cycles and stored over molecular sieves 4 Å. Deuterated solvents were used as received, degassed *via* three freeze-pump cycles and stored over molecular sieves 4 Å. The ^1H NMR and ^{31}P spectra were recorded on a Bruker HD 500, a Bruker HD 300 or a Bruker HD 250 NMR spectrometer (Bruker Corporation, Billerica, USA). Chemical shifts are reported in ppm relative to the residual proton signals of the solvent (for ^1H). $w_{½}$ is the line width of a signal at half its maximum intensity. Integrals of the broad signals ligand set were obtained directly or by peak fitting (in case of overlapping signals) using the MestreNova software package (Mestrelab, Santiago de Compostela, Spain). IR measurements were conducted on a Bruker Alpha ATR-IR spectrometer (Bruker Corporation, Billerica, USA). The UV/VIS measurement were recorded on an AnalytikJena Specord S600 using WinASPECT software. Elemental analysis were performed by the "in-house" service of the Chemistry Department of the Philipps University Marburg, Germany using a CHN(S) analyser vario MICRO Cube (Elementar Analysensysteme GmbH, Langenselbold, Germany). $[Mn(N\{SiMe_3\}_2)_2]$,[16] $[Fe(N\{SiMe_3\}_2)_2]$,[15] $[Co(N\{SiMe_3\}_2)_2]$[20] and [(sIDipp)PH][30] were prepared according to literature procedures. In this regard, we note that significant amounts of $[Co(OEt_2)\{N(SiMe_3)_2\}_2]$ is sometimes present after the final destillative isolation at >100°C during the synthesis of adduct free $[Co\{N(SiMe_3)_2\}_2]$ in Et_2O. This can be mitigated by prolonged drying of crude $[Co\{N(SiMe_3)_2\}_2]$ under gentle heating for several hours.

[M{PH(sIDipp)}{N(SiMe$_3$)$_2$}$_2$] (M = Mn − Co). One equivalent [M{N(SiMe$_3$)$_2$}$_2$] (M = Mn − Co) (0.15 mmol) were allowed to stir for several minutes with one equivalent [(sIDipp)PH] (0.15 mmol) in *n*-pentane. Thereby, a color change to beige (Mn), brown (Fe) or green (Co) was observed. The concentrated solutions were cooled to −40 °C for crystallization. After several days, obtained crystals were isolated *via* filtration and subsequent drying *in vacuo*. **[Mn]** − **[Co]** were obtained in moderate yields (42% – 98%).

[Mn{PH(sIDipp)}{N(SiMe$_3$)$_2$}$_2$] ([Mn]). Using 56 mg [Mn{N(SiMe$_3$)$_2$}$_2$], yellow crystalline **[Mn]** could be obtained in yields of 98%. **Yield:** 118 mg (0.14 mmol, 98%). Crystals, suitable for x-ray diffraction analysis, were obtained from a solution of **[Mn]** in *n*-pentane at −40 °C. **^{1}H NMR** (300.2 MHz, C_6D_6, 300 K, ppm): δ = 8.43 (bs, $w_{½}$ = 650 Hz), 3.24 (bs, $w_{½}$ = 260 Hz), 1.28 (s, $w_{½}$ = 49 Hz); (500.1 MHz, toluene-d_8, 193 K, ppm): δ = 3.20 (bs, $w_{½}$ = 330 Hz), 1.27 (bs, $w_{½}$ = 480 Hz), 0.13 (bs, $w_{½}$ = 130 Hz). **^{31}P NMR** (202.5 MHz, toluene-d_8, ppm): 300 K: no signal detectable; 193 K: δ = −120.0 (free [(sIDipp)PH]). Elemental analysis $C_{39}H_{76}MnN_4PSi_4$ (799.32 g/mol): calcd: N 7.01, C 58.60, H 9.58; found: N 7.31, C 58.85, H 9.30%. **IR** (ATR, cm^{-1}): $\tilde{\nu}$ = 2960 (m), 2889 (m), 2869 (m), 1587 (w), 1478 (m), 1454 (m), 1430 (m), 1397 (m), 1347 (w), 1325 (w), 1296 (s), 1238 (s), 1178 (w), 1107 (w), 1056 (w), 998 (s), 969 (s), 885 (m), 863 (s), 841 (s), 823 (vs), 804 (vs), 758 (m), 749 (s), 711 (w), 699 (w), 666 (s), 623 (m), 611 (m), 557 (m), 490 (m), 452 (w), 431 (w), 409 (m). **EVANS** (500.1 MHz, 300 K, C_6D_6 +1% TMS): μ_{eff} = 5.25 μ_B; $\mu_{S.O.}$ = 5.92 μ_B.

[Fe{PH(sIDipp)}{N(SiMe$_3$)$_2$}$_2$] ([Fe]). Using 56 mg [Fe{N(SiMe$_3$)$_2$}$_2$], yellow crystalline **[Fe]** could be obtained in yields of 42%. **Yield:** 50 mg (0.06 mmol, 42%). Crystals, suitable for x-ray diffraction analysis, were obtained from a solution of **[Fe]** in *n*-pentane at −40 °C. **^{1}H NMR** (300.2 MHz, C_6D_6, 300 K, ppm): δ = 42.6 (bs, $w_{½}$ = 1980 Hz), 4.64 (bs, $w_{½}$ = 130 Hz), 2.11 (bs, $w_{½}$ = 43 Hz), 1.09 (bs, $w_{½}$ = 130 Hz), 1.01 (s, $w_{½}$ = 28.5 Hz); (500.1 MHz, toluene-d_8, 193 K, ppm): δ = 46.1 (bs, $w_{½}$ = 280 Hz), 33.8 (bs, $w_{½}$ = 390 Hz), 9.72 (bs, $w_{½}$ = 520 Hz), 5.84 (bs, $w_{½}$ = 350 Hz), 3.31 (bs, $w_{½}$ = 260 Hz), 1.00 − 1.49 (m), −2 (bs, $w_{½}$ = 2270 Hz), −5.76 (bs, $w_{½}$ = 280 Hz), −9.50 (bs, $w_{½}$ = 210 Hz), −14.9 (bs, $w_{½}$ = 870 Hz), −18.53 (bs, $w_{½}$ = 130 Hz), −34 (bs, $w_{½}$ = 1130 Hz), **^{31}P NMR** (202.5 MHz, toluene-d_8, ppm): 300 K: no signal detectable; 193 K: δ = −115.3 (free [(sIDipp)PH]). Elemental analysis $C_{39}H_{76}FeN_4PSi_4$ (800.22 g/mol): calcd: N 7.01, C 58.61, H 9.46; found: N 6.83, C 59.94, H 9.28%. **IR** (ATR, cm^{-1}): $\tilde{\nu}$ = 3072 (w), 2961 (m), 2948 (m), 2892 (m), 2868 (m), 1587 (w), 1478 (m), 1454 (m), 1431 (m), 1396 (m), 1366 (w), 1346 (w), 1325 (w), 1294 (m), 1276 (m), 1239 (s), 1180 (w), 1104 (w), 1057 (w), 976 (s), 948 (s), 885 (m), 845 (s), 826 (vs), 803 (s), 785 (s), 751 (m), 704 (w), 666 (s), 613 (m), 556 (m), 528)w), 482 (m), 459 (m), 414 (m). **EVANS** (500.1 MHz, 300 K, C_6D_6 +1% TMS): μ_{eff} = 3.69 μ_B; $\mu_{S.O.}$ = 4.90 μ_B.

[Co{PH(sIDipp)}{N(SiMe$_3$)$_2$}$_2$] ([Co]). Using 57 mg [Co{N(SiMe$_3$)$_2$}$_2$], yellow crystalline **[Co]** could be obtained in yields of 53%. **Yield:** 64 mg (0.08 mmol, 53%). Crystals, suitable for x-ray diffraction analysis, were obtained from a solution of **[Co]** in *n*-pentane at −40 °C. **^{1}H NMR** (500.1 MHz, toluene-d_8, 300 K, ppm): δ = 42.8 (bs, $w_{½}$ = 1400 Hz), 12 (bs, $w_{½}$ = 5400 Hz), 5.49 (s, $w_{½}$ = 30 Hz), 5.17 (bs, $w_{½}$ = 330 Hz), −6.55 (bs, 36 H, $w_{½}$ = 210 Hz, Si(C**H**$_3$)$_3$), −26.4 (bs, $w_{½}$ = 350 Hz). (500.1 MHz, toluene-d_8, 193 K, ppm): δ = 109.4 (bs, 2 H, $w_{½}$ = 340 Hz), 100.4 (bs, 2 H, $w_{½}$ = 260 Hz), 64.3 (bs, 2 H, $w_{½}$ = 720 Hz), 34.2 (bs, 2 H, $w_{½}$ = 480 Hz), 30.2 (bs, 6 H, $w_{½}$ = 1200 Hz), 16.60 (s, 6 H, $w_{½}$ = 93 Hz, CH(C**H**$_3$)$_2$), 9.36 (s, 6 H, $w_{½}$ = 97 Hz, CHC**H**$_3$), 1.2 (bs, 6 H, $w_{½}$ = 140 Hz), −0.41 (bs, 1 H, $w_{½}$ = 52 Hz), −4.83 (bs, 2 H, $w_{½}$ = 180 Hz), −21.5 (bs, 2 H, $w_{½}$ = 110 Hz), −25.4 (bs, 36 H, $w_{½}$ = 680 Hz, Si(C**H**$_3$)$_3$), −35.2 (bs, 1 H, $w_{½}$ = 390 Hz).**^{31}P NMR** (202.5 MHz, toluene-d_8, ppm): 300 K: no signal detectable; 193 K: δ = −117.5 (free [(sIDipp)PH]). Elemental analysis $C_{39}H_{76}CoN_4PSi_4$ (803.31 g/mol): calcd: N 6.98, C 58.39, H 9.42; found: N 6.27, C 59.61, H 9.19%. **IR** (ATR, cm^{-1}): $\tilde{\nu}$ = 3074 (w), 2959 (m), 2894 (m), 2871 (w), 1588 (w), 1482 (m), 1454 (m), 1434 (m), 1402 (m), 1386 (w), 1365 (w), 1345 (w), 1326 (w), 1293 (m), 1278 (m), 1240 (s), 1180 (w), 1150 (w), 1105 (w), 1055 (w), 985 (s), 920 (m), 881 (m), 828 (vs), 803 (s), 778 (s), 756 (s), 703 (m), 665 (s), 612 (m), 583 (w), 555 (m), 482 (m), 431 (m), 417 (w). **EVANS** (500.1 MHz, 300 K, C_6D_6 +1% TMS): μ_{eff} = 4.34 μ_B; $\mu_{S.O.}$ = 3.87 μ_B.

X-ray diffraction analysis: Data for compound **[Co]** (CCDC 2095757) were collected at 100 K on a Bruker Quest D8 diffractometer (Bruker Corporation, Billerica, USA) using an Incoatec Microfocus Source Mo-Kα radiation and equipped with an Oxford Instrument Cooler Device (Oxford Instruments, Abingdon, UK) and Photon 100 detector. Data for compounds **[Mn]** (CCDC 2095759) and **[Fe]** (CCDC 2095758) were collected at 100 K on a STOE IPDS2 diffractometer (STOE & Cie GmbH, Darmstadt, Germany) using a graphite-monochromated Mo-Kα radiation (λ = 0.71073 Å) and equipped with an Oxford Instrument Cooler Device (Oxford Instruments, Abingdon, UK). The structures have been solved using either OLEX SHELXT V2014/1[31] and refined by means of least-squares procedures on a F^2 with the aid of the program SHELXL-2016/6[32] included in the software package WinGX version 1.63.[33] The atomic scattering factors were taken from International Tables for X-ray Crystallography.[34] All non-hydrogen atoms were refined anisotropically. All hydrogen atoms were refined by using a riding model. Absorption corrections were introduced by using the MULTISCAN and X-Red programs.[35] Drawings of molecules are performed with the program DIAMOND (Crystal Impact, Bonn, Germany) with 50% probability displacement ellipsoids for non-H atoms. Additional details are given in the Supporting Information.

Keywords: phosphinidene • 3d transition metal • silylamides • structure • NMR spectroscopy

[1] a) L. Weber, *Ber. Dtsch. Chem. Ges.* **2007**, *2007*, 4095; b) F. Mathey, *Dalton Trans.* **2007**, 1861; c) K. Lammertsma, M. J. M. Vlaar, *Ann. Chem. Pharm.* **2002**, *2002*, 1127; d) A. Doddi, M. Peters, M. Tamm, *Chem. Rev.* **2019**, *119*, 6994; e) I. A. J. Arduengo, H. V. R. Dias, J. C. Calabrese, *Chem. Lett.* **1997**, *26*, 143.

[2] a) L. Weber, *Ber. Dtsch. Chem. Ges.* **2000**, *2000*, 2425; b) F. Mathey, *Angew. Chem. Int. Ed.* **2003**, *42*, 1578; c) R. R. Rodrigues, C. L. Dorsey, C. A. Arceneaux, T. W. Hudnall, *Chem. Commun.* **2014**, *50*, 162; d) O. Back, M. Henry-Ellinger, C. D. Martin, D. Martin, G. Bertrand, *Angew. Chem. Int. Ed.* **2013**, *52*, 2939.

[3] A. J. Arduengo III, C. J. Carmalt, J. A. C. Clyburne, A. H. Cowley, R. Pyati, *Chem. Commun.* **1997**, 981.

[4] O. Lemp, M. Balmer, K. Reiter, F. Weigend, C. von Hänisch, *Chem. Commun.* **2017**, *53*, 7620.

[5] A. Doddi, D. Bockfeld, M. Tamm, *Z. Anorg. Allg. Chem.* **2019**, *645*, 44.

[6] D. Bockfeld, A. Doddi, P. G. Jones, M. Tamm, *Eur. J. Inorg. Chem.* **2016**, *2016*, 3704.

[7] A. Doddi, D. Bockfeld, A. Nasr, T. Bannenberg, P. G. Jones, M. Tamm, *Chem. Eur. J.* **2015**, *21*, 16178.

[8] T. G. Larocque, G. G. Lavoie, *New J. Chem.* **2014**, *38*, 499.

[9] T. Krachko, M. Bispinghoff, A. M. Tondreau, D. Stein, M. Baker, A. W. Ehlers, J. C. Slootweg, H. Grützmacher, *Angew. Chem. Int. Ed.* **2017**, *56*, 7948.

[10] L. L. Liu, D. A. Ruiz, F. Dahcheh, G. Bertrand, *Chem. Commun.* **2015**, *51*, 12732.

[11] M. Peters, A. Doddi, T. Bannenberg, M. Freytag, P. G. Jones, M. Tamm, *Inorg. Chem.* **2017**, *56*, 10785.
[12] M. Bispinghoff, H. Grützmacher, *CHIMIA* **2016**, *70*, 279.
[13] M. Bispinghoff, A. M. Tondreau, H. Grützmacher, C. A. Faradji, P. G. Pringle, *Dalton Trans.* **2016**, *45*, 5999.
[14] O. Lemp, C. von Hänisch, *Phosphorus, Sulfur, and Silicon and the Related Elements* **2016**, *191*, 659.
[15] H. Bürger, U. Wannagat, *Monatsh. Chem.* **1963**, *94*, 1007.
[16] H. Bürger, U. Wannagat, *Monatsh. Chem.* **1964**, *95*, 1099.
[17] C. G. Werncke, L. Vendier, S. Sabo-Etienne, J.-P. Sutter, C. Pichon, S. Bontemps, *Eur. J. Inorg. Chem.* **2017**, *2017*, 1041.
[18] A. Eichhöfer, Y. Lan, V. Mereacre, T. Bodenstein, F. Weigend, *Inorg. Chem.* **2014**, *53*, 1962.
[19] T. Bodenstein, A. Eichhöfer, *Dalton Trans.* **2019**, *48*, 15699.
[20] A. M. Bryan, G. J. Long, F. Grandjean, P. P. Power, *Inorg. Chem.* **2013**, *52*, 12152.
[21] P.-H. Lin, N. C. Smythe, S. I. Gorelsky, S. Maguire, N. J. Henson, I. Korobkov, B. L. Scott, J. C. Gordon, R. T. Baker, M. Murugesu, *J. Am. Chem. Soc.* **2011**, *133*, 15806.
[22] a) B. M. Day, K. Pal, T. Pugh, J. Tuck, R. A. Layfield, *Inorg. Chem.* **2014**, *53*, 10578; b) K. Pal, O. B. Hemming, B. M. Day, T. Pugh, D. J. Evans, R. A. Layfield, *Angew. Chem. Int. Ed.* **2016**, *55*, 1690; c) B. M. Day, T. Pugh, D. Hendriks, C. F. Guerra, D. J. Evans, F. M. Bickelhaupt, R. A. Layfield, *J. Am. Chem. Soc.* **2013**, *135*, 13338; d) Y. Liu, L. Deng, *J. Am. Chem. Soc.* **2017**, *139*, 1798; e) A. Massard, P. Braunstein, A. A. Danopoulos, S. Choua, P. Rabu, *Organometallics* **2015**, *34*, 2429.
[23] R. A. Layfield, J. J. W. McDouall, M. Scheer, C. Schwarzmaier, F. Tuna, *Chem. Commun.* **2011**, *47*, 10623.
[24] a) A. Panda, M. Stender, M. M. Olmstead, P. Klavins, P. P. Power, *Polyhedron* **2003**, *22*, 67; b) Y.-F. Deng, T. Han, Z. Wang, Z. Ouyang, B. Yin, Z. Zheng, J. Krzystek, Y.-Z. Zheng, *Chem. Commun.* **2015**, *51*, 17688; c) W. Zhou, A. N. Desnoyer, J. A. Bailey, B. O. Patrick, K. M. Smith, *Inorg. Chem.* **2013**, *52*, 2271; d) I. Müller, C. Schneider, C. Pietzonka, F. Kraus, C. G. Werncke, *Inorganics* **2019**, *7*, 117; e) G. Margraf, F. Schödel, I. Sänger, M. Bolte, M. Wagner, H.-W. Lerner, *Z. Naturforsch. B Chem. Sci.* **2012**, *67*, 549; f) M. Faust, A. M. Bryan, A. Mansikkamäki, P. Vasko, M. M. Olmstead, H. M. Tuononen, F. Grandjean, G. J. Long, P. P. Power, *Angew. Chem. Int. Ed.* **2015**, *54*, 12914; g) M. Andruh, H. W. Roesky, M. Noltemeyer, H.-G. Schmidt, *Z. Naturforsch. B Chem. Sci.* **1994**, *49*, 31; h) M. M. Olmstead, P. P. Power, S. C. Shoner, *Inorg. Chem.* **1991**, *30*, 2547.
[25] A. Doddi, D. Bockfeld, T. Bannenberg, P. G. Jones, M. Tamm, *Angew. Chem. Int. Ed.* **2014**, *53*, 13568.
[26] W. Lin, T. Bodenstein, V. Mereacre, K. Fink, A. Eichhöfer, *Inorg. Chem.* **2016**, *55*, 2091.
[27] A. Reckziegel, C. Pietzonka, F. Kraus, C. G. Werncke, *Angew. Chem. Int. Ed.* **2020**, *59*, 8527.
[28] R. Weller, I. Müller, C. Duhayon, S. Sabo-Etienne, S. Bontemps, C. G. Werncke, *Dalton Trans.* **2021**, *50*, 4890.
[29] C.-Y. Lin, J. C. Fettinger, P. P. Power, *Inorg. Chem.* **2017**, *56*, 9892.
[30] M. Balmer, Y. J. Franzke, F. Weigend, C. von Hänisch, *Chem. Eur. J.* **2020**, *26*, 192.
[31] O. V. Dolomanov, L. J. Bourhis, R. J. Gildea, J. Howard, H. Puschmann, *J. Appl. Crystallogr.* **2009**, *42*, 339.
[32] G. M. Sheldrick, *Acta. Crystallogr. C* **2015**, *71*, 3.
[33] L. J. Farrugia, *J. Appl. Crystallogr.* **1999**, *32*, 837.
[34] *International tables for crystallography*, International Union of Crystallography; Springer, Chester, England, New York, **2006**.
[35] SADABS-2016/2, *Bruker*, **2016**.

Entry for the Table of Contents

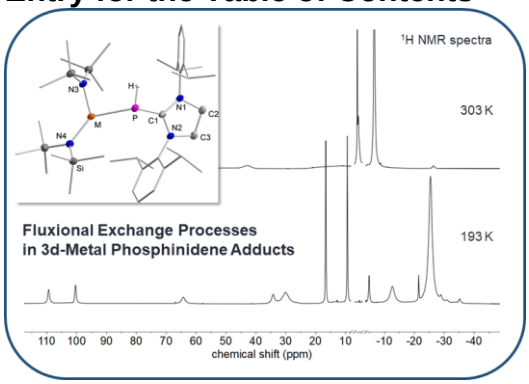

Additional Author information for the electronic version of the article.

Author: ORCID identifier
Author: ORCID identifier
Author: ORCID identifier

5.7 „Synthesis of the Open-Shell 3d-Transition Metal(II) Bis(phosphinidenide) [Mn(P(sIDipp))$_2$]“

Ruth Weller, Markus Balmer, Carsten von Hänisch, C. Gunnar Werncke

- eingereichtes Manuskript -

Abstract

The synthesis and characterization of the first open-shell transition metal phosphinidenide is presented. By reacting [MnL$_2$] (L = −N(SiMe$_3$)$_2$) with [(sIDipp)PK] (sIDipp = 1,3-bis(2,6-di-*iso*-propylphenyl)-imidazolidine-2-ylidene), the formation of [Mn(P(sIDipp))$_2$] instead of the initially expected adduct [KMn(sIDipp)L$_2$], is observed. Interestingly, a solvent change from toluene to *n*-pentane leads to the formation of [(sIDipp)PK$_2$(Et$_2$O)$_4$][MnL$_3$], which can be seen as intermediate in the formation process of [Mn(P(sIDipp))$_2$]. Contrary to manganese, the highly reducing phosphinidenide [(sIDipp)P]$^-$ cannot be stabilized in an analogous fashion by coordination to a low-coordinate high-spin iron(II) center.

Zusammenfassung

In dieser Publikation wird die Synthese des ersten offenschaligen Übergangsmetall-Phosphinidenid-Komplexes [Mn(P(sIDipp))$_2$], **1**, beschrieben. Dieser wurde anfänglich in einer 1:1-Umsetzung von [MnL$_2$] (L = −N(SiMe$_3$)$_2$) mit [(sIDipp)PK] in Toluol dargestellt und als kristalliner Feststoff nach der Überschichtung mit 18-Krone-6 erhalten. Die durch Röntgendiffraktometrie erhaltene Molekülstruktur weist ein Inversionszentrum im zentralen Manganzentrum und eine lineare P−Mn−P-Achse auf. Das sterisch und elektronisch ungesättigte Metallzentrum wird durch die zusätzliche Ausbildung intramolekularer Wechselwirkungen mit den Aryl-Substituenten des Ligandrückgrats stabilisiert.

Weder eine Reduktion mit KC$_8$ noch eine Oxidation mit Silbertriflat (AgOTf) war erfolgreich, jedoch ist ein irreversibler Oxidationsprozess im Zyklovoltammogramm zu sehen. PPMS-Messungen (engl.: physical properties measurement system) bei H = 1 T bestätigen CURIE-WEISS‘sches Verhalten von **1** und ein effektives Moment μ_{eff} von 5.83 μ_B. Dieser Wert stimmt gut mit dem zu erwartenden Spin-Only Wert für eine *High-Spin* d^5-Elektronenkonfiguration überein. ($\mu_{S.O.}$ = 5.92 μ_B).

Der durch die Ligandaustauschreaktion freiwerdende Ligand L wird durch den Präkursor [MnL$_2$] abgefangen und das Mangan-Trisamid K{18c6}[MnL$_3$] gebildet. Durch diesen Prozess wird sowohl die Ausbeute von **1** minimiert als auch dessen Isolierung erschwert, da das Trisamid, verglichen mit **1**, ähnliche Lösungseigenschaften besitzt. Erst durch einen Wechsel des Maskierungsreagenz zu crypt-222 und das Anpassen der Stöchiometrien gelang eine elementaranalytisch saubere Isolierung von **1**.

Interessanterweise führte ein Lösungsmittelwechsel von Toluol zu *n*-Pentan zur Bildung des ionischen Komplexes [(sIDipp)PK$_2$(Et$_2$O)$_4$][MnL$_3$] (**2a**). Es wird vermutet, dass **1** über die intermediäre Entstehung von **2a** ermöglicht wird (**Schema 28**). Bei dem Versuch, das Eisen-haltige Analogon von **1** darzustellen, konnten lediglich vereinzelte Kristalle von **2b**, [(sIDipp)PK$_2$(Et$_2$O)$_4$][FeL$_3$], erhalten und röntgenkristallographisch untersucht werden.

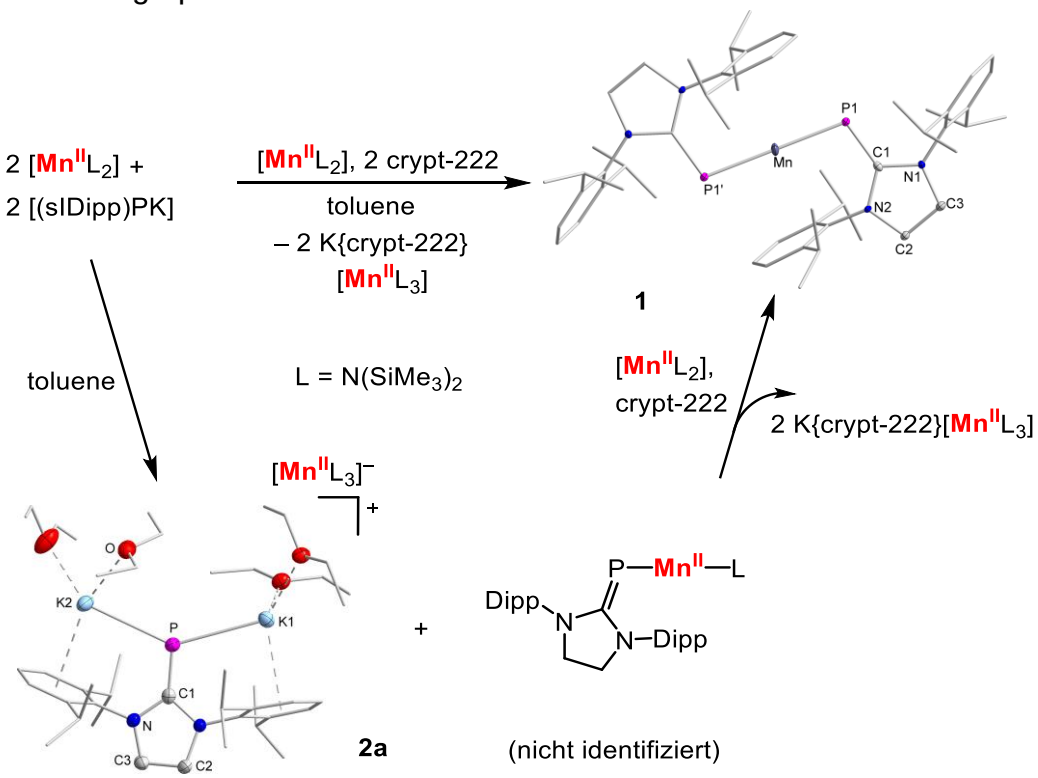

Schema 28. Vorgeschlagener Mechanismus zur Entstehung von **1**.

Beiträge der Autoren

Die Planung und Durchführung des Projektes sowie die Synthese und Charakterisierung aller neu erworbenen Verbindungen lag in meiner Hand. Dazu zählen alle Messungen mittels ^{1}H- und ^{31}P-NMR-, IR- und UV/Vis-Spektroskopie. Der Präkursor [(sIDipp)PK] wurde von Markus Balmer bzw. Hannah Gottschling im

Arbeitskreis von Prof. Dr. Carsten von Hänisch dargestellt und für dieses Projekt zur Verfügung gestellt. Zusätzlich war ich für die Aufnahmen der Daten von **2a** und **2b**, gemessen am Diffraktometer IPDS2 der Firma STOE, zuständig. Die Daten für **1** wurden von Dr. C. Gunnar Werncke am Quest D8 Diffraktometer der Firma BRUKER aufgenommen. Alle Datensätze, die mittels Einkristallstrukturanalyse erhalten wurden, wurden von mir gelöst und verfeinert. Evans-Messungen wurden mit Unterstützung der hausinternen NMR-Abteilung des Fachbereichs Chemie der Philipps-Universität Marburg unter der Leitung von Dr. Xiulan Xie aufgenommen und durch mich ausgewertet. Die Messung und Auswertung des Zyklovoltammogramms erfolgte durch Christian Schneider. Die magnetische PPMS-Messung wurde durch die hausinterne Serviceabteilung der Phillips-Universität Marburg unter der Leitung von Clemens Pietzonka durchgeführt und durch mich ausgewertet. Das Manuskript wurde von mir in Zusammenarbeit mit Dr. C. Gunnar Werncke und mit der Unterstützung von Prof. Dr. Carsten von Hänisch verfasst.

ARTICLE

Synthesis of the Open-Shell 3d-Transition Metal(II) Bis(phosphinidenide) [Mn{P(sIDipp)}$_2$]

Received 00th January 20xx,
Accepted 00th January 20xx

DOI: 10.1039/x0xx00000x

Ruth Weller,[a] Markus Balmer,[b] Carsten von Hänisch,[a] C. Gunnar Werncke*,[a]

The synthesis and characterization of the first homoleptic open-shell transition metal phosphinidenide is presented. By reacting [MnL$_2$] (L = −N(SiMe$_3$)$_2$) with [(sIDipp)PK] (sIDipp = 1,3-bis(2,6-di-*iso*-propylphenyl)-imidazolidine-2-ylidene), the formation of [Mn{P(sIDipp)}$_2$] instead of the initially expected adduct [KMn{P(sIDipp)}L$_2$] is observed. Interestingly, a solvent change from toluene to *n*-pentane leads to the formation of [(sIDipp)PK$_2$(Et$_2$O)$_4$][MnL$_3$], which can be seen as intermediate in the formation process of [Mn{P(sIDipp)}$_2$]. Contrary to manganese, the highly reducing phosphinidenide [(sIDipp)P]$^-$ cannot be stabilized in an analogous fashion by coordination to a low-coordinate high-spin iron(II) center.

Introduction

In recent years, stabilized 'parent' phosphinidenes, [PH], represent the phosphorous analoga of well-established carbenes and nitrenes. They are attracting interest since ROBINSON firstly stabilized those highly reactive fragments by *N*-heterocyclic carbenes (NHCs) in 2010, in which the phosphorous is formally in a +I oxidation state.[1] Thereby, the [(NHC)PH] species can either be described as a phosphaalkene (**I**) with one or a NHC stabilized [PH] (**III**) with two lone pairs (**Figure 1**). They can be potentially used for the coordination to one or two transition metal(s).[2,3,4]

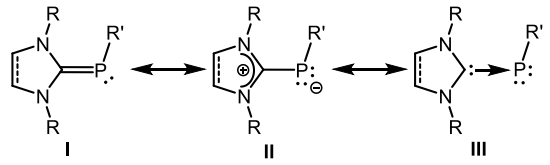

Figure 1. Mesomeric strutures in free phosphinidenes.[2]

Recently, some of us managed the deprotonation of the very basic [PH] unit in [(NHC)PH] (NHC = sIMes (1,3-bis{2,4,6-trimethylphenyl}imidazolidine-2-ylidene), sIDipp (1,3-bis{2,6-di-*iso*-propylphenyl}-imidazolidine-2-ylidene)) with benzyl potassium. The two resulting phosphinidenides [(sIMes)PK][5] and [(sIDipp)PK][6] are insoluble in aromatic and aliphatic solvents or decompose in others, which attributes to the lack of a solid state structure (similar to solvent free benzyl potassium).

Nonetheless, these phosphinidenides could be employed in salt elimination reactions with main group metal halogenides that lead for example to homoleptic group IV tetrel(II) phosphinidenides.[6–8] Further, reaction with potassium hexamethyldisilazanide gave ladder-like structures.[7] Attempts for the introduction of anionic phosphinidenides as ligands in transition metal complexes proved so far difficult. As such only a few stable diamagnetic examples were reported to this date (**Figure 2**). TAMM and co-workers presented the reaction of [(NHC)PSiMe$_3$] with ruthenium(II) and rhodium(III) chloride complexes, which gave complexes with terminal or bridging phosphindenides with suggested M–P double bond character.[2,3] Further, a homoleptic mercury bis(phosphenidenide) was also reported by PRINGLE and co-workers.[9] Even less is known about respective 3d-transition metal complexes, which were obtained only indirectly: either by activation of the 2-phosphaethynolate anion [PCO]$^-$ by a NHC stabilized nickel(I) cyclopentadienide[10] or a P$_6$-ring contraction of the triple decker complex [(Cp*V)$_2$(μ,$\eta^{6:6}$-P$_6$)] with ^{Me}NHC.[11]

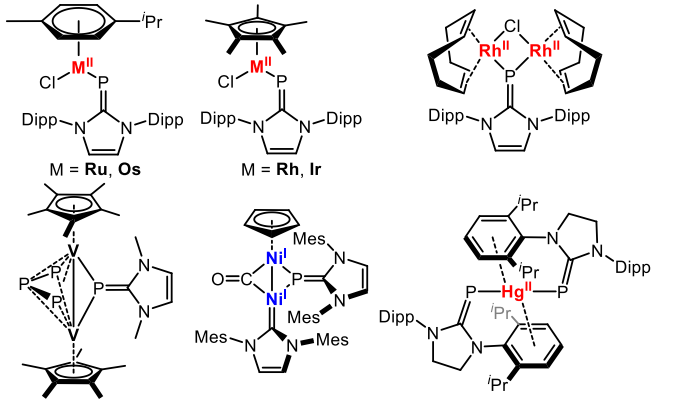

Figure 2. Known transition metal complexes bearing a phosphinidenide moiety (Dipp =2,6-di-*iso*-propylphenyl; Mes = 2,4,6-trimethylphenyl).[2,3,9–11]

[a] R. Weller, Prof. Dr. C. von Hänisch, Dr. C. G. Werncke, Department of Chemistry, Philipps-Universität Marburg, Hans-Meerwein-Straße 4, D- 35032 Marburg, Germany, E-Mail: gunnar.werncke@chemie.uni-marburg.de
[b] Dr. M. Balmer, Dockweiler Chemicals GmbH, Philipps-Universität Marburg, Hans-Meerwein-Straße 4, D- 35032 Marburg, Germany
[c] Electronic Supplementary Information (ESI) available:Analytical details concerning UV/Vis-, NMR-, IR-spectroscopy, cyclovoltammetry, magnetic measurements. See DOI: 10.1039/x0xx00000x

Results and Discussion

To introduce phosphinidenides into the coordination sphere of a paramagnetic 3d-transition metal, we fathomed the addition of [(sIDipp)PK] to the Lewis acidic metal(II) hexamethyldisilazanides [ML_2] (M = Mn, Fe; L = –$N(SiMe_3)_2$) of iron and manganese, which were shown to solubilise and stabilize benzyl potassium.[12] First, a suspension of [(sIDipp)PK][5] was treated with one equivalent of [MnL_2] and allowed to stir over night in toluene, which resulted in a brownish/yellow emulsion. After solvent removal under reduced pressure, one equivalent of 18-crown-6 was added to the residue before redissolving in diethyl ether and layering with *n*-pentane to yield yellow crystals amongst others. In contrast to the expected adduct K{18c6}[Mn(sIDipp)L_2], x-ray diffraction analysis revealed the formation of the homoleptic manganese phosphinidenide [Mn{P(sIDipp)}$_2$] (**1, Figure 3)**.

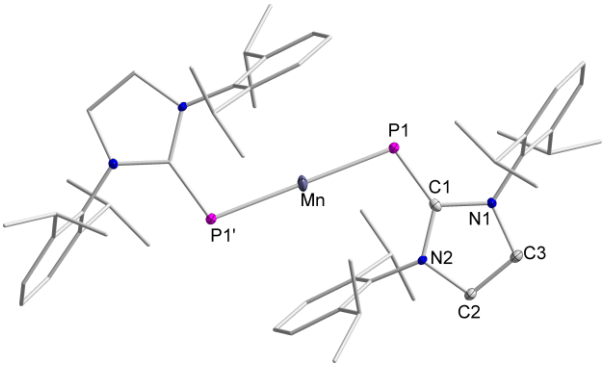

Figure 3. Crystal structure of **1**. All hydrogen atoms are omitted for clarity. Selected bond lengths and angles: Mn–P1 2.4206(6) Å, P1–C1: 1.738(2) Å, C2–C3: 1.510(3) Å, Mn–C^{ipso}: 2.988(2) Å, P1–Mn–P1' 180.0°, Mn–P1–C1 104.68(8)°.

In solid state, **1** shows a linear, symmetry generated geometry at the manganese center with a P1–Mn–P1' bond angle of 180°. Adjacent aryl rings of their NHC substituents are clearly pointing towards the metal atom (Mn–C^{ipso}: 2.988(2) Å), indicating further stabilization of the unsaturated manganese(II) ion. Consequently, the Mn–P1–C1 bond angle is bent to 104.68(8)°. The Mn–P1 bond distance amounts 2.4206(6) Å, whereas the C1–P1 length (1.738(2) Å) is slightly shorter than in comparable two-coordinated main group complexes, as well as in the ruthenium complexes by Tamm.[2,13] All discussed bond lengths and angles assume the presence of a phosphaalkene with a P=C1 double bond character binding to the metal through M–P σ-bonds.[6] As mentioned before, transition metal phosphinidenides are still rare species, whereas **1** now represents the first example of an open-shell phosphenidenide in general and a homoleptic 3d-metal phosphenidenide in particular. In this context it is also worthy to note that homoleptic 3d-metal phosphides with open-shell ions are also rare,[14] which can be attributed to the highly reducing nature of the phosphides (as for phosphinidenides). The initial isolation of **1** was accompanied by inseparable colorless crystals, which were later identified as the manganese(II) trisamide K{18c6}[MnL_3]. This indicated that the manganese hexamethyldisilazanide not only undergoes ligand exchange with [(sIDipp)PK] but also functions as a scavenger of the liberated $KN(SiMe_3)_2$.

Unfortunately, the presence of the trisamide made isolation of **1** very challenging. Adjusting for the stoichiometry and simplified purification, three equivalents of [MnL_2] were reacted with two equivalents of [(sIDipp)PK] in toluene. Subsequently, the crude product was treated with two equivalents crypt–222 in diethyl ether, giving crystalline substrate **1** and K{crypt-222}[MnL_3] after cooling to –40 °C for several days. All crystals were isolated *via* decantation and, as the trisamide is not soluble in toluene, **1** could be isolated *via* extraction in toluene. After drying *in vacuo*, elemental pure [Mn{P(sIDipp)}$_2$] (**1**) was obtained in yields of 36%.

Interestingly, a solvent change from toluene to *n*-pentane leads to the formation of a beige solid, which turned out to be the complex salt [(sIDipp)$PK_2(Et_2O)_4$][MnL_3] (**2a**, **Figure 4**) In the cationic part of **2a**, the phosphorous atom is surrounded in a trigonal planar fashion by one NHC moiety and two potassium atoms. Each potassium ion exhibits interactions with a flanking aryl ring of the sIDipp substituent (K–aryl approx. 3.02 Å) and are further coordinated by two diethyl ether molecules. The K1–P–K2 bond angle amounts to 139.28(3)° with K–P–C1 bond angles of 109.45(8)° (K1) and 111.18(8) (K2), respectively. The P–C1 bond length of 1.708(2) Å can be compared to the analogue bond in the ladder-like complex [K_4{(sIMes)P}$_2${$N(SiMe_3)_2$}$_2$] (1.708(3) Å).[7] The P–K distances in **2a** are with length of 3.2065(9) Å (K1) and 3.1946(9) Å (K2), respectively, in agreement with values found in literature.[7,15] **2a** could be obtained in a rational fashion reacting equimolar amounts of [MnL_2], [(sIDipp)PK] and $KN(SiMe_3)_2$ in yields of 71% (**Scheme 1**). The presence of coordinating Et_2O in the vicinity of a $[(NHC)P]^-$ unit is remarkable given the readily deprotonation of this solvent by [(NHC)PK].[7] In **2a** it is likely overcome by coordination of the phosphinidenide to a second potassium ion.

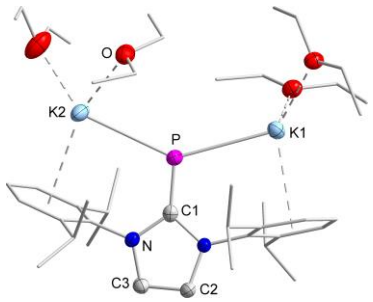

Figure 4. Cationic part of the crystal structure of **2a**. All hydrogen atoms are omitted for clarity. Selected bond lengths and angles: P–K1 3.2065(9) Å, P–K2 3.1946(9) Å, P–C1: 1.708(2) Å, C2–C3: 1.513(3) Å, K1–aryl: 3.0199(6) Å, K2–aryl: 3.0234(6) Å, K1–P–K2 139.28(3)°, K1–P–C1 109.45(8)°, K2–P–C1 111.18(8)°.

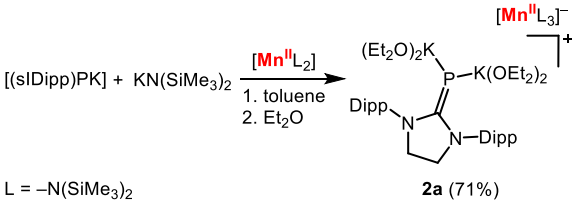

Scheme 1. Direct synthetic path towards complex **2a**.

We assume the formation of **1** commences with an initial ligand exchange of [MnL_2], forming the unidentified heteroleptic complex [Mn{P(sIDipp)}L] (**Scheme 2**). The liberated KL reacts with a second equivalent [MnL_2] yielding [$KMnL_3$]. The latter reacts further with a second phosphinidenide, forming **2a**. In a next step, [Mn{P(sIDipp)}L] undergoes a second ligand exchange by reacting with either [(sIDipp)PK] or **2a**. More regular approaches towards **1** by reacting [(sIDipp)PK] with $MnCl_2$ (or an NHC adduct [(NHC)$MnCl_2$]) in toluene proved not successful. This can be attributed to the low solubility of both educts whereas the use of polar solvents such as Et_2O or THF is precluded due to its deprotonation by [(NHC)PK].[7]

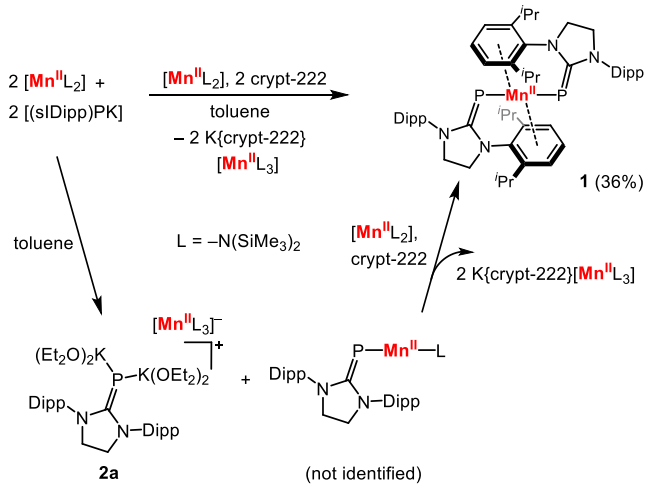

Scheme 2. Proposed mechanism to yield complex **1**.

Attempts to obtain an iron derivative of **1** yielded mostly intractable blackish products, from which only [(sIDipp)$PK_2(Et_2O)_4$][FeL_3], **2b**, could be identified *via* means of x-ray diffraction analysis. Its structural features mimic the one of the manganese containing complex **2a**. This indicated that the highly reducing phosphinidenide [(sIDipp)P]$^-$ fragment might be not suitable for coordination to a low-coordinate, high-spin iron(II) ion.

A solution state magnetic measurement of **2a** *via* the Evans method gave a μ_{eff} of 5.17 μ_B, which is slightly lower than the expected spin-only value for a d^5 configuration ($\mu_{S.O.}$ = 5.92 μ_B). For **1**, solid state measurements were performed *via* a physical properties measurements system (PPMS) in a field of H = 1 T in a temperature range of 5 to 300 K (**Figure 5**). The linear $1/\chi$ vs *T* shows the presence of isolated manganese ions (see Figure S11).The χT vs *T* curve could be fit using the Curie-Weiß law and gave a magnetic moment for **1** of 5.83 μ_B confirming a high-spin manganese(II) complex.[16,17] The curve does not plateau around 5.92 μ_B (4.38 $cm^3\,mol^{-1}\,K$) at higher temperatures, which would be expected from a d^5 ion.[16,18] It is attributed to a substantial temperature-independent paramagnetism (χ_{TIP} = 9.468(6) 10^{-3} emu mol^{-1}) whose origin is still unclear.

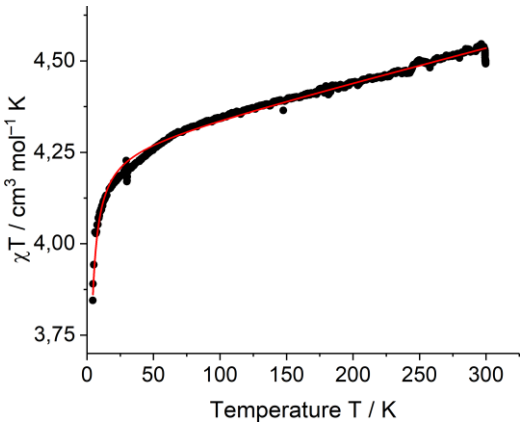

Figure 5. Temperature dependence of the molar magnetic susceptibility times temperature product (χT vs. T) for compound **1**. Data were collected under an applied dc field of 1 T in a temperature range of 5 to 300 K. Molar diamagnetic correction = 10^{-15} emu mol^{-1}, χ_{TIP} = 9.468(6) x 10^{-3} emu mol^{-1}, n_{eff} = 5.837(1) μ_B f.u.$^{-1}$ (f.u. = formula unit), $\chi_M T$ = 4.50 $cm^3\,mol^{-1}\,K$ (300 K), Θ = −0.463(6) K.

The paramagnetic nature of the manganese centers in both complexes **1** and **2a** causes pronounced line broadening and shifting of the signals, prohibiting any ^1H and ^{31}P NMR spectroscopic assignments and observations. In due course, the extremely high moisture and dioxygen sensitivity of **1** became apparent, which usually leads to rapid formation of the parent phosphinidene [(sIDipp)PH]. UV/Vis spectroscopic examinations of **1** and **2a** showed similar absorption maxima, which are located at 378 nm (ε = 2760 L $mol^{-1}\,cm^{-1}$, **2a**) and around 380 nm (ε = 2750 L $mol^{-1}\,cm^{-1}$, **1**). As such they can be attributed to transitions within the phosphinidenide ligand. In the cyclic voltammogram of **1** an irreversible one-electron oxidation process at $E_{1/2}$ = −0.66 V (versus Fc/Fc^+, Figure S9) is observed. Attempts to reduce or oxidize **1** with potassium graphite or silver triflate, respectively, were unsuccessful as employed **1** was reobtained.

Conclusions

Overall, we report on the synthesis of the first open-shell transition metal phosphinidenide. The linear complex [Mn{P(sIDipp)}$_2$] is obtained *via* ligand exchange by reacting [Mn{N(SiMe$_3$)$_2$}$_2$]with the phosphinidenide [(sIDipp)PK]. The electronically and sterically unsaturated manganese ion in [Mn{P(sIDipp)}$_2$] shows secondary interactions with adjacent aryl rings. The highly sensitive [Mn{P(sIDipp)}$_2$] is found in a high-spin state, and proves robust towards chemical one-electron oxidation or reduction. An intermediate of its formation was obtained *via* isolation of the dipotassium salt of the employed phosphinidenide [(sIDipp)$PK_2(Et_2O)_4$][MnL_3]. It can deliberately be obtained *via* reaction of [(sIDipp)PK] with [Mn{N(SiMe$_3$)$_2$}$_2$] in the presence of KN(SiMe$_3$)$_2$.

Experimental Section

Materials and Methods

All manipulations were carried out in a glovebox under a dry argon atmosphere unless indicated otherwise. Used solvents were dried by continuous distillation over sodium metal for several days. Deuterated solvents were used as received, degassed *via* three freeze-pump cycles and stored over molecular sieves 4 Å. The ^{1}H and ^{31}P NMR spectra were recorded on a Bruker HD 500, a Bruker HD 300 or a Bruker HD 250 NMR spectrometer (Bruker Corporation, Billerica, USA). Chemical shifts are reported in ppm relative to the residual proton signals of the solvent (for ^{1}H). $w_{1/2}$ is the line width of a signal at half its maximum intensity. Integrals of the broad signals ligand set were obtained directly or by peak fitting (in case of overlapping signals) using the MestreNova software package (Mestrelab, Santiago de Compostela, Spain). For CV measurements, a microcell HC "closed" stand (rhd instruments) was used in combination with a temperature controller (rhd instruments) and an AUTOLAB PGSTAT 204 (Metrohm GmbH) potentiostat/galvanostat. The measurements were performed at 25 ± 0.1 °C, using a TSC 1600 Closed (rhd instruments) Pt cell in a three-electrode configuration with Pt wires acting as pseudo reference and as working electrode. To secure reproducible conditions, the electrodes were freshly polished, rinsed with THF and dried *in vacuo* for 2 hours. 3 mM of analyte and 0.1 M nBu$_4$N[PF$_6$], which acted as electrolyte, were used in the default measurement setup. The [FeCp$_2$] / [FeCp$_2$]$^+$ (Fc/Fc+) redox couple was utilized as external standard. IR measurements were conducted on a Bruker Alpha ATR-IR spectrometer (Bruker Corporation, Billerica, USA). The UV/VIS measurements were recorded on an AnalytikJena Specord S600 using WinASPECT software. Elemental analysis were performed by the "in-house" service of the Chemistry Department of the Philipps University Marburg, Germany using a CHN(S) analyser vario MICRO Cube (Elementar Analysensysteme GmbH, Langenselbold, Germany). Crypt-222 and KN(SiMe$_3$)$_2$ were obtained commercially and used as received. [Mn{N(SiMe$_3$)$_2$}$_2$][19] and [(sIDipp)PK][8] were prepared according to literature procedures.

[Mn{P(sIDipp)}$_2$] (**1**): 61 mg (0.16 mmol, 3 equiv.) [Mn{N(SiMe$_3$)$_2$}$_2$] and 50 mg [(sIDipp)PK] (0.11 mmol, 2 equiv.) were suspended in 2 mL toluene. After stirring over night at room temperature, the solvent of the yellow solution was evaporated off. The residue was redissolved in Et$_2$O and layered with a saturated solution of crypt-222 (0.11 mmol, 2 equiv.) in Et$_2$O before cooling to −40 °C for crystallization. After several days, a crystalline mixture was obtained. **1** was extracted by adding toluene and subsequent filtration. The filtrate was dried *in vacuo* and [Mn{P(sIDipp)}$_2$] (**1**) was obtained as orange solid in yields of 36%. Crystals, suitable for x-ray diffraction analysis, were obtained from a *n*-pentane layered solution of **1** in Et$_2$O at −40 °C. **Yield:** 21 mg (0.02 mmol, 36%). **^{1}H NMR** (300.2 MHz, THF-d_8, 300 K, ppm): δ = 26.6 (bs, w$_{½}$ = 4760 Hz), 7.07 − 7.17 (m), 3.57* (s), 3.38 (s, w$_{½}$ = 25 Hz), 2.58 (bs, w$_{½}$ = 44 Hz), 2.30 (s, w$_{½}$ = 8.2 Hz), 1.11 (m). * Signal is overlapping with a solvent peak. **^{31}P NMR** (121.5 MHz, 300 K, ppm): δ = Due to the influence of the paramagnetic manganese center on the phosphorous atom no signal is detectable. Elemental analysis $C_{54}H_{76}MnN_4P_2$ (898.12 g/mol): calcd: N 6.24, C 72.22, H 8.53; found: N 6.46, C 72.05, H 8.37%. **IR** (ATR, cm^{-1}): $\tilde{\nu}$ = 3068 (w), 3022 (w), 2957 (m), 2925 (m), 2863 (m), 1587 (w), 1464 (m), 1484 (w), 1446 (m), 1380 (s), 1344 (m), 1324 (m), 1291 (w), 1269 (m), 1252 (w), 1226 (vs), 1201 (s), 1189 (m), 1177 (m), 1145 (m), 1125 (w), 1091 (m), 1057 (m), 996 (w), 936 (m), 899 (m), 871 (m), 793 (s), 760 (w), 750 (m), 726 (m), 698 (m), 652 (w), 632 (w), 615 (m), 571 (w), 556 (s), 492 (s), 434 (m), 419 (m).

[(sIDipp)PK$_2$(Et$_2$O)$_4$][ML$_3$] (M = Mn (**2a**), Fe (**2b**)): 50 mg (0.11 mmol, 1 equiv.) [(sIDipp)PK] and 22 mg KN(SiMe$_3$)$_2$ (0.11 mmol, 1 equiv.) were suspended in 2 mL toluene at -40 °C. After stirring for 30 minutes, a cooled solution (-40 °C) of one equivalent [M{N(SiMe$_3$)$_2$}$_2$] (M = Mn, Fe) (0.11 mmol) in 1 mL toluene was added to the suspension. The orange solution was allowed to stir for another 30 minutes while it was slowly warmed to room temperature. The solvent was evaporated to a minimum before a few drops of diethyl ether were added. It was layered with *n*-pentane and cooled to -40 °C for several days. For manganese, grown crystals were isolated by decanting off the solvent, washing with *n*-pentane and drying *in vacuo*. Orange [(sIDipp)PK$_2$(Et$_2$O)$_4$][MnL$_3$] (**2a**) was obtained in yields of 71%. **Yield:** 81 mg (0.08 mmol, 71%). **^{1}H NMR** (300.2 MHz, THF-d_8, 300 K, ppm): δ = 28.4 (bs, w$_{½}$ = 4450 Hz), 7.17 (m), 3.86 (s, w$_{½}$ = 23 Hz), 3.37 (s, w$_{½}$ = 11 Hz), 2.30 (s, w$_{½}$ = 8.2 Hz), 1.32 (s, w$_{½}$ = 30 Hz), 1.24 (s, w$_{½}$ = 30 Hz), 1.11 (m), -0.23 (s, w$_{½}$ = 9.7 Hz). **^{31}P NMR** (121.5 MHz, 300 K, ppm): δ = Due to the influence of the paramagnetic manganese center on the phosphorous atom no signal is detectable. Elemental analysis $C_{45}H_{92}MnK_2N_5PSi_6$ (1035.88 g/mol): calcd: N 6.76, C 52.18, H 8.95; found: N 6.29, C 52.84, H 9.09%. **IR** (ATR, cm^{-1}): $\tilde{\nu}$ = 2942 (m), 2890 (m), 2867 (m), 1463 (w), 1446 (m), 1382 (m), 1361 (m), 1328 (w), 1269 (m), 1229 (s), 1189 (m), 1148 (w), 1095 (m), 1056 (w), 998 (vs), 933 (w), 869 (s), 823 (vs), 808 (w), 772 (s), 748 (s), 702 (m), 659 (s), 607 (s), 563 (m), 470 (m), 432 (w). **EVANS** (500.1 MHz, 300 K, THF-d_8 +1% TMS): μ_{eff} = 5.17 μ_B; $\mu_{S.O.}$ = 5.92 μ_B.

Obtained orange crystals of [(sIDipp)PK$_2$(Et$_2$O)$_4$][FeL$_3$] (**2b**) were consistently contaminated with intractable blackish oily substances that prohibited further analysis.

X-ray diffraction analysis

Data for compound **1** (CCDC 2113238) were collected at 100 K on a Bruker Quest D8 diffractometer (Bruker Corporation, Billerica, USA) using an Incoatec Microfocus Source Mo-Kα radiation and equipped with an Oxford Instrument Cooler Device (Oxford Instruments, Abingdon, UK) and Photon 100 detector. Data for compounds **2a** (CCDC 2113239), **2b** (CCDC 2113240) and **K{crypt.222}[MnL$_3$]** (CCDC 2115445) were collected on a STOE IPDS2T diffractometer (STOE & Cie GmbH, Darmstadt, Germany) using a graphite-monochromated Mo-Kα radiation (λ = 0.71073 Å) and equipped with an Oxford Instrument Cooler Device (Oxford Instruments, Abingdon, UK). The structures have been solved using either OLEX SHELXT V2014/1[20] and refined by means of least-squares procedures on an F^2 with the aid of the program SHELXL-2016/6[21] included in the software package WinGX version 1.63.[22] The atomic

scattering factors were taken from International Tables for X-ray Crystallography.[23] All non-hydrogen atoms were refined anisotropically. All hydrogen atoms were refined by using a riding model. Disorders were found for **2a** and **2b** in one coordinated Et_2O molecule each and were modelled accordingly. Absorption corrections were introduced by using the MULTISCAN and X-Red programs.[24] Drawings of molecules are performed with the program DIAMOND (Crystal Impact, Bonn, Germany) with 50% probability displacement ellipsoids for non-H atoms. Additional details are given in the Supporting Information.

Conflicts of interest

There are no conflicts to declare.

Acknowledgements

We thank the Philipps University, the Deutsche Forschungsgesellschaft (Grant WE5627/4-1 for C.G.W and Grant HA 3466/9-1 for C.v.H.) and the Dockweiler GmbH for financial support. We thank C. Schneider for the cyclovoltammetric measurements.

References

1 a) M. Y. Abraham, Y. Wang, Y. Xie, P. Wei, H. F. Schaefer, P. v. R. Schleyer and G. H. Robinson, *Chem. Eur. J.*, 2010, **16**, 432–435; b) K. Hansen, T. Szilvási, B. Blom, S. Inoue, J. Epping and M. Driess, *J. Am. Chem. Soc.*, 2013, **135**, 11795–11798; c) A. M. Tondreau, Z. Benkő, J. R. Harmer and H. Grützmacher, *Chem. Sci.*, 2014, **5**, 1545–1554;

2 A. Doddi, D. Bockfeld, T. Bannenberg, P. G. Jones and M. Tamm, *Angew. Chem. Int. Ed.*, 2014, **53**, 13568–13572.

3 M. Peters, A. Doddi, T. Bannenberg, M. Freytag, P. G. Jones and M. Tamm, *Inorg. Chem.*, 2017, **56**, 10785–10793.

4 a) D. Bockfeld, A. Doddi, P. G. Jones and M. Tamm, *Eur. J. Inorg. Chem.*, 2016, **2016**, 3704–3713; b) L. L. Liu, D. A. Ruiz, F. Dahcheh and G. Bertrand, *Chem. Commun.*, 2015, **51**, 12732–12735; c) M. Bispinghoff and H. Grützmacher, *CHIMIA*, 2016, **70**, 279–283;

5 O. Lemp, M. Balmer, K. Reiter, F. Weigend and C. von Hänisch, *Chem. Commun.*, 2017, **53**, 7620–7623.

6 M. Balmer, Y. J. Franzke, F. Weigend and C. von Hänisch, *Chem. Eur. J.*, 2020, **26**, 192–197.

7 M. Balmer, F. Weigend and C. von Hänisch, *Chem. Eur. J.*, 2019, **25**, 4914–4919.

8 M. Balmer and C. von Hänisch, *Z. Anorg. Allg. Chem.*, 2020, **646**, 648–652.

9 M. Bispinghoff, A. M. Tondreau, H. Grützmacher, C. A. Faradji and P. G. Pringle, *Dalton Trans.*, 2016, **45**, 5999–6003.

10 G. Hierlmeier, A. Hinz, R. Wolf and J. M. Goicoechea, *Angew. Chem. Int. Ed.*, 2018, **57**, 431–436.

11 M. Piesch, S. Reichl, M. Seidl, G. Balázs and M. Scheer, *Angew. Chem. Int. Ed.*, 2019, **58**, 16563–16568.

12 a) C. G. Werncke, J. Pfeiffer, I. Müller, L. Vendier, S. Sabo-Etienne and S. Bontemps, *Dalton Trans.*, 2019, **48**, 1757–1765; b) R. Weller, L. Völlinger and C. G. Werncke, *Ber. Dtsch. Chem. Ges.*, 2021, DOI: 10.1002/ejic.202100716;

13 A. Doddi, D. Bockfeld, T. Bannenberg and M. Tamm, *Chem. Eur. J.*, 2020, **26**, 14878–14887.

14 a) S. C. Goel, M. Y. Chiang, D. J. Rauscher and W. E. Buhro, *J. Am. Chem. Soc.*, 1993, **115**, 160–169; b) K. Kaniewska, Ł. Ponikiewski, N. Szynkiewicz, B. Cieślik, J. Pikies, J. Krzystek, A. Dragulescu-Andrasi, S. A. Stoian and R. Grubba, *Dalton Trans.*, 2020, **49**, 10091–10103;

15 a) G. W. Rabe, H. Heise, G. P. A. Yap, L. M. Liable-Sands, I. A. Guzei and A. L. Rheingold, *Inorg. Chem.*, 1998, **37**, 4235–4245; b) R. Wolf and E. Hey-Hawkins, *Z. Anorg. Allg. Chem.*, 2006, **632**, 727–734; c) M. S. Winston and J. E. Bercaw, *Organometallics*, 2010, **29**, 6408–6416;

16 C. G. Werncke, E. Suturina, P. C. Bunting, L. Vendier, J. R. Long, M. Atanasov, F. Neese, S. Sabo-Etienne and S. Bontemps, *Chem. Eur. J.*, 2016, **22**, 1668–1674.

17 A. E. Ashley, A. R. Cowley, J. C. Green, D. R. Johnston, D. J. Watkin and D. L. Kays, *Eur. J. Inorg. Chem.*, 2009, **2009**, 2547–2552.

18 C. Ni, J. C. Fettinger, G. J. Long and P. P. Power, *Dalton Trans.*, 2010, **39**, 10664–10670.

19 H. Bürger and U. Wannagat, *Monatsh. Chem.*, 1964, **95**, 1099–1102.

20 O. V. Dolomanov, L. J. Bourhis, R. J. Gildea, J. Howard and H. Puschmann, *J. Appl. Crystallogr.*, 2009, **42**, 339–341.

21 G. M. Sheldrick, *Acta. Crystallogr. C*, 2015, **71**, 3–8.

22 L. J. Farrugia, *J. Appl. Crystallogr.*, 1999, **32**, 837–838.

23 *International tables for crystallography*, International Union of Crystallography; Springer, Chester, England, New York, 1st edn., 2006.

24 a) SADABS-2016/2, *Bruker*, 2016; b) X.-R. 1. X-Area, *STOE*, 2016;

6 Zusammenfassung

Im Rahmen dieser Doktorarbeit wurden neuartige (quasi-)lineare 3d-Metall(II)- und 3d-Metall(I)-Komplexe synthetisiert und deren Eigenschaften sowie Reaktivitäten hinsichtlich verschiedener Substrate näher erforscht.

Der Fokus lag zunächst auf der Synthese Silylamid-basierter Verbindungen des Typs $[M(N(Dipp)SiR_3)_2]^{0,-}$ (M = Cr − Co) mit elektronenreichen Phenyl- bzw. Allylsubstituenten (SiR_3 = $SiPh_{3-n}Me_n$ (n = 1 − 3), $SiMe_2(allyl)$) im Ligandrückgrat (**Schema 29**). In den divalenten Metall(II)-Derivaten führt die Präsenz von Phenyleinheiten zur Ausbildung sekundärer Metall−Aren-Wechselwirkungen, welche stark abgewinkelte N−M−N-Achsen verursachen. Im Fall von Eisen und Kobalt verschwinden diese Interaktionen durch Reduktion zu den entsprechenden Metall(I)-Komplexen mit KC_8 in Anwesenheit von 18-Krone-6. Auf struktureller Ebene konnte so gezeigt werden, dass anionische Metall(I)-Ionen eine − im Vergleich zu ihren divalenten und neutralen Analoga − vernachlässigbare LEWIS-Azidität besitzen. Ähnliche Ergebnisse wurden bei dem Einbau der Propenyleinheit in Metall(II)-Komplexe von Chrom bis Kobalt erzielt. Besonders erwähnenswert ist hierbei das Mangan-Derivat, in welchem erstmals eine intramolekulare Mangan−Alken-Wechselwirkung dokumentiert wurde. Aufgrund langer Metall−Alken-Abstände und einem C═C-Doppelbindungscharakter im Propenylfragment sind die sekundären Interaktionen trotz abgewinkelter N−M−N-Achsen jedoch als schwach anzusehen. Die Reduktion mit KC_8 in Anwesenheit von 18-Krone-6 führt, konträr zu den Arylsubstituenten, zu verstärkten π-Rückbindungen (Co), die im Fall von Chrom sogar bis hin zu einer intermolekularen C−C-Kopplungsreaktion der Allyleinheiten unter Bildung eines binuklearen Chrom(II)-Alkyl-Komplexes reicht. Diese Ergebnisse zeigen, dass lineare, anionische 3d-Metall(I)-Komplexen eher als elektronenreich angesehen werden sollten. Die Umsetzungen der beiden Kobalt(I)-Komplexe $K\{18c6\}[Co(N(Dipp)SiMe_2R)_2]$ (R = Ph, allyl) mit dem Organoazid $Dipp{-}N_3$ ergaben seltene Beispiele trigonaler *High-Spin*-Kobalt-Imido-Komplexe. Interessanterweise findet im Fall von $K\{18c6\}[Co(N(Dipp)((N(Dipp)SiMe_2(allyl))_2]$ keine Reaktion zwischen dem intramolekular gebundenen Alken und der Imidyl-Einheit statt.

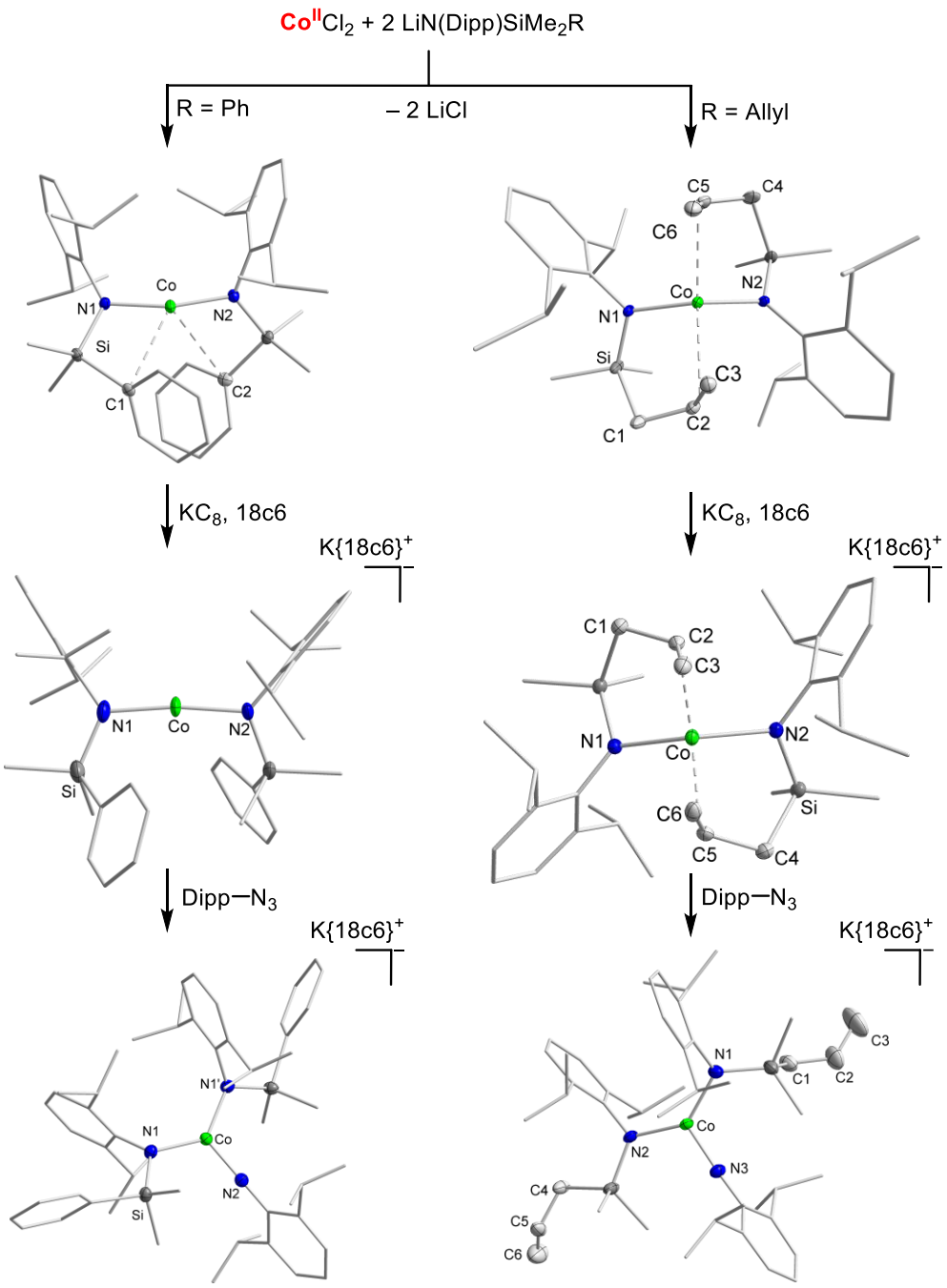

Schema 29. Einfluss elektronenreicher Substituenten in zweifach-koordinierten Silylamid-Komplexen und anschließender Umsetzung mit Dipp-Azid am Beispiel von Kobalt.

Weitere Untersuchungen innerhalb dieser Doktorarbeit beschäftigten sich mit der Wahl des Reduktionsmittels sowie der Variation des kationischen Gegenions. Am Beispiel von [Fe(N(Dipp)SiMe$_3$)$_2$] wurde gezeigt, dass die Reduktion eines Metall(II)-Silylamids nicht nur auf Kalium (in Form von KC_8) beschränkt ist, sondern auch auf weitere Alkalimetalle wie Natrium (in Na/NaCl, 5% v/v) oder Lithium (elementar) ausgeweitet werden kann (**Schema 30**). Während die Reduktion zu den Eisen(I)-Verbindungen des Typs M^A[Fe(N(Dipp)SiMe$_3$)$_2$] (M^A = Na, Li) in Lösung mittels ^{1}H-NMR Spektroskopie verfolgt werden konnte, war die Isolierung im Festkörper nur in Anwesenheit eines

Kryptanden möglich. Dies steht im Kontrast zu den neutralen, Kalium-haltigen Analoga [KM(N(Dipp)SiR$_3$)$_2$] (Cr (R = ^{i}Pr), Mn − Co (R = Me)), die im Zuge dieser Arbeit erfolgreich synthetisiert und isoliert wurden (**Schema 30**). In ihnen ist das K$^+$-Ion entweder intermolekular in Form polymerer Ketten (Cr − Fe) oder intramolekular (Fe, Co) zwischen den Arylsubstituenten interkaliert. Unterschiedlichste räumliche Ligand-Anordnungen (*cis*, *trans* oder orthogonal) zeigen, dass nicht nur intra-, sondern auch intermolekulare Wechselwirkungen die Geometrie der Komplexionen ohne Beeinflussung der Metall−Amid-Bindungslängen bestimmen. Die in der Literatur diskutierten intramolekularen Dispersionswechselwirkungen sind somit wichtige, aber keine essenziellen Stabilisierungsfaktoren in linearen 3d-Metall(I)-Verbindungen.

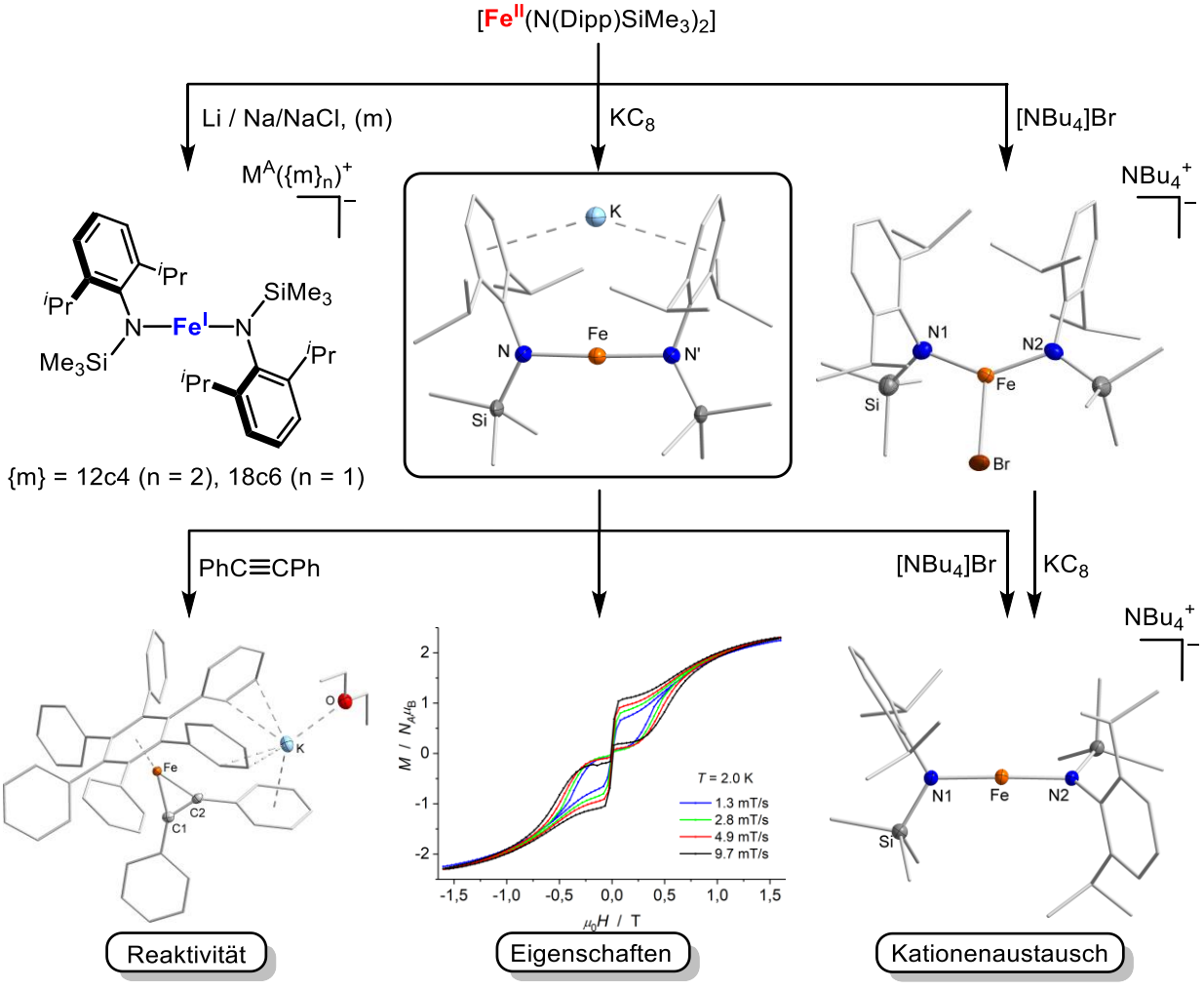

Schema 30. Überblick über die in dieser Arbeit vorgenommenen Untersuchungen an Silylamid-basierten Komplexen am Beispiel von [Fe(N(Dipp)SiMe$_3$)$_2$].

Durch Zugabe weniger Äquivalente LEWIS-basischer Substrate wie Diethylether, THF oder DMAP konnte erneut bestätigt werden, dass die Metall(I)-Zentren als eher elektronenreich behandelt werden sollten, da die kleinen Moleküle im Festkörper ausschließlich an das Kaliumkation und nicht an das Metall(I)-Atom koordinieren.

^{1}H-NMR spektroskopische Untersuchungen des Kobaltderivats zeigten zudem Ionenseparierung in stark koordinierenden Lösungsmitteln (z. B. THF), während das Kaliumion in nicht bzw. schwach koordinierenden Lösungsmitteln (Toluol, Diethylether oder *n*-Pentan) in der Nähe des Metallanions bleibt.

Anhand von [KFe(N(Dipp)SiMe$_3$)$_2$] wurden die elektronischen und magnetischen Eigenschaften der Neutralkomplexe untersucht. Diese Eisenverbindung stellt ein seltenes Beispiel eines Übergangsmetall-basierten Einzelmolekülmagneten dar. Messungen mithilfe der SQUID-Methode zeigen eine ‚close-waist' Hysterese unterhalb der Blocktemperatur T_B von 4.5 K (**Schema 30**). Die Barriere des Spinumkehrs von U_{eff} = 184 cm^{-1} stimmt gut mit einem magnetischen Übergang zwischen Grund- und angeregtem Zustand bei 180 cm^{-1} überein, welcher mittels feldabhängiger IR-Spektroskopie ermittelt und durch quantenchemische Berechnungen (AILFT) bestätigt wurde. Die Ergebnisse sind erstaunlich, da die intramolekulare Kaliumstabilisierung die N–M–N-Achse leicht abwinkelt und eine erniedrigte Symmetrie im System vorliegt. Mit diesen ungewöhnlichen Eigenschaften wurden die synthetischen Möglichkeiten und das Potenzial zur Konstruktion einkerniger SIMs erweitert.

Statt einem Ladungsausgleich durch ein anorganisches Alkalimetall ist die Stabilisierung der metallorganischen Metall(I)-Ionen ebenso durch ein organisches Gegenion möglich. Die Komplexe NBu$_4$[M(N(Dipp)SiMe$_3$)$_2$] (M = Fe, Co) können durch Umsetzung der Neutralkomplexe [KM(N(Dipp)SiMe$_3$)$_2$] (M = Fe, Co) mit [NBu$_4$]Br durch einen Kationenaustauch unter Abspaltung von KBr in moderaten Ausbeuten dargestellt werden (**Schema 30**). Ein alternativer Zugang besteht über die neu entwickelten, trigonalen Metall(II)-Halogenido-Komplexe, NBu$_4$[M(Br)L$_2$] (M = Mn − Co, L = −N(SiMe$_3$)$_2$, −N(Dipp)SiMe$_3$), durch Reduktion mit KC$_8$ oder, gezeigt am Beispiel von Kobalt, durch Umsetzung mit KHBEt$_3$. Bei Verwendung von KC$_8$ ist die Isolierung der Metall(I)-Komplexe jedoch auf wenige Derivate und geringe Ausbeuten beschränkt. Die Synthese der Halogenido-Komplexe erfolgt durch eine Additionsreaktion zwischen den Metall(II)-Präkursoren [ML$_2$] (M = Mn − Co, L = −N(SiMe$_3$)$_2$, −N(Dipp)SiMe$_3$) und dem organischen Salz [NBu$_4$]Br. Im Fall von Chrom führte dieselbe Vorgehensweise entweder zu einem zweifachen Ligandaustausch (L = −N(Dipp)SiMe$_3$) oder einer intramolekularen Deprotonierung (L = −N(SiMe$_3$)$_2$).

Analog konnte das üblicherweise unlösliche Benzylkalium (BnK) an die divalenten Silylamide addiert und die neutralen Komplexe [KM(Bn)(N(SiMe$_3$)$_2$)$_2$] (M = Mn, Co) synthetisiert und isoliert werden. Auch hier wird das Kaliumion, ähnlich zu den oben

beschriebenen Neutralkomplexen [KM(N(Dipp)SiR$_3$)$_2$] (Cr (R = ^{i}Pr), Mn − Co (R = Me)), intermolekular zwischen dem benzylischen Ring und zwei Silylamid-Liganden interkaliert. Die sich so formenden polymeren Ketten können durch Zugabe von 18-Krone-6 und anschließender Interkalation des Kations in das Maskierungsreagenz aufgebrochen werden.

Ebenso wurde nachgewiesen, dass die Anwesenheit eines Maskierungsreagenz die Reaktivität von Metall(I)-Komplexen beeinflusst. Während die stöchiometrische Umsetzung des internen Alkins Diphenylacetylen mit den ladungsseparierten Komplexen K{18c6}[M(N(Dipp)SiMe$_3$)$_2$] (M = Mn, Fe) *side-on*-koordinierte η^2-Alkin-Komplexe ergeben, wird das Olefin durch die Neutralkomplexe [KM(N(Dipp)SiMe$_3$)$_2$] (M = Mn, Fe) unter sukzessiver Abspaltung von Silylamid-Liganden bis hin zu dem Hexaphenylbenzol-Derivat [K(Et$_2$O)$_n$Fe(HPB)(η^2-PhCCPh)] (n = 0, 1) zyklotrimerisiert (**Schema 30**). Dabei konnten ungewöhnliche Intermediate isoliert werden, die für die Aufklärung Übergangsmetall-katalysierter Alkintrimerisierungen sehr aufschlussreich sein können. Die Ergebnisse lassen auf eine Labilisierung der Metall−Amid-Bindungen durch die intramolekulare Kaliumstabilisierung schließen.

Mittels ^{1}H-NMR spektroskopischen Untersuchungen wurden am Beispiel von Eisen auch die katalytischen Eigenschaften von Silylamid-basierten Komplexen bezüglich Alkinisomerisierungen erforscht (**Schema 31**).

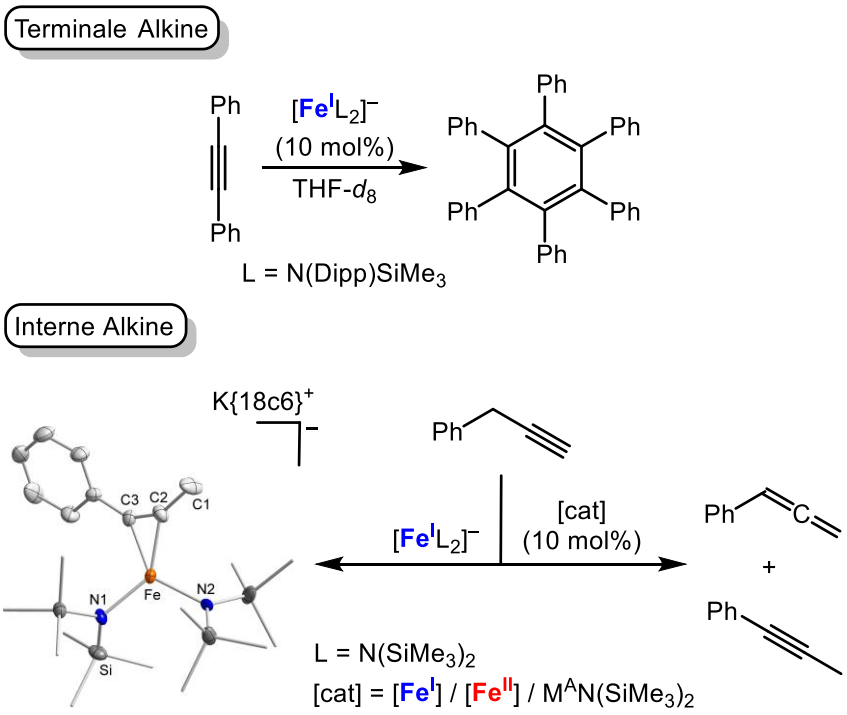

Schema 31. Übersicht über mögliche Alkinisomerisierungen mithilfe verschiedener Eisen- und Alkalimetall-basierter Silylamide.

Es konnte gezeigt werden, dass K{18c6}[Fe(N(Dipp)SiMe$_3$)$_2$] die Zyklotrimerisierung interner Alkine katalysiert, auch wenn diese Fähigkeit bisher auf Diphenylacetylen beschränkt ist. Interessanterweise ist dies mit dem Hexamethyldisilazanid-Komplex K{18c6}[Fe(N(SiMe$_3$)$_2$)$_2$] nicht möglich, obwohl dieser sterisch weniger anspruchsvoll ist und beide Verbindungen bei stöchiometrischen Umsetzungen *side-on*-Komplexe ausbilden.[252]

Dem gegenüber werden für terminale Alkine keine Trimerisierungsreaktionen beobachtet. Stattdessen findet im Fall des benzylischen Alkins 3-Phenylpropin eine katalytische Umlagerung der Dreifachbindung statt. Dabei lagert das innerhalb weniger Minuten gebildete Phenylallen innerhalb von 24 Stunden (K{18c6}[Fe(N(Dipp)SiMe$_3$)$_2$]) bzw. einem Tag (K{18c6}[Fe(N(SiMe$_3$)$_2$)$_2$]) zu 1-Phenylpropin weiter um.

Diese 1,3-H-Atomumlagerung konnte auch im Festkörper durch die Isolierung des olefinischen Eisenkomplexes K{18c6}[Fe(PhCCMe)(N(SiMe$_3$)$_2$)$_2$] nachgewiesen werden, welcher durch die stöchiometrische Umsetzung von K{18c6}[Fe(N(SiMe$_3$)$_2$)$_2$] mit 3-Phenylpropin entsteht. Alternativ kann dieser auch durch eine Additionsreaktion zwischen besagtem Präkursor und 1-Phenylpropin dargestellt werden.

Mit dem sterisch anspruchsvolleren Ligandsystem –N(Dipp)SiMe$_3$ konnte mittels ^{1}H-NMR Spektroskopie lediglich die Umlagerung zu Phenylallen beobachtet und kein Komplex isoliert werden. In Zusammenhang mit den Ergebnissen der katalytischen Studien lässt dies auf eine höhere Bindungsaffinität des Olefins hinsichtlich des sterisch anspruchsloseren Komplexes K{18c6}[Fe(N(SiMe$_3$)$_2$)$_2$] schließen. Dadurch werden der Substrataustausch und damit auch die katalytische Umsetzung verlangsamt.

Während die katalytische Umlagerung zu Phenylallen auch mit dem trigonalen Eisen(II)-Trisamid K{18c6}[Fe(N(SiMe$_3$)$_2$)$_3$] zu beobachten ist, bleibt die neutrale Eisen(II)-Spezies [Fe(N(SiMe$_3$)$_2$)$_2$] bezüglich Alkinen inaktiv. Mechanistisch wird von De- bzw. Reprotonierungsprozessen ausgegangen, da auch die metallfreien Alkalisalze M^{A}N(SiMe$_3$)$_2$ (M^A = K, Li) die Alkinumlagerung katalysieren. Im Fall von Kalium ist die Isomerisierung bereits nach wenigen Minuten vollendet und damit wesentlich effizienter als die oben beschriebenen Eisenkomplexe.

Ein weiteres Ziel dieser Arbeit war es, (quasi-)lineare 3d-Metall(II/I)-Komplexe mit Phosphor-basierten Ligandsystemen zu entwickeln. Dafür wurden die divalenten

Hexamethyldisilazanide [M(N(SiMe$_3$)$_2$)$_2$] (M = Mn − Co) mit dem Phosphiniden [(sIDipp)PH] bzw. dem deprotonierten Analogon [(sIDipp)PK] umgesetzt (**Schema 32**). Während mit dem ‚parent' Phosphiniden labile, dreifach-koordinierte Addukte des Typs [M(PH(sIDipp))(N(SiMe$_3$)$_2$)$_2$] (M = Mn − Co) gebildet werden, findet durch Verwendung des normal unlöslichen Kalium-Phosphinidenids im Fall von Mangan ein Ligandaustausch statt. Nach der intermediären Bildung des ionischen Komplexes [(sIDipp)PK$_2$(Et$_2$O)$_4$][MnL$_3$] wird der zweifach-koordinierte Komplex [Mn(P(sIDipp))$_2$] gebildet, welcher die erste dokumentierte offenschalige Übergangsmetall-Phosphinidenid-Verbindung darstellt. Im Festkörper wird das Manganzentrum linear von den Liganden umgeben und zusätzlich durch intramolekulare Metall−Aren-Wechselwirkungen stabilisiert. Ein Oxidationsversuch mit Silbertriflat sowie eine angestrebte Reduktion mit KC$_8$ waren nicht erfolgreich.

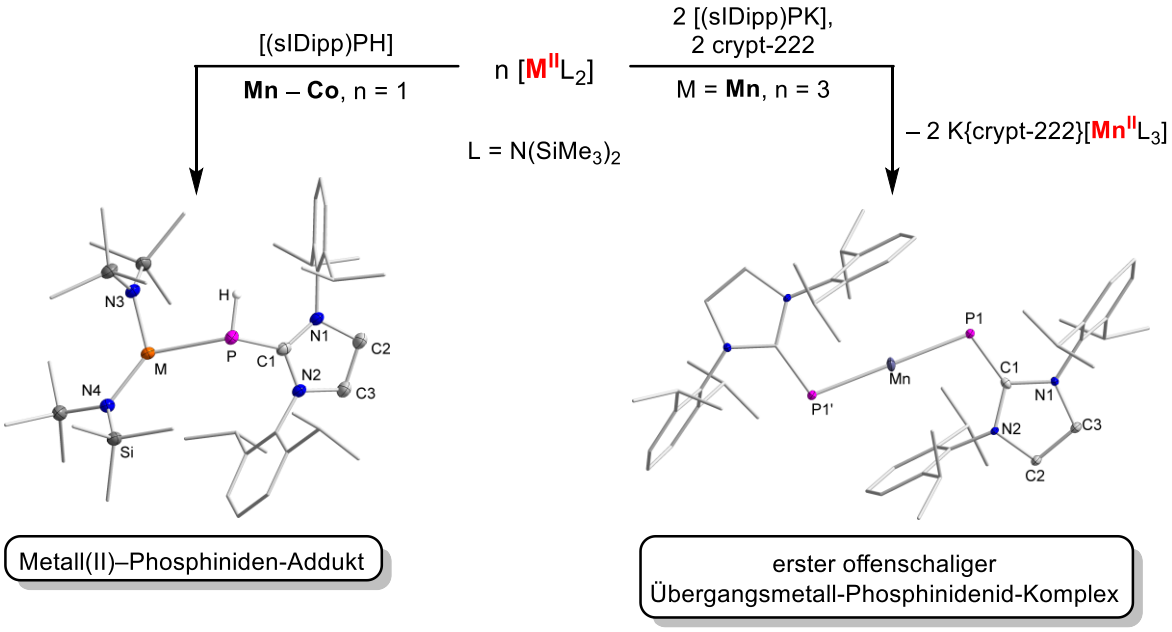

Schema 32. Entstehung verschiedener Reaktionsprodukte durch Umsetzung von [M(N(SiMe$_3$)$_2$)$_2$] (M = Mn − Co) mit [(sIDipp)PR] (R = H, K).

Durch die Studien innerhalb dieser Arbeit konnte das Wissen über homoleptische, (quasi-)lineare 3d-Metall(II/I)-Komplexe erweitert werden. Es wurden sowohl synthetische Grenzen Silylamid-basierter Derivate ausgelotet als auch der Einfluss struktureller Veränderungen auf die molekularen Eigenschaften sowie die Reaktivitäten hinsichtlich verschiedener Substrate erforscht. Ebenso konnte das Spektrum linearer 3d-Metall(II)-Komplexe auf eine Phosphor-basierte Verbindung ausgedehnt werden.

7 English Summary

Within the framework of this PhD thesis, a number of novel (quasi-)linear 3d-metal(II)- and 3d-metal(I) complexes could be synthesized. Additionally, their properties as well as their reactivities, with respect to different substrates, were explored.

The initial focus lay on the synthesis of silylamide-based compounds of the type $[M(N(Dipp)SiR_3)_2]^{0,-}$ (M = Cr − Co) with electron rich phenyl or allyl substituents (SiR_3 = $SiPh_{3-n}Me_n$ (n = 1 − 3), $SiMe_2$(allyl)) in the ligand backbone (**Scheme 1**). In the divalent metal(II) derivatives, the presence of phenyl moieties led to the formation of secondary metal−arene interactions causing strongly angled N−M−N axes. In the case of iron and cobalt, these interactions disappear by reduction to the corresponding metal(I) complexes with KC_8 in the presence of 18-crown-6. Thus, at a structural level, anionic metal(I) ions were shown to have − compared to their divalent and neutral counterparts − negligible LEWIS acidity. Similar results were obtained for the incorporation of the propenyl moiety into metal(II) complexes from chromium to cobalt. Here, the manganese derivative is of particularly noteworthy as an intramolecular manganese−alkene interaction is documented for the first time. Due to long metal−alkene distances and a C═C double bond character in the propenyl fragment, the secondary interactions are, however, considered weak despite strongly bent N−M−N axes. Contrary to the observations for the aryl derivatives, reduction with KC_8 in the presence of 18-crown-6 leads to enhanced π-backbonding (Co), which even extends to an intermolecular C−C coupling reaction of the allyl moieties to form a binuclear metal(II)-alkyl complex in the case of chromium. These results indicate that anionic, linear 3d-metal(I) complexes should be seen as electron rich. The conversion of the two cobalt(I) complexes $K\{18c6\}[Co(N(Dipp)SiMe_2R)_2]$ (R = Ph, allyl) with the organoazide Dipp-N_3 gave rare examples of trigonal *high-spin* cobalt-imido complexes. Interestingly, no reaction between the intramolecularly bound alkene and the imidyl moiety took place in the case of $K\{18c6\}[Co(N(Dipp))\ (N(Dipp)SiMe_2(allyl))_2]$.

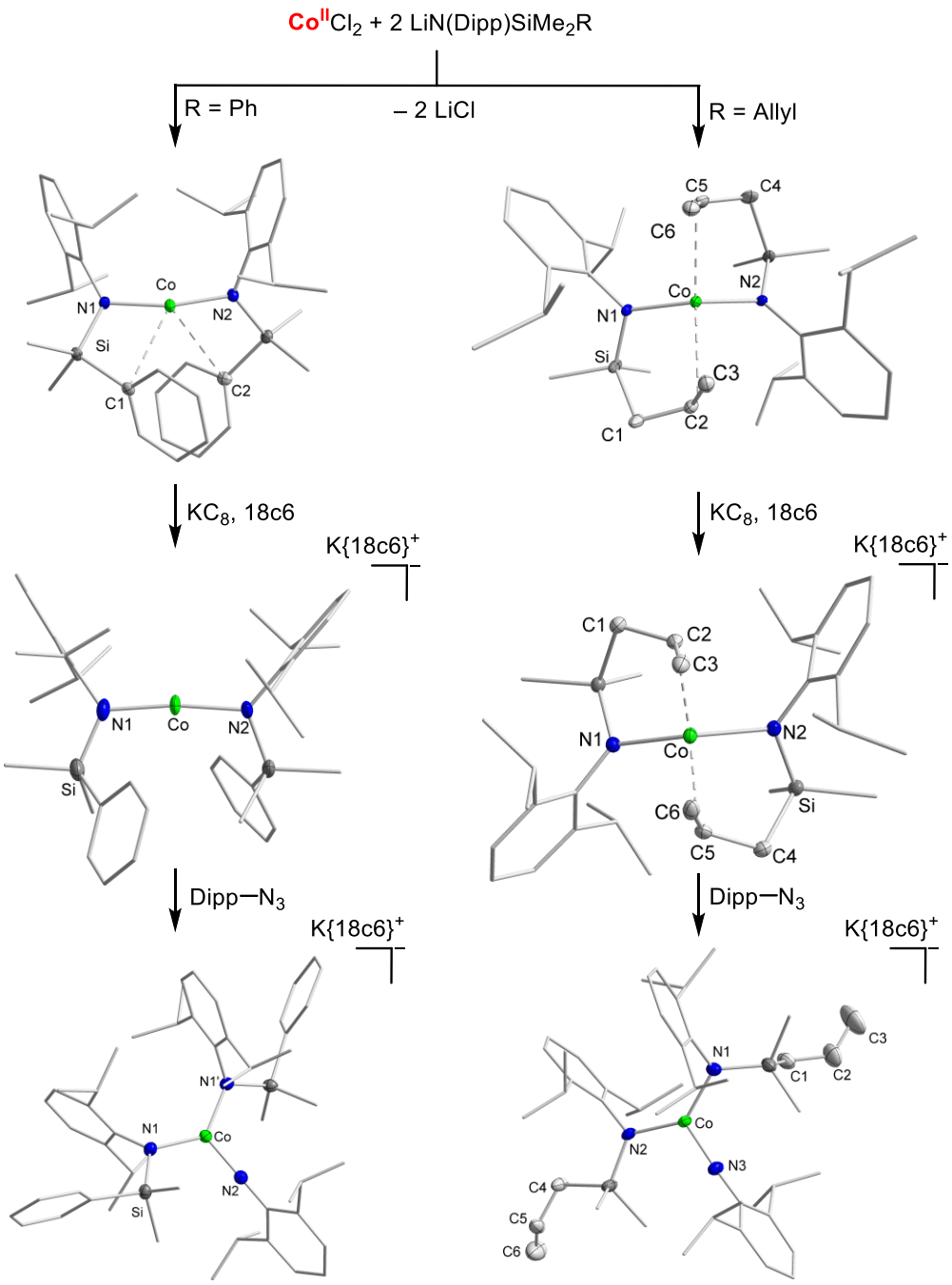

Scheme 1. Influence of electron rich substituents in two-coordinated silylamide complexes and subsequent reaction with Dipp azide at the example of cobalt.

Further investigations within this thesis dealt with the choice of the reducing agent as well as the variation of the cationic counter ion. In case of $[Fe(N(Dipp)SiMe_3)_2]$, it was shown that the reduction of a metal(II) silylamide is not limited to potassium (in form of KC_8), but can also be extended to other alkali metals such as sodium (in Na/NaCl, 5% v/v) or lithium (elemental) (**Scheme 2**). While the reduction to the iron(I) compounds $M^A[Fe(N(Dipp)SiMe_3)_2]$ (M^A = Na, Li) could be followed by ^1H NMR spectroscopy in solution, isolation in solid state was only possible in the presence of a cryptand. This contrasts with the neutral, potassium-containing analogues $[KM(N(Dipp)SiR_3)_2]$ (Cr

(R = ^{i}Pr), Mn − Co (R = Me)), which were successfully synthesized and isolated in the course of this work (**Scheme 2**), too. In them, the K^{+}-ion is intercalated either intermolecularly in form of polymeric chains (Cr − Fe) or intramolecularly (Fe, Co) between the two aryl substituents. A wide variety of spatial ligand arrangements (*cis*, *trans* or orthogonal) show that not only intra- but also intermolecular interactions determine the geometry of the complex ions without affecting the metal−amide bond lengths. Intramolecular dispersion forces discussed in literature are thus important but not essential for stabilizing linear 3d-metal(I) compounds.

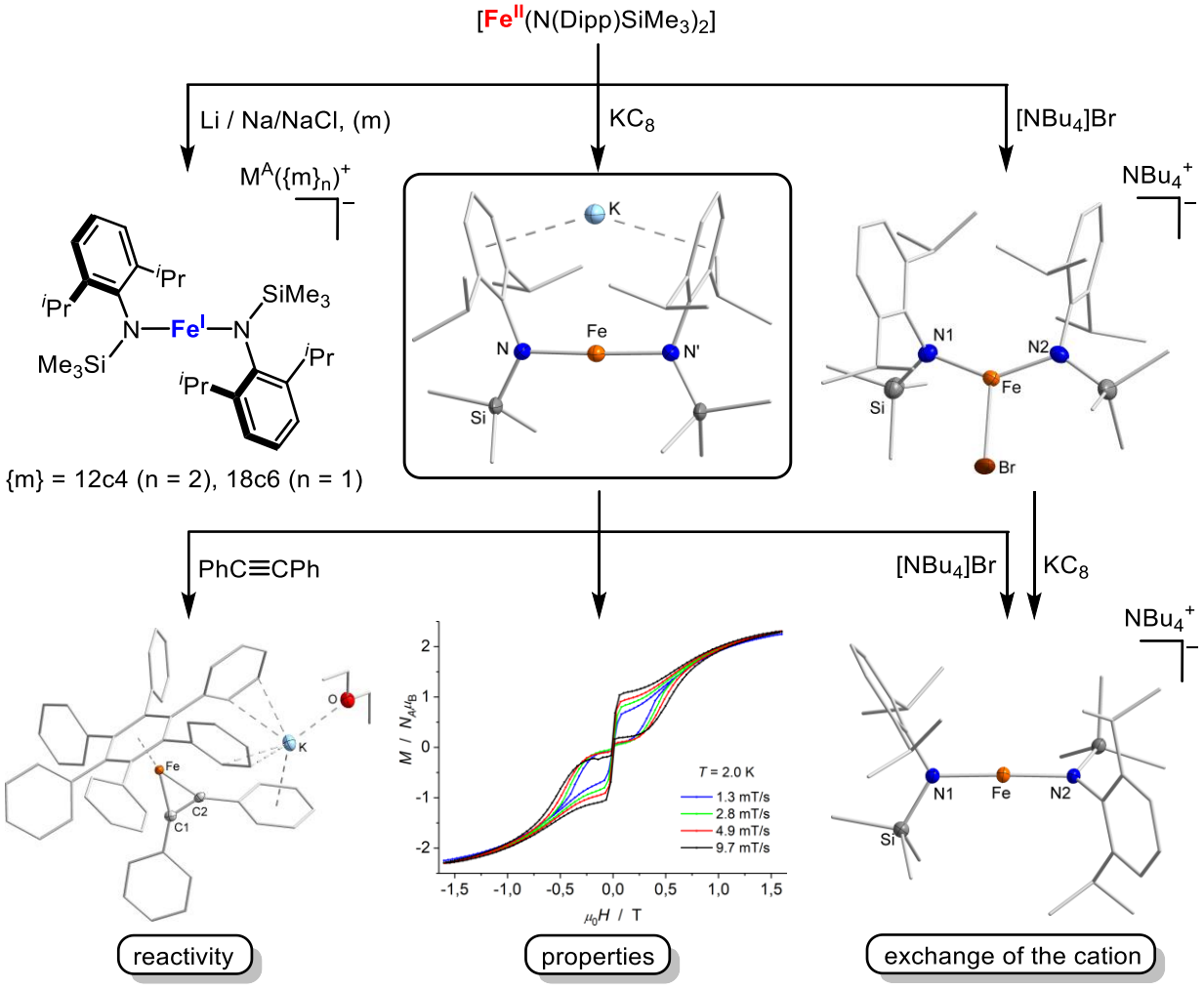

Scheme 2. Overview of the studies on silylamide-based complexes carried out in this work using [Fe(N(Dipp)SiMe$_3$)$_2$] as an example.

Addition of a few equivalents of LEWIS-basic substrates such as diethyl ether, THF or DMAP, reconfirmed that 3d-metal(I) centres should be treated as rather electron rich, since the tested molecules coordinate exclusively to the potassium cation and not to the metal(I) atoms in solid state. For cobalt, ^{1}H NMR spectroscopic studies showed ion separation in strongly coordinating solvents (e. g. THF), while the potassium ion

remains close to the metal anion in non- or weakly coordinating solvents like toluene, diethyl ether, or *n*-pentane.

The electronic and magnetic properties of the neutral complexes were investigated using the iron derivative [KFe(N(Dipp)SiMe$_3$)$_2$]. The compound represents a rare example of a transition metal-based single-molecule magnet. Measurements using the SQUID method show a 'close-waist' hysteresis below a block temperature T_B of 4.5 K (**Scheme 2**). The magnetic barrier of spin reversal (U_{eff} = 184 cm^{-1}) agrees well with a magnetic transition between ground and excited state at 180 cm^{-1}. This was determined by field-dependent IR spectroscopy and further confirmed by quantum chemical calculations (*via* AILFT). The results are surprising as the intramolecular potassium stabilization slightly angles the N−M−N axis, which lowers the symmetry in the system. With these unusual properties, the synthetic possibilities and the potential for constructing mononuclear SIMs are extended.

Instead of charge balancing by an inorganic alkali metal, the stabilization of the organometallic metal(I) ions is also possible by organic counter ions. By reacting the neutral complexes [KM(N(Dipp)SiMe$_3$)$_2$] (M = Fe, Co) with [NBu$_4$]Br, the metal(I) complexes NBu$_4$[M(N(Dipp)SiMe$_3$)$_2$] (M = Fe, Co) can be prepared *via* cation exchange upon elimination of KBr in moderate yields (**Scheme 2**). An alternative approach *via* reduction of the newly developed trigonal metal(II) halido complexes, NBu$_4$[M(Br)L$_2$] (M = Mn − Co, L = −N(SiMe$_3$)$_2$, -N(Dipp)SiMe$_3$) with KC$_8$ is also possible or, shown at the example of cobalt, by reacting them with KHBEt$_3$. However, when KC$_8$ is used, the isolation of the metal(I) complexes is limited to a few derivatives and low yields.

The halido complexes were obtained through addition reactions between the metal(II) precursors [ML$_2$] (M = Mn − Co, L = −N(SiMe$_3$)$_2$, −N(Dipp)SiMe$_3$) and the organic salt [NBu$_4$]Br. In the case of chromium, the same procedure led to either a two-fold ligand exchange (L = −N(Dipp)SiMe$_3$) or an intramolecular deprotonation (L = −N(SiMe$_3$)$_2$).

Similarly, the usually insoluble benzyl potassium (BnK) could be added to the divalent silylamides. Thus, the neutral complexes [KM(Bn)(N(SiMe$_3$)$_2$)$_2$] (M = Mn, Co) were synthesized and isolated. Similar to the neutral derivatives [KM(N(Dipp)SiR$_3$)$_2$] (Cr (R = ^{i}Pr), Mn − Co (R = Me)), *vide supra*, the potassium ion is intercalated intermolecularly between the benzylic ring and two silylamide ligands. The formed polymeric chains can be sequestered by addition of 18-crown-6 and subsequent intercalation of the cation into the masking reagent.

Within this work it was also demonstrated that the presence of a masking reagent affects the reactivity of metal(I) complexes, as well. While the stoichiometric reactions of the internal alkyne diphenyl acetylene with the charge separated complexes K{18c6}[M(N(Dipp)SiMe$_3$)$_2$] (M = Mn, Fe) give *side-on* coordinated η^2-alkyne complexes, the same olefin is trimerised by the neutral [KM(N(Dipp)SiMe$_3$)$_2$] (M = Mn, Fe) with successive decoordination of the silylamide ligands. This gave unusual intermediates, such as the hexaphenyl benzene derivative [K(Et$_2$O)$_n$Fe(HPB)(η^2-PhCCPh)] (n = 0, 1) (**Scheme 2**), which are very informative for the elucidation of transition metal-catalysed alkyne trimerisation. Further, the results overall suggest a weakening of the metal−amide bonds by intramolecular potassium stabilization.

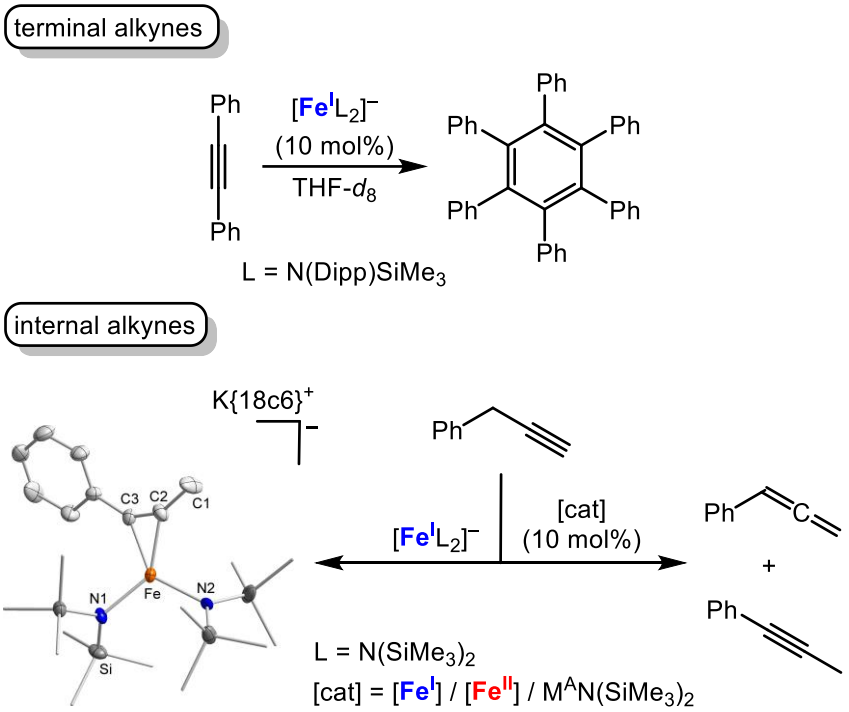

Scheme 3. Overview of possible alkyne isomerisation processes using different iron- and alkali metal-based silylamides.

Using iron as an example, the catalytic properties of silylamide-based complexes with respect to alkyne isomerisation were explored by means of ^{1}H NMR spectroscopy (**Scheme 3**). It was shown that K{18c6}[Fe(N(Dipp)SiMe$_3$)$_2$] catalyses the cyclotrimerisation of internal alkynes, although this ability has so far been limited to diphenyl acetylene. Interestingly, this rearrangement is not possible with the hexamethyldisilazanide complex K{18c6}[Fe(N(SiMe$_3$)$_2$)$_2$], although the sterical demand is lower and both compounds form *side-on* complexes in stoichiometric reactions.

In contrast, no trimerisation reactions were observed for terminal alkynes. Instead, a catalytic shift of the triple bond takes place in the case of the benzylic alkyne 3-phenyl

propyne. After the initial formation of phenyl allene, it subsequently rearranges further to 1-phenyl propyne within the course of 24 hours (K{18c6}[Fe(N(Dipp)SiMe$_3$)$_2$]) or one week (K{18c6}[Fe(N(SiMe$_3$)$_2$)$_2$]).

This 1,3-H atom shift was also evident in solid state through isolation of the olefinic iron complex K{18c6}[Fe(PhCCMe)(N(SiMe$_3$)$_2$)$_2$], which was synthesized *via* the stoichiometric reaction of K{18c6}[Fe(N(SiMe$_3$)$_2$)$_2$] with 3-phenyl propyne. Alternatively, the reaction between the divalent precursor and 1-phenyl propyne leads to the same product.

With the sterically more encumbered ligand system −N(Dipp)SiMe$_3$, the shift stops at phenyl allene although no complex was isolated upon stoichiometric reactions. Relating to the results of the catalytic studies, this suggests a higher binding affinity of the olefin to the sterically less demanding complex K{18c6}[Fe(N(SiMe$_3$)$_2$)$_2$], which thus slows down the substrate conversion.

While a catalytic shift to phenyl allene can also be observed with the trigonal iron(II) trisamide K{18c6}[Fe(N(SiMe$_3$)$_2$)$_3$], the neutral iron(II) species [Fe(N(SiMe$_3$)$_2$)$_2$] remains inactive with respect to alkynes. Mechanistically, de- or reprotonation processes are assumed since the metal-free alkali salts M^{A}N(SiMe$_3$)$_2$ (M^A = K, Li) also catalyse the 1,3-H atom shift. In case of potassium, isomerisation is completed within a few minutes and is thus much more efficient than the iron complexes described above.

Another goal of this work was the development of (quasi-)linear 3d-metal(II/I) complexes with phosphorus-containing ligand systems. For this purpose, the divalent hexamethyldisilazanides [M(N(SiMe$_3$)$_2$)$_2$] (M = Mn − Co) were reacted with the phosphinidene [(sIDipp)PH] or its deprotonated analogue [(sIDipp)PK], respectively (**Scheme 4**). While labile, tri-coordinated adducts of the type [M(PH(sIDipp))(N(SiMe$_3$)$_2$)$_2$] (M = Mn − Co) are formed with the 'parent' phosphinidene, the use of the salt-like phosphinidenide allows for a ligand exchange in case of manganese. After the initial formation of the ionic complex [(sIDipp)PK$_2$(Et$_2$O)$_4$][MnL$_3$] as intermediate, the two-coordinated complex [Mn(P(sIDipp))$_2$] is formed. This compound represents the first documented open-shell transition metal phosphinidenide complex. In solid state, the manganese centre is coordinated in a linear fashion and is additionally stabilized by intramolecular metal−arene interactions. Oxidation with silver triflate as well as the initially targeted reduction with KC$_8$ were not successful.

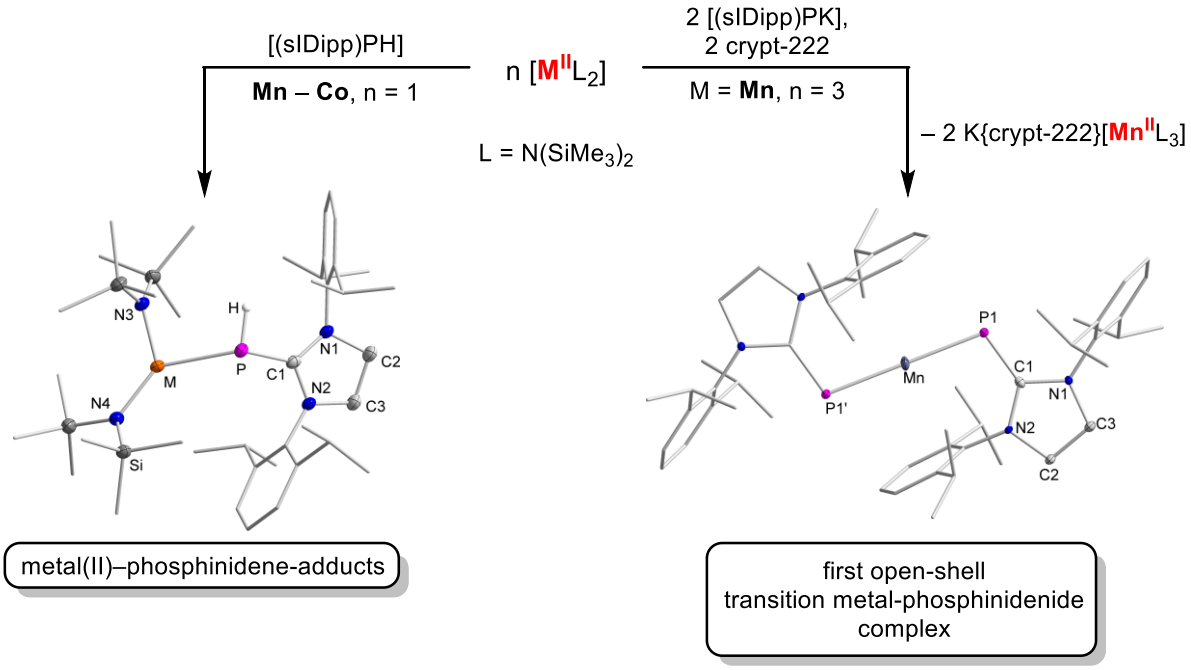

Scheme 4. Formation of different products by reaction of $[M(N(SiMe_3)_2)_2]$ (M = Mn – Co) with [(sIDipp)PR] (R = H, K).

Through the studies within this thesis, the knowledge about homoleptic, (quasi-)linear 3d-metal(II/I) complexes is extended. Synthetic limits of silylamide-based derivatives as well as the influence of structural changes on molecular properties and reactivities with respect to different substrates were explored. Also, the spectrum of linear 3d-metal(II) complexes could be extended to a phosphorus-based compound.

8 Literaturverzeichnis

[1] L. H. Gade, *Koordinationschemie*, WILEY-VCH Verlag GmbH, Weinheim, **1998**.
[2] H. Kopp, *Geschichte Der Chemie, Bd. I*, Braunschweig, **1843**.
[3] D. Seyferth, *Organometallics* **2001**, *20*, 1488–1498.
[4] C. Elschenbroich, *Organometallics*, WILEY-VCH Verlag GmbH, Weinheim, **2006**.
[5] R. A. Love, T. F. Koetzle, G. J. B. Williams, L. C. Andrews, R. Bau, *Inorg. Chem.* **1975**, *14*, 2653–2657.
[6] A. Werner, *Z. Anorg. Chem.* **1893**, *3*, 267–330.
[7] U. Müller, *Anorganische Strukturchemie*, Vieweg+Teubner, Wiesbaden, **2008**.
[8] H. Bethe, *Ann. Phys.* **1929**, *3*, 133–208.
[9] R. S. Mulliken, *Phys. Rev.* **1932**, *40*, 55.
[10] J. H. Van Vleck, *J. Chem. Phys.* **1935**, *3*, 803–806.
[11] L. Pauling, *The Nature of the Chemical Bond*, Ithaca, NY, **1940**.
[12] C. J. Ballhausen, M. A. Weiner, *J. Electrochem. Soc.* **1963**, *110*, 97C.
[13] C. J. Moffit, W.; Ballhausen, *C. Annu. Rev. Phys. Chem.* **1956**, *7*, 107–136.
[14] C. K. Jørgensen, *Modern Aspects of Ligand Field Theory*, Elsevier: New York, New York, **1971**.
[15] P. P. Power, *Chem. Rev.* **2012**, *112*, 3482–3507.
[16] D. P. Bradley, D. C.; Mehrotra, R. C.; Gaur, *Metal Alkoxides*, Academic Press: London, **1978**.
[17] D. C. Bradley, *Adv. Inorg. Chem. Radiochem.* **1972**, *15*, 259–322.
[18] R. C. Lappert, M. F.; Power, P. P.; Sanger, A. R.; Srivastava, *Metal and Metalloid Amides.*, Ellis-Horwood: Chichester, **1980**.
[19] A. Lappert, M. F.; Power, P. P.; Protchenko, A.; Seeber, *Metal Amide Chemistry*, **2008**.
[20] H. Bürger, U. Wannagat, *Monatsh. Chem.* **1963**, *94*, 1007–1012.
[21] H. Bürger, U. Wannagat, *Monatsh. Chem.* **1964**, *95*, 1099–1102.
[22] D. C. Bradley, M. B. Hursthouse, P. F. Rodesiler, *Chem. Commun.* **1969**, 14–15.
[23] S. Alvarez, *Coord. Chem. Rev.* **1999**, *193–195*, 13–41.
[24] C. C. Cummins, *Chem. Commun.* **1998**, *7*, 1777–1786.
[25] D. W. Eller, P.G.; Bradley, D. C.; Hursthouse, M. B.; Meek, *Coord. Chem. Rev.* **1977**, *24*, 1–95.
[26] P. B. Hitchcock, M. F. Lappert, R. G. Smith, R. A. Bartlett, P. P. Power, *J. Chem. Soc., Chem. Commun.* **1988**, *3*, 1007–1009.
[27] C. C. Cummins, *Prog. Inorg. Chem.* **1998**, *47*, 885.
[28] D. L. Kays, *Dalton Trans.* **2011**, *40*, 769–778.
[29] R. Bradley, D. C.; Hursthouse, M. B.; Abdul Malik, K. M.; Möseler, *Transit. Met. Chem.* **1978**, *3*, 253–254.
[30] M. M. Olmstead, P. P. Power, S. C. Shoner, *Inorg. Chem.* **1991**, *30*, 2547–2551.
[31] B. D. Murray, P. P. Power, *Inorg. Chem.* **1984**, *23*, 4584–4588.
[32] A. M. Bryan, G. J. Long, F. Grandjean, P. P. Power, *Inorg. Chem.* **2013**, *52*, 12152–12160.
[33] A. J. Bradley, C. D.; Hursthouse, M. B.; Newig, C. W.; Welch, *J. Chem. Soc., Chem. Commun.* **1972**, 567–568.
[34] A. Eichhöfer, Y. Lan, V. Mereacre, T. Bodenstein, F. Weigend, *Inorg. Chem.* **2014**, *53*, 1962–1974.
[35] M. Faust, A. M. Bryan, A. Mansikkamäki, P. Vasko, M. M. Olmstead, H. M.

Tuononen, F. Grandjean, G. J. Long, P. P. Power, *Angew. Chem. Int. Ed.* **2015**, *54*, 12914–12917.
[36] R. A. Andersen, K. Faegri, J. C. Green, A. Haaland, M. F. Lappert, W. P. Leung, K. Rypdal, J. C. Green, M. F. Lappert, W. P. Leung, *Inorg. Chem.* **1988**, *27*, 1782–1786.
[37] N. H. Buttrus, C. Eaborn, P. B. Hitchcock, J. D. Smith, A. C. Sullivan, *J. Chem. Soc., Chem. Commun.* **1985**, 1380–1381.
[38] R. A. Bartlett, P. P. Power, *J. Am. Chem. Soc.* **1987**, *109*, 7563–7564.
[39] R. A. Andersen, A. Haaland, K. Rypdal, H. V. Volden, *J. Chem. Soc., Chem. Commun.* **1985**, *160*, 1807–1808.
[40] W. M. Reiff, C. E. Schulz, M. H. Whangbo, J. I. Seo, Y. S. Lee, G. R. Potratz, C. W. Spicer, G. S. Girolami, *J. Am. Chem. Soc.* **2009**, *131*, 404–405.
[41] M. Atanasov, J. M. Zadrozny, J. R. Long, F. Neese, *Chem. Sci.* **2013**, *4*, 139–156.
[42] M. A. Companion, A. L.; Komarynsky, *J. Chem. Educ.* **1964**, *41*, 257–262.
[43] A. M. Bryan, W. A. Merrill, W. M. Reiff, J. C. Fettinger, P. P. Power, *Inorg. Chem.* **2012**, *51*, 3366–3373.
[44] B. Vest, Z. Varga, M. Hargittai, A. Hermann, P. Schwerdtfeger, *Chem. - A Eur. J.* **2008**, *14*, 5130–5143.
[45] H. Lücken, *Magnetochemie*, B. G. Teubner, Leipzig, **1999**.
[46] H. Lueken, *Magnetochemie*, Teubner Studienbücher, Leipzig, **1999**.
[47] A. Weiss, H. Witte, *Magnetochemie*, Chemie Verlag, Weinheim, **1973**.
[48] A. K. Bar, C. Pichon, J. P. Sutter, *Coord. Chem. Rev.* **2016**, *308*, 346–380.
[49] A. M. Bryan, C.-Y. Y. Lin, M. Sorai, Y. Miyazaki, H. M. Hoyt, A. Hablutzel, A. LaPointe, W. M. Reiff, P. P. Power, C. E. Schulz, *Inorg. Chem.* **2014**, *53*, 12100–12107.
[50] D. Shao, X. Y. Wang, *Chin. J. Chem.* **2020**, *38*, 1005–1018.
[51] S. Bond, C. J. Milios, R. E. P. Winpenny, **2014**, DOI 10.1007/430.
[52] J. M. Frost, K. L. M. Harriman, M. Murugesu, *Chem. Sci.* **2016**, *7*, 2470–2491.
[53] R. Bagai, G. Christou, *Chem. Soc. Rev.* **2009**, *38*, 1011–1026.
[54] D. Gatteschi, R. Sessoli, *Angew. Chem. Int. Ed.* **2003**, *42*, 268–297.
[55] M. Mannini, F. Pineider, C. Danieli, F. Totti, L. Sorace, P. Sainctavit, M. A. Arrio, E. Otero, L. Joly, J. C. Cezar, A. Cornia, R. Sessoli, *Nature* **2010**, *468*, 417–421.
[56] S. Hill, R. S. Edwards, N. Aliaga-Alcalde, G. Christou, *Science* **2003**, *302*, 1015–1018.
[57] W. Wernsdorfer, I. Chiorescu, R. Sessoli, D. Gatteschi, D. Mailly, *Phys. B Condens. Matter* **1999**, *284–288*, 1231–1232.
[58] M. N. Leuenberger, D. Loss, *Nature* **2001**, *410*, 789–793.
[59] M. Mannini, F. Pineider, P. Sainctavit, C. Danieli, E. Otero, C. Sciancalepore, A. M. Talarico, M. A. Arrio, A. Cornia, D. Gatteschi, R. Sessoli, *Nat. Mater.* **2009**, *8*, 194–197.
[60] R. Sessoli, D. Gatteschi, A. Caneschi, M. A. Novak, *Nature* **1993**, *365*, 141–143.
[61] T. Lis, *Acta Crystallogr. Sect. B Struct. Crystallogr. Cryst. Chem.* **1980**, *36*, 2042–2046.
[62] J. Gatteschi, D.; Sessoli, R.; Villain, *Molecular Nanomagnets*, Oxford University Press, Oxford, UK, **2006**.
[63] S. Da Jiang, B. W. Wang, H. L. Sun, Z. M. Wang, S. Gao, *J. Am. Chem. Soc.* **2011**, *133*, 4730–4733.
[64] F. S. Guo, B. M. Day, Y. C. Chen, M. L. Tong, A. Mansikkamäki, R. A. Layfield, *Science* **2018**, *362*, 1400–1403.
[65] A. Cornia, A. C. Fabretti, R. Sessoli, L. Sorace, D. Gatteschi, A.-L. Barra, C.

Daiguebonne, T. Roisnel, *Acta Cryst.* **2002**, *C58*.
[66] S. Karasawa, G. Zhou, H. Morikawa, N. Koga, *J. Am. Chem. Soc.* **2003**, *125*, 13676–13677.
[67] D. E. Freedman, W. H. Harman, T. D. Harris, G. J. Long, C. J. Chang, J. R. Long, *J. Am. Chem. Soc.* **2010**, *132*, 1224–1225.
[68] P. C. Bunting, M. Atanasov, E. Damgaard-Møller, M. Perfetti, I. Crassee, M. Orlita, J. Overgaard, J. Van Slageren, F. Neese, J. R. Long, *Science* **2018**, *362*, eaat7319.
[69] X. N. Yao, J. Z. Du, Y. Q. Zhang, X. B. Leng, M. W. Yang, S. Da Jiang, Z. X. Wang, Z. W. Ouyang, L. Deng, B. W. Wang, S. Gao, *J. Am. Chem. Soc.* **2017**, *139*, 373–380.
[70] J. M. Zadrozny, D. J. Xiao, M. Atanasov, G. J. Long, F. Grandjean, F. Neese, J. R. Long, *Nat. Chem.* **2013**, *5*, 577–581.
[71] W. A. Merrill, T. A. Stich, M. Brynda, G. J. Yeagle, J. C. Fettinger, R. De Hont, W. M. Reiff, C. E. Schulz, R. D. Britt, P. P. Power, *J. Am. Chem. Soc.* **2009**, *131*, 12693–12702.
[72] J. M. Zadrozny, M. Atanasov, A. M. Bryan, C. Y. Lin, B. D. Rekken, P. P. Power, F. Neese, J. R. Long, *Chem. Sci.* **2013**, *4*, 125–138.
[73] S. C. Goel, M. Y. Chiang, D. J. Rauscher, W. E. Buhro, *J. Am. Chem. Soc.* **1993**, *115*, 160–169.
[74] T. Hatanaka, R. Miyake, Y. Ishida, H. Kawaguchi, *J. Organomet. Chem.* **2011**, *696*, 4046–4050.
[75] H. Chen, M. M. Olmstead, D. C. Pestana, P. P. Power, *Inorg. Chem.* **1991**, *30*, 1783–1787.
[76] C.-Y. Lin, J.-D. Guo, J. C. Fettinger, S. Nagase, F. Grandjean, G. J. Long, N. F. Chilton, P. P. Power, *Inorg. Chem.* **2013**, *52*, 13584–13593.
[77] I. C. Cai, M. I. Lipschutz, T. D. Tilley, *Chem. Commun.* **2014**, *50*, 13062–13065.
[78] C. Ni, P. P. Power, *Chem. Commun.* **2009**, 5543–5545.
[79] C. G. Werncke, E. Suturina, P. C. Bunting, L. Vendier, J. R. Long, M. Atanasov, F. Neese, S. Sabo-Etienne, S. Bontemps, *Chem. – A Eur. J.* **2016**, *22*, 1668–1674.
[80] M. Hargittai, *Coord. Chem. Rev.* **1988**, *91*, 35–88.
[81] P. P. Power, *J. Organomet. Chem.* **2004**, *689*, 3904–3919.
[82] D. K. Kennepohl, S. Brooker, G. M. Sheldrick, H. W. Roesky, **1991**, *1*, 2223–2225.
[83] M. W. Rathke, *Org. Synth.* **1973**, *53*, 66.
[84] C. G. Werncke, I. Müller, *Chem. Commun.* **2020**, *56*, 2268–2271.
[85] R. J. Wehmschulte, P. P. Power, *Organometallics* **1995**, *14*, 3264–3267.
[86] S. N. König, C. Schädle, C. Maichle-Mössmer, R. Anwander, *Inorg. Chem.* **2014**, *53*, 4585–4597.
[87] P. P. Power, **2012**.
[88] H. Chen, R. A. Bartlett, M. M. Olmstead, P. P. Power, S. C. Shoner, *J. Am. Chem. Soc.* **1990**, *112*, 1048–1055.
[89] P. P. Power, *Comments Inorg. Chem.* **1989**, *8*, 177.
[90] C. Ni, P. P. Power, *Struct. Bond.* **2010**, *136*, 59.
[91] P. P. Power, *Chemtracts: Inorg. Chem.* **1994**, *6*, 181.
[92] H. Y. Au-Yeung, C. H. Lam, C.-K. Lam, W.-Y. Wong, H. K. Lee, *Inorg. Chem.* **2007**, *46*, 7695–7697.
[93] A. E. Ashley, A. R. Cowley, J. C. Green, D. R. Johnston, D. J. Watkin, D. L. Kays, *Eur. J. Inorg. Chem.* **2009**, 2547–2552.
[94] G. Moula, T. Matsumoto, M. E. Miehlich, K. Meyer, K. Tatsumi, *Angew. Chem.*

Int. Ed. **2018**, *57*, 11594–11597.
[95] T. Nguyen, A. Panda, M. M. Olmstead, A. F. Richards, M. Stender, M. Brynda, P. P. Power, *J. Am. Chem. Soc.* **2005**, *127*, 8545–8552.
[96] M. A. Matchett, M. Y. Chiang, W. E. Buhro, *Inorg. Chem.* **1994**, *33*, 1109–1114.
[97] S. C. Goel, M. Y. Chiang, W. E. Buhro, **1990**, *112*, 5636–5637.
[98] K. Kaniewska, Ł. Ponikiewski, N. Szynkiewicz, B. Cieślik, J. Pikies, J. Krzystek, A. Dragulescu-Andrasi, S. A. Stoian, R. Grubba, *Dalton Trans.* **2020**, *49*, 10091–10103.
[99] K. D. Dillon, F. Mathey, J. F. Nixon, *Phosphorous: The Carbon Copy*, Wiley, Chichester, **1998**.
[100] K. Lammertsma, M. J. M. Vlaar, *Eur. J. Org. Chem.* **2002**, 1127–1138.
[101] H. Aktaş, J. Chris Slootweg, K. Lammertsma, *Angew. Chem. Int. Ed.* **2010**, *49*, 2102–2113.
[102] X. Li, S. I. Weissman, T. Lin, P. P. Gaspar, *J. Am. Chem. Soc.* **1994**, *116*, 7899–7900.
[103] G. Bucher, M. L. G. Borst, A. W. Ehlers, K. Lammertsma, S. Ceola, M. Huber, D. Grote, W. Sander, *Angew. Chem. Int. Ed.* **2005**, *44*, 3289–3293.
[104] L. Dostál, *Coord. Chem. Rev.* **2017**, *353*, 142–158.
[105] L. Liu, D. A. Ruiz, D. Munz, G. Bertrand, *Chem* **2016**, *1*, 147–153.
[106] F. Mathey, N. H. T. Huy, A. Marinetti, *Helv. Chim. Acta* **2001**, *84*, 2938–2957.
[107] G. Frison, F. Mathey, A. Sevin, *J. Organomet. Chem.* **1998**, *570*, 225–234.
[108] A. W. Ehlers, E. J. Baerends, K. Lammertsma, *J. Am. Chem. Soc.* **2002**, *124*, 2831–2838.
[109] R. Melenkivitz, D. J. Mindiola, G. L. Hillhouse, *J. Am. Chem. Soc.* **2002**, *124*, 3846–3847.
[110] T. W. Graham, K. A. Udachin, M. Z. Zgierski, A. J. Carty, *Organometallics* **2011**, *30*, 1382–1388.
[111] T. L. Breen, D. W. Stephan, *Organometallics* **1996**, *15*, 4509–4514.
[112] T. Sasamori, N. Takeda, M. Fujio, M. Kimura, S. Nagase, N. Tokitoh, *Angew. Chem. Int. Ed.* **2002**, *41*, 139–141.
[113] D. S. J. Arney, R. C. Schnabel, B. C. Scott, C. J. Burns, *J. Am. Chem. Soc.* **1996**, *118*, 6780–6781.
[114] A. H. Cowley, *Acc. Chem. Res.* **1997**, *30*, 445–451.
[115] A. B. Burg, W. J. Mahler, *J. Am. Chem. S* **1961**, *83*, 2388–2389.
[116] A. J. Arduengo, J. C. Calabrese, A. H. Cowley, H. V. R. Dias, J. R. Goerlich, W. J. Marshall, B. Riegel, *Inorg. Chem.* **1997**, *2*, 2151–2158.
[117] A. J. Arduengo, R. L. Harlow, M. Kline, *J. Am. Chem. Soc.* **1991**, *113*, 361–363.
[118] A. J. Arduengo, H. V. R. Dias, J. C. Calabrese, *Chem. Lett.* **1997**, 143–144.
[119] L. Weber, *Eur. J. Inorg. Chem.* **2007**, *2*, 4095–4117.
[120] G. Frison, A. Sevin, *J. Organomet. Chem.* **2002**, *643–644*, 105–111.
[121] Y. Wang, Y. Xie, M. Y. Abraham, R. J. Gilliard, P. Wei, H. F. Schaefer, P. V. R. Schleyer, G. H. Robinson, *Organometallics* **2010**, *29*, 4778–4780.
[122] M. Balmer, F. Weigend, C. von Hänisch, *Chem. – A Eur. J.* **2019**, *25*, 4914–4919.
[123] A. Doddi, D. Bockfeld, T. Bannenberg, P. G. Jones, M. Tamm, *Angew. Chem. Int. Ed.* **2014**, *53*, 13568–13572.
[124] A. M. Tondreau, Z. Benkő, J. R. Harmer, H. Grützmacher, *Chem. Sci.* **2014**, *5*, 1545–1554.
[125] M. Cicač-Hudi, J. Bender, S. H. Schlindwein, M. Bispinghoff, M. Nieger, H. Grützmacher, D. Gudat, *Eur. J. Inorg. Chem.* **2016**, *2016*, 649–658.
[126] O. Lemp, M. Balmer, K. Reiter, F. Weigend, C. Von Hänisch, *Chem. Commun.*

2017, *53*, 7620–7623.
[127] M. Balmer, Y. J. Franzke, F. Weigend, C. von Hänisch, *Chem. - A Eur. J.* **2020**, *26*, 192–197.
[128] O. Lemp, C. Von Hänisch, *Phosphorus Sulfur Silicon Relat. Elem.* **2016**, *191*, 659–661.
[129] A. J. Arduengo, C. J. Carmalt, J. A. C. Clyburne, A. H. Cowley, R. Pyati, *Chem. Commun.* **1997**, *78*, 981–982.
[130] O. Back, M. Henry-Ellinger, C. D. Martin, D. Martin, G. Bertrand, *Angew. Chem. Int. Ed.* **2013**, *52*, 2939–2943.
[131] A. J. Arduengo, R. Krafczyk, R. Schmutzler, H. A. Craig, J. R. Goerlich, W. J. Marshall, M. Unverzagt, *Tetrahedron* **1999**, *55*, 14523–14534.
[132] M. Peters, A. Doddi, T. Bannenberg, M. Freytag, P. G. Jones, M. Tamm, *Inorg. Chem.* **2017**, *56*, 10785–10793.
[133] A. Doddi, M. Peters, M. Tamm, *Chem. Rev.* **2019**, *119*, 6994–7112.
[134] A. Doddi, D. Bockfeld, T. Bannenberg, M. Tamm, *Chem. – A Eur. J.* **2020**, *26*, 14878–14887.
[135] M. Bispinghoff, A. M. Tondreau, H. Grützmacher, C. A. Faradji, P. G. Pringle, *Dalton Trans.* **2016**, *45*, 5999–6003.
[136] C. A. Laskowski, G. L. Hillhouse, *J. Am. Chem. Soc.* **2008**, *130*, 13846–13847.
[137] C. A. Laskowski, D. J. Bungum, S. M. Baldwin, S. A. Del Ciello, V. M. Iluc, G. L. Hillhouse, *J. Am. Chem. Soc.* **2013**, *135*, 18272–18275.
[138] M. I. Lipschutz, T. D. Tilley, *Organometallics* **2014**, *33*, 5566–5570.
[139] A. A. Danopoulos, P. Braunstein, K. Y. Monakhov, J. Van Leusen, P. Kögerler, M. Clémancey, J. M. Latour, A. Benayad, M. Tromp, E. Rezabal, G. Frison, *Dalton Trans.* **2017**, *46*, 1163–1171.
[140] J. Hicks, C. Jones, *Organometallics* **2015**, *34*, 2118–2121.
[141] M. I. Lipschutz, X. Yang, R. Chatterjee, T. D. Tilley, *J. Am. Chem. Soc.* **2013**, *135*, 15298–15301.
[142] T. Inatomi, Y. Fukahori, Y. Yamada, R. Ishikawa, S. Kanegawa, Y. Koga, K. Matsubara, *Catal. Sci. Technol.* **2019**, *9*, 1784–1793.
[143] M. I. Lipschutz, T. Chantarojsiri, Y. Dong, T. D. Tilley, *J. Am. Chem. Soc.* **2015**, *137*, 6366–6372.
[144] R. J. Witzke, T. D. Tilley, *Chem. Commun.* **2019**, *55*, 6559–6562.
[145] C. Ni, B. D. Ellis, J. C. Fettinger, G. J. Long, P. P. Power, *Chem. Commun.* **2008**, 1014–1016.
[146] H. Lei, J. C. Fettinger, P. P. Power, *Inorg. Chem.* **2012**, *51*, 1821–1826.
[147] C. Ni, B. D. Ellis, T. A. Stich, J. C. Fettinger, G. J. Long, R. D. Britt, P. P. Power, *J. Chem. Soc., Dalton Trans.* **2009**, *2*, 5401–5405.
[148] T. R. Dugan, X. Sun, E. V. Rybak-Akimova, O. Olatunji-Ojo, T. R. Cundari, P. L. Holland, *J. Am. Chem. Soc.* **2011**, *133*, 12418–12421.
[149] P. Zhao, Z. Brown, J. C. Fettinger, F. Grandjean, G. J. Long, P. P. Power, *Organometallics* **2014**, *33*, 1917–1920.
[150] R. Wolf, M. Brynda, C. Ni, G. J. Long, P. P. Power, *J. Am. Chem. Soc.* **2007**, *129*, 6076–6077.
[151] Y. Dong, M. I. Lipschutz, R. J. Witzke, J. A. Panetier, T. D. Tilley, **2021**, DOI 10.1021/acscatal.1c02926.
[152] Q. Zhang, L. Xiang, L. Deng, *Organometallics* **2012**, *31*, 4537–4543.
[153] S. C. Meier, A. Holz, J. Kulenkampff, A. Schmidt, D. Kratzert, D. Himmel, D. Schmitz, E. W. Scheidt, W. Scherer, C. Bülow, M. Timm, R. Lindblad, S. T. Akin, V. Zamudio-Bayer, B. von Issendorff, M. A. Duncan, J. T. Lau, I. Krossing, *Angew. Chem. Int. Ed.* **2018**, *57*, 9310–9314.

[154] Z. Ouyang, J. Du, L. Wang, J. L. Kneebone, M. L. Neidig, L. Deng, *Inorg. Chem.* **2015**, *54*, 8808–8816.
[155] A. A. Danopoulos, D. Pugh, *J. Chem. Soc., Dalton Trans.* **2007**, *874*, 30–31.
[156] J. Du, W. Chen, Q. Chen, X. Leng, Y. Meng, S. Gao, L. Deng, *Organometallics* **2020**, *39*, 729–739.
[157] K. Matsubara, S. Miyazaki, Y. Koga, Y. Nibu, T. Hashimura, T. Matsumoto, *Organometallics* **2008**, *27*, 6020–6024.
[158] P. P. Samuel, K. C. Mondal, H. W. Roesky, M. Hermann, G. Frenking, S. Demeshko, F. Meyer, A. C. Stückl, J. H. Christian, N. S. Dalal, L. Ungur, L. F. Chibotaru, K. Pröpper, A. Meents, B. Dittrich, *Angew. Chem. Int. Ed.* **2013**, *52*, 11817–11821.
[159] B. Dittrich, C. M. Wandtke, A. Meents, K. Pröpper, K. C. Mondal, P. P. Samuel, N. Amin Sk, A. P. Singh, H. W. Roesky, N. Sidhu, *ChemPhysChem* **2015**, *16*, 412–419.
[160] K. C. Mondal, P. P. Samuel, Y. Li, H. W. Roesky, S. Roy, L. Ackermann, N. S. Sidhu, G. M. Sheldrick, E. Carl, S. Demeshko, S. De, P. Parameswaran, L. Ungur, L. F. Chibotaru, D. M. Andrada, *Eur. J. Inorg. Chem.* **2014**, 818–823.
[161] Y. S. Meng, Z. Ouyang, M. W. Yang, Y. Q. Zhang, L. Deng, B. W. Wang, S. Gao, *Inorg. Chem. Front.* **2019**, *6*, 1050–1057.
[162] Y. S. Meng, Z. Mo, B. W. Wang, Y. Q. Zhang, L. Deng, S. Gao, *Chem. Sci.* **2015**, *6*, 7156–7162.
[163] Z. Mo, D. Chen, X. Leng, L. Deng, *Organometallics* **2012**, *31*, 7040–7043.
[164] P. P. Samuel, K. C. Mondal, N. Amin Sk, H. W. Roesky, E. Carl, R. Neufeld, D. Stalke, S. Demeshko, F. Meyer, L. Ungur, L. F. Chibotaru, J. Christian, V. Ramachandran, J. Van Tol, N. S. Dalal, *J. Am. Chem. Soc.* **2014**, *136*, 11964–11971.
[165] A. J. Arduengo, S. F. Camper, J. C. Calabrese, *J. Am. Chem. Soc.* **1994**, *116*, 4391–4394.
[166] S. Caddick, F. G. N. Cloke, G. K. B. Clentsmith, P. B. Hitchcock, D. McKerrecher, L. R. Titcomb, M. R. V. Williams, *J. Organomet. Chem.* **2001**, *617–618*, 635–639.
[167] S. Caddick, F. G. N. Cloke, P. B. Hitchcock, A. K. D. K. Lewis, *Angew. Chem. Int. Ed.* **2004**, *43*, 5824–5827.
[168] Z. C. Cao, S. J. Xie, H. Fang, Z. J. Shi, *J. Am. Chem. Soc.* **2018**, *140*, 13575–13579.
[169] Z. Mo, D. Chen, X. Leng, L. Deng, *Organometallics* **2012**, *31*, 7040–7043.
[170] Y.-S. Meng, Z. Mo, B.-W. Wang, Y.-Q. Zhang, L. Deng, S. Gao, *Chem. Sci.* **2015**, *6*, 7156–7162.
[171] P. P. Samuel, R. Neufeld, K. Chandra Mondal, H. W. Roesky, R. Herbst-Irmer, D. Stalke, S. Demeshko, F. Meyer, V. C. Rojisha, S. De, P. Parameswaran, A. C. Stückl, W. Kaim, J. H. Christian, J. K. Bindra, N. S. Dalal, *Chem. Sci.* **2015**, *6*, 3148–3153.
[172] G. Ung, J. Rittle, M. Soleilhavoup, G. Bertrand, J. C. Peters, *Angew. Chem. Int. Ed.* **2014**, *53*, 8427–8431.
[173] Z. Mo, Z. Ouyang, L. Wang, K. L. Fillman, M. L. Neidig, L. Deng, *Org. Chem. Front.* **2014**, *1*, 1040–1044.
[174] C.-Y. Y. Lin, J. C. Fettinger, N. F. Chilton, A. Formanuik, F. Grandjean, G. J. Long, P. P. Power, *Chem. Commun.* **2015**, *51*, 13275–13278.
[175] M. K. Thomsen, A. Nyvang, J. P. S. Walsh, P. C. Bunting, J. R. Long, F. Neese, M. Atanasov, A. Genoni, J. Overgaard, *Inorg. Chem.* **2019**, *58*, 3211–3218.
[176] C. G. Werncke, P. C. Bunting, C. Duhayon, J. R. Long, S. Bontemps, S. Sabo-

Etienne, *Angew. Chem. Int. Ed.* **2015**, *54*, 245–248.
[177] C. Y. Lin, J. C. Fettinger, F. Grandjean, G. J. Long, P. P. Power, *Inorg. Chem.* **2014**, *53*, 9400–9406.
[178] A. Reckziegel, C. Pietzonka, F. Kraus, C. G. Werncke, *Angew. Chem. Int. Ed.* **2020**, *59*, 8527–8531.
[179] A. Reckziegel, C. Pietzonka, F. Kraus, C. G. Werncke, *Angew. Chem.* **2020**, *132*, 8605–8609.
[180] C. Schneider, S. Demeshko, F. Meyer, C. G. Werncke, *Chem. - A Eur. J.* **2021**, *27*, 6348–6353.
[181] J. K. Kochi, *J. Organomet. Chem.* **2002**, *653*, 11–19.
[182] T. J. Anderson, G. D. Jones, D. A. Vicic, *J. Am. Chem. Soc.* **20047**, *126*, 8100–8101.
[183] B. D. Sherry, A. Fürstner, *Acc. Chem. Res.* **2008**, *41*, 1500–1511.
[184] L. S. Yamout, M. Ataya, F. Hasanayn, P. L. Holland, A. J. M. Miller, A. S. Goldman, *J. Am. Chem. Soc.* **2021**, *143*, 9744–9757.
[185] I. Müller, C. Schneider, C. Pietzonka, F. Kraus, C. G. Werncke, *Inorganics* **2019**, *7*, 117–138.
[186] C. G. Werncke, J. Pfeiffer, I. Müller, L. Vendier, S. Sabo-Etienne, S. Bontemps, *Dalton Trans.* **2019**, *48*, 1757–1765.
[187] A. Reckziegel, M. Kour, B. Battistella, S. Mebs, K. Beuthert, R. Berger, C. G. Werncke, *Angew. Chem. Int. Ed.* **2021**, *60*, 15376–15380.
[188] I. Müller, C. G. Werncke, *Chem. - A Eur. J.* **2021**, *27*, 4932–4938.
[189] M. Lipschutz, T. Don Tilley, *Chem. Commun.* **2012**, *48*, 7146–7148.
[190] I. Müller, *Dissertation*, Marburg, **2020**.
[191] D. L. J. Broere, E. Ruijter, *Synth.* **2012**, *44*, 2639–2672.
[192] J. J. Li, *Name Reactions*, Springer-Verlag, Berlin Heidelberg, **2006**.
[193] J. A. Varela, C. Saá, *Chem. Rev.* **2003**, *103*, 3787–3801.
[194] S. E. Gibson, A. Stevenazzi, *Angew. Chem. Int. Ed.* **2003**, *42*, 1800–1810.
[195] I. U. Khand, G. R. Knox, P. L. Pauson, W. E. Watts, *J. Chem. Soc., Dalton Trans.* **1971**, *36a*.
[196] H. E. Simmons, R. D. Smith, *J. Am. Chem. Soc.* **1958**, *80*, 5323–5324.
[197] D. M. P. Mingos, *J. Organomet. Chem.* **2001**, *635*, 1–8.
[198] J. Chatt, L. A. Duncanson, L. M. Venanzi, *J. Chem. Soc.* **1955**, 4456–4460.
[199] S. Willemsen, *Dissertation*, Berlin, **1999**.
[200] T. Engel, P. Reid, *Physikalische Chemie*, Pearson Studium, München, **2006**.
[201] M. S. Nechaev, V. M. Rayon, G. Frenking, *J. Phys. Chem. A* **2004**, *108*, 3134–3142.
[202] C. Martín, M. Sierra, E. Alvarez, T. R. Belderrain, P. J. Pérez, *Dalton Trans.* **2012**, *41*, 5319–5325.
[203] G. B. Wijeratne, E. M. Zolnhofer, S. Fortier, L. N. Grant, P. J. Carroll, C. H. Chen, K. Meyer, J. Krzystek, A. Ozarowski, T. A. Jackson, D. J. Mindiola, J. Telser, *Inorg. Chem.* **2015**, *54*, 10380–10397.
[204] V. V. Burlakov, A. V. Polyakov, A. I. Yanovsky, Y. T. Struchkov, V. B. Shur, M. E. Vol'pin, U. Rosenthal, H. Görls, *J. Organomet. Chem.* **1994**, *476*, 197–206.
[205] C. J. Adams, I. M. Bartlett, N. G. Connelly, D. J. Harding, O. D. Hayward, A. J. Martín, A. G. Orpen, M. J. Quayle, P. H. Rieger, *J. Chem. Soc., Dalton Trans.* **2002**, *2*, 4281–4288.
[206] E. Salt, Julian, S. Girolami, Gregory, G. Wilkinson, M. Motevalli, M. Thornton-Pett, B. Hursthouse, Michael, *J. Chem. Soc., Dalton Trans.* **1985**, 685–692.
[207] A. A. Danopoulos, G. Wilkinson, T. K. N. Sweet, M. B. Hursthouse, *J. Chem. Soc., Dalt. Trans.* **1996**, 271–281.

[208] D. J. Wink, B. Timothy Creagan, *J. Am. Chem. Soc.* **1990**, *112*, 8585–8586.
[209] Y. Ortin, Y. Coppel, N. Lugan, R. Mathieu, M. J. McGlinchey, *Chem. Commun.* **2001**, *1*, 1690–1691.
[210] C. P. Casey, T. L. Dzwiniel, S. Kraft, I. A. Guzei, *Organometallics* **2003**, *22*, 3915–3920.
[211] M. Akita, S. Kakuta, S. Sugimoto, M. Terada, M. Tanaka, Y. Moro-oka, *Organometallics* **2001**, *20*, 2736–2750.
[212] M. Barrow, N. L. Cromhout, D. Cunningham, A. R. Manning, P. McArdle, *J. Organomet. Chem.* **2000**, *612*, 61–68.
[213] S. A. Stoian, Y. Yu, J. M. Smith, P. L. Holland, E. L. Bominaar, E. Munck, *Inorg. Chem.* **2005**, *44*, 4915–4922.
[214] Y. Yu, J. M. Smith, C. J. Flaschenriem, P. L. Holland, *Inorg. Chem.* **2006**, *45*, 5742–5751.
[215] S. C. Bart, E. J. Hawrelak, E. Lobkovsky, P. J. Chirik, *Organometallics* **2005**, *24*, 5518–5527.
[216] W. H. Monillas, J. F. Young, G. P. A. Yap, K. H. Theopold, *Dalton Trans.* **2013**, *42*, 9198–9210.
[217] F. Dai, G. P. A. Yap, K. H. Theopold, *J. Am. Chem. Soc.* **2013**, *135*, 16774–16776.
[218] E. S. Akturk, G. P. A. Yap, K. H. Theopold, *Chem. Commun.* **2015**, *51*, 15402–15405.
[219] A. Enachi, D. Baabe, M. K. Zaretzke, P. Schweyen, M. Freytag, J. Raeder, M. D. Walter, *Chem. Commun.* **2018**, *54*, 13798–13801.
[220] Z. Mo, J. Xiao, Y. Gao, L. Deng, *J. Am. Chem. Soc.* **2014**, *136*, 17414–17417.
[221] R. Wolf, N. Ghavtadze, K. Weber, E. M. Schnöckelborg, B. De Bruin, A. W. Ehlers, K. Lammertsma, *Dalton Trans.* **2010**, *39*, 1453–1456.
[222] R. J. Witzke, D. Hait, K. Chakarawet, M. Head-Gordon, T. D. Tilley, *ACS Catal.* **2020**, *10*, 7800–7807.
[223] W. H. Monillas, G. P. A. Yap, K. H. Theopold, *Angew. Chem. Int. Ed.* **2007**, *46*, 6692–6694.
[224] S. F. McWilliams, E. Bill, G. Lukat-Rodgers, K. R. Rodgers, B. Q. Mercado, P. L. Holland, *J. Am. Chem. Soc.* **2018**, *140*, 8586–8598.
[225] W. Chen, Q. Chen, Y. Ma, X. Leng, S. Di Bai, L. Deng, *Chin. Chem. Lett.* **2020**, *31*, 1342–1344.
[226] J. Du, L. Wang, M. Xie, L. Deng, *Angew. Chem. Int. Ed.* **2015**, *54*, 12640–12644.
[227] W. H. Monillas, G. P. A. Yap, L. A. MacAdams, K. H. Theopold, *J. Am. Chem. Soc.* **2007**, *129*, 8090–8091.
[228] G. Bai, P. Wei, A. K. Das, D. W. Stephan, *Dalton Trans.* **2006**, *60*, 1141–1146.
[229] M. Horitani, K. Grubel, S. F. McWilliams, B. D. Stubbert, B. Q. Mercado, Y. Yu, P. M. Gurubasavaraj, N. S. Lees, P. L. Holland, B. M. Hoffman, *Chem. Sci.* **2017**, *8*, 5941–5948.
[230] J. Cheng, Q. Chen, X. Leng, S. Ye, L. Deng, *Inorg. Chem.* **2019**, *58*, 13129–13141.
[231] A. Kapat, T. Sperger, S. Guven, F. Schoenebeck, *Science* **2019**, *363*, 391–396.
[232] M. Hassam, A. Taher, G. E. Arnott, I. R. Green, W. A. L. Van Otterlo, *Chem. Rev.* **2015**, *115*, 5462–5569.
[233] E. H. P. Tan, G. C. Lloyd-Jones, J. N. Harvey, A. J. J. Lennox, B. M. Mills, *Angew. Chem. Int. Ed.* **2011**, *50*, 9602–9606.
[234] J. E. Gano, E. J. Jacob, P. Sekher, G. Subramaniam, L. A. Eriksson, D. Lenoir, *J. Org. Chem.* **1996**, *61*, 6739.
[235] P. Griess, *Ann. Chem. Pharm.* **1862**, *121*, 257–280.

[236] E. F. V. Scriven, K. Turnbull, *Chem. Rev.* **1988**, *88*, 297–368.
[237] S. Bräse, C. Gil, K. Knepper, V. Zimmermann, *Angew. Chem. Int. Ed.* **2005**, *44*, 5188–5240.
[238] S. Cenini, E. Gallo, A. Caselli, F. Ragaini, S. Fantauzzi, C. Piangiolino, *Coord. Chem. Rev.* **2006**, *250*, 1234–1253.
[239] A. Grünwald, S. S. Anjana, D. Munz, *Eur. J. Inorg. Chem.* **2021**, 1–21.
[240] D. A. Iovan, T. A. Betley, *J. Am. Chem. Soc.* **2016**, *138*, 1983–1993.
[241] K. M. Carsch, I. M. DiMucci, D. A. Iovan, A. Li, S. L. Zheng, C. J. Titus, S. J. Lee, K. D. Irwin, D. Nordlund, K. M. Lancaster, T. A. Betley, *Science* **2019**, *365*, 1138–1143.
[242] Y. M. Badiei, A. Krishnaswamy, M. M. Melzer, T. H. Warren, *J. Am. Chem. Soc.* **2006**, *128*, 15056–15057.
[243] Y. Dong, J. T. Lukens, R. M. Clarke, S.-L. Zheng, K. M. Lancaster, T. A. Betley, *Chem. Sci.* **2020**, *11*, 1260–1268.
[244] D. T. Shay, G. P. A. A. Yap, L. N. Zakharov, A. L. Rheingold, K. H. Theopold, *Angew. Chem.* **2005**, *44*, 1532–1534.
[245] E. R. King, E. T. Hennessy, T. A. Betley, **2011**, 4917–4923.
[246] W. Mao, D. Fehn, F. W. Heinemann, A. Scheurer, D. Munz, K. Meyer, *Angew. Chem.* **2021**, 16616–16622.
[247] Y. Park, S. P. Semproni, H. Zhong, P. J. Chirik, *Angew. Chem. Int. Ed.* **2021**, *60*, 14376–14380.
[248] E. R. King, G. T. Sazama, T. A. Betley, *J. Am. Chem. Soc.* **2012**, *134*, 17858–17861.
[249] T. A. Betley, J. C. Peters, **2003**, *9*, 10782–10783.
[250] X. Hu, K. Meyer, **2004**, *940*, 16322–16323.
[251] V. Di, C. Engineering, M. Beckman, C. Synthesis, D. M. Jenkins, T. A. Betley, J. C. Peters, **2002**, *51*, 11238–11239.
[252] I. Müller, D. Munz, C. G. Werncke, *Inorg. Chem.* **2020**, *14*, 9521–9537.
[253] N. Krause, A. S. Hashmi, *Modern Allene Chemistry*, WILEY-VCH Verlag GmbH, Weinheim, **2004**.
[254] P. Wang, J. Cheng, D. Wang, C. Yang, X. Leng, L. Deng, *Organometallics* **2020**, DOI 10.1021/acs.organomet.0c00383.
[255] D. Bockfeld, A. Doddi, P. G. Jones, M. Tamm, *Eur. J. Inorg. Chem.* **2016**, *2016*, 3704–3713.
[256] C. G. Werncke, L. Vendier, S. Sabo-Etienne, J.-P. P. Sutter, C. Pichon, S. Bontemps, *Eur. J. Inorg. Chem.* **2017**, *2017*, 1041–1406.

9 Wissenschaftliche Beiträge

Publikationen

Alle in dieser Arbeit enthaltenen Publikationen sind durch fett markierte Titel gekennzeichnet.

8. ***„Magnetic Blocking in a Conformationally Restricted Quasilinear Iron(I) Silylamide”,*** R. Weller, M. Atanasov, S. Demeshko, I. Mohelsky, M. Orlita, F. Meyer, F. Neese, C. G. Werncke*, Manuskript in Vorbereitung.*

7. ***„Synthesis of the Open-Shell 3d-transition metal(II) Bis(phosphinidenide) [Mn(P(sIDipp))$_2$]“***, R. Weller, M. Balmer, C. von Hänisch, C. G. Werncke, *eingereichtes Manuskript*.

6. ***„NHC-Stabilized Parent Phosphinidene Adducts of Metal(II) Hexamethyldisilazanides of Manganese − Cobalt and Their Lability in Solution”***, R. Weller, A. Gonzalez, H. Gottschling, C. von Hänisch, C. G. Werncke, *eingereichtes Manuskript*.

5. **„*Catalytic 1,3-H Atom Shift of a Terminal Benzylic Alkyne by Iron and Alkali Metal Silylamides − Switching between Allene and Internal Alkyne*”**, R. Weller, I. Müller, C. G. Werncke, *eingereichtes Manuskript.*

4. ***„On the Synthesis and Reduction of Trigonal Halido Bis(silylamido) Metalates of Chromium to Cobalt“***, R. Weller, L. Völlinger, C. G. Werncke, *Eur. J. Inorg. Chem.* **2021**, 4383−4392; DOI: 10.1002/ejic.202100716.

3. ***“Homoleptic quasilinear metal(I/II) silylamides of Cr − Co with phenyl and allyl functions − impact of the oxidation state on secondary ligand interactions”***, R. Weller, L. Ruppach, A. Shlyaykher, F. Tambornino, C. G. Werncke, *Dalton Trans.* **2021**, *50*, 10947−10963. DOI: 10.1039/d1dt01543e.

2. ***„Quasilinear 3d-metal(I) complexes [KM(N(Dipp)SiR$_3$)$_2$] (M = Cr − Co) − structural diversity, solution state behaviour and reactivity”***, R. Weller, I. Müller, C. Duhayon, S. Sabo-Etienne, S. Bontemps, C. G. Werncke, *Dalton Trans*. **2021**, *50*, 4890−4903; DOI: 10.1039/d1dt00121c.

1. „*Hexa-peri-hexabenzocoronene decorated with an allenylidene ruthenium complex − almost a flyswatter*“, R. Lorenz, D. Reger, R. Weller, N. Jux, N. Burzlaff, *Dalton Trans*. **2020**, *49*, 13134−13141; DOI: 10.1039/d0dt02729d.

Präsentationen

Posterbeiträge

4. Online-Vortragstagung für Anorganische Chemie der FG Wöhler-Vereinigung und Festkörperchemie und Materialforschung, September **2020**: „*Synthesis of neutral and linear 3d-transition metal(I) silylamides*“

3. 15. Koordinationschemie-Treffen, März **2019**: „*Synthese neutraler, quasilinearer 3d-Übergangsmetall(I)-Silylamide*“

2. ACS Publications Forum, Oktober **2018**: „*Synthesis of neutral and linear two-coordinated 3d-transition metal(I) silylamides*“

1. 19. Vortragstagung für Anorganische Chemie der FG Wöhler-Vereinigung und Festkörperchemie und Materialforschung, September **2018**: „*Synthesis of neutral and linear 3d-transition metal(I) silylamides*“

Vorträge

3. Hirschegg-Tagung, August **2019**: „*Synthese neuartiger zweifach-koordinierter Metall(I)-Komplexe*“

2. Anorganisch-chemisches Symposium, Juli **2019**: „*Synthese neuartiger zweifach-koordinierter Metall(I)-Komplexe*“

1. Anorganisch-chemisches Symposium, Juli **2018**: „*Synthese neuartiger zweifach-koordinierter Metall(I)-Komplexe*“

10 Wissenschaftlicher Werdegang

Der Inhalt dieses Kapitels wurde aus Datenschutzgründen aus der elektronischen Version entfernt.

11 Elektronische Zusatzinformationen

Auf den folgenden Seiten werden die elektronischen Zusatzinformationen („Supporting Information“, ESI) der im kumulativen Teil enthaltenen Publikationen aufgeführt.

11.1 Zusatzinformationen zu Publikation 1

„Homoleptic quasilinear metal(I/II) silylamides of Cr − Co with phenyl and allyl functions − impact of the oxidation state on secondary ligand interactions“

Ruth Weller, Lutz Ruppach, Alena Shlyaykher, Frank Tambornino, C. Gunnar Werncke

Dalton Transactions **2021**, *50*, 10947−10963.
DOI: 10.1039/d1dt01543e
https://pubs.rsc.org/en/content/articlelanding/2021/dt/d1dt01543e

Electronic Supplementary Material (ESI) for Dalton Transactions.

Homoleptic Quasilinear Metal(I/II) Silylamides of Cr – Co with Phenyl and Allyl Functions – Impact of Oxidation State on Secondary Ligand Interactions

Ruth Weller,[a] Lutz Ruppach,[a] Alena Shlyaykher,[a] Frank Tambornino,[a] C. Gunnar Werncke*,[a]

Table of Content

1 NMR Spectra

−N(Dipp)Si(Me$_2$Ph) (L^1) containing compounds

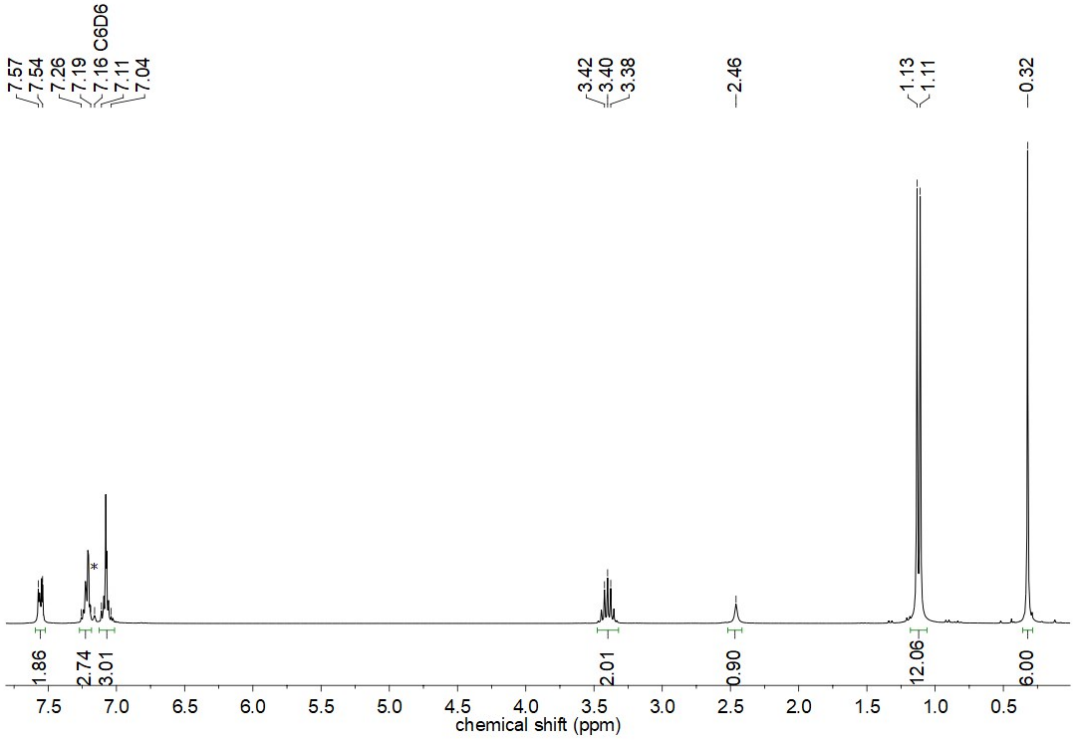

Figure S1. ^{1}H NMR spectrum (300.2 MHz, 300 K) of **HL^1** in C_6D_6. (* solvent)

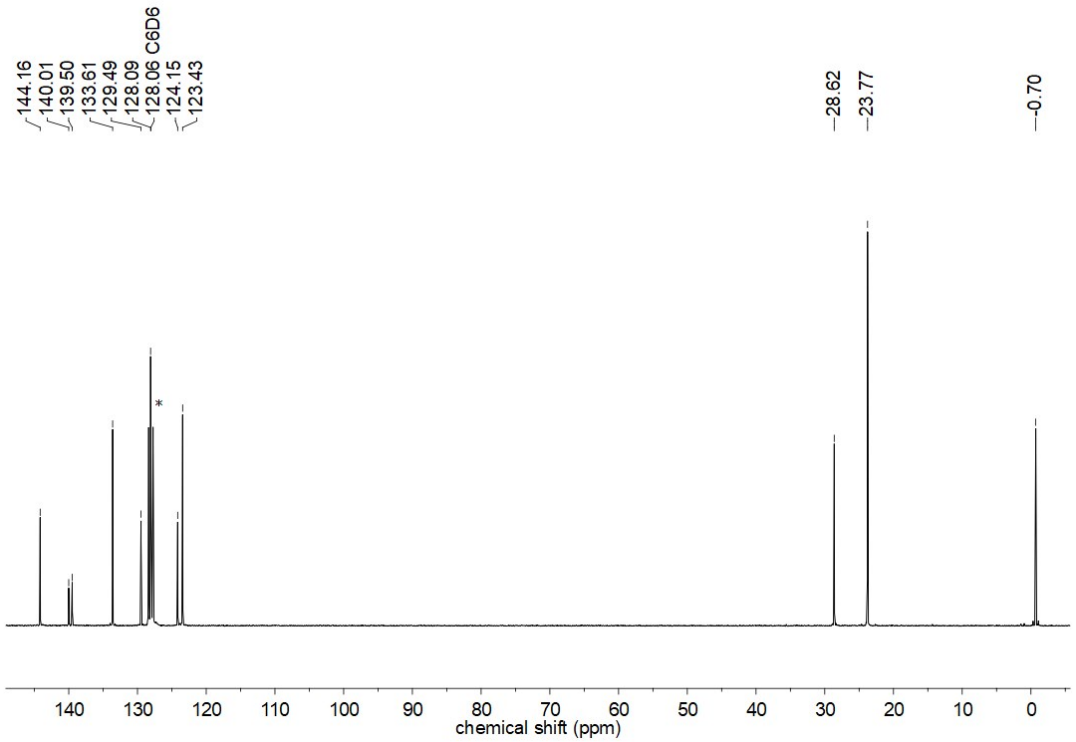

Figure S2. ^{13}C NMR spectrum (75.5 MHz, 300 K) of **HL^1** in C_6D_6. (* solvent)

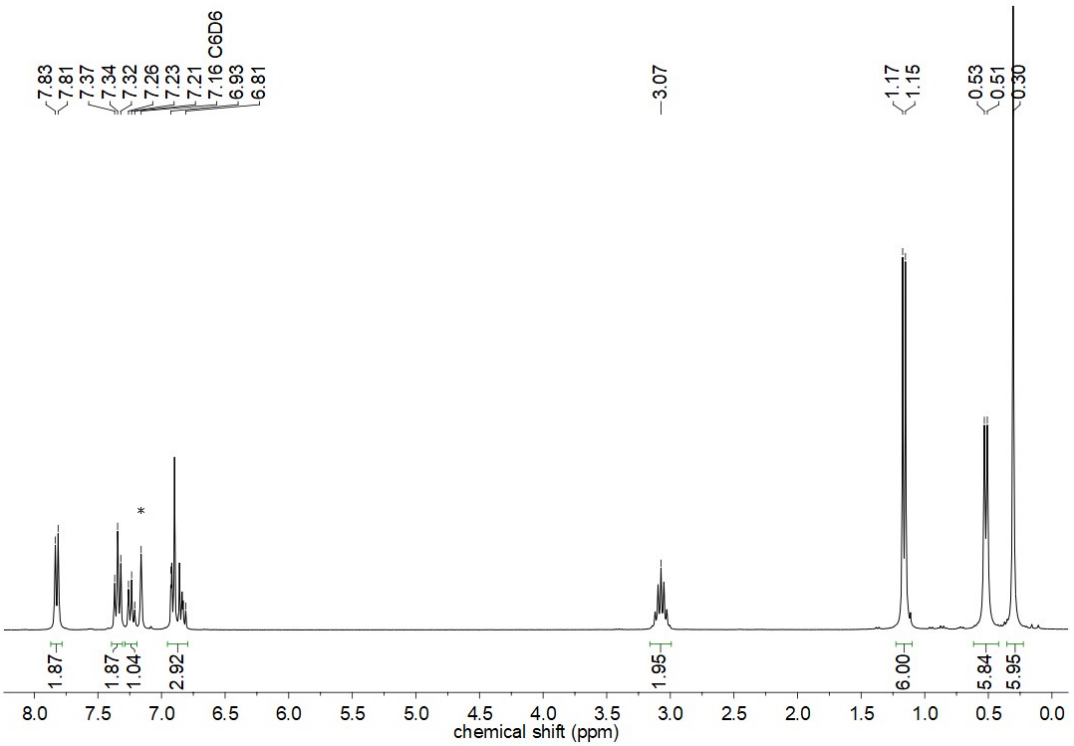

Figure S3. ^{1}H NMR spectrum (300.2 MHz, 300 K) of **LiL^{1}** in C_6D_6. (* solvent)

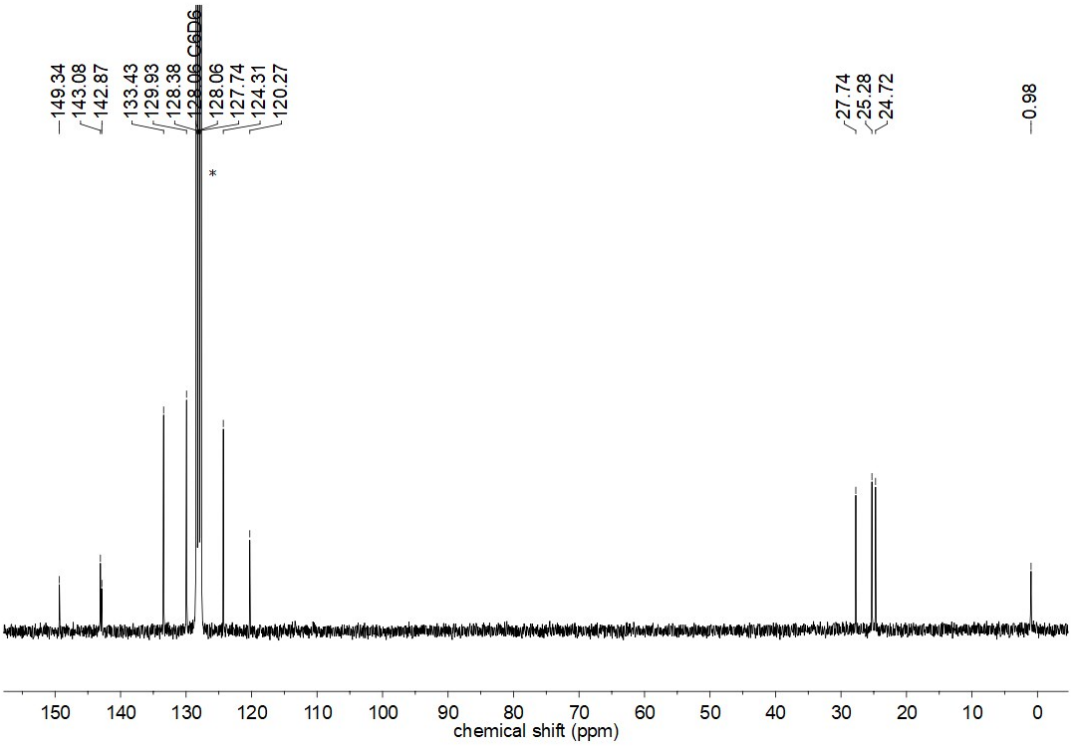

Figure S4. ^{13}C NMR spectrum (75.5 MHz, 300 K) of **LiL^{1}** in C_6D_6. (* solvent)

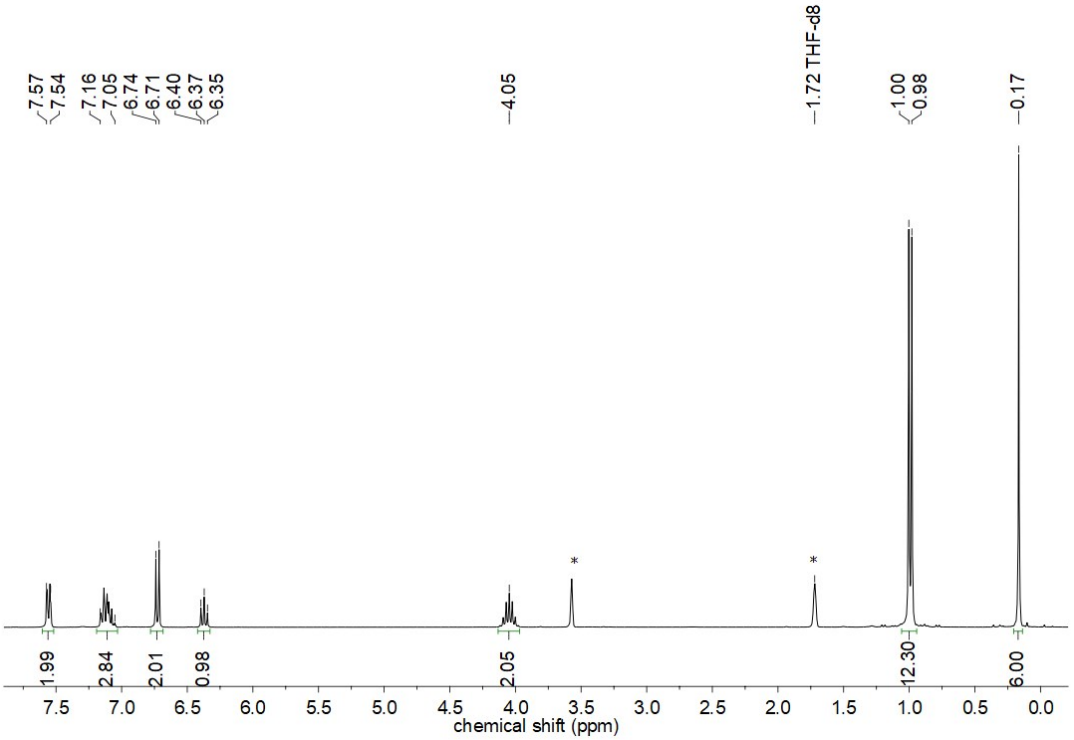

Figure S5. ^{1}H NMR spectrum (300.2 MHz, 300 K) of **LiL^{1}** in THF-d_8. (* solvent)

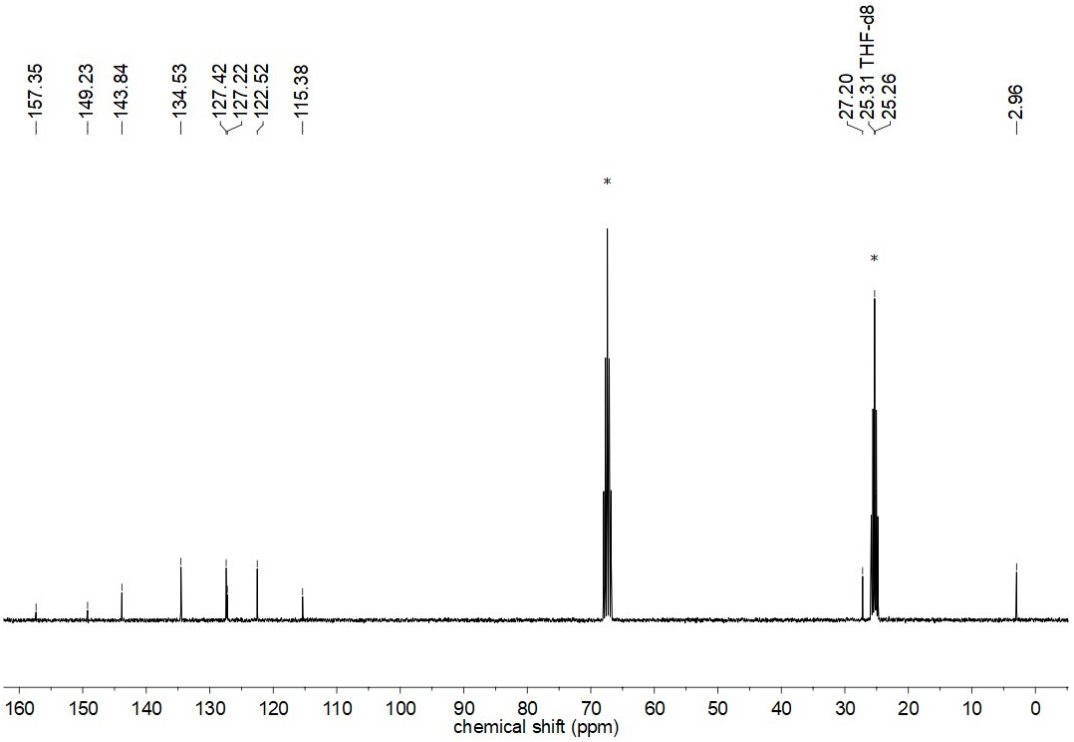

Figure S6. ^{13}C NMR spectrum (75.5 MHz, 300 K) of **LiL^{1}** in THF-d_8. (* solvent)

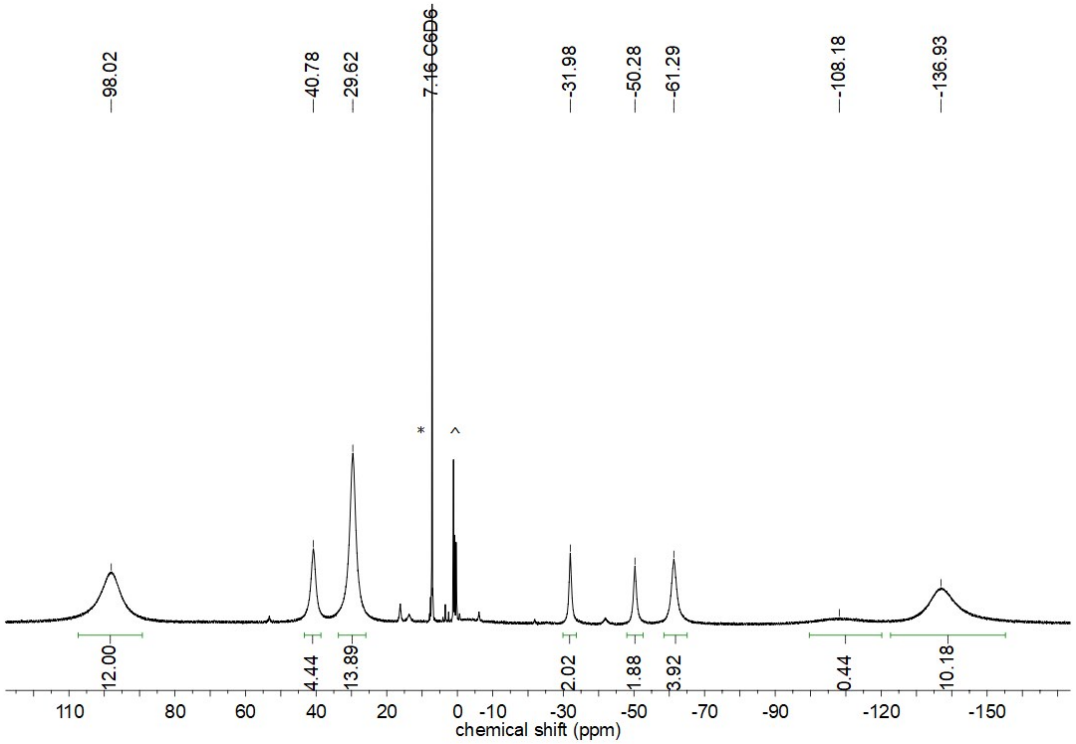

Figure S7. ^{1}H NMR spectrum (300.2 MHz, 300 K) of **[FeL$^1_2$]** in C_6D_6. (* solvent, ^ impurities)

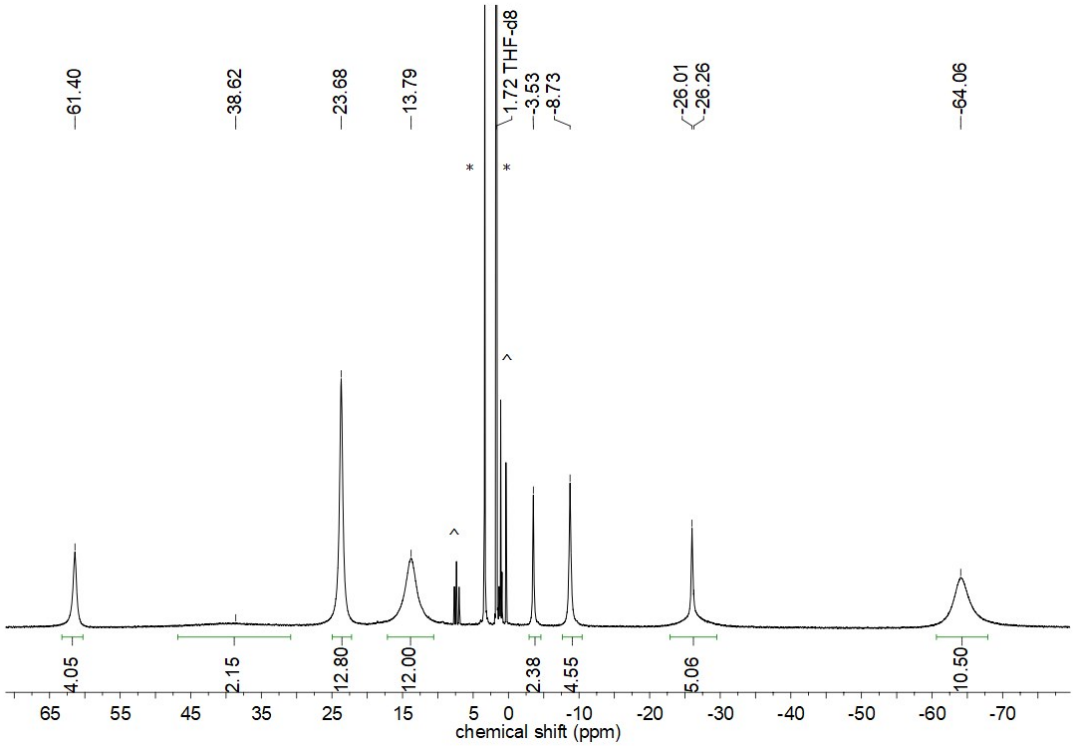

Figure S8. ^{1}H NMR spectrum (300.2 MHz, 300 K) of **[FeL$^1_2$]** in THF-d_8. (* solvent, ^ impurities)

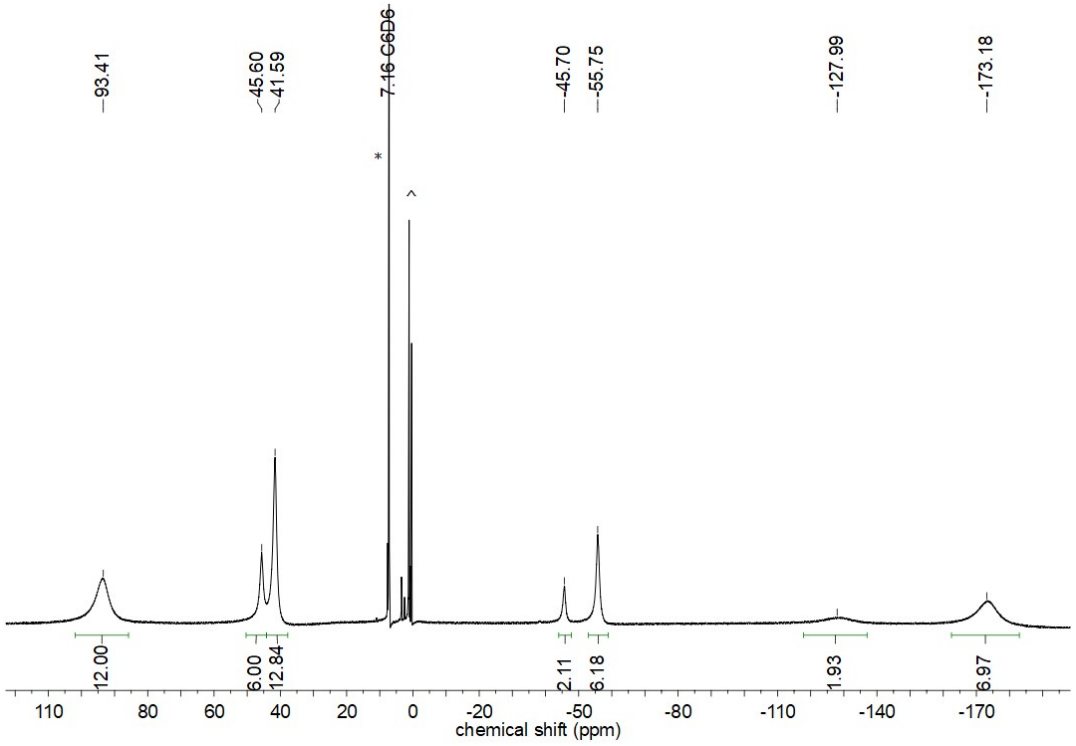

Figure S9. ^{1}H NMR spectrum (300.2 MHz, 300 K) of **[CoL$^1_2$]** in C_6D_6. (* solvent, ^ impurities)

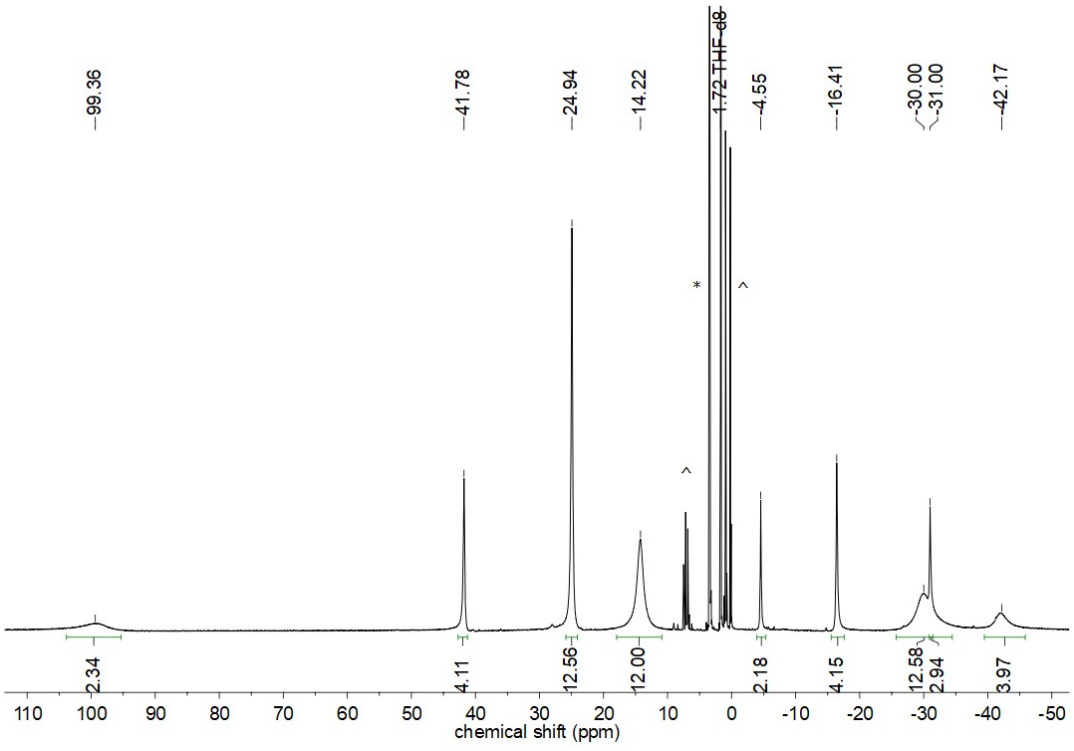

Figure S10. ^{1}H NMR spectrum (300.2 MHz, 300 K) of **[CoL$^1_2$]** in THF-d_8. (* solvent, ^ impurities)

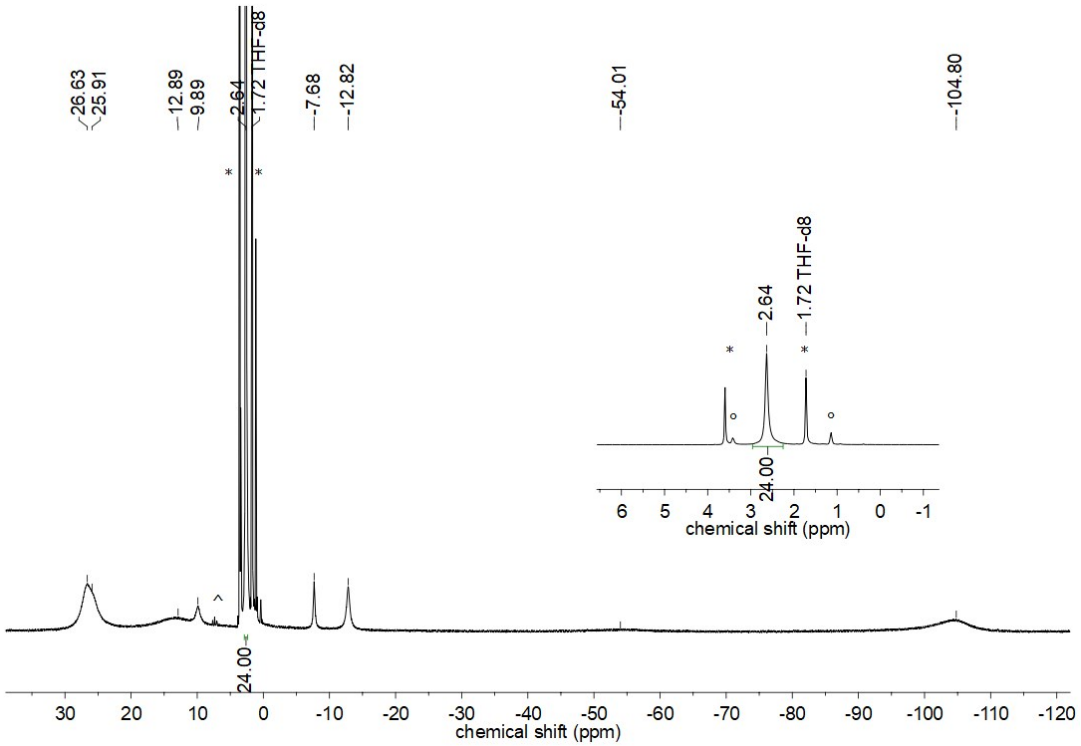

Figure S11. ^{1}H NMR spectrum (300.2 MHz, 300 K) of K{18c6}**[FeL$^{1}_{2}$]** in THF-d_8. (* solvent, ° diethyl ether)

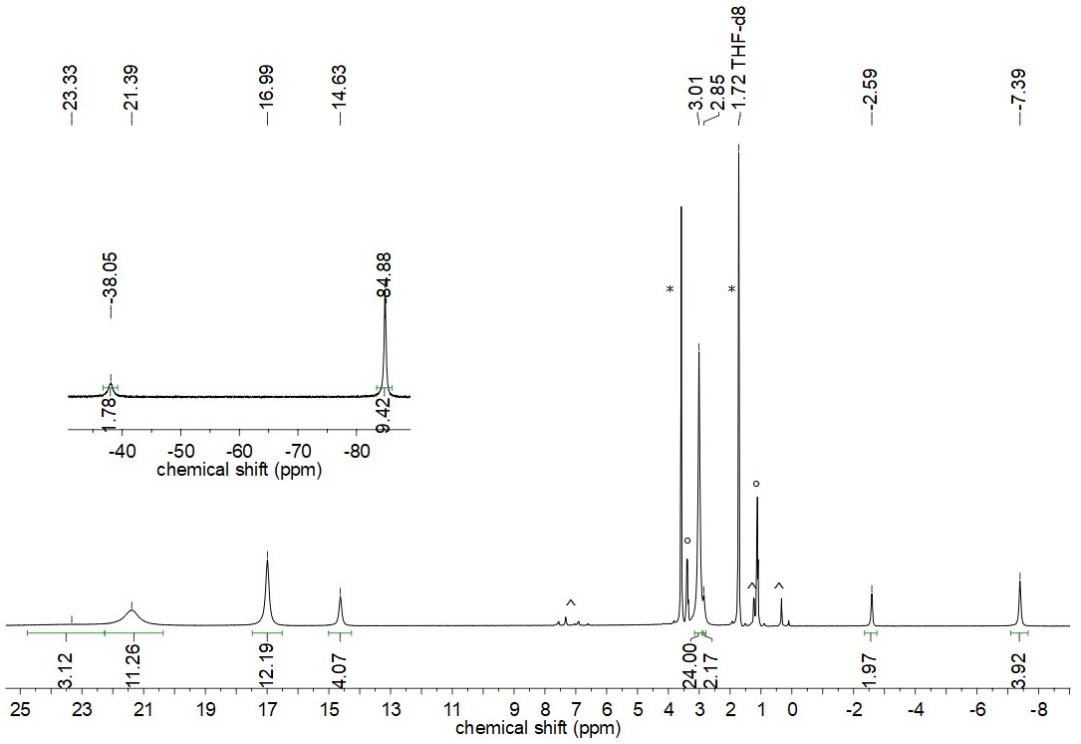

Figure S12. ^{1}H NMR spectrum (300.2 MHz, 300 K) of K{18c6}**[CoL$^{1}_{2}$]** in THF-d_8. (* solvent, ^ impurities, ° diethyl ether)

−N(Dipp)SiMePh$_2$ (L^2) containing compounds

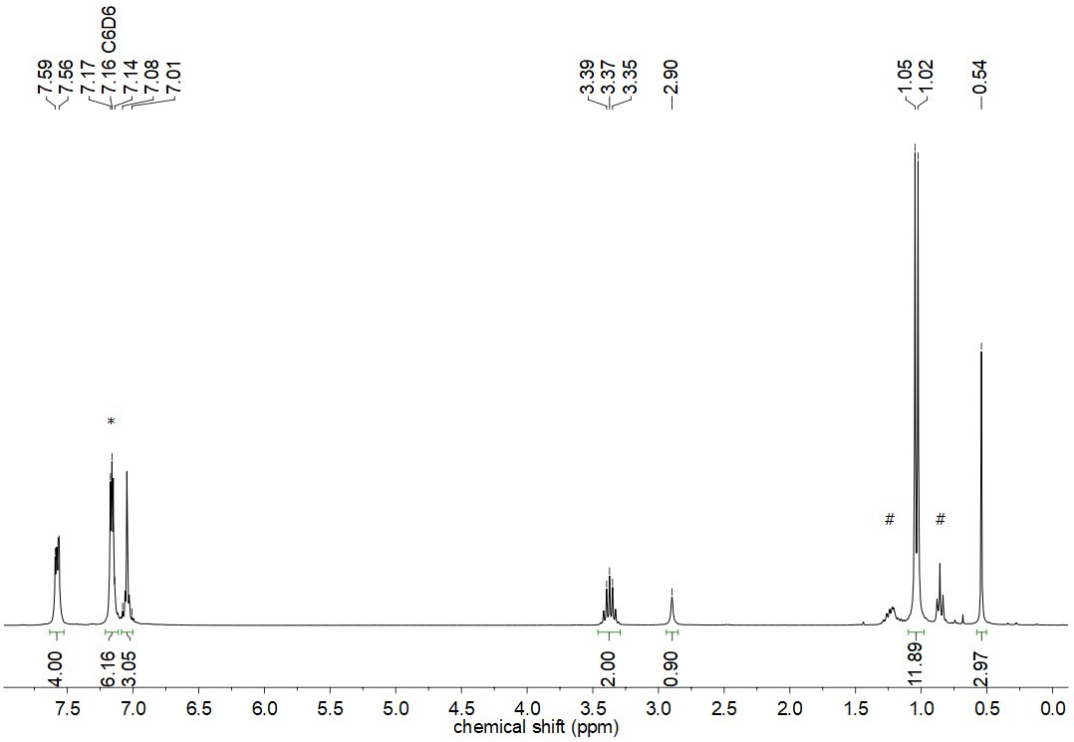

Figure S13. ^{1}H NMR spectrum (300.2 MHz, 300 K) of **HL^2** in C_6D_6. (* solvent, # *n*-pentane)

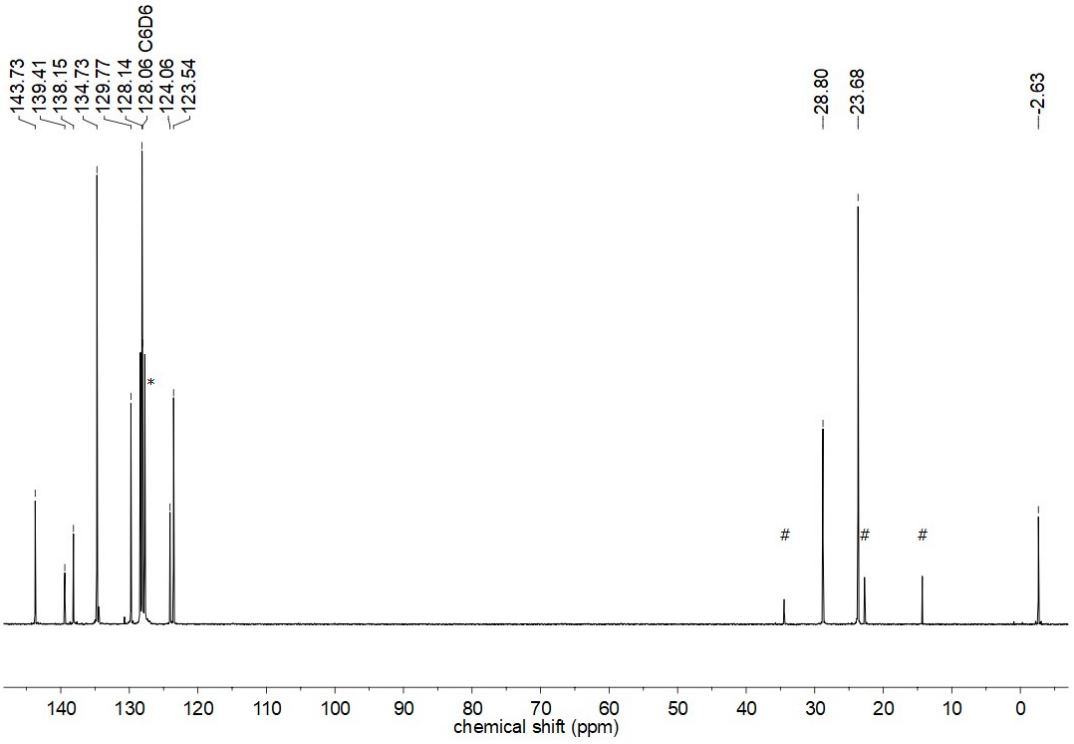

Figure S14. ^{13}C NMR spectrum (300.2 MHz, 300 K) of **HL^2** in C_6D_6. (* solvent, # *n*-pentane)

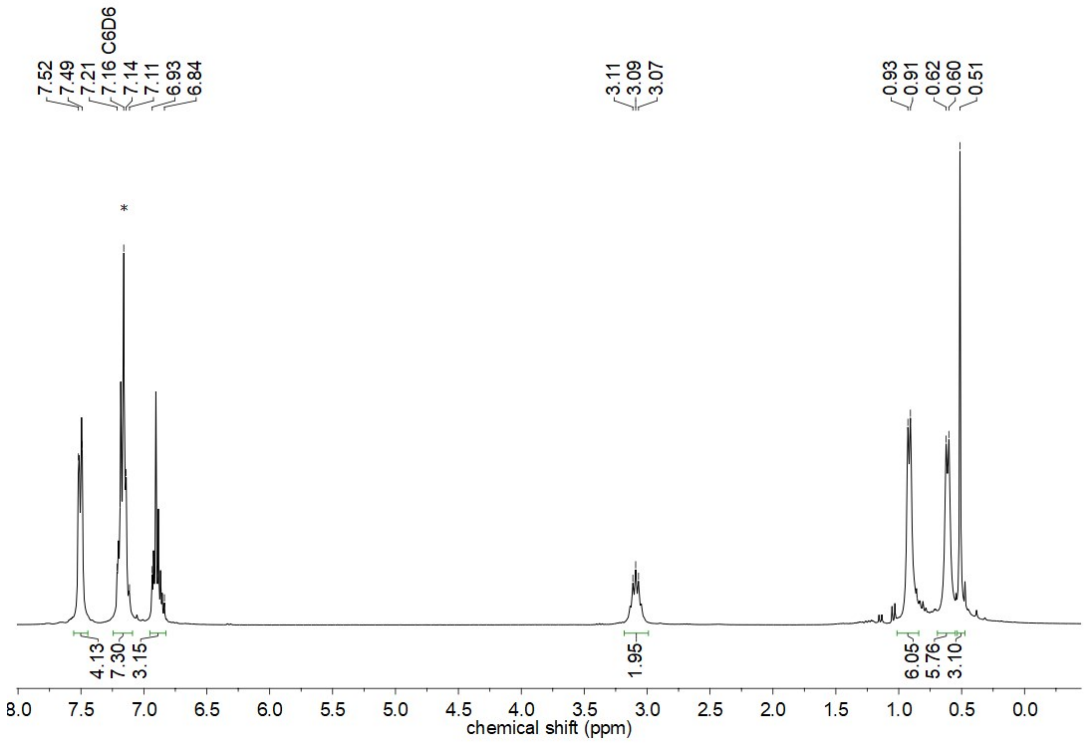

Figure S15. ^{1}H NMR spectrum (300.2 MHz, 300 K) of **LiL²** in C_6D_6. (* solvent)

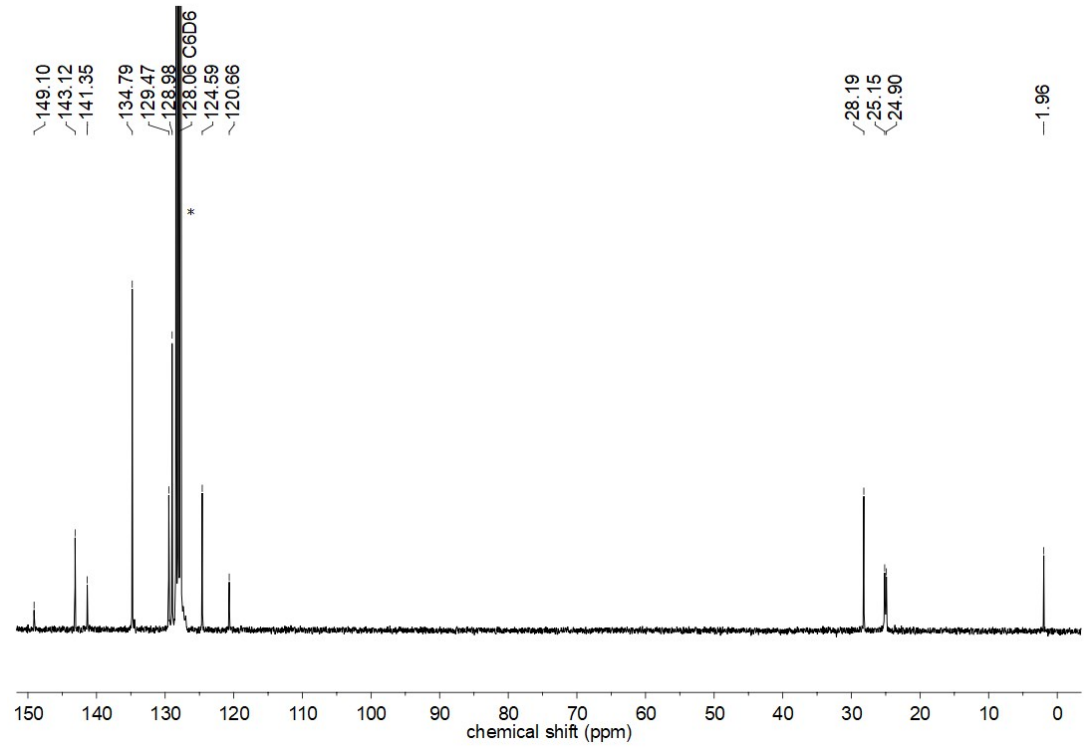

Figure S16. ^{13}C NMR spectrum (75.5 MHz, 300 K) of **LiL²** in C_6D_6. (* solvent)

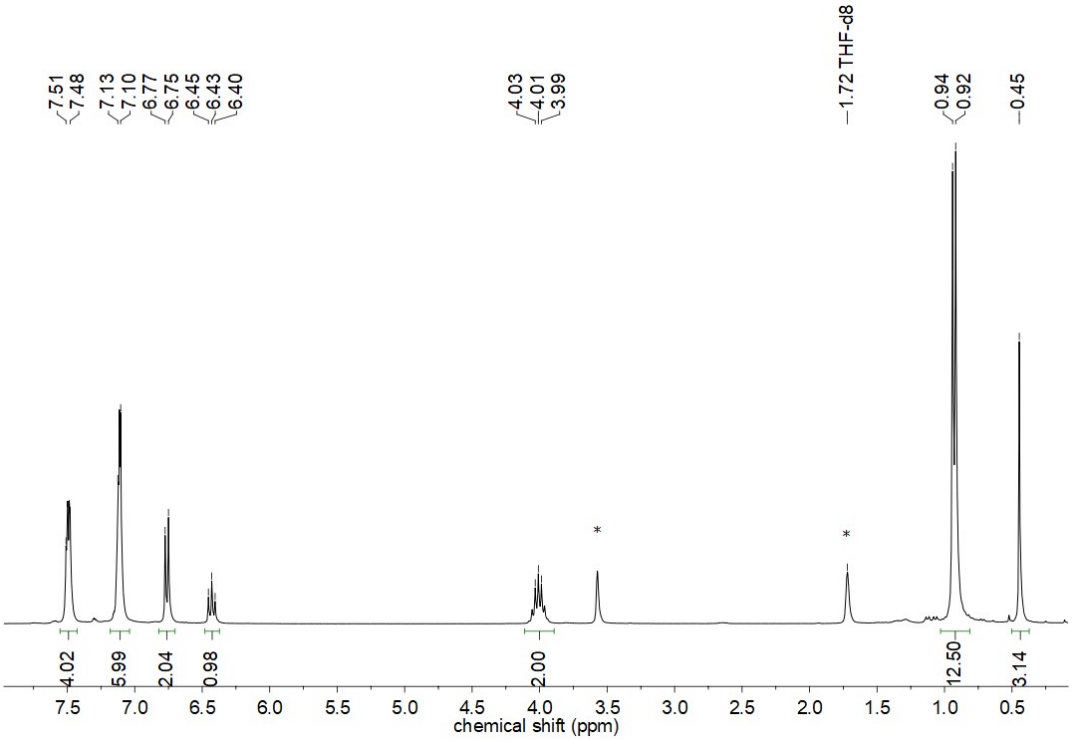

Figure S17. ^{1}H NMR spectrum (300.2 MHz, 300 K) of **LiL^{2}** in THF-d_8. (* solvent)

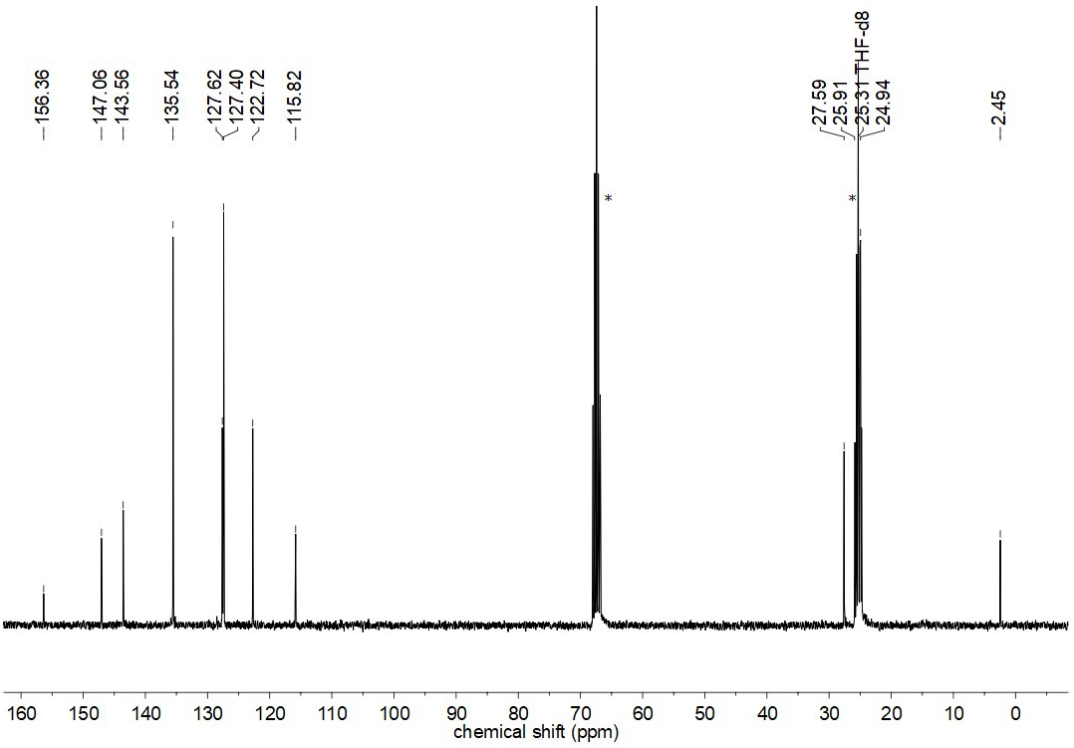

Figure S18. ^{13}C NMR spectrum (75.5 MHz, 300 K) of **LiL^{2}** in THF-d_8. (* solvent)

−N(Dipp)SiPh$_3$ (L^3) containing compounds

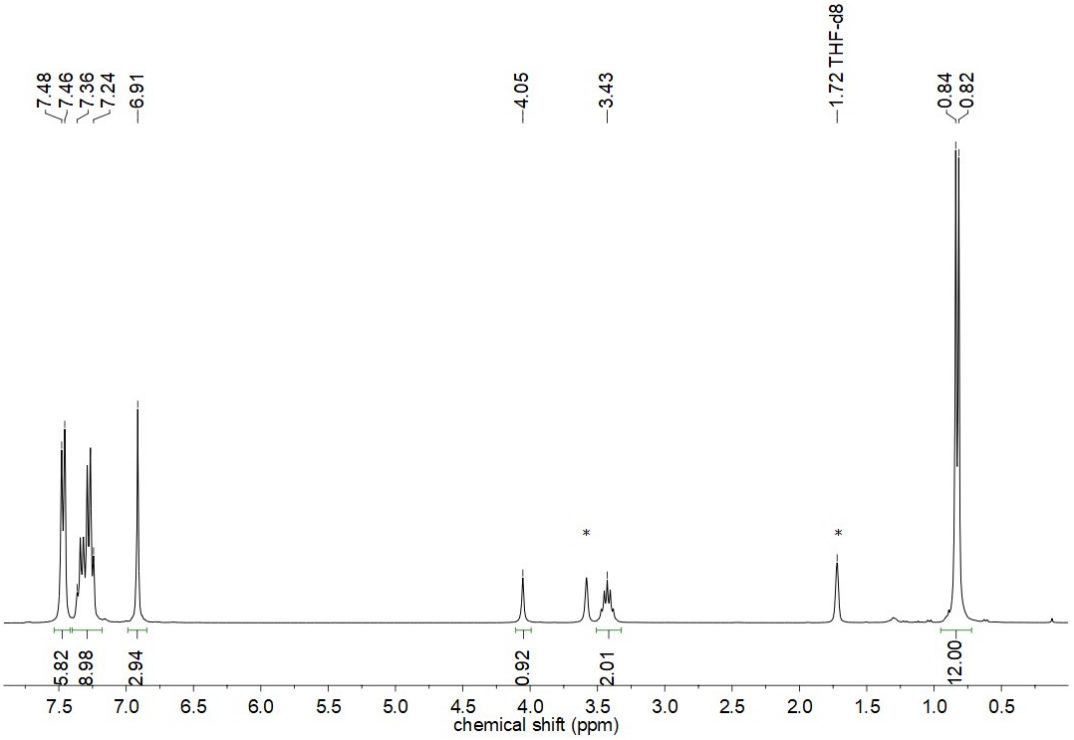

Figure S19. ^{1}H NMR spectrum (300.2 MHz, 300 K) of **HL^3** in THF-d_8. (* solvent)

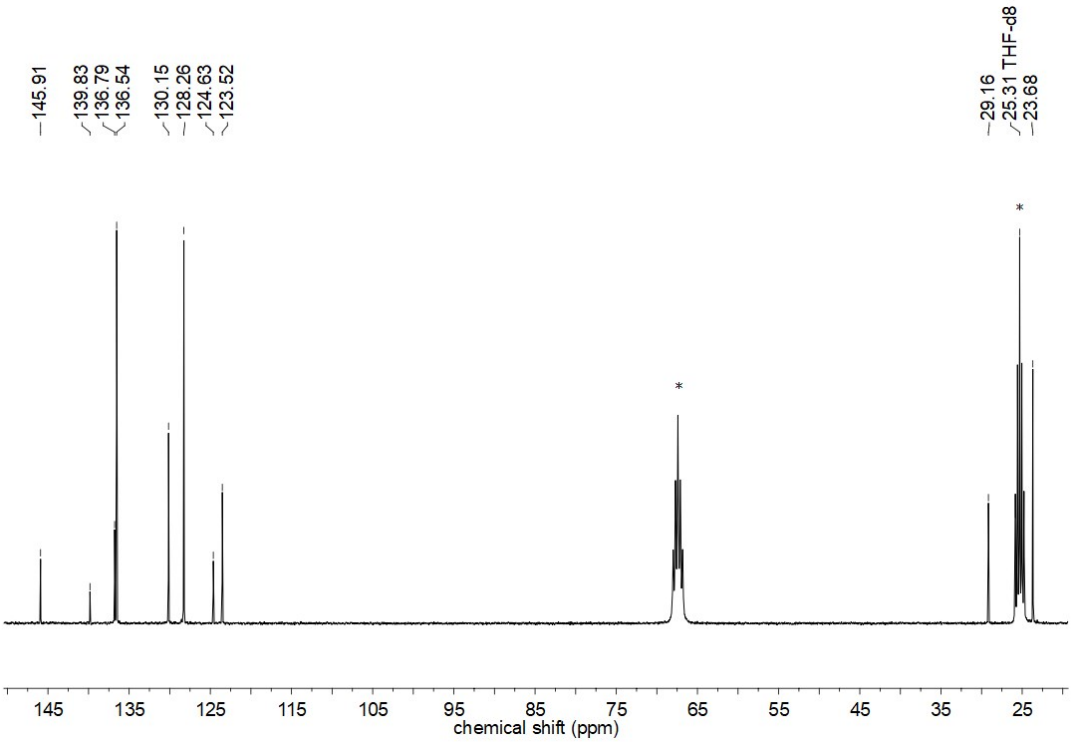

Figure S20. ^{13}C NMR spectrum (75.5 MHz, 300 K) of **HL^3** in THF-d_8. (* solvent)

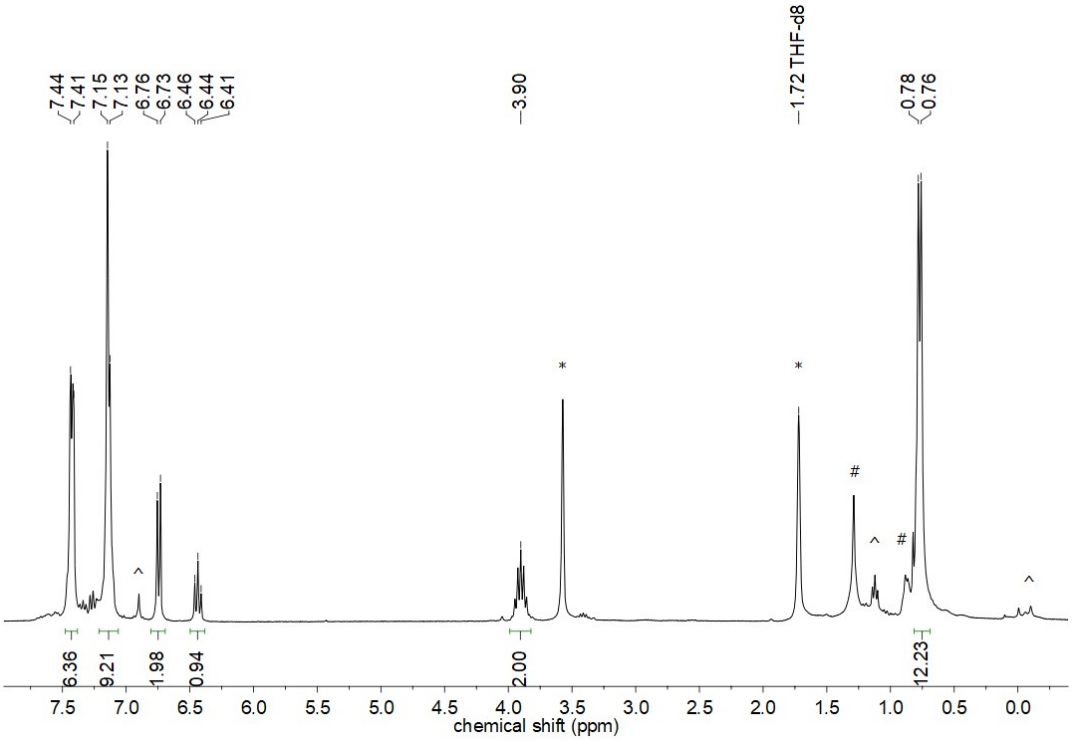

Figure S21. ^{1}H NMR spectrum (300.2 MHz, 300 K) of **LiL^{3}** in THF-d_8. (* solvent, # *n*-pentane, ^ impurities)

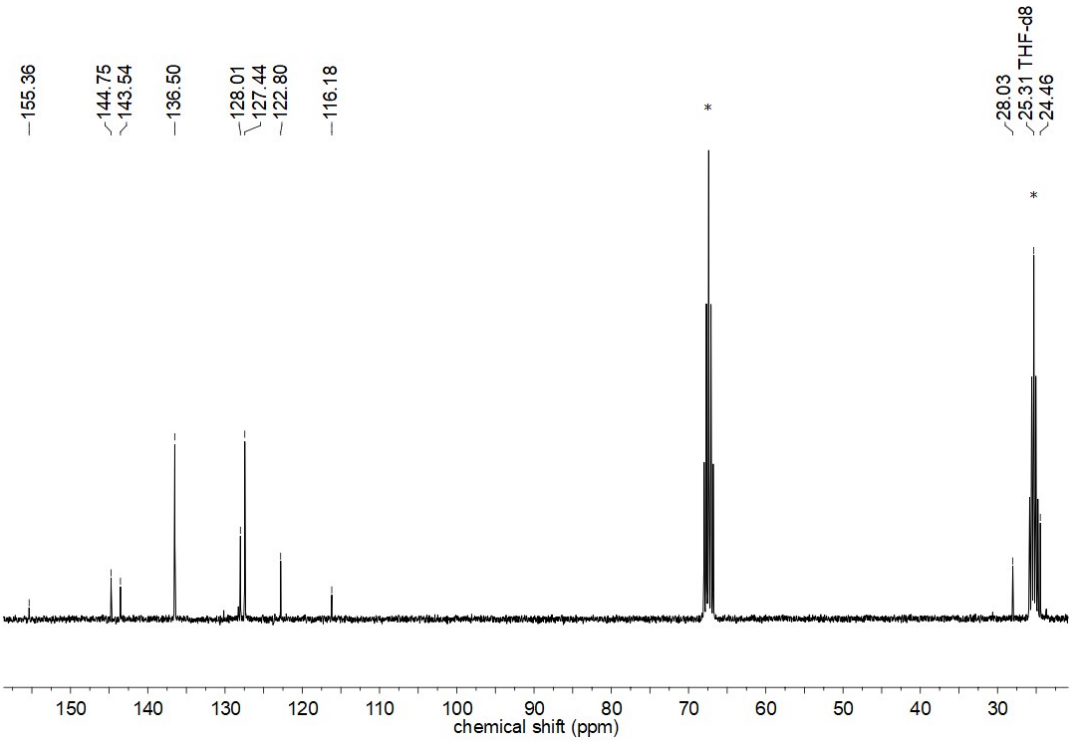

Figure S22. ^{13}C NMR spectrum (75.5 MHz, 300 K) of **LiL^{3}** in THF-d_8. (* solvent)

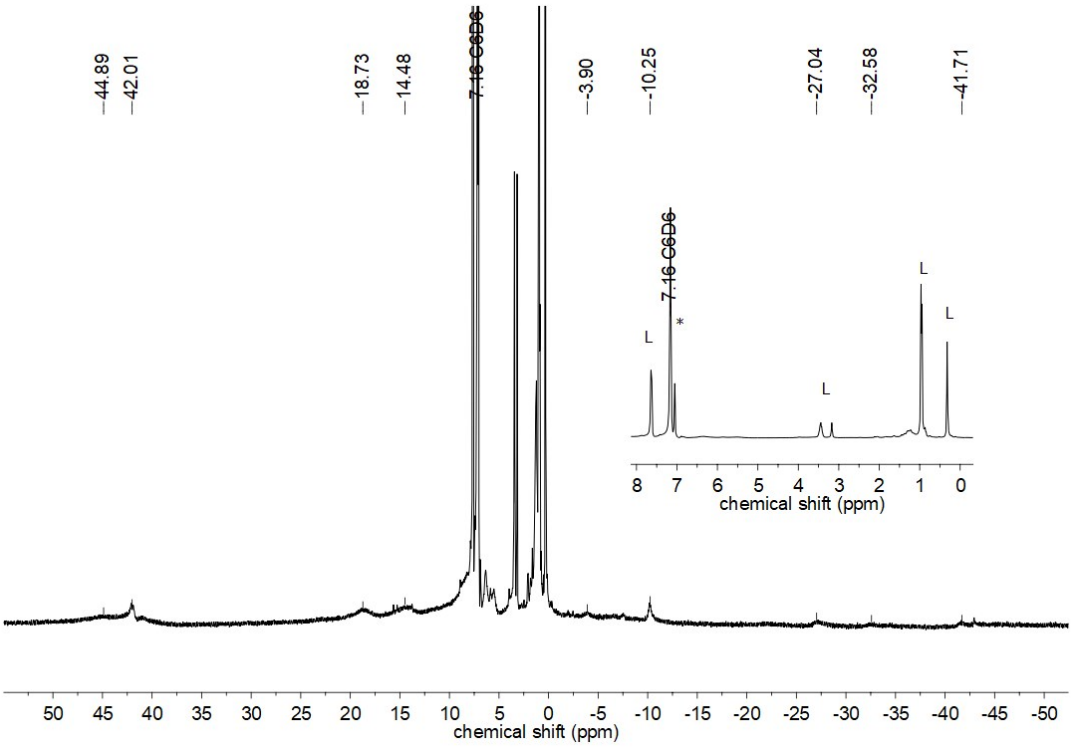

Figure S23. ^{1}H NMR spectrum (300.2 MHz, 300 K) of **[FeL$^{3}_{2}$]** in C_6D_6. (* solvent, ^{L} ligand impurities)

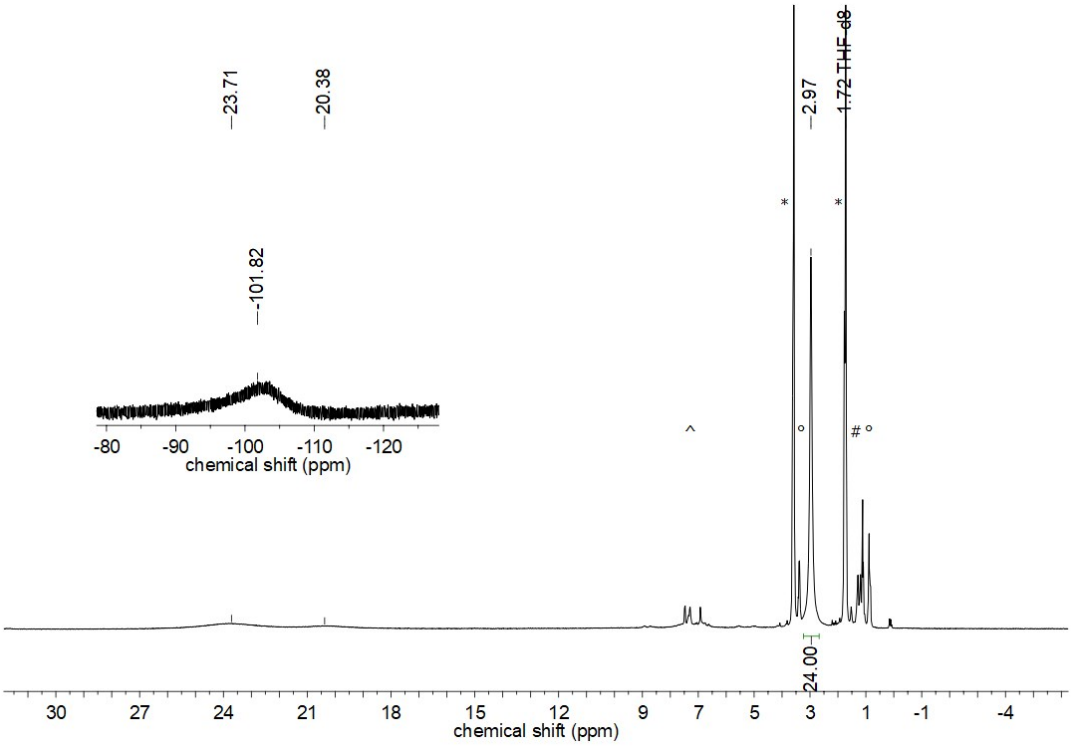

Figure S24. ^{1}H NMR spectrum (300.2 MHz, 300 K) of K{18c6}**[FeL$^{3}_{2}$]** in THF-d_8. (* solvent, ^ impurities, ° diethyl ether, # *n*-pentane)

−N(Dipp)SiMe$_2$(allyl) (L^4) containing compounds

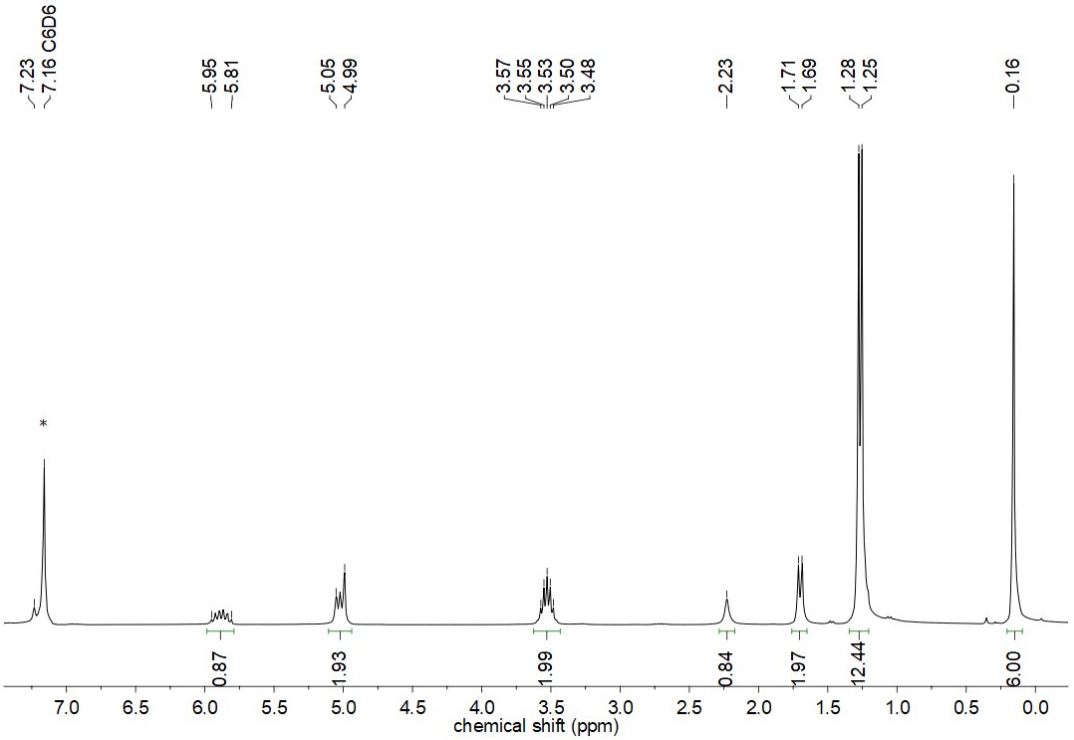

Figure S25. ^{1}H NMR spectrum (300.2 MHz, 300 K) of **HL^4** in C_6D_6. (* solvent)

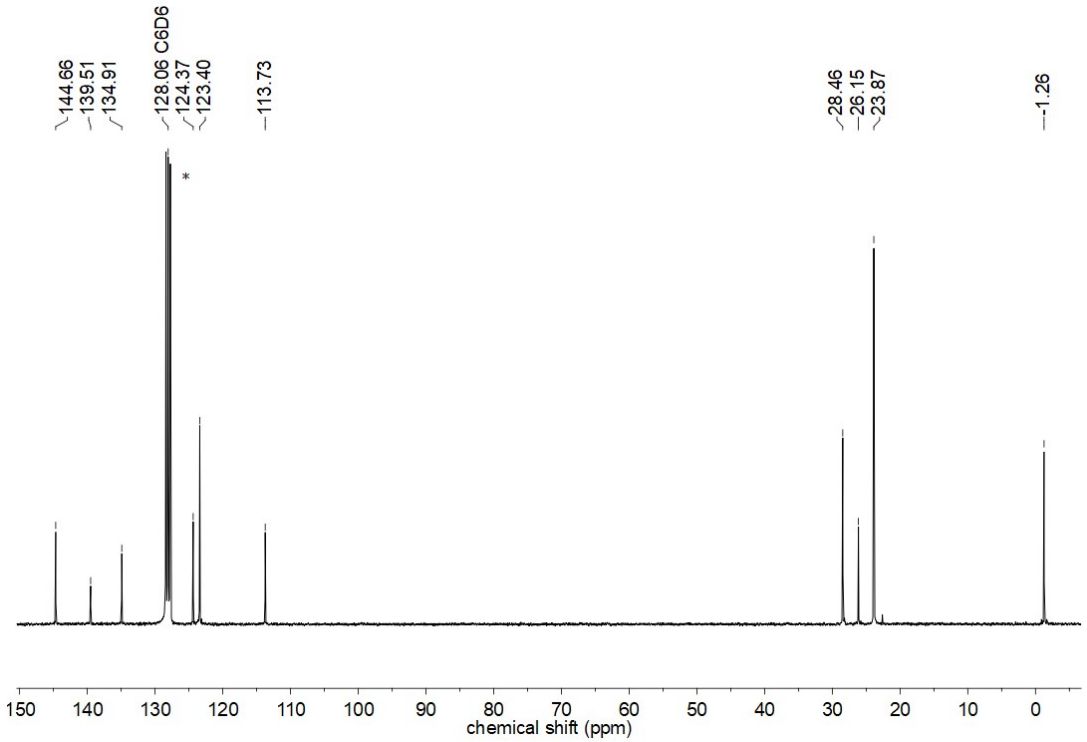

Figure S26. ^{13}C NMR spectrum (75.5 MHz, 300 K) of **HL^4** in C_6D_6. (* solvent)

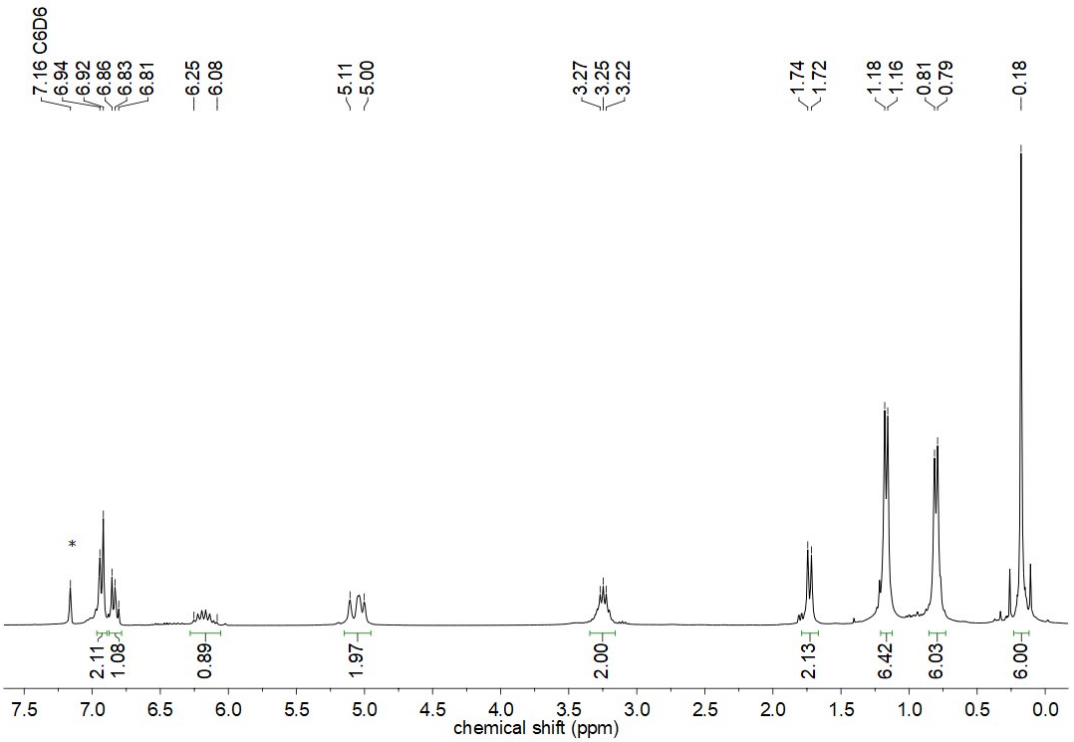

Figure S27. ^{1}H NMR spectrum (300.2 MHz, 300 K) of **LiL^{4}** in C_6D_6. (* solvent)

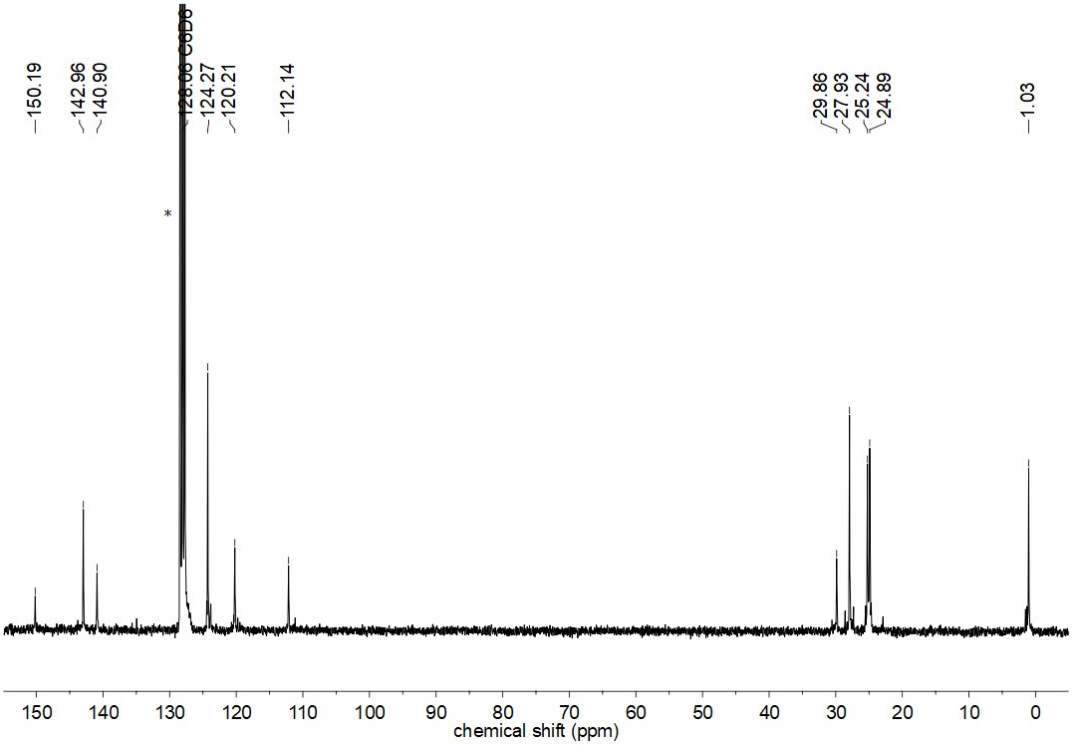

Figure S28. ^{13}C NMR spectrum (75.5 MHz, 300 K) of **LiL^{4}** in C_6D_6. (* solvent)

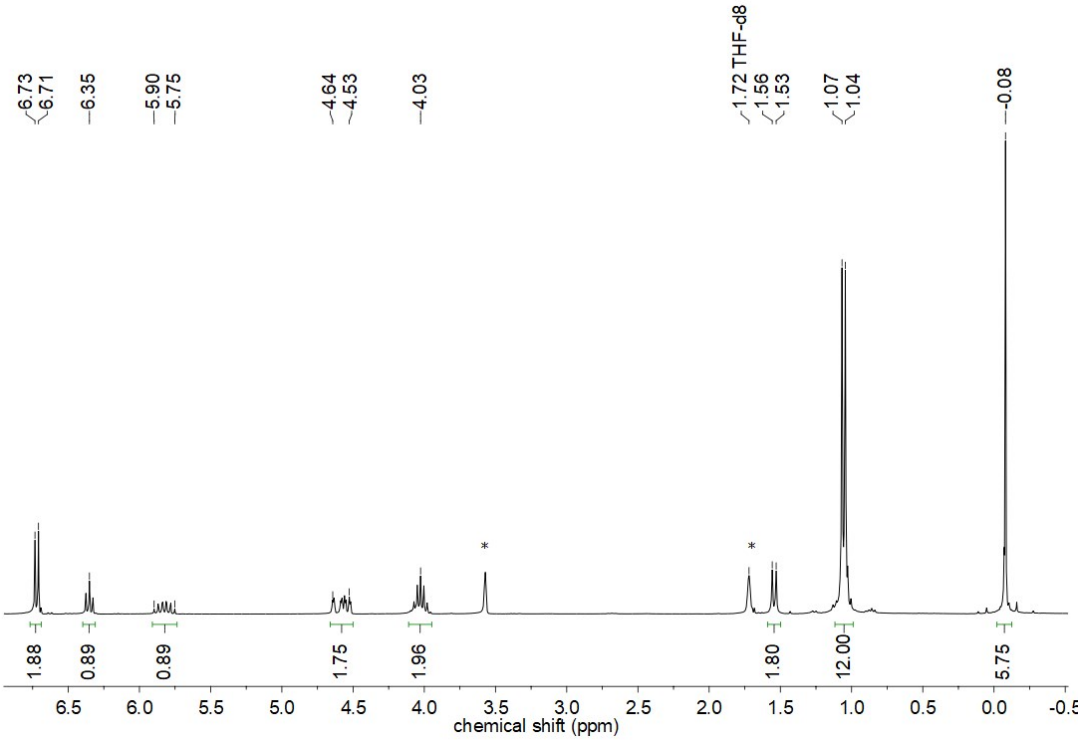

Figure S29. ^{1}H NMR spectrum (300.2 MHz, 300 K) of **LiL^{4}** in THF-d_8. (* solvent)

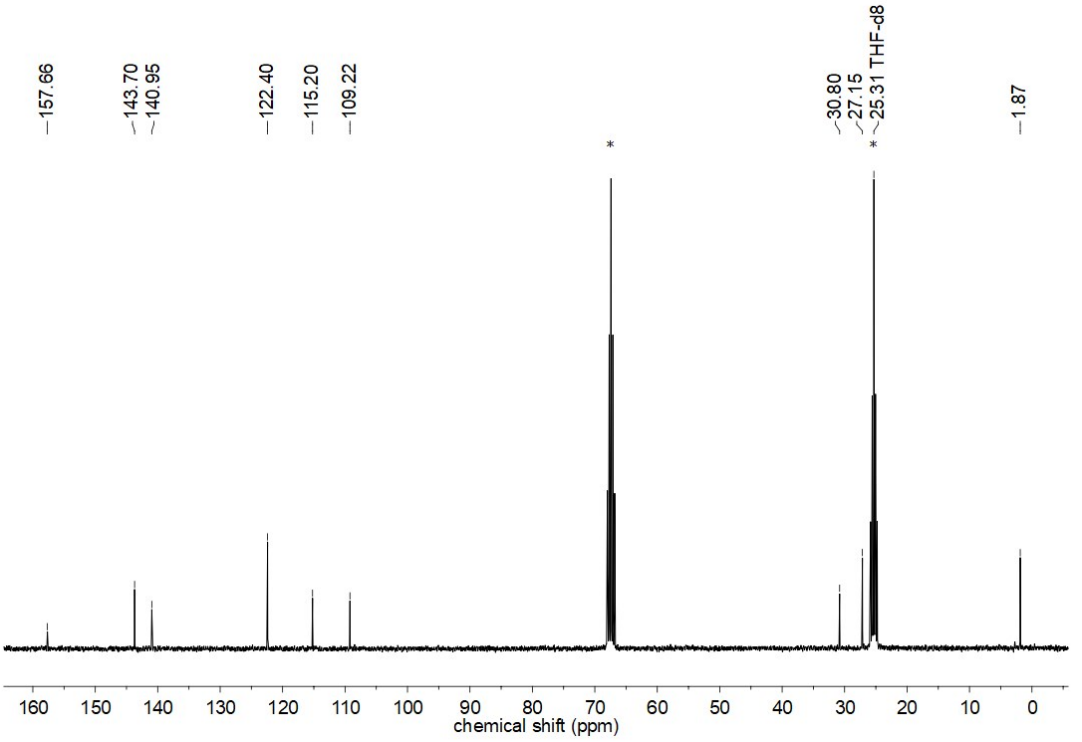

Figure S30. ^{13}C NMR spectrum (75.5 MHz, 300 K) of **LiL^{4}** in THF-d_8. (* solvent)

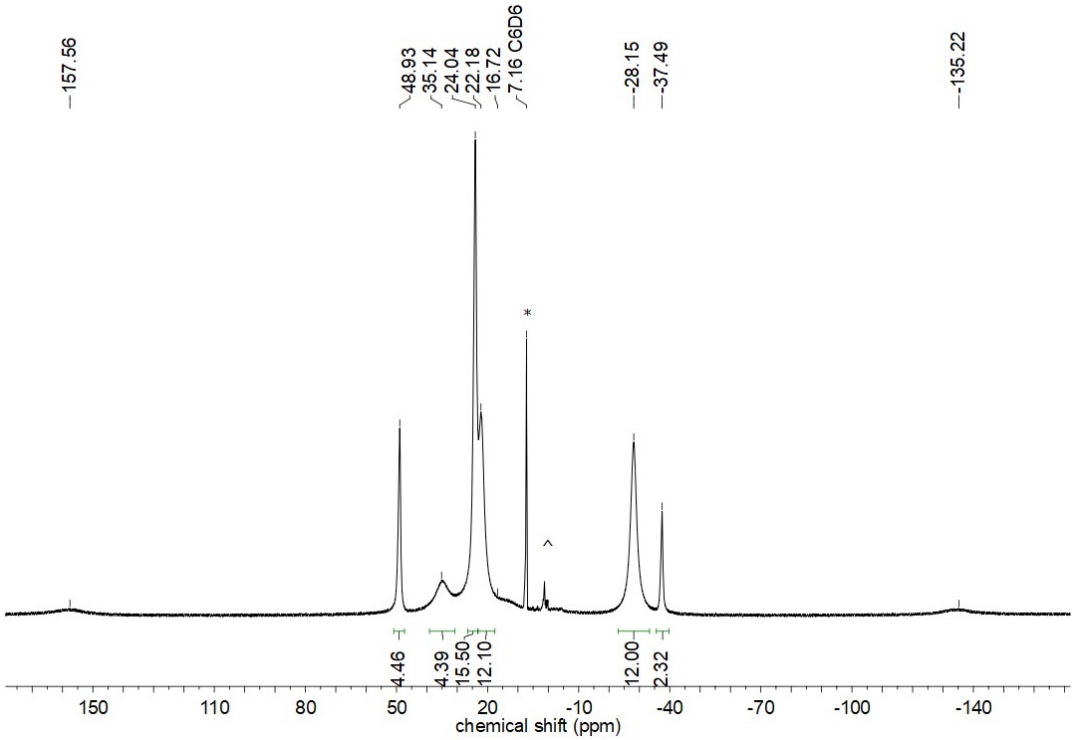

Figure S31. ^{1}H NMR spectrum (300.2 MHz, 300 K) of **[FeL$^4_2$]** in C_6D_6. (* solvent, ^ impurities)

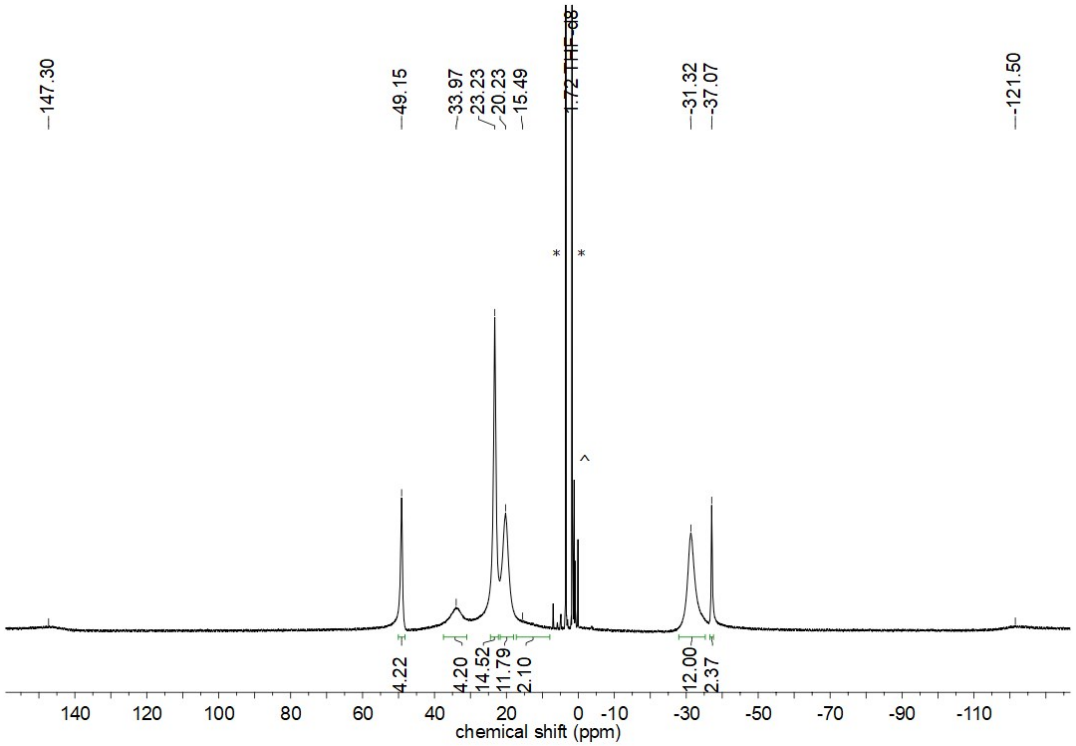

Figure S32. ^{1}H NMR spectrum (300.2 MHz, 300 K) of **[FeL$^4_2$]** in THF-d_8. (* solvent, ^ impurities)

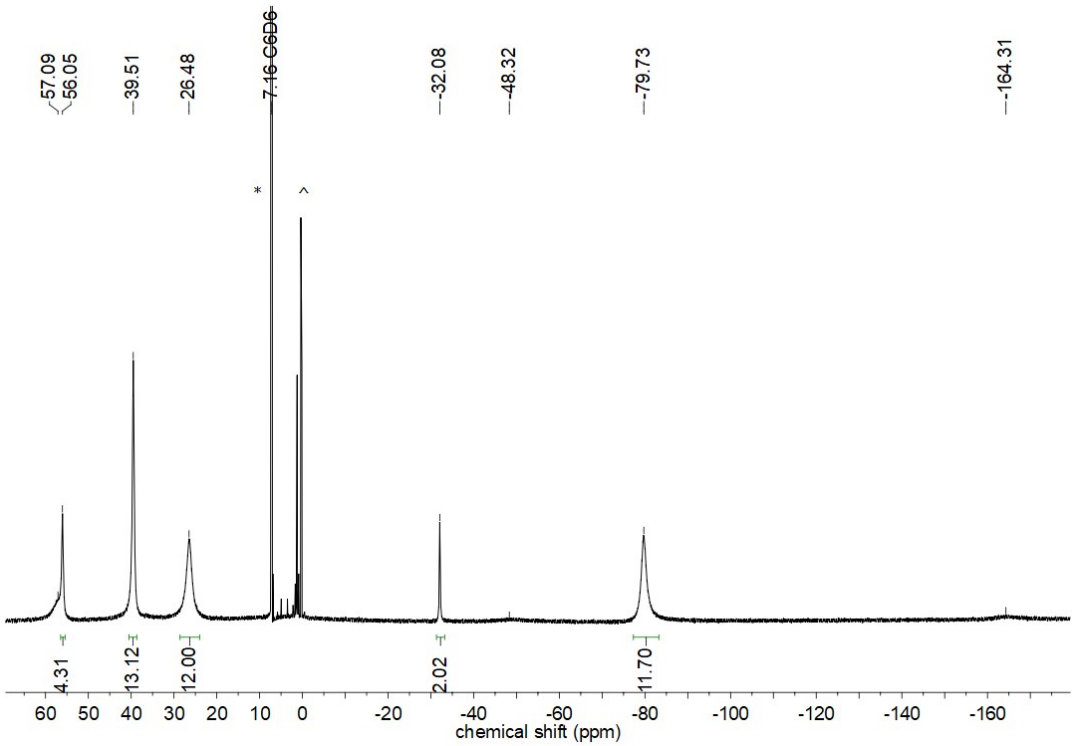

Figure S33. ^{1}H NMR spectrum (300.2 MHz, 300 K) of **[CoL$^4_2$]** in C_6D_6. (* solvent, ^ impurities)

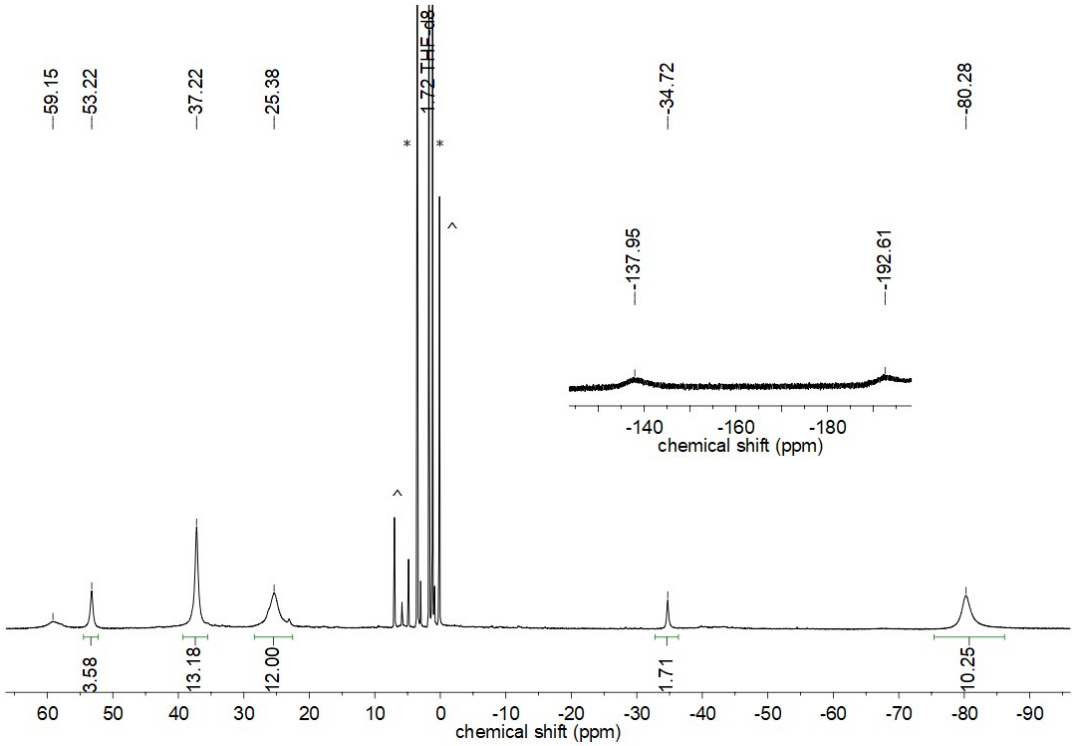

Figure S34. ^{1}H NMR spectrum (300.2 MHz, 300 K) of **[CoL$^4_2$]** in THF-d_8. (* solvent, ^ impurities)

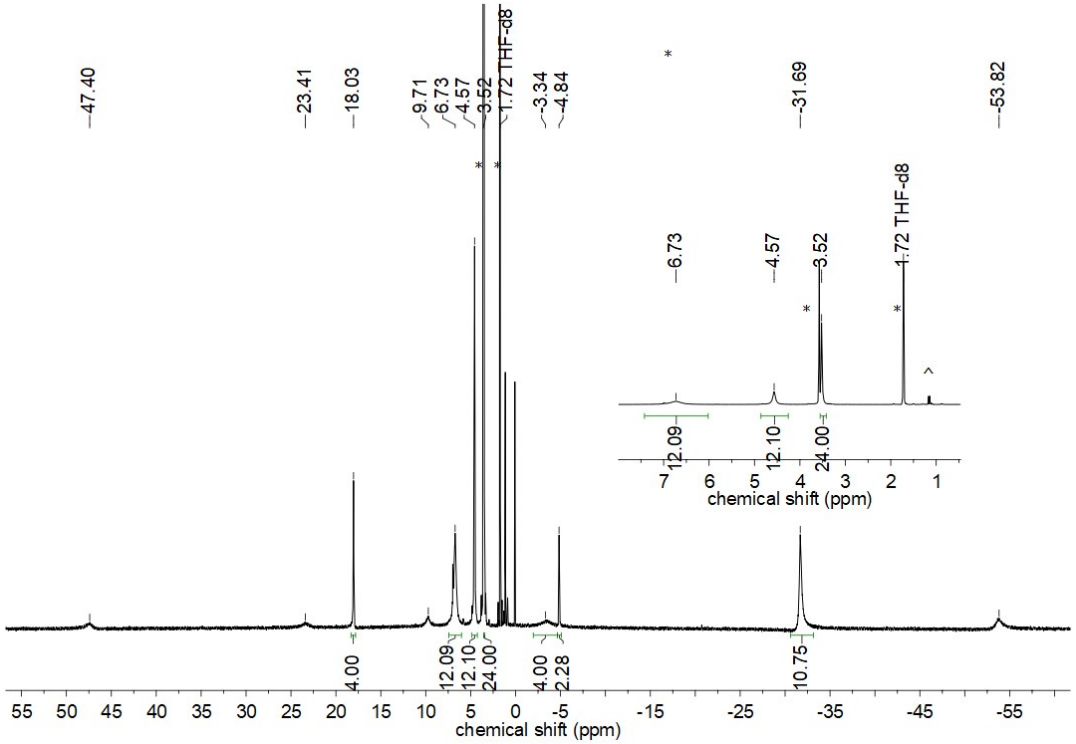

Figure S35. ^{1}H NMR spectrum (300.2 MHz, 300 K) of K{18c6}**[CoL$^{4}_{2}$]** in THF-d_8. (* solvent, ^ impurities)

Imido complexes

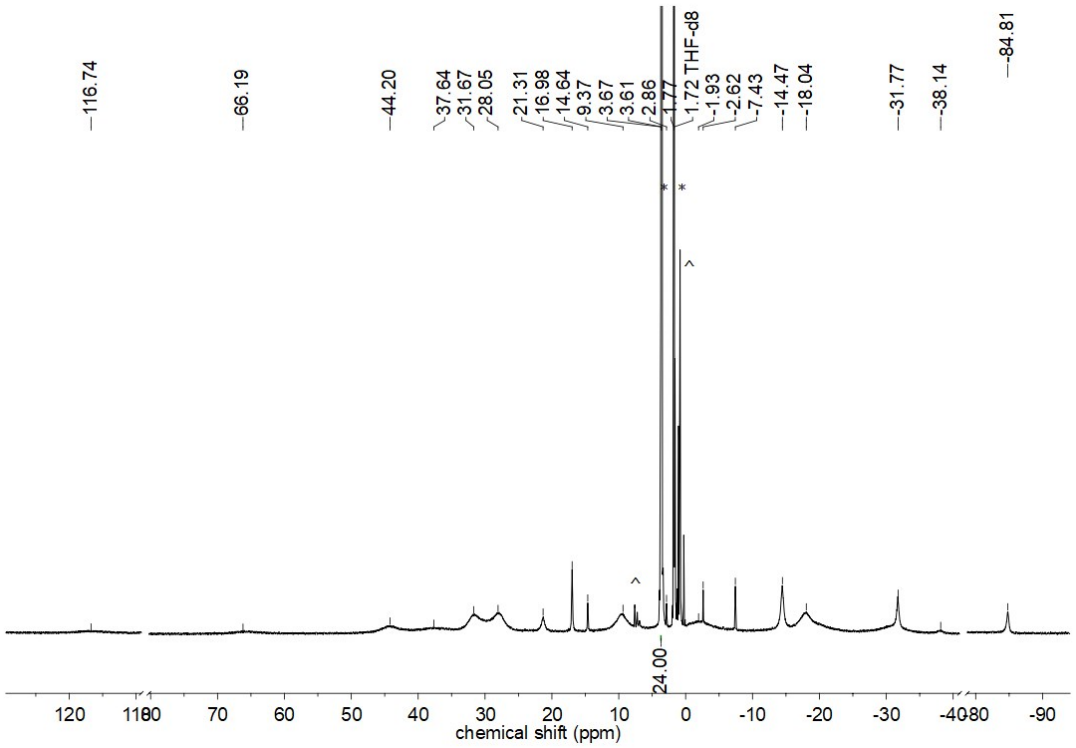

Figure S36. ^{1}H NMR spectrum (300.2 MHz, 300 K) of K{18c6}**[Co(NDipp)L$^{1}_{2}$]** in THF-d_8. (* solvent, ^ impurities)

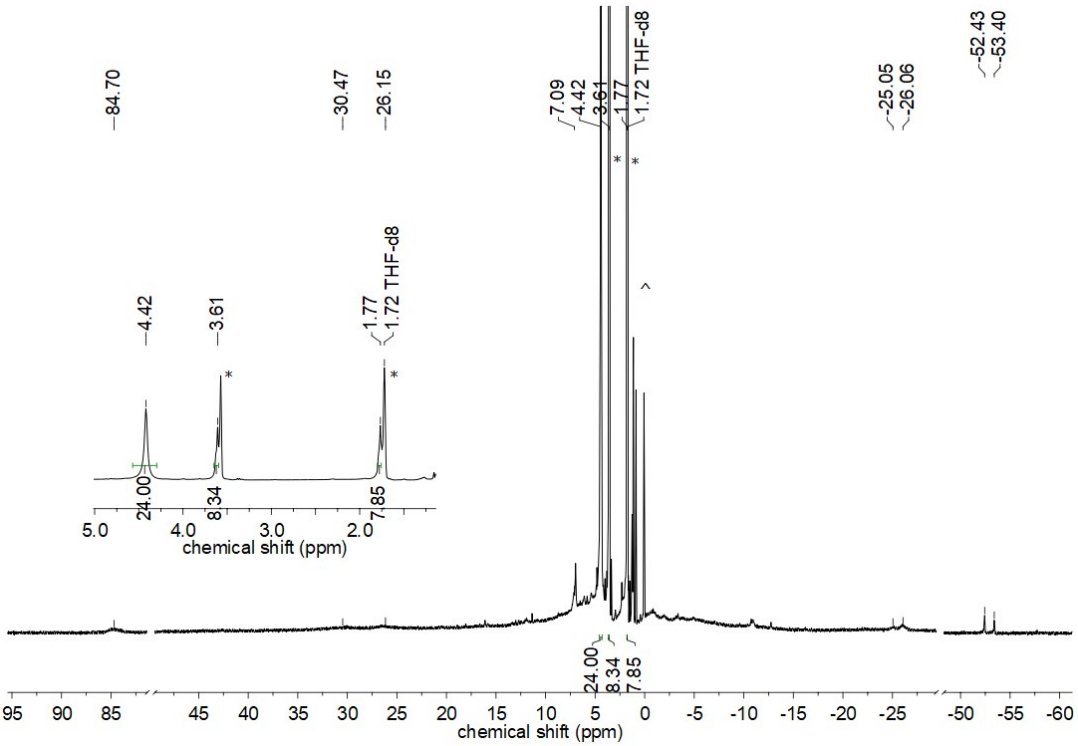

Figure S37. ^{1}H NMR spectrum (300.2 MHz, 300 K) of K{18c6}**[Co(NDipp)L$^{4}_{2}$]** in THF-d_8. (* solvent, ^ impurities)

2 UV/Vis spectra

−N(Dipp)SiMe$_2$Ph (L^1) containing compounds

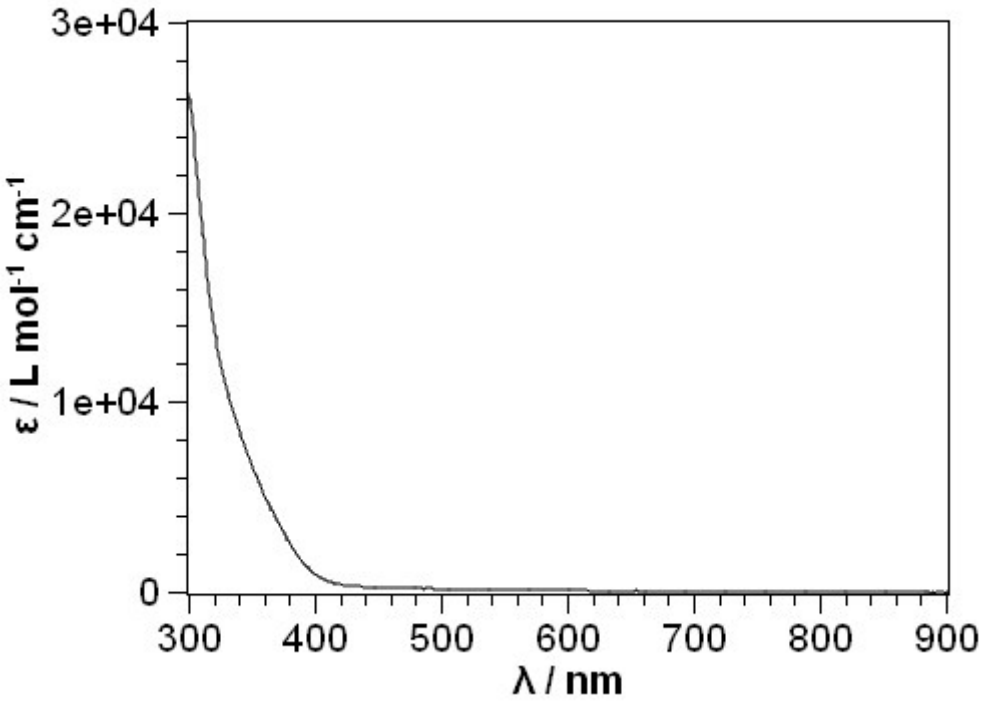

Figure S38. UV/Vis spectrum of **[MnL$^1_2$]** in Et$_2$O.

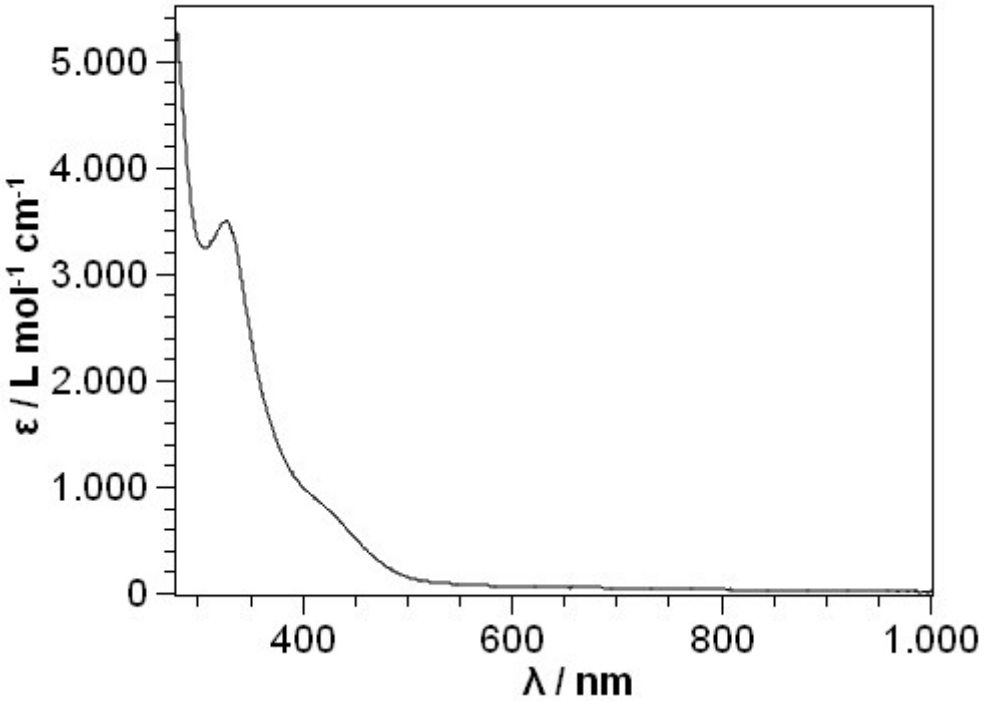

Figure S39. UV/Vis spectrum of **[FeL$^1_2$]** in Et$_2$O.

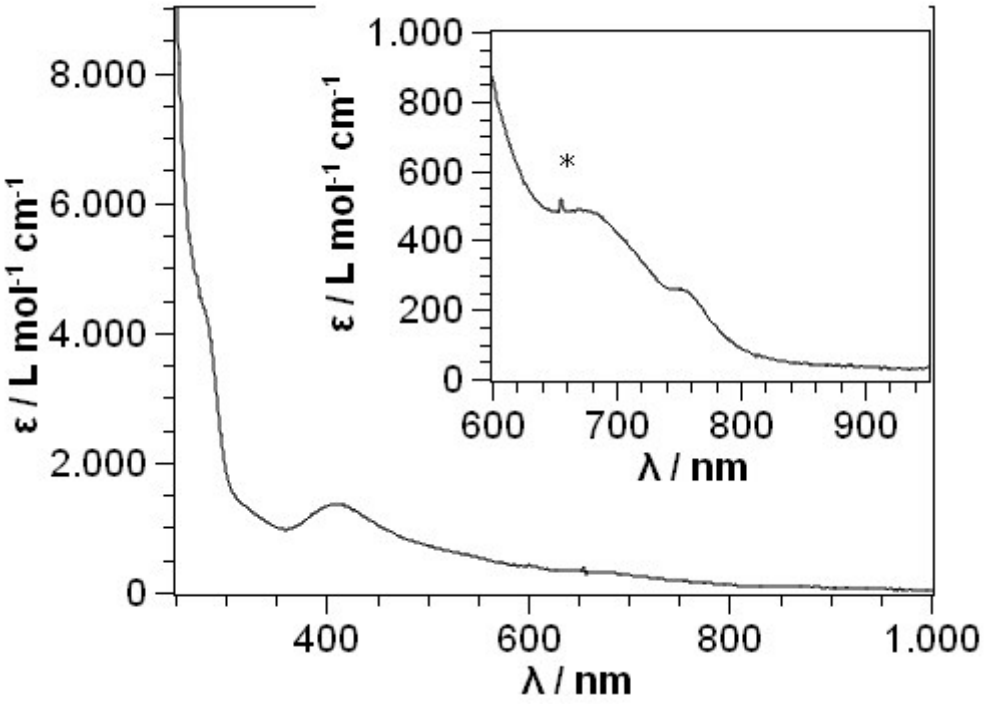

Figure S40. UV/Vis spectrum of **[CoL$^1_2$]** in Et_2O. The signal caused by detector exchange is indicated by *.

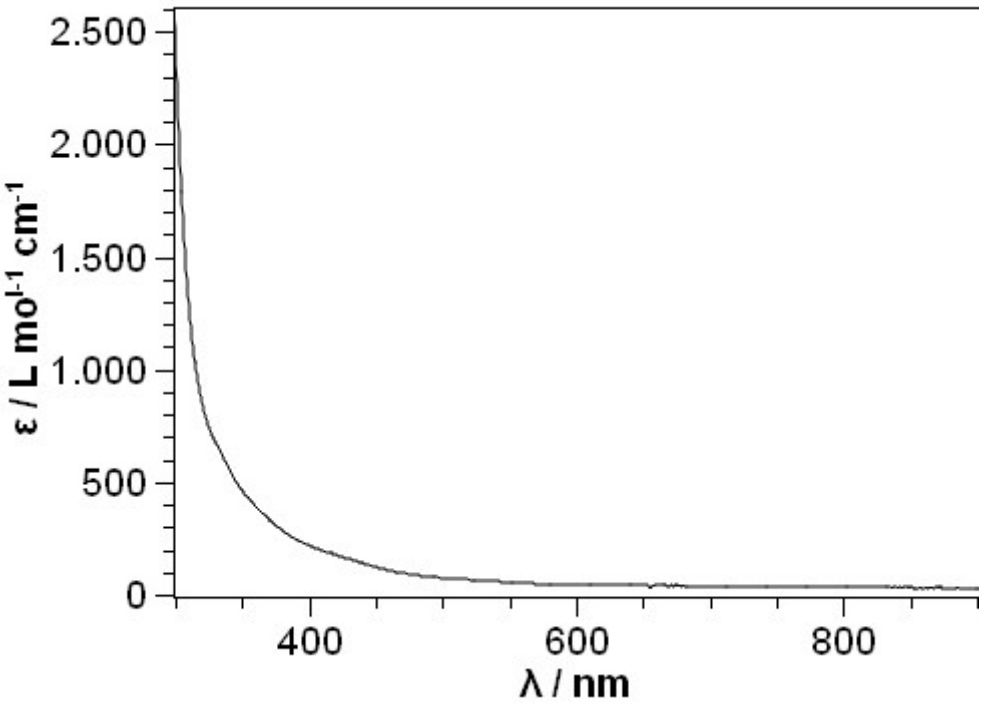

Figure S41. UV/Vis spectrum of K{18c6}**[MnL^{1}L^{1*}]** in THF.

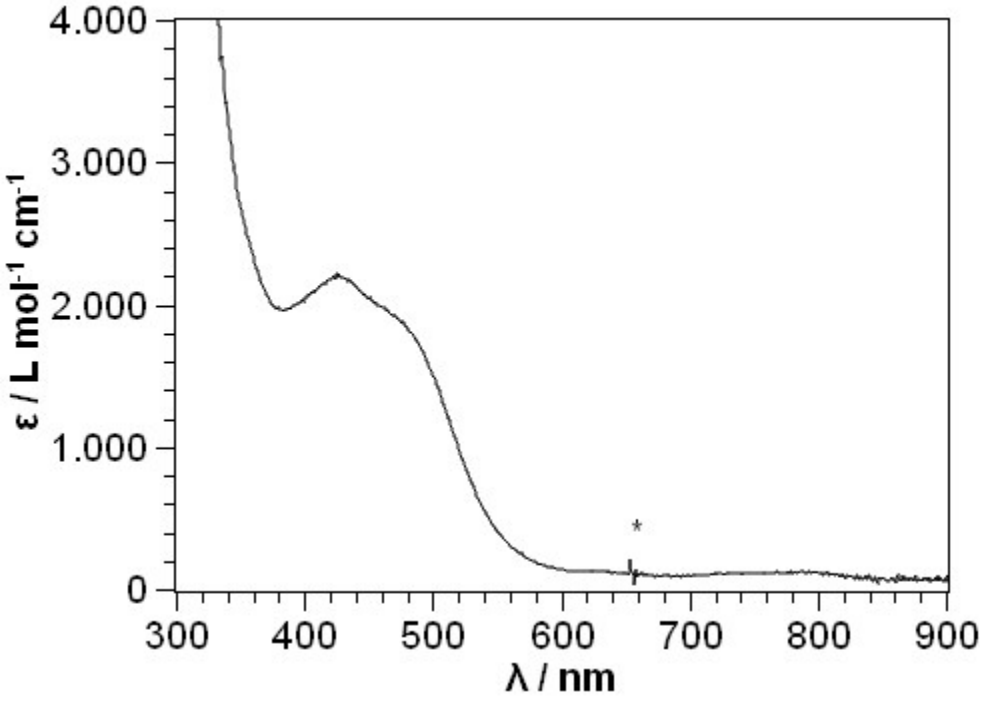

Figure S42. UV/Vis spectrum of K{18c6}**[FeL$^1_2$]** in Et_2O.

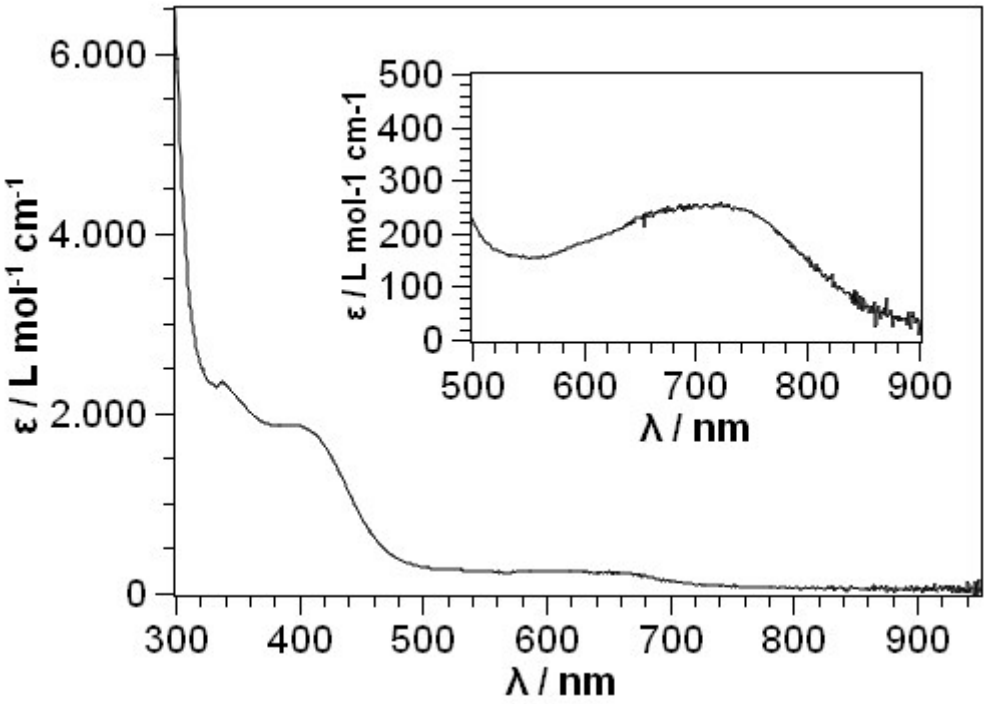

Figure S43. UV/Vis spectrum of K{18c6}**[CoL$^1_2$]** in Et_2O.

−N(Dipp)SiMePh$_2$ (L^2) containing compounds

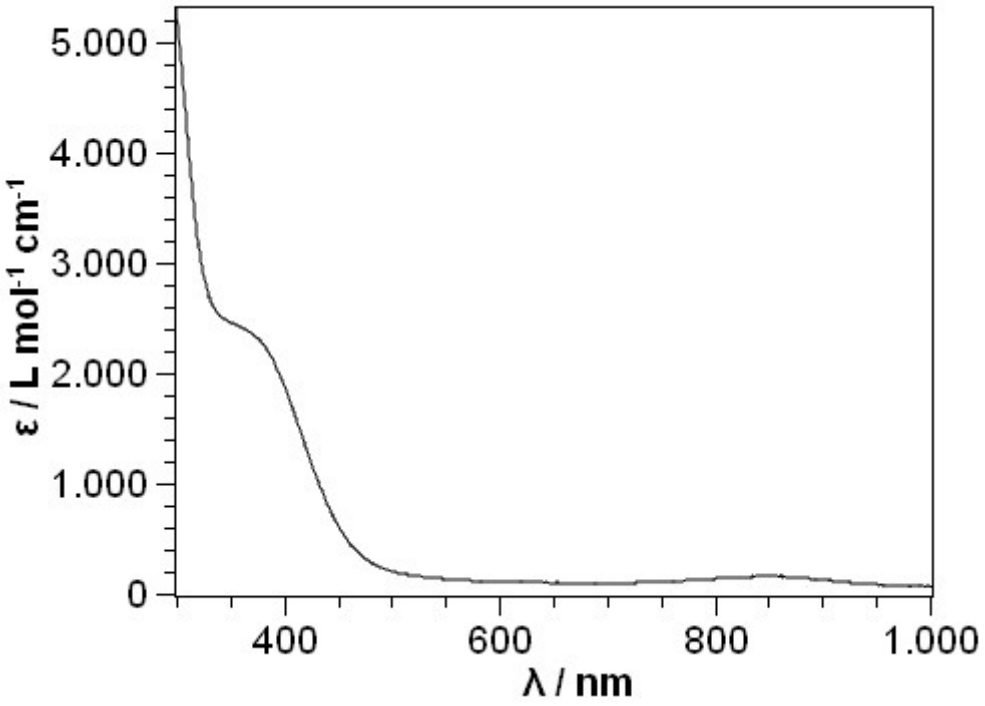

Figure S44. UV/Vis spectrum of **[CrL$^2_2$]** in Et_2O.

−N(Dipp)SiPh$_3$ (L^3) containing compounds

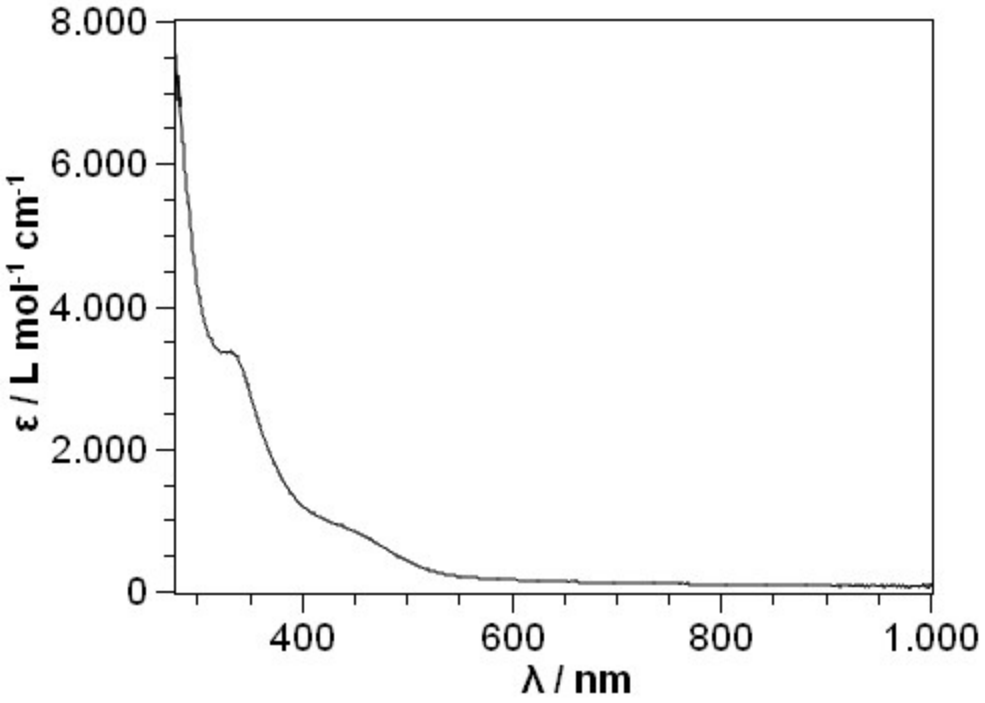

Figure S45. UV/Vis spectrum of **[FeL$^3_2$]** in Et_2O.

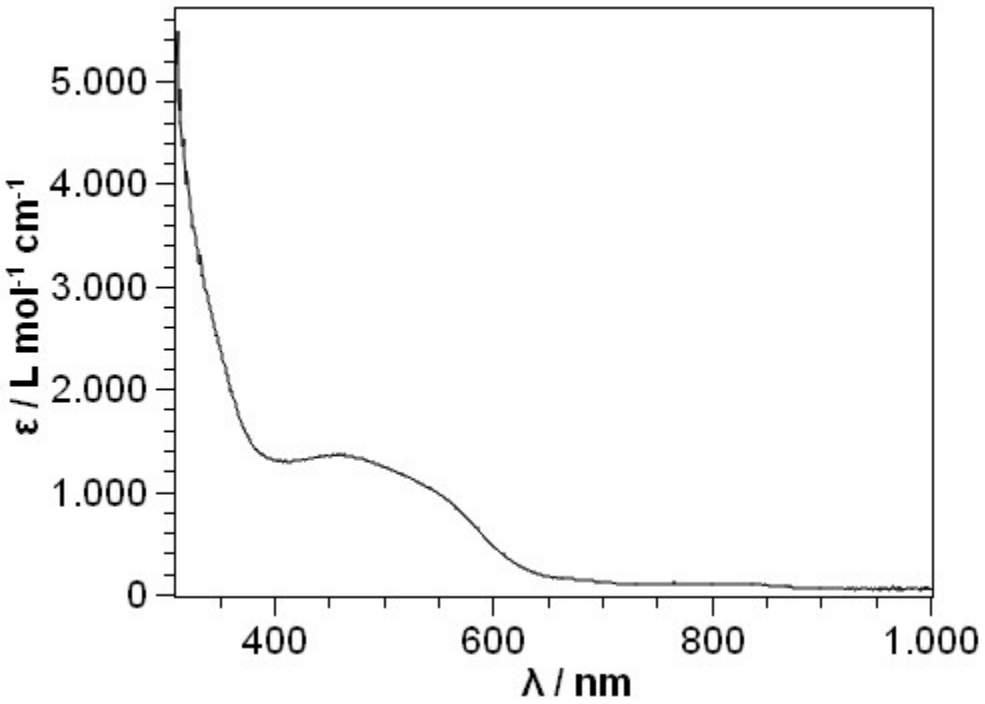

Figure S46. UV/Vis spectrum of K{18c6}**[FeL$^3_2$]** in THF.

−N(Dipp)SiMe$_2$(allyl) (L^4) containing compounds

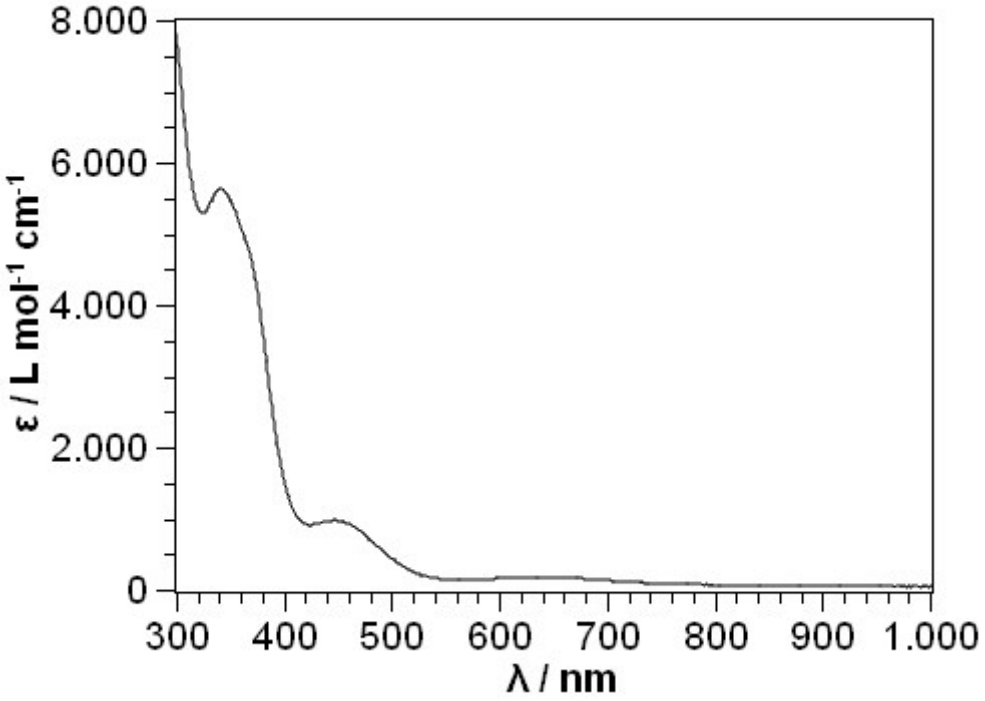

Figure S47. UV/Vis spectrum of **[CrL$^4_2$]** in Et_2O.

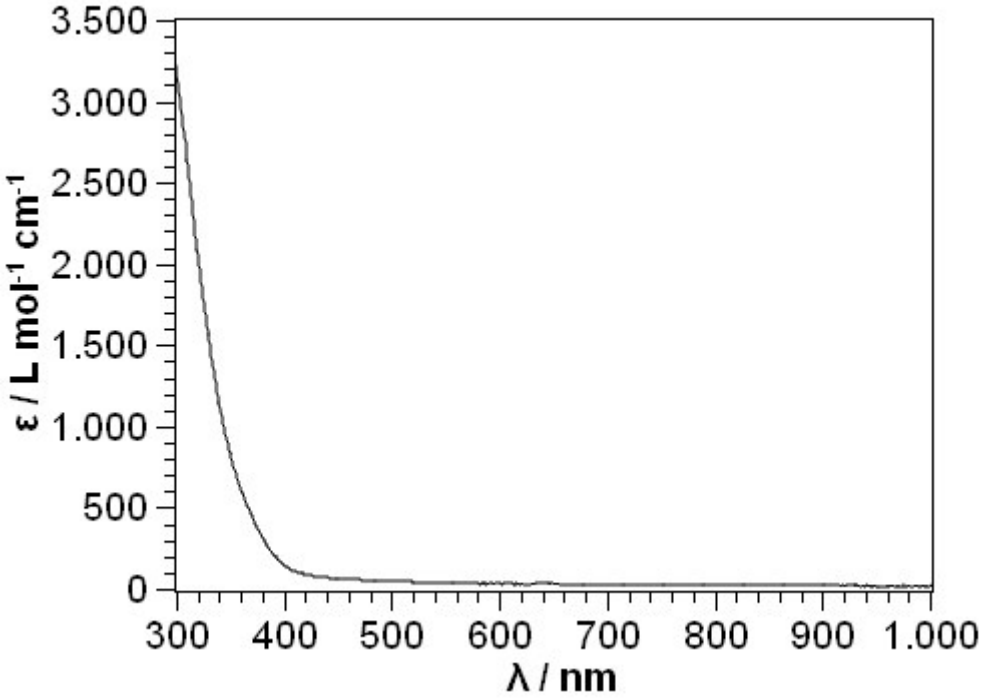

Figure S48. UV/Vis spectrum of **[MnL$^4_2$]** in Et_2O.

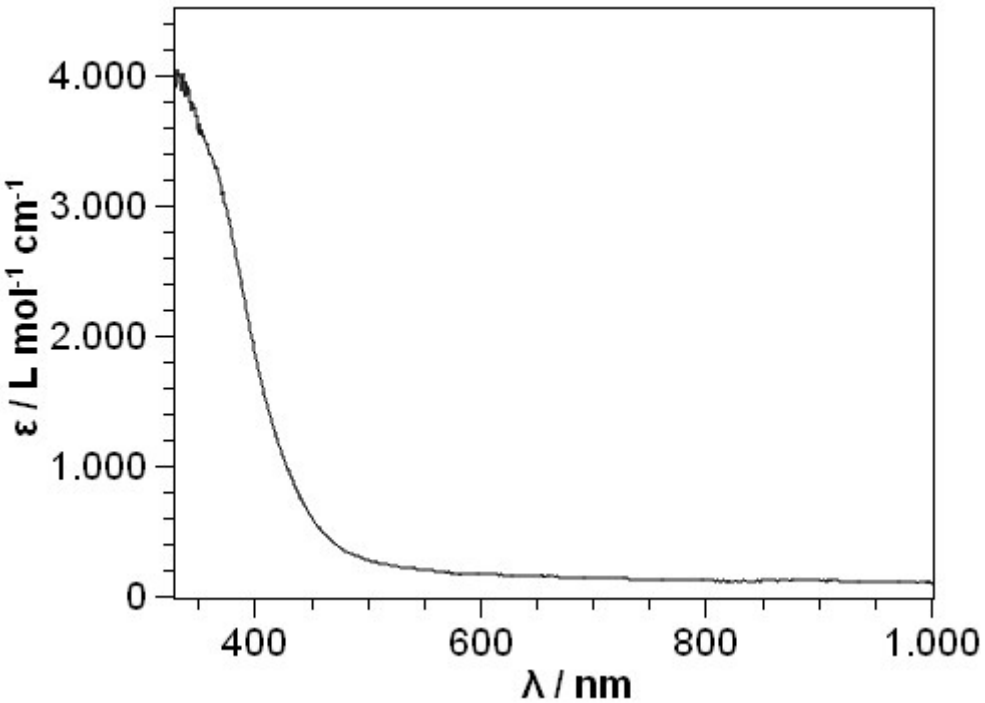

Figure S49. UV/Vis spectrum of **[FeL$^4_2$]** in Et_2O.

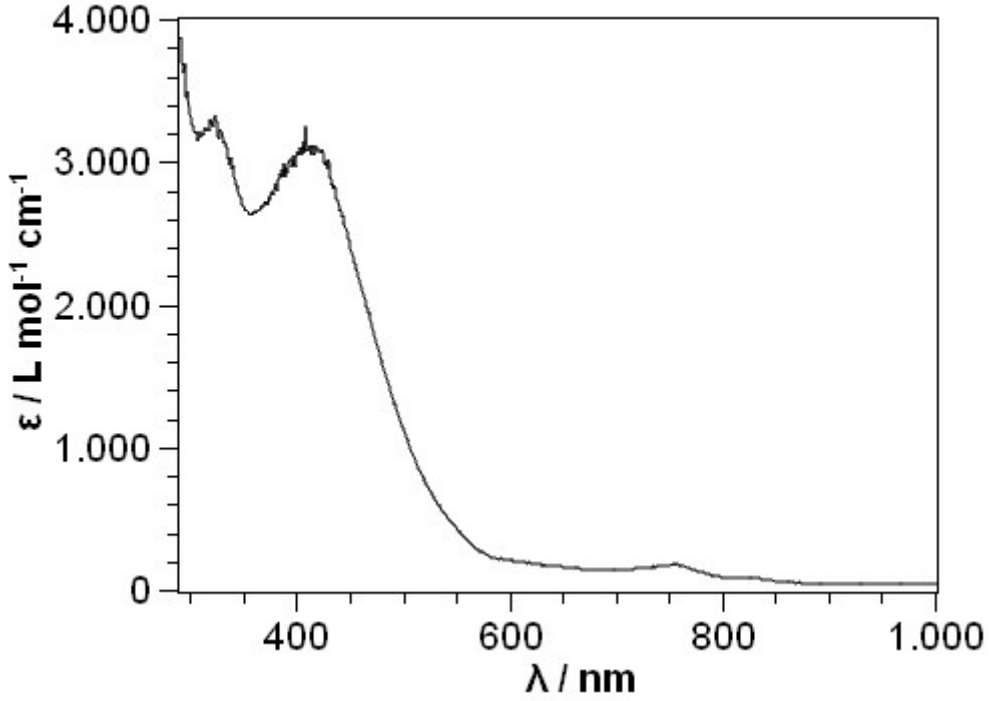

Figure S50. UV/Vis spectrum of **[CoL$^4_2$]** in Et_2O.

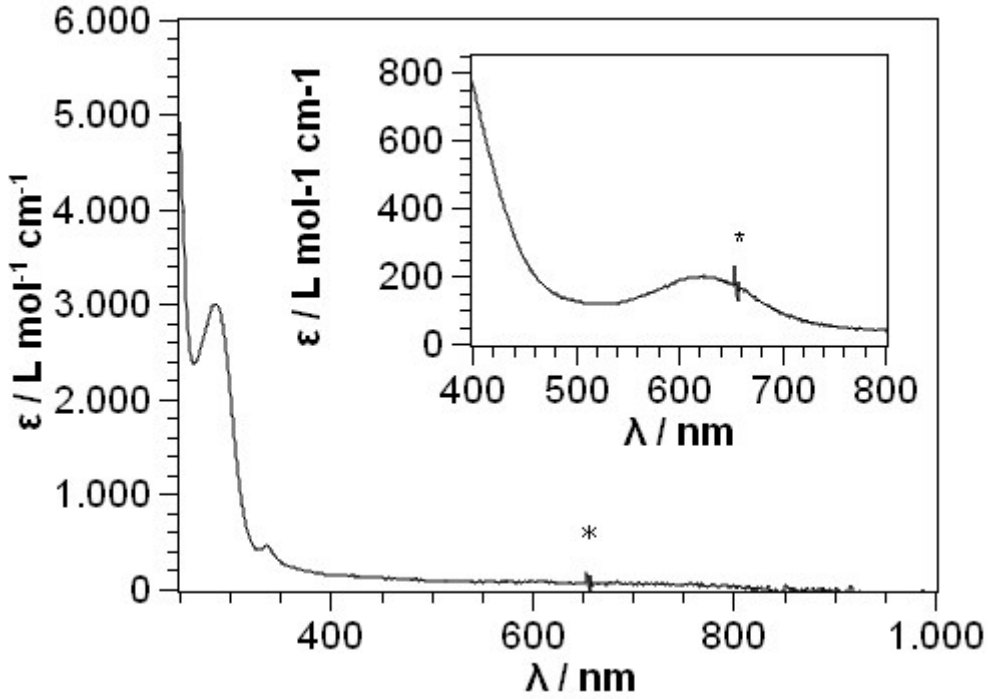

Figure S51. UV/Vis spectrum of $(K\{18c6\})_2$**[CrL$^4_2$]$_2$** in THF. The signal caused by detector exchange is indicated by *.

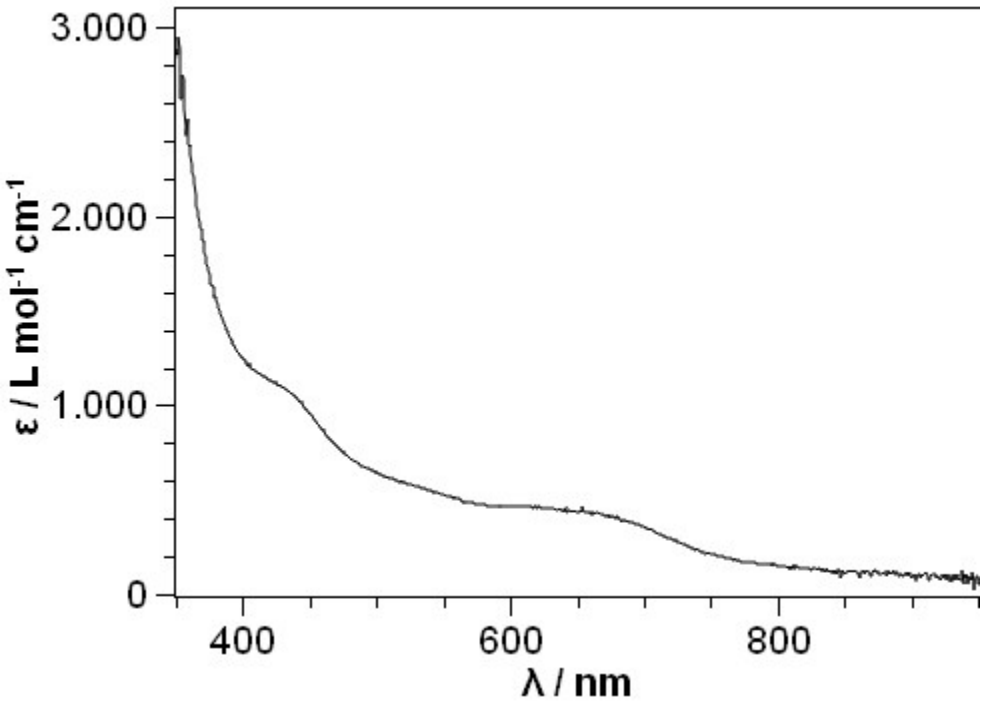

Figure S52. UV/Vis spectrum of K{18c6}**[CoL$^4_2$]** in THF.

Imido complexes

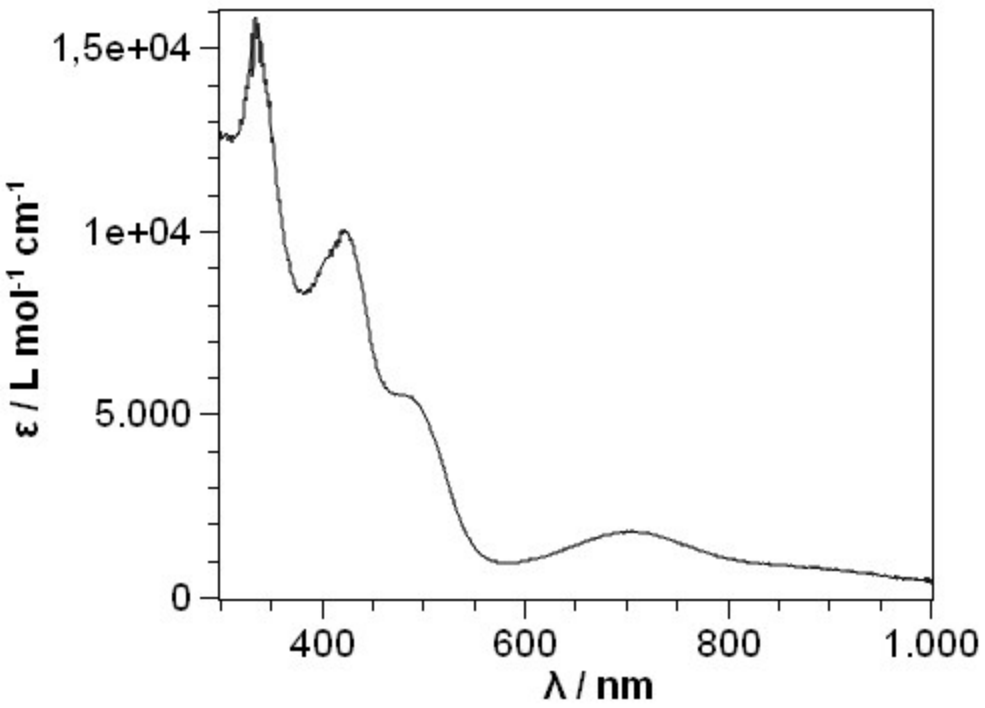

Figure S53. UV/Vis spectrum of K{18c6}**[Co(NDipp)L$^1_2$]** in THF.

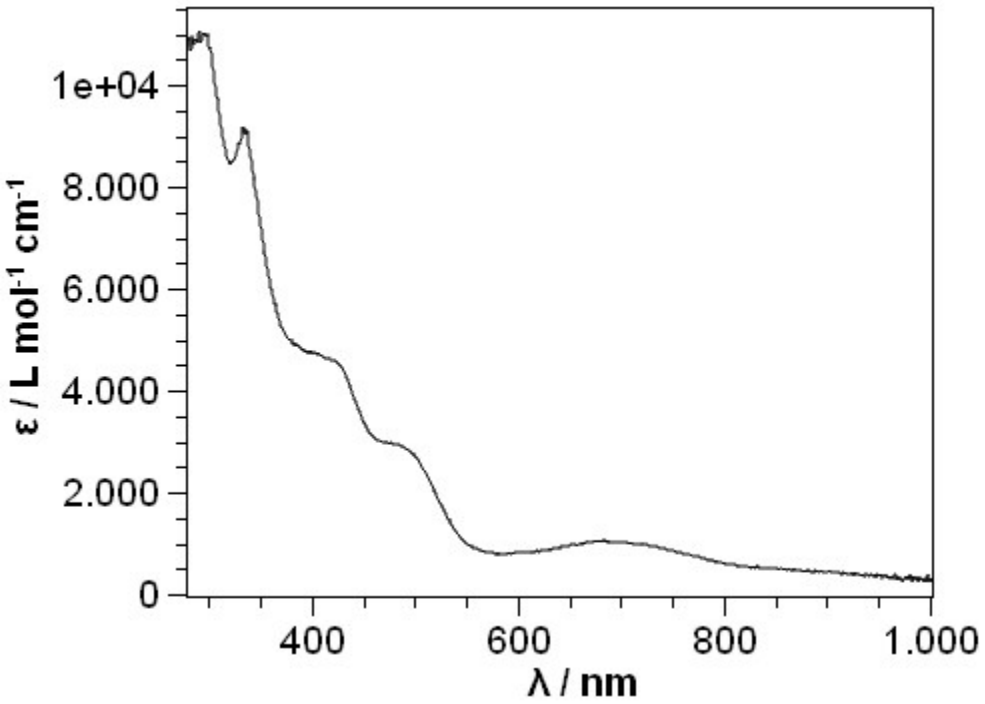

Figure S54. UV/Vis spectrum of K{18c6}**[Co(NDipp)L$^4_2$]** in THF.

3 IR spectra

−N(Dipp)Si(Me_2Ph) (L^1) containing compounds

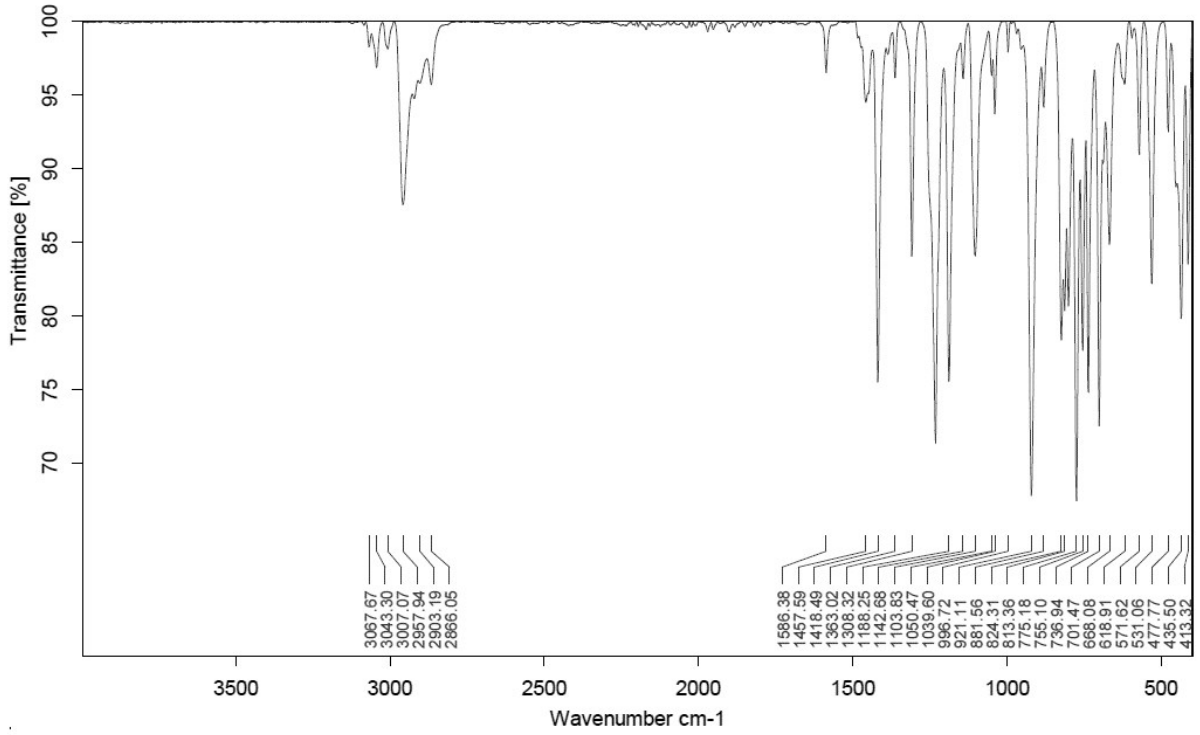

Figure S55. IR spectrum of **LiL^1**.

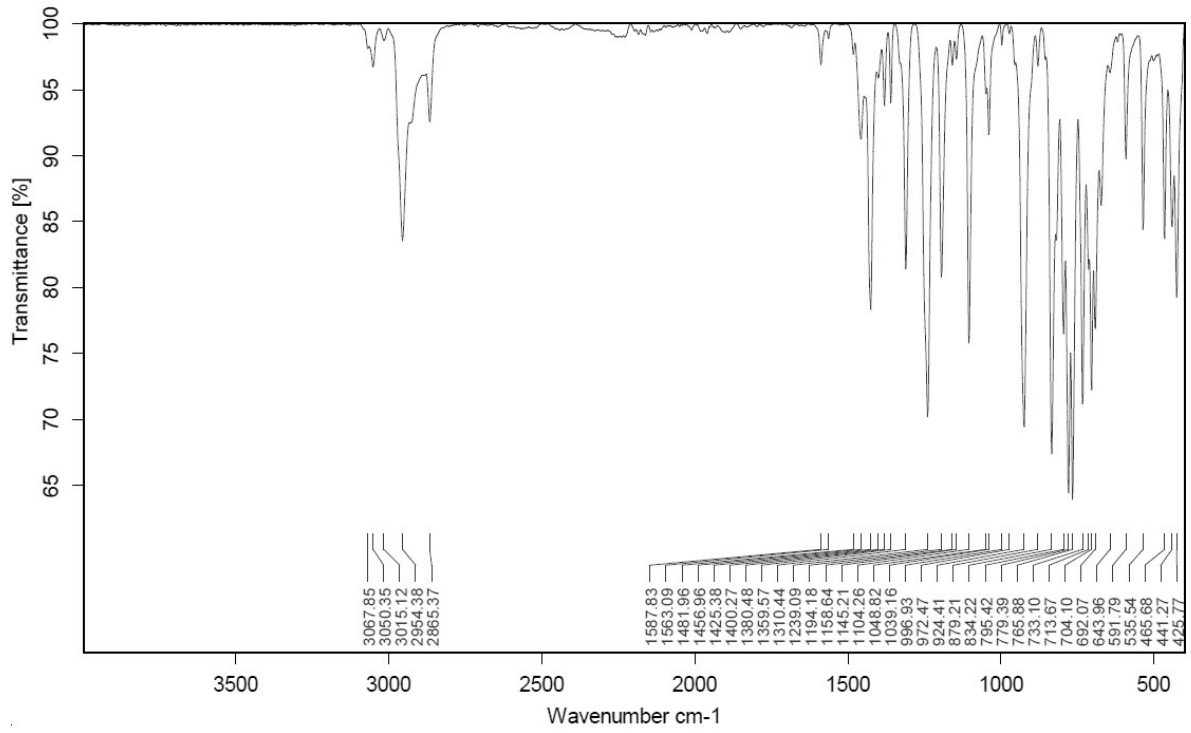

Figure S56. IR spectrum of **[MnL^1_2]**.

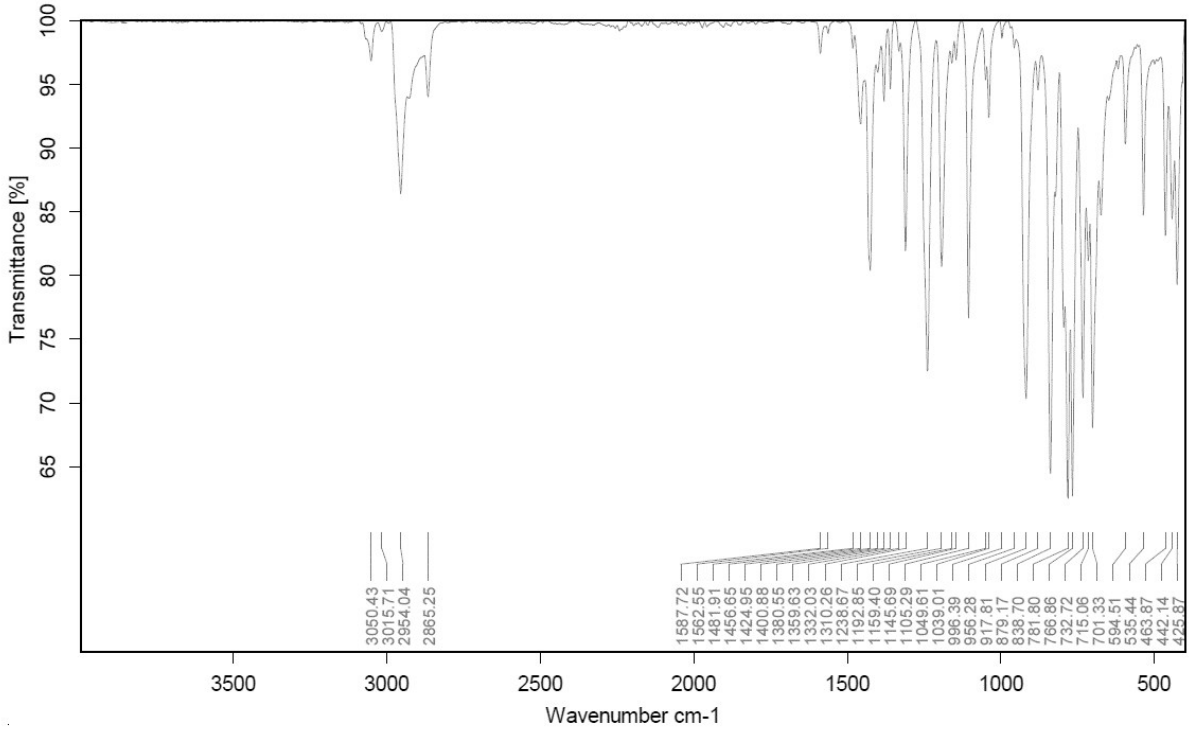

Figure S57. IR spectrum of **[FeL$^1_2$]**.

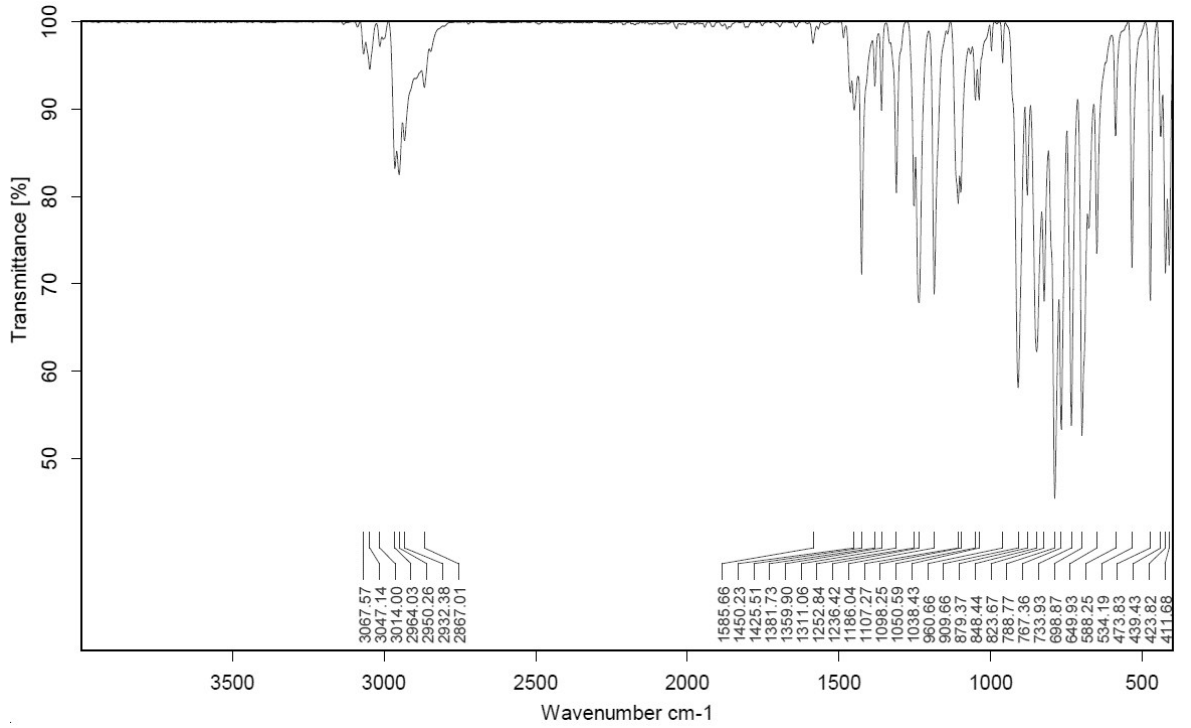

Figure S58. IR spectrum of **[CoL$^1_2$]**.

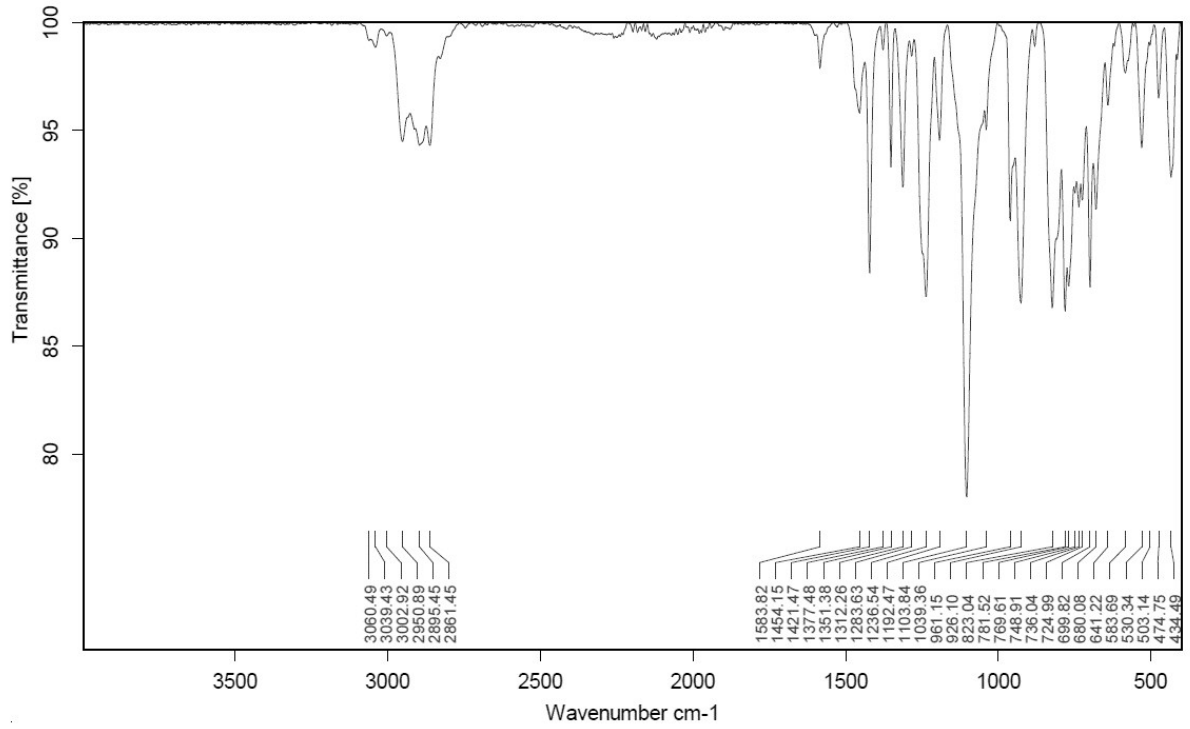

Figure S59. IR spectrum of K{18c6}**[MnL^{1}L^1*]**.

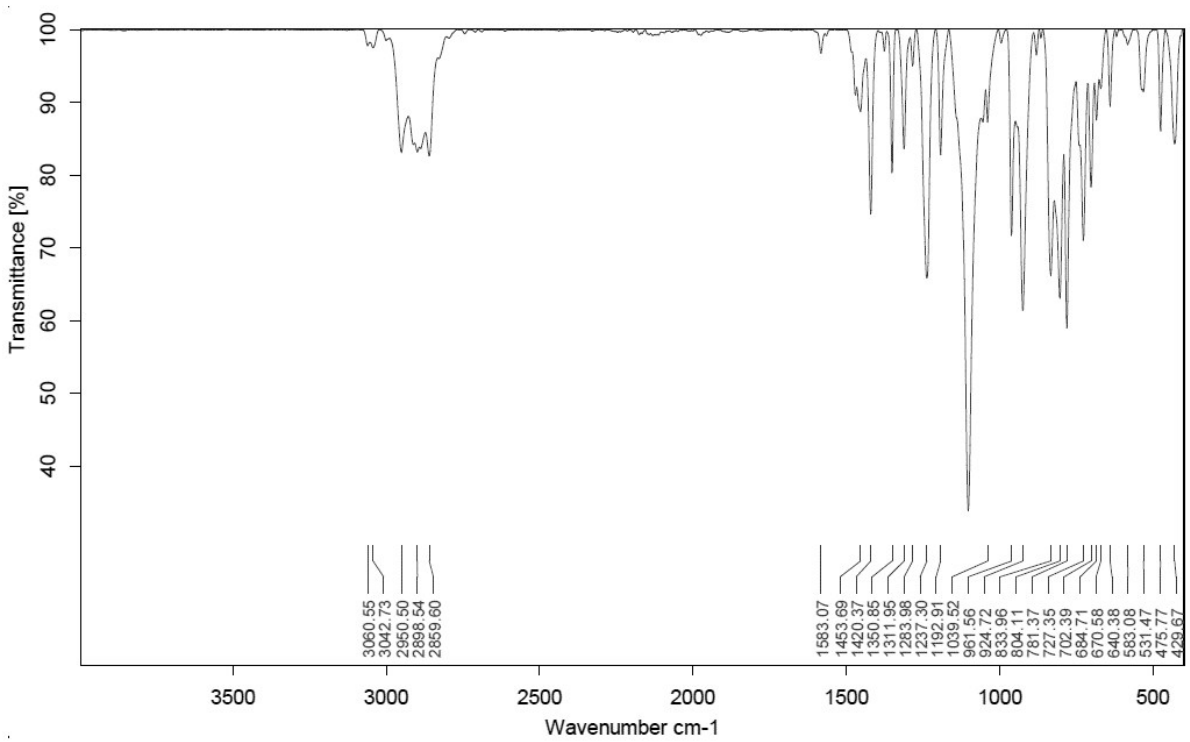

Figure S60. IR spectrum of K{18c6}**[FeL$^1_2$]**.

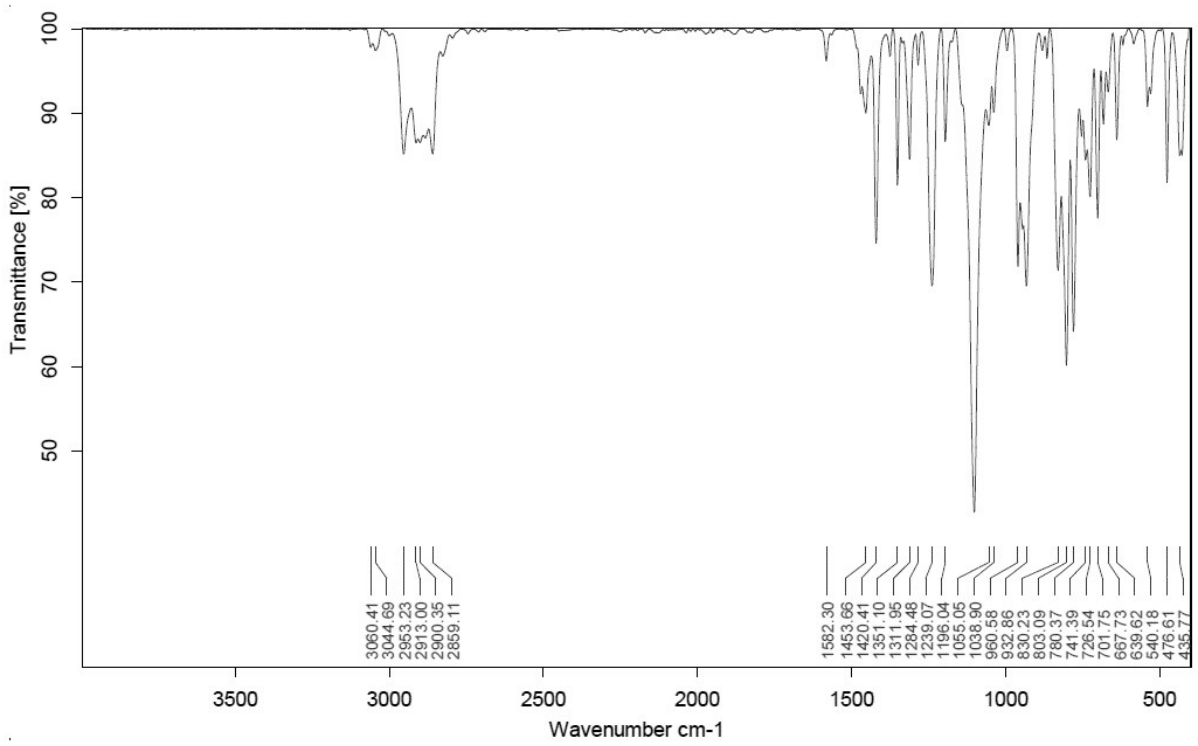

Figure S61. IR spectrum of K{18c6}**[CoL$^1_2$]**.

−N(Dipp)SiMePh$_2$ (L^2) containing compounds

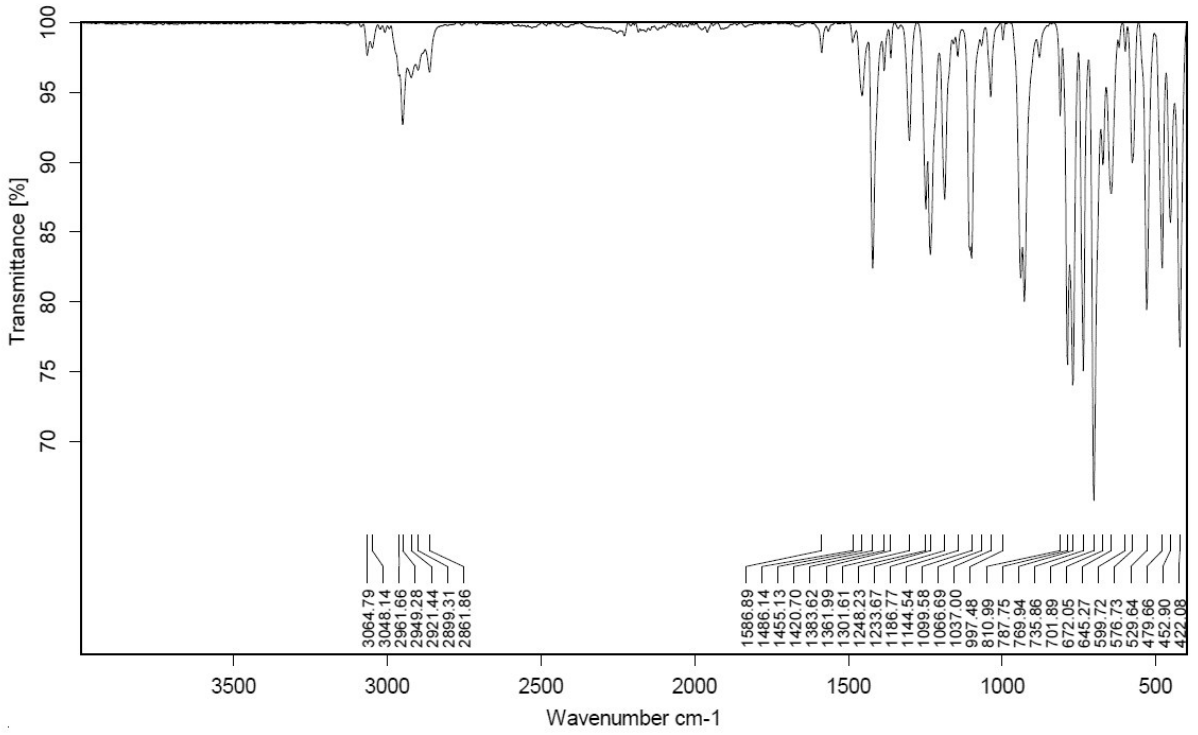

Figure S62. IR spectrum of **LiL^2**.

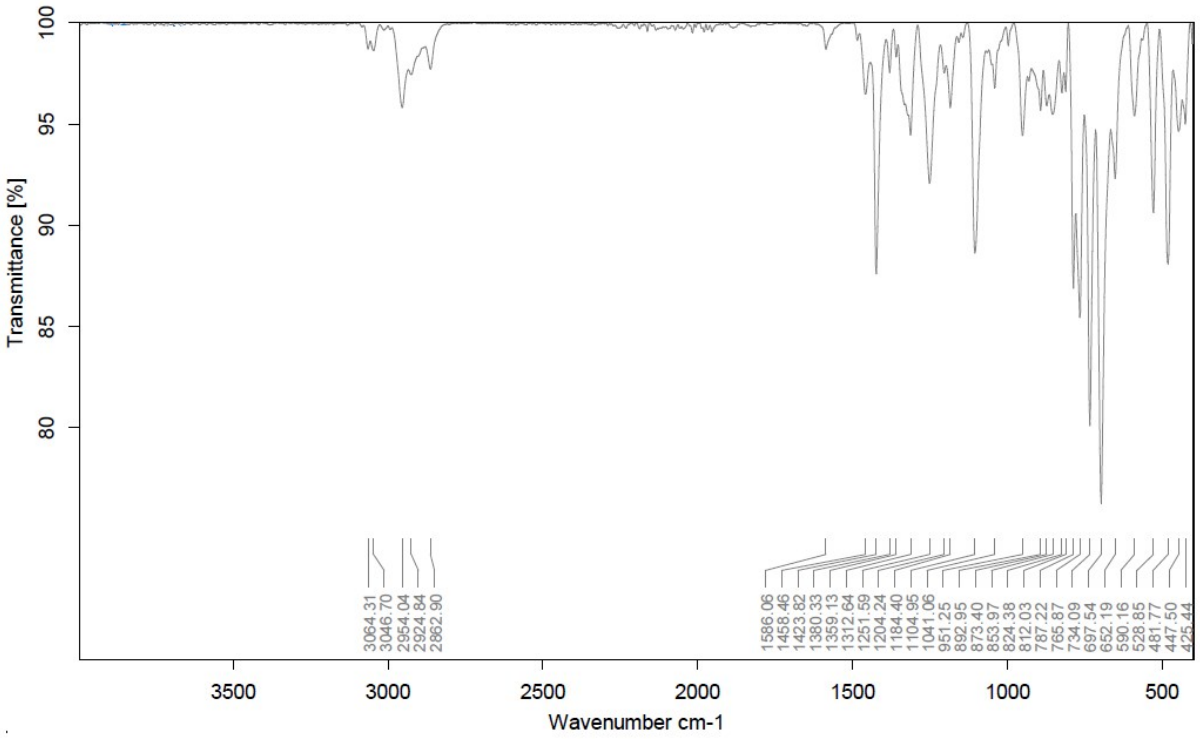

Figure S63. IR spectrum of **[CrL$^2_2$]**.

−N(Dipp)SiPh$_3$ (L^3) containing compounds

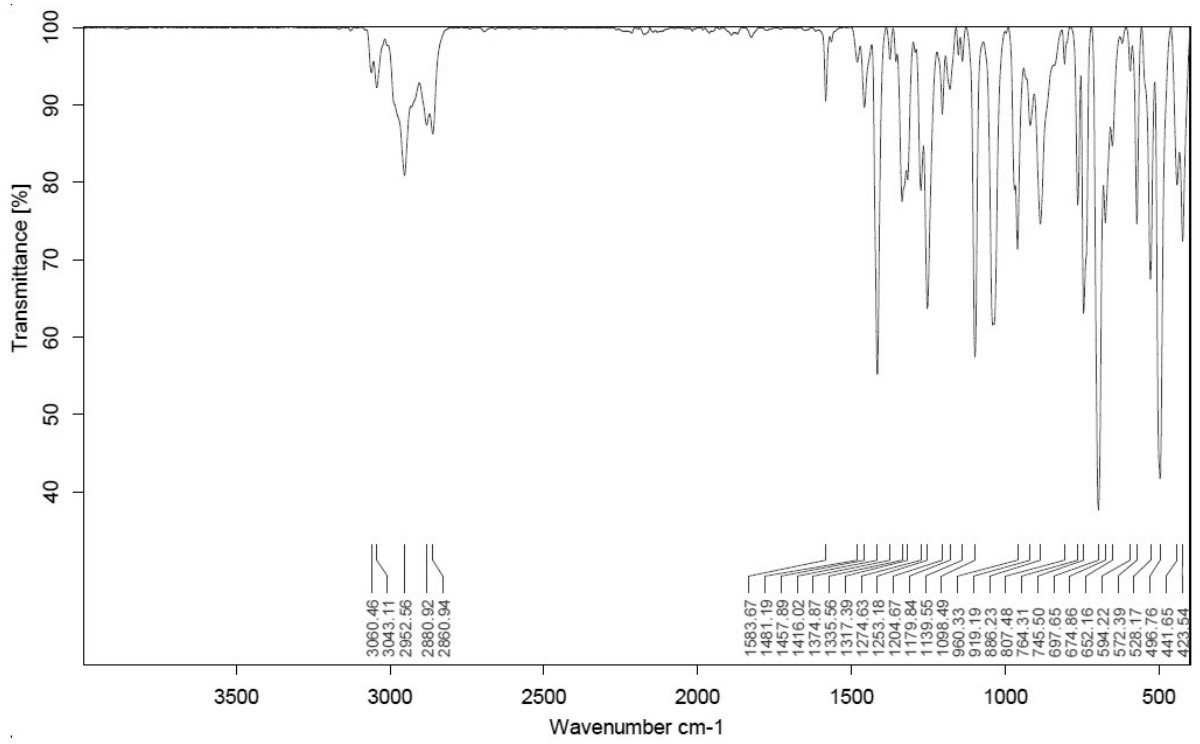

Figure S64. IR spectrum of **LiL^3**.

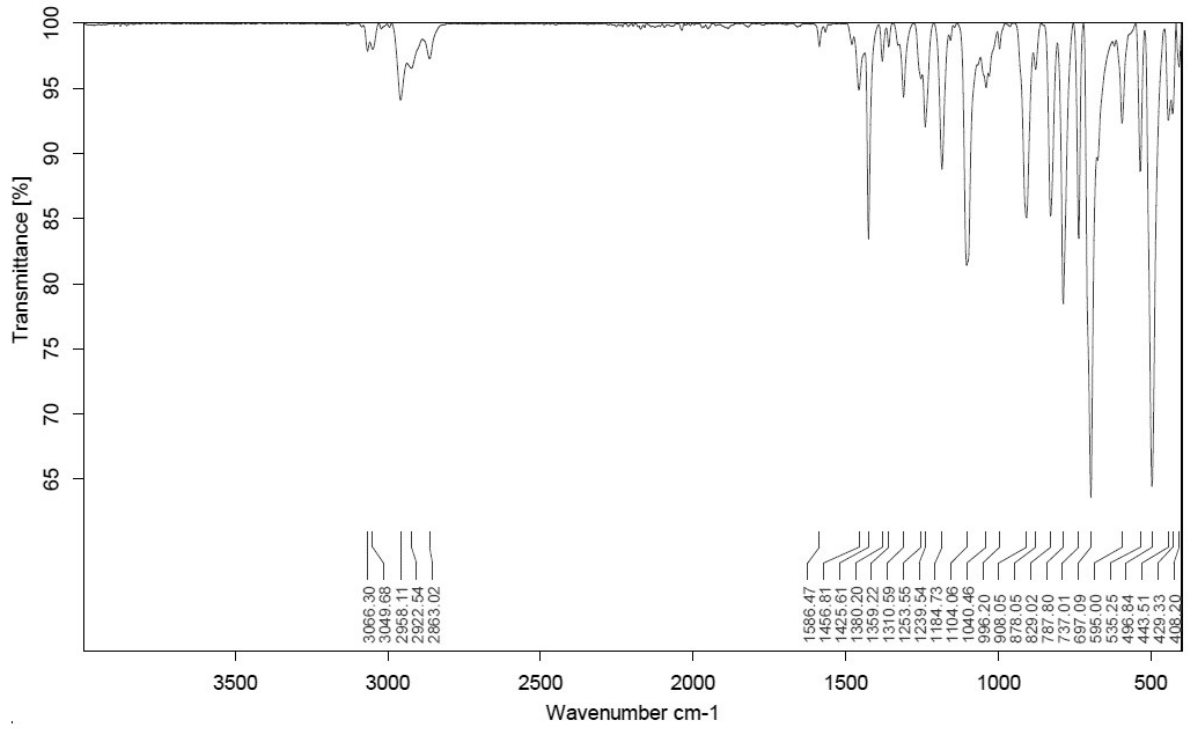

Figure S65. IR spectrum of **[FeL$^3_2$]**.

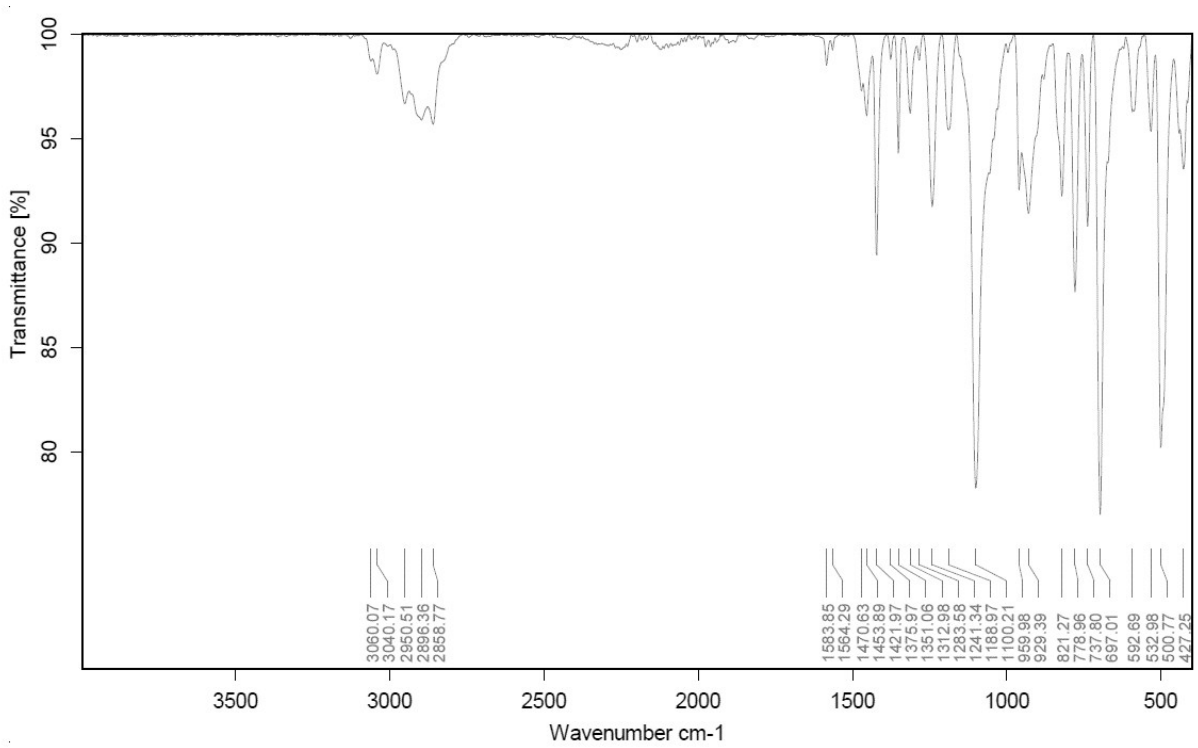

Figure S66. IR spectrum of K{18c6}**[FeL$^3_2$]**.

−N(Dipp)SiMe$_2$(allyl) (L^4) containing compounds

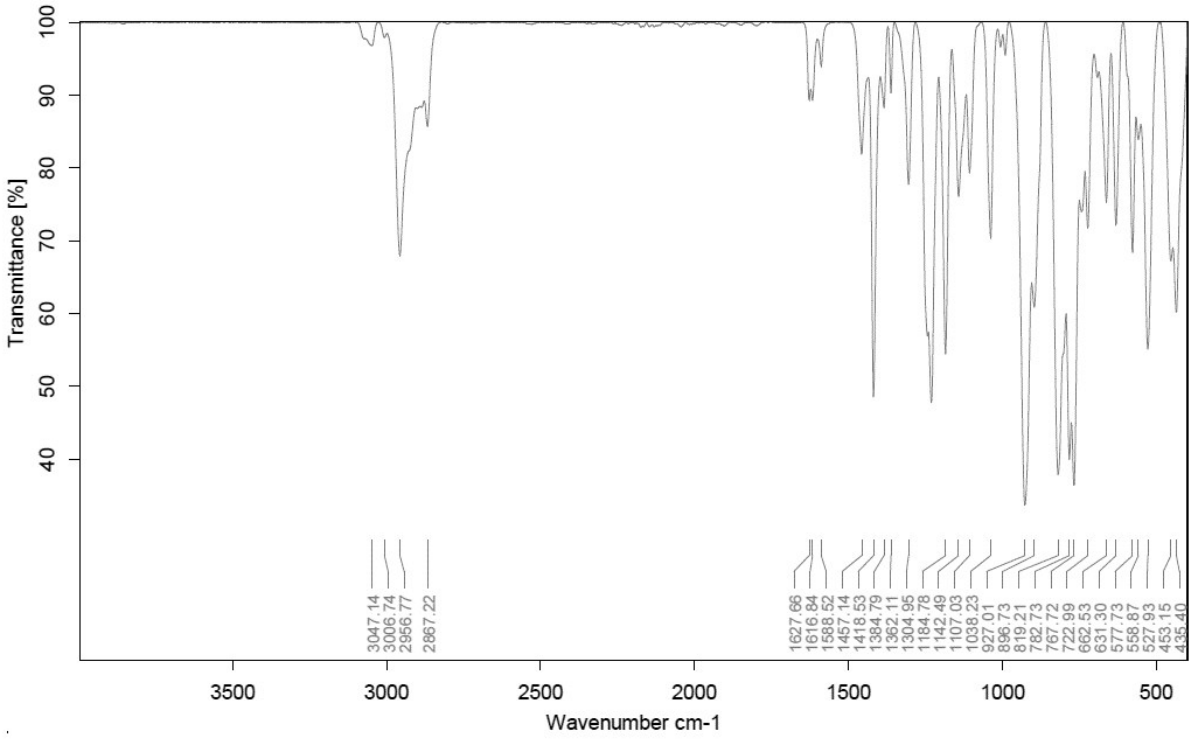

Figure S67. IR spectrum of **LiL^4**.

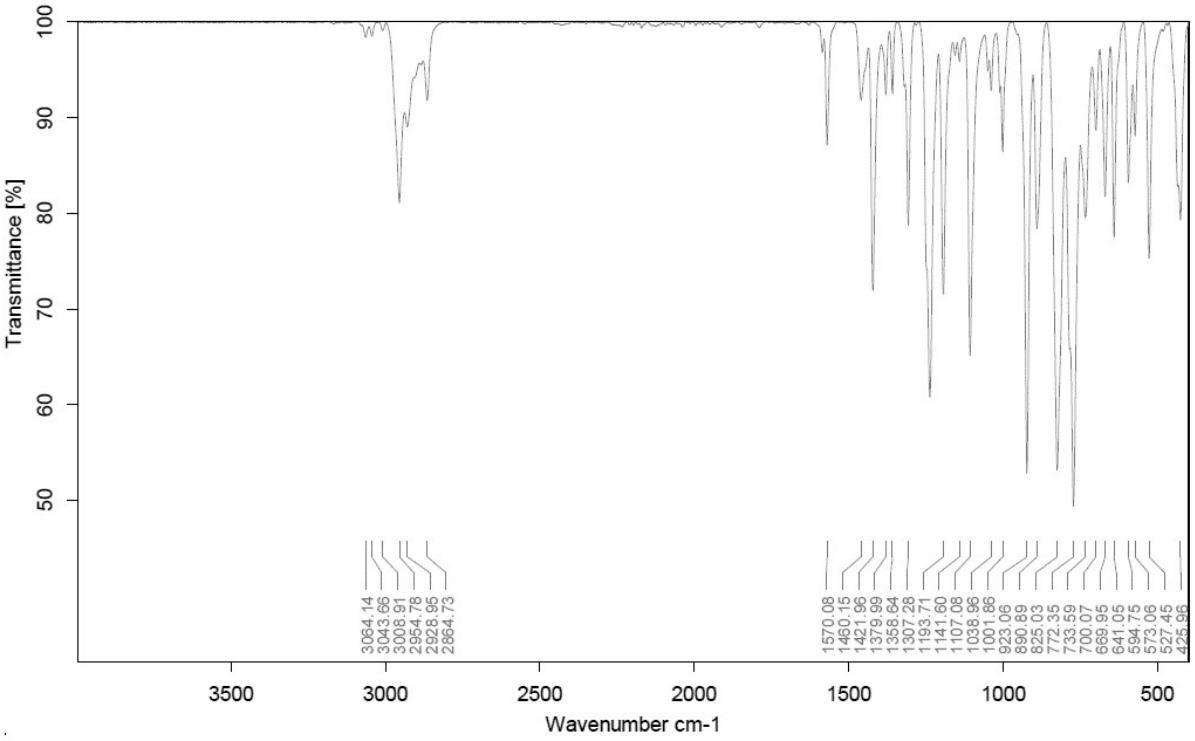

Figure S68. IR spectrum of **[CrL$^4_2$]**.

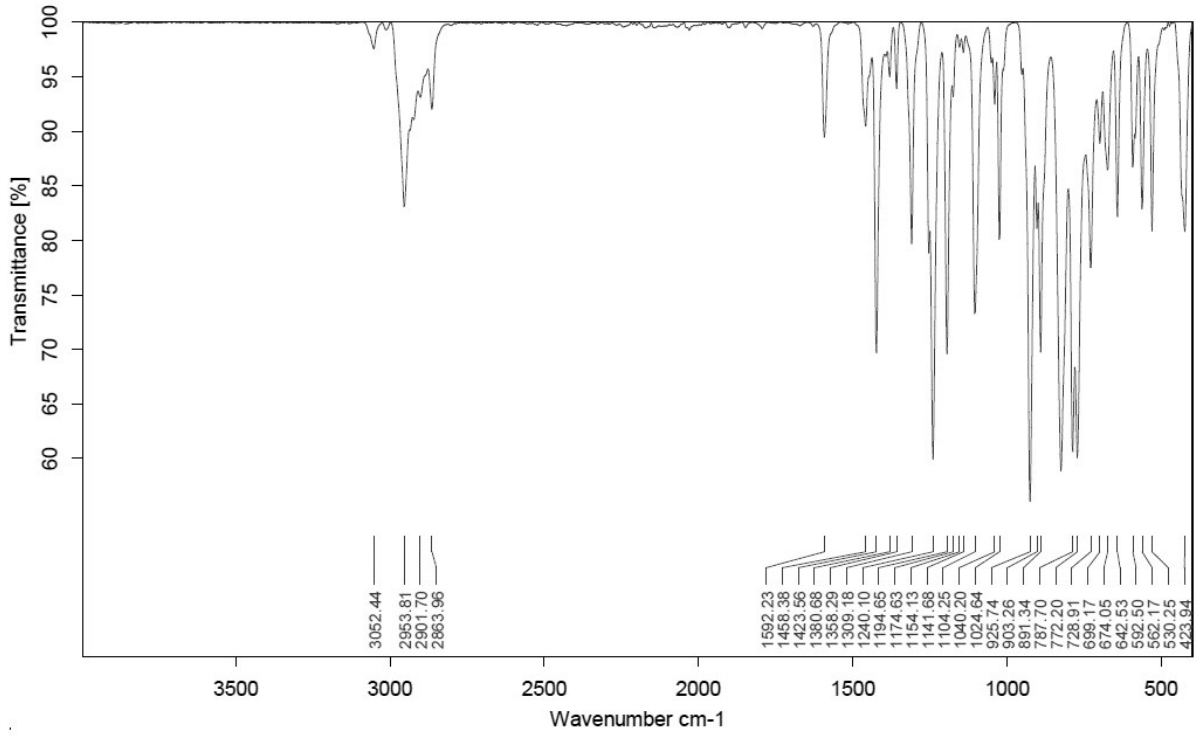

Figure S69. IR spectrum of **[MnL$^4_2$]**.

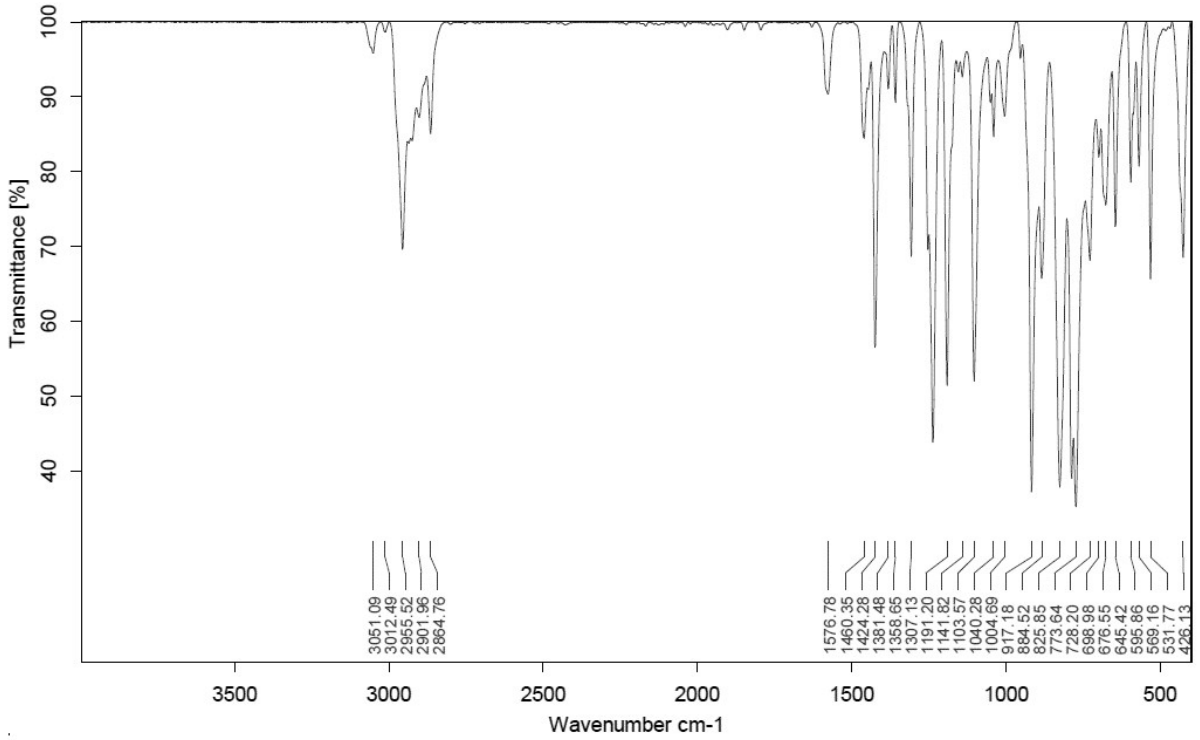

Figure S70. IR spectrum of **[FeL$^4_2$]**.

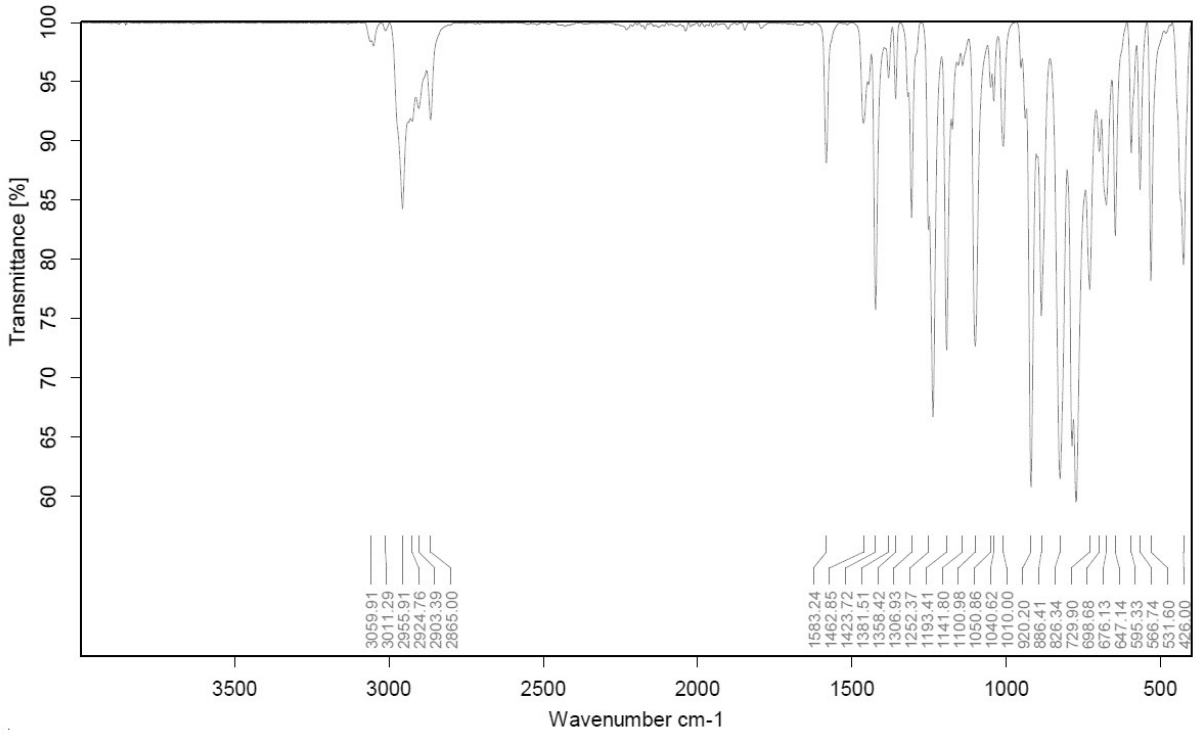

Figure S71. IR spectrum of **[CoL$^4_2$]**.

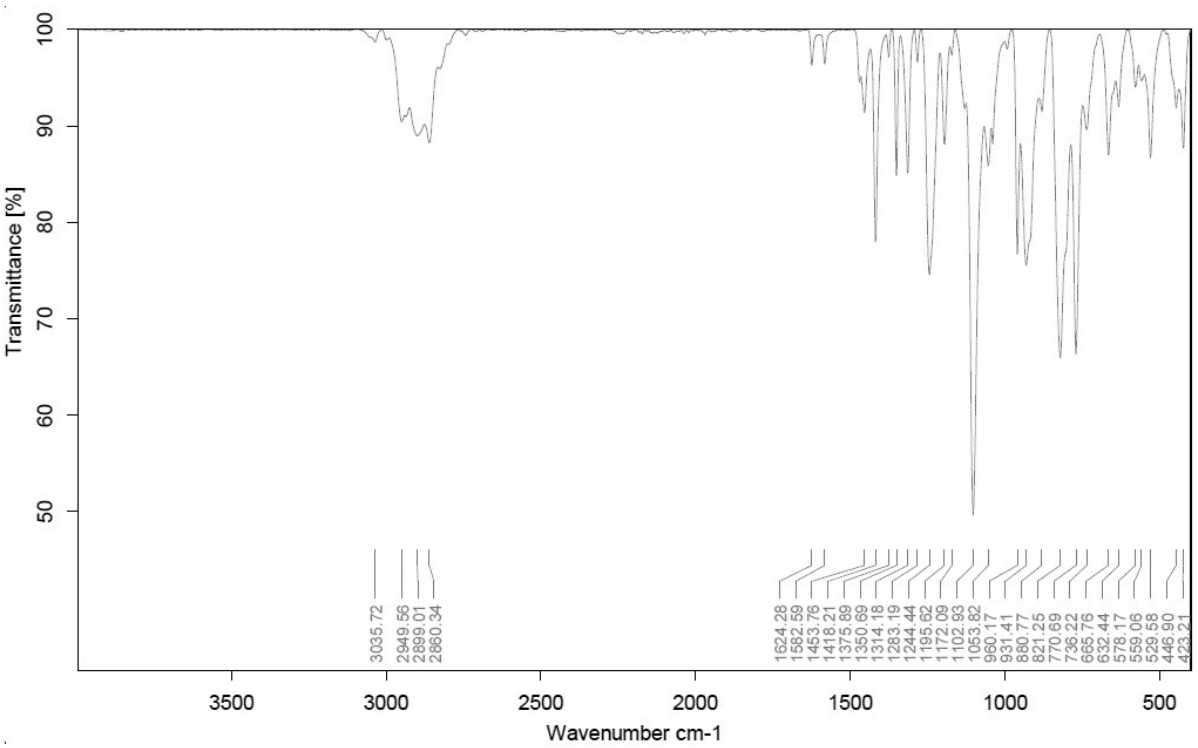

Figure S72. IR spectrum of (K{18c6})$_2$**[CrL$^4_2$]$_2$**.

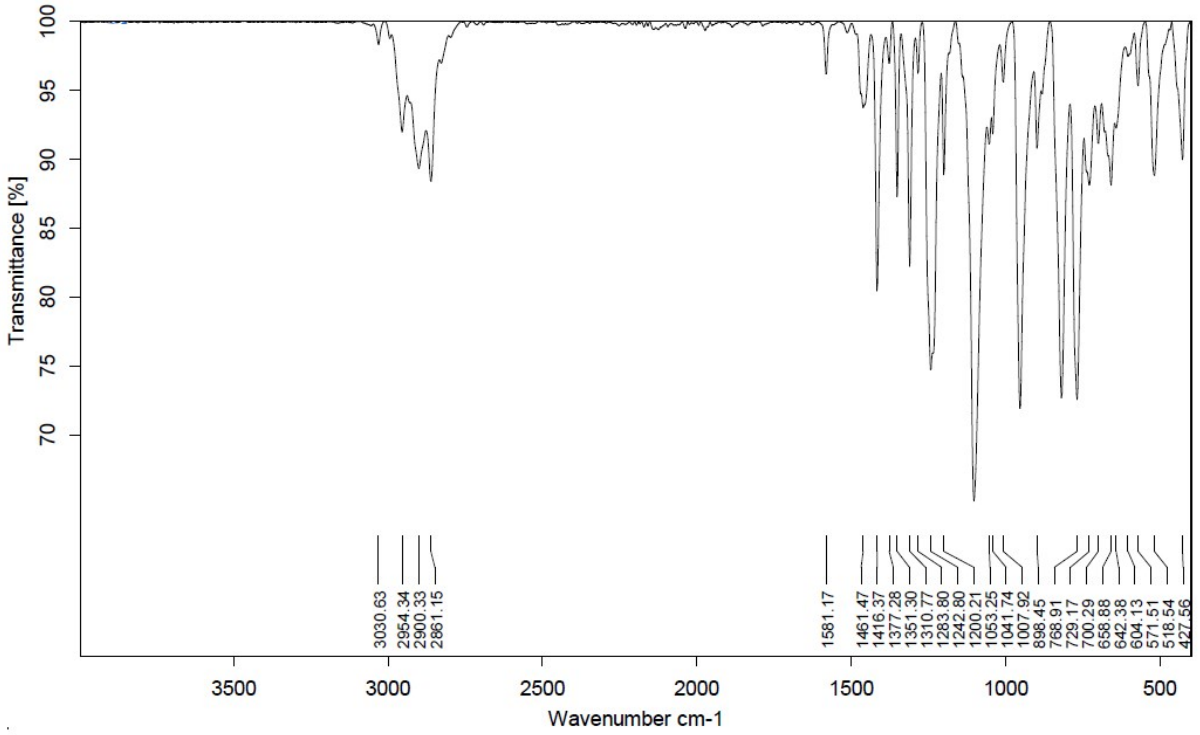

Figure S73. IR spectrum of K{18c6}**[CoL$^4_2$]**.

Imido complexes

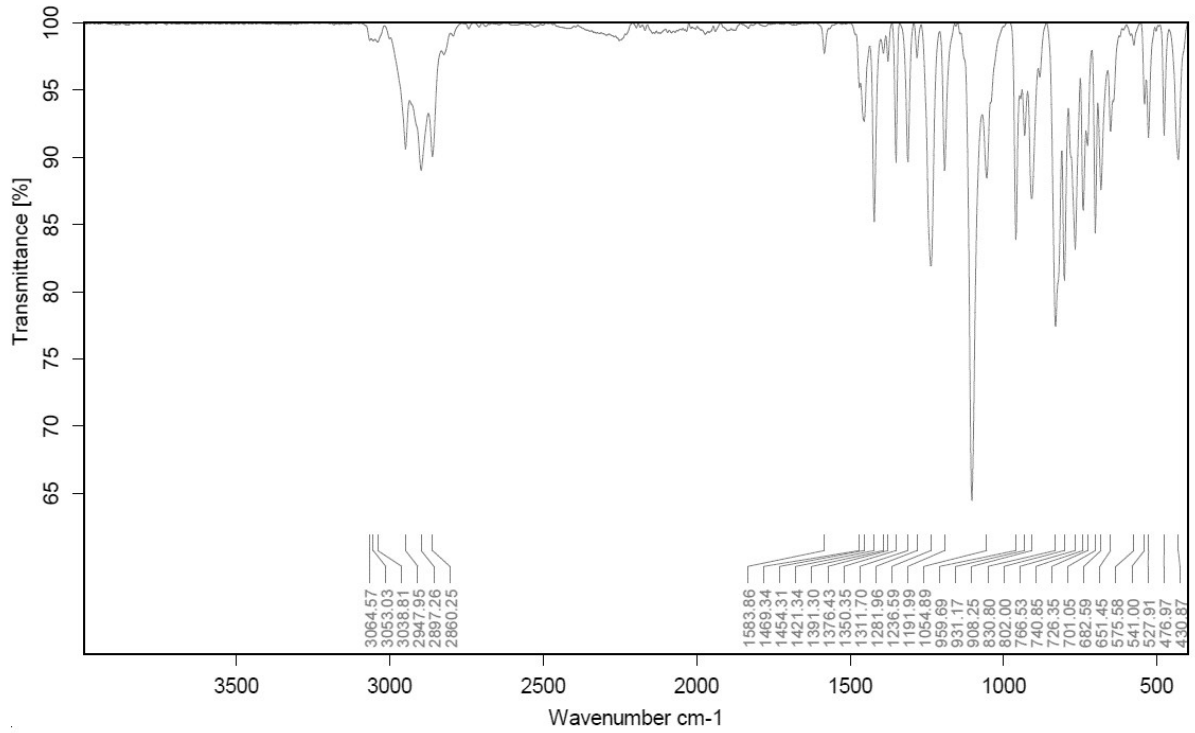

Figure S74. IR spectrum of K{18c6}**[Co(NDipp)L$^1_2$]**.

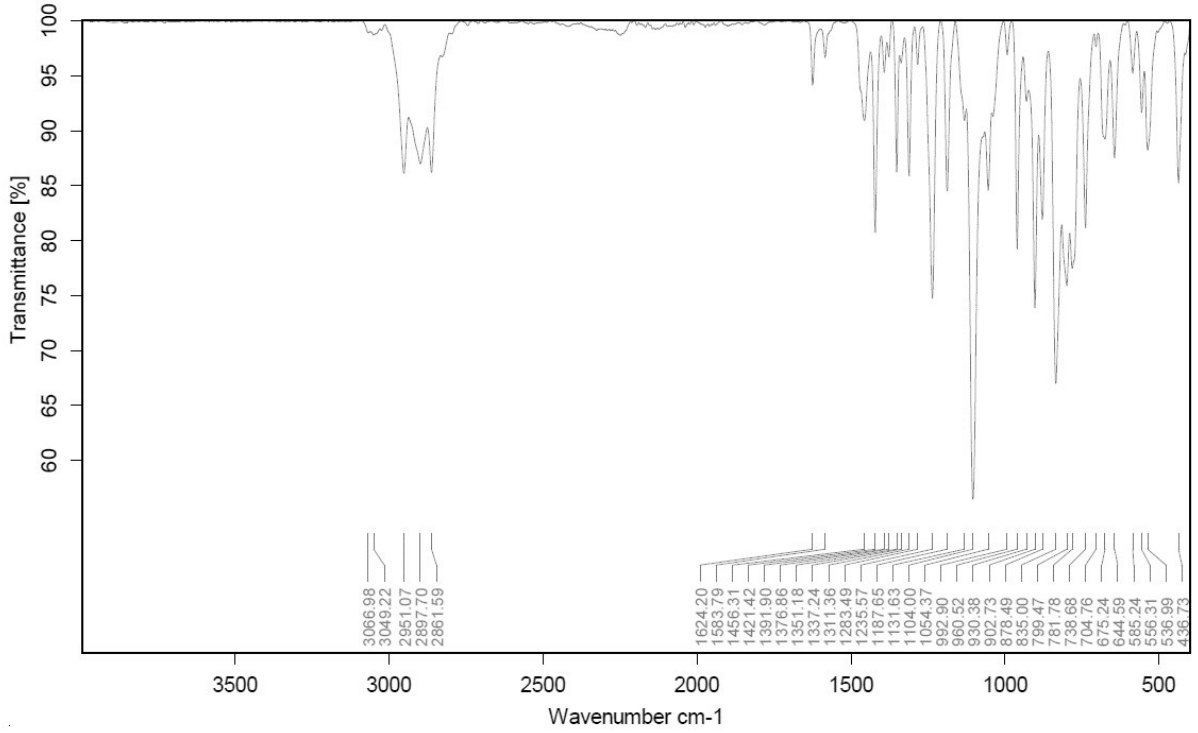

Figure S75. IR spectrum of K{18c6}**[Co(NDipp)L$^4_2$]**.

4 X-Ray Diffraction Analysis and Molecular Structures

−N(Dipp)SiMe$_2$Ph (L^1) containing compounds

Table S1. Crystal data and structure refinement of **LiL^1**

Empirical formula	$C_{40}H_{56}Li_2N_2Si_2$
Formula weight	634.92
Temperature /K	100.0
Crystal system	monoclinic
Space group	$P2_1/n$
a /Å	11.4917(10)
b /Å	12.5476(17)
c /Å	12.9022(11)
α /°	90
β /°	92.171(7)
γ /°	90
Volume /Å^3	1859.1(3)
Z	2
ρ_{calc} /g·cm^3	1.134
μ /mm^{-1}	0.125
F(000)	688.0
Crystal size /mm^3	0.931 × 0.293 × 0.188
Radiation	MoKα (λ = 0.71073)
2Θ range for data collection/°	4.808 to 53.434
Index ranges	−13 ≤ *h* ≤ 14, −15 ≤ *k* ≤ 15, −15 ≤ *l* ≤ 16
Reflections collected	16372
Independent reflections	3939 [R_{int} = 0.0744, R_{sigma} = 0.0671]
Data/restraints/parameters	3939/0/320
Goodness-of-fit on F^2	0.899
Final *R* indexes [*I*>=2σ (*I*)]	R_1 = 0.0377, wR_2 = 0.0812
Final *R* indexes [all data]	R_1 = 0.0700, wR_2 = 0.0886
Largest diff. peak/hole / e Å^{-3}	0.30/−0.22

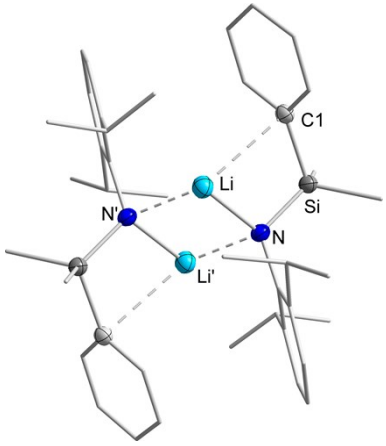

Figure S76. Molecular structure of (**LiL^1**)$_2$. All hydrogen atoms are omitted for clarity.

Table S2. Crystal data and structure refinement of **[MnL$^1_2$]**

Empirical formula	$C_{40}H_{56}MnN_2Si_2$
Formula weight	675.98
Temperature /K	100
Crystal system	triclinic
Space group	P−1
a /Å	11.5053(6)
b /Å	19.5096(13)
c /Å	19.5355(11)
α /°	117.392(4)
β /°	97.873(4)
γ /°	90.877(5)
Volume /Å^3	3841.3(4)
Z	4
ρ_{calc} /g·cm^3	1.169
μ /mm^{-1}	0.435
F(000)	1452.0
Crystal size /mm^3	0.413 × 0.199 × 0.144
Radiation	MoKα (λ = 0.71073)
2Θ range for data collection/°	5.008 to 54.178
Index ranges	−14 ≤ *h* ≤ 13, −24 ≤ *k* ≤ 24, −24 ≤ *l* ≤ 24
Reflections collected	38338
Independent reflections	38338 [R_{int} = 0.2443, R_{sigma} = 0.1343]
Data/restraints/parameters	38338/0/836
Goodness-of-fit on F^2	0.911
Final *R* indexes [*I*>=2σ (*I*)]	R_1 = 0.0633, wR_2 = 0.1460
Final *R* indexes [all data]	R_1 = 0.1521, wR_2 = 0.1750
Largest diff. peak/hole / e Å^{-3}	0.63/−0.86

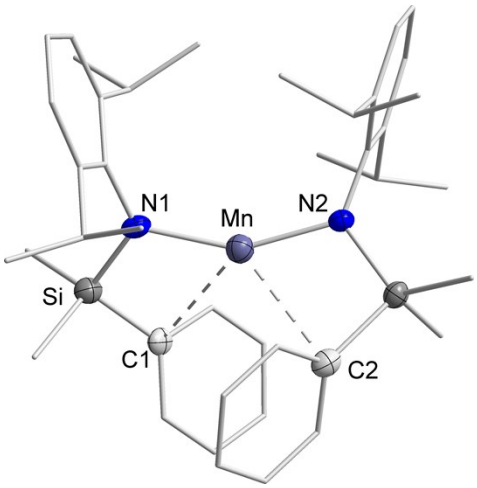

Figure S77. Molecular structure of **[MnL$^1_2$]**. All hydrogen atoms and a second, independent molecule are omitted for clarity. The structure was refined as a twin, twin ratio refined to 0.2465(8).

Table S3. Crystal data and structure refinement of **[FeL$^1_2$]**

Empirical formula	$C_{80}H_{112}Fe_2N_4Si_4$
Formula weight	1353.79
Temperature /K	100.01
Crystal system	triclinic
Space group	P−1
a /Å	11.4603(5)
b /Å	19.4567(9)
c /Å	19.5695(9)
α /°	117.2580(10)
β /°	90.819(2)
γ /°	97.965(2)
Volume /Å^3	3826.6(3)
Z	2
ρ_{calc} /g·cm^3	1.175
μ /mm^{-1}	0.485
F(000)	1456.0
Crystal size /mm^3	0.262 × 0.186 × 0.124
Radiation	MoKα (λ = 0.71073)
2Θ range for data collection/°	4.054 to 54.578
Index ranges	−14 ≤ *h* ≤ 14, −25 ≤ *k* ≤ 25, −24 ≤ *l* ≤ 25
Reflections collected	73224
Independent reflections	17162 [R_{int} = 0.0571, R_{sigma} = 0.0531]
Data/restraints/parameters	17162/0/835
Goodness-of-fit on F^2	1.038
Final *R* indexes [*I*>=2σ (*I*)]	R_1 = 0.0408, wR_2 = 0.0755
Final *R* indexes [all data]	R_1 = 0.0686, wR_2 = 0.0838
Largest diff. peak/hole / e Å^{-3}	0.35/−0.30

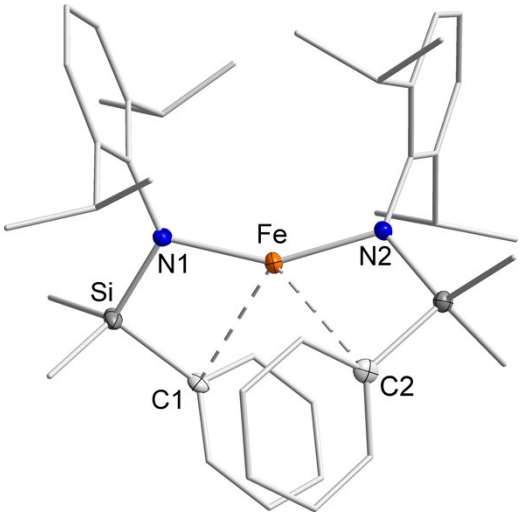

Figure S78. Molecular structure of **[FeL$^1_2$]**. All hydrogen atoms and a second, independent molecule are omitted for clarity.

Table S4. Crystal data and structure refinement of **[CoL$^1_2$]**

Empirical formula	$C_{40}H_{56}CoN_2Si_2$
Formula weight	680.008
Temperature/K	99.96
Crystal system	triclinic
Space group	P−1
a/Å	11.5124(5)
b/Å	19.4083(8)
c/Å	19.4427(8)
α/°	116.737(1)
β/°	98.024(1)
γ/°	91.028(2)
Volume/Å^3	3825.7(3)
Z	4
ρ_{calc}g/cm^3	1.181
μ/mm^{-1}	0.540
F(000)	1462.5
Crystal size/mm^3	0.486 × 0.213 × 0.192
Radiation	Mo Kα (λ = 0.71073)
2Θ range for data collection/°	4.24 to 58.5
Index ranges	−15 ≤ *h* ≤ 15, −26 ≤ *k* ≤ 26, −26 ≤ *l* ≤ 25
Reflections collected	75032
Independent reflections	19910 [R_{int} = 0.0525, R_{sigma} = 0.0618]
Data/restraints/parameters	19910/0/885
Goodness-of-fit on F^2	1.053
Final *R* indexes [*I*>=2σ (*I*)]	R_1 = 0.0456, wR_2 = 0.0801
Final *R* indexes [all data]	R_1 = 0.0844, wR_2 = 0.0924
Largest diff. peak/hole / e Å^{-3}	0.63/−0.66

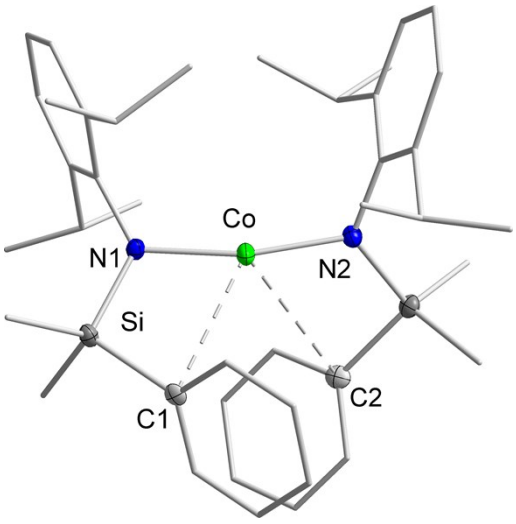

Figure S79. Molecular structure of **[CoL$^1_2$]**. All hydrogen atoms and a second, independent molecule are omitted for clarity.

Table S5. Crystal data and structure refinement of K{18c6}**[MnL^{1}L^{1*}]**

Empirical formula	$C_{52}H_{79}KMnN_2O_6Si_2$
Formula weight	978.39
Temperature/K	100
Crystal system	monoclinic
Space group	Pn
a/Å	13.0249(6)
b/Å	14.7896(6)
c/Å	14.3462(6)
α/°	90
β/°	101.315(2)
γ/°	90
Volume/Å^3	2709.8(2)
Z	2
ρ_{calc}g/cm^3	1.199
μ/mm^{-1}	3.457
F(000)	1050.0
Crystal size/mm^3	0.212 × 0.134 × 0.115
Radiation	Cu Kα (λ = 1.54186)
2Θ range for data collection/°	5.976 to 151.934
Index ranges	−14 ≤ *h* ≤ 16, −18 ≤ *k* ≤ 16, −18 ≤ *l* ≤ 14
Reflections collected	33826
Independent reflections	11326 [R_{int} = 0.0421, R_{sigma} = 0.0412]
Data/restraints/parameters	11326/3659/1058
Goodness-of-fit on F^2	0.945
Final *R* indexes [*I*>=2σ (*I*)]	R_1 = 0.0484, wR_2 = 0.1211
Final *R* indexes [all data]	R_1 = 0.0812, wR_2 = 0.1371
Largest diff. peak/hole / e Å^{-3}	0.24/−0.23
Flack parameter	0.529(12)

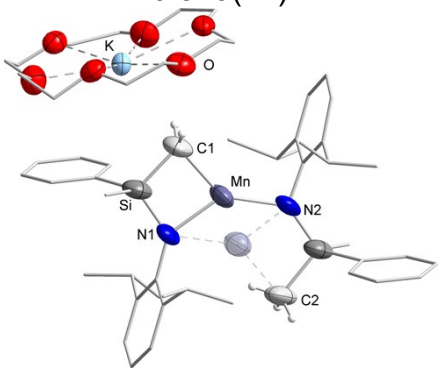

Figure S80. Molecular structure of K{18c6}**[MnL^{1}L^{1*}]**. Unnecessary hydrogen atoms are omitted for clarity. The structure was refined as a twin, twin ratio refined to 0.529(12). Disorders were found for all atoms with different occupancies (anion: part 1 (depicted): 69%; part 2 (indicated for Mn): 31%; K{18c6}: both part 3 (depicted) / 4: 50%)

Table S6. Crystal data and structure refinement of K{18c6}**[FeL$^1_2$]**

Empirical formula	$C_{56}H_{90}FeKN_2O_7Si_2$
Formula weight	1054.42
Temperature /K	100.0
Crystal system	triclinic
Space group	P−1
a /Å	18.141(2)
b /Å	19.9930(19)
c /Å	20.561(2)
α /°	60.863(7)
β /°	66.609(9)
γ /°	79.327(9)
Volume /Å^3	5977.9(13)
Z	4
ρ_{calc} /g·cm^3	1.172
μ /mm^{-1}	0.410
F(000)	2276.0
Crystal size /mm^3	0.702 × 0.604 × 0.161
Radiation	Mo Kα (λ = 0.71073)
2Θ range for data collection/°	4.894 to 50
Index ranges	−21 ≤ *h* ≤ 21, −23 ≤ *k* ≤ 23, −24 ≤ *l* ≤ 22
Reflections collected	41617
Independent reflections	20923 [R_{int} = 0.0650, R_{sigma} = 0.0742]
Data/restraints/parameters	20923/174/1394
Goodness-of-fit on F^2	1.042
Final *R* indexes [*I*>=2σ (*I*)]	R_1 = 0.0773, wR_2 = 0.2276
Final *R* indexes [all data]	R_1 = 0.1104, wR_2 = 0.2420
Largest diff. peak/hole / e Å^{-3}	0.98/−0.53

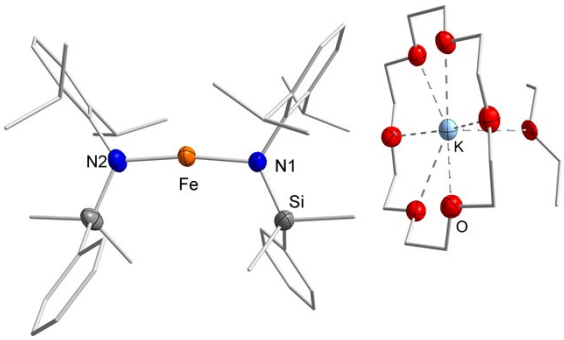

Figure S81. Molecular structure of K{18c6}**[FeL$^1_2$]**. All hydrogen atoms and a second, independent molecule with disorders in two phenyl rings and two *iso*-propyl groups (all parts: 50%) are omitted for clarity. A disorder in the Et_2O molecule (part 1 (depicted): 70%; part 2: 30%) is found. The dataset is based on a measurement comprising approximately 75% data for the crystal presented here + 25% data from other individuums, which could not be indexed. Partial reflection overlap of the parasitic scattering leads to a high wR_2 value.

Table S7. Crystal data and structure refinement of K{18c6}**[CoL$^1_2$]**

Empirical formula	$C_{52}H_{80}CoKN_2O_6Si_2$
Formula weight	983.39
Temperature /K	100.0
Crystal system	triclinic
Space group	P−1
a /Å	10.688(2)
b /Å	15.427(3)
c /Å	17.610(4)
α /°	85.095(6)
β /°	75.862(6)
γ /°	77.123(6)
Volume /Å^3	2743.5(10)
Z	2
ρ_{calc} /g·cm^3	1.190
μ /mm^{-1}	0.478
F(000)	1056.0
Crystal size /mm^3	0.62 × 0.274 × 0.124
Radiation	MoKα (λ = 0.71073)
2Θ range for data collection/°	4.172 to 49.998
Index ranges	−12 ≤ *h* ≤ 12, −18 ≤ *k* ≤ 16, −20 ≤ *l* ≤ 20
Reflections collected	29137
Independent reflections	9518 [R_{int} = 0.1123, R_{sigma} = 0.1104]
Data/restraints/parameters	9518/6/599
Goodness-of-fit on F^2	1.050
Final *R* indexes [*I*>=2σ (*I*)]	R_1 = 0.0683, wR_2 = 0.1386
Final *R* indexes [all data]	R_1 = 0.1335, wR_2 = 0.1551
Largest diff. peak/hole / e Å^{-3}	0.65/−0.43

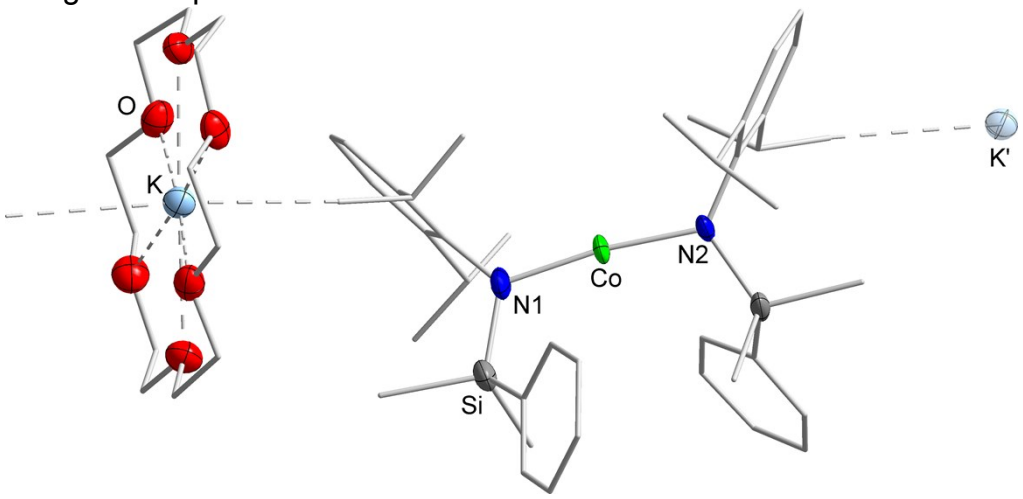

Figure S82. Molecular structure of K{18c6}**[CoL$^1_2$]**. All hydrogen atoms are omitted for clarity. A disorder in one methyl group (part 1 (depicted): 30%; part 2: 70%) is found.

−N(Dipp)SiMePh$_2$ (L^2) containing compounds

Table S8. Crystal data and structure refinement of **LiL^2**

Empirical formula	$C_{37}H_{54}LiNO_3Si$
Formula weight	595.84
Temperature /K	100.0
Crystal system	triclinic
Space group	P1
a /Å	10.0915(5)
b /Å	10.2440(5)
c /Å	17.2833(9)
α /°	87.900(2)
β /°	86.203(2)
γ /°	76.965(2)
Volume /Å^3	1736.41(15)
Z	2
ρ_{calc} /g·cm^3	1.140
μ /mm^{-1}	0.102
F(000)	648.0
Crystal size /mm^3	0.412 × 0.36 × 0.176
Radiation	MoKα (λ = 0.71073)
2Θ range for data collection/°	4.082 to 58.948
Index ranges	−13 ≤ *h* ≤ 13, −14 ≤ *k* ≤ 14, −23 ≤ *l* ≤ 23
Reflections collected	101241
Independent reflections	18604 [R_{int} = 0.0344, R_{sigma} = 0.0281]
Data/restraints/parameters	18604/3/803
Goodness-of-fit on F^2	1.047
Final *R* indexes [*I*>=2σ (*I*)]	R_1 = 0.0373, wR_2 = 0.0926
Final *R* indexes [all data]	R_1 = 0.0423, wR_2 = 0.0952
Largest diff. peak/hole / e Å^{-3}	0.76/−0.41
Flack parameter	0.001(15)

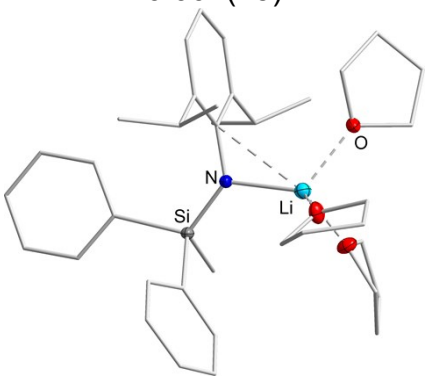

Figure S83. Molecular structure of **LiL^2**. All hydrogen atoms and a second, independent molecule with a disorder in one THF molecule (part 1: 70%; part 2: 30%) are omitted for clarity.

Table S9. Crystal data and structure refinement of **[CrL$^2_2$]**

Empirical formula	$C_{50}H_{60}Cr_{0.82}Li_{0.35}N_2Si_2$
Formula weight	790.51
Temperature /K	100.0
Crystal system	triclinic
Space group	P−1
a /Å	11.8650(11)
b /Å	12.9730(13)
c /Å	16.4026(16)
α /°	84.911(8)
β /°	88.653(8)
γ /°	68.582(7)
Volume /Å^3	2341.0(4)
Z	2
ρ_{calc} /g·cm^3	1.121
μ /mm^{-1}	0.291
F(000)	846.0
Crystal size /mm^3	0.233 × 0.203 × 0.121
Radiation	Mo Kα (λ = 0.71073)
2Θ range for data collection/°	4.986 to 53.542
Index ranges	−14 ≤ *h* ≤ 14, −14 ≤ *k* ≤ 16, −20 ≤ *l* ≤ 20
Reflections collected	20595
Independent reflections	9847 [R_{int} = 0.0399, R_{sigma} = 0.0426]
Data/restraints/parameters	9847/53/612
Goodness-of-fit on F^2	1.068
Final *R* indexes [*I*>=2σ (*I*)]	R_1 = 0.0337, wR_2 = 0.0822
Final *R* indexes [all data]	R_1 = 0.0506, wR_2 = 0.0863
Largest diff. peak/hole / e Å^{-3}	0.37/−0.30

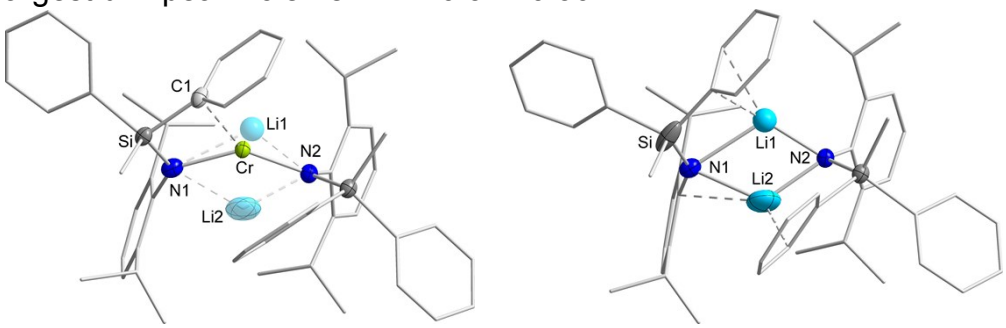

Figure S84. Molecular structure of **[CrL$^2_2$]** (left). All hydrogen atoms are omitted for clarity. One free *n*-pentane molecule is disordered over multiple positions on a symmetry element and has thus been squeezed. A disorder in one $SiMePh_2$ fragment and one phenyl group (part 1 (depicted): 83%; part 2: 17%) is found. Additionally, the chromium atom is only present in part 1 (83%), while co-crystallized dimeric $(LiL^2)_2$ is present in part 2 (17%, left: indicated; right: isolated). Due to its proximity to the chromium atom, Li1 could not be modelled anisotropically.

−N(Dipp)SiPh$_3$ (L^3) containing compounds

Table S10. Crystal data and structure refinement of **HL^3**

Empirical formula	$C_{60}H_{66}N_2Si_2$
Formula weight	871.32
Temperature /K	100.0
Crystal system	monoclinic
Space group	$P2_1$
a /Å	10.9870(13)
b /Å	8.9441(7)
c /Å	12.9460(13)
α /°	90
β /°	93.863(9)
γ /°	90
Volume /Å^3	1269.3(2)
Z	1
ρ_{calc} /g·cm^3	1.140
μ /mm^{-1}	0.110
F(000)	468.0
Crystal size /mm^3	0.543 × 0.46 × 0.157
Radiation	MoKα (λ = 0.71073)
2Θ range for data collection/°	5.034 to 53.616
Index ranges	−13 ≤ *h* ≤ 13, −10 ≤ *k* ≤ 11, −16 ≤ *l* ≤ 16
Reflections collected	11229
Independent reflections	5138 [R_{int} = 0.0319, R_{sigma} = 0.0294]
Data/restraints/parameters	5138/1/297
Goodness-of-fit on F^2	1.023
Final *R* indexes [*I*>=2σ (*I*)]	R_1 = 0.0319, wR_2 = 0.0811
Final *R* indexes [all data]	R_1 = 0.0365, wR_2 = 0.0826
Largest diff. peak/hole / e Å^{-3}	0.28/−0.15
Flack parameter	0.00(4)

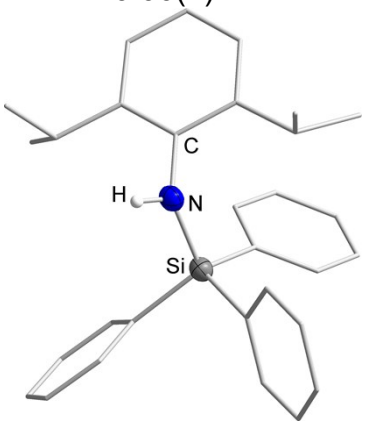

Figure S85. Molecular structure of **HL^3**. Unnecessary hydrogen atoms are omitted for clarity.

Table S11. Crystal data and structure refinement of **LiL^3**

Empirical formula	$C_{38}H_{48}LiNO_2Si$
Formula weight	585.80
Temperature /K	100.0
Crystal system	orthorhombic
Space group	Pbca
a /Å	10.6101(7)
b /Å	16.8895(10)
c /Å	38.289(3)
α /°	90
β /°	90
γ /°	90
Volume /Å^3	6861.3(8)
Z	8
ρ_{calc} /g·cm^3	1.134
μ /mm^{-1}	0.101
F(000)	2528.0
Crystal size /mm^3	0.288 × 0.192 × 0.181
Radiation	MoKα (λ = 0.71073)
2Θ range for data collection/°	4.656 to 53.492
Index ranges	−13 ≤ *h* ≤ 13, −21 ≤ *k* ≤ 20, −48 ≤ *l* ≤ 48
Reflections collected	55029
Independent reflections	7263 [R_{int} = 0.1141, R_{sigma} = 0.1028]
Data/restraints/parameters	7263/0/404
Goodness-of-fit on F^2	0.797
Final *R* indexes [*I*>=2σ (*I*)]	R_1 = 0.0379, wR_2 = 0.0819
Final *R* indexes [all data]	R_1 = 0.0958, wR_2 = 0.0892
Largest diff. peak/hole / e Å^{-3}	0.25/−0.24

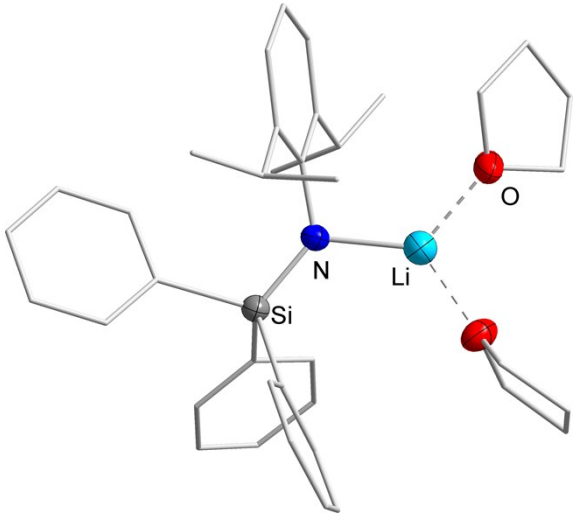

Figure S86. Molecular structure of **LiL^3**. All hydrogen atoms are omitted for clarity. A disorder in one THF molecule (both part 1 (depicted) / 2: 50%) is found.

Table S12. Crystal data and structure refinement of **LiL³**

Empirical formula	$C_{38}H_{48}LiNO_2Si$
Formula weight	585.80
Temperature /K	100.0
Crystal system	orthorhombic
Space group	$P2_12_12_1$
a /Å	9.750(3)
b /Å	15.312(5)
c /Å	45.002(11)
α /°	90
β /°	90
γ /°	90
Volume /Å³	6719(3)
Z	8
ρ_{calc} /g·cm³	1.158
μ /mm⁻¹	0.103
F(000)	2528.0
Crystal size /mm³	0.287 × 0.155 × 0.11
Radiation	MoKα (λ = 0.71073)
2Θ range for data collection/°	4.552 to 52.13
Index ranges	−12 ≤ *h* ≤ 12, −18 ≤ *k* ≤ 18, −55 ≤ *l* ≤ 55
Reflections collected	97307
Independent reflections	13263 [R_{int} = 0.0433, R_{sigma} = 0.0272]
Data/restraints/parameters	13263/0/810
Goodness-of-fit on F^2	1.073
Final *R* indexes [*I*>=2σ (*I*)]	R_1 = 0.0405, wR_2 = 0.0950
Final *R* indexes [all data]	R_1 = 0.0459, wR_2 = 0.0975
Largest diff. peak/hole / e Å⁻³	0.53/−0.25
Flack parameter	0.00(2)

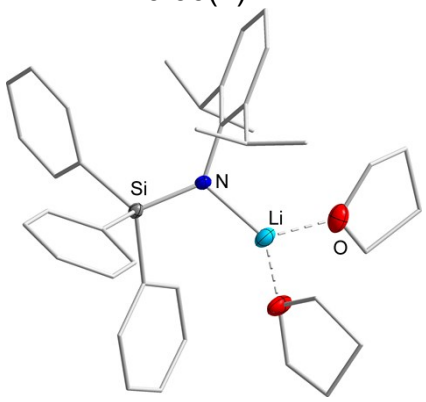

Figure S87. Molecular structure of **LiL³**. All hydrogen atoms and a second, independent molecule with a disorder in one THF molecule (part 1: 70%; part 2: 30%) are omitted for clarity. A disorder in one THF molecule (both part 1 (depicted) / 2: 50%) is found.

Table S13. Crystal data and structure refinement of **[FeL$^3_2$]**

Empirical formula	$C_{60}H_{64}FeN_2Si_2$
Formula weight	925.16
Temperature /K	99.99
Crystal system	triclinic
Space group	P−1
a /Å	12.2746(11)
b /Å	13.7722(10)
c /Å	17.6349(11)
α /°	72.165(2)
β /°	88.812(2)
γ /°	86.503(2)
Volume /Å^3	2832.6(4)
Z	2
ρ_{calc} /g·cm^3	1.085
μ /mm^{-1}	0.344
F(000)	984.0
Crystal size /mm^3	0.167 × 0.104 × 0.068
Radiation	MoKα (λ = 0.71073)
2Θ range for data collection/°	4.422 to 49.998
Index ranges	−14 ≤ *h* ≤ 14, −16 ≤ *k* ≤ 16, −20 ≤ *l* ≤ 20
Reflections collected	66757
Independent reflections	9966 [R_{int} = 0.1147, R_{sigma} = 0.0766]
Data/restraints/parameters	9966/18/588
Goodness-of-fit on F^2	1.081
Final *R* indexes [*I*>=2σ (*I*)]	R_1 = 0.0584, wR_2 = 0.1302
Final *R* indexes [all data]	R_1 = 0.0930, wR_2 = 0.1391
Largest diff. peak/hole / e Å^{-3}	0.77/−0.82

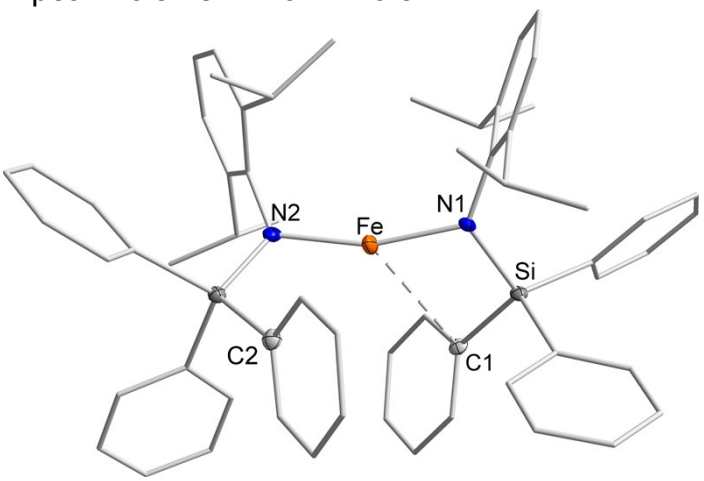

Figure S88. Molecular structure of **[FeL$^3_2$]**. All hydrogen atoms are omitted for clarity. One free *n*-pentane molecule is disordered over multiple positions and has thus been squeezed.

Table S14. Crystal data and structure refinement of K{18c6}**[FeL$^3_2$]**

Empirical formula	$C_{80}H_{104}FeKN_2O_8Si_2$
Formula weight	1372.78
Temperature /K	100.0
Crystal system	triclinic
Space group	P−1
a /Å	12.5267(8)
b /Å	13.5299(9)
c /Å	24.9620(15)
α /°	79.978(2)
β /°	88.219(2)
γ /°	73.252(2)
Volume /Å^3	3988.6(4)
Z	2
ρ_{calc} /g·cm^3	1.143
μ /mm^{-1}	0.323
F(000)	1470.0
Crystal size /mm^3	0.263 × 0.243 × 0.144
Radiation	MoKα (λ = 0.71073)
2Θ range for data collection/°	3.808 to 50
Index ranges	−14 ≤ *h* ≤ 14, −16 ≤ *k* ≤ 16, −29 ≤ *l* ≤ 29
Reflections collected	54903
Independent reflections	14023 [R_{int} = 0.0870, R_{sigma} = 0.1105]
Data/restraints/parameters	14023/186/903
Goodness-of-fit on F^2	1.037
Final *R* indexes [*I*>=2σ (*I*)]	R_1 = 0.0713, wR_2 = 0.1399
Final *R* indexes [all data]	R_1 = 0.1203, wR_2 = 0.1515
Largest diff. peak/hole / e Å^{-3}	0.44/−0.49

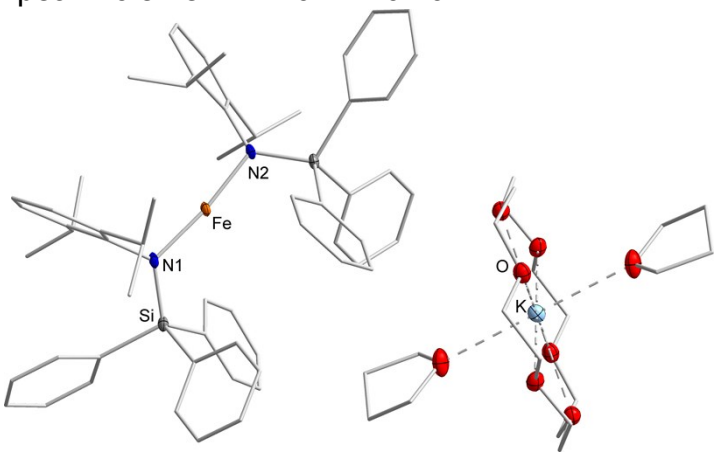

Figure S89. Molecular structure of K{18c6}**[FeL$^3_2$]**. All hydrogen atoms are omitted for clarity. One free *n*-pentane molecule is disordered over multiple positions and has thus been squeezed. A disorder in the THF molecule (both part 1 (depicted) / part 2: 50%) is found.

−N(Dipp)SiMe$_2$(allyl) (L^4) containing compounds

Table S15. Crystal data and structure refinement of **[CrL$^4_2$]**

Empirical formula	$C_{34}H_{56}CrN_2Si_2$
Formula weight	600.98
Temperature /K	100.0
Crystal system	triclinic
Space group	P−1
a /Å	9.5587(5)
b /Å	12.8751(7)
c /Å	16.1547(8)
α /°	67.981(2)
β /°	86.382(2)
γ /°	70.002(2)
Volume /Å^3	1727.15(16)
Z	2
ρ_{calc} /g·cm^3	1.156
μ /mm^{-1}	0.424
F(000)	652.0
Crystal size /mm^3	0.445 × 0.226 × 0.206
Radiation	MoKα (λ = 0.71073)
2Θ range for data collection/°	4.548 to 56.518
Index ranges	−12 ≤ *h* ≤ 12, −16 ≤ *k* ≤ 17, −21 ≤ *l* ≤ 21
Reflections collected	26070
Independent reflections	8502 [R_{int} = 0.0302, R_{sigma} = 0.0360]
Data/restraints/parameters	8502/0/380
Goodness-of-fit on F^2	1.027
Final *R* indexes [*I*>=2σ (*I*)]	R_1 = 0.0364, wR_2 = 0.0893
Final *R* indexes [all data]	R_1 = 0.0485, wR_2 = 0.0957
Largest diff. peak/hole / e Å^{-3}	0.53/−0.51

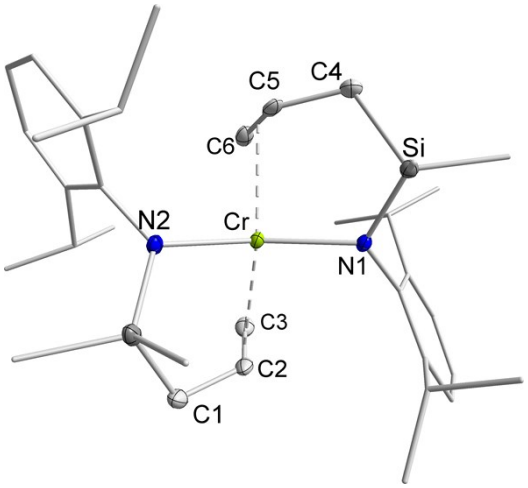

Figure S90. Molecular structure of **[CrL$^4_2$]**. All hydrogen atoms are omitted for clarity.

Table S16. Crystal data and structure refinement of **[MnL$^4_2$]**

Empirical formula	$C_{34}H_{56}MnN_2Si_2$
Formula weight	603.92
Temperature /K	100.0
Crystal system	monoclinic
Space group	$P2_1/n$
a /Å	15.9153(12)
b /Å	13.0196(8)
c /Å	17.0810(16)
α /°	90
β /°	97.079(7)
γ /°	90
Volume /Å^3	3512.4(5)
Z	4
ρ_{calc} /g·cm^3	1.142
μ /mm^{-1}	0.468
F(000)	1308.0
Crystal size /mm^3	0.491 × 0.029 × 0.016
Radiation	MoKα (λ = 0.71073)
2Θ range for data collection/°	5.736 to 53.5
Index ranges	−20 ≤ *h* ≤ 20, −16 ≤ *k* ≤ 16, −21 ≤ *l* ≤ 21
Reflections collected	31624
Independent reflections	7421 [R_{int} = 0.0466, R_{sigma} = 0.0466]
Data/restraints/parameters	7421/0/372
Goodness-of-fit on F^2	0.941
Final *R* indexes [*I*>=2σ (*I*)]	R_1 = 0.0357, wR_2 = 0.0830
Final *R* indexes [all data]	R_1 = 0.0603, wR_2 = 0.0892
Largest diff. peak/hole / e Å^{-3}	0.36/−0.27

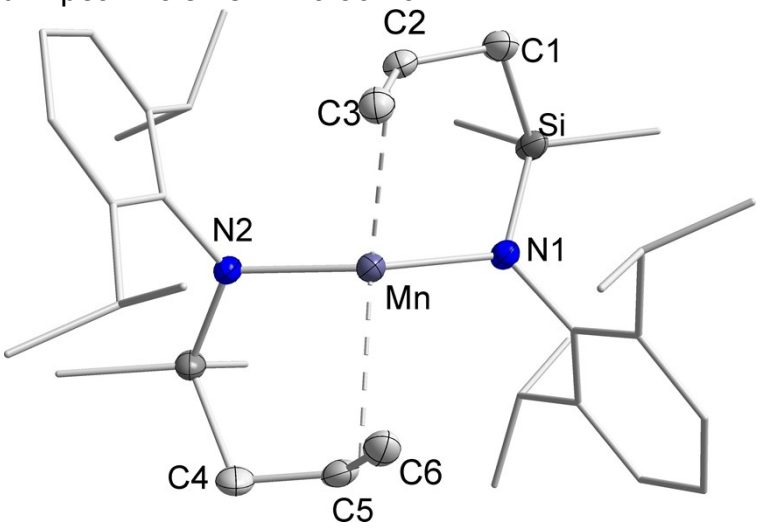

Figure S91. Molecular structure of **[MnL$^4_2$]**. All hydrogen atoms are omitted for clarity.

Table S17. Crystal data and structure refinement of **[FeL$^4_2$]**

Empirical formula	$C_{34}H_{56}FeN_2Si_2$
Formula weight	604.83
Temperature /K	99.99
Crystal system	monoclinic
Space group	$P2_1/n$
a /Å	15.7788(7)
b /Å	13.0161(6)
c /Å	17.0238(8)
α /°	90
β /°	97.370(2)
γ /°	90
Volume /Å^3	3467.4(3)
Z	4
ρ_{calc} /g·cm^3	1.159
μ /mm^{-1}	0.528
F(000)	1312.0
Crystal size /mm^3	0.34 × 0.339 × 0.24
Radiation	MoKα (λ = 0.71073)
2Θ range for data collection/°	4.826 to 59.104
Index ranges	−21 ≤ *h* ≤ 21, −18 ≤ *k* ≤ 17, −23 ≤ *l* ≤ 23
Reflections collected	45644
Independent reflections	9681 [R_{int} = 0.0314, R_{sigma} = 0.0264]
Data/restraints/parameters	9681/0/388
Goodness-of-fit on F^2	1.020
Final *R* indexes [*I*>=2σ (*I*)]	R_1 = 0.0305, wR_2 = 0.0733
Final *R* indexes [all data]	R_1 = 0.0399, wR_2 = 0.0776
Largest diff. peak/hole / e Å^{-3}	0.41/−0.29

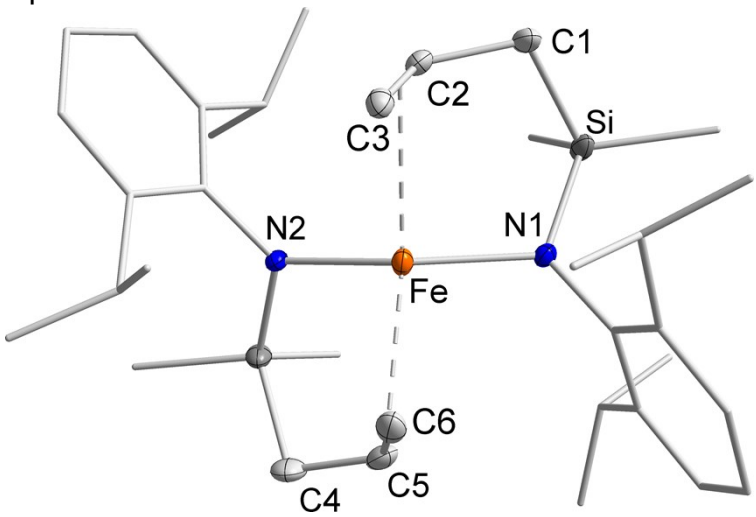

Figure S92. Molecular structure of **[FeL$^4_2$]**. All hydrogen atoms (partially disordered with both part 1 / 2: 50% due to free rotation of CH_3 fragments) are omitted for clarity.

Table S18. Crystal data and structure refinement of **[CoL$^4_2$]**

Empirical formula	$C_{34}H_{56}CoN_2Si_2$
Formula weight	607.91
Temperature /K	100.0
Crystal system	monoclinic
Space group	$P2_1/n$
a /Å	15.7778(8)
b /Å	13.0041(7)
c /Å	17.0121(9)
α /°	90
β /°	97.284(2)
γ /°	90
Volume /Å^3	3462.3(3)
Z	4
ρ_{calc} /g·cm^3	1.166
μ /mm^{-1}	0.589
F(000)	1316.0
Crystal size /mm^3	0.64 × 0.344 × 0.298
Radiation	MoKα (λ = 0.71073)
2Θ range for data collection/°	4.562 to 68.872
Index ranges	−25 ≤ *h* ≤ 25, −20 ≤ *k* ≤ 20, −27 ≤ *l* ≤ 27
Reflections collected	117460
Independent reflections	14585 [R_{int} = 0.0360, R_{sigma} = 0.0224]
Data/restraints/parameters	14585/0/404
Goodness-of-fit on F^2	1.050
Final *R* indexes [*I*>=2σ (*I*)]	R_1 = 0.0305, wR_2 = 0.0744
Final *R* indexes [all data]	R_1 = 0.0413, wR_2 = 0.0789
Largest diff. peak/hole / e Å^{-3}	0.43/−0.38

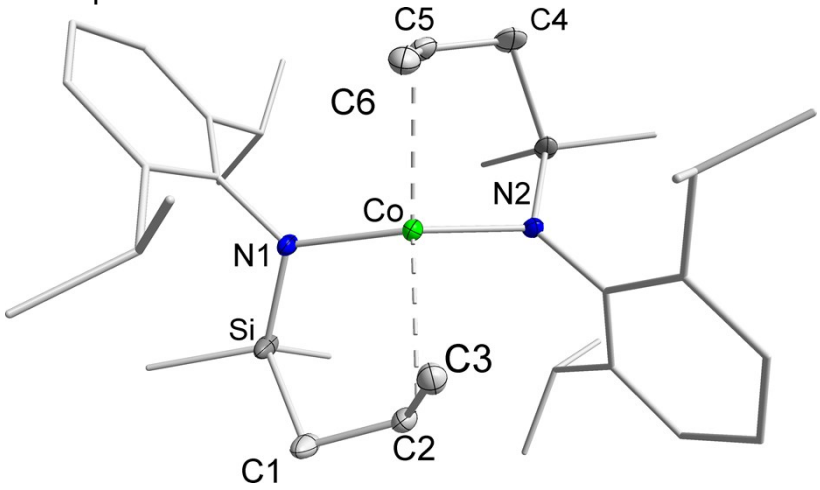

Figure S93. Molecular structure of **[CoL$^4_2$]**. All hydrogen atoms (partially disordered with both part 1 / 2: 50% due to free rotation of CH_3 fragments) are omitted for clarity.

Table S19. Crystal data and structure refinement of (K{18c6})$_2$**[CrL$^4_2$]$_2$**

Empirical formula	$C_{54}H_{94}CrKN_2O_8Si_2$
Formula weight	1046.59
Temperature /K	99.88
Crystal system	monoclinic
Space group	C2/c
a /Å	31.9234(17)
b /Å	12.8832(6)
c /Å	33.0790(16)
α /°	90
β /°	101.405(2)
γ /°	90
Volume /Å^3	13335.9(11)
Z	8
ρ_{calc} /g·cm^3	1.043
μ /mm^{-1}	0.314
F(000)	4528.0
Crystal size /mm^3	0.321 × 0.269 × 0.224
Radiation	MoKα (λ = 0.71073)
2Θ range for data collection/°	3.96 to 51.478
Index ranges	−33 ≤ *h* ≤ 38, −15 ≤ *k* ≤ 15, −40 ≤ *l* ≤ 39
Reflections collected	47610
Independent reflections	12301 [R_{int} = 0.0548, R_{sigma} = 0.0750]
Data/restraints/parameters	12301/1260/986
Goodness-of-fit on F^2	1.030
Final *R* indexes [*I*>=2σ (*I*)]	R_1 = 0.1095, wR_2 = 0.2809
Final *R* indexes [all data]	R_1 = 0.1809, wR_2 = 0.3278
Largest diff. peak/hole / e Å^{-3}	0.42/−0.45

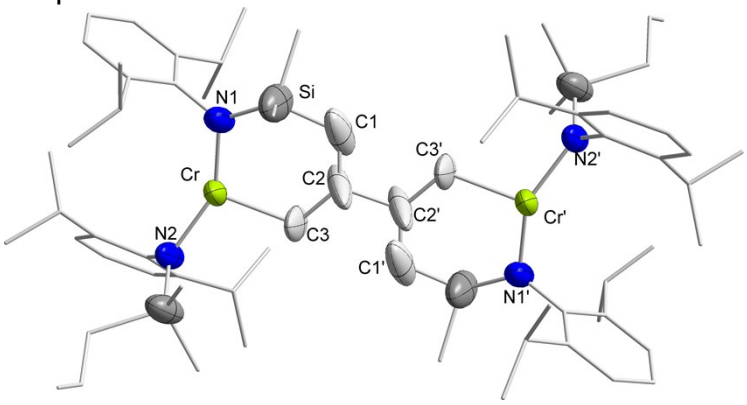

Figure S94. Anionic section of (K{18c6})$_2$**[CrL$^4_2$]$_2$**. All hydrogen atoms are omitted for clarity. The structure suffered from intrinsic crystallographic flaws, due to weakly diffracting crystals, which could not be overcome despite multiple attempts. Disorders were found for the crown ether, THF molecules, *iso*-propyl groups and the allyl moiety in different occupancies of 50% (part 1/2), 75% (part 3) or 25% (part 4/5).

Table S20. Crystal data and structure refinement of K{18c6}**[CoL$^4_2$]**

Empirical formula	$C_{46}H_{80}CoKN_2O_6Si_2$
Formula weight	911.33
Temperature /K	100.0
Crystal system	monoclinic
Space group	$P2_1/n$
a /Å	13.0369(5)
b /Å	22.1041(11)
c /Å	18.2404(7)
α /°	90
β /°	110.376(3)
γ /°	90
Volume /Å^3	4927.4(4)
Z	4
ρ_{calc} /g·cm^3	1.228
μ /mm^{-1}	0.527
F(000)	1968.0
Crystal size /mm^3	0.415 × 0.395 × 0.101
Radiation	MoKα (λ = 0.71073)
2Θ range for data collection/°	4.97 to 53.496
Index ranges	−16 ≤ *h* ≤ 16, −27 ≤ *k* ≤ 27, −23 ≤ *l* ≤ 22
Reflections collected	39565
Independent reflections	10419 [R_{int} = 0.0402, R_{sigma} = 0.0362]
Data/restraints/parameters	10419/0/574
Goodness-of-fit on F^2	1.025
Final *R* indexes [*I*>=2σ (*I*)]	R_1 = 0.0316, wR_2 = 0.0703
Final *R* indexes [all data]	R_1 = 0.0527, wR_2 = 0.0764
Largest diff. peak/hole / e Å^{-3}	0.30/−0.33

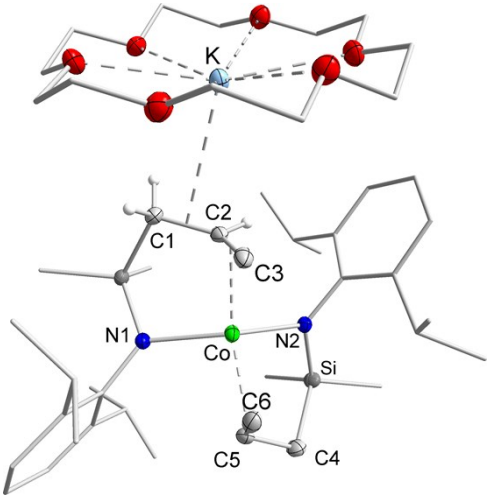

Figure S95. Molecular structure of K{18c6}**[CoL$^4_2$]**. Unnecessary hydrogen atoms are omitted for clarity.

Imido cobalt complexes

Table S21. Crystal data and structure refinement of K{18c6}**[Co(NDipp)L$^1_2$]**

Empirical formula	$C_{72}H_{113}CoKN_3O_8Si_2$
Formula weight	1302.86
Temperature /K	100.0
Crystal system	monoclinic
Space group	C2/c
a /Å	10.1708(6)
b /Å	25.7371(18)
c /Å	28.1136(15)
α /°	90
β /°	90.265(5)
γ /°	90
Volume /Å^3	7359.1(8)
Z	4
ρ_{calc} /g·cm^3	1.176
μ /mm^{-1}	0.375
F(000)	2816.0
Crystal size /mm^3	0.501 × 0.218 × 0.152
Radiation	MoKα (λ = 0.71073)
2Θ range for data collection/°	5.18 to 53.508
Index ranges	−12 ≤ *h* ≤ 12, −32 ≤ *k* ≤ 32, −35 ≤ *l* ≤ 35
Reflections collected	31700
Independent reflections	7779 [R_{int} = 0.0427, R_{sigma} = 0.0293]
Data/restraints/parameters	7779/0/422
Goodness-of-fit on F^2	1.053
Final *R* indexes [*I*>=2σ (*I*)]	R_1 = 0.0341, wR_2 = 0.0871
Final *R* indexes [all data]	R_1 = 0.0469, wR_2 = 0.0913
Largest diff. peak/hole / e Å^{-3}	0.66/−0.46

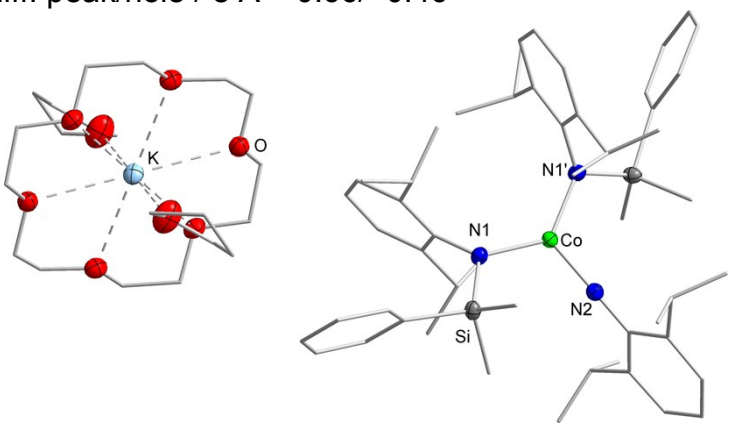

Figure S96. Molecular structure of K{18c6}**[Co(NDipp)L$^1_2$]**. All hydrogen atoms are omitted for clarity. A disorder in the THF molecule (part 1 (depicted): 75%; part 2: 25%) is omitted for clarity.

Table S22. Crystal data and structure refinement of K{18c6}**[Co(NDipp)L$^4_2$]**

Empirical formula	$C_{70}H_{121}CoKN_3O_9Si_2$
Formula weight	1302.90
Temperature /K	100.03
Crystal system	triclinic
Space group	P−1
a /Å	13.0565(5)
b /Å	15.5862(7)
c /Å	19.4665(8)
α /°	102.682(2)
β /°	100.886(2)
γ /°	94.621(2)
Volume /Å^3	3764.4(3)
Z	2
ρ_{calc} /g·cm^3	1.148
μ /mm^{-1}	0.367
F(000)	1412.0
Crystal size /mm^3	0.358 × 0.238 × 0.203
Radiation	MoKα (λ = 0.71073)
2Θ range for data collection/°	3.866 to 61.622
Index ranges	−17 ≤ *h* ≤ 18, −19 ≤ *k* ≤ 22, −27 ≤ *l* ≤ 27
Reflections collected	77935
Independent reflections	19892 [R_{int} = 0.0429, R_{sigma} = 0.0479]
Data/restraints/parameters	19892/26/876
Goodness-of-fit on F^2	1.037
Final *R* indexes [*I*>=2σ (*I*)]	R_1 = 0.0595, wR_2 = 0.1282
Final *R* indexes [all data]	R_1 = 0.0922, wR_2 = 0.1432
Largest diff. peak/hole / e Å^{-3}	0.81/−0.71

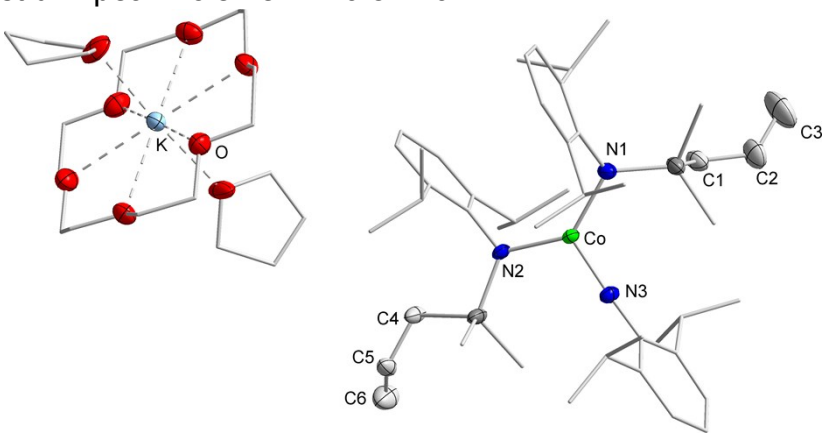

Figure S97. Molecular structure of K{18c6}**[Co(NDipp)L$^4_2$]**. All hydrogen atoms and one free, disordered THF molecule (part 1: 70%; part 2: 30%) are omitted for clarity. Disorders in both coordinated THF molecules (part 1 (depicted) / part 2: 50%) and both allyl moieties (part 1 (depicted): 70%; part 2: 30%) are omitted for clarity.

11.2 Zusatzinformationen zu Publikation 2

„Quasilinear 3d-metal(I) complexes [KM(N(Dipp)SiR_3)$_2$] (M = Cr − Co) − structural diversity, solution state behaviour and reactivity”

Ruth Weller, Igor Müller, Carine Duhayon, Sylviane Sabo-Etienne, Sébastian Bontemps, C. Gunnar Werncke

Dalton Transactions **2021**, *50*, 4890−4903.
DOI: 10.1039/d1dt00121c
https://pubs.rsc.org/en/content/articlehtml/2021/dt/d1dt00121c

Electronic Supplementary Material (ESI) for Dalton Transactions.

Quasilinear 3d-Metal(I) Complexes [KM(N(Dipp)SiR$_3$)$_2$] (M = Cr – Co) – Structural Diversity, Solution State Behaviour and Reactivity

Ruth Weller,[a] I. Müller,[a] Carine Duhayon,[b] Sylviane Sabo-Etienne,[b] Sébastien Bontemps,[b] C. Gunnar Werncke*

[a]Department of Chemistry, Philipps-University Marburg, Hans-Meerwein-Straße 4, D-35032 Marburg, Germany, E-Mail: gunnar.werncke@chemie.uni-marburg.de; [b]CNRS, LCC (Laboratoire de Chimie de Coordination), 205 route de Narbonne, 31077 Toulouse and Université de Toulouse, UPS, INPT, 31077 Toulouse, France

Table of Content

1 NMR Spectra

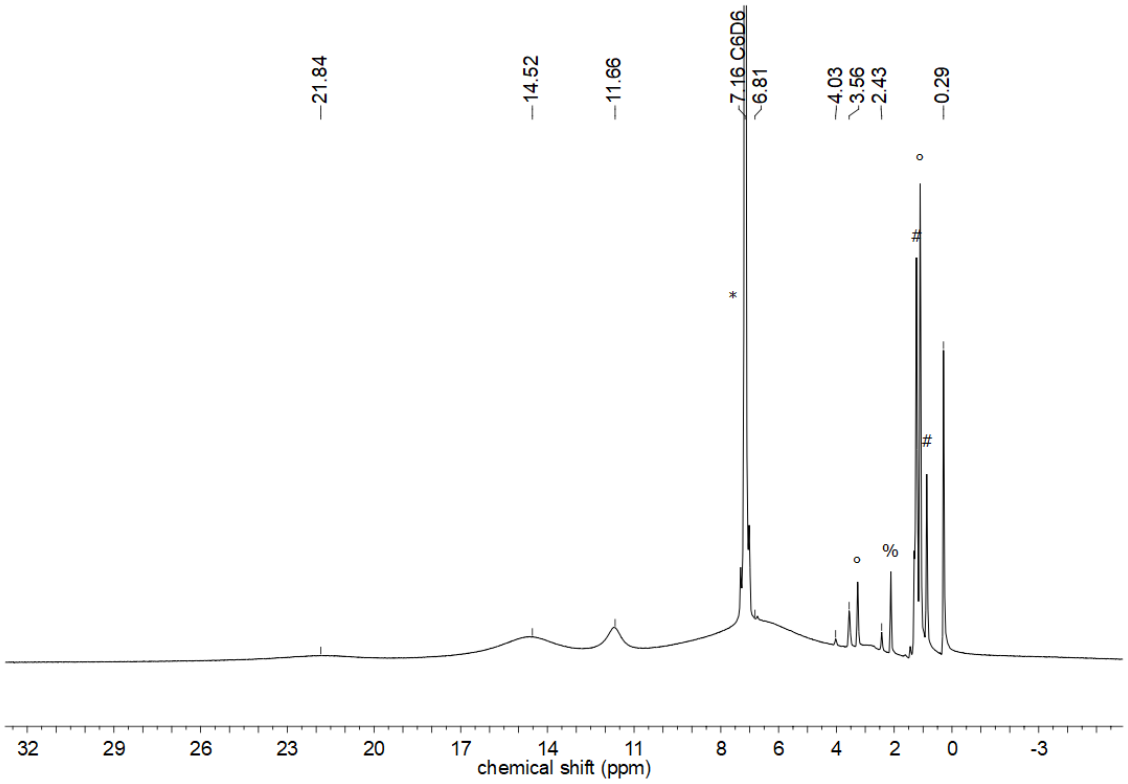

Figure S 1. ^{1}H NMR spectrum (500.1 MHz) of [KCr(L^{1})$_2$] (**1**) in C_6D_6 at 300 K. (* solvent, ° diethyl ether, # *n*-pentane, % toluene)

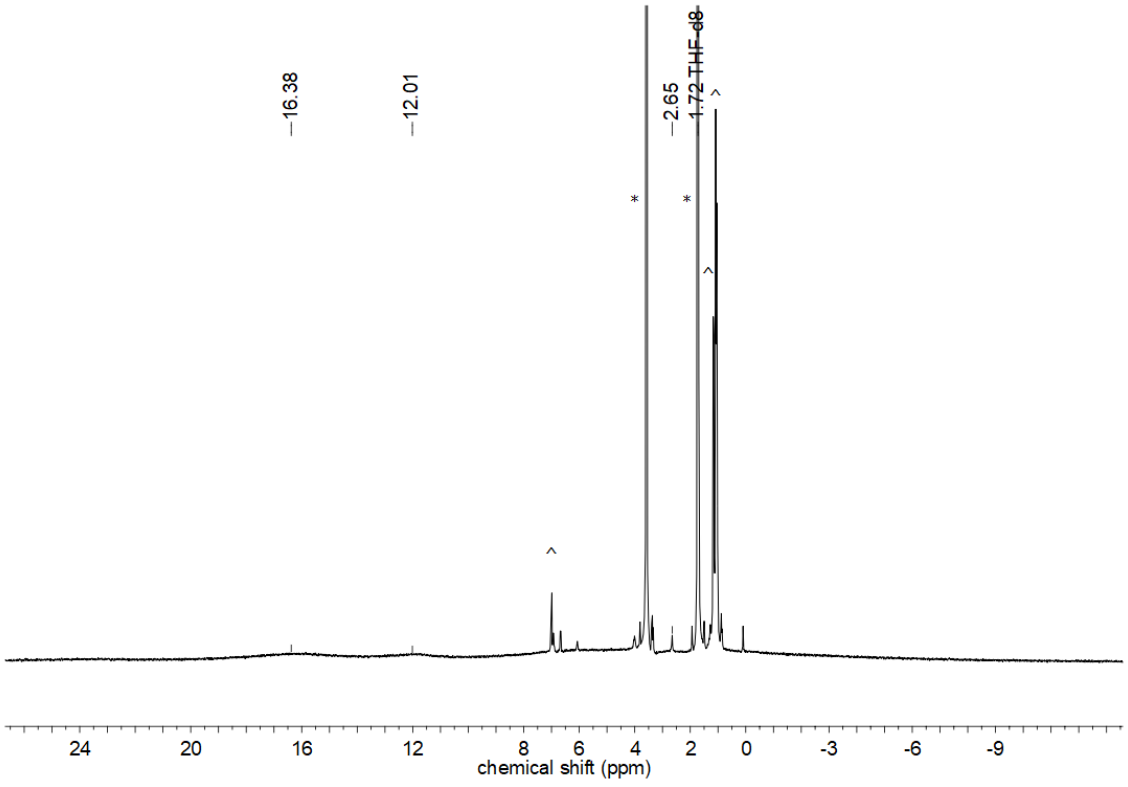

Figure S 2. ^{1}H NMR spectrum (500.1 MHz) of [KCr(L^{1})$_2$] (**1**) in THF-d_8 at 300 K. (* solvent, ^ impurities)

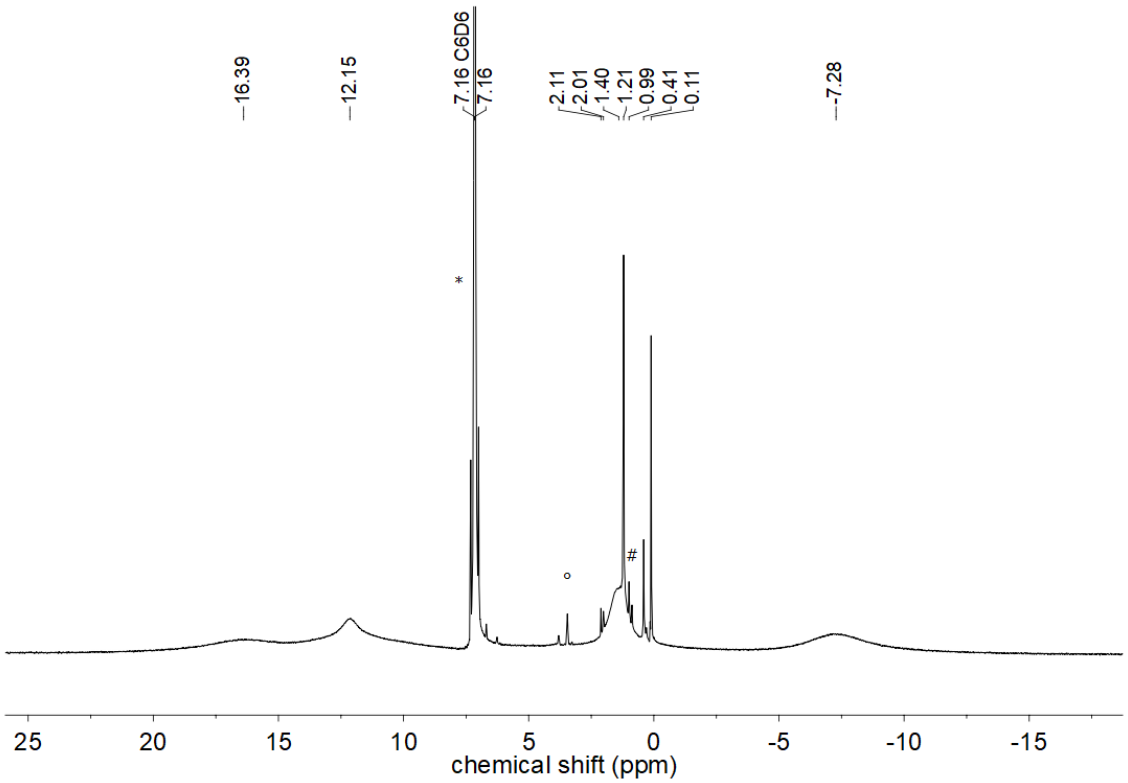

Figure S 3. ^{1}H NMR spectrum (500.1 MHz) of [KMn(L^{2})$_2$] (**2**) in C_6D_6 at 300 K. (* solvent, ° diethyl ether, $^{\#}$ *n*-pentane)

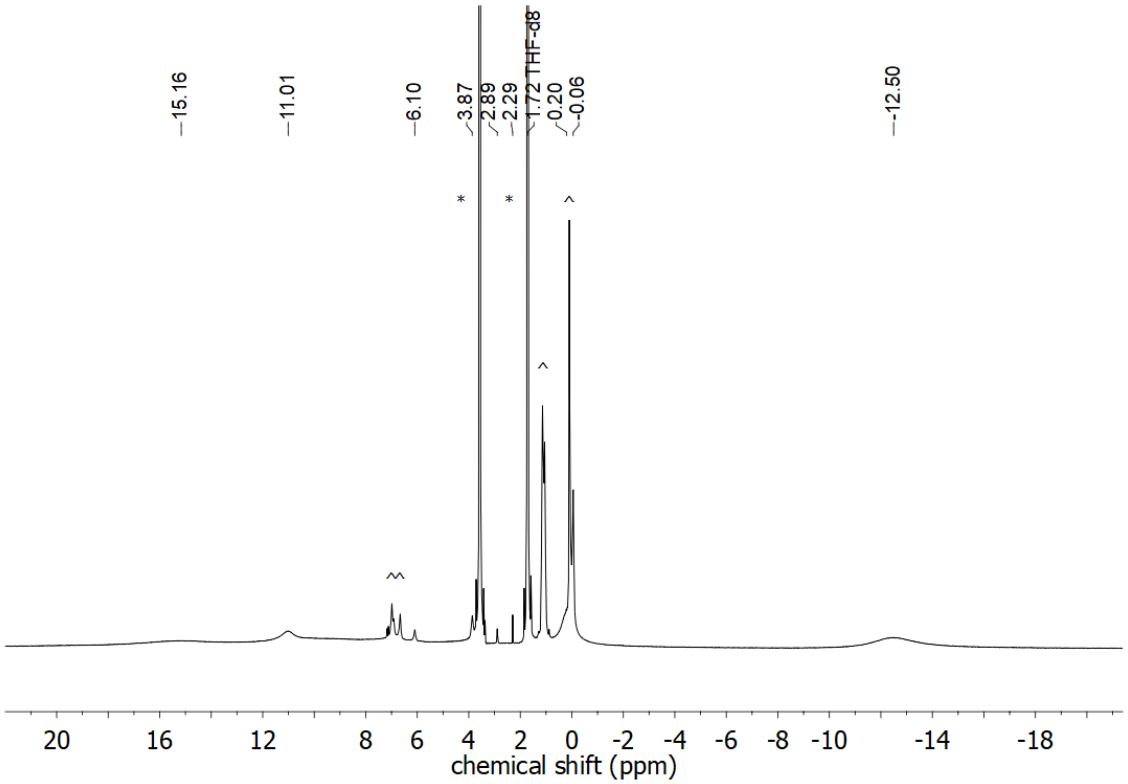

Figure S 4. ^{1}H NMR spectrum (500.1 MHz) of [KMn(L^{2})$_2$] (**2**) in THF-d_8 at 300 K. (* solvent, ^ impurities)

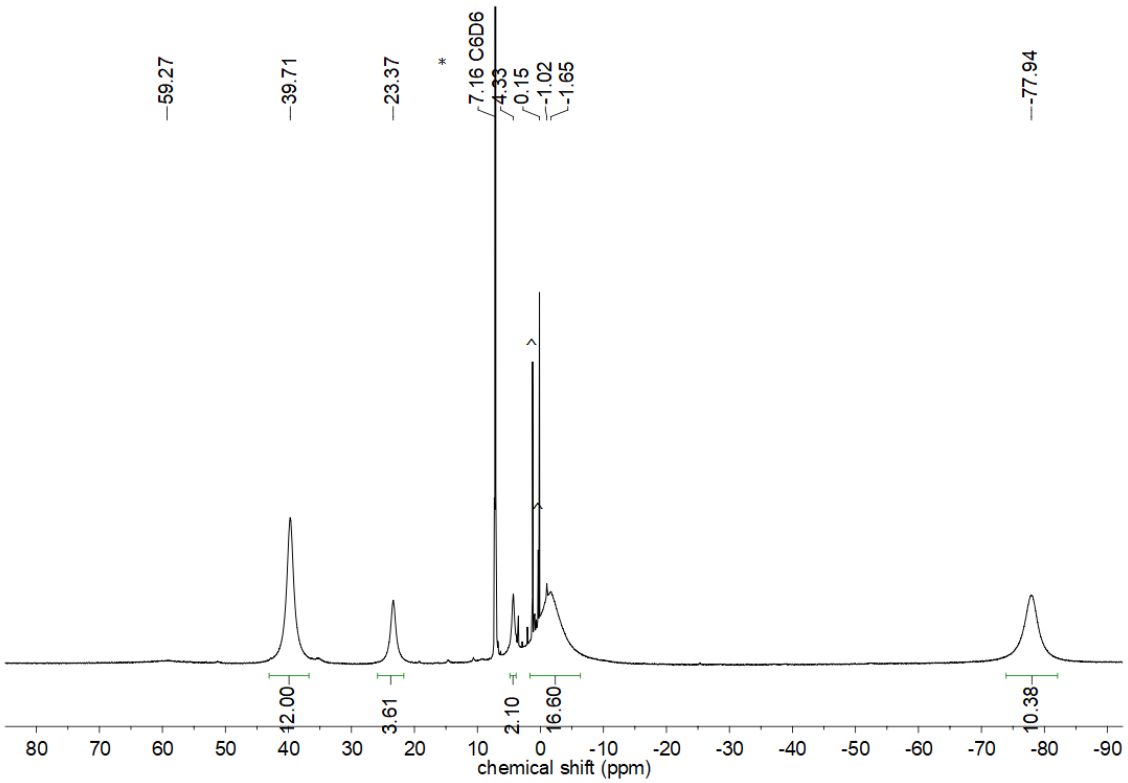

Figure S 5. ^{1}H NMR spectrum (500.1 MHz) of [KFe(L^{2})$_2$] (**3**) in C_6D_6 at 300 K. (* solvent, ^ impurities)

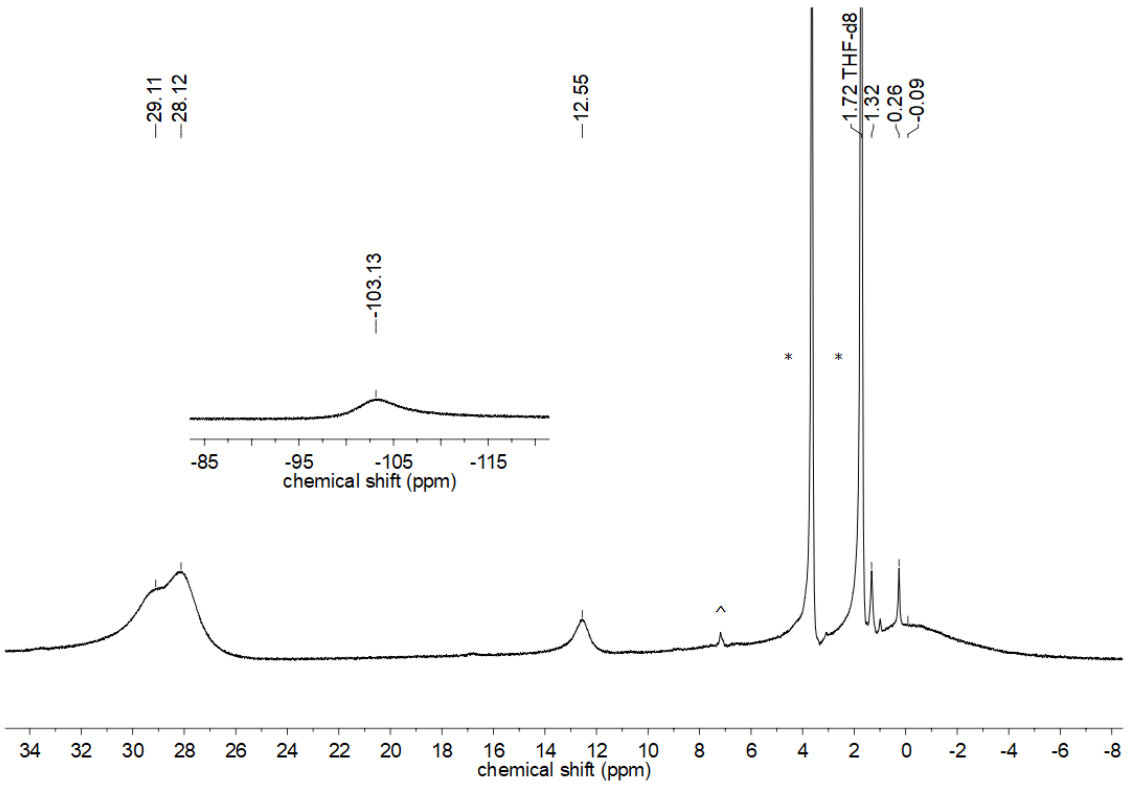

Figure S 6. ^{1}H NMR spectrum (500.1 MHz) of [KFe(L^{2})$_2$] (**3**) in THF-d_8 at 300 K. (* solvent, ^ impurities)

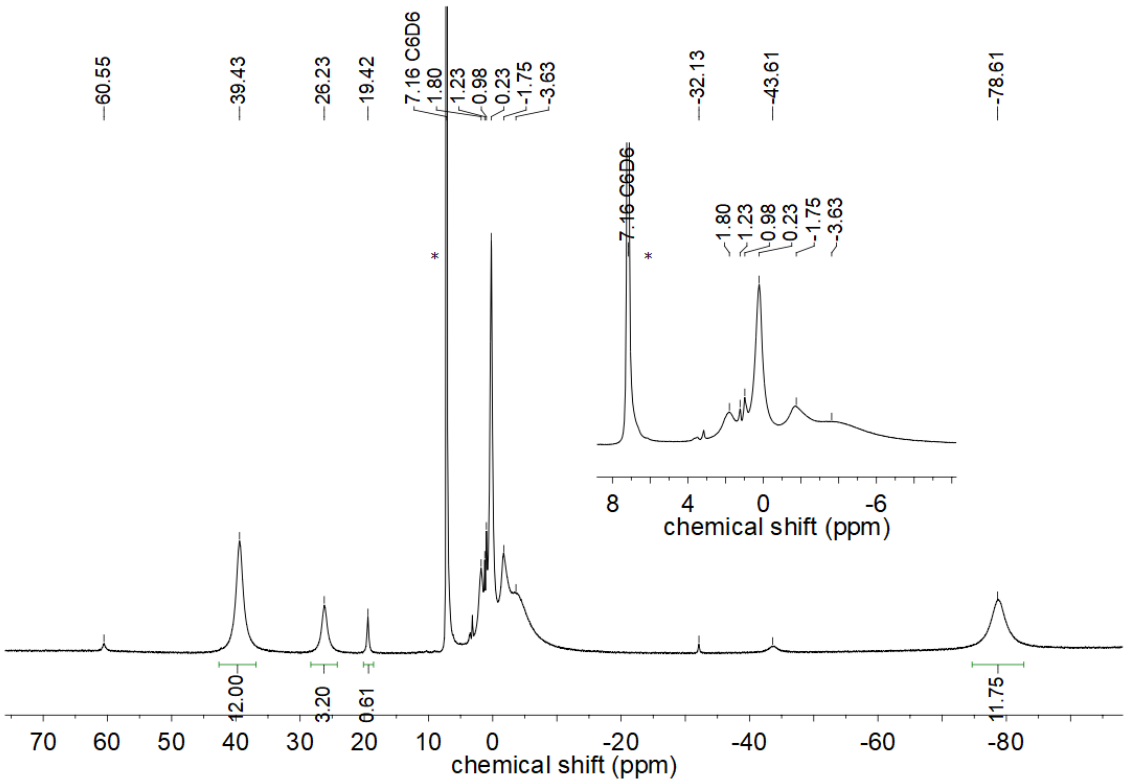

Figure S 7. ^{1}H NMR spectrum (500.1 MHz) of [K(DMAP)$_2$Fe(L^2)$_2$] (**3**.2DMAP) in C_6D_6 at 300 K. (* solvent, ^ impurities)

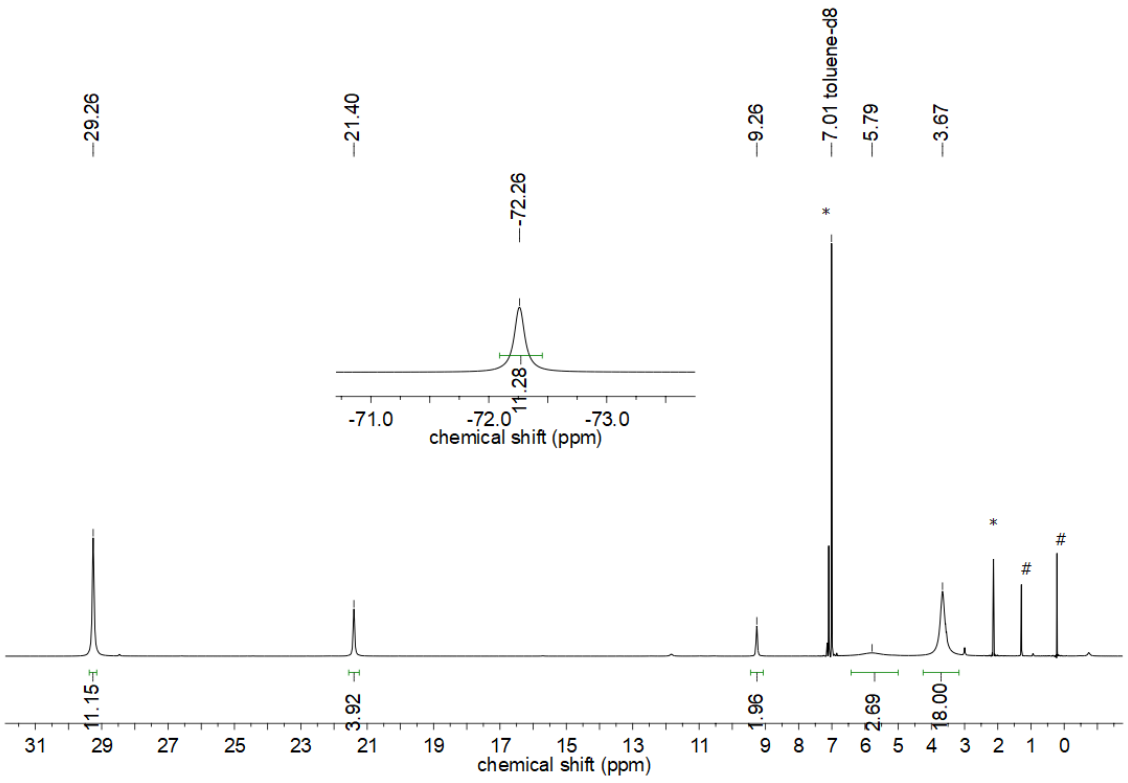

Figure S 8. ^{1}H NMR spectrum (500.1 MHz) of [KCo(L^2)$_2$] (**4**) in toluene-d_8 at 300 K. (* solvent, $^{\#}$ *n*-pentane)

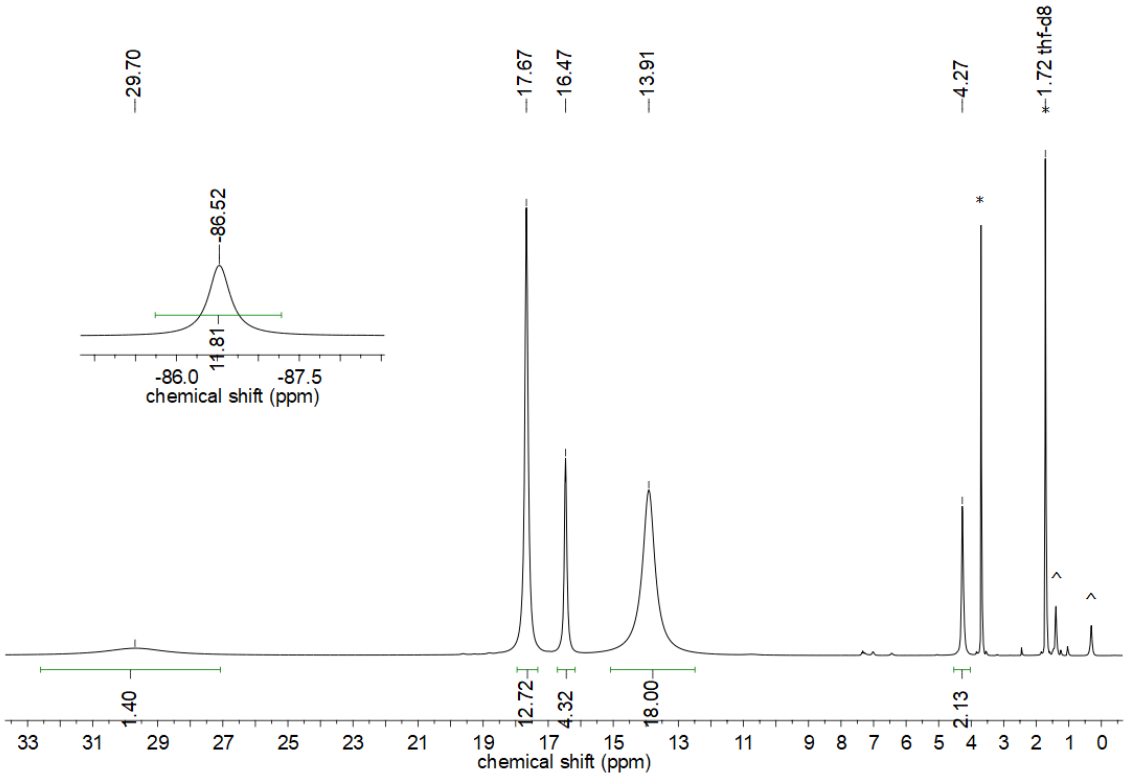

Figure S 9. ^{1}H NMR spectrum (500.1 MHz) of [KCo(L^{2})$_2$] (**4**) in THF-d_8 at 300 K. (* solvent, ^ impurities)

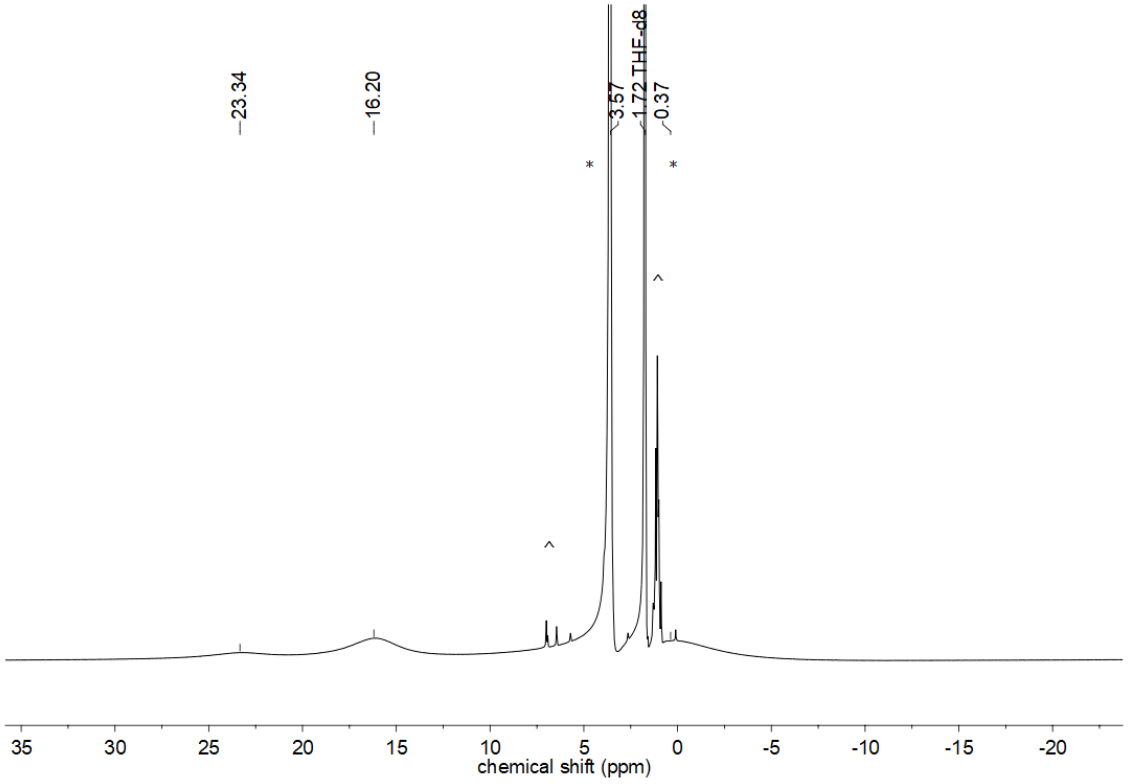

Figure S 10. ^{1}H NMR spectrum (500.1 MHz) of [K{18c6}][Cr(L^{1})$_2$] (**5**) in THF-d_8 at 300 K. (* solvent, ^ impurities)

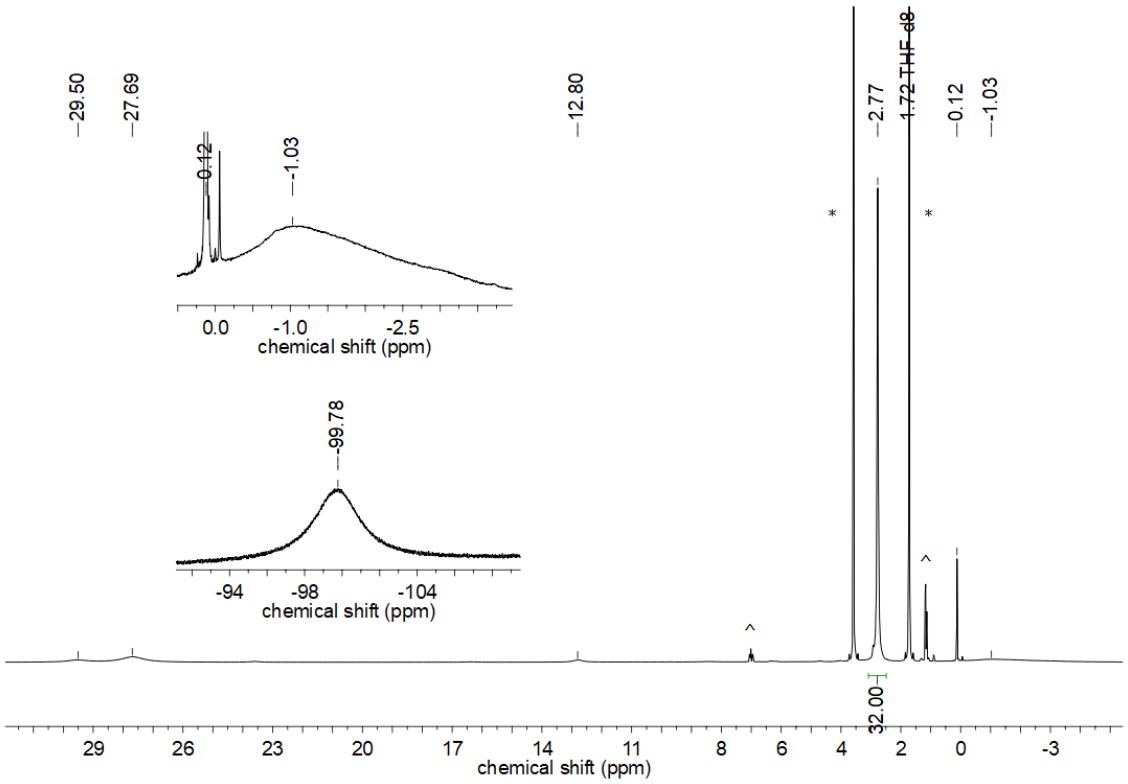

Figure S 11. ^{1}H NMR spectrum (500.1 MHz) of [Li{12c4}$_2$][Fe(L^2)$_2$] (**6**) in THF-d_8 at 300 K. (* solvent, ^ impurities)

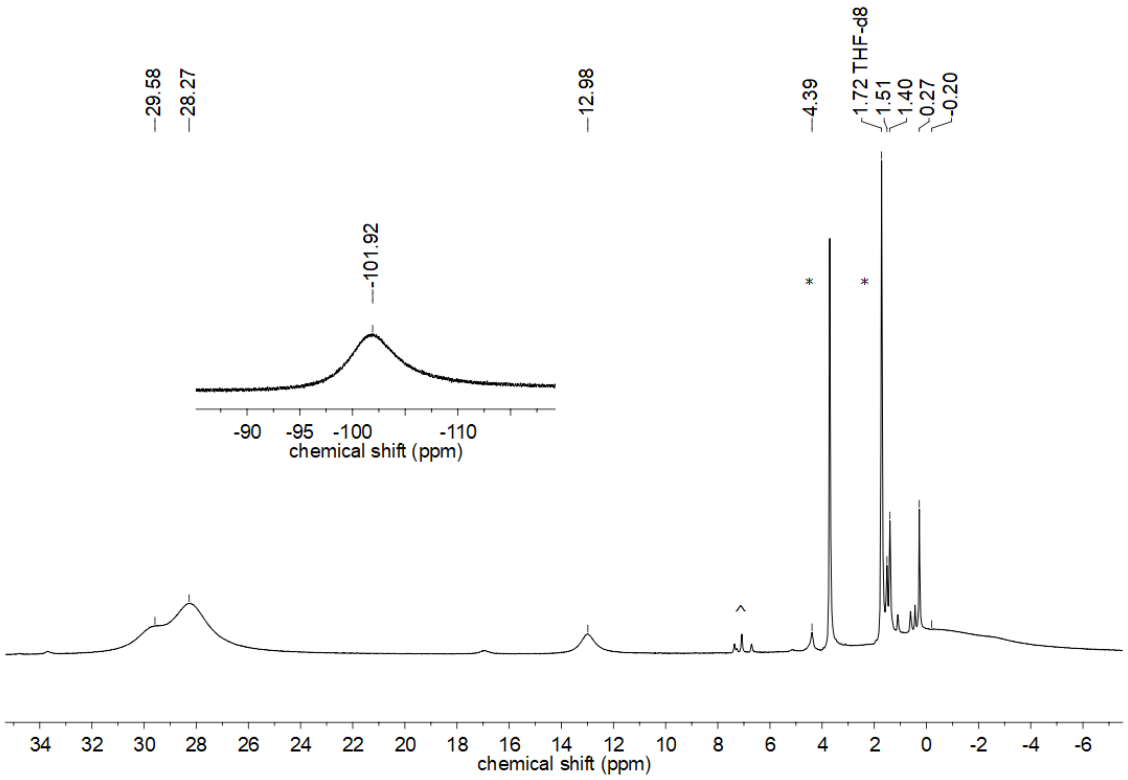

Figure S 12. *In Situ* ^{1}H NMR spectrum (300.2 MHz) of [LiFe(L^2)$_2$] in THF-d_8 at 300 K. (* solvent, ^ impurities)

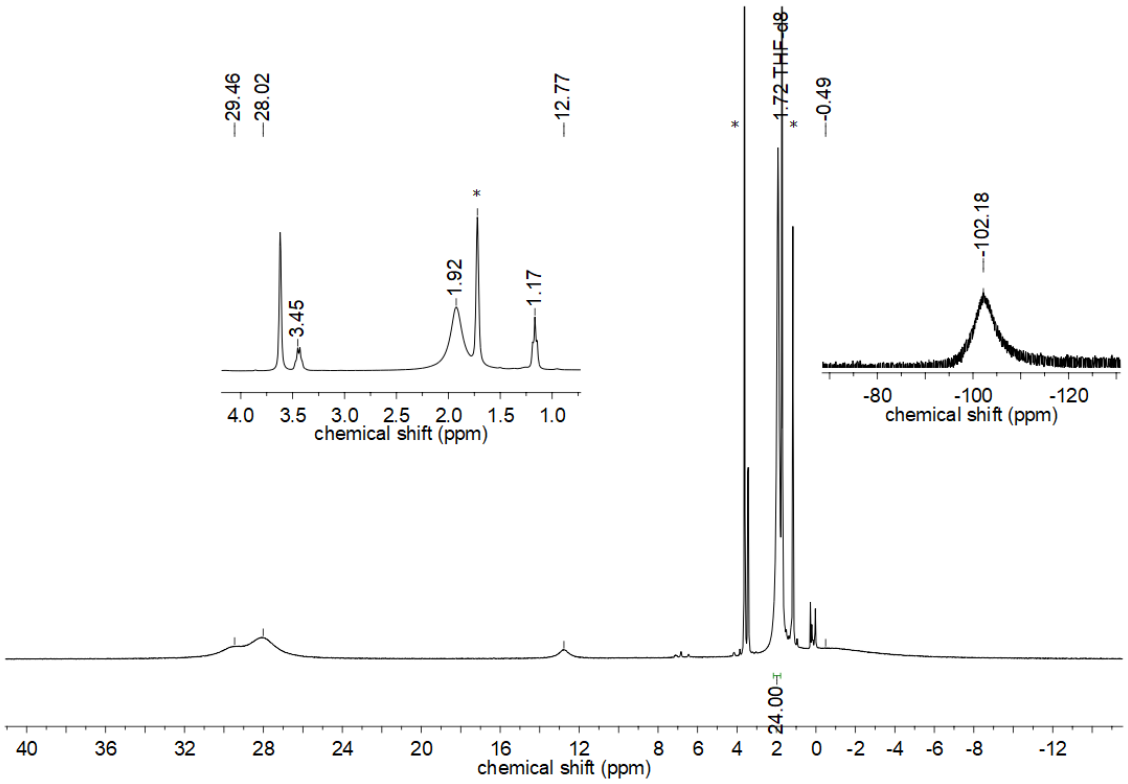

Figure S 13. ^{1}H NMR spectrum (500.1 MHz) of [Na{18c6}][Fe(L^{2})$_2$] (**7**) in THF-d_8 at 300 K. (* solvent)

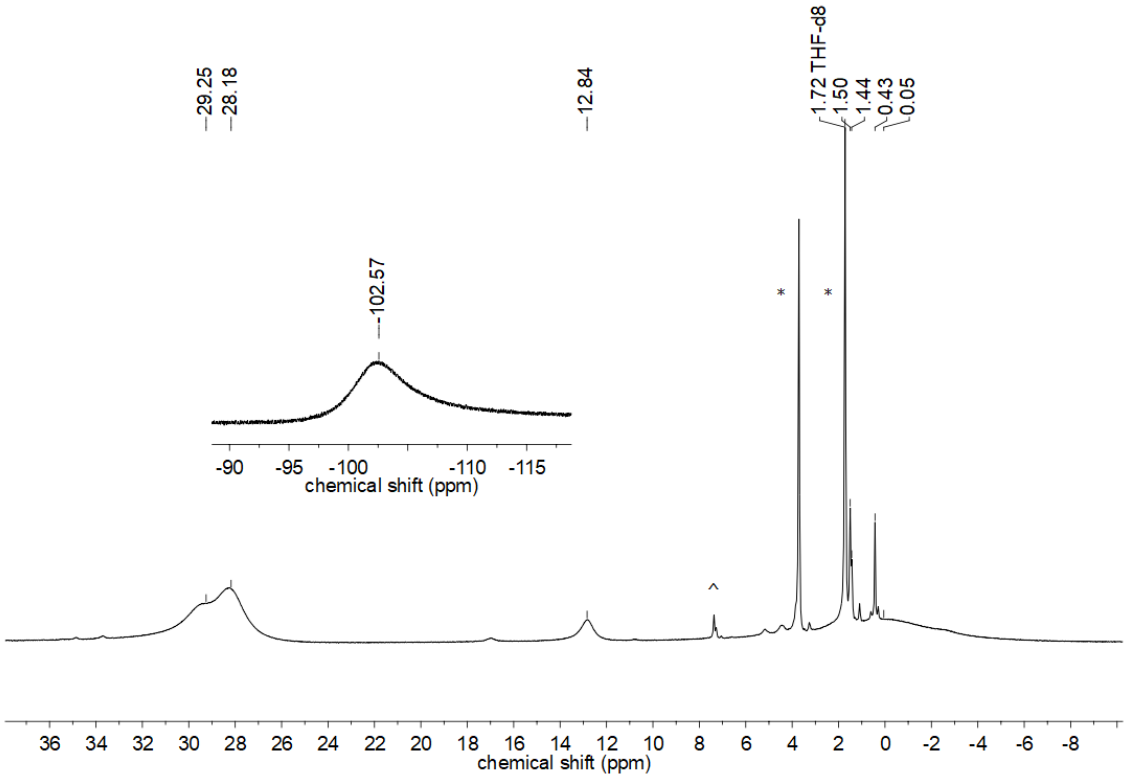

Figure S 14. *In Situ* ^{1}H NMR spectrum (300.2 MHz) of [NaFe(L^{2})$_2$] in THF-d_8 at 300 K. (* solvent, ^ impurities)

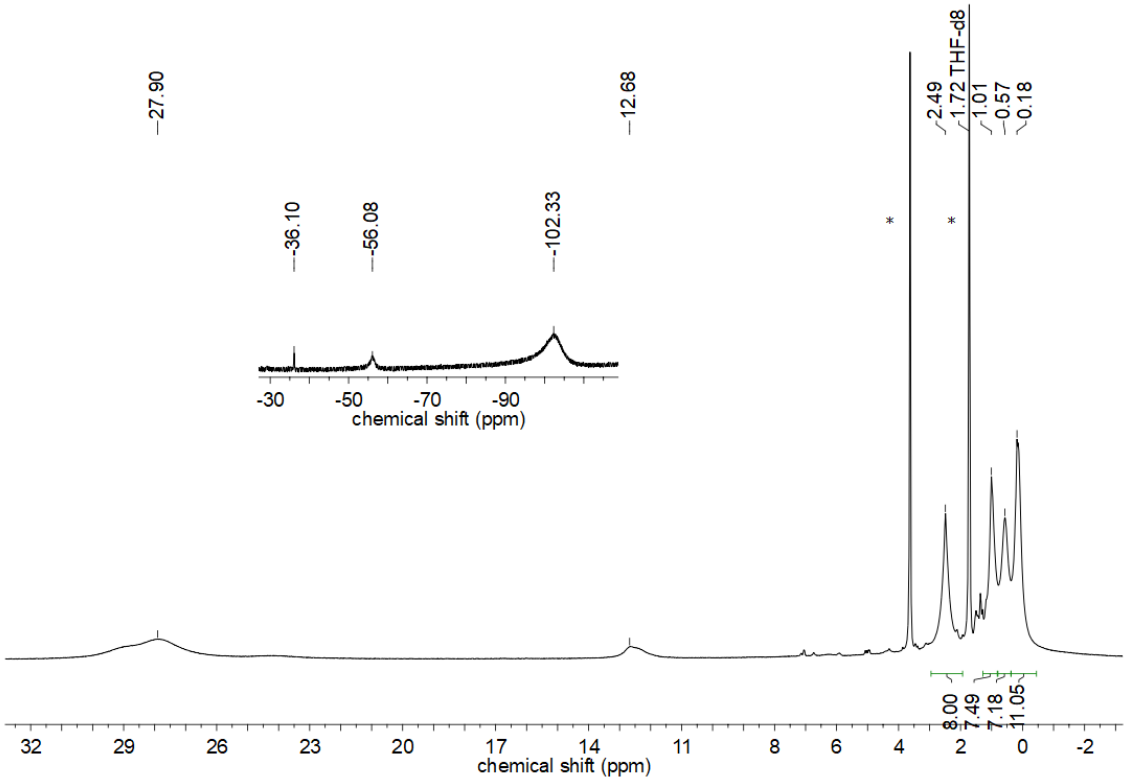

Figure S 15. ^{1}H NMR spectrum (500.1 MHz) of [NBu$_4$][Fe(L^2)$_2$] (**8**) in THF-d_8 at 300 K. (* solvent)

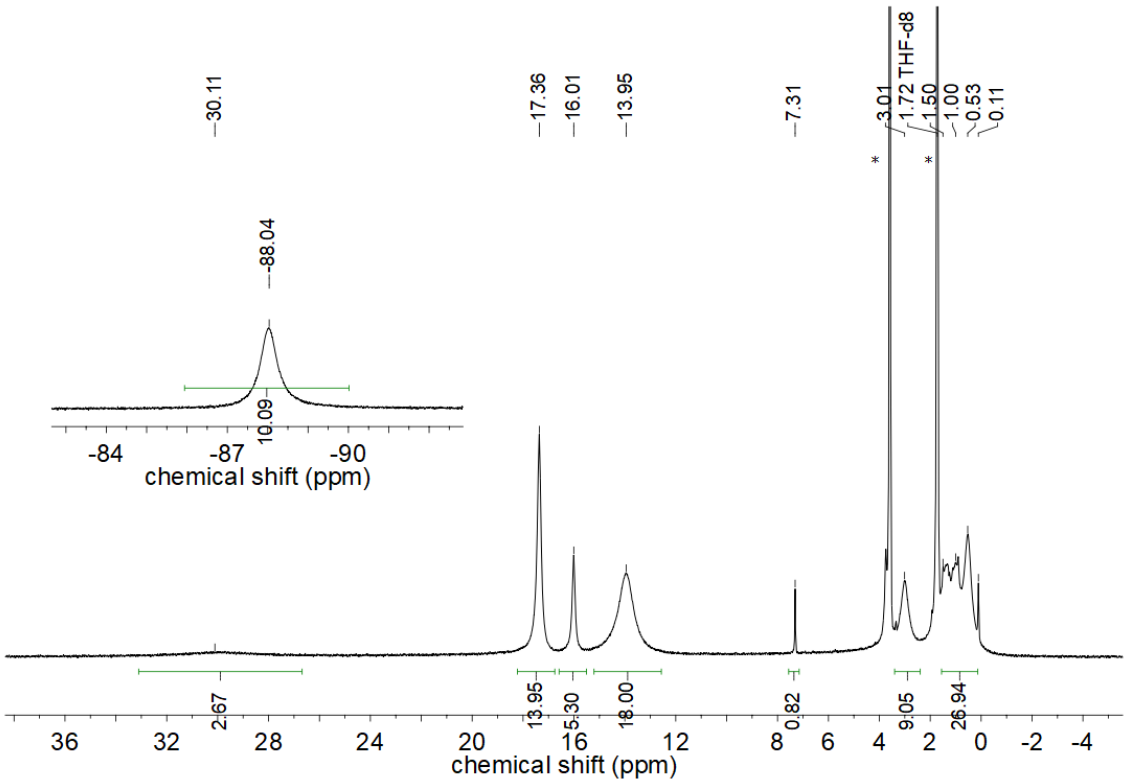

Figure S 16. ^{1}H NMR spectrum (500.1 MHz) of [Bu$_4$N][Co(L^2)$_2$] (**9**) in THF-d_8 at 300 K. (* solvent)

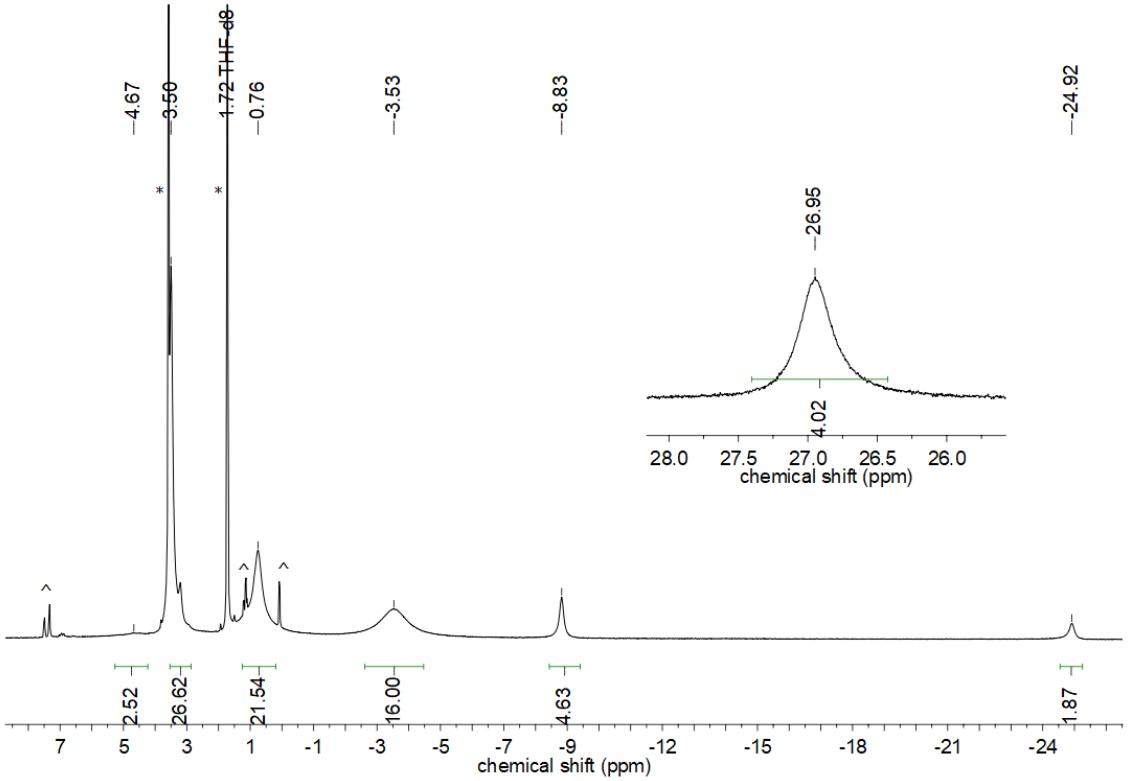

Figure S 17. ^{1}H NMR spectrum (300.2 MHz) of [K{18c6}][Fe(L^{2})$_2$)(η^{2}-PhCCPh)] (**10**) in THF-d_8 at 300 K. (* solvent, ^ impurities and residual diphenyl acetylene)

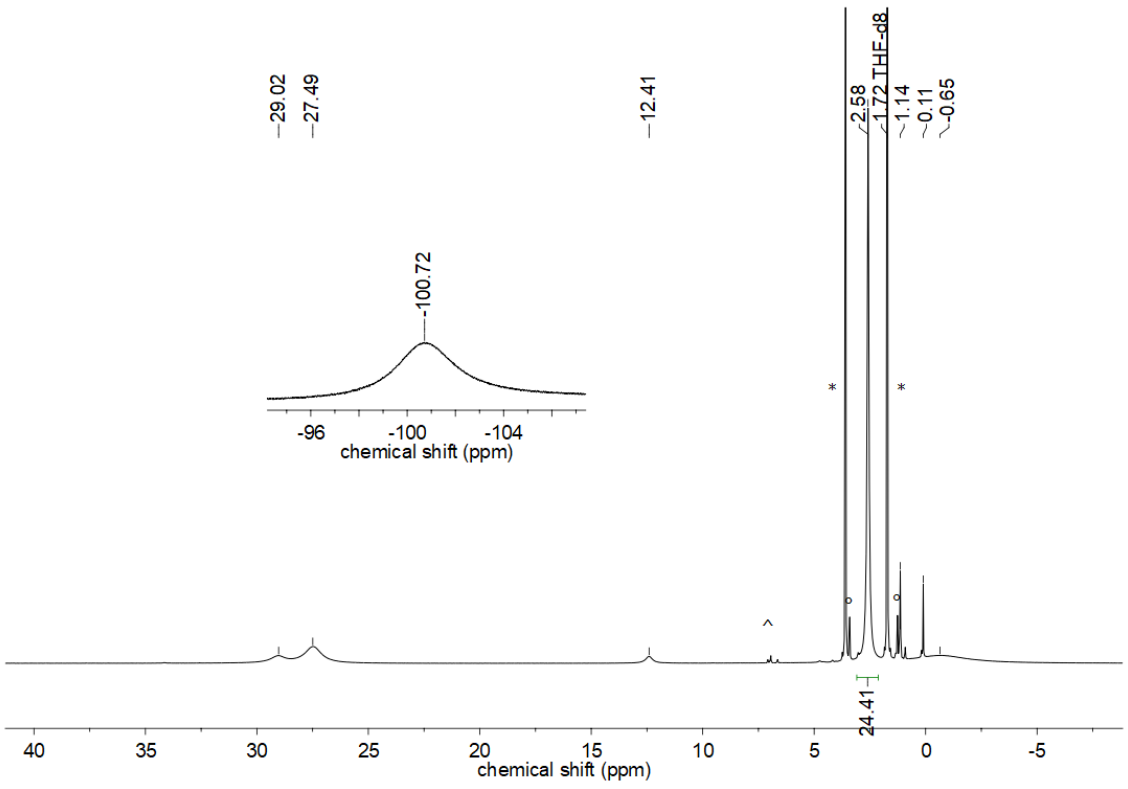

Figure S 18. ^{1}H NMR spectrum (500.1 MHz) of [K{18c6}][Fe(L^{2})$_2$] in THF-d_8 at 300 K. (* solvent, ° diethyl ether, ^ impurities)

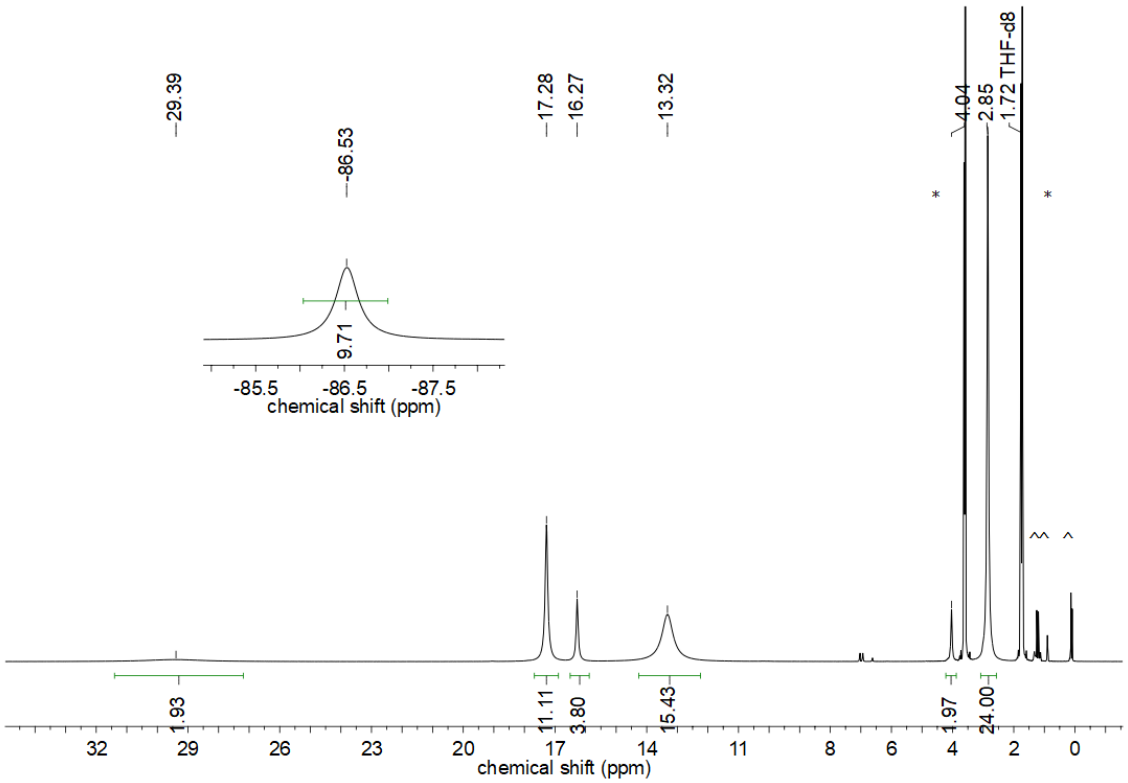

Figure S 19. ^{1}H NMR spectrum (500.1 MHz) of [K{18c6}][Co(L^{2})$_2$] in THF-d_8 at 300 K. (* solvent, ^ impurities)

Temperature-dependent ^{1}H NMR spectra of 4

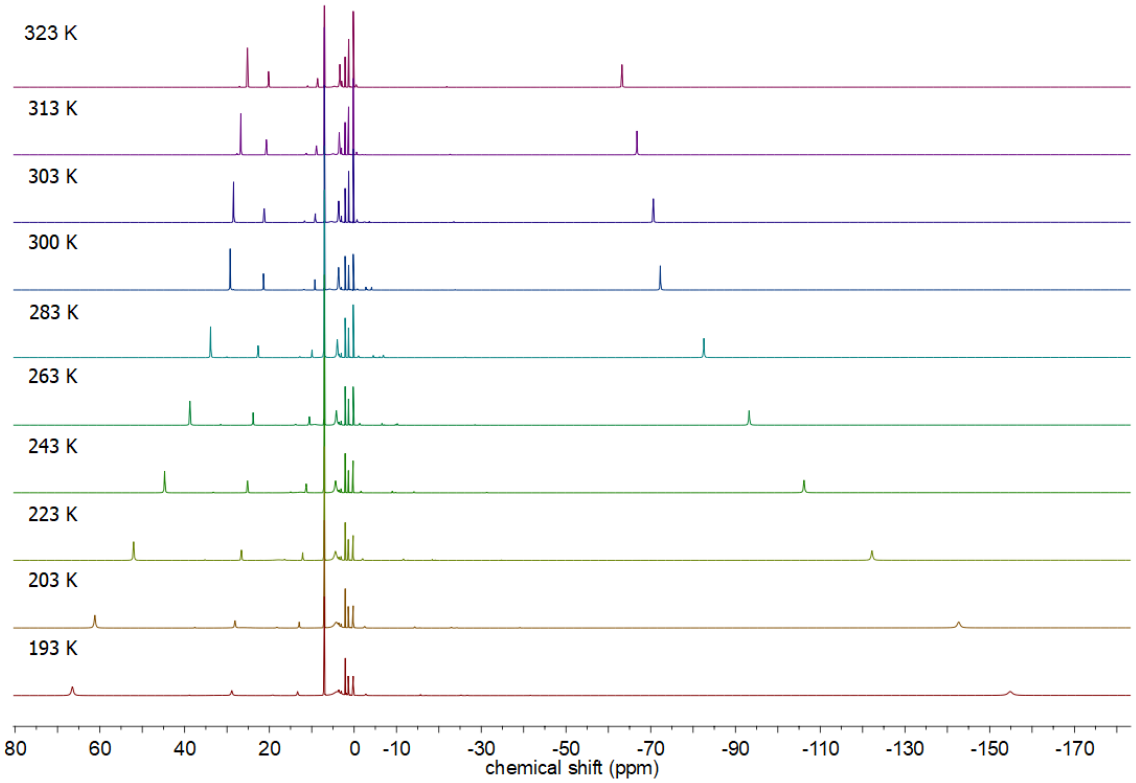

Figure S 20. Temperature-dependent ^{1}H NMR spectrum (500.1 MHz) of [KCo(L^{2})$_2$] (**4**) in toluene-d_8 from 323 K to 193 K.

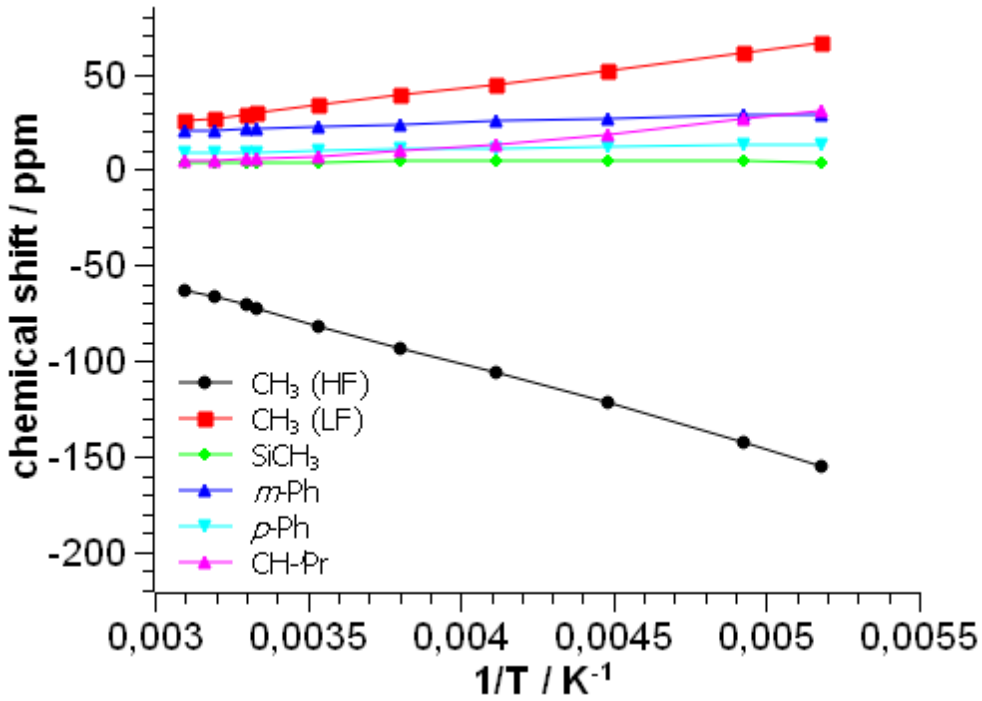

Figure S 21. Curie-Weiss plot of the temperature dependent ^{1}H NMR spectrum of [KCo(L^{2})$_2$] (**4**) in toluene-d_8 (HF: high field; LF: low field).

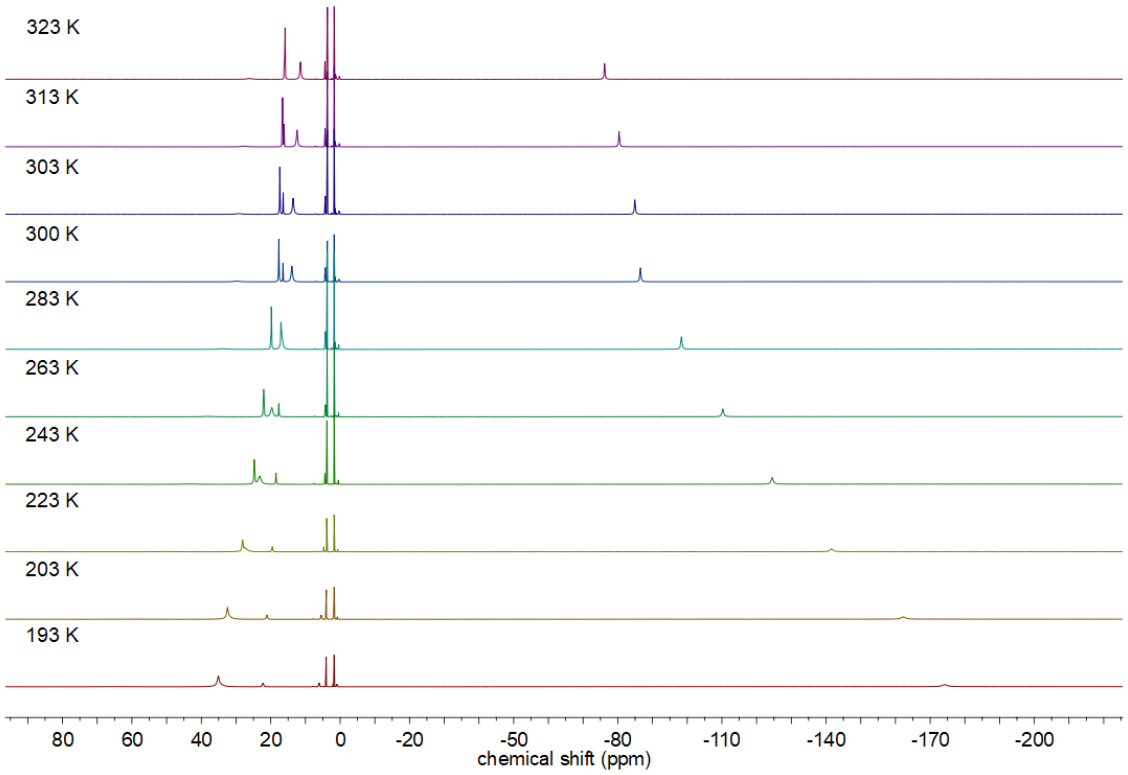

Figure S 22. Temperature-dependent ^{1}H NMR spectrum (500.1 MHz) of [KCo(L^{2})$_2$] (**4**) in THF-d_8 from 323 K to 193 K.

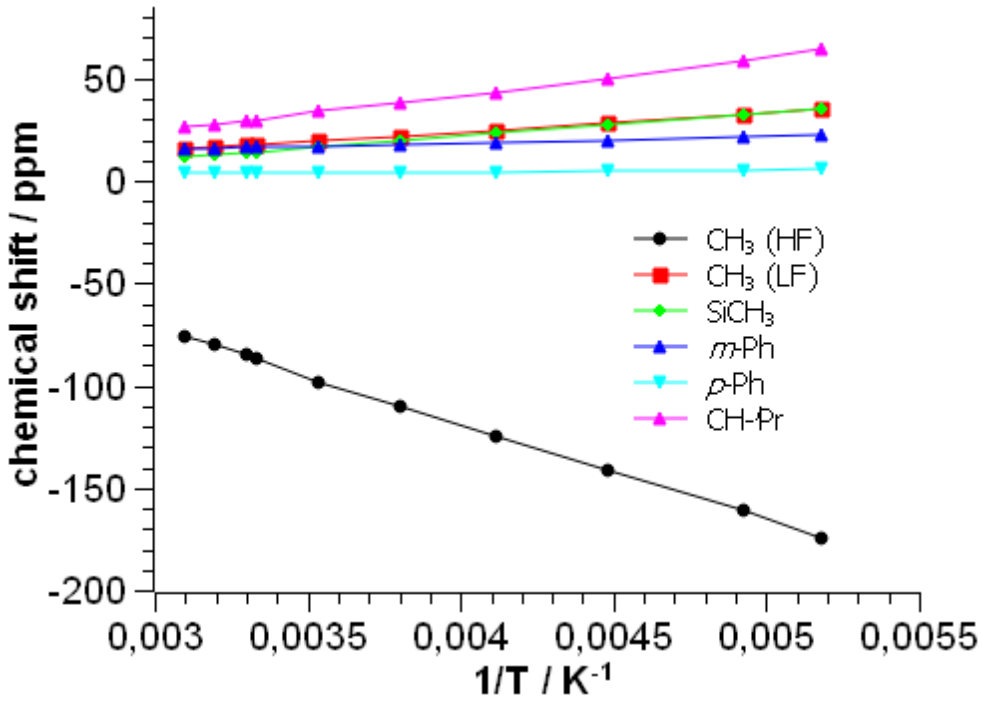

Figure S 23. Curie-Weiss plot of the temperature dependent ^{1}H NMR spectrum of [KCo(L^{2})$_2$] (**4**) in THF-d_8 (HF: high field; LF: low field).

Gradual addition of coordinating solvent to 4 in toluene-d_8

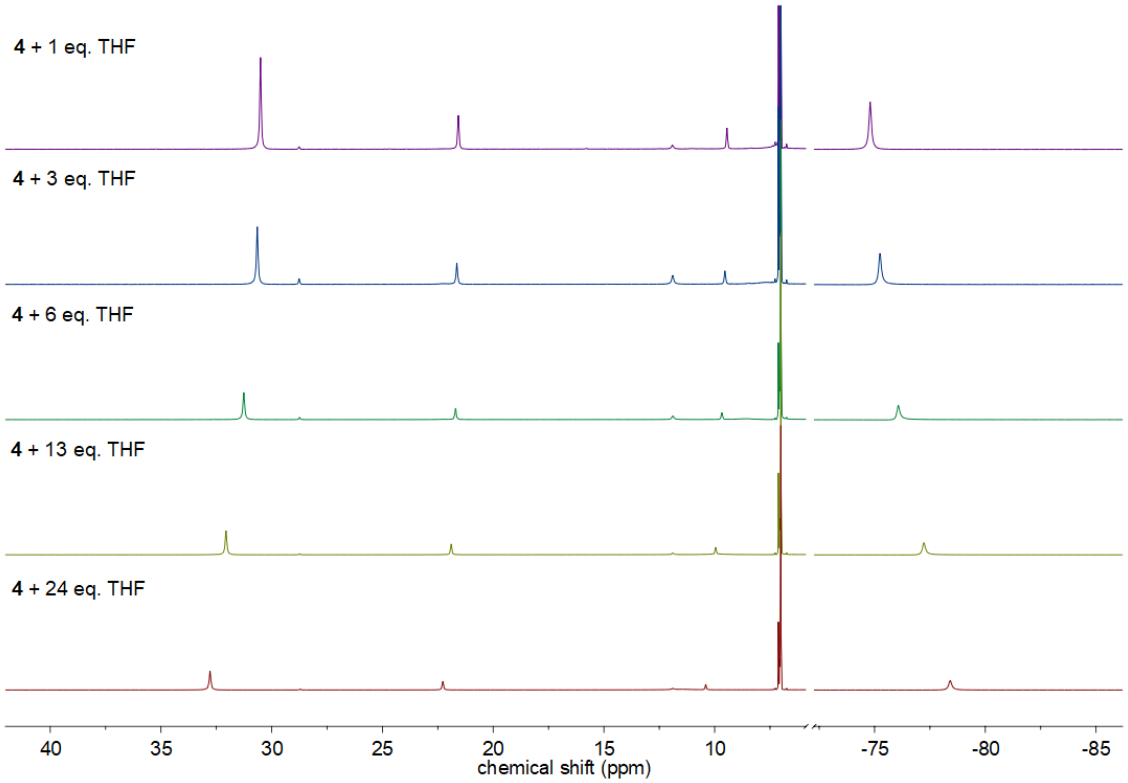

Figure S 24. Paramagnetic region of the ^{1}H NMR spectrum (300.2 MHz) of [KCo(L^2)$_2$] (**4**) in toluene-d_8 at 300 K by gradual addition of THF.

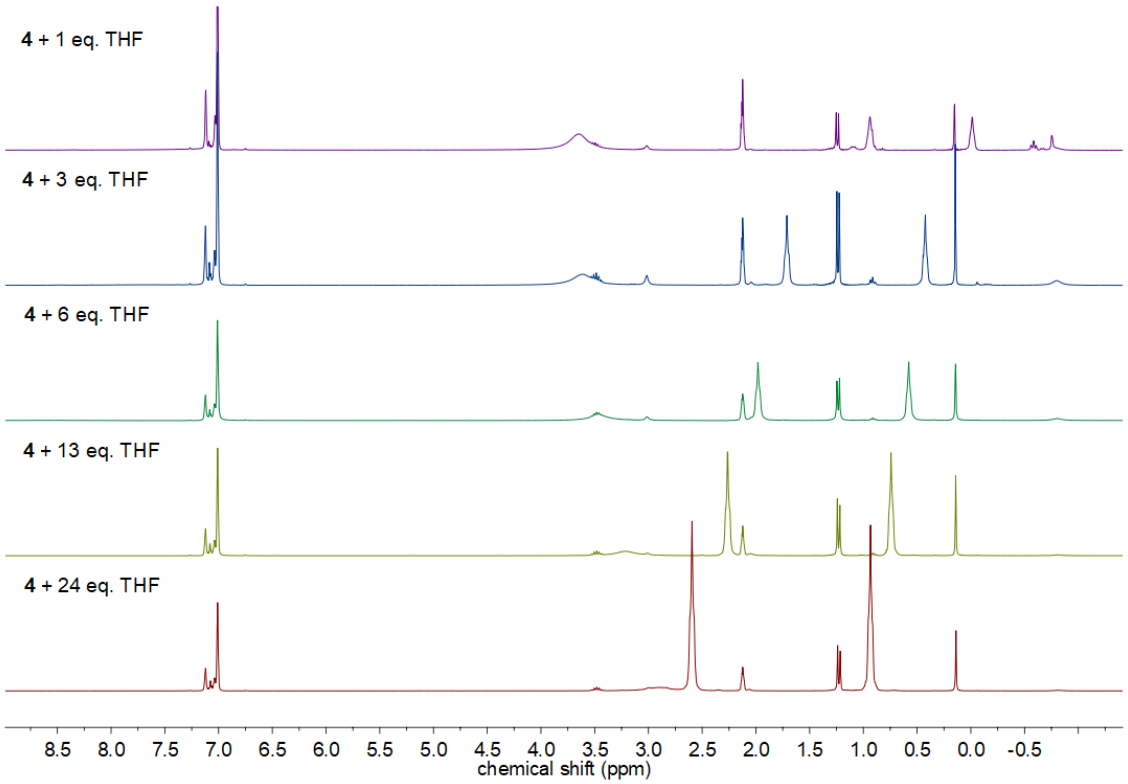

Figure S 25. Diamagnetic region of the ^{1}H NMR spectrum (300.2 MHz) of [KCo(L^2)$_2$] (**4**) in toluene-d_8 at 300 K by gradual addition of THF.

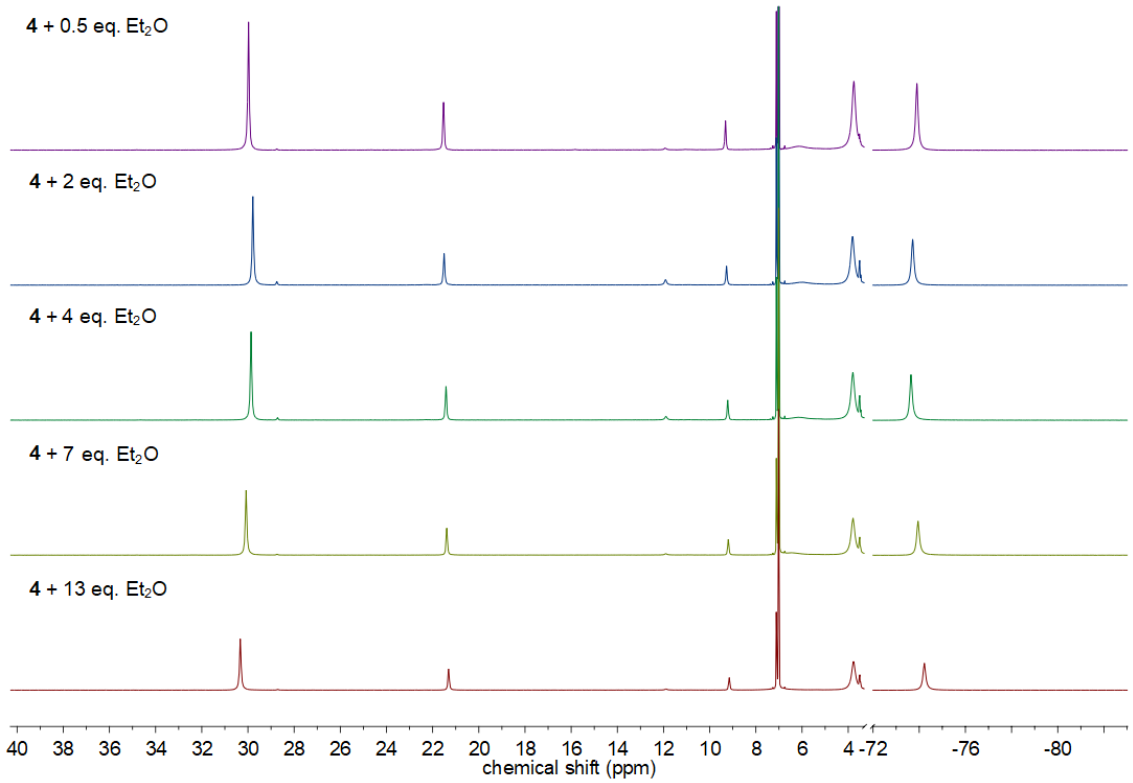

Figure S 26. Paramagnetic region of the ^{1}H NMR spectrum (300.2 MHz) of [KCo(L^{2})$_2$] (**4**) in toluene-d_8 at 300 K by gradual addition of Et_2O.

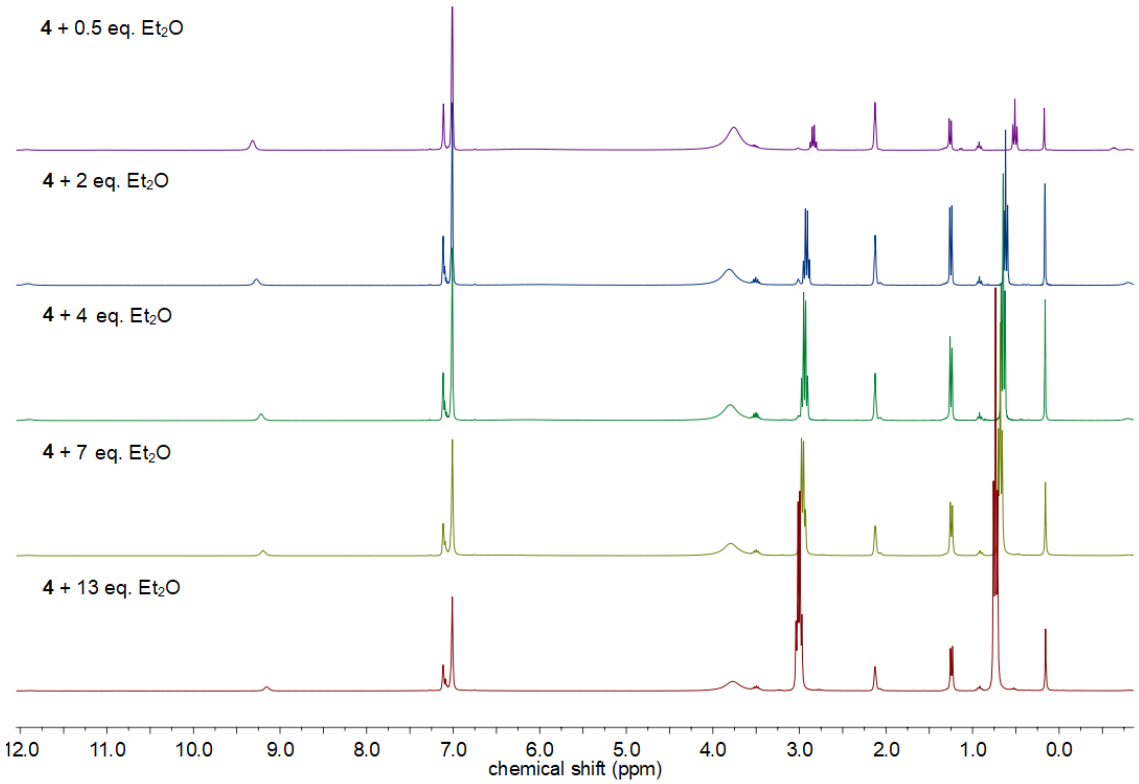

Figure S 27. Diamagnetic region of the ^{1}H NMR spectrum (300.2 MHz) of [KCo(L^{2})$_2$] (**4**) in toluene-d_8 at 300 K by gradual addition of Et_2O.

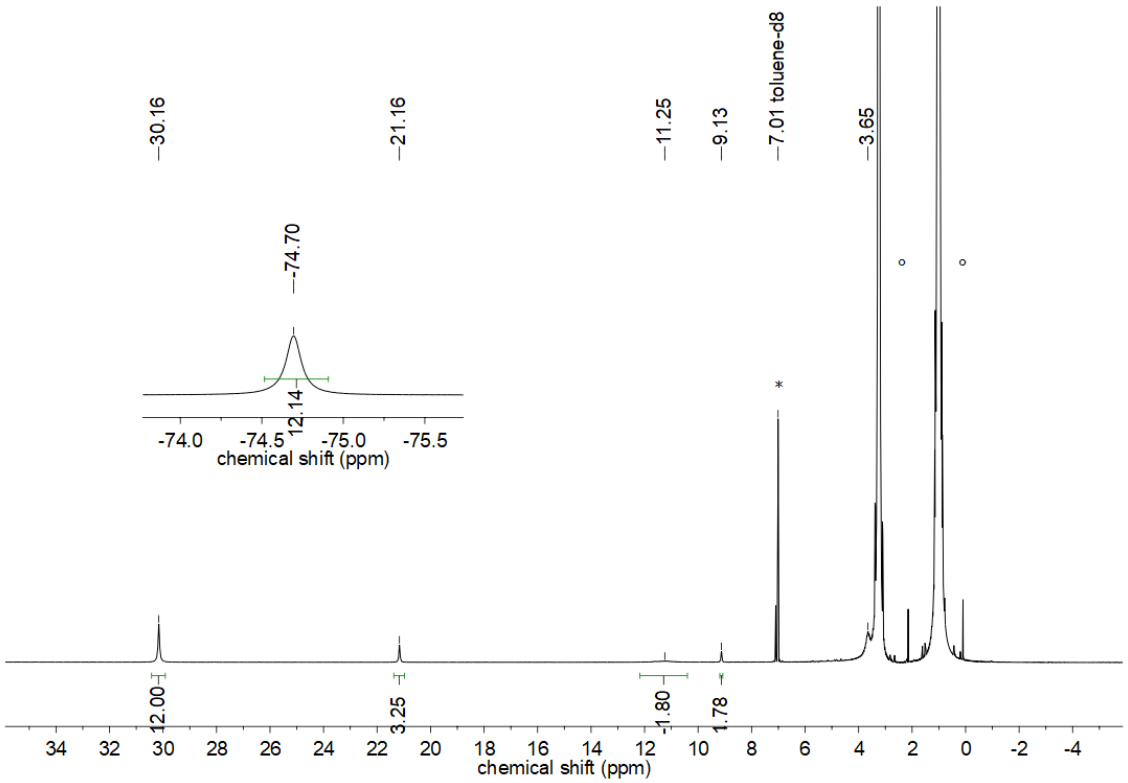

Figure S 28. ^{1}H NMR spectrum (300.2 MHz) of [KCo(L^{2})$_2$] (**4**) in toluene-d_8/Et$_2$O (1:1 v/v) at 300 K. (* solvent, ° diethyl ether)

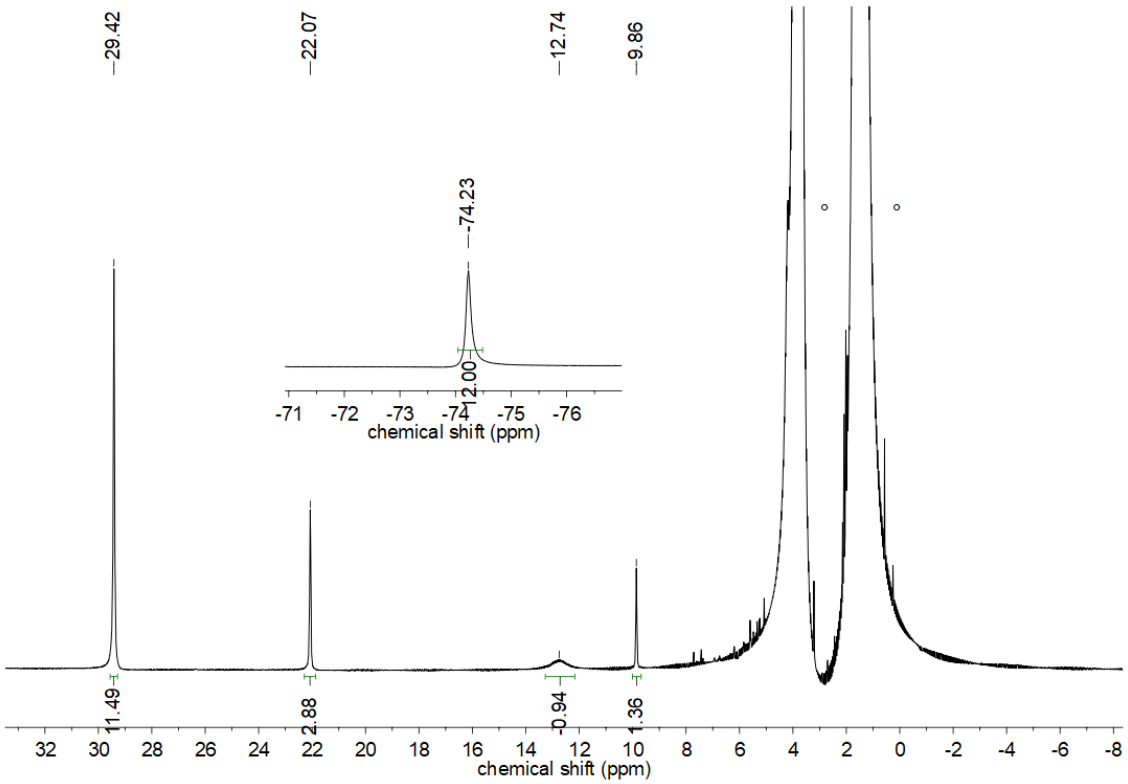

Figure S 29. ^{1}H NMR spectrum (300.2 MHz) of [KCo(L^{2})$_2$] (**4**) in Et$_2$O at 300 K. (° diethyl ether)

^{1}H NMR studies of 3 with diethyl ether

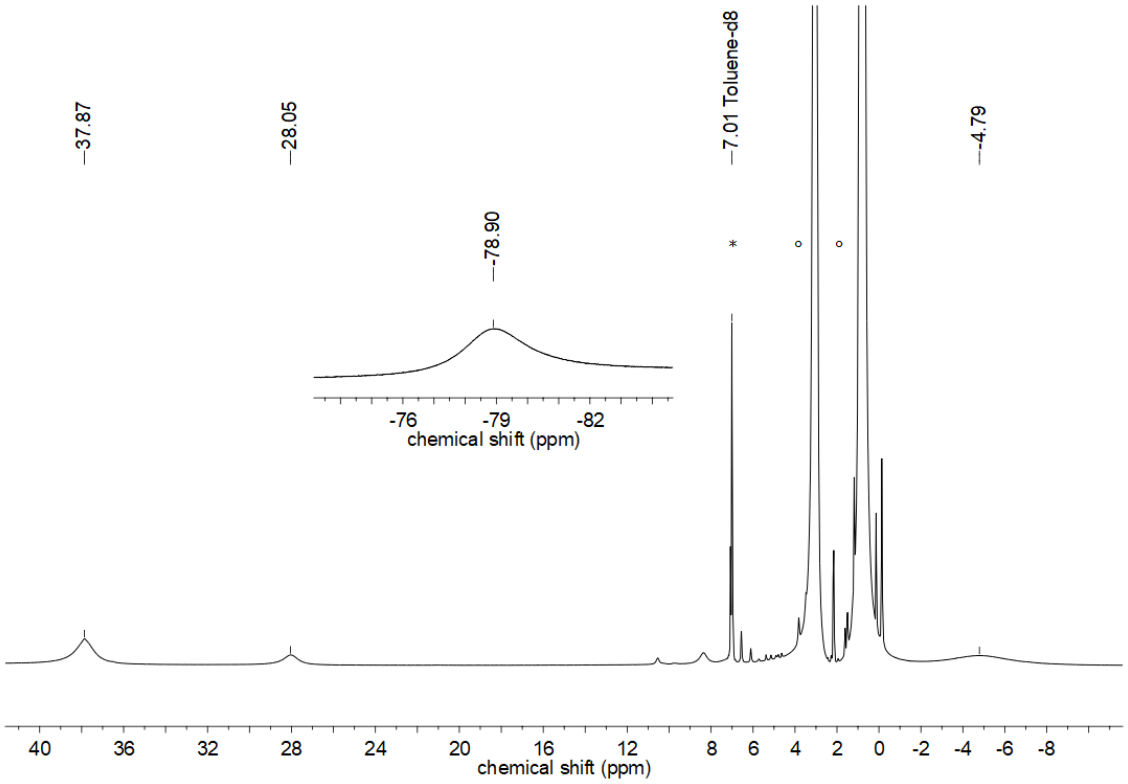

Figure S 30. ^{1}H NMR spectrum (300.2 MHz) of [KFe(L^2)$_2$] (**3**) in toluene-d_8/Et_2O (1:1 v/v) at 300 K. (* solvent, ° diethyl ether)

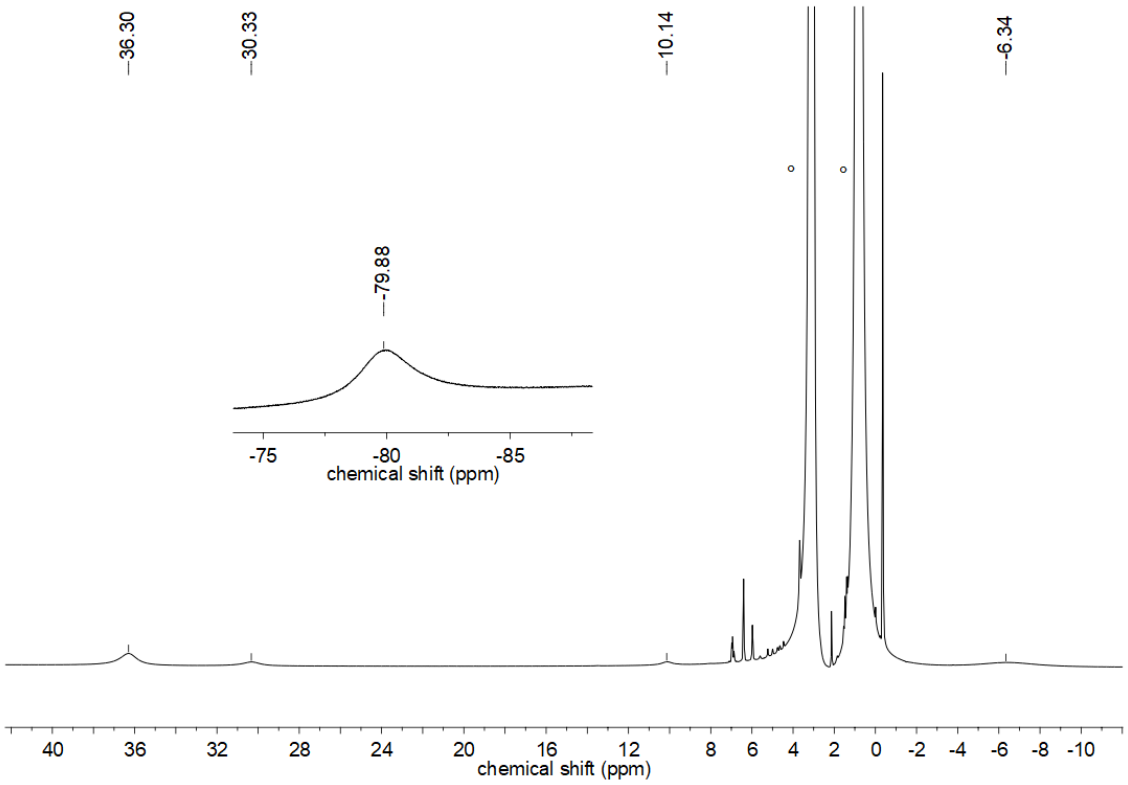

Figure S 31. ^{1}H NMR spectrum (300.2 MHz) of [KFe(L^2)$_2$] (**3**) in Et_2O at 300 K. (° diethyl ether)

***In Situ* ^{1}H NMR's of reacting 2 and 3 with diphenyl acetylene**

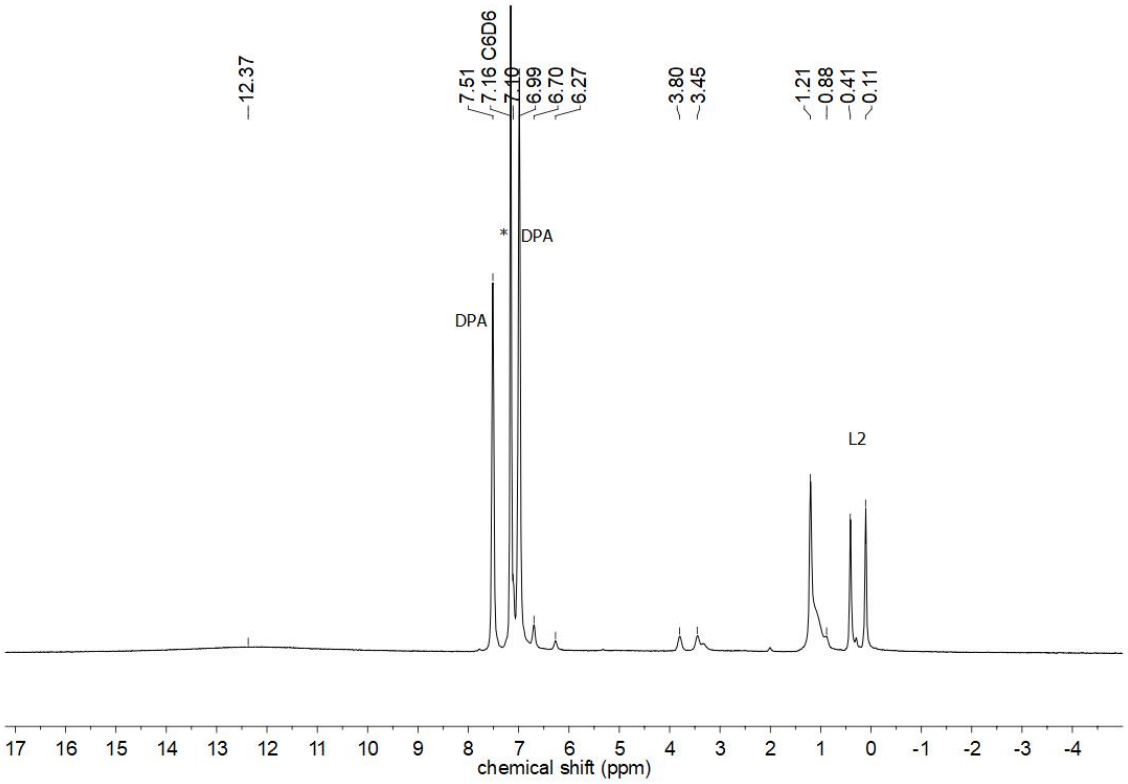

Figure S 32. *In Situ* ^{1}H NMR spectrum (300.2 MHz) of [KMn(L^2)$_2$] (**2**) with diphenyl acetylene in C_6D_6 at 300 K. (* solvent, ^{DPA} diphenyl acetylene, ^{L2} released KL^2 during the reaction)

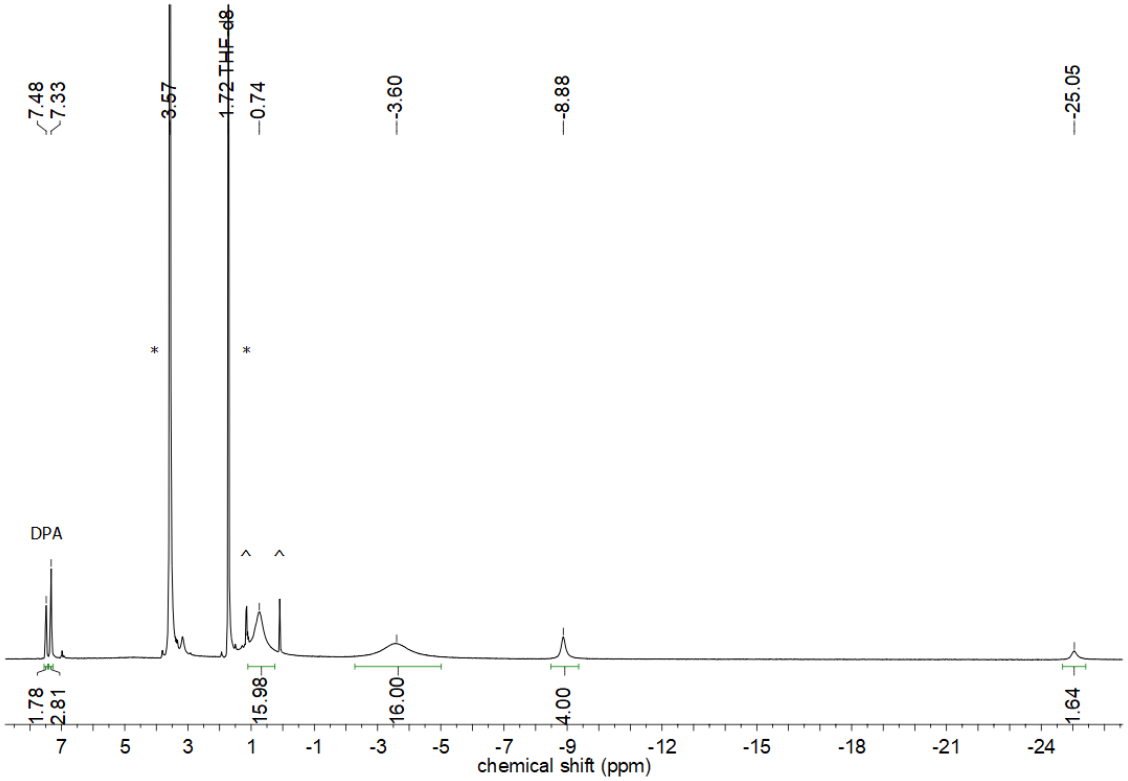

Figure S 33. *In Situ* ^{1}H NMR spectrum (300.2 MHz) of [K{18c6}][Fe(L^{2})$_2$] with diphenyl acetylene in THF-d_8 at 300 K. (* solvent, ^{DPA} diphenyl acetylene, ^ impurities)

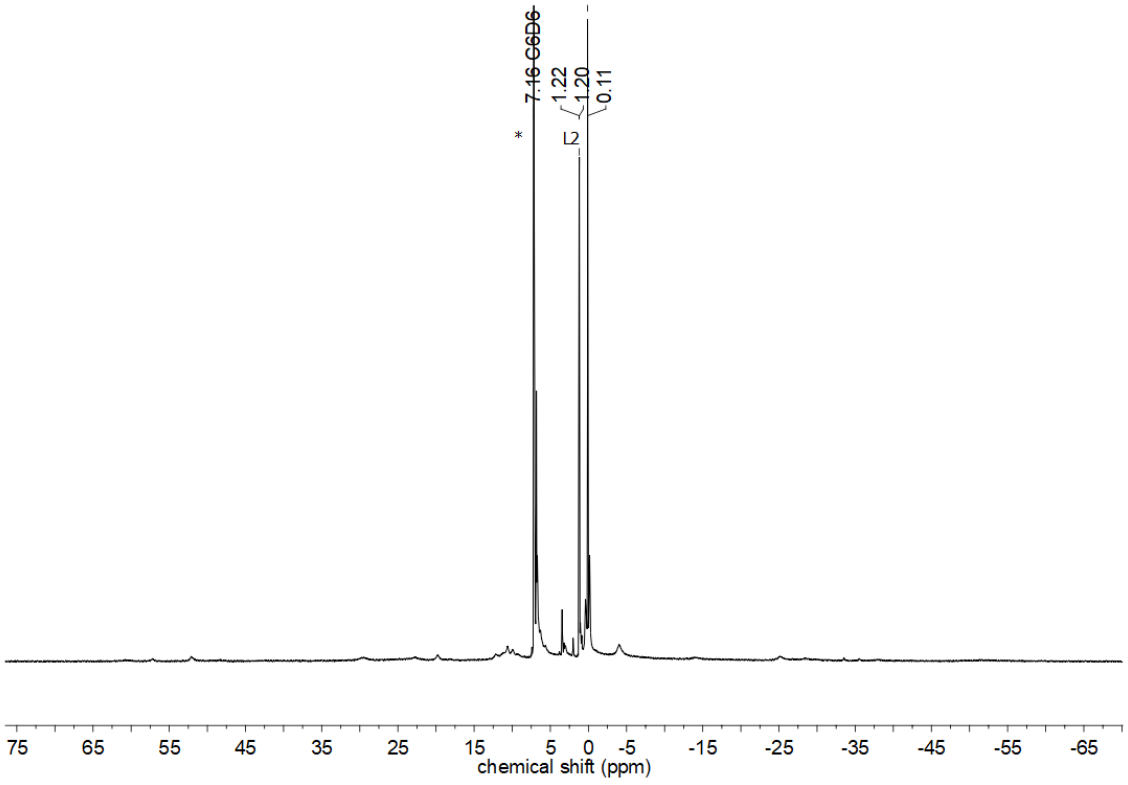

Figure S 34. *In Situ* ^{1}H NMR spectrum (300.2 MHz) of [KFe(L^{2})$_2$] (**3**) with diphenyl acetylene in C_6D_6 at 300 K. (* solvent, ^{L2} released KL^{2} during the reaction)

2 UV/Vis spectra

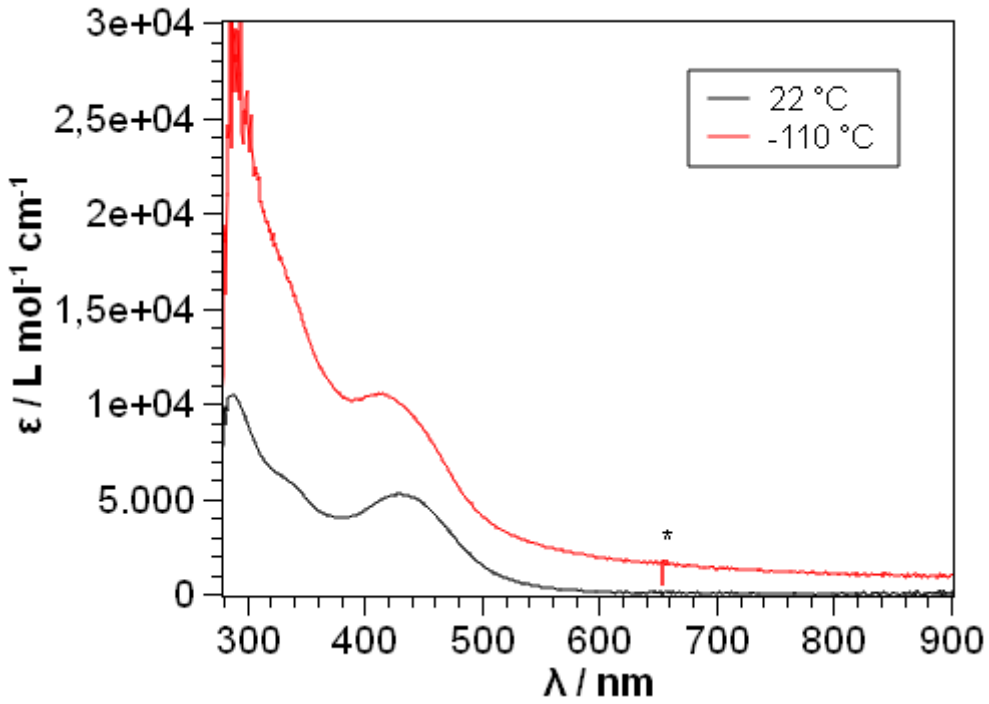

Figure S 35. UV/Vis spectrum of [KCr(L^1)$_2$] (**1**) in toluene. The signal caused by detector exchange is indicated by *.

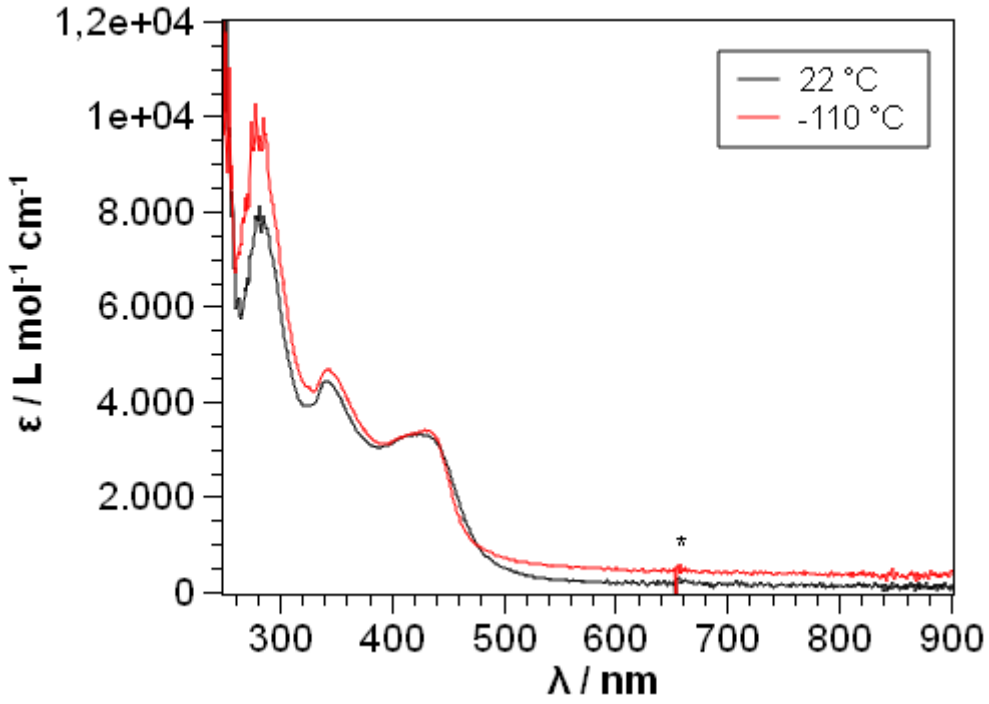

Figure S 36. UV/Vis spectrum of [KCr(L^1)$_2$] (**1**) in THF. The signal caused by detector exchange is indicated by *.

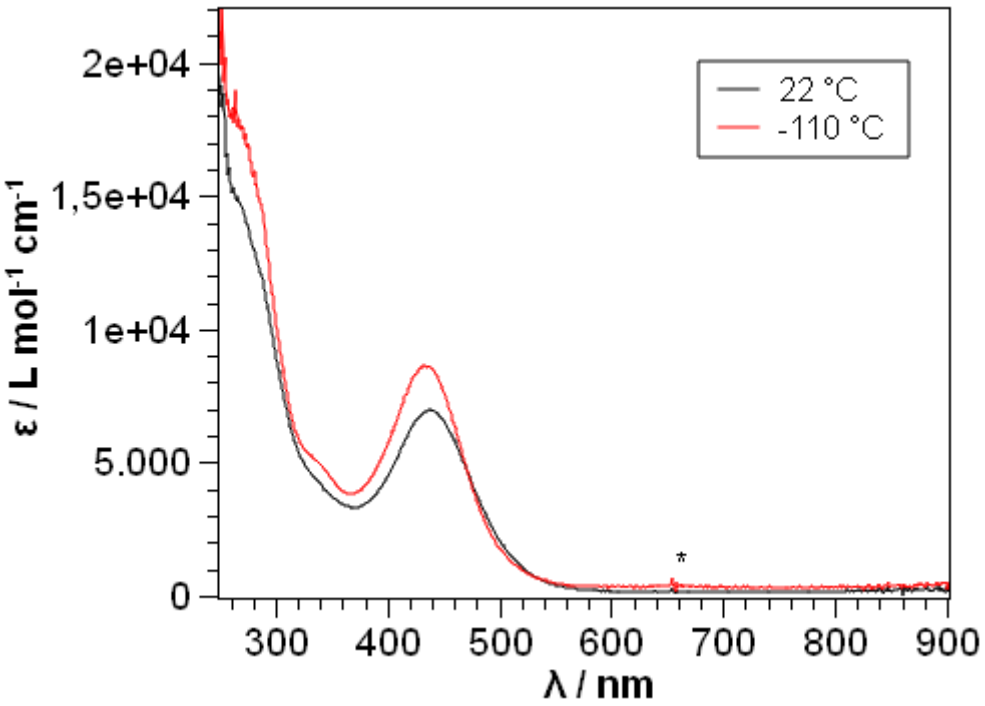

Figure S 37. UV/Vis spectrum of [KCr(L^1)$_2$] (**1**) in Et_2O. The signal caused by detector exchange is indicated by *.

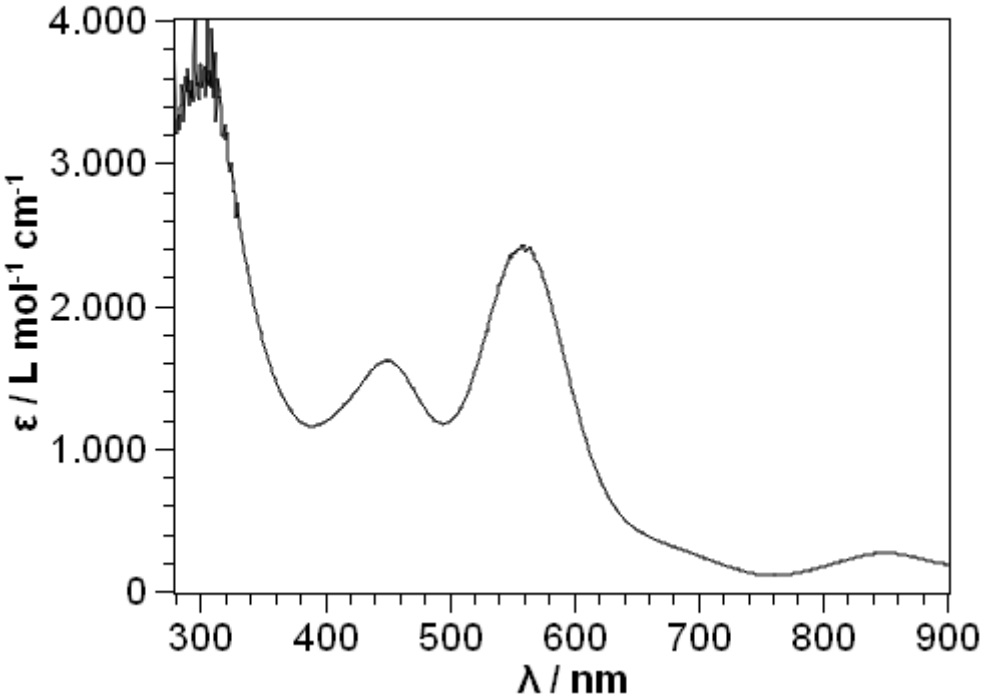

Figure S 38. UV/Vis spectrum of [KMn(L^2)$_2$] (**2**) in Et_2O.

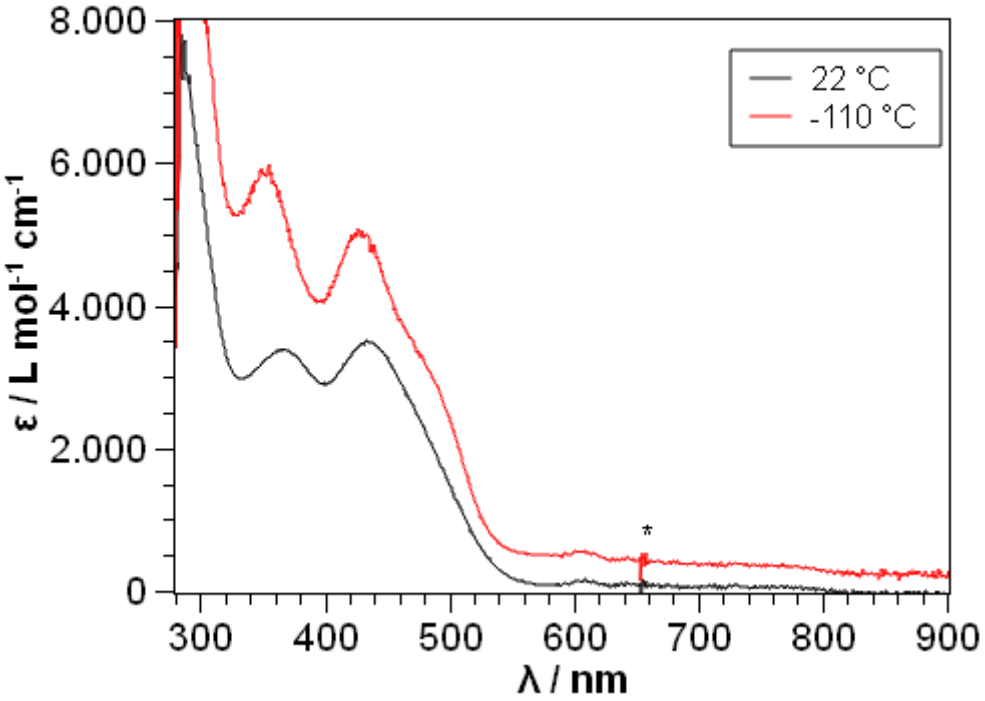

Figure S 39. UV/Vis spectrum of [KFe(L^2)$_2$] (**3**) in toluene. The signal caused by detector exchange is indicated by *.

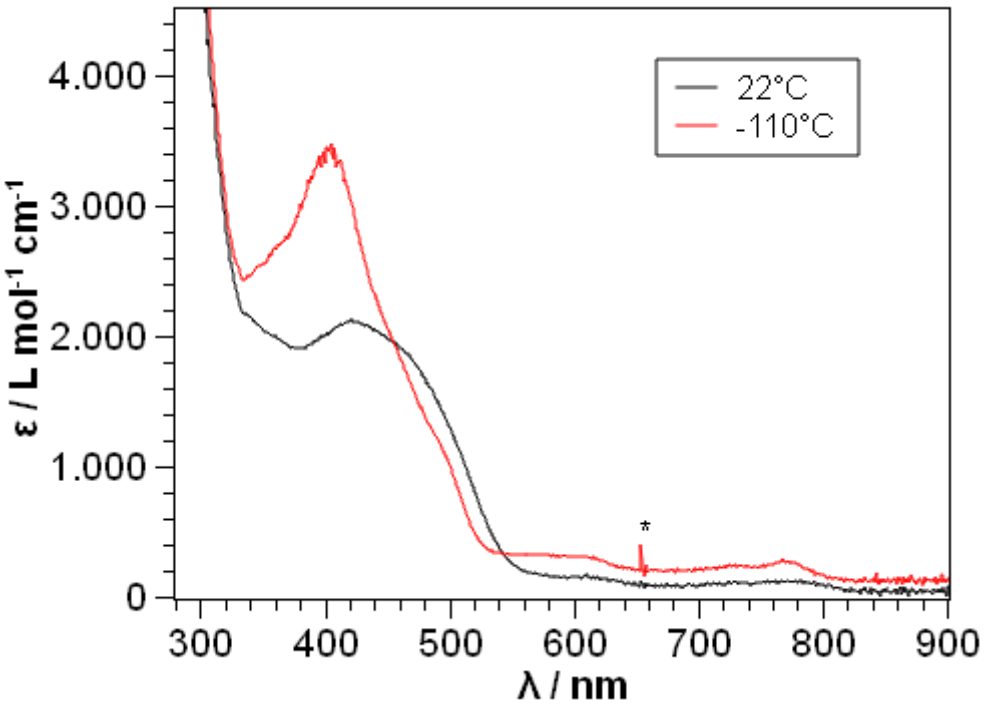

Figure S 40. UV/Vis spectrum of [KFe(L^2)$_2$] (**3**) in THF. The signal caused by detector exchange is indicated by *.

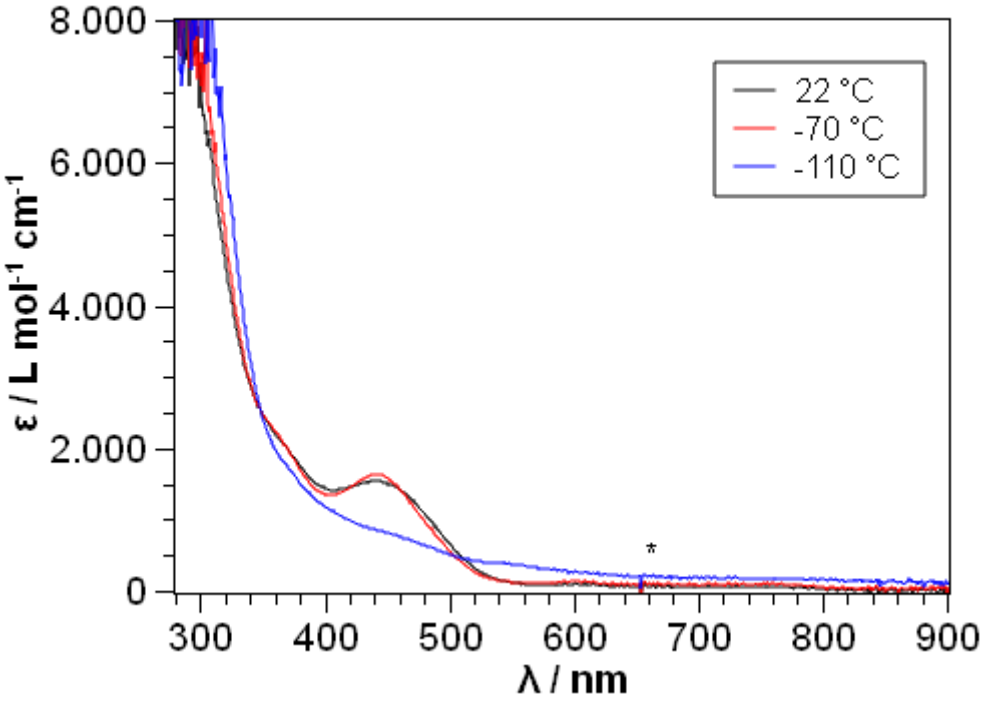

Figure S 41. UV/Vis spectrum of [KFe(L^2)$_2$] (**3**) in Et_2O. The signal caused by detector exchange is indicated by *.

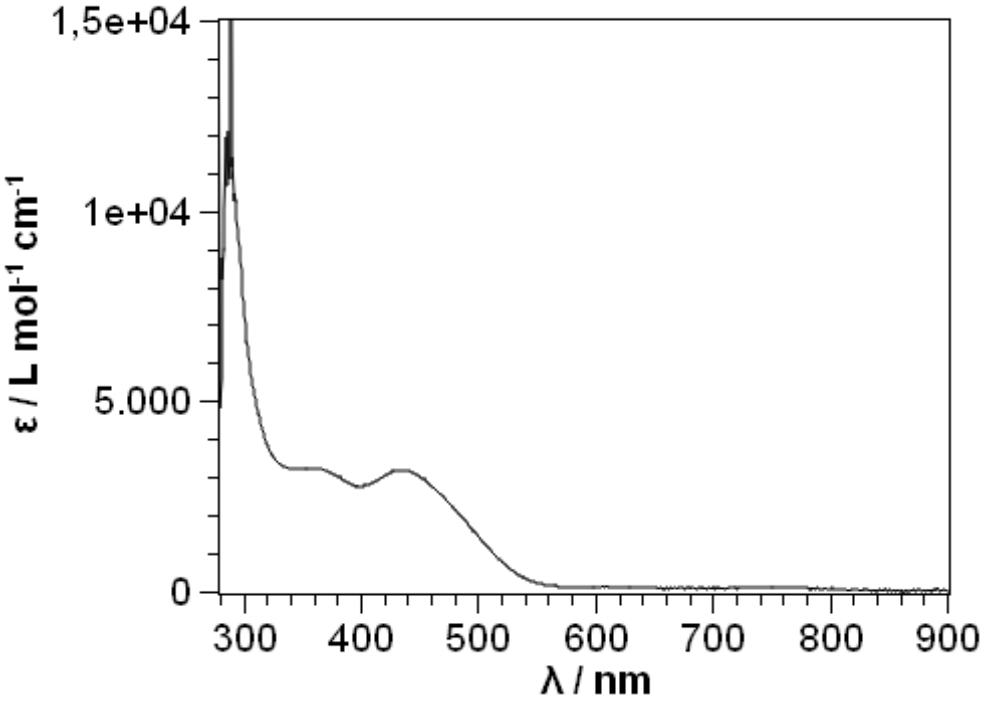

Figure S 42. UV/Vis spectrum of [K(DMAP)$_2$Fe(L^2)$_2$] (**3**.2DMAP) in toluene.

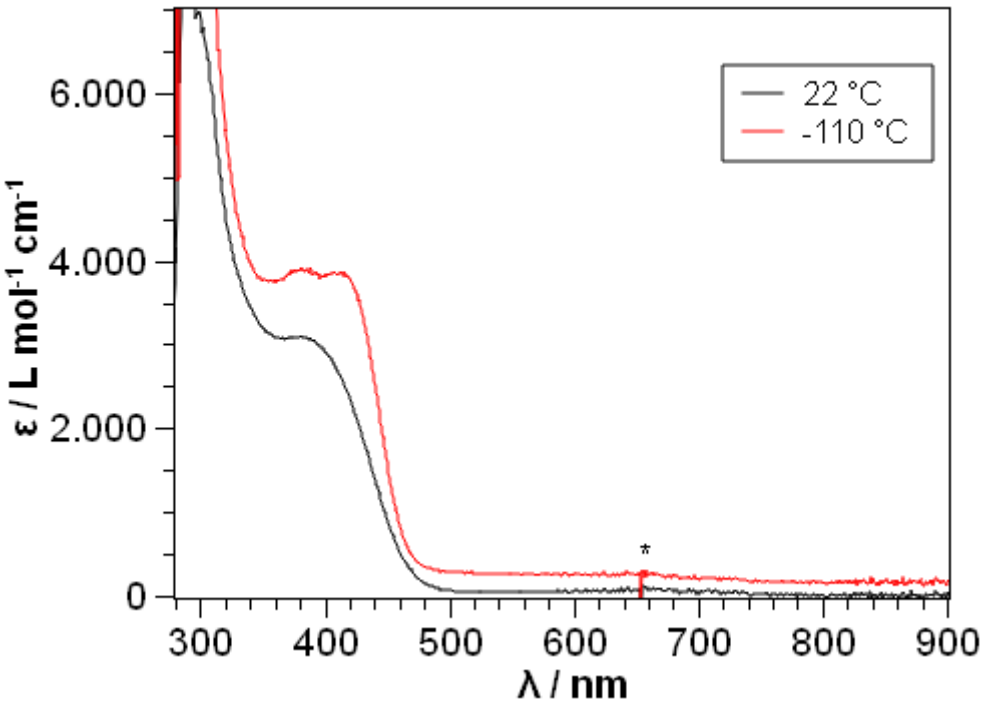

Figure S 43. UV/Vis spectrum of [KCo(L^2)$_2$] (**4**) in toluene. The signal caused by detector exchange is indicated by *.

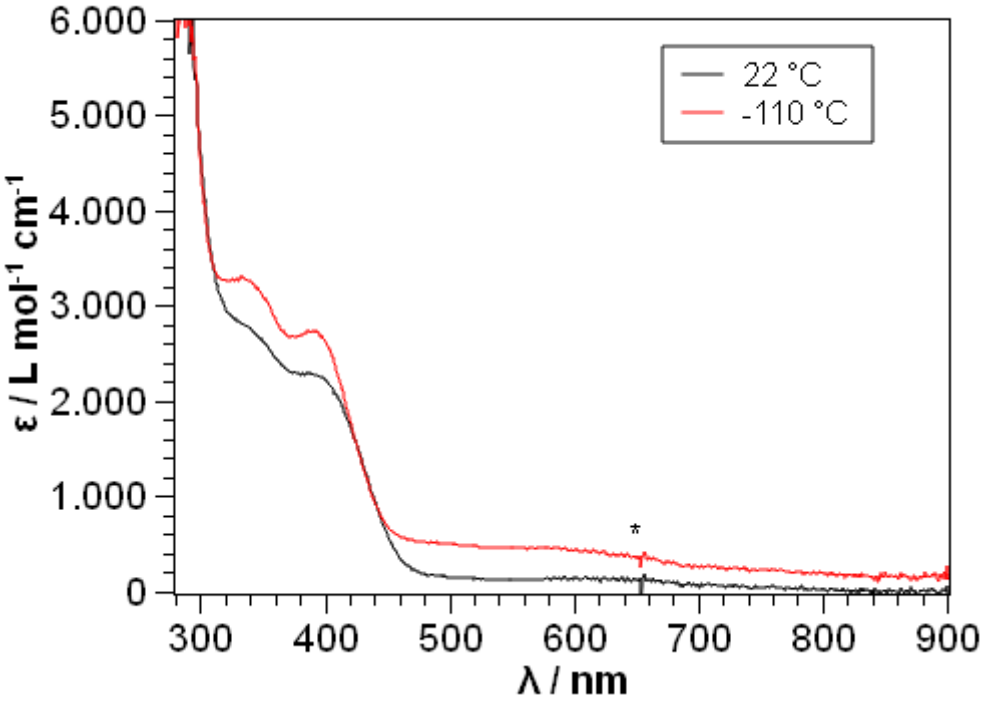

Figure S 44. UV/Vis spectrum of [KCo(L^2)$_2$] (**4**) in THF. The signal caused by detector exchange is indicated by *.

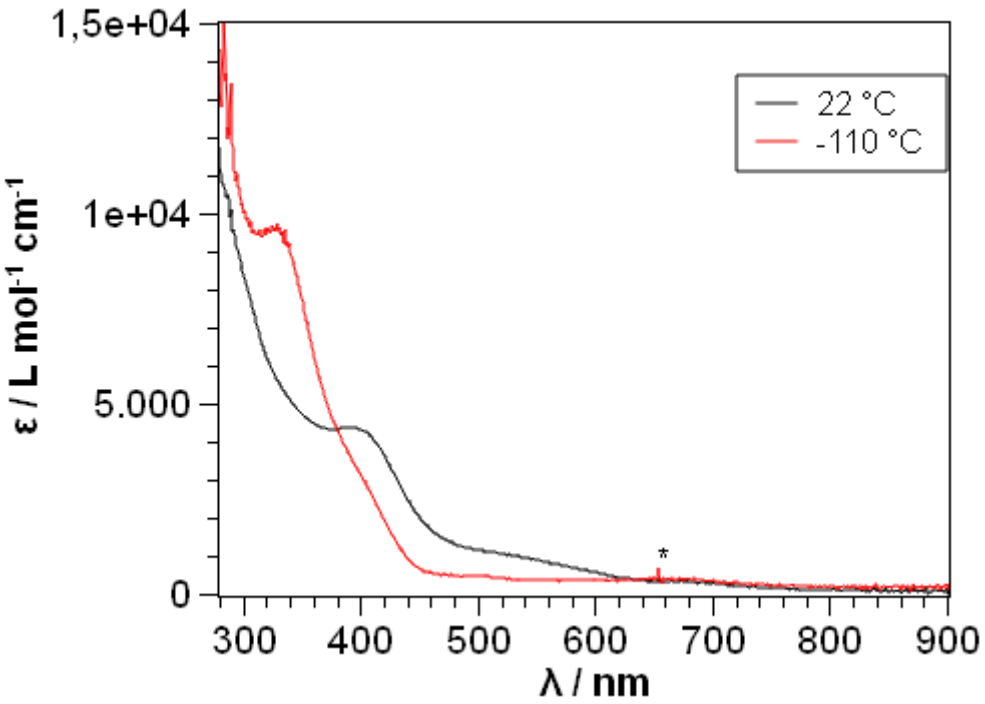

Figure S 45. UV/Vis spectrum of [KCo(L^2)$_2$] (**4**) in Et_2O. The signal caused by detector exchange is indicated by *.

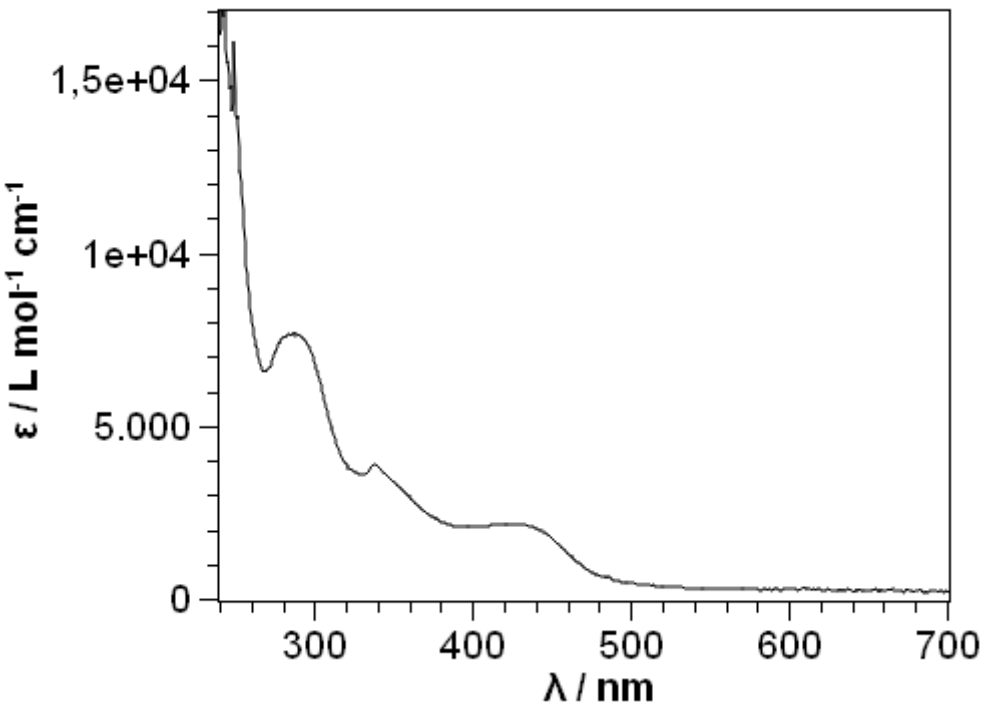

Figure S 46. UV/Vis spectrum of [K{18c6}][Cr(L^1)$_2$] (**5**) in THF.

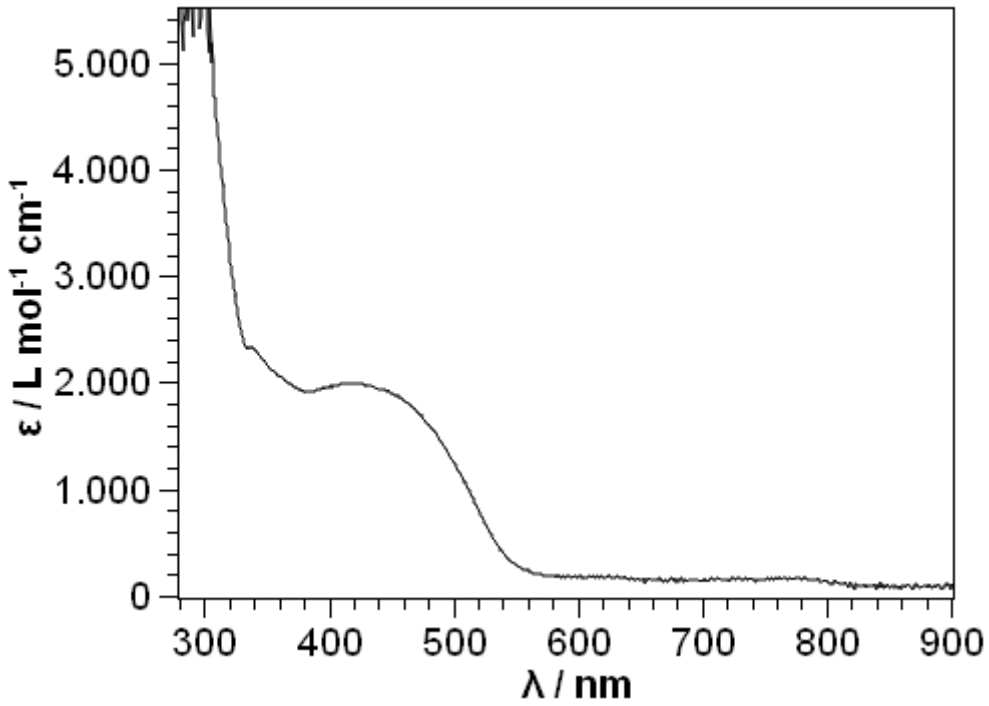

Figure S 47. UV/Vis spectrum of [Li{12c4}$_2$][Fe(L^2)$_2$] (**6**) in THF.

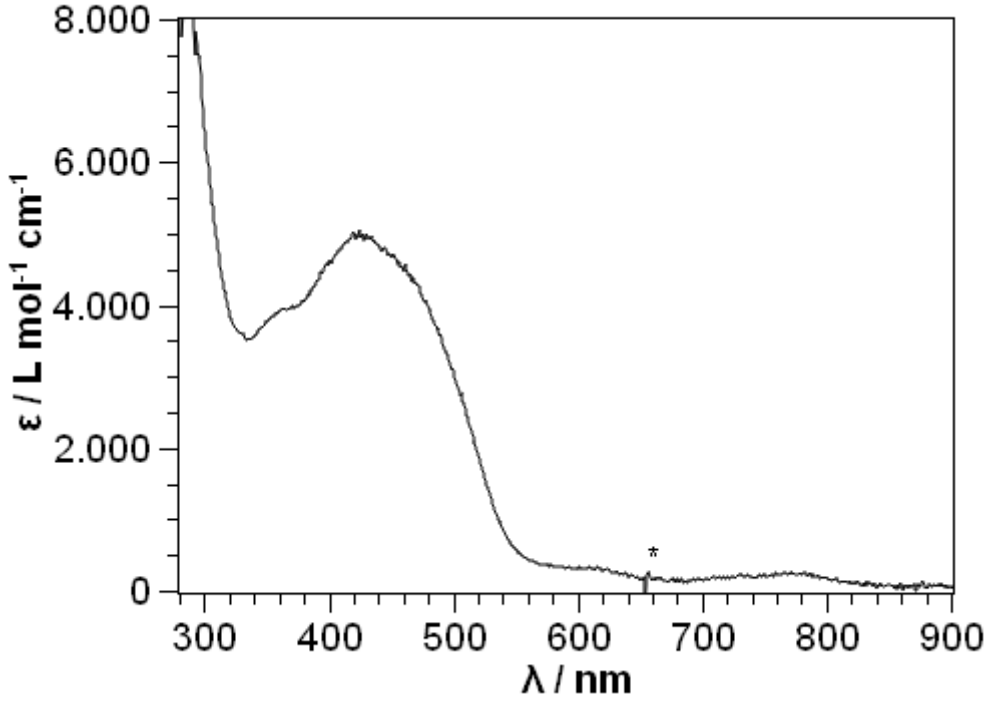

Figure S 48. UV/Vis spectrum of [Na{18c6}][Fe(L^2)$_2$] (**7**) in THF. The signal caused by detector exchange is indicated by *.

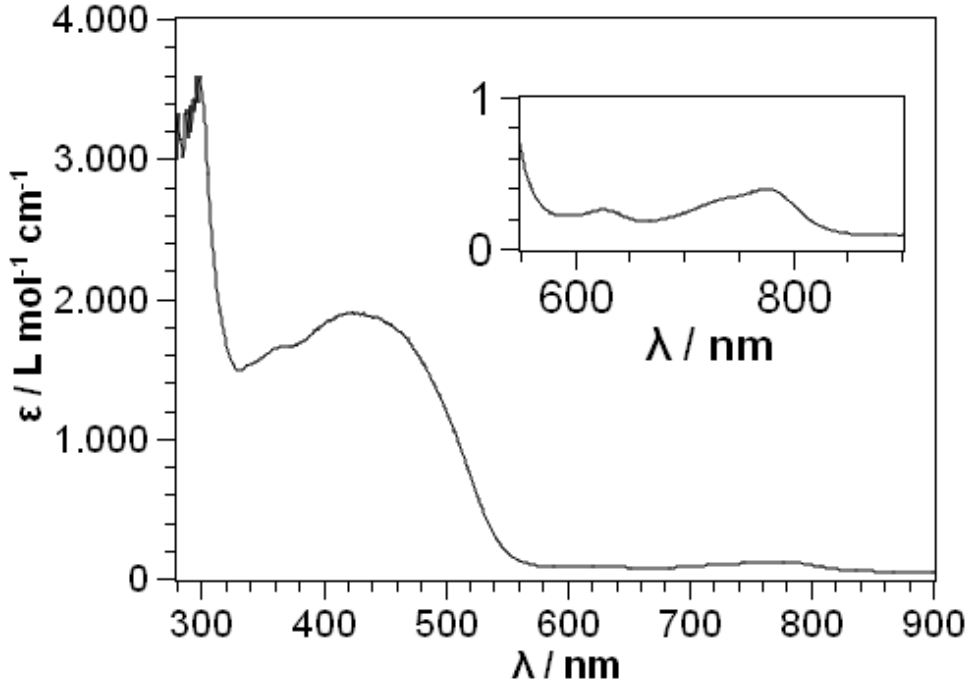

Figure S 49. UV/Vis spectrum of $[NBu_4][Fe(L^2)_2]$ (**8**) in THF.

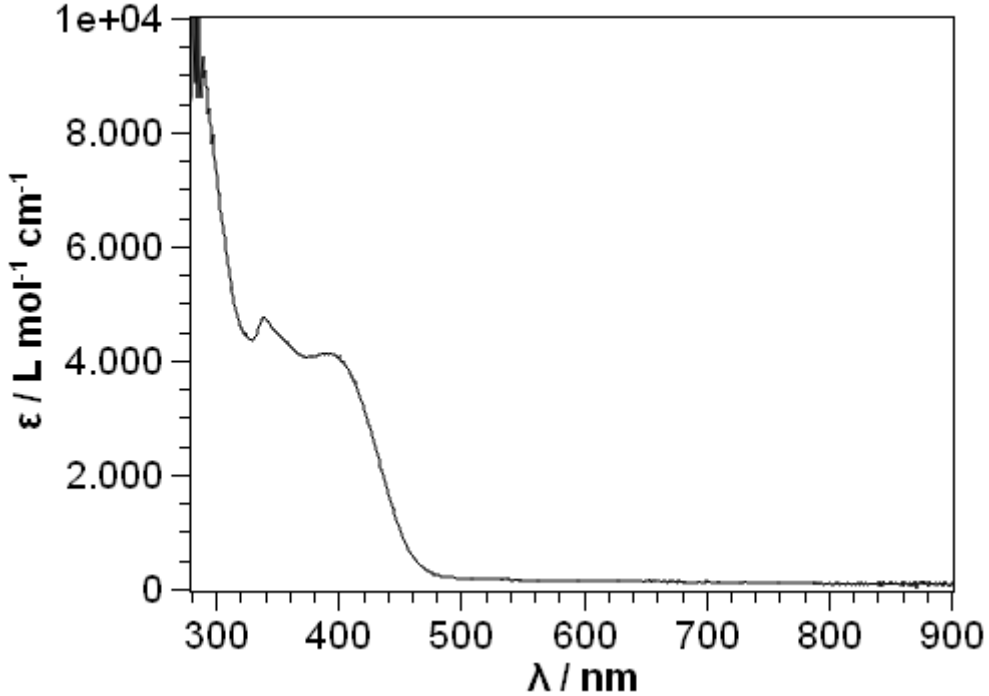

Figure S 50. UV/Vis spectrum of $[NBu_4][Co(L^2)_2]$ (**9**) in THF.

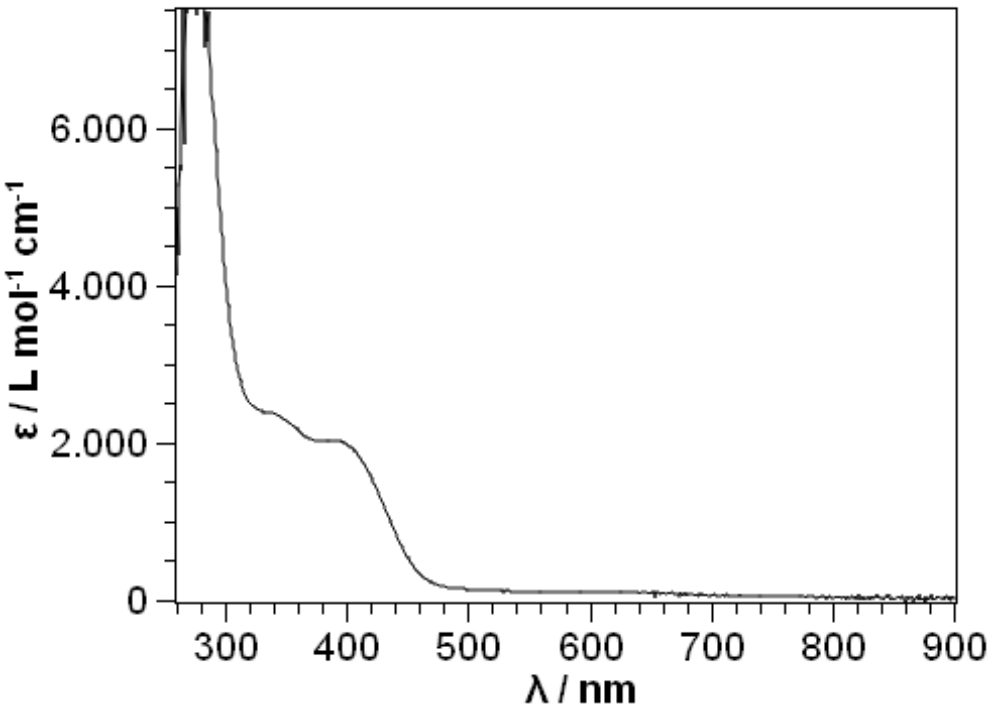

Figure S 51. UV/Vis spectrum of [K{18c6}][Co(L^2)$_2$] in THF.

Table S 1. Location of UV/Vis absorption maxima in compounds **1** − **9** and [K{18c6}][M(L^2)$_2$] (M = Fe, Co, L^2 = −N(Dipp)SiMe$_3$)) in the range from 280 − 900 nm. *UV/Vis spectrum was recorded but no absorption coefficients were given in the original report.

		solvent	T	λ(ε) / nm(Lmol^{-1}cm^{-1})
Cr	**1**	toluene	r.t.	431 (5210)
			−100 °C	419 (10430)
		THF	r.t.	286 (>7930), 343 (4440), 426 (3320)
			−100 °C	286 (9980), 343 (4680), 428 (3370)
		Et_2O	r.t.	435 (6940)
			−100 °C	433 (8670)
	5	THF	r.t.	288 (7710), 338 (3880), 421 (2160)
Mn	**2**	Et_2O	r.t.	448 (1610), 565 (2410), 849 (2650)
Fe	**3**	toluene	r.t.	368 (3380), 432 (3490), 602 (140)
			−100 °C	355 (5970), 430 (5040), 606 (560)
		THF	r.t.	421 (2120), 610 (160), 773 (120)
			−100 °C	408 (3430), 610 (310), 771 (480)
		Et_2O	r.t.	442 (1540), 601 (100)
			−100 °C	no maximum
	3.2DMAP	toluene	r.t.	360 (3230), 434 (3190), 607 (130)
	6	THF	r.t.	422 (1990), 771 (170)
	7	THF	r.t.	420 (5020), 613 (320), 771 (260)
	8	THF	r.t.	364 (1660), 420 (1900)
	K{18c6}[Fe(L^2)$_2$][1]	THF	r.t.	428 (4000), 626 (100)
Co	**4**	toluene	r.t.	385 (3080)
			−100 °C	387 (3910), 410 (3850)
		THF	r.t.	336 (2800), 385 (2300)
			−100 °C	334 (3300), 388 (2740)
		Et_2O	r.t.	393 (3560)
			−100 °C	334 (9540)
	9	THF	r.t.	340 (4770), 390 (4120)
	K{18c6}[Co(L^2)$_2$]* [1]	THF	r.t.	337 (2380), 391 (2030), 629 (100)

3 IR spectra

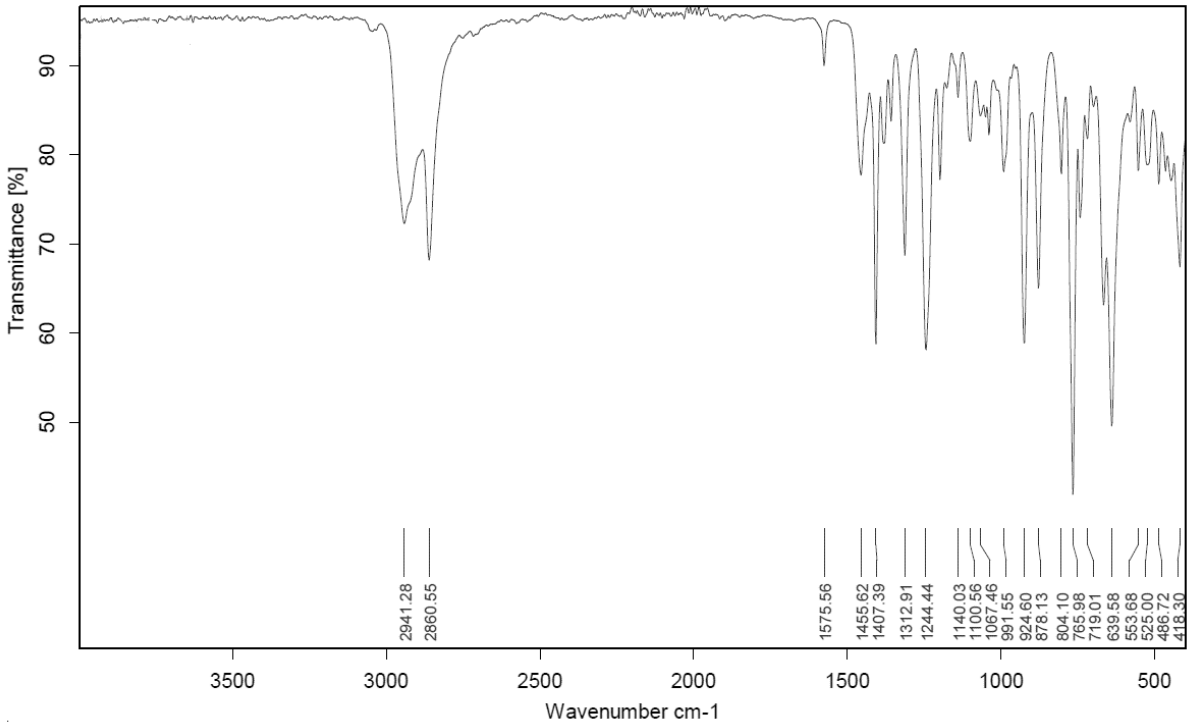

Figure S 52. IR spectrum of $[KCr(L^1)_2]_n$ (**1**).

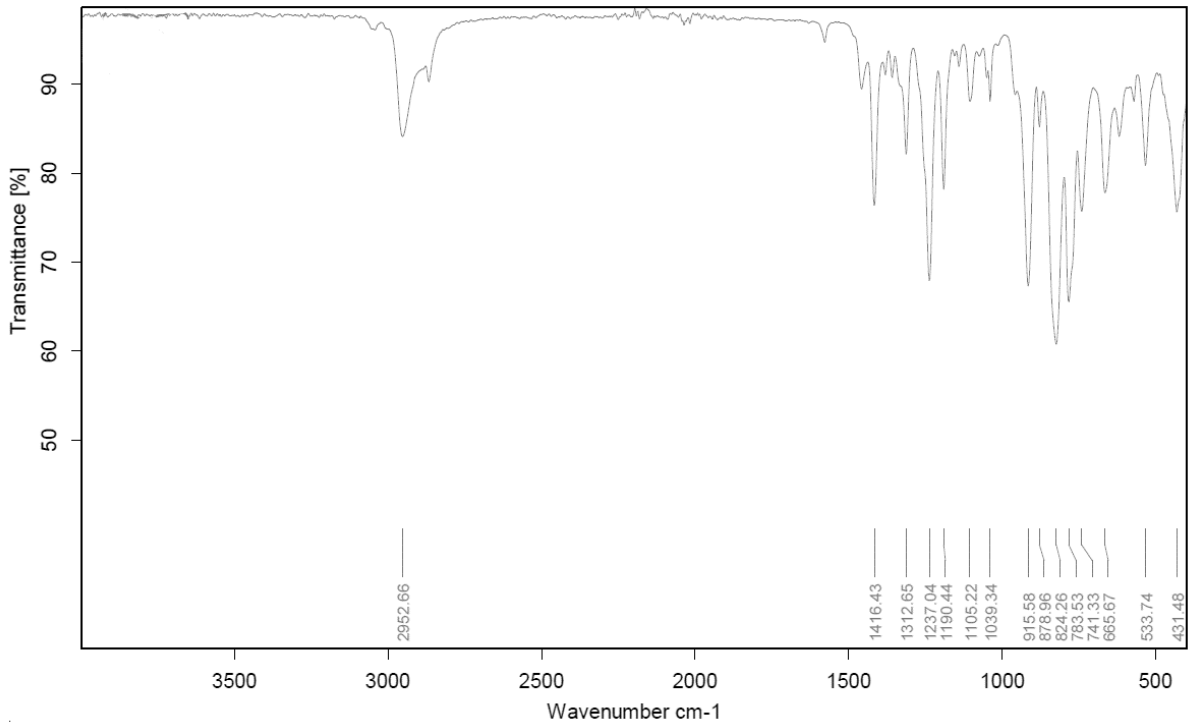

Figure S 53. IR spectrum of $[KMn(L^2)_2]$ (**2**).

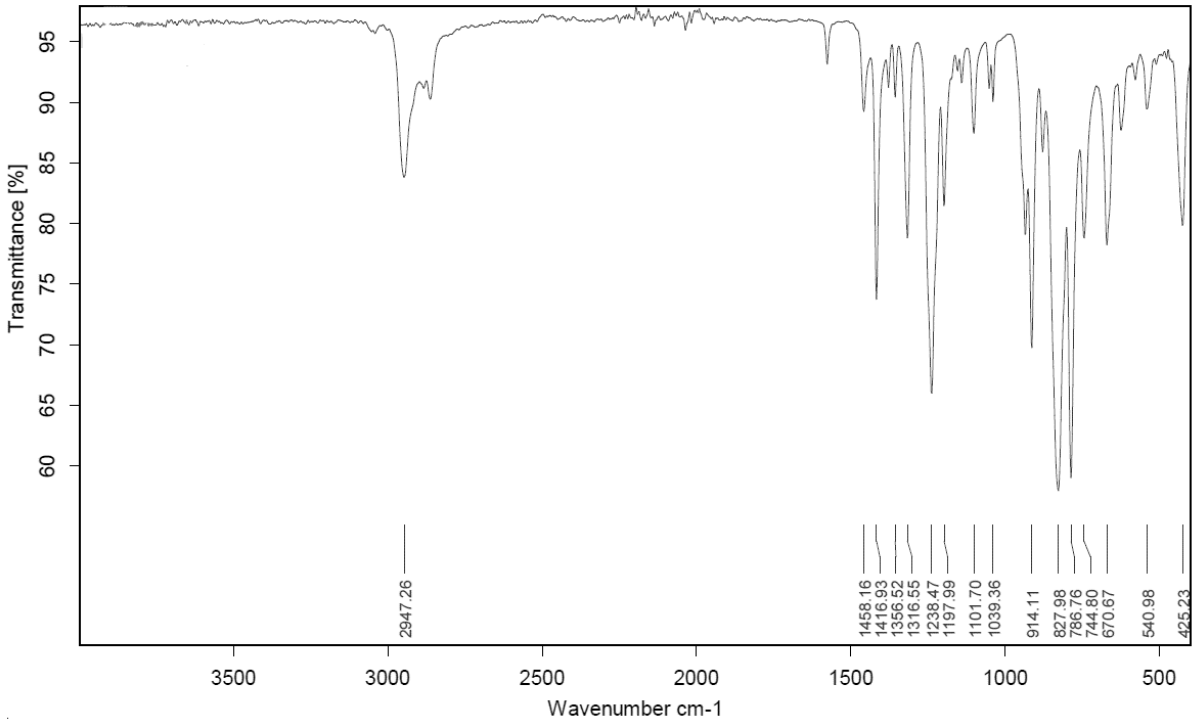

Figure S 54. IR spectrum of [KFe(L^2)$_2$] (**3**).

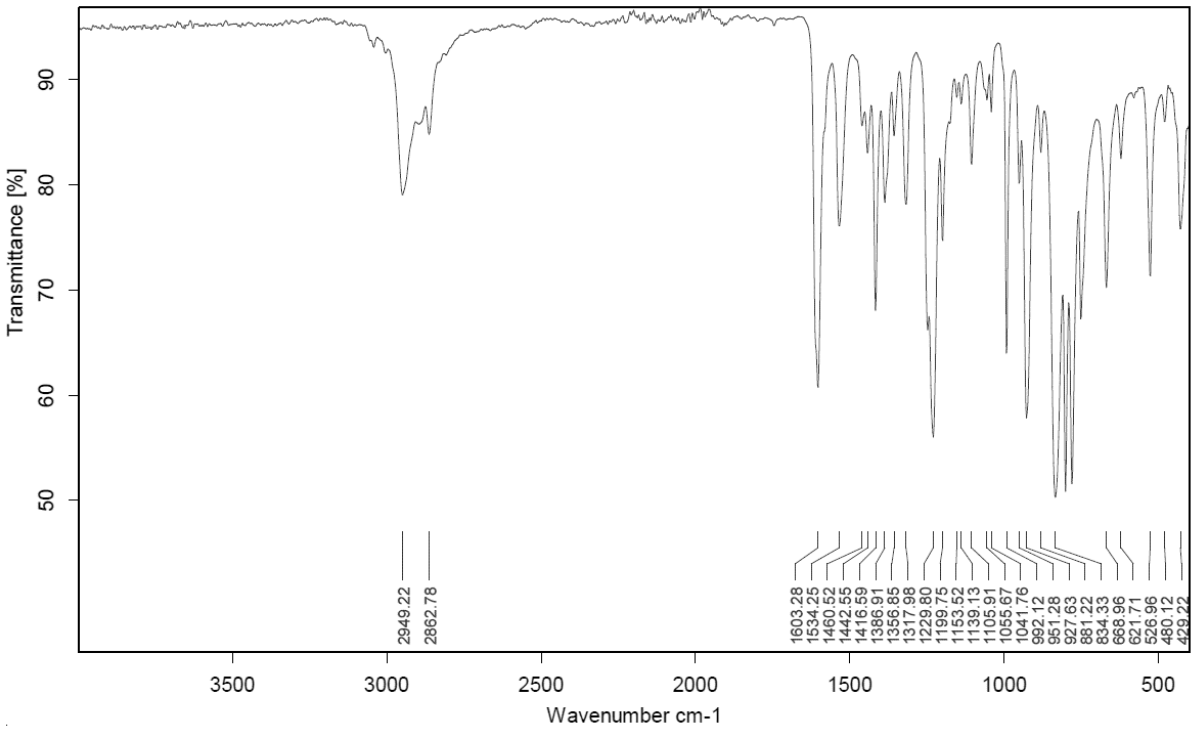

Figure S 55. IR spectrum of [K(DMAP)$_2$Fe(L^2)$_2$] (**3**.2DMAP).

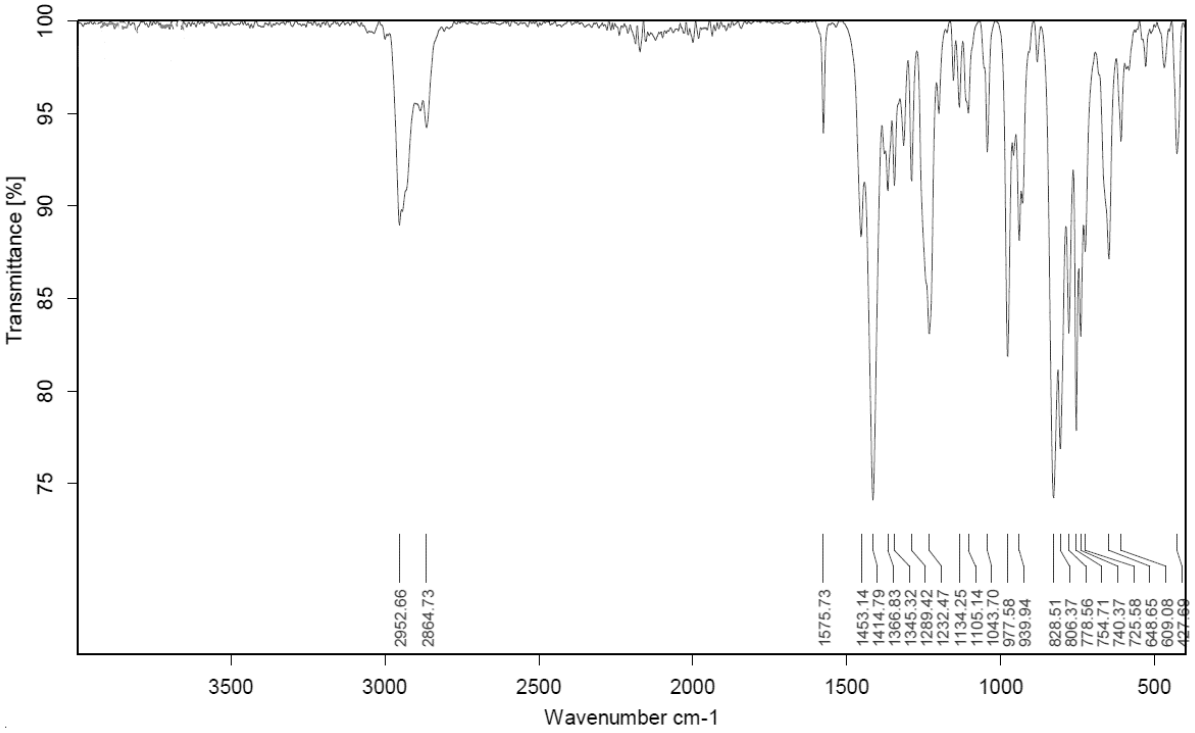

Figure S 56. IR spectrum of [KCo(L^2)$_2$] (**4**).

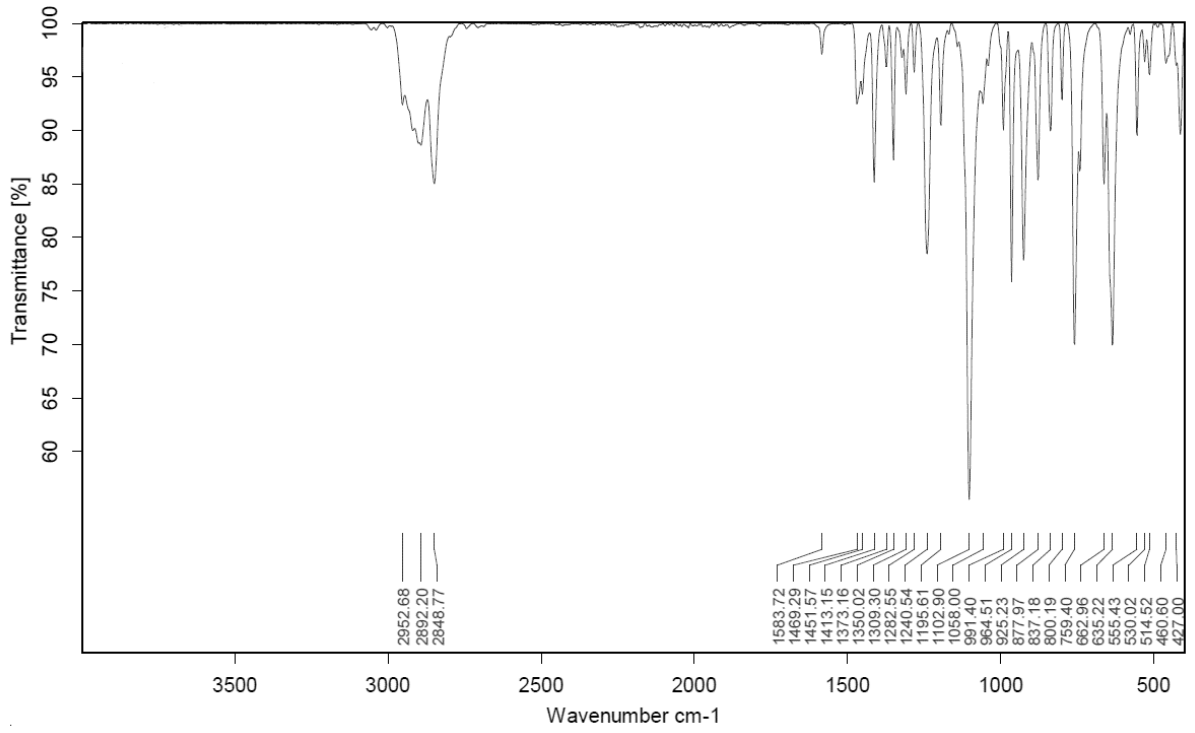

Figure S 57. IR spectrum of [K{18c6}(thf)$_2$][Cr(L^1)$_2$] (**5**).

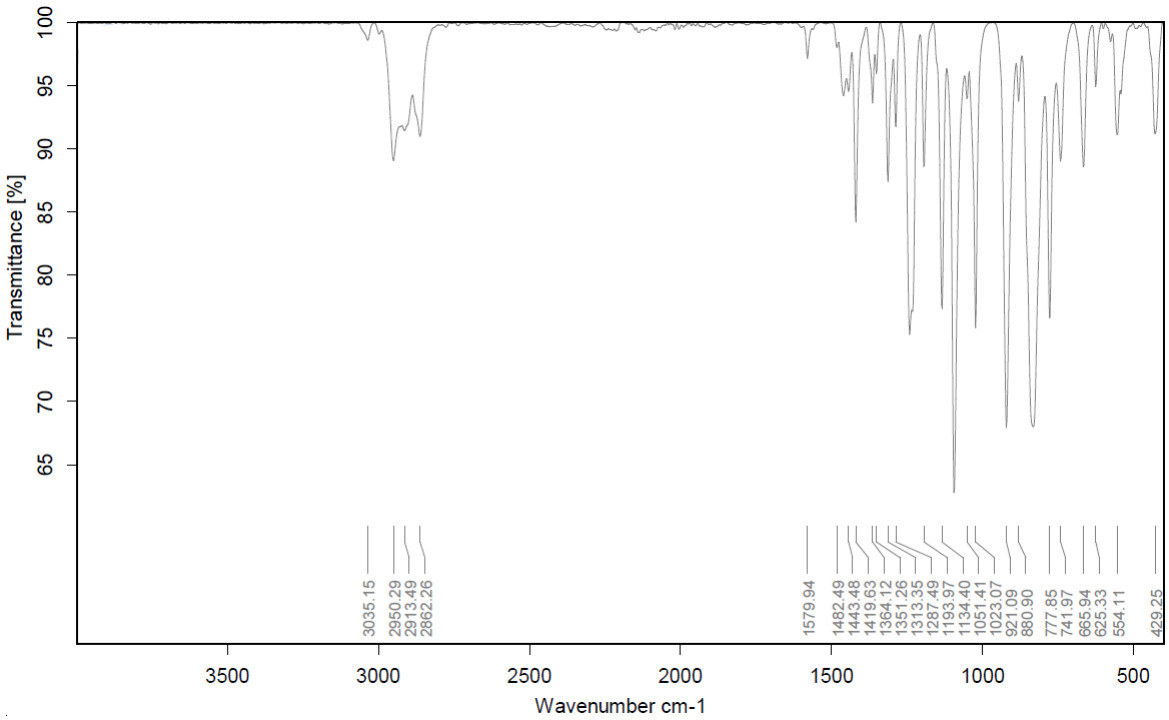

Figure S 58. IR spectrum of [Li{12c4}$_2$][Fe(L^2)$_2$] (**6**).

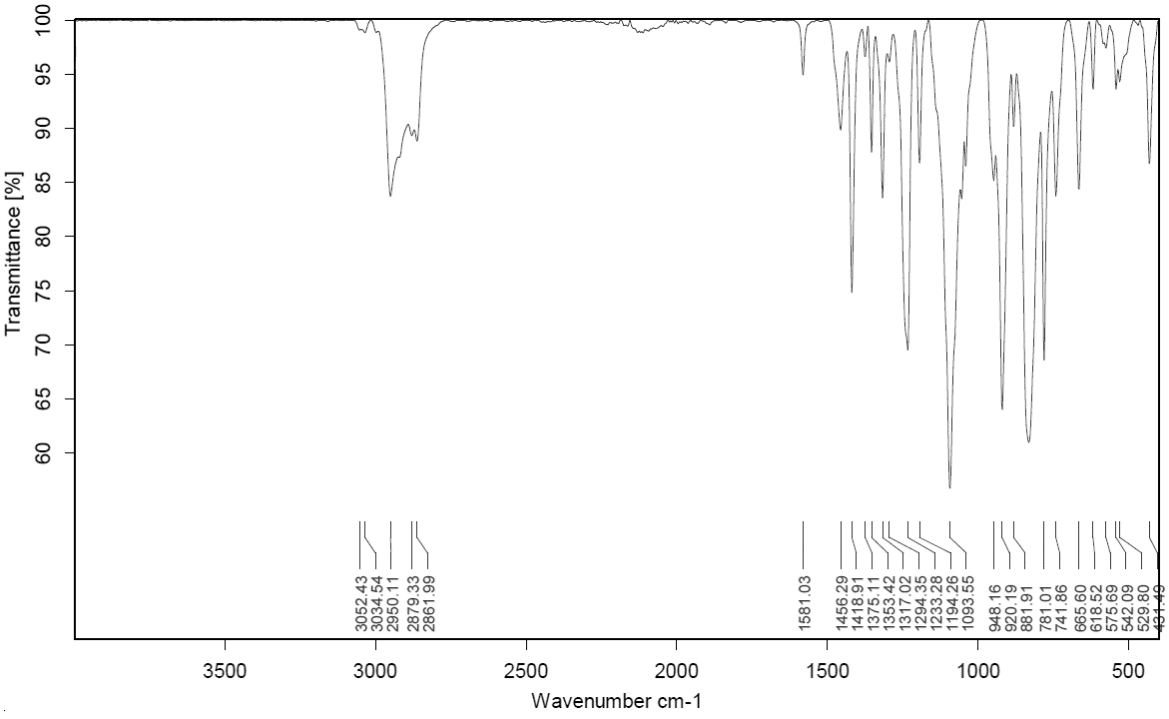

Figure S 59. IR spectrum of [Na{18c6}][Fe(L^2)$_2$] (**7**).

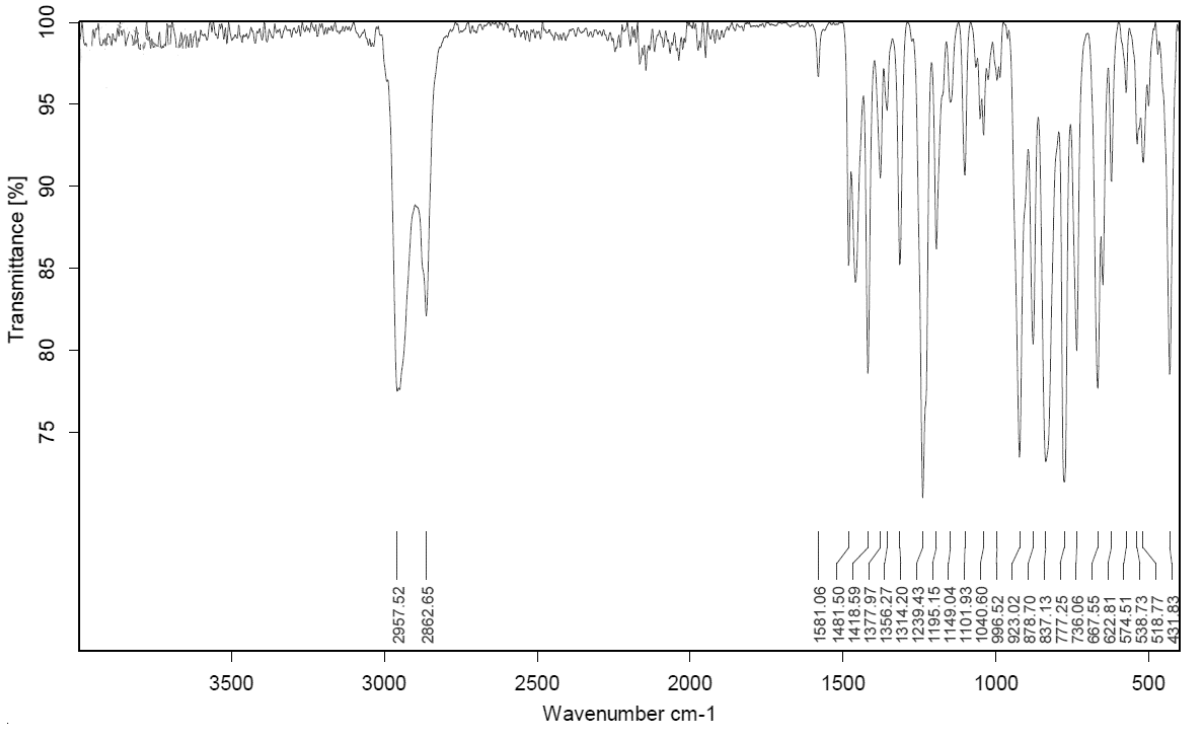

Figure S 60. IR spectrum of $[NBu_4][Fe(L^2)_2]$ (**8**).

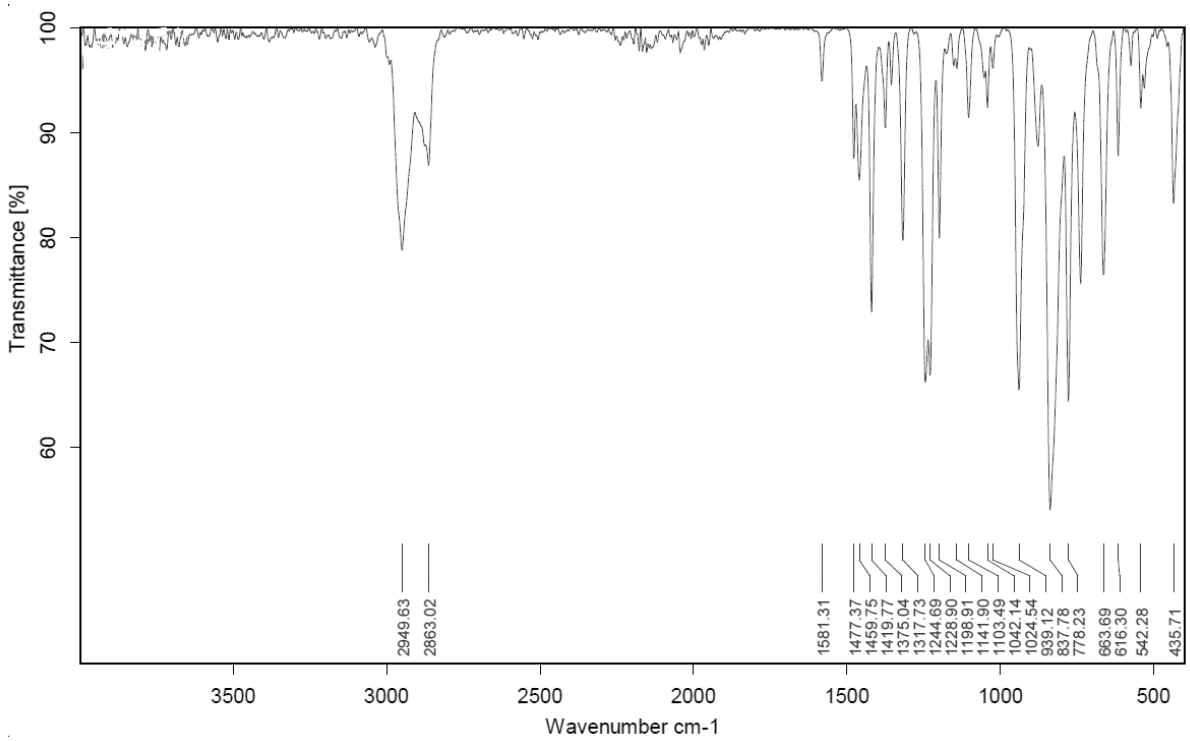

Figure S 61. IR spectrum of $[NBu_4][Co(L^2)_2]$ (**9**).

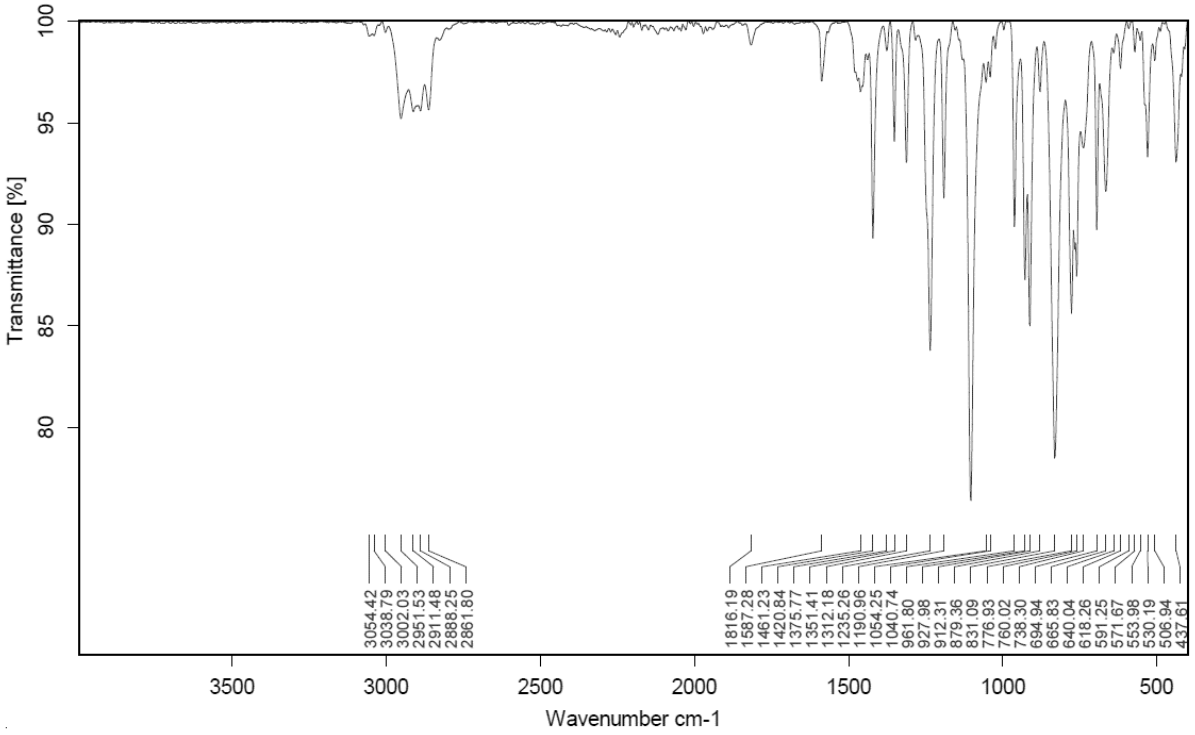

Figure S 62. IR spectrum of [K{18c6}][Fe(L^2)$_2$)(η^2-PhCCPh)] (**10**).

4 X-Ray Diffraction Analysis and Molecular Structures

$[KCr(L^1)_2]$ (1)

Table S 2. Crystal data and structure refinement of **1**

Empirical formula	$C_{42}H_{76}CrKN_2Si_2$
Formula weight	756.32
Temperature/K	99.99
Crystal system	orthorhombic
Space group	Pbcn
a/Å	22.7750(14)
b/Å	22.3023(13)
c/Å	17.1996(10)
α/°	90
β/°	90
γ/°	90
Volume/$Å^3$	8736.3(9)
Z	8
$\rho_{calc}g/cm^3$	1.150
μ/mm^{-1}	0.441
F(000)	3304.0
Crystal size/mm^3	0.157 × 0.124 × 0.109
Radiation	MoKα (λ = 0.71073)
2Θ range for data collection/°	4.354 to 49.998
Index ranges	−27 ≤ h ≤ 27, −26 ≤ k ≤ 26, −20 ≤ l ≤ 20
Reflections collected	119181
Independent reflections	7685 [R_{int} = 0.1694, R_{sigma} = 0.0597]
Data/restraints/parameters	7685/36/453
Goodness-of-fit on F^2	1.043
Final R indexes [I>=2σ (I)]	R_1 = 0.0562, wR_2 = 0.1031
Final R indexes [all data]	R_1 = 0.0895, wR_2 = 0.1112
Largest diff. peak/hole / e $Å^{-3}$	0.35/−0.41

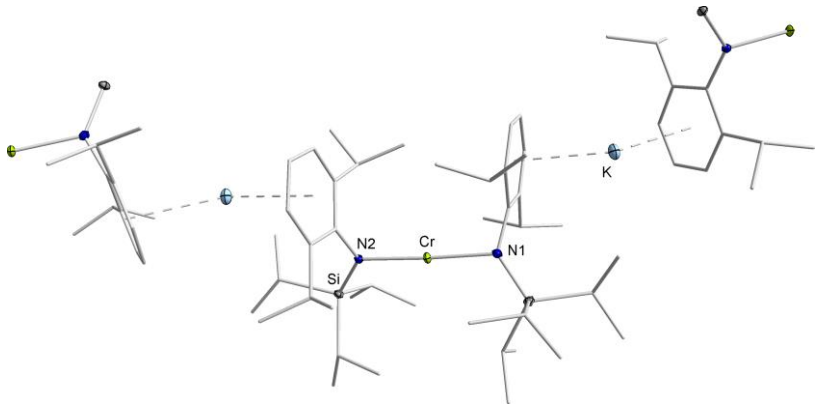

Figure S 63. Molecular structure of $[KCr^{I}(L^1)_2]_n$ (**1**). All hydrogen atoms are omitted for clarity.

Table S 3. Crystal data and structure refinement of **1**.3THF

Empirical formula	$C_{54}H_{98}CrKN_2O_3Si_2$
Formula weight	970.62
Temperature/K	100.0
Crystal system	triclinic
Space group	P−1
a/Å	11.886(2)
b/Å	14.190(2)
c/Å	17.464(3)
α/°	93.330(5)
β/°	95.457(5)
γ/°	97.740(5)
Volume/Å^3	2898.0(8)
Z	2
ρ_{calc}g/cm^3	1.112
μ/mm^{-1}	0.350
F(000)	1062.0
Crystal size/mm^3	0.3 × 0.2 × 0.1
Radiation	MoKα (λ = 0.71073)
2Θ range for data collection/°	4.394 to 29.706
Index ranges	−8 ≤ h ≤ 8, −10 ≤ k ≤ 10, −12 ≤ l ≤ 11
Reflections collected	23343
Independent reflections	2232 [R_{int} = 0.0445, R_{sigma} = 0.0224]
Data/restraints/parameters	2232/1424/433
Goodness-of-fit on F^2	1.182
Final R indexes [I>=2σ (I)]	R_1 = 0.1311, wR_2 = 0.2766
Final R indexes [all data]	R_1 = 0.1331, wR_2 = 0.2776
Largest diff. peak/hole / e Å^{-3}	0.69/−0.39

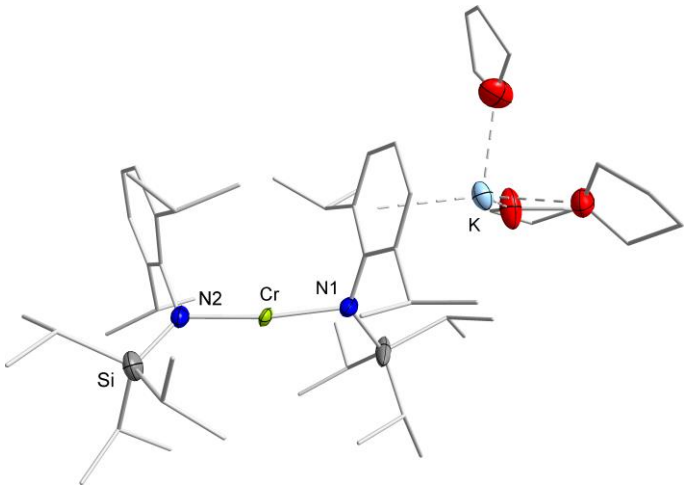

Figure S 64. Molecular structure of [K(THF)$_3$Cr^{I}(L^1)$_2$] (**1**.3THF). All hydrogen atoms are omitted for clarity. Disorders were found for one THF molecule (part 1: 63%, part 2: 37%) and two *iso*-propyl groups of a Si(^{i}Pr)$_3$ unit (part 1/2: 50%).

[KMn(L^2)$_2$] (2)

Table S 4. Crystal data and structure refinement of **2**

Empirical formula	$C_{30}H_{52}KMnN_2Si_2$
Formula weight	590.97
Temperature/K	100.01
Crystal system	monoclinic
Space group	$P2_1/n$
a/Å	11.6778(6)
b/Å	17.5423(9)
c/Å	17.8495(8)
α/°	90
β/°	108.652(2)
γ/°	90
Volume/Å^3	3464.5(3)
Z	4
ρ_{calc}g/cm^3	1.1329
μ/mm^{-1}	0.590
F(000)	1275.2
Crystal size/mm^3	0.236 × 0.179 × 0.132
Radiation	Mo Kα (λ = 0.71073)
2Θ range for data collection/°	4.36 to 53.36
Index ranges	−14 ≤ h ≤ 14, −22 ≤ k ≤ 22, −22 ≤ l ≤ 22
Reflections collected	76754
Independent reflections	7299 [R_{int} = 0.1314, R_{sigma} = 0.0575]
Data/restraints/parameters	7299/0/533
Goodness-of-fit on F^2	1.011
Final R indexes [I>=2σ (I)]	R_1 = 0.0357, wR_2 = 0.0767
Final R indexes [all data]	R_1 = 0.0509, wR_2 = 0.0824
Largest diff. peak/hole / e Å^{-3}	0.84/−0.51

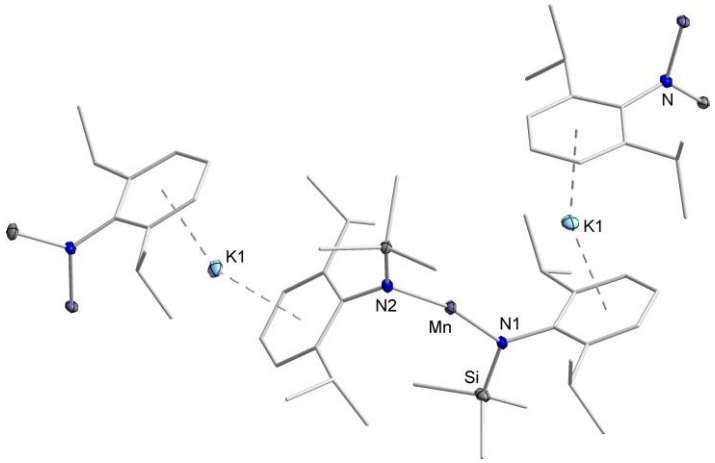

Figure S 65. Molecular structure of [KMn^I(L^2)$_2$]$_n$ (**2**). All hydrogen atoms are omitted for clarity.

[KFe(L^2)$_2$] (3)

Table S 5. Crystal data and structure refinement of **3**

Empirical formula	$C_{30}H_{52}FeKN_2Si_2$
Formula weight	591.86
Temperature/K	100.0
Crystal system	triclinic
Space group	P-1
a/Å	11.8776(6)
b/Å	14.0736(7)
c/Å	14.4037(7)
α/°	115.309(2)
β/°	91.001(2)
γ/°	110.473(2)
Volume/Å^3	1999.11(18)
Z	2
ρ_{calc}g/cm^3	0.983
μ/mm^{-1}	0.558
F(000)	638.0
Crystal size/mm^3	0.5 × 0.386 × 0.278
Radiation	MoKα (λ = 0.71073)
2Θ range for data collection/°	3.734 to 52
Index ranges	−14 ≤ h ≤ 14, −17 ≤ k ≤ 17, −17 ≤ l ≤ 17
Reflections collected	72350
Independent reflections	7861 [R_{int} = 0.0405, R_{sigma} = 0.0193]
Data/restraints/parameters	7861/0/363
Goodness-of-fit on F^2	1.086
Final R indexes [I>=2σ (I)]	R_1 = 0.0296, wR_2 = 0.0836
Final R indexes [all data]	R_1 = 0.0341, wR_2 = 0.0851
Largest diff. peak/hole / e Å^{-3}	0.31/−0.26

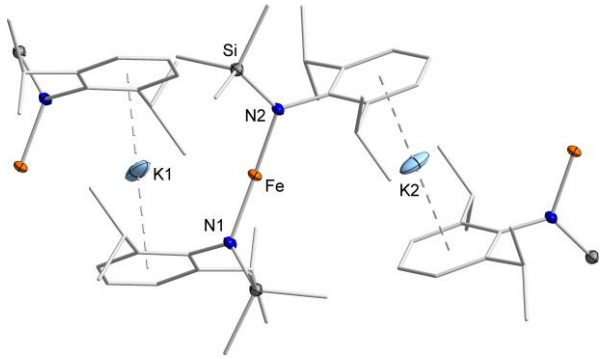

Figure S 66. Molecular structure of [KFe(L^2)$_2$]$_n$ (**3**). All hydrogen atoms are omitted for clarity. Disordering the potassium ion over two positions did not lead to a better, stable structure refinement. one free *n*-pentane molecule is heavily disordered over multiple positions. Attempts to model the disorders did not lead to satisfactory. It was thus squeezed.

Table S 6. Crystal data and structure refinement of **3**.Et_2O

Empirical formula	$C_{34}H_{62}Fe_1K_1N_2O_1Si_2$
Formula weight	666.00
Temperature/K	100
Crystal system	monoclinic
Space group	P 1 2_1/n 1
a/Å	10.4002(6)
b/Å	16.5542(9)
c/Å	22.9563(13)
α/°	90
β/°	95.379(2)
γ/°	90
Volume/$Å^3$	3934.9(4)
Z	4
$\rho_{calc}g/cm^3$	1.124
μ/mm^{-1}	0.576
F(000)	1444.000
Crystal size/mm^3	0.15 × 0.15 × 0.15
Radiation	MoKα (λ = 0.71073)
2Θ range for data collection/°	2 to 32
Index ranges	−15 ≤ h ≤ 15, 0 ≤ k ≤ 24, 0 ≤ l ≤ 16
Reflections collected	98693
Independent reflections	8758
Data/restraints/parameters	7182/0/370
Goodness-of-fit on F^2	1.057
Final R indexes [I>=2σ (I)]	R1 = 0.0299, wR2 = 0.0296
Final R indexes [all data]	R1 = 0.0405, wR2 = 0.0439
Largest diff. peak/hole / e $Å^{-3}$	0.84/−0.36

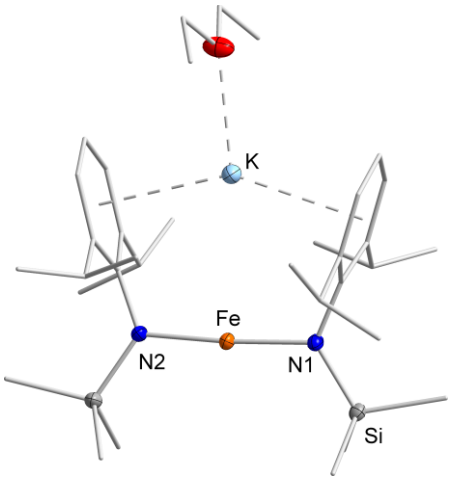

Figure S 67. Molecular structure of [K(Et_2O)Fe(L^2)$_2$] (**3**.Et_2O). All hydrogen atoms are omitted for clarity. Some data are probably incomplete due to strategy errors.

Table S 7. Crystal data and structure refinement of **3**.2DMAP

Empirical formula	$C_{176}H_{288}Fe_4K_4N_{24}Si_8$
Formula weight	3344.81
Temperature/K	100
Crystal system	monoclinic
Space group	C2/c
a/Å	20.857(3)
b/Å	13.086(2)
c/Å	19.863(3)
α/°	90
β/°	117.192(10)
γ/°	90
Volume/Å^3	4822.1(14)
Z	1
ρ_{calc}g/cm^3	1.152
μ/mm^{-1}	0.483
F(000)	1804.0
Crystal size/mm^3	0.687 × 0.104 × 0.098
Radiation	MoKα (λ = 0.71073)
2Θ range for data collection/°	3.808 to 50
Index ranges	−24 ≤ h ≤ 21, −15 ≤ k ≤ 15, −23 ≤ l ≤ 23
Reflections collected	18133
Independent reflections	4259 [R_{int} = 0.0940, R_{sigma} = 0.0594]
Data/restraints/parameters	4259/0/254
Goodness-of-fit on F^2	0.938
Final R indexes [I>=2σ (I)]	R_1 = 0.0634, wR_2 = 0.1572
Final R indexes [all data]	R_1 = 0.0848, wR_2 = 0.1679
Largest diff. peak/hole / e Å^{-3}	0.54/−0.78

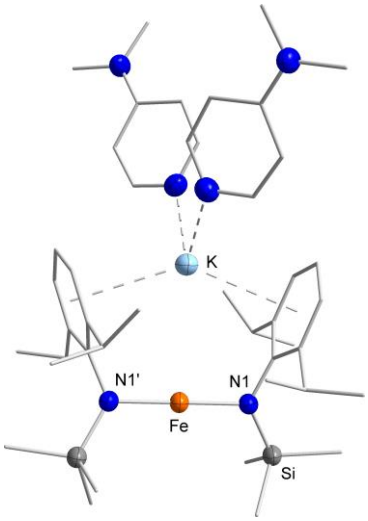

Figure S 68. Molecular structure of [K(DMAP)$_2$Fe(L^2)$_2$] (**3**.2DMAP). All hydrogen atoms are omitted for clarity.

[K(C$_7$H$_8$)Co(L^2)$_2$] (4)

Table S 8. Crystal data and structure refinement of **4**

Empirical formula	$C_{37}H_{60}CoKN_2Si_2$
Formula weight	687.08
Temperature/K	100.0
Crystal system	monoclinic
Space group	C2/c
a/Å	24.6815(11)
b/Å	25.6246(11)
c/Å	15.9053(7)
α/°	90
β/°	128.3810(10)
γ/°	90
Volume/Å^3	7885.5(6)
Z	8
ρ_{calc}g/cm^3	1.157
μ/mm^{-1}	0.627
F(000)	2960.0
Crystal size/mm^3	0.567 × 0.191 × 0.143
Radiation	MoKα (λ = 0.71073)
2Θ range for data collection/°	4.558 to 52.212
Index ranges	−30 ≤ h ≤ 30, −31 ≤ k ≤ 31, −17 ≤ l ≤ 19
Reflections collected	141451
Independent reflections	7826 [R_{int} = 0.0701, R_{sigma} = 0.0234]
Data/restraints/parameters	7826/0/414
Goodness-of-fit on F^2	1.211
Final R indexes [I>=2σ (I)]	R_1 = 0.0399, wR_2 = 0.0788
Final R indexes [all data]	R_1 = 0.0508, wR_2 = 0.0817
Largest diff. peak/hole / e Å^{-3}	0.28/−0.31

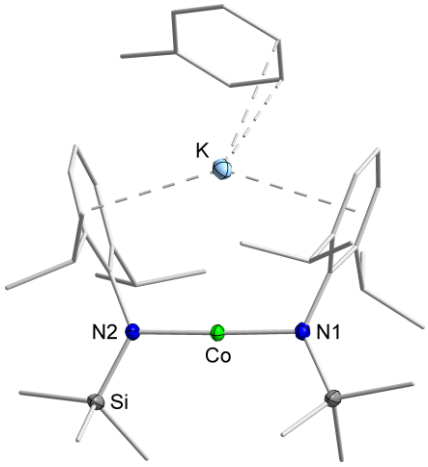

Figure S 69. Molecular structure of [K(C$_7$H$_8$)Co(L^2)$_2$] (**4**). All hydrogen atoms are omitted for clarity.

[K{18c6}(THF)$_2$][Cr(L^1)$_2$] (5)

Table S 9. Crystal data and structure refinement of **5**

Empirical formula	$C_{62}H_{116}CrKN_2O_8Si_2$
Formula weight	1164.82
Temperature/K	100.0
Crystal system	orthorhombic
Space group	Pbca
a/Å	17.2978(7)
b/Å	23.0874(9)
c/Å	34.2506(14)
α/°	90
β/°	90
γ/°	90
Volume/Å^3	13678.4(10)
Z	8
ρ_{calc}g/cm^3	1.131
μ/mm^{-1}	0.312
F(000)	5096.0
Crystal size/mm^3	0.338 × 0.243 × 0.16
Radiation	MoKα (λ = 0.71073)
2Θ range for data collection/°	4.256 to 52.23
Index ranges	−21 ≤ h ≤ 21, −28 ≤ k ≤ 28, −41 ≤ l ≤ 42
Reflections collected	239756
Independent reflections	13578 [R_{int} = 0.0914, R_{sigma} = 0.0297]
Data/restraints/parameters	13578/2/722
Goodness-of-fit on F^2	1.054
Final R indexes [I>=2σ (I)]	R_1 = 0.0364, wR_2 = 0.0724
Final R indexes [all data]	R_1 = 0.0544, wR_2 = 0.0782
Largest diff. peak/hole / e Å^{-3}	0.28/−0.24

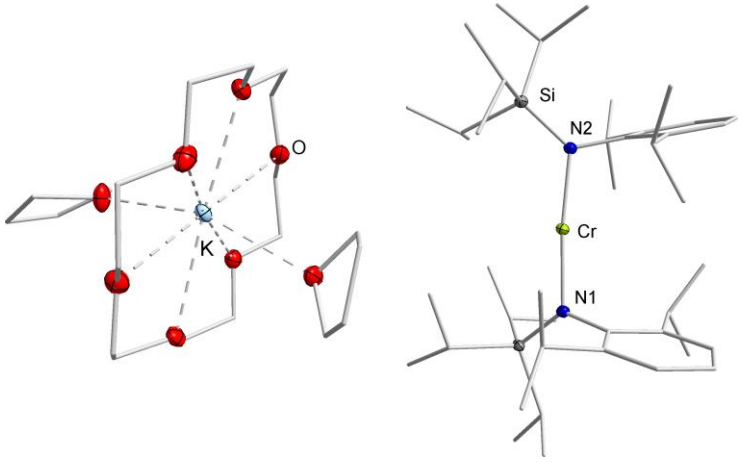

Figure S 70. Molecular structure of [K{18c6}(THF)$_2$][Cr(L^1)$_2$] (**5**). All hydrogen atoms and a disorder in one THF molecule are omitted for clarity.

[Li{12c4}$_2$][Fe(L^2)$_2$] (6)

Table S 10. Crystal data and structure refinement of **6**

Empirical formula	$C_{46}H_{84}FeLiN_2O_8Si_2$
Formula weight	912.12
Temperature/K	100.0
Crystal system	triclinic
Space group	P-1
a/Å	11.6888(8)
b/Å	14.5127(10)
c/Å	16.4126(12)
α/°	70.550(2)
β/°	83.481(2)
γ/°	77.315(2)
Volume/Å^3	2558.7(3)
Z	2
ρ_{calc}g/cm^3	1.184
μ/mm^{-1}	0.390
F(000)	990.0
Crystal size/mm^3	0.395 × 0.248 × 0.242
Radiation	MoKα (λ = 0.71073)
2Θ range for data collection/°	4.346 to 61.008
Index ranges	−14 ≤ h ≤ 16, −20 ≤ k ≤ 20, −23 ≤ l ≤ 23
Reflections collected	50692
Independent reflections	14042 [R_{int} = 0.0418, R_{sigma} = 0.0499]
Data/restraints/parameters	14042/471/564
Goodness-of-fit on F^2	1.098
Final R indexes [I>=2σ (I)]	R_1 = 0.0826, wR_2 = 0.1912
Final R indexes [all data]	R_1 = 0.0979, wR_2 = 0.1996
Largest diff. peak/hole / e Å^{-3}	1.46/−0.85

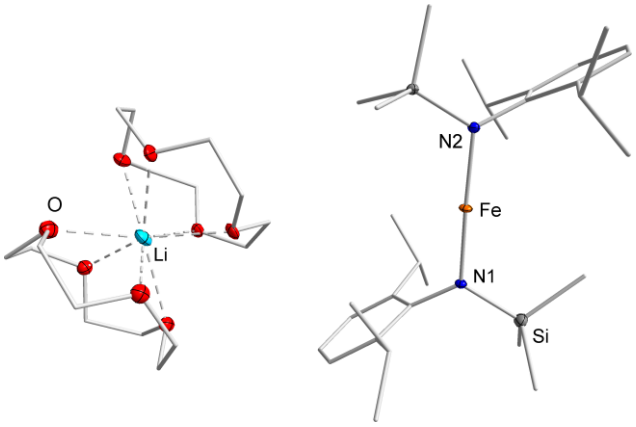

Figure S 71. Molecular structure of [Li{12c4}$_2$][Fe(L^2)$_2$] (**6**). All hydrogen atoms are omitted for clarity. The structure was refined as a twin, twin ratio refined to 0.0863(9).

[Na{18c6}(Et_2O)][Fe(L^2)$_2$] (7)

Table S 11. Crystal data and structure refinement of **7**

Empirical formula	$C_{46}H_{86}FeN_2NaO_7Si_2$
Formula weight	914.18
Temperature/K	100.0
Crystal system	triclinic
Space group	P−1
a/Å	12.392(3)
b/Å	13.002(3)
c/Å	18.053(3)
α/°	71.086(15)
β/°	76.889(16)
γ/°	70.636(15)
Volume/Å^3	2572.7(10)
Z	2
ρ_{calc}g/cm^3	1.180
μ/mm^{-1}	0.395
F(000)	994.0
Crystal size/mm^3	0.893 × 0.503 × 0.2
Radiation	MoKα (λ = 0.71073)
2Θ range for data collection/°	3.45 to 53.888
Index ranges	−15 ≤ h ≤ 14, −16 ≤ k ≤ 16, −23 ≤ l ≤ 22
Reflections collected	23621
Independent reflections	10961 [R_{int} = 0.2177, R_{sigma} = 0.1943]
Data/restraints/parameters	10961/54/578
Goodness-of-fit on F^2	0.909
Final R indexes [I>=2σ (I)]	R_1 = 0.0828, wR_2 = 0.2018
Final R indexes [all data]	R_1 = 0.1415, wR_2 = 0.2306
Largest diff. peak/hole / e Å^{-3}	1.03/−0.86

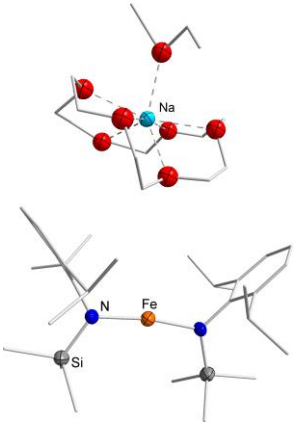

Figure S 72. Molecular structure of [Na{18c6}(Et_2O)][Fe(L^2)$_2$] (**7**). All hydrogen atoms are omitted for clarity. A disorder of the 18-crown-6 unit with occupations of 50% for both part 1 (depicted) and part 2 is found.

[NBu$_4$][Fe(L^2)$_2$] (8)

Table S 12. Crystal data and structure refinement of **8**

Empirical formula	$C_{184}H_{352}Fe_4N_{12}Si_8$
Formula weight	3180.87
Temperature/K	100
Crystal system	monoclinic
Space group	$P2_1/n$
a/Å	18.298(2)
b/Å	13.8270(10)
c/Å	21.446(3)
α/°	90
β/°	114.323(10)
γ/°	90
Volume/Å^3	4944.3(10)
Z	1
ρ_{calc}g/cm^3	1.068
μ/mm^{-1}	0.385
F(000)	1756.0
Crystal size/mm^3	0.372 × 0.246 × 0.173
Radiation	MoKα (λ = 0.71073)
2Θ range for data collection/°	4.862 to 53.478
Index ranges	−23 ≤ h ≤ 23, −17 ≤ k ≤ 17, −26 ≤ l ≤ 27
Reflections collected	44120
Independent reflections	10436 [R_{int} = 0.0915, R_{sigma} = 0.0680]
Data/restraints/parameters	10436/0/487
Goodness-of-fit on F^2	0.994
Final R indexes [I>=2σ (I)]	R_1 = 0.0394, wR_2 = 0.0746
Final R indexes [all data]	R_1 = 0.0793, wR_2 = 0.0839
Largest diff. peak/hole / e Å^{-3}	0.24/−0.35

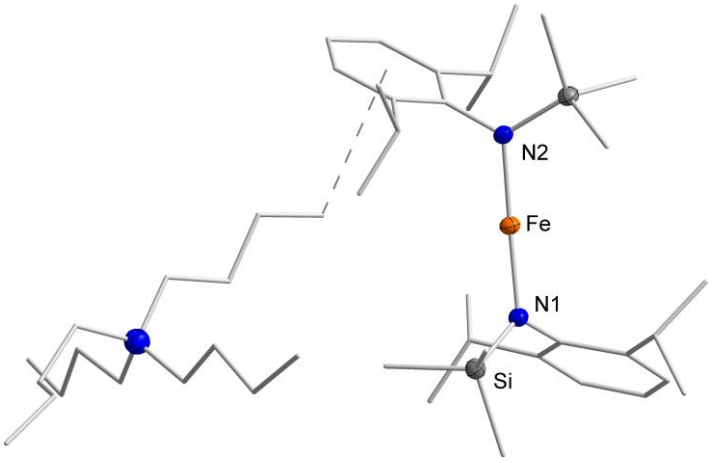

Figure S 73. Molecular structure of [NBu$_4$][Fe(L^2)$_2$] (**8**). All hydrogen atoms are omitted for clarity.

[NBu$_4$][Co(L^2)$_2$] (9)

Table S 13. Crystal data and structure refinement of **9**

Empirical formula	$C_{184}H_{352}Co_4N_{12}Si_8$
Formula weight	3193.20
Temperature/K	100
Crystal system	orthorhombic
Space group	$P2_12_12_1$
a/Å	10.7553(6)
b/Å	19.9389(8)
c/Å	22.5989(11)
α/°	90
β/°	90
γ/°	90
Volume/Å^3	4846.3(4)
Z	1
ρ_{calc}g/cm^3	1.094
μ/mm^{-1}	0.435
F(000)	1760.0
Crystal size/mm^3	0.432 × 0.293 × 0.185
Radiation	MoKα (λ = 0.71073)
2Θ range for data collection/°	3.604 to 49.998
Index ranges	−12 ≤ h ≤ 12, −23 ≤ k ≤ 23, −26 ≤ l ≤ 26
Reflections collected	36221
Independent reflections	8508 [R_{int} = 0.0503, R_{sigma} = 0.0302]
Data/restraints/parameters	8508/0/488
Goodness-of-fit on F^2	1.040
Final R indexes [I>=2σ (I)]	R_1 = 0.0286, wR_2 = 0.0720
Final R indexes [all data]	R_1 = 0.0317, wR_2 = 0.0731
Largest diff. peak/hole / e Å^{-3}	0.25/−0.20
Flack parameter	0.152(12)

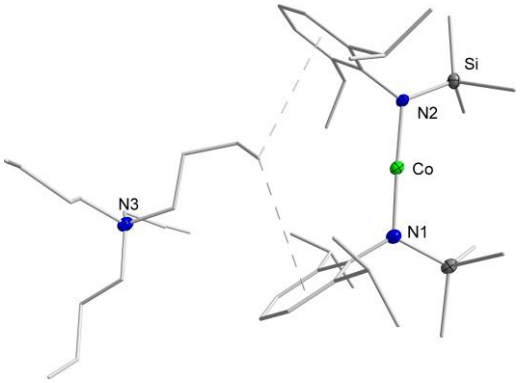

Figure S 74. Molecular structure of [NBu$_4$][Co(L^2)$_2$] (**9**). All hydrogen atoms are omitted for clarity. The structure was refined as an inversion twin, twin ratio refined to 0.152(12).

[K{18c6}(THF)$_2$][Fe(L^2)$_2$)(η^{2}-PhCCPh)] (10)

Table S 17. Crystal data and structure refinement of **10**

Empirical formula	$C_{64}H_{102}N_2O_8Si_2KFe$
Formula weight	1178.60
Temperature/K	100.0
Crystal system	triclinic
Space group	P−1
a/Å	11.0677(6)
b/Å	13.4596(7)
c/Å	22.1320(11)
α/°	83.532(2)
β/°	88.471(2)
γ/°	87.653(2)
Volume/Å^3	3272.4(3)
Z	2
ρ_{calc}g/cm^3	1.196
μ/mm^{-1}	0.383
F(000)	1274.0
Crystal size/mm^3	0.312 × 0.239 × 0.072
Radiation	MoKα (λ = 0.71073)
2Θ range for data collection/°	4.528 to 50.626
Index ranges	−12 ≤ h ≤ 13, −16 ≤ k ≤ 16, −26 ≤ l ≤ 26
Reflections collected	117177
Independent reflections	11928 [R_{int} = 0.0554, R_{sigma} = 0.0299]
Data/restraints/parameters	11928/0/720
Goodness-of-fit on F^2	1.043
Final R indexes [I>=2σ (I)]	R_1 = 0.0367, wR_2 = 0.0731
Final R indexes [all data]	R_1 = 0.0508, wR_2 = 0.0773
Largest diff. peak/hole / e Å^{-3}	0.36/−0.33

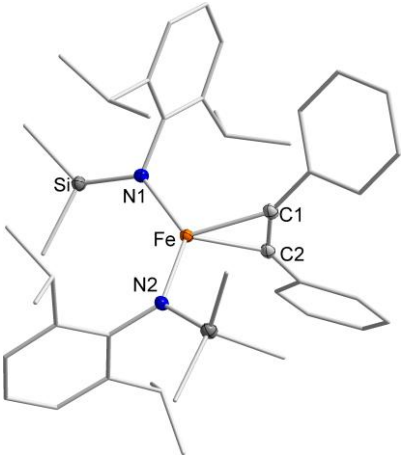

Figure S 75. Molecular structure of [K{18c6}(THF)$_2$][Fe(L^2)$_2$)(η^{2}-PhCCPh)] (**10**). All hydrogen atoms and the K{18c6}(THF)$_2$ cation are omitted for clarity.

[K(Et$_2$O)Fe(η^6-HPB)(η^{2-}PhCCPh)] (11.Et$_2$O**)**

Table S 15. Crystal data and structure refinement of **11**.Et2O

Empirical formula	$C_{60}H_{50}FeKO$
Formula weight	881.95
Temperature/K	110.0
Crystal system	monoclinic
Space group	$P2_1/n$
a/Å	19.3467(7)
b/Å	11.2945(4)
c/Å	21.4705(9)
α/°	90
β/°	102.4730(13)
γ/°	90
Volume/Å^3	4580.8(3)
Z	4
ρ_{calc}g/cm^3	1.279
μ/mm^{-1}	0.462
F(000)	1852.0
Crystal size/mm^3	0.26 × 0.08 × 0.07
Radiation	MoKα (λ = 0.71073)
2Θ range for data collection/°	4.312 to 50.652
Index ranges	−23 ≤ h ≤ 23, −13 ≤ k ≤ 13, −25 ≤ l ≤ 25
Reflections collected	115901
Independent reflections	8348 [R_{int} = 0.0574, R_{sigma} = 0.0218]
Data/restraints/parameters	8348/0/594
Goodness-of-fit on F^2	1.029
Final R indexes [I>=2σ (I)]	R_1 = 0.0368, wR_2 = 0.0870
Final R indexes [all data]	R_1 = 0.0470, wR_2 = 0.0920
Largest diff. peak/hole / e Å^{-3}	0.59/−0.50

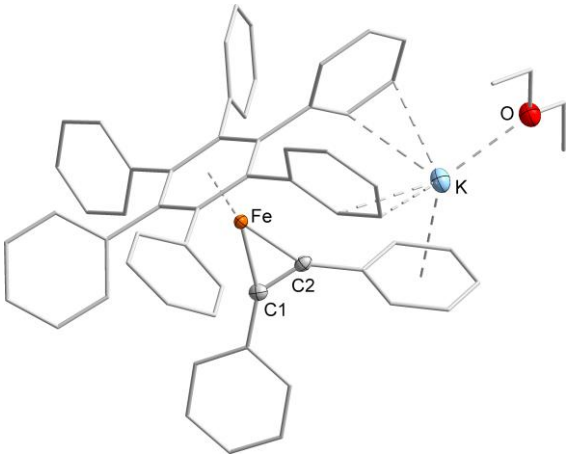

Figure S 76. Molecular structure of [K(Et$_2$O)Fe(η^6-HPB)(η^{2-}PhCCPh)] (**11**.Et$_2$O). All hydrogen atoms are omitted for clarity.

[KFe(η^6-HPB)(η^{2-}PhCCPh)] (11)

Table S 16. Crystal data and structure refinement of **11**

Empirical formula	$C_{56}H_{40}FeK$
Formula weight	807.83
Temperature/K	99.99
Crystal system	monoclinic
Space group	$P2_1/c$
a/Å	10.4506(4)
b/Å	18.1974(7)
c/Å	23.8299(9)
α/°	90
β/°	97.1120(10)
γ/°	90
Volume/Å^3	4497.0(3)
Z	4
ρ_{calc}g/cm^3	1.193
μ/mm^{-1}	0.463
F(000)	1684.0
Crystal size/mm^3	0.194 × 0.135 × 0.075
Radiation	MoKα (λ = 0.71073)
2Θ range for data collection/°	4.476 to 52.172
Index ranges	−11 ≤ h ≤ 12, −22 ≤ k ≤ 22, −29 ≤ l ≤ 29
Reflections collected	70523
Independent reflections	8887 [R_{int} = 0.0621, R_{sigma} = 0.0363]
Data/restraints/parameters	8887/0/550
Goodness-of-fit on F^2	1.045
Final R indexes [I>=2σ (I)]	R_1 = 0.0411, wR_2 = 0.0897
Final R indexes [all data]	R_1 = 0.0572, wR_2 = 0.0952
Largest diff. peak/hole / e Å^{-3}	0.31/−0.36

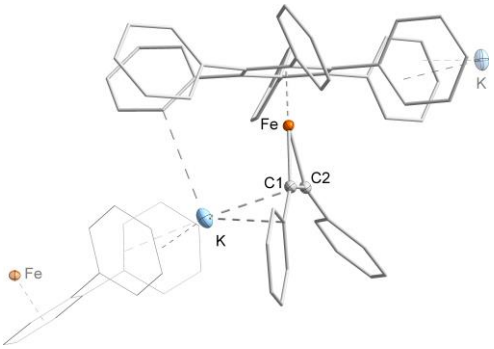

Figure S 77. Molecular structure of [KFe(η^6-HPB)(η^{2-}PhCCPh)] (**11**). All hydrogen atoms and a disorder in one phenyl ring (part 1: 75%, depicted; part 2: 25%) are omitted for clarity. A free diethyl ether molecule is located on a symmetry element and is heavily disordered over multiple positions. Attempts to model the disorder did not lead to satisfactory results and further gave higher R-values. It was thus squeezed.

Table S 19. Crystal data and structure refinement of **12**

Empirical formula	$C_{74}H_{103}K_2Mn_2N_2O_4Si_2$
Formula weight	1328.84
Temperature/K	100.0
Crystal system	triclinic
Space group	P-1
a/Å	12.905(11)
b/Å	13.215(8)
c/Å	14.360(9)
α/°	104.35(5)
β/°	107.84(6)
γ/°	105.11(6)
Volume/Å^3	2103(3)
Z	1
ρ_{calc}g/cm^3	1.049
μ/mm^{-1}	0.468
F(000)	709.0
Crystal size/mm^3	0.942 × 0.456 × 0.229
Radiation	MoKα (λ = 0.71073)
2Θ range for data collection/°	3.188 to 49.994
Index ranges	−15 ≤ h ≤ 15, −15 ≤ k ≤ 15, −17 ≤ l ≤ 17
Reflections collected	15985
Independent reflections	7390 [R_{int} = 0.1069, R_{sigma} = 0.0991]
Data/restraints/parameters	7390/3/409
Goodness-of-fit on F^2	0.949
Final R indexes [I>=2σ (I)]	R_1 = 0.0868, wR_2 = 0.2314
Final R indexes [all data]	R_1 = 0.1224, wR_2 = 0.2483
Largest diff. peak/hole / e Å^{-3}	0.86/−0.64

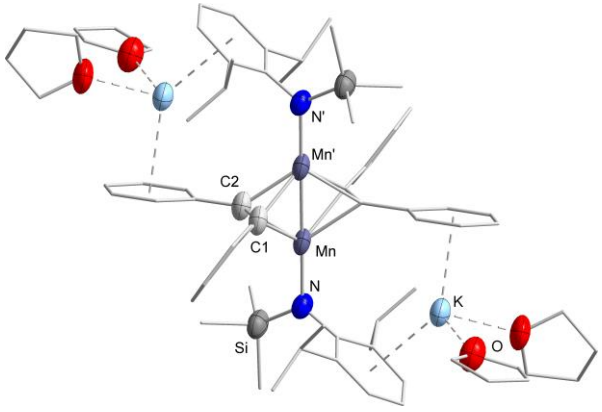

Figure S 78. Molecular structure of **12**. All hydrogen atoms and disorders in one *iso*-propyl group and one trimethylsilyl group are omitted for clarity. Two free toluene molecules are heavily disordered over multiple positions. Attempts to model the disorders did not lead to satisfactory results and further gave higher R-values. They were thus squeezed.

Table S 18. Crystal data and structure refinement of **13**

Empirical formula	$C_{78}H_{70}K_2Mn_2O_2$
Formula weight	1227.42
Temperature/K	100.0
Crystal system	monoclinic
Space group	$P2_1/c$
a/Å	17.6490(9)
b/Å	18.4355(9)
c/Å	19.6687(11)
α/°	90
β/°	93.540(2)
γ/°	90
Volume/Å^3	6387.4(6)
Z	4
ρ_{calc}g/cm^3	1.276
μ/mm^{-1}	0.573
F(000)	2568.0
Crystal size/mm^3	0.729 × 0.113 × 0.103
Radiation	MoKα (λ = 0.71073)
2Θ range for data collection/°	4.418 to 50.202
Index ranges	−18 ≤ h ≤ 21, −21 ≤ k ≤ 21, −23 ≤ l ≤ 23
Reflections collected	37162
Independent reflections	11297 [R_{int} = 0.0750, R_{sigma} = 0.0891]
Data/restraints/parameters	11297/1548/879
Goodness-of-fit on F^2	1.040
Final R indexes [I>=2σ (I)]	R_1 = 0.0829, wR_2 = 0.1868
Final R indexes [all data]	R_1 = 0.1366, wR_2 = 0.2107
Largest diff. peak/hole / e Å^{-3}	0.70/−0.77

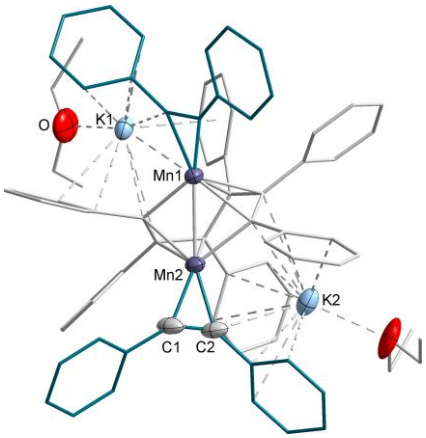

Figure S 79. Molecular structure of **13**. All hydrogen atoms are omitted for clarity. Disorders in both diethyl ether adducts and two phenyl rings with occupations of 50% for both part 1 (depicted) and part 2 are found.

[K{18c6}][Fe(L^2)$_2$] x Et$_2$O

Table S 14. Crystal data and structure refinement of [K{18c6}][Fe(L^2)$_2$] x Et$_2$O

Empirical formula	$C_{184}H_{344}Fe_4K_4N_8O_{28}Si_8$
Formula weight	3721.17
Temperature/K	100
Crystal system	monoclinic
Space group	$P2_1/n$
a/Å	10.3333(7)
b/Å	34.0397(14)
c/Å	15.5254(9)
α/°	90
β/°	95.062(5)
γ/°	90
Volume/Å^3	5439.6(5)
Z	1
ρ_{calc}g/cm^3	1.136
μ/mm^{-1}	0.442
F(000)	2020.0
Crystal size/mm^3	0.888 × 0.304 × 0.225
Radiation	MoKα (λ = 0.71073)
2Θ range for data collection/°	4.944 to 53.622
Index ranges	−13 ≤ h ≤ 13, −43 ≤ k ≤ 43, −19 ≤ l ≤ 18
Reflections collected	42532
Independent reflections	11480 [R_{int} = 0.0441, R_{sigma} = 0.0347]
Data/restraints/parameters	11480/0/548
Goodness-of-fit on F^2	1.046
Final R indexes [I>=2σ (I)]	R_1 = 0.0422, wR_2 = 0.1070
Final R indexes [all data]	R_1 = 0.0648, wR_2 = 0.1172
Largest diff. peak/hole / e Å^{-3}	0.59/−0.69

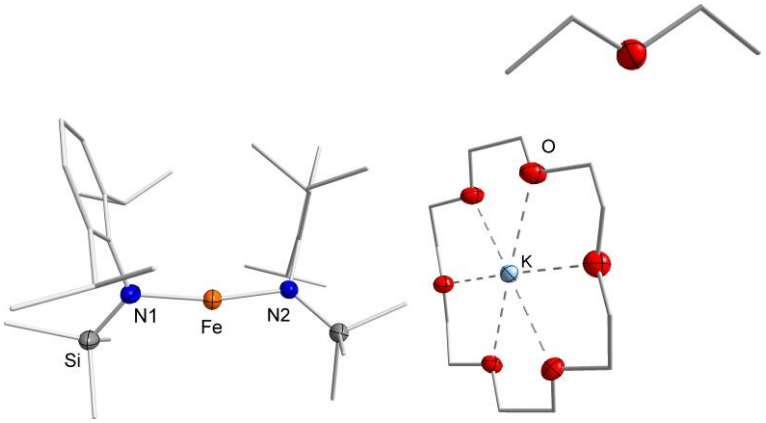

Figure S 80. Molecular structure of [K{18c6}][Fe(L^2)$_2$] x Et$_2$O. All hydrogen atoms are omitted for clarity.

References

(1) Lin, C.-Y.; Fettinger, J. C.; Grandjean, F.; Long, G. J.; Power, P. P. Synthesis, Structure, and Magnetic and Electrochemical Properties of Quasi-Linear and Linear Iron(I), Cobalt(I), and Nickel(I) Amido Complexes // Synthesis, structure, and magnetic and electrochemical properties of quasi-linear and linear iron(I), cobalt(I), and nickel(I) amido complexes. *Inorg. Chem.* **2014**, *53*, 9400–9406.

11.3 Zusatzinformationen zu Publikation 3

“On the Synthesis and Reduction of Trigonal Halido Bis(silylamido) Metalates of Chromium to Cobalt“

Ruth Weller, Lena Völlinger, C. Gunnar Werncke

Eur. J. Inorg. Chem. **2021**, 4383−4392.
DOI: 10.1002/ejic.202100716
https://doi.org/10.1002/ejic.202100716

European Journal of Inorganic Chemistry

Supporting Information

On the Synthesis and Reduction of Trigonal Halido Bis (silylamido) Metalates of Chromium to Cobalt

Ruth Weller, Lena Völlinger, and C. Gunnar Werncke*

Table of Content

1 ^{1}H NMR Spectra of isolated complexes

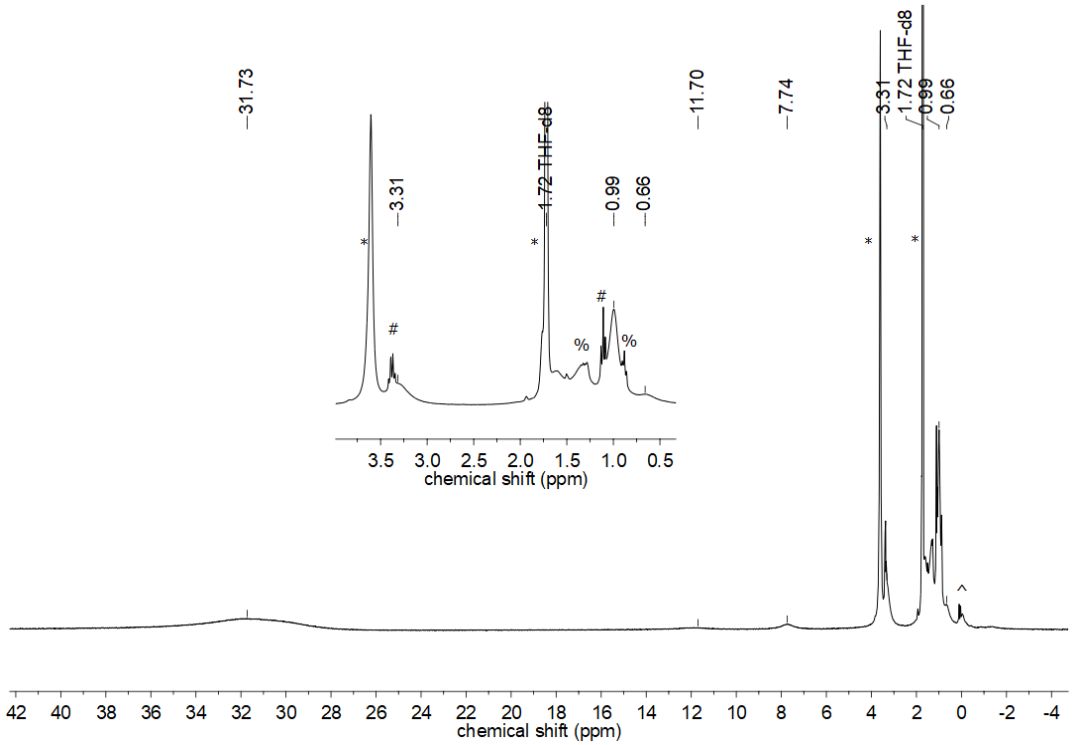

Figure S1. ^{1}H NMR spectrum (300.2 MHz, 300 K) of **[NBu$_4$][Cr$_2$(Br)L$^1_2$L^{1*}]** in THF-d_8. (* solvent, ^ decomposition, # diethyl ether, % *n*-pentane)

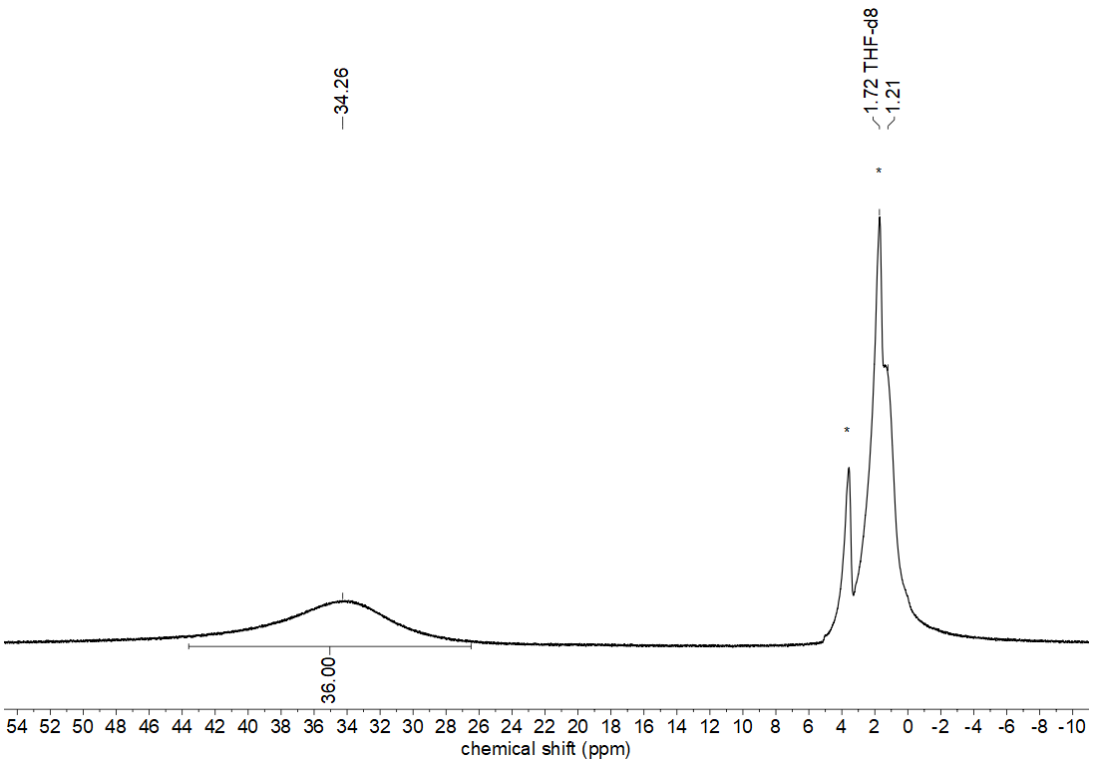

Figure S2. ^{1}H NMR spectrum (300.2 MHz, 300 K) of **[NBu$_4$][Mn(Br)L$^1_2$]** in THF-d_8. (* solvent)

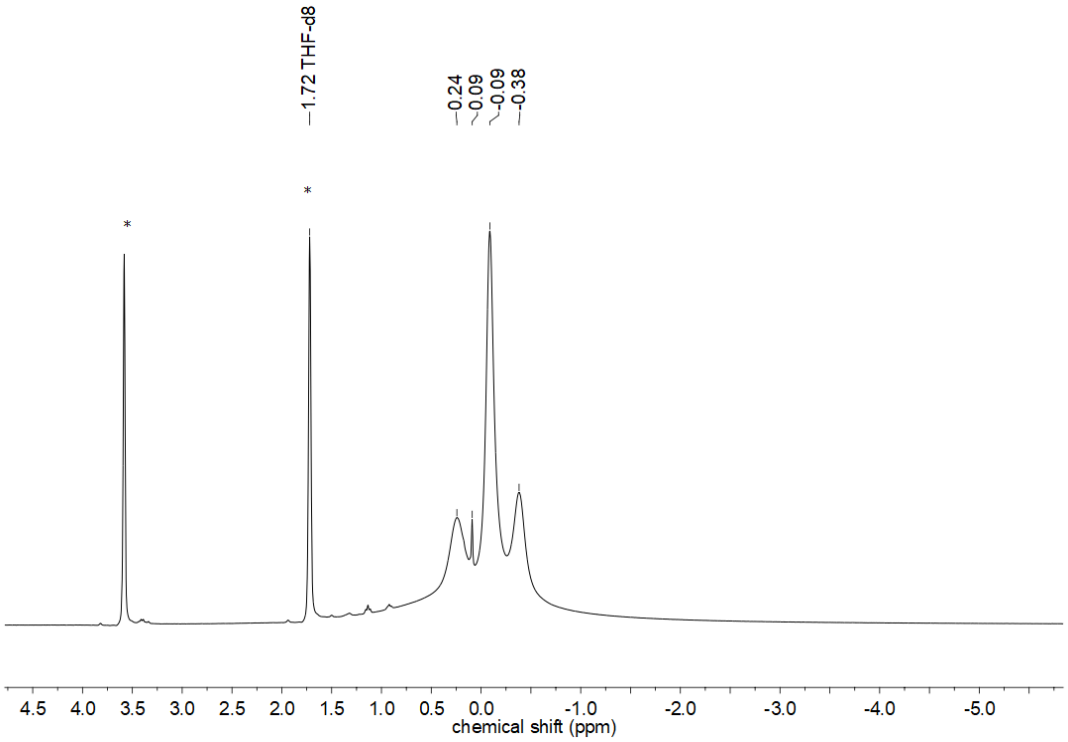

Figure S3. ^{1}H NMR spectrum (300.2 MHz, 300 K) of **[NBu$_4$][Fe(Br)L$^1_2$]** in THF-d_8. (* solvent)

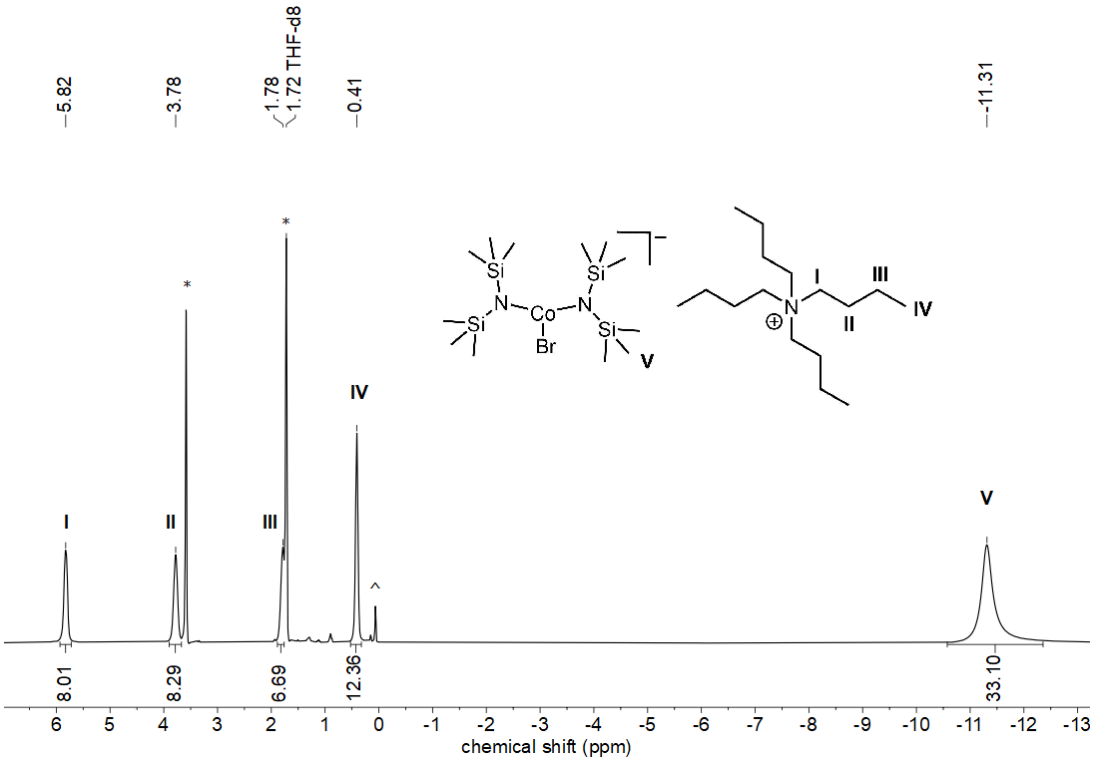

Figure S4. ^{1}H NMR spectrum (300.2 MHz, 300 K) of **[NBu$_4$][Co(Br)L$^1_2$]** in THF-d_8. (* solvent, ^ decomposition)

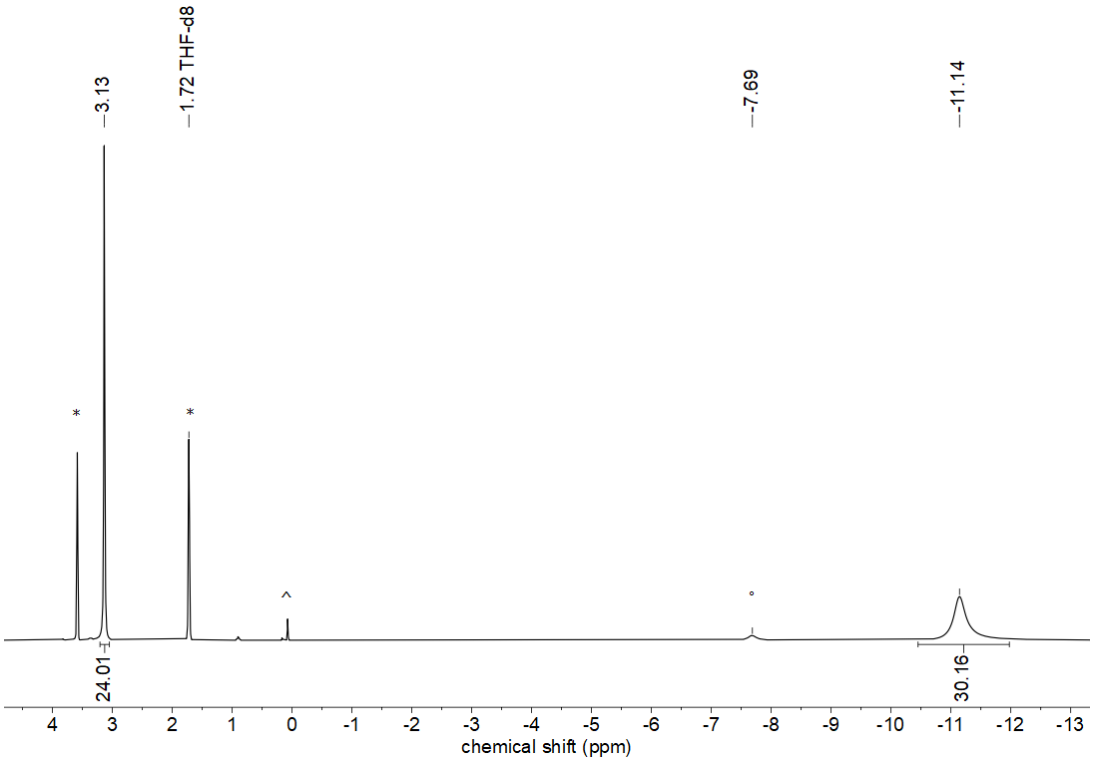

Figure S5. ^{1}H NMR spectrum (300.2 MHz, 300 K) of **[K{18c6}][Co(Br)L$^{1}_{2}$]** in THF-d_8. (* solvent, ^ decomposition, ° [CoL$^{1}_{3}$]$^{-}$)

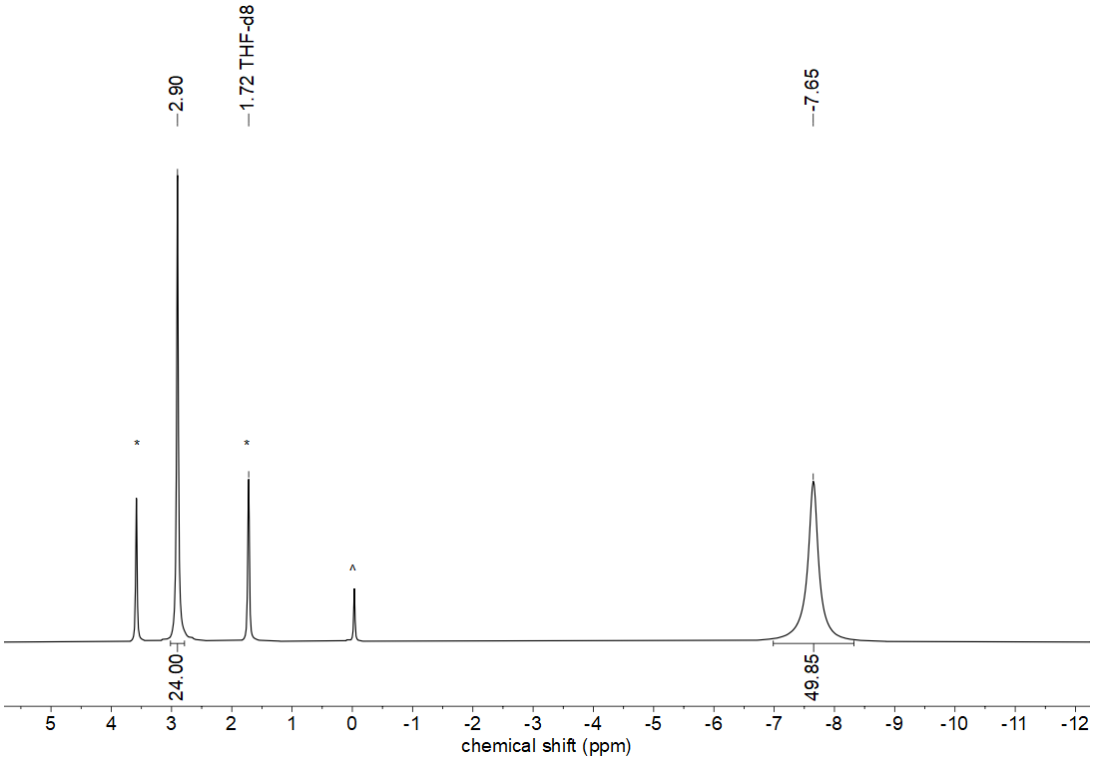

Figure S6. ^{1}H NMR spectrum (300.2 MHz, 300 K) of **[K{18c6}][CoL$^{1}_{3}$]** in THF-d_8. (* solvent, ^ decomposition)

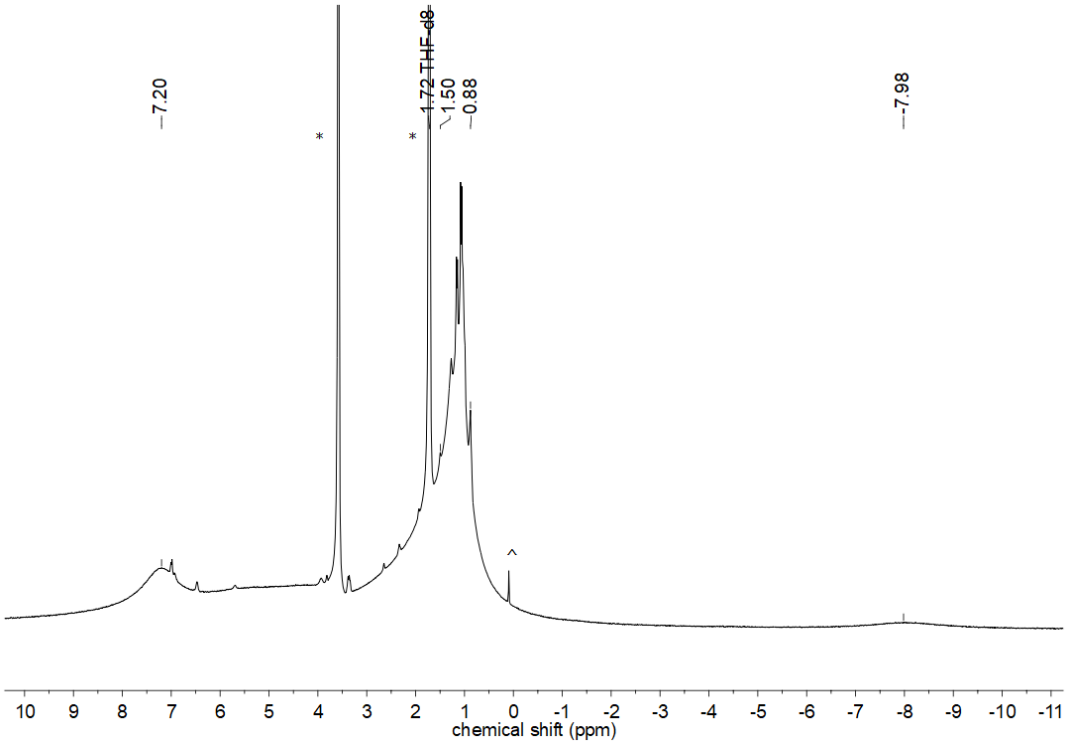

Figure S7. ^{1}H NMR spectrum (300.2 MHz, 300 K) of **[NBu$_4$][Cr(Br)$_2$L^3]** in THF-d_8. (* solvent, ^ decomposition)

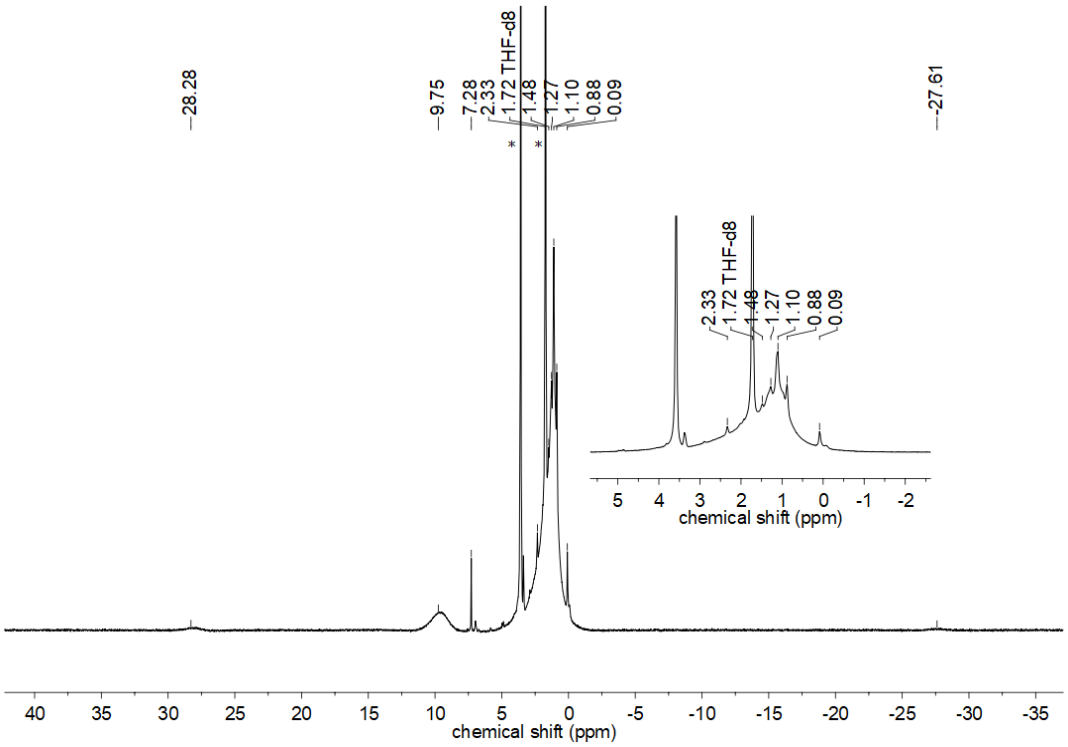

Figure S8. ^{1}H NMR spectrum (300.2 MHz, 300 K) of **[NBu$_4$][Mn(Br)L$^2_2$]** in THF-d_8. (* solvent)

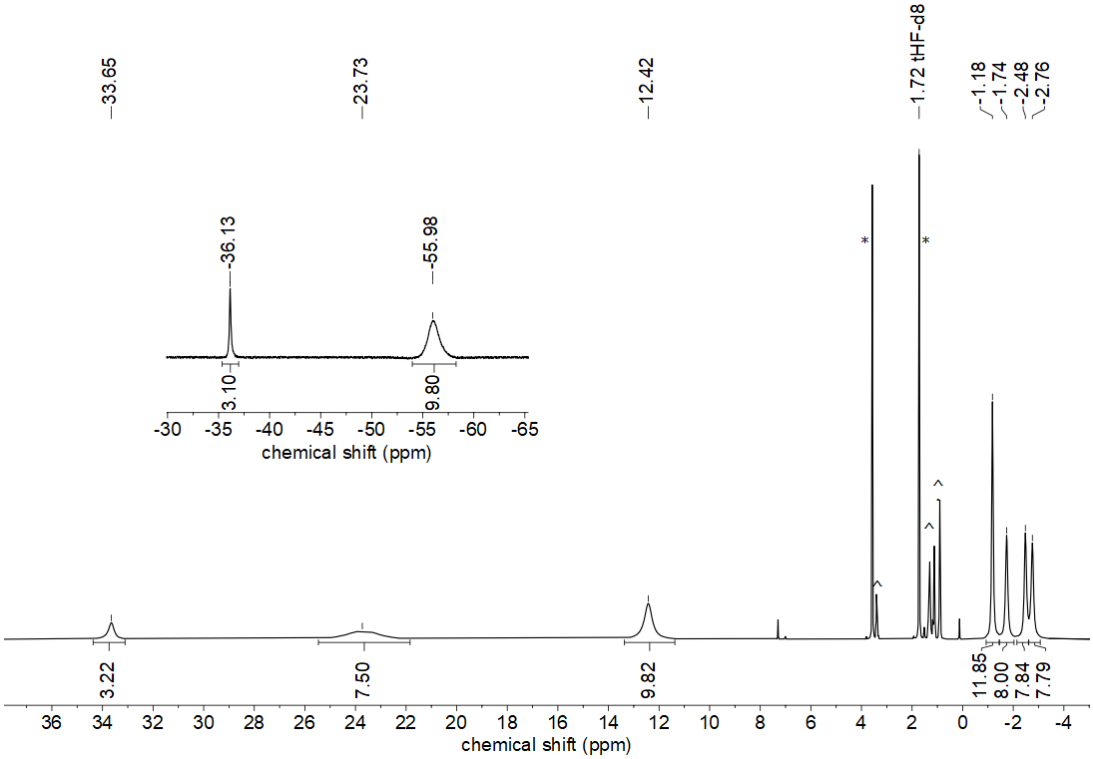

Figure S9. ^{1}H NMR spectrum (300.2 MHz, 300 K) of **[NBu$_4$][Fe(Br)L$^2_2$]** in THF-d_8. (* solvent, ^ decomposition)

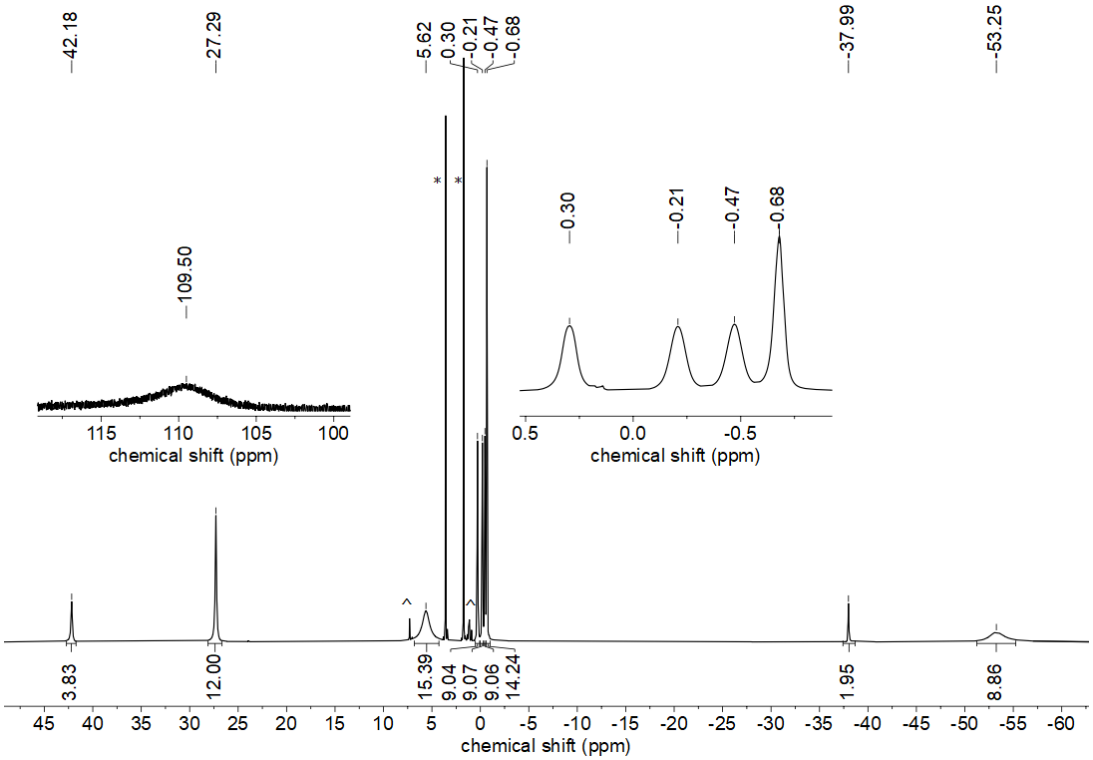

Figure S10. ^{1}H NMR spectrum (300.2 MHz, 300 K) of **[NBu$_4$][Co(Br)L$^2_2$]** in THF-d_8. (* solvent, ^ decomposition)

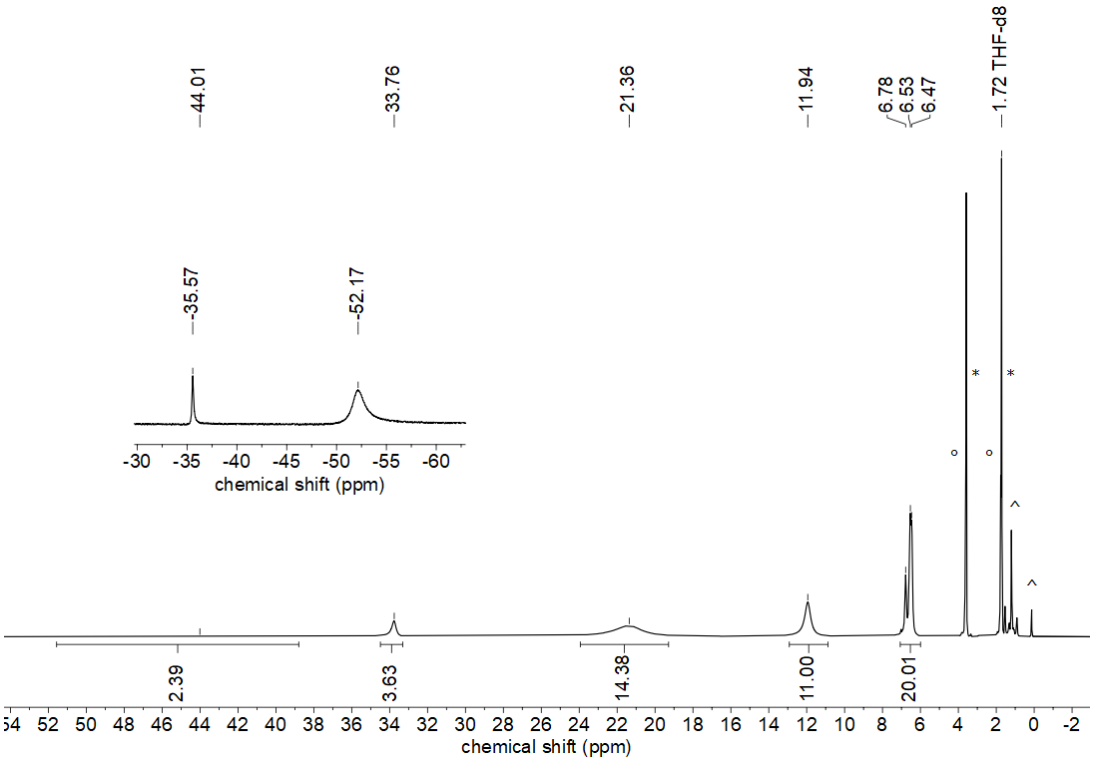

Figure S11. ^{1}H NMR spectrum (300.2 MHz, 300 K) of **[PPh$_4$][Fe(Br)L$^2_2$]** in THF-d_8. (* solvent, ° THF$_{coord}$, ^ impurities)

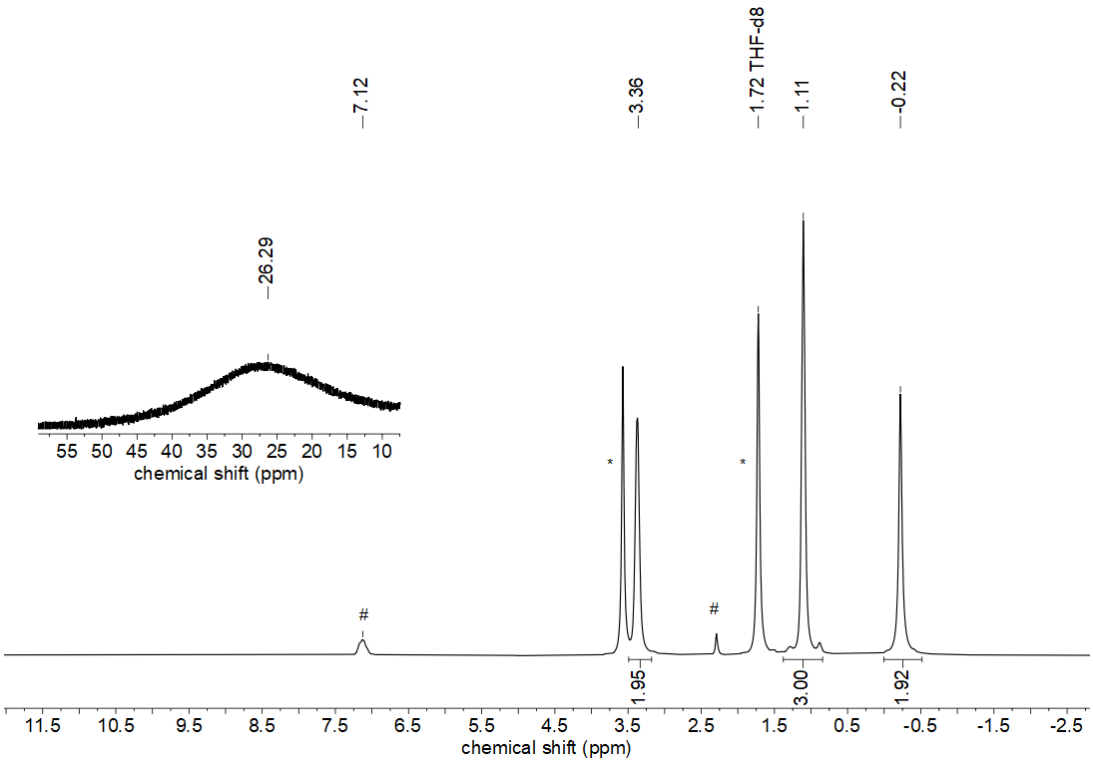

Figure S12. ^{1}H NMR spectrum (300.2 MHz, 300 K) of **[KMn(Bn)L$^1_2$]** in THF-d_8. (* solvent, # free BnK)

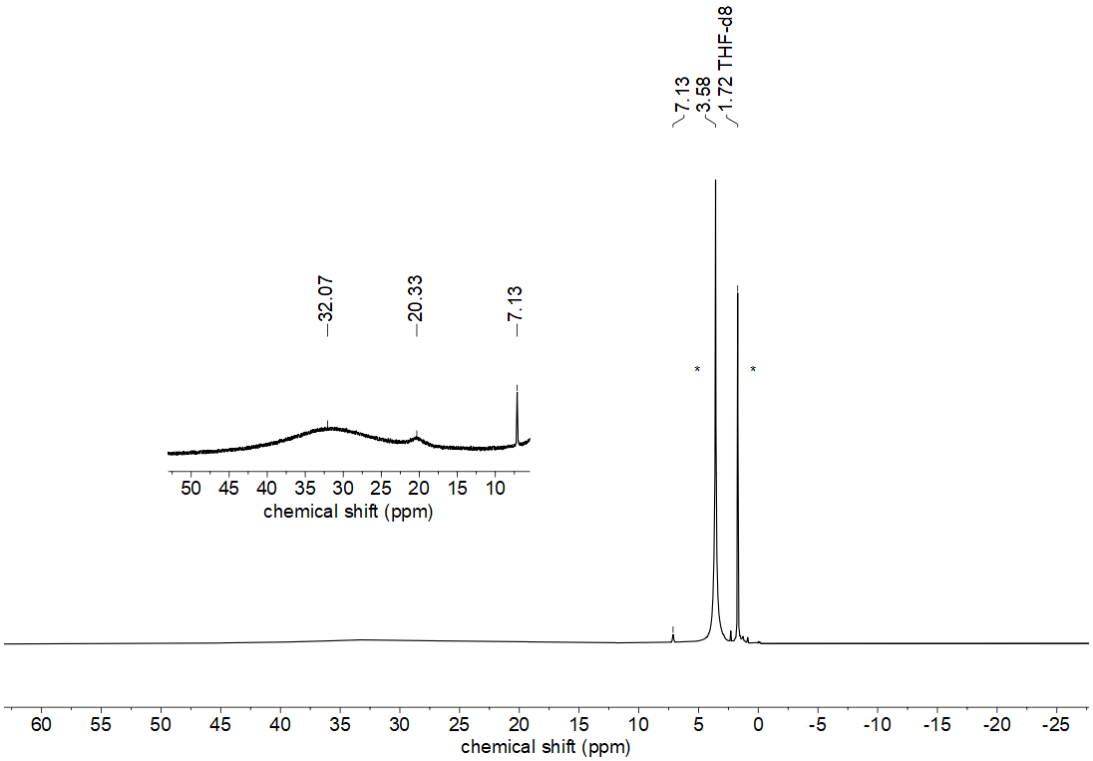

Figure S13. ^{1}H NMR spectrum (300.2 MHz, 300 K) of **[K{18c6}][Mn(Bn)L$^{1}_{2}$]** in THF-d_8. (* solvent) * Signal of 18-crown-6 is overlapping with the solvent signal at 3.58 ppm.

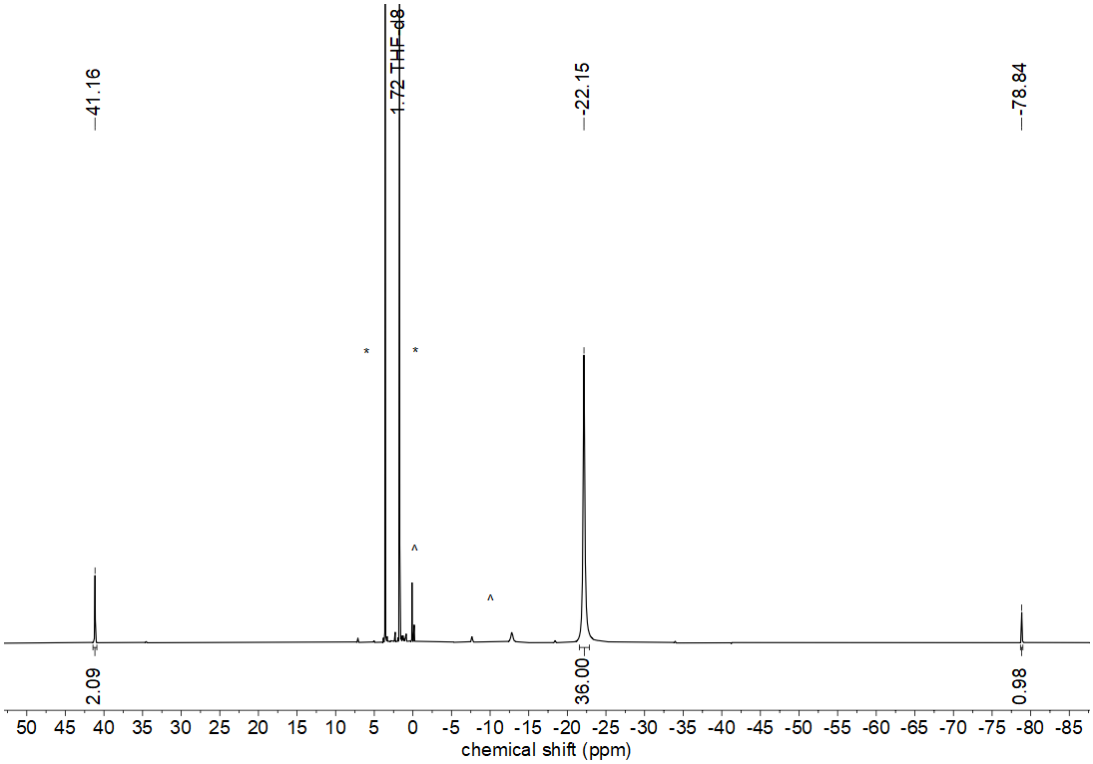

Figure S14. ^{1}H NMR spectrum (300.2 MHz, 300 K) of **[KCo(Bn)L$^{1}_{2}$]** in THF-d_8. (* solvent, ^ decomposition/impurities)

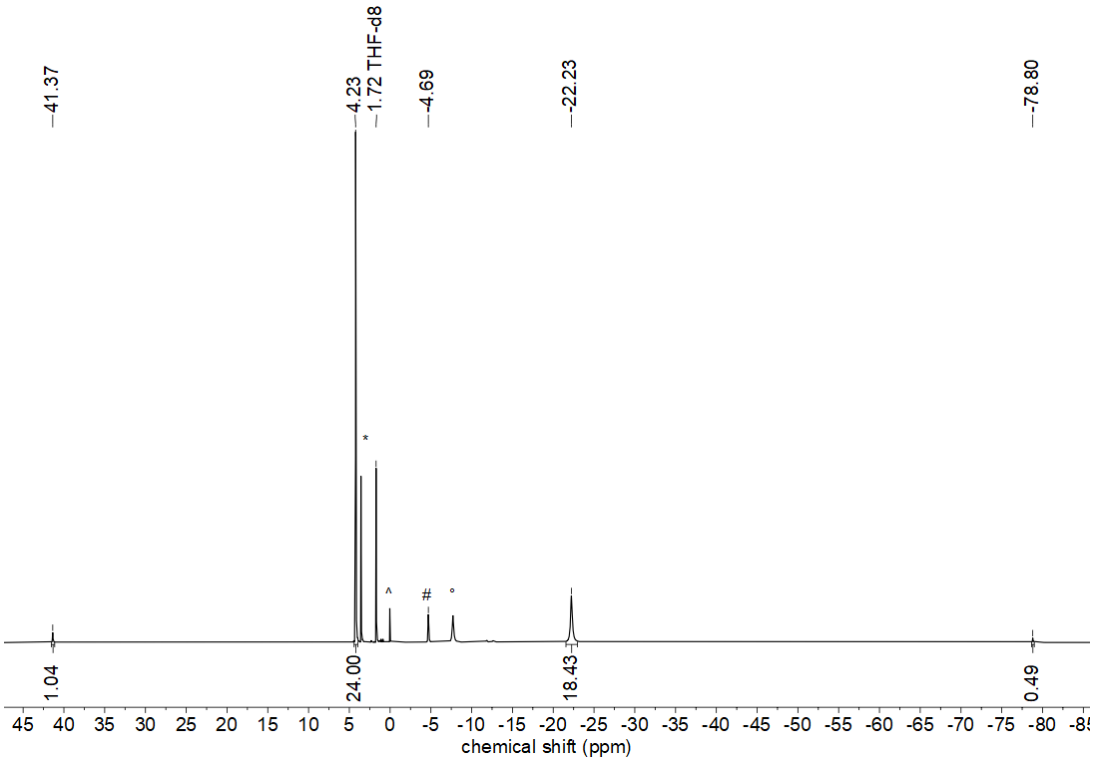

Figure S15. ^{1}H NMR spectrum (300.2 MHz, 300 K) of **[K{18c6}][Co(Bn)L$^{1}_{2}$]** in THF-d_8. (* solvent, ^ decomposition, # $[CoL^{1}_{2}]^{-}$, ° $[CoL^{1}_{3}]^{-}$)

Reactivity studies *via* ^{1}H NMR spectroscopy

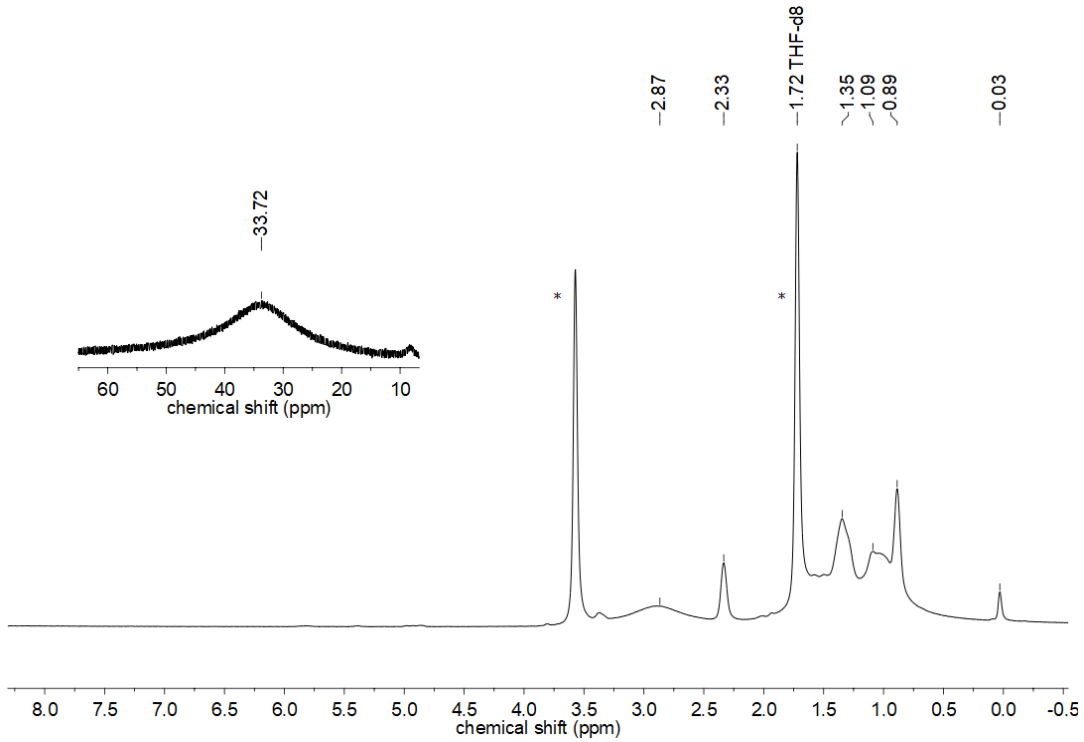

Figure S16. *In situ* ^{1}H NMR spectrum (300.2 MHz, 300 K) of reacting **[NBu$_4$][Mn(Br)L$^1_2$]** with KC_8 in THF-d_8. (* solvent)

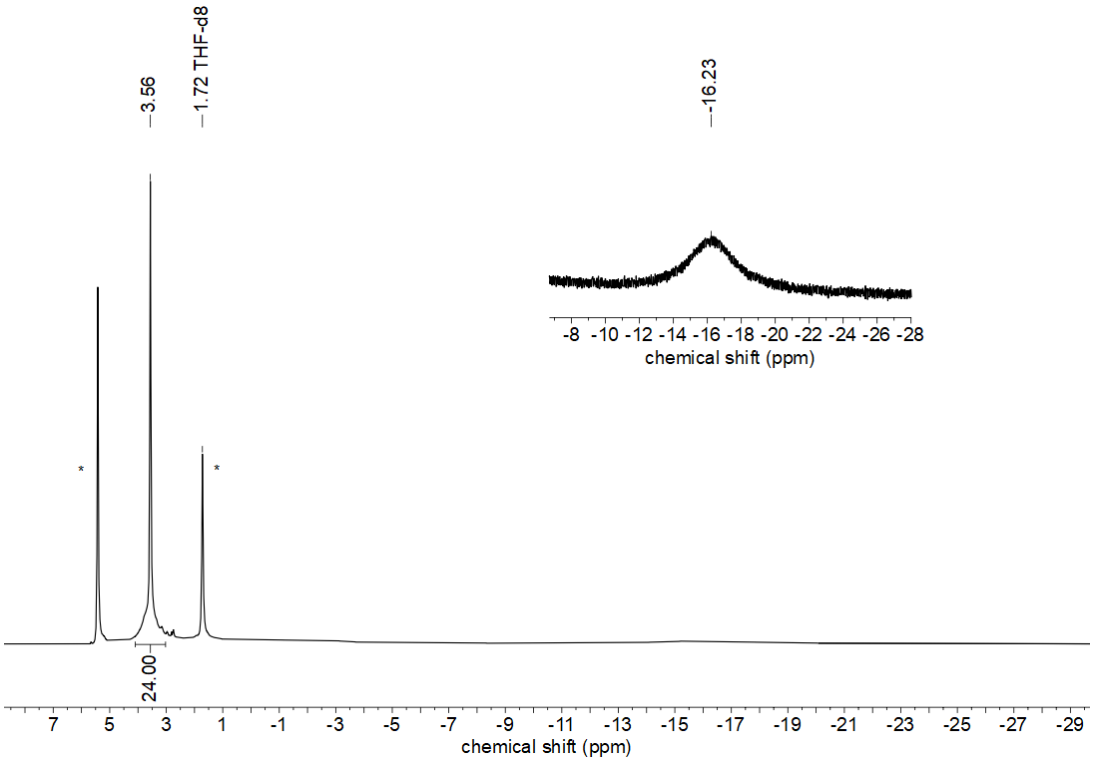

Figure S17. *In situ* ^{1}H NMR spectrum (300.2 MHz, 300 K) of reacting **[K{18c6}][Fe(Br)L$^1_2$]** with KC_8 in THF-d_8. (* solvent)

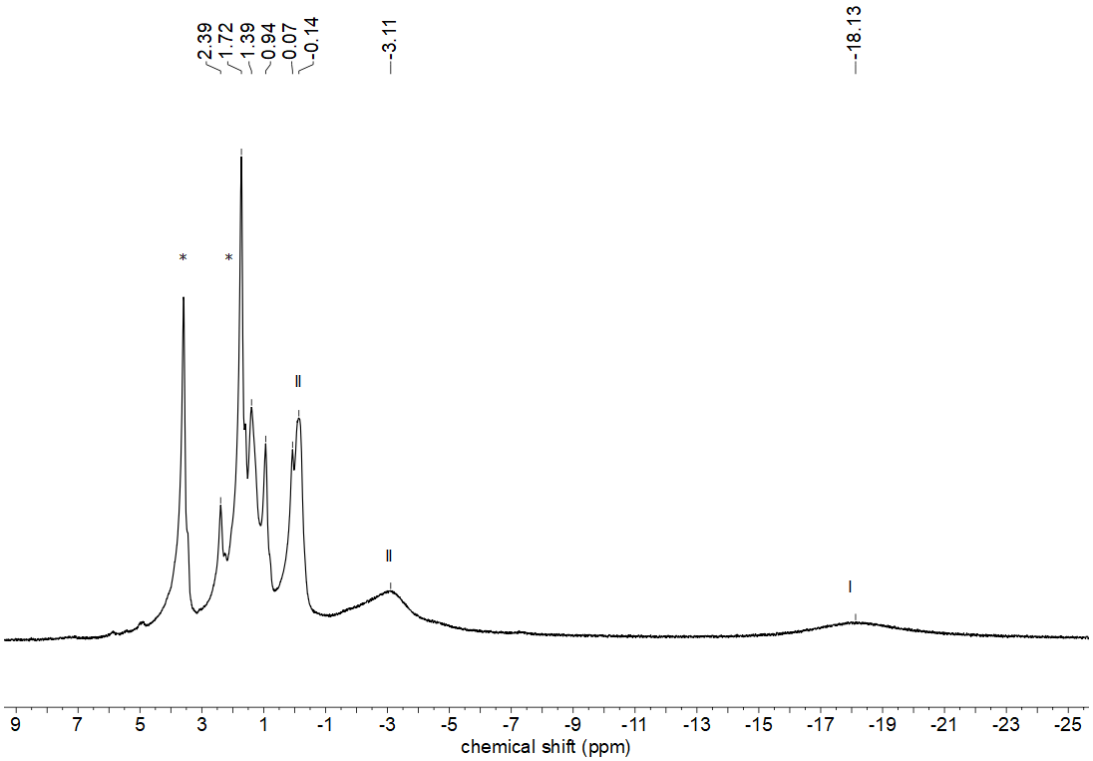

Figure S18. *In situ* ^{1}H NMR spectrum (300.2 MHz, 300 K) of reacting **[NBu$_4$][Fe(Br)L$^1_2$]** with KC_8 in THF-d_8 ("II" $[Fe(Br)L^1_2]^-$, "I" $[Fe^{I}(N(SiMe_3)_2)_2]^-$). (* solvent)

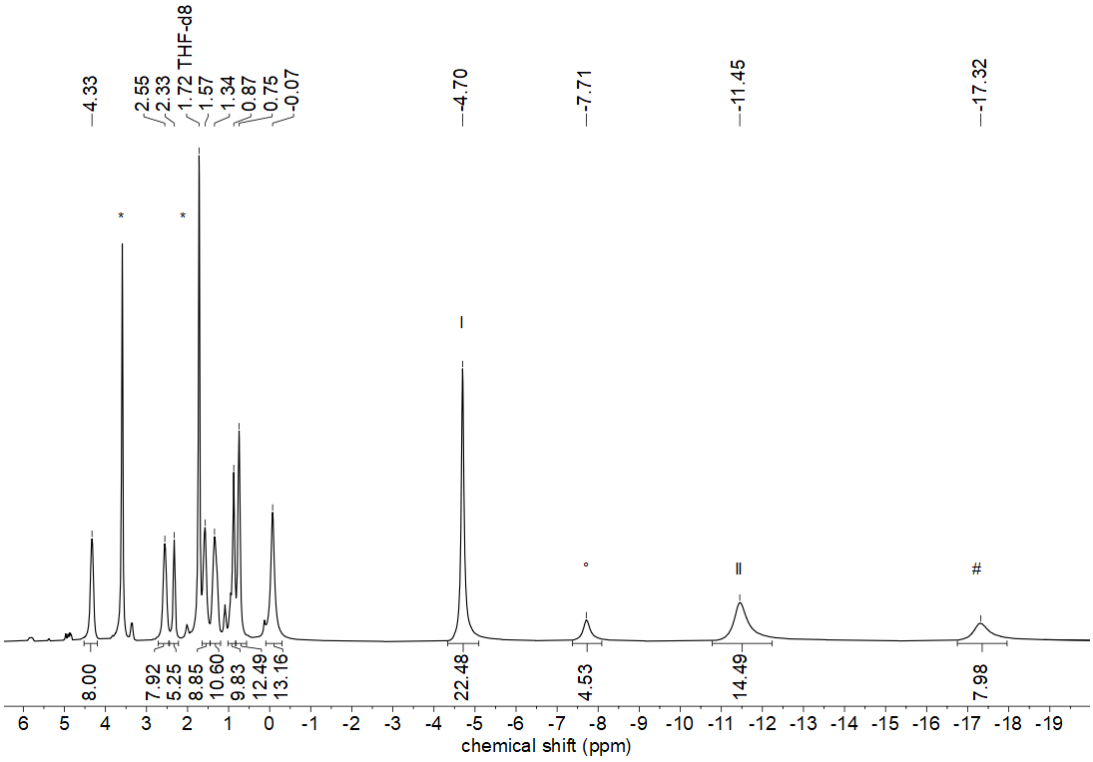

Figure S19. *In situ* ^{1}H NMR spectrum (300.2 MHz, 300 K) of the reduction of **[NBu$_4$][Co(Br)L$^1_2$]** with KC_8 in THF-d_8. (* solvent, "II" $[Co(Br)L^1_2]^-$, "I" $[CoL^1_2]^-$ ° $[CoL^1_3]^-$; # unknown species)

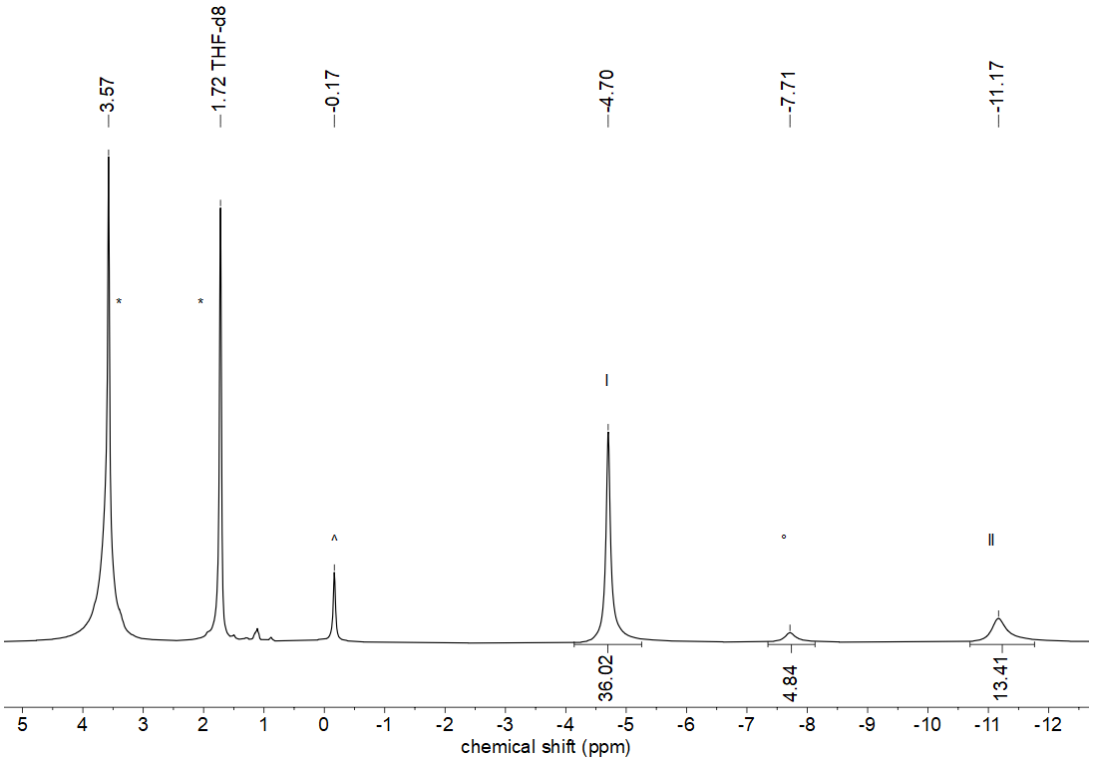

Figure S20. *In situ* ^{1}H NMR spectrum (300.2 MHz, 300 K) of reacting **[K{18c6}][Co(Br)L$^{1}_{2}$]** with KC_8 in THF-d_8. (* solvent, "II" $[Co(Br)L^{1}_{2}]^{-}$, ° $[CoL^{1}_{3}]^{-}$; "I" $[CoL^{1}_{2}]^{-}$, ^ decomposition). * Signal of 18-crown-6 is overlapping with the solvent signal at 3.57 ppm.

Temperature dependent ^{1}H NMR spectroscopy of [NBu$_4$][Co(Br)L$^1_2$] and [K{18c6}][Co(Br)L$^1_2$]

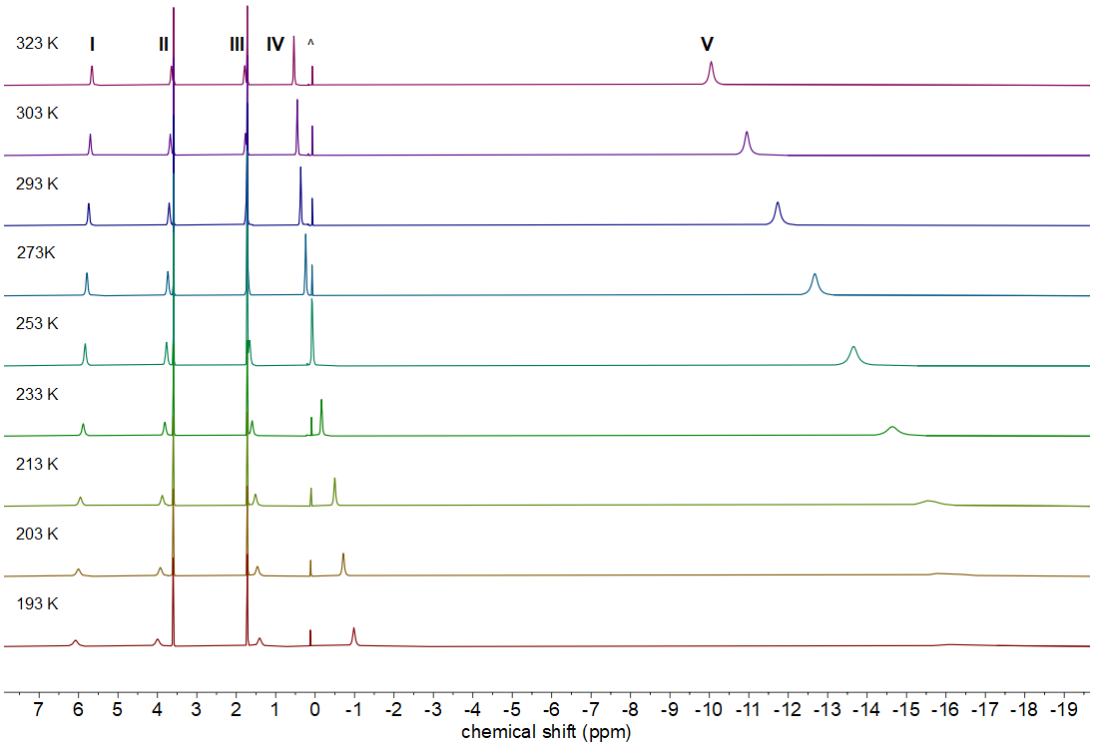

Figure S21. Temperature dependent ^{1}H NMR spectrum (500.1 MHz) of **[NBu$_4$][Co(Br)L$^1_2$]** in THF-d_8 from 323 K to 193 K. (^ decomposition)

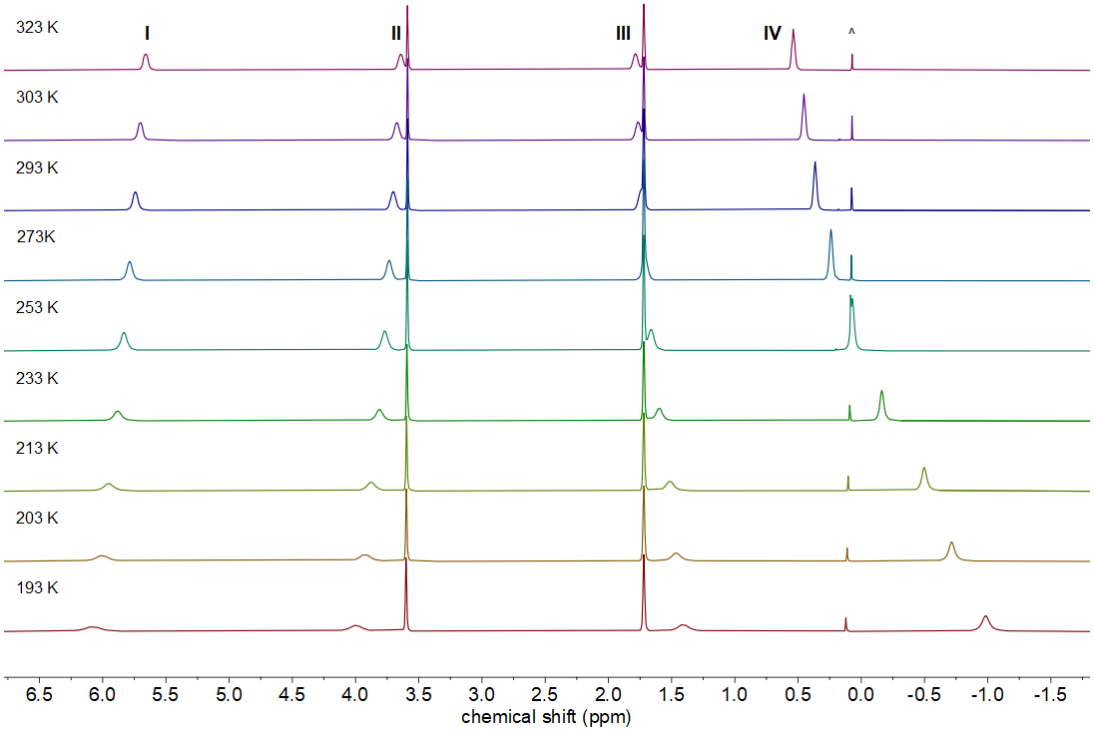

Figure S22. Section of the temperature dependent ^{1}H NMR spectrum (500.1 MHz) of **[NBu$_4$][Co(Br)L$^1_2$]** in THF-d_8 from 323 K to 193 K from −2 ppm to 6.5 ppm. (^ decomposition)

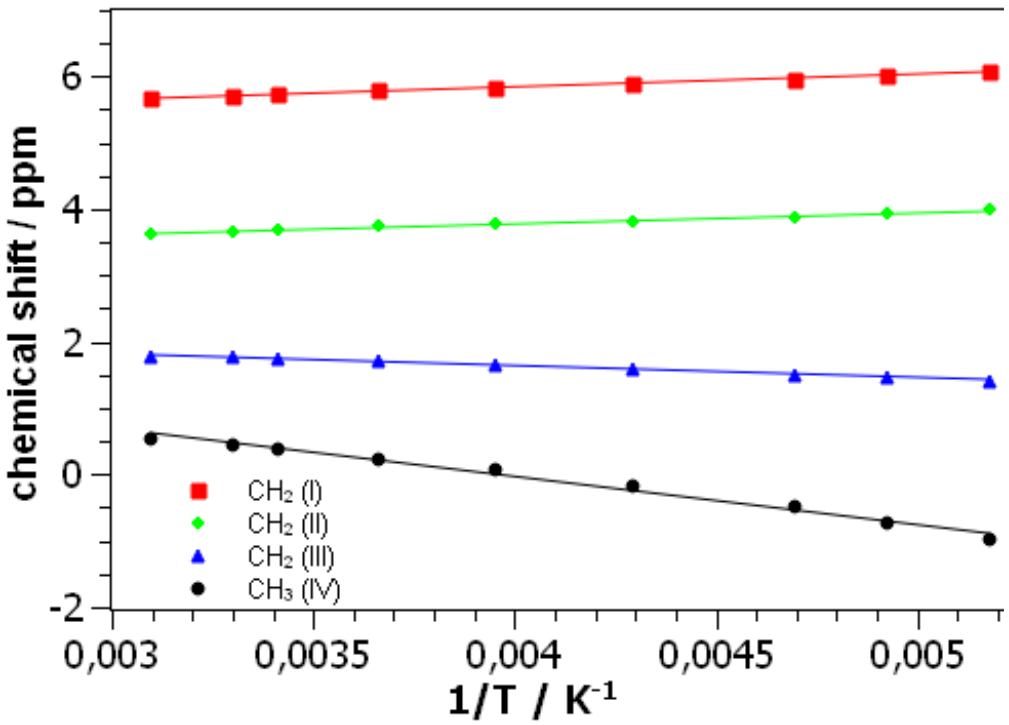

Figure S23. Curie-Weiss plot of the temperature dependent ^{1}H NMR spectrum of **[NBu$_4$][Co(Br)L$^1_2$]** in THF-d_8.

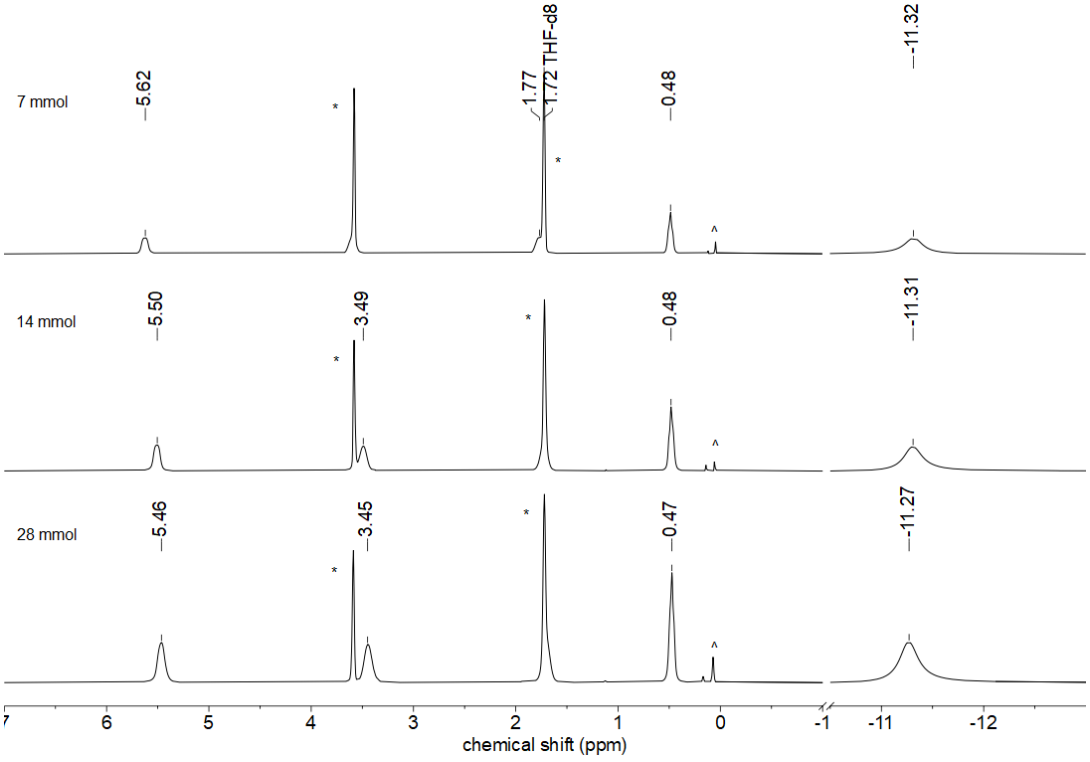

Figure S24. Dilution effects of **[NBu$_4$][Co(Br)L$^1_2$]** in THF-d_8 measured by ^{1}H NMR spectroscopy (500.1 MHz, 300 K) (* solvent, ^ decomposition).

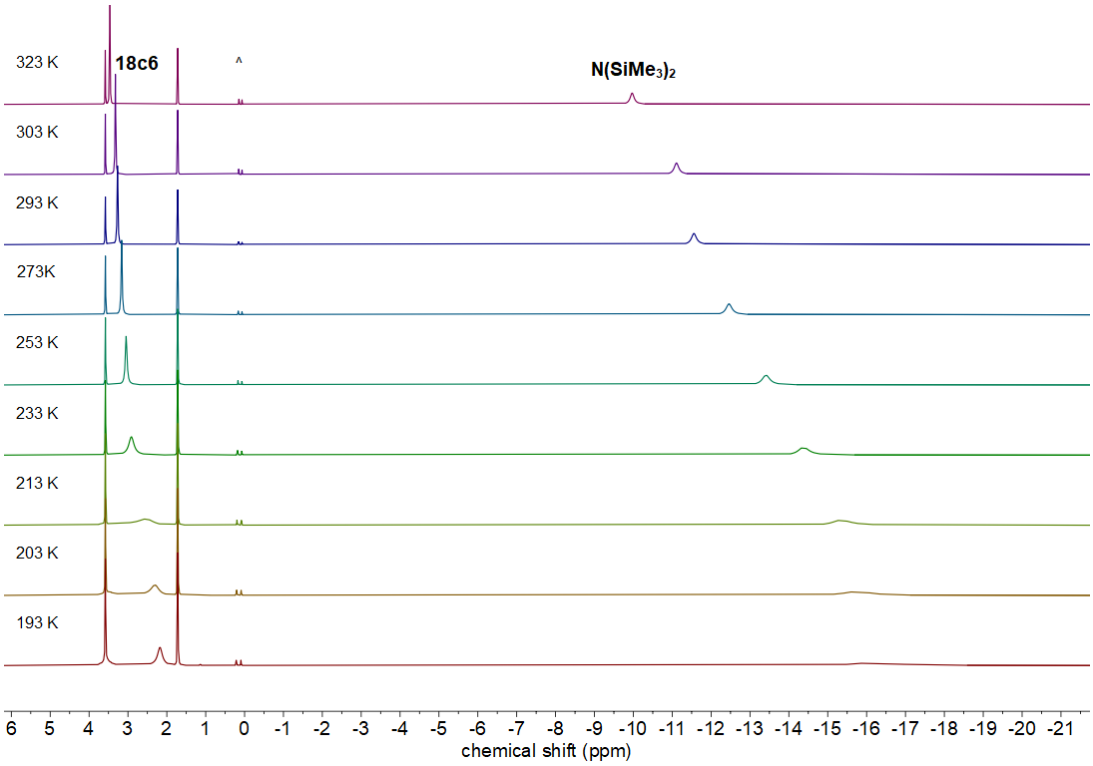

Figure S25. Temperature dependent ^{1}H NMR spectrum (500.1 MHz) of **[K{18c6}][Co(Br)L$^{1}_{2}$]** in THF-d_8 from 323 K to 193 K. (^ decomposition)

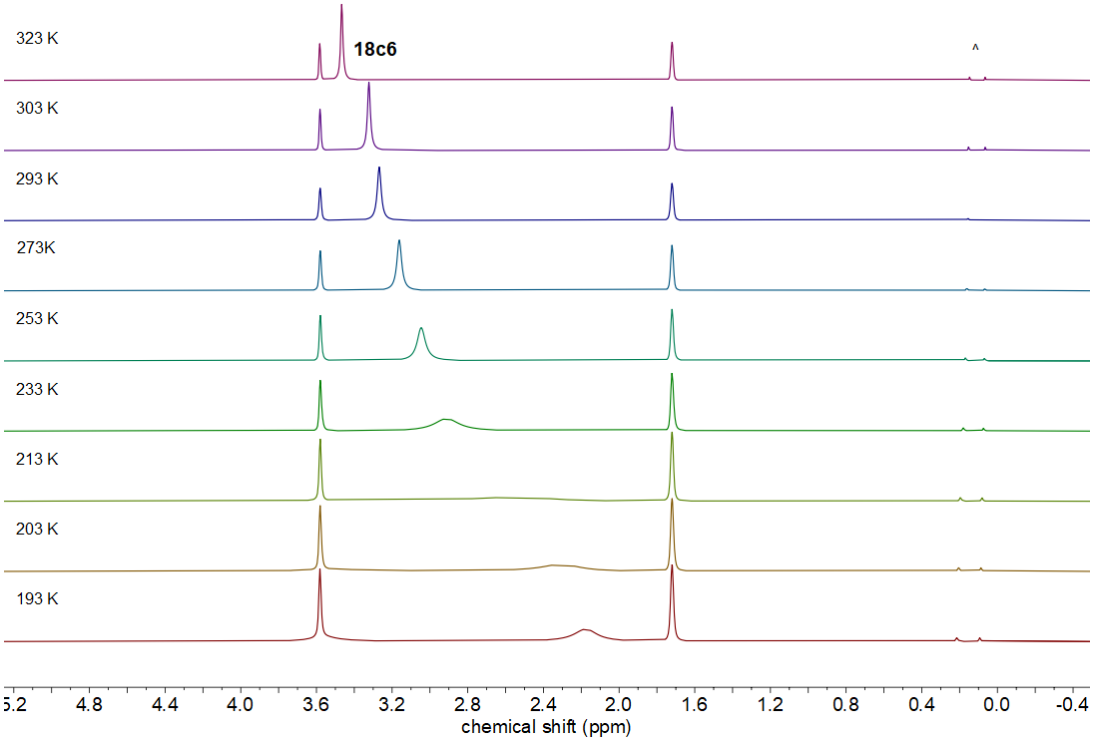

Figure S26. Section of the temperature dependent ^{1}H NMR spectrum (500.1 MHz) of **[K{18c6}][Co(Br)L$^{1}_{2}$]** in THF-d_8 from 323 K to 193 K from 0 ppm to 5 ppm. (^ decomposition)

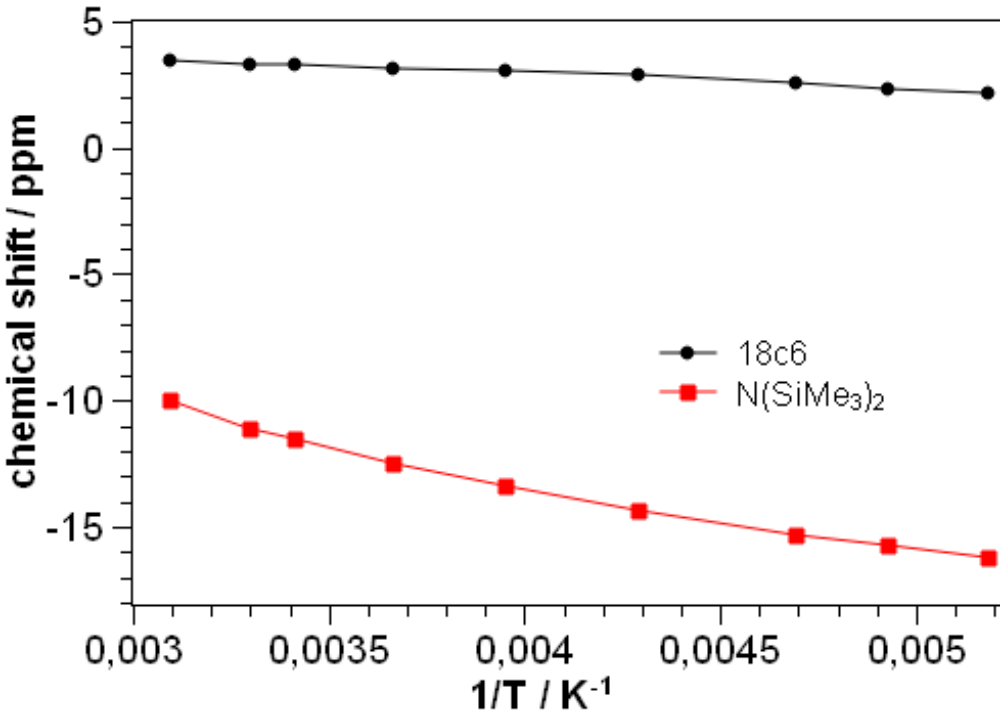

Figure S27. Curie-Weiss plot of the temperature dependent ^{1}H NMR spectrum of **[K{18c6}][Co(Br)L$^{1}_{2}$]** in THF-*d*$_{8}$.

2 IR spectra

$N(SiMe_3)_2$

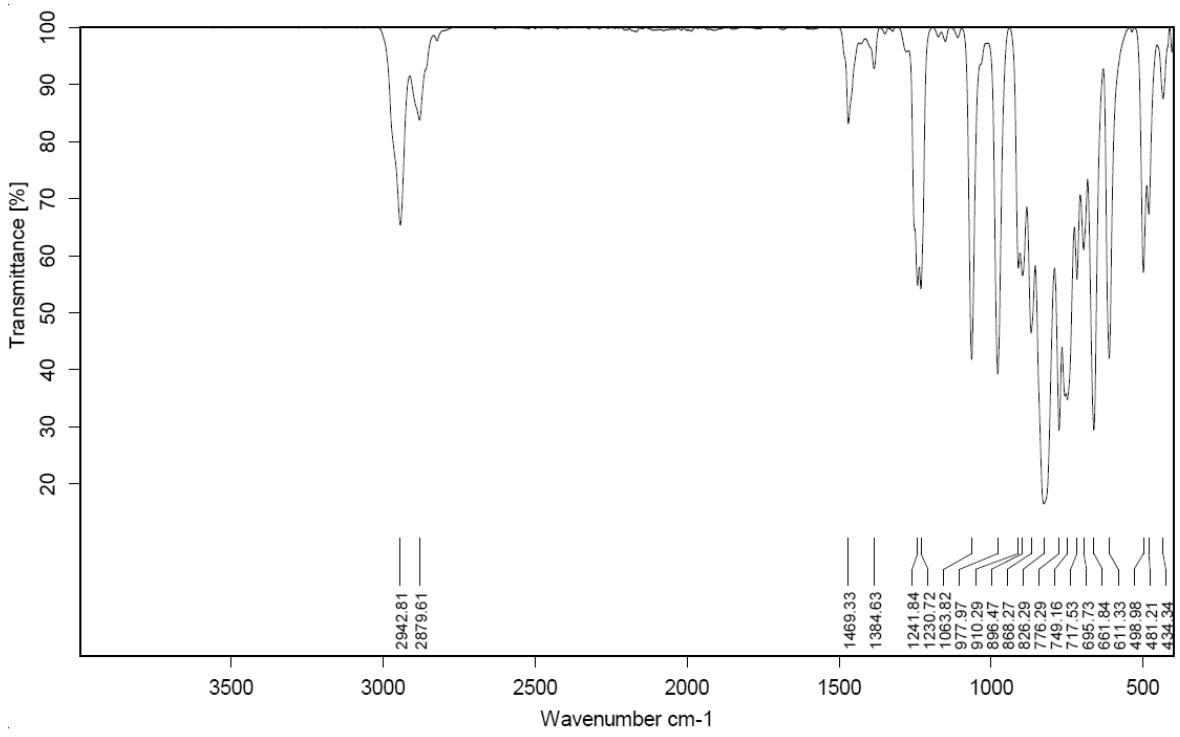

Figure S28. IR spectrum of **$[NBu_4][Cr_2(Br)L^1{}_2L^{1*}]$**.

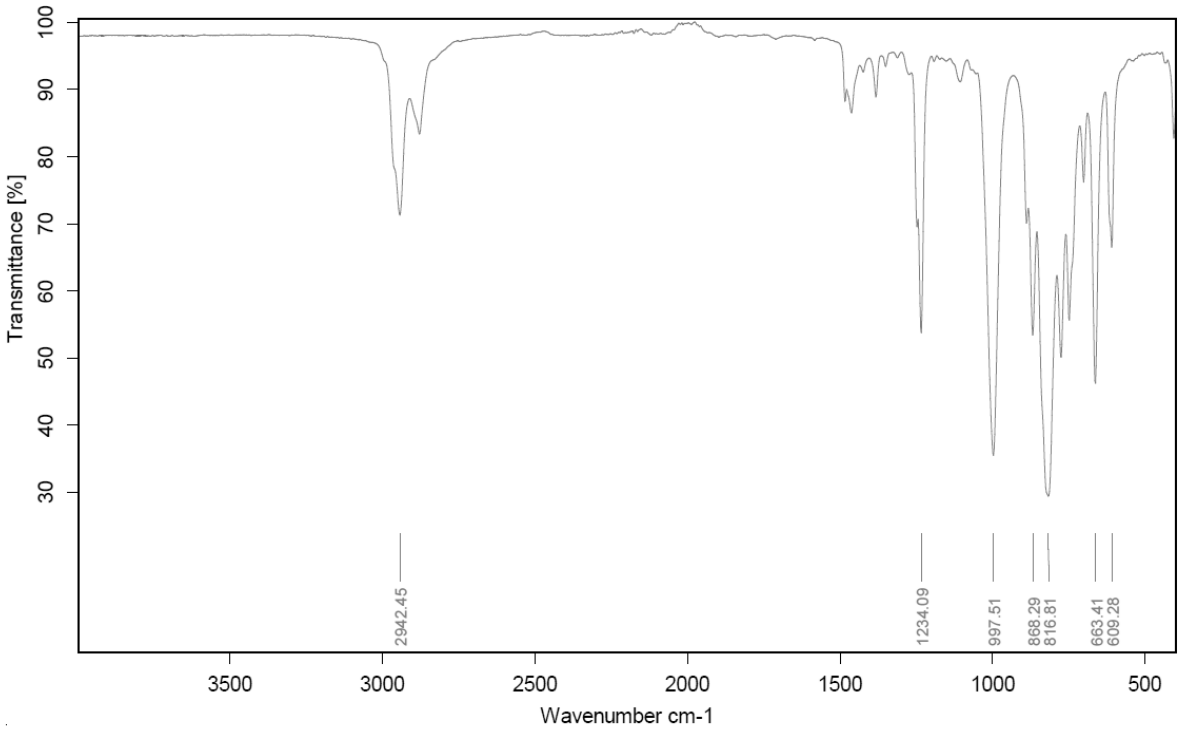

Figure S29. IR spectrum of **$[NBu_4][Mn(Br)L^1{}_2]$**.

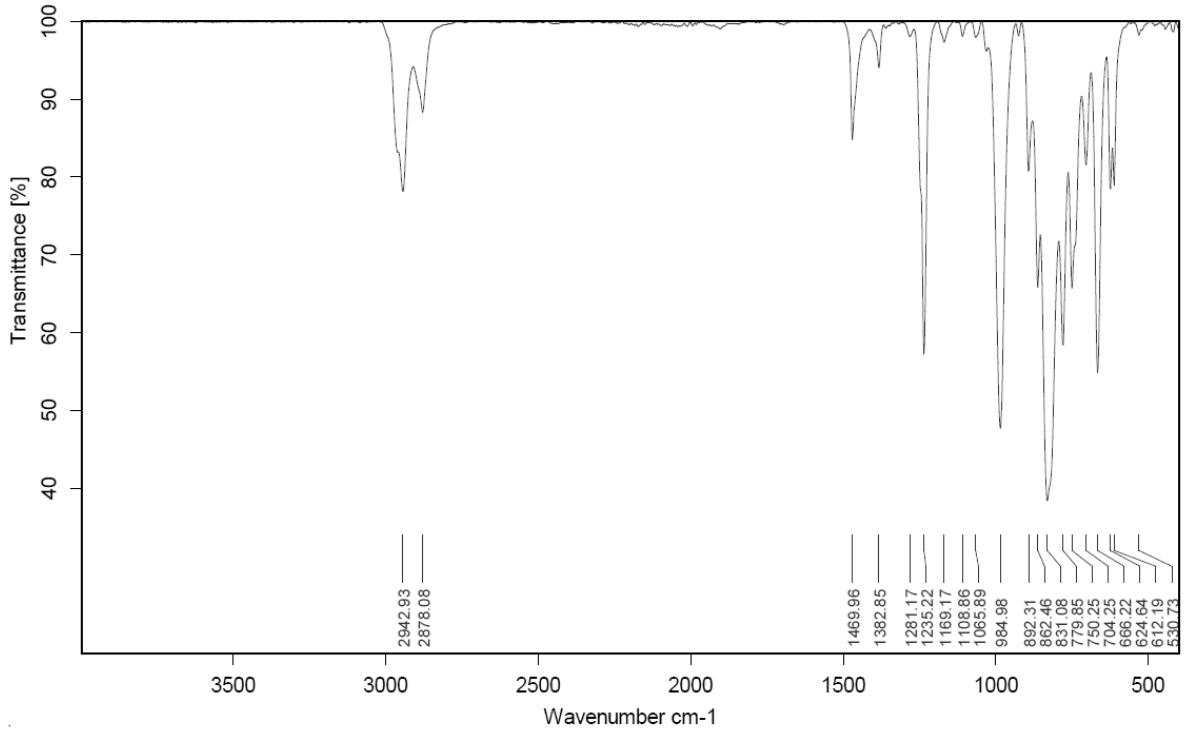

Figure S30. IR spectrum of **[NBu$_4$][Fe(Br)L$^1_2$]**.

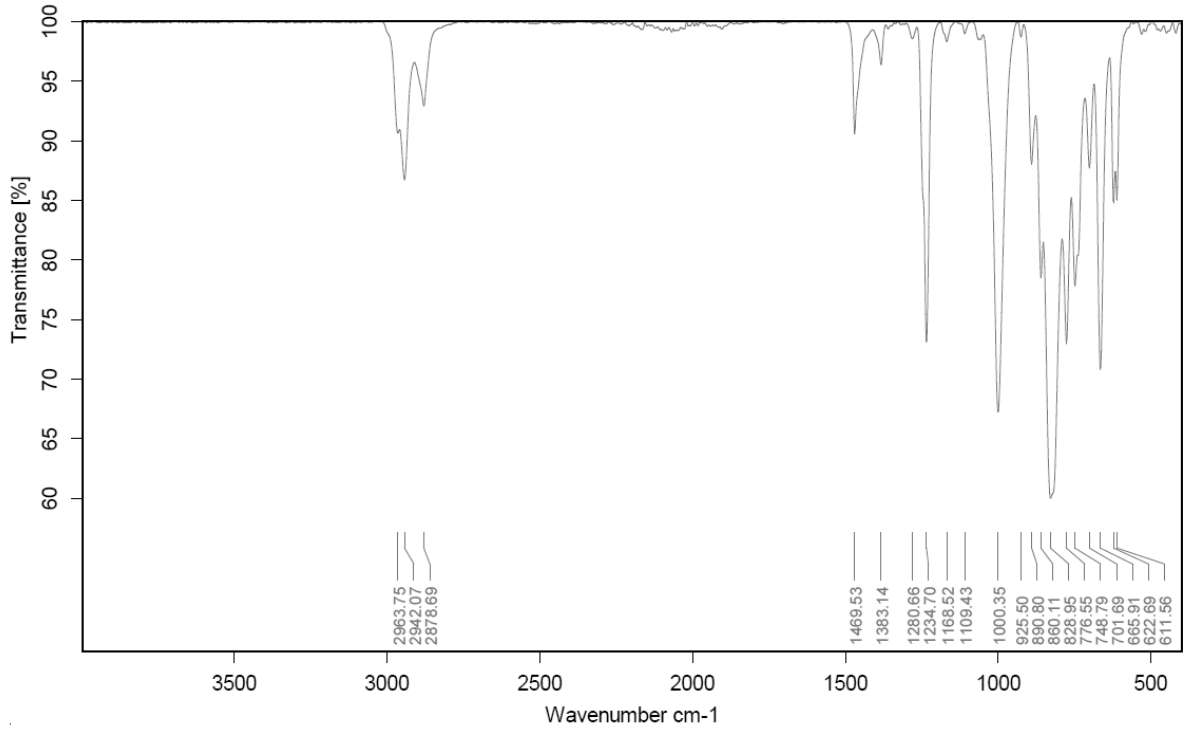

Figure S31. IR spectrum of **[NBu$_4$][Co(Br)L$^1_2$]**.

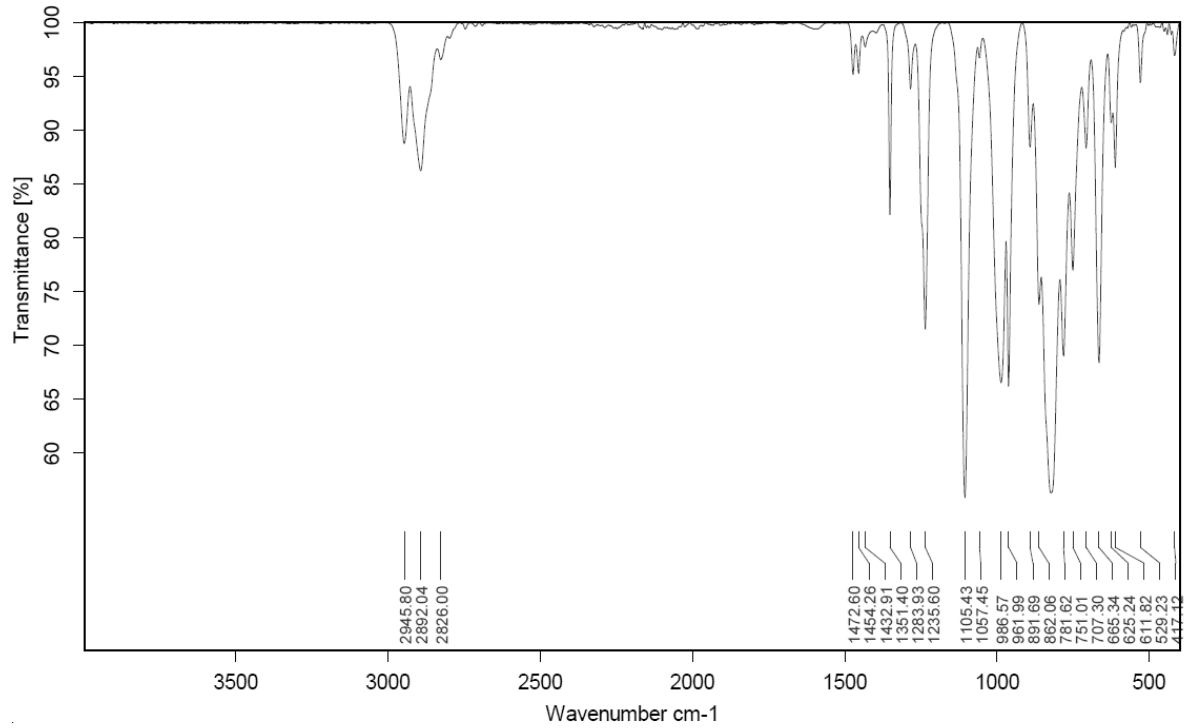

Figure S32. IR spectrum of **[K{18c6}][Co(Br)L$^{1}_{2}$]**.

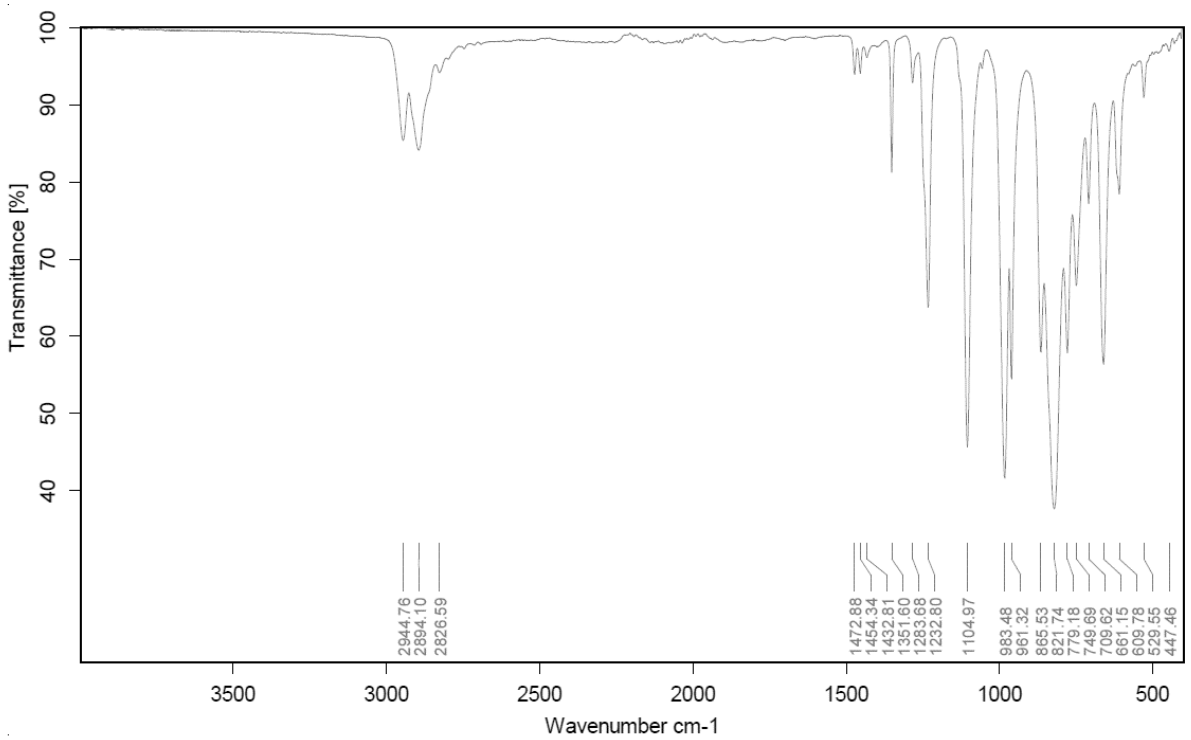

Figure S33. IR spectrum of **[K{18c6}][CoL$^{1}_{3}$]**.

N(Dipp)SiR$_3$ (R = ^{i}Pr (Cr), Me (Mn − Co))

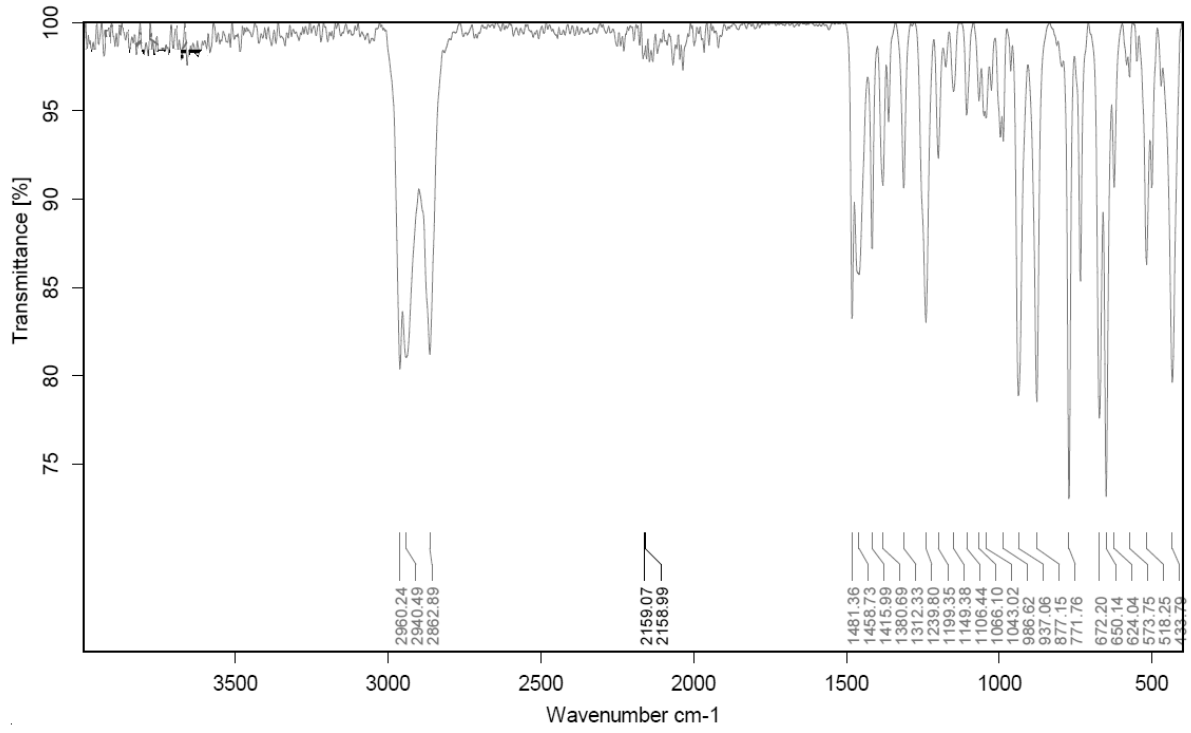

Figure S34. IR spectrum of **[NBu$_4$][Cr(Br)$_2$L^3]**.

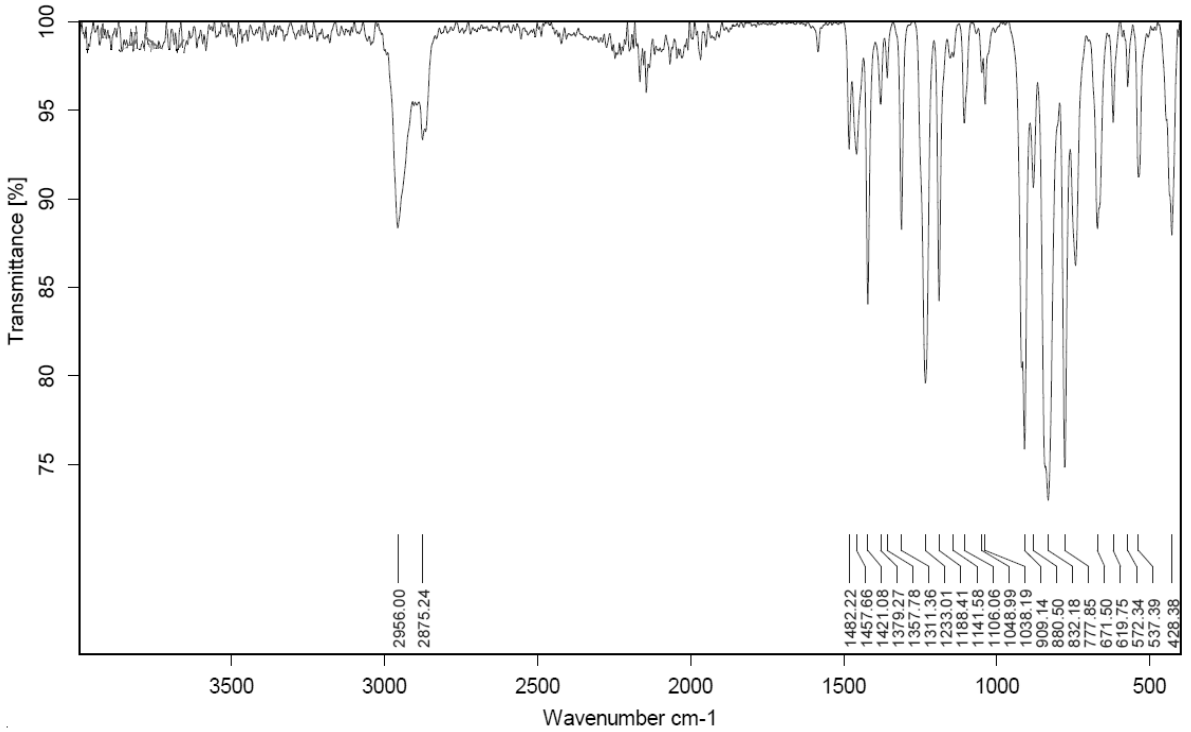

Figure S35. IR spectrum of **[NBu$_4$][Mn(Br)L$^2_2$]**.

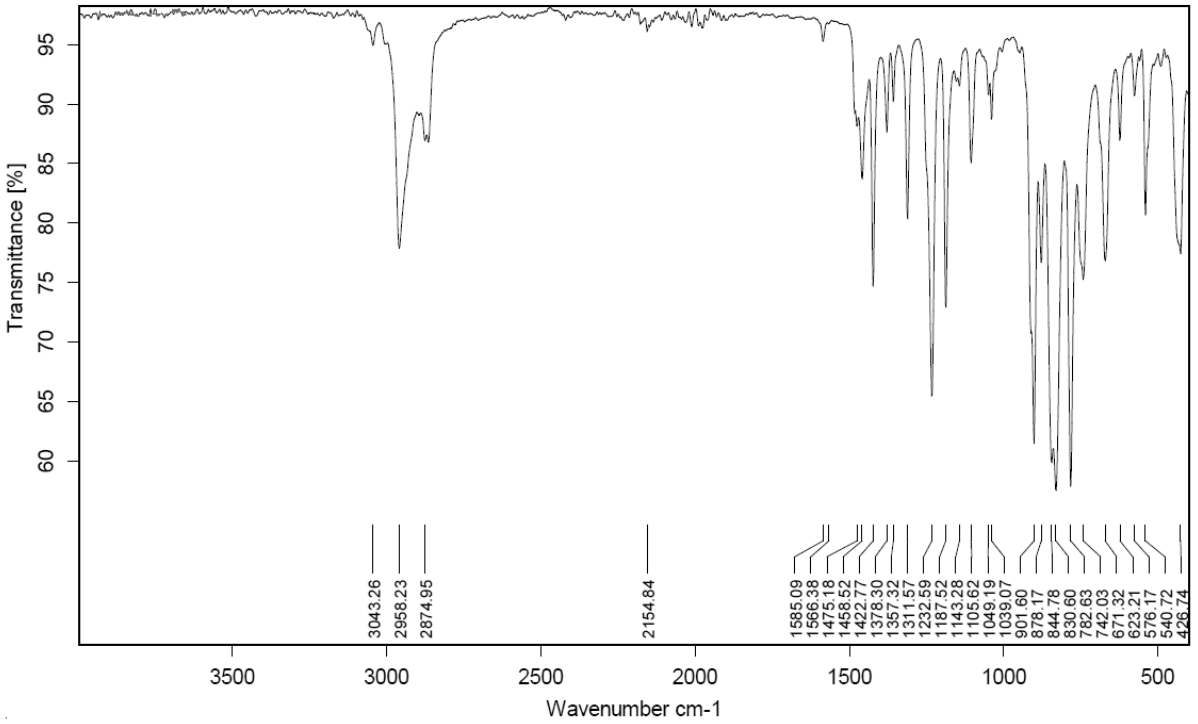

Figure S36. IR spectrum of **[NBu$_4$][Fe(Br)L$^2_2$]**.

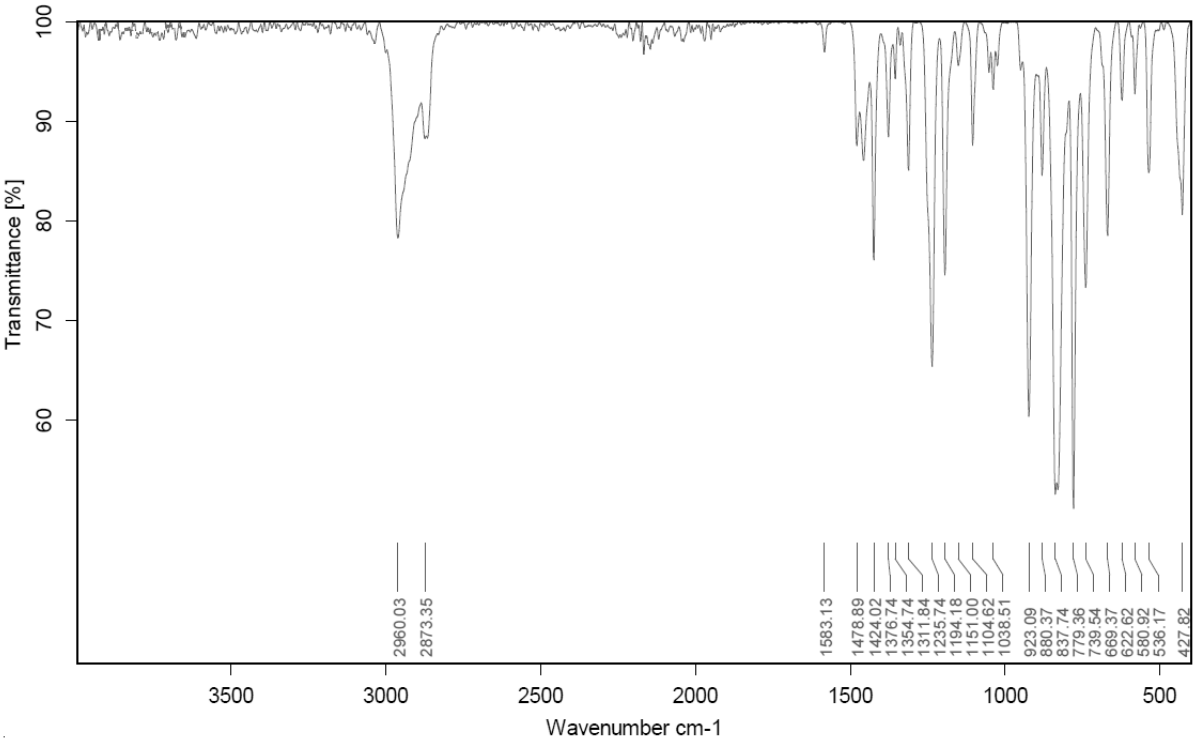

Figure S37. IR spectrum of **[NBu$_4$][Co(Br)L$^2_2$]**.

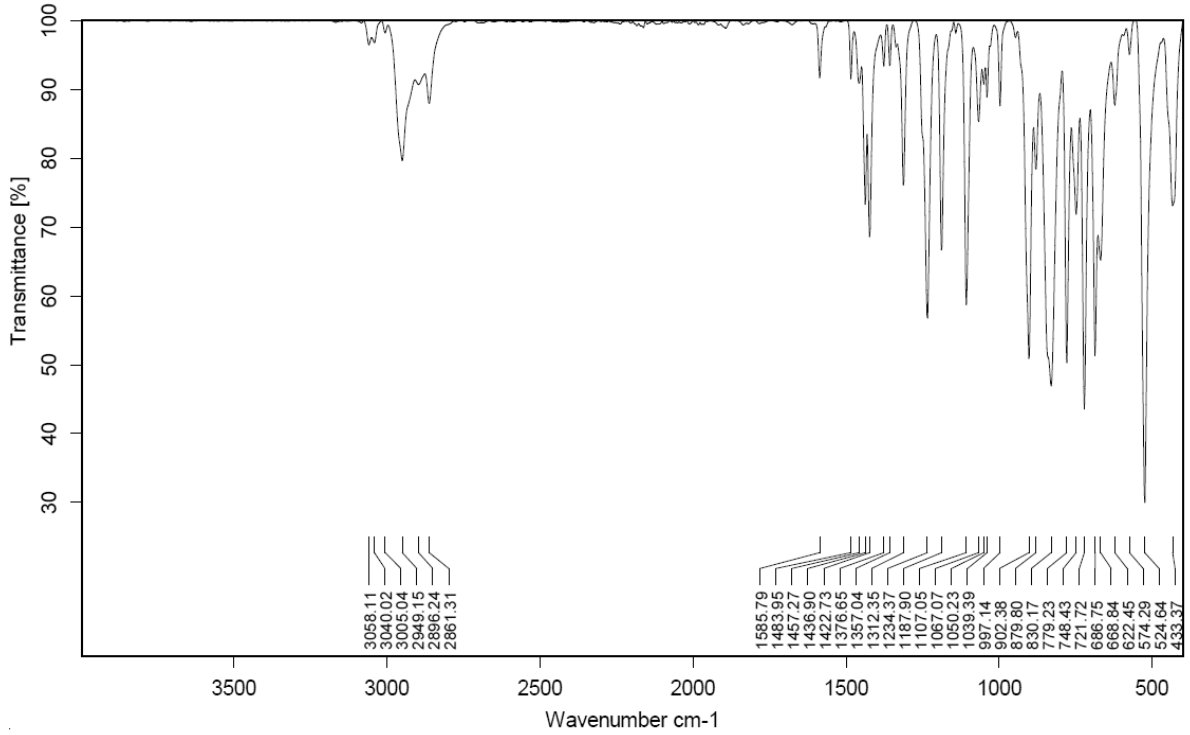

Figure S38. IR spectrum of **[PPh_4][Fe(Br)L^2_2]**.

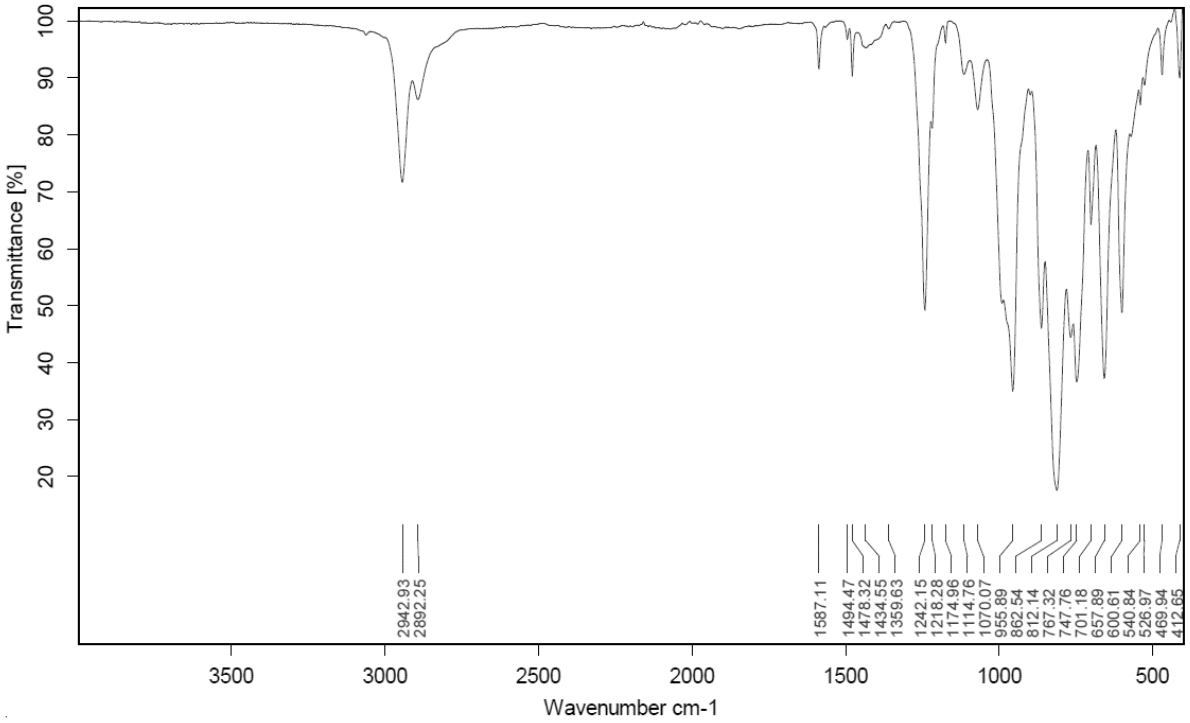

Figure S39. IR spectrum of **[KMn(Bn)L^1_2]**.

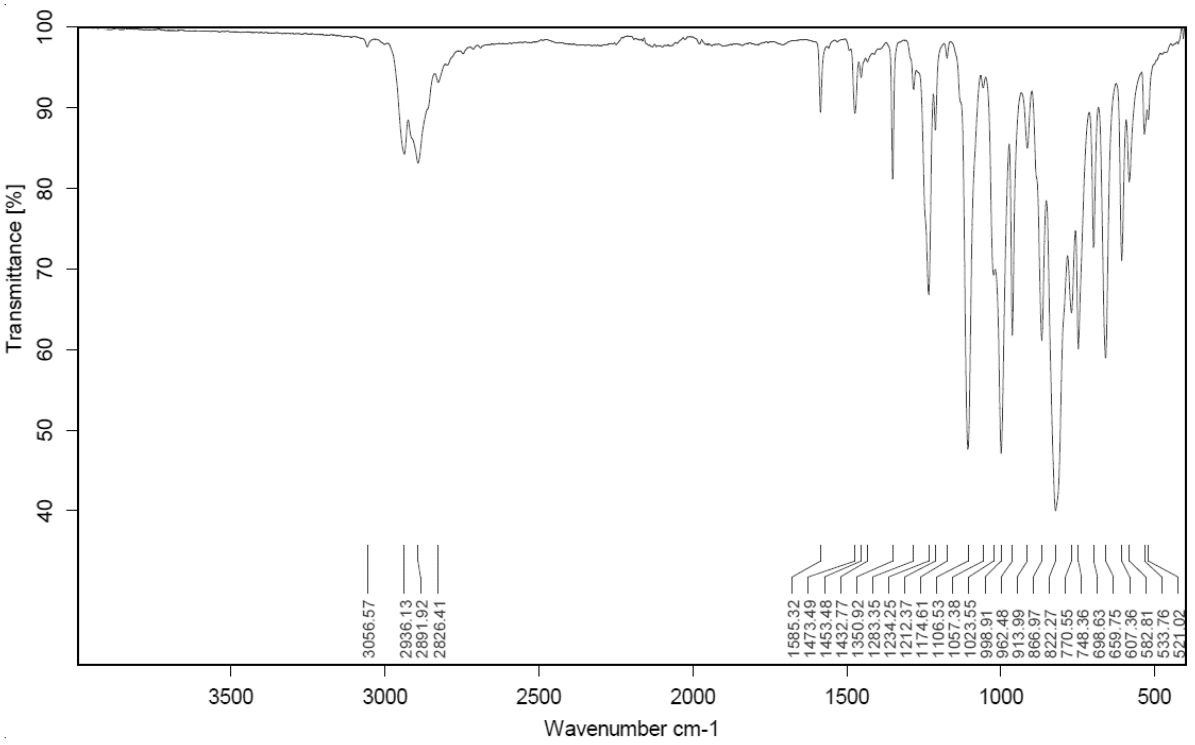

Figure S40. IR spectrum of **[K{18c6}][Mn(Bn)L^1_2]**.

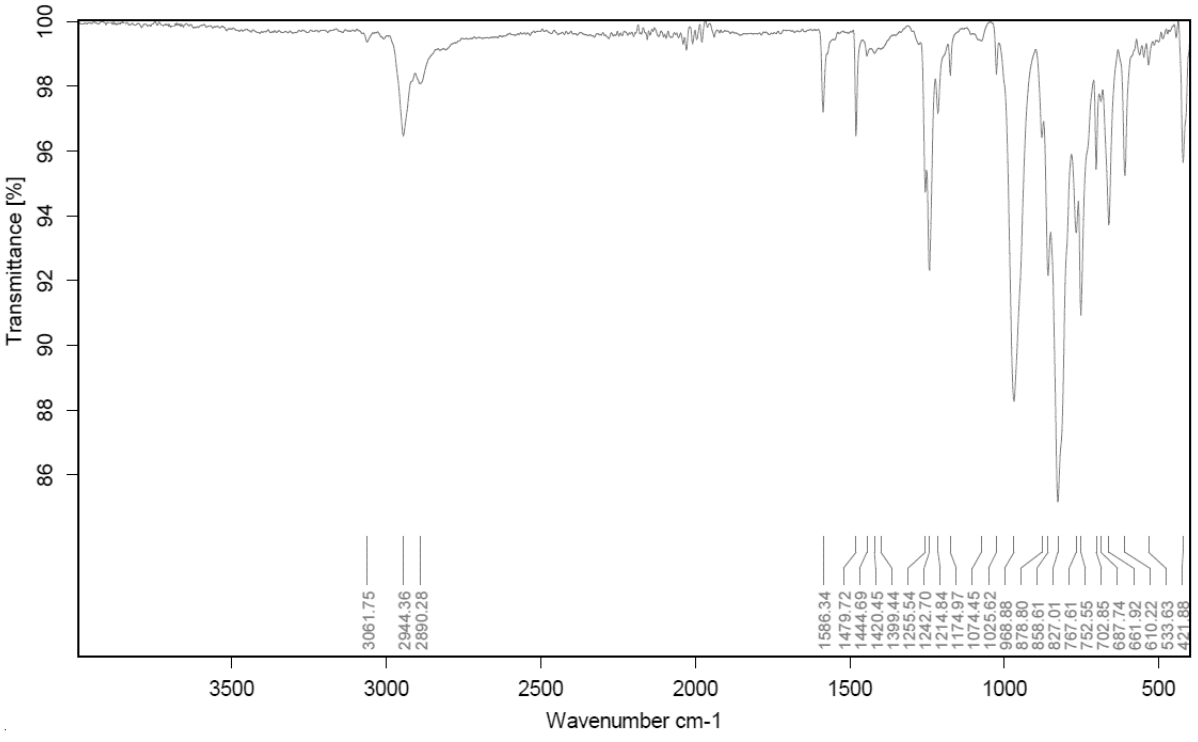

Figure S41. IR spectrum of **[KCo(Bn)L^1_2]**.

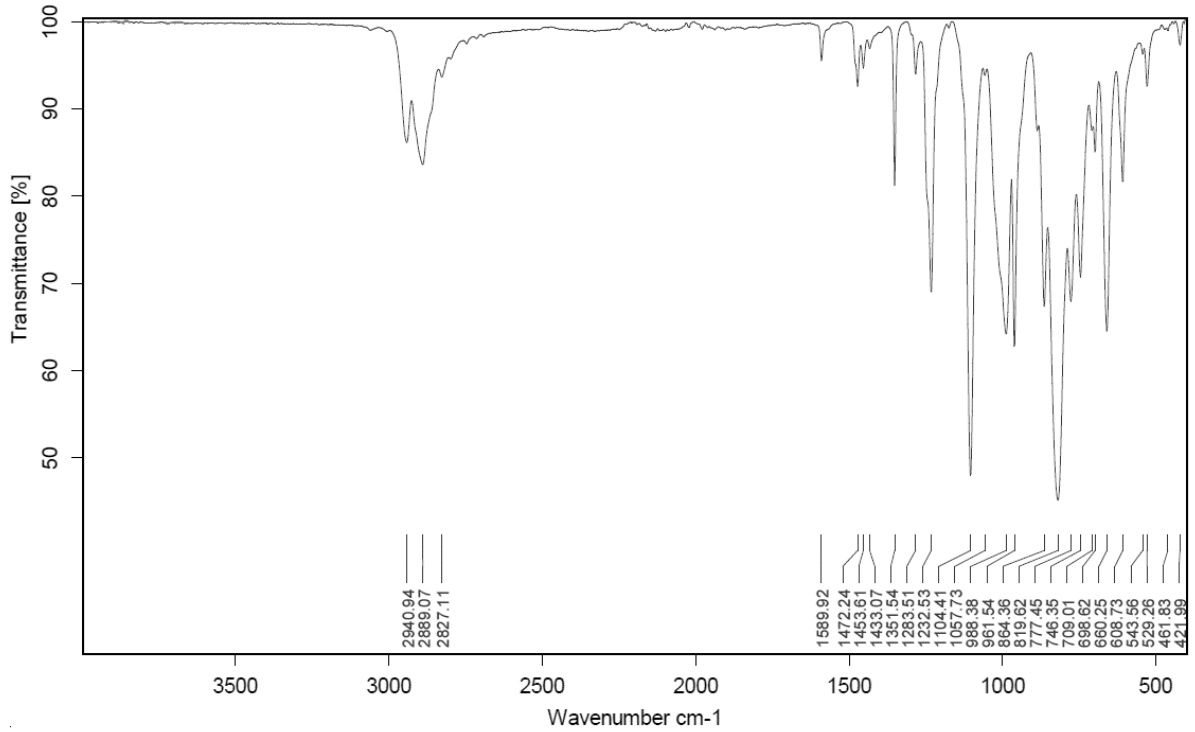

Figure S42. IR spectrum of **[K{18c6}][Co(Bn)L$^{1}_{2}$]**.

3 X-Ray Diffraction Analysis and Molecular Structures

$N(SiMe_3)_2$

Table S1. Crystal data and structure refinement of **$[NBu_4][Cr_2(Br)L^1{}_2L^{1*}]$**

Empirical formula	$C_{38}H_{99}BrCr_2N_4OSi_6$
Formula weight	980.66
Temperature/K	100.0
Crystal system	monoclinic
Space group	$P2_1/c$
a/Å	18.3201(14)
b/Å	19.8196(17)
c/Å	17.8047(15)
α/°	90
β/°	117.633(6)
γ/°	90
Volume/Å^3	5727.4(9)
Z	4
ρ_{calc}g/cm^3	1.137
μ/mm^{-1}	1.231
F(000)	2120.0
Crystal size/mm^3	0.792 × 0.279 × 0.154
Radiation	MoKα (λ = 0.71073)
2Θ range for data collection/°	4.816 to 49.998
Index ranges	−21 ≤ *h* ≤ 21, −23 ≤ *k* ≤ 23, −19 ≤ *l* ≤ 21
Reflections collected	39241
Independent reflections	10087 [R_{int} = 0.0579, R_{sigma} = 0.0564]
Data/restraints/parameters	10087/48/488
Goodness-of-fit on F^2	0.993
Final *R* indexes [*I*>=2σ (*I*)]	R_1 = 0.0475, wR_2 = 0.1218
Final *R* indexes [all data]	R_1 = 0.0833, wR_2 = 0.1312
Largest diff. peak/hole / e Å^{-3}	0.78/−0.75

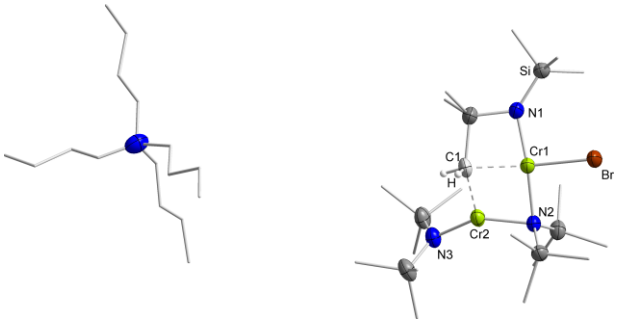

Figure S43. Molecular structure of **$[NBu_4][Cr_2(Br)L^1{}_2L^{1*}]$**. All hydrogen atoms and one free, disordered solvent molecule, (part 1: Et_2O (50%) /part 2: THF (50%)) are omitted for clarity. Disorders in two butyl groups with occupations of 50% for both part 1 (depicted) and part 2 are found.

Table S2. Crystal data and structure refinement of **[NBu$_4$][Mn(Br)L$^1_2$]**

Empirical formula	$C_{28}H_{72}BrMnN_3Si_4$
Formula weight	698.09
Temperature/K	100
Crystal system	monoclinic
Space group	$P2_1/n$
a/Å	11.8696(6)
b/Å	55.434(4)
c/Å	18.8265(11)
α/°	90
β/°	90.708(4)
γ/°	90
Volume/Å^3	12386.5(13)
Z	12
ρ_{calc}g/cm^3	1.123
μ/mm^{-1}	1.423
F(000)	4524.0
Crystal size/mm^3	0.883 × 0.243 × 0.243
Radiation	MoKα (λ = 0.71073)
2Θ range for data collection/°	4.518 to 49.998
Index ranges	−12 ≤ *h* ≤ 14, −65 ≤ *k* ≤ 65, −22 ≤ *l* ≤ 22
Reflections collected	67797
Independent reflections	21604 [R_{int} = 0.1025, R_{sigma} = 0.0894]
Data/restraints/parameters	21604/0/1048
Goodness-of-fit on F^2	0.954
Final *R* indexes [*I*>=2σ (*I*)]	R_1 = 0.0921, wR_2 = 0.2265
Final *R* indexes [all data]	R_1 = 0.1282, wR_2 = 0.2487
Largest diff. peak/hole / e Å^{-3}	1.02/−1.21

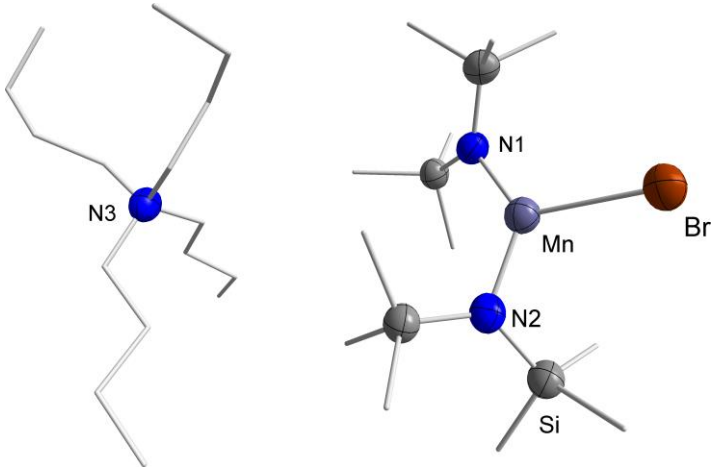

Figure S44. Molecular structure of **[NBu$_4$][Mn(Br)L$^1_2$]**. All hydrogen atoms and two independent molecules are omitted for clarity.

Table S3. Crystal data and structure refinement of **[NBu$_4$][Fe(Br)L$^1_2$]**

Empirical formula	$C_{28}H_{72}BrFeN_3Si_4$
Formula weight	699.00
Temperature/K	270.0
Crystal system	orthorhombic
Space group	Pnn2
a/Å	23.0421(10)
b/Å	32.4243(15)
c/Å	11.5606(6)
α/°	90
β/°	90
γ/°	90
Volume/Å^3	8637.2(7)
Z	2
ρ_{calc}g/cm^3	1.075
μ/mm^{-1}	1.404
F(000)	3024.0
Crystal size/mm^3	0.2 × 0.142 × 0.069
Radiation	MoKα (λ = 0.71073)
2Θ range for data collection/°	3.942 to 46.512
Index ranges	−25 ≤ *h* ≤ 25, −36 ≤ *k* ≤ 34, −12 ≤ *l* ≤ 12
Reflections collected	74946
Independent reflections	12410 [R_{int} = 0.1046, R_{sigma} = 0.0828]
Data/restraints/parameters	12410/1183/1219
Goodness-of-fit on F^2	1.024
Final *R* indexes [*I*>=2σ (*I*)]	R_1 = 0.0539, wR_2 = 0.1178
Final *R* indexes [all data]	R_1 = 0.1186, wR_2 = 0.1464
Largest diff. peak/hole / e Å^{-3}	0.52/−0.26
Flack parameter	0.335(17)

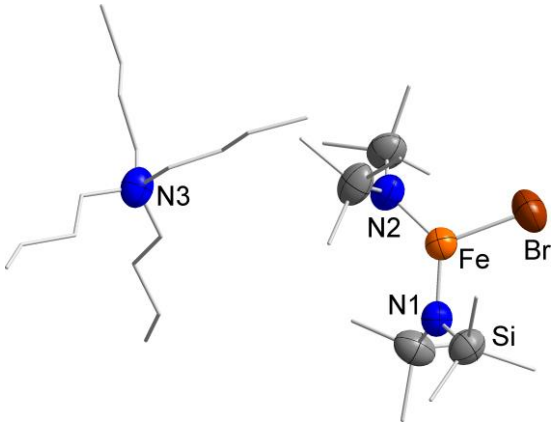

Figure S45. Molecular structure of **[NBu$_4$][Fe(Br)L$^1_2$]**. All hydrogen atoms, disorders in the cation (both part 1 / 2: ~ 50%) and a second, independent molecule are omitted for clarity. The structure was refined as a twin with a twin ration of 0.335(17).

Table S4. Crystal data and structure refinement of **[NBu$_4$][Co(Br)L$^1_2$]**

Empirical formula	$C_{28}H_{72}BrCoN_3Si_4$
Formula weight	702.08
Temperature/K	230.03
Crystal system	orthorhombic
Space group	Pnna
a/Å	23.1094(13)
b/Å	32.0134(18)
c/Å	11.4451(7)
α/°	90
β/°	90
γ/°	90
Volume/Å^3	8467.2(8)
Z	8
ρ_{calc}g/cm^3	1.102
μ/mm^{-1}	1.481
F(000)	3032.0
Crystal size/mm^3	0.51 × 0.32 × 0.24
Radiation	MoKα (λ = 0.71073)
2Θ range for data collection/°	5.09 to 50.636
Index ranges	−27 ≤ *h* ≤ 27, −34 ≤ *k* ≤ 38, −13 ≤ *l* ≤ 13
Reflections collected	66731
Independent reflections	7705 [R_{int} = 0.0351, R_{sigma} = 0.0223]
Data/restraints/parameters	7705/892/532
Goodness-of-fit on F^2	1.031
Final *R* indexes [*I*>=2σ (*I*)]	R_1 = 0.0356, wR_2 = 0.0876
Final *R* indexes [all data]	R_1 = 0.0547, wR_2 = 0.0966
Largest diff. peak/hole / e Å^{-3}	0.52/−0.34

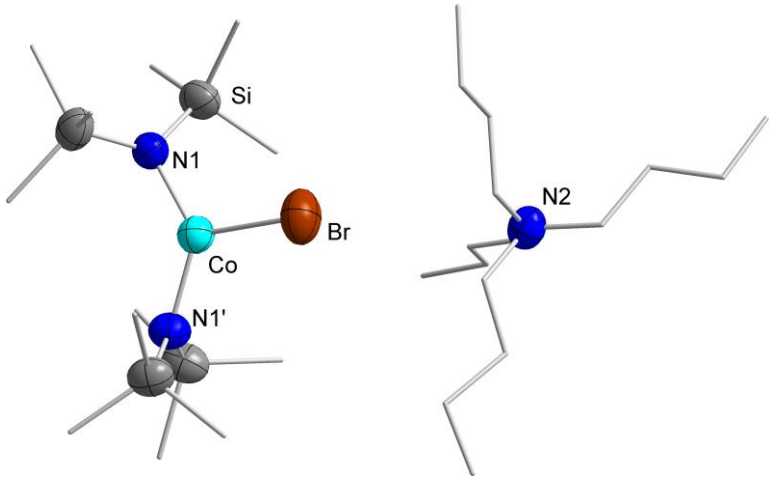

Figure S46. Molecular structure of **[NBu$_4$][Co(Br)L$^1_2$]**. All hydrogen atoms and disorders in one trimethylsilyl group (part 1 (depicted): 80%, part 2: 20%) and in all butyl groups (part 1/part 2: 50%) are omitted for clarity.

Table S5. Crystal data and structure refinement of **[K{18c6}][Co(Br)L$^1_2$]**

Empirical formula	$C_{24}H_{60}BrCoKN_2O_6Si_4$
Formula weight	763.04
Temperature/K	100.0
Crystal system	orthorhombic
Space group	$P2_12_12_1$
a/Å	19.3848(12)
b/Å	21.4223(15)
c/Å	28.887(2)
α/°	90
β/°	90
γ/°	90
Volume/Å^3	11995.9(14)
Z	12
ρ_{calc}g/cm^3	1.267
μ/mm^{-1}	1.685
F(000)	4836.0
Crystal size/mm^3	0.384 × 0.285 × 0.239
Radiation	MoKα (λ = 0.71073)
2Θ range for data collection/°	4.824 to 53.628
Index ranges	−24 ≤ *h* ≤ 24, −27 ≤ *k* ≤ 27, −33 ≤ *l* ≤ 36
Reflections collected	107921
Independent reflections	25373 [R_{int} = 0.1441, R_{sigma} = 0.1062]
Data/restraints/parameters	25373/0/1091
Goodness-of-fit on F^2	0.941
Final *R* indexes [*I*>=2σ (*I*)]	R_1 = 0.0662, wR_2 = 0.1456
Final *R* indexes [all data]	R_1 = 0.1084, wR_2 = 0.1603
Largest diff. peak/hole / e Å^{-3}	1.23/-0.98
Flack parameter	0.133(11)

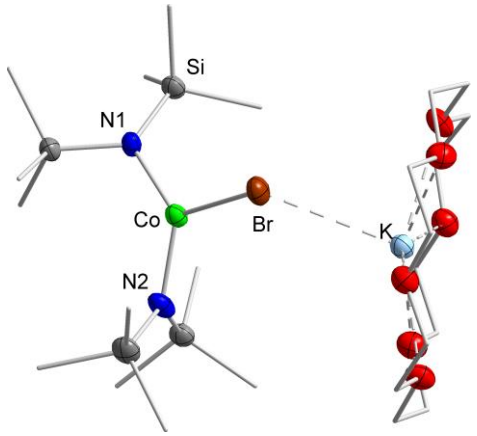

Figure S47. Molecular structure of **[K{18c6}][Co(Br)L$^1_2$]**. All hydrogen atoms are omitted for clarity. The structure was refined as an inversion twin, twin ration refined to 0.133(11).

Table S6. Crystal data and structure refinement of **[K{18c6}(thf)$_2$][CoL$^1_3$]**

Empirical formula	$C_{38}H_{98}CoKN_3O_8Si_6$
Formula weight	991.76
Temperature/K	100.0
Crystal system	monoclinic
Space group	$P2_1/n$
a/Å	15.5099(6)
b/Å	17.4058(7)
c/Å	21.6265(11)
α/°	90
β/°	92.056(2)
γ/°	90
Volume/Å^3	5834.6(4)
Z	4
ρ_{calc}g/cm^3	1.129
μ/mm^{-1}	0.530
F(000)	2164.0
Crystal size/mm^3	0.371 × 0.268 × 0.24
Radiation	MoKα (λ = 0.71073)
2Θ range for data collection/°	4.436 to 52
Index ranges	–19 ≤ h ≤ 19, –21 ≤ k ≤ 21, –23 ≤ l ≤ 26
Reflections collected	41243
Independent reflections	11458 [R_{int} = 0.0842, R_{sigma} = 0.0686]
Data/restraints/parameters	11458/7/558
Goodness-of-fit on F^2	1.024
Final *R* indexes [*I*>=2σ (*I*)]	R_1 = 0.0423, wR_2 = 0.0831
Final *R* indexes [all data]	R_1 = 0.0859, wR_2 = 0.0921
Largest diff. peak/hole / e Å^{-3}	0.40/–0.38

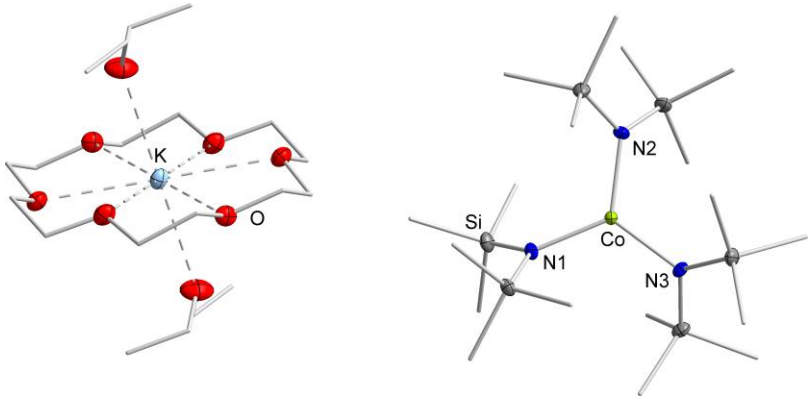

Figure S48. Molecular structure of **[K{18c6}(thf)$_2$][CoL$^1_3$]**. All hydrogen atoms and a second, independent molecule with a disorder in the THF molecule (part 1 (depicted) / part 2: 50%) are omitted for clarity. Selected bond length and angles: Co−N1 1.9717(17) Å, Co−N2 1.9619(19) Å, Co−N3 1.9743(18), N1−Co−N2 119.46(8) °, N1−Co−N3 120.62(8) °, N2−Co−N3 119.92(8) °.

N(Dipp)SiR$_3$ (R = ^{i}Pr (Cr), Me (Mn − Co))

Table S7. Crystal data and structure refinement of **KL^3**

Empirical formula	$C_{21}H_{38}KNSi$
Formula weight	371.71
Temperature/K	100.0
Crystal system	monoclinic
Space group	$P2_1/c$
a/Å	12.0182(5)
b/Å	18.2406(8)
c/Å	20.6241(9)
α/°	90
β/°	97.895(2)
γ/°	90
Volume/Å^3	4478.3(3)
Z	8
ρ_{calc}g/cm^3	1.103
μ/mm^{-1}	0.294
F(000)	1632.0
Crystal size/mm^3	0.487 × 0.256 × 0.205
Radiation	MoKα (λ = 0.71073)
2Θ range for data collection/°	4.336 to 52.28
Index ranges	−14 ≤ *h* ≤ 14, −22 ≤ *k* ≤ 22, −25 ≤ *l* ≤ 25
Reflections collected	113225
Independent reflections	8914 [R_{int} = 0.0502, R_{sigma} = 0.0218]
Data/restraints/parameters	8914/0/453
Goodness-of-fit on F^2	1.043
Final *R* indexes [*I*>=2σ (*I*)]	R_1 = 0.0326, wR_2 = 0.0747
Final *R* indexes [all data]	R_1 = 0.0427, wR_2 = 0.0791
Largest diff. peak/hole / e Å^{-3}	0.34/−0.26

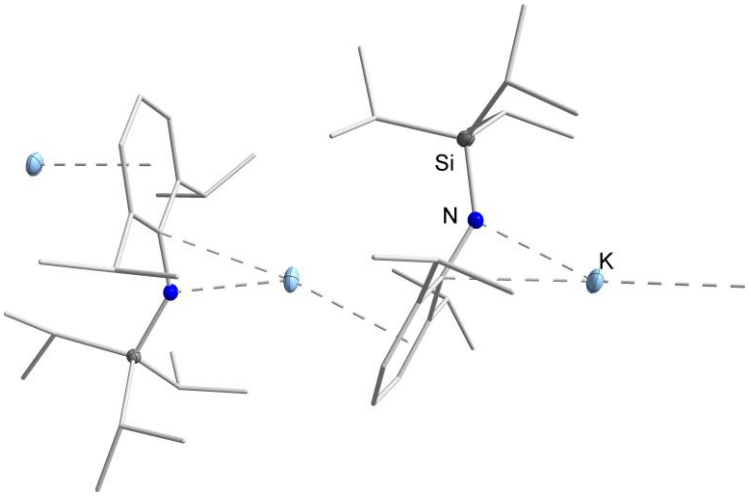

Figure S49. Molecular structure of **KL^3**. All hydrogen atoms are omitted for clarity.

Table S8. Crystal data and structure refinement of **[NBu$_4$][Cr(Br)$_2$L^3]**

Empirical formula	$C_{37}H_{74}Br_2CrN_2Si$
Formula weight	786.89
Temperature/K	100.0
Crystal system	monoclinic
Space group	$P2_1/n$
a/Å	16.1172(18)
b/Å	13.5085(12)
c/Å	20.707(2)
α/°	90
β/°	108.517(9)
γ/°	90
Volume/Å^3	4274.9(8)
Z	4
ρ_{calc}g/cm^3	1.223
μ/mm^{-1}	2.190
F(000)	1672.0
Crystal size/mm^3	0.4098 × 0.1831 × 0.1298
Radiation	MoKα (λ = 0.71073)
2Θ range for data collection/°	2.81 to 53.79
Index ranges	−20 ≤ *h* ≤ 20, −16 ≤ *k* ≤ 16, −26 ≤ *l* ≤ 26
Reflections collected	26220
Independent reflections	9046 [R_{int} = 0.0689, R_{sigma} = 0.0751]
Data/restraints/parameters	9046/0/402
Goodness-of-fit on F^2	0.904
Final *R* indexes [*I*>=2σ (*I*)]	R_1 = 0.0365, wR_2 = 0.0746
Final *R* indexes [all data]	R_1 = 0.0749, wR_2 = 0.0819
Largest diff. peak/hole / e Å^{-3}	0.58/−0.25

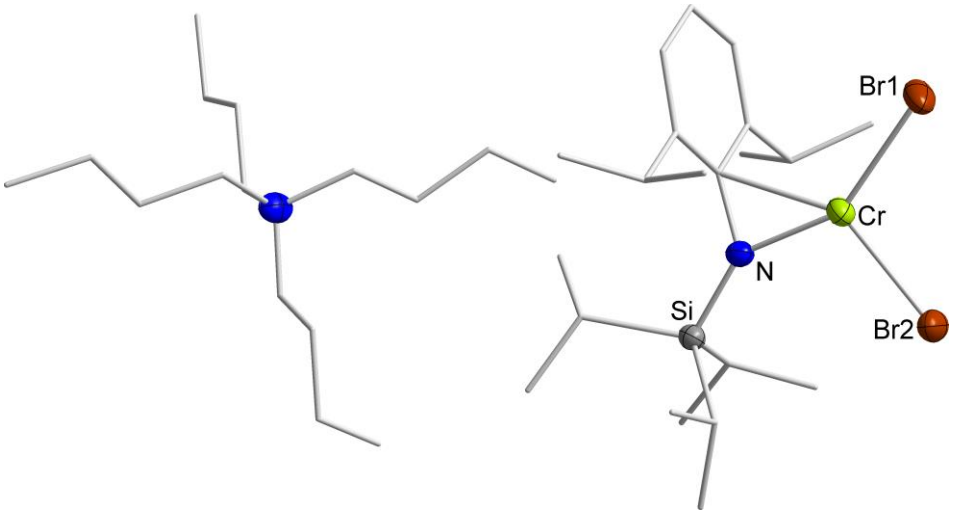

Figure S50. Molecular structure of **[NBu$_4$][Cr(Br)$_2$L^3]**. All hydrogen atoms are omitted for clarity.

Table S9. Crystal data and structure refinement of **[NBu$_4$][Mn(Br)L$^2_2$]**

Empirical formula	$C_{46}H_{88}BrMnN_3Si_2$
Formula weight	874.22
Temperature/K	99.99
Crystal system	triclinic
Space group	P−1
a/Å	9.5944(8)
b/Å	22.6205(17)
c/Å	36.514(3)
α/°	91.570(2)
β/°	92.865(2)
γ/°	95.203(3)
Volume/Å^3	7878.2(11)
Z	6
ρ_{calc}g/cm^3	1.106
μ/mm^{-1}	1.088
F(000)	2838.0
Crystal size/mm^3	0.793 × 0.127 × 0.112
Radiation	MoKα (λ = 0.71073)
2Θ range for data collection/°	4.314 to 50
Index ranges	−11 ≤ *h* ≤ 11, −26 ≤ *k* ≤ 26, −43 ≤ *l* ≤ 43
Reflections collected	119838
Independent reflections	27740 [R_{int} = 0.0907, R_{sigma} = 0.0957]
Data/restraints/parameters	27740/55/1529
Goodness-of-fit on F^2	1.028
Final *R* indexes [*I*>=2σ (*I*)]	R_1 = 0.0649, wR_2 = 0.1276
Final *R* indexes [all data]	R_1 = 0.1138, wR_2 = 0.1389
Largest diff. peak/hole / e Å^{-3}	0.50/−1.02

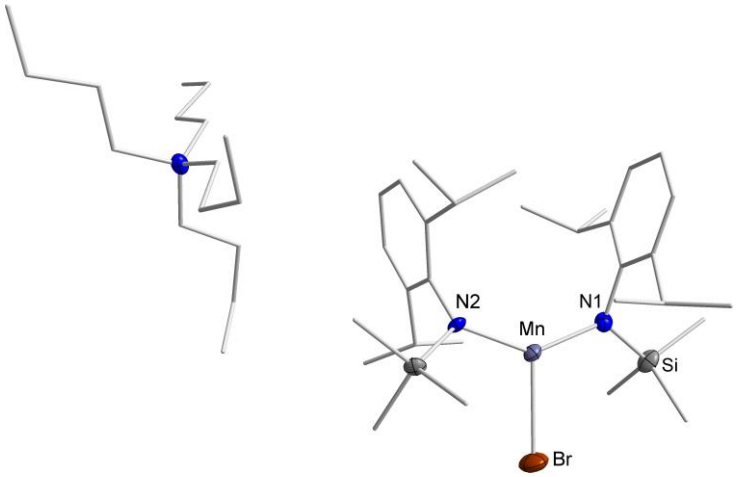

Figure S51. Molecular structure of **[NBu$_4$][Mn(Br)L$^2_2$]**. All hydrogen atoms and two independent molecules (one with disorders in one SiMe$_3$ group and the bromido ligand (part 1: 80% / part 2: 20%)) are omitted for clarity.

Table S10. Crystal data and structure refinement of **[NBu$_4$][Fe(Br)L$^2_2$]**

Empirical formula	$C_{46}H_{88}BrFeN_3Si_2$
Formula weight	875.13
Temperature/K	100.0
Crystal system	orthorhombic
Space group	Pbca
a/Å	25.2435(15)
b/Å	18.1557(11)
c/Å	25.2898(15)
α/°	90
β/°	90
γ/°	90
Volume/Å^3	11590.7(12)
Z	8
ρ_{calc}g/cm^3	1.003
μ/mm^{-1}	1.018
F(000)	3792.0
Crystal size/mm^3	0.425 × 0.278 × 0.21
Radiation	MoKα (λ = 0.71073)
2Θ range for data collection/°	4.244 to 51.462
Index ranges	−30 ≤ *h* ≤ 30, −22 ≤ *k* ≤ 22, −30 ≤ *l* ≤ 30
Reflections collected	303659
Independent reflections	11025 [R_{int} = 0.1101, R_{sigma} = 0.0289]
Data/restraints/parameters	11025/4/556
Goodness-of-fit on F^2	1.004
Final *R* indexes [*I*>=2σ (*I*)]	R_1 = 0.0439, wR_2 = 0.0938
Final *R* indexes [all data]	R_1 = 0.0683, wR_2 = 0.1049
Largest diff. peak/hole / e Å^{-3}	0.54/−0.56

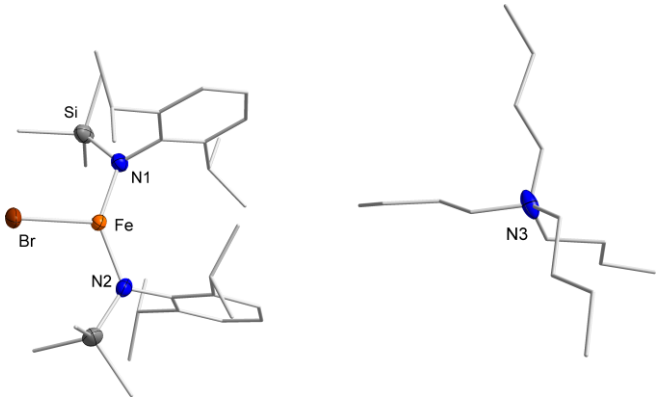

Figure S52. Molecular structure of **[NBu$_4$][Fe(Br)L$^2_2$]**. All hydrogen atoms and disorders (part 1 (depicted) / part 2: 50%) in one *iso*-propyl group and two butyl group are omitted for clarity. One free *n*-pentane molecule is heavily disordered over multiple positions. Attempts to model the disorders did not lead to satisfactory results, why it was thus squeezed.

Table S11. Crystal data and structure refinement of **[NBu$_4$][Co(Br)L$^2_2$]**

Empirical formula	$C_{46}H_{88}BrCoN_3Si_2$
Formula weight	878.21
Temperature/K	230.15
Crystal system	monoclinic
Space group	$P2_1$
a/Å	11.8960(5)
b/Å	15.7934(7)
c/Å	14.0473(6)
α/°	90
β/°	93.0360(10)
γ/°	90
Volume/Å^3	2635.5(2)
Z	2
ρ_{calc}g/cm^3	1.107
μ/mm^{-1}	1.159
F(000)	950.0
Crystal size/mm^3	0.355 × 0.349 × 0.272
Radiation	MoKα (λ = 0.71073)
2Θ range for data collection/°	5.078 to 52.728
Index ranges	−14 ≤ *h* ≤ 14, −19 ≤ *k* ≤ 19, −17 ≤ *l* ≤ 17
Reflections collected	92428
Independent reflections	10767 [R_{int} = 0.0341, R_{sigma} = 0.0227]
Data/restraints/parameters	10767/1/497
Goodness-of-fit on F^2	1.021
Final *R* indexes [*I*>=2σ (*I*)]	R_1 = 0.0264, wR_2 = 0.0630
Final *R* indexes [all data]	R_1 = 0.0338, wR_2 = 0.0665
Largest diff. peak/hole / e Å^{-3}	0.34/−0.36
Flack parameter	0.255(7)

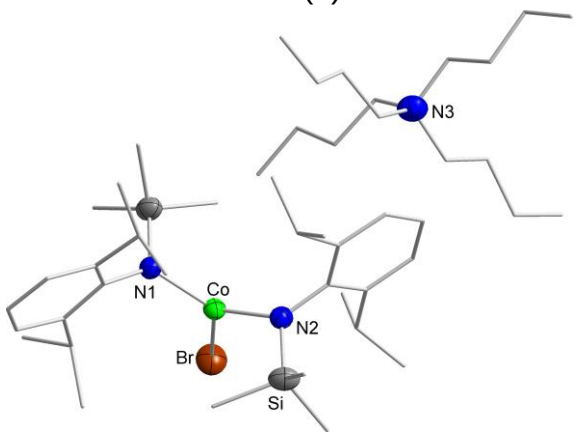

Figure S53. Molecular structure of **[NBu$_4$][Co(Br)L$^2_2$]**. All hydrogen atoms are omitted for clarity. The structure was refined as a twin with a twin ration of 0.255(7).

Table S12. Crystal data and structure refinement of **[PPh$_4$][Fe(Br)L$^2_2$]**

Empirical formula	$C_{58}H_{80}BrFeN_2OPSi_2$
Formula weight	1044.15
Temperature/K	100.0
Crystal system	monoclinic
Space group	$P2_1/c$
a/Å	15.1183(7)
b/Å	37.3788(15)
c/Å	30.2947(13)
α/°	90
β/°	93.929(2)
γ/°	90
Volume/Å^3	17079.4(13)
Z	4
ρ_{calc}g/cm^3	1.218
μ/mm^{-1}	1.076
F(000)	6648.0
Crystal size/mm^3	0.448 × 0.305 × 0.185
Radiation	MoKα (λ = 0.71073)
2Θ range for data collection/°	4.188 to 44.06
Index ranges	−15 ≤ *h* ≤ 15, −39 ≤ *k* ≤ 39, −31 ≤ *l* ≤ 31
Reflections collected	205859
Independent reflections	20951 [R_{int} = 0.0551, R_{sigma} = 0.0237]
Data/restraints/parameters	20951/12/1678
Goodness-of-fit on F^2	1.063
Final *R* indexes [*I*>=2σ (*I*)]	R_1 = 0.0529, wR_2 = 0.1367
Final *R* indexes [all data]	R_1 = 0.0629, wR_2 = 0.1434
Largest diff. peak/hole / e Å^{-3}	1.23/−1.30

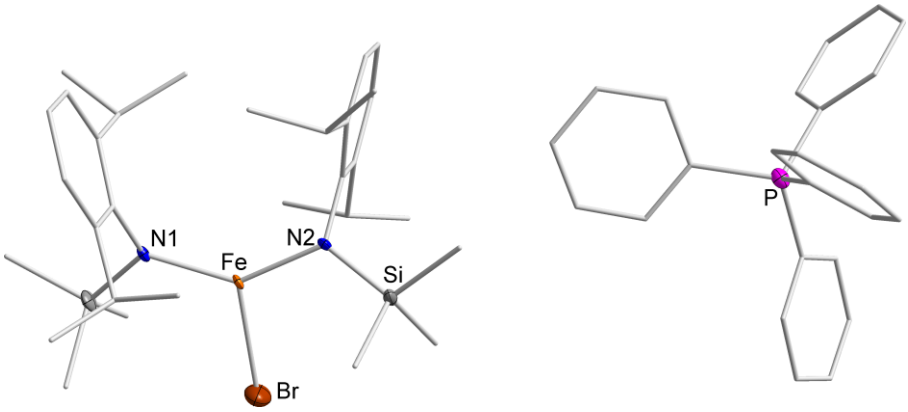

Figure S54. Molecular structure of **[PPh$_4$][Fe(Br)L$^2_2$]**. All hydrogen atoms, two independent molecules (one with a disorder in the bromido ligand (part 1: 95%/ part 2: 5%) and one free THF molecule are omitted for clarity.

Table S13. Crystal data and structure refinement of **[KMn(Bn)L$^1_2$]**

Empirical formula	$C_{19}H_{43}KMnN_2Si_4$
Formula weight	505.95
Temperature/K	100.0
Crystal system	monoclinic
Space group	$P2_1/n$
a/Å	9.1933(4)
b/Å	20.9352(8)
c/Å	15.0703(6)
α/°	90
β/°	91.1860(10)
γ/°	90
Volume/Å^3	2899.9(2)
Z	4
ρ_{calc}g/cm^3	1.159
μ/mm^{-1}	0.772
F(000)	1084.0
Crystal size/mm^3	0.545 × 0.17 × 0.074
Radiation	MoKα (λ = 0.71073)
2Θ range for data collection/°	4.738 to 53.162
Index ranges	$-11 \le h \le 11$, $-26 \le k \le 26$, $-18 \le l \le 18$
Reflections collected	53239
Independent reflections	6055 [R_{int} = 0.0483, R_{sigma} = 0.0255]
Data/restraints/parameters	6055/0/256
Goodness-of-fit on F^2	1.047
Final *R* indexes [I>=2σ (I)]	R_1 = 0.0304, wR_2 = 0.0665
Final *R* indexes [all data]	R_1 = 0.0387, wR_2 = 0.0696
Largest diff. peak/hole / e Å^{-3}	0.58/−0.33

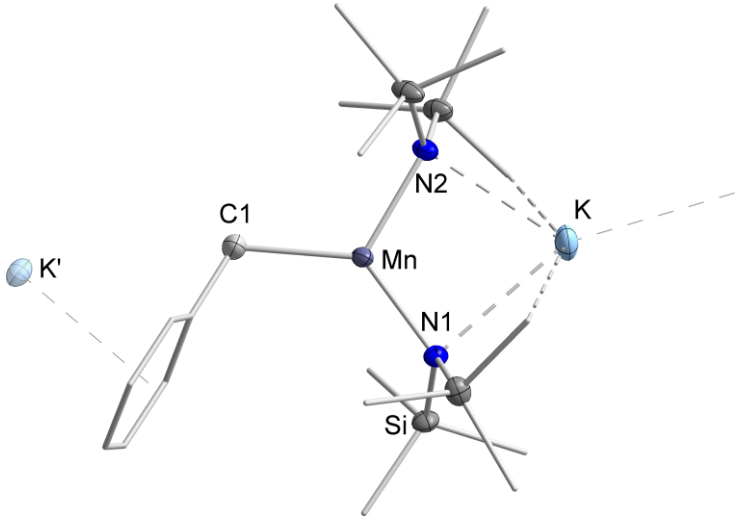

Figure S55. Molecular structure of **[KMn(Bn)L$^1_2$]**. All hydrogen atoms are omitted for clarity.

Table S14. Crystal data and structure refinement of **[K{18c6}][Mn(Bn)L$^1_2$]**

Empirical formula	$C_{31}H_{67}KMnN_2O_6Si_4$
Formula weight	770.26
Temperature/K	100.0
Crystal system	triclinic
Space group	P−1
a/Å	8.9881(4)
b/Å	20.0230(9)
c/Å	24.1825(11)
α/°	92.009(2)
β/°	94.467(2)
γ/°	91.954(2)
Volume/Å^3	4333.2(3)
Z	4
ρ_{calc}g/cm^3	1.181
μ/mm^{-1}	0.549
F(000)	1660.0
Crystal size/mm^3	0.437 × 0.158 × 0.121
Radiation	MoKα (λ = 0.71073)
2Θ range for data collection/°	4.47 to 52.176
Index ranges	−11 ≤ *h* ≤ 11, −24 ≤ *k* ≤ 24, −29 ≤ *l* ≤ 29
Reflections collected	91842
Independent reflections	17133 [R_{int} = 0.0595, R_{sigma} = 0.0444]
Data/restraints/parameters	17133/57/889
Goodness-of-fit on F^2	1.192
Final *R* indexes [*I*>=2σ (*I*)]	R_1 = 0.0546, wR_2 = 0.1120
Final *R* indexes [all data]	R_1 = 0.0716, wR_2 = 0.1168
Largest diff. peak/hole / e Å^{-3}	0.68/−0.39

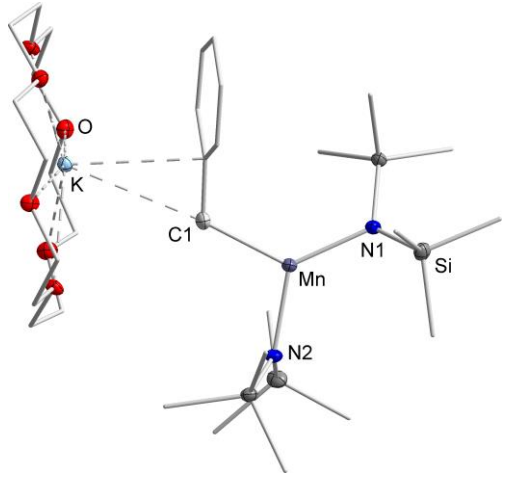

Figure S56. Molecular structure of **[K{18c6}][Mn(Bn)L$^1_2$]**. All hydrogen atoms and a second, independent molecule with a disorder in the benzyl moiety (part 1: 60% / part 2: 40%) are omitted for clarity.

Table S15. Crystal data and structure refinement of **[KCo(Bn)L$^1_2$]**

Empirical formula	$C_{19}H_{43}CoKN_2Si_4$
Formula weight	509.94
Temperature/K	100.0
Crystal system	monoclinic
Space group	$P2_1/n$
a/Å	9.3097(4)
b/Å	20.7693(10)
c/Å	14.8718(7)
α/°	90
β/°	91.621(2)
γ/°	90
Volume/Å^3	2874.4(2)
Z	4
ρ_{calc}g/cm^3	1.178
μ/mm^{-1}	0.916
F(000)	1092.0
Crystal size/mm^3	0.462 × 0.23 × 0.204
Radiation	MoKα (λ = 0.71073)
2Θ range for data collection/°	4.784 to 52.528
Index ranges	−11 ≤ *h* ≤ 11, −25 ≤ *k* ≤ 25, −18 ≤ *l* ≤ 18
Reflections collected	70318
Independent reflections	5807 [R_{int} = 0.0356, R_{sigma} = 0.0157]
Data/restraints/parameters	5807/0/256
Goodness-of-fit on F^2	1.040
Final *R* indexes [*I*>=2σ (*I*)]	R_1 = 0.0260, wR_2 = 0.0635
Final *R* indexes [all data]	R_1 = 0.0317, wR_2 = 0.0653
Largest diff. peak/hole / e Å^{-3}	0.43/−0.28

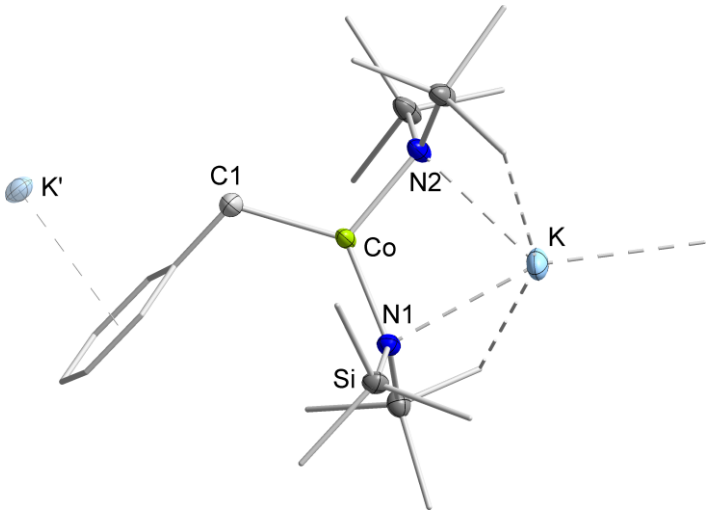

Figure S57. Molecular structure of **[KCo(Bn)L$^1_2$]**. All hydrogen atoms are omitted for clarity.

Table S16. Crystal data and structure refinement of **[K{18c6}(thf)][Mn(Bn)L$^1_2$]**

Empirical formula	$C_{35}H_{75}CoKN_2O_7Si_4$
Formula weight	846.36
Temperature/K	100.0
Crystal system	monoclinic
Space group	$P2_1/c$
a/Å	11.1616(8)
b/Å	13.5261(8)
c/Å	31.9577(18)
α/°	90
β/°	98.445(3)
γ/°	90
Volume/Å^3	4772.4(5)
Z	4
ρ_{calc}g/cm^3	1.178
μ/mm^{-1}	0.588
F(000)	1828.0
Crystal size/mm^3	0.424 × 0.309 × 0.261
Radiation	MoKα (λ = 0.71073)
2Θ range for data collection/°	4.762 to 58
Index ranges	−15 ≤ *h* ≤ 15, −18 ≤ *k* ≤ 18, −43 ≤ *l* ≤ 43
Reflections collected	78844
Independent reflections	12673 [R_{int} = 0.0386, R_{sigma} = 0.0255]
Data/restraints/parameters	12673/0/513
Goodness-of-fit on F^2	1.051
Final *R* indexes [*I*>=2σ (*I*)]	R_1 = 0.0356, wR_2 = 0.0775
Final *R* indexes [all data]	R_1 = 0.0483, wR_2 = 0.0809
Largest diff. peak/hole / e Å^{-3}	0.36/−0.33

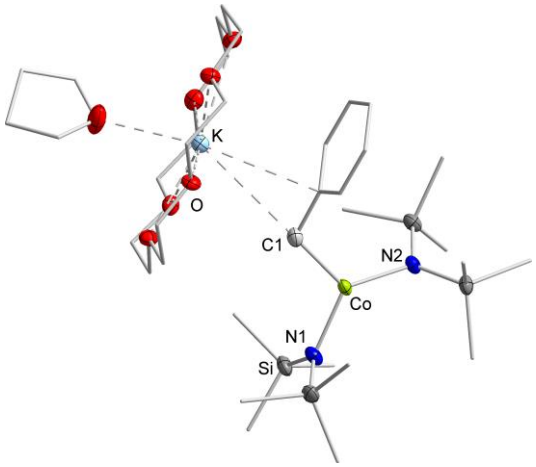

Figure S58. Molecular structure of [**K{18c6}(thf)][Mn(Bn)L$^1_2$]**. All hydrogen atoms and a disorder in the THF molecule (part 1 (depicted): 67% / part 2: 33%) are omitted for clarity.

11.4 Zusatzinformationen zu Publikation 4

„Catalytic 1,3-H Atom Shift of a Terminal Benzylic Alkyne by Iron and Alkali Metal Silylamides − Switching between Allene and Internal Alkyne”

Ruth Weller, Igor Müller, C. Gunnar Werncke

- eingereichtes Manuskript -

Catalytic 1,3-H Atom Shift of a Terminal Benzylic Alkyne by Silylamides of Iron and Alkali Metals

Ruth Weller,[1] Igor Müller,[1] C. Gunnar Werncke*[1]

[1]Department of Chemistry, Philipps-University Marburg, Hans-Meerwein-Straße 4, 35043 Marburg, Germany; gunnar.werncke@chemie.uni-marburg.de, +49 6421 282 5627;

Table of Contents

1 ^{1}H NMR Spectra

1.1 ^{1}H NMR Spectra of the Isolated Complexes

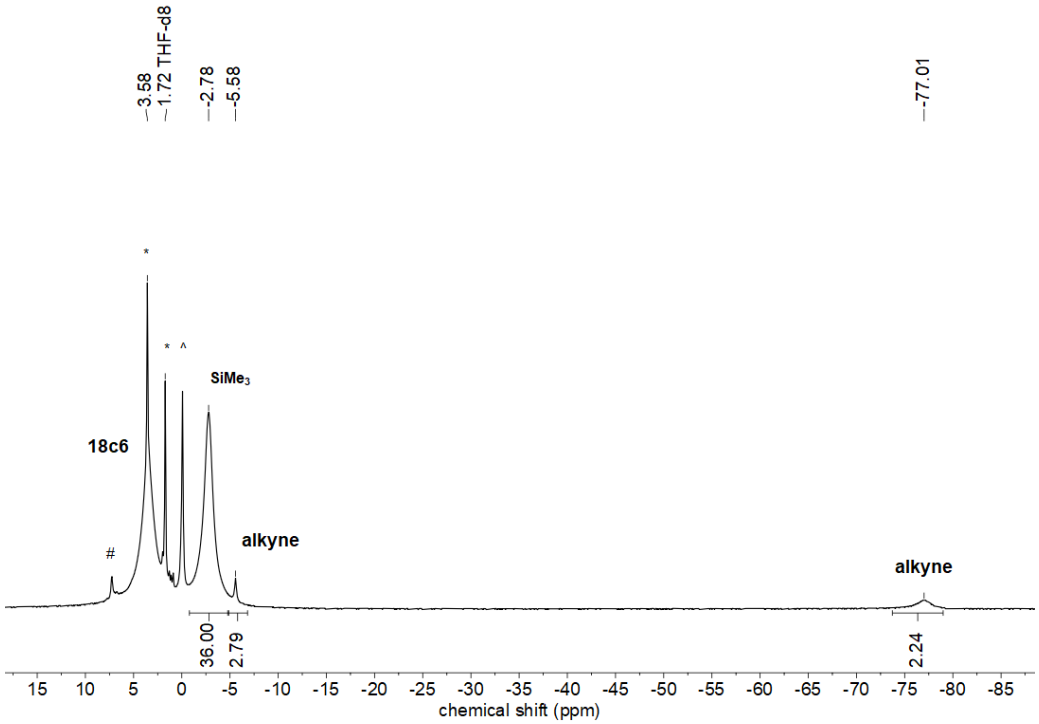

Figure S1. ^{1}H NMR spectrum (300.1 MHz, 300 K) of [K{18c6}][Fe(N{SiMe$_3$}$_2$)$_2$(η^2-PhCCMe)] (**1**) in THF-d_8. (* solvent, # free alkyne, ^ decomposition)

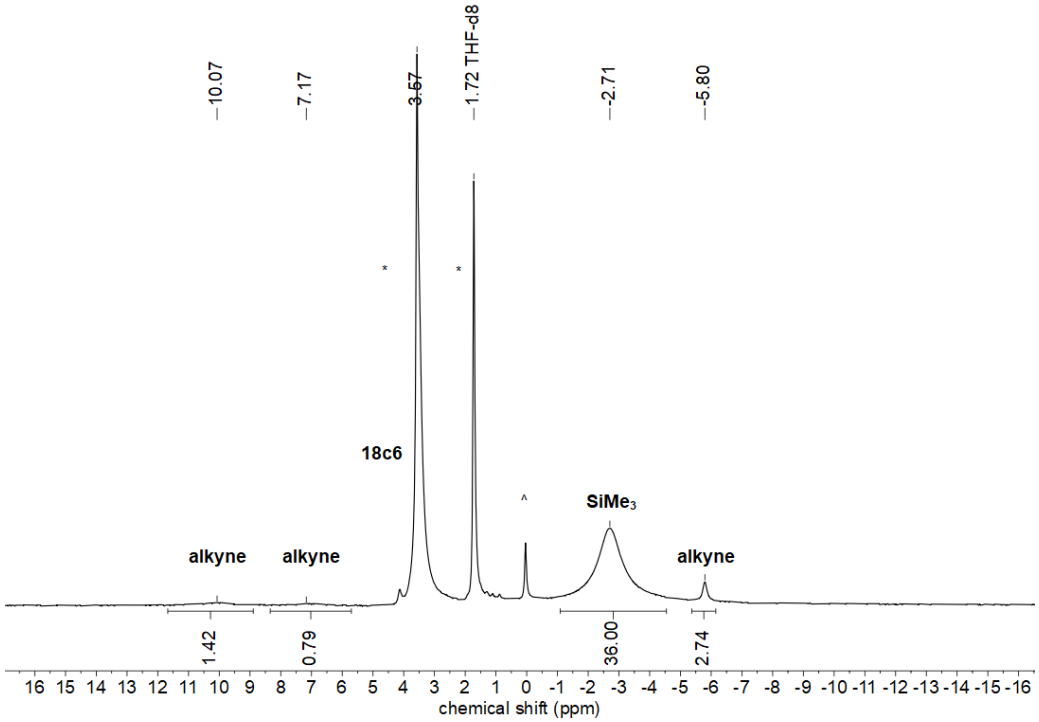

Figure S2. ^{1}H NMR spectrum (300.1 MHz, 300 K) of [K{18c6}][Fe(N{SiMe$_3$}$_2$)$_2$(η^2-PhCCH)] (**2**) in THF-d_8. (* solvent, ^ decomposition)

1.2 Catalytic Insights

Reactions with [K{18c6}][Fe(N{SiMe$_3$}$_2$)$_2$] (A)

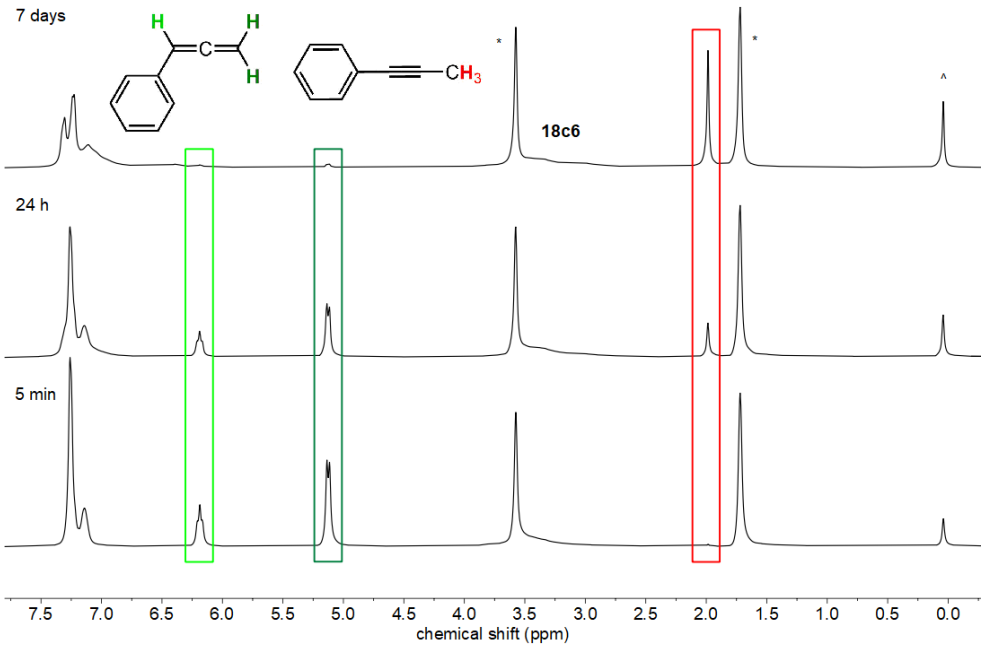

Figure S3. Time dependent *in situ* ^{1}H NMR spectrum (300.1 MHz, 300 K) of reacting **A** (1 equiv.) with 3-phenyl propyne (10 equiv.) at room temperature in THF-d_8. After 7 days conversion to 1-phenyl propyne (85%) was observed. (* solvent, ^ decomposition)

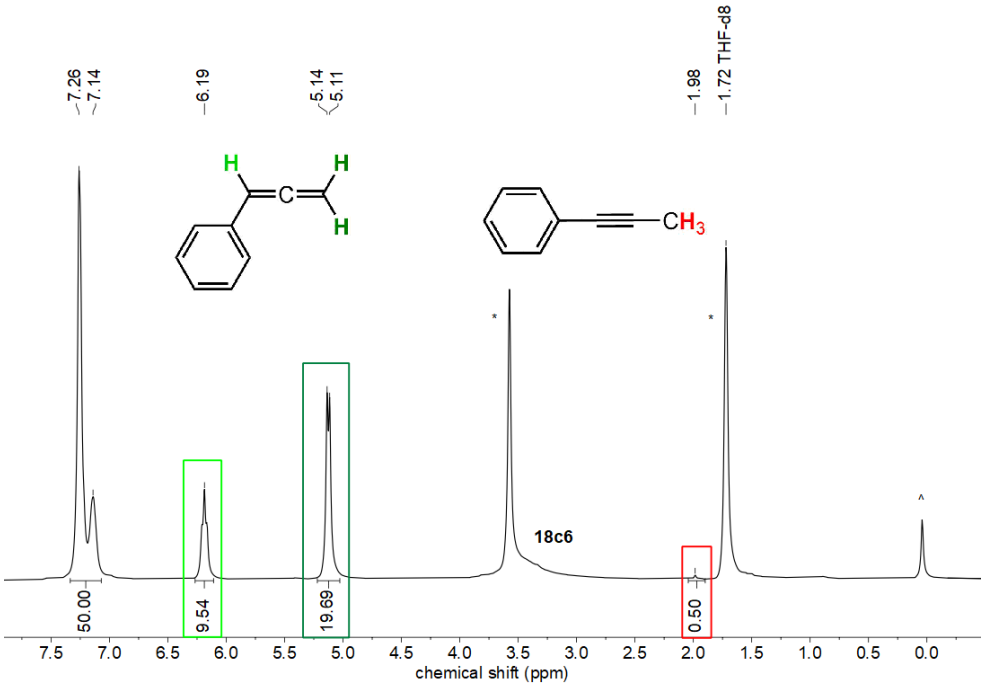

Figure S4. *In situ* ^{1}H NMR spectrum (300.1 MHz, 300 K) of reacting **A** (1 equiv.) with 3-phenyl propyne (10 equiv.) at room temperature in THF-d_8 after 5 minutes reaction time. Full conversion to phenyl allene (>99%) was observed, which slowly converts into 1-phenyl propyne (<1%). (* solvent, ^ decomposition)

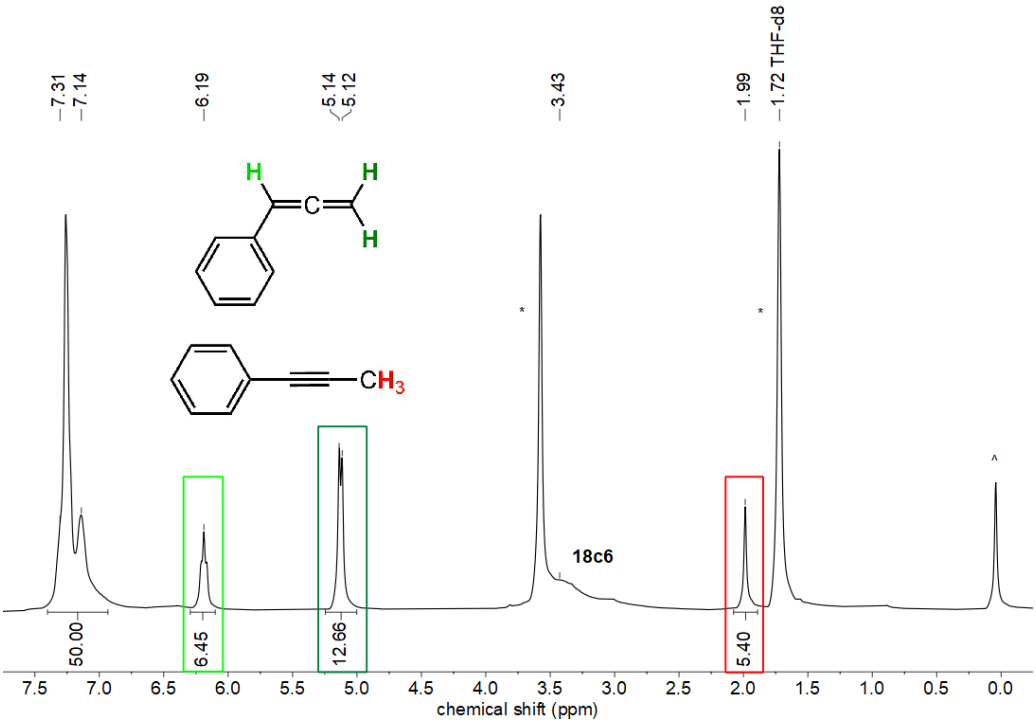

Figure S5. *In situ* ^{1}H NMR spectrum (300.1 MHz, 300 K) of reacting **A** (1 equiv.) with 3-phenyl propyne (10 equiv.) at room temperature in THF-d_8 after 24 hours reaction time. Subsequent conversion of phenyl allene (76%) to 1-phenyl propyne (24%) was observed. (* solvent, ^ decomposition)

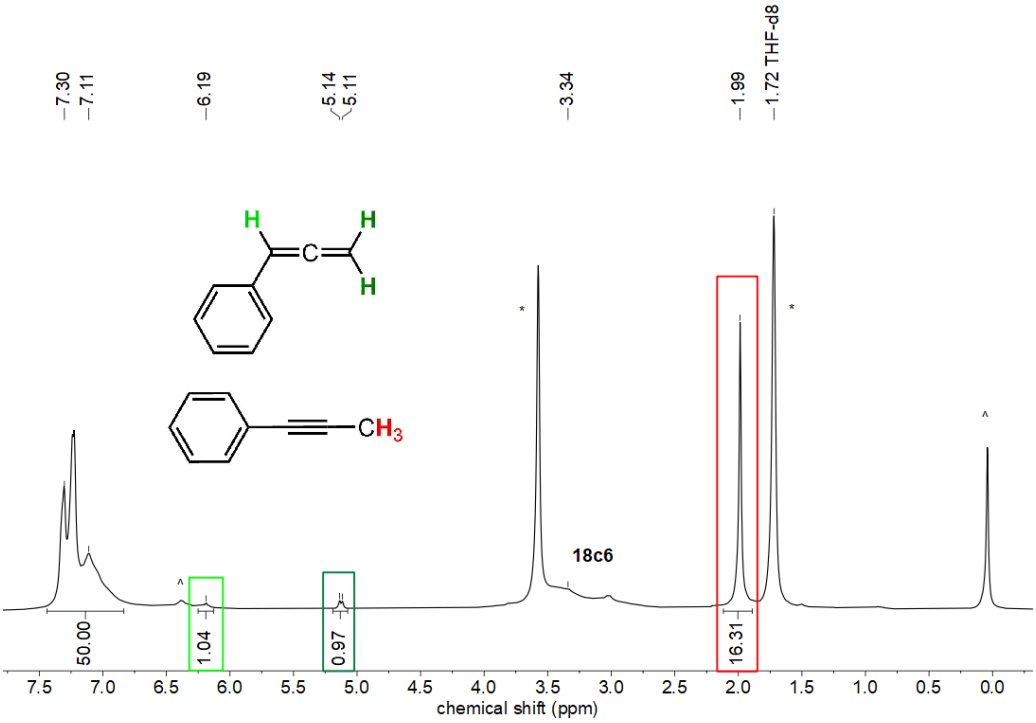

Figure S6. *In situ* ^{1}H NMR spectrum (300.1 MHz, 300 K) of reacting **A** (1 equiv.) with 3-phenyl propyne (10 equiv.) at room temperature in THF-d_8 after 7 days reaction time. Subsequent conversion of phenyl allene (15%) to 1-phenyl propyne (85%) was observed. (* solvent, ^ decomposition)

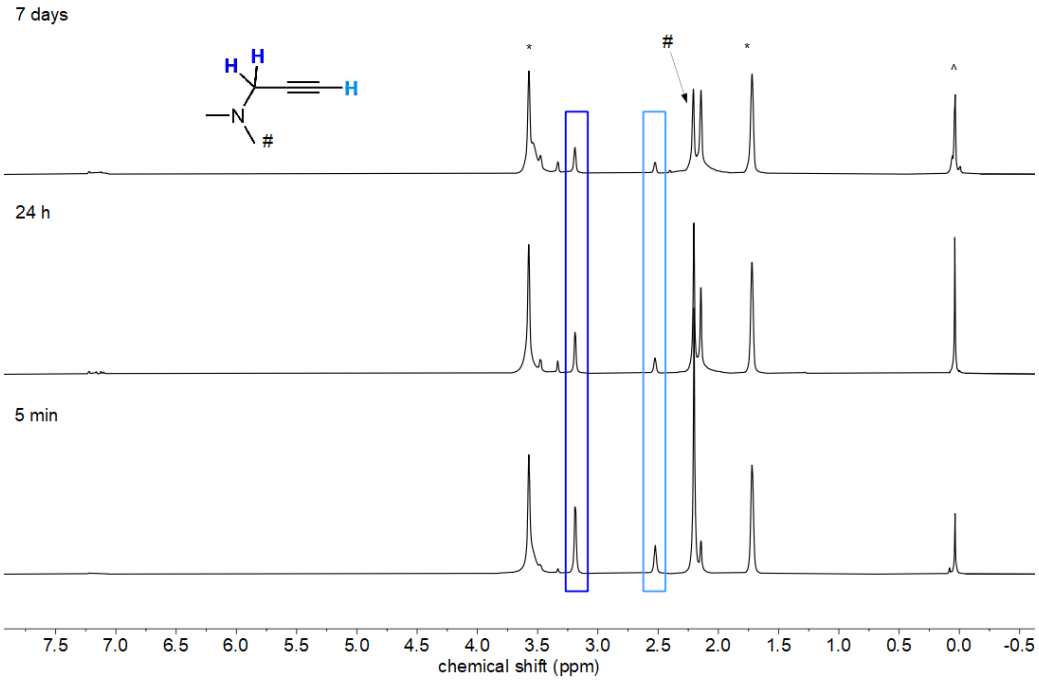

Figure S7. Time dependent *in situ* ^{1}H NMR spectrum (300.1 MHz, 300 K) of reacting **A** (1 equiv.) with *N,N*-dimethylpropargylamine (10 equiv.) at room temperature in THF-d_8. After 7 days reaction time, partial conversion (57%) was observed. (* solvent, ^ decomposition)

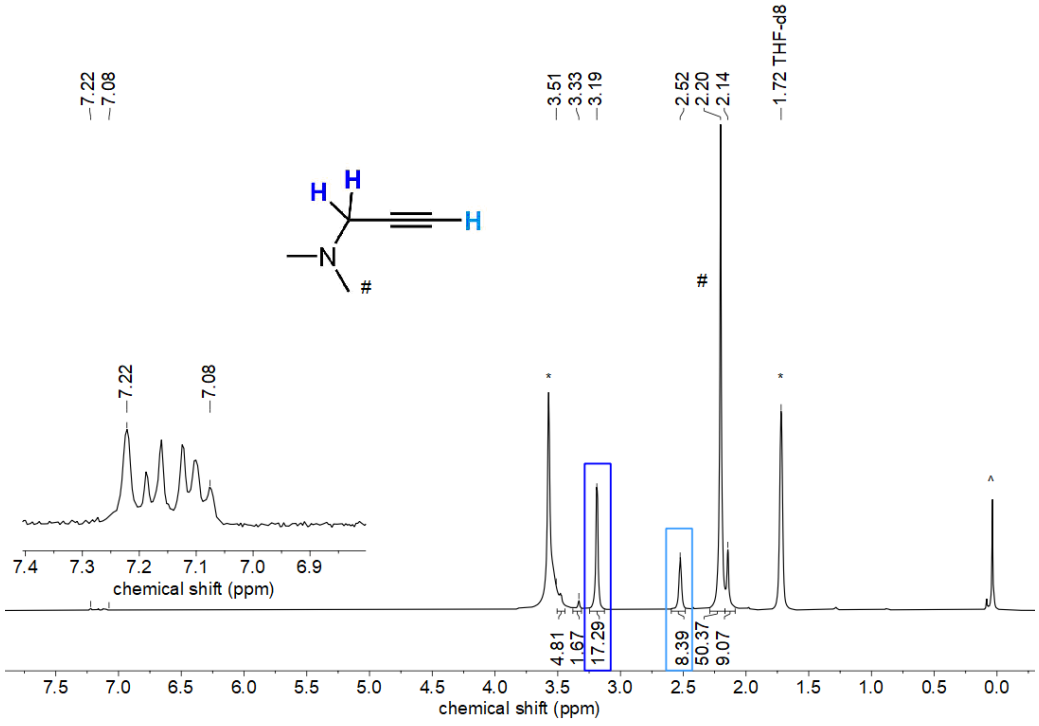

Figure S8. *In situ* ^{1}H NMR spectrum (300.1 MHz, 300 K) of reacting **A** (1 equiv.) with *N,N*-dimethylpropargylamine (10 equiv.) at room temperature in THF-d_8 after 5 minutes reaction time. Partial conversion (15%) was observed. (* solvent, ^ decomposition)

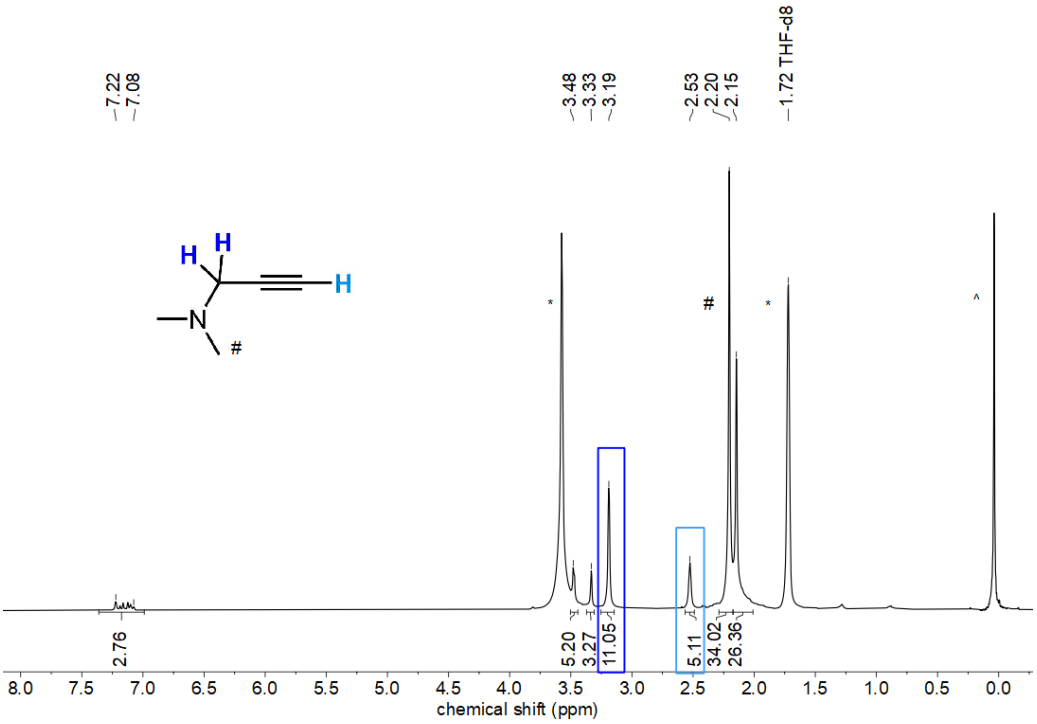

Figure S9. *In situ* ^{1}H NMR spectrum (300.1 MHz, 300 K) of reacting **A** (1 equiv.) with *N,N*-dimethylpropargylamine (10 equiv.) at room temperature in THF-d_8 after 24 hours reaction time. Partial conversion (43%) was observed. (* solvent, ^ decomposition

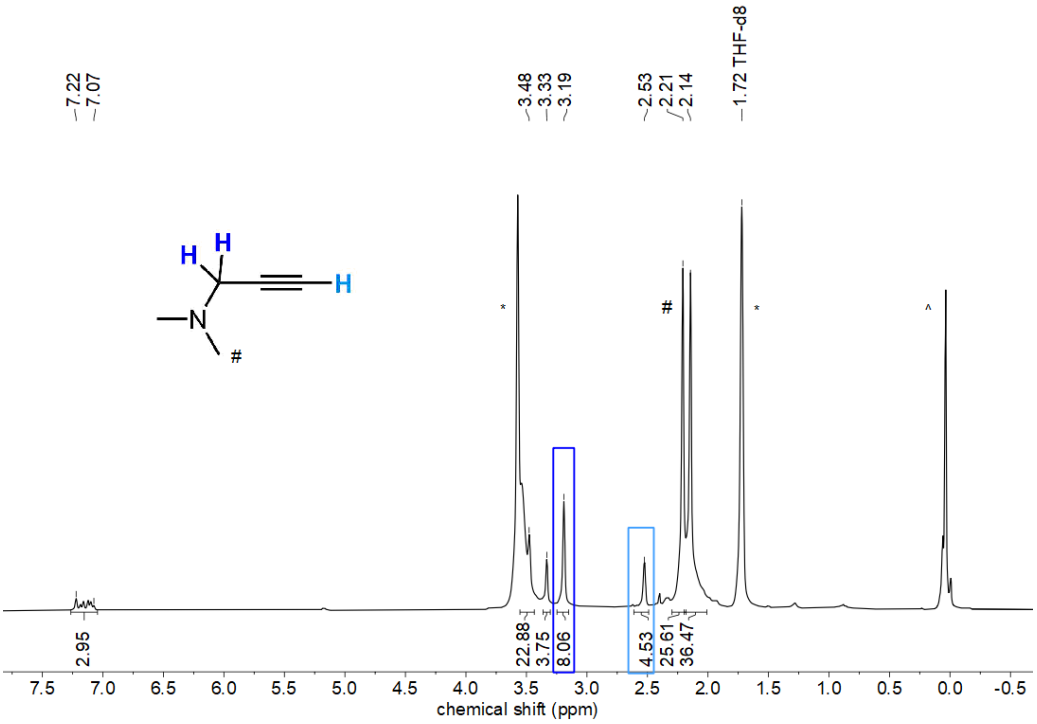

Figure S10. *In situ* ^{1}H NMR spectrum (300.1 MHz, 300 K) of reacting **A** (1 equiv.) with *N,N*-dimethylpropargylamine (10 equiv.) at room temperature in THF-d_8 after 7 days reaction time. Partial conversion (57%) was observed. (* solvent, ^ decomposition)

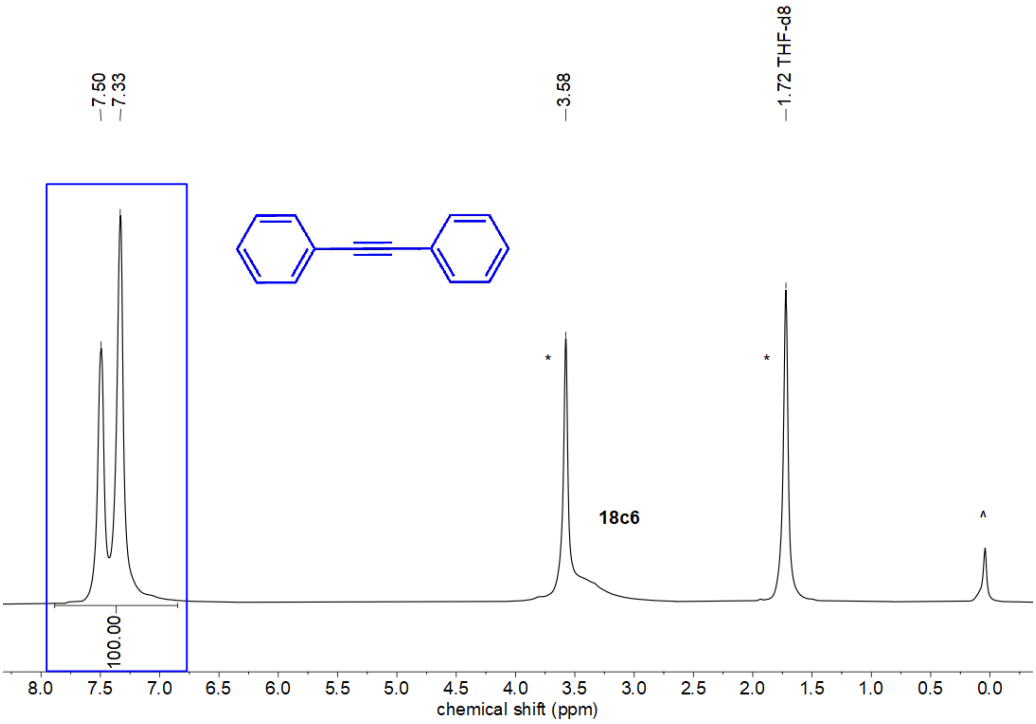

Figure S11. *In situ* ^{1}H NMR spectrum (300.1 MHz, 300 K) of reacting **A** (1 equiv.) with diphenyl acetylene (10 equiv.) at room temperature in THF-d_8 after 7 days reaction time. No conversion was observed. (* solvent, ^ decomposition)

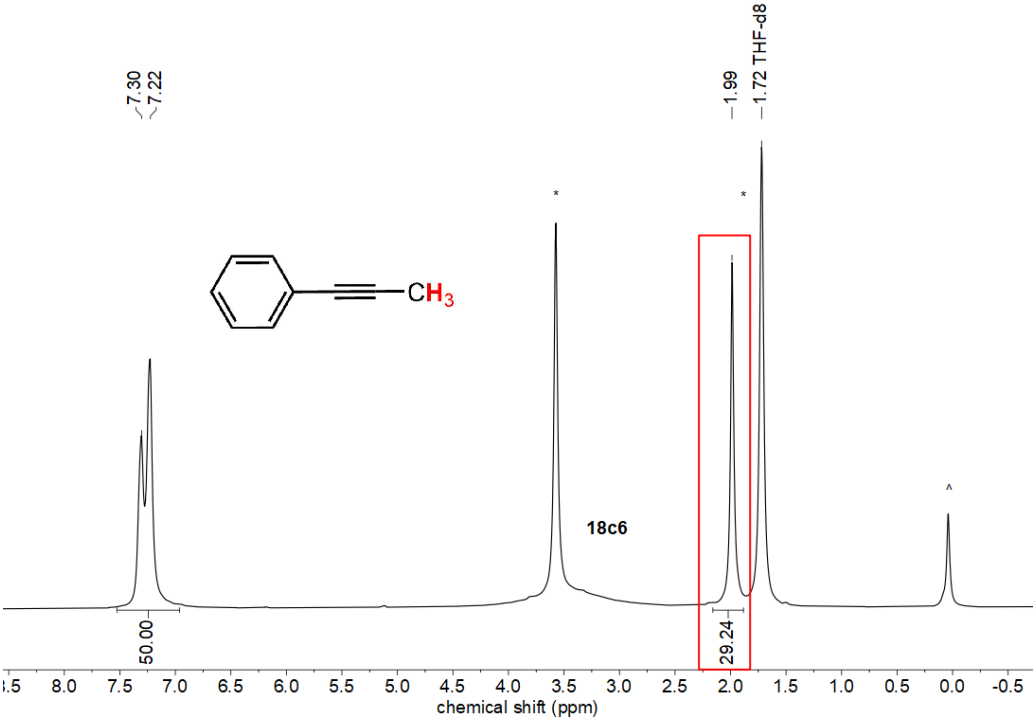

Figure S12. *In situ* ^{1}H NMR spectrum (300.1 MHz, 300 K) of reacting **A** (1 equiv.) with 1-phenyl propyne (10 equiv.) at room temperature in THF-d_8 after 7 days reaction time. No conversion was observed. (* solvent, ^ decomposition)

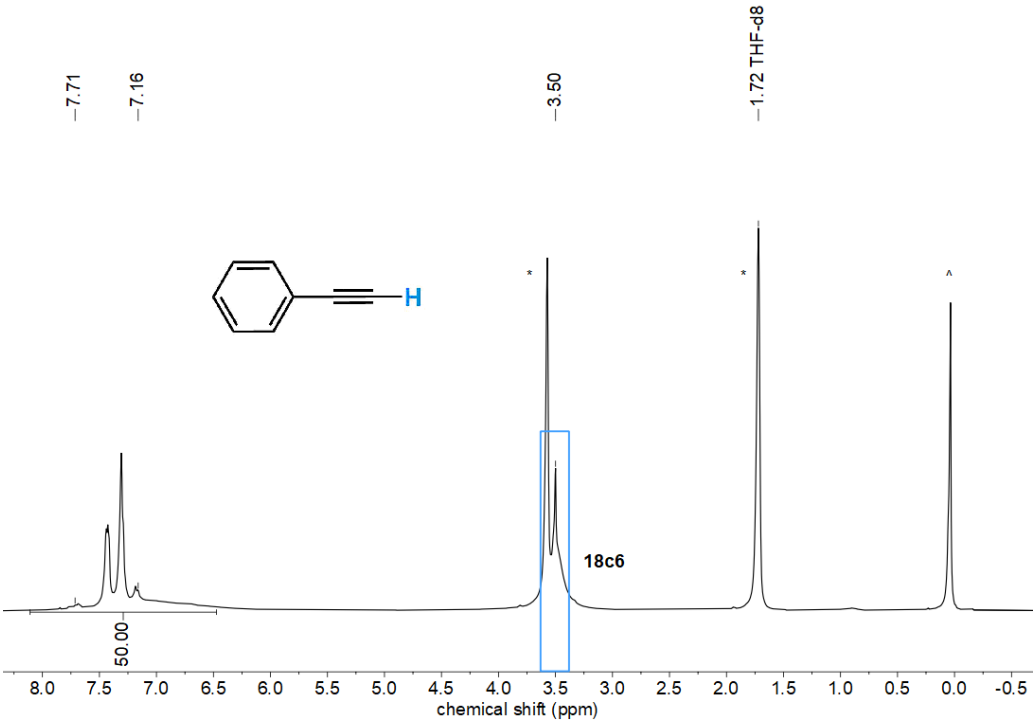

Figure S13. *In situ* ^{1}H NMR spectrum (300.1 MHz, 300 K) of reacting **A** (1 equiv.) with phenyl acetylene (10 equiv.) at room temperature in THF-d_8 after 7 days reaction time. No conversion but partial decomposition was observed. (* solvent, ^ decomposition)

Reactions with [K{18c6}][Fe(N{Dipp}SiMe$_3$)$_2$] (B)

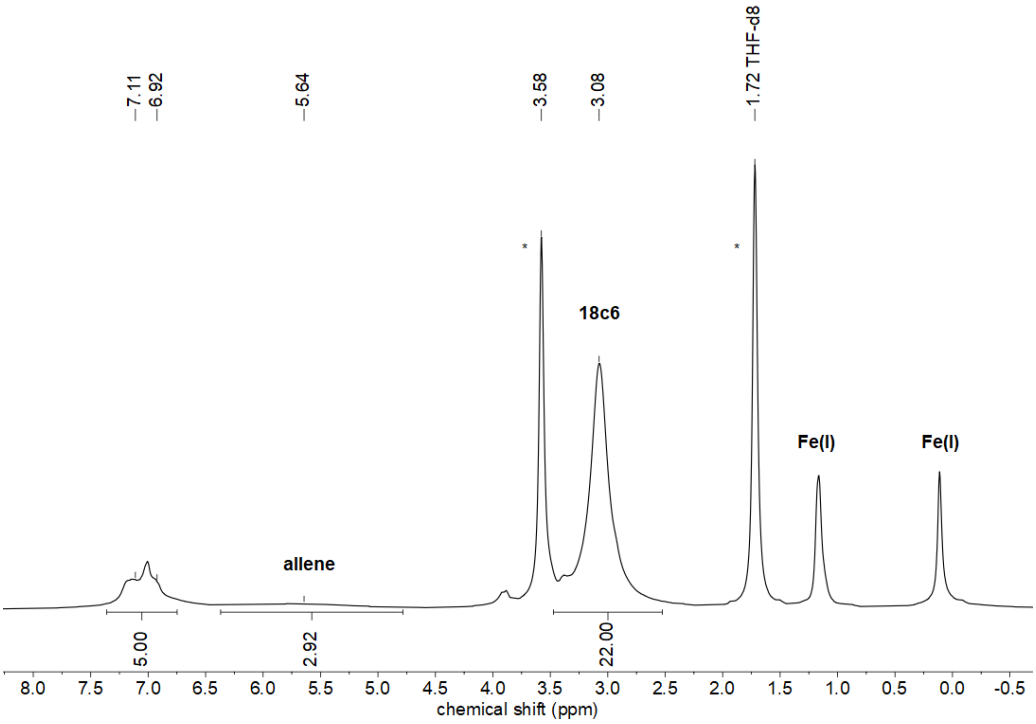

Figure S14. *In situ* ^{1}H NMR spectrum (300.1 MHz, 300 K) of reacting **B** (1 equiv.) with 3-phenyl propyne (1 equiv.) at room temperature in THF-d_8. (* solvent)

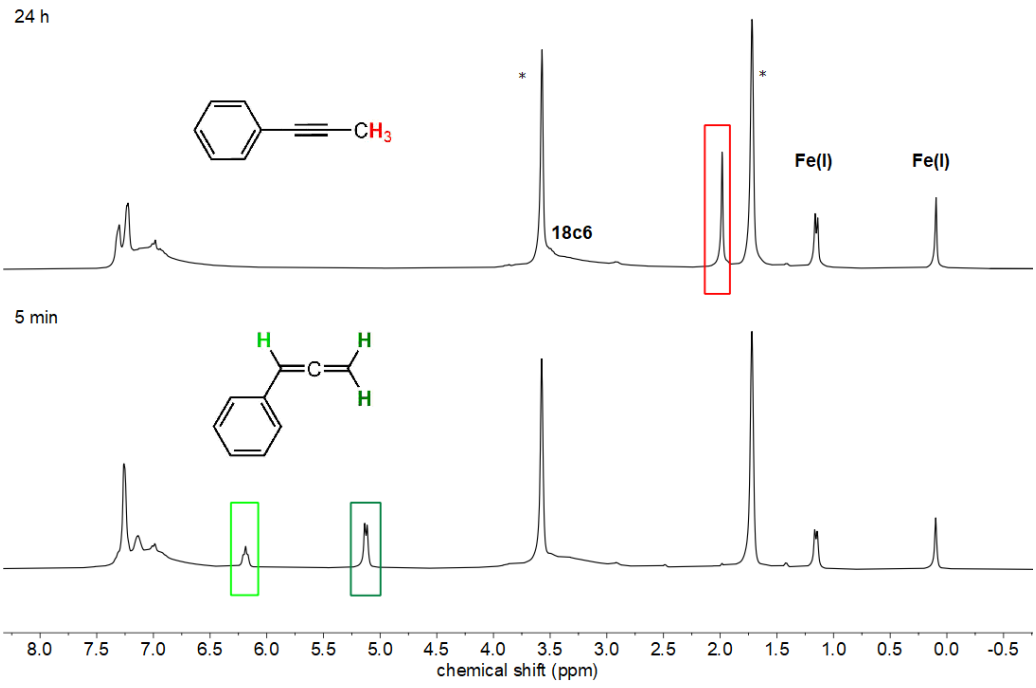

Figure S15. Time dependent *in situ* ^{1}H NMR spectrum (300.1 MHz, 300 K) of reacting **B** (1 equiv.) with 3-phenyl propyne (10 equiv.) at room temperature in THF-d_8. After 24 hours reaction time, full conversion to 1-phenyl propyne (>99%) was observed. (* solvent)

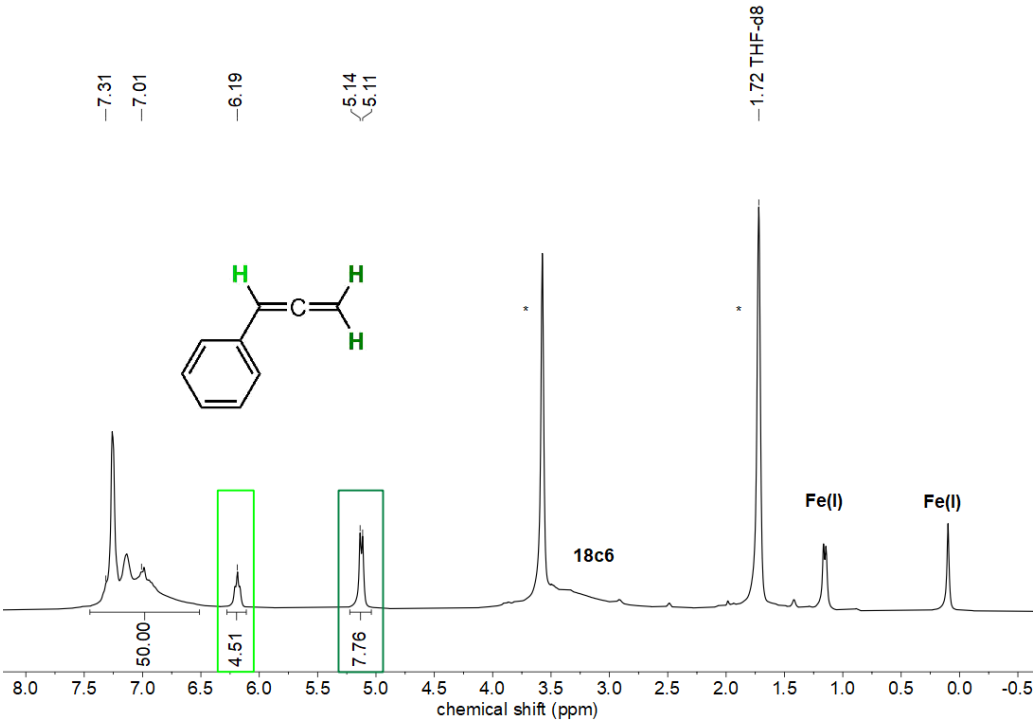

Figure S16. *In situ* ^{1}H NMR spectrum (300.1 MHz, 300 K) of reacting **B** (1 equiv.) with 3-phenyl propyne (10 equiv.) at room temperature in THF-d_8 after 5 minutes reaction time. Full conversion to phenyl allene (>99%) was observed. (* solvent)

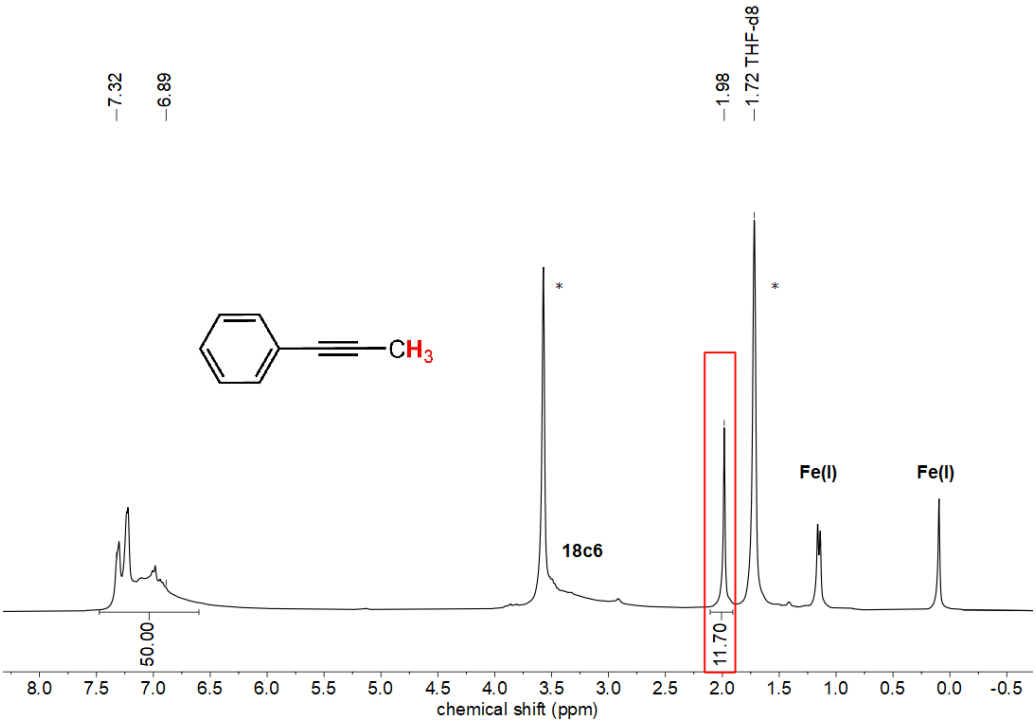

Figure S17. *In situ* ^{1}H NMR spectrum (300.1 MHz, 300 K) of reacting **B** (1 equiv.) with 3-phenyl propyne (10 equiv.) at room temperature in THF-d_8 after 24 hours reaction time. Full conversion to 1-phenyl propyne (>99%) was observed. (* solvent)

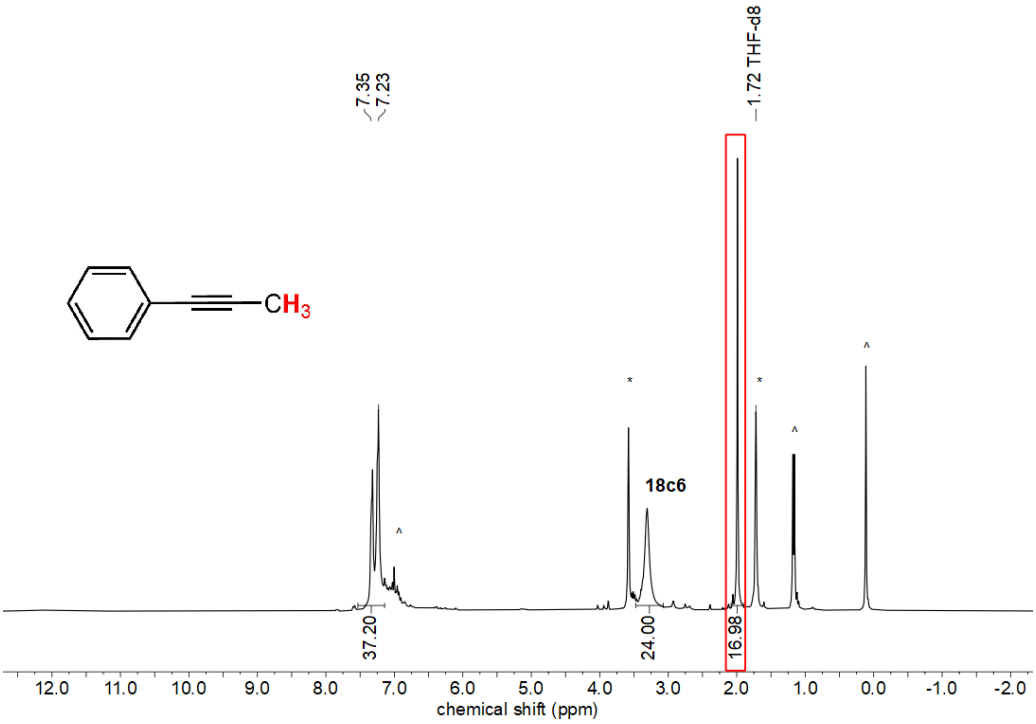

Figure S18. *in situ* ^{1}H NMR spectrum (300.1 MHz, 300 K) of reacting **B** (1 equiv.) with 1-phenyl propyne (10 equiv.) at room temperature in THF-d_8 after 7 days reaction time. No conversion was observed. (* solvent, ^ catalyst)

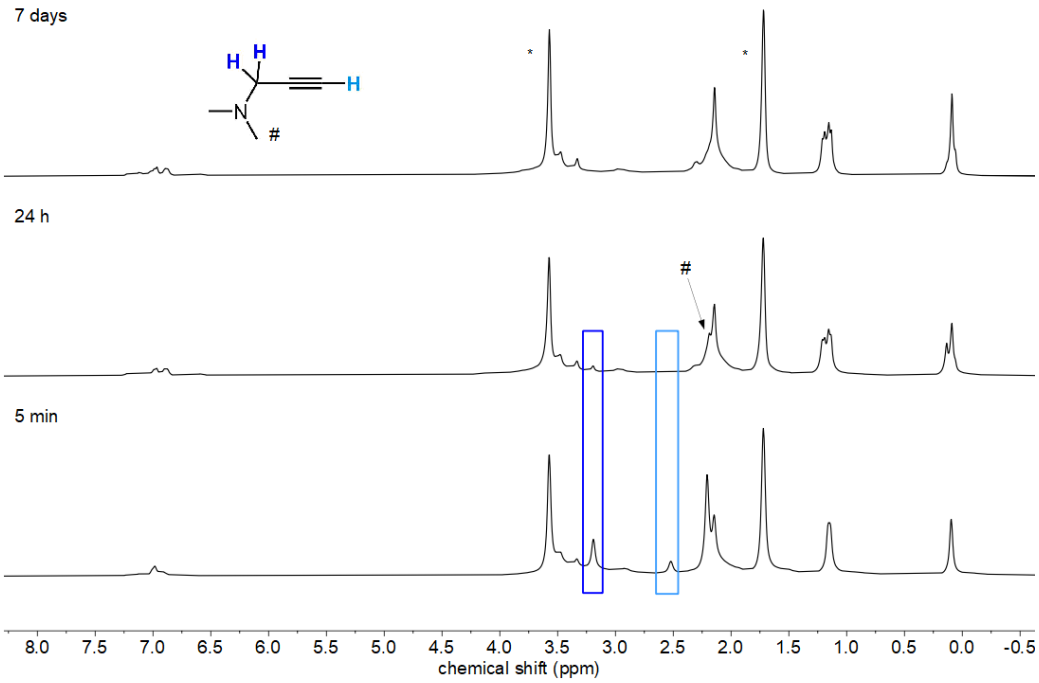

Figure S19. Time dependent *in situ* ^{1}H NMR spectrum (300.1 MHz, 300 K) of reacting **B** (1 equiv.) with *N,N*-dimethylpropargylamine (10 equiv.) at room temperature in THF-d_8. After 7 days reaction time, full conversion (>99%) was observed using the NMe_2-signals of the educt (#). (* solvent)

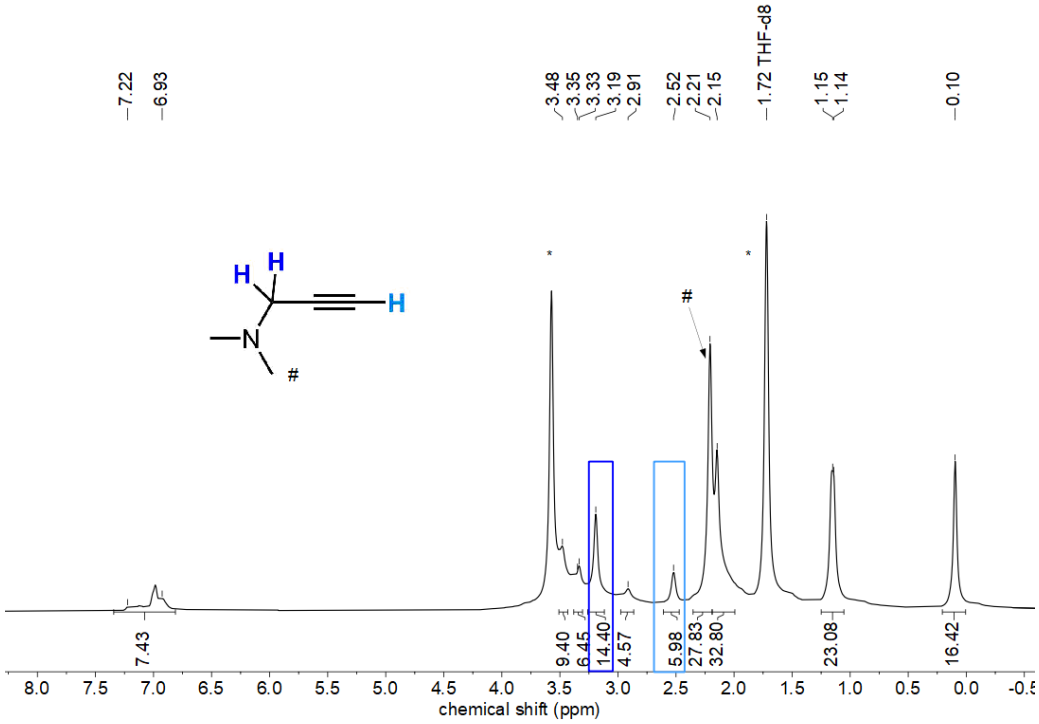

Figure S20. *In situ* ^{1}H NMR spectrum (300.1 MHz, 300 K) of reacting **B** (1 equiv.) with *N,N*-dimethylpropargylamine (10 equiv.) at room temperature in THF-d_8 after 5 minutes reaction time. Partial conversion (53%) was observed using the NMe_2-signals of the educt (#). (* solvent)

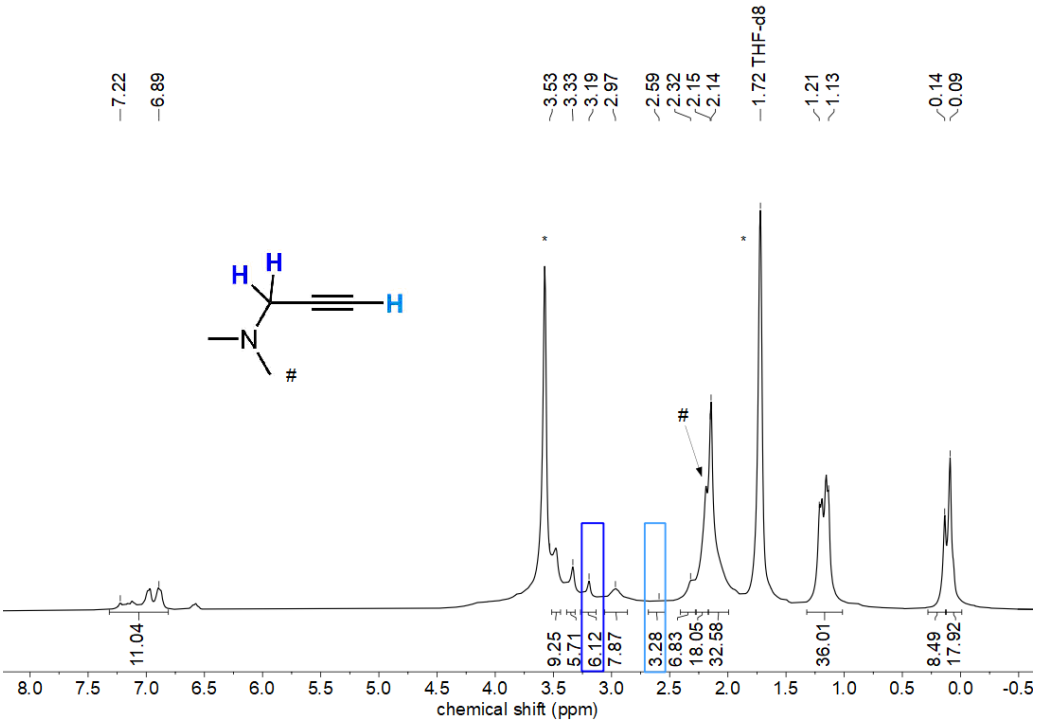

Figure S21. *In situ* ^{1}H NMR spectrum (300.1 MHz, 300 K) of reacting **B** (1 equiv.) with *N,N*-dimethylpropargylamine (10 equiv.) at room temperature in THF-d_8 after 24 hours reaction time. (* solvent)

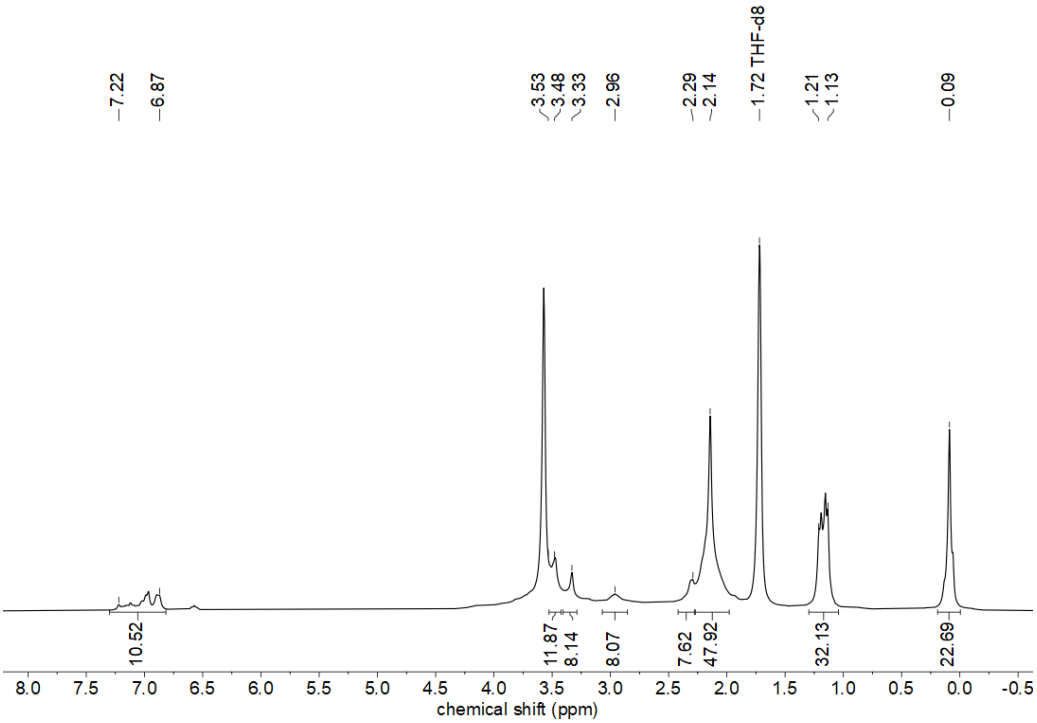

Figure S22. *In situ* ^{1}H NMR spectrum (300.1 MHz, 300 K) of reacting **B** (1 equiv.) with *N,N*-dimethylpropargylamine (10 equiv.) at room temperature in THF-d_8 after 7 days reaction time. Full conversion (>99%) was observed using the NMe_2-signals of the educt (#). (* solvent)

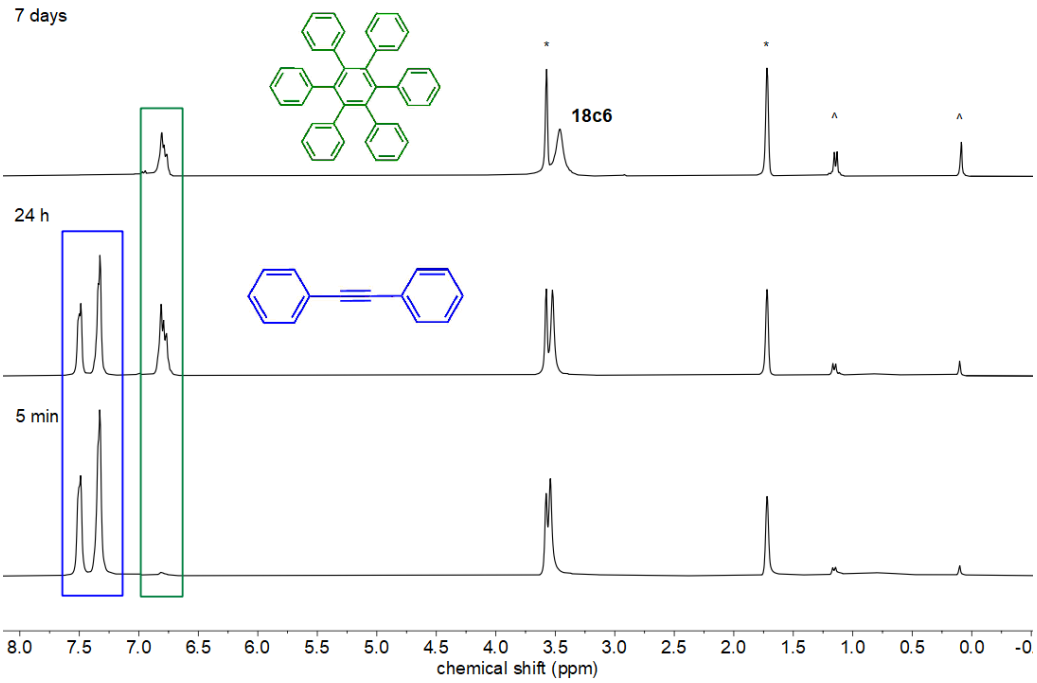

Figure S23. Time dependent *in situ* ^{1}H NMR spectrum (300.1 MHz, 300 K) of reacting **B** (1 equiv.) with diphenyl acetylene (10 equiv.) at room temperature in THF-d_8. After 7 days, a full conversion to hexaphenyl benzene was observed, which mostly precipitates as white solid. (* solvent, ^ catalyst)

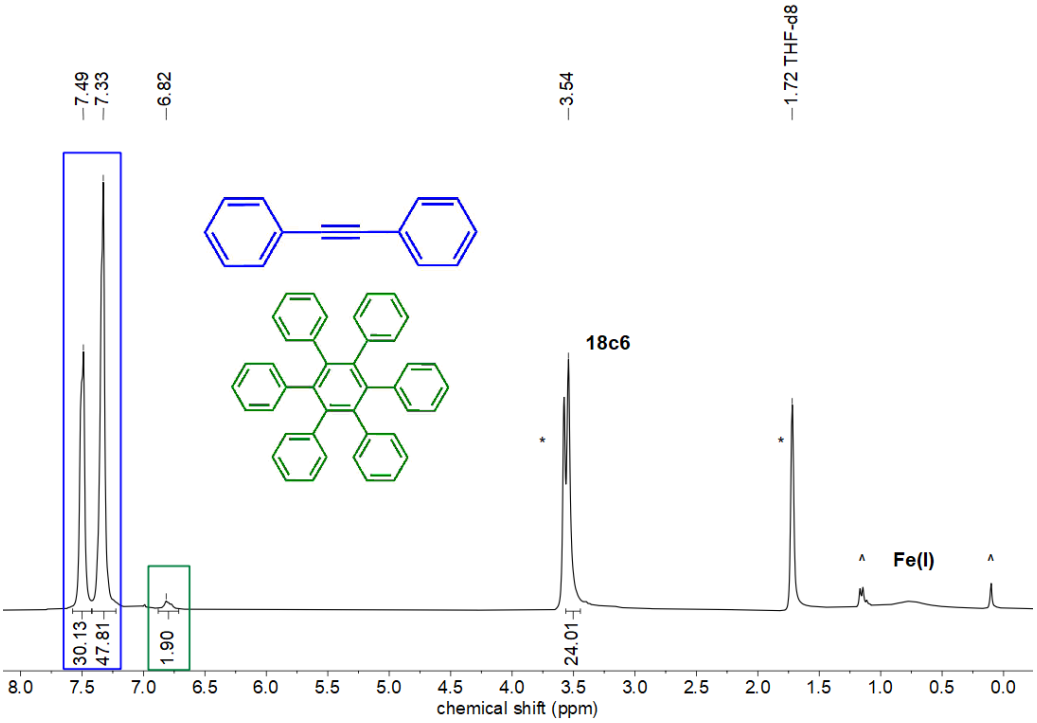

Figure S24. *in situ* ^{1}H NMR spectrum (300.1 MHz, 300 K) of reacting **B** (1 equiv.) with diphenyl acetylene (10 equiv.) at room temperature in THF-d_8 after 5 minutes reaction time. Partial conversion to hexaphenyl benzene (20%) was observed, which mostly precipitates as white solid. (* solvent, ^ catalyst)

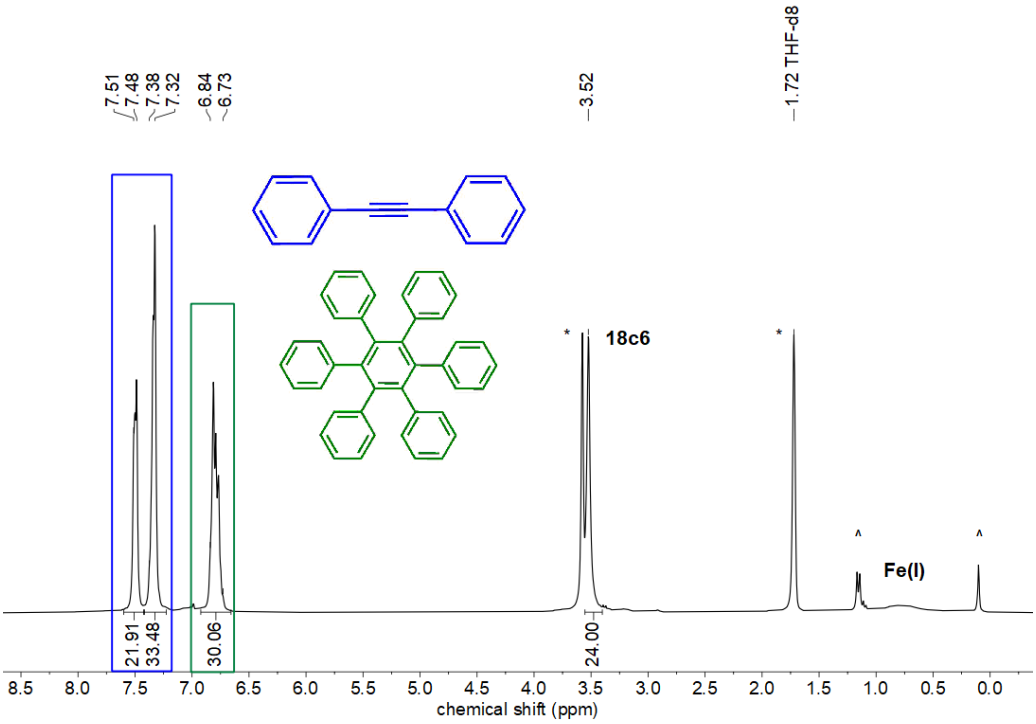

Figure S25. *in situ* ^{1}H NMR spectrum (300.1 MHz, 300 K) of reacting **B** (1 equiv.) with diphenyl acetylene (10 equiv.) at room temperature in THF-d_8 after 24 hours reaction time. Partial conversion to hexaphenyl benzene (45%) was observed, which mostly precipitates as white solid. (* solvent, ^ catalyst)

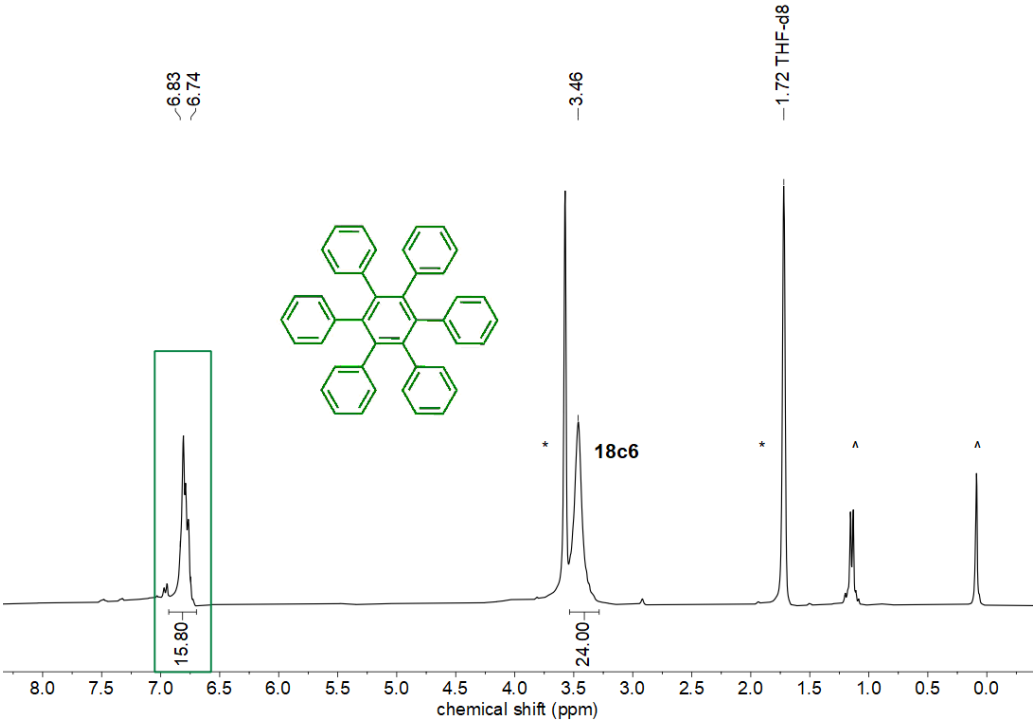

Figure S26. *in situ* ^{1}H NMR spectrum (300.1 MHz, 300 K) of reacting **B** (1 equiv.) with diphenyl acetylene (10 equiv.) at room temperature in THF-d_8 after 7 days reaction time. Full conversion to hexaphenyl benzene (>99%) was observed, which mostly precipitates as white solid. (* solvent, ^ catalyst)

Reactions with [K{18c6}][Fe(N{SiMe$_3$}$_2$)$_3$] (C)

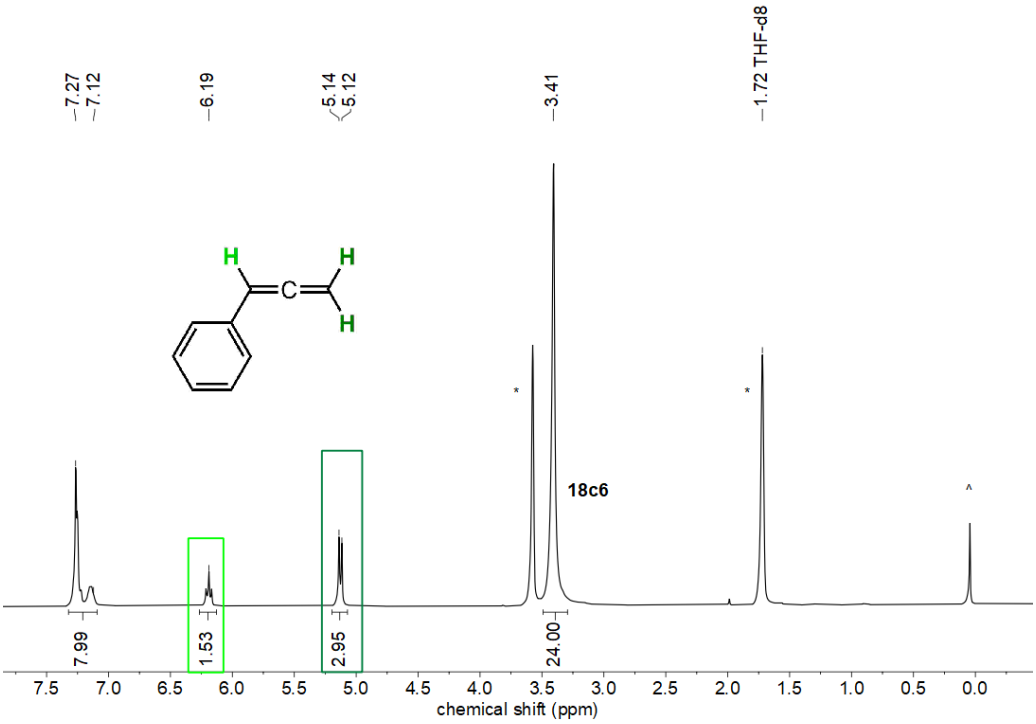

Figure S27. *In situ* ^{1}H NMR spectrum (300.1 MHz, 300 K) of reacting **C** (1 equiv.) with 3-phenyl propyne (1 equiv.) at room temperature in THF-d_8. Conversion to phenyl allene was observed. (* solvent, ^ decomposition)

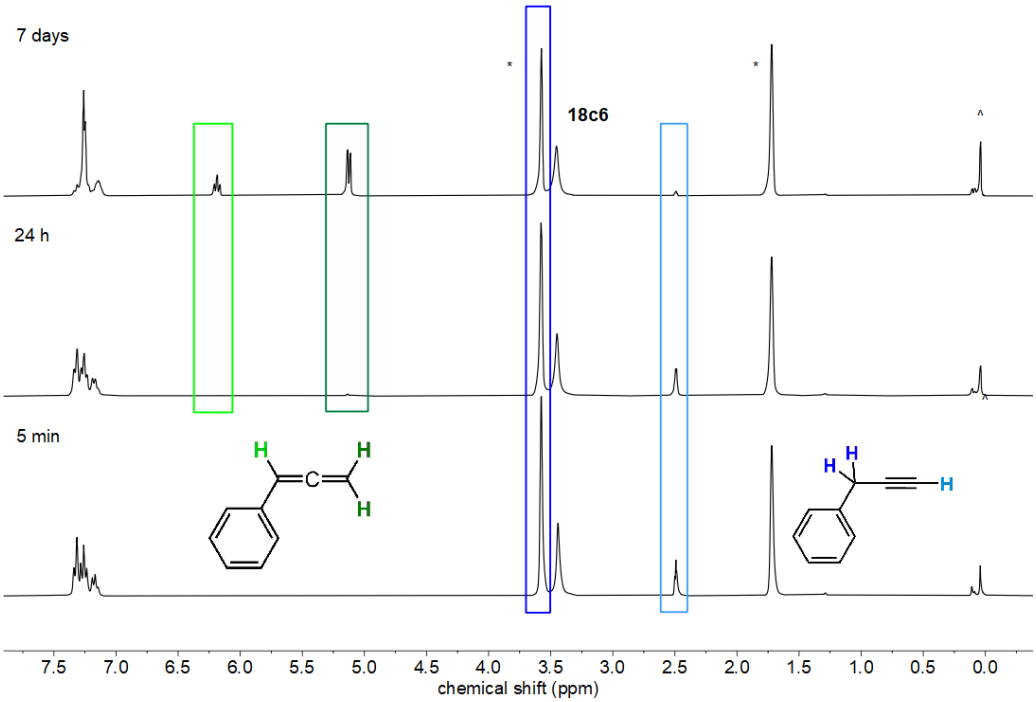

Figure S28. Time dependent *in situ* ^{1}H NMR spectrum (300.1 MHz, 300 K) of reacting **C** (1 equiv.) with 3-phenyl propyne (10 equiv.) at room temperature in THF-d_8. After 7 days partial conversion to phenyl allene (85%) was observed. (* solvent, ^ decomposition)

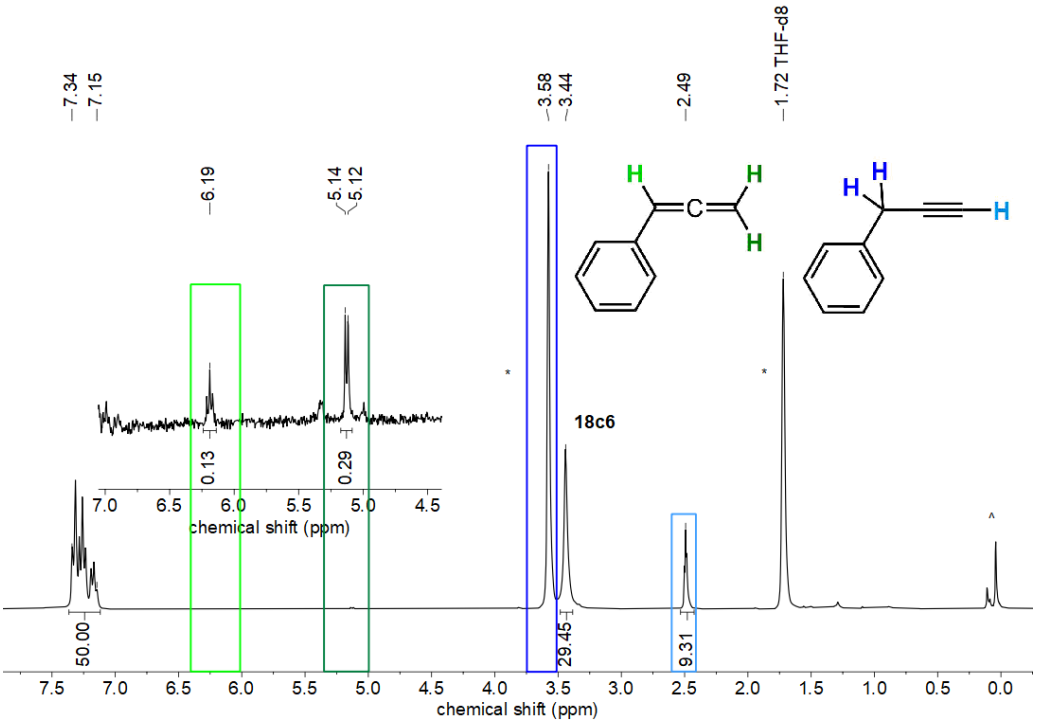

Figure S29. *In situ* ^{1}H NMR spectrum (300.1 MHz, 300 K) of reacting **C** (1 equiv.) with 3-phenyl propyne (10 equiv.) at room temperature in THF-d_8 after 5 minutes reaction time. Partial conversion to phenyl allene (2%) was observed. (* solvent, ^ decomposition)

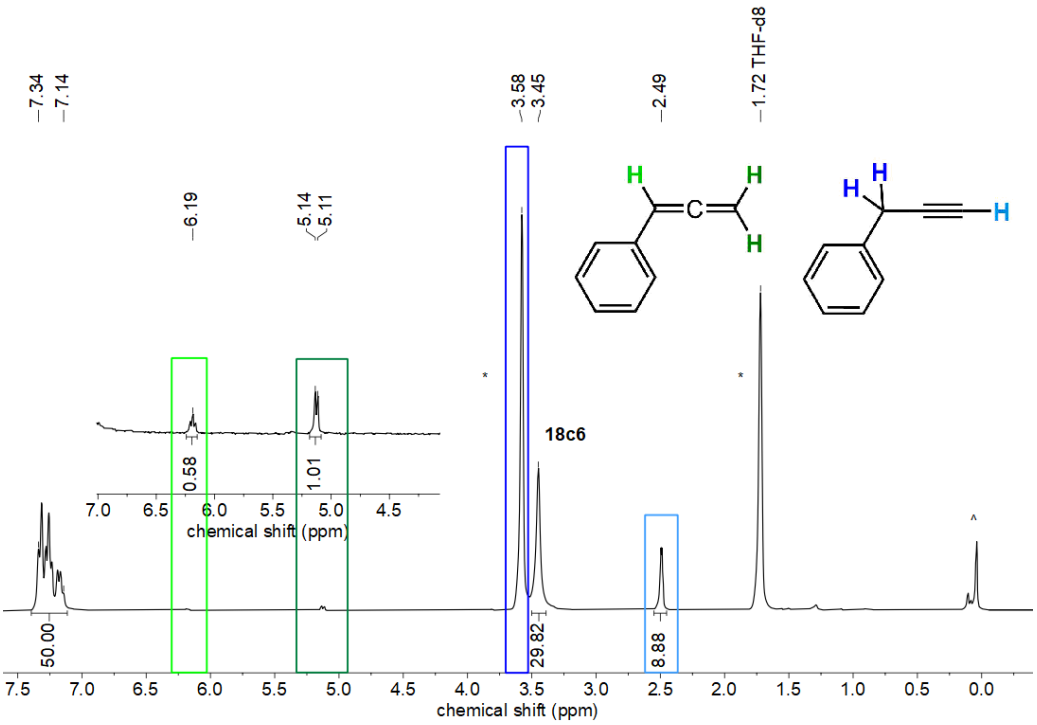

Figure S30. *In situ* ^{1}H NMR spectrum (300.1 MHz, 300 K) of reacting **C** (1 equiv.) with 3-phenyl propyne (10 equiv.) at room temperature in THF-d_8 after 24 hours reaction time. Partial conversion to phenyl allene (6%) was observed. (* solvent, ^ decomposition)

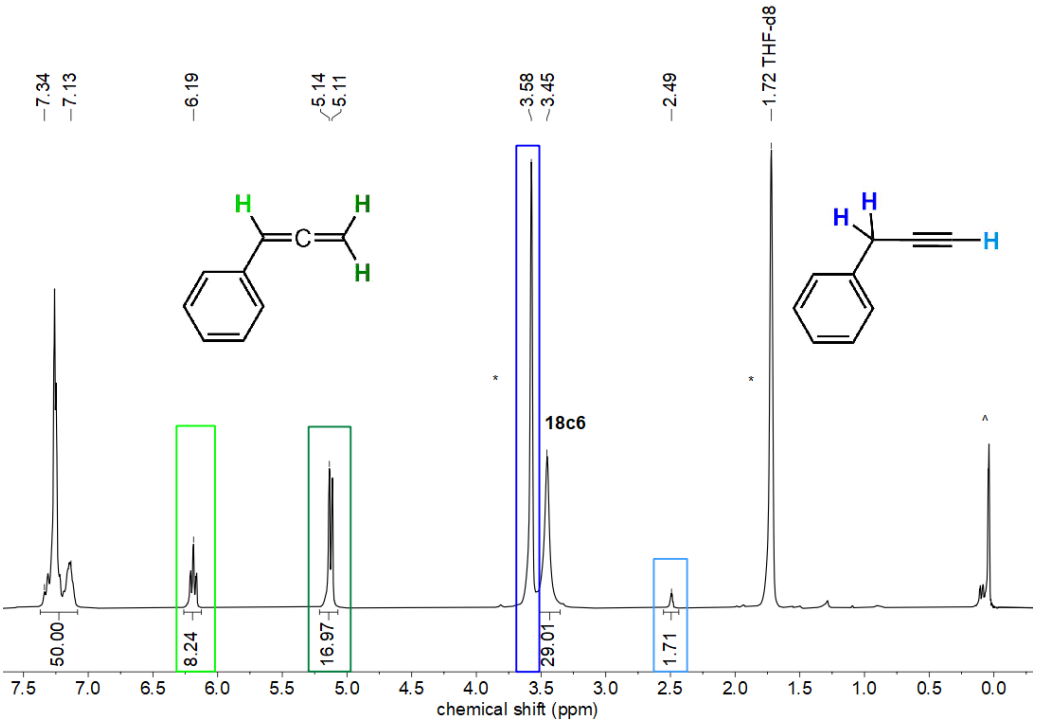

Figure S31. *In situ* ^{1}H NMR spectrum (300.1 MHz, 300 K) of reacting **C** (1 equiv.) with 3-phenyl propyne (10 equiv.) at room temperature in THF-d_8 after 7 days reaction time. Partial conversion to phenyl allene (85%) was observed. (* solvent, ^ decomposition)

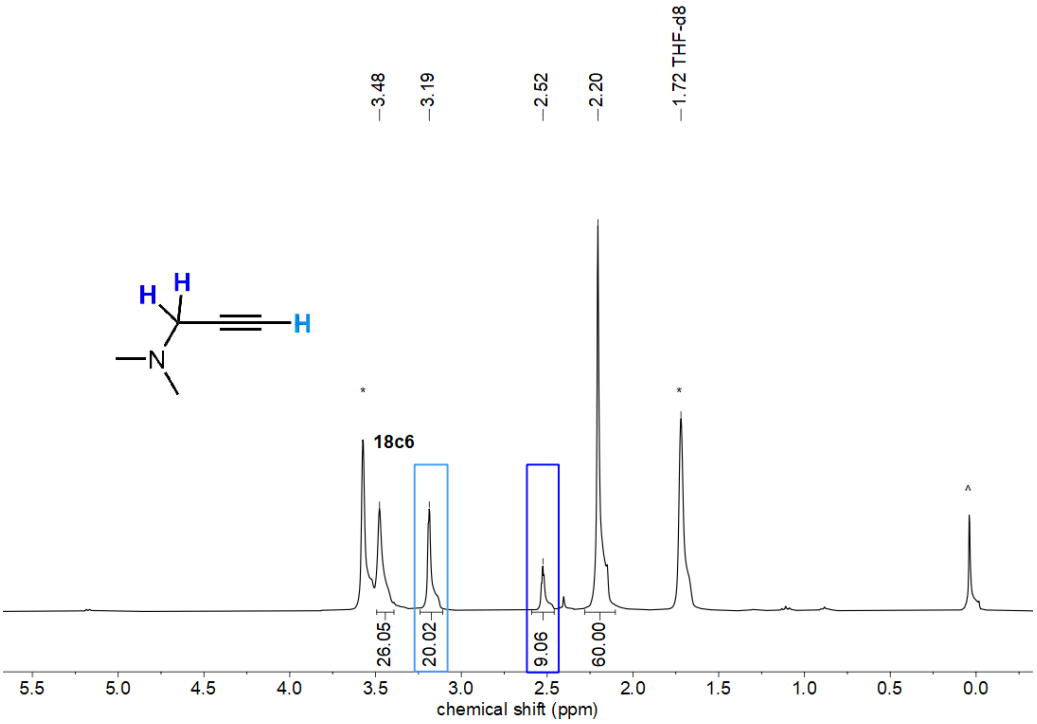

Figure S32. *In situ* ^{1}H NMR spectrum (300.1 MHz, 300 K) of reacting **C** (1 equiv.) with *N*,*N*-dimethylpropargylamine (10 equiv.) at room temperature in THF-d_8 after 7 days reaction time. No conversion was observed. (* solvent, ^ decomposition).

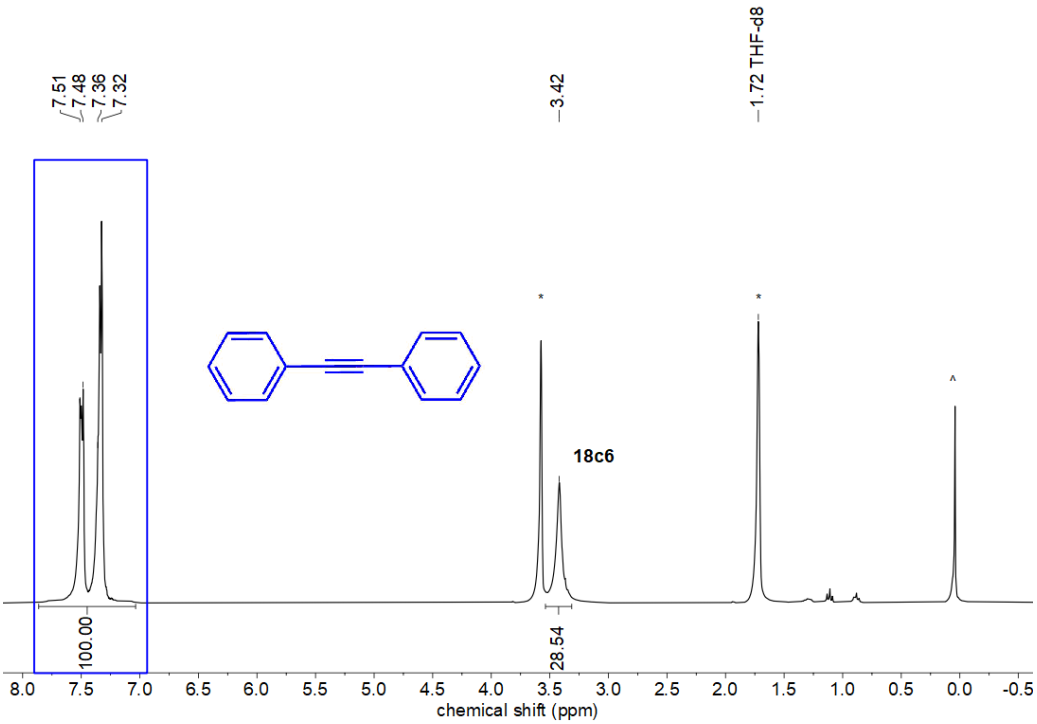

Figure S33. *In situ* ^{1}H NMR spectrum (300.1 MHz, 300 K) of reacting **C** (1 equiv.) with diphenyl acetylene (10 equiv.) at room temperature in THF-d_8 after 7 days reaction time. No conversion but partial decomposition was observed. (* solvent, ^ decomposition).

Reactions with [Fe(N{SiMe$_3$}$_2$)$_2$] (D)

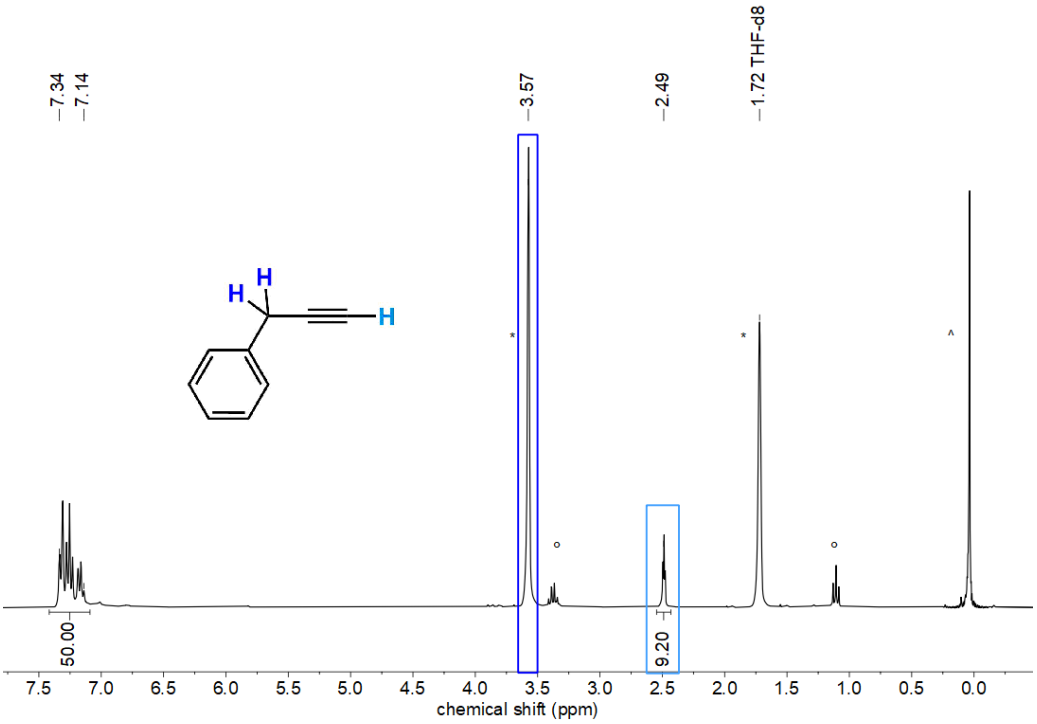

Figure S34. *In situ* ^{1}H NMR spectrum (300.1 MHz, 300 K) of reacting **D** (1 equiv.) with 3-phenyl propyne (10 equiv.) at room temperature in THF-d_8 after 7 days reaction time. No conversion but partial decomposition was observed. (* solvent, ^ decomposition, ° diethyl ether)

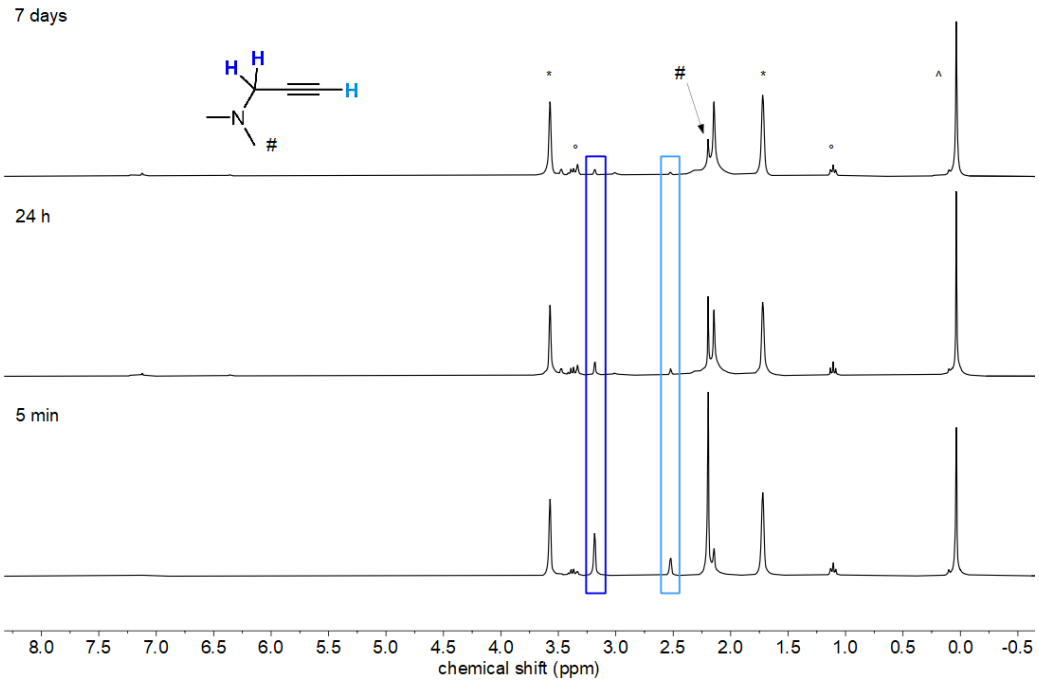

Figure S35. Time dependent *in situ* ^{1}H NMR spectrum (300.1 MHz, 300 K) of reacting **D** (1 equiv.) with *N*,*N*-dimethylpropargylamine (10 equiv.) at room temperature in THF-d_8. After 7 days reaction time, partial conversion (75%) was observed. (* solvent, ^ decomposition)

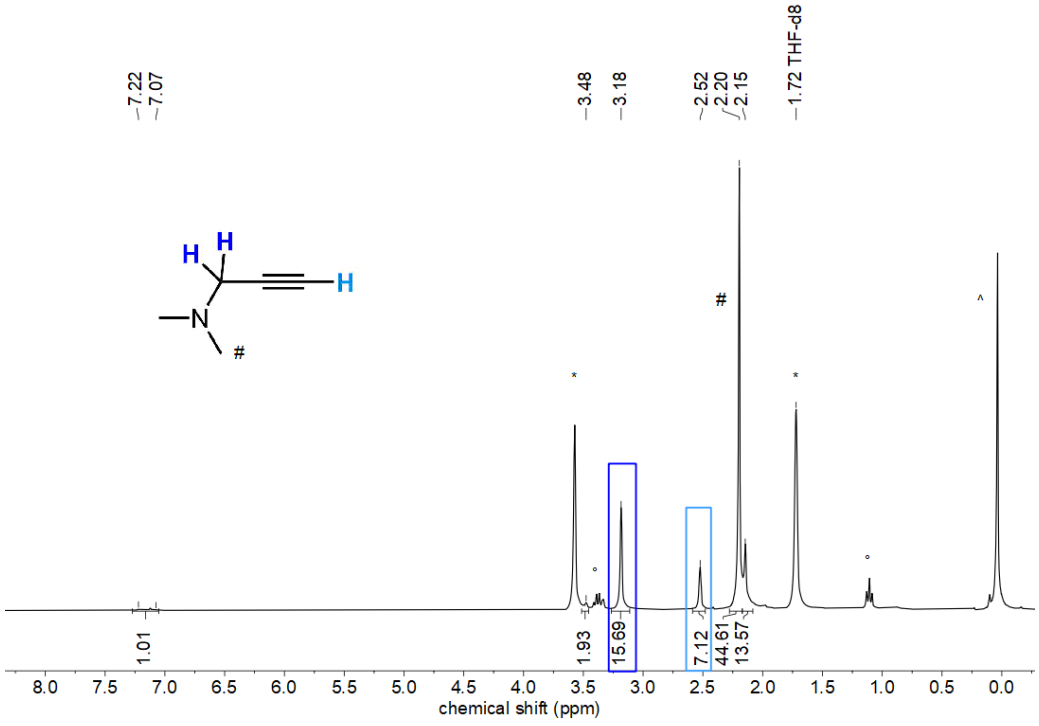

Figure S36. *In situ* ^{1}H NMR spectrum (300.1 MHz, 300 K) of reacting **D** (1 equiv.) with *N*,*N*-dimethylpropargylamine (10 equiv.) at room temperature in THF-d_8 after 5 minutes reaction time. Partial conversion (23%) was observed. (* solvent, ^ decomposition)

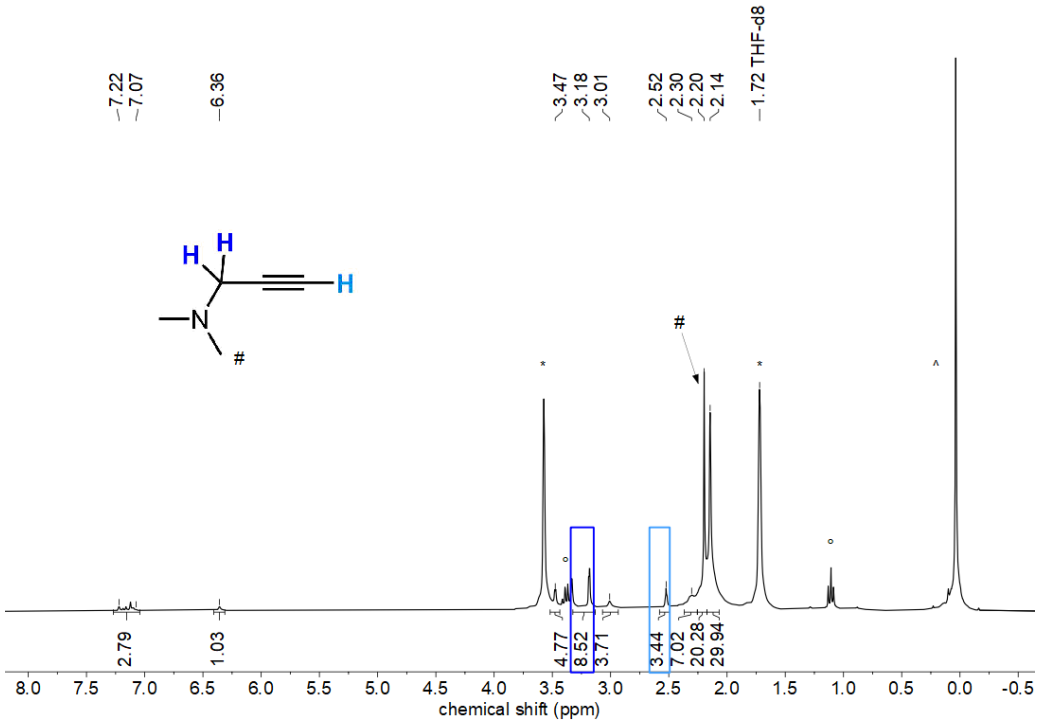

Figure S37. *In situ* ^{1}H NMR spectrum (300.1 MHz, 300 K) of reacting **D** (1 equiv.) with *N*,*N*-dimethylpropargylamine (10 equiv.) at room temperature in THF-d_8 after 24 hours reaction time. Partial conversion (67%) was observed. (* solvent, ° diethyl ether, ^ decomposition)

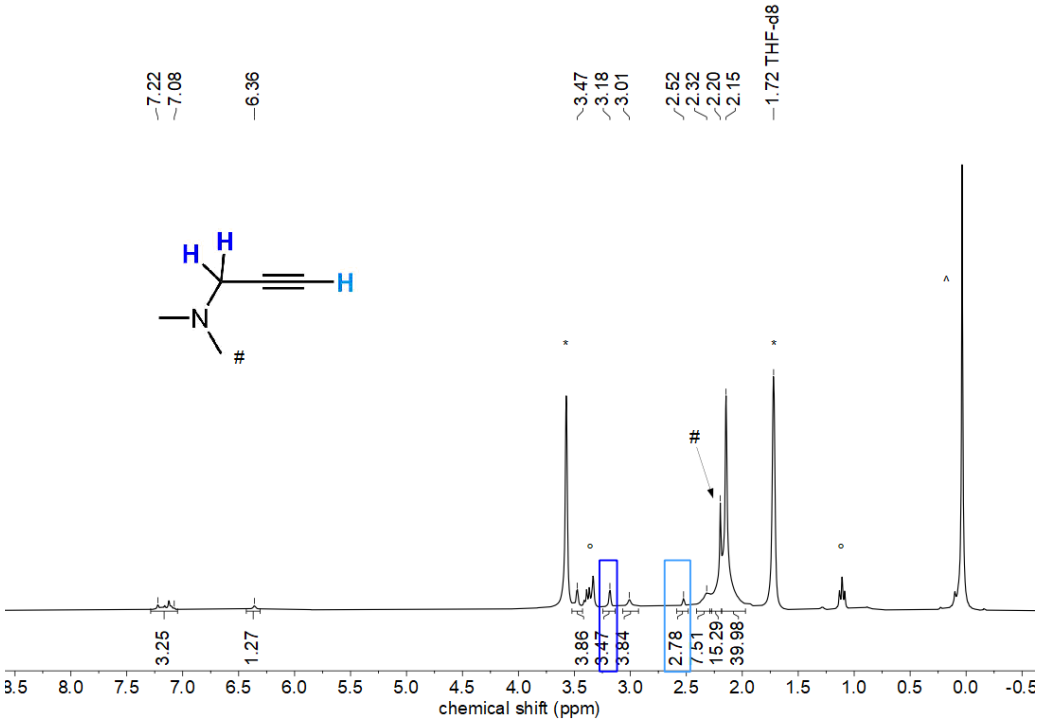

Figure S38. *In situ* ^{1}H NMR spectrum (300.1 MHz, 300 K) of reacting **D** (1 equiv.) with *N*,*N*-dimethylpropargylamine (10 equiv.) at room temperature in THF-d_8 after 7 days reaction time. Partial conversion (75%) was observed. (* solvent, ° diethyl ether, ^ decomposition)

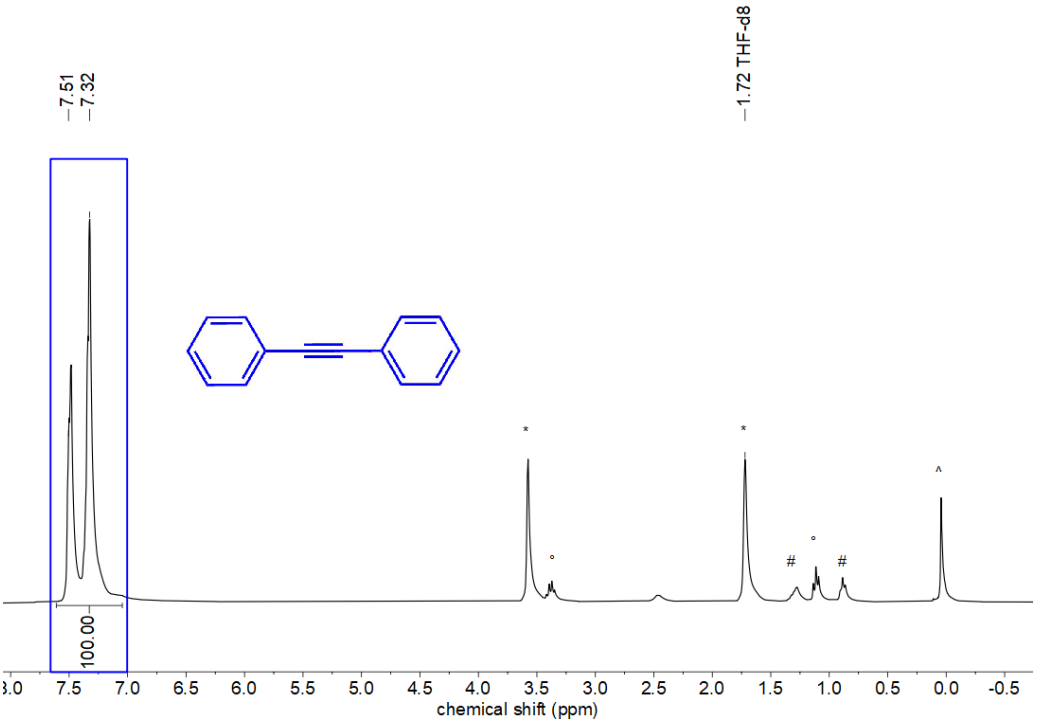

Figure S39. *In situ* ^{1}H NMR spectrum (300.1 MHz, 300 K) of reacting **D** (1 equiv.) with diphenyl acetylene (10 equiv.) at room temperature in THF-d_8 after 7 days reaction time. No conversion was observed. (* solvent, ^ decomposition, ° diethyl ether, $^{\#}$ *n*-pentane)

Reactions with $KN(SiMe_3)_2$ (E)

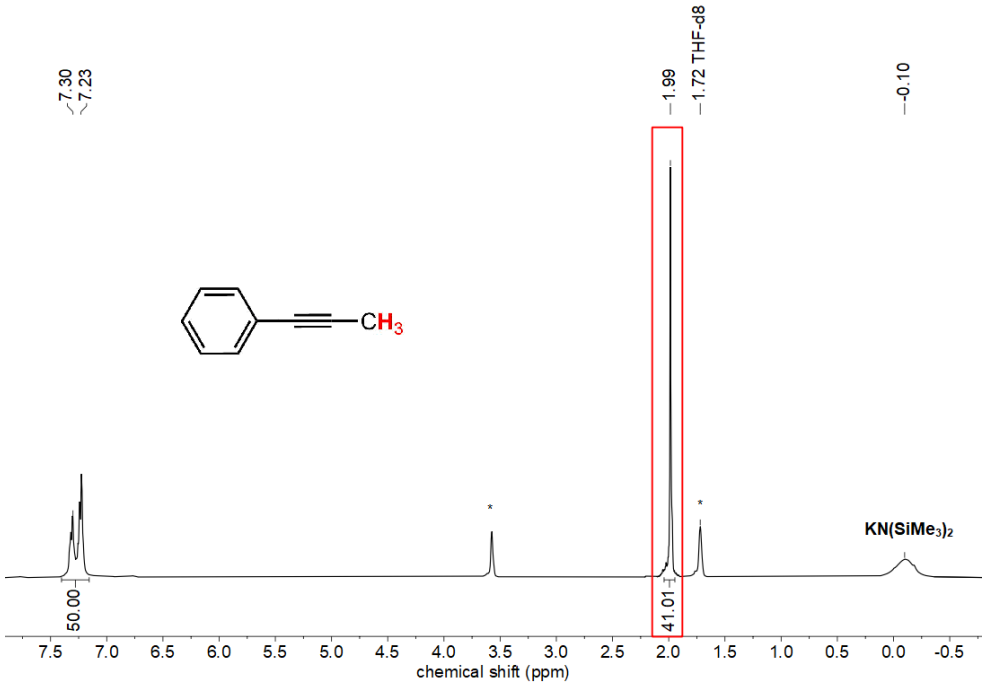

Figure S40. *In situ* ^{1}H NMR spectrum (300.1 MHz, 300 K) of reacting **E** (1 equiv.) and 3-phenyl propyne (10 equiv.) at room temperature in THF-d_8. After 5 min reaction time, full conversion (>99%) to 1-phenyl propyne (>99%) was observed. (* solvent)

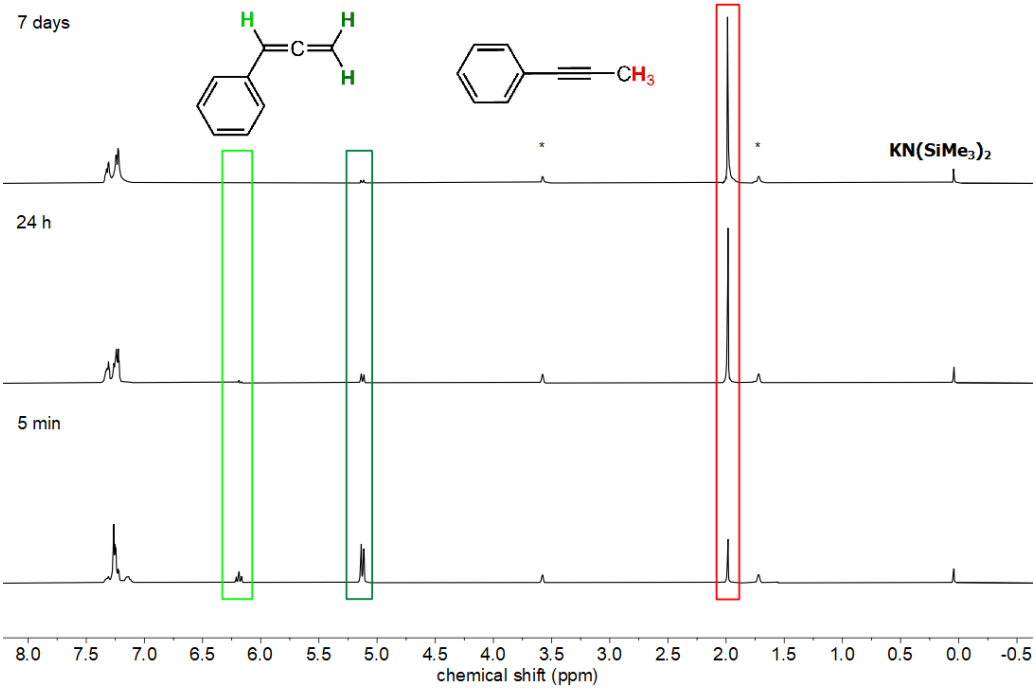

Figure S41. Time dependent *in situ* ^{1}H NMR spectrum (300.1 MHz, 300 K) of reacting **E** (1 equiv.) with 3-phenyl propyne (100 equiv.) at room temperature in THF-d_8. After 7 days reaction time almost full conversion to 1-phenyl propyne (94%) was observed. (* solvent)

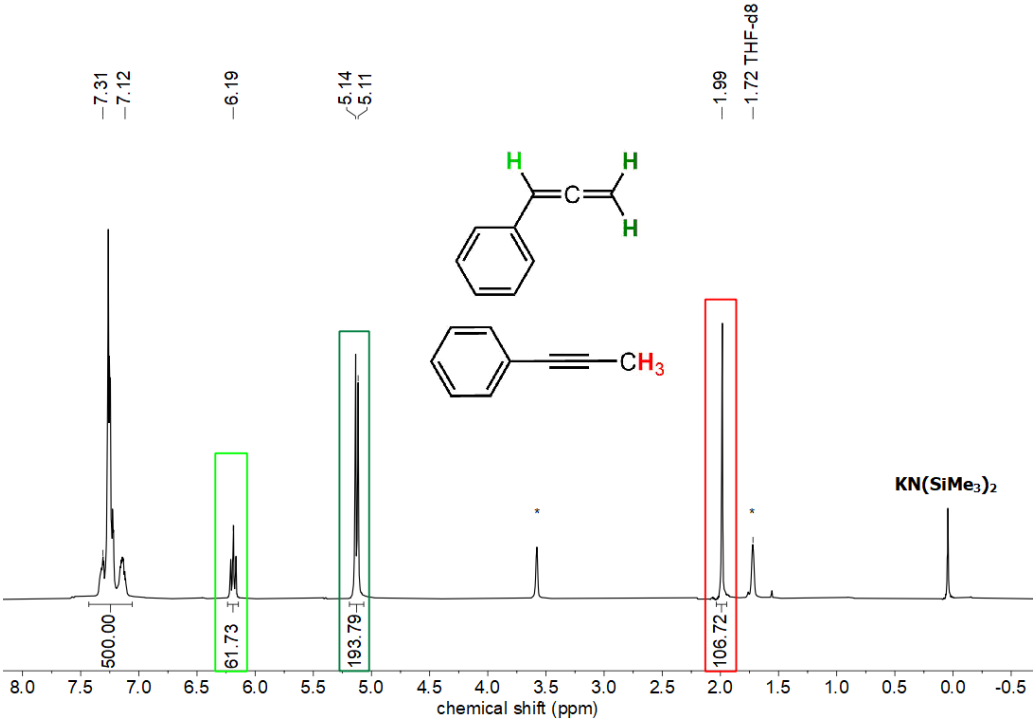

Figure S42. *In situ* ^{1}H NMR spectrum (300.1 MHz, 300 K) of reacting **E** (1 equiv.) and 3-phenyl propyne (100 equiv.) at room temperature in THF-d_8. After 5 min reaction time, full conversion to phenyl allene (still 71%) and subsequent conversion to 1-phenyl propyne (29%) was observed. (* solvent)

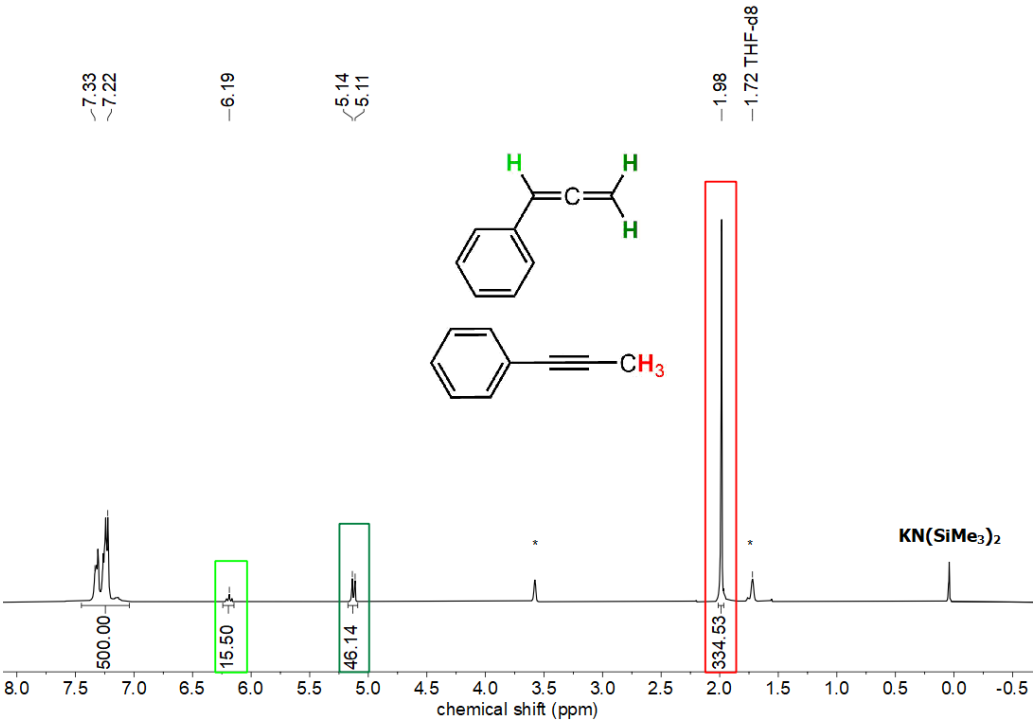

Figure S43. *In situ* ^{1}H NMR spectrum (300.1 MHz, 300 K) of reacting **E** (1 equiv.) and 3-phenyl propyne (100 equiv.) at room temperature in THF-d_8. After 24 hours reaction time, subsequent conversion from phenyl allene (still 16%) to 1-phenyl propyne (84%) was observed. (* solvent)

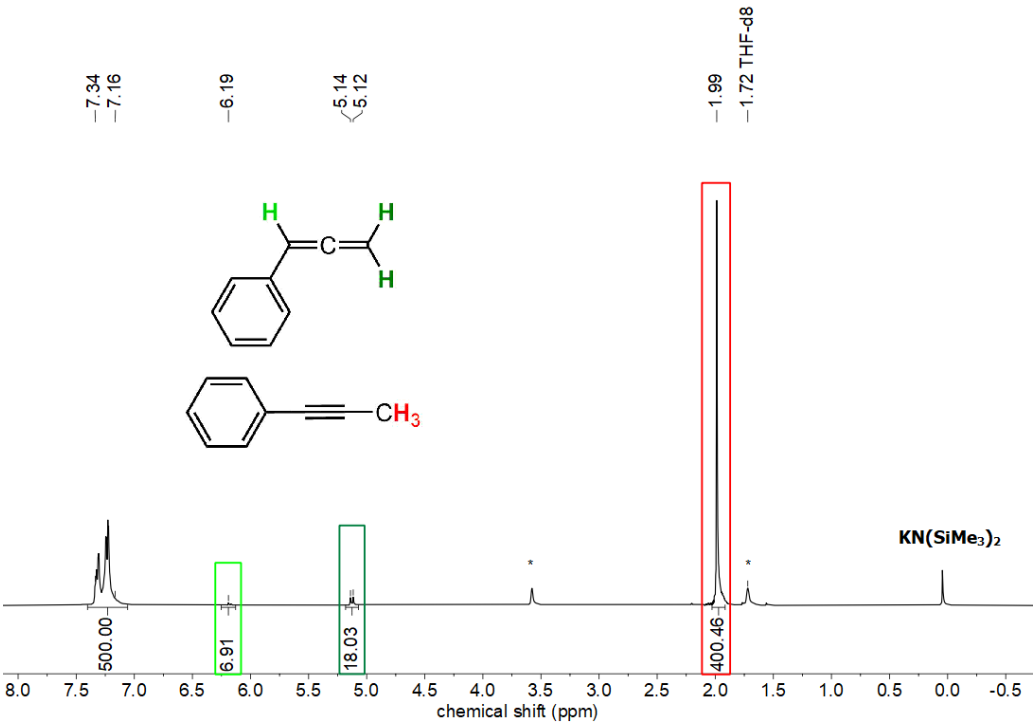

Figure S44. *In situ* ^{1}H NMR spectrum (300.1 MHz, 300 K) of reacting **E** (1 equiv.) and 3-phenyl propyne (100 equiv.) at room temperature in THF-d_8. After 7 days reaction time, almost full conversion to 1-phenyl propyne (94%) was observed. (* solvent, ^ decomposition)

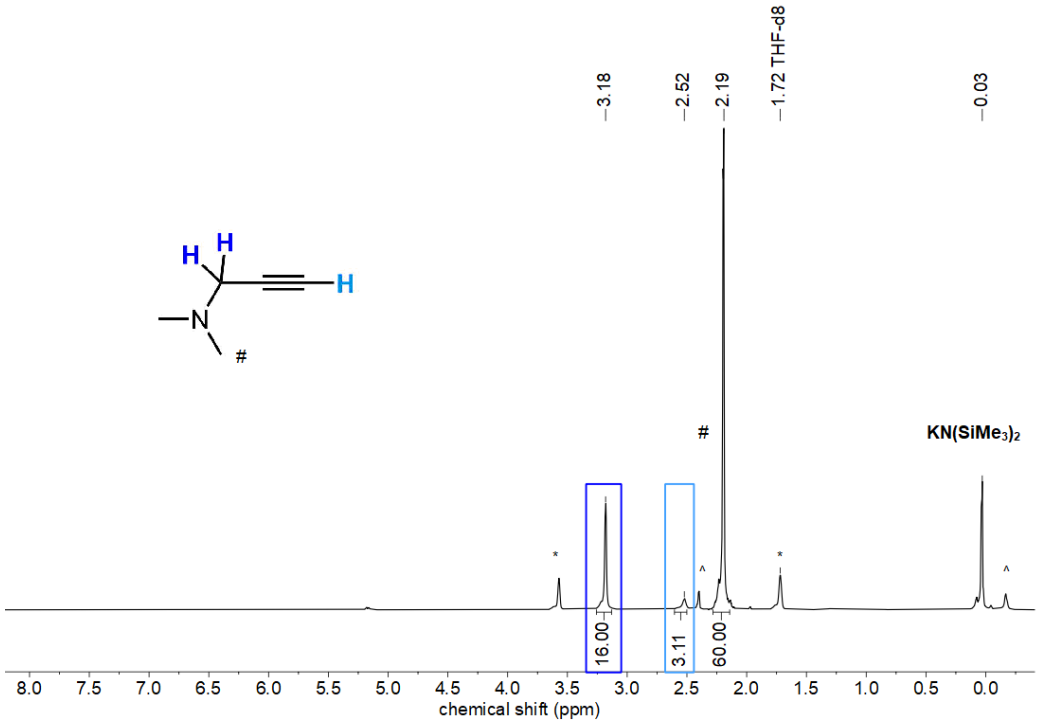

Figure S45. *In situ* ^{1}H NMR spectrum (300.1 MHz, 300 K) of reacting **E** (1 equiv.) with *N*,*N*-dimethylpropargylamine (10 equiv.) at room temperature in THF-d_8 after 7 days reaction time. No conversion was observed. (* solvent, ^ decomposition)

Reactions with $LiN(SiMe_3)_2$ (F)

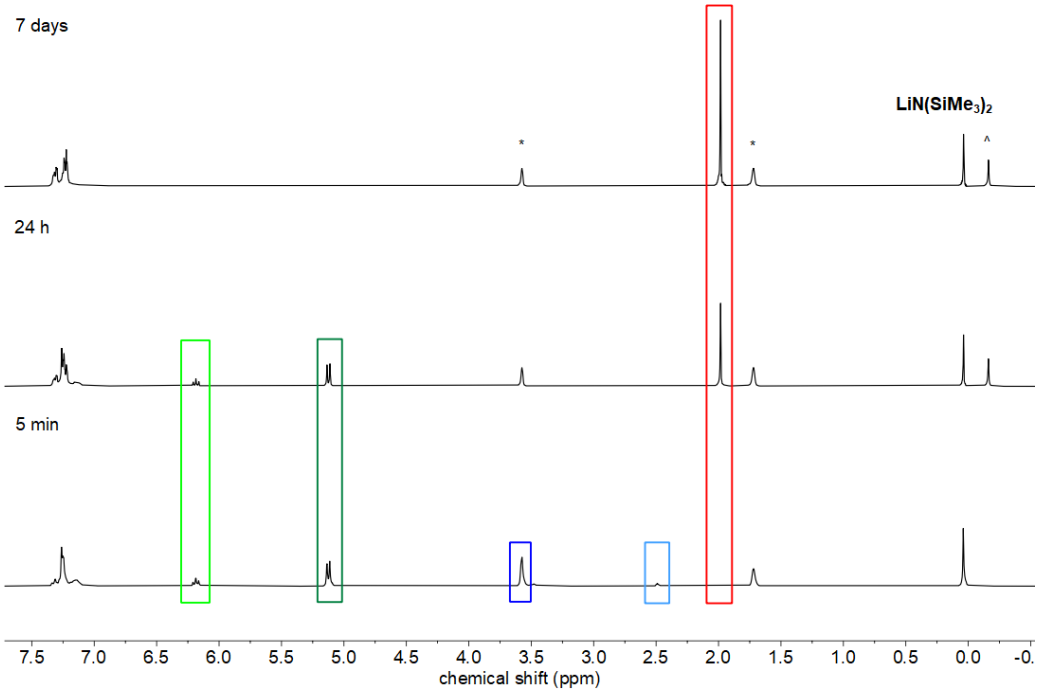

Figure S46. Time dependent *in situ* ^{1}H NMR spectrum (300.1 MHz, 300 K) of reacting **F** (1.0 equiv.) with 3-phenyl propyne (10 equiv.) at room temperature in THF-d_8. After 7 days full conversion to 1-phenyl propyne (>99%) was observed. (* solvent, ^ decomposition)

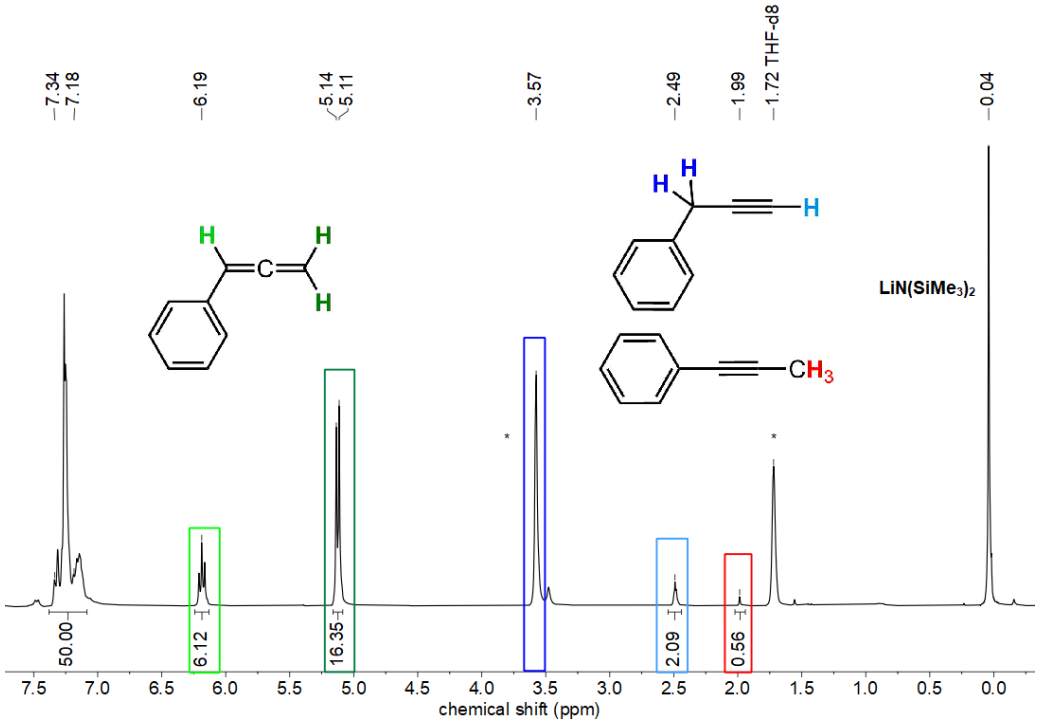

Figure S47. *In situ* ^{1}H NMR spectrum (300.1 MHz, 300 K) of reacting **F** (1.0 equiv.) with 3-phenyl propyne (10 equiv.) at room temperature in THF-d_8 after 5 minutes. Partial conversion to phenyl allene (still 77%) and further reaction to 1-phenyl propyne (2%) was observed. (* solvent)

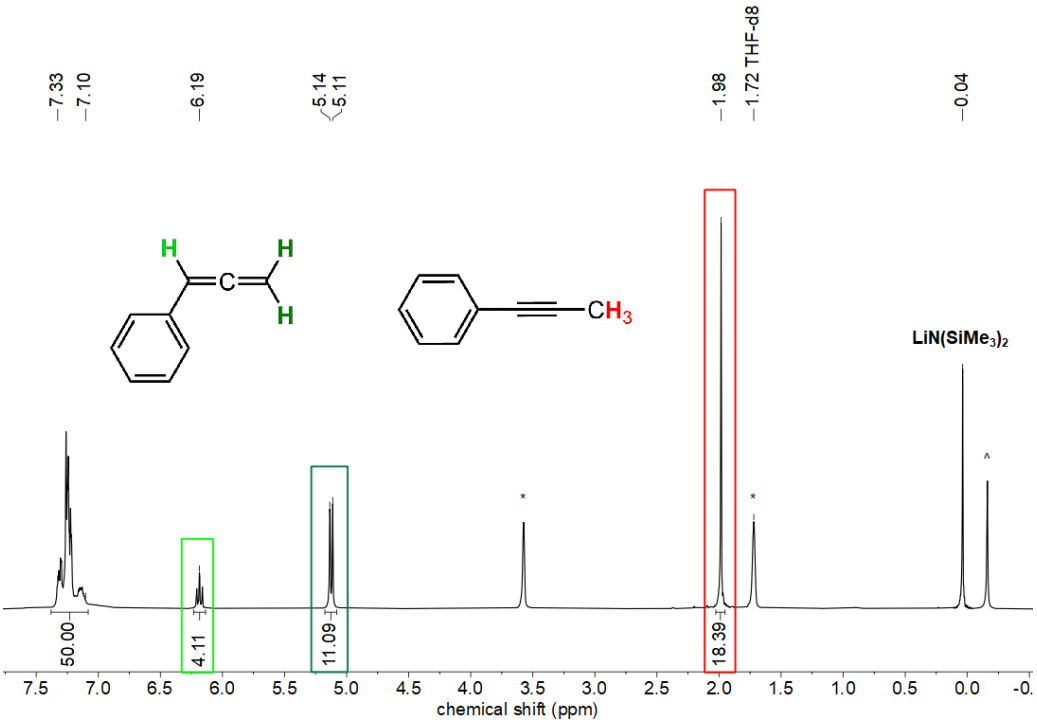

Figure S48. *In situ* ^{1}H NMR spectrum (300.1 MHz, 300 K) of reacting **F** (1.0 equiv.) with 3-phenyl propyne (10 equiv.) at room temperature in THF-d_8 after 24 hours. Full conversion to phenyl allene (still 56%) and further reaction to 1-phenyl propyne (44%) was observed. (* solvent, ^ decomposition)

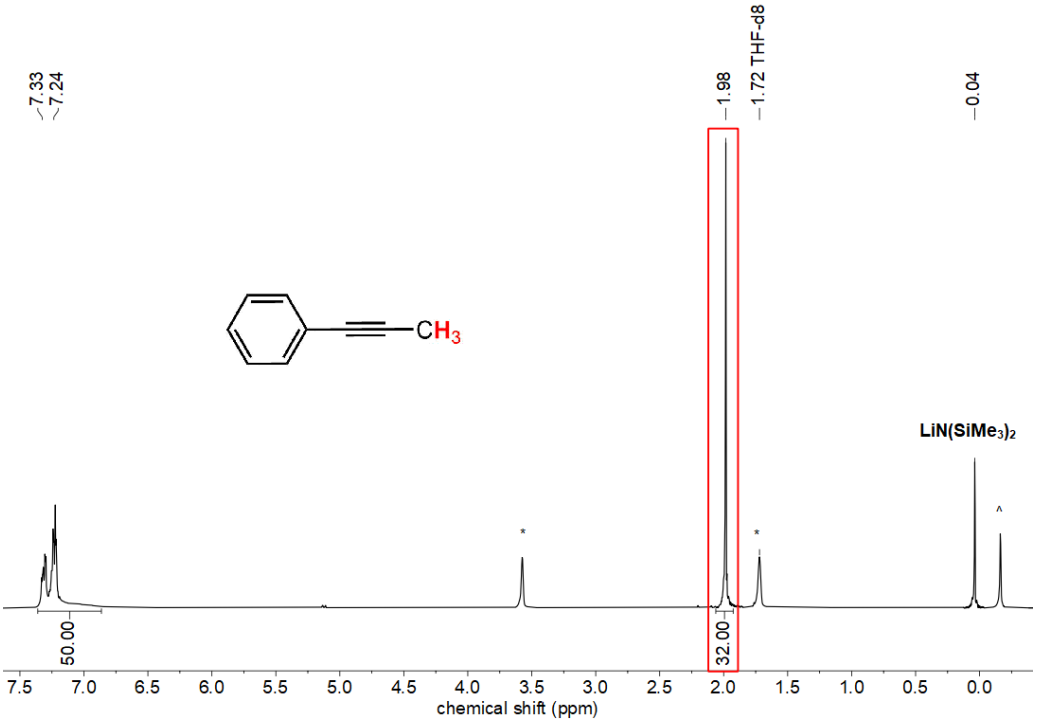

Figure S49. *In situ* ^{1}H NMR spectrum (300.1 MHz, 300 K) of reacting **F** (1.0 equiv.) with 3-phenyl propyne (10 equiv.) at room temperature in THF-d_8 after 7 days. Full conversion to 1-phenyl propyne (>99%) was observed. (* solvent, ^ decomposition)

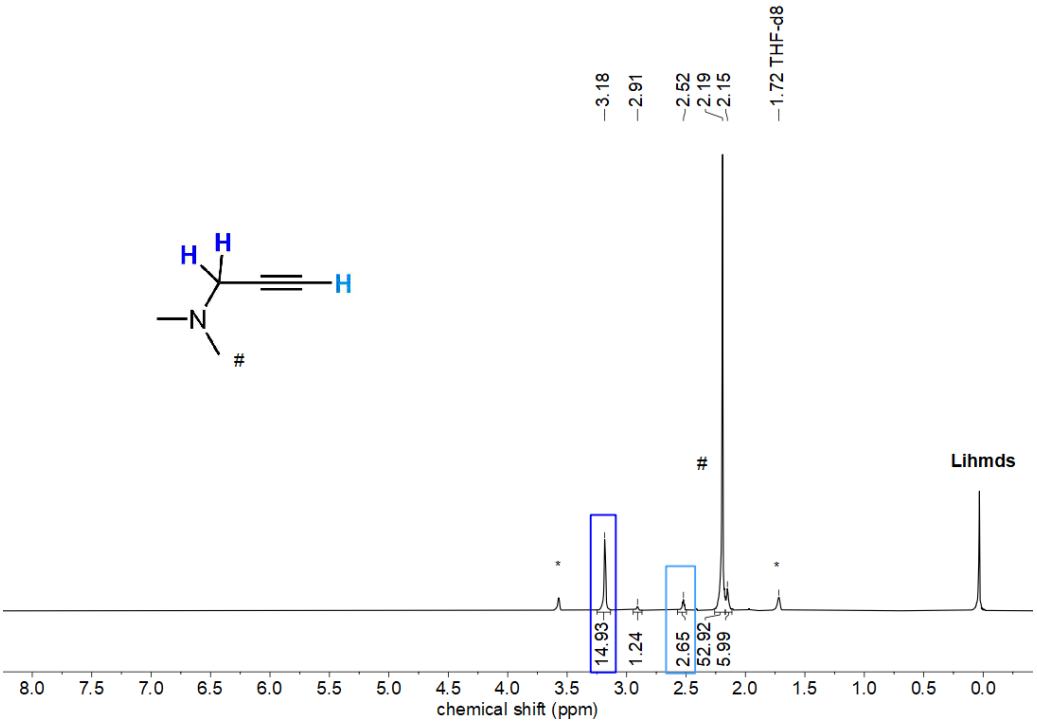

Figure S50. *In situ* ^{1}H NMR spectrum (300.1 MHz, 300 K) of reacting **F** (1.0 equiv.) with *N*,*N*-dimethylpropargylamine (10 equiv.) at room temperature in THF-d_8 after 7 days. Partial conversion (10%) was observed. (* solvent)

2 IR Spectra

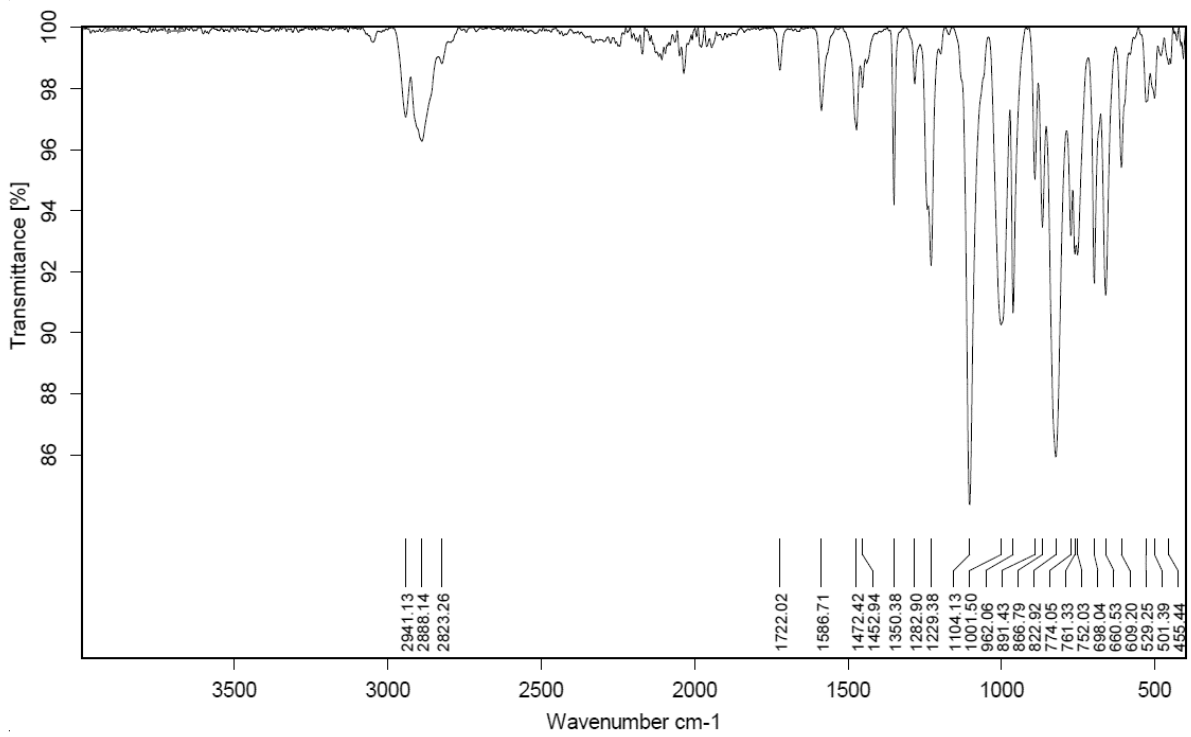

Figure S51. IR spectrum of [K{18c6}][Fe(N{SiMe$_3$}$_2$)$_2$(η^2-PhCCMe)] (**1**).

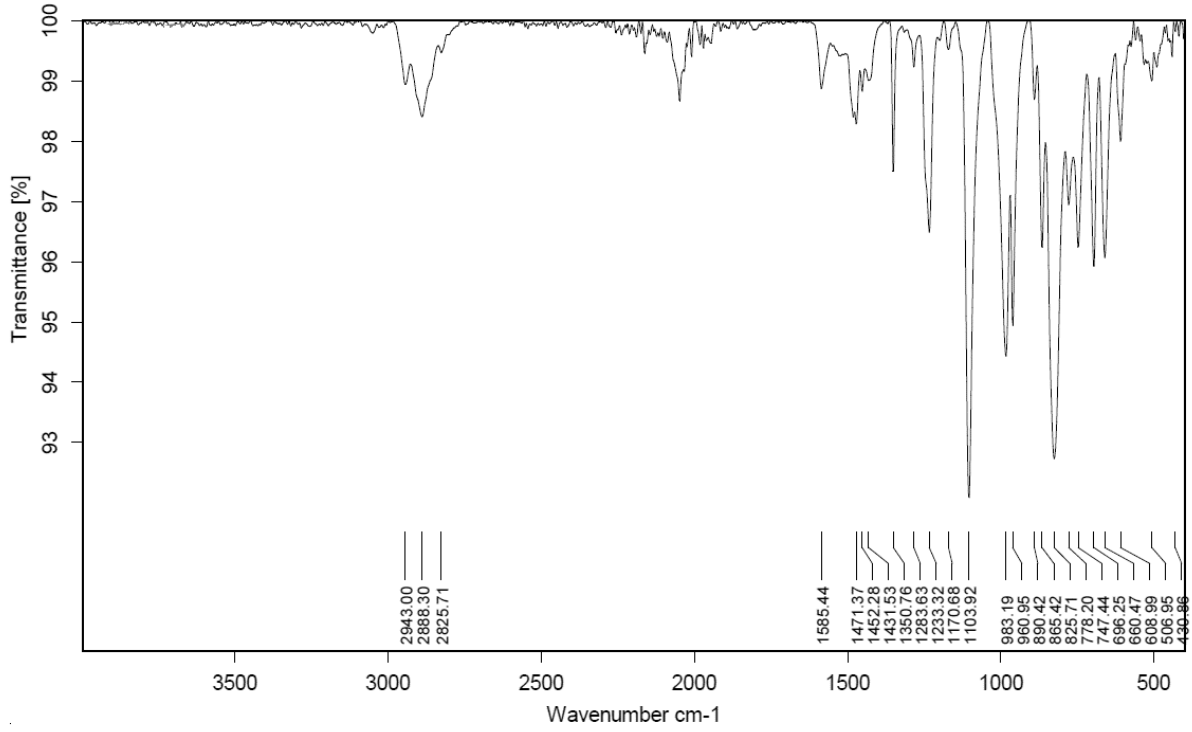

Figure S52. IR spectrum of [K{18c6}][Fe(N{SiMe$_3$}$_2$)$_2$(η^2-PhCCH)] (**2**).

3 UV/Vis Spectra

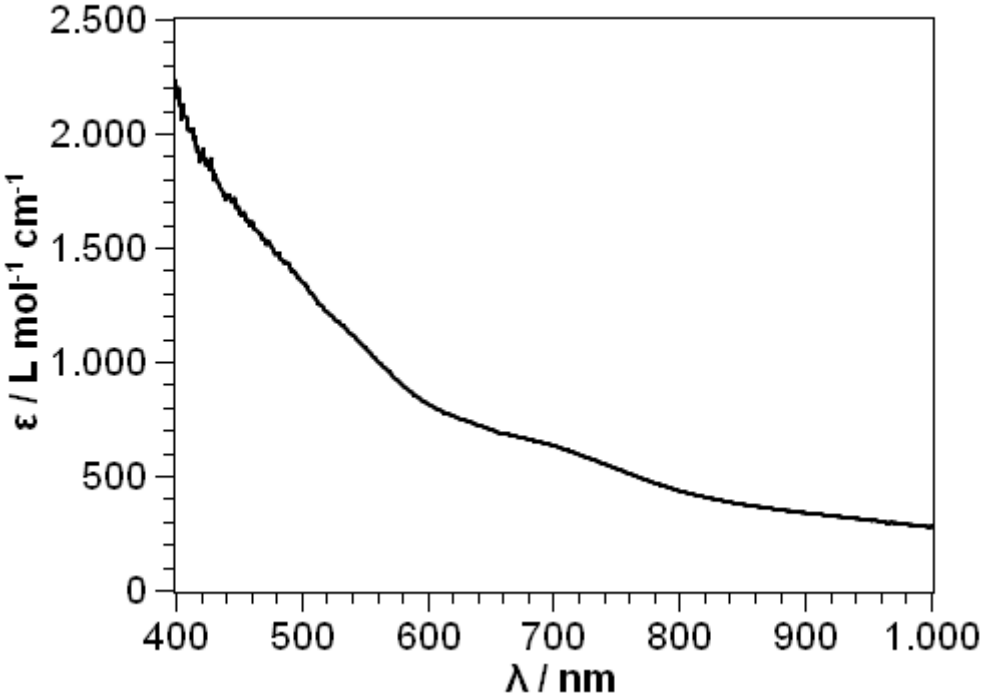

Figure S53. UV/vis spectrum of [K{18c6}][Fe(N{SiMe$_3$}$_2$)$_2$(η^2-PhCCMe)] (**1**) in Et$_2$O.

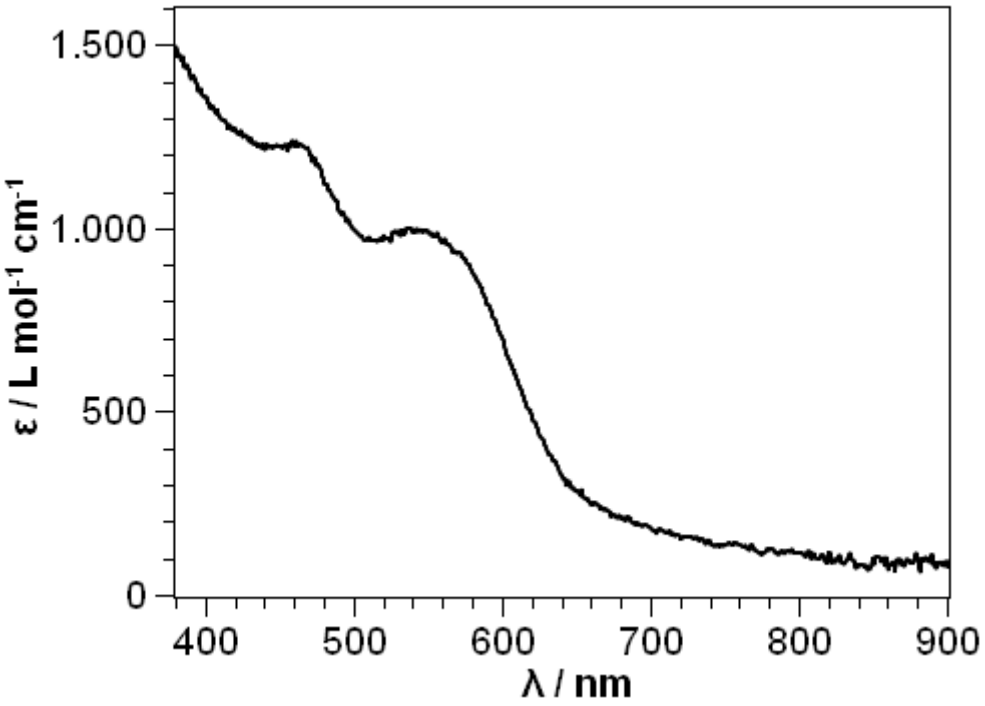

Figure S54. UV/vis spectrum of [K{18c6}][Fe(N{SiMe$_3$}$_2$)$_2$(η^2-PhCCH)] (**2**) in Et$_2$O.

4 X-Ray Diffraction Analysis and Molecular Structures

Table S1. Crystal data and structure refinement of **1**.

Empirical formula	$C_{33}H_{68}FeKN_2O_6Si_4$
Formula weight	796.20
Temperature / *K*	100.0
Crystal system	monoclinic
Space group	$P2_1/n$
a/Å	16.4150(16)
b/Å	13.2604(12)
c/Å	20.7970(19)
α/°	90
β/°	98.928(3)
γ/°	90
Volume / Å^3	4472.0(7)
Z	4
ρ_{calc} g/cm^3	1.183
μ/mm^{-1}	0.576
F(000)	1716.0
Crystal size / mm^3	0.177 × 0.164 × 0.128
Radiation	MoKα (λ = 0.71073)
2Θ range for data collection /°	4.258 to 49.994
Index ranges	−19 ≤ *h* ≤ 19, −15 ≤ *k* ≤ 15, −24 ≤ *l* ≤ 24
Reflections collected	59594
Independent reflections	7854 [R_{int} = 0.1334, R_{sigma} = 0.0742]
Data/restraints/parameters	7854/0/440
Goodness-of-fit on F^2	1.170
Final *R* indexes [I>=2σ (I)]	R_1 = 0.1010, wR_2 = 0.2118
Final *R* indexes [all data]	R_1 = 0.1331, wR_2 = 0.2213
Largest diff. peak/hole / e Å^{-3}	1.09/−0.58

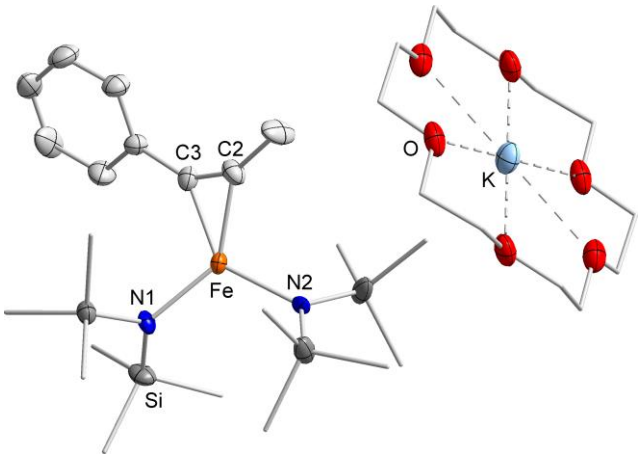

Figure S55. Molecular structure of **1**. All hydrogen atoms are omitted for clarity.

Table S2. Crystal data and structure refinement of **2**.

Empirical formula	$C_{32}H_{66}FeKN_2O_6Si_4$
Formula weight	782.17
Temperature / *K*	100.0
Crystal system	monoclinic
Space group	$P2_1/n$
a/Å	15.4733(14)
b/Å	13.1341(12)
c/Å	21.626(2)
α/°	90
β/°	94.876(3)
γ/°	90
Volume / Å^3	4379.1(7)
Z	4
ρ_{calc} g/cm^3	1.186
μ/mm^{-1}	0.587
F(000)	1684.0
Crystal size / mm^3	0.399 × 0.135 × 0.116
Radiation	MoKα (λ = 0.71073)
2Θ range for data collection /°	4.396 to 51
Index ranges	−18 ≤ *h* ≤ 18, −15 ≤ *k* ≤ 15, −26 ≤ *l* ≤ 26
Reflections collected	90751
Independent reflections	8146 [R_{int} = 0.1194, R_{sigma} = 0.0534]
Data/restraints/parameters	8146/109/687
Goodness-of-fit on F^2	1.039
Final *R* indexes [I>=2σ (I)]	R_1 = 0.0418, wR_2 = 0.0817
Final *R* indexes [all data]	R_1 = 0.0789, wR_2 = 0.0905
Largest diff. peak/hole / e Å^{-3}	0.39/−0.27

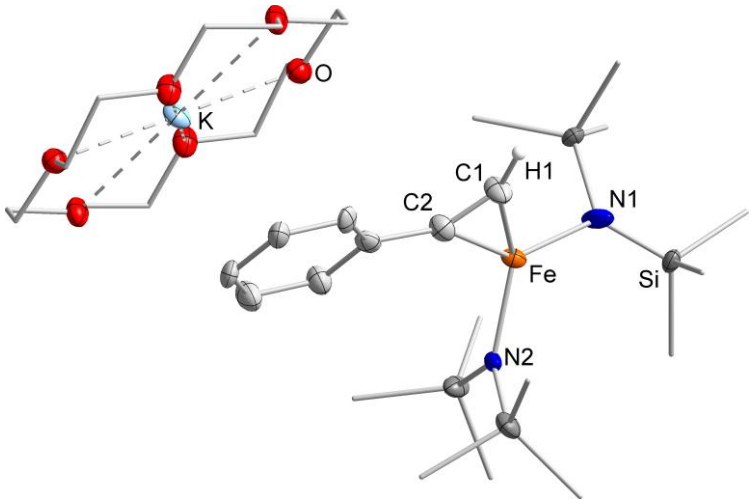

Figure S56. Molecular structure of **2**. Irrelevant hydrogen atoms are omitted for clarity. A disorder (both part 1/ part 2 (depicted): 50%) in the anion is found.

11.5 Zusatzinformationen zu Publikation 5

„Magnetic Blocking in a Conformationally Restricted Quasilinear Iron(I) Silylamide”

Ruth Weller, Mihail Atanasov, Serhiy Demeshko, Ivan Mohelsky, Milan Orlita, Franc Meyer, Frank Neese, C. Gunnar Werncke

- Manuskript in Vorbereitung -

Magnetic Blocking in a Conformationally Restricted Quasilinear Iron(I) Silylamide

Ruth Weller,[a] Mihail Atanasov,[b] Serhiy Demeshko,[c] Ivan Mohelsky,[d] Milan Orlita,[d] Franc Meyer,[c] Frank Neese,[b] C. Gunnar Werncke[a]

[a] M. Sc. R. Weller, Dr. C. G. Werncke Title(s)
Department of Chemistry
Philipps-University Marburg
Hans-Meerwein-Straße 4, 35043 Marburg, Germany
E-mail: gunnar.werncke@chemie.uni-marburg.de

[b] Dr. S. Demeshko, Prof. Dr. F. Meyer
Institut für Anorganische Chemie
Universität Göttingen
Tammannstr. 4, D-37077 Göttingen, Germany

[c] Prof. D. M. Atanasov, Prof. Dr. F. Neese
Max-Planck-Institut für Kohlenforschung
Kaiser-Wilhelm-Platz 1, 45470 Mülheim an der Ruhr, Germany

[b] I. Mohelsky, Dr. M. Orlita
LAB National des Champs Magnétiques Intenses
LNCMI - CNRS
25 Martyrs Avenue, BP 166, 38042 Grenoble Cedex 9, France

Table of Content

1 Experimentals

Materials and Methods

All manipulations were carried out in a glovebox under a dry argon atmosphere, unless indicated otherwise. Used solvents were dried by continuous distillation over sodium metal for several days. Deuterated solvents were used as received, degassed *via* three freeze-pump cycles and stored over molecular sieves 4 Å. The ^{1}H NMR spectra were recorded on a Bruker AV 500, a Bruker HD 500 or a Bruker HD 300 NMR spectrometer (Bruker Corporation, Billerica, USA). Chemical shifts are reported in ppm relative to the residual proton signals of the solvent (for ^{1}H). $w_{1/2}$ is the line width of a signal at half its maximum intensity. Integrals of the broad signals ligand set were obtained directly or by peak fitting (in case of overlapping signals) using the MestreNova software package (Mestrelab, Santiago de Compostela, Spain). Elemental analysis were performed by the "in-house" service of the Chemistry Department of the Philipps University Marburg, Germany using a CHN(S) analyser vario MICRO Cube (Elementar Analysensysteme GmbH, Langenselbold, Germany). [Fe(N(Dipp)SiMe$_3$)$_2$][1] was prepared according to literature procedures.

[KFe(N(Dipp)SiMe$_3$)$_2$] (1)

One equivalent of [Fe(N(Dipp)SiMe$_3$)$_2$] (200 mg, 0.36 mmol) was dissolved in 5 mL toluene. After adding KC_8 (0.40 mmol, 1.1 equiv.) the reaction mixture was stirred for several minutes at room temperature, while a change in colour to red was observed. The graphite was filtered off and all volatiles were evaporated off. Successful synthesis was revealed by ^{1}H NMR spectroscopy and combustion analysis that matches to polymeric form of **1**.[2] Crystals, suitable for x-ray diffraction analysis, were obtained from a saturated solution of **1** in toluene at −40 °C. **Yield:** 187 mg (0.32 mmol, 88%). **IR** (ATR, cm^{-1}): $\tilde{\nu}$ = 3051 (w), 2948 (m), 2885 (w), 2864 (m), 1576 (w), 1458 (m), 1417 (s), 1378 (m), 1357 (m), 1316 (m), 1238 (s), 1197 (m), 1155 (w), 1141 (w), 1101 (m), 1052 (m), 1040 (m), 936 (m), 915 (s), 878 (m), 827 (vs), 787 (s), 746 (m), 671 (m), 627 (m), 579 (w), 535 (m), 422 (m).

2 X-Ray Diffraction Analysis and Molecular Structure

Data for compound [KFe(N(Dipp)SiMe$_3$)$_2$] (**1**) (CCDC 2113327) were collected on a STOE IPDS2 diffractometer (STOE & Cie GmbH, Darmstadt, Germany) using a graphite-monochromated Mo-Kα radiation (λ = 0.71073 Å) and equipped with an Oxford Instrument Cooler Device (Oxford Instruments, Abingdon, UK). The structure has been solved using either OLEX SHELXT V2014/1[3] and refined by means of least-squares procedures on an F^2 with the aid of the program SHELXL-2016/6[4] included in the software package WinGX version 1.63[5] or using CRYSTALS[6]. The atomic scattering factors were taken from International Tables for X-ray Crystallography.[7] All non-hydrogen atoms were refined anisotropically. All hydrogen atoms were refined by using a riding model. Disorders were found in the trimethylsilyl moiety and modelled accordingly. The absorption correction was introduced by using the MULTISCAN and X-Red programs.[8,9] The drawing of the molecule is performed with the program DIAMOND (Crystal Impact, Bonn, Germany) with 50% probability displacement ellipsoids for non-H atoms.

Table S1. Crystal data and structure refinement of **1**

Empirical formula	$C_{30}H_{52}FeKN_2Si_2$
Formula weight	591.86
Temperature/K	293(2)
Crystal system	orthorhombic
Space group	Pccn
a/Å	13.4245(19)
b/Å	13.3935(17)
c/Å	18.137(3)
α/°	90
β/°	90
γ/°	90
Volume/Å^3	3261.1(8)
Z	4
ρ_{calc}g/cm^3	1.206
μ/mm^{-1}	0.684
F(000)	1276.0
Crystal size/mm^3	0.514 × 0.418 × 0.178
Radiation	Mo Kα (λ = 0.71073)
2Θ range for data collection/°	5.422 to 53.914
Index ranges	–17 ≤ h ≤ 17, –16 ≤ k ≤ 16, –22 ≤ l ≤ 22
Reflections collected	21899
Independent reflections	3478 [R_{int} = 0.0624, R_{sigma} = 0.0556]
Data/restraints/parameters	3478/6/195
Goodness-of-fit on F^2	0.993
Final *R* indexes [*I*>=2σ (*I*)]	R_1 = 0.0420, wR_2 = 0.1032
Final *R* indexes [all data]	R_1 = 0.0761, wR_2 = 0.1168
Largest diff. peak/hole / e Å^{-3}	0.54/–0.31

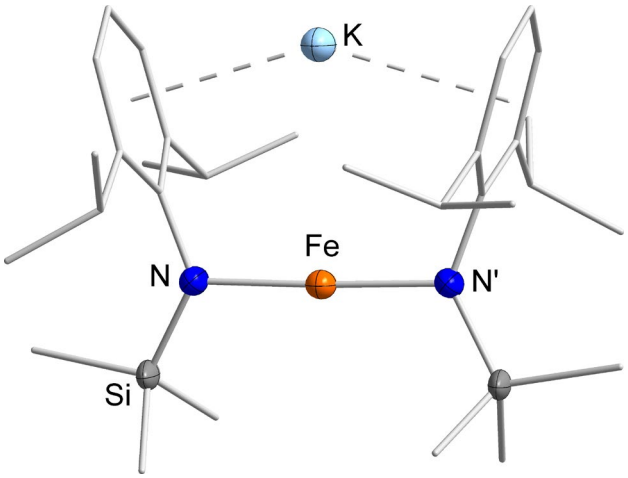

Figure S1. Molecular structure of the mononuclear complex **1**. All hydrogen atoms and a disorder in the trimethylsilyl group are omitted for clarity. The structure was refined as a rotation twin.

3 Mößbauer Measurement

The Mössbauer spectrum was recorded with a ^{57}Co source in a Rh matrix using an alternating constant acceleration *Wissel* Mössbauer spectrometer operated in the transmission mode and equipped with a *Janis* closed-cycle helium cryostat. Isomer shifts are given relative to iron metal at ambient temperature. Simulation of the experimental data was performed with the *MF* program using *Lorentzian* line sextets: E. Bill, Max-Planck Institute for Chemical Energy Conversion, Mülheim/Ruhr, Germany.

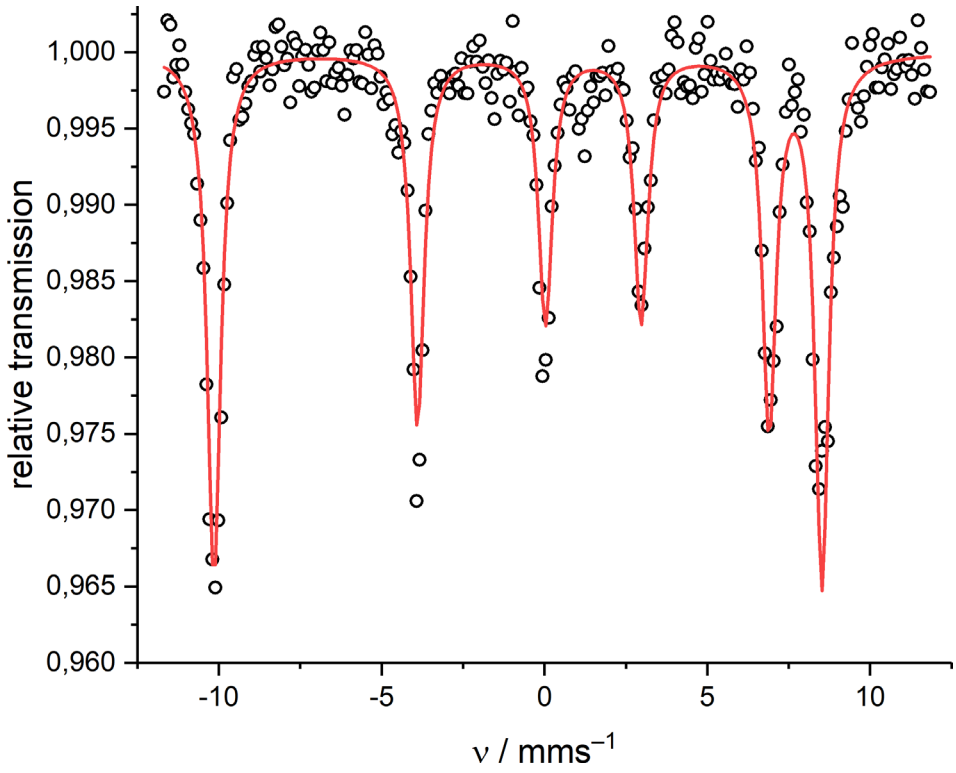

Figure S2. Zero field ^{57}Fe Mössbauer spectrum of solid **1** at 7 K. The red line represents a fit with δ = 0.34 mm/s, ΔE_Q = −2.31 mm/s, H_{int} = 58 T.

4 Magnetic Measurements

Temperature-dependent magnetic susceptibility measurements were carried out with a *Quantum-Design* MPMS3 SQUID magnetometer equipped with a 7 Tesla magnet in the range from 2 to 210 K in a magnetic field of 0.5 T. The polycrystalline sample was contained in a polycarbonate capsule, covered with a few drops of low viscosity perfluoropolyether based inert oil Fomblin Y45 to fix the crystals, and fixed in a non-magnetic sample holder. The maximum measuring temperature of 210 K was chosen because of the pour point of the oil, in order to keep the oil in the frozen state and to avoid therefore the orientation of the crystals parallel to the magnetic field. Each raw data file for the measured magnetic moment was corrected for the diamagnetic contribution of the capsule and of the inert oil according to $M^{dia} = \chi_g \cdot m \cdot H$, with experimentally obtained gram susceptibility of the capsule ($\chi_g = -5.60 \cdot 10^{-7}$ emu/(g·Oe) and of the oil ($\chi_g = -3.82 \cdot 10^{-7}$ emu/(g·Oe)). The molar susceptibility data were corrected for the diamagnetic contribution according to χ_M^{dia}(sample) = $-0.5 \cdot M\ 10^{-6}$ cm^3 mol^{-1}.[10]

Experimental $\chi_M T$ vs. T data were modelled using a fitting procedure to the following spin Hamiltonian for one iron(I) $S = 3/2$ ion with Zeeman splitting and zero-field splitting:

$$\hat{H} = \mu_B \vec{B} \boldsymbol{g} \vec{S} + D[\hat{S}_z^2 - \frac{1}{3}S(S+1) + {}^{E}/_{D}\,(\hat{S}_x^2 - \hat{S}_y^2)] \quad \text{(eq. 1)}$$

Full-matrix diagonalization of the spin Hamiltonian was performed with the *julX_2s* program (E. Bill, Max-Planck Institute for Chemical Energy Conversion, Mülheim/Ruhr, Germany, **2014**). Matrix diagonalization is done with the routine ZHEEV from the LAPACK numerical package. Parameter optimization is performed with the simplex routine AMOEBA from NUMERICAL RECIPES.

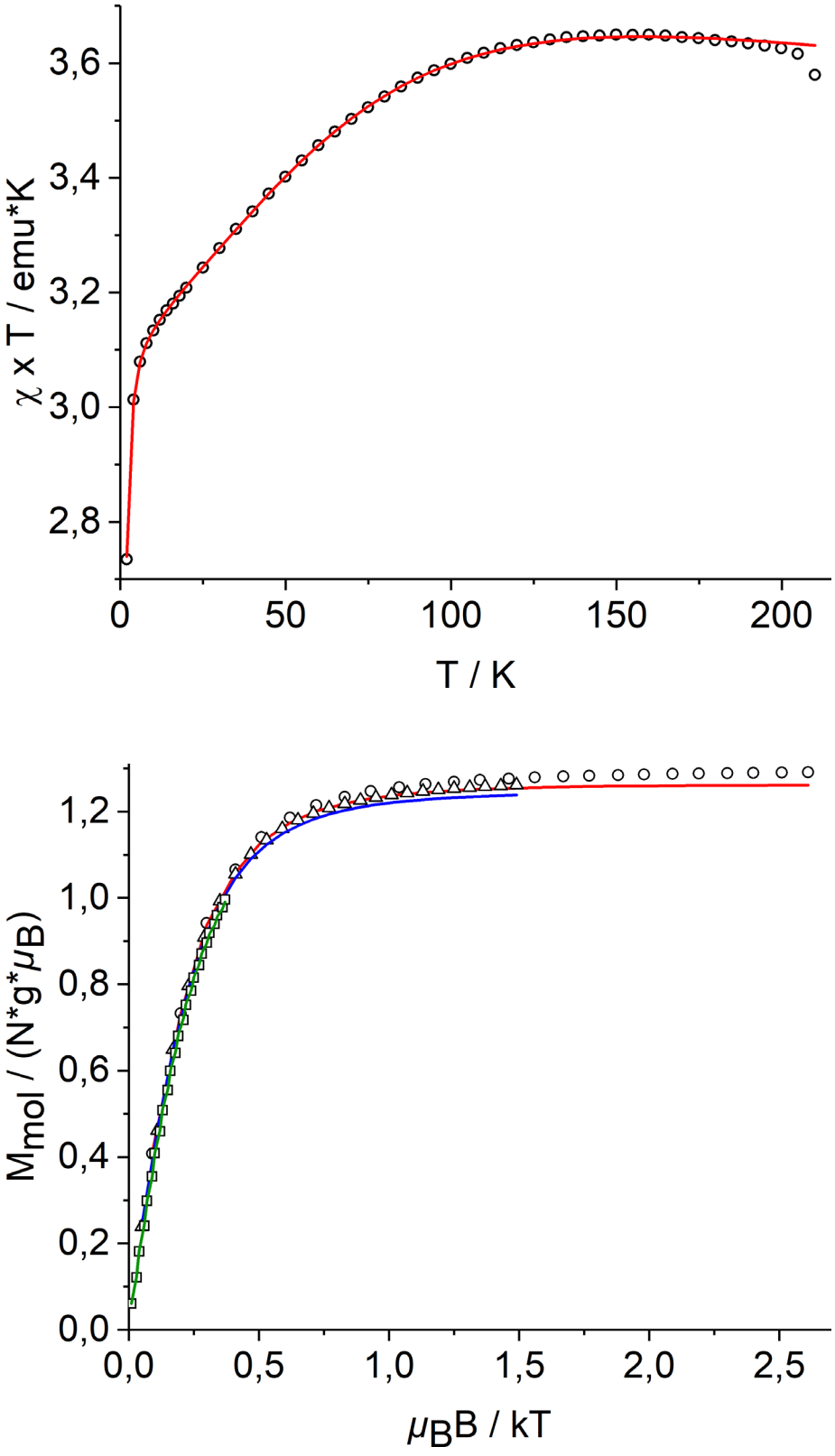

Figure S3. Temperature dependence of $\chi_M T$ at 5000 Oe (top) and VTVH magnetisation measurements at 1, 4 and 7 T (bottom). The best fit values are g_x = 2.27, g_y = 2.27, g_z = 3.31 and D = –104 cm^{-1} (E/D = 0).

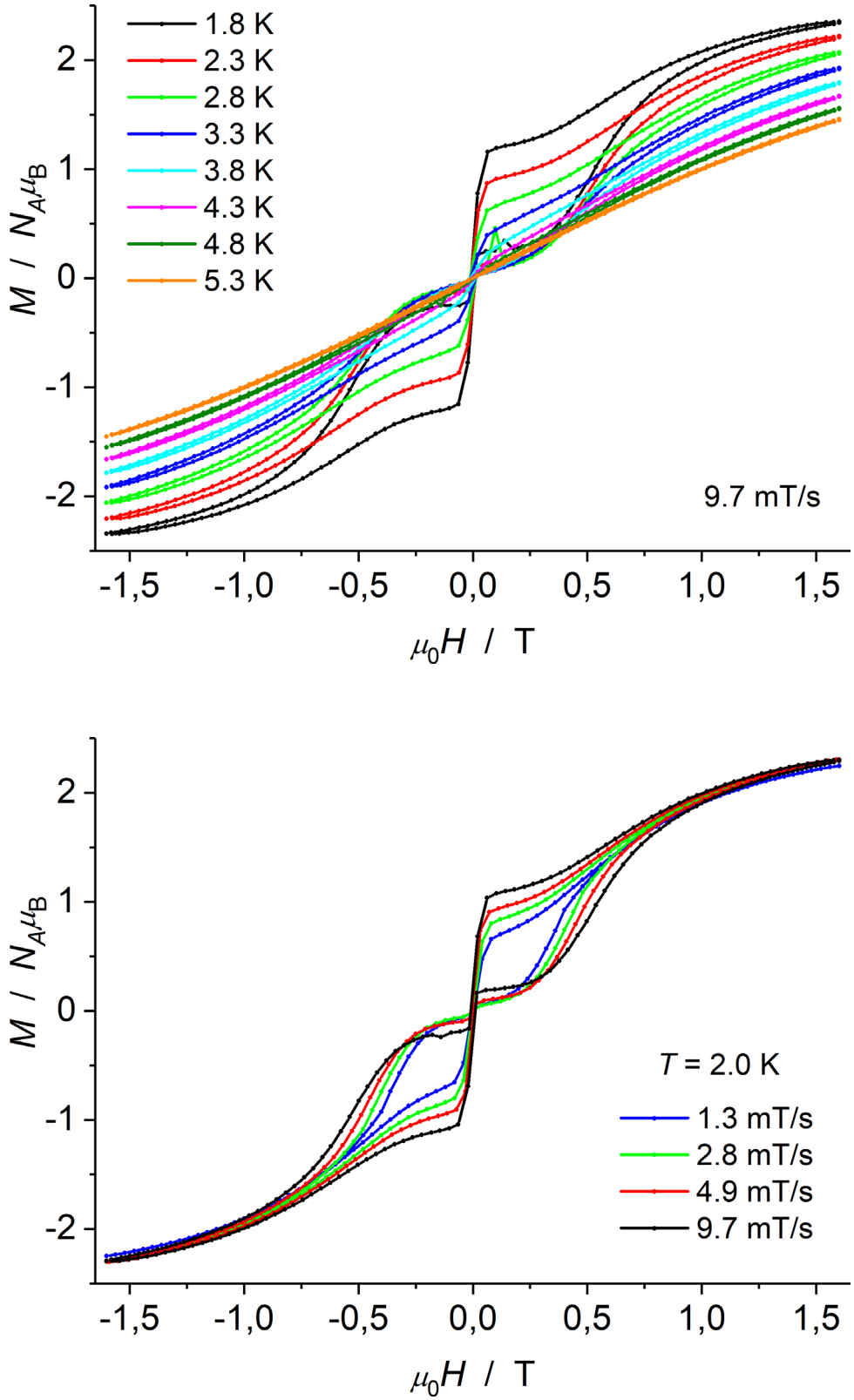

Figure S4. Magnetic hysteresis loop over the temperature range 1.8 to 5.3 K (top) and for various field sweep rates at 2.0 K (bottom).

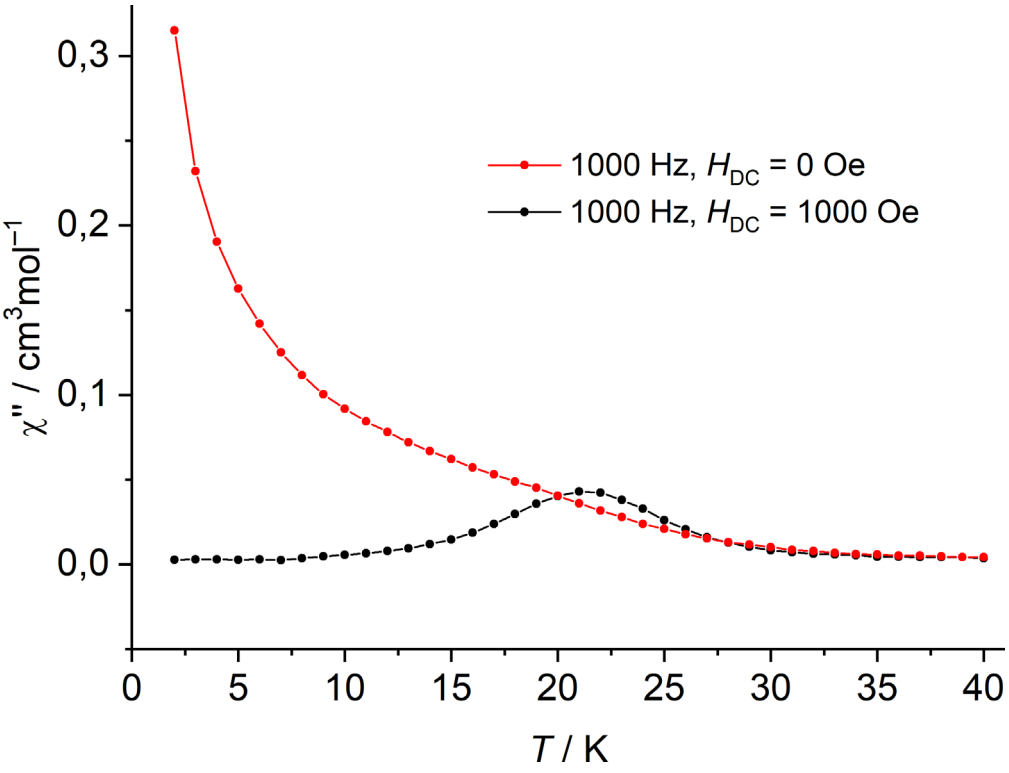

Figure S5. Temperature dependence of χ'' at 1000 Hz in the absence of a dc field an in the applied field of 1000 Oe.

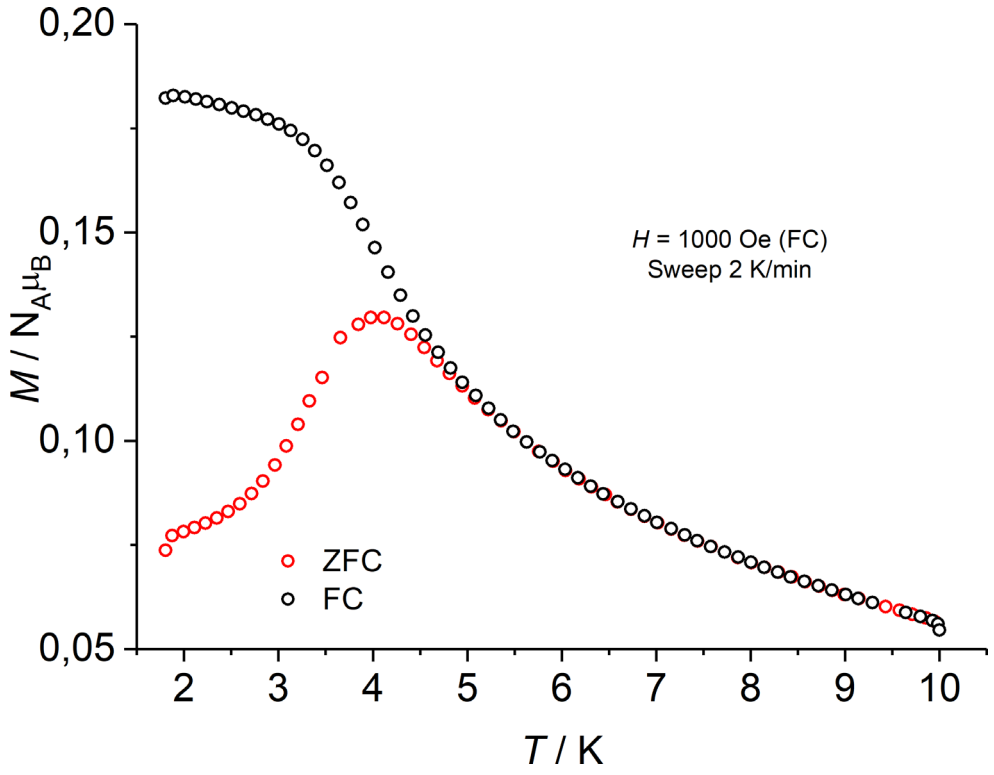

Figure S6. Zero-field-cooled/field-cooled (ZFC/FC) magnetisation measurements.

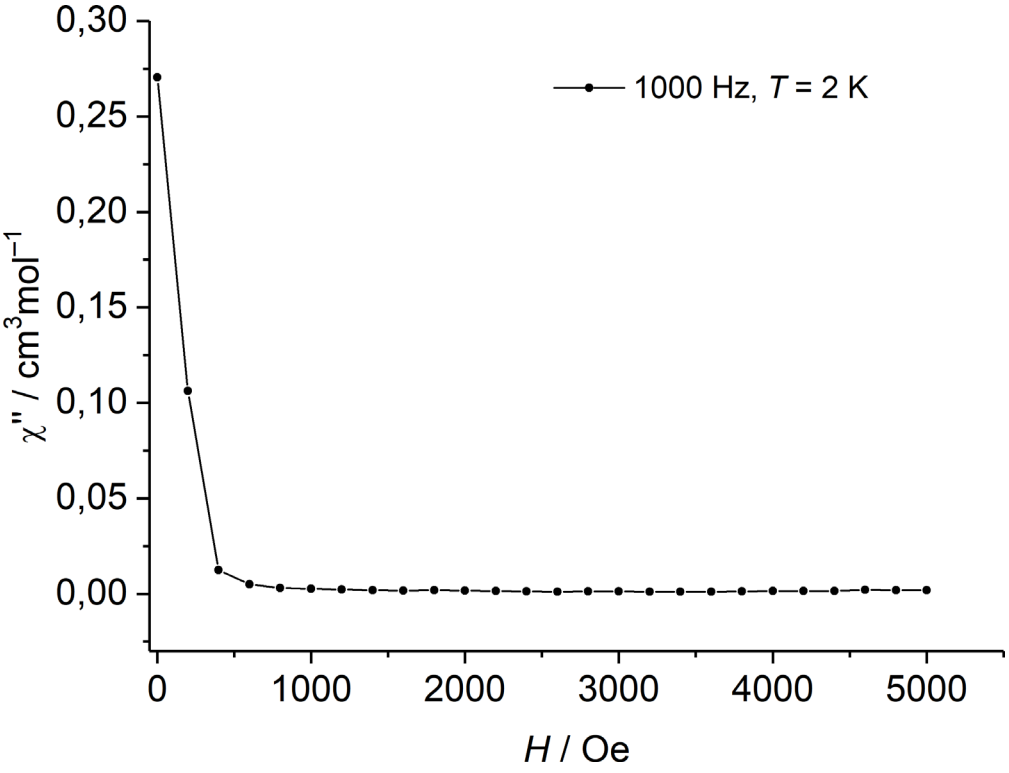

Figure S6. Field dependence of χ'' at 2 K using 1000 Hz ac frequency.

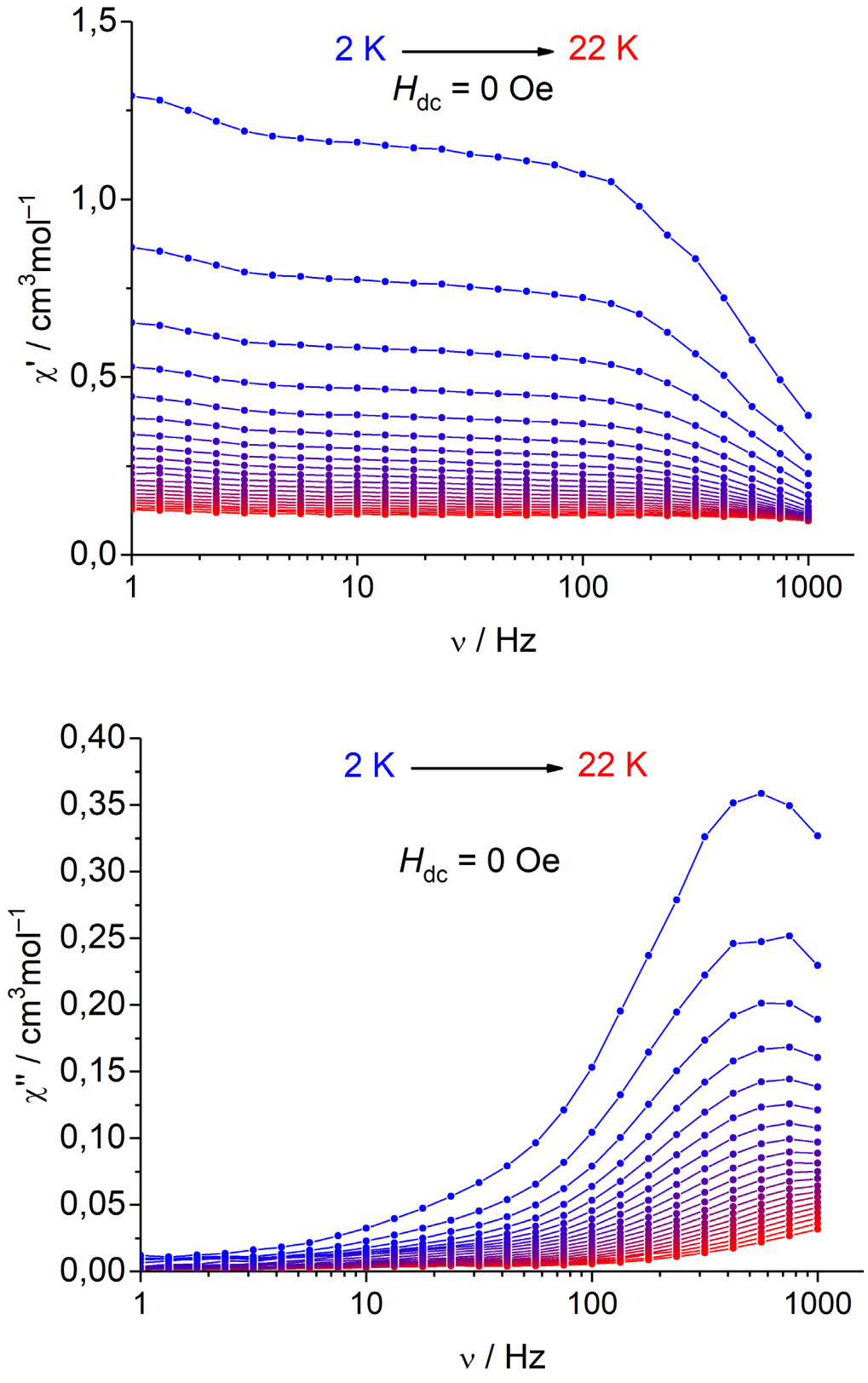

Figure S7. Frequency dependence of χ' (top) and χ'' (bottom) at various temperatures in the absence of a dc field. The measurements were done between 2 and 22 K with steps of 1 K.

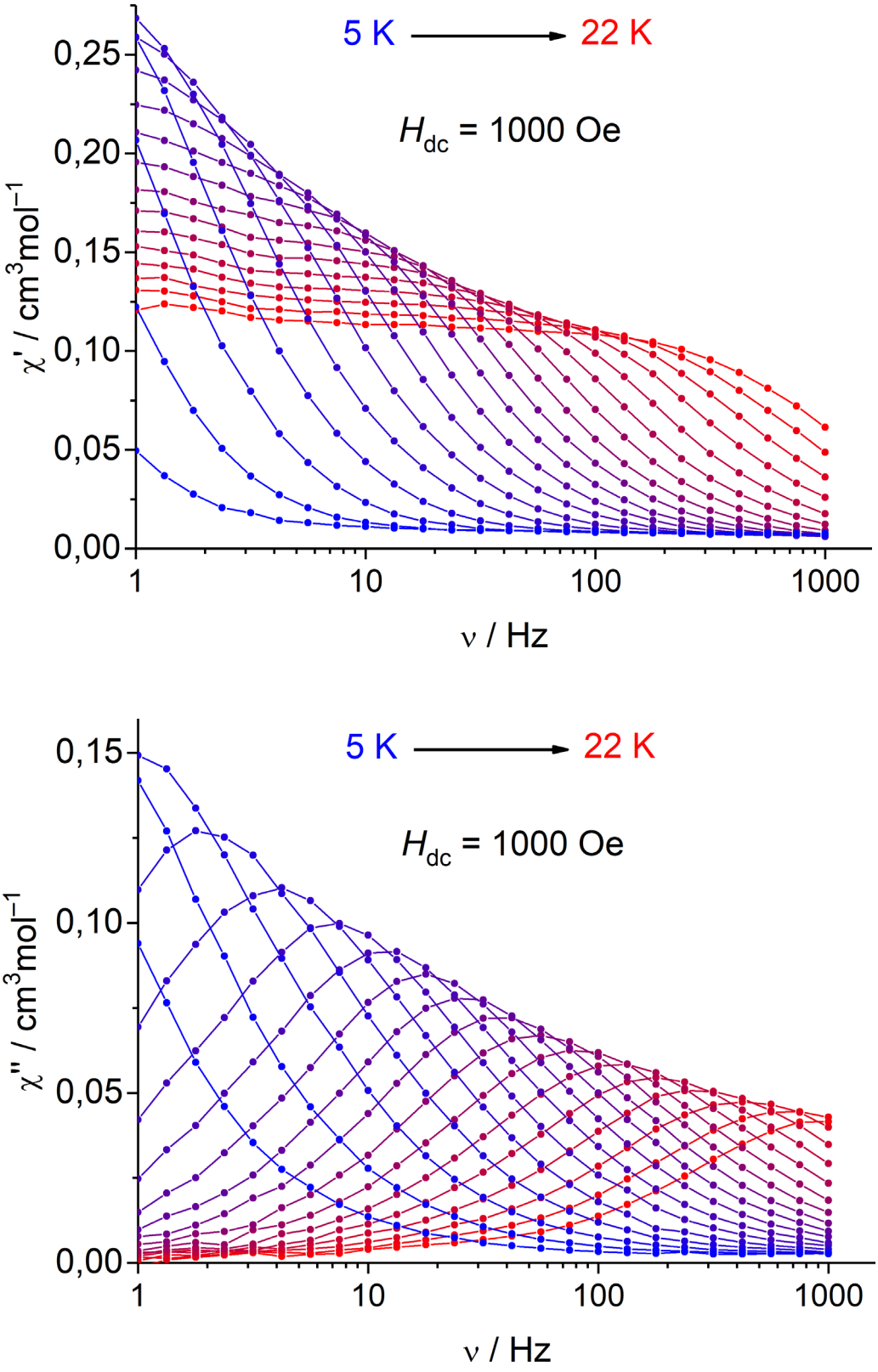

Figure S8. Frequency dependence of χ' (top) and χ'' (bottom) at various temperatures with an applied dc field of H_{dc} = 1000 Oe. The measurements were done between 5 and 22 K with steps of 1 K.

Frequency dependent ac magnetic susceptibility measurements of **1** at various temperatures (**Figure S8**) were performed to determine the relaxation barrier U_{eff}. For this reason, the resulting χ' and χ'' values were used for constructing the Cole−Cole diagrams (**Figure S9**) and simultaneously fitted using the CC-Fit program.[11]

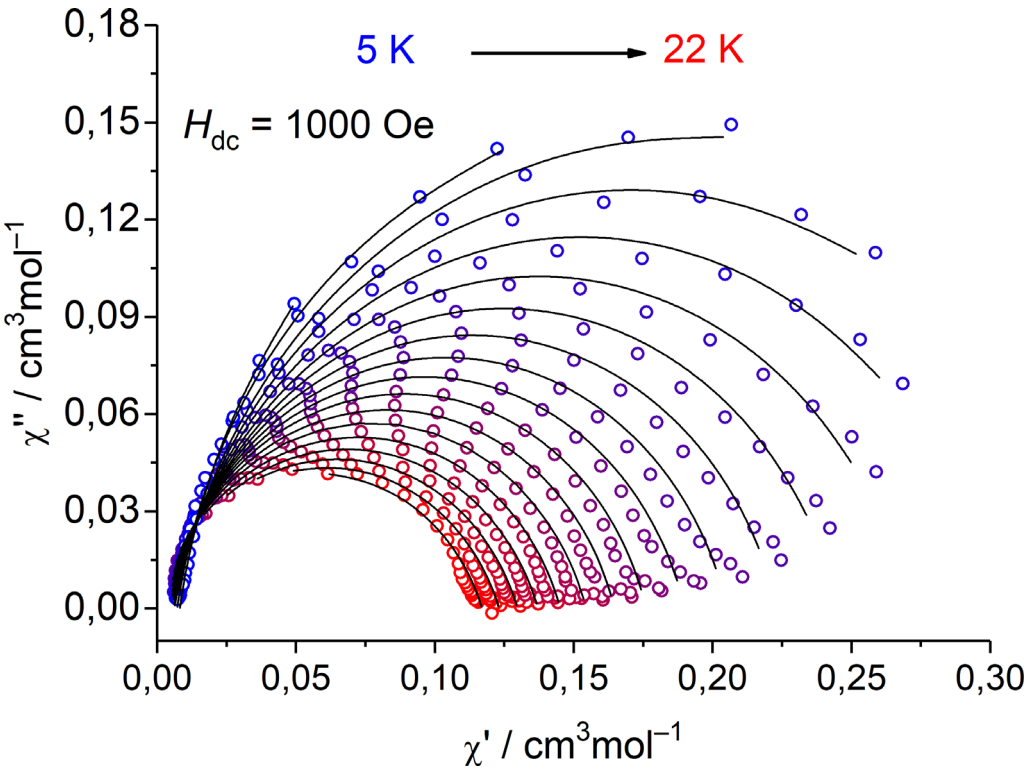

Figure S9. Cole–Cole diagrams of ac measurements with an applied dc field of H_{dc} = 1000 Oe between 5 and 22 K with steps of 1 K; the black solid lines represent the fit curves.

Temperature dependence of the obtained relaxation times τ is depictured in **Figure S10**.

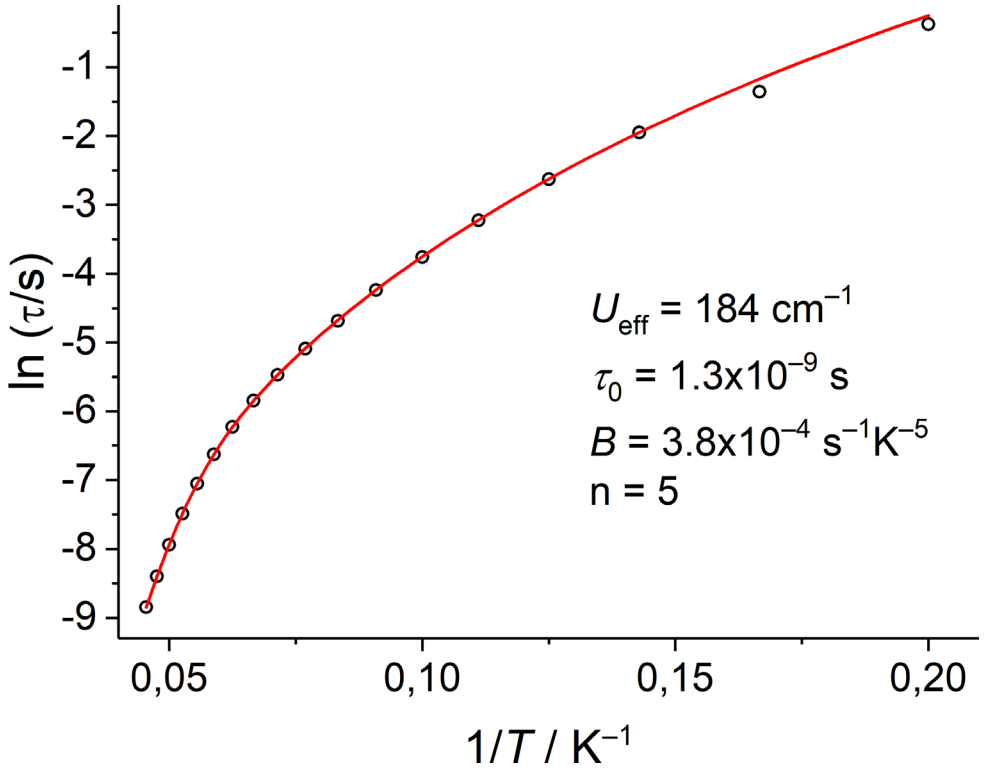

Figure S10. Arrhenius plot of the temperature dependence of τ at H_{dc} = 1000 Oe.

The obtained points are clearly deviated from the linear Arrhenius law, so, additional relaxation processes have to be considered. In general, the temperature dependence of the relaxation times can be described with three different types of relaxation: direct, Raman, Orbach processes and quantum tunneling of the magnetization (QTM).[12] In the case of **1**, whole temperature range can be well fitted assuming Raman and Orbach relaxation processes (eq. 2).

$$\tau^{-1} = BT^n + \tau_0^{-1} exp\left(-U_{eff}/k_B T\right) \qquad \text{(eq. 2)}$$

The obtained best fit parameters are B = 3.8·10^{-4} s^{-1}·K^{-5}, n = 5, U_{eff} = 184 cm^{-1} and τ_0 = 1.3·10^{-9} s.

5 Raman Spectroscopy

The Raman spectra were measured with a Monovista CRS+ confocal Raman microscope of the company 'Spectroscopy & Imaging GmbH'. A 532 nm solid-state laser and a 300 grooves nm^{-1} (low resolution mode, FWHM: < 4.62 cm^{-1}) grating was used. The sample was transferred into a dried and melted off glass capillary prior to the measurement.

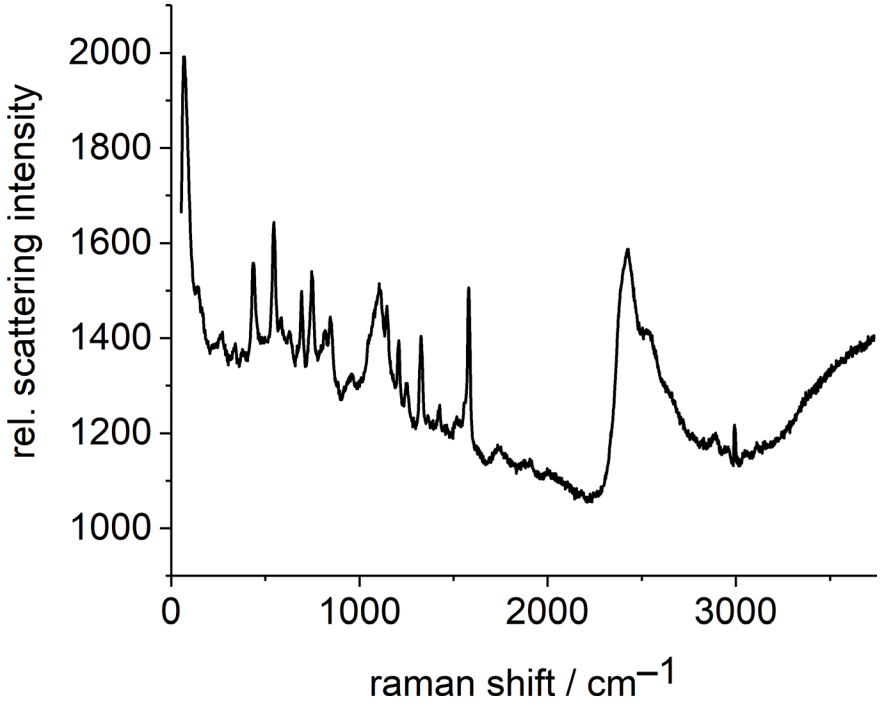

Figure S11. Raman spectrum of crystalline **1**.

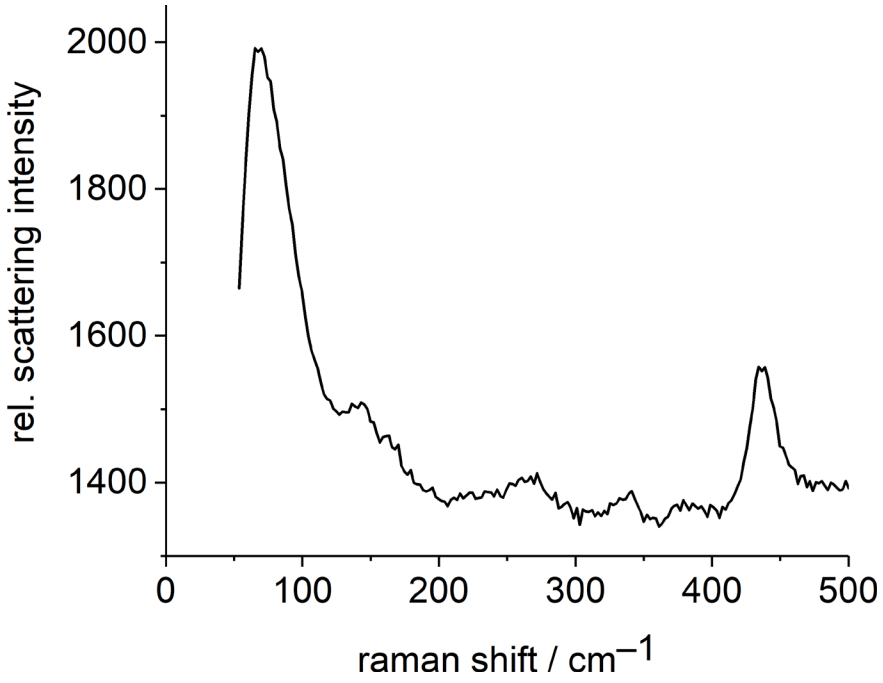

Figure S12. Zoom in of Raman spectrum of crystalline **1** from 50 cm^{-1} to 500 cm^{-1}.

6 IR Spectroscopy

6.1 ATR-IR spectroscopy

The IR measurement was conducted on a Bruker Alpha ATR-IR spectrometer (Bruker Corporation, Billerica, USA).

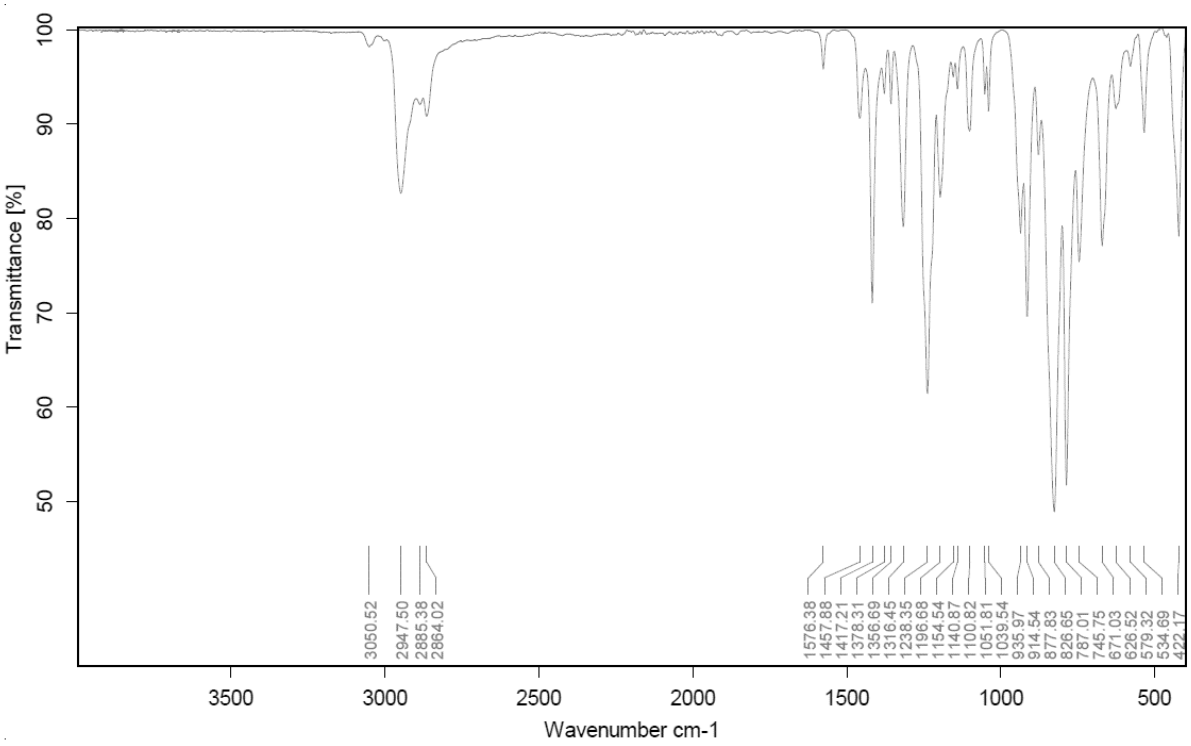

Figure S13. ATR-IR spectrum of **1**.

6.2 Magneto-IR Spectroscopy

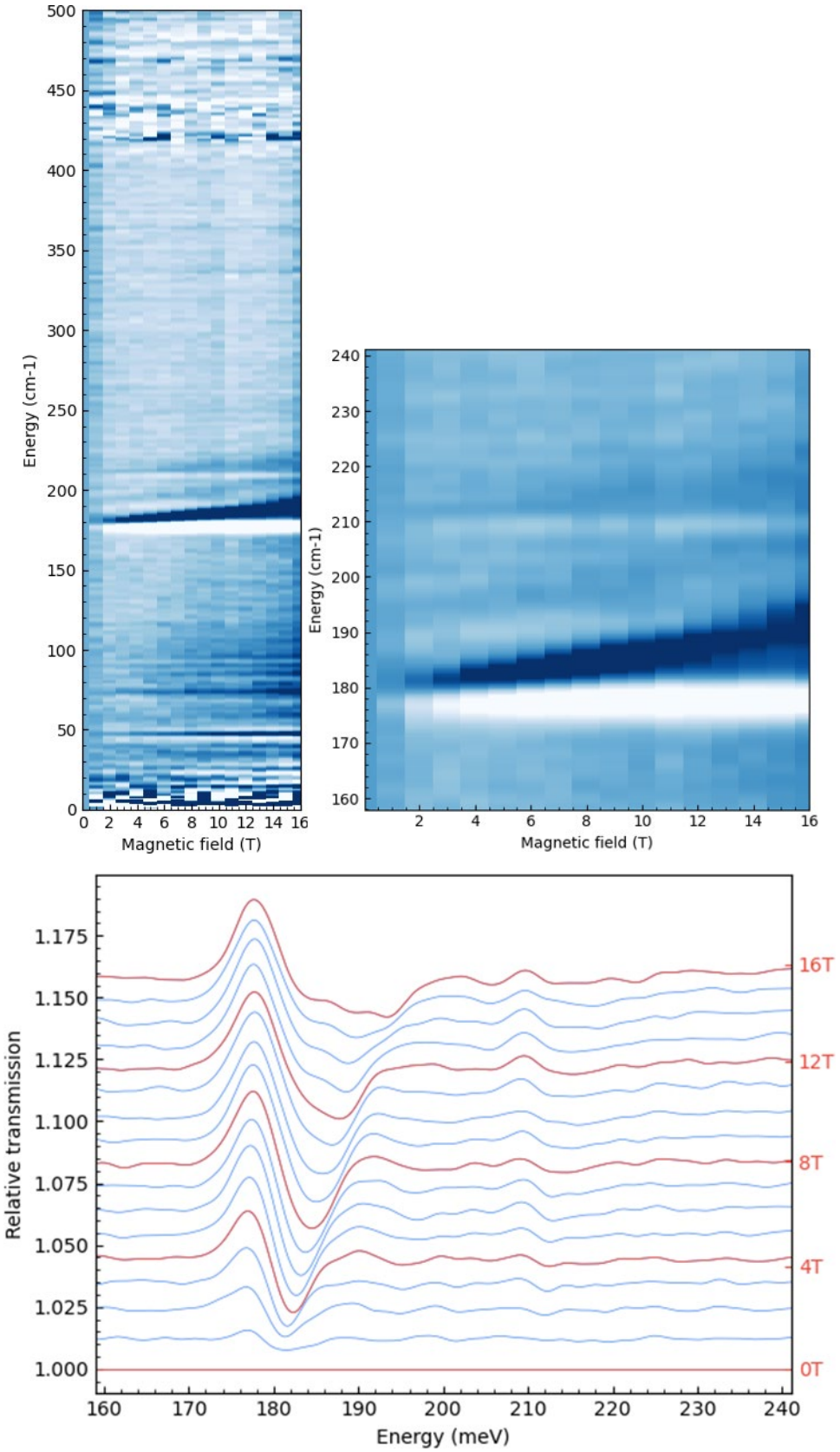

Figure S14. Top: Far-IR region of complex **1** under an applied field of 0 − 16 T at 4 K (left) and a zoom in to energies from 160 − 240 cm^{-1} (right). Bottom: Different Spectra given in relation to the zero field spectrum.

8 Computational Details

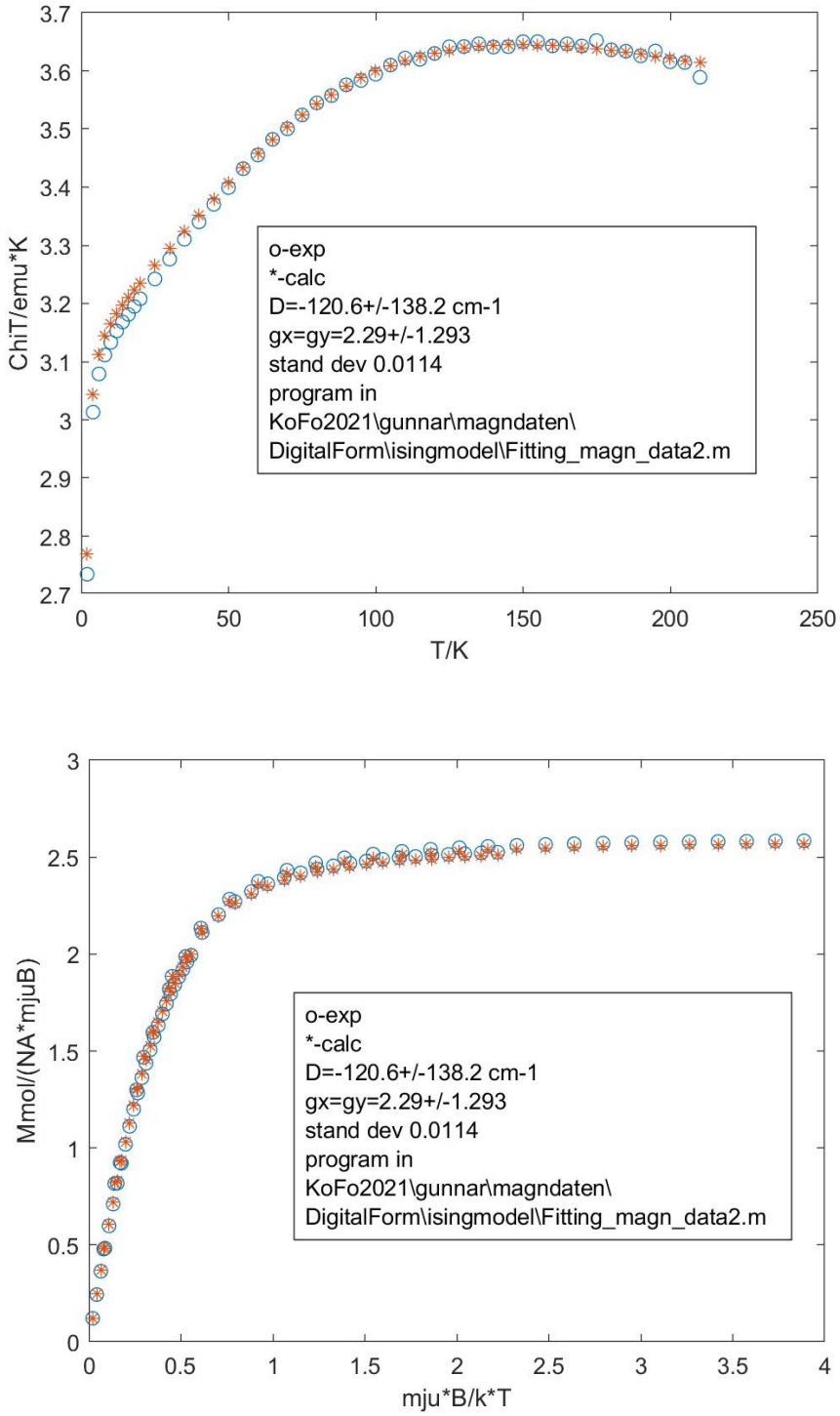

Figure S15. Calculated temperature dependence of $\chi_M T$ (top) and VTVH magnetisation measurements at 1, 4 and 7 T (bottom) of **1**.

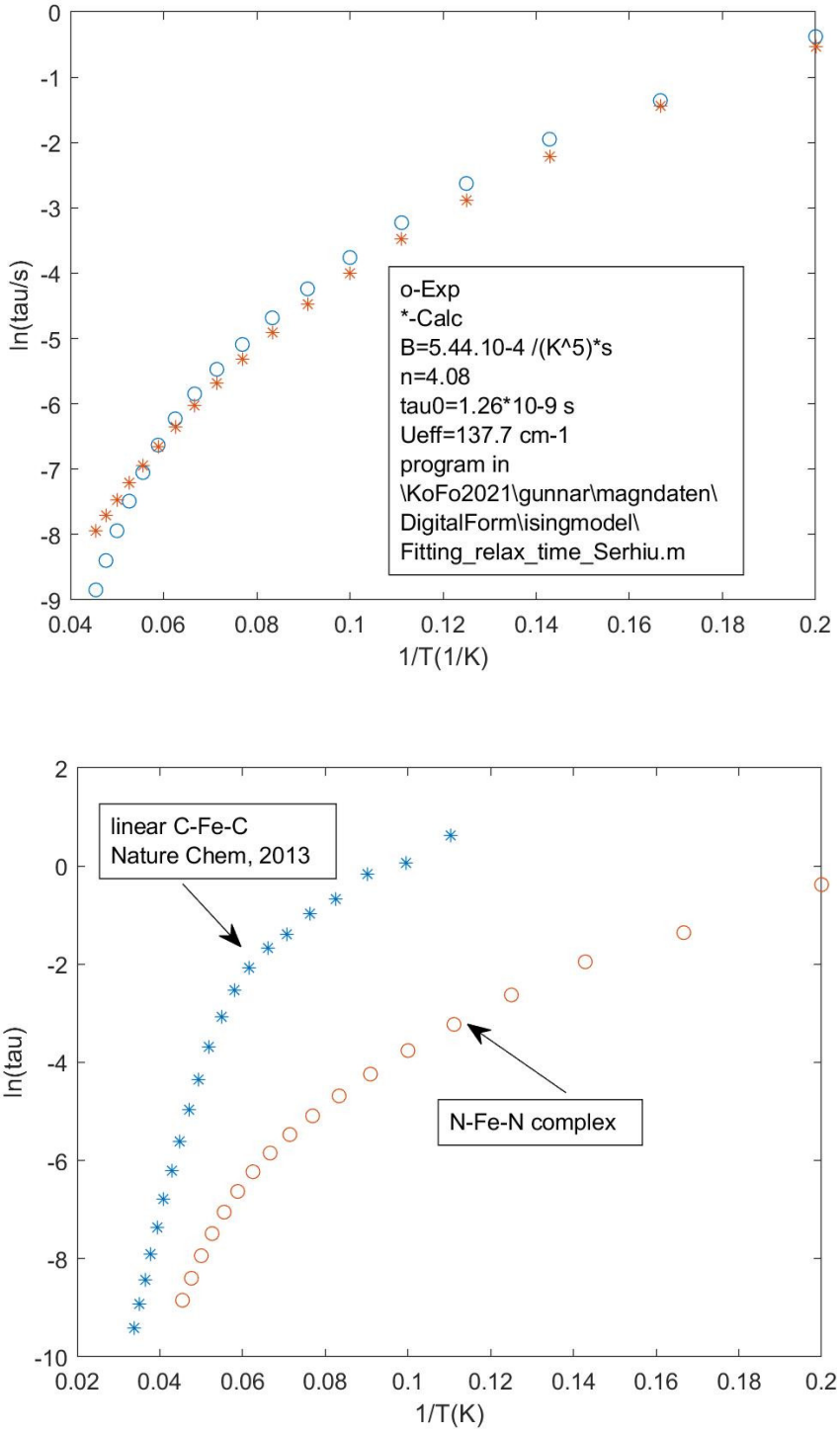

Figure S16. Calculated arrhenius plots of **1**.

References

[1] Lin, C.-Y.; Guo, J.-D.; Fettinger, J. C.; Nagase, S.; Grandjean, F.; Long, G. J.; Chilton, N. F.; Power, P. P. *Inorg. Chem.* **2013**, *52*, 13584–13593.

[2] Weller, R.; Müller, I.; Duhayon, C.; Sabo-Etienne, S.; Bontemps, S.; Werncke, C. G. *Dalton Trans.* **2021**, *50*, 4890–4903.

[3] Dolomanov, O. V.; Bourhis, L. J.; Gildea, R. J.; Howard, J.; Puschmann, H. *J. Appl. Crystallogr.* **2009**, *42*, 339–341.

[4] Sheldrick, G. M. *Acta. Crystallogr. C* **2015**, *71*, 3–8.

[5] Farrugia, L. J. *J. Appl. Crystallogr.* **1999**, *32*, 837–838.

[6] Betteridge, P. W.; Carruthers, J. R.; Cooper, R. I.; Prout, K.; Watkin, D. J. *J. Appl. Crystallogr.* **2003**, *36*, 1487.

[7] *International tables for crystallography*, 1st online ed.; International Union of Crystallography; Springer: Chester, England, New York, 2006.

[8] SADABS-2016/2. *Bruker*, 2016.

[9] X-Area, X.-R. 1. *STOE*, 2016.

[10] Kahn, O. *Molecular magnetism*; VCH: New York, NY, 1993.

[11] Reta, D.; Chilton, N. F. *Phys. Chem. Chem. Phys.* **2019**, *21*, 23567–23575.

[12] Carlin, R. L. *Magnetochemistry*; Springer Berlin Heidelberg: Berlin, Heidelberg, 1986.

11.6 Zusatzinformationen zu Publikation 6

“NHC-Stabilized Parent Phosphinidene Adducts of Metal(II) Hexamethyldisilazanides of Manganese − Cobalt and Their Lability in Solution”

Ruth Weller, Andres Gonzalez, Hannah Gottschling, Carsten von Hänisch, C. Gunnar Werncke

- eingereichtes Manuskript -

NHC-Stabilized Parent Phosphinidene Adducts of Metal(II) Hexamethyldisilazanides of Manganese – Cobalt and Their Lability in Solution

Ruth Weller,[a] Andres Gonzalez,[a] Hannah Gottschling,[a] Carsten von Hänisch,[a] C. Gunnar Werncke*[a]

[a] R. Weller, A. Gonzalez, H. Gottschling, Prof. Dr. C. von Hänisch, Dr. C. G. Werncke
Department of Chemistry
Philipps-Universität Marburg
Hans-Meerwein-Straße 4, D- 35032 Marburg, Germany
E-Mail: gunnar.werncke@chemie.uni-marburg.de

Table of Content

1 NMR Spectra

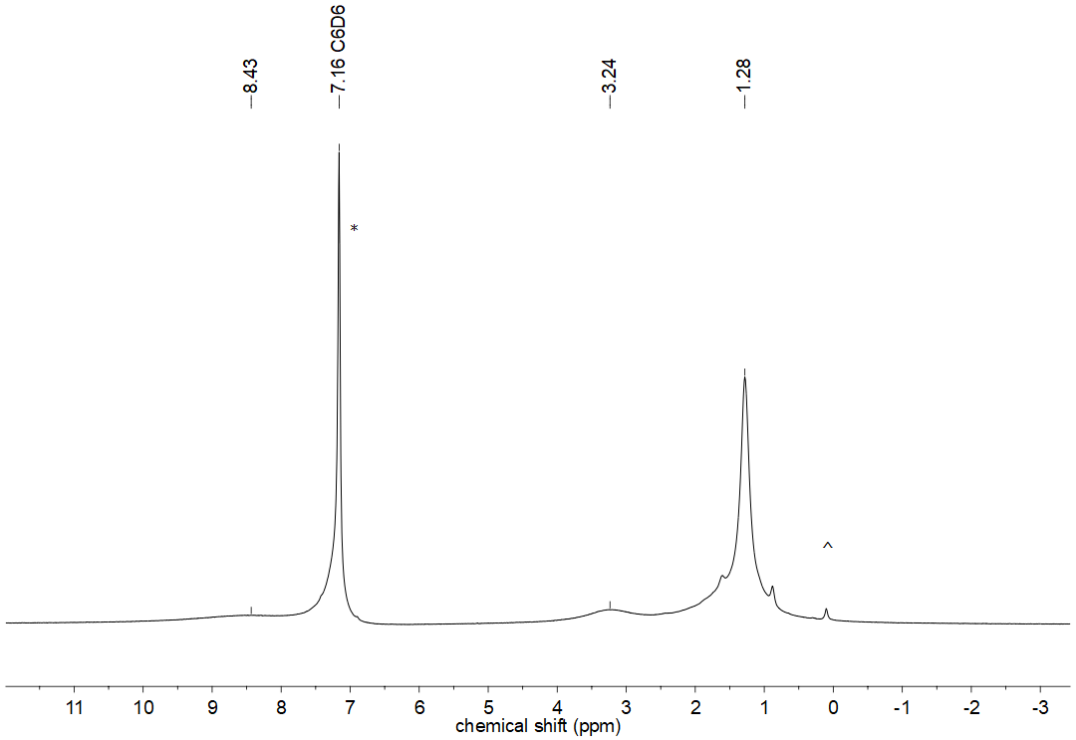

Figure S1. ^{1}H NMR spectrum (300.2 MHz) of **[Mn]** in C_6D_6 at 300 K. (* solvent, ^ impurities)

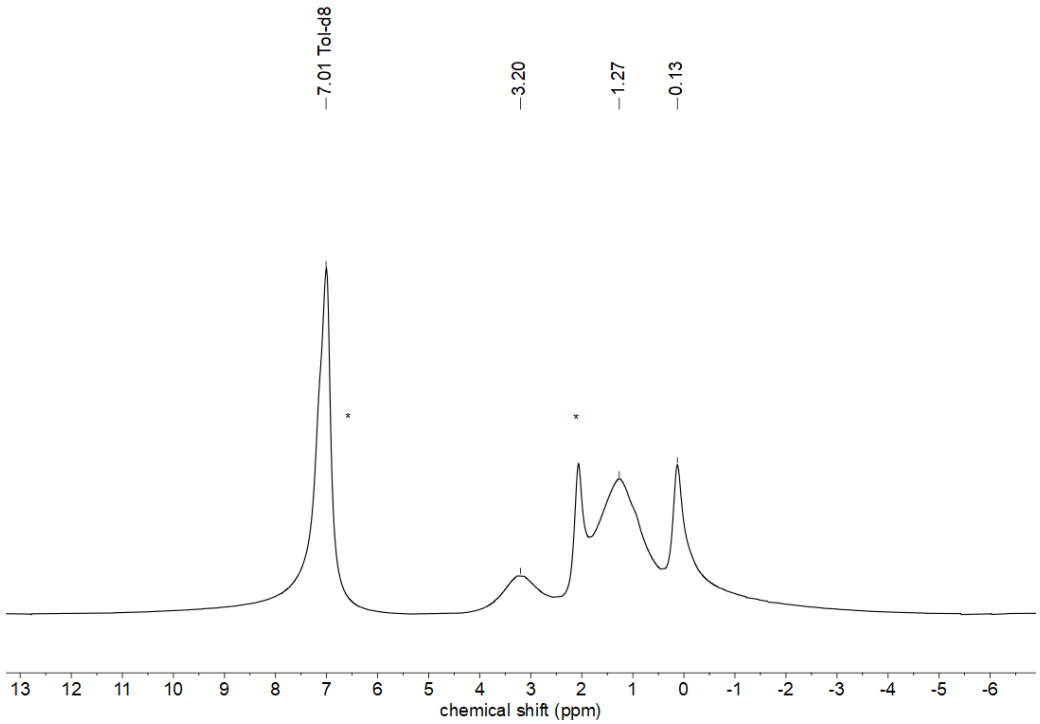

Figure S2. ^{1}H NMR spectrum (500.1 MHz) of **[Mn]** in toluene-d_8 at 193 K. (* solvent)

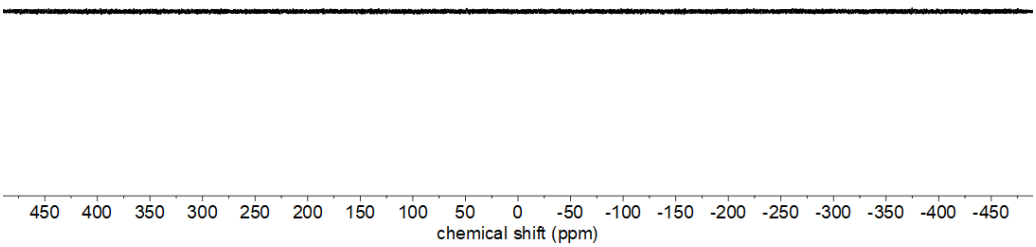

Figure S3. ^{31}P NMR spectrum (202.5 MHz) of **[Mn]** in toluene-d_8 at 300 K.

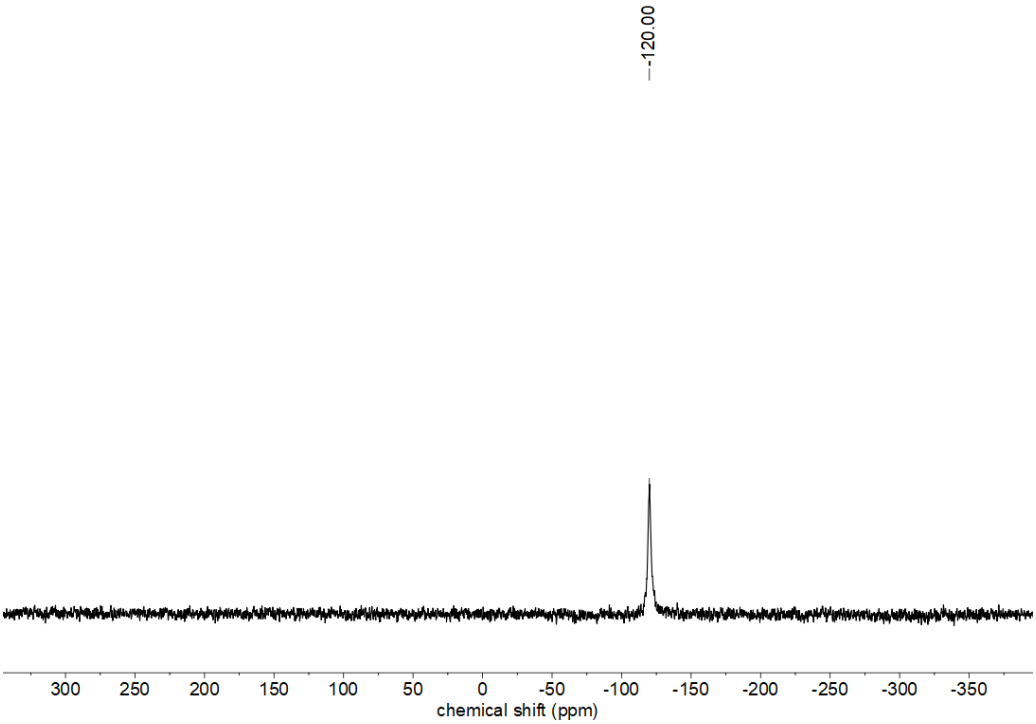

Figure S4. ^{31}P NMR spectrum (202.5 MHz) of **[Mn]** in toluene-d_8 at 193 K.

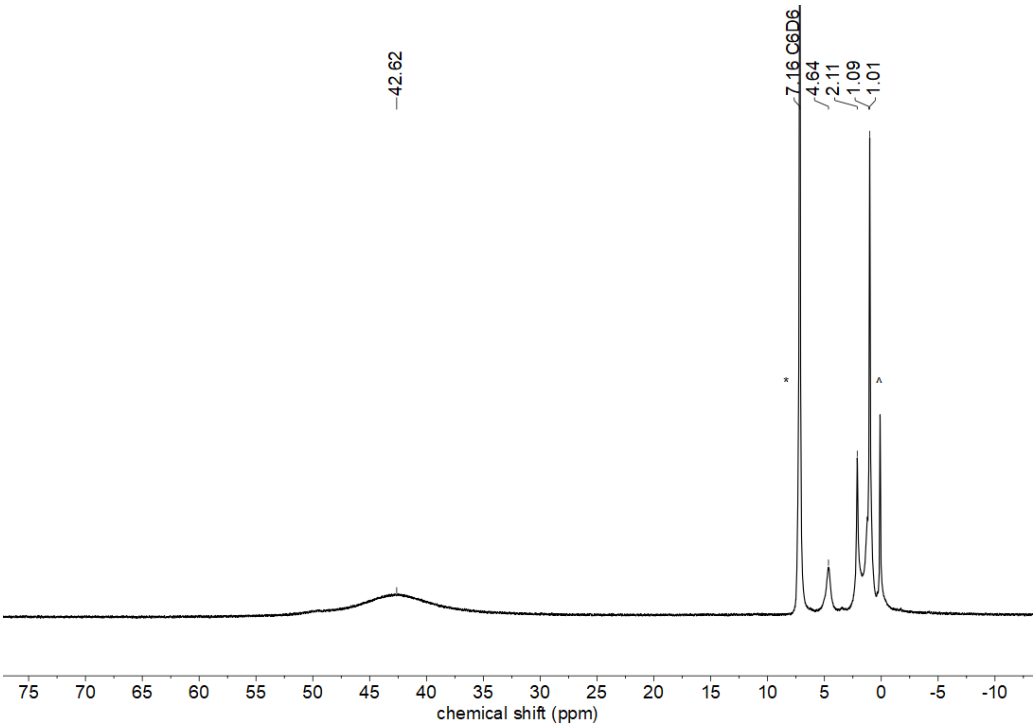

Figure S5. ^{1}H NMR spectrum (300.2 MHz) of **[Fe]** in C_6D_6 at 300 K. (* solvent, ^ impurities/decomposition)

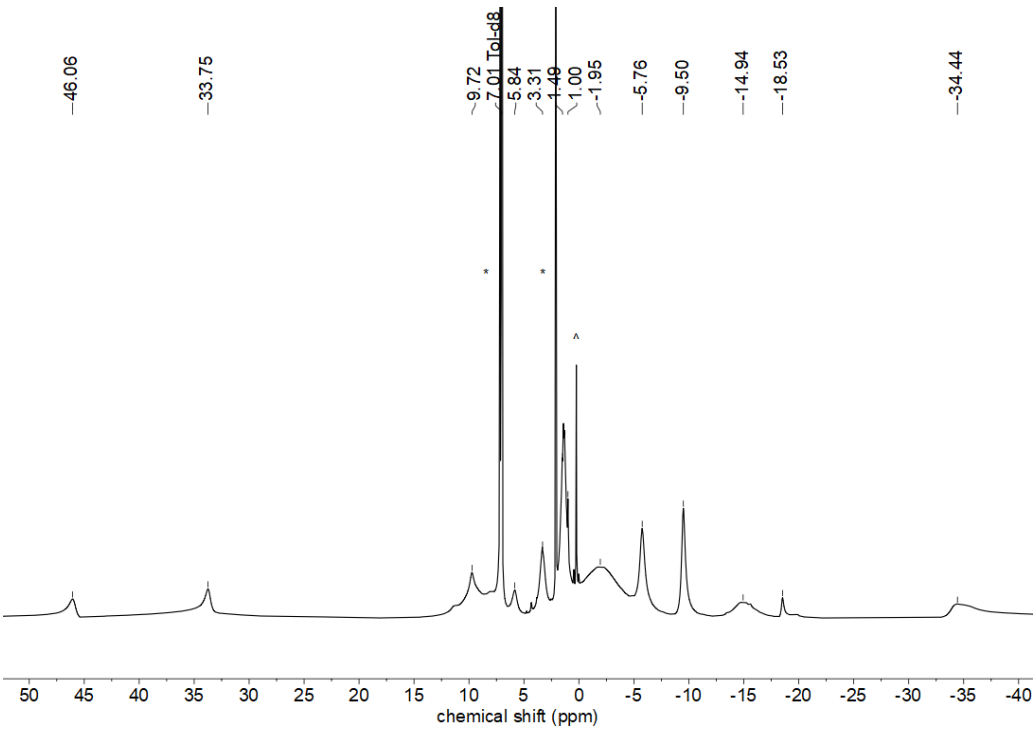

Figure S6. ^{1}H NMR spectrum (500.1 MHz) of **[Fe]** in toluene-d_8 at 193 K. (* solvent, ^ impurities/decomposition)

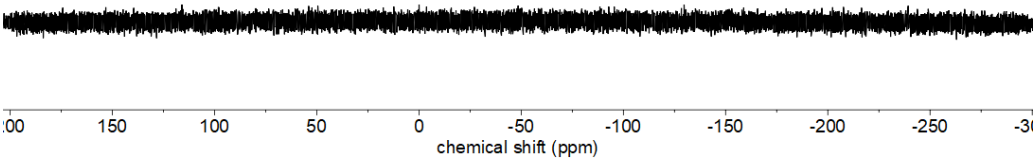

Figure S7. ^{31}P NMR spectrum (202.5 MHz) of **[Fe]** in toluene-d_8 at 300 K.

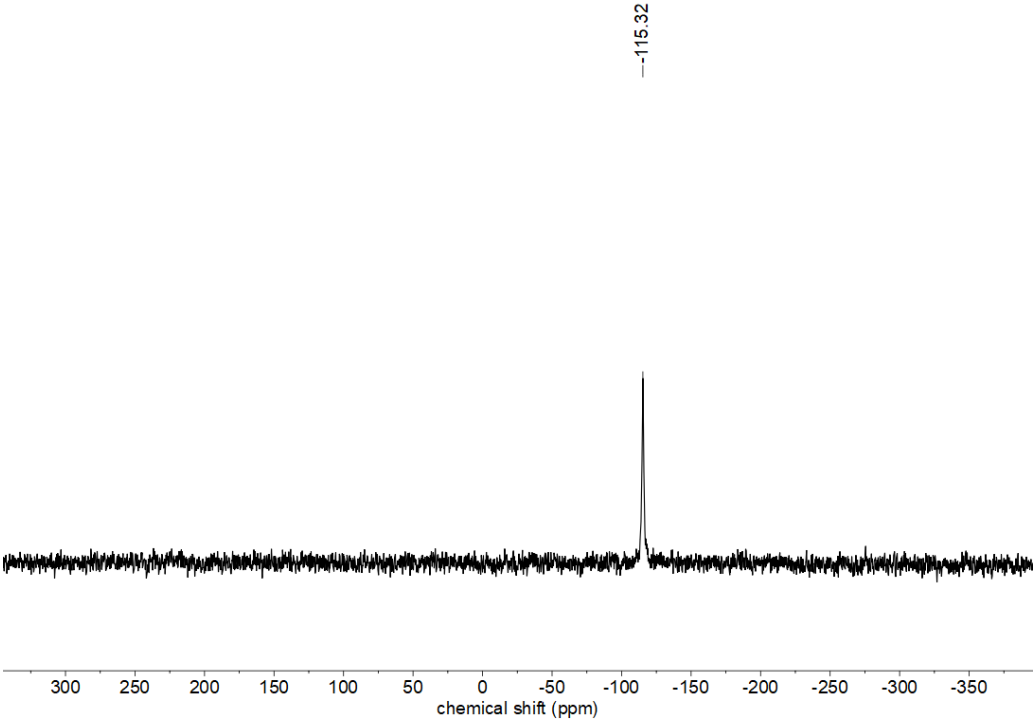

Figure S8. ^{31}P NMR spectrum (202.5 MHz) of **[Fe]** in toluene-d_8 at 193 K.

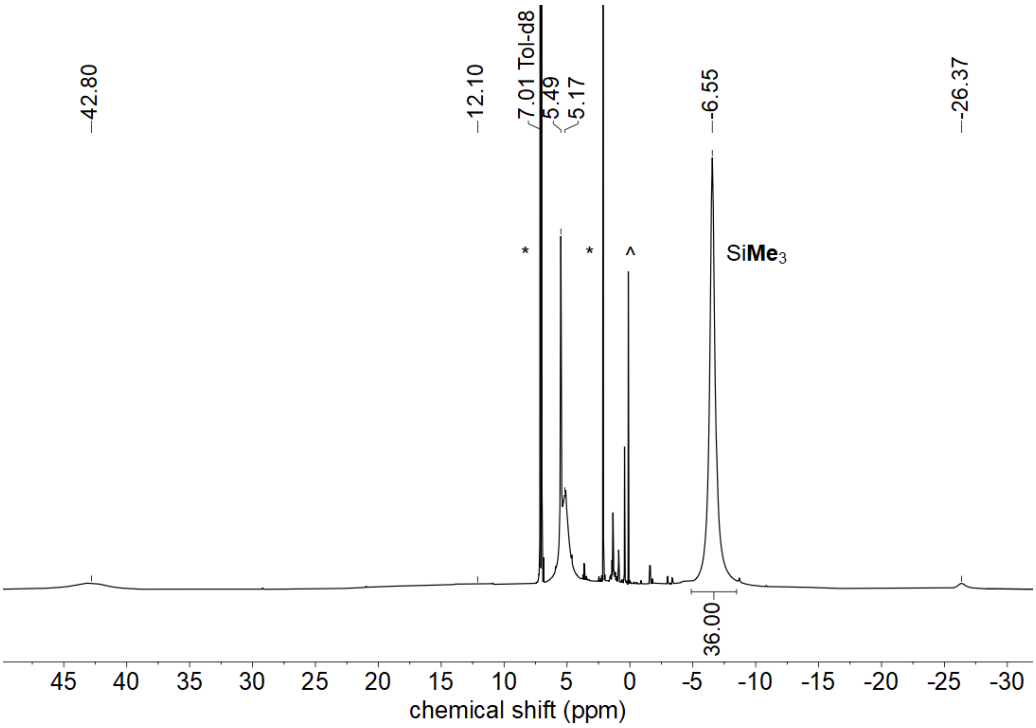

Figure S9. ^{1}H NMR spectrum (300.2 MHz, 300 K) of **[Co]** in toluene-d_8 at 300 K. (* solvent, ^ impurities)

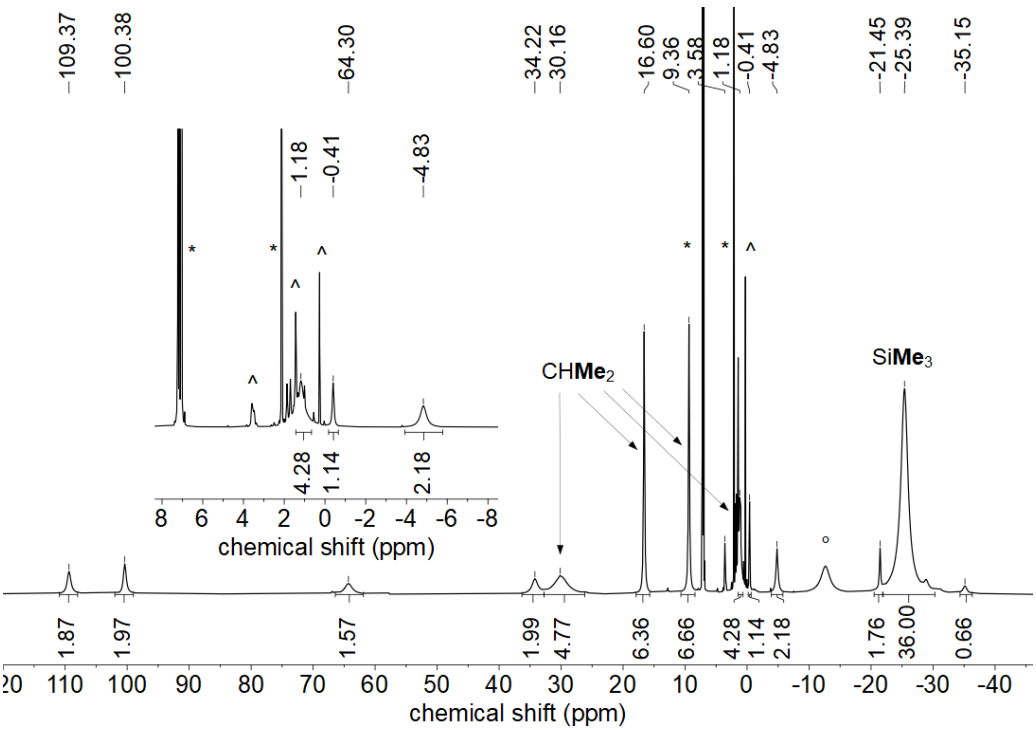

Figure S10. ^{1}H NMR spectrum (300.2 MHz, 300 K) of **[Co]** in toluene-d_8 at 193 K. (* solvent, ^ impurities)

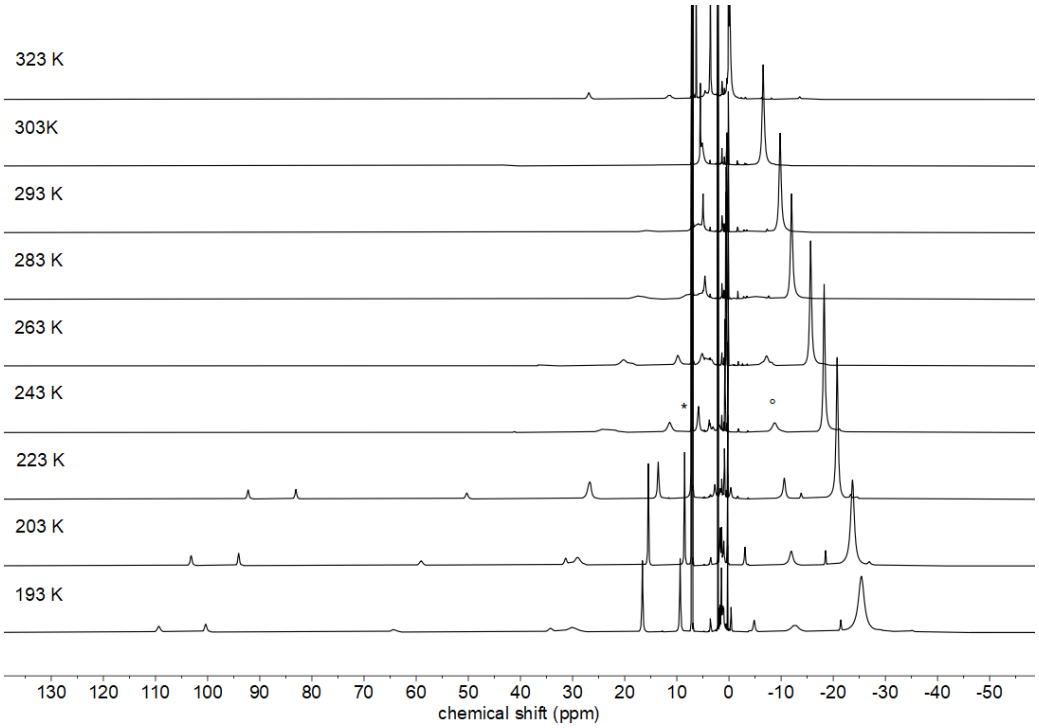

Figure S11. Temperature dependent ^{1}H NMR spectrum (500.1 MHz) of **[Co]** in toluene-d_8 from 193 K to 323 K. (* solvent, ° impurities)

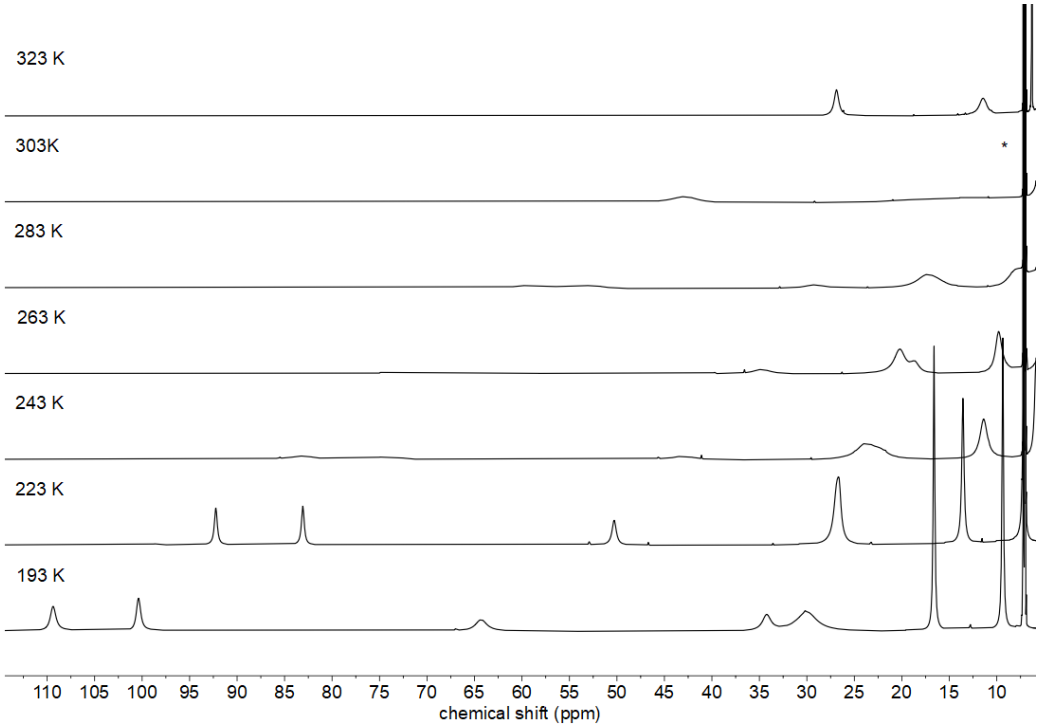

Figure S12. Low-Field of the temperature dependent ^{1}H NMR spectrum (500.1 MHz) of **[Co]** in toluene-d_8 from 193 K to 323 K. (* solvent)

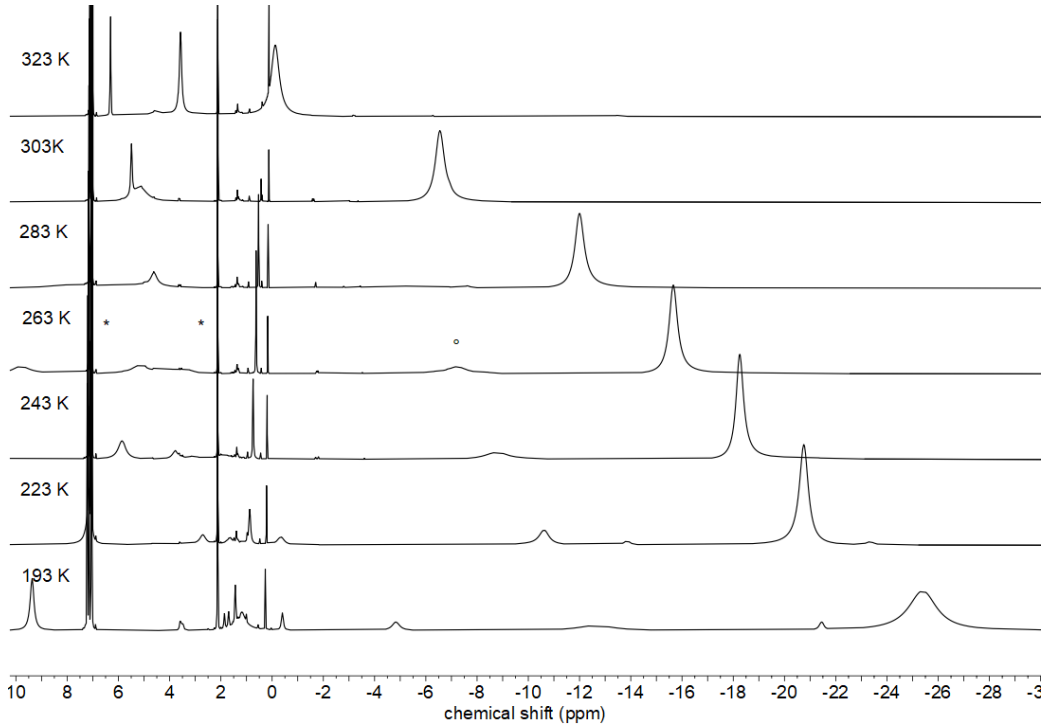

Figure S13. High-Field of the temperature dependent ^{1}H NMR spectrum (500.1 MHz) of **[Co]** in toluene-d_8 from 193 K to 323 K. (* solvent, ° impurities)

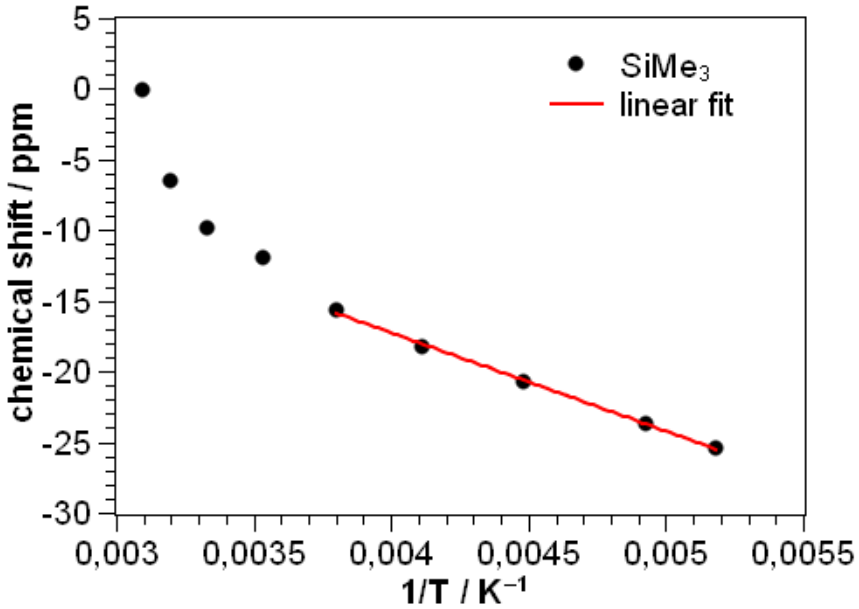

Figure S14. Curie-Weiss plot of the temperature dependent ^{1}H NMR spectrum of **[Co]** for the trimethylsilyl signal in toluene-d_8 with a linear fit for temperatures below 270 K.

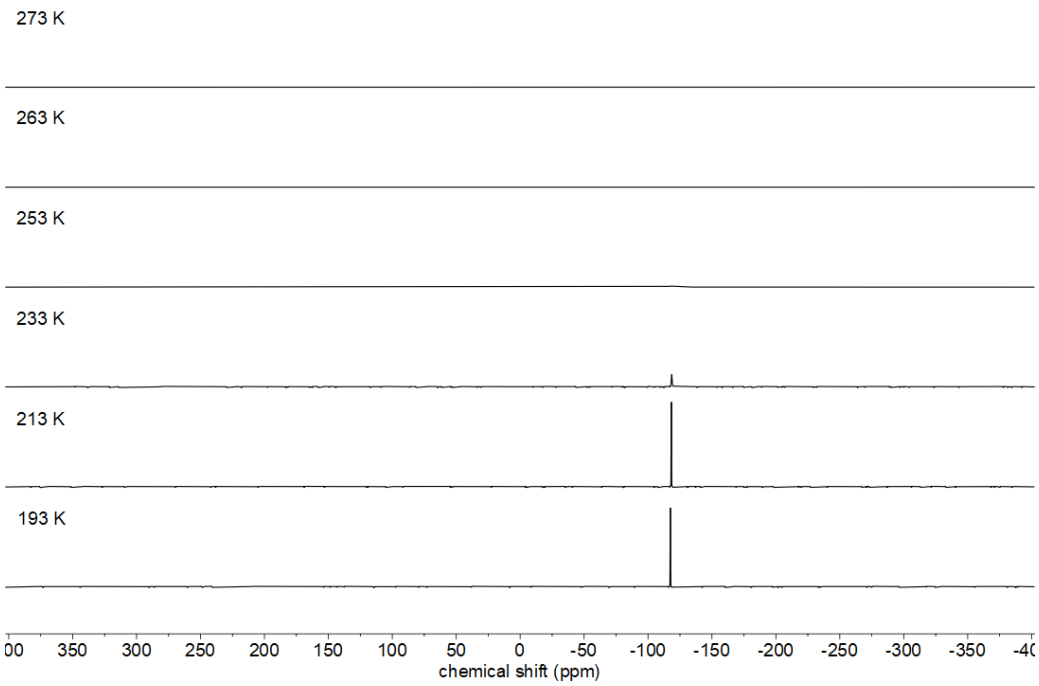

Figure S15. Temperature dependent ^{31}P NMR spectrum (202.5 MHz) of **[Co]** in toluene-d_8 from 193 K to 273 K.

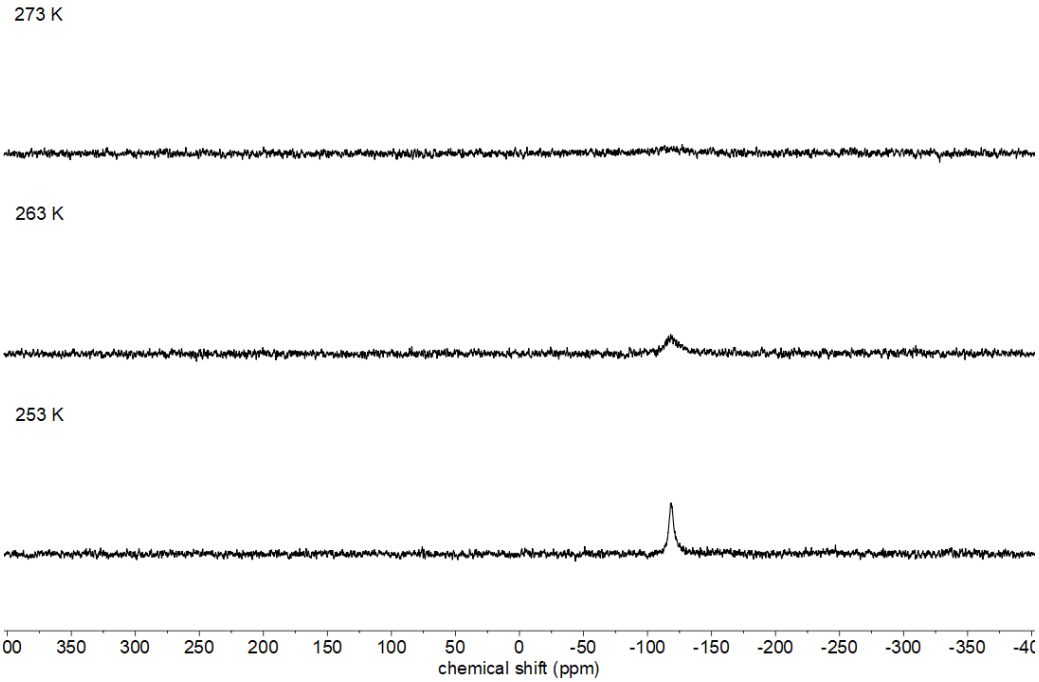

Figure S16. Temperature dependent ^{31}P NMR spectrum (202.5 MHz) of **[Co]** in toluene-d_8 from 253 k to 273 K.

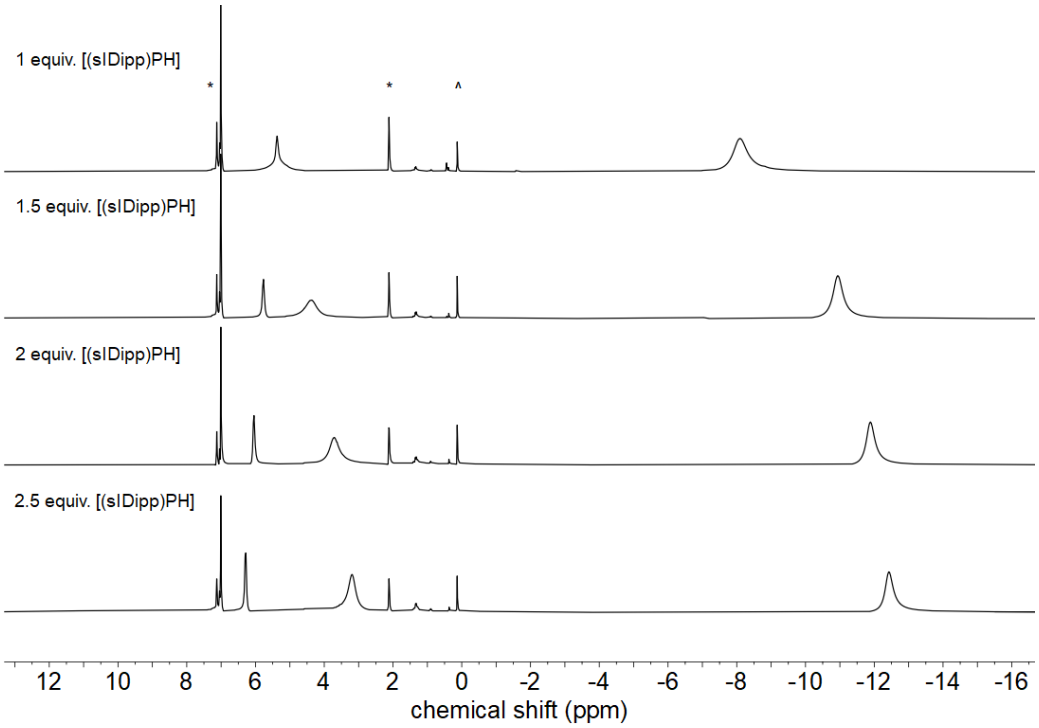

Figure S17. High-Field of the ^{1}H NMR spectra (300.2 MHz) of [Co{N(SiMe$_3$)$_2$}$_2$] in toluene-d_8 with addition of a variable amount of [(sIDipp)PH].

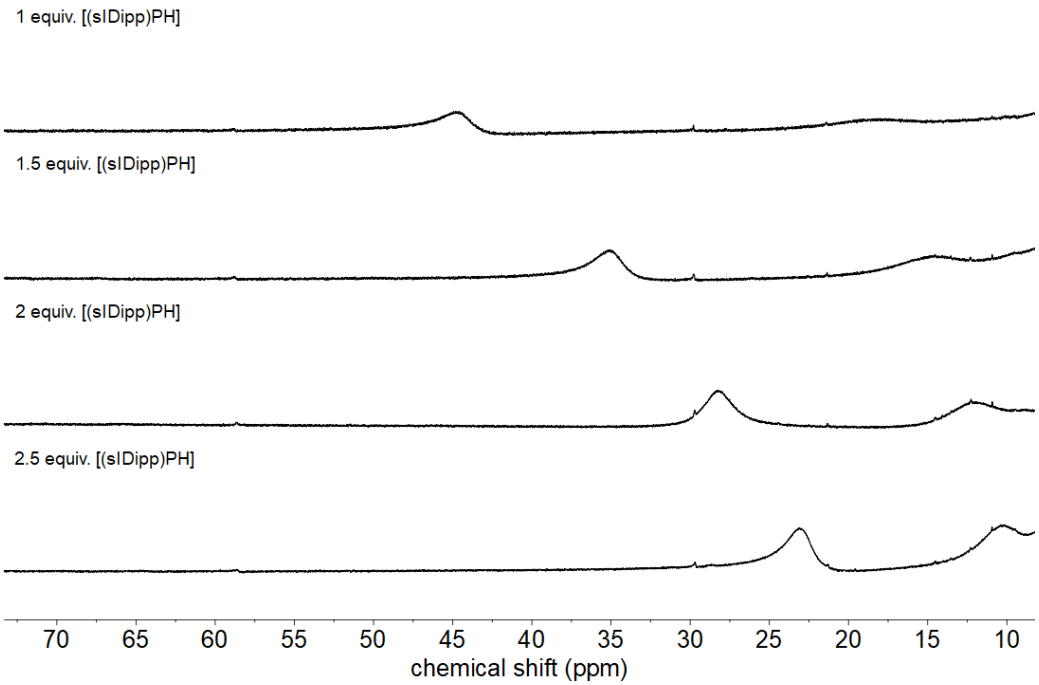

Figure S18. Low-Field of the ^{1}H NMR spectra (300.2 MHz) of [Co{N(SiMe$_3$)$_2$}$_2$] in toluene-d_8 with addition of a variable amount of [(sIDipp)PH].

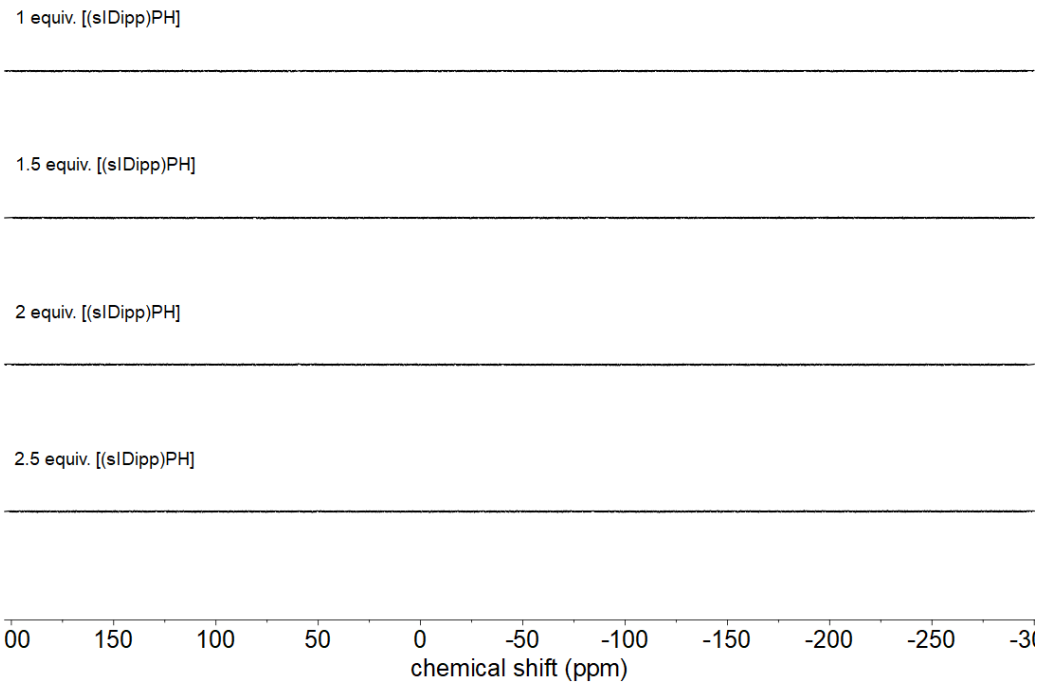

Figure S19. ^{31}P NMR spectra (202.5 MHz) of [Co{N(SiMe$_3$)$_2$}$_2$] in toluene-d_8 with addition of a variable amount of [(sIDipp)PH].

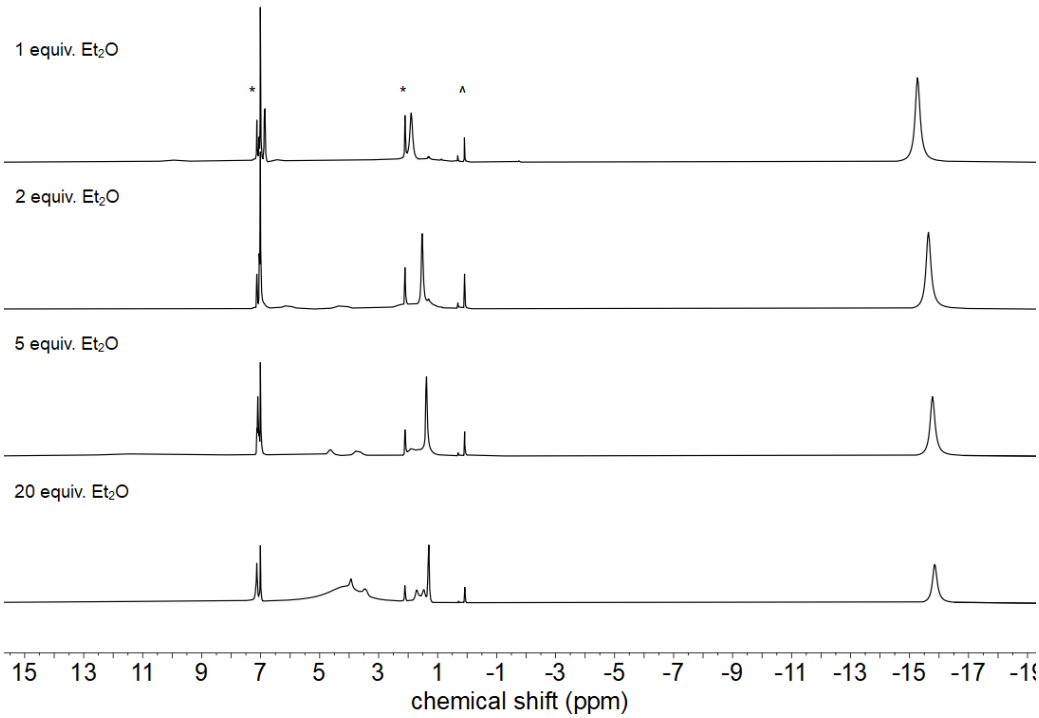

Figure S20. High-Field of the ^{1}H NMR spectra (300.2 MHz) of **[Co]** in toluene-d_8 with addition of a variable amount of diethyl ether.

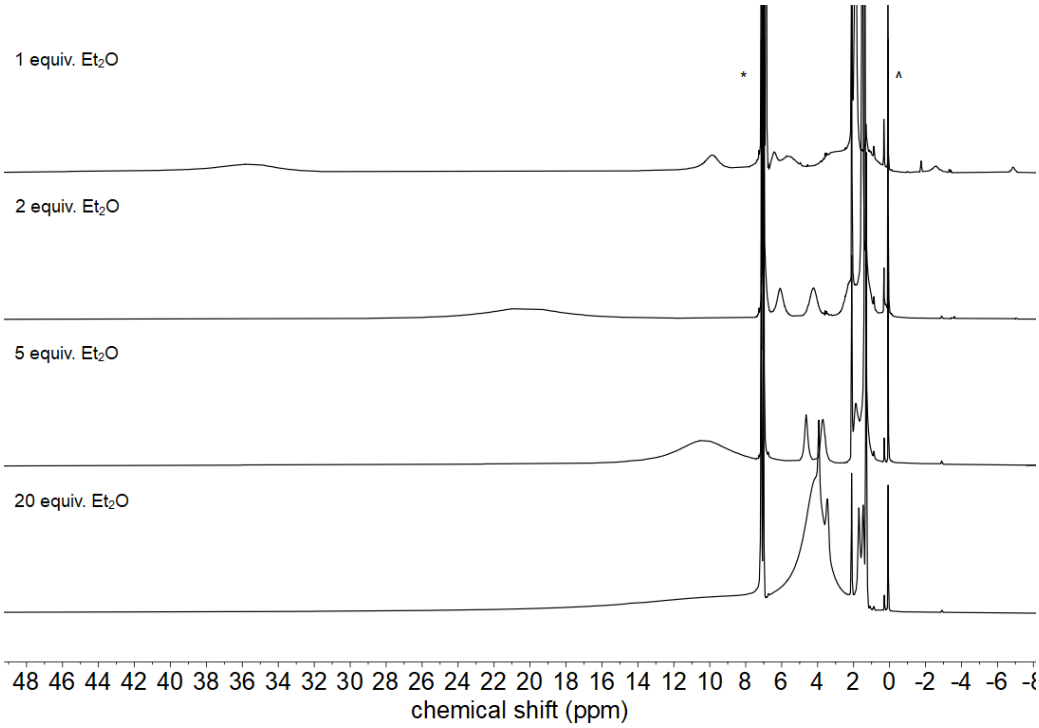

Figure S21. Low-Field of the ^{1}H NMR spectra (300.2 MHz) of **[Co]** in toluene-d_8 with addition of a variable amount of diethyl ether.

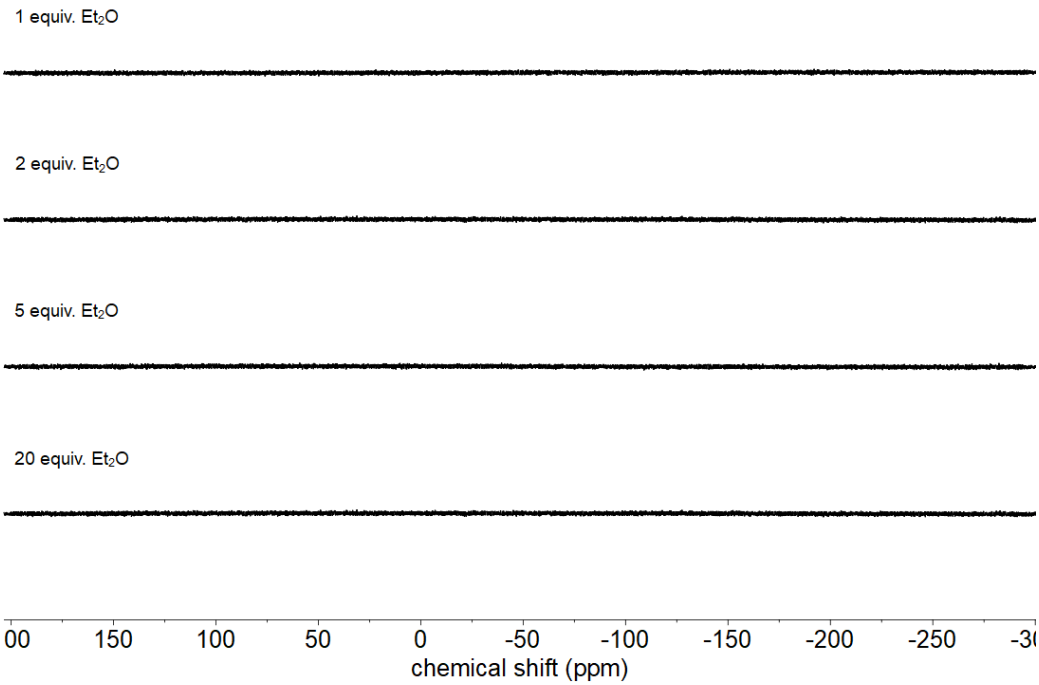

Figure S22. ^{31}P NMR spectra (202.5 MHz) of **[Co]** in toluene-d_8 with addition of a variable amount of diethyl ether.

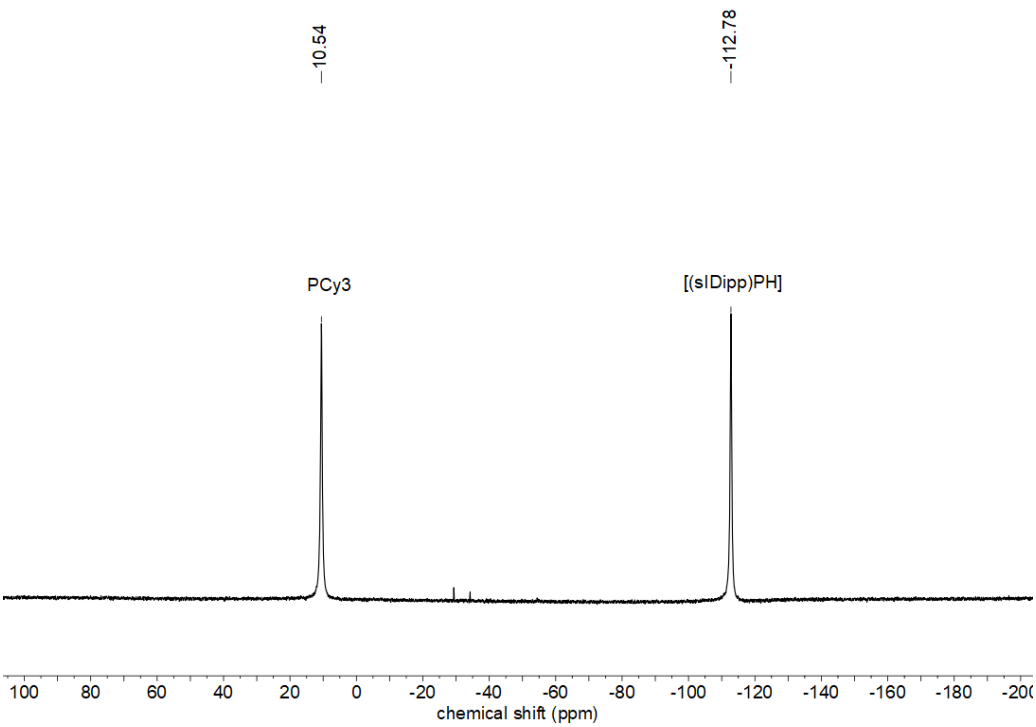

Figure S23. ^{31}P NMR spectrum (202.5 MHz) of **[Co]** with 1 equiv. PCy_3 in toluene-d_8 at 300 K.

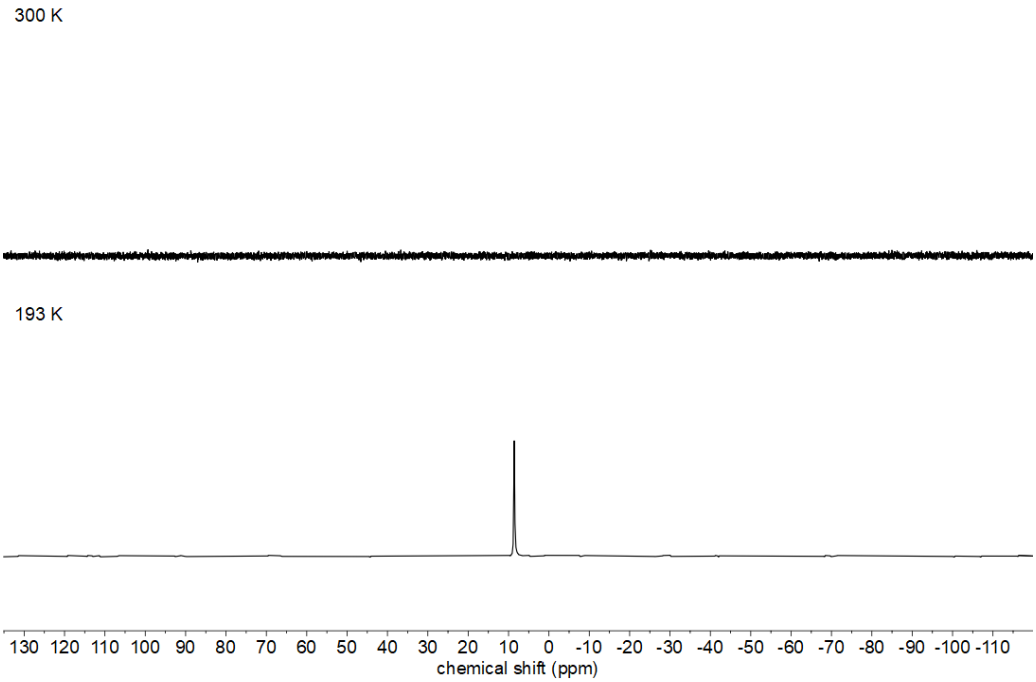

Figure S24. ^{31}P NMR spectrum (202.5 MHz) of $[Co\{N(SiMe_3)_2\}_2]$ with 1 equiv. PCy_3 in toluene-d_8 at 300 K.

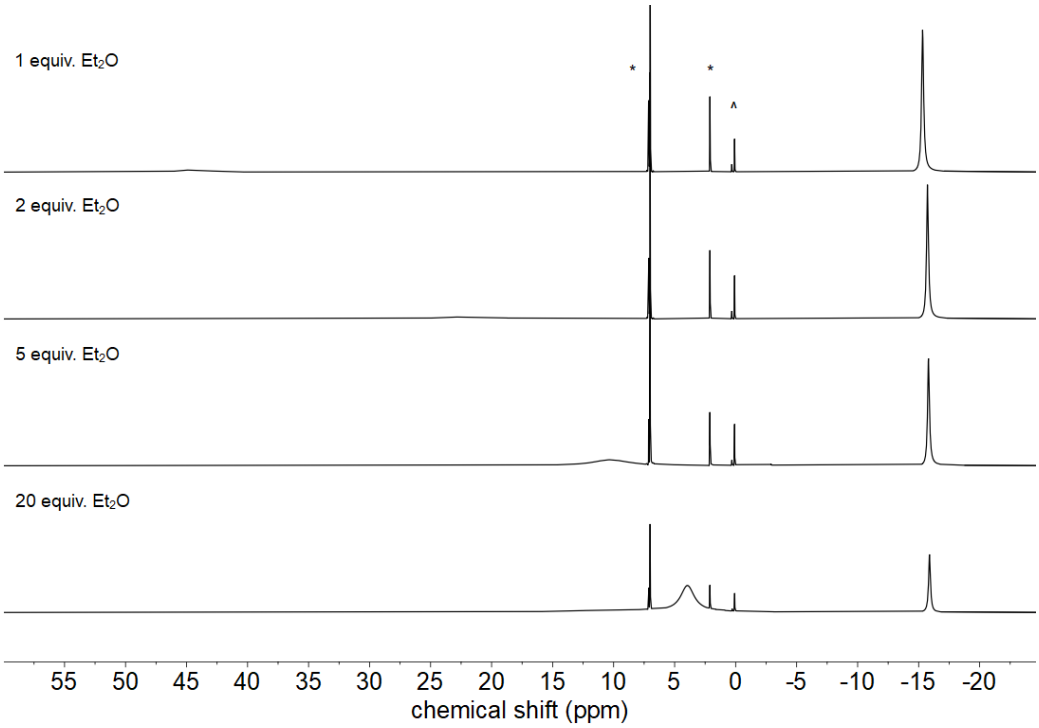

Figure S25. High-Field of the ^{1}H NMR spectra (300.2 MHz) of [Co{N(SiMe$_3$)$_2$}$_2$] in toluene-*d*$_8$ with addition of a variable amount of diethyl ether.

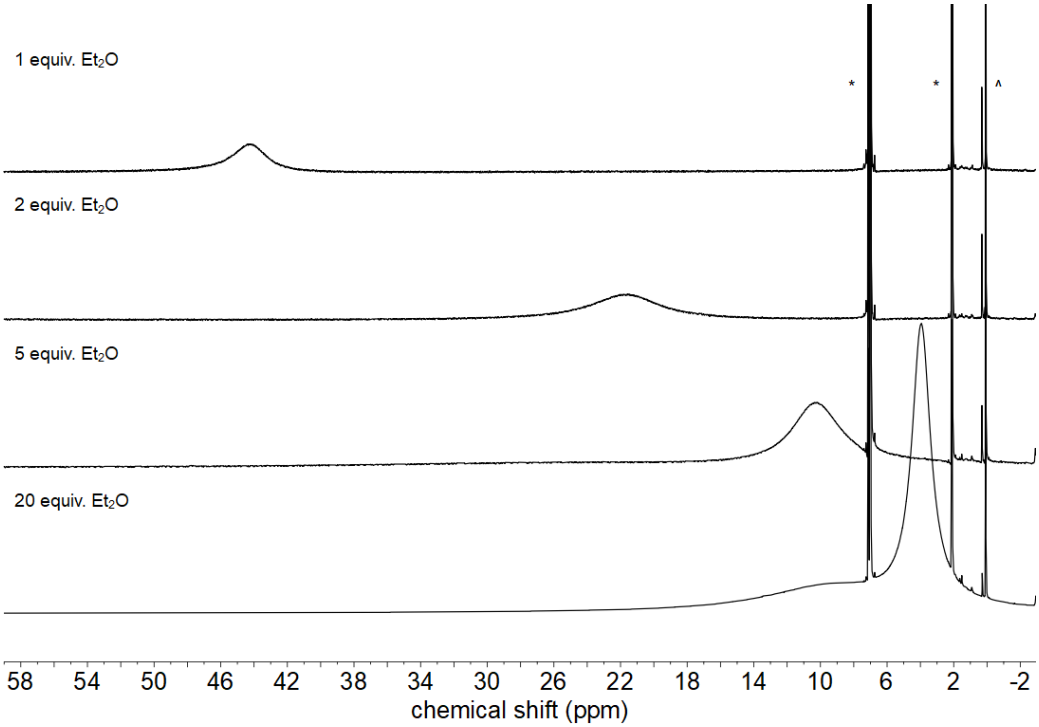

Figure S26. Low-Field of the ^{1}H NMR spectra (300.2 MHz) of [Co{N(SiMe$_3$)$_2$}$_2$] in toluene-*d*$_8$ with addition of a variable amount of diethyl ether.

2 UV/Vis Spectra

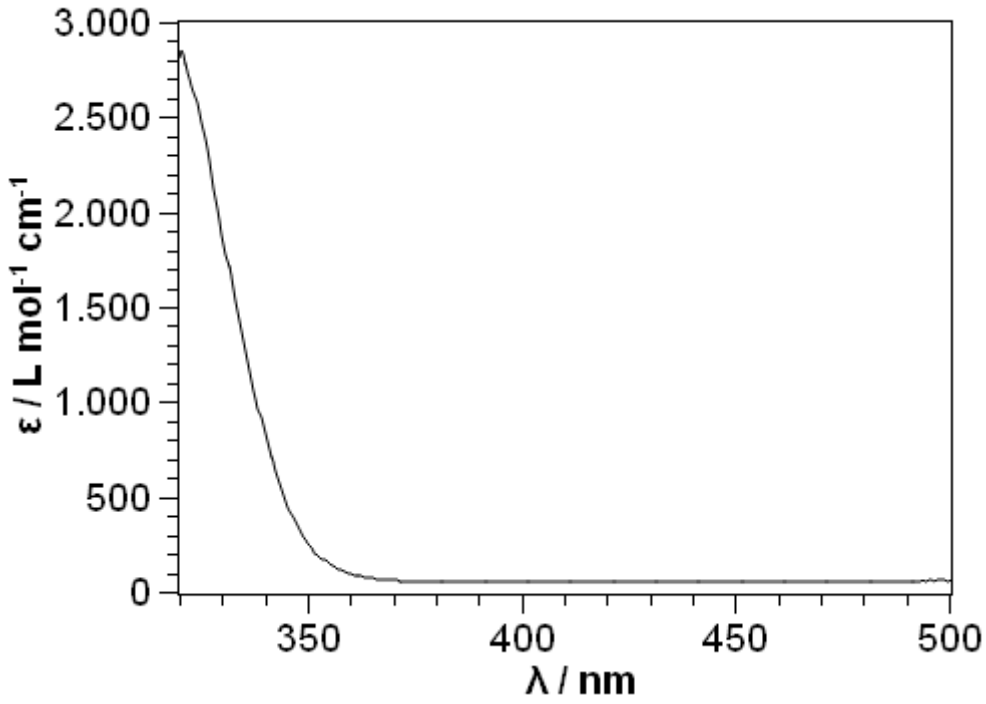

Figure S27. UV/Vis spectrum of **[Mn]** at 293 K in *n*-pentane.

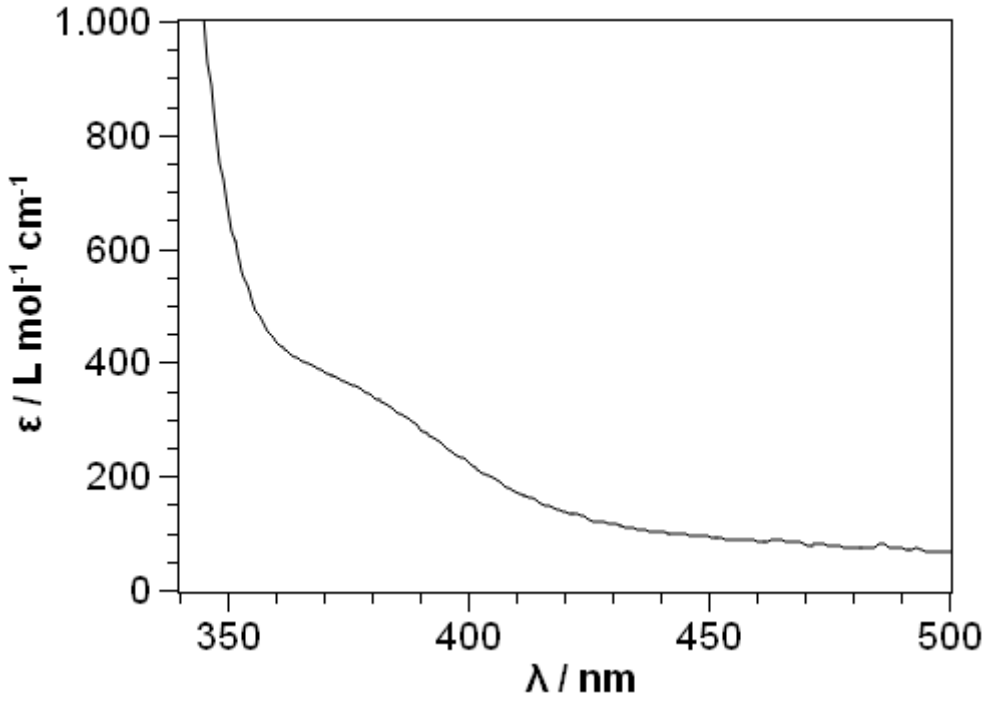

Figure S28. UV/Vis spectrum of **[Fe]** at 293 K in *n*-pentane.

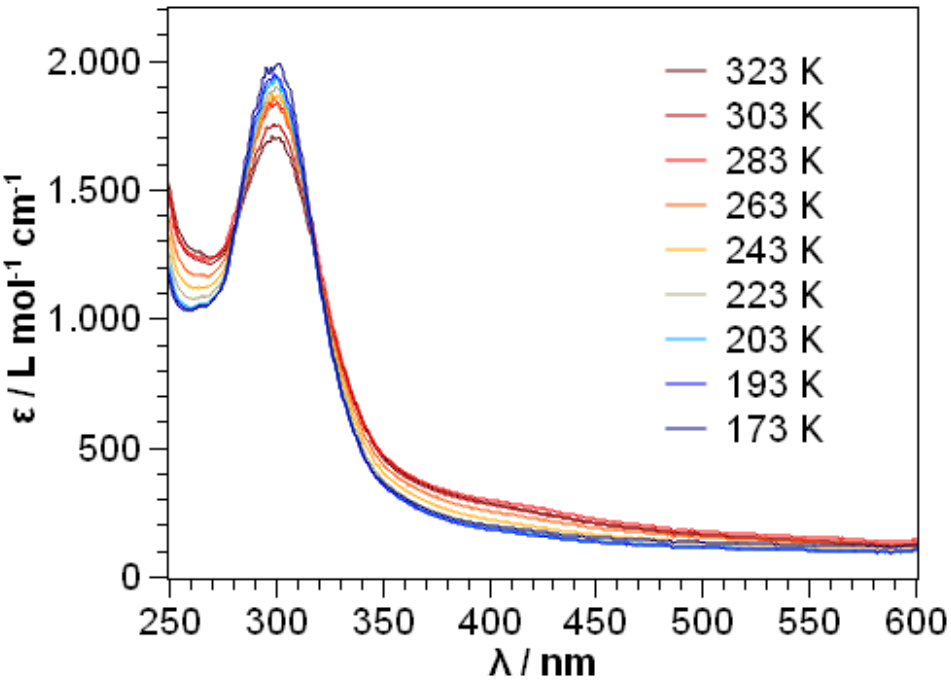

Figure S29. UV/Vis spectrum of **[Co]** at different temperatures in *n*-pentane in the region from 250 nm to 600 nm.

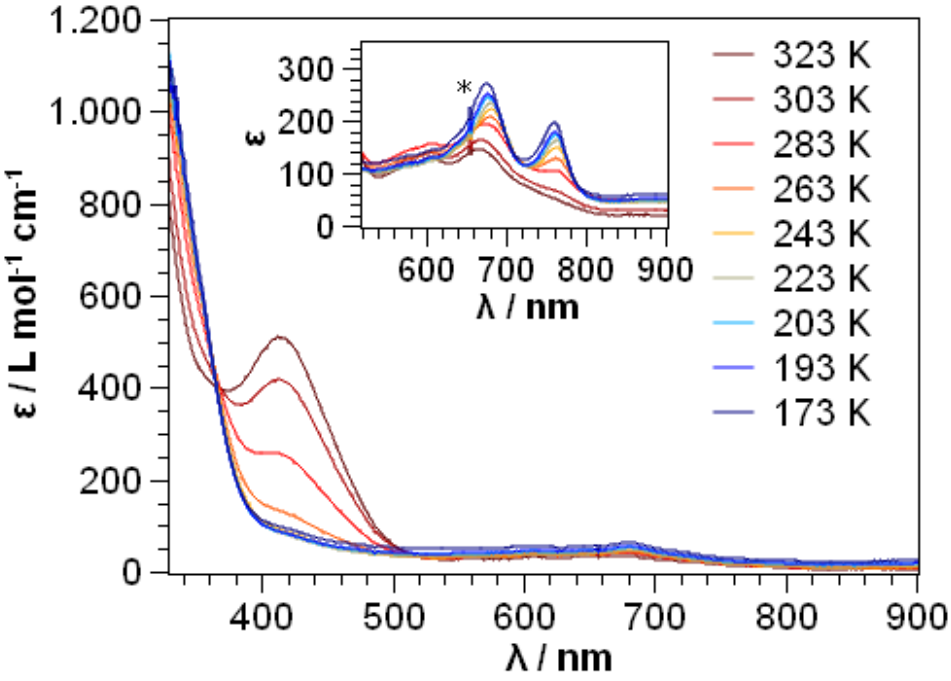

Figure S30. Zoom into the UV/Vis spectrum of **[Co]** at different temperatures in *n*-pentane in the region from 340 nm to 900 nm. (* signal caused by lamp exchange)

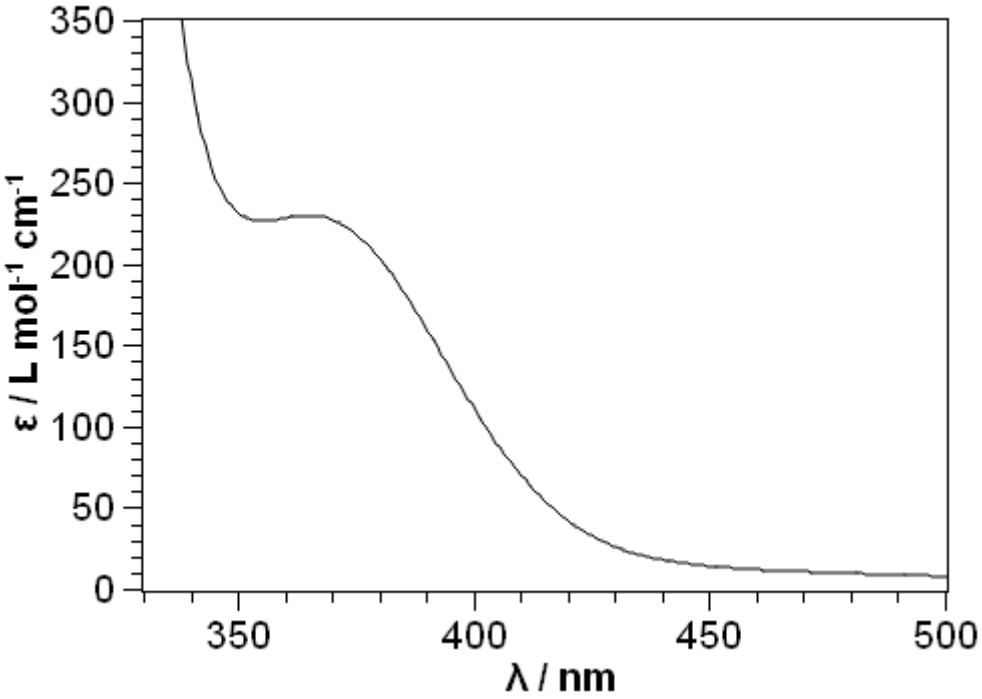

Figure S31. UV/Vis spectrum of [Fe{N(SiMe$_3$)$_2$}$_2$] at 22 °C in *n*-pentane.

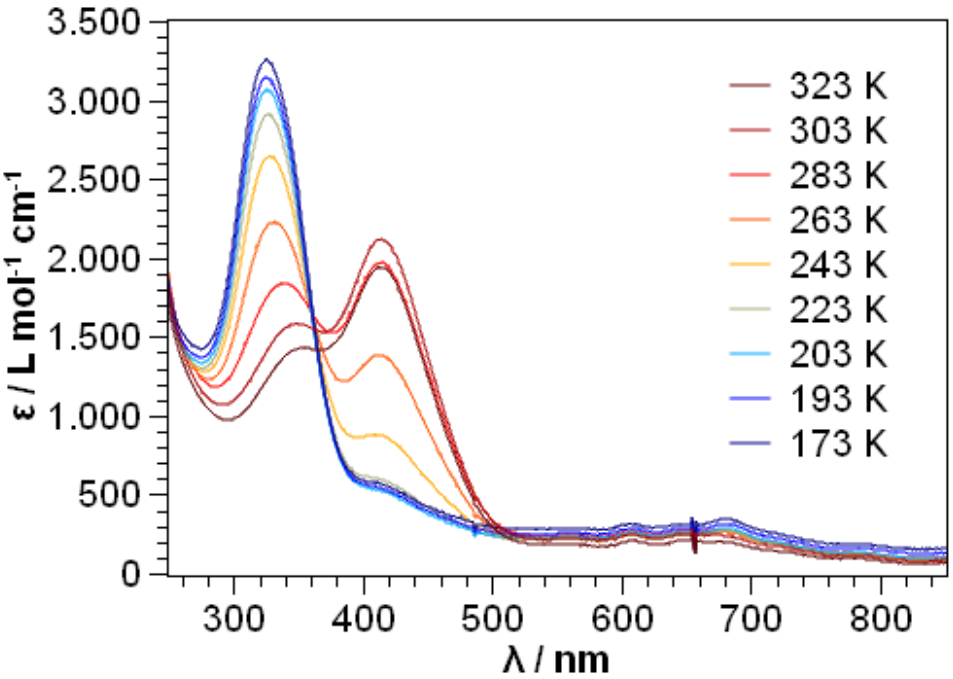

Figure S32. UV/Vis spectrum of [Co{N(SiMe$_3$)$_2$}$_2$] at different temperatures in *n*-pentane.

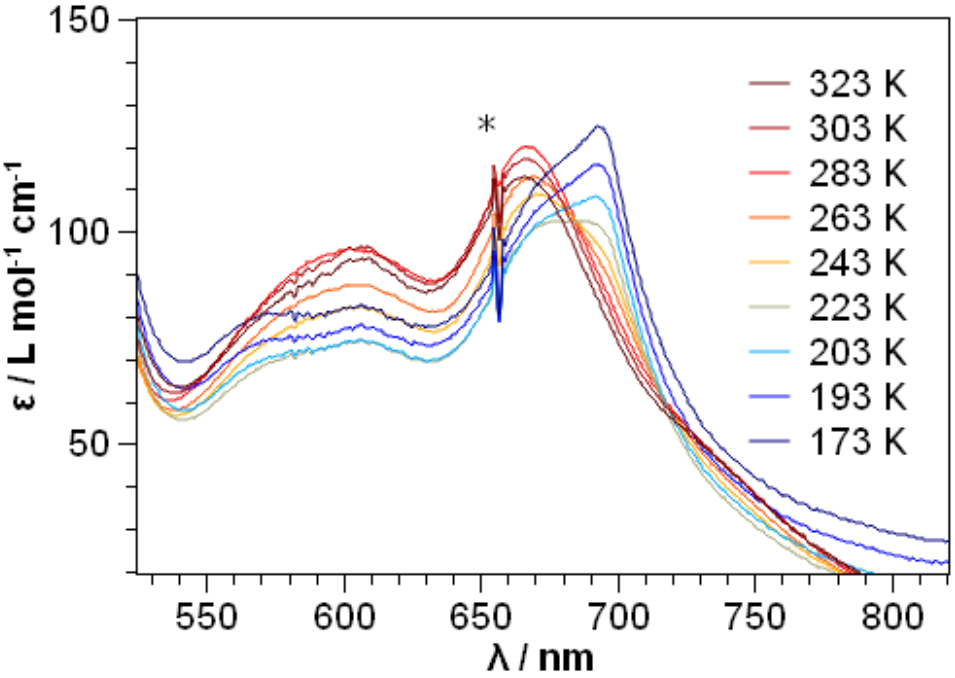

Figure S33. Zoom into the UV/Vis spectrum of $[Co\{N(SiMe_3)_2\}_2]$ at different temperatures in *n*-pentane in the region from 500 nm to 820 nm. (* signal caused by lamp exchange)

3 IR Spectra

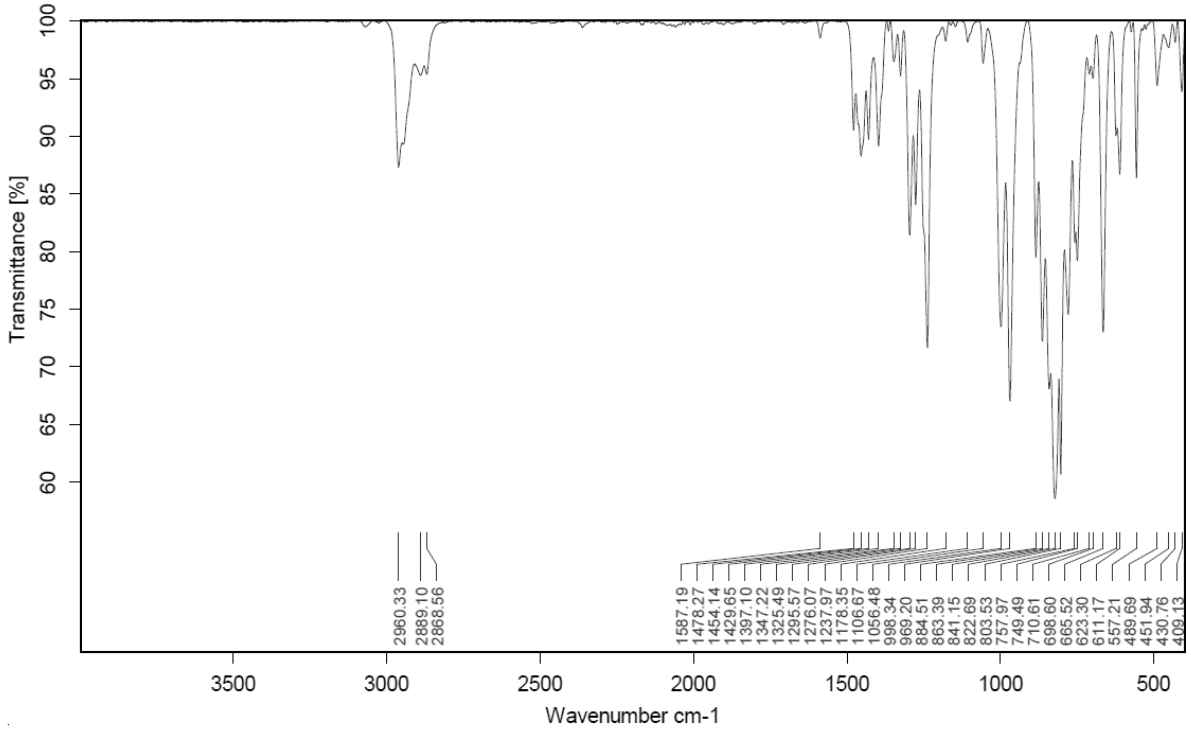

Figure S34. IR spectrum of **[Mn]**.

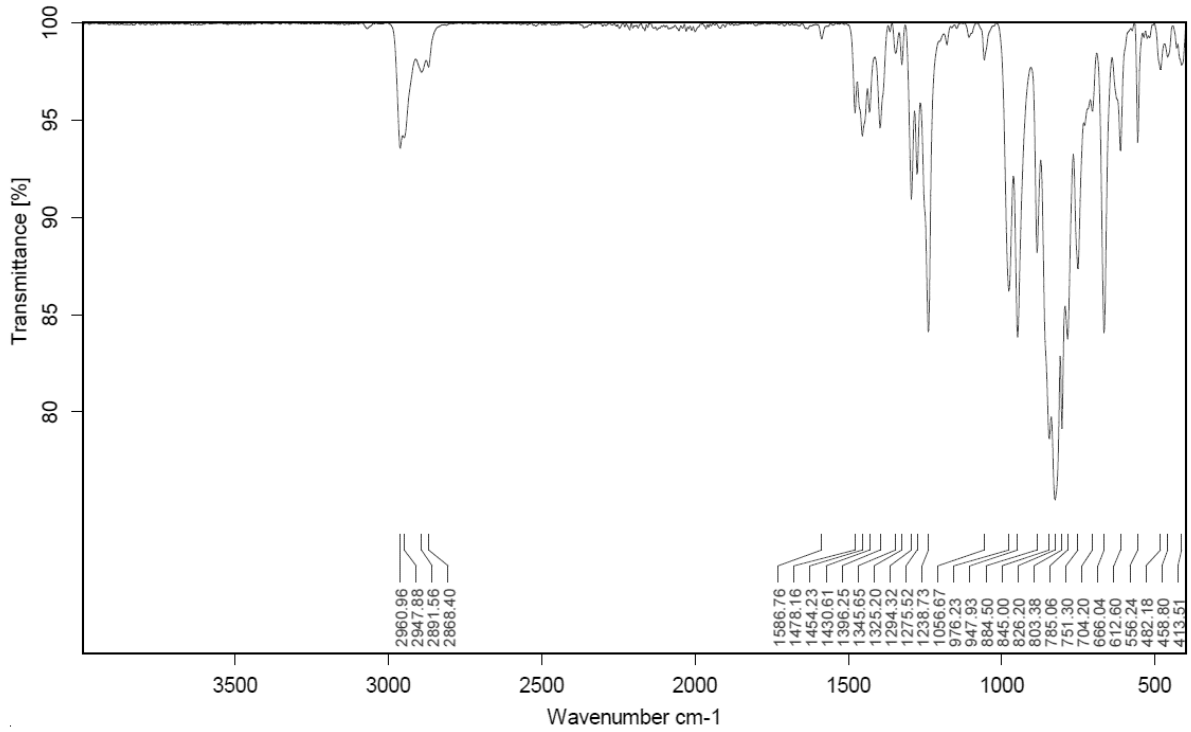

Figure S35. IR spectrum of **[Fe]**.

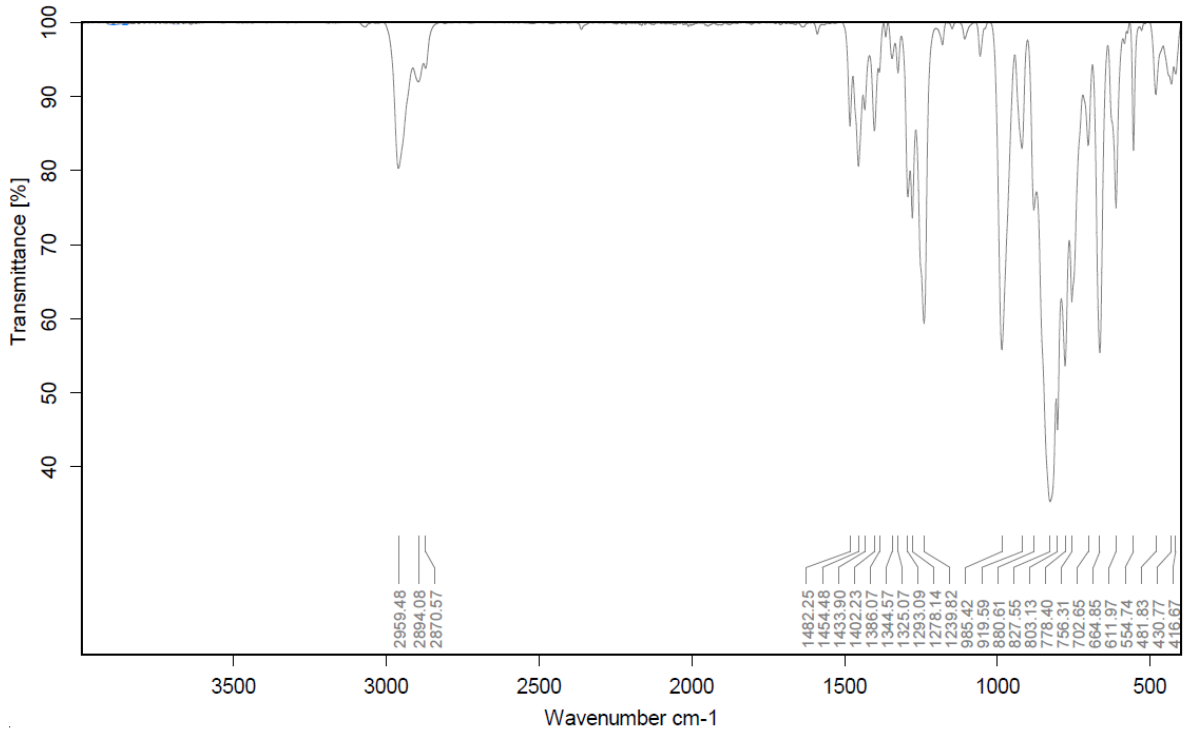

Figure S36. IR spectrum of **[Co]**.

4 X-Ray Diffraction Analysis and Molecular Structures

Table S1. Crystal data and structure refinement of **[Mn]**

Empirical formula	$C_{78}H_{150}Mn_2N_8P_2Si_8$
Formula weight	1596.59
Temperature/K	100.0
Crystal system	monoclinic
Space group	$P2_1/c$
a/Å	19.645
b/Å	28.369
c/Å	18.704
α/°	90
β/°	113.18
γ/°	90
Volume/Å^3	9582.1
Z	4
ρ_{calc}g/cm^3	1.107
μ/mm^{-1}	0.438
F(000)	3464.0
Crystal size/mm^3	0.767 × 0.466 × 0.297
Radiation	MoKα (λ = 0.71073)
2Θ range for data collection/°	4.12 to 50
Index ranges	$-23 \le h \le 23$, $-33 \le k \le 31$, $-22 \le l \le 20$
Reflections collected	37629
Independent reflections	16857 [R_{int} = 0.0698, R_{sigma} = 0.0949]
Data/restraints/parameters	16857/0/931
Goodness-of-fit on F^2	0.901
Final *R* indexes [*I*>=2σ (*I*)]	R_1 = 0.0499, wR_2 = 0.1012
Final *R* indexes [all data]	R_1 = 0.1134, wR_2 = 0.1156
Largest diff. peak/hole / e Å^{-3}	0.48/−0.29

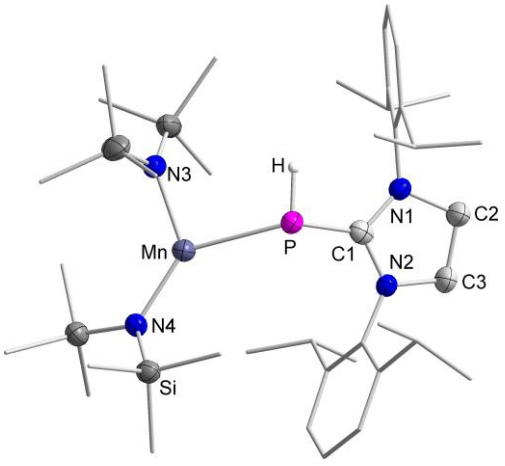

Figure S37. Molecular structure of **[Mn]**. Irrelevant hydrogen atoms and a second, independent molecule are omitted for clarity.

Table S2. Crystal data and structure refinement of **[Fe]**

Empirical formula	$C_{78}H_{150}Fe_2N_8P_2Si_8$
Formula weight	1598.41
Temperature/K	100.0
Crystal system	monoclinic
Space group	$P2_1/c$
a/Å	18.7424(15)
b/Å	28.0245(17)
c/Å	19.6241(17)
α/°	90
β/°	113.141(6)
γ/°	90
Volume/Å^3	9478.2(13)
Z	4
ρ_{calc}g/cm^3	1.120
μ/mm^{-1}	0.482
F(000)	3472.0
Crystal size/mm^3	0.947 × 0.709 × 0.115
Radiation	MoKα (λ = 0.71073)
2Θ range for data collection/°	4.742 to 56.362
Index ranges	−24 ≤ *h* ≤ 24, −35 ≤ *k* ≤ 35, −23 ≤ *l* ≤ 23
Reflections collected	70034
Independent reflections	19779 [R_{int} = 0.0616, R_{sigma} = 0.0533]
Data/restraints/parameters	19779/0/931
Goodness-of-fit on F^2	0.952
Final *R* indexes [*I*>=2σ (*I*)]	R_1 = 0.0377, wR_2 = 0.0927
Final *R* indexes [all data]	R_1 = 0.0610, wR_2 = 0.1001
Largest diff. peak/hole / e Å^{-3}	0.73/−0.36

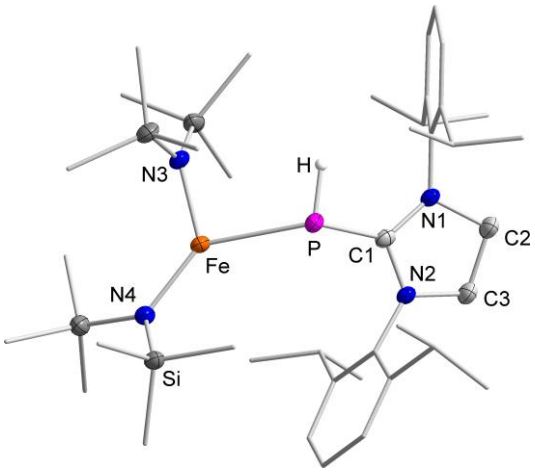

Figure S38. Molecular structure of **[Fe]**. Irrelevant hydrogen atoms and a second, independent molecule are omitted for clarity.

Table S3. Crystal data and structure refinement of **[Co]**

Empirical formula	$C_{39}H_{75}CoN_4PSi_4$
Formula weight	802.29
Temperature/K	100.0
Crystal system	monoclinic
Space group	$P2_1/n$
a/Å	12.0359(8)
b/Å	20.6625(14)
c/Å	19.2983(14)
α/°	90
β/°	90.270(2)
γ/°	90
Volume/Å^3	4799.3(6)
Z	4
ρ_{calc}g/cm^3	1.110
μ/mm^{-1}	0.520
F(000)	1740.0
Crystal size/mm^3	0.379 × 0.351 × 0.205
Radiation	MoKα (λ = 0.71073)
2Θ range for data collection/°	4.442 to 49.996
Index ranges	$-14 \le h \le 14$, $-24 \le k \le 24$, $-22 \le l \le 22$
Reflections collected	41828
Independent reflections	8441 [R_{int} = 0.0528, R_{sigma} = 0.0404]
Data/restraints/parameters	8441/0/466
Goodness-of-fit on F^2	1.048
Final *R* indexes [I>=2σ (I)]	R_1 = 0.0428, wR_2 = 0.0995
Final *R* indexes [all data]	R_1 = 0.0658, wR_2 = 0.1071
Largest diff. peak/hole / e Å^{-3}	1.38/−0.42

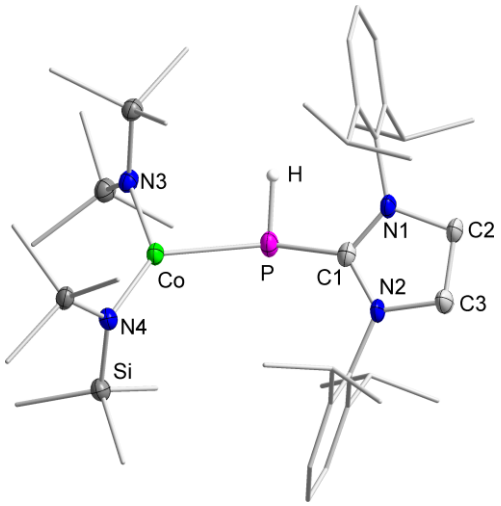

Figure S39. Molecular structure of **[Co]**. Irrelevant hydrogen atoms are omitted for clarity.

11.7 Zusatzinformationen zu Publikation 7

„Synthesis of the Open-Shell 3d-Transition Metal(II) Bis(phosphinidenide) [Mn(P(sIDipp))$_2$]“

Ruth Weller, Markus Balmer, Carsten von Hänisch, C. Gunnar Werncke

- eingereichtes Manuskript -

Synthesis of the Open-Shell 3d-Transition Metal(II) Bis(phosphinidenide) [Mn{P(sIDipp)}$_2$]

Ruth Weller,[a] Markus Balmer,[b] Carsten von Hänisch,[a] C. Gunnar Werncke*,[a]

[a] R. Weller, Prof. Dr. C. von Hänisch, Dr. C. G. Werncke
Department of Chemistry
Philipps-Universität Marburg
Hans-Meerwein-Straße 4,
D – 35032 Marburg, Germany
E-Mail: gunnar.werncke@chemie.uni-marburg.de

[b] Dr. M. Balmer
Dockweiler Chemicals GmbH
Philipps-Universität Marburg
Hans-Meerwein-Straße 4
D – 35032 Marburg, Germany

Table of Content

1 NMR Spectra

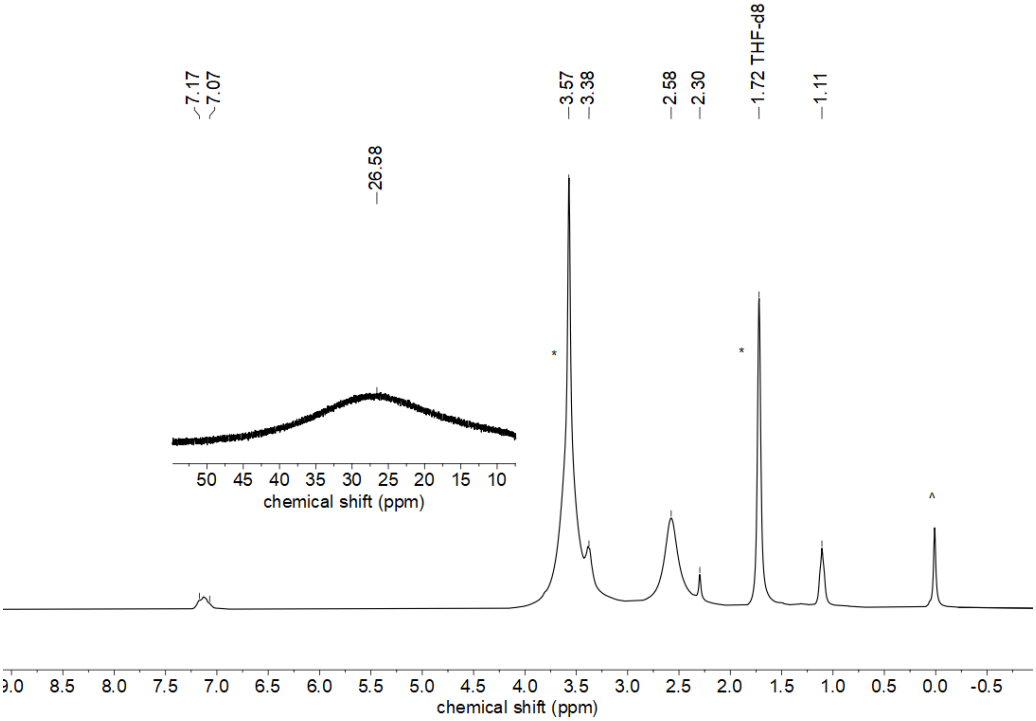

Figure S1. ^{1}H NMR spectrum (300.2 MHz, 300 K) of **1** in THF-d_8. (* solvent, ^ decomposition)

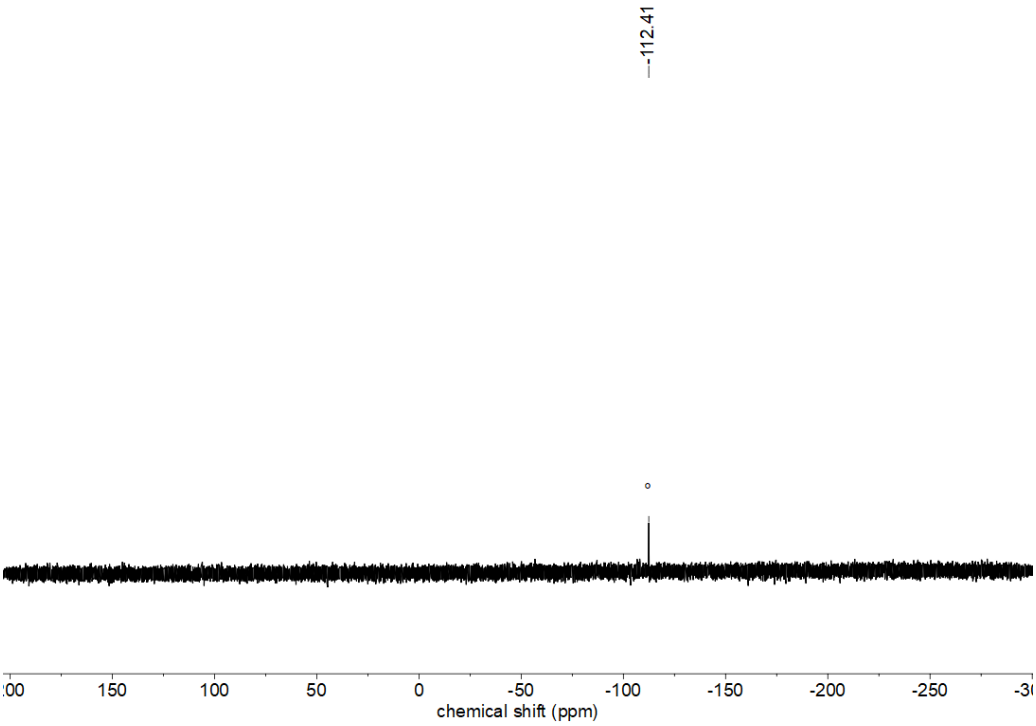

Figure S2. ^{31}P NMR spectrum (300.2 MHz, 300 K) of **1** in THF-d_8. (° free [(sIDipp)PH][1])

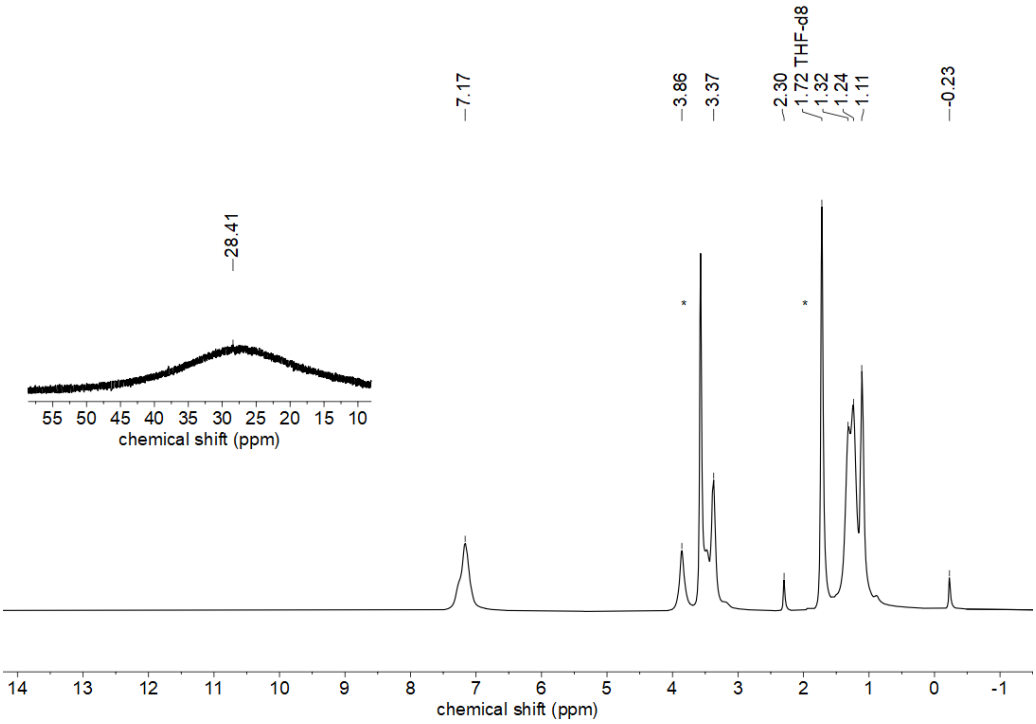

Figure S3. ^{1}H NMR spectrum (300.2 MHz, 300 K) of **2a** in THF-d_8. (* solvent)

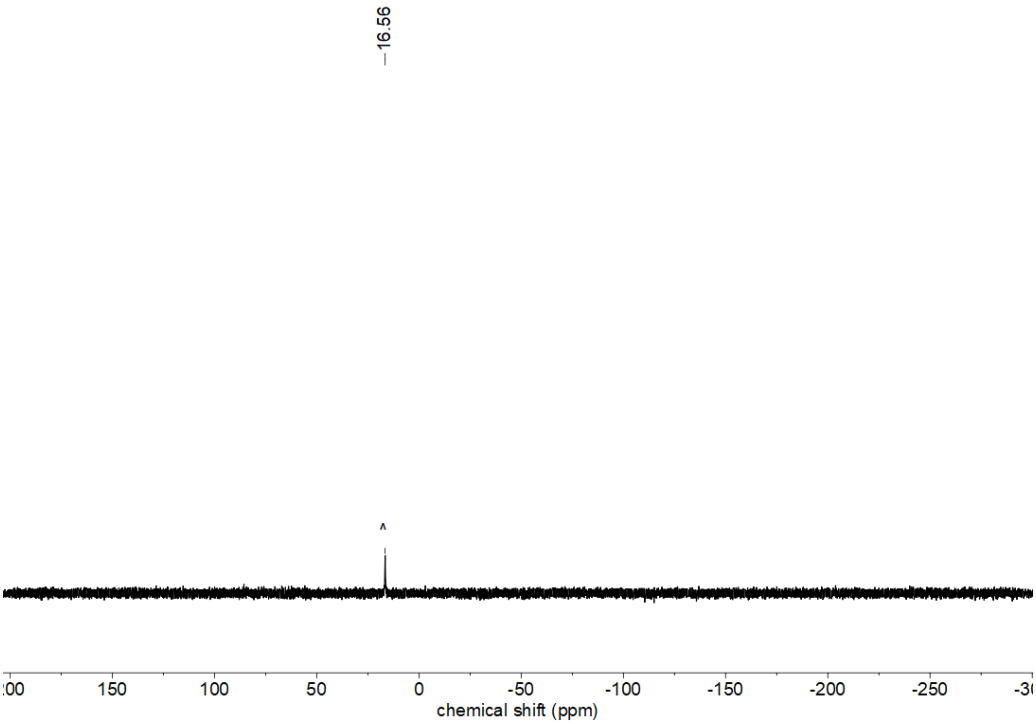

Figure S4. ^{31}P NMR spectrum (300.2 MHz, 300 K) of **2a** in THF-d_8. (^ decomposition)

2 UV/Vis Spectra

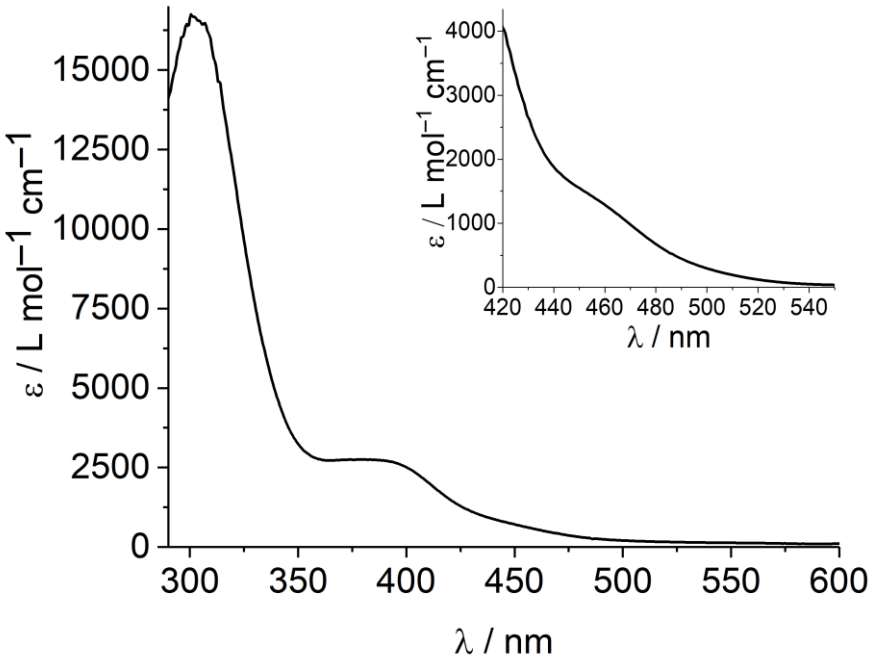

Figure S5. UV/Vis spectrum of **1** in toluene at room temperature.

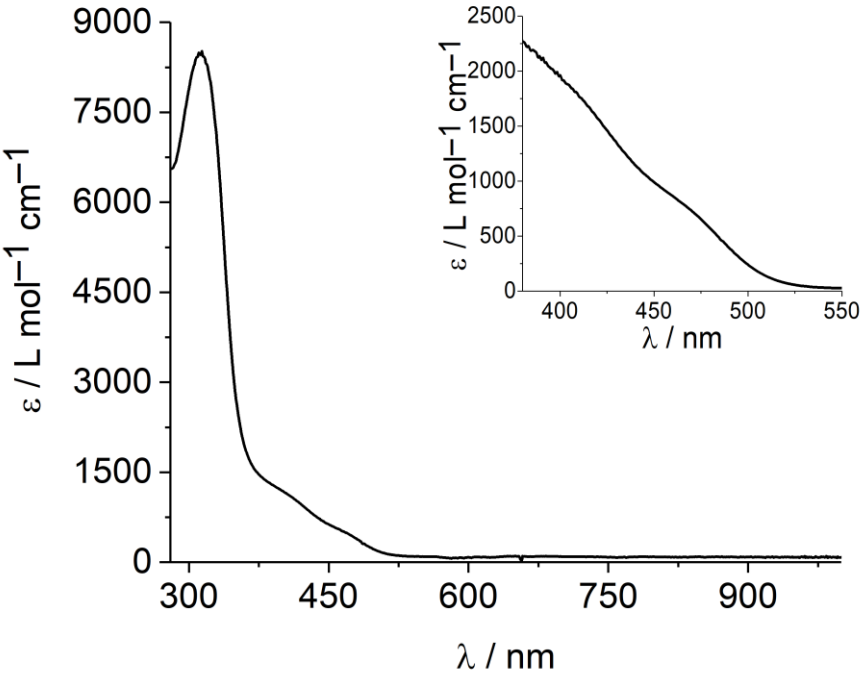

Figure S6. UV/Vis spectrum of **2a** in diethyl ether at room temperature.

3 IR Spectra

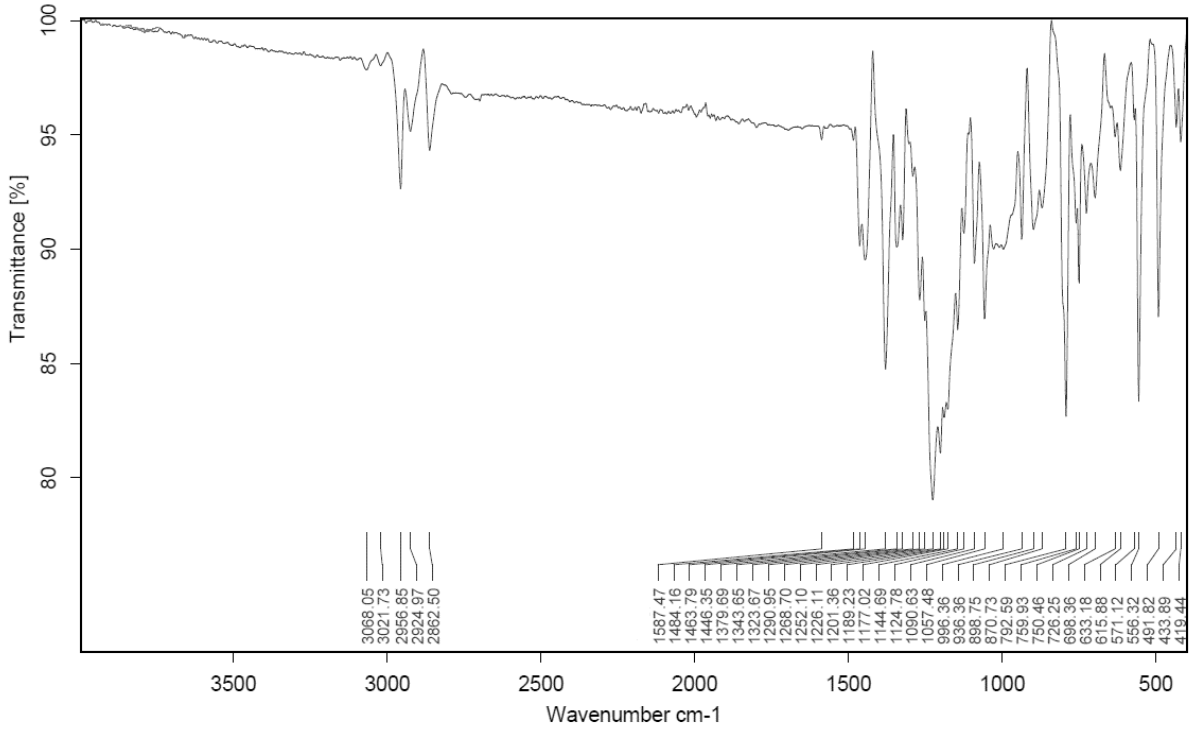

Figure S7. IR spectrum of **1**.

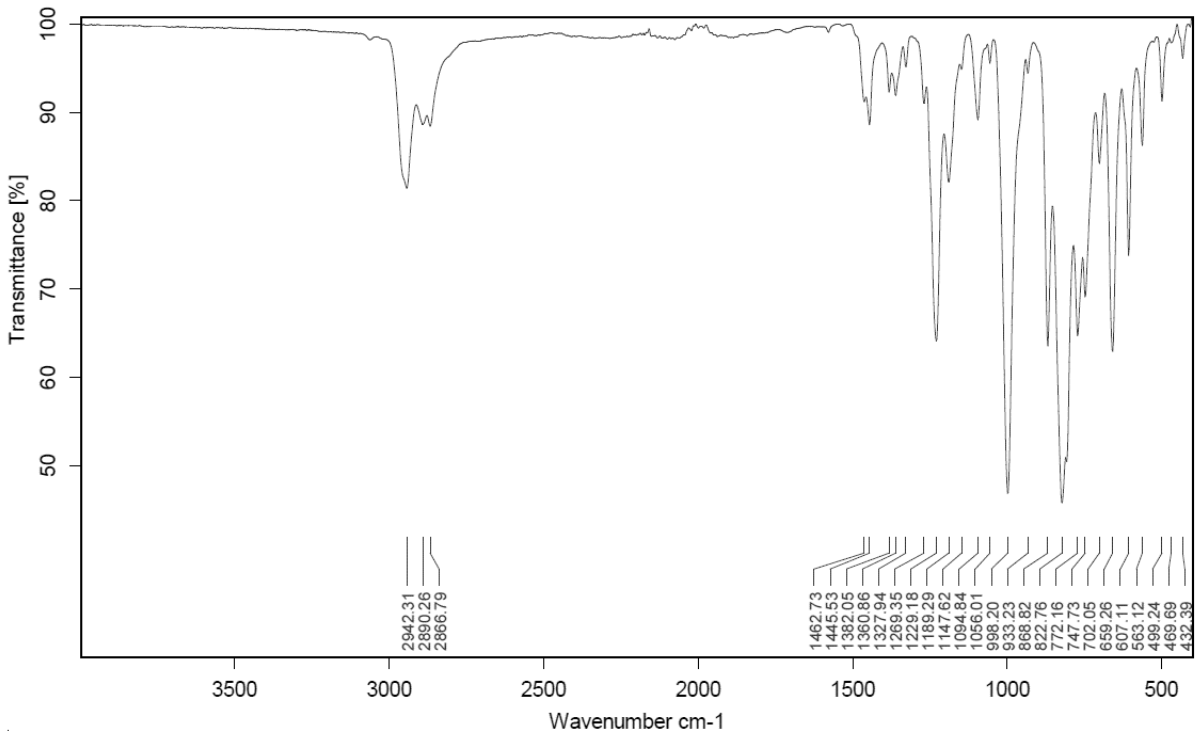

Figure S8. IR spectrum of **2a**.

4 Cyclic Voltammetry

The redox behavior of **1** was examined by cyclic voltammetry. A microcell HC “closed” stand (rhd instruments) was used in combination with a temperature controller (rhd instruments) and an AUTOLAB PGSTAT 204 (Metrohm GmbH) potentiostat/galvanostat. The measurements were performed at 25±0.1 °C, using a TSC 1600 Closed (rhd instruments) Pt cell in a three-electrode configuration with Pt wires acting as pseudo reference and as working electrode. To secure reproducible conditions, the electrodes were freshly polished, rinsed with THF and dried *in vacuo* for 2 hours. 3 mM of analyte and 0.1 M *n*-$NBu_4[PF_6]$, which acted as electrolyte, were used in the default measurement setup. The $[FeCp_2]$ / $[FeCp_2]^+$ (Fc/Fc^+) redox couple was utilized as internal standard. The measurements were performed at two different scan rates (100 and 200 mV/s), with two full cycles per scan rate. However, due to the fast decomposition of **1** under the measurement conditions it was not possible to get reliable voltammograms at scan rates < 200 mV/s. Peak potentials and currents of the second cycle of each measurement were determined using the NOVA Software (ver. 1.10.1.9, Metrohm GmbH).

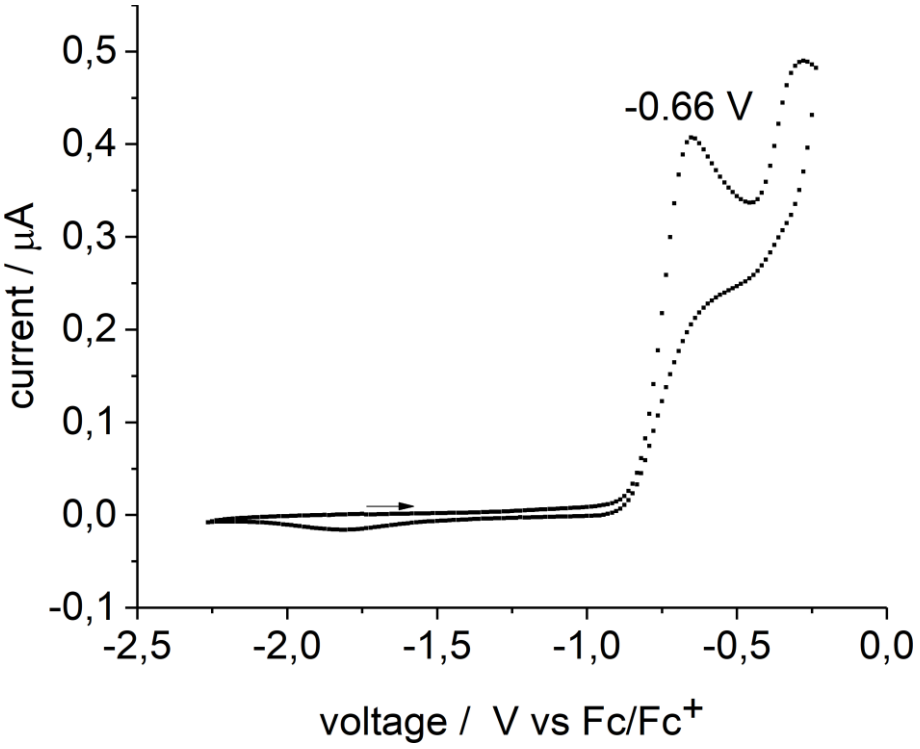

Figure S9. CV spectrum of **1** in THF at a scan rate of 100 mV/s (0.1 M $NBu_4[PF_6]$, vs. Fc/Fc^+).

5 Magnetic Measurements

Magnetic data of complex **1** were recorded using a dried crystalline sample and were corrected for diamagnetic contributions from the sample holder and the diamagnetic susceptibility of the compound using Pascal constants. Obtained paramagnetic susceptibility χ_{para} was fitted using the Curie-Weiss-law $\chi_{CW} = \left(\frac{N_A \mu_B^2 n_{eff}}{3k_B}\right) 2 \frac{1}{T-\theta}$ (n_{eff} = effective magnetic moment in Bohr's magnetons per formula unit, Θ = Weiss temperature) with contributions from a temperature independent paramagnetism χ_{TIP} using the overall equation $\chi_{para}T = (\chi_{TIP} + \chi_{CW})T$.

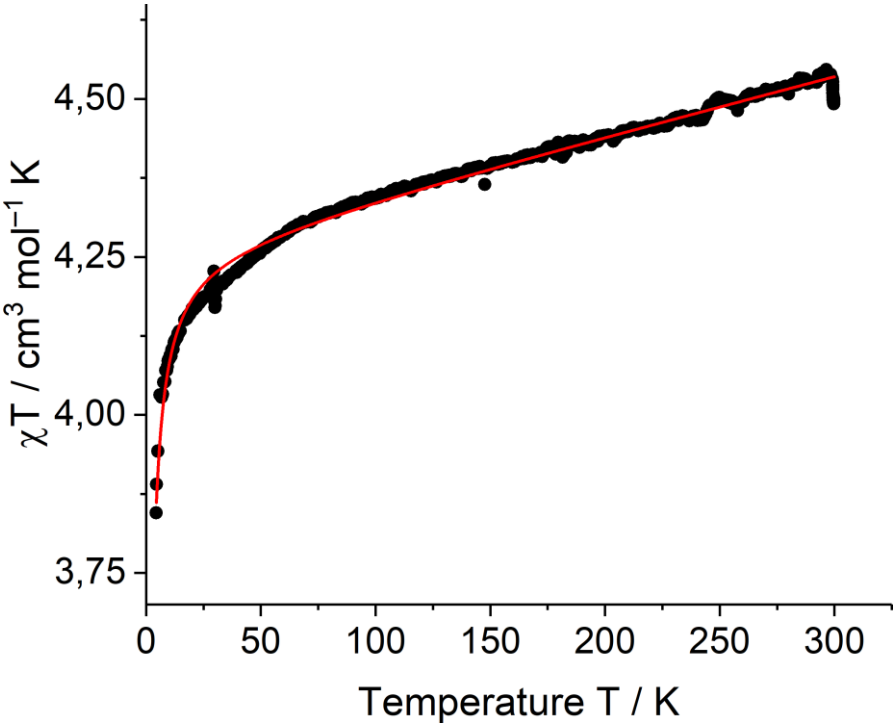

Figure S10. Temperature dependence of the molar magnetic susceptibility times temperature product (χT vs. T) for compound **1**. Data were collected under an applied dc field of 1 T in a temperature range of 5 to 300 K. Molar diamagnetic correction = 10^{-15} emu mol^{-1}, χ_{TIP} = 9.468(6) x 10^{-3} emu mol^{-1}, n_{eff} = 5.837(1) μ_B f.u.$^{-1}$ (f.u. = formula unit), $\chi_M T$ = 4.50 cm^3 mol^{-1} K (300 K), Θ = −0.463(6) K.

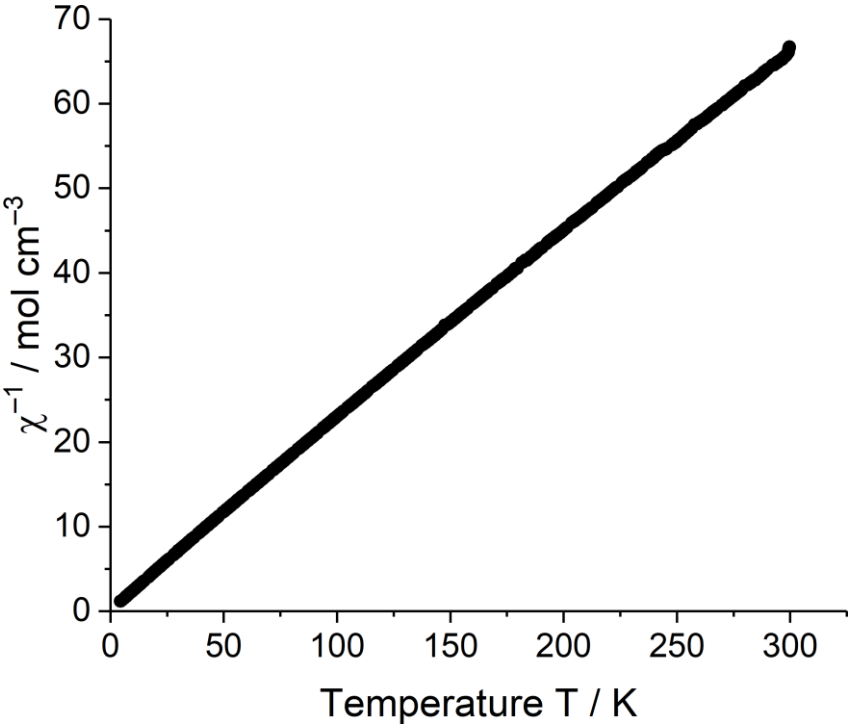

Figure S11. Reciprocal molar magnetic susceptibilities (χ^{-1}) for compound **1**. Data were collected under an applied dc field of 1 T in a temperature range of 5 to 300 K.

6 X-Ray Diffraction Analysis and Molecular Structures

Table S1. Crystal data and structure refinement of **1**

Empirical formula	$C_{54}H_{76}MnN_4P_2$
Formula weight	898.06
Temperature/K	100.01
Crystal system	triclinic
Space group	*P*−1
a/Å	10.7707(5)
b/Å	10.8284(6)
c/Å	12.2278(6)
α/°	110.589(2)
β/°	103.611(2)
γ/°	96.697(2)
Volume/Å^3	1266.00(11)
Z	1
ρ_{calc}g/cm^3	1.178
μ/mm^{-1}	0.362
F(000)	483.0
Crystal size/mm^3	0.176 × 0.172 × 0.086
Radiation	MoKα (λ = 0.71073)
2Θ range for data collection/°	4.578 to 51.464
Index ranges	−13 ≤ *h* ≤ 13, −13 ≤ *k* ≤ 13, −14 ≤ *l* ≤ 14
Reflections collected	22106
Independent reflections	4814 [R_{int} = 0.0808, R_{sigma} = 0.0645]
Data/restraints/parameters	4814/0/285
Goodness-of-fit on F^2	1.023
Final *R* indexes [*I*>=2σ (*I*)]	R_1 = 0.0469, wR_2 = 0.0854
Final *R* indexes [all data]	R_1 = 0.0784, wR_2 = 0.0937
Largest diff. peak/hole / e Å^{-3}	0.30/−0.33

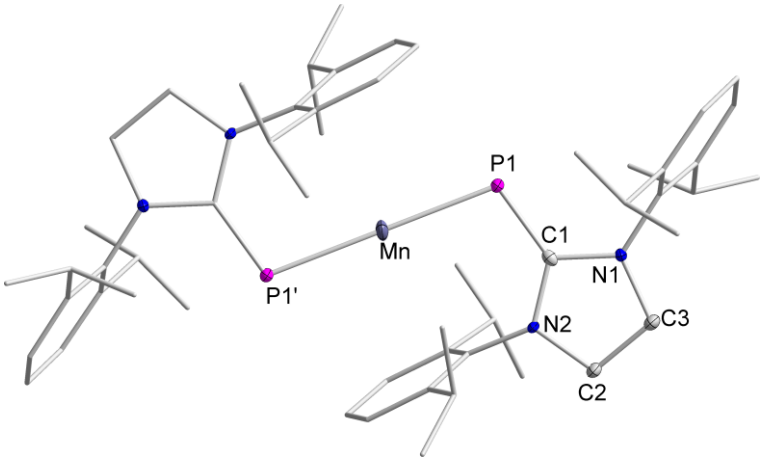

Figure S12. Molecular structure of **1**. All hydrogen atoms are omitted for clarity.

Table S2. Crystal data and structure refinement of **2a**

Empirical formula	$C_{61}H_{132}K_2MnN_5O_4PSi_6$
Formula weight	1332.36
Temperature/K	100
Crystal system	monoclinic
Space group	$P2_1/n$
a/Å	16.9431(12)
b/Å	26.5429(14)
c/Å	18.8061(13)
α/°	90
β/°	102.993(6)
γ/°	90
Volume/Å^3	8240.9(9)
Z	4
ρ_{calc}g/cm^3	1.074
μ/mm^{-1}	0.408
F(000)	2908.0
Crystal size/mm^3	0.747 × 0.695 × 0.392
Radiation	MoKα (λ = 0.71073)
2Θ range for data collection/°	2.7 to 49.998
Index ranges	−17 ≤ *h* ≤ 20, −27 ≤ *k* ≤ 31, −22 ≤ *l* ≤ 22
Reflections collected	45951
Independent reflections	14522 [R_{int} = 0.0955, R_{sigma} = 0.0907]
Data/restraints/parameters	14522/12/774
Goodness-of-fit on F^2	0.908
Final *R* indexes [*I*>=2σ (*I*)]	R_1 = 0.0407, wR_2 = 0.0813
Final *R* indexes [all data]	R_1 = 0.0887, wR_2 = 0.0906
Largest diff. peak/hole / e Å^{-3}	0.26/−0.34

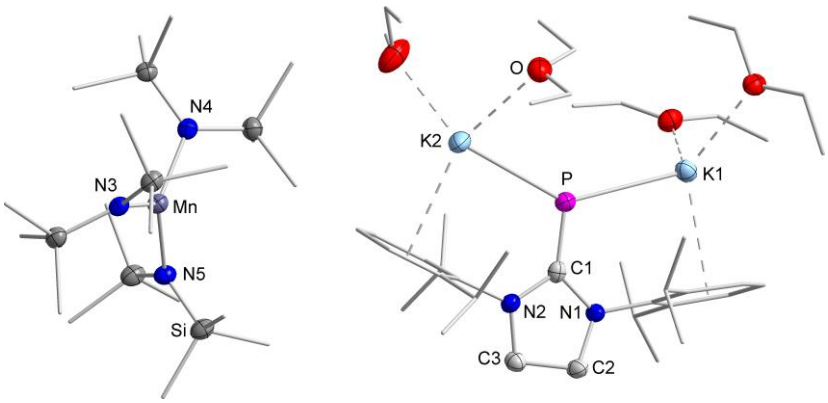

Figure S13. Molecular structure of [sIDippPK$_2$(Et$_2$O)$_4$][Mn(N(SiMe$_3$)$_2$)$_3$] (**2a**). All hydrogen atoms are omitted for clarity. A disorder in one diethyl ether molecule (part 1 (depicted) /part 2: 50%) is found.

Table S3. Crystal data and structure refinement of **2b**

Empirical formula	$C_{61}H_{132}FeK_2N_5O_4PSi_6$
Formula weight	1333.27
Temperature/K	100
Crystal system	monoclinic
Space group	$P2_1/n$
a/Å	16.9890(17)
b/Å	26.471(3)
c/Å	18.6846(19)
α/°	90
β/°	103.571(8)
γ/°	90
Volume/Å^3	8168.0(15)
Z	4
ρ_{calc}g/cm^3	1.084
μ/mm^{-1}	0.434
F(000)	2912.0
Crystal size/mm^3	0.407 × 0.221 × 0.081
Radiation	MoKα (λ = 0.71073)
2Θ range for data collection/°	2.72 to 50
Index ranges	−20 ≤ h ≤ 20, −31 ≤ k ≤ 31, −22 ≤ l ≤ 22
Reflections collected	60892
Independent reflections	14385 [R_{int} = 0.1788, R_{sigma} = 0.1277]
Data/restraints/parameters	14385/25/774
Goodness-of-fit on F^2	0.896
Final *R* indexes [*I*>=2σ (*I*)]	R_1 = 0.0590, wR_2 = 0.1338
Final *R* indexes [all data]	R_1 = 0.1261, wR_2 = 0.1525
Largest diff. peak/hole / e Å^{-3}	0.95/−0.57

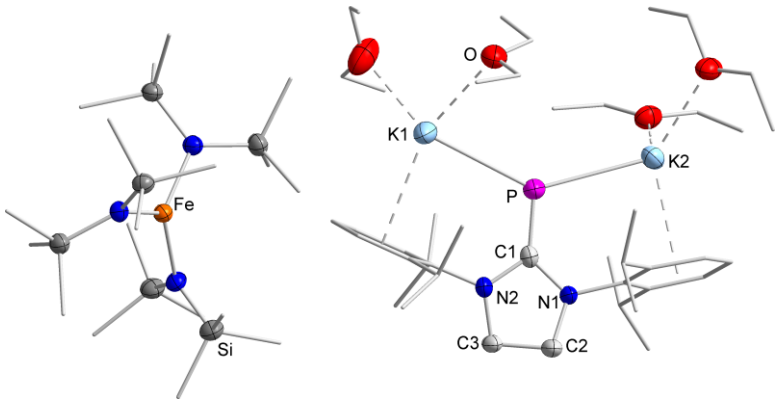

Figure S14. Molecular structure of [sIDippPK$_2$(Et$_2$O)$_4$][Fe{N(SiMe$_3$)$_2$}$_3$] (**2b**). All hydrogen atoms are omitted for clarity. A disorder in one diethyl ether molecule (part 1 (depicted) /part 2: 50%) is found.

Table S4. Crystal data and structure refinement of **K{crypt-222}[MnL$_3$]**

Empirical formula	$C_{36}H_{90}KMnN_5O_6Si_6$
Formula weight	951.70
Temperature/K	100.0
Crystal system	triclinic
Space group	P−1
a/Å	11.4888(9)
b/Å	15.4353(12)
c/Å	16.6387(12)
α/°	84.190(6)
β/°	77.760(6)
γ/°	89.530(6)
Volume/Å^3	2868.4(4)
Z	2
ρ_{calc}g/cm^3	1.102
μ/mm^{-1}	0.467
F(000)	1034.0
Crystal size/mm^3	0.58 × 0.336 × 0.16
Radiation	Mo Kα (λ = 0.71073)
2Θ range for data collection/°	4.836 to 53.468
Index ranges	−14 ≤ *h* ≤ 14, −19 ≤ *k* ≤ 19, −20 ≤ *l* ≤ 21
Reflections collected	29082
Independent reflections	12109 [R_{int} = 0.0490, R_{sigma} = 0.0465]
Data/restraints/parameters	12109/0/514
Goodness-of-fit on F^2	1.016
Final R indexes [*I*>=2σ (*I*)]	R_1 = 0.0323, wR_2 = 0.0805
Final R indexes [all data]	R_1 = 0.0466, wR_2 = 0.0842
Largest diff. peak/hole / e Å^{-3}	0.32/−0.51

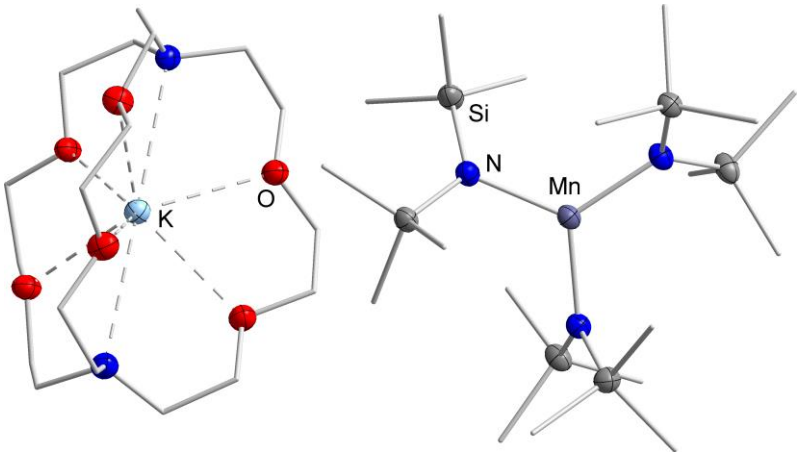

Figure S15. Molecular structure of **K{crypt-222}[MnL$_3$]**. All hydrogen atoms are omitted for clarity. One free molecule of diethyl ether is lying on a symmetry element and disordered over multiple position, why it has thus been squeezed.

References

[1] M. Bispinghoff, A. M. Tondreau, H. Grützmacher, C. A. Faradji, P. G. Pringle, *Dalton Trans.* **2016**, *45*, 5999.

Danksagung

Der Inhalt der Danksagung wurde aus Datenschutzgründen aus der elektronischen Version entfernt.